UNIVERSITY OF CALIFORNIA SAN DIEGO

Earthquake Simulator Testing and Associated Study on Performance and Design of Seismic Collectors in Steel Buildings

A dissertation submitted in partial satisfaction of the requirements

for the degree Doctor of Philosophy

in

Structural Engineering

by

Chao-Hsien Li

Committee in charge:

Professor Chia-Ming Uang, Chair
Professor Joel P. Conte
Professor Robert B. Fleischman
Professor Machel L. Morrison
Professor Pui-Shum Shing
Professor Kenneth Vecchio

2022

The Dissertation of Chao-Hsien Li is approved, and it is acceptable in quality and form for publication on microfilm and electronically.

University of California San Diego

2022

DEDICATION

This dissertation is dedicated to my grandparents in loving memory.

TABLE OF CONTENTS

LIST OF FIGURES

LIST OF TABLES

ACKNOWLEDGEMENTS

This research was supported by the National Science Foundation (NSF) under Grant CMMI-1662816, Engineering for Natural hazards (ENH) and 2019 NSF Supplement. The experimental research was supported by industry partners American Institute of Steel Construction (AISC), The California Field Ironworkers Administrative Trust, The Herrick Corporation, Annie-Johnson Company, CoreBrace, and Testing & Inspection Services. The project advisory board includes representatives from Degenkolb Engineers, Walter P. Moore, and the California Office of Statewide Health Planning and Development (OSHPD). These supports are greatly appreciated.

Experimental testing was performed by using the NHERI@UCSD Large High Performance Outdoor Shake Table (LHPOST). The research was indebted to the commitment and hard work of the staff members: Messrs. Alex Sherman, Robert Beckley, and Jeremy Fitcher. The author would like to thank the staff members of Charles Lee Powell Structural Research Laboratories: Messrs. Andrew Sander, Darren McKay, Abdullah Hamid, Noah Aldrich, Mike Sanders, and Dr. Christopher Latham and the staff members of Caltrans Seismic Response Modification Device (SRMD) Test Facility: Messrs. Danny Innamorato and Edward Stovin for their technical assistance towards the completion of this test program. Accomplishing a three-phase testing program at LHPOST in a timely manner in Summer 2019 was just like winning an epic war. I will always cherish the memories of working with laboratory staff during my Ph.D. journey.

Foremost, I would like to express my deep appreciation to my advisor, Professor Chia-Ming Uang, for his unwavering support, encouragement, and guidance during my Ph.D. study and research at the University of California, San Diego (UCSD). I have benefited greatly from his wealth of knowledge, research attitude, and meticulous editing. He has set an example of

excellence as a researcher, mentor, instructor, and role model. I have been so fortunate to have a supervisor who cared about my professional growth and helped me gain a substantial teaching experience at UCSD. I am also very grateful that Prof. Uang gave me opportunities to conduct shake table tests at the unique LHPOST facility and work on several research projects in cooperation with other researchers and industrial partners.

Special thanks are extended to Professor Robert B. Fleischman from University of Arizona (UA) for leading and coordinating this NSF collaborative research among three universities (UA, UCSD, and Lehigh University) and providing invaluable guidance for this doctoral work. I would also like to thank the committee members Professor Pui-Shum Shing, Professor Joel P. Conte, Prof. Machel L. Morrison, and Professor Kenneth Vecchio for all their guidance through this process; their discussion, ideas, and feedback have been invaluable.

Last but not least, a big "Thank You" to my family and relatives, my parents, aunts, and siblings for their endless support throughout the years. Special thanks to my beautiful wife, Meng-Hsuan, for taking care of everything and to my wonderful child, Chuan-En, for being such a good boy always cheering me up.

Parts of Chapters 1, 2, 3, 4, 6, and 7 are based on material published in the 17th World Conference on Earthquake Engineering, titled "Earthquake simulator testing on behavior of seismic collectors in steel buildings" with co-authors Uang C.-M., and Fleischman R.B. (2020). Materials were also submitted for publication in the 12th National Conference on Earthquake Engineering, titled "Shake Table Tests on Seismic Response of Collectors in Steel Buildings" with co-authors Uang C.-M., and Fleischman R.B. (2022). I serve as the first author of these papers.

VITA

2005 Bachelor of Science in Civil Engineering, National Taiwan University

2007 Master of Science in Civil Engineering, National Taiwan University

2008-2017 Assistant Researcher, National Center for Research on Earthquake Engineering

2022 Doctor of Philosophy in Structural Engineering, University of California San Diego

PUBLICATIONS

Refereed Journals

Li, C.H., Vidmar, Z, Saxey, B., Reynolds, M. and Uang, C.M. (2022). "A Procedure for Assessing Low-Cycle Fatigue Life of Buckling-Restrained Braces," *Journal of Structural Engineering*, ASCE. 148(2): 04021259. DOI: 10.1061/(ASCE)ST.1943-541X.0003237

Sabelli, R., Saxey, B., **Li, C.H.** and Thornton, W.A. (2021). "Design for local web shear at brace connections: An adaptation of the Uniform Force Method," *Engineering Journal,* AISC. 58(4): 223-265.

Lin, J.L., Chow, T.K., **Li, C.H**. and Yeh, Y.K. (2021). "A Comparative Study of Seismic Performance of Steel Framed Buildings with Varied Plan-Asymmetric Properties," *Journal of Earthquake and Tsunami,* 15(4): 2150016. DOI: 10.1142/S1793431121500160.

Tsai, C.Y., Tsai, K.C., **Li, C.H**., Wu, C.C, Lin, K.C. and Jhuang, S.J. (2020). "Seismic Fracture Evaluation of Diaphragm Joints in Welded Beam-to-Box Column Moment Connections," *Earthquake Engineering & Structural Dynamics,* 49(13): 1344-1362. DOI: 10.1002/eqe.3293.

Chen, P.C., Ting, G.C. and **Li, C.H.** (2020). "A versatile small-scale structural laboratory for novel experimental earthquake engineering," *Earthquakes and Structures*, 18(3): 337-348. DOI: 10.12989/eas.2020.18.3.337

Wang, K.J., Chuang, M.C., Tsai, K.C., **Li, C.H.**, Chin, P.Y., and Chueh, S.Y. (2019). "Hybrid testing with model updating on steel panel damper substructures using a multi-axial testing system," *Earthquake Engineering & Structural Dynamics*, 48(3): 347-365, DOI: 10.1002/eqe.3139.

Li, C.H., Tsai, K.C., Su, L., Lin, P.C., and Lin, T.H. (2018). "Experimental investigations on seismic behavior and design of bottom vertical boundary elements in multi-story steel plate shear walls," *Earthquake Engineering & Structural Dynamics*, 47(14): 2777-2801, DOI: 10.1002/eqe.3106.

Tsai, K.C., Hsu, C.H., **Li, C.H.**, and Chin, P.Y. (2018). "Experimental and analytical investigations of steel panel dampers for seismic applications in steel moment frames," *Earthquake Engineering & Structural Dynamics*, 47(6): 1416-1439, DOI: 10.1002/eqe.3023.

Chuang, M.C., Hsieh, S.H., Tsai, K.C., **Li, C.H**., Wang, K.J. and Wu, A.C. (2018). "Parameter identification for on-line model updating in hybrid simulations using a gradient-based method," *Earthquake Engineering & Structural Dynamics*, 47(2): 269-293, DOI: 10.1002/eqe.2950.

Wu, A.C., Tsai, K.C., Yang, H.H., Huang, J.L., **Li, C.H.**, Wang, KJ., and Khoo, H.H. (2017). "Hybrid experimental performance of a full-scale two-story buckling-restrained braced RC frame," *Earthquake Engineering & Structural Dynamics,* 46(8):1223-1244, DOI: 10.1002/eqe.2853.

Li, C.H., Tsai, K.C., Huang, H.Y., and Tsai, C.Y. (2017). "Cyclic Tests of Steel Plate Shear Walls Using Box-shape Vertical Boundary Elements With or Without Infill Concrete," *Earthquake Engineering & Structural Dynamics*, 46(14): 2537-2264, DOI: 10.1002/eqe.2917.

Clayton, P.M., Dowden, D.M., **Li, C.H.**, Berman, J.W., Bruneau, M., Lowes, L.N., and Tsai, K.C. (2016) "Self-Centering Steel Plate Shear Walls for Improving Seismic Resilience," Special Issue: Frontiers of Structural and Civil Engineering, Vol. 10, 283–290. DOI:10.1007/s11709-016-0344-z.

Dowden, D.M., Clayton, P.M., **Li, C.H.**, Berman, J.W., Bruneau, M., Lowes, L.N., and Tsai, KC. (2016). "Full-Scale Pseudodynamic Testing of Self-Centering Steel Plate Shear Walls," *Journal of Structural Engineering*, ASCE, 142(1): 04015100, DOI: 10.1061/(ASCE)ST.1943-541X.0001367.

Sen, A.D., Roeder, C.W., Berman, J.W., Lehman, D.E., **Li, C.H.**, Wu, A.C., and Tsai, K.C. (2016). "Experimental Investigation of Chevron Concentrically Braced Frames with Yielding Beams," *Journal of Structural Engineering*, ASCE, 142(12): 04016123, DOI: 10.1061/(ASCE)ST.1943-541X.0001597.

Pan, K.Y., Wu, A.C., Tsai, K.C., **Li, C.H.**, and Khoo, H.H. (2016). "Seismic retrofit of reinforced concrete frames using buckling-restrained brace with bearing block load transfer mechanism," *Earthquake Engineering & Structural Dynamics*, 45(14): 2303-2326, DOI: 10.1002/eqe.2763.

Lin, P.C., Tsai, K.C., Wu, A.C., Chuang, M.C., **Li, C.H.**, and Wang K.J. (2015). "Seismic design and experiment of single and coupled corner gusset connections in a full-scale two-story buckling-restrained braced frame," *Earthquake Engineering & Structural Dynamics*, 44(13): 2155-2177, DOI: 10.1002/eqe.2577.

Li, C.H., Tsai, K.C., and Lee, H.C. (2014). "Seismic design and testing of the bottom vertical boundary elements in steel plate shear walls. Part 2: experimental studies," *Earthquake Engineering & Structural Dynamics*, 43(14): 2155-2177, DOI: 10.1002/eqe.2442.

Tsai, K.C., **Li, C.H.**, and Lee, H.C. (2014). "Seismic design and testing of the bottom vertical boundary elements in steel plate shear walls. Part 1: design methodology," *Earthquake Engineering & Structural Dynamics*, 43(15): 2237-2259, DOI: 10.1002/eqe.2443.

Li, C.H., Tsai, K.C., Chang, J.T., Lin, C.H., Chen, J.C., Lin, T.H., and Chen, P.C. (2012), "Cyclic test of a coupled steel plate shear wall substructure," *Earthquake Engineering & Structural Dynamics*, 41(9): 1277–1299, DOI: 10.1002/eqe.1180.

Yu, Y.J., Tsai, K.C., **Li, C.H.**, Weng, Y.T., and Tsai, C.Y. (2012). "Earthquake response analyses of a full-scale five-story steel frame equipped with two types of dampers," *Earthquake Engineering & Structural Dynamics*, 42(9): 2237-2259, DOI: 10.1002/eqe.2273.

Li, C.H., Tsai, K.C., Lin, C.H., and Chen, P.C. (2010). "Cyclic tests of four two-story narrow steel plate shear walls. Part 2: experimental results and design implications," *Earthquake Engineering & Structural Dynamics*, 39(7): 801-826, DOI: 10.1002/eqe.964.

Tsai, K.C., **Li, C.H.**, Lin, C.H., Tsai, C.Y. and Yu, Y.J. (2010). "Cyclic tests of four two-story narrow steel plate shear walls—Part 1: Analytical studies and specimen design," *Earthquake Engineering & Structural Dynamics*, 39(7): 775-799, DOI: 10.1002/eqe.977.

Technical Reports

Li, C.H. and Uang, C.M. (2021). "Earthquake Simulator Testing and Associated Study on Seismic Behavior and Design of Collectors in Steel Buildings," *Report No. SSRP-21/05*, University of California, San Diego, La Jolla, CA.

Li, C.H. and Uang, C.M. (2021). "Experimental Investigation on Cyclic Behavior of Buckling-Restrained Braces Experiencing Fire," *Report No. TR-21/03*, University of California, San Diego, La Jolla, CA.

Li, C.H. and Uang, C.M. (2021). "Qualification Testing of CoreBrace All-Steel Buckling-Restrained Braces (S Series)," *Report No. TR-21/02*, University of California, San Diego, La Jolla, CA.

Li, C.H. and Uang, C.M. (2021). "Qualification Testing of CoreBrace Bolted Buckling-Restrained Braces (P Series)," *Report No. TR-21/01*, University of California, San Diego, La Jolla, CA.

Li, C.H. and Uang, C.M. (2020). "Strain Aging Effect on Cyclic Response of Buckling-Restrained Braces," *Report No. TR-20/06*, University of California, San Diego, La Jolla, CA.

Li, C.H. and Uang, C.M. (2020). "CoreBrace BRB Collar Tests for San Francisco Tower Project," *Report No. TR-20/05*, University of California, San Diego, La Jolla, CA.

Li, C.H., Mansing, R., Reynolds, R. and Uang, C.M. (2020). "Qualification Testing of CoreBrace Bolted Buckling-Restrained Braces (J Series)," *Report No. TR-20/03*, University of California, San Diego, La Jolla, CA.

Mansing, R., **Li, C.H.**, Reynolds, R. and Uang, C.M. (2020). "Qualification Testing of CoreBrace Bolted Buckling-Restrained Braces (H Series)," *Structural Systems Research Project Report No. TR-20/02*, University of California, San Diego, La Jolla, CA.

Li, C.H. and Uang, C.M. (2020). "CoreBrace BRB Qualification Tests for Seattle Waterfront Pedestrian Bridge Project," *Report No. TR-20/01*, University of California, San Diego, La Jolla, CA.

Mansing, R., **Li, C.H.**, and Uang, C.M. (2019). "Qualification Testing of CoreBrace Buckling-Restrained Braces with Perforated Steel Cores," *No. TR-19/06*, University of California, San Diego, La Jolla, CA.

Li, C.H., Reynolds, R. and Uang, C.M. (2018). "Fatigue Testing of CoreBrace Buckling-Restrained Braces," *Report No. TR-18/06*, University of California, San Diego, La Jolla, CA.

ABSTRACT OF THE DISSERTATION

Earthquake Simulator Testing and Associated Study on Performance and Design of Seismic Collectors in Steel Buildings

by

Chao-Hsien Li

Doctor of Philosophy in Structural Engineering

University of California San Diego, 2022

Professor Chia-Ming Uang, Chair

Collectors are structural components that play a critical role to transmit inertia forces in the floor diaphragms to the vertical seismic-force resisting system in a building structure. Yet little research has been done on collectors. A three-phase test program was conducted on a half-scale, two-story steel building by using the NHERI@UCSD large high performance outdoor shake table. The main objectives of this project were to investigate the inertial force load path in the floor diaphragms and the seismic behavior of collectors and their connections.

Phase 1 tests were performed as a "single-story phase" with only the first story with a composite slab constructed. An innovative experimental technique was developed such that the absolute acceleration history response of any floor in a multi-story prototype building experiencing nonlinear response and higher-mode effects could be simulated by using a re-usable single-story specimen through a transfer function approach. Test results validated this testing technique.

Phase 2 tests were conducted after a second story with a bare steel roof deck was added to the test building; the conventional testing method with the scaled historical ground acceleration as the input motion was used. In Phase 3, two buckling-restrained braces were added to the second story to modify the building dynamic characteristics and the collector seismic load path. Earthquake simulation tests were conducted again until the failure of side-lap connections of the roof deck occurred.

Test results showed that the current collector design would overestimate the axial forces in the roof collectors because it neglects the effect of flexural rigidity of the collector connections, which would mobilize gravity columns to transfer some inertial forces to the story below. An improved design method for estimating the roof collector axial forces that considers the flexural rigidity of the collector connections was proposed. Test results also showed that the unintended moment demand produced by the connection rigidity would cause the steel connections in composite collectors to experience axial forces higher than that assumed in design. Recommendations including connection design requirements and collector width-to-thickness ratios were also made.

1. INTRODUCTION

1.1 Background

Building structures are typically composed of horizontal spanning elements such as beams, floor diaphragms and, roof decks as well as vertical elements, such as columns, diagonal braces, and walls. Together these elements comprise an integral 3-D system that resists both vertical and lateral loads. Earthquake horizontal forces are actually the inertial effects generated by the building mass being accelerated horizontally; the great majority of the earthquake forces is usually generated from the mass of the roof and floor diaphragm systems. The seismic resistance of a building is composed of a continuous lateral load path from the horizontal floor diaphragm systems to the primary vertical elements of seismic force-resisting system (SFRS), which in turn transmit the forces to the foundation.

Collectors, or drag struts, are key structural elements that "collect" inertial forces in the floor of roof diaphragms and then deliver them to the primary vertical elements of SFRS. As shown in Figure 1.1, in the cases where the SFRS only occupies a partial length of a frame line across the floor diaphragm, collectors are located along the remaining parts of that frame line and serve to collect the diaphragm shears before transferring them to the SFRS. In addition, these collectors must transfer the forces through connections to the columns. In steel structure buildings, collectors commonly used by the designers are either special reinforcement in the floor slab or steel beams beneath the slab.

Loss of collectors is potentially catastrophic, as has been shown by failures of collectors in concrete structures, including the collapse of CTV building (Figure 1.2) in the 2011 Christchurch earthquake (Royal Commission 2012), and the collapse of nine parking garages in the 1994 Northridge earthquake (EERI 1994), in which shear or core walls were undamaged, but the floor

system was detached, resulting in collapse of the gravity load resisting system. Despite the critical nature of seismic collectors, little research has focused on collectors, and both the seismic behavior and demands on these elements are not well understood.

Current design code provisions for collectors recognize their critical role through special load combinations that include the System Overstrength Factor Ω_0, resulting in large design forces. This design approach is an attempt to ensure that the collector elements remain elastic. Likewise, seismic collectors are typically designed for direct axial force actions and gravity load for idealized conditions without a consideration of actual boundary conditions, the composite slab effect or the effect of frame drift. This design intent permits relaxation of some of the more stringent detailing requirements associated with special seismic details [e.g., the WUF-W moment connection (AISC 2016a)] that undergo major inelastic action. It is unclear if the collector connections will remain elastic under the combination of seismic effects (including compatible deformations) and gravity effects. Thus, establishing realistic values for all aspects of the design, including gravity design, is crucial for making recommendations for the design steel seismic collectors and their connections.

Due to the cyclic nature of earthquake loads, collectors must alternately carry tension and compression while under the presence of effects from gravity load and frame lateral drift. In the cases where the collectors are provided by beams in the floor or roof systems of a steel building, the collectors must be designed both as tension and compression members. Both collector connection strength and collector element stability are key aspects of collector design. Tension design focuses on the collector connections. The collector itself is designed as a beam-column, since the member is under combined flexure (due to gravity load) and axial load (due to collector action). The controlling compression limit state for a steel collector depends on the bracing

condition of the floor or roof system, including strong-axis or weak axis flexural buckling, torsional or constrained-axis flexural torsional buckling (AISC 2018).

In many modern steel building structures, SFRS are allocated in only a few of the frame bays within the floor plan, resulting in very long collector lines. Composite action between the stee beam and concrete slab is attained through the shear studs. In general, the magnitude of collector force increases with the area tributary to the collector line. The assumed uniform transfer of inertial forces into the collectors leads to a linear collector axial force diagram (AISC 2018; Sabelli et al. 2011). Thus, collector forces are larger in the bays nearer to the SFRS (see Figure 1.3).

The connections used to transmit the collector forces across the gravity load-resisting columns or to the vertical members of SFRS vary depending on the magnitude of the collector force. For lower-level collector forces, the conventional shear tab connection used for gravity load design can be sued to carry the combined shear and tension, sometimes supplemented by collector reinforcing bars in the slab that are properly anchored in the slab, as described in a design example in the AISC Seismic Design Manual (AISC 2018). As collector forces grow, a modified version of the shear tab connection employing multiple bolt rows, termed the multiple bolt row shear tab (MST) connection [Figure 1.4(a)], is often employed. As the collector force demands increase further, a typical collector connection design involves connecting the top flange to the column. One typical detail in the US involves welding the top flange, which is called the top flange weld (TFW) connection [Figure 1.4(b)]. When the strength of this detail is still insufficient, both flanges are welded to the column, and the connections is termed the all flange weld (AFW) connection in this study.

Currently there is no “standard” collector connection details and design procedure. In addition to the three typical collector connections (MST, TFW, and AFW), designers do come up

with other types of connections. Figure 1.5 shows the TFW collector connection with horizontally slotted bolt holes in the web, which are intended to minimize the moment demands. Figure 1.6 shows the bolted flange plate collector connection which utilizes the bolted joints on both collector flanges to transfer the collector forces. Figure 1.7 shows the double shear tab collector connection, which puts all the bolts in double shear so as to reduce the number of bolts.

Although various types of collector connections are used in practice, no physical testing has yet been done to evaluate their performance. Understanding the performance of seismic collectors and their connections for the development of a rational design procedure is challenging as it is a system issue involving several components of different materials at each floor level in a multistory. Equally challenging is the identification of the load path from the distributed inertia forces in the floor diaphragm to SFRS, especially from physical testing. This lack of knowledge impacts not only new construction but also the assessment and retrofit of existing buildings, especially critical care facilities in high seismic regions. This also applies to older non-seismic compliant steel buildings nationwide, where inadequate or non-existent seismic collectors are often a major concern.

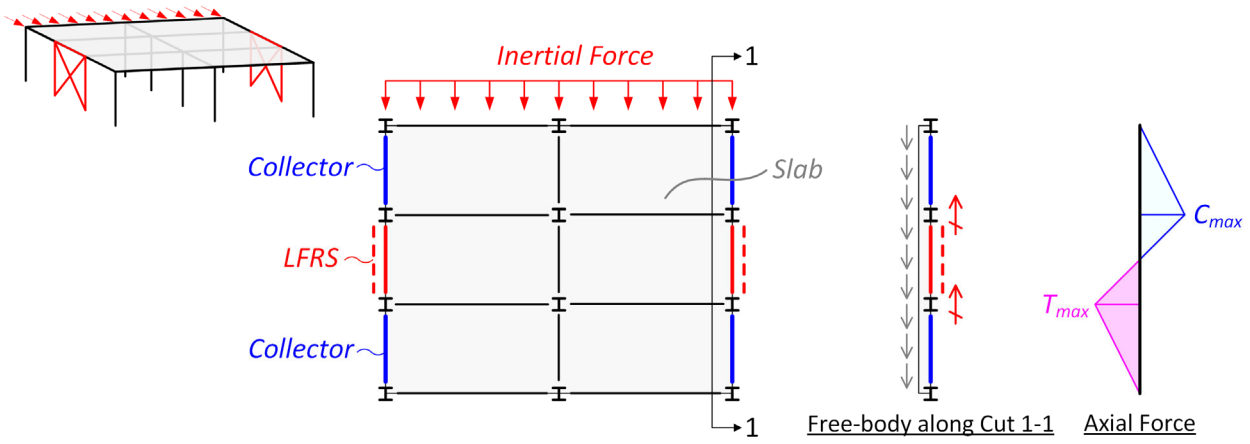

(a) Collectors in Floor Diaphram (b) Collector Actions

Figure 1.1 (a) Collectors in a Floor Diaphragm; and (b) Collector Actions (Sabelli et al. 2011)

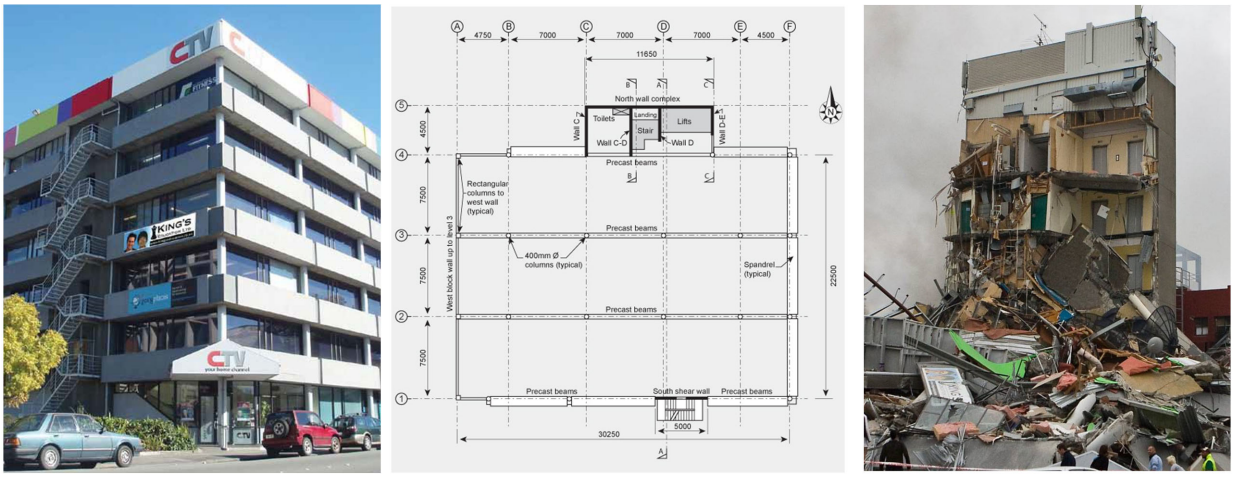

(a) CTV Building (b) Floor Plan (c) State after Collapse

Figure 1.2 Collapse of CTV Building in 2011 Christchurch, New Zealand earthquake (Royal Commission 2012)

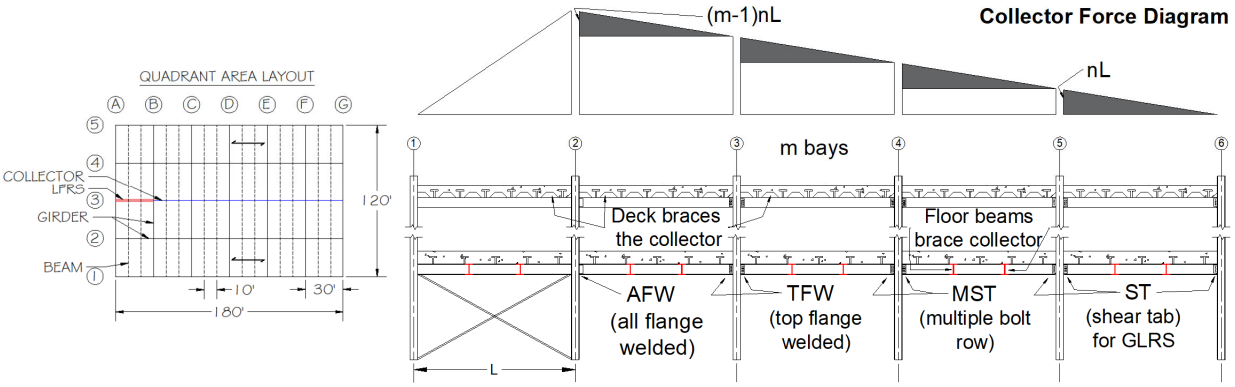

Figure 1.3 Collector Line and Axial Force Diagram (Anshul et al. 2018)

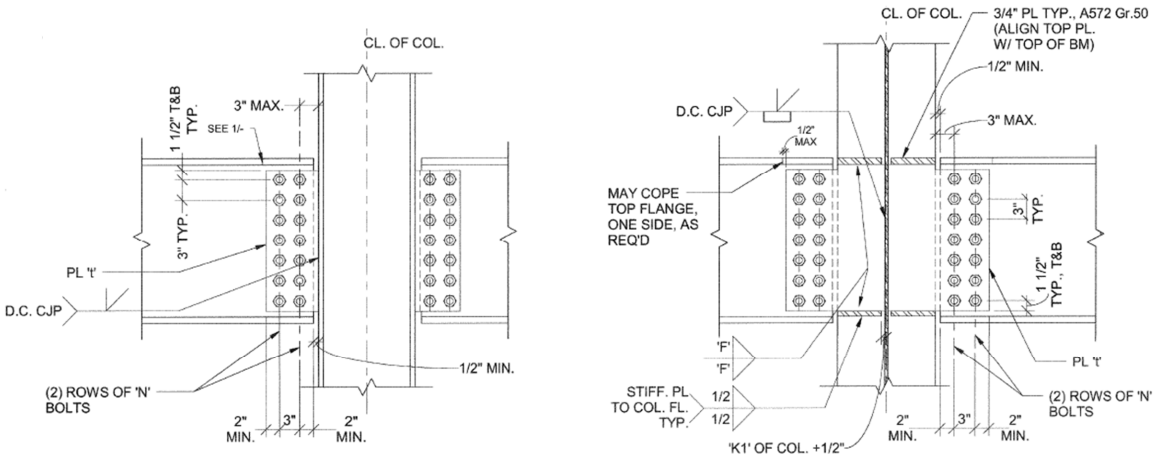

(a) Multiple Bolt Row Shear Tab (MST) Connection

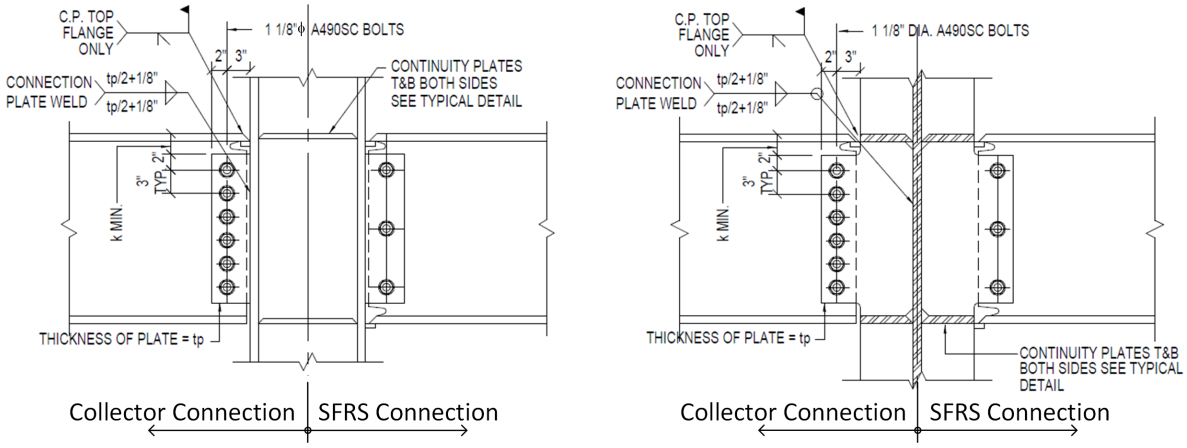

(b) Top Flange Weld (TFW) Collector Connection

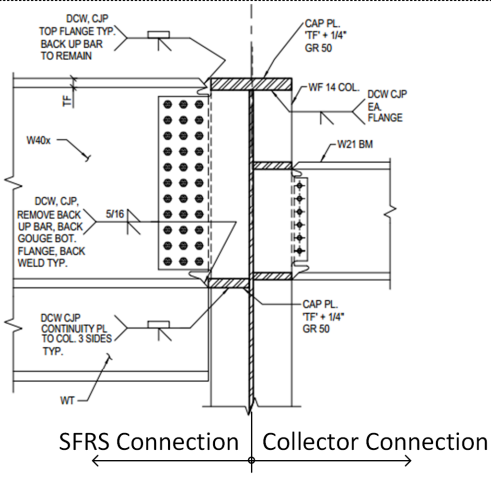

(c) ALL Flange Weld (AFW) Collector Connection

Figure 1.4 Typical Collector-to-Column Connections (Courtesy of The Herrick Corporation)

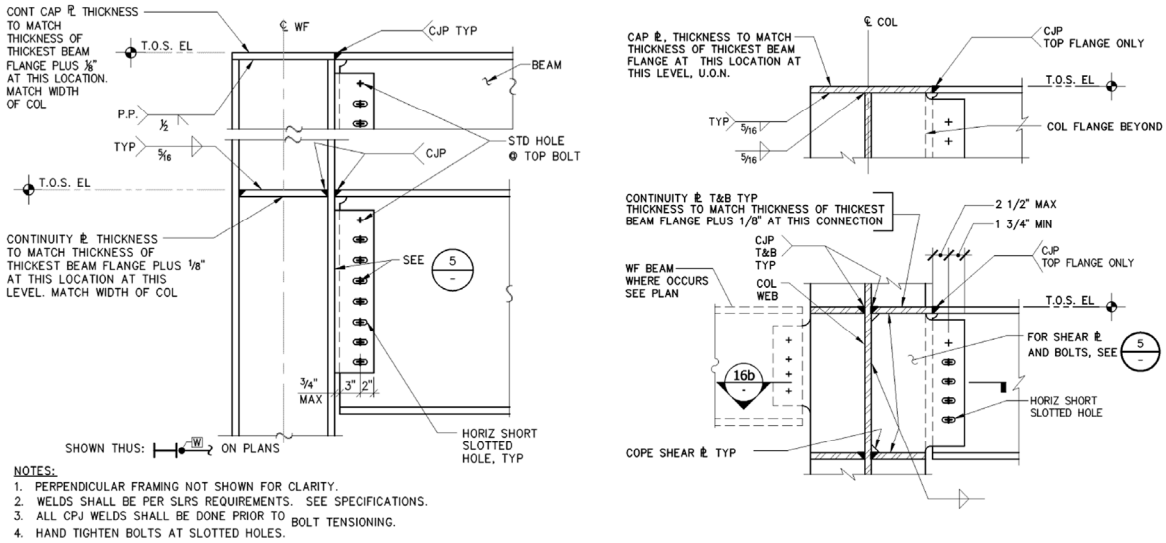

Figure 1.5 TFW Collector Connection with Slotted Holes (Courtesy of The Herrick Corporation)

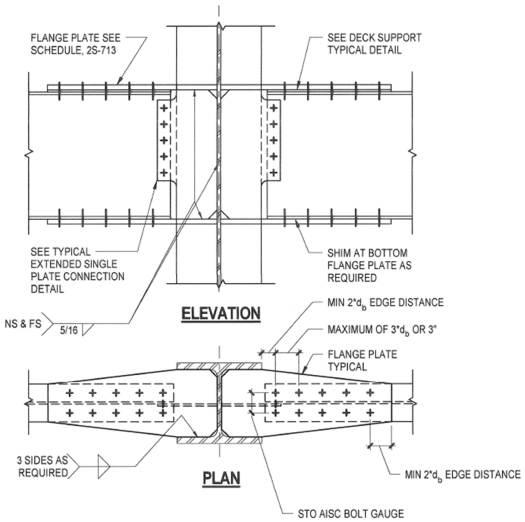

Figure 1.6 Bolted Flange Plate Collector Connection (Courtesy of The Herrick Corporation)

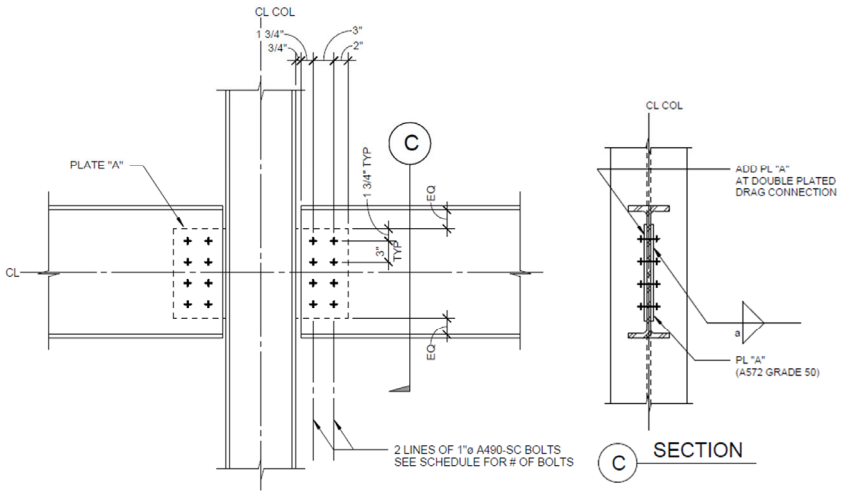

Figure 1.7 Double Shear Tab Collector Connection (Courtesy of The Herrick Corporation)

1.2 UA-UCSD-LU Collaborative Research Project

This study is part of a National Science Foundation (NSF) Engineering for Natural Hazard (ENH) research project conducted through the collaboration among researchers from the University of Arizona, University of California, San Diego (UCSD), and Lehigh University. The main goal of this joint research is to advance knowledge on the seismic performance, analysis, and design of collectors in steel buildings with composite floor and roof systems.

In this project, an integrated experimental and analytical program makes use of the NSF Natural Hazard Engineering Research Infrastructure (NHERI) Facilities, including (1) large-scale testing of collector elements and collector connections at the NHERI Lehigh Experimental Facility, (2) shake table testing of a two-story structure with seismic collectors in a steel composite floor and an unfilled roof deck at the NHERI@UCSD Large High Performance Outdoor Shake Table (LHPOST), and (3) nonlinear static and dynamic analysis of steel seismic collectors in steel composite floor systems and unfilled deck roof systems at all three universities.

The joint research aims to provide new knowledge on (1) the collector seismic load path, (2) collector limit states, including collector connection failure and collector member stability modes, (3) the effect of the composite slab on connection design, (4) collector properties (strength, stiffness and deformation capacity) in the presence of other actions (gravity load, frame lateral drift), and (5) modeling of collector connections for numerical simulation of seismic response.

The research team also works with the American Institute of Steel Construction (AISC) and an advisory panel composed of experts from seismic design consultants and regulatory agencies to evaluate seismic collector details, from code minimum to best practice designs, and to develop relevant and impactful design recommendations.

1.3 Objective and Scope of Research

The main objectives of this research project, which involved shake table testing and associated analytical studies, include (1) investigating the collector load paths in the floor and roof diaphragms, (2) examining the seismic behavior and performance of steel collectors and collector-to-column connections, (3) evaluating the adequacy of current design practice, and (4) developing collector connection modeling and frame analysis procedure.

In this research, a 3-Phase shake table test program were planned on a half-scale, two-story, multi-bay steel test building with a composite floor diaphragm at the second floor and a metal deck diaphragm at the roof level. Three commonly used collector connections, including the all flange weld (AFW), top flange weld (TFW), and bolted web (BW) details, were employed in the test building. Phase 1 of this program involved the testing with only the first story of the test building with a composite slab was constructed. An innovative testing methodology was developed such that the floor absolute acceleration time history of any floor in a multi-story building could be simulated by using this single-story specimen through a transfer function approach.

A series of analytical studies by using the line element frame models were also conducted and the combined experimental and numerical simulation results for Phase 1 testing were used to investigate the load path. In addition, a parallel analytical study was carried out to develop the modeling techniques for seismic analysis of steel building structures with collectors and composite floor diaphragm.

Phase 2 tests were conducted after the second story with a bare steel roof deck was added to the test building. Three commonly used collector connections were also employed for the bare steel roof collectors. The two-story structure was treated as a building and tested with the conventional earthquake simulation testing by using the time-scaled historic ground motions as

the input motions. The Phase 2 test results were used to investigate the seismic behavior of composite and bare steel collectors as well as their connections. Test results were used to evaluate the adequacy of the current practice and develop the associated design recommendations. Phase 2 test results were also used to develop approximation methods for predicting the collector force demand and the rotational stiffnesses of collector connections.

In Phase 3, a pair of buckling-restrained braces (BRBs) were added to the 2nd story of the test building to modify the building dynamic characteristics and the collector seismic load path. Earthquake simulation testing conducted until a failure of the bare steel roof deck occurred.

1.4 Literature Review

1.4.1 Diaphragm Force for Collector Design

Collectors and the floor diaphragms in multistory building need to be designed for the peak floor acceleration excited by the earthquakes with considering the higher mode effect. Although each floor should be designed for the peak response acceleration for that floor, it would be overly conservative to design the vertical elements of the SFRS for the sum of all the individual peaks because each floor reaches its peak response at a different time during a seismic event. Thus, as shown in Figure 1.8, two different sets of seismic design forces in the building code are used for seismic design of the building structures (Sabelli et al. 2011):

(1) One set of design forces, F_x, is for the design of SFRS. In practice, this set of forces is typically determined by using the Equivalent Lateral Force (ELF) procedure or the modal response spectrum analysis procedure. For discussion purpose, this set of forces is called the "seismic design force". Again, seismic design forces do not necessarily reflect the maximum inertial forces induced at a particular diaphragm level.

(2) A second set design forces, F_{px}, which is related to the peak acceleration response, is applied to the design of the diaphragm system including the collectors. For discussion purpose, this set of forces is called the "diaphragm design force" as it is used for design of diaphragm system.

Section 12.10 in the modern building code ASCE 7 (ASCE 2016) stipulates that the diaphragm design force at level x of a building, F_{px}, is computed as:

$$F_{px} = \frac{\sum_{i=x}^{n} F_i}{\sum_{\iota=x}^{n} w_\iota} w_{px} \tag{1.1}$$

where F_i is the seismic design force applied to level i. w_i is the weight tributary to level i, while w_{px} is the weight tributary to diaphragm at level x. The force determined from Eq. (1.1) shall not be less than

$$F_{px} = 0.2 S_{DS} I_e w_{px} \tag{1.2}$$

where S_{DS} is the design spectral response acceleration parameter at short periods, while I_e is the seismic importance factor. Also, the force determined from Eq. (1.1) needs not exceed

$$F_{px} = 0.4 S_{DS} I_e w_{px} \tag{1.3}$$

Note that the diaphragm design force determined from Eq. (1.1) is constructed based on the seismic design force, F_x, which is typically determined from the ELF procedure and thus it is related to the response modification factor R and the system overstrength factor Ω_0. On the other hand, Eqs. (1.2) and (1.3) are used to define the minimum and maximum values for F_{px}, respectively. These two equations are related to the response spectrum parameter S_{DS} but are not dependent on the system parameters R and Ω_0.

Failure of connections between concrete diaphragms and concrete shear walls in the 1994 Northridge earthquake triggered code changes for collectors. With an attempt to ensure the collectors remain elastic during the design earthquake, ASCE 7 Section 12.10.2 regulates that, for structures assigned to Seismic Design Categories (SDC) C through F, collector elements and their connections shall be designed to resist the maximum of the following:

(1) Force calculated using the seismic load effects including overstrength factor Ω_0 with seismic design forces, F_x, determined by the ELF procedure or the modal response spectrum analysis.

(2) Force calculated using the seismic load effects including overstrength factor Ω_0 with diaphragm design forces, F_{px}, determined by Eq (1.1).

(3) Force calculated using the load combinations with seismic with diaphragm design forces, F_{px}, determined by Eq (1.2).

Other than using the above-mentioned conventional method, in performance-based seismic design, nonlinear time history analysis is typically used to determine the design forces in the diaphragms and collectors (Sabelli et al. 2011). Input ground motions are sometimes selected and scaled with a focus on the fundamental period of vibration. However, because peak diaphragm accelerations and design forces may be affected by higher vibration modes, the selection and scaling procedure needs to properly address these vibration modes. Different ground motions will result in differing degrees of response in a given structure, and thus multiple ground motions are typically used is the analysis.

In addition, ASCE 7 Section 12.10.3 stipulates an alternative procedure for determining the design forces for diaphragm and collectors. This “new” diaphragm design force procedure was firstly adopted in the 2016 version of ASCE 7 (ASCE 2016) in recognition of large peak inertial forces that can develop during a seismic event. These forces can be substantially larger than the

design forces computed from the conventional method. It has been shown that diaphragms designed using conventional design procedure may be subjected to inelasticity during design level earthquakes (Rodriguez et al, 2007). Figure 1.9 compares the conventional and new ASCE 7 diaphragm design forces, indicating an impact on collector design (Anshul et al. 2018).

Note that the conventional diaphragm design procedures using seismic design forces reduced by the response modification factor, R, associated with the SFRS. By contrast, the alternative diaphragm design procedure using larger and more accurate elastic design forces incorporated with a diaphragm design force reduction factor, R_S, that reduces the diaphragm demands based on the ductility and overstrength in the diaphragm. So far, the alternative procedure is being mandated only for precast concrete diaphragms in buildings assigned to SDC C through F, and are being offered as an alternative to the conventional method for other precast concrete diaphragms, cast-in-place concrete diaphragms, and wood-sheathed diaphragms supported by wood framing. Thus, there is no currently available code-prescribed R_S factor for composite slab or bare steel metal deck diaphragms. However, the values of R_S for different types of diaphragms have been proposed by the latest NERHRP Recommended Seismic Provisions (FEMA 2020) including R_S = 2.5 for bare steel deck diaphragms satisfying specific special detailing requirements.

1.4.2 Seismic Responses of Shear Tab Beam-to-Column Connections

No experiment has done on collector-to-column connections so far. However, some typical collector connections (e.g., AFW, TFW, and MST connections) used in the current practice are modified from the shear tab beam-to-column connections (also referred to as the single-plate connections) intended for gravity frames.

A series of quasi-static cyclic tests on full-scale beam-to-column assemblies with shear tab connections were conducted by Liu and Astaneh-Asl (2000; 2004) at the University of California,

Berkeley (UCB), as shown in Figure 1.10(a). Among thirteen test specimens with shear tab connections, nine of them were constructed with concrete slabs to represent the composite shear tab connections, while the remaining four were the bare steel connections. Test results showed that these specimens exhibited ductile behavior up to inter-story drift levels on the order of 0.06–0.14 rad. This indicates that both bare steel and composite shear tab connections have sufficiently large rotational capacity such that they can retain their gravity load-carrying capacity at a rotation angle far beyond that of most steel moment frame connections. The rotation capacity of the shear tab connections is inherently resulted from plastic deformation of the shear tab, elongation of bolt holes, and slip of bolts in the connection. Brittle fracture with limited rotational capacity is possible if the shear tab and beam web are too thick to permit these local ductile inelastic deformations, or if the shear tab welds do not have adequate capacity.

Figure 1.10(b) shows the typical moment-rotation response for bare steel shear tab connections. Test results showed that this type of connection can reach a moment capacity on the order of 15–20% of the plastic moment capacity of the beam. The moment-rotation curves are often non-symmetric, mainly due to the following reasons. First, the initial moment in the connection due to gravity load makes the connection appear weaker in one direction, since the applied seismic deformation immediately increases the moment in one direction while decreases the moment in the other. Secondly, the binding between the steel beam flange and the column flange causes the connection to be much stronger in the negative moment direction than in the positive moment direction at rotations larger than about 0.06 rad. Note that this added strength was not observed in all tests and it came only at very large rotations, and it depends on variables such as the clearance gap, which varies from beam to beam and from fabricator to fabricator. Thus, this added resistance cannot be counted on seismic design.

Figure 1.10(c) shows the typical moment-rotation response for composite shear tab connections. Test results indicated that the connection could develop a moment capacity on the order of 30–60% of the beam plastic moment capacity. The moment rotation curves are invariably non-symmetric, which is mainly caused by the presence of concrete slab. The composite slab increases the moment capacity significantly in positive bending. However, the composite action was lost at a level of about 0.04 rad drift, with the crushing of the concrete causing a significant drop in moment capacity. On the other hand, the composite slab has very little effect under negative bending. Hence, for a composite shear tab connection, it is appropriate to compute the positive moment capacity based on composite and the negative moment capacity based on the bare steel section. Like bare steel connections, composite-shear-tab connections may also develop additional bending moment at large rotations due to binding action. Again, this binding action does not provide an increase in resistance that can be effectively used in seismic design.

Liu and Astaneh-Asl (2004) proposed a backbone moment-rotation curve for the composite shear tab connections. In Figure 1.11(a) the first quadrant represents the positive bending response, and the third quadrant represents negative bending response. For a bare steel shear tab connection, both positive and negative bending would have the same response as shown in the third quadrant. The responses shown in Figure 1.10(b) and (c) are for a ductile connection. Note that failure modes (or limit states) must be evaluated as part of the connection model development. Possible ductile failure modes for composite gravity connections include (1) gross yielding of shear tab, (2) gross yielding of beam web, (3) bearing at bolt holes, and (4) concrete slab crushing. Potential non-ductile failure modes include (1) net section fracture of shear tab, (2) net section fracture of beam web, (3) bolt fracture, and (4) weld fracture.

To evaluate the governing failure mode, the shear tab is discretized at each bolt location based on the bolt spacing and edge distances as shown in Figure 1.11(b). The discretized segments are called equivalent bolt elements. The shear and tension capacity of an equivalent bolt element is compared to the bolt and weld fracture capacities to establish which failure mode will govern in the loading directions parallel and perpendicular to the beam span. The lowest capacity governs the connection capacity and the connection behavior, which is referred to as $F_{\parallel}$ for shear and $F_{\perp}$ for tension. These capacities should be evaluated using the strength equations of the AISC Specification (AISC 2016c), where the expected material strengths are used and the resistance factors are set to 1.0. If the non-ductile modes do not govern, then the connection is assumed to be ductile and can be represented by the cyclic backbone curve shown in Figure 1.11(a).

The moment at connection slip, M_{slip}, is based on a plastic distribution of bolt friction forces as shown in Figure 1.11(c) and (d) for positive and negative bending, respectively. The bolt slip force, F_{slip}, is computed as:

$$F_{slip} = \mu T_b \tag{1.4}$$

where μ is the friction coefficient, and T_b is the minimum pretension force. The values of μ and T_b can be referred to the AISC Specification. For the composite connection:

$$M_{slip} = 0.67 F_{slip} \cdot (\text{no. of tension bolt}) \cdot d \tag{1.5}$$

where d is the distance between the bolt group centroid and top of concrete slab. For the bare steel connection:

$$M_{slip} = 1.5 F_{slip} \cdot (\text{no. of tension bolt}) \cdot d \tag{1.6}$$

where d is the distance between centroids of tension and compression bolts. As illustrated in Figure 1.11(a), the rotation at connection slip, θ_{slip}, is assumed to be 0.0042 rad. The initial stiffness of the connection is equal to M_{slip}/θ_{slip}.

As illustrated by the idealized force distribution in Figure 1.11(e), the positive moment capacity, M_{max}^{+}, can be determined by multiplying the tension resistance of bolts on the lower portion of the shear tab by an effective moment arm. Based on test results, bolts near the top of the shear tab are assumed to resist the applied beam shear, with the remaining bolts available to provide positive moment resistance. For a expected gravity-induced shear force, V_g, the number of equivalent bolt elements required to provide shear resistance is determined from $N_v = V_g/F_{\|}$ rounded up to the nearest integer. The maximum normal force that can be developed is the lesser between the total tension resistance of the equivalent bolt element, T, and the compression capacity of the concrete slab, C, where

$$C = 0.85 f_c' b_{eff} a \tag{1.7}$$

where f_c' is the compressive strength of concrete. Effective slab width, b_{eff}, is taken as the width of column face. Slab depth is taken as $a = h_c$ for deck parallel to the beam and $a = 0.6h_c$ for deck perpendicular to the beam. If $T \geq C$, concrete slab is the weak link and governs the connection capacity. Otherwise, T governs the connection capacity and the effective slab compression depth, a_{eff} is computed as:

$$a_{eff} = T/0.85 f_c' b_{eff} \tag{1.8}$$

As shown in Figure 1.11(e), the lever arm dimension d is then determined based on the distance between the centroid of the bolt tension force T and the compression depth (lesser of slab thickness a or a_{eff}). The positive moment capacity, M_{max}^{+} , can then be calculated as:

$$M_{max}^{+} = d \cdot \min(T, C) \tag{1.9}$$

As illustrated in Figure 1.11(a), M_{max}^{+} is assumed to be reached at a connection rotation of 0.03 rad for a composite connection. Beyond this, the moment resistance is reduced linearly to $M_{drop} = M_{max}^{-}$ at a rotation of 0.04 rad, where M_{max}^{-} is the the negative moment capacity of the connection.

Tests conducted by Liu and Astaneh-Asl (2000a, 2004) showed that the presence of a slab could increase the negative moment capacity, M_{max}^{-}, up to 50% above the bare steel connection, due to continuity of the slab, metal deck and slab reinforcement. However, such contribution in negative bending was inconsistent. Therefore, it was suggested to evaluate the negative moment capacity based on the bare steel connection. Similar to the calculation for M_{max}^{+} , the number of gravity shear bolts N_v is determined first; however, for negative bending, this number is not rounded up to the nearest integer. The bolts at the bolt group centroid are assumed to resist the shear load and assigned as shear bolts, starting at the center and distributed evenly above and below the centroid. The remaining bolts are assumed to resist flexure. A fully plastic force distribution is shown in Figure 1.11(f). Assuming that each equivalent bolt strength is governed by the tension capacity, $F_{\perp}$, M_{max}^{+} is computed as:

$$M_{max}^{-} = d \cdot T \tag{1.10}$$

where the lever arm dimension *d* is taken as the distance between flexure bolts centroids, and the bolt tension force, T, is based on the bolted joint strength. It was assumed that M_{max}^{-} is reached at 0.02 rad.

FEMA 355D (FEMA 2000) also provides two simplified equations to predict the rotational stiffnesses, k_s, of composite and bare steel shear tab connections, respectively. The stiffness of the connection depends upon the depth of the bolt group, d_{bg}, [see Figure 1.12(a)] since deeper bolt groups provide increased connection stiffness. Therefore, as shown Figure 1.12(b), two equations

from linear regression of test data from the UCB test results (Liu and Astaneh-Asl 2000; 2004) and some other historical test data (Richard et al., 1980; Astaneh-Asl et al., 1989) were derived:

$$k_S = 28000\left(d_{bg} - 5.6"\right) \tag{1.11}$$

For composite shear tab connections, k_S is estimated as:

$$k_S = 28000\left(d_{bg} - 3.3"\right) \tag{1.12}$$

Note that this stiffness is not the maximum stiffness of the connection. It is a secant stiffness to the rotation at which 50% to 75% of the maximum resistance is achieved. The UCB test results showed that, for the bare steel shear tab connections, the rotational stiffness, k_S, was about 10% of the bending stiffness (EI/L) of the beam. For the composite shear tab connections, k_S, was between 30% and 150% of EI/L.

1.4.3 Modeling of Floor Diaphragm Systems

So far, there is limited research on modeling of the in-plane response of steel-concrete composite slabs. Thus, past research on modeling of in-plane behavior of concrete slab and shear wall is reviewed. Lu and Panagiotou (2013) proposed a Beam-Truss model (Figure 1.13) for nonplanar reinforced concrete walls. This modeling approach was validated by experimentally measured responses. The model used nonlinear diagonal truss elements to represent the diagonal field of concrete in compression. The angle of the diagonals with respect to the horizontal elements is θ_d [Figure 1.13(h)] was suggested to be ranged between 40° and 50°. The area of each diagonal is the product of the thickness of the panel and the effective width $b_{eff} = a \cdot \sin(\theta_d)$, where a is the length of the subpanel [Figure 1.13(f)]. In addition, nonlinear fiber-section Euler-Bernoulli beam elements were employed to represent the steel and concrete in the vertical direction, while nonlinear truss elements were used to represent concrete and steel rebars in the horizontal direction.

Linear beams were used in parallel with the horizontal truss elements to model the out-of-plane flexural rigidity of the wall segments.

The concrete material model used for the vertical and horizontal elements should reflect the compressive and tension strengths that can be developed in the concrete. For the diagonal truss elements, the concrete material model was suggested to be compression-only (i.e., zero tensile strength). In addition, it should account for the biaxial strain field on the concrete compressive behavior as described by Vecchio and Collins (1986). Thus, the compressive stress-strain behavior is dependent on the strain, ε_n, normal to the axis of the truss element, which is measured by the zero stiffness strain gauge elements intentionally placed in the model. With the measured, ε_n, for the reduction in diagonal compressive strength due to biaxial tension can be obtained by multiplying the instantaneous compressive strength of the diagonal trusses by a stress reduction factor β.

For the modeling of bare steel roof diaphragm, Tremblay et al. (2004) simulated the cyclic testing (Essa et al. 2003) on a screwed-nailed steel deck diaphragm specimen by using a deep horizontal plane truss as shown in Figure 1.14. A Wayne-Stewart model (Stewart 1987) was employed for the diagonal trusses to capture the cyclically pinched hysteresis responses of in-pane shear force-deformation behavior of the diaphragm. A good agreement between analytical and experimental results confirmed the validity of the plane truss model.

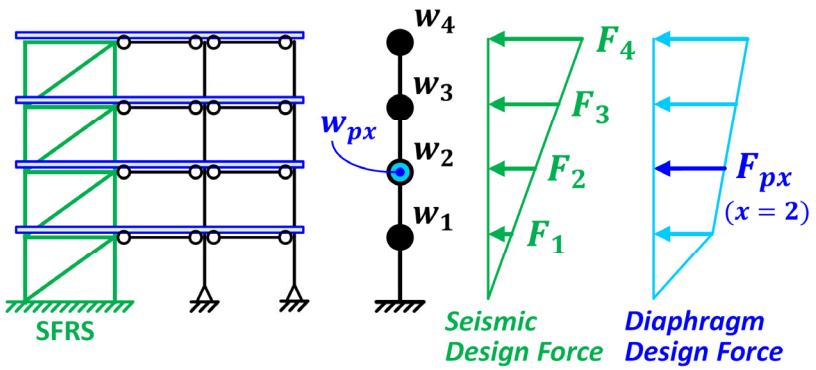

Figure 1.8 Seismic Design Force and Diaphragm Design Force

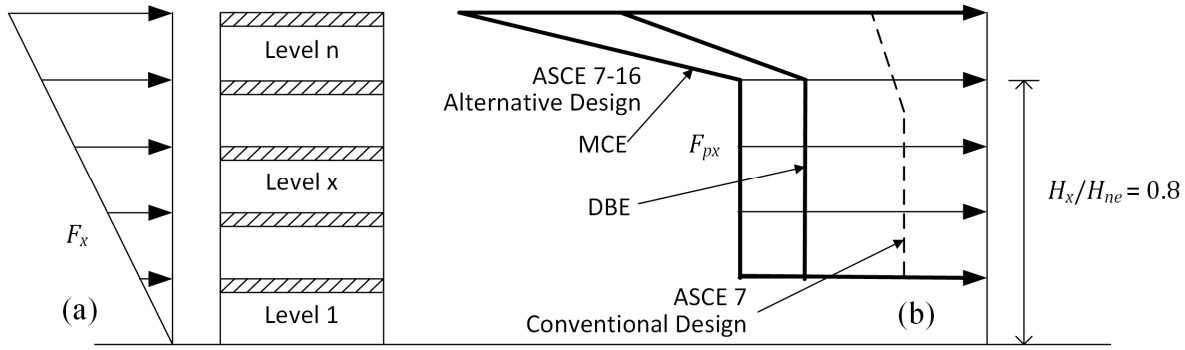

Figure 1.9 Comparison between (a) Seismic Design Force and (b) Conventional and Alternative Diaphragm Design Forces (Anshul et al. 2018)

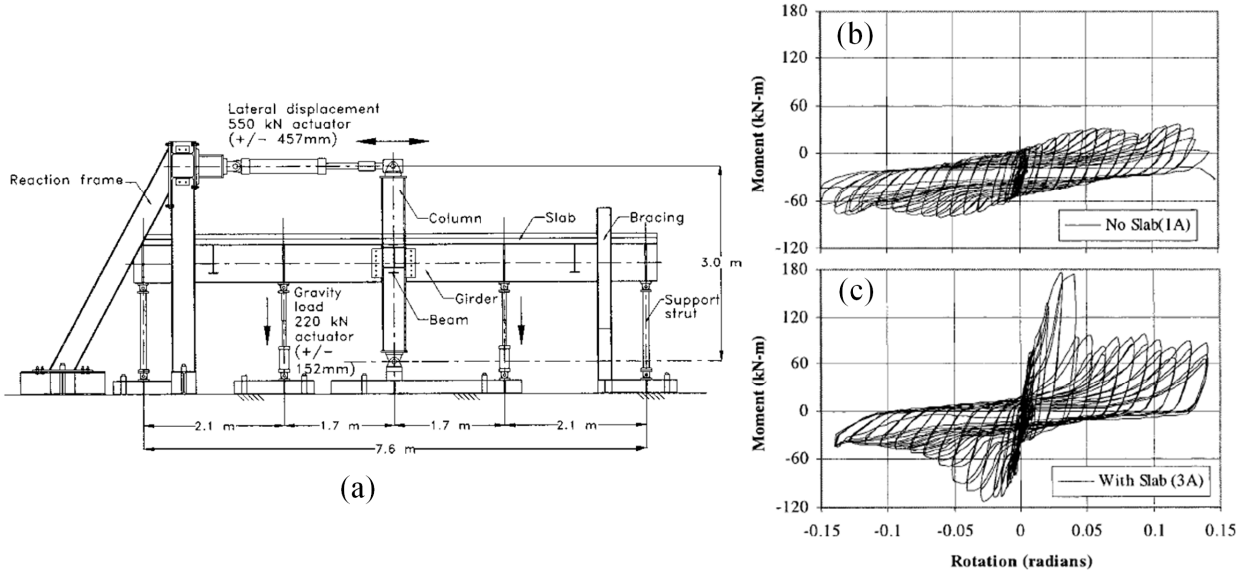

Figure 1.10 (a) UCB Test Setup, and Moment-Rotation Responses of (b) Bare Steel and (c) Composite Shear Tab Connections (Liu and Astaneh-Asl 2000; 2004)

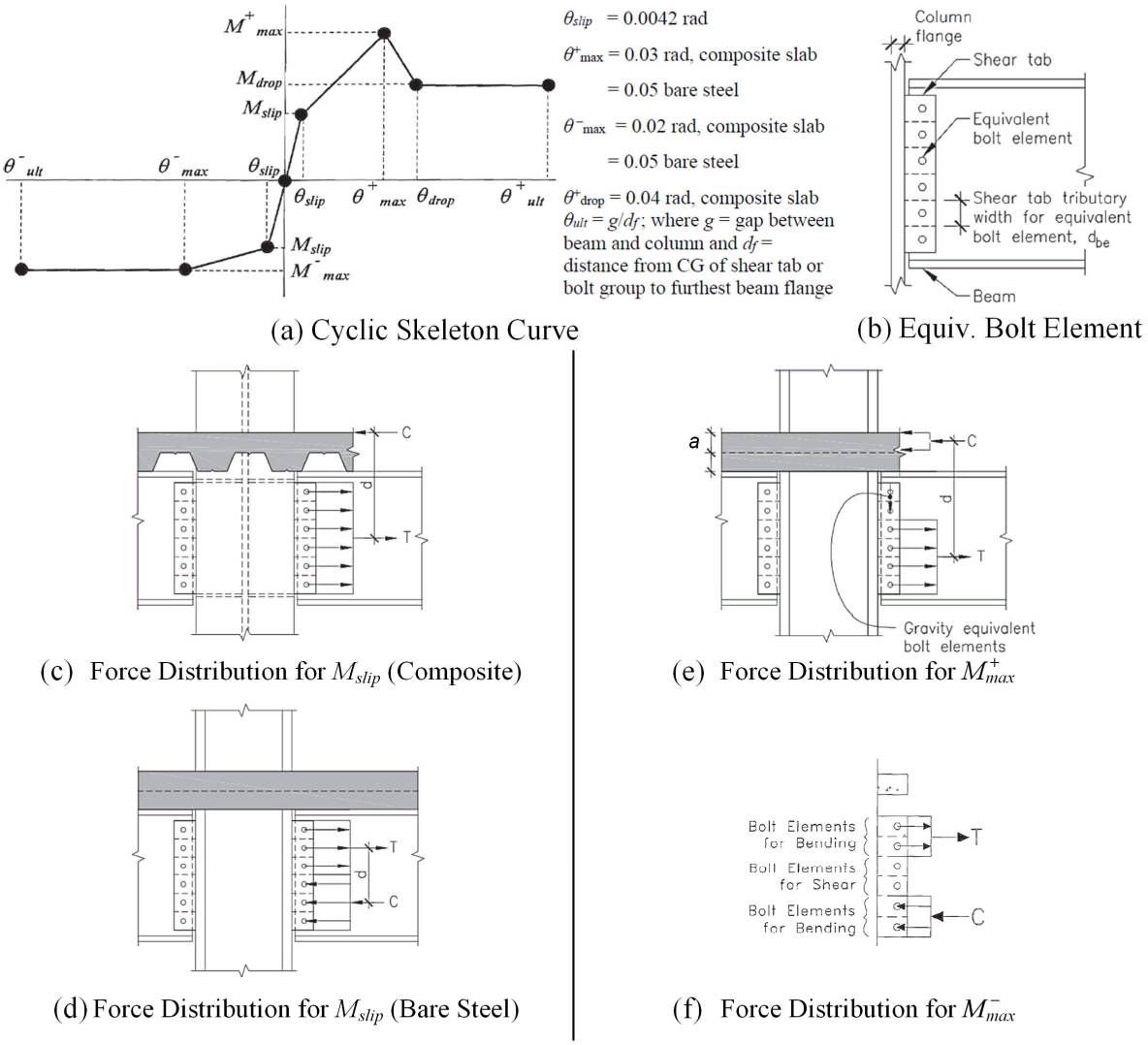

Figure 1.11 Moment-Rotation Model for Composite Shear Tab Connection (Liu and Astaneh-Asl 2004)

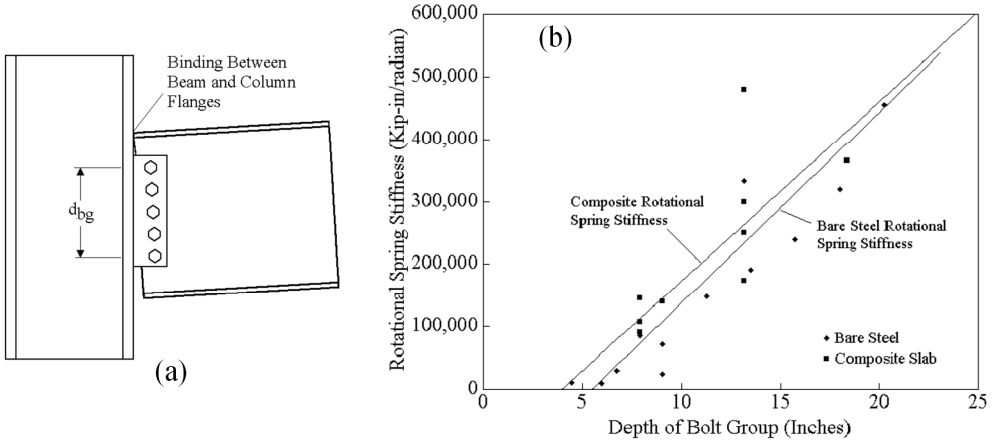

Figure 1.12 (a) Depth of Bolt Group, and (b) Rotational Stiffness versus Depth of Bolt Group Relationships for Shear Tab Connections (FEMA 2000)

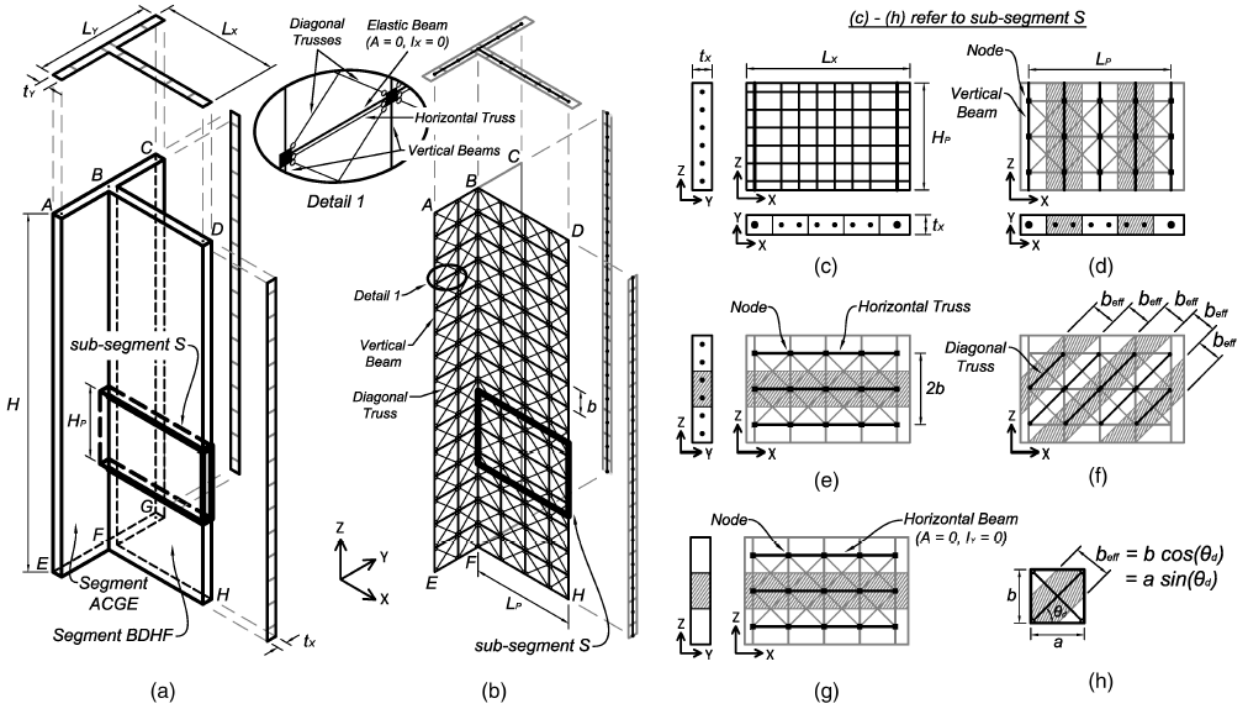

Figure 1.13 Beam-Truss Model (Lu and Panagiotou 2013)

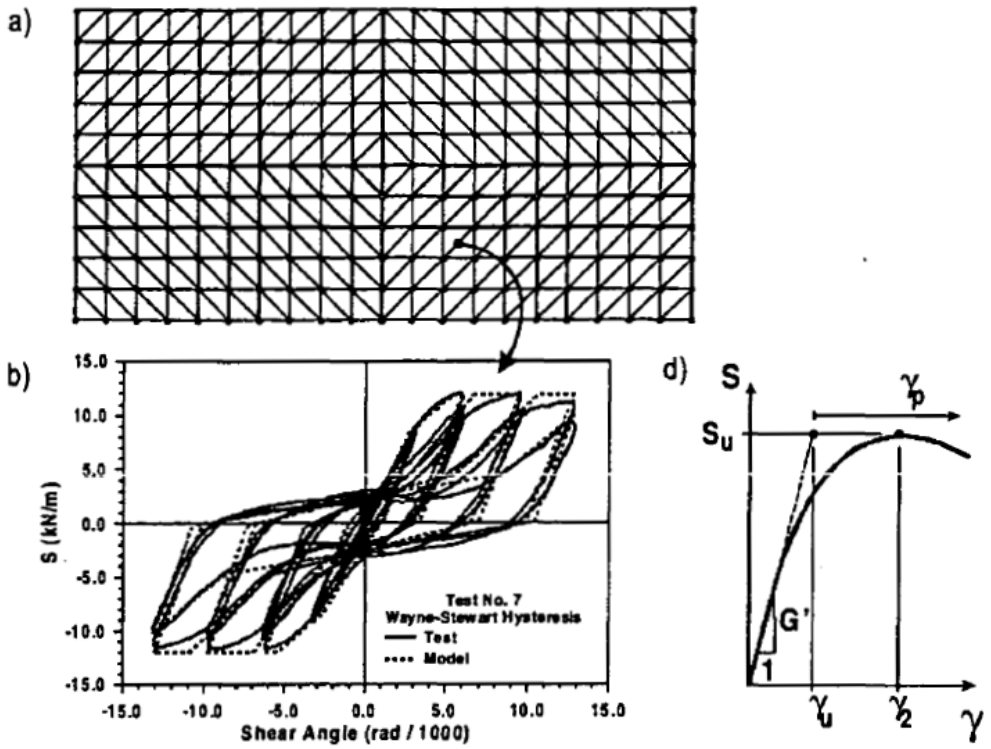

Figure 1.14 Plane Truss Model for Roof Diaphragm (Tremblay et al. 2004)

1.5 Organization of Dissertation

The remainder of the dissertation is organized as follows:

- Chapter 2 describes the development of a testing methodology for floor acceleration simulation for Phase 1 testing. This includes the derivation of transfer function for generating the required input motion for shake table tests and the numerical verification of the testing methodology.
- Chapter 3 describes Phase 1 shake table test program, including the specimen design, test setup, instrumentation, loading protocol, and data reduction.
- Chapter 4 describes Phase 1 test results. The first part of this chapter is the general description of the global responses of the test building for all tests. The second part presents in detail the specimen responses of Test 1-3, which was tested with the highest intensity in this phase. This part begins with an evaluation of the proposed testing methodology for floor acceleration simulation, followed by the detailed specimen responses, including the strain profiles and experimentally derived member forces in collectors and moment-rotation responses of collector connections.
- Chapter 5 describes numerical simulation of Phase 1 testing and design implications. The first part describes the modeling of the test specimen and analysis results. The second part presents the design implications learned from experimental and analytical results, which include the prediction of rotational stiffness of collector connections, the effective slab width of composite collector, and the prediction of collector axial force demand.
- Chapter 6 describes Phase 2 test program, including the specimen design, test setup, instrumentation, loading protocol, and data reduction.
- Chapter 7 describes Phase 2 shake table test results. The first part is the general description of the global responses of the test building for all tests. The second part presents in detail the

specimen responses from Test 2B-5, which was tested with the highest intensity in this phase. Detailed specimen responses, including strain profiles and member experimentally derived forces in collectors, and the moment-rotation responses of collector connections are presented.

- Chapter 8 describes design implications learned from Phase 2 testing. This chapter begins with the effective slab width determination for composite collectors. Subsequently, a proposed method for predicting the rotational stiffness of collector connections and a proposed lateral load analysis for the topmost gravity frame with collectors were developed. Design recommendations on collectors and collector connections are presented.
- Chapter 9 describes Phase 3 shake table test program, including the specimen design, test setup, loading protocol, instrumentation, data reduction, and general test results.
- Chapter 10 provides a summary and conclusions from this research and suggestions for future research.

Part of this chapter is based on the material published in the 17th World Conference on Earthquake Engineering, titled "Earthquake simulator testing on behavior of seismic collectors in steel buildings" with co-authors Uang C.-M., and Fleischman R.B. (2020). Materials were also submitted for publication in the 12th National Conference on Earthquake Engineering, titled "Shake Table Tests on Seismic Response of Collectors in Steel Buildings" with co-authors Uang C.-M., and Fleischman R.B. (2022). The author of this dissertation serves as the first author of these papers.

2. DEVELOPMENT OF TESTING METHODOLOGY FOR FLOOR ACCELERATION SIMULATION

2.1 General

The main objective of the Phase 1 test program was to investigate the load path of inertial forces in the composite floor diaphragm system in steel buildings and to investigate the seismic behavior of steel collectors and their connections. Therefore, the main goal of the test program is to excite a test specimen to produce realistic floor accelerations in a multistory building. However, distributed inertial forces in a floor diaphragm cannot be simulated easily by using a quasi-static testing or pseudo dynamic testing technique in the laboratory. Hence, the shake table test at the NHERI@UCSD LHPOST is ideal for this research.

The earthquake-induced floor accelerations in a multi-story building are quite often affected by the higher mode responses. Although it is ideal that a multi-story test building be constructed for this purpose, it is very expensive and time-consuming to do so. Therefore, a testing methodology for the floor acceleration simulation was developed in this research to allow a single-story test frame to reproduce the floor acceleration time history from any floor in a prototype multi-story building. Figure 2.1 illustrates the concept and challenge for floor acceleration simulation. As shown in Figure 2.1(a), a 12-story building (Torabian et al. 2017) designed by the Steel Diaphragm Innovation Initiative (SDII) research team (https://steeli.org/) was chosen to be the prototype structure. This 12-story building was designed with buckling-restrained braced frames (BRBFs) for its lateral force-resisting system (LFRS). See Appendix F for detailed description of the prototype structure. A series of nonlinear time history analyses were performed on a numerical model representing the prototype building to obtain the floor absolute acceleration responses under various intensities of earthquake events. Some numerically predicted floor acceleration responses,

denoted as $\ddot{u}_i^t(t)$, were selected to be the target responses. The subscript "i" represents the i-th floor, while the superscript "t" means the "absolute" (or "total") acceleration.

As shown in Figure 2.1(b), a single-story test frame composed of a LFRS with a floor diaphragm and multiple bays of gravity frames is intended for shake table testing. This single-story test frame can be idealized as a single-degree-of-freedom (SDOF) system. The LFRS contributes to the structural dynamic properties of this SDOF system. Further, multiple bays of gravity frame are needed for the investigation on how the inertial forces in the floor system are collected by a series of collectors and connections and then transferred into the LFRS. The challenge of this test program lies in generating a shake table input acceleration, $\ddot{u}_g^*(t)$, that can excite the single-story test frame to reproduce the target floor acceleration, $\ddot{u}_i^t(t)$. To tackle this "inverse" problem which estimates the required input motion from a target output response for a system, a linearly elastic single-story test frame is designed such that the elastic frequency-domain structural dynamic theory can be used to develop the procedure for generating the required input table accelerations. This elastic test frame then can be used repeatedly to simulate the target acceleration time history at any given floor of the prototype or any other prototype.

2.2 Development of Testing Methodology

Figure 2.2(a) shows the mathematical model of an SDOF system subjected to an input ground acceleration, $\ddot{u}_g^*(t)$. The equation of motion for this system is

$$m\ddot{u}^*(t) + c\dot{u}^*(t) + ku^*(t) = -m\ddot{u}_g^*(t) \tag{2.1}$$

where m, c, and k are the mass, damping coefficient, and stiffness, respectively; $\ddot{u}^*$, $\dot{u}^*$, and u^* are the relative acceleration, relative velocity, and relative displacement, respectively. Note that the superscript "*" is used to represent that these quantities belong to the test specimen so as to be

distinguish them from those quantities of the prototype structure. Equation (2.1) can be rewritten as:

$$\ddot{u}^*(t) + 2\xi\omega_n\dot{u}^*(t) + \omega_n^2 u^*(t) = -\ddot{u}_g^*(t) \tag{2.2}$$

where ω_n and ξ are the natural angular frequency and damping ratio, respectively. Taking a Fourie transform of Eq. (2.2) and considering the properties $\dot{u}^*(\omega) = i\omega u^*(\omega)$ and $\ddot{u}^*(\omega) = -\omega^2 u^*(\omega)$, the equation of motion can be further rewritten as:

$$-\omega^2 u^*(\omega) + i2\xi\omega_n\omega u^*(\omega) + \omega_n^2 u^*(\omega) = -\ddot{u}_g^*(\omega) \tag{2.3}$$

This equation gives the relationship between $u^*(\omega)$ and $\ddot{u}_g^*(\omega)$ so that the transfer function, $H_0(\omega)$, for an SDOF system [see Figure 2.2(a)] can be obtained:

$$H_0(\omega) = \frac{u^*(\omega)}{\ddot{u}_g^*(\omega)} = \frac{1}{\omega^2 - i2\xi\omega_n\omega - \omega_n^2} \tag{2.4}$$

However, the SDOF system with an output of absolute (total) acceleration, $\ddot{u}^{t*}$, as shown in Figure 2.2(b), is more of interest for this research because the inertial force of the diaphragm and its collectors and chords are directly related to $\ddot{u}^{t*}$. The transfer function, $H(\omega)$, for this system can be derived by taking a Fourie transform of $\ddot{u}^{t*}(t)$. The absolute acceleration is

$$\ddot{u}^{t*}(t) = \ddot{u}^*(t) + \ddot{u}_g^*(t) \tag{2.5}$$

Taking a Fourie transform of Equation (2.5) yields

$$\begin{aligned}\ddot{u}^{t*}(\omega) = \ddot{u}^*(\omega) + \ddot{u}_g^*(\omega) = -\omega^2 u^*(\omega) + \ddot{u}_g^*(\omega) = -\omega^2 H_0(\omega)\ddot{u}_g^*(\omega) + \ddot{u}_g^*(\omega) \\ = [1 - \omega^2 H_0(\omega)]\ddot{u}_g^*(\omega)\end{aligned} \tag{2.6}$$

So the transfer function, $H(\omega)$, between the absolute acceleration, $\ddot{u}^{t*}(\omega)$, and the ground acceleration, $\ddot{u}_g^*(\omega)$, is obtained:

$$H(\omega) = \frac{\ddot{u}^t(\omega)}{\ddot{u}_g(\omega)} = [1 - \omega^2 H_0(\omega)] = \frac{i2\xi\omega_n\omega + \omega_n^2}{-\omega^2 + i2\xi\omega_n\omega + \omega_n^2} \tag{2.7}$$

To use Eq. (2.7) to generate the required input shake table motion for the SDOF test specimen shown in Figure 2.1(b), a fast Fourier transform (FFT) of $\ddot{u}_i^t(t)$, the target *i*-th floor absolute acceleration in the prototype building, is conducted to obtain the frequency-domain response $\ddot{u}_i^t(\omega)$. Then the required input acceleration for the test frame, $\ddot{u}_g^*(\omega)$, in the frequency domain can be calculated as:

$$\ddot{u}_g^*(\omega) = \frac{\ddot{u}_i^t(\omega)}{H(\omega)} \tag{2.8}$$

Finally, an inverse fast Fourier transform (IFFT) of $\ddot{u}_g^*(\omega)$ is performed to obtain the required input shake table acceleration for the test specimen, $\ddot{u}_g^*(t)$ in the time domain. It is noted that, by using this test methodology, the structural dynamic characteristics such as natural frequency and damping ratio of the single-story test frame has nothing to do with those of the multi-story prototype structure.

2.3 Numerical Verification

Figure 2.3 shows an example structure and the associated numerical model for a numerical verification of the proposed testing technique. As shown in Figure 2.3(a), the 4-story BRBF (4F-BRBF) in the AISC Seismic Design Manual (AISC 2018) was chosen to be the protype structure. A two-dimensional (2-D) frame model was developed to represent the half one 4F-BRBF by using the nonlinear structural analysis software PISA3D (Lin et al. 2012). This prototype model has a fundamental period T_1 = 0.819 sec (ω_1 = 7.67 rad/sec) for its first mode with 2% Rayleigh damping for the 1st and 2nd modes. A nonlinear time history analysis with an input motion from the 1994 Northridge earthquake record ('Vasquez Rock Park' Station) scaled to the maximum

considered earthquake (MCE) level at the period T_1 was carried out. For scaling of the ground motion, the MCE response spectrum was constructed based on the ASCE 7 (ASCE 2016) and the assumed spectral response accelerations S_{DS} = 1.0 and S_{D1} = 0.6. As illustrated in Figure 2.4(a), the numerically computed third-floor absolute acceleration time history, $\ddot{u}_3^t(t)$, was then selected as the target floor acceleration for specimen model.

Figure 2.3(b) shows a trial single-story test specimen intended to simulate $\ddot{u}_3^t(t)$. This test frame is composed of 1-bay moment frame and 13 gravity columns interconnected by a composite floor. The single-bay pin-based moment resisting frame (MRF) in the interior longitudinal frame serves as the LFRS for the test frame, which leads to a long collector line running across the remaining three bays of the interior frame. The total lateral stiffness, k, of the pin-based MRF can be computed by a plane frame analysis shown in Figure 2.5, which lead to the following:

$$k = \frac{F^*}{u^*} = \frac{24EI_c}{H^3}\left[1 - \frac{\frac{I_c}{H} + \frac{3}{2}\left(\frac{I_b}{L}\right)}{\frac{I_c}{H} + 2\left(\frac{I_b}{L}\right)}\right] \tag{2.9}$$

where H and L are the height and span length of the MRF, respectively; I_c and I_b are the moments of inertia of the column and beam in the MRF.

The corresponding numerical model for the interior frame was developed by using PISA3D as well. Elastic beam elements were used for this specimen model. The mass source for this is the composite slab and the masses of the columns were lumped at the top ends in the interior frame. All the columns in this model were pin-supported and all the collectors were modeled as pin-ended beams. A modal analysis shows that the fundamental period of this specimen model was T_n^* = 0.19 sec (ω_n^* = 33.07 rad/sec). The Rayleigh damping was assumed to be 2% for the 1st and 2nd modes. Based on the transfer function shown in Eqs. (2.7), the required input ground motions for the specimen model, $\ddot{u}_g^*(t)$, was generated [see Figure 2.4(b)]. Subsequently, a time history analysis

on the specimen model with the input ground motion, $\ddot{u}_g^*(t)$, was carried out to obtain the output absolute acceleration, $\ddot{u}^{t*}(t)$, of the specimen model. Figure 2.4(c) shows that the achieved floor accelerations of the specimen model, $\ddot{u}^{t*}(t)$, matches the target floor acceleration, $\ddot{u}_3^t(t)$, of the prototype structure very well, which confirms the effectiveness of the proposed testing methodology in reproducing any target floor acceleration response.

In addition to the floor acceleration, the collector-to-column connection rotation is another physical quantity of interest in this research. However, the testing methodology does not guarantee that the test specimen can simulate the prototype deformation. Since the proposed procedure requires an elastic specimen, the specimen model responds within the elastic range. By contrast, the prototype 4F-BRBF model experiences a good amount of inelastic deformation under the MCE level earthquake ground motion. Hence, it is expected that the deformation in the test specimen can be much smaller than that in the protype structure.

For the prototype model [see Figure 2.6(a)], the pin-ended rigid beams between the BRBF and the leaning gravity column are considered as collectors in this model. Take the rotation of the joint between the collector and BRBF columns on the 3rd floor (denoted as Joint X) as an example to compare with those of the two collector-to-column joints (denoted as Joints A and B) in Figure 2.6(b) in the specimen model. As expected, Figure 2.6(c) shows that the rotations of Joints A and B are much smaller than that at Joint X. In addition, the prototype model had a significant residual displacement while the elastic specimen model does not have this issue. In the specimen model, the rotation of the collector-to-column joint adjacent to the MRF, Joint A, is also smaller than that of Joint B, which represents the collector-to-column joints at gravity columns. This is because the beam in the MRF would somewhat restrain the rotation of the top ends of the MRF columns, while the pin-ended collectors provide no restraint on the rotation of the column top ends.

2.4 Improvements on Test Specimen Configuration

The above-mentioned analytical studies indicate that the test specimen composed of LFRS and gravity frames in a regular configuration [see Figure 2.3(b)] would not be able to reproduce the prototype collector-to-column joint rotation responses. In addition, the specimen responses in the joint rotation would be much smaller than the prototype structure responses. Note that the current practice on collector design only considers the acceleration-triggered axial force demands combined with the flexural demand due to gravity. The deformation-triggered seismic flexural demands are ignored. This may be due to the simplification of collector-to-column joints as pin-connections in the analytical models used in the design offices so that the seismic forces would not induce flexural demands in the collectors. However, in the real world, the collector-to-column joints would possess certain amount of rotational rigidity so that the rotation of joints would result in flexural demands on these joints. Hence, it is preferable that the shake table tests can induce a considerable magnitude of rotations at the collector-to-column joint although the proposed testing methodology does not allow the test specimen to reproduce the prototype collector-column joint rotation time histories.

In order to increase the collector joint rotation responses in the test specimen, as shown in Figure 2.7(a), a revised specimen configuration was considered. The LFRS of the specimen was revised to be a pin-based L-shaped frame. In addition, a pin-connection is used between the beam of the L-shaped frame and the adjacent gravity column GC 1 to increase the rotation of the collector end there. A frame analysis as shown in Figure 2.7(b) was conducted to estimate the lateral stiffness, k, of the L-shaped frame, resulting in the following equation:

$$k = \frac{F^*}{u^*} = \frac{12EI_c}{H^3}\left[1 - \frac{\frac{I_c}{H} + \frac{3}{4}\left(\frac{I_b}{L}\right)}{\frac{I_c}{H} + \frac{I_b}{L}}\right] \tag{2.10}$$

By using a shorter height for the gravity columns, it can be shown that the collector joints would experience a larger rotation:

$$\theta_{Jt}^{*} = \theta_{GF}^{*} = \left(\frac{H}{H'}\right)\theta_{LFRS}^{*} \tag{2.11}$$

where θ_{Jt}^{*} is the rotation of collector-to-column joints, θ_{GF}^{*} is the story drift angle of the gravity frame, and θ_{LFRS}^{*} is the story drift angle of the LFRS (i.e., L-shaped frame). H is the story height of the LFRS, while H' is the story height of the gravity frame. It is shown that, with the intentionally shorter gravity columns, θ_{Jt}^{*} can be magnified from θ_{LFRS}^{*} by an amplification factor of H/H'. That is to say, the magnitude of collector-to-column joint rotations in the specimen can be tuned by adjusting the ratio H/H'.

Figure 2.8 shows the PISA3D analysis results for a numerical verification on the revised test program. Again, the analytical 3rd floor acceleration, $\ddot{u}_3^t(t)$, of the prototype 4F-BRBF model was taken as the target response [see Figure 2.8(a)]. Modal analysis results showed that the fundamental period of the revised specimen model was T_n^* = 0.20 sec (ω_n^* = 31.42 rad/sec). The Rayleigh damping was assumed as 2% for the 1st and 2nd modes for the specimen model. The required input acceleration, $\ddot{u}_g^*(t)$, was computed again for the specimen model to reproduce the target floor acceleration. A time history analysis with input motion $\ddot{u}_g^*(t)$ was carried out on the specimen model [see Figure 2.8(b)]. Figure 2.8(c) shows the comparison of collector-to-column joint rotation responses between the prototype and specimen models. Although the specimen cannot reproduce the time history of the prototype collector-to-column joint rotation, the magnitude of joint rotations in the revised specimen was closer to that of the prototype structure responses.

Figure 2.8(d) shows a comparison of responses of the collector-to-column joint rotation (top half) and floor acceleration (bottom half) in a time window from 5th to 11th seconds. The

collector-to-column joint rotation time history in the specimen does not follow the prototype structure response, while the specimen reproduces the prototype floor acceleration very well. Since the specimen behaves elastically, the collector-to-column joint rotation and the floor acceleration are completely out of phase by 180 degrees in the specimen. Hence, in the specimen, the peak floor acceleration coincides with the peak collector-to-column joint rotation (at time t_1). By contrast, for the prototype structure, there is no significant relationship between the two responses. The peak collector-to-column joint rotation (at time t_2) does not coincide with the peak floor acceleration (at time t_1). This could be due to the inelastic responses of the prototype structure. Furthermore, at the time (t_1) when the 3rd floor acceleration of prototype structure reaches the peak value, the rotation of 3rd floor collector-to-column joint is not large. On the other hand, at the time (t_2) when the collector-to-column joint rotation reaches peak value, the floor acceleration is very low. Theses indicate that, in an inelastic response, the acceleration-triggered axial force and deformation-triggered flexural demand in the collectors might not reach peak values at the same time. By contrast, as the specimen behaves elastically during the shake table tests, the collectors would experience the peak axial force and peak flexural demand simultaneously.

Theoretically, by shortening the gravity column height to H', the magnitude of the collector-to-column joint rotation in the elastic specimen can be tuned to match the peak response expected in the inelastic prototype structure. However, imposing this level of deformation to the collector-to-column joints in test specimen could be too stringent because of the coincidence of peak axial force and peak flexural demands in the specimen collectors. Furthermore, as well be shown later from testing, the collector-to-column joints have a certain amount of flexural rigidity such that the gravity columns would resist some story shear. Shortening the gravity column height too much for the specimen would result in an unreasonably high flexural stiffness of the gravity

column, which would distort the amount of how the inertial force that is dragged into the collectors. Other than trying to match the magnitude of the specimen responses to exactly match that of the prototype structure, a mild shortening of gravity columns was eventually adopted in the design of the test building (as shown in Section 2.3) to amplify the collector-to-column joint rotation to some acceptable level.

Part of this chapter is based on the material published in the 17th World Conference on Earthquake Engineering, titled "Earthquake simulator testing on behavior of seismic collectors in steel buildings" with co-authors Uang C.-M., and Fleischman R.B. (2020). Materials were also submitted for publication in the 12th National Conference on Earthquake Engineering, titled "Shake Table Tests on Seismic Response of Collectors in Steel Buildings" with co-authors Uang C.-M., and Fleischman R.B. (2022). The author of this dissertation serves as the first author of these papers.

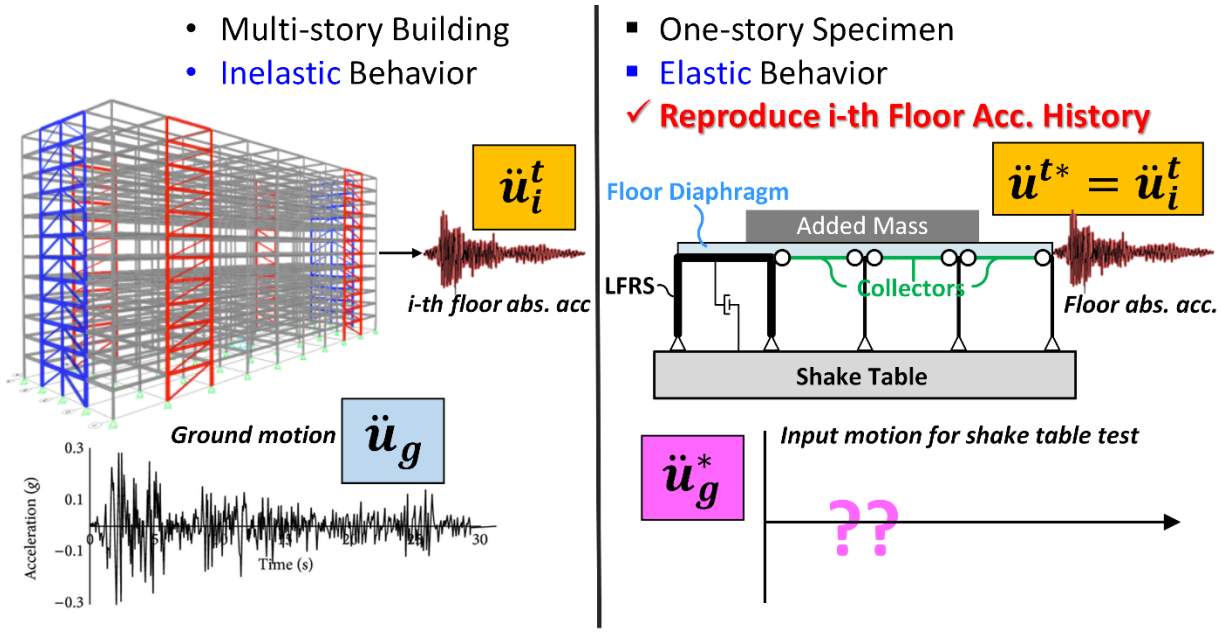

(a) Prototype Structure (b) Test Specimen

Figure 2.1 Concept for Floor Acceleration Simulation Testing

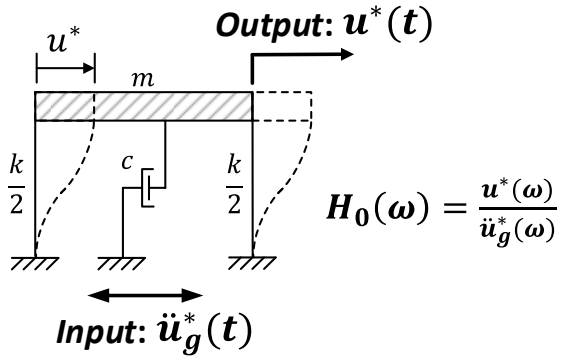

(a) Output: Relative Displacement

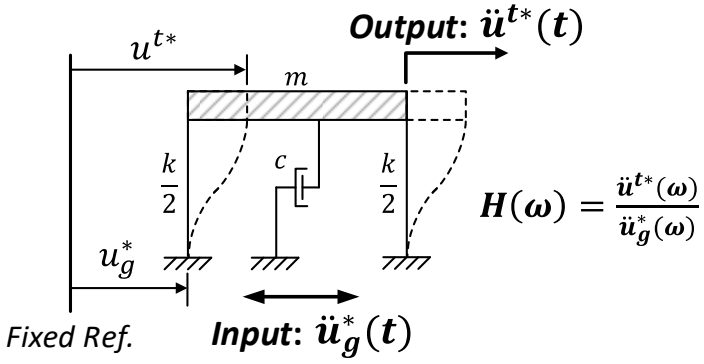

(b) Output: Absolute Acceleration

Figure 2.2 Mathematical Model of a SDOF System Subjected to a Ground Motion

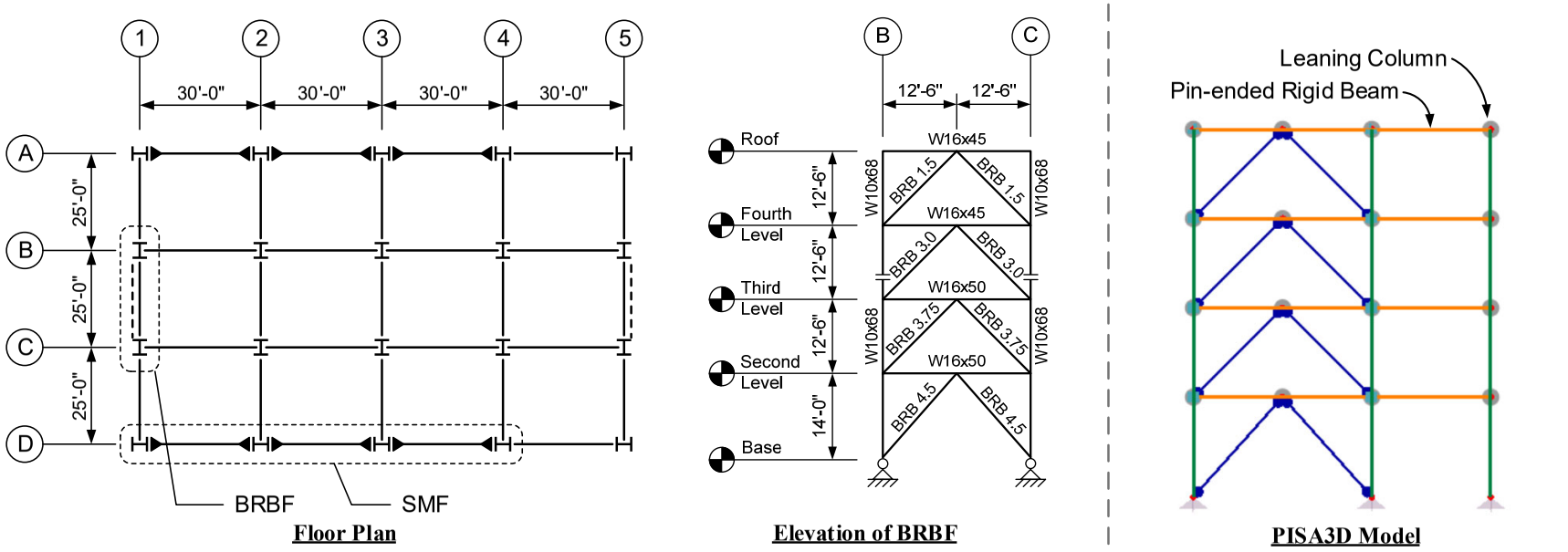

(a) Prototype Structure

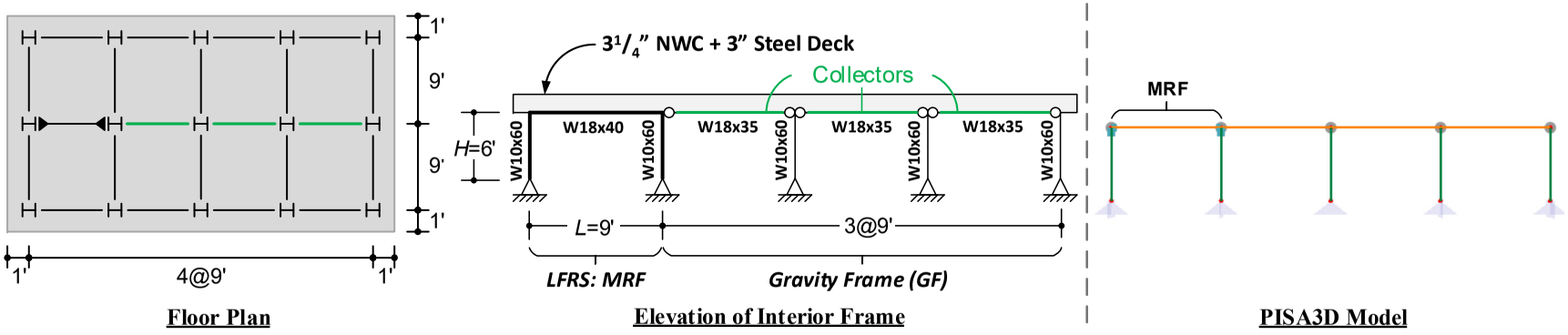

(b) Test Specimen

Figure 2.3 Example Structure and Analytical Models for Numerical Verification of Proposed Testing Methodology

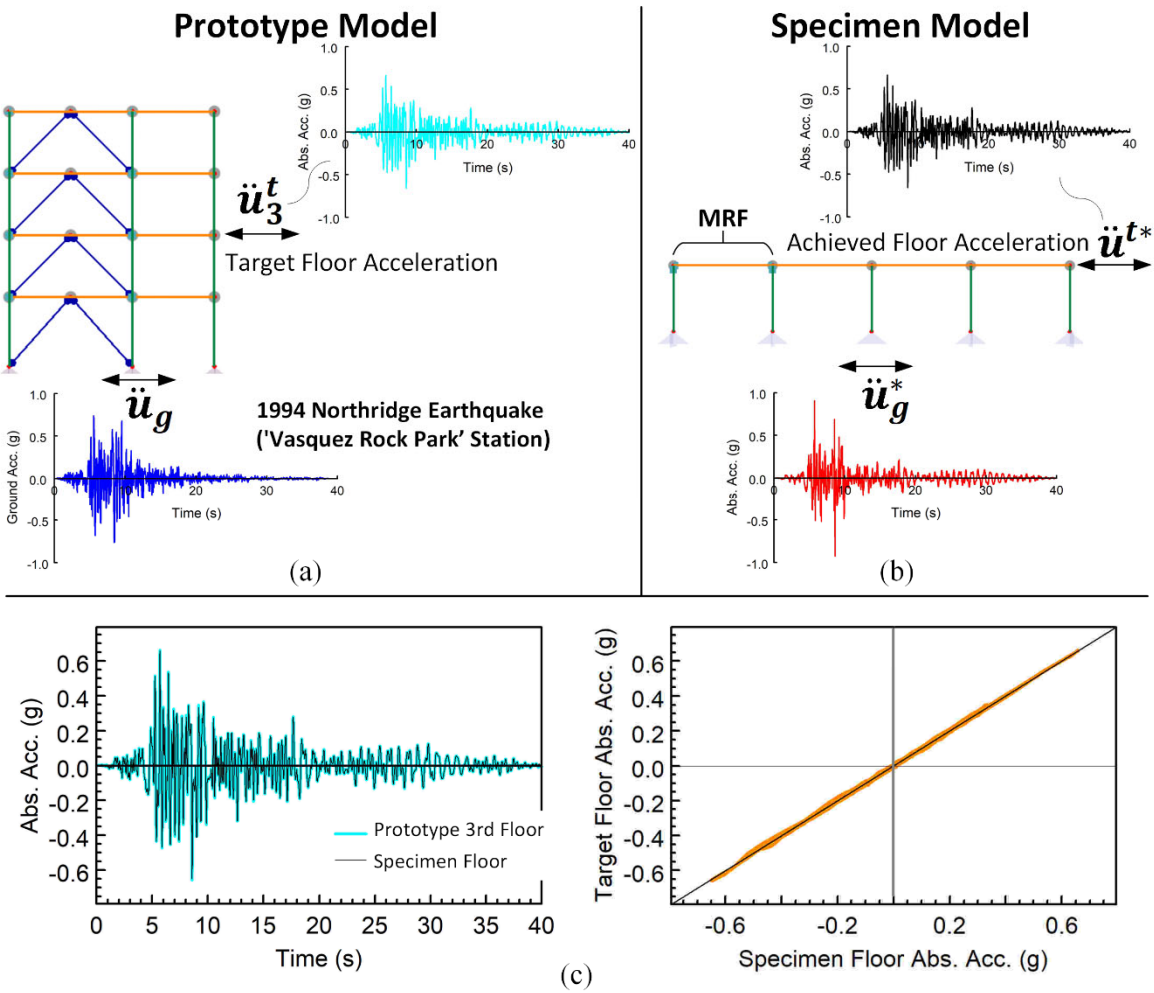

Figure 2.4 Time History Analysis Results on Floor Accelerations for (a) Prototype, (b) Specimen Models, and (c) Comparison of Target and Achieved Accelerations

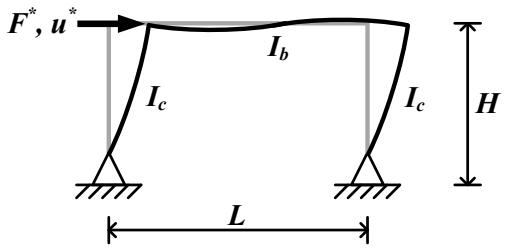

Figure 2.5 Frame Analysis of Pin-based Moment Resisting Frame

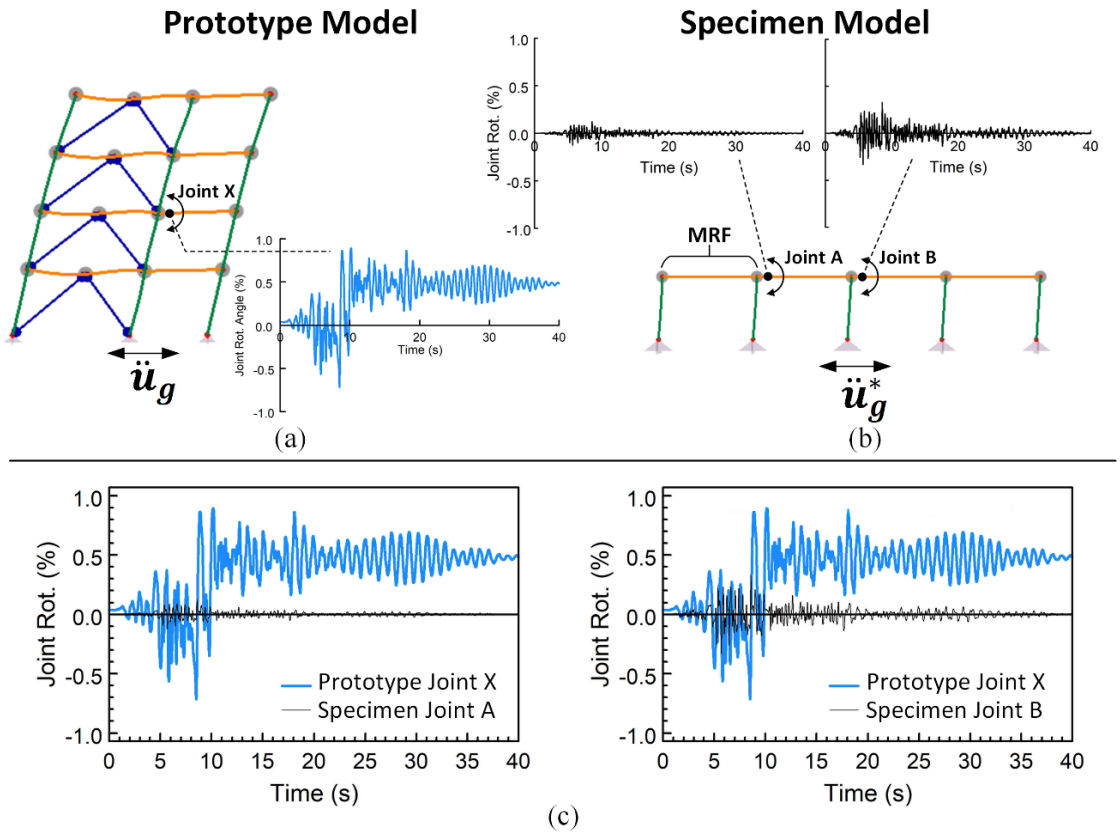

Figure 2.6 Analysis Results on Collector-to-Column Joint Rotations for (a) Prototype, (b) Specimen Models, and (c) Comparison of Results between two Models

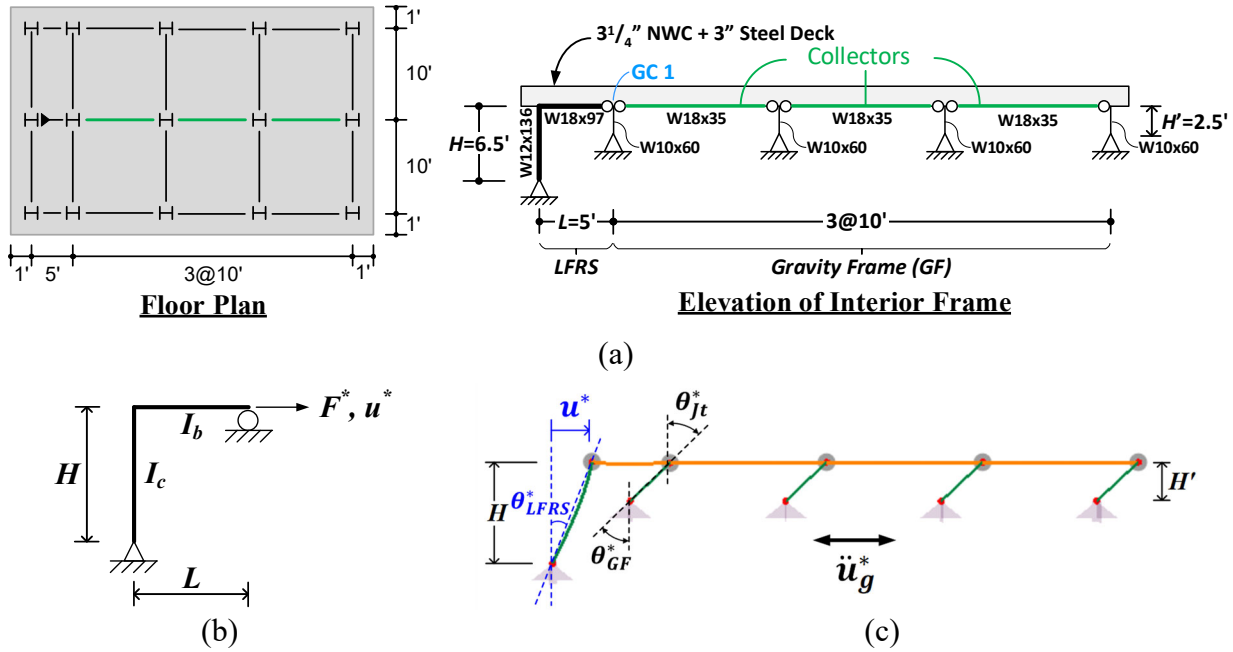

Figure 2.7 (a) Revised Specimen Configuration: (b) Frame Analysis of L-shaped Frame, and (c) Associated Deformed Shape

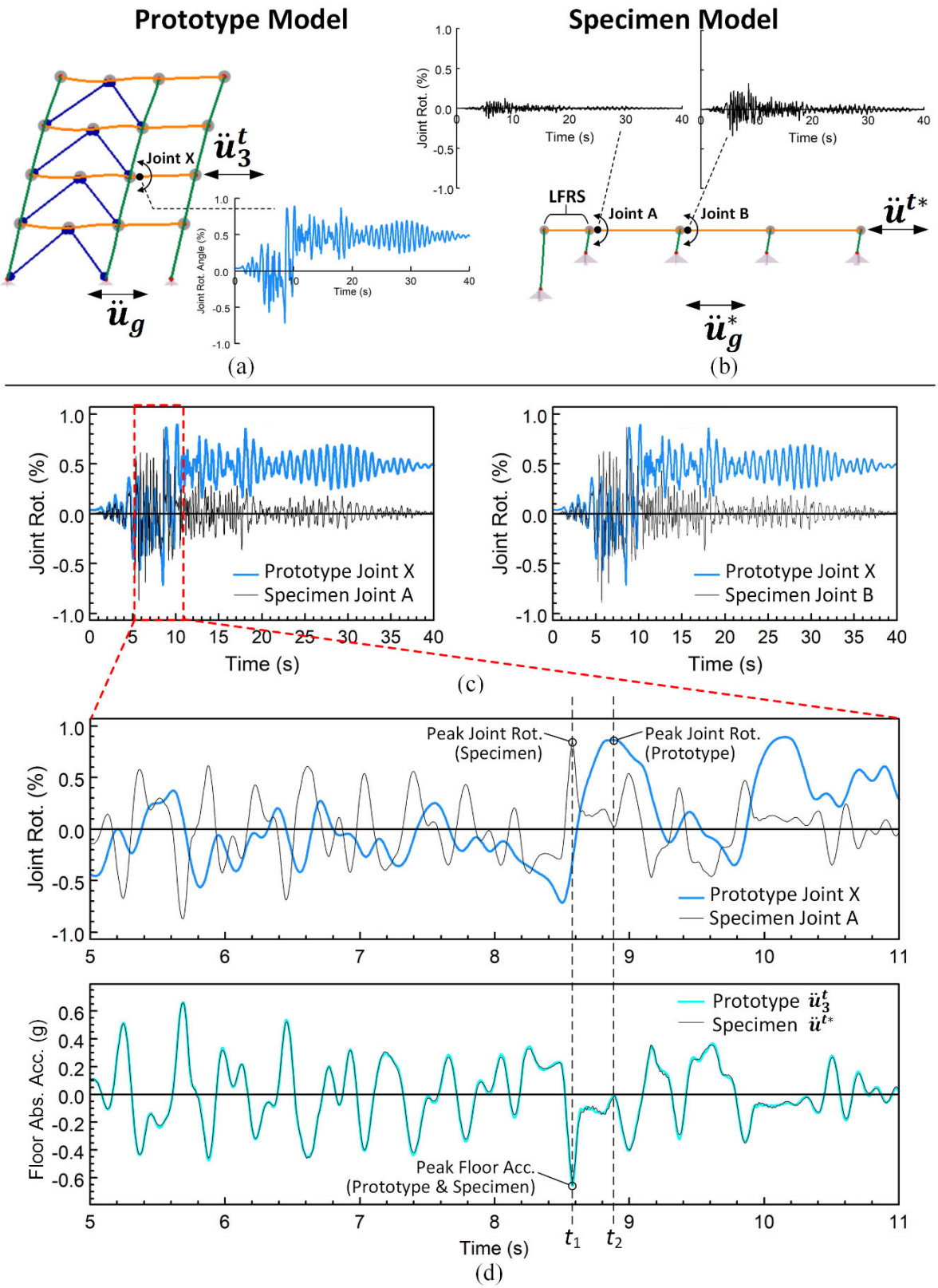

Figure 2.8 Comparison between (a) Prototype and (b) Revised Specimen Models, (c) Collector Connection Rotations, and (d) Floor Accelerations

3. PHASE 1 TEST PROGRAM

3.1 General

In Phase 1 test program, a single-story test building was tested at the NHERI@UCSD Large High Performance Outdoor Shake Table (LHPOST) by using the proposed floor acceleration simulation testing methodology as introduced in Chapter 2. Three floor acceleration simulation tests were performed to excite the testing building to reproduce the 5^{th} floor acceleration responses of a prototype 12-story building structure under the earthquakes with intensities at 20%, 50%, 100% of design earthquake level, respectively.

The main objective of the Phase 1 test program is to investigate the load path of the inertial forces among the composite floor diaphragm system in steel buildings and investigate the seismic behavior of steel collectors. This chapter describes the testing program including specimen design test setup and instrumentation plan. The associated test results are presented in Chapter 4, while the implications and interpretations of the test results along with numerical simulation results are presented in Chapter 5.

3.2 Test Specimen and Setup

3.2.1 Test Building

For Phase 1 test program, a 0.5-scale one-story test building with a composite floor slab was designed to simulate the earthquake-induced acceleration time-history response of any floor of a prototype multi-story building such that a realistic inertial force transfer mechanism could be reproduced in the floor diaphragm system of the test building. Figure 3.1 though Figure 3.10 show the important information of the Phase 1 test building. For the complete design drawings for the test building, refer to Appendix A.

As shown in Figure 3.1(a), the floor plan of the single-story test building was 38 feet long and 18 feet wide. The composite slab, made with 2-in. concrete over $1^1/_2$-in. metal deck, extends beyond the beam centerlines around the perimeter of the building by one foot. In the longitudinal (West-East) direction, which was the direction of shaking, there were two 14-ft long bays, one 5-ft long bay, and one 5-ft long cantilever span. Two longitudinal frames, called Frame N and Frame S [see Figure 3.1(b)], were relatively located at the north and south sides of the specimen. Two W12×170 cantilever columns (on Column Line 1) at the west end of the building constituted the lateral force-resisting system (LFRS) in the longitudinal direction. The remaining six W8×40 columns (on Column Lines 1, 2, and 3) served as the gravity columns. To resist the shaking in the longitudinal direction, the edge beams running along Column Lines N and S served as the collectors, while the edge beams at the west and east sides of the floor plan functioned as the diaphragm chords. The north half of the metal deck was oriented to be parallel to collectors, while the south half was perpendicular to the collectors. On each collector line, the four collectors from west to east are designated "Collector 1", "Collector 2", "Collector 3", and "Collector 4", respectively. The 14-ft long Collectors 1 and 2 were made of W14×30 shape, The 5-ft long Collectors 3 and 4, the two chords, and the remaining floor beams were made of W14×26 shape. In the transverse direction of the specimen, four single-bay chevron braced frames [see Figure 3.1(c)] were employed on Column Lines 1, 2, 3, and 4 to take out the torsional action and the translational motion in the transverse direction from the 1st mode of the structure.

For the test building, all the W-shape members were made of A992 steel. All the braces were made with long leg back-to-back A36 double angle section 2L5×3×$^3/_8$. All the plates, including continuity plates, stiffeners, and gusset plates, were made of A572 Gr. 50 steel. For the composite slab, the 20-ga. thick, $1^1/_2$-in. deep Verco PLB-36 deck was used and the fill was lightweight

concrete with a specified compressive strength, f_c' = 4 ksi. The edge form L11$^1/_2$″×3$^1/_2$″×10 ga. was employed for the 1-ft slab overhang. The wire mesh 6×6-W1.4×W1.4 (10 ga.) was placed in the concrete slab. Headed studs with a $^1/_2$-in. diameter were placed on the beams (collectors, chords and floor beams) at a center-to-center spacing of 6 in. For the collector-to-column connections, beam-to-column connections, beam-to-beam connections, and gusset plate connections, all the connection bolts were pre-tensioned by using $^5/_8$″-diameter A325 T.C. bolts.

Figure 3.1(b) shows the elevation of the longitudinal frames (Frames S and N). For each longitudinal frame, the cantilever column (Columns S1 or N1) at the west end of the frame served as the LFRS. The cantilever column was embedded into a 3′ tall reinforced concrete (RC) footing (designated as RC Footing 1), which was mounted to the shake table and provided a fixed-base condition for the steel column. The remaining gravity columns were pin supported. A 4′-3″ tall RC footing (designated as RC footings 2 and 3), serving as a spacer, was placed underneath the pin support of each gravity column. The story height of LFRS (from the top of RC footing 1 to the beam center line) was 8-ft, while the story height of gravity frame (from the pin-support to the beam center line) was 6′-4″. A shorter story height for the gravity frame was intentionally used to increase the rotation of the collector-to-column collections. It is noted that the cantilever column, which is the type of LFRS occupying the least floor area, was selected to make the LFRS for the test building to accommodate the longest span for the collectors. Since Collectors 1 and 2, on the two 14-ft spans (Spans 1 and 2, respectively), are the main subject of this research. The Collectors 3 and 4, on the two 5-ft spans (Spans 3 and 4, respectively) and the slab over these two spans were constructed to carry more added weights such that a higher inertial force demand can be delivered into Collectors 1 and 2. In each longitudinal frame, a diagonal double-angle brace was employed to support the cantilever span (Span 4).

As the inertial force dragged into the collectors and then transmitted to the LFRS, the axial force demands in the collectors and their connections increased gradually from east to west of the test building. The closer to LFRS the collector is located, the higher the axial forced demand is. Hence, three types of collector-to-column connection detail, which are commonly used in the U.S. practice, were employed. Figure 3.2 and Figure 3.3 show the three connections details used in Frame S and N, respectively. For the collector-to-column connections at the cantilever columns (Column S1 and N1), the all-flange weld (AFW) detail [see Figure 3.2(a) and Figure 3.3(a)] was used. In addition to the bolted connection between shear tab and collector web, complete-joint-penetration (CJP) groove welds were used for the top and bottom flanges of the collector. The weld access hole per AWS D1.1/D1.1 (AWS 2015) was employed, and the steel backings was not removed for each flange. Continuity plates were installed in the panel zone at the elevations aligned up with the collector top and bottom flanges. Note that the continuity plates were welded to the column flanges and column web by using CJP and double fillet welds, respectively.

For the collector-to-column connections at the gravity columns on Column Line 2 (Columns S2 or N2), the top flange weld (TFW) detail [see Figure 3.2(b) and Figure 3.3(b)] was employed. In addition to the bolted web, only the collector top flange was connected to the column by using CJP weld. In the panel zone, the continuity plates were only installed at the elevation aligned with the collector top flanges. Note that the welding details used for the flange welds and continuity plates in AFW connection were adopted for TFW connections. In addition, a horizontal stiffener was installed underneath the extended shear tab connecting the transverse beam to the column web. The stiffener was connected to the column flanges by using double fillet welds, while a gap was left between the stiffener and the column web.

Lastly, for the remaining collector-to-column connections at the gravity columns (Columns S3, N3, S4, and N4) on Column Lines 3 and 4, the bolted-web (BW) connection detail, actually a shear tab connection, was used [see Figure 3.2(c) and Figure 3.3(c)]. The shear tabs were welded to the column flange by using double fillet weld. With a $^1/_2$-in. beam setback, five $^5/_8$″-diameter A325 T.C. bolts with a 2″-spacing and $1^1/_4$″-edge distances were used for each shear tab connection. Note that similar five-bolt shear tab connections were used for AFW and TFW connections as well. However, the center of the shear tab connection was aligned with the steel collector center line for BW connections, while the shear tabs in AFW and TFW connections were located at an elevation resulting in the topmost bolt $2^7/_8$ inches below the top face of the collector. For BW connections, no continuity plate was installed in the panel zone. For the transverse beam-to-column connection, a pair of horizontal stiffeners were welded to the column flanges and relatively placed above and below the extended shear tab. A gap was left between each stiffener and the column web.

Figure 3.4(a) and Figure 3.4(b) show the composite cross sections for the collectors in Frames S and N, respectively. Figure 3.5 and Figure 3.6 show the details of the transverse beam-to-column connections and the beam-to-beam connections, respectively. For each of these connections, an extended shear tab connection was used. Figure 3.7 shows the details of the pin-support for the gravity columns. For each W8×40 gravity column, a $^3/_4$″-thick base plate was welded to the column bottom end and an 8″-long double-angle shape, 2L6×6×$^3/_4$, was bolted to the bottom side of the column base plate. With $1^1/_{16}$″-diameter bolt holes, a 1″-diameter A325 bolt served as the “pin” to connect the double-angle to the stem of an inverted T-shaped fixture built up from 1″-thick plates. Figure 3.8 shows the details of the 3′-tall RC footing, designated as RC footing 1, for the cantilever columns. The footing was made of normal weight concrete with a specified compressive strength, f_c' = 8 ksi and a steel cage formed by #6 and #4 rebars respectively

oriented in the longitudinal and transverse directions. The W12×170 column was embedded into the RC footing with an embedment length of 2′-6″. With four $^{7}/_{8}$″-diameter thread rods, a $^{3}/_{4}$″-thick column base plate was welded to the column for positioning the column before pouring of the concrete. To increase the rigidity and strength of the embedded column base connection, two 1′-7″ long W10×60 beam segments were welded to the column flanges and stuck out horizontally at the mid-height of footing. In addition, one hundred $^{3}/_{4}$″-diameter headed studs were welded to the steel column and beam segments for each footing. Figure 3.9 shows two types of 4′-3″ tall RC footings that served as the spacers underneath the gravity columns. Figure 3.9(a) shows the footing, named RC footing 2, for the gravity columns on Column Lines 2 and 3, while Figure 3.9(b) shows the footing, named RC footing 3, for the gravity columns on Column Line 4. These footings were made of normal weight concrete with f_c' = 5 ksi and a steel cage formed by #6 and #4 rebars respectively oriented in the longitudinal and transverse directions of the test frame.

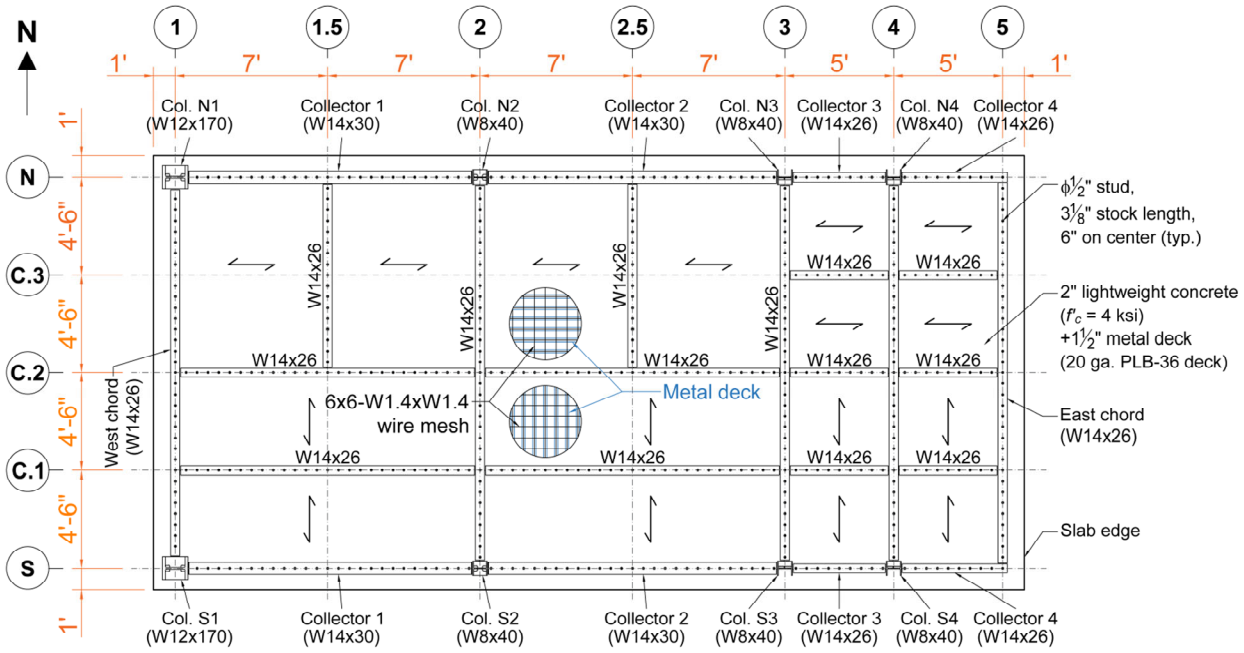

(a) Floor Plan

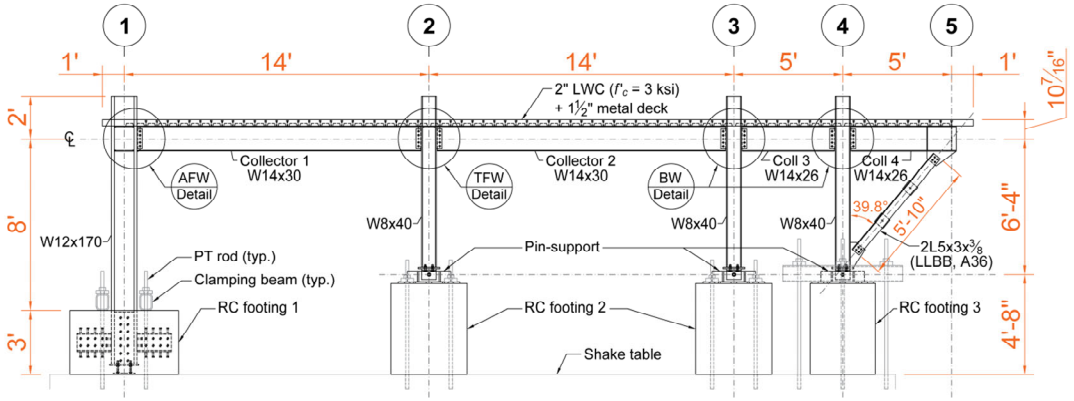

(b) Longitudinal Frame Elevation (Frame S)

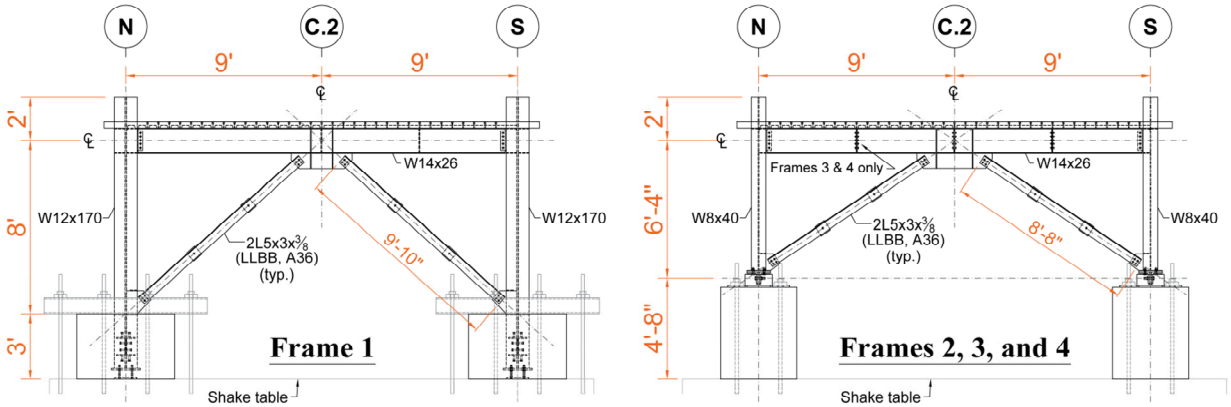

(c) Transverse Frame Elevations

Figure 3.1 Phase 1 Test Building: Overview

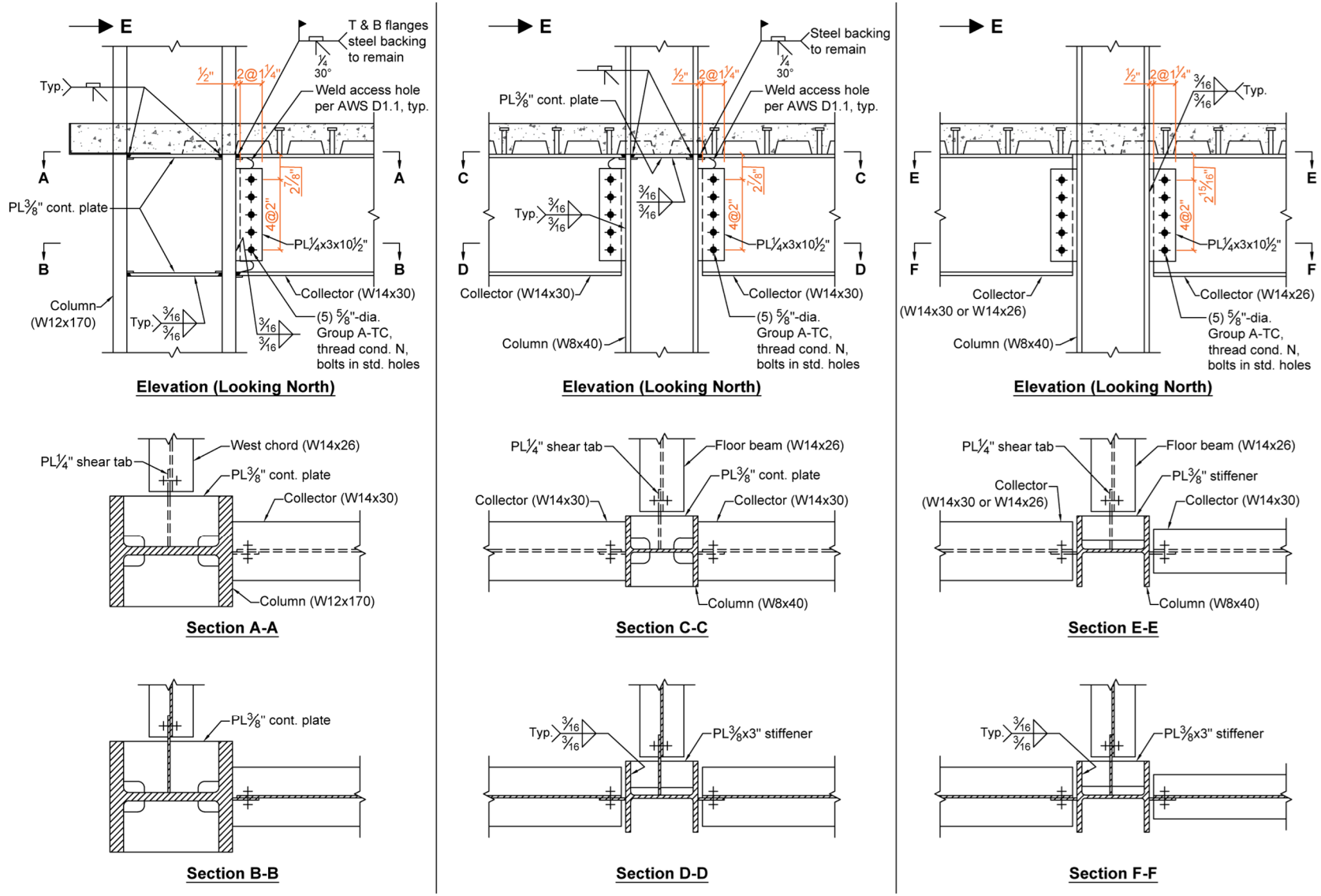

(a) All Flange Weld (AFW) (b) Top Flange Weld (TFW) (c) Bolted Web (BW)

Figure 3.2 Phase 1 Test Building: Collector-to-Column Connections in Frame S (Deck Perpendicular to Collectors)

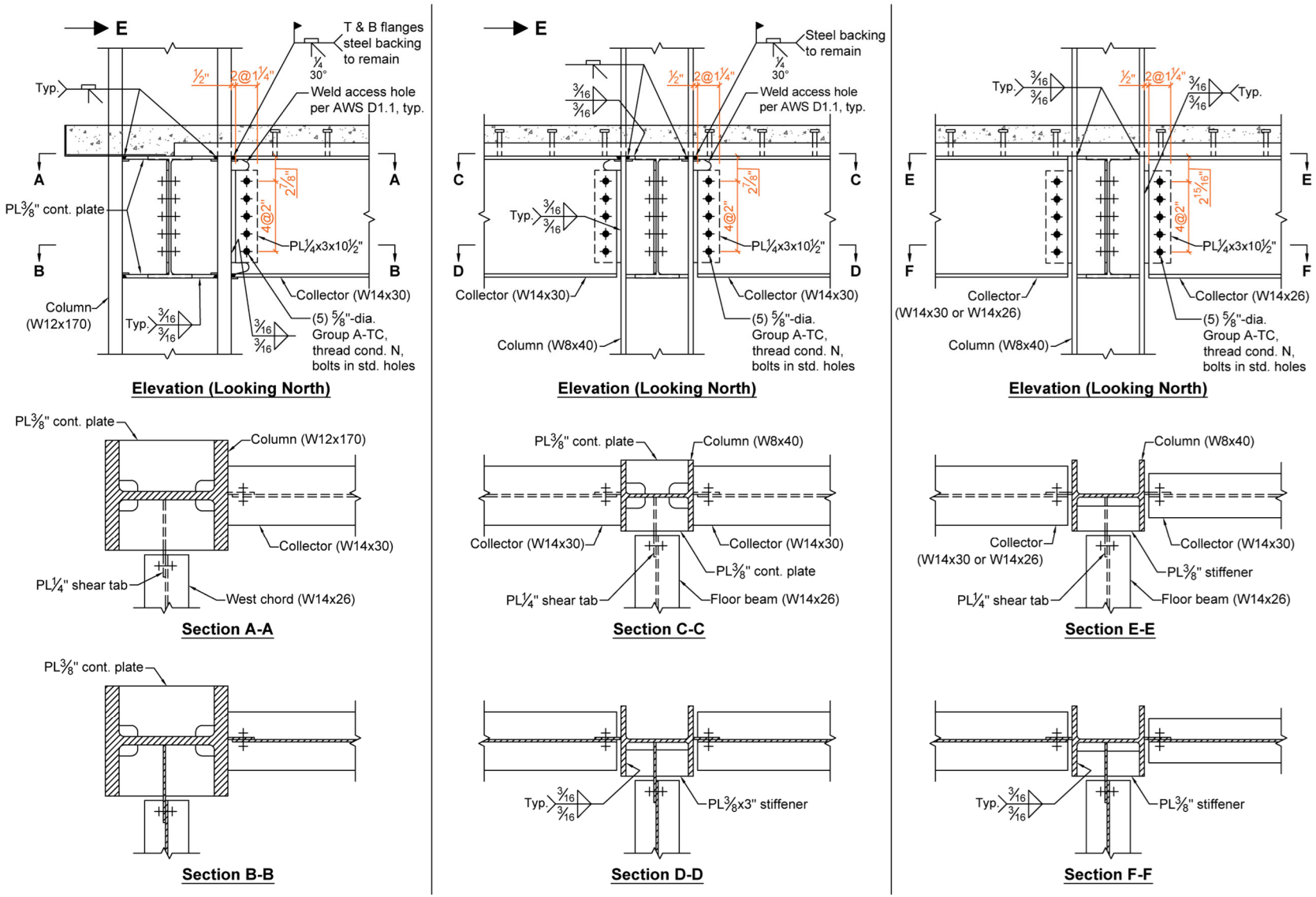

(a) All Flange Weld (AFW) (b) Top Flange Weld (TFW) (c) Bolted Web (BW)

Figure 3.3 Phase 1 Test Building: Collector-to-Column Connections in Frame N (Deck Parallel to Collectors)

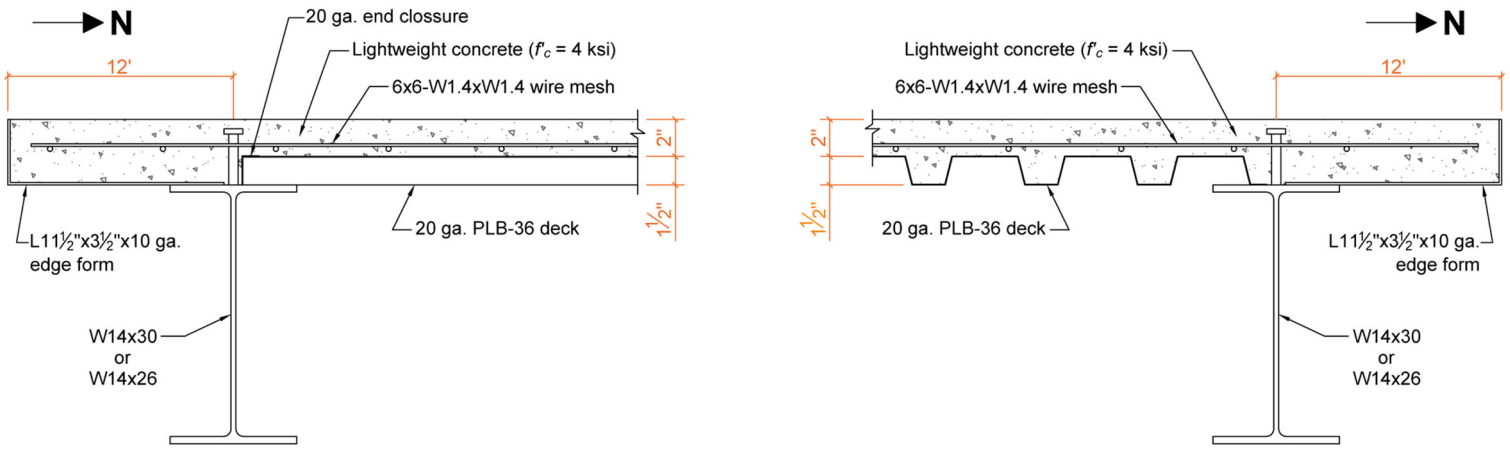

(a) Frame S (b) Frame N

Figure 3.4 Phase 1 Test Building: Composite Cross Sections of Collectors

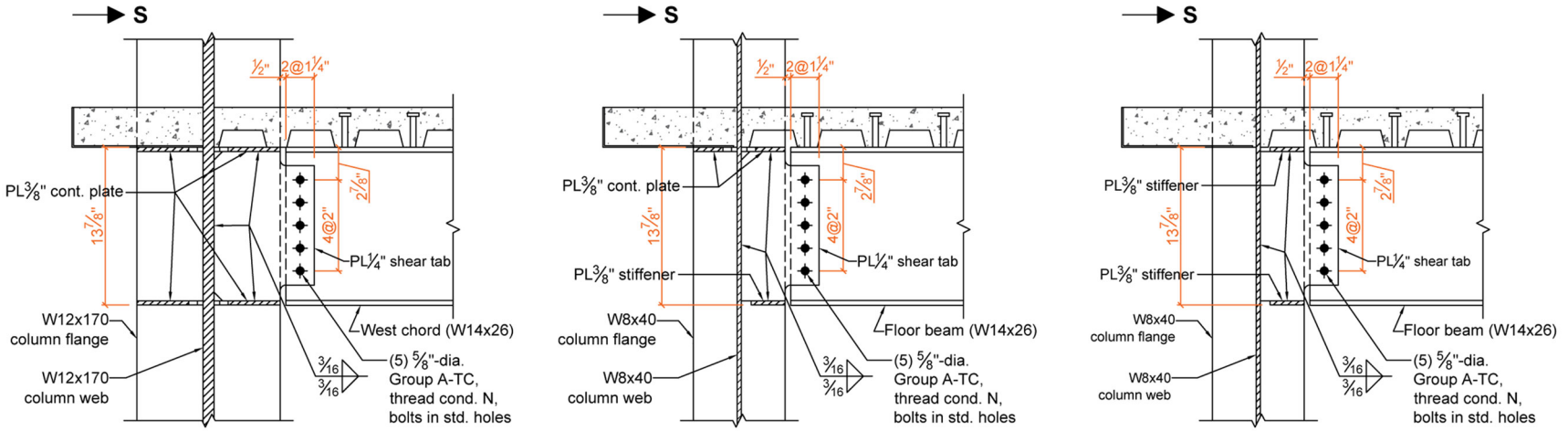

(a) Frame 1 (b) Frame 2 (c) Frames 3 and 4

Figure 3.5 Phase 1 Test Building: Transverse Beam-to-Column Connections

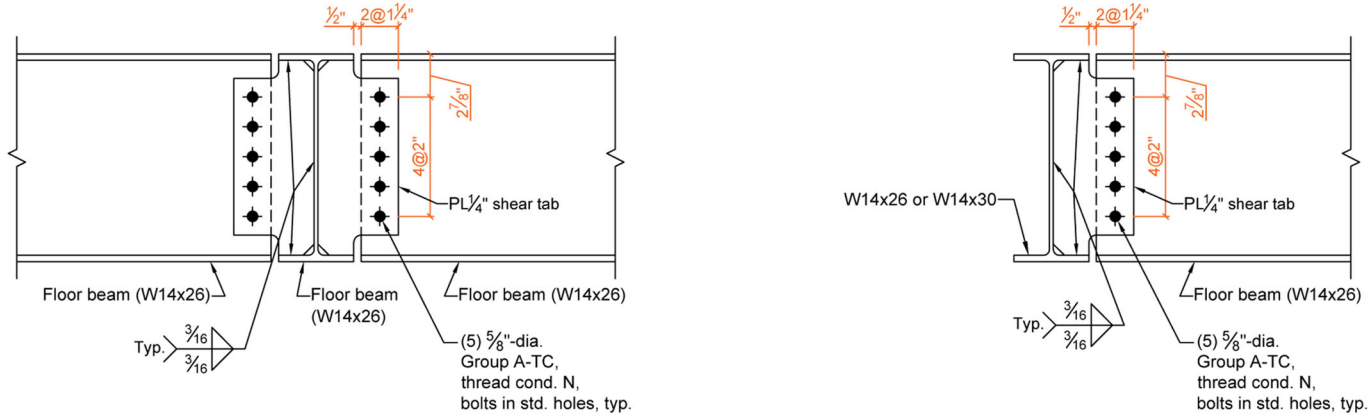

(a) Double-sided

(b) Single-sided

Figure 3.6 Phase 1 Test Building: Beam-to-Beam Connections

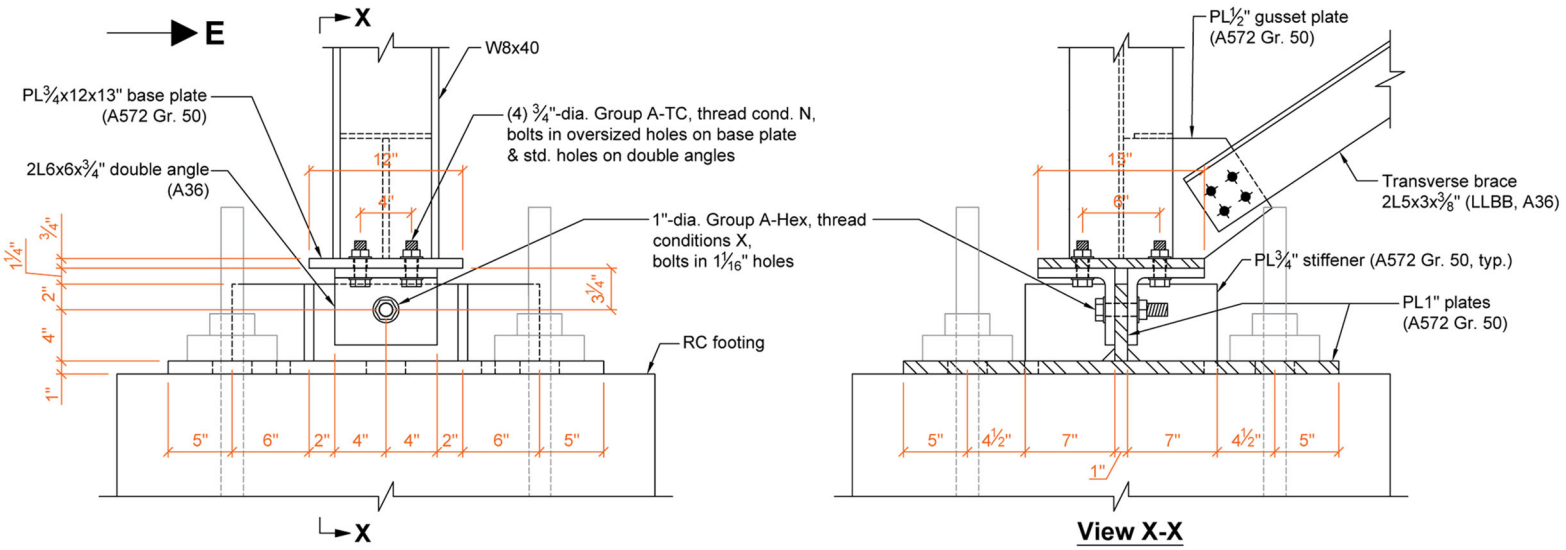

Figure 3.7 Phase 1 Test Building: Pin-Support

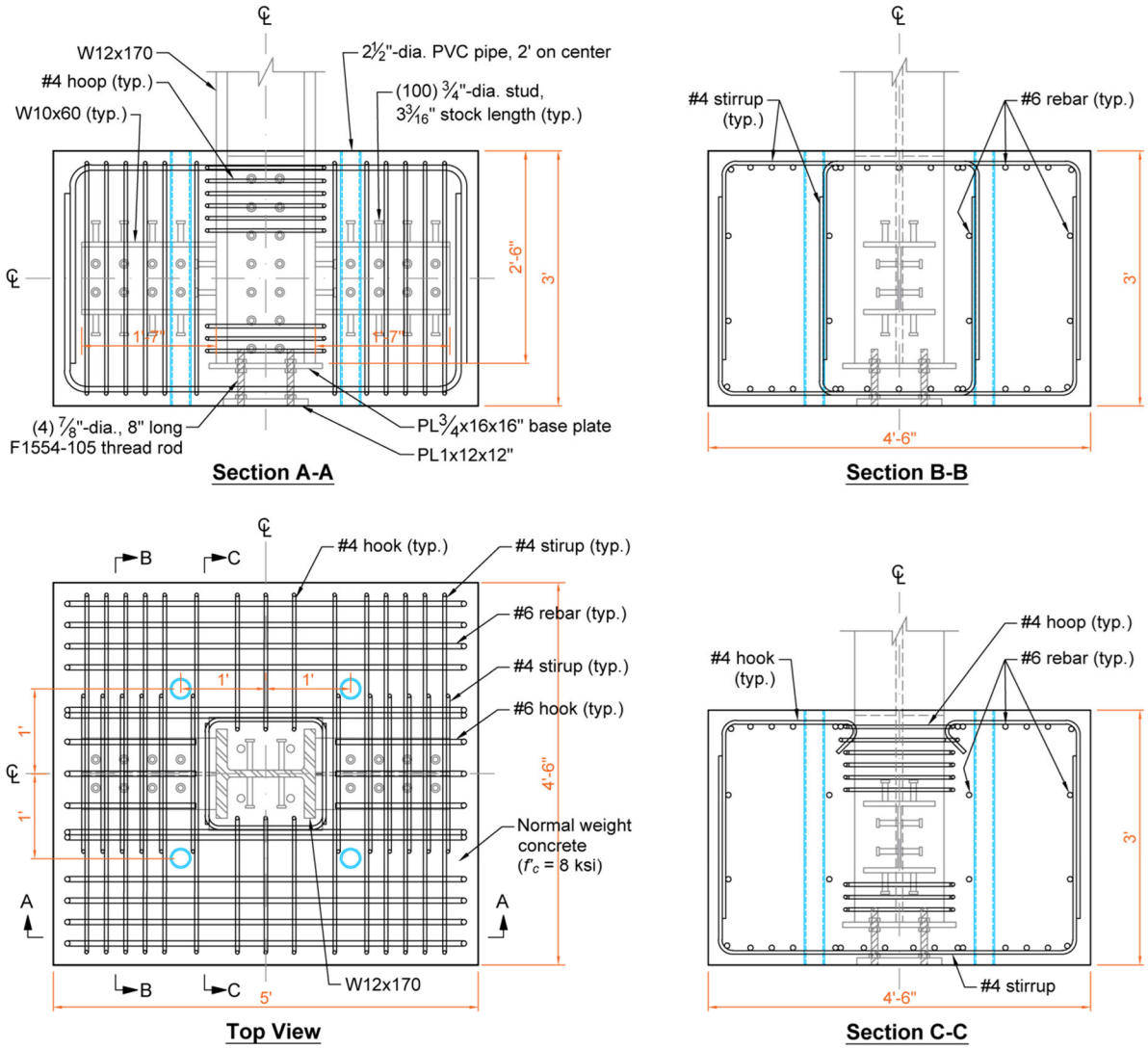

Figure 3.8 Phase 1 Test Building: RC Footing 1 (for Cantilever Columns)

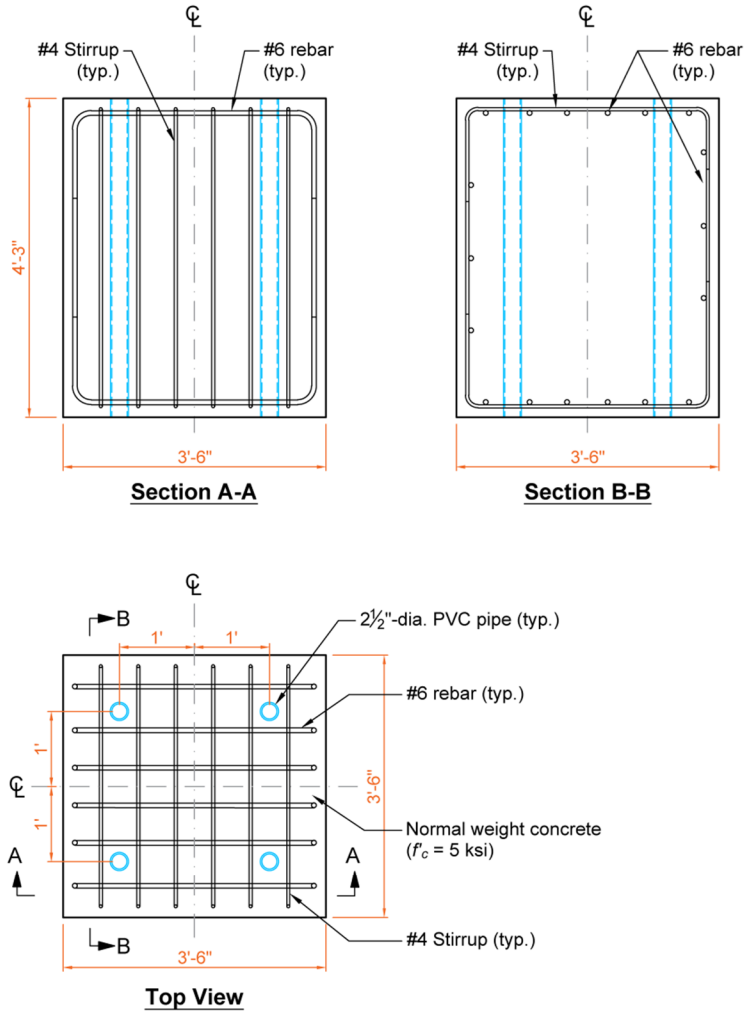

(a) RC Footing 2

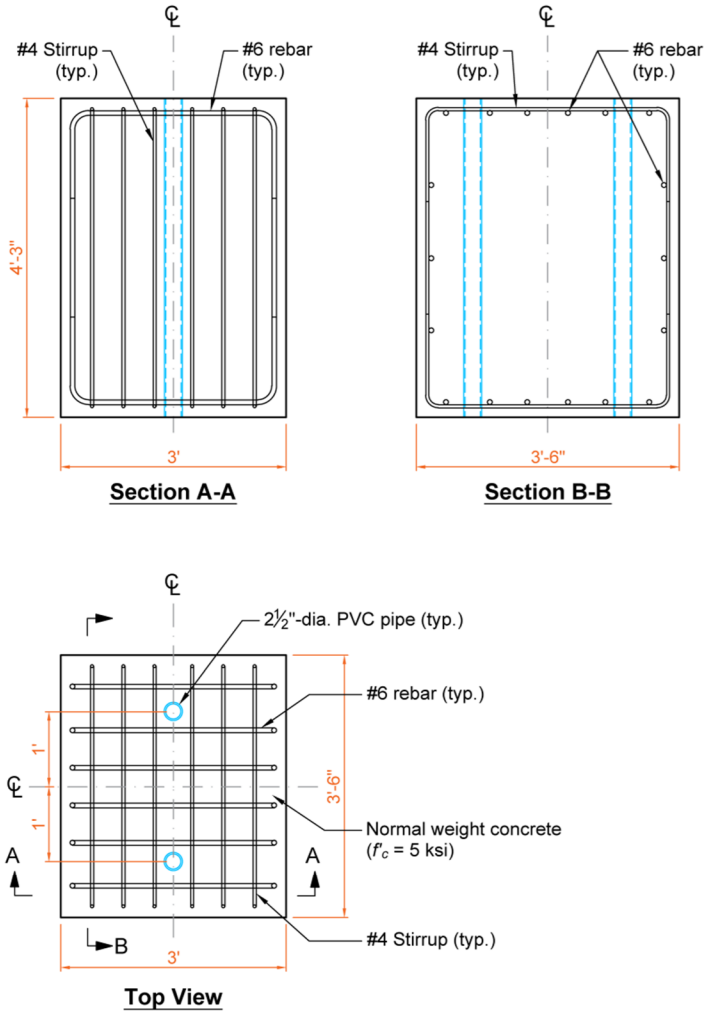

(b) RC Footing 3

Figure 3.9 Phase 1 Test Building: RC Footings 2 and 3 (for Gravity Columns)

Figure 3.10 Phase 1 Test Building (without Added Mass) Assembled on Shake Table

Figure 3.11 All Flange Weld (AFW) Connection

Figure 3.12 Top Flange Weld (TFW) Connections

Figure 3.13 Bolted Web (BW) Connections

Figure 3.14 Pin-support for Gravity Column

3.2.2 Test Setup

The test building was constructed on the NHERI@UCSD Large High Performance Outdoor Shake Table (LHPOST). Figure 3.18 demonstrates the procedures of construction of test building and setup. Figure 3.15 and Figure 3.19 show the overview of Phase 1 test setup. Eight RC footings were mounted to the shake table through $1^{3}/_{4}$″-dia. DYWIDAG post-tensioning (PT) rods, tensioned to 200 kips each. For each of the two cantilever column footings (designated as RC footing 1), as shown in Figure 3.15 (c), a pair of clamping beams made from HSS9×7×$^{5}/_{8}$ were placed on the top of footing to accommodate four PT rods outside the footing area, resulting in eight PT rods in total used for each footing. For each of the four footings designated as RC footing 2, four PT rods were used to anchor the footing together with the steel pin-support. For each of the four gravity column footings designated as RC footing 2, four PT rods were used to anchor the footing together with a steel pin-support on the footing. For each of the two gravity column footings designated as RC footing 3, a pair of clamping beams made from HSS9×7×$^{5}/_{8}$ were placed on the top of a steel pin-support on the footing to accommodate four PT rods outside the footing area, resulting in five PT rods in total used for mounting the footing together with the pin-support.

Several RC blocks, serving as the added mass, were attached onto the composite slab through $1^{3}/_{8}$″-dia. DYWIDAG post-tensioning (PT) rods, tensioned to 150 kips each. As shown in Figure 3.15(a) and (b), the four groups of added mass blocks relatively spanned over the four spans (named Spans 1, 2, 3, and 4, relatively, from west to east) of the testing building in the longitudinal direction. In the transverse direction, the added masses were concentrated at the central region of the slab so that the RC blocks were located away from the collectors and would not markedly affect the stiffness and strength of the collectors.

Figure 3.16 shows the detailed dimensions and locations of the added mass blocks. Figure 3.17 shows the details for clamping the RC blocks onto the slab. To reduce the loss of PT forces during the stressing of the rods, a coupler made from HSS6.000×0.500 was used to increase the length of the stressed segment of each rod. Two types of bearing plates (denoted as Types 1 and 2 in Figure 3.17) were placed underneath at the PT locations to spread out the bearing forces acting on the bottom of slab, preventing the crush of the slab. The total added weights (designated as Added Weights 1, 2, 3, and 4, respectively), including each group of RC blocks together with the associated PT rods, nuts, washers, and bearing plates, on Spans 1, 2, 3, and 4 were 26.02 kips, 27.00 kips, 11.45 kips, and 16.12 kips, respectively.

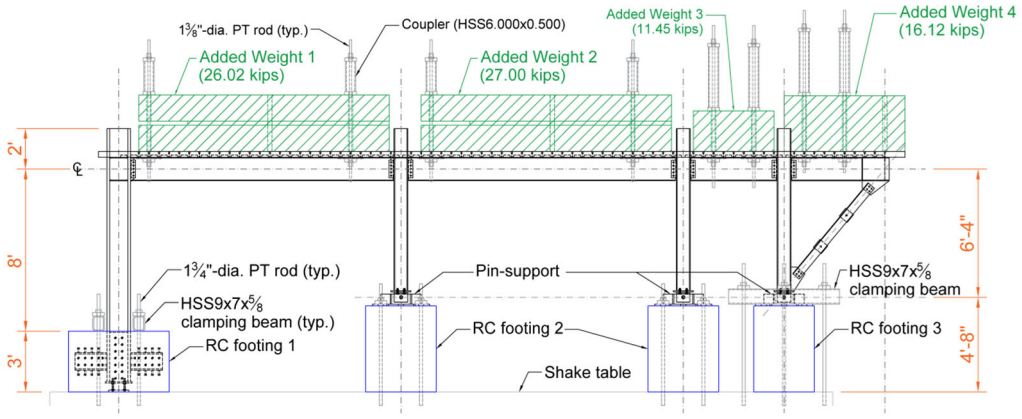

(a) Elevation View

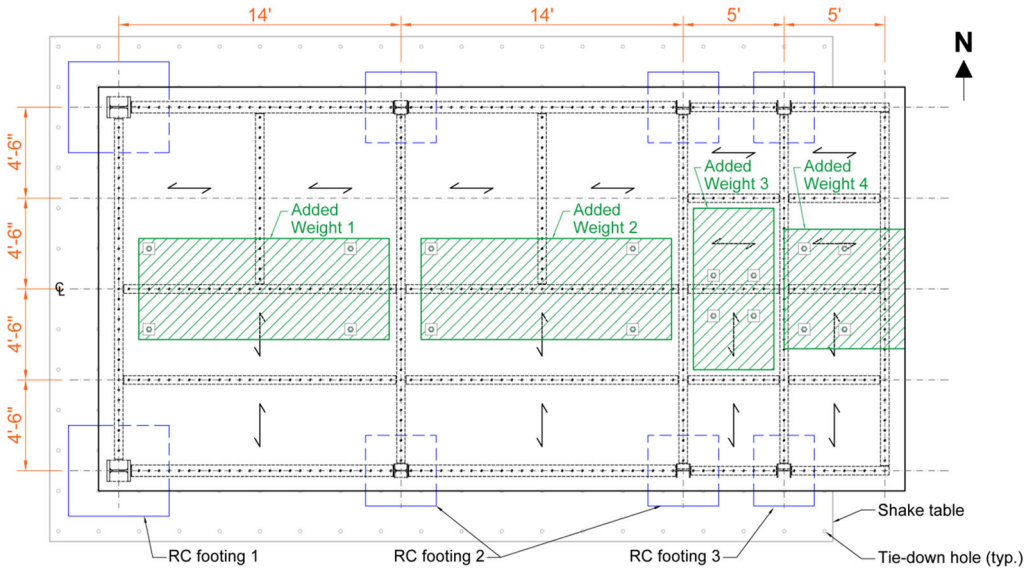

(b) Plan View of 2nd Floor Level

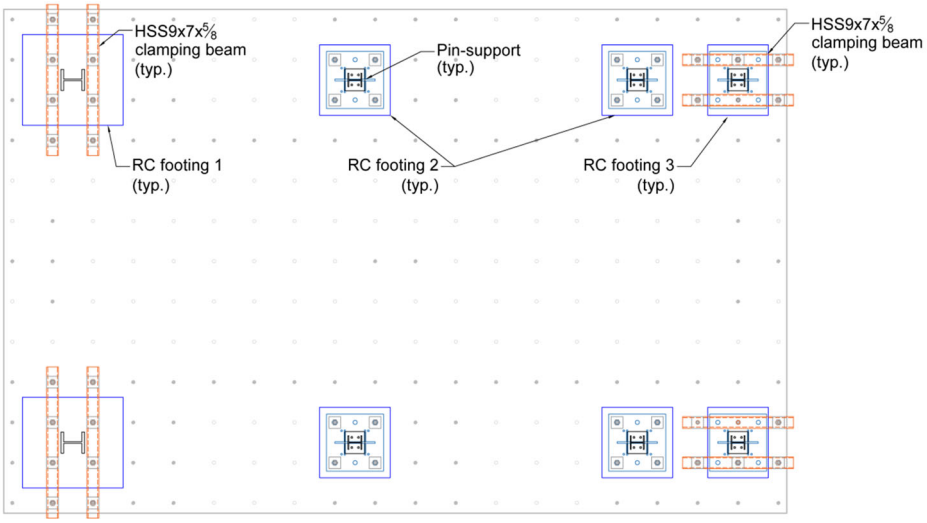

(c) Plan View of Ground Level

Figure 3.15 Phase 1 Test Setup

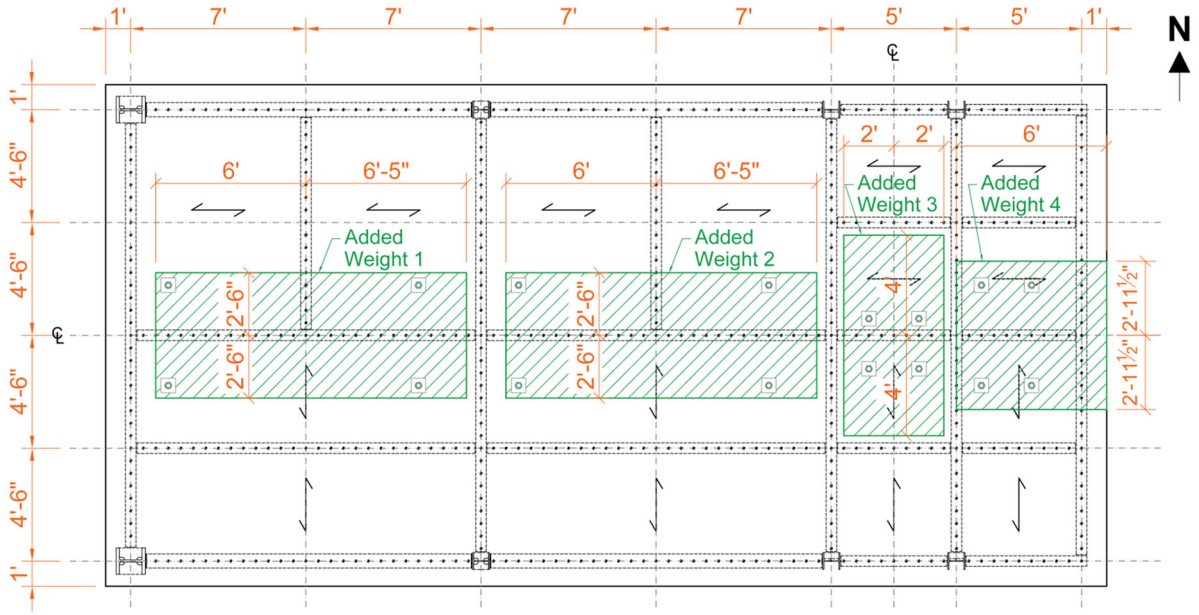

(a) Plan View

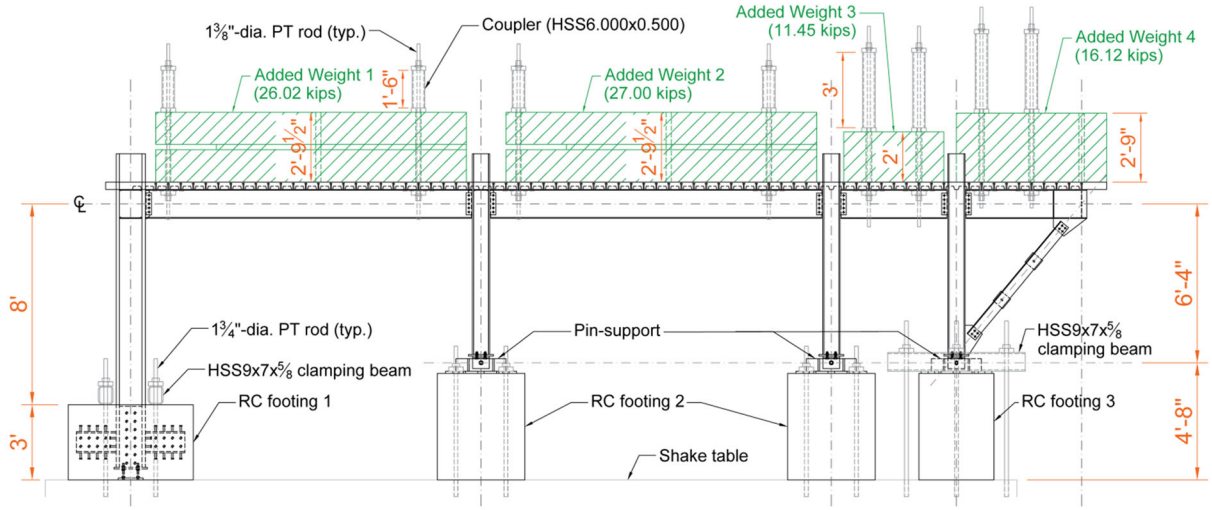

(b) Elevation View

Figure 3.16 Additional Weight Layout for Phase 1 Test

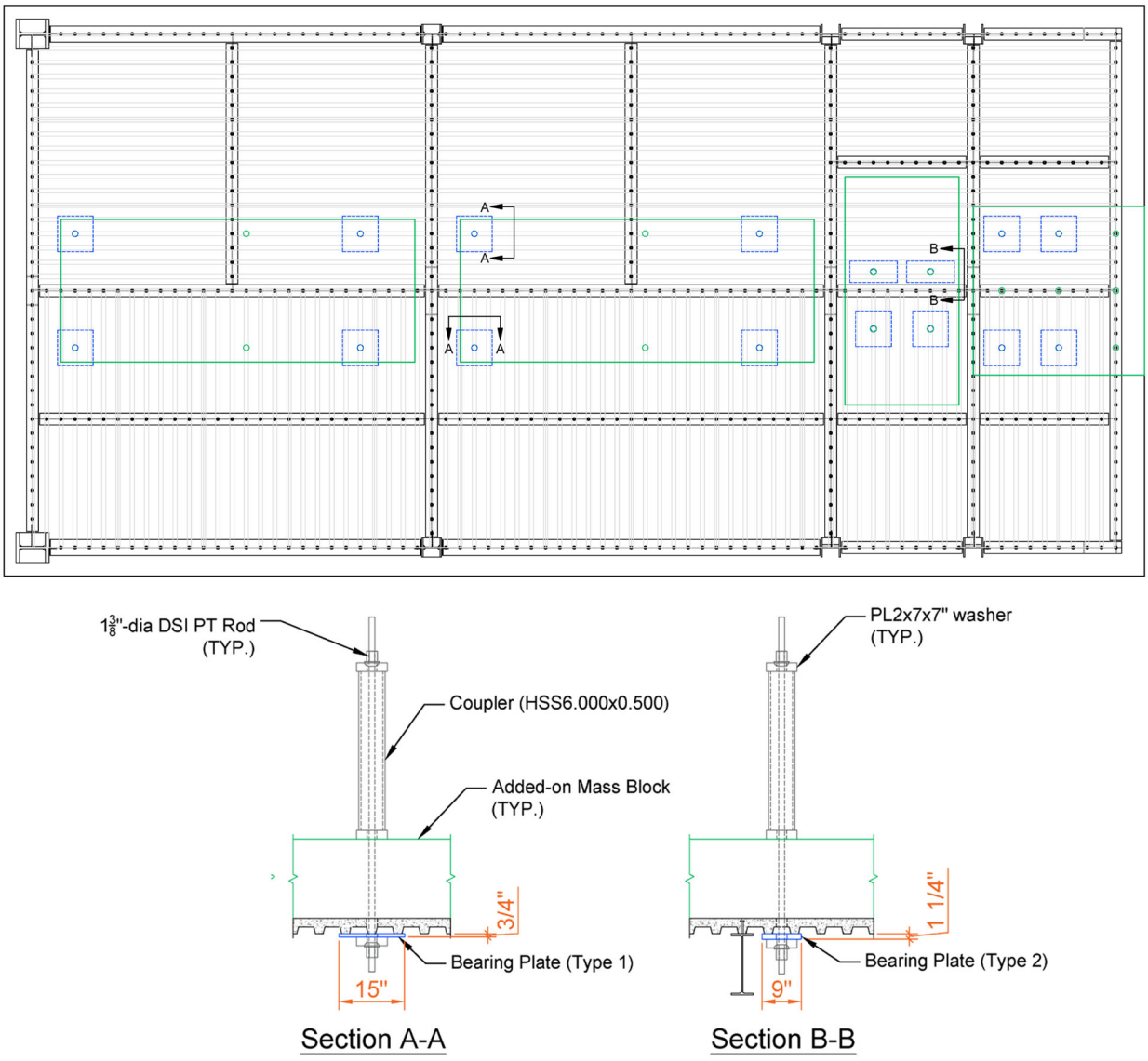

(a) Clamping Details

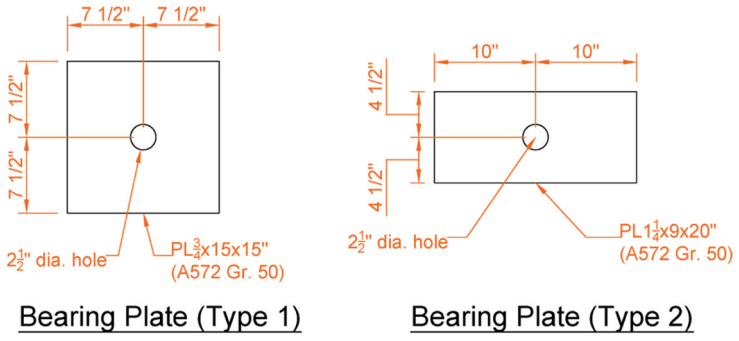

(b) Bearing Plates

Figure 3.17 Clamping of Additional Weight

(a) Construction of RC Footings 2 and 3

(b) Steel Cages and Formworks for Column 1

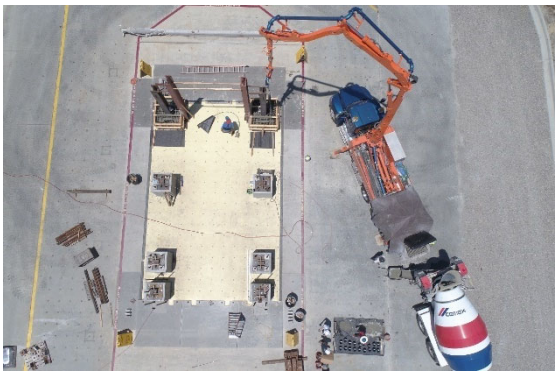

(c) Pouring Concrete Footings for Column 1

(d) Placement of Pin-supports for Gravity Columns

(e) Erection of Steel Frame

(f) Tensioning of Post-tensioning Rods

(g) Field Bolting and Field Welding

(h) UT Inspection and Welding Repair

Figure 3.18 Construction Test Building and Setup

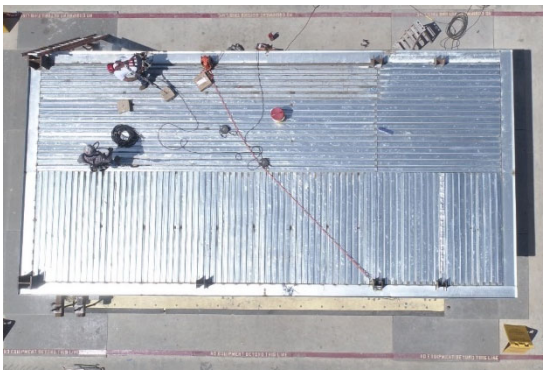

(i) Installation of Metal Deck

(j) Welding of Headed Anchor Stud

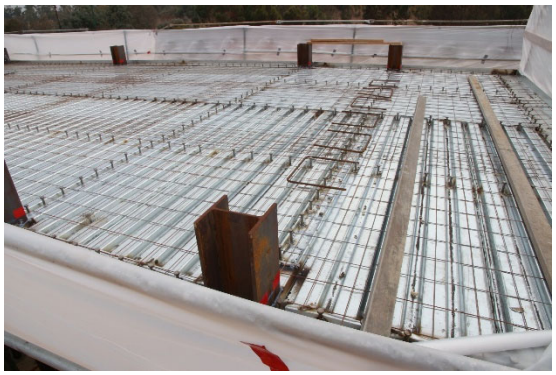

(k) Placement of Wire Mesh

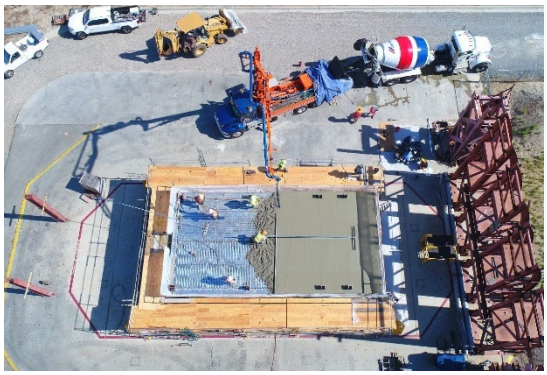

(l) Pouring of Concrete Slab

(m) Finishing for Concrete Slab

(n) Core Drilling of Concrete Slab

(o) Installation of Added Mass Blocks

Figure 3.18 Construction Test Building and Setup (continued)

Figure 3.19 Photos of Phase 1 Test Setup

3.2.3 Seismic Weight Calculations

To illustrating the calculations of seismic weights tributary to the composite slab floor (2nd floor) of the test building, the node and beam designations respectively shown in Figure 3.20 and Figure 3.21 are employed. Figure 3.20 also shows the weights from the columns, braces, and beam-to-beam connections are treated as nodal weights. The weights of the beams (steel collectors, chord, and floor beams shown in Figure 3.21) are considered as line weights. Figure 3.22 shows that the weights from the composite slab and added weights are simplified as area weights.

Two seismic weights are of interest in this research. The first one is the total seismic weight tributary to the 2nd floor, denoted as W_{2F}. which is used for seismic force determination in practice. As shown in Figure 3.23, W_{2F} includes the weights from the composite slab, added weights, steel beams, columns, double-angle braces, and the bolts and plates used for the connections. The second seismic weight of interest is that tributary to collector lines on the 2nd floor, denoted as W'_{2F}, which is used for the determination of the collector axial force demand. As shown in Figure 3.24, the weight sources of W'_{2F} are almost the same as those of W_{2F} except that the weights from the columns and the diagonal braces in the longitudinal frames are not included in W'_{2F} because the inertial forces generated from the masses of columns and longitudinal braces would not be transmitted into the collectors.

Table 3.1 shows the seismic weight calculation results for the seismic weight from six components. The considerations for the six components are summarized as follows:

(1) Concrete slab and metal deck

Based on the geometry of the composite slab profile, the slab can be divided into two regions: interior and exterior slabs. The interior slab was composed of corrugated metal deck, which was the 20-ga. thick, $1^1/_2$-in. deep Verco PLB-36 deck, and 2-in. thick lightweight concrete

above the deck. Based on the product catalog, the unit weight (per unit area) for the interior composite slab, denoted as $\overline{w_0}$, is 25.50 psf. In addition, the exterior slab, which was the 1-ft slab overhang, was made by using the edge form L11$^1/_2$″×3$^1/_2$″×10 ga. the area weight for the interior composite slab, denoted as $\overline{w_0^*}$, is 39.26 psf. See Table 3.1(a) for the weight calculation results on composite slab.

(2) Added weights

As shown in Figure 3.16, four groups of added mass blocks, were installed onto the composite slab. Together with the PT rods, couplers, washers, bearing plates used for installation of mass blocks, the total weights for the four added weight groups from west to east (denoted as Added Weights 1, 2, 3, and 4 in Figure 3.16) were W_{a1} = 25,965 lbs, W_{a2} = 26,945 lbs, W_{a3} = 11,245 lbs, and W_{a4} = 15,884 lbs, respectively. See Table 3.1(b) for the calculations of added weights.

(3) Steel columns

The seismic weight from the steel columns considers the part of the columns in the upper half of the story and the part extending out above the 2nd floor. It includes the weight from the continuity plates and stiffeners in the column panel zones. In addition, the shear tabs and the bolts used for the collector-to-column or beam-to-column connections are also considered as a part of the column weight. See Table 3.1(c) for the calculations of column weights. For numerical simulation, the calculated seismic weight tributary to each column is considered as a nodal load applied on the nodes marked by red circles in Figure 3.20.

(4) Steel beams

The seismic weight tributary to each steel beam (collector, chord, or floor beam) was calculated by multiplying a linear weight by the clear beam length. The linear weight includes the

beam self-weight and the headed studs spaced 6-in. on center on the beams. To avoid the double counting of the concrete slab weight at the shear stud locations, the weight of the shear studs was determined by a factor $n_w = 1 - \rho_c/\rho_s$, where ρ_c = 110 pcf and ρ_s = 490 pcf are the unit weight of the concrete and steel, respectively. See Table 3.1(d) for the weight calculation results on steel beams.

(5) Steel double-angle braces

The seismic weight from the steel double-angle braces considers the self-weight of the braces and the gusset plates connections in the upper half story. For inconvenience, the shear tabs, bolts, and stiffeners on the beams at the brace-to-beam intersections are included as well. For numerical simulation, these weights are lumped to the nodes at the brace-to-beam intersections, which are marked by blue circles in Figure 3.20, as nodal loads or nodal masses. See Table 3.1(e) for the weight calculation results on double-angle braces.

(6) Beam-to-beam connections

The seismic weight from the beam-to-beam joints considers the shear tabs and stiffeners at the brace-to-beam connections. For numerical simulation, these weights are lumped to the nodes at the beam-to-beam intersections, marked by orange circles in Figure 3.20, as nodal loads or nodal masses. See Table 3.1(e) for the weight calculation results on beam-to-beam joints.

As shown in Figure 3.22 the seismic weights from the composite slab and added mass can be simplified as uniform area load applied on the floor, which can be used to determine the lumped masses or weights for the nodes on the floors, such as the nodes in shown in Figure 3.20. Table 3.2 shows the calculations on these area loads. The area loads from the interior and exterior slabs are $\overline{w_0}$ = 25.5 psf and $\overline{w_0^*}$ = 39.6 psf, respectively. The area loads for four groups of added weights

(Added Weights 1, 2, 3, and 4, respectively) are $\overline{w_{a1}}$ = 418.23 psf, $\overline{w_{a2}}$ = 434.02 psf, $\overline{w_{a3}}$ = 351.39 psf, and $\overline{w_{a4}}$ = 447.43 psf, respectively.

Table 3.3 shows the summary of the seismic weight tributary to the 2nd floor. The total seismic weight for the seismic force determination is W_{2F} = 113.300 kips. The contributions from composite slab, added weights, steel beams, steel columns, double-angle braces, and beam-to-beam joints are 19.41%, 70.64%, 6.11%, 2.91%, 0.82%, and 0.10%, respectively. The total seismic weight tributary to collector lines is W'_{2F} = 109.873 kips. The contributions from composite slab, added weights, steel beams, double-angle braces, and beam-to-beam joints are 20.02%, 72.85%, 6.30%, 0.73%, and 0.10%, respectively.

To determine the collector axial force demand triggered by the floor acceleration, it requires the calculations of seismic weight tributary to each collector. Figure 3.24 illustrates that the seismic weight, W'_{Ni} or W'_{Si}, tributary to the *i*-th span of the north or south collector line, respectively. Also, the following relationship holds:

$$W'_{2F} = \sum_{i=1}^{4} W'_{Ni} + \sum_{i=1}^{4} W'_{Si} \tag{3.1}$$

For simplicity, it is assumed that seismic weight is uniformly distributed along the collector, so that the linear weight, w'_{Ni} or w'_{Si}, to the *i*-th span of the north or south collector line, respectively, can be determined from:

$$\begin{aligned} w'_{Ni} &= W'_{Ni}/L_i \\ w'_{Si} &= W'_{Si}/L_i \end{aligned} \tag{3.2}$$

where L_i is the *i*-th span length.

Table 3.4 and

Table 3.5 shows the calculations for seismic weights tributary to the north and south collector lines, respectively. Figure 3.25 demonstrates the variation of the linear seismic weight tributary to the collectors along the collector lines. Figure 3.26 shows that the inertial forces, F_I', on the slab triggered by a floor acceleration, a_{flr}, are transferred into the collectors through the shear forces between the slab and collectors. In practice, it is considered a rational approach to assume that these shear forces are uniformly distributed. Therefore, the shear forces, v_{Ni}' and v_{Si}', which are acting along the i-th span of north and south collector lines, respectively, can be determined from:

$$v_{Ni}' = w_{Ni}' \times \frac{a_{flr}}{g}$$
$$v_{Si}' = w_{Si}' \times \frac{a_{flr}}{g} \tag{3.3}$$

These shear forces can be used to compute the axial force demand in the collectors.

Table 3.1 Seismic Weights from Various Components Tributary to 2nd Floor

(a) Concrete Slab and Metal Deck

Item	Unit Weight (psf)		Width	Length	Area	Weight
	Concrete	Metal Deck	(ft)	(ft)	(ft^2)	(lbs)
Interior Slab	23.20	2.30	18	38	684	17442
Exterior Slab	32.08	7.18	1	116	116	4554
					Total	21996

(b) Added Weights

Added Weight No.	RC Block	1-3/8"-dia. PT Rod			HSS6.000×0.500			Washer		Bearing Plate 1		Bearing Plate 2		Total Weight
		Unit Wt.	Length	Qty	Unit Wt.	Length	Qty	Each Wt.	Qty	Each Wt.	Qty	Each Wt.	Qty	
	(lbs)	(lb/ft)	(ft)	-	(lbs/ft)	(ft)	-	(lbs)	-	(lbs)	-	(lbs)	-	(lbs)
1	25120	5.56	7	4	29.4	1.5	4	27.08	12	47.04	4	62.38	0	25965
2	26100	5.56	7	4	29.4	1.5	4	27.08	12	47.04	4	62.38	0	26945
3	10170	5.56	8	4	29.4	3	4	27.08	12	47.04	2	62.38	2	11245
4	14840	5.56	8	4	29.4	3	4	27.08	12	47.04	4	62.38	0	15884
													Total	80039

(c) Columns

Node No.	Column		Cont. Plate		Stiffener		Shear Tab 1		Shear Tab 2		Bolt		Total Weight
	Unit Wt.	Length	Each Wt.	Qty	Each Wt.	Qty	Each Wt.	Qty	Each Wt.	Qty	Each Wt.	Qty	
	(plf)	(in.)	(lbs)	-	(lbs)	-	(lbs)	-	(lbs)	-	(lbs)	-	(lbs)
A1	170	72	6.76	4	0	0	2.24	1	8.30	1	0.353	10	1061
A9	170	72	6.76	4	0	0	2.24	1	8.30	1	0.353	10	1061
G1	40	52	2.95	2	2.28	1	2.24	2	6.43	1	0.353	15	198
G9	40	52	2.95	2	2.28	1	2.24	2	6.43	1	0.353	15	198
M1	40	52	0	0	2.28	2	2.24	2	6.43	1	0.353	15	194
M9	40	52	0	0	2.28	2	2.24	2	6.43	1	0.353	15	194
O1	40	52	0	0	2.28	2	2.24	2	6.43	1	0.353	15	194
O9	40	52	0	0	2.28	2	2.24	2	6.43	1	0.353	15	194
												Total	3294

Table 3.1 Seismic Weights from Various Components Tributary to 2nd Floor (continued)

(d) Collectors and Floor Beams

Beam Group No.	Beam No.	Beam		Headed Stud Unit Wt.	Length	Each Beam Wt.	Qty	Weight
		Shape	Unit Wt.					
			(lb/ft)	(lb/ft)	in.	(lbs)	-	(lbs)
1	AG1, AG9	W14×30	30	0.35	156.875	396.8	2	794
2	GM1, GM9	W14×30	30	0.35	159.250	402.8	2	806
3	MO1, MO9	W14×26	26	0.35	50.750	111.4	2	223
4	OQ1, OQ9	W14×26	26	0.35	57.890	127.1	2	254
5	AG5, AG7, GM5, GM7	W14×26	26	0.35	161.970	355.7	4	1423
6	MO3, MO5, MO7, OQ3, OQ5, OQ7	W14×26	26	0.35	53.970	118.5	6	711
7	A19	W14×26	26	0.35	202.400	444.4	1	444
8	G19, M19, Q19	W14×26	26	0.35	206.930	454.4	3	1363
9	Q19	W14×26	26	0.35	209.970	461.1	1	461
10	D15, J15	W14×26	26	0.35	101.120	222.0	2	444
							Total	6923

(e) Double-Angle Braces

Node No.	Double-Angle Brace			Gusset Plate		Stitch Plate		Shear Tab		Stiffener 1		Stiffener 2		Bolt 1		Bolt 2		Total Weight
	Area	Half-Length	Qty	Each Wt.	Qty	Each Wt.	Qty	Each Wt.	Qty	Each Wt.	Qty	Each Wt.	Qty	Each Wt.	Qty	Each Wt.	Qty	
	(in^2)	(in.)	-	(lbs)	-	(lbs)	-	(lbs)	-	(lbs)	-	(lbs)	-	(lbs)	-	(lbs)	-	(lbs)
A5	5.72	59	2	37.36	1	5.13	1	5.00	1	3.32	4	2.14	4	0.353	5	0.417	10	214
G5	5.72	52	2	47.13	1	5.13	1	5.00	2	3.32	4	2.14	4	0.353	10	0.417	10	196
M5	5.72	52	2	47.13	1	5.13	1	5.00	2	3.32	4	2.14	4	0.353	10	0.417	10	196
O5	5.72	52	2	47.13	1	5.13	1	5.00	2	3.32	4	2.14	4	0.353	10	0.417	10	196
Q1	5.72	35	1	10.91	1	5.13	1	5.00	1	3.32	2	0	0	0.353	5	0.417	5	66
Q9	5.72	35	1	10.91	1	5.13	1	5.00	1	3.32	2	0	0	0.353	5	0.417	5	66
																	Total	933

Table 3.1 Seismic Weights from Various Components Tributary to 2nd Floor (continued)

(f) Beam-to-Beam Connections

Node	Shear Tab		Bolt		Total Weight
	Each Wt.	Qty	Each Wt.	Qty	
	(lbs)	-	(lbs)	-	(lbs)
A7	5.00	1	0.353	5	6.77
D1	5.00	1	0.353	5	6.77
D5	5.00	1	0.353	5	6.77
G7	5.00	2	0.353	10	13.53
J1	5.00	1	0.353	5	6.77
J5	5.00	1	0.353	5	6.77
M3	5.00	1	0.353	5	6.77
M7	5.00	2	0.353	10	13.53
O3	5.00	2	0.353	10	13.53
O7	5.00	2	0.353	10	13.53
Q3	5.00	1	0.353	5	6.77
Q5	5.00	1	0.353	5	6.77
Q7	5.00	1	0.353	5	6.77
				Total	115

Table 3.2 Area Load from Slab and Added Weights

Item	Area Occupied			Total Weight (lbs)	Area Load, $\overline{w}$ (psf)
	Width (in.)	Length (in.)	Area (ft^2)		
Interior Slab	216	456	684	17,442	$\overline{w_0}$ =25.5
Exterior Slab	12	1392	116	4,554	$\overline{w_0^*}$ =39.6
Added Weight 1	149	60	62.083	25,965	$\overline{w_1}$ = 418.23
Added Weight 2	149	60	62.083	26,945	$\overline{w_2}$ = 434.02
Added Weight 3	48	96	32.000	11,245	$\overline{w_3}$ = 351.39
Added Weight 4	72	71	35.500	15,884	$\overline{w_4}$ = 447.43

Table 3.3 Summary of Seismic Weights Tributary to 2nd Floor

(a) for Collector Force Determination

Item	Slab	Added Weight	Steel Beam	Double-Angle Brace	Beam-to-Beam Connection	Total
Weight (kips)	21.996	80.039	6.923	0.801	0.115	109.873
Mass (kip-sec/in.^{2})	0.0570	0.2073	0.0179	0.0021	0.0003	0.2846
Percentage (%)	20.02%	72.85%	6.30%	0.73%	0.10%	-

(b) for Seismic Force Determination

Item	Slab	Added Weight	Steel Beam	Double-Angle Brace	Beam-to-Beam Connection	Column	Total
Weight (kips)	21.996	80.039	6.923	0.933	0.115	3.294	113.300
Mass (kip-sec/in.^{2})	0.0570	0.2073	0.0179	0.0024	0.0003	0.0085	0.2935
Percentage (%)	19.41%	70.64%	6.11%	0.82%	0.10%	2.91%	-

Table 3.4 Seismic Weights Tributary to Each Span of North Collector Line

Span No.	Span length	Interior Slab		Exterior Slab		Added Weight	Steel Beam				Brace	Beam-to-Beam Connection	Total Weight, W'_{Ni}	Linear Weight, w'_{Ni}
							W14×30		W14×26					
		A_T	Unit Wt.	A_T	Unit Wt.		L_T	Unit Wt.	L_T	Unit Wt.				
	(ft)	(ft^2)	(psf)	(ft^2)	(psf)	(lbs)	(in.)	(lb/ft)	(in.)	(lb/ft)	(lbs)	(lbs)	(kips)	(kips/ft)
1	14	126	25.50	24	39.26	12983	335.04	26.35	156.88	30.35	155.83	10.15	18.436	1.3169
2	14	126	25.50	14	39.26	13473	285.57	26.35	159.25	30.35	97.85	16.91	18.380	1.3128
3	5	45	25.50	5	39.26	5622	235.17	26.35	0	30.35	97.85	10.15	7.590	1.5181
4	5	45	25.50	15	39.26	7942	295.56	26.35	0	30.35	48.93	16.91	10.393	2.0786
												Total W'_N =	54.800	kips
												Avg. $\overline{w'_N}$ =	1.4421	kips/ft

Table 3.5 Seismic Weights Tributary to Each Span of South Collector Line

Span No.	Span length	Interior Slab		Exterior Slab		Added Weight	Steel Beam				Brace	Beam-to-Beam Connection	Total Weight, W'_{Si}	Linear Weight, w'_{Si}
							W14×30		W14×26					
		A_T	Unit Wt.	A_T	Unit Wt.		L_T	Unit Wt.	L_T	Unit Wt.				
	(ft)	(ft^2)	(psf)	(ft^2)	(psf)	(lbs)	(in.)	(lb/ft)	(in.)	(lb/ft)	(lbs)	(lbs)	(kips)	(kips/ft)
1	14	126	25.50	24	39.26	12983	395.89	26.35	156.88	30.35	155.83	16.91	18.577	1.3269
2	14	126	25.50	14	39.26	13473	346.42	26.35	159.25	30.35	97.85	13.53	18.510	1.3221
3	5	45	25.50	5	39.26	5622	235.17	26.35	0	30.35	97.85	13.53	7.594	1.5188
4	5	45	25.50	15	39.26	7942	295.56	26.35	0	30.35	48.93	16.91	10.393	2.0786
												Total W'_S =	55.074	kips
												Avg. $\overline{w'_S}$ =	1.4493	kips/ft

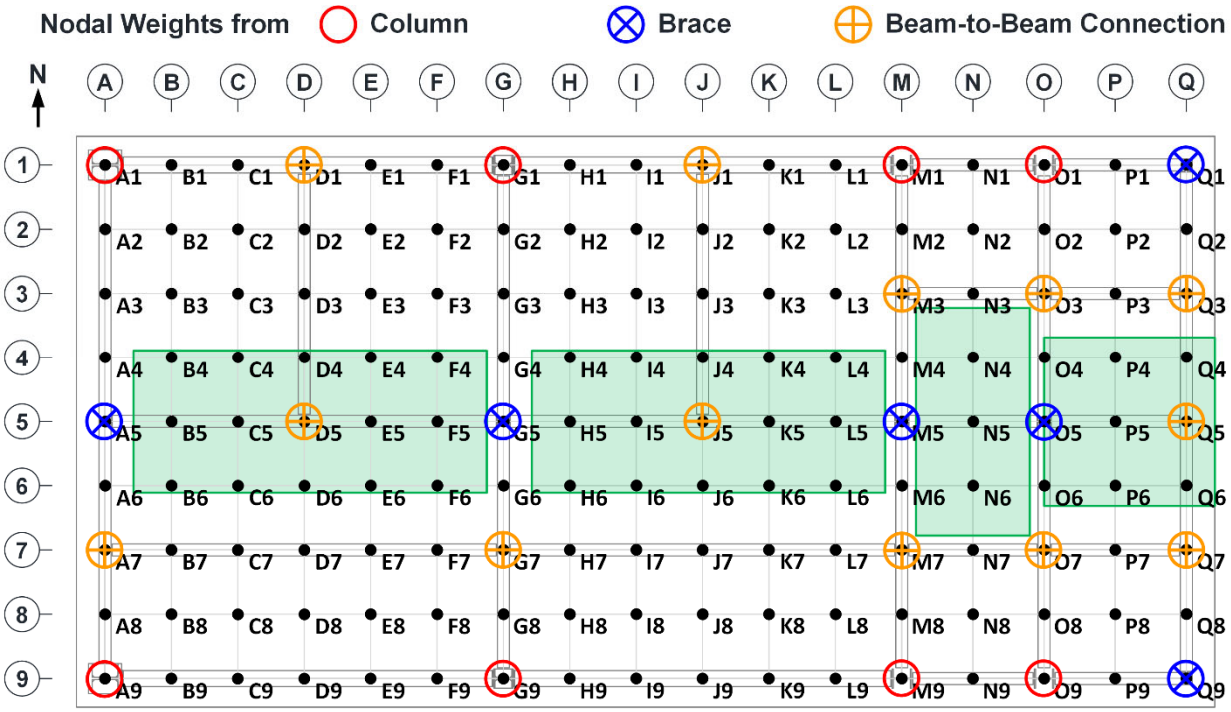

Figure 3.20 Node Designations and Nodal Weights

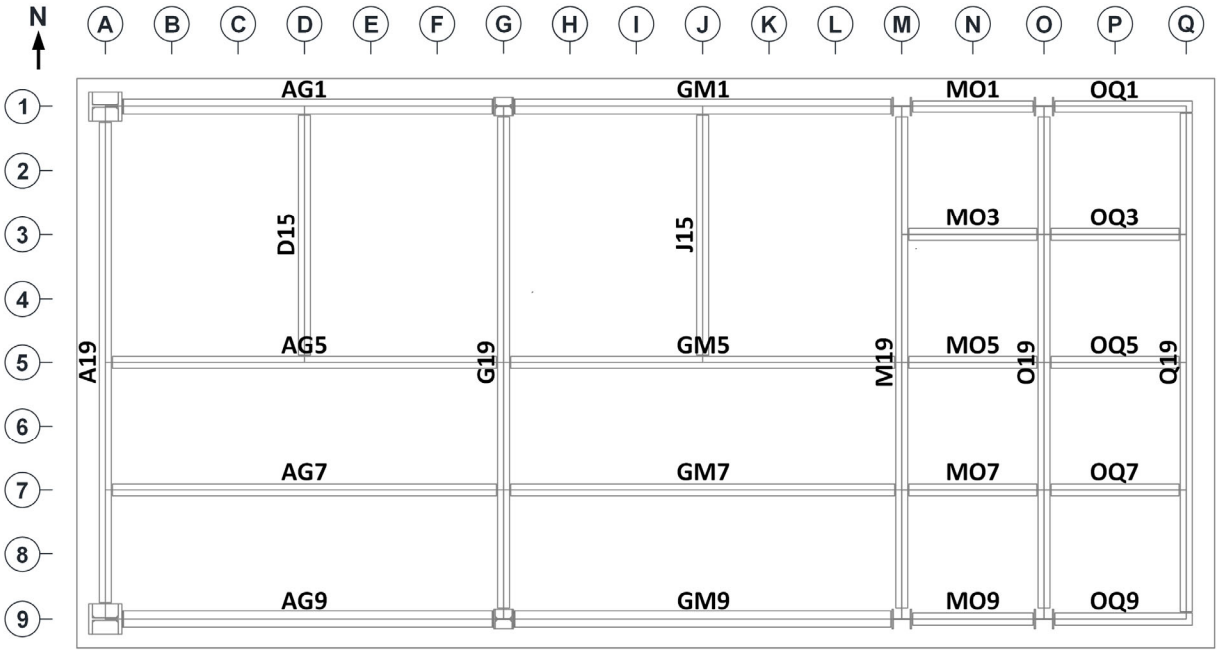

Figure 3.21 Beam Designations

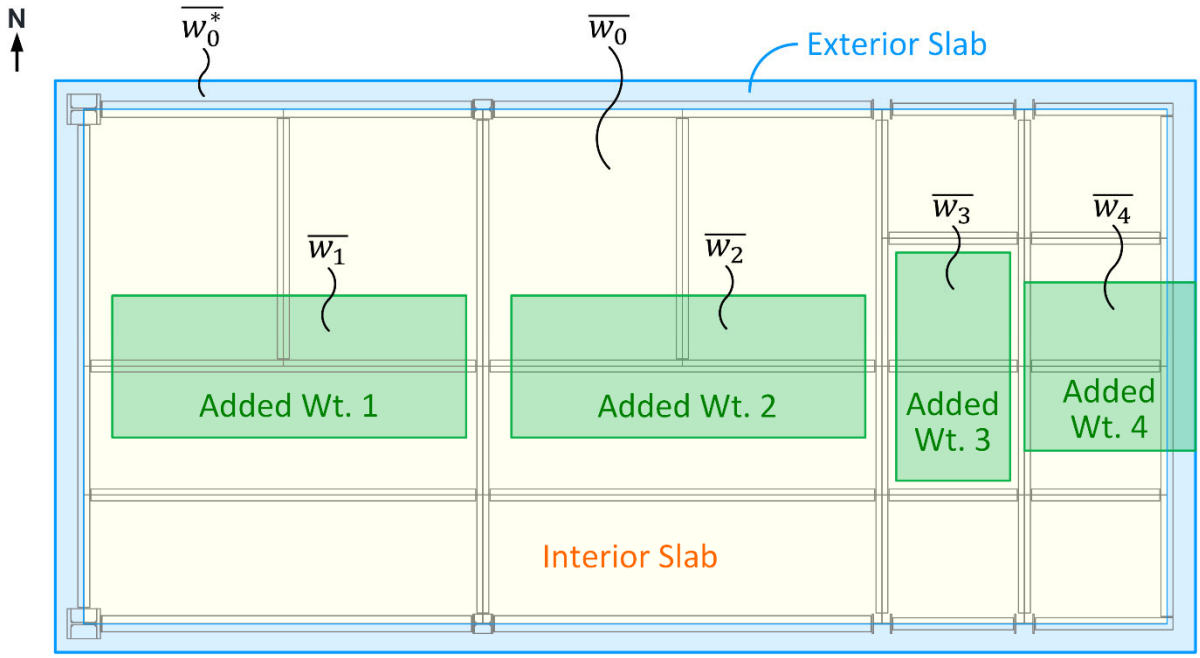

Figure 3.22 Area Weights

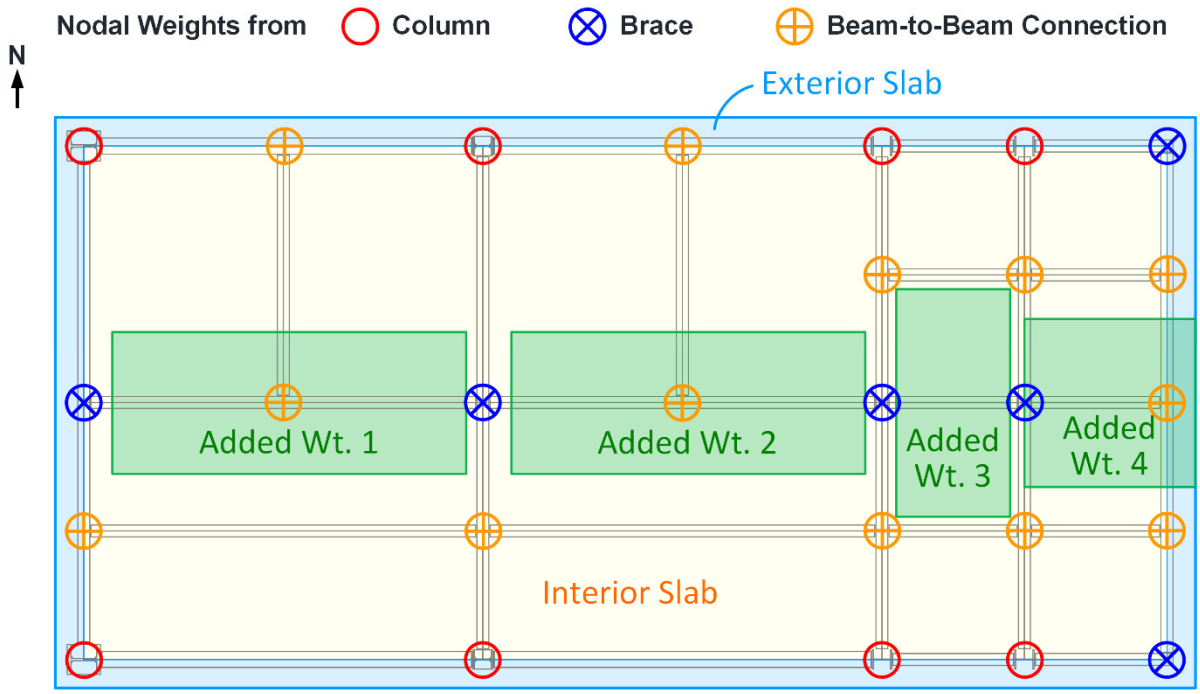

Figure 3.23 Tributary Seismic Weights at 2nd Floor

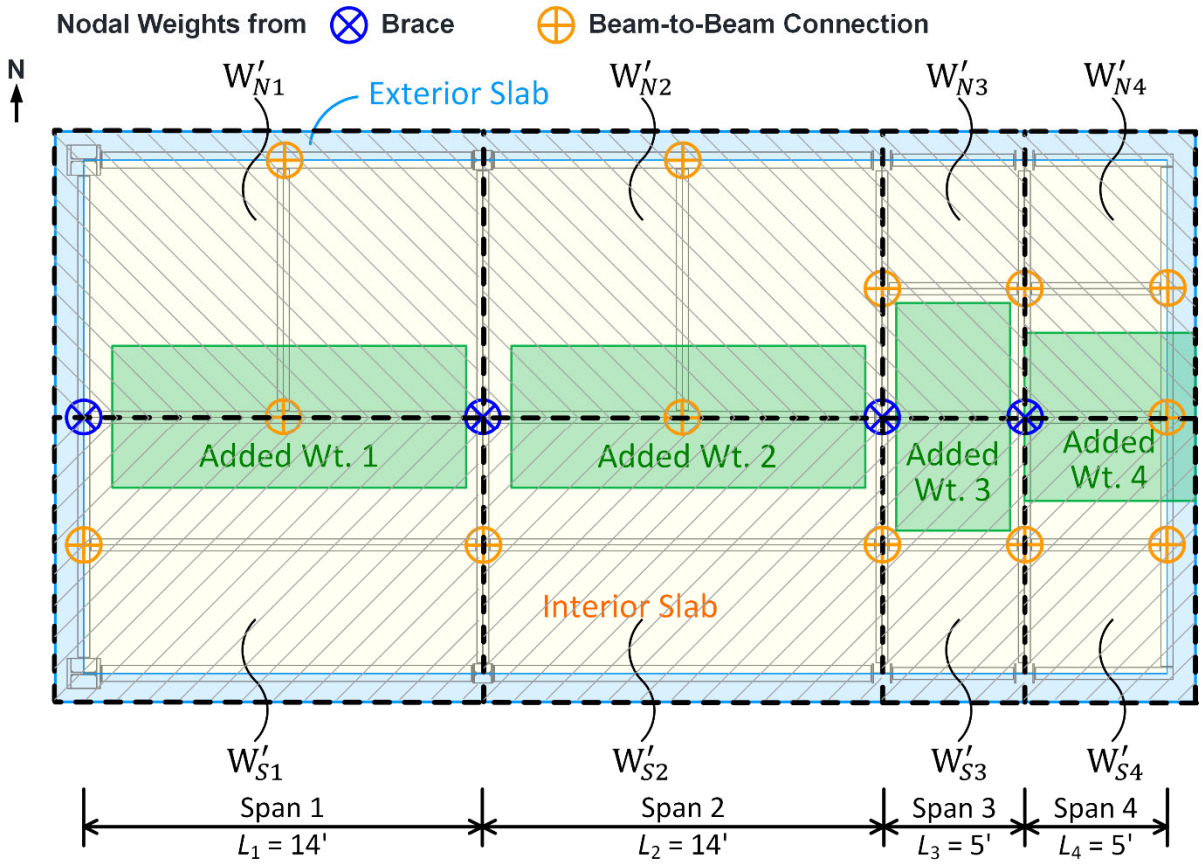

Figure 3.24 Seismic Weights Tributary to Each Span of Collector Lines

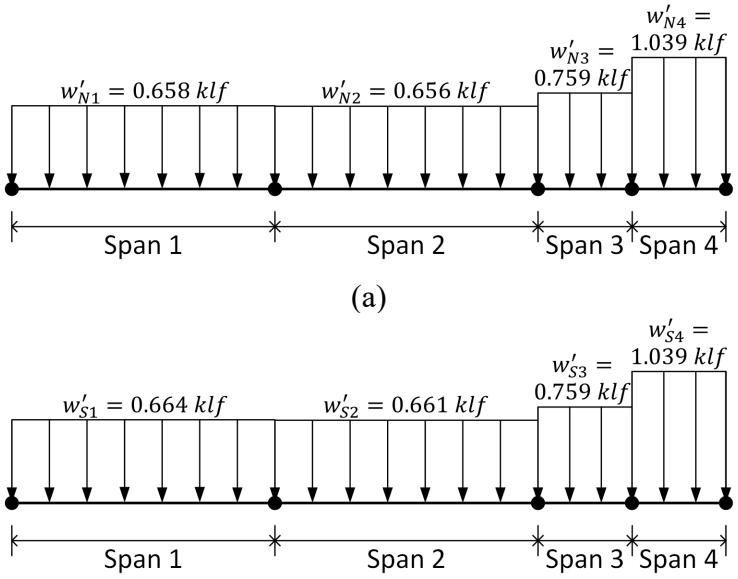

Figure 3.25 Linear Seismic Weights Tributary to (a) North and (b)South Collector Lines

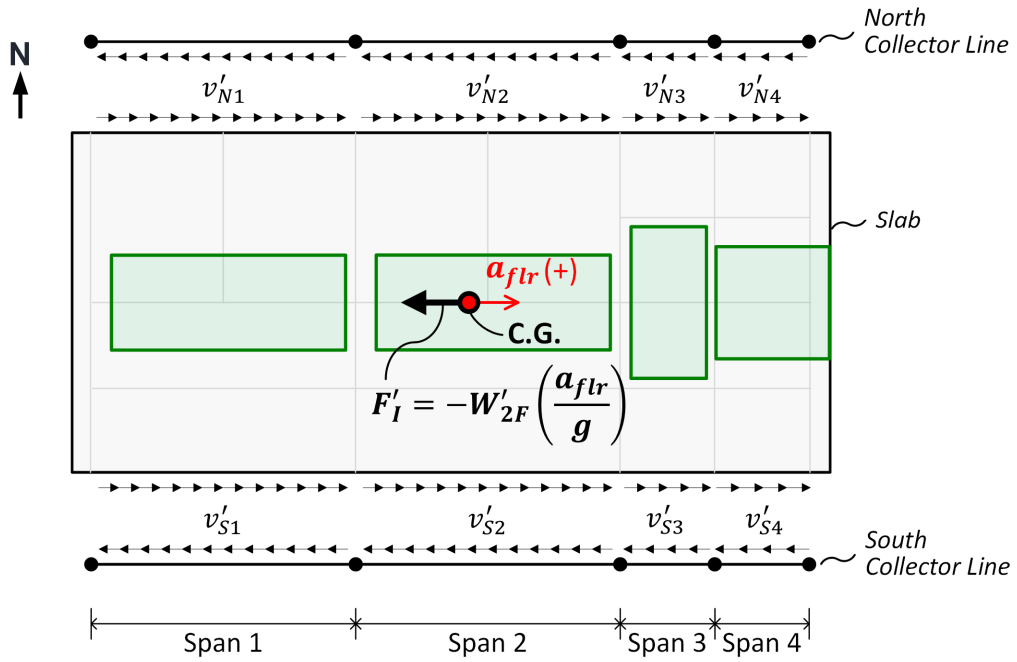

(a)

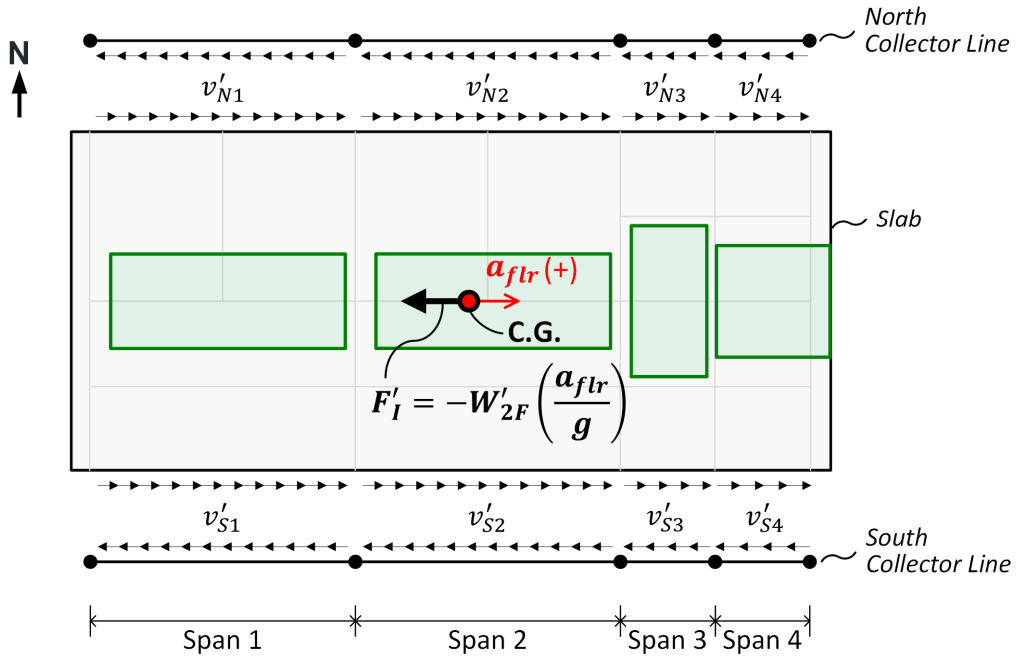

(b)

Figure 3.26 Shear Force Flows Acting along Collector Lines due to (a) Positive and (b) Negative Floor Accelerations

3.2.4 Comparison of Test Specimen and Prototype Structure

A 12-story building with buckling restrained braced frames (BRBFs) for the seismic force-resisting system (SFRS) from the version 1.0 of the Steel Diaphragm Innovation Initiative (SDII) building archetypes (Torabian et al. 2017) was selected as the prototype structure for this research. See Appendix F for detailed description of the prototype structure. Figure 3.27 shows the comparison of floor plans between the prototype structure and test specimen. The longitudinal direction of the prototype building is the direction of interest in this study because significant force demands would be induced in the long collector line between the two BRBFs in each perimeter frame in this direction. For simplicity, the floor area tributary [shown by dashed line in Figure 3.27(a)-top] to one BRBF together with half of its adjacent collector line was considered for design of the long collector line. Note that, for comparison purpose, the floor area considered for the collector line design shown in Figure 3.27(a)-bottom was plotted on the same scale as the test specimen floor plane shown in Figure 3.27(b). The two 14′-long collectors, denoted as Collectors 1 and 2, in the test specimen were intended to represent the two 33′-4″ long collectors (also designated Collectors 1 and 2) in the prototype structure. The model/prototype ratio for the collector beam span is 0.42.

In addition, Figure 3.28 shows the comparison of the cross sections of the composite collectors in prototype structure and test specimen. Table 3.6 lists the comparisons of the dimensions of the collectors in the prototype structure and test specimen. The model/prototype ratios of various dimensions are ranging from 0.44 to 0.65 except for two outliers: the average rib width of deck, w_r, and steel beam flange, b_f. The model/prototype ratios for w_r and b_f were 0.354 and 0.814, respectively. The low model/prototype ratio for w_r is due to the configuration of the available shallow metal deck used for the test specimen. The high model/prototype ratio for b_f is

due to the difference in the design methodologies adopted to determine the collector section between prototype and specimen. For prototype design, the collector section was determined by the member force check without considering the design of the collector-to-column connections. By contrast, for the test specimen, the selection of collector section was governed by the design of the collector-to-column connections. Since the AFW and TFW connections were employed for the 14′-ft long collectors, the axial force strength of the connections was mainly determined from the beam flange area. Hence, a section with a longer flange width was selected to provide adequate welds between the beam flange and column, which resulted in a high model/prototype ratio for b_f. However, in general, the model/prototype ratios tabulated in Table 3.6 indicates that the collectors in the test specimen can represent an approximately 0.5-scale collector.

Figure 3.27(a) and (b) also show the floor areas (A_T) tributary the collectors in the specimen and prototype building, respectively. Note that these tributary areas to the collectors are defined based on the assumption that the inertial force generated from the seismic mass in the area will be transfer to the corresponding collector. It is different from the commonly seen tributary area that is used for the gravity load design. In addition, the total seismic weight in the tributary area of a collector is defined as the tributary seismic weight to the W_T collector. As listed in Table 3.7, the model/prototype ratios for A_T and W_T are 0.076 and 0.116, respectively, both of which are smaller than the theoretical ratio of 0.25 for a 0.5-scale specimen based on the similitude-based scaling laws (Table 3.8 lists the similitude relationships for the key parameters based on scaling laws). Hence, these two parameters (A_T and W_T) were distorted in the specimen. A low A_T in the specimen is unavoidable because the transverse dimension of the test building is restricted by the shake table area. To increase the tributary weight W_T to collectors, heavy added-on RC blocks were placed on the specimen. However, only a part of floor area in the specimen was used to

accommodate the mass blocks because the added weights were intentionally concentrated at the central region of the floor, away from collectors, to avoid affecting the stiffness of the collectors. In addition, it was only allowed to pile up a limited number of mass blocks for each group of added masses because it is undesirable to have the center of added mass too far away from the slab. Hence, the resulting W_T to the collectors in the specimen was unavoidably lower than the theoretical value. Lastly, the average area weight $\overline{W_T}$ applied on the floor is estimated by dividing W_T by A_T. The model/prototype ratio for $\overline{W_T}$ is 1.538, which is higher than the theoretical value of 1.0 per solitude laws. This suggests that the area gravity load from added mass on the specimen is higher than the average superimposed gravity load on the prototype floors.

However, the low tributary area and low tributary weights to the collectors in the specimen is considered acceptable. This is because cantilever columns (i.e., LFRS) of the test building was designed to remain elastic even though the specimen is subjected to a floor acceleration up to 2.7 g, which is much higher than the target peak floor acceleration required in Phase 1 test program. In other words, the LFRS of the test building was intentionally "overdesigned" so that, although seismic weight tributary to the collectors was low, high inertial force demands on the collectors can be generated by scaling up the input motion such that a high floor acceleration can be produced.

Table 3.6 Comparisons of Dimensions of Collectors in Prototype and Specimen

Dimension	Unit	Prototype	Specimen	Specimen /Prototype Ratio	Note for Dimension
L	(in.)	400	168	0.420	Collector beam span
t_c	(in.)	4.5	2	0.444	Thickness of concrete above metal deck
h_r	(in.)	3	1.5	0.500	Height of metal deck
w_r	(in.)	6	2.125	0.354	Average rib width of metal deck
s_r	(in.)	12	6	0.500	Rib spacing of metal deck
d	(in.)	21.1	13.8	0.654	Steel beam height
b_f	(in.)	8.27	6.73	0.814	Steel beam flange width
t_w	(in.)	0.43	0.23	0.535	Steel beam web thickness
t_f	(in.)	0.685	0.385	0.562	Steel beam flange thickness

Table 3.7 Comparisons of Tributary Floor Area and Tributary Seismic Weights of Collectors in Prototype and Specimen

Parameter	Unit	Prototype	Specimen	Specimen /Prototype Ratio	Theoretical Model/Prototype Ratio for 0.5-scale Specimen
Tributary Area, A_T	(ft^2)	1666.67	126	0.076	0.25
Tributary Weight, W_T	(kips)	159.16	18.5	0.116	0.25
Area Weight, $\overline{W_T}$	(psf)	95.50	146.83	1.538	1

Table 3.8 Similitude Relationship

Parameter	Model/Prototype Ratio	Model/Prototype Ratio for 0.5-scale Specimen
Length	L	0.500
Time	$\sqrt{L}$	0.707
Mass	L^2	0.250
Displacement	L	0.500
Velocity	$\sqrt{L}$	0.707
Acceleration	1	1
Stress	1	1
Strain	1	1
Force	L^2	0.250
Moment	L^3	0.125
Energy	L^3	0.125
Area	L^2	0.250
Moment of Inertia	L^4	0.0625

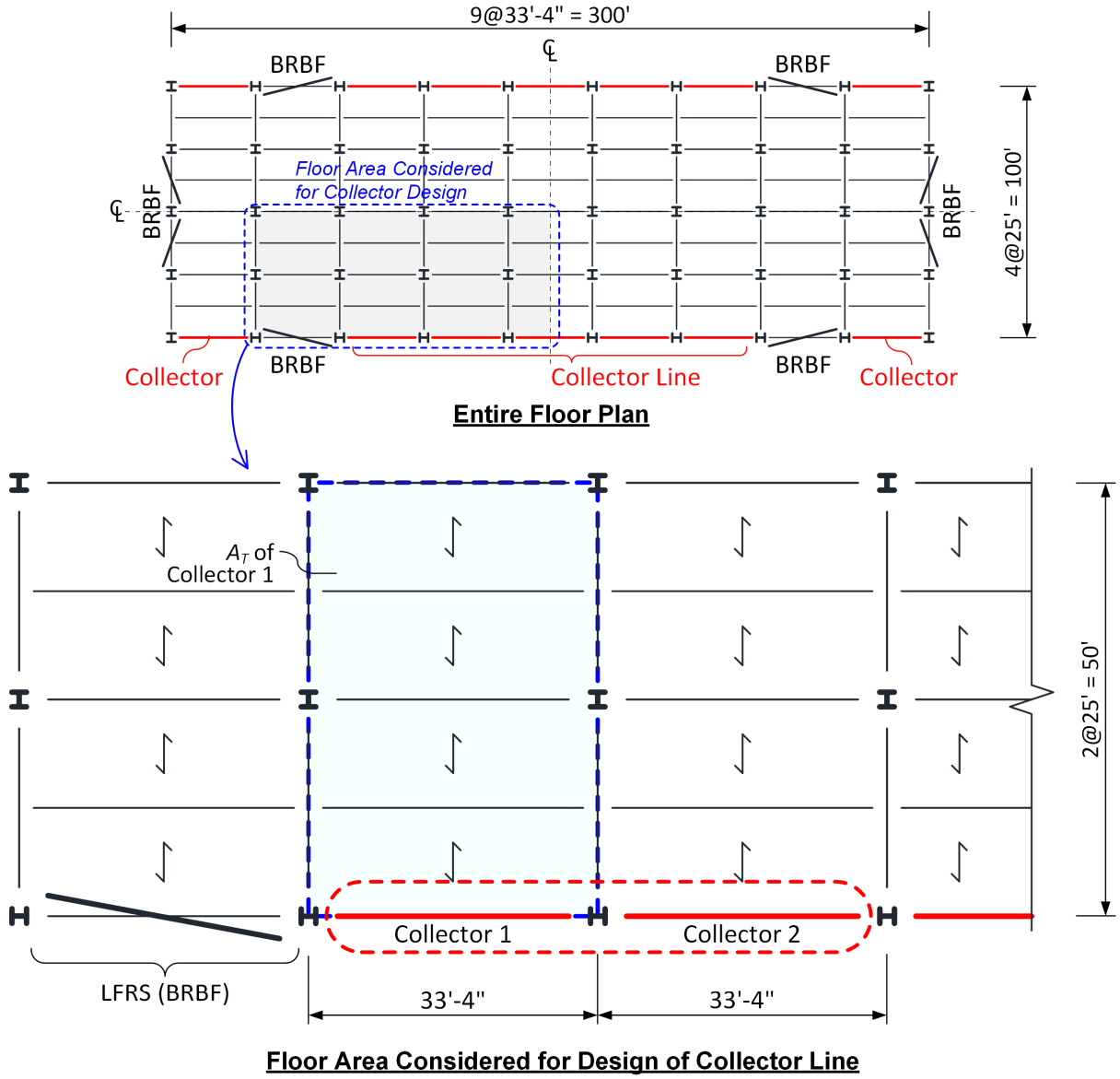

(a) Prototype Structure

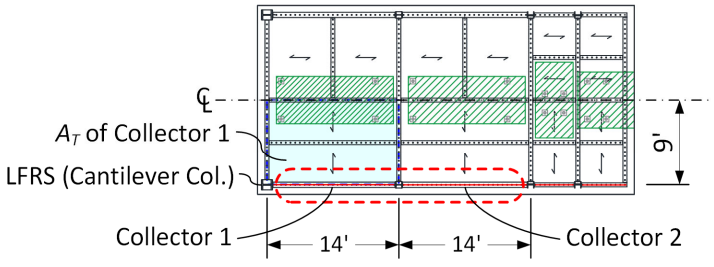

(b) Test Specimen

Figure 3.27 Comparison of Floor Plans in (a) Prototype Structure and (b) Test Specimen

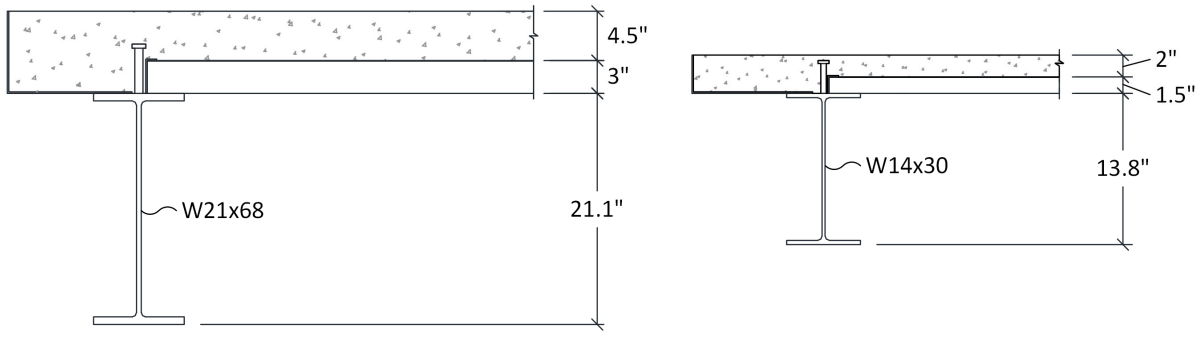

(a) Prototype Structure (b) Test Specimen

Figure 3.28 Comparison of Collector Sections in (a) Prototype Structure and (b) Test Specimen

3.3 Specimen Design Strengths per Current Practice

3.3.1 Collector Compressive Strength

Collector beams with composite slabs are continuously braced for minor axis flexural buckling. The composite slab also provides significant continuous torsional bracing. This continuous torsional bracing is often sufficient to preclude torsional buckling altogether. This can be verified by using the approaches developed by Helwig and Yura (1999). However, for simplicity, designers usually conservatively neglect the effect of the continuous torsional bracing from the slab and consider the constrained-axis torsional buckling about the top flange [see Figure 3.29(d)] for the collector design. Hence, the compressive strength of a collector with composite slab is governed by the weaker strength between the major axis flexural bucking and constrained-axis torsional bucking.

For the 14′-long W14×30 collectors in the Phase 1 test building, the effective lengths with respect to the major-axis flexural, minor-axis flexural, and torsional buckling modes, respectively denoted as L_{cx}, L_{cy}, and L_{cz}, are taken as:

$L_{cx} = (KL)_x = 1.0(14\text{ ft}) = 14\text{ ft}$

$L_{cy} = 0$ (lateral movement is braced by the slab)

$$L_{cz} = (KL)_z = \begin{cases} 14\text{ ft}, & \text{for south collectors} \\ 7\text{ ft}, & \text{for north collectors} \end{cases}$$

Note that the effective length factors, K_x and K_z, are conservatively assumed as 1.0.

For major axis flexural buckling mode [Figure 3.29(a)], the elastic buckling stress, F_e, is computed by:

$$F_e = \frac{\pi^2 E}{\left(\frac{L_{cx}}{r_x}\right)^2} \tag{3.4}$$

On the other hand, as suggested in the AISC *Specification* (AISC 2016c) Commentary Section E4, the elastic buckling stress, F_e, for the constrained-axis torsional buckling [Figure 3.29(d)], is determined from

$$F_e = \omega \left[\frac{\pi^2 E I_y}{(L_{cz})^2} \left(\frac{h_o^2}{4} + a^2 \right) + GJ \right] \frac{1}{A_g \bar{r_o}^2} \tag{3.5}$$

where E and G are Young's modulus and shear modulus of steel, respectively. A_g, I_y, and J are gross cross-sectional area, minor-axis moment of inertia about, and torsional constant of the steel section. a is the distance from the centroid to lateral restraint on the member minor axis. h_o is the distance between flange centroids. The polar radius of gyration about the shear center is $\bar{r_o} = \sqrt{{r_x}^2 + {r_y}^2 + a^2}$, where r_x and r_y are the radii of gyration about major axis and minor axis for the steel section, respectively. ω is the factor to address the effects of bracing flexibility, taken as 0.9.

Inserting the expression for $\bar{r_o}$ in the denominator term in Eq. (3.5) and taking $a = d/2$, for the case when the restraint is at the top flange, Eq. (3.5) is rewritten as:

$$F_e = 0.9 \left[\frac{\pi^2 E I_y (h_o^2 + d^2)}{4(L_{cz})^2} + GJ \right] \frac{1}{I_x + I_y + 0.25 A_g d^2} \tag{3.6}$$

where d is the depth of the steel section and I_x is the moment of inertia about the major axis.

For each of the two buckling modes considered, the corresponding critical stress, F_{cr}, is determined per AISC *Specification* Section E3 with the following equations

$$F_{cr} = \begin{cases} \left(0.658^{\frac{F_y}{F_e}} \right) F_y, & \frac{F_y}{F_e} \leq 2.25 \\ 0.877 F_e, & \frac{F_y}{F_e} > 2.25 \end{cases} \tag{3.7}$$

Since there is no compactness requirement for the collector beam in the current building codes (AISC 2016b, 2016c), it is allowed to employ slender sections for collectors. When a collector section is slender for axial compression, the effective area, A_e, of the section accounting

for local buckling effect is determined per AISC *Specification* Section E7. For the W14×30 collectors made of A992 steel (F_y = 50 ksi), the flange is compact ($b_f/2t_f = 8.74 < \lambda_r = 0.56\sqrt{E/F_y} = 13.49$), while the web is slender ($h/t_w = 45.4 > \lambda_r = 1.49\sqrt{E/F_y} = 35.88$). The effective width for the web, h_e, is determined from:

$$h_e = \begin{cases} h, & \lambda \le \lambda_r \sqrt{\dfrac{F_y}{F_{cr}}} \\ h\left(1 - c_1\sqrt{\dfrac{F_{el}}{F_{cr}}}\right)\sqrt{\dfrac{F_{el}}{F_{cr}}}, & \lambda > \lambda_r \sqrt{\dfrac{F_y}{F_{cr}}} \end{cases} \tag{3.8}$$

where h is the clear height of the web. c_1 is the effective width imperfection adjustment factor (= 0.18 for stiffened elements). c_2 is computed as $\left(1 - \sqrt{1 - 4c_1}\right)/(2c_1)$. λ is the width-to-thickness ratio of the web. λ_r is the limiting width-to-thickness ratio for members subject to axial compression. F_{el} is the elastic local bucking stress and computed as $[(c_2\lambda_r)/\lambda]^2 F_y$.

Subsequently, the effective area, A_e, of the section is estimated from:

$$A_e = A_g - t_w(h - h_e) \tag{3.9}$$

Finally, the design compressive strength is computed by:

$$\phi_c P_n = \phi_c(F_{cr}A_e) = 0.9F_{cr}A_e \tag{3.10}$$

Note that A_e is replaced by A_g when collector section is compact. The smaller of the design compressive strengths of the two bucking modes considered is the governing compressive strength of the collector. Table 3.9 and Table 3.10 show the calculations of $\phi_c P_n$ for the 14′-long W14×30 collectors in Frames S and N, respectively.

3.3.2 Collector Flexural Strength for Gravity Design

The design flexural strength of collector for gravity design was computed per Section I3.2 of the AISC Specification (AISC 2016c). Table 3.11 and Table 3.12 show the calculations of the design positive flexural strength, $\phi_b M_n$, for the composite section of the north and south 14-ft long collectors, respectively. As the steel collector section (W14×30) has a web width-to-thickness ratio $h/t_w = 45.4 \leq 3.76\sqrt{E/F_y} = 90.6$, the nominal positive flexural strength, M_n was determined from the plastic stress distribution for the limit state of yielding. The nominal strengths for steel and concrete, F_y = 50 ksi and f_c' = 4 ksi, respectively, were used for the calculations of M_n.

The compression force, C_c, in the concrete slab was determined from the smallest of:

$$C_{c1} = A_s F_y \tag{3.11}$$

$$C_2 = 0.85 f_c' h_c b_{eff} \tag{3.12}$$

$$C_3 = \Sigma Q_n \tag{3.13}$$

where A_s is the cross-sectional area of the steel section, h_c is the thick of concrete slab above the metal deck, and b_{eff} is the effective slab width, which was determined per Section I3.1a of the AISC Specification. ΣQ_n is the sum of nominal strengths of steel headed stud anchors between the point of maximum positive moment and the point of zero moment. It is assumed that the collector under the gravity loads acts as a simply supported beam subjected to a uniform load. Thus, the number of studs (= 13) allocated at each half span of the 14-ft collector was used to compute ΣQ_n. The nominal shear strength, Q_n, of one steel headed stud anchor was determined as follows (AISC 2016c):

$$Q_n = 0.5 A_{sa} \sqrt{f_c' E_c} \leq R_g R_p A_{sa} F_u \tag{3.14}$$

where A_{sa} is the cross-sectional area of the steel headed stud, E_c is the modulus of elasticity of concrete, which was determined from $E_c = w_c^{1.5}\sqrt{f_c'}$ (ksi), and F_u is the specified minimum tensile strength of a steel headed stud anchor. R_g and R_p are reduction factors for stud design.

The effective thickness of concrete slab, a, was determined from:

$$a = \frac{C_c}{0.85 f_c' b_{eff}} \tag{3.15}$$

At the assumed limit states, the distance from the concrete slab force (C_c) to the steel top flange, Y_2, was determined as:

$$a = Y_{con} - \frac{a}{2} \tag{3.16}$$

where Y_{con} is the distance from the top of steel collector to top of concrete slab.

For calculation of M_n, the combination of a root of the web and its adjacent fillets for the steel collector section was idealized as a rectangular shape with a depth of $K_{dep} = \left(k - t_f\right)$ and an area $K_{area} = \left(A_s - 2A_f - A_w\right)/2$, where k is the dimension of the k-area, t_f is the flange thickness, $A_f = b_f t_f$ is the flange area, and $A_w = (d - 2k)t_w$ is the web area. d, b_f, and t_w are the depth, flange width, and web thickness of the steel section, respectively.

Assuming the plastic neutral axis (PNA) is located whing the steel web, the distance from the bottom of the steel section to the PNA, y_{PNA}, was computed as:

$$y_{PNA} = k + \frac{1}{t_w}\left[\frac{A_s}{2} + \frac{C_c}{2F_y} - K_{area} - A_f\right] \tag{3.17}$$

Then, M_n was calculated by summing up the moments generated by steel and concrete components of the composite section under the plastic stress distribution.

3.3.3 B1 and B2 Multipliers for Collector Design

In this section, the B_1 and B_2 multipliers per in AISC *Specification* (AISC 2016c) Appendix 8 were computed to evaluate the second-order effects on the collector design. The B_2 multiplier, accounting for P-Δ effect, is determined from:

$$B_2 = \frac{1}{1 - \frac{\alpha P_{story}}{P_{e\,story}}} \geq 1 \tag{3.18}$$

where α = 1.0 for LRFD and P_{story} is the total vertical load supported by the story. The total seismic weight tributary to the 2nd floor of test specimen, W_{2F}, was used to estimate P_{story}, i.e., $P_{story} = W_{2F}$ = 113.3 kips. $P_{e\,story}$ is the elastic critical buckling strength for the story in the direction of translation being considered and computed by:

$$P_{e\,story} = R_M \frac{HL}{\Delta_H} \tag{3.19}$$

where

H = total story shear, in the direction of translation being considered, produced by the lateral forces used to compute Δ_H

L = story height, taken as the height (= 8 ft) of the cantilever columns in the test building

Δ_H = first-order interstory drift, in the direction of translation being considered

$R_M = 1 - 0.15\left(P_{mf}/P_{story}\right)$

P_{mf}= total vertical load in columns in the story that are part of moment frames in the direction of translation being considered

Note that H/Δ_H represents the lateral stiffness of the test building in the longitudinal direction. For simplicity, it is assumed that the rigidity of the TFW ad BW collector-to-column connections is negligible and that the lateral stiffness of the test building is provided by the two

cantilever columns and the collectors framing to these two columns through AFW connections. A L-shape frame model (see Figure 3.30), composed of a cantilever column and a beam with one end connected to the column and the other end supported by a roller, was used to estimate the lateral stiffness of each longitudinal frame of the test building. By summing up the stiffnesses from two longitudinal frame, the total lateral stiffness of the specimen, H/Δ_H, is estimated as:

$$\frac{H}{\Delta_H} = (2\ \text{Frames}) \times \frac{3EI_c}{{L_c}^3}\left[4 - 3\left[\frac{1}{1+\frac{3}{4}\left(\frac{I_b/L_b}{I_c/L_c}\right)}\right]\right] \tag{3.20}$$

This gives the result: H/Δ_H = 392.91 kips/in. Furthermore, P_{mf} (= 5.76 kips) is estimated by the summation of the vertical loads carried by the two cantilever columns, which is the total of the weights located in the tributary areas (see Figure 3.31) of the cantilever columns. With P_{mf} and P_{story}, the value of R_M (= 0.9924) is determined. Plugging the values of R_M, L, and H/Δ_H into Eq. (3.19), the value of $P_{e\ story}$ is obtained (= 37,432 kips). Finally, by using Eq. (3.18), the value of B_2 is determined (= 1.003).

The B_1 multiplier, accounting for the P-δ effect on the collector, is determined from:

$$B_1 = \frac{C_m}{1-\frac{\alpha P_r}{P_{e1}}} \geq 1 \tag{3.21}$$

where α = 1.0 for LRFD. The equivalent uniform moment factor, C_m, is conservatively taken as 1.0 because gravity loads served as the transverse loading between the supports of the collector. P_r is the required second-order axial strength and calculated by $P_{nt} + B_2 P_{lt}$. It is assumed that P_{nt} = 0 because the gravity-induced axial force in the collector is negligible. P_{lt} is estimated by the axial force in the Collector 1 induced by a floor acceleration of 2.0 g. It is assumed that the total inertial force generated from the seismic weight tributary to two collector lines, W'_{2F}, will be

transferred to and evenly shared by the two cantilever columns. Thus, the west end of each Collector 1 will see the axial force:

$$P_{lt} = \left(\frac{1}{2}\right) \times W'_{2F} \times \left(\frac{a_{flr}}{g}\right) \tag{3.22}$$

where the floor acceleration, a_{flr}, is taken as 2 g. This resulted in $P_{lt} = W'_{2F}$ = 109.9 kips.

In addition, the elastic critical buckling strength of the member in the plane of bending, P_{e1}, is determined from:

$$P_{e1} = \frac{\pi^2 EI^*}{(L_{c1})^2} \tag{3.23}$$

where EI^* is taken as EI_x of the collector. I_x is the moment of inertia about the major axis (x-axis of the section). The effective length of the collector in the plane of bending is taken as $L_{c1} = (KL)_x$= 1.0(14 ft) = 14 ft. The computed P_{e1} is 2,951 kips. Plugging the values of the variables into Eq. (3.21), the value of B_1 is obtained (= 1.039).

3.3.4 Collector-to-Column Connection Strength

Three types of collector-to-column connections (AFW, TFW and BW connections) were employed for test building. In current practice, engineers usually compute the axial force resistance, $\phi R_{n,total}$, of a collector connection and check it with the resultant force demand, R_u, at the collector end. Note that the resultant force R_u is determined from the following equation:

$$R_u = \sqrt{{P_a}^2 + {V_g}^2} \tag{3.24}$$

where P_a is the floor acceleration-triggered axial force, while V_g is the gravity-induced shear force in the collector. On the other hand, the general formula for the design strength of these three types of connections can be expressed as follows:

$$\phi R_{n,total} = n_f \phi R_{n,f} + \phi R_{n,w} \tag{3.25}$$

where $\phi R_{n,total}$ = total design strength of the connection; $\phi R_{n,f}$ = design strength of each welded flange; $\phi R_{n,w}$= design strength of bolted connection at collector web; and n_f = number of welded flanges. Note that n_f = 2, 1, and 0 for the AFW, TFW and BW connections, respectively.

To determine the strength of each welded flange, $\phi R_{n,f}$, two limit states are considered. One is yielding of the flange and its corresponding design strength, $\phi R_{n,f1}$, is computed by:

$$\phi R_{n,f1} = \phi_t F_y A_f \tag{3.26}$$

where ϕ_t = 0.90; F_y is the yield stress of flange; and A_f is the flange area (= $b_f t_f$). The other is fracture of the flange weld and its corresponding design strength, $\phi R_{n,f2}$, is estimated as:

$$\phi R_{n,f2} = \phi F_{nw} A_f \tag{3.27}$$

where ϕ = 0.75 and F_{nw} is the nominal stress of weld metal. Finally, the smaller strength between these two limit states gives the governing strength, $\phi R_{n,f}$, for the welded flange as follows:

$$\phi R_{n,f} = \min\left(\phi R_{n,f1}, \phi R_{n,f2}\right) \tag{3.28}$$

To determine the strength of bolted connection at collector web, $\phi R_{n,w}$, seven limit states are considered. They include: (1) gross section yield of shear tab; (2) net section fracture of shear tab; (3) shear rupture of bolts; (4) bearing or tear-out of bolt holes on shear tab; (5) bearing or tear-out of bolt holes on collector beam web; (6) block shear rupture of shear tab; and (7) block shear rupture of collector beam web. Table 3.13 and Table 3.14 show the calculations of the design strengths of AFW and TFW connections, respectively. Table 3.15 and Table 3.16 show the calculations of the design strengths of the BW connections in the W14×30 and W14×26 collectors, respectively.

Table 3.9 Design Compressive Strength for South Collector

Effective Lengths					
L_{cx} =	168	in.	L_{cz} =	168	in.
Material Properties					
E =	29000	ksi	F_y =	50	ksi
G =	11154	ksi			
Section Information					
Section	W14×30		I_x =	291	in.^{4}
A_g =	8.85	in.^{2}	I_y =	19.6	in.^{4}
d =	13.8	in.	r_x =	5.73	in.
b_f =	6.73	in.	r_y =	1.49	in.
t_w =	0.27	in.	h_o =	13.4	in.
t_f =	0.385	in.	J =	0.38	in.^{4}
Compactness Check					
Element	λ		λ_r		Classification
Flange	$b_f/2t_f$ =	8.74	$0.56\sqrt{E/F_y}$ =	13.49	Compact
Web	h/t_w =	45.4	$1.49\sqrt{E/F_y}$ =	35.88	Slender
$\phi_c P_n$ for Major-Axis Flexural Buckling			$\phi_c P_n$ for Constrain-Axis Torsional Buckling		
L_{cx}/r_x =	29.32		ω =	0.9	
F_e =	332.96	ksi	F_e =	27.82	ksi
F_y/F_e =	0.15		F_y/F_e =	1.80	
F_{cr} =	46.95	ksi	F_{cr} =	23.56	ksi
$\lambda_r\sqrt{F_y/F_{cr}}$ =	37.03	$< \lambda$	$\lambda_r\sqrt{F_y/F_{cr}}$ =	52.27	$\geq \lambda$
c_1 =	0.22		c_1 =	0.22	
c_2 =	1.485		c_2 =	1.485	
F_{el} =	68.92	ksi	F_{el} =	68.92	ksi
h =	12.26	in.	h =	12.26	in.
h_e =	10.89	in.	h_e =	12.26	in.
A_e =	8.48	in.^{2}	A_e =	8.85	in.^{2}
$\phi_c P_n$ =	358.4	kips	$\phi_c P_n$ =	187.7	kips
Governing $\phi_c P_n$ = 187.7 kips					

Table 3.10 Design Compressive Strength for North Collector

Effective Lengths					
L_{cx} =	168	in.	L_{cz} =	84	in.
Material Properties					
E =	29000	ksi	F_y =	50	ksi
G =	11154	ksi			
Section Information					
Section	W14×30		I_x =	291	in.^{4}
A_g =	8.85	in.^{2}	I_y =	19.6	in.^{4}
d =	13.8	in.	r_x =	5.73	in.
b_f =	6.73	in.	r_y =	1.49	in.
t_w =	0.27	in.	h_o =	13.4	in.
t_f =	0.385	in.	J =	0.38	in.^{4}
Compactness Check					
Element	λ		λ_r		Classification
Flange	$b_f/2t_f$ =	8.74	$0.56\sqrt{E/F_y}$ =	13.49	Compact
Web	h/t_w =	45.4	$1.49\sqrt{E/F_y}$ =	35.88	Slender
$\phi_c P_n$ for Major-Axis Flexural Buckling			$\phi_c P_n$ for Constrain-Axis Torsional Buckling		
L_{cx}/r_x =	29.32		ω =	0.9	
F_e =	332.96	ksi	F_e =	95.64	ksi
F_y/F_e =	0.15		F_y/F_e =	0.52	
F_{cr} =	46.95	ksi	F_{cr} =	40.17	ksi
$\lambda_r\sqrt{F_y/F_{cr}}$ =	37.03	$< \lambda$	$\lambda_r\sqrt{F_y/F_{cr}}$ =	40.03	$< \lambda$
c_1 =	0.22		c_1 =	0.22	
c_2 =	1.485		c_2 =	1.485	
F_{el} =	68.92	ksi	F_{el} =	68.92	ksi
h =	12.26	in.	h =	12.26	in.
h_e =	10.89	in.	h_e =	11.43	in.
A_e =	8.48	in.^{2}	A_e =	8.63	in.^{2}
$\phi_c P_n$ =	358.4	kips	$\phi_c P_n$ =	311.9	kips
Governing $\phi_c P_n$ = 311.9 kips					

Table 3.11 Design Positive Flexural Strength of North Collector

Steel Beam Section			Composite Slab			Headed Stud Anchor		
Section	W14×30		f_c' =	4	ksi	Condition	Deck Parallel	
F_y =	50	ksi	w_c =	110	pcf	N_{stud} =	13	in.
d =	13.8	in.	E_c =	2408	ksi	d_{sa} =	0.5	in.
b_f =	6.73	in.	b =	33	in.	A_{sa} =	0.1963	in.^{2}
t_w =	0.27	in.	h_c =	2	in.	F_u =	65	ksi
t_f =	0.385	in.	h_r =	1.5	in.	R_g =	0.85	
k =	0.785	in.	w_r =	2.125	in.	R_p =	0.75	
A_s =	8.85	in.^{2}	w_r/h_r =	1.42		Q_{n1} =	9.635	kips
A_f =	2.59105	in.^{2}	C_{c1} =	442.5	kips	Q_{n2} =	8.136	kips
A_w =	3.3021	in.^{2}	C_{c2} =	224.4	kips	Q_n =	8.136	kips
K_{area} =	0.1829	in.^{2}	C_{c3} =	105.8	kips	ΣQ_n =	105.8	kips
K_{dep} =	0.4	in.	C_c =	105.8	kips			

Design Positve Flexural Strenth, $\phi_b M_n$

			Component	Area (in.^{2})	Force (kips)	y (in.)	$y - y_{PNA}$ (in.)	M_n (kip-in.)
a =	0.943	in.						
Y_{con} =	3.5	in.						
Y_2 =	3.029	in.	Steel #1	2.5911	129.55	0.193	-10.62	1376.49
y_{PNA} =	10.82	in.	Steel #2	0.1829	9.14	0.585	-10.23	93.58
$\frac{C_c}{F_y A_s}$ =	23.90%		Steel #3	2.7088	135.44	5.801	-5.02	679.39
ϕ_b =	0.9		Steel #4	0.5933	29.67	11.916	1.10	32.60
			Steel #5	0.1829	9.14	13.215	2.40	21.93
			Steel #6	2.5911	129.55	13.608	2.79	361.46
			Concrete	-	105.77	16.829	6.01	635.81
							Total =	3201.24
$\phi_b M_n$ =	240	kip-ft						

[Note]

1. C_{c1}= $A_s F_y$; C_{c2}= $0.85 f_c' A_c$; C_{c3}= ΣQ_n; and C_c= min (C_{c1}, C_{c2}, C_{c3})
2. Q_{n1}=$0.5 A_{sa}\sqrt{f_c' E_c}$; Q_{n2}=$R_g R_p A_{sa} F_u$; and Q_n= min (Q_{n1}, Q_{n2})

Table 3.12 Design Positive Flexural Strength of South Collector

Steel Beam Section			Composite Slab			Headed Stud Anchor		
Section	W14×30		f_c' =	4	ksi	Condition	Deck Perpendicular	
F_y =	50	ksi	w_c =	110	pcf	N_{stud} =	0.5	in.
d =	13.8	in.	E_c =	2408	ksi	d_{sa} =	0.1963	in.
b_f =	6.73	in.	b =	33	in.	A_{sa} =	65	in.^{2}
t_w =	0.27	in.	h_c =	2	in.	F_u =	1	ksi
t_f =	0.385	in.	h_r =	1.5	in.	R_g =	0.6	
k =	0.785	in.	w_r =	2.125	in.	R_p =	9.635	
A_s =	8.85	in.^{2}	w_r/h_r =	1.42		Q_{n1} =	7.658	kips
A_f =	2.59105	in.^{2}	C_{c1} =	442.5	kips	Q_{n2} =	7.658	kips
A_w =	3.3021	in.^{2}	C_{c2} =	224.4	kips	Q_n =	99.5	kips
K_{area} =	0.1829	in.^{2}	C_{c3} =	99.5	kips	ΣQ_n =	0.5	kips
K_{dep} =	0.4	in.	C_c =	99.5	kips			

Design Positve Flexural Strenth, $\phi_b M_n$

			Component	Area (in.^{2})	Force (kips)	y (in.)	$y - y_{PNA}$ (in.)	M_n (kip-in.)
a =	0.887	in.						
Y_{con} =	3.5	in.						
Y_2 =	3.056	in.	Steel #1	2.5911	129.55	0.193	-10.39	1346.63
y_{PNA} =	10.59	in.	Steel #2	0.1829	9.14	0.585	-10.00	91.47
$\frac{C_c}{F_y A_s}$ =	22.50%		Steel #3	2.6465	132.33	5.686	-4.90	648.54
ϕ_b =	0.9		Steel #4	0.6556	32.78	11.801	1.21	39.79
			Steel #5	0.1829	9.14	13.215	2.63	24.03
			Steel #6	2.5911	129.55	13.608	3.02	391.31
			Concrete	-	99.55	16.856	6.27	624.11
							Total =	3165.89
$\phi_b M_n$ =	237	kip-ft						

[Note]

1. $C_{c1} = A_s F_y$; $C_{c2} = 0.85 f_c' A_c$; $C_{c3} = \Sigma Q_n$; and $C_c = \min(C_{c1}, C_{c2}, C_{c3})$

2. $Q_{n1} = 0.5 A_{sa} \sqrt{f_c' E_c}$; $Q_{n2} = R_g R_p A_{sa} F_u$; and $Q_n = \min(Q_{n1}, Q_{n2})$

Table 3.13 Design Strength for AFW Connection

Collector Connection Type = AFW			n_f = 2					
Bolt Parameters			Bolt Hole Layout			Collector (W14×30)		
d_b =	0.625	in.	d_h =	0.6875		d =	13.8	in.
A_b =	0.31	in.^{2}	$\overline{n_b}$ =	5		b_f =	6.73	in.
Type	A325-N		n_r =	1		t_w =	0.27	in.
F_{nt} =	90	ksi	n_b =	5		t_f =	0.385	in.
F_{nv} =	54	ksi	s_v =	2		F_y =	50	ksi
μ =	0.3		e_v =	1.25		F_u =	65	ksi
D_u =	1.13		s_h =	0		Shear Tab		
h_f =	1		e_h =	1.25		l =	10.5	in.
T_b =	19	kips	e_{hw} =	1.25		w =	3	in.
$\overline{n_s}$ =	1		Design Coefficient			t_p =	0.25	in.
			U =	1		F_{yp} =	50	ksi
			U_{bs} =	1		F_{up} =	65	ksi

Design Strength of Each Welded Flange, $\phi R_{n,f}$								
Yield of Flange			Fracture of Weld					
ϕ_t =	0.9		ϕ =	0.75				
A_f =	2.591	in.^{2}	A_f =	2.591	in.^{2}			
F_y =	50	ksi	F_{nw} =	70	ksi			
$\phi R_{n,f1}$ =	116.6	kips	$\phi R_{n,f2}$ =	136.0	kips			
Governing $\phi R_{n,f}$ =	116.6	kips	(Controlling Limit State: Yield of Flange)					

Design Strength of Bolted Connection at Collector Web, $\phi R_{n,w}$								
Gross Section Yield of Shear Tab			Net Section Fracture of Shear Tab			Shear Rupture of Bolts		
ϕ_t =	0.9		ϕ =	0.75		ϕ =	0.75	
A_p =	2.625	in.^{2}	A_n =	1.6875	in.^{2}	ϕr_n =	12.43	kips
$\phi R_{n,w1}$ =	118.1	kips	$\phi R_{n,w2}$ =	82.3	kips	$\phi R_{n,w3}$ =	62.1	kips
Bearing/Tearout (B/T) of Bolt Holes on Shear Tab			Bearing/Tearout (B/T) of Bolt Holes on Collector Web			Bolt Slip Resistance		
ϕ =	0.75		ϕ =	0.75		ϕ =	1.0	
$l_{c,e}$ =	0.90625	in.	$l_{c,e}$ =	0.90625	in.	ϕr_n =	6.44	kips
$l_{c,s}$ =	0	in.	$l_{c,s}$ =	0	in.	$\phi R_{n,w8}$ =	32.2	kips
$r_{n,e}$ =	17.67	kips	$r_{n,e}$ =	19.09	kips			
$r_{n,s}$ =	0	kips	$r_{n,s}$ =	0	kips			
$\phi R_{n,w4}$ =	66.3	kips	$\phi R_{n,w5}$ =	71.6	kips			
Block Shear Rupture (BSR) of Shear Tab			Block Shear Rupture (BSR) of Collector Web					
ϕ =	0.75		ϕ =	0.75				
A_{nt} =	1.25	in.^{2}	A_{nt} =	1.35	in.^{2}			
A_{gv} =	0.625	in.^{2}	A_{gv} =	0.675	in.^{2}			
A_{nv} =	0.4375	in.^{2}	A_{nv} =	0.4725	in.^{2}			
$\phi R_{n,w6}$ =	73.7	kips	$\phi R_{n,w7}$ =	79.6	kips			
Governing $\phi R_{n,w}$ =	62.1	kips	(Controlling Limit State: Shear Rupture of Bolts)					

Total Design Strength of Collector Connection, $\phi R_{n,total}$		
Governing $\phi R_{n,total}$ =	295.3	kips

Table 3.14 Design Strength for TFW Connection

Collector Connection Type =	TFW		n_f =	1	
Bolt Parameters			**Bolt Hole Layout**		
d_b =	0.625	in.	d_h =	0.6875	
A_b =	0.31	in.^{2}	$\overline{n_b}$ =	5	
Type	A325-N		n_r =	1	
F_{nt} =	90	ksi	n_b =	5	
F_{nv} =	54	ksi	s_v =	2	
μ =	0.3		e_v =	1.25	
D_u =	1.13		s_h =	0	
h_f =	1		e_h =	1.25	
T_b =	19	kips	e_{hw} =	1.25	
$\overline{n_s}$ =	1		**Design Coefficient**		
			U =	1	
			U_{bs} =	1	

Collector (W14×30)		
d =	13.8	in.
b_f =	6.73	in.
t_w =	0.27	in.
t_f =	0.385	in.
F_y =	50	ksi
F_u =	65	ksi
Shear Tab		
l =	10.5	in.
w =	3	in.
t_p =	0.25	in.
F_{yp} =	50	ksi
F_{up} =	65	ksi

Design Strength of Each Welded Flange, $\phi R_{n,f}$

Yield of Flange			Fracture of Weld		
ϕ_t =	0.9		ϕ =	0.75	
A_f =	2.591	in.^{2}	A_f =	2.591	in.^{2}
F_y =	50	ksi	F_{nw} =	70	ksi
$\phi R_{n,f1}$ =	116.6	kips	$\phi R_{n,f2}$ =	136.0	kips

Governing $\phi R_{n,f}$ = 116.6 kips (Controlling Limit State: Yield of Flange)

Design Strength of Bolted Connection at Collector Web, $\phi R_{n,w}$

Gross Section Yield of Shear Tab			Net Section Fracture of Shear Tab			Shear Rupture of Bolts		
ϕ_t =	0.9		ϕ =	0.75		ϕ =	0.75	
A_p =	2.625	in.^{2}	A_n =	1.6875	in.^{2}	ϕr_n =	12.43	kips
$\phi R_{n,w1}$ =	118.1	kips	$\phi R_{n,w2}$ =	82.3	kips	$\phi R_{n,w3}$ =	62.1	kips
Bearing/Tearout (B/T) of Bolt Holes on Shear Tab			**Bearing/Tearout (B/T) of Bolt Holes on Collector Web**			**Bolt Slip Resistance**		
ϕ =	0.75		ϕ =	0.75		ϕ =	1.0	
$l_{c,e}$ =	0.90625	in.	$l_{c,e}$ =	0.90625	in.	ϕr_n =	6.44	kips
$l_{c,s}$ =	0	in.	$l_{c,s}$ =	0	in.	$\phi R_{n,w8}$ =	32.2	kips
$r_{n,e}$ =	17.67	kips	$r_{n,e}$ =	19.09	kips			
$r_{n,s}$ =	0	kips	$r_{n,s}$ =	0	kips			
$\phi R_{n,w4}$ =	66.3	kips	$\phi R_{n,w5}$ =	71.6	kips			
Block Shear Rupture (BSR) of Shear Tab			**Block Shear Rupture (BSR) of Collector Web**					
ϕ =	0.75		ϕ =	0.75				
A_{nt} =	1.25	in.^{2}	A_{nt} =	1.35	in.^{2}			
A_{gv} =	0.625	in.^{2}	A_{gv} =	0.675	in.^{2}			
A_{nv} =	0.4375	in.^{2}	A_{nv} =	0.4725	in.^{2}			
$\phi R_{n,w6}$ =	73.7	kips	$\phi R_{n,w7}$ =	79.6	kips			

Governing $\phi R_{n,w}$ = 62.1 kips (Controlling Limit State: Shear Rupture of Bolts)

Total Design Strength of Collector Connection, $\phi R_{n,total}$

Governing $\phi R_{n,total}$ = 178.7 kips

Table 3.15 Design Strength for BW Connection in W14×30 Collector

Collector Connection Type =	BW		n_f =	0			
Bolt Parameters			**Bolt Hole Layout**			**Collector (W14×30)**		
d_b =	0.625	in.	d_h =	0.6875		d =	13.8	in.
A_b =	0.31	in.^{2}	$\overline{n_b}$ =	5		b_f =	6.73	in.
Type	A325-N		n_r =	1		t_w =	0.27	in.
F_{nt} =	90	ksi	n_b =	5		t_f =	0.385	in.
F_{nv} =	54	ksi	s_v =	2		F_y =	50	ksi
μ =	0.3		e_v =	1.25		F_u =	65	ksi
D_u =	1.13		s_h =	0		**Shear Tab**		
h_f =	1		e_h =	1.25		l =	10.5	in.
T_b =	19	kips	e_{hw} =	1.25		w =	3	in.
$\overline{n_s}$ =	1		**Design Coefficient**			t_p =	0.25	in.
			U =	1		F_{yp} =	50	ksi
			U_{bs} =	1		F_{up} =	65	ksi

Design Strength of Each Welded Flange, $\phi R_{n,f}$

Yield of Flange			Fracture of Weld		
ϕ_t =	0.9		ϕ =	0.75	
A_f =	2.591	in.^{2}	A_f =	2.591	in.^{2}
F_y =	50	ksi	F_{nw} =	70	ksi
$\phi R_{n,f1}$ =	116.6	kips	$\phi R_{n,f2}$ =	136.0	kips

Governing $\phi R_{n,f}$ = 116.6 kips (Controlling Limit State: Yield of Flange)

Design Strength of Bolted Connection at Collector Web, $\phi R_{n,w}$

Gross Section Yield of Shear Tab			Net Section Fracture of Shear Tab			Shear Rupture of Bolts		
ϕ_t =	0.9		ϕ =	0.75		ϕ =	0.75	
A_p =	2.625	in.^{2}	A_n =	1.6875	in.^{2}	ϕr_n =	12.43	kips
$\phi R_{n,w1}$ =	118.1	kips	$\phi R_{n,w2}$ =	82.3	kips	$\phi R_{n,w3}$ =	62.1	kips
Bearing/Tearout (B/T) of Bolt Holes on Shear Tab			**Bearing/Tearout (B/T) of Bolt Holes on Collector Web**			**Bolt Slip Resistance**		
ϕ =	0.75		ϕ =	0.75		ϕ =	1.0	
$l_{c,e}$ =	0.90625	in.	$l_{c,e}$ =	0.90625	in.	ϕr_n =	6.44	kips
$l_{c,s}$ =	0	in.	$l_{c,s}$ =	0	in.	$\phi R_{n,w8}$ =	32.2	kips
$r_{n,e}$ =	17.67	kips	$r_{n,e}$ =	19.09	kips			
$r_{n,s}$ =	0	kips	$r_{n,s}$ =	0	kips			
$\phi R_{n,w4}$ =	66.3	kips	$\phi R_{n,w5}$ =	71.6	kips			
Block Shear Rupture (BSR) of Shear Tab			**Block Shear Rupture (BSR) of Collector Web**					
ϕ =	0.75		ϕ =	0.75				
A_{nt} =	1.25	in.^{2}	A_{nt} =	1.35	in.^{2}			
A_{gv} =	0.625	in.^{2}	A_{gv} =	0.675	in.^{2}			
A_{nv} =	0.4375	in.^{2}	A_{nv} =	0.4725	in.^{2}			
$\phi R_{n,w6}$ =	73.7	kips	$\phi R_{n,w7}$ =	79.6	kips			

Governing $\phi R_{n,w}$ = 62.1 kips (Controlling Limit State: Shear Rupture of Bolts)

Total Design Strength of Collector Connection, $\phi R_{n,total}$

Governing $\phi R_{n,total}$ = 62.1 kips

Table 3.16 Design Strength for BW Connection W14×26 Collector

Collector Connection Type =	BW		n_f =	0			
Bolt Parameters			**Bolt Hole Layout**			**Collector (W14×26)**		
d_b =	0.625	in.	d_h =	0.6875		d =	13.8	in.
A_b =	0.31	in.^{2}	$\overline{n_b}$ =	5		b_f =	6.73	in.
Type	A325-N		n_r =	1		t_w =	0.27	in.
F_{nt} =	90	ksi	n_b =	5		t_f =	0.385	in.
F_{nv} =	54	ksi	s_v =	2		F_y =	50	ksi
μ =	0.3		e_v =	1.25		F_u =	65	ksi
D_u =	1.13		s_h =	0		**Shear Tab**		
h_f =	1		e_h =	1.25		l =	10.5	in.
T_b =	19	kips	e_{hw} =	1.25		w =	3	in.
$\overline{n_s}$ =	1		**Design Coefficient**			t_p =	0.25	in.
			U =	1		F_{yp} =	50	ksi
			U_{bs} =	1		F_{up} =	65	ksi

Design Strength of Each Welded Flange, $\phi R_{n,f}$

Yield of Flange			Fracture of Weld		
ϕ_t =	0.9		ϕ =	0.75	
A_f =	2.113	in.^{2}	A_f =	2.113	in.^{2}
F_y =	50	ksi	F_{nw} =	70	ksi
$\phi R_{n,f1}$ =	95.1	kips	$\phi R_{n,f2}$ =	110.9	kips

Governing $\phi R_{n,f}$ = 95.1 kips (Controlling Limit State: Yield of Flange)

Design Strength of Bolted Connection at Collector Web, $\phi R_{n,w}$

Gross Section Yield of Shear Tab			Net Section Fracture of Shear Tab			Shear Rupture of Bolts		
ϕ_t =	0.9		ϕ =	0.75		ϕ =	0.75	
A_p =	2.625	in.^{2}	A_n =	1.6875	in.^{2}	ϕr_n =	12.43	kips
$\phi R_{n,w1}$ =	118.1	kips	$\phi R_{n,w2}$ =	82.3	kips	$\phi R_{n,w3}$ =	62.1	kips
Bearing/Tearout (B/T) of Bolt Holes on Shear Tab			**Bearing/Tearout (B/T) of Bolt Holes on Collector Web**			**Bolt Slip Resistance**		
ϕ =	0.75		ϕ =	0.75		ϕ =	1.0	
$l_{c,e}$ =	0.90625	in.	$l_{c,e}$ =	0.90625	in.	ϕr_n =	6.44	kips
$l_{c,s}$ =	0	in.	$l_{c,s}$ =	0	in.	$\phi R_{n,w8}$ =	32.2	kips
$r_{n,e}$ =	17.67	kips	$r_{n,e}$ =	18.03	kips			
$r_{n,s}$ =	0	kips	$r_{n,s}$ =	0	kips			
$\phi R_{n,w4}$ =	66.3	kips	$\phi R_{n,w5}$ =	67.6	kips			
Block Shear Rupture (BSR) of Shear Tab			**Block Shear Rupture (BSR) of Collector Web**					
ϕ =	0.75		ϕ =	0.75				
A_{nt} =	1.25	in.^{2}	A_{nt} =	1.275	in.^{2}			
A_{gv} =	0.625	in.^{2}	A_{gv} =	0.6375	in.^{2}			
A_{nv} =	0.4375	in.^{2}	A_{nv} =	0.44625	in.^{2}			
$\phi R_{n,w6}$ =	73.7	kips	$\phi R_{n,w7}$ =	75.2	kips			

Governing $\phi R_{n,w}$ = 62.1 kips (Controlling Limit State: Shear Rupture of Bolts)

Total Design Strength of Collector Connection, $\phi R_{n,total}$

Governing $\phi R_{n,total}$ = 62.1 kips

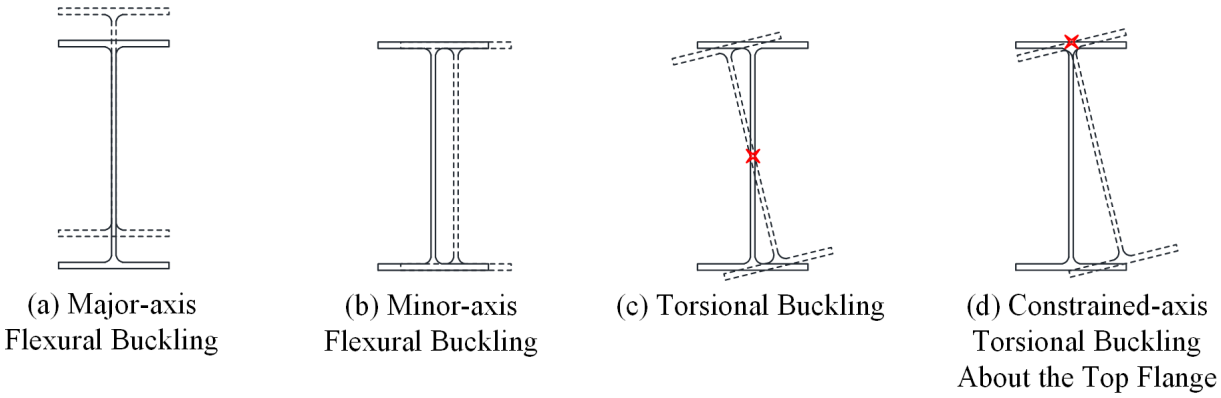

Figure 3.29 Types of Collector Buckling

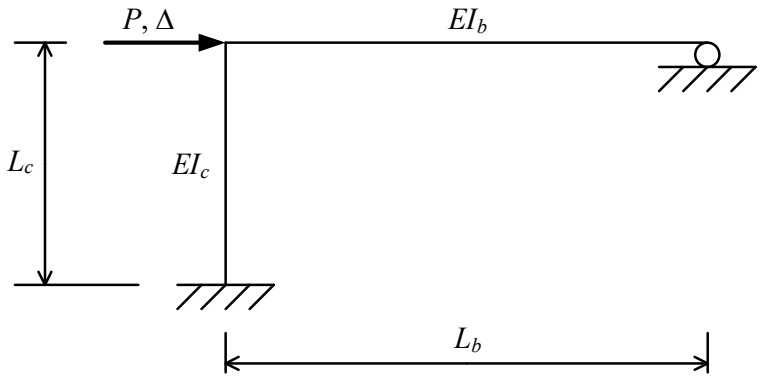

Figure 3.30 L-shaped Frame Model Considered for Estimation of Specimen Lateral Stiffness

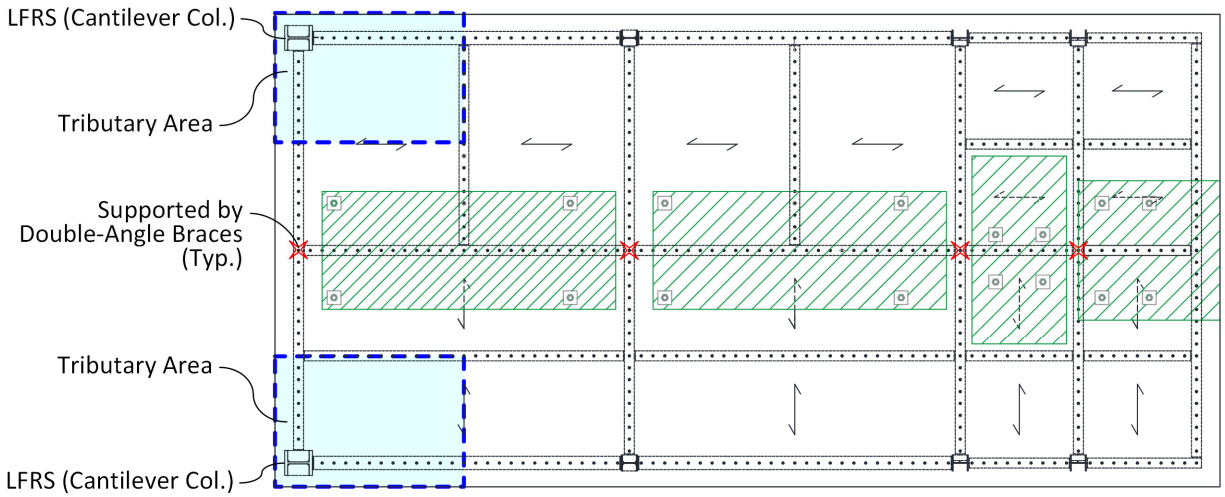

Figure 3.31 Tributary Areas of Cantilever Columns

3.4 Instrumentation and Data Filtering

Phase 1 test building was thoroughly instrumented with a combination of accelerometers, displacement transducers, uniaxial electrical resistance strain gauges, and strain gauge rosettes. Instrumentation plans are shown in Figure 3.32 through Figure 3.35. A total of 285 separate data channels were used for Phase 1 tests. All sensors were sampled at a rate of 256 Hz throughout each recorded motion. The measured sensor signals were filtered using an 8^{th} order Butterworth low-pass filter with a cutoff frequency of 30 Hz and a zero-phase digital filtering process built into MATLAB (Mathworks 2019). Prior to each motion, the gages were biased such that the initial readings of all instruments were zero.

Figure 3.32 shows the strain gauges layout. Strain gauges and rosettes were located at several sections along each column and collector. Uniaxial strain gauges were placed on both flanges at two elevations for each column to recover the member force distributions, such as moment diagram or axial force diagram. The collectors were heavily instrumented at the sections 7 inch (about half steel beam depth) away from the column faces of the collector-to-column connections at Column Lines 1, 2, and 3. For these critical sections, in addition to the gauges placed at five elevations along the steel collector section depth, a concrete-embedded strain gauge and a concrete surface gauge (see Figure 3.36) were place in the concrete slab so that the strain profile of the composite section can be measured. In addition, strain gauges were placed on the steel flanges at the mid-span and quarter span of each 14-ft long collector (Collectors 1 or 2) and at the mid-span of east and west chords. Furthermore, each double-angle brace was instrumented with a strain gauge. Strain gage sections were distributed over the frames to both recover an accurate moment diagram and to provide redundancy in the case of damaged or malfunctioned gages.

Figure 3.33 shows the displacement transducers layout. Displacement transducers were used to measure rotations of the collector-to-column connections and pin-supports, slip of the concrete slab, and shear deformations in the panel zones. Figure 3.37 and Figure 3.38 show the setup of the displacement transducers used to measure the rotation of the collector-to-column connections. Figure 3.39 shows a typically instrumented pin-support. Figure 3.40 shows the setup of the displacement transducers used to measure the slip of the concrete slab. Figure 3.41 shows a typically instrumented panel zone.

Figure 3.34 shows the string potentiometer layout. String potentiometers were placed on the reference columns and a reference frame, which were fixed outside of the shake table, to measure the absolute displacements of the test building at the footing level and 2nd floor. Figure 3.35 shows the accelerometer layout. On the test building, accelerometers were located at the top ends of the columns on Column Lines 1 and 4 and at the mid span of the east chord to monitor accelerations in three orthogonal directions at these locations. In addition, an accelerometer, designated as A19, oriented horizontally in the East-West direction, was installed on the added mass block on the 2nd span.

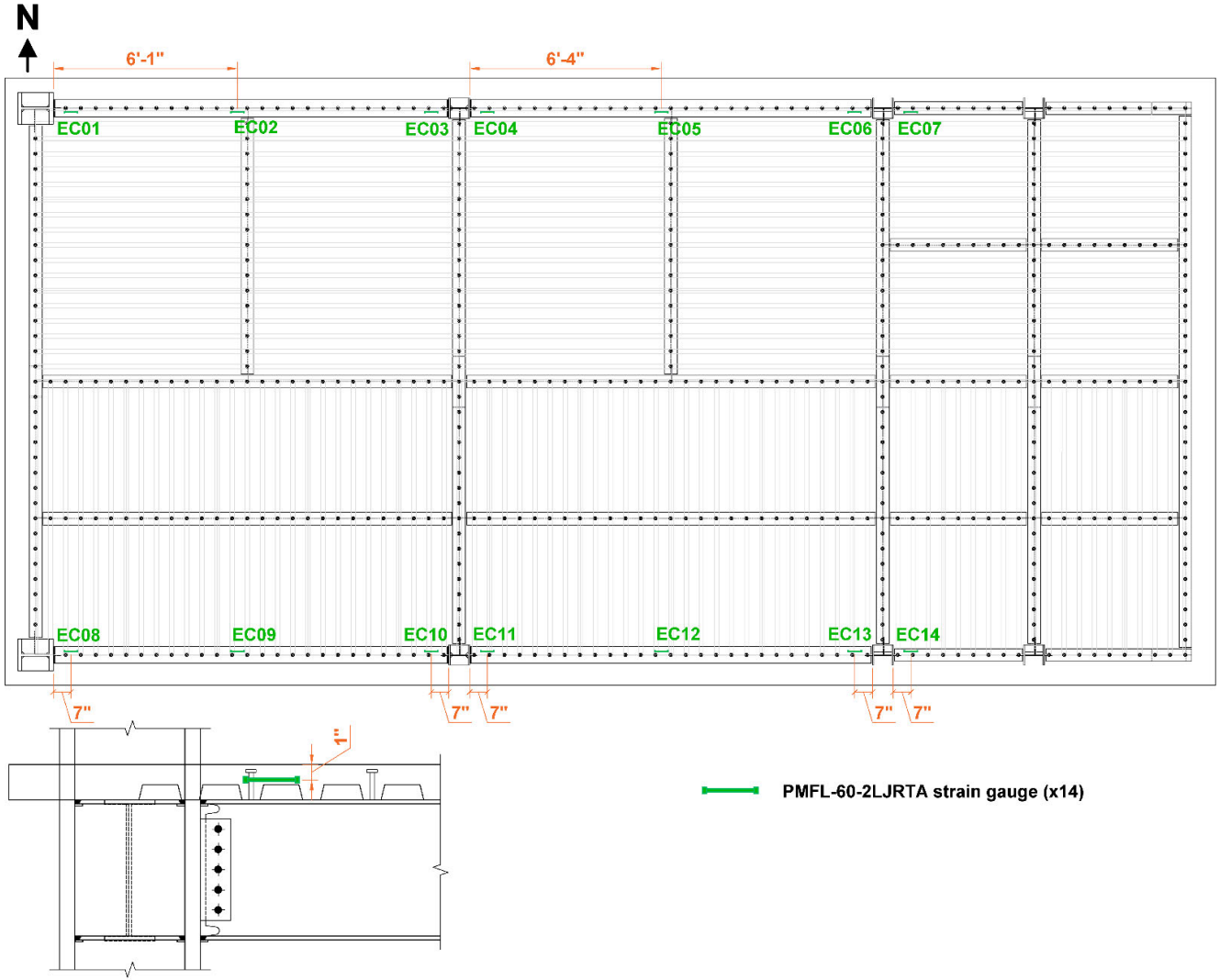

(a) Concrete-embedded Strain Gauges

Figure 3.32 Instrumentation Plan for Phase 1 Test: Strain Gauge Layout

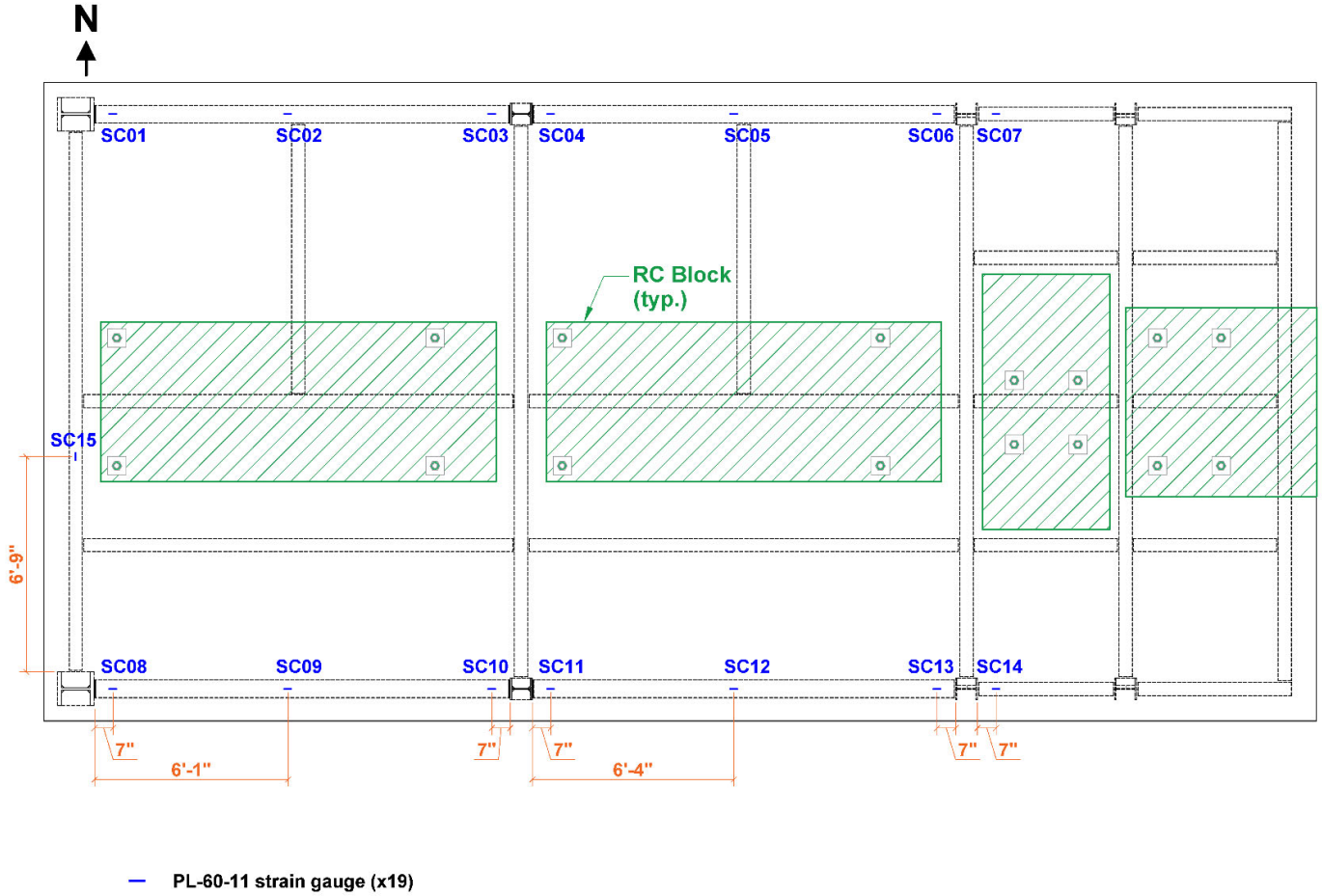

(b) Concrete Surface Strain Gauges

Figure 3.32 Instrumentation Plan for Phase 1 Test: Strain Gauge Layout (continued)

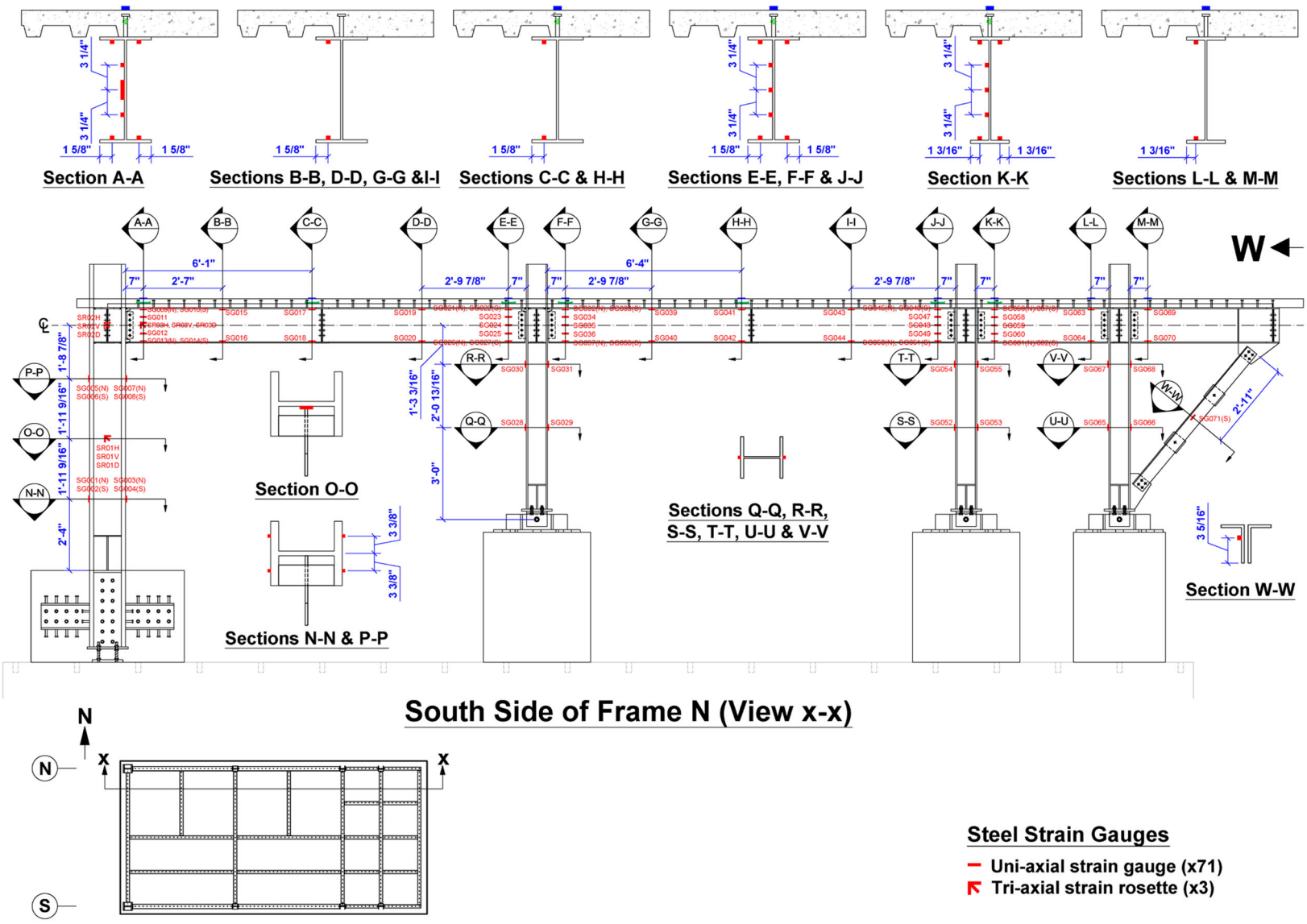

(c) Steel Strain Gauges on Frame N

Figure 3.32 Instrumentation Plan for Phase 1 Test: Strain Gauge Layout (continued)

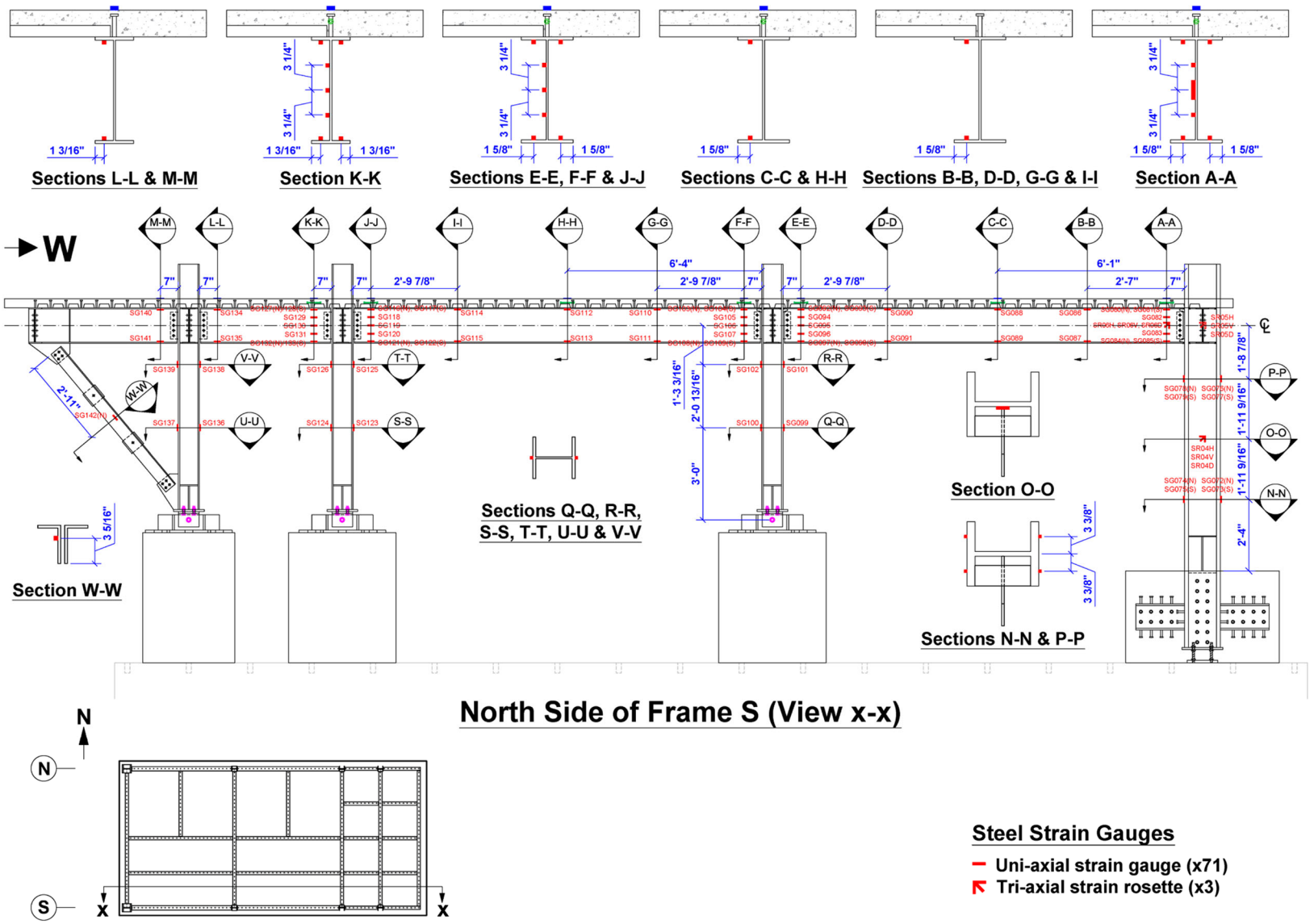

(d) Steel Strain Gauges on Frame S

Figure 3.32 Instrumentation Plan for Phase 1 Test: Strain Gauge Layout (continued)

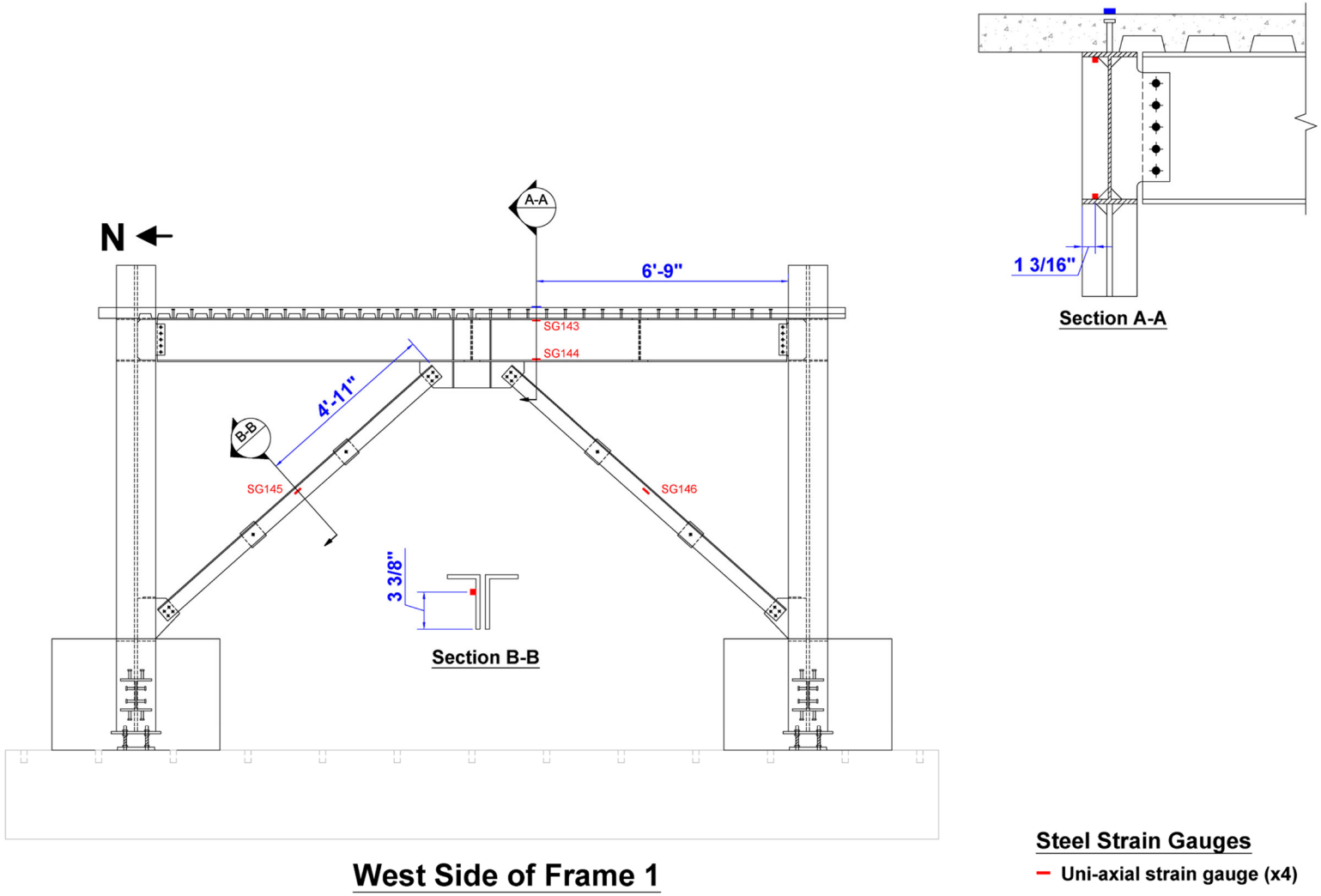

(e) Steel Strain Gauges on Frame 1

Figure 3.32 Instrumentation Plan for Phase 1 Test: Strain Gauge Layout (continued)

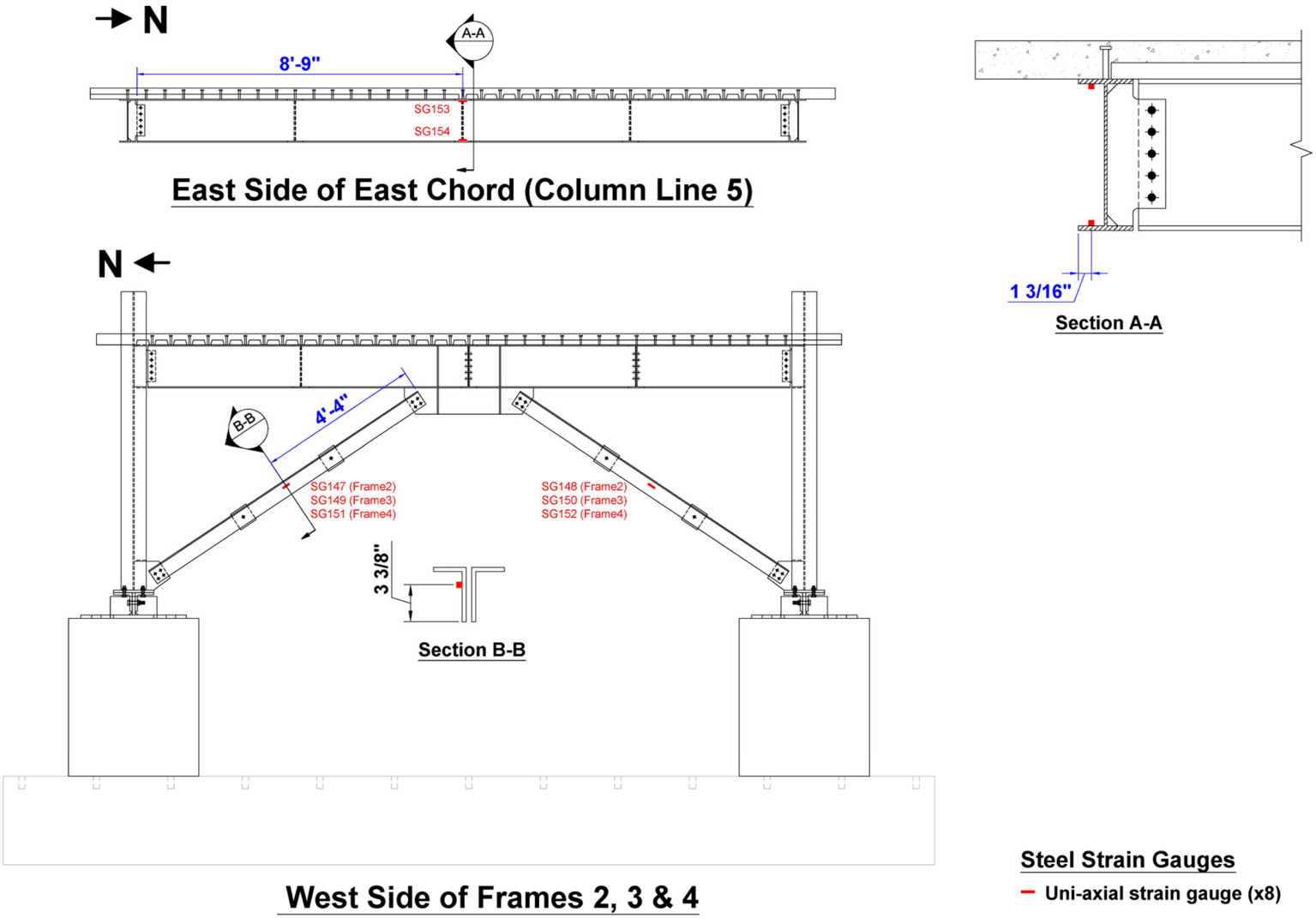

(f) Steel Strain Gauges on East Chord and Frames 2, 3, and 4

Figure 3.32 Instrumentation Plan for Phase 1 Test: Strain Gauge Layout (continued)

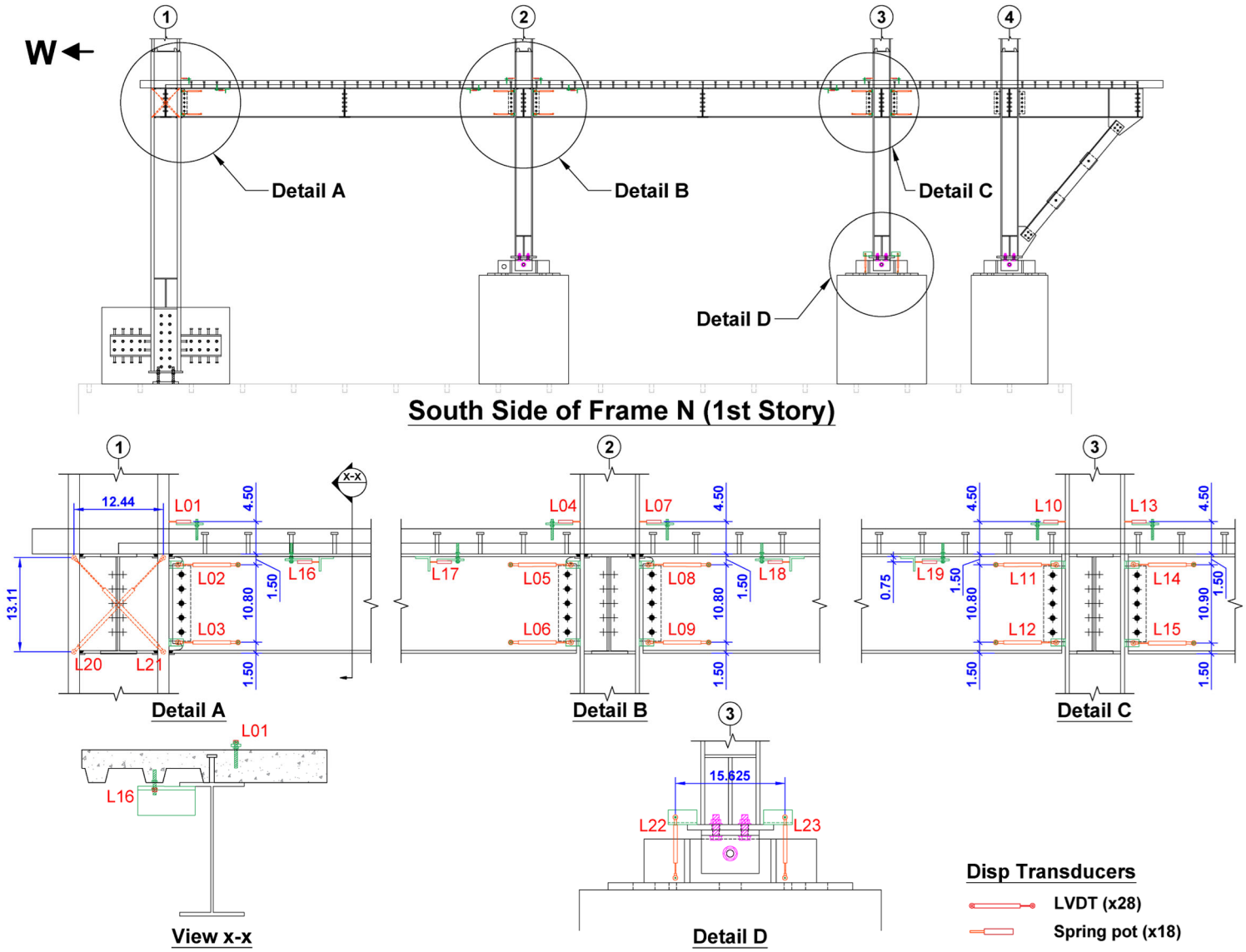

(a) Displacement Transducers on Frame N

Figure 3.33 Instrumentation Plan for Phase 1 Test: Displacement Transducer Layout

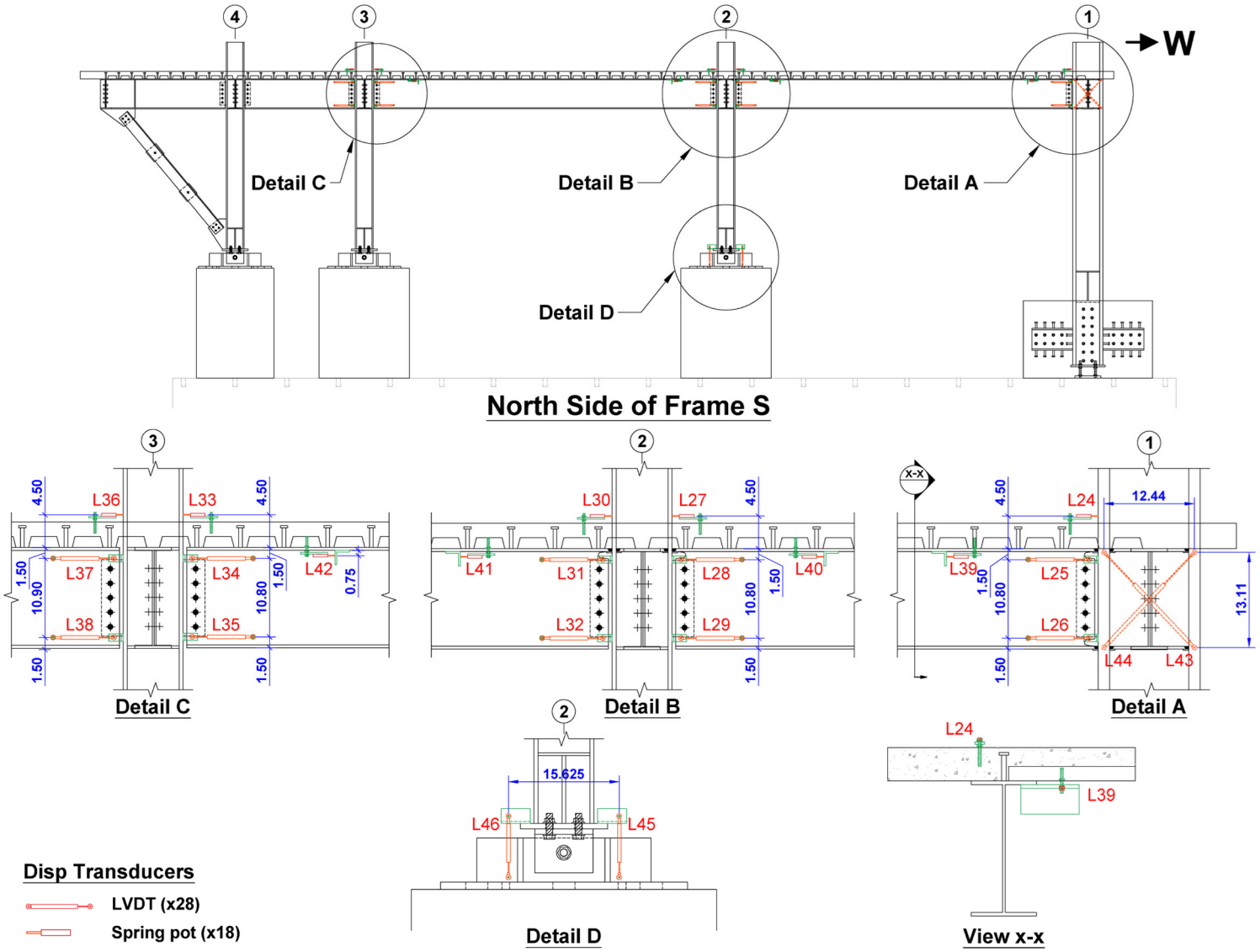

(b) Displacement Transducers on Frame S

Figure 3.33 Instrumentation Plan for Phase 1 Test: Displacement Transducer Layout (continued)

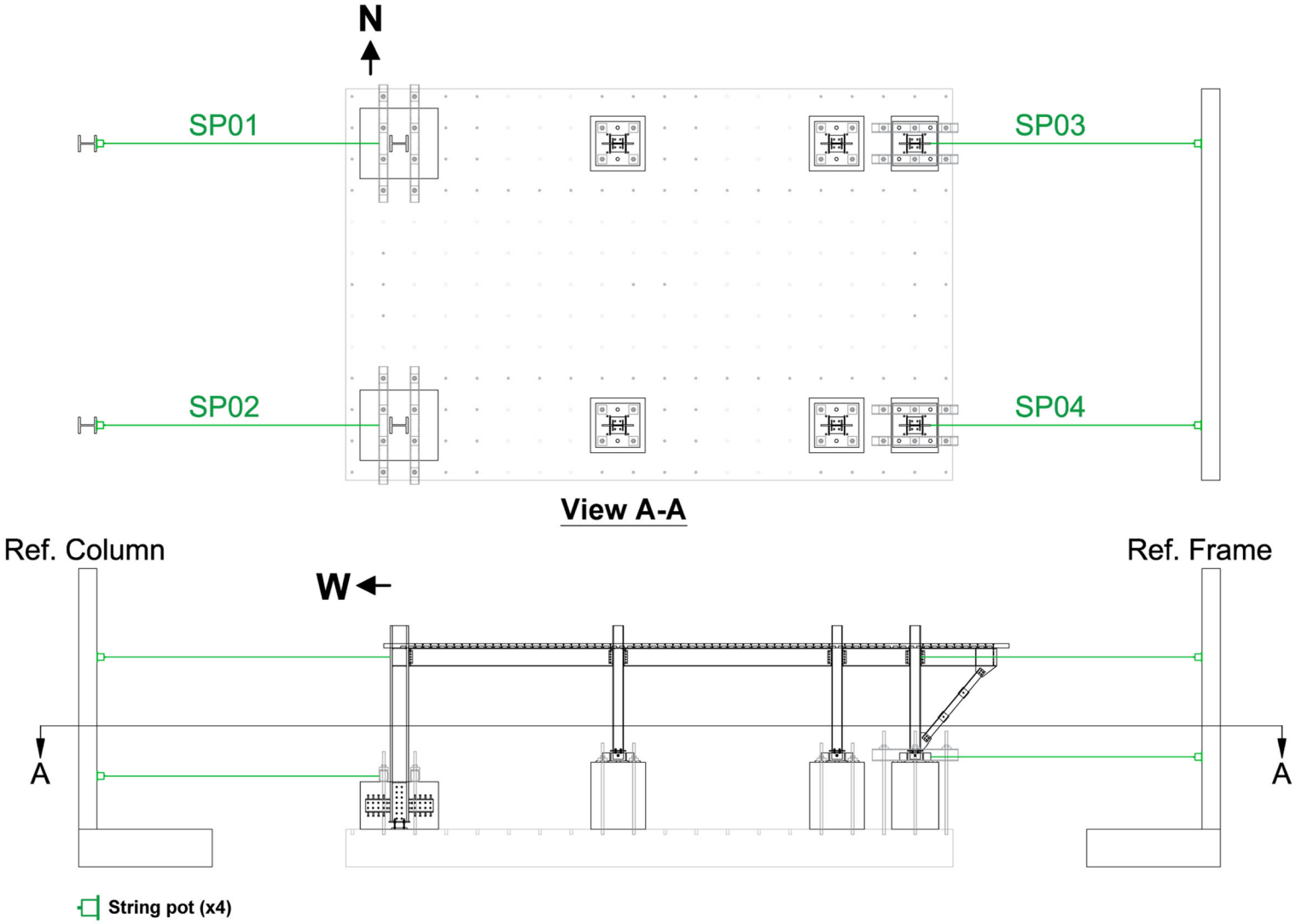

(a) String Pots on Footing Level

Figure 3.34 Instrumentation Plan for Phase 1 Test: String Potentiometer Layout

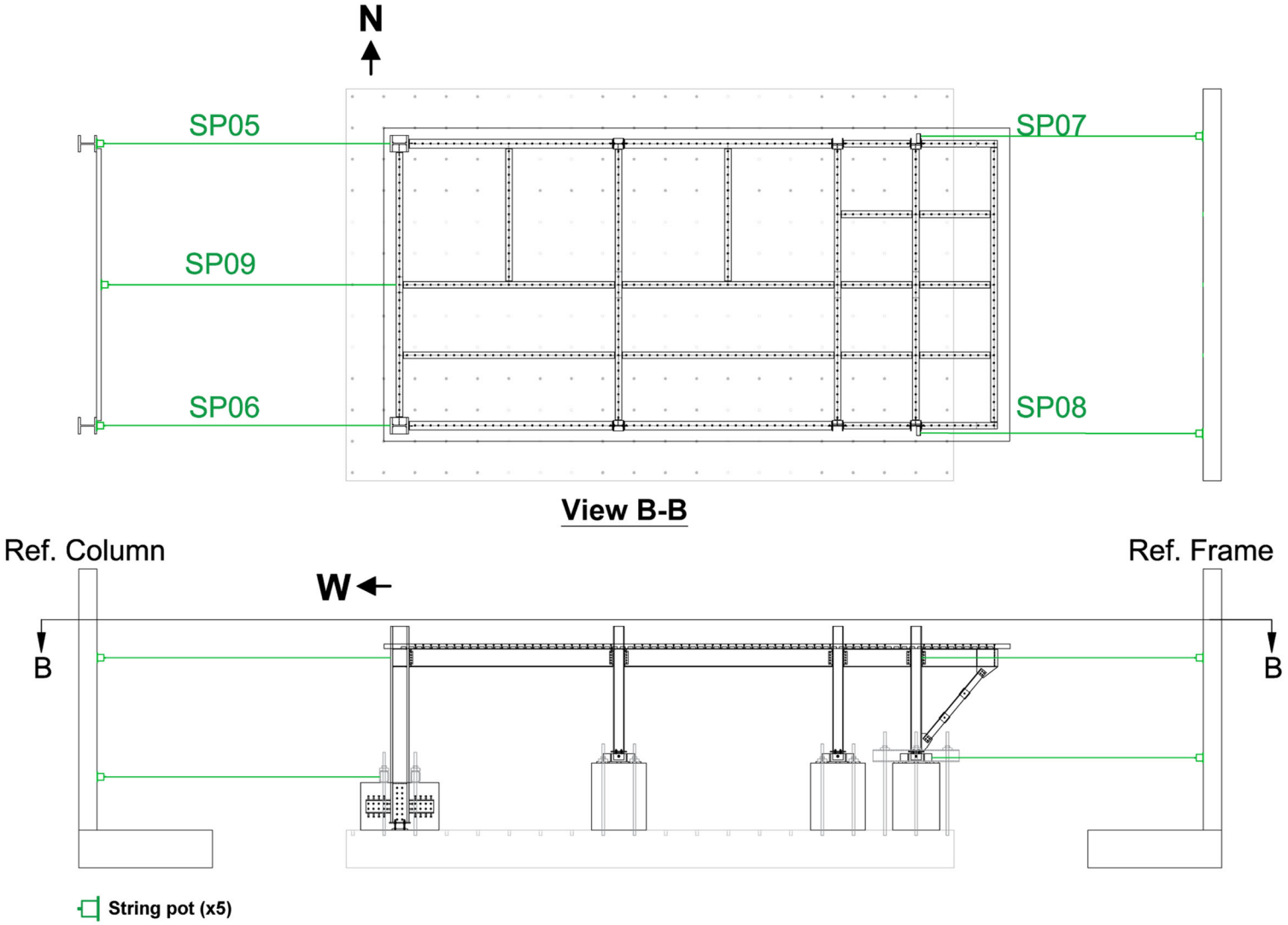

(b) String Pots on 2nd Floor Level

Figure 3.34 Instrumentation Plan for Phase 1 Test: String Potentiometer Layout (continued)

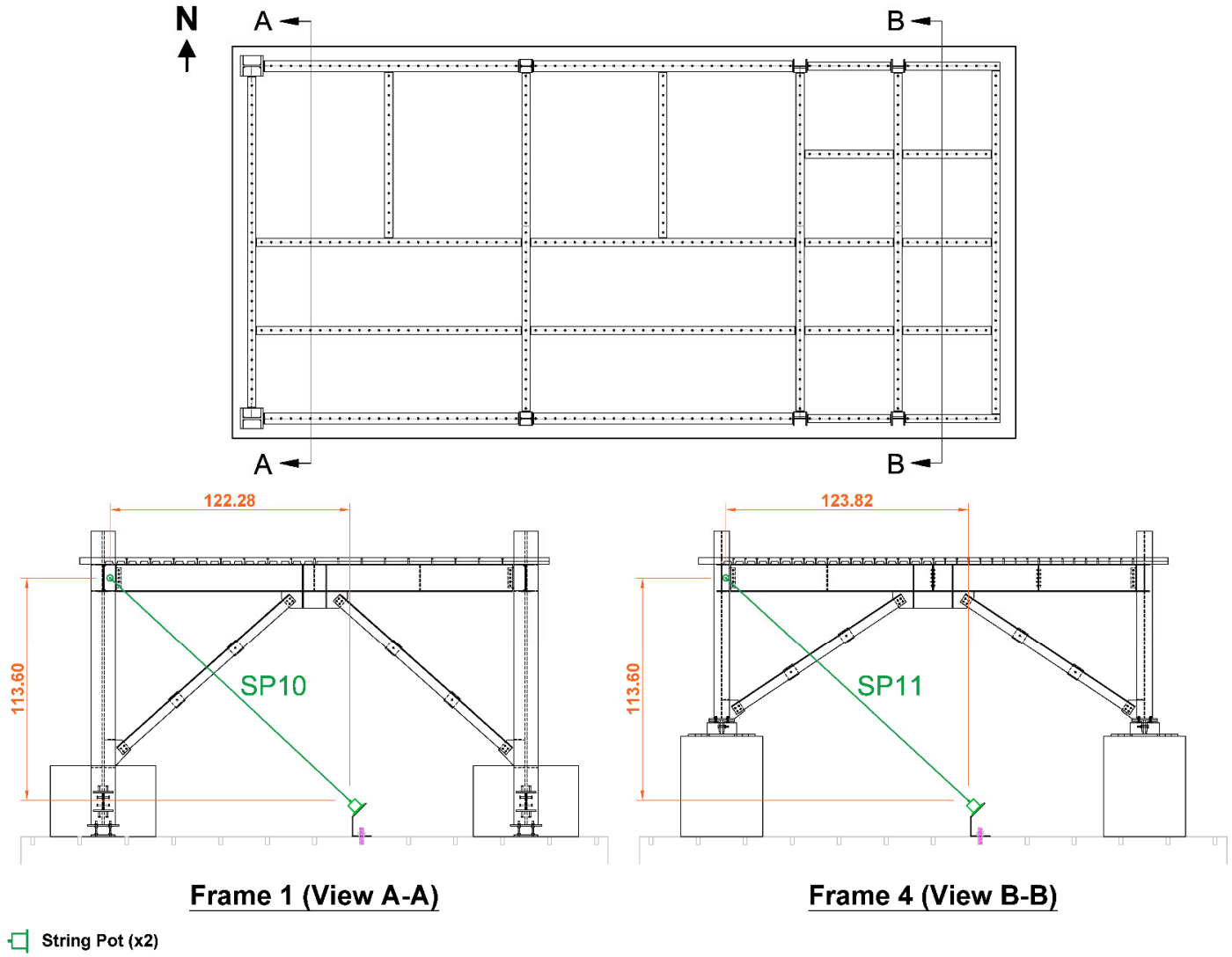

(c) Diagonal String Pots for Measuring Transverse Displacement

Figure 3.34 Instrumentation Plan for Phase 1 Test: String Potentiometer Layout (continued)

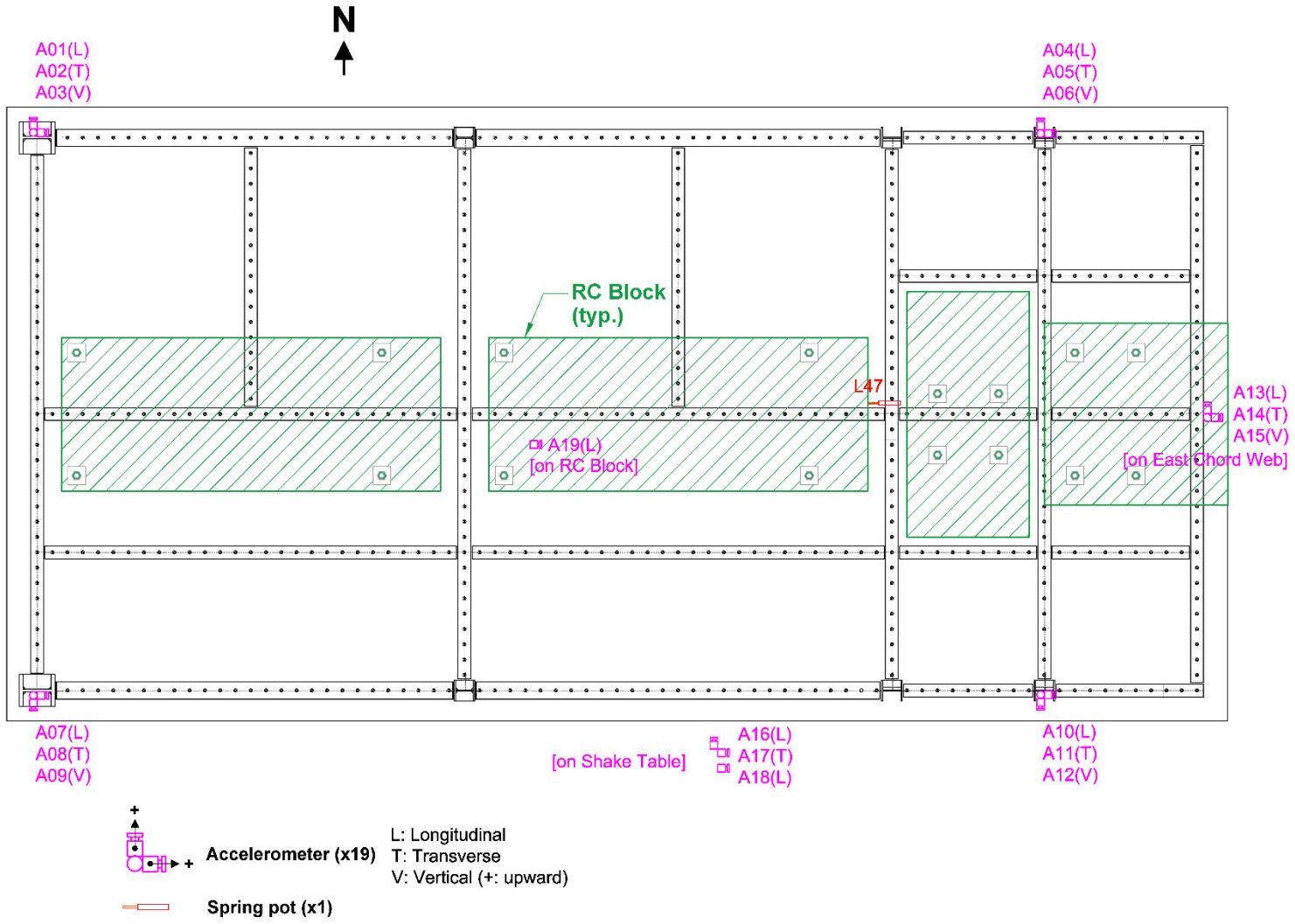

Figure 3.35 Instrumentation Plan for Phase 1 Test: Accelerometer Layout

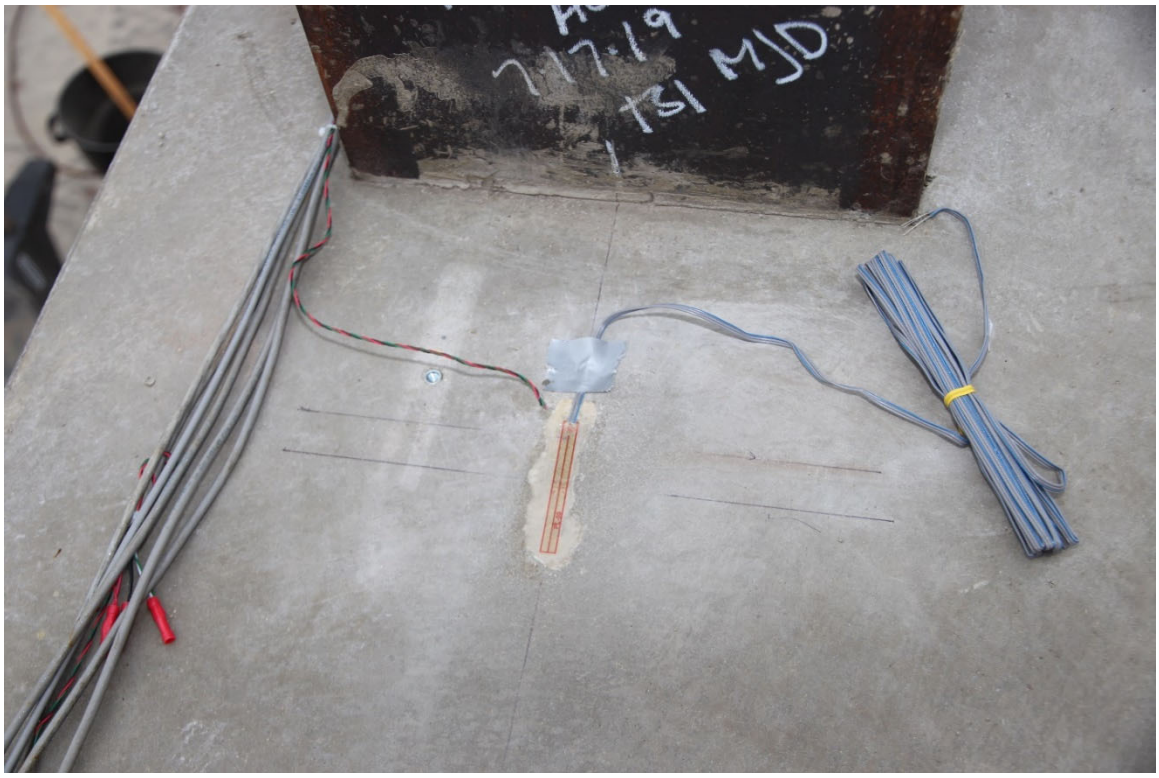

Figure 3.36 Concrete Surface Strain Gauge

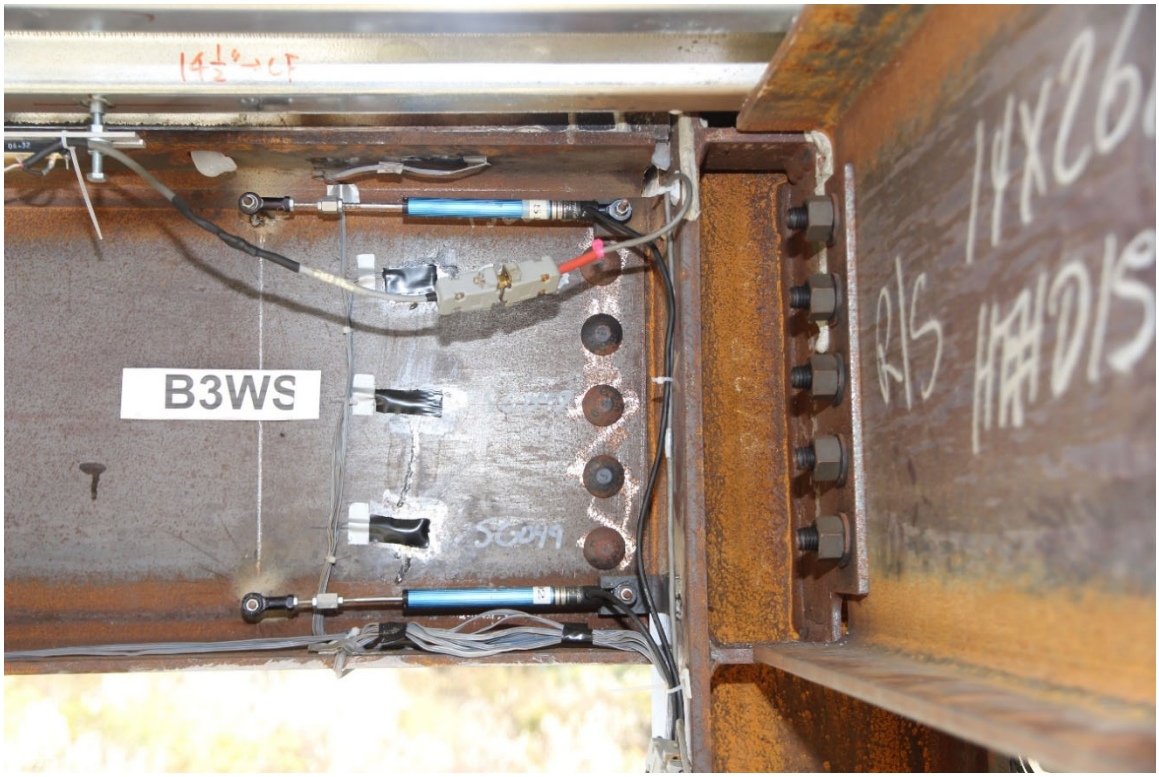

Figure 3.37 Displacement Transducers Installed at Steel Collector-to-Column Connection

Figure 3.38 Displacement Transducer Installed between Slab and Column

Figure 3.39 Displacement Transducers Installed at Gravity Column Pin-support

Figure 3.40 Displacement Transducer Installed between Slab and Collector

Figure 3.41 Displacement Transducers Installed at Cantilever Column Panel Zone

3.5 Material Properties

A992 steel was specified for all the beams and columns, A572 Gr. 50 Steel was specified for the additional plates, including shear tabs, continuity plates, gusset plates, and stiffeners, and A36 steel was specified for the double-angle braces. The specified grades and material properties based on tensile coupon test results are summarized in Table 3.17. Tensile test results in the form of stress-strain curves are shown in Figure 3.42. All materials satisfied ASTM requirements except the W12×170 column flange and web coupons.

The specified concrete compressive strengths, f_c', for the 2nd floor slab, cantilever column footings, gravity column footings were 4 ksi, 8 ksi, and 5 ksi, respectively. Table 3.18 shows the results of the concrete cylinder tests that were conducted on the Phase 1 test day. A325 (Group A) high-strength bolts were specified for the collector-to-column connections, transverse beam-to-column connections, beam-to-beam connections, and gusset plate connections.

Table 3.17 Steel Tensile Coupon Test Results

Component	Steel Type	Nominal Thickness (in.)	Measured Thickness (in.)	F_y (ksi)	F_u (ksi)	Elong.[a] (%)
W12×170 Column Flange	A992	1.560	1.520	48.52	66.54	45.8
W12×170 Column Web	A992	0.960	1.022	49.40	66.73	47.2
W8×40 Column Flange	A992	0.560	0.510	52.77	68.31	41.7
W8×40 Column Web	A992	0.360	0.357	54.70	69.36	34.7
W14×30 Collector Flange-1	A992	0.385	0.362	53.52	75.25	34.8
W14×30 Collector Flange-2	A992	0.385	0.364	53.81	75.02	32.6
W14×30 Collector Web-1	A992	0.270	0.271	55.56	75.19	34.6
W14×30 Collector Web-2	A992	0.270	0.271	55.33	75.23	32.3
W14×26 Collector Flange	A992	0.420	0.392	52.63	70.27	37.9
W14×26 Collector Web	A992	0.255	0.269	54.60	69.35	36.5
Shear Tab (PL$^1/_4$")	A572 Gr. 50	0.250	0.253	70.37	76.57	21.1
a) Elongation values are based on test results of coupons with 2 in. gage length						

Table 3.18 Concrete Cylinder Test Results

Component	Age (Days)	f_c' of Each Cylinder (ksi)		Average f_c' (ksi)
Gravity Column Footings -Truck #1	68	#1:	6.357	6.181
		#2:	6.103	
		#3:	6.082	
Gravity Column Footings -Truck #2	68	#1:	5.424	5.348
		#2:	5.234	
		#3:	5.386	
Cantilever Column Footings	53	#1:	8.432	8.182
		#2:	8.673	
		#3:	7.441	
2nd Floor Slab	15	#1:	3.968	4.218
		#2:	4.468	
		#3:	4.217	

Test Date: 8/20/2019

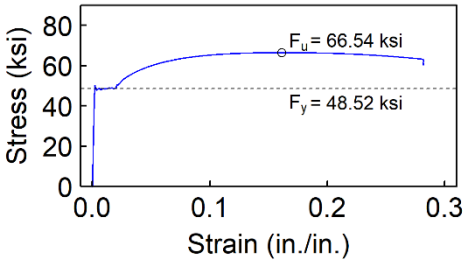

(a) W12x170 Column Flange

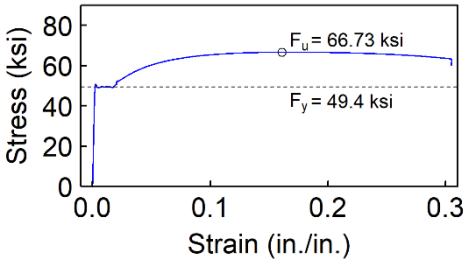

(b) W12x170 Column Web

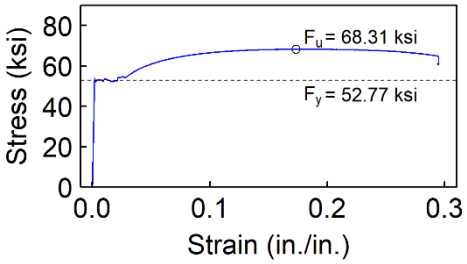

(c) W8x40 Column Flange

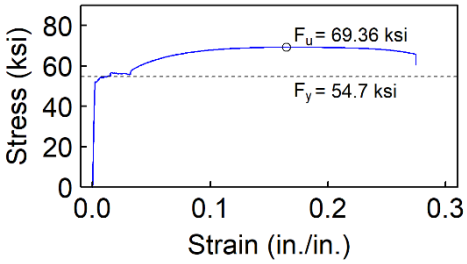

(d) W8x40 Column Web

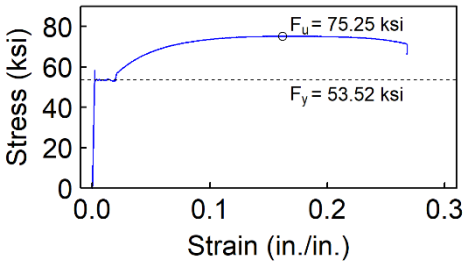

(e) W14x26 Collector Flange-1

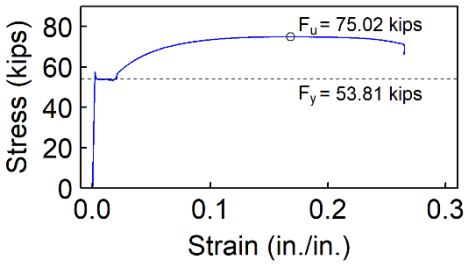

(f) W14x30 Collector Flange-2

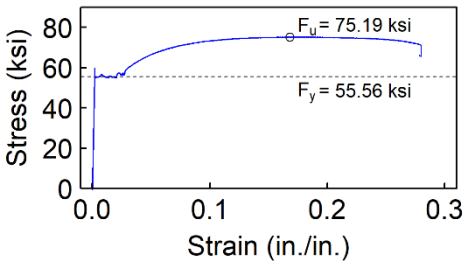

(g) W14x30 Collector Web-1

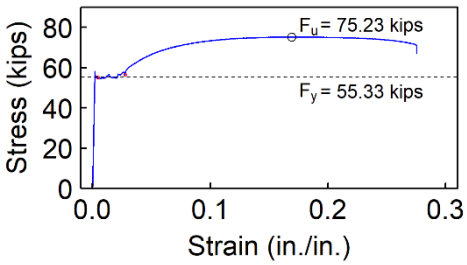

(h) W14x30 Collector Web-2

Figure 3.42 Steel Coupon Stress-Strain Curves

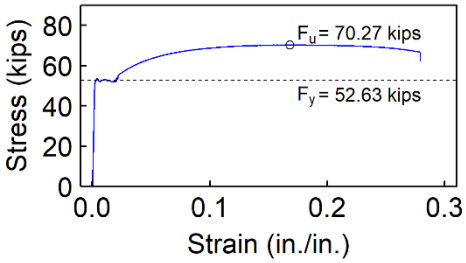

(i) W14x26 Collector Flange

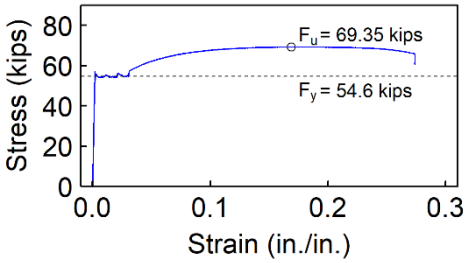

(j) W14x26 Collector Web

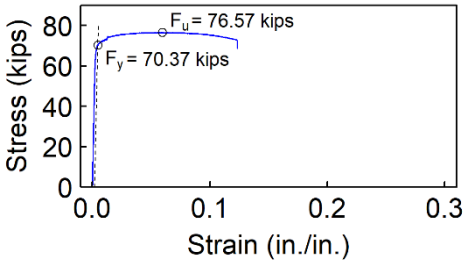

(k) Shear Tab for 2nd Floor Collector

Figure 3.42 Steel Coupon Stress-Strain Curves (continued)

3.6 Testing Protocol

3.6.1 General

As shown in Table 3.19, Phase 1 testing was composed of three main tests, which were carried out by using the proposed floor acceleration simulation testing methodology, and several dynamic characterization tests. The three main tests, designated as Tests 1-1, 1-2, and 1-3, respectively, were conducted to excite the testing building to reproduce the 5^{th} floor acceleration responses of a prototype 12-story building structure under the earthquakes with intensities at 20%, 50%, 100% of design earthquake level, respectively. The target prototype floor acceleration responses were obtained from the time history analyses on a frame model representing the protype structure. The dynamic characterization tests were performed by using a 2-munite white noise motion with a peak ground acceleration (PGA) at 0.1 g or a short duration impulse type motion with a PGA at 0.2 g to assess the dynamic characteristics (natural periods and damping) of the specimen between main tests to detect and track accumulating damage of the specimen. In addition, the fundamental period and damping assessed by the dynamic characterization test prior to each main test were employed to generate the input motion for the main test. Section 3.6.2 introduces the time history analyses for obtaining target prototype floor accelerations, while Section 3.6.3 presents the detailed procedures for generating input motions for main tests.

3.6.2 Time History Analyses on Prototype Structure Model

Time history analyses were performed on a frame model representing the prototype structure to obtain the floor acceleration responses of the prototype structure subjected to earthquakes at various intensity levels. The 12-story SDII building was chosen as the prototype structure in this program. As shown in Figure 3.43, a 2-dimensional (2-D) frame model was constructed by using

the structural analysis software PISA3D (Lin et al. 2009) to simulate the response of half of the prototype building structure in the longitudinal direction. Note that the except for the beams in the two buckling-restrained braced frames (BRBFs), all the beams in the exterior frame were collectors. In addition to constructing a frame model to present an exterior longitudinal frame, an elastic leaning column was developed to simulate the $P-\Delta$ effect from the interior part of half the building loads. For the exterior frame model, the columns and beams were modeled by beam-column element with the lumped plasticity approach and bilinear material model. For simplicity, all the collector-to-column connections were assumed as by pin-connections. The diagonal Buckling-restrained Braces (BRBs) were modeled by truss elements with a material model adopting two-surface plastic hardening rule (Dafalias and Popov, 1976). The parameters of the material model for BRBs were finely tuned such that, as shown in Figure 3.44, the hysteretic responses of a single BRB truss model well matched the nonlinear properties [strength adjustment factor (β or ω) versus core strain relationships] provided by a BRB supplier, CoreBrace, LLC.

Figure 3.45 illustrates the assignment of gravity loads to the 2-D frame model. The loads tributary to the exterior frame were applied on the exterior frame model in terms of uniform line loads on the beams and point loads on the columns. The total gravity loads tributary to each floor of the interior frame were lumped as a point load applied on the leaning column. The gravity load combination of $1.0D + 0.2L_0$, where D and L_0 are dead load and unreduced live load, respectively, was applied to the analytical model prior to the time history analysis. Figure 3.46 illustrates the mass assignments for the 2D-model. To simulate the phenomenon that inertial forces among the floor diaphragm would be eventually dragged into the collectors in the exterior frame, the total mass tributary to each column was lumped as a nodal mass assigned to each column. No mass was

assigned to the leaning column. The mass sources considered were the area dead load on the floors, exterior walls, and partition walls.

Figure 3.47 shows the modal analysis results on the first three modes. The periods for the 1st, 2nd, and 3rd modes were T_1 = 2.833 sec, T_2 = 1.005 sec, and T_3 = 0.594 sec, respectively. A 2% Rayleigh damping for the 1st and 2nd modes was employed for the model. A ground motion record (Beverly Hills-14145 Mulhol Station) from the 1994 Northridge Earthquake was selected and scaled to three intensity levels: 20%, 50%, and 100% Design Earthquake (DE) levels for time history analyses on the prototype structure model. For ground motion scaling, a DE spectrum per ASCE-7 (ASCE 2016) was constructed with S_{DS} = 1.03 and S_{D1} = 0.569[see Figure 3.48(b)] and T1-method was used. The ground motion was linearly scaled such that the spectral acceleration of the ground motion matches 20%, 50%, or 100% of the DE spectrum value at the period T_1. Figure 3.48 shows the 100% DE-scaled ground motion.

Figure 3.49 through Figure 3.54 show the key results of the time history analyses on the prototype structure for three intensity levels of input ground motions. See Figure 3.49, Figure 3.51, and Figure 3.53 for the floor acceleration responses at intensities of 20%, 50% and 100% DE, respectively. See Figure 3.50, Figure 3.52, and Figure 3.54 for the story drift angle responses at intensities of 20%, 50% and 100% DE, respectively. The prototype structure model responded elastically during the earthquake at 20% DE level. From the fast Fourier transforms (FFTs) of the floor accelerations shown in Figure 3.49(b), it can be found that most of the floors exhibited an acceleration response dominated by the 2nd mode. For those floors with 2nd mode-dominated acceleration response, the period corresponding to the peak responses of the FFTs and spectra matched T_2 very well. On the other hands. The prototype structure model experienced moderate and significant inelasticity during the earthquake at 50% and 100% DE levels, respectively.

Similarly, for these two intensity levels, most floor exhibited an 2nd mode-dominated acceleration response. However, for these 2nd mode-dominated floors, the period corresponding to peak responses of the FFTs was close to but slightly deviated from T_2. The deviation is more promising for the responses at 100% DE levels. These suggest that the inelasticity of the structure lead to this period deviation. Finally, the 5th floor accelerations at three intensities were selected to be the target accelerations for the test specimen because all of them had a considerable peak acceleration and a promising 2nd-mode dominated behavior.

3.6.3 Generation of Input Accelerations

Figure 3.55 shows the procedure for generating the shake table input motion for each floor acceleration simulation testing on the scaled test specimen. The analytical 5th floor acceleration response of the prototype structure model, $\ddot{u}^t(t)$, which was obtained form a time history analysis for an input ground motion, $\ddot{u}_g(t)$ with a duration of t_d, was selected to be the basis of the target floor acceleration for the specimen. Since the test building was a 1/2-scale specimen (i.e., scale factor l_d = 0.5), based on the similitude law, the time of the floor acceleration time history, $\ddot{u}^t(t)$, was scaled by a factor of $\sqrt{l_d} = \sqrt{0.5}$. Then, the scaled acceleration time history, $\ddot{u}^t_{sq}(t)$, with a duration of $\sqrt{l_d}t_d$ was taken as the target floor acceleration for the test specimen.

Prior to each floor acceleration simulation testing, a dynamic characterization test, such as white-noise or impulse tests, was conducted to identify the fundamental period, T_n, and damping ratio, ξ, of the specimen. Considering the single-story test building as an SDOF system, the transfer function in the frequency domain, $H(\omega)$, between the output absolute acceleration, $\ddot{u}^{t*}(\omega)$, and the input ground acceleration, $\ddot{u}^*_g(\omega)$ of the specimen was determined from Equation

(2.7) with two experimentally-determined parameters: natural angular frequency $\omega_n = 2\pi/T_n$ and damping ratio ξ.

With the transfer function, $H(\omega)$, the required shake table input motion in the frequency-domain was determined from $\ddot{u}_g^*(\omega) = \ddot{u}_{sq}^t(\omega)/H(\omega)$, where $\ddot{u}_{sq}^t(\omega)$ was obtained by taking fast Fourier transform (FFT) of $\ddot{u}_{sq}^t(t)$. Subsequently, by performing an inverse fast Fourier transform (IFFT) on $\ddot{u}_g^*(\omega)$, the required input motion time history for the test frame, $\ddot{u}_g^*(t)$, was obtained. Subsequently, along with a baseline correction and a filtering with cut-in and cut-out frequencies at 0.2 Hz and 30 Hz, respectively, the time series $\ddot{u}_g^*(t)$ was extended at both ends with zero padding, each of duration 10 seconds, to obtain the finalized shake table input motion, $\ddot{u}_g^{**}(t)$. Note that the input motion, $\ddot{u}_g^{**}(t)$, was intended to make the middle portion, with a duration of $\sqrt{l_d}t_d$, of the floor acceleration response, $\ddot{u}^{t*}(t)$, achieved by the specimen can reproduce the target floor acceleration, $\ddot{u}_{sq}^t(t)$. Finally, Figure 3.56 summarizes the three intensity levels of time history analyses and floor acceleration simulation tests in Phase 1 test program.

Table 3.19 Test Matrix (Phase 1)

Phase 1 Tests		
Test No.	Description	Test Date
WN 1-0	White Noise Test	8/19/2019
IM 1-0	Impulse Test	8/20/2019
1-1	Floor Acc. Simulation Test (20% DE)	8/20/2019
IM 1-1	Impulse Test	8/20/2019
1-2	Floor Acc. Simulation Test (50% DE)	8/20/2019
IM 1-1	Impulse Test	8/20/2019
1-3	Floor Acc. Simulation Test (100% DE)	8/20/2019
WN 1-3	White Noise Test	8/20/2019
IM 1-3	Impulse Test	8/20/2019

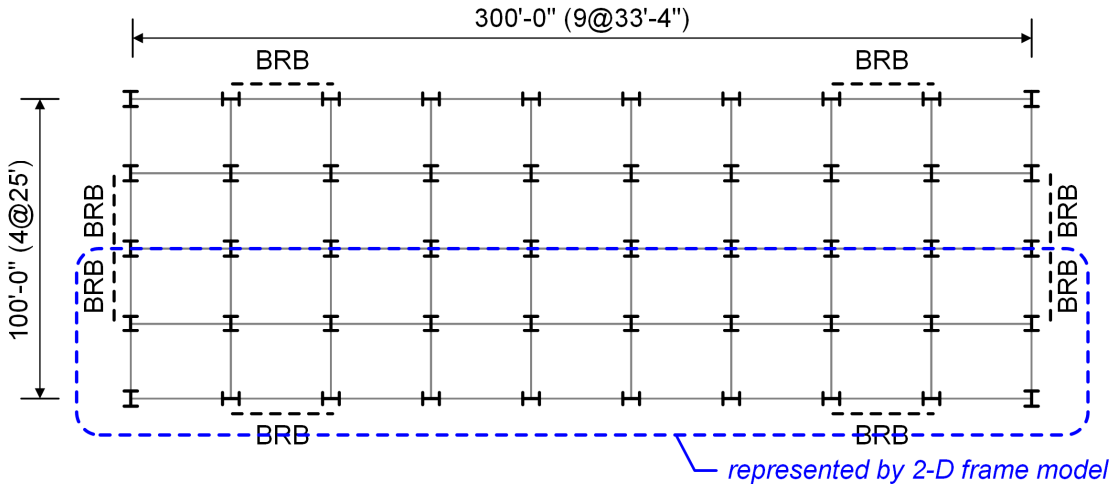

(a) Floor Plan

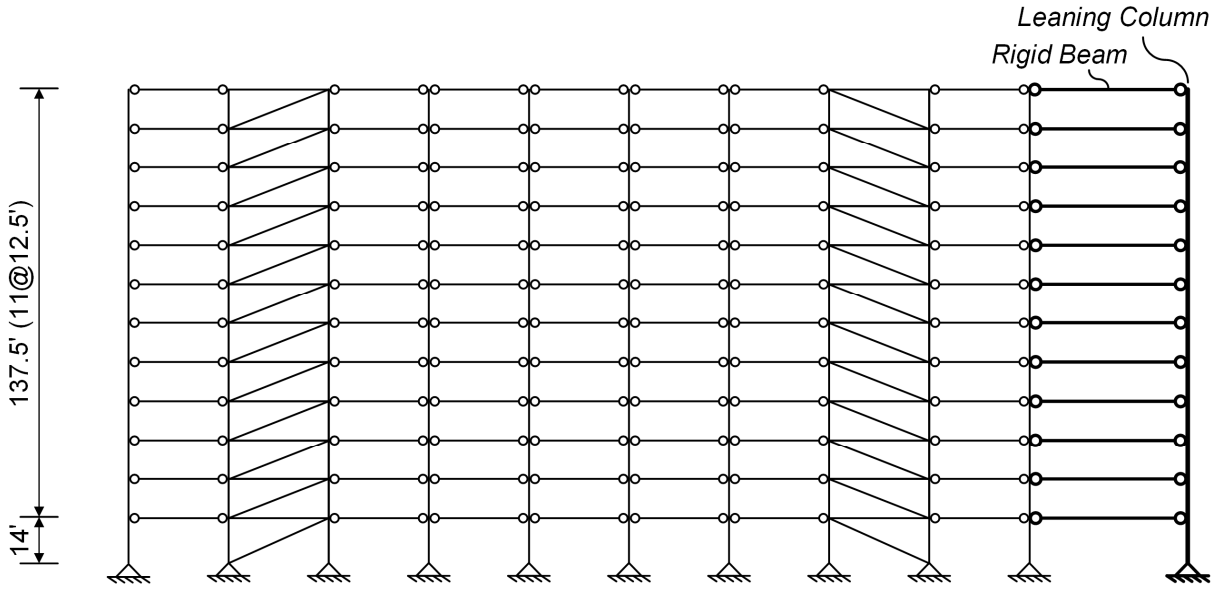

(a) 2-D Frame Model

Figure 3.43 (a) Floor Plan and (b) 2-D Frame Model for Prototype Structure

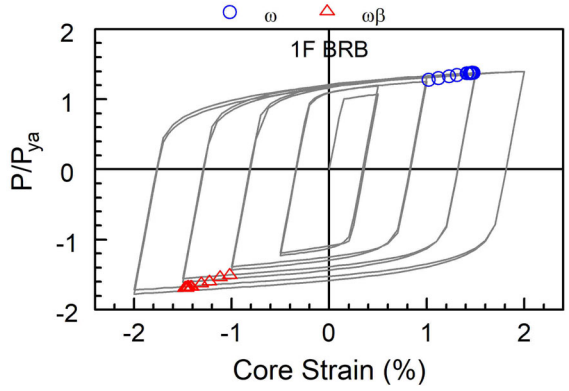

Figure 3.44 Analytical Hysteresis Responses of Buckling-restrained Braces

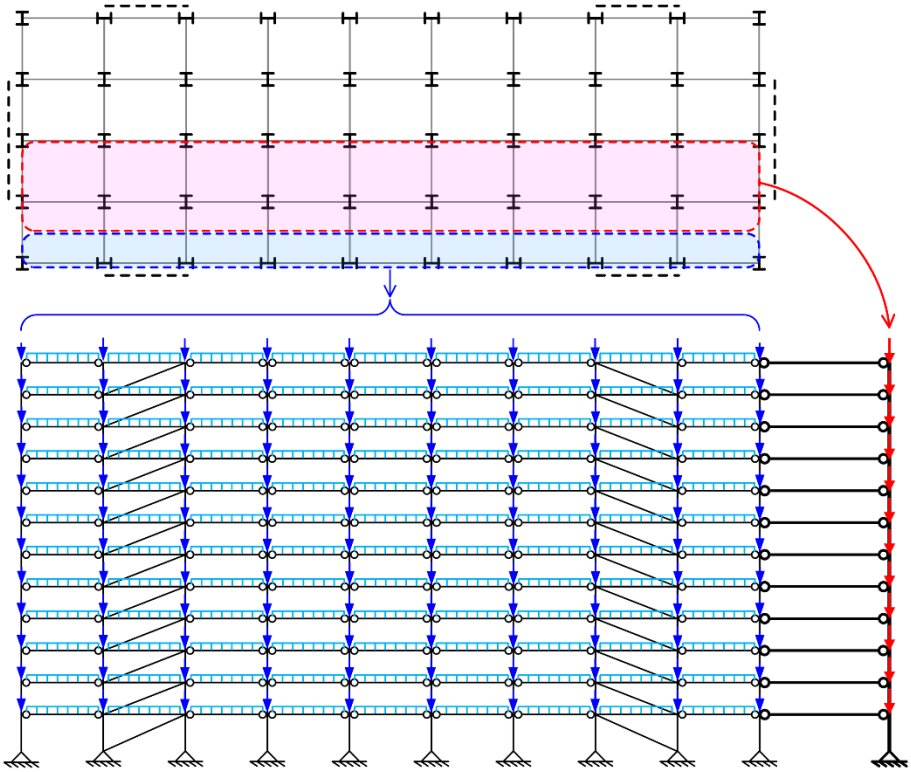

Figure 3.45 Assignment of Gravity Loads to 2-D Frame Model for Prototype Structure

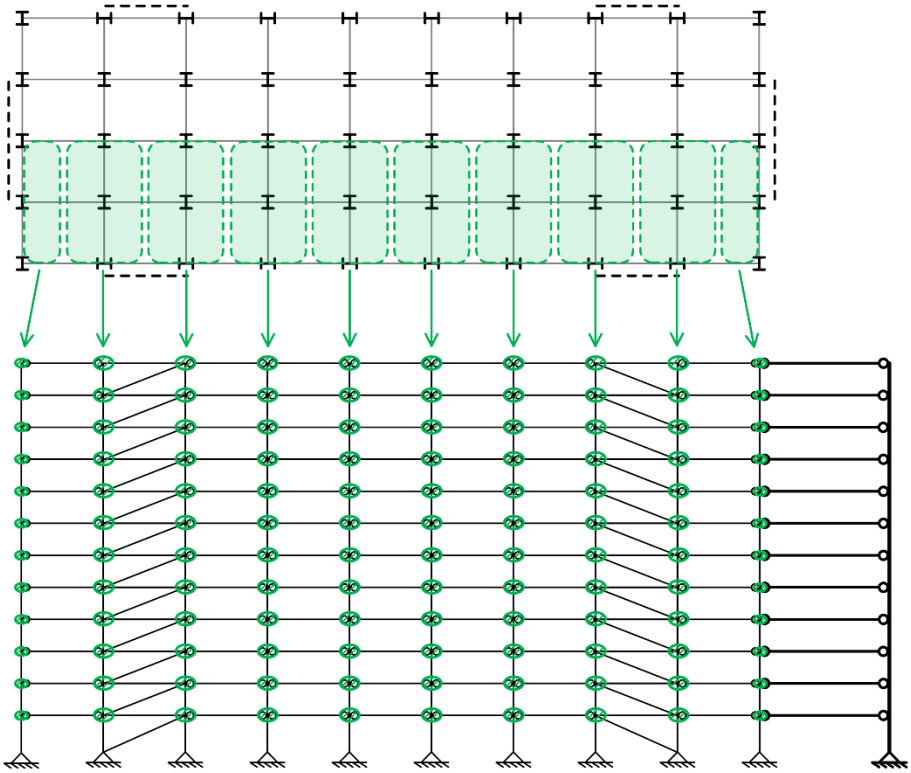

Figure 3.46 Assignment of Masses to 2-D Frame Model for Prototype Structure

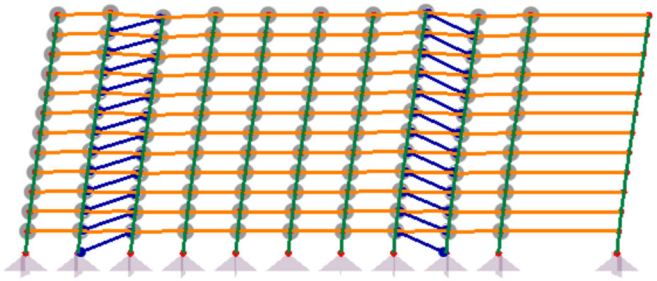

(a) 1st Mode (T_1 = 2.833 sec)

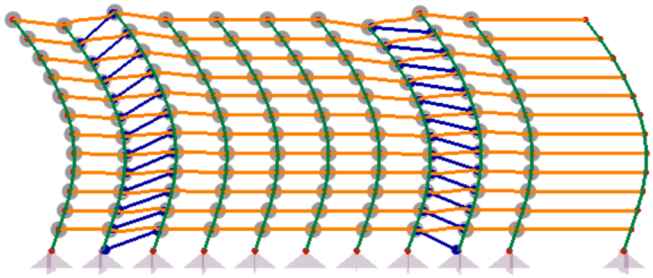

(b) 2nd Mode (T_2 = 1.005 sec)

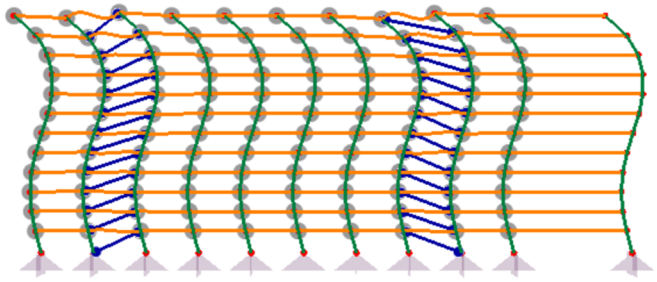

(c) 3rd Mode (T_3 = 0.594 sec)

Figure 3.47 Model Analysis Results for Prototype Model

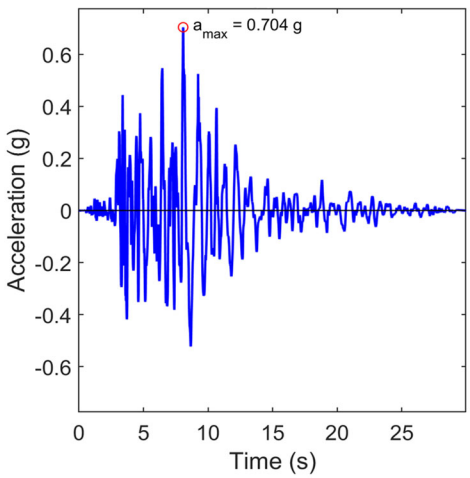

(a) Scaled Ground Acceleration

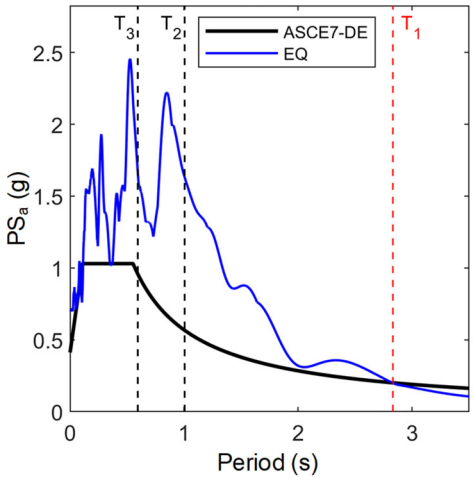

(b) Response Spectrum

Figure 3.48 Input Motion Scaled to 100% Design Earthquake (DE) Level for Prototype Model

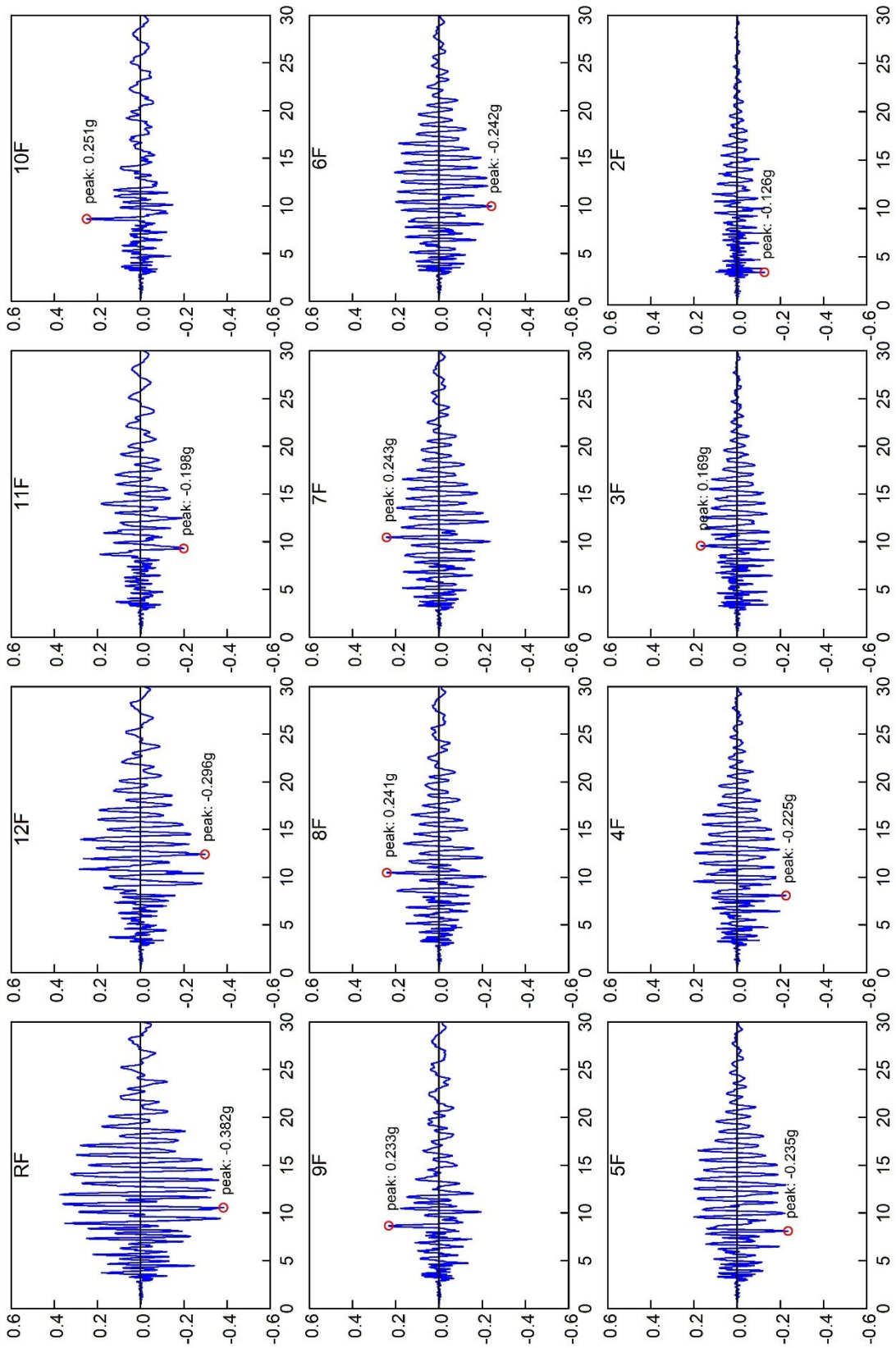

(a) Time Histories

Figure 3.49 Results of Time History Analysis on Prototype Model at 20% Design Earthqaule Level: Floor Accelerations

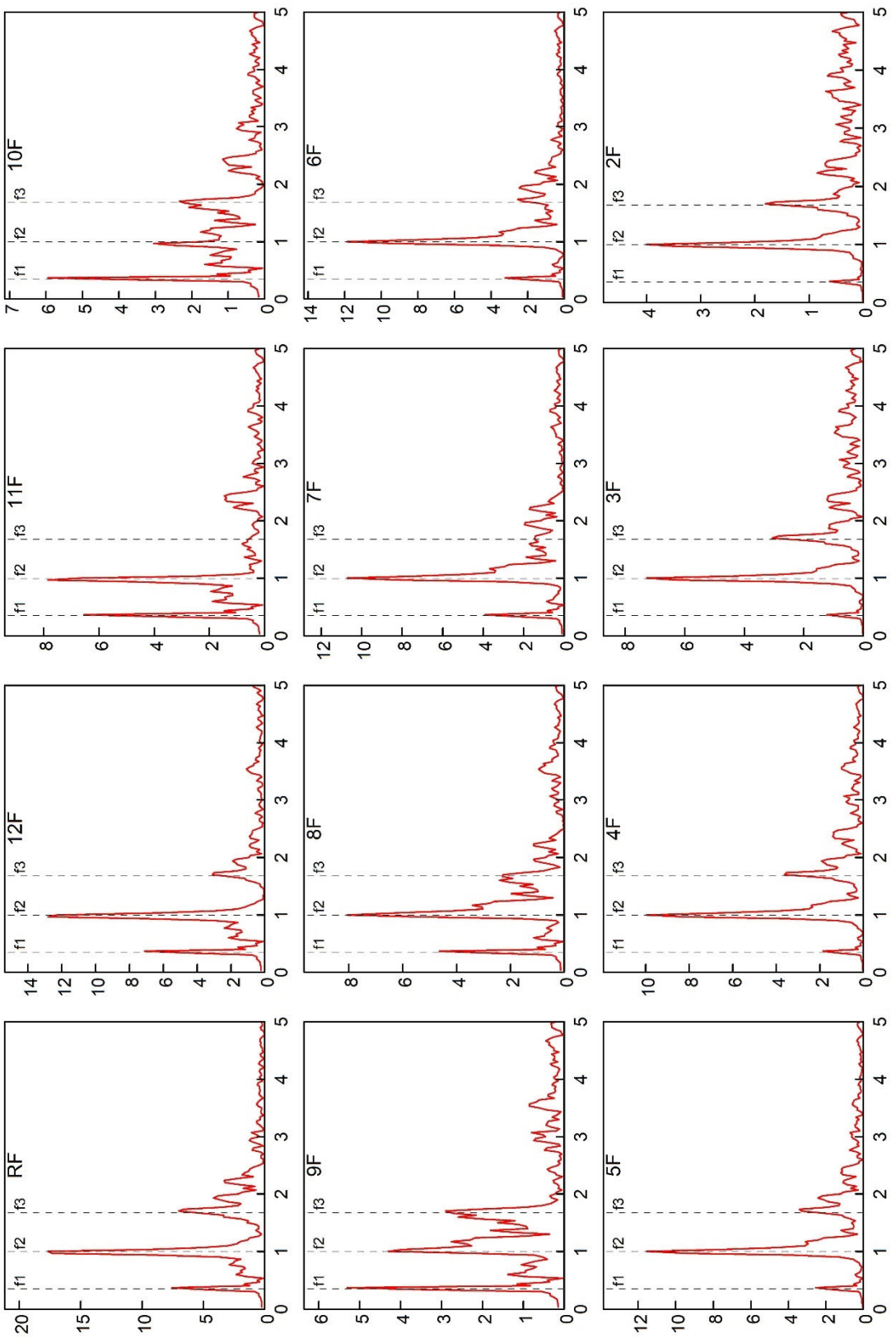

(b) Fast Fourier Transforms

Figure 3.49 Results of Time History Analysis on Prototype Model at 20% Design Earthqaule Level (continued)

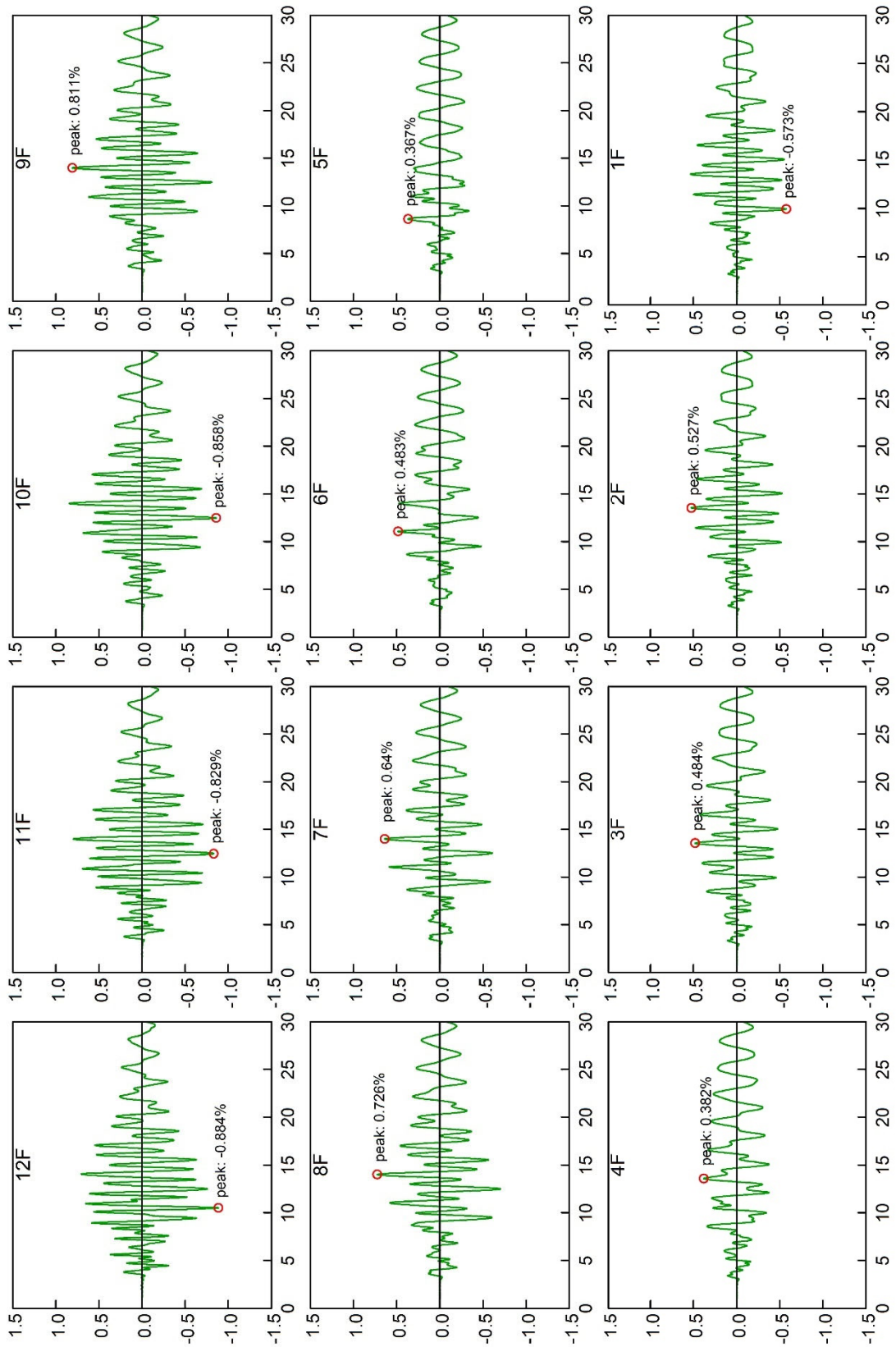

Figure 3.50 Results of Time History Analysis on Prototype Model at 20% Design Earthqaule Level: Story Drift Angles

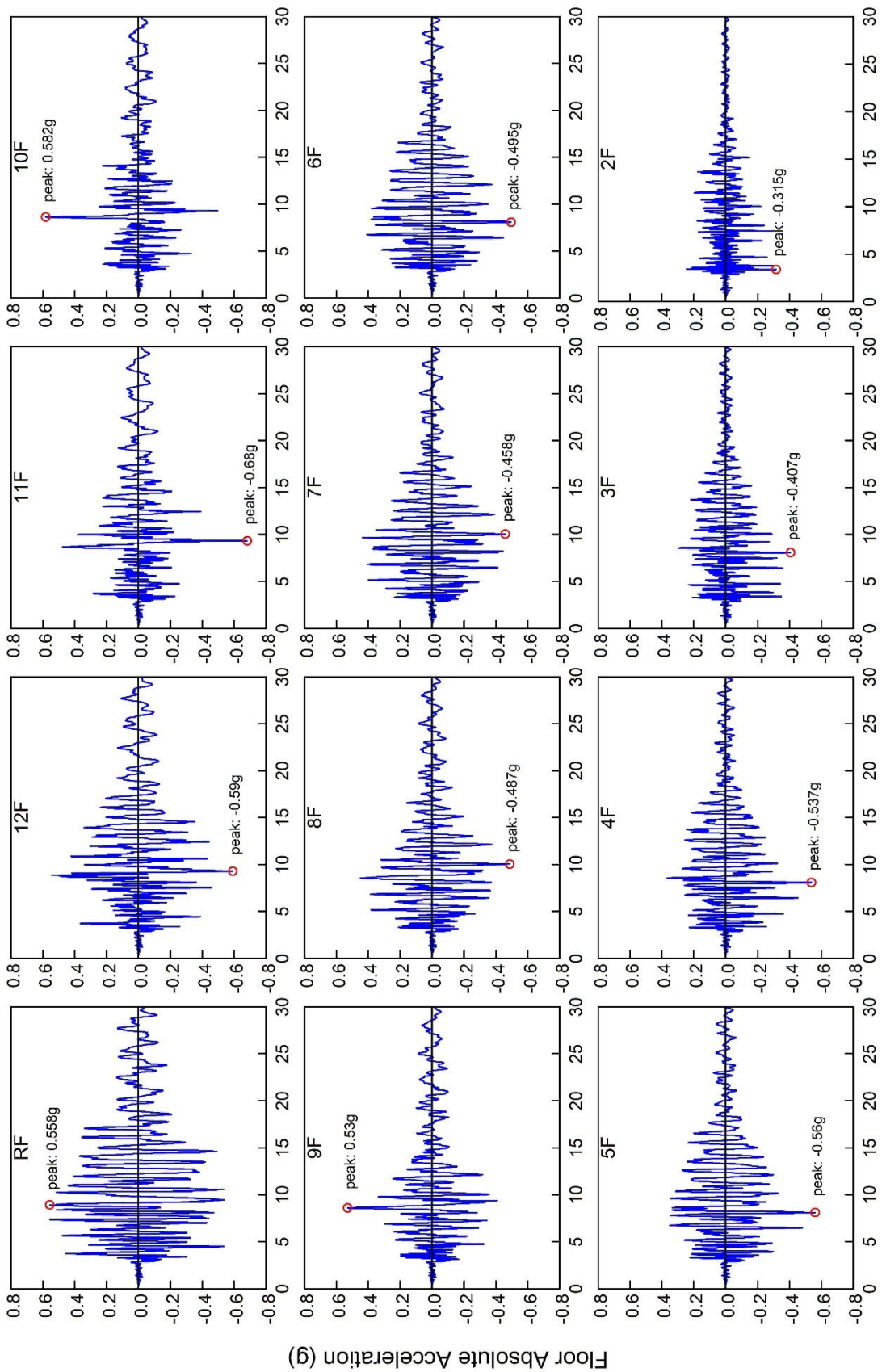

(a) Time Histories

Figure 3.51 Results of Time History Analysis on Prototype Model at 50% Design Earthqaule Level: Floor Accelerations

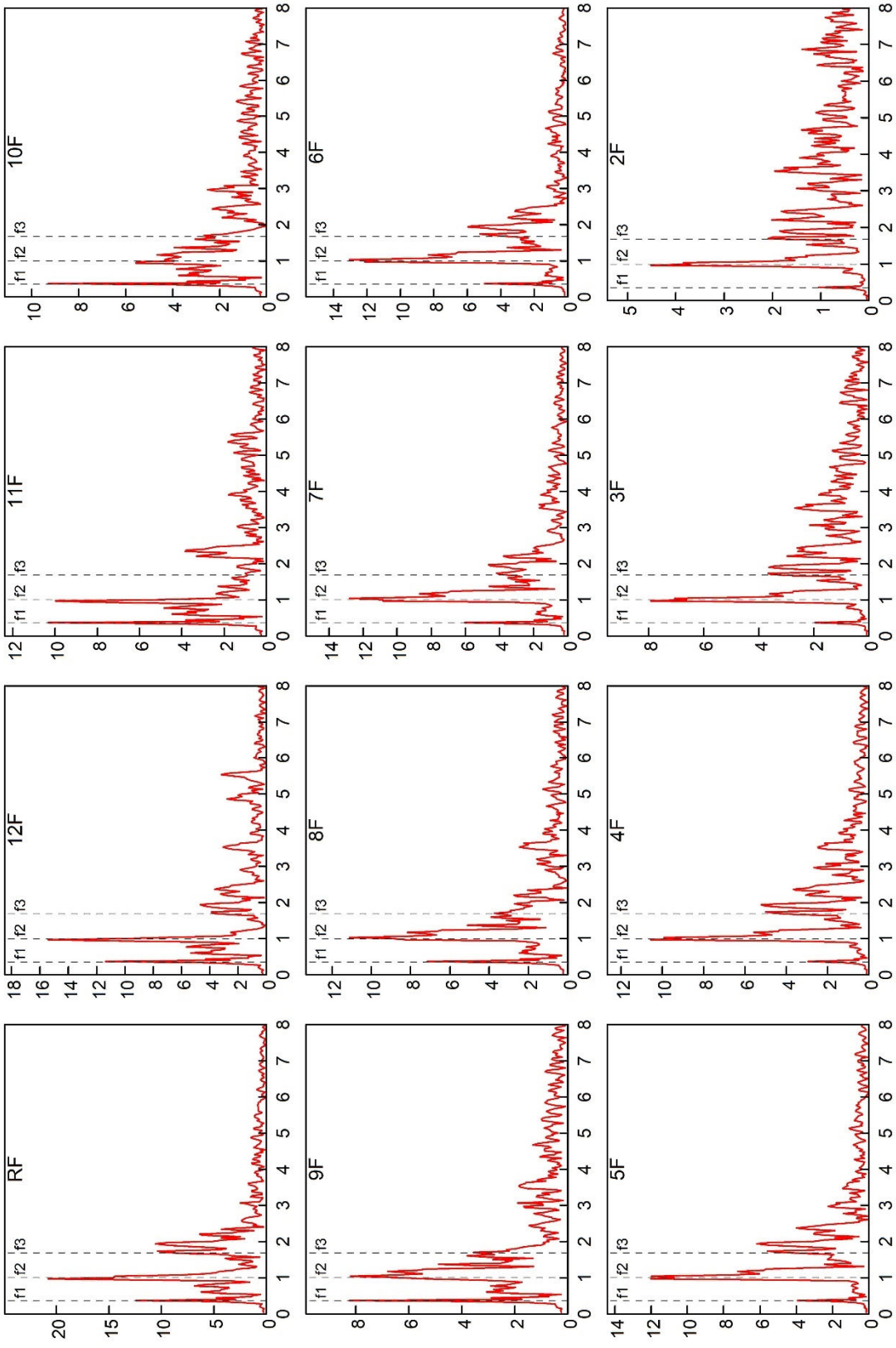

(b) Fast Fourier Transforms

Figure 3.51 Results of Time History Analysis on Prototype Model at 50% Design Earthqaule Level: Floor Accelerations (continued)

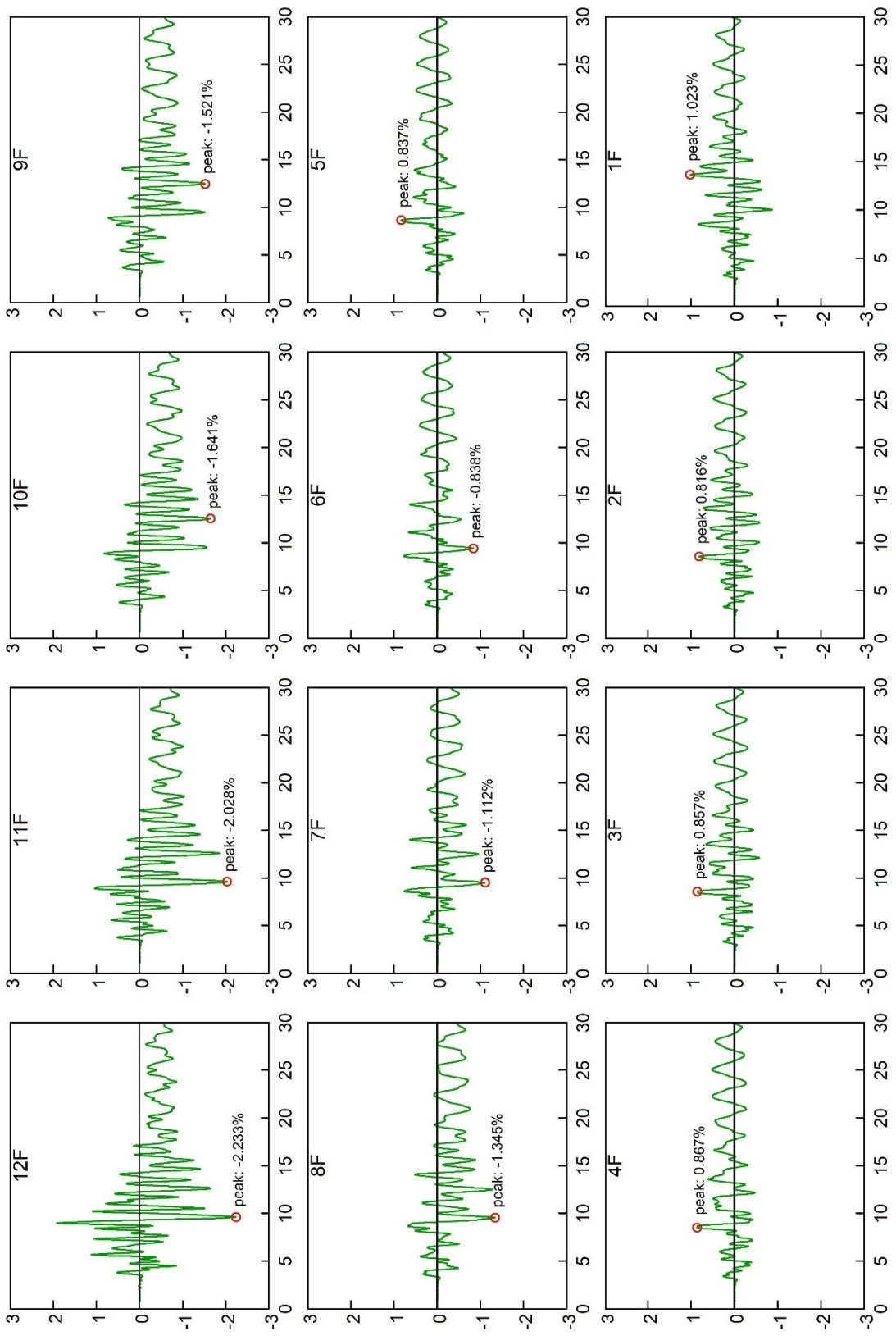

Figure 3.52 Results of Time History Analysis on Prototype Model at 50% Design Earthqaule Level: Story Drift Angles

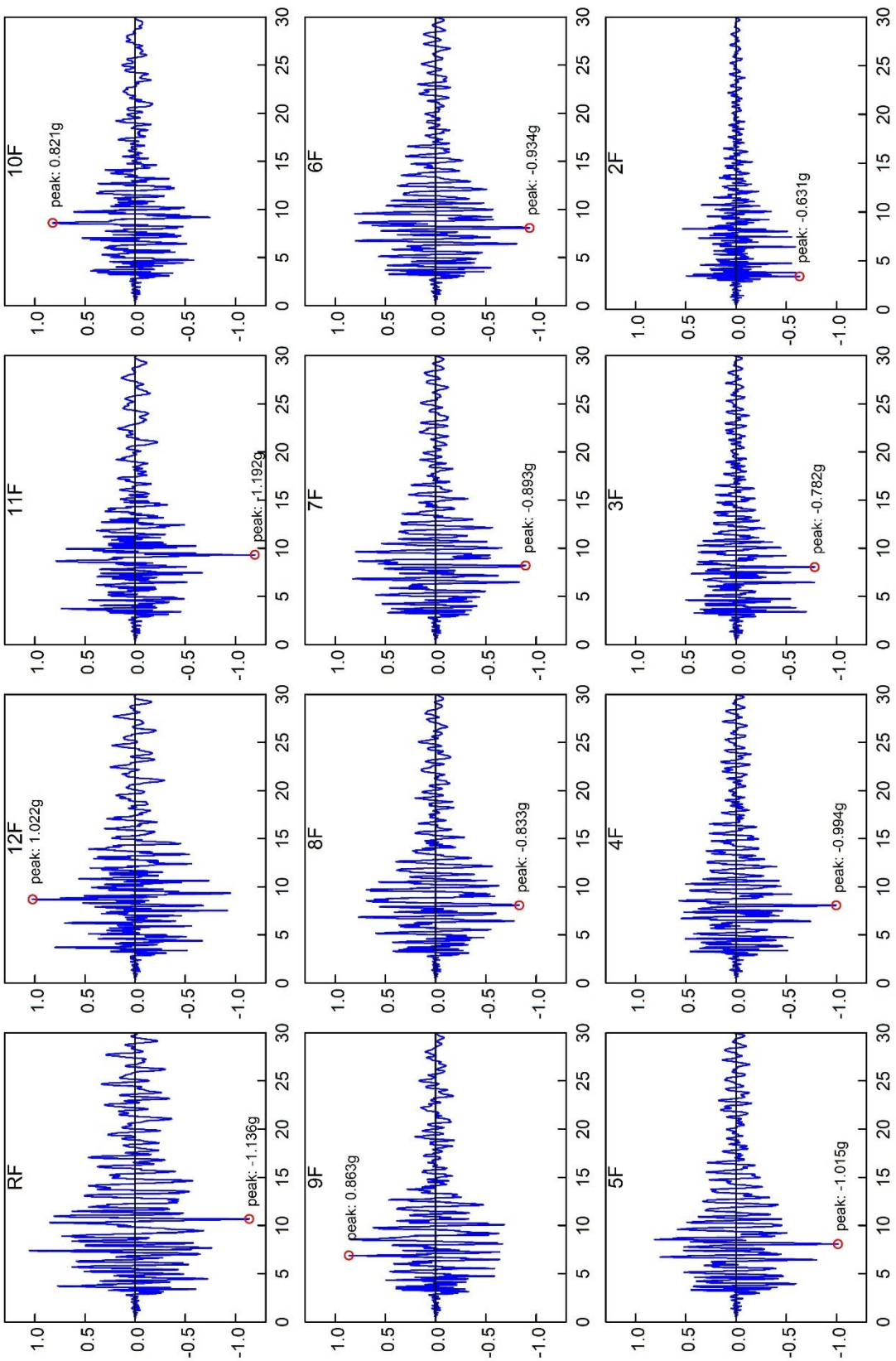

(a) Time Histories

Figure 3.53 Results of Time History Analysis on Prototype Model at 100% Design Earthqaule Level: Floor Accelerations

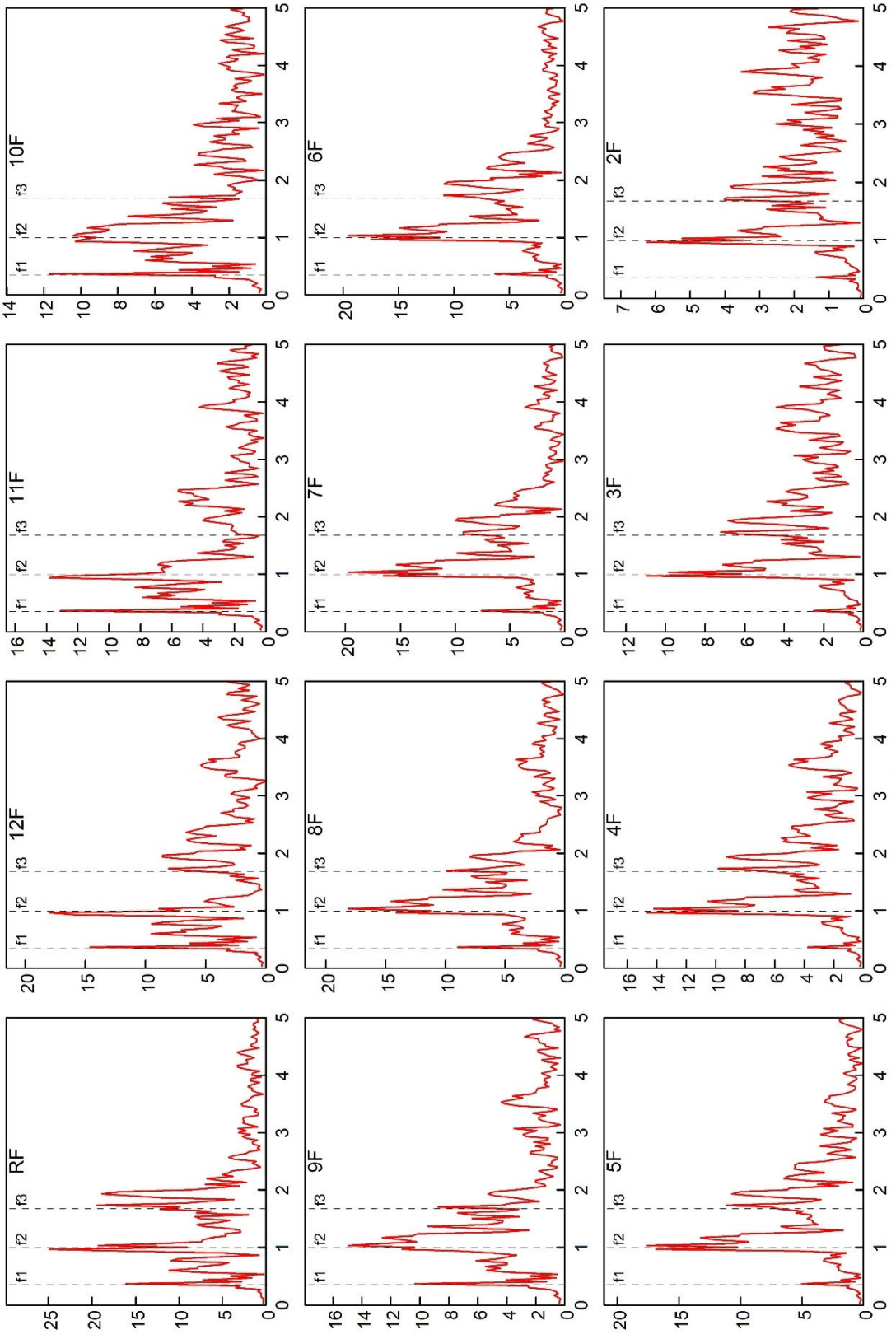

(b) Fast Fourier Transforms

Figure 3.53 Results of Time History Analysis on Prototype Model at 100% Design Earthqaule Level: Floor Accelerations (continued)

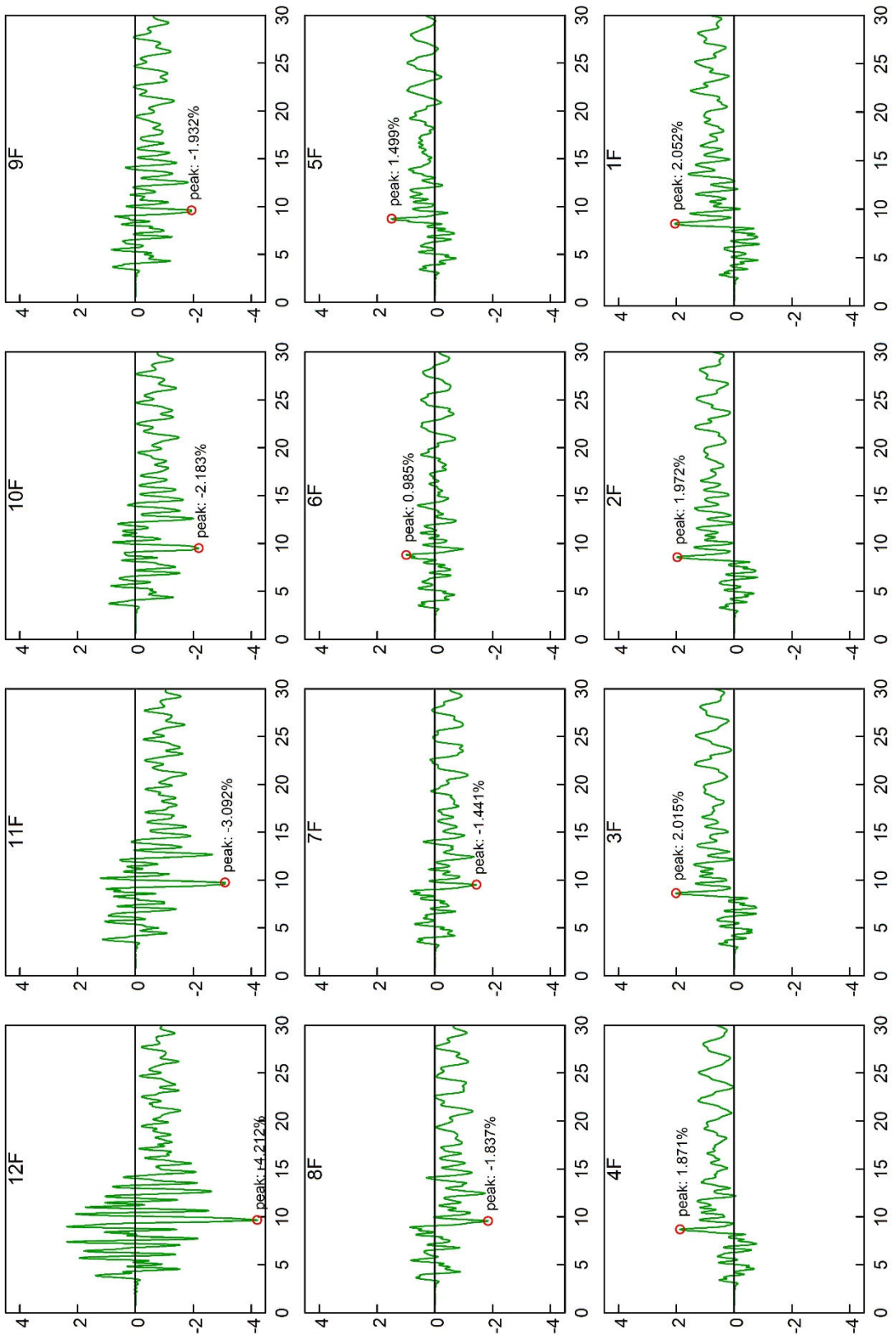

Figure 3.54 Results of Time History Analysis on Prototype Model at 100% Design Earthqaule Level: Story Drift Angles

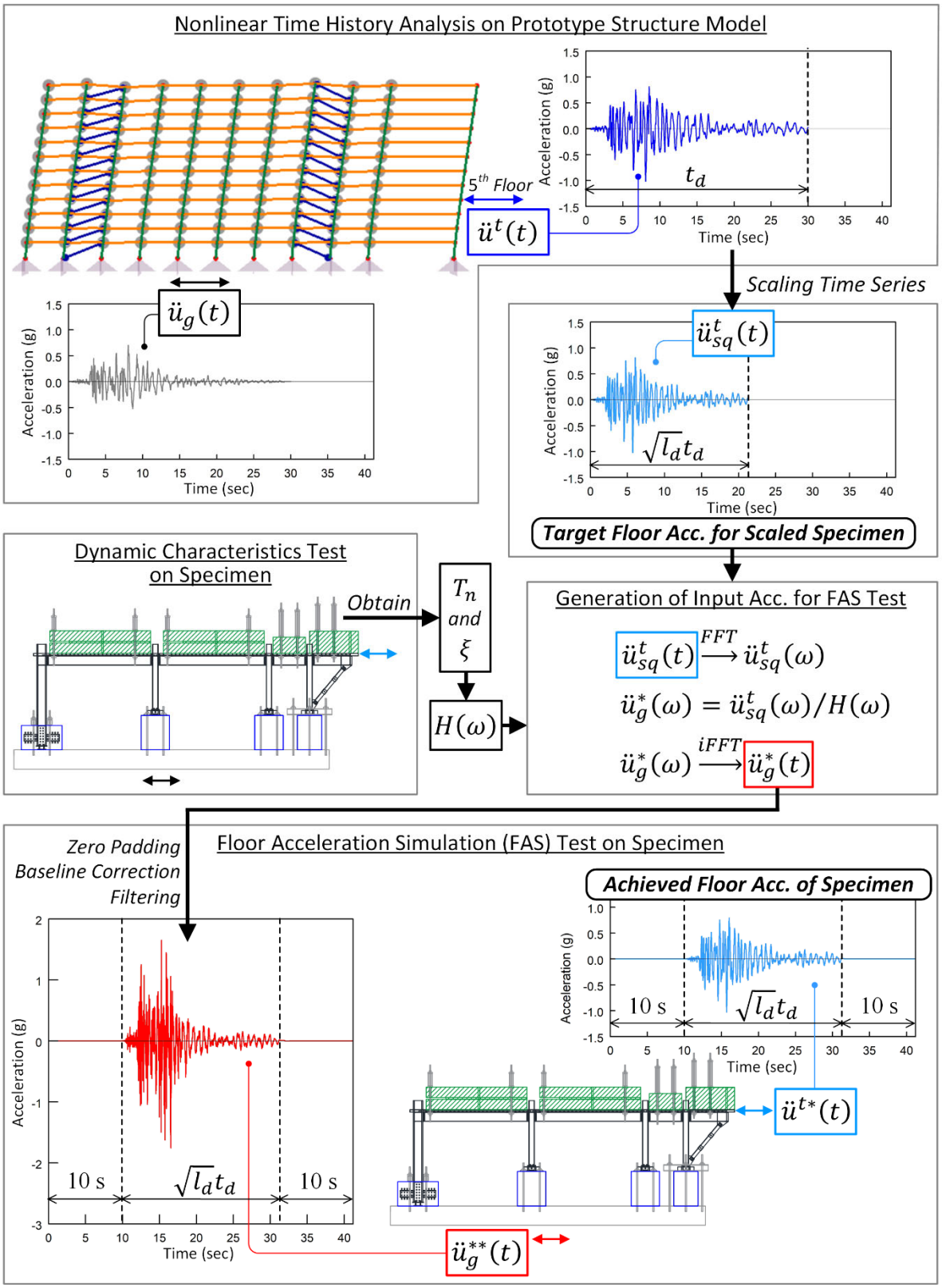

Figure 3.55 Generation of Input Acceleration for Floor Acceleration Simulation Testing

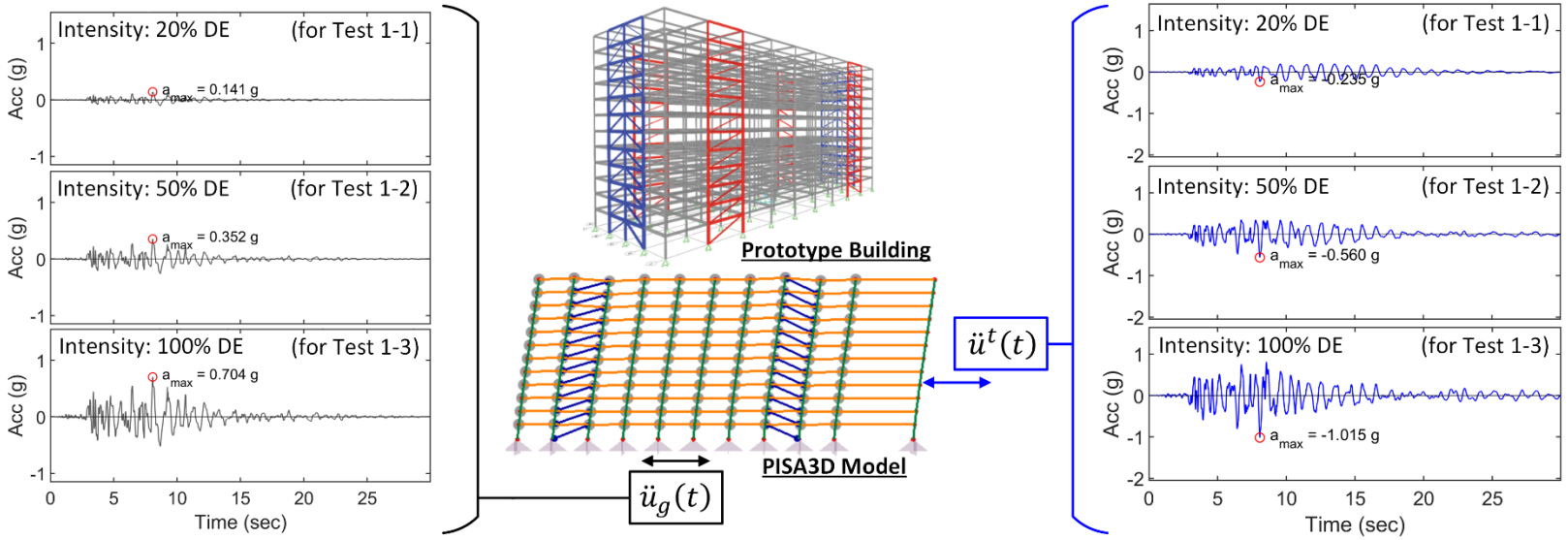

(a)

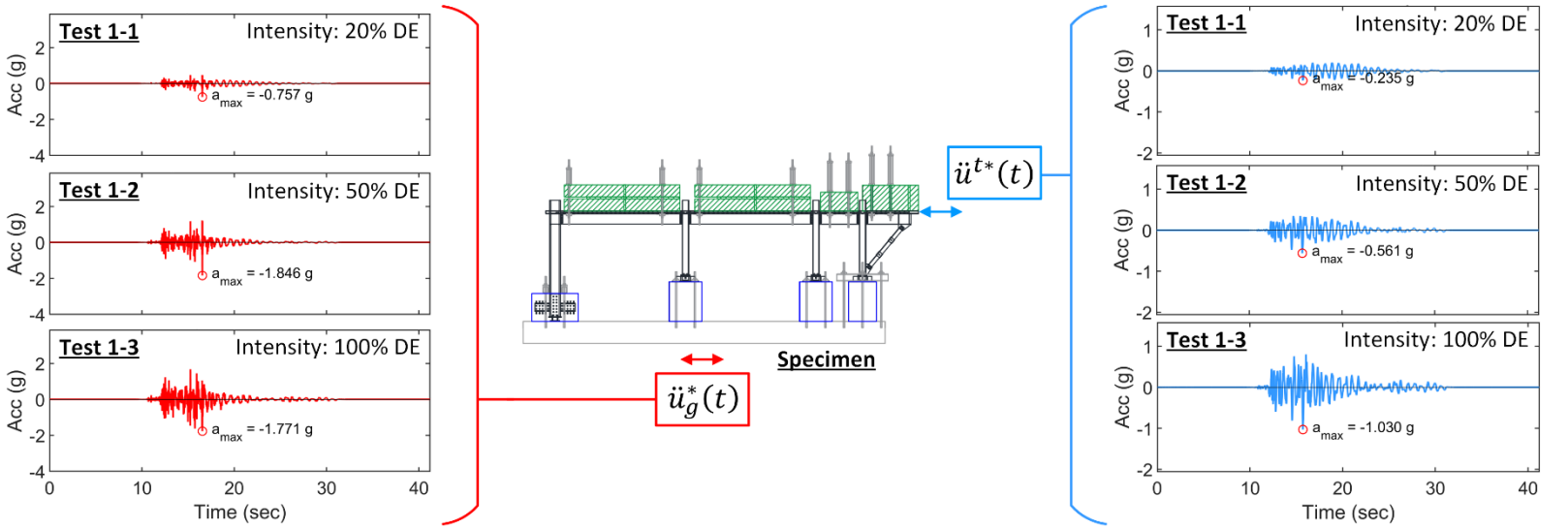

(b)

Figure 3.56 Three Intensity Levels of (a) Time History Analyses on Prototype Model and (b) Phase 1 Main Tests on Specimens

3.7 Data Reduction

3.7.1 Sign Conventions for Key Responses

Figure 3.57 shows the sign convention for displacements and inter-story drift. In the longitudinal direction of the test building, the motion (displacement, velocity, or acceleration) from west to east is considered positive. In the vertical direction, the motion upward is considered positive. Figure 3.58 indicates the positive direction of member forces (axial force, shear force, and bending moment, denoted as P, V, and M, respectively) in the longitudinal frame. Figure 3.59(a) shows the sign convention for the rotations at collector-to-column connections and pin-supports. Notes that the direction of the rotation of collector-to-column connection follows that of the bending moment in the collector. The positive rotation of the pin-support is corresponding to a positive inter-story drift angle. Figure 3.60(a) shows the sign convention for the rotations at the collector-to-column centerline intersections due to the panel zone deformation.

3.7.2 Inter-Story Drift and Floor Acceleration

Figure 3.34(a) and (b) show that the specimen absolute displacement in the longitudinal direction at four column locations were measured at the footing and 2nd floor levels, respectively. As shows Figure 3.57, the 2nd floor absolute displacements at Columns N1, S1, N4 and S4 are denoted as u^t_{2F-N1}, u^t_{2F-S1}, u^t_{2F-N4}, and u^t_{2F-S4}, respectively. The "$2F$" in the subscript represents the 2nd floor level. Similarly, the four measured absolute displacements at the footing level are designated u^t_{Ft-N1}, u^t_{Ft-S1}, u^t_{Ft-N4}, and u^t_{Ft-S4}, respectively. The "Ft" in the subscript represents the footing level. The quality check for Test 1-3 presented in Appendix D shows that the absolute displacement responses at the four column locations at each level were nearly identical.

Hence, the average of absolute displacements at the four column locations at each level is taken as the representative response for the entire level, which leads to:

$$u_{Ft}^{t} = \frac{u_{Ft-N1}^{t} + u_{Ft-S1}^{t} + u_{Ft-N4}^{t} + u_{Ft-S4}^{t}}{4} \tag{3.29}$$

$$u_{2F}^{t} = \frac{u_{2F-N1}^{t} + u_{2F-S1}^{t} + u_{2F-N4}^{t} + u_{2F-S4}^{t}}{4} \tag{3.30}$$

where u_{Ft}^{t} and u_{2F}^{t} are the representative absolute displacements for the footing and 2nd floor levels, respectively. Furthermore, the inter-story drift and story drift angle, respectively denoted as Δ_1 and θ_1, are determined from:

$$\Delta_1 = u_{2F}^{t} - u_{Ft}^{t} \tag{3.31}$$

$$\theta_1 = \Delta_1 / H_1 \tag{3.32}$$

where H_1 is the story height of the gravity frame. Note that the story height of LFRS (i.e., the cantilever column), H_1^*, is different from H_1. The story drift of LFRS, θ_1^*, is determined from:

$$\theta_1^* = \Delta_1 / H_1^* \tag{3.33}$$

Considering the subject of this research, collectors, existed in the gravity frame and the rotations of most of the collector-to-column connections would be closer to θ_1 than to θ_1^*, the story drift of the gravity frame, θ_1, is taken to report the story drift angle for the entire test building.

Like the displacement measurement, accelerometers were installed on the second floor at the four column locations. The 2nd floor absolute accelerations in the longitudinal direction at the four column locations are denoted as $\ddot{u}_{2F-N1}^{t}$, $\ddot{u}_{2F-S1}^{t}$, $\ddot{u}_{2F-N4}^{t}$, and $\ddot{u}_{2F-S4}^{t}$, respectively. In addition, a longitudinal accelerometer, labeled as A19, was placed on the added mass block near the center of the total mass on the 2nd floor. Thus, the acceleration measured by A19 is designated $\ddot{u}_{2F-CM}^{t}$, where "CM" in the subscript represents the center of mass. Furthermore, the longitudinal

and vertical accelerations at the mid-span of east chord, respectively denoted as $\ddot{u}^t_{2F-EC}$ and $\ddot{v}^t_{2F-EC}$, were measured to monitor the actions of the cantilever slab. Note that "EC" represents the east chord. The quality check for Test 1-3 presented in Appendix D shows that response of $\ddot{u}^t_{2F-CM}$ was very similar to those 2nd floor accelerations measured at the four column locations and east chord although the magnitude of the peak acceleration near the mass center was slightly lower than the accelerations at the columns. Considering that majority of the mass on the slab was placed around the middle of the slab in the transverse direction, the accelerations near the slab center, $\ddot{u}^t_{2F-CM}$, is taken to serve as the acceleration of the entire 2nd floor, $\ddot{u}^t_{2F}$.

3.7.3 Collector Connection Rotations and Panel Zone Deformation

Figure 3.59(b) illustrates the measurement of rotation at a collector-to-column connection. For each instrumented collector connection, a pair of LVDT displacement transducers were installed to measure the horizontal relative displacements between column face and steel collector web near the top and bottom flanges, which are denoted as δ_{st} and δ_{sb}, respectively. In addition, a spring potentiometer was placed on the top of the concrete slab to measure the horizontal relative displacement between column face and slab, δ_{ct}. The rotation of collector connection, θ_{Jt}, were determined from two approaches. The first one is to evaluate θ_{Jt} by using the rotation of the steel collector section, θ_{JtS}, which is determined from:

$$\theta_{JtS} = \frac{\delta_{sb} - \delta_{st}}{d_{ss}} \tag{3.34}$$

where d_{ss} is the vertical distance between the two transducers placed in the steel section. The second approach is to assess θ_{Jt} by suing the rotation of the composite collector section, θ_{JtC}, which is calculated by:

$$\theta_{JtC} = \frac{\delta_{sb} - \delta_{ct}}{d_{sc}} \tag{3.35}$$

where d_{sc} is the vertical distance between the transducer near the bottom steel flange to that on the top of slab. For W14×30 collectors, d_{ss} and d_{sc} are 10.80 and 16.80 in., respectively. For W14×26 collectors, d_{ss} and d_{sc} are 10.90 and 16.90 in., respectively.

Figure 3.59(c) shows the measurement of rotation at the pin-support of a gravity column. For each instrumented pin-support, a pair of LVDT displacement transducers were installed to measure the vertical relative displacements between the column and support on the west and east sides column, denoted as δ_W and δ_E, respectively. The rotation of the pin-support, θ_{pin}, is determined from:

$$\theta_{pin} = \frac{\delta_W - \delta_E}{d_{pin}} \tag{3.36}$$

where d_{pin} is the horizontal distance between the two transducers at each pin-support.

Figure 3.60(b) shows that a pair of LVDT displacement transducers were installed at the panel zone of each AFW connection to measure the deformations of the two diagonals of the panel zone. Note that δ_{TW} denotes the deformation of the diagonal from the top-west corner to the bottom-east corner, while δ_{TE} denotes the deformation of the diagonal from the top-east corner to the bottom-west corner. Based on the concept shown in Figure 3.60(c), the average panel zone shear deformation, γ_{pz}, is computed by:

$$\gamma_{pz} = \frac{\sqrt{w_{pz}^2 + d_{pz}^2}}{2w_{pz}d_{pz}}(\delta_{TW} - \delta_{TE}) \tag{3.37}$$

where w_{pz} and d_{pz} are the width and depth of the panel zone measure points. In addition, the shear measured γ_{pz} is used to evaluate the rotation at the collector-to-column intersection point, θ_{pz}, in the centerline frame model [see Figure 3.60(a)] representing the test specimen.

3.7.4 Member Force Recovery for Columns and Diagonal Braces

The member force recovery for the columns is conducted based on the measured axial strains on the column flanges. Figure 3.61(a) shows that for each column, strain gauges were placed on both column flanges at two selected elevations along the column height. These elevations are selected because the column sections there are away from the potential plastic hinge location so that the elastic beam theory can be applied to the compute the section forces. In addition, the measured sections are away from the potential inflection point such that considerable flexural strains would be developed there. Figure 3.61(b) and (c) demonstrates the linear strain profile obtained from the measured strain data for each instrumented section in cantilever columns and gravity columns, respectively. For each instrumented column section, the measured strains on the west and east flanges are denoted as ε_W and ε_E, respectively. Note that, in gravity columns, ε_W or ε_E is determined from the average of strains measured from the two gauges on the west or east flange, respectively. Based on the elastic beam theory, the axial force (P) and bending moment (M) of each instrumented column section can be computed by:

$$P = \frac{E_s A(\varepsilon_W + \varepsilon_E)}{2} \tag{3.38}$$

$$M = \frac{E_s S_x(\varepsilon_W - \varepsilon_E)}{2} \tag{3.39}$$

where E_s is the Young's modulus of the steel. A and S_x are the cross-sectional area and the section modulus around strong axis of the column section, respectively.

As shown in Figure 3.61(a), it assumed that the column moment diagrams due to the frame sway action are linear. For each column, the measured bending moments from Eq. (3.39) at the lower and upper instrumented sections are denoted as M_L and M_U, respectively. Recognizing that

shear force in the column is the slope of the bending moment diagram and considering the sign convention used for member forces (see Figure 3.58), the column shear, V_c, is determined from:

$$V_c = -\left(\frac{M_U - M_L}{y_U - y_L}\right) \tag{3.40}$$

where y_U and y_L are elevations of the upper and lower instrumented sections measured from the column base, respectively.

As shown in Figure 3.61(a) also illustrates the recovery of the axial force in the diagonal double-angle braces of in the longitudinal frames. A strain gauge was installed on the brace to measure the axial strain, ε_{br}, in the brace. Assuming each brace behaves as an elastic two-force member, the brace axial force, P_{br}, is computed by:

$$P_{br} = E\varepsilon_{br}A_{br} \tag{3.41}$$

3.7.5 Base Shear Calculation

Prior to describing the data reduction, it will be beneficial to describe how base shears were calculated for discussion purposes. The base shear, for use in seismic design, is the total horizontal force resisted by the building structural elements. Two methods were used to derive the seismic base shear from the instrumentation. Portions of mass, m_i, were considered tributary to certain accelerometers, a_i, and the first estimation of base shear was calculated as:

$$V_a(t) = -\sum_i m_i\, a_i(t) \tag{3.42}$$

In theory, Equation (3.42) should lead to a large estimation of the base shear because a_i measures the absolute acceleration. Recall that the basic differential equation of motion for a *N* degree-of-freedom (DOF) linear dynamical system is:

$$\mathbf{m}\ddot{\boldsymbol{u}} + \mathbf{c}\dot{\boldsymbol{u}} + \mathbf{k}\boldsymbol{u} = -\mathbf{m}\boldsymbol{i}\ddot{u}_g \tag{3.43}$$

where $\mathbf{m}$, $\mathbf{c}$, and $\mathbf{k}$ are the $N \times N$ mass, damping and stiffness matrices of the system, $\ddot{\boldsymbol{u}}$, $\dot{\boldsymbol{u}}$, and $\boldsymbol{u}$ are the $N \times 1$ nodal relative accelerations, velocities, and displacement vectors at times t, and $\boldsymbol{i}$ is the influence vector containing nodal accelerations corresponding to uniform unit acceleration of all nodes in the direction of the ground motion, $\ddot{u}_g(t)$. Then, rearranging Equation (3.43) as:

$$V_a(t) = -\mathbf{m}\left(\ddot{\boldsymbol{u}}(t) + \boldsymbol{i}\ddot{u}_g(t)\right) = \mathbf{c}\dot{\boldsymbol{u}}(t) + \mathbf{k}\boldsymbol{u}(t) = f_D(t) + f_S(t) \tag{3.44}$$

shows the base shear estimate of Equation (3.42), for a linear system overestimates the actual base shear, f_S, by the damping force f_D. It will be shown the damping of these system is quite low such that f_D is small compared to f_S. Therefore, Equation (3.42) should provide a close estimate of the base shear with appropriate tributary mass assignments and good quality accelerometer data.

For the single-story Phase 1 test building, the base shear $V_a(t)$ was estimated as:

$$V_a(t) = -\sum_i m_i\, a_i(t) \approx -\left(\frac{W_{2F}}{g}\right)\ddot{u}_{2F}^t(t) \tag{3.45}$$

where W_{2F} is the total weight tributary to the 2nd floor, while $\ddot{u}_{2F}^t(t)$ is the acceleration time history measured near the center of mass on the 2nd floor. This base shear estimation approach can be justified when the acceleration responses among the floor diaphragm is uniform, which has been confirmed by the quality check for Test 1-3 as presented in Appendix D.

The second method of calculating the base shear was to sum up the measured story shear taken by columns and diagonal braces in the longitudinal frames. Figure 3.61 shows the member force recovery for the columns and braces were based on the readouts of the strain gauges on these members. Also see Section 3.7.4 for the details of these member force recovery. The time history of the base shear taken by Frame N, $V_{bN}(t)$, was estimated as:

$$V_{bN}(t) = \sum_{i=1}^{4} V_{cNi}\,(t) + P_{brN}(t)\sin\theta \tag{3.46}$$

where V_{cN1} to V_{cN4} represent the measured column shear forces for Columns N1 to N4, respectively. P_{brN} is the measured axial force of the north diagonal brace, while θ is the inclination angle between the brace and the vertical. Likewise, the time history of the base shear taken by Frame S, $V_{bS}(t)$, was approximated as:

$$V_{bS}(t) = \sum_{i=1}^{4} V_{cSi}\,(t) + P_{brS}(t)\sin\theta \tag{3.47}$$

where V_{cS1} to V_{cS4} represent the measured column shear forces for Columns S1 to S4, respectively. P_{brS} is the measured axial force of the south brace. Then, the total base shear of the test building, $V_b(t)$, was determined by summing up the story shears taken by Frames N and S:

$$V_b(t) = V_{bN}(t) + V_{bS}(t) \tag{3.48}$$

Because this is an estimate of the restoring force $f_S(t)$ directly and does not include damping forces, it is expected to be smaller and more accurate than Eq. (3.45). This method is only reliable and valid when those instrumented sections remain elastic.

Both methods were applied to Phase 1 specimen for every test in this phase. It was found that both methods resulted in close base shear estimates with V_a always slightly larger than V_b. Because V_b was found to result in a smoother curve (less "noisy") and its theoretical advantage over V_a, Eqs. (3.46) through (3.48) were used as the primary method of base shear determination for presentation and discussion in this research.

3.7.6 Member Force Recovery for Collectors

Considering the inertial forces would be transferred trough the composite section of the collectors and the geometric discontinuity at various collector-to-column connections would result in a complexity of strain profile, where the elastic Euler-Bernoulli beam theory may not hold, the member force recovery for the composite collectors was conducted by using the fiber section

approach. Figure 3.62(a) and Figure 3.63(a) respectively show the cross section of the composite collectors in Frame N and S, where the metal deck is parallel and perpendicular to the collectors, respectively. Due to the shear lag phenomenon of the stress distribution across the slab width, the effective width concept was employed to analyze the section forces for composite collectors. Since the collectors were located on the periphery of the test building, the composite section is not symmetric and the effective widths of concrete slab on the two sides of steel beam centerline would be different. For discussion purpose, the effective widths for the exterior and interior are denoted as $b_{eff,e}$ and $b_{eff,i}$, respectively. With these effective slab widths, the stress distribution in the slab can be simplified as a uniform stress across the effective width range with a magnitude equal to the maximum stress resulting from the effects of shear lag in the actual slab.

An accurate section analysis for a composite section requires a good estimate on the effective slab width. Unfortunately, for Phase 1 tests, the concrete strain gages used at collector sections were only aligned with the steel beam centerline so that the stress distribution across the slab width could not be measured. However, in Phase 2 tests, multiple concrete strain gauges were deployed across the slab width for four collector sections [see Figure 6.23(a)] such that the stress distribution along the slab width could be measured and the effective slab width could be evaluated. Figure 3.64 shows the effective slab widths used to perform the collector member force recovery for Phase 1 tests. All the test results regarding the collector member forces presented in Chapter 4 were obtained based on these effective slab widths. Note that the effective slab width for Collectors 1 and 2 were determined based on the results of Test 2A-5, while the code-prescribed effective width (AISC 2016c) was used for Collectors 3 and 4. In addition, a parametric study was conducted to eluate the effect of effective slab widths on the collector member forces and the associated results can be seen in Chapter 5.

Figure 3.62(b) shows the composite section considered in the section analysis for a collector with metal deck parallel to the collector. Note that the interior slab can be separated into two layers: (1) the concrete above the top of metal deck and (2) the concrete below the top of metal deck. For this orientation of metal deck, the contribution from the concrete below the top of metal deck should be considered for the interior slab. The effective width the of interior slab for the concrete below the top of the metal deck, $b_{eff,ib}$, is estimated as:

$$b_{eff,ib} = \sum_i b_i = b_{eff,i} - (s_r - w_r)\left(\left\lfloor \frac{(b_{eff,i} - b_1)}{s_r} \right\rfloor + 1\right) \geq b_1 + w_r \left\lfloor \frac{(b_{eff,i} - b_1)}{s_r} \right\rfloor \quad (3.49)$$

where s_r (= 6 in.) and w_r (= $2^1/_8$ in.) are the spacing and average width of the concrete rib, respectively. Note that b_1, which was estimated as $^1/_2'' + w_r/2 = 1^5/_{16}''$. considering the actual position of the metal deck, represents a width measured from the steel beam centerline to the far end of the first concrete rib. The modified brackets "$\lfloor \cdot \rfloor$" represents an operator taking the integer quotient. On the other hand, Figure 3.63(b) the composite section considered in the section analysis for a collector with metal deck perpendicular to the collector. For interior slab with this orientation of metal deck, the contribution from the concrete below the top of the metal deck is negligible.

Figure 3.62(b) and Figure 3.63(b) also illustrate the discretization strategy for the fiber sections representing the composite collector sections. As the strain gauges on the collector cross sections were deployed near the steel beam centerline along the depth-direction of the section, it only allows to construct a one-dimensional strain profile are along the depth of the section. Hence, one-dimensional fiber sections (i.e., layer sections) were used for the test data reduction in this research [see Figure 3.62(c) and Figure 3.63(c)]. The concrete slab part is uniformly discretized into seven layers, each of 0.5-in. thickness, resulting in four and three layers for the concretes above and below the top of metal deck. By merging the effective widths from exterior and interior

slabs, the total effective slab widths for the concrete above and below the top of metal deck, relatively denoted as $b_{eff,t}$ and $b_{eff,b}$, are computed by:

$$b_{eff,t} = b_{eff,i} + b_{eff,e} \tag{3.50}$$

$$b_{eff,b} = \begin{cases} b_{eff,ib} + b_{eff,e} & ,for\ deck\ parallel\ to\ collector \\ b_{eff,e} & ,for\ deck\ perpendicular\ to\ collector \end{cases} \tag{3.51}$$

The part of steel section is separated into eleven sections. Each steel flange constitutes a layer with a thickness of t_f and a width of b_f. Adjacent to each flange layer, a "fillet layer" is assigned to each web end region combined with flange-to-web fillets. The width and thickness for each web toe layer, respectively denoted as d_k and b_k, are determined from:

$$d_k = k - t_f \tag{3.52}$$

$$b_k = \frac{A_k}{d_k} = \frac{\left(A_s - 2A_f - A_w\right)/2}{d_k} \tag{3.53}$$

where

A_s = cross-sectional area of steel section

A_f = flange area = $b_f t_f$

A_w = web area = $(d - 2k)t_w$

A_k = area of web end region combined with fillet area = $\left(A_s - 2A_f - A_w\right)/2$

d = depth of steel section

k = distance from the outer face of the flange to the web toe of fillet

Note that k_{des} value tabulated in Table 1-1 in the AISC Steel Construction Manual (AISC 2016d) is used for k. Furthermore, five "bolt layers" are assigned within the steel beam web such that each bolt layer is aligned with a bolt center and has a layer thickness equal to the vertical bolt spacing,

s_v (= 2″). Lastly, the remaining two layers are assigned to the beam web areas between each web toe layer and its nearby bolt layer.

As shown in Figure 3.62(c) and Figure 3.63(c), for each fiber section, fibers are numbered from bottom to top. The bottom flange fiber is designated Fiber 1, while the top concrete fiber is labeled as Fiber 18. Table 3.20 tabulates the effective slab widths used for the fiber sections to compute the collector member forces presented in Chapter 4. Table 3.21 lists the key information of the fibers, including the thickness (t_{fib}), width (w_{fib}), area (A_{fib}), and coordinate (y_{fib}) of each fiber, used for various instrumented collector sections for Phase 1 tests. Note that y_{fib} is the coordinate with reference to an origin at the mid-height of the steel section.

Figure 3.65 illustrates the force recovery for five sections at collector ends by using the measured strain data with fiber section approach. As shown in Figure 3.65(a), the designations of the locations for these five sections are: Loc 1 and Loc 5 of Collector 1; Loc 1 and Loc 5 of Collector 2; and Loc 1 of Collector 3. Figure 3.65(b) shows that each of these sections were instrumented with strain gauges at seven elevations along the depth of the section. Two concrete strain gauges were relatively placed at the top surface of the slab and 1 in. below the top face of the slab. In addition, a pair of strain gauges were installed on the inner face of the steel flange, while three strain gauges were placed on the steel webs at the middle and quarter points of the height of steel section. As shown in Figure 3.65(c), the measured strains at seven elevations from bottom to top of each section are denoted as ε_1 to ε_7, respectively. Note that the measured strains on the steel flanges, ε_1 and ε_5, were determined by taking strain of the two gauges on each flange. Figure 3.65(c) also shows the assumed strain profile based on the measured strain data. Note that the Euler-Bernoulli beam theory would not be applied at these sections because of the geometric discontinuity at the collector connection region. Hence, it is assumed that the seven measured

strains are uniformly distributed across their corresponding tributary heights, which are bordered by the centerlines dividing the spacing between measure points in half. Lastly, Figure 3.65(d) illustrates the mapping of measured strains to the fiber strains. If the tributary height of a fiber is within the range of tributary width of a specific measured strain, this measured strain is directly assigned to that fiber. If the tributary height of a fiber overlaps two adjacent tributary heights of measured strains, a weighted average of the two measured strains is computed and then assigned to that fiber.

Figure 3.66 illustrates the force recovery for six sections within the collector span by using the measured strain data with fiber section approach. As shown in Figure 3.66(a), the designations of the locations for these six sections are: Loc 2, Loc 3, and Loc 4 of Collector 1; and Loc 2, Loc 3, and Loc 4 of Collector 2. The Loc 3 sections, which are near the mid-span of the collectors, were instrumented with three strain gauges: one gauge on each steel flange and one on the top surface of the slab [see Figure 3.66(b)]. The Loc 2 and Loc 4 sections, which are near the quarter-span of the collectors, were instrumented with only two strain gauges: one on each steel flange. Since these sections are way from the collector ends and sufficient headed studs were placed on the collectors, it is assumed that composite action, which leads to a linear strain profile across the composite section, can be achieved at these instrumented sections within collector span. Hence, as shown in Figure 3.66(c), the measured strain profiles for these sections within the collector span were obtained by a linear regression line that best fits the two or three data points from strain gauges on each section. Figure 3.66(d) illustrates the mapping of linear measured strain profile to the fiber strains [Figure 3.66(c)]. The strain of the measured profile corresponding to the centroid of a fiber was computed and then assigned to that fiber.

For Phase 1 tests, all the measured strains on the steel were within the elastic range. Thus, the fiber stress, σ_{fib}, of a steel fiber is determined from the linear elastic constitutive relation:

$$\sigma_{fib} = E_s \varepsilon_{fib} \tag{3.54}$$

On the other hand, a constitutive relationship adapted from the models proposed by Popovics (1973) and Mander et al. (1988) was used to estimate the compressive branch of the monotonic stress-strain (σ- ε) curve for the concrete slab:

$$\sigma = -f_c' \left|\frac{\varepsilon}{\varepsilon_{co}}\right| \frac{n}{n - 1 + \left|\frac{\varepsilon}{\varepsilon_{co}}\right|^n}, \quad \varepsilon \leq 0 \tag{3.55}$$

in which

$$n = \frac{E_c}{E_c - E_{sec}} \tag{3.56}$$

$$E_c = 33(w_c^{1.5})\sqrt{f_c' \, (psi)} \tag{3.57}$$

$$E_{sec} = \frac{f_c'}{\varepsilon_{co}} \tag{3.58}$$

Note that the compressive strength of the unconfined concrete, f_c' (= 4.218 ksi) is determined form the averaged strength form three concrete cylinders tested on the same day as the Phase 1 tests. The unit weight of the concrete w_c is 110 pcf and the strain at the maximum compressive strength, ε_{co}, is assumed as -0.002.

For estimating the tensile branch of the monotonic σ- ε curve for the concrete slab, the equations proposed by Belarbi and Hsu (1994) for the pre-cracking and post-cracking stages were adapted as:

$$\sigma = E_c \varepsilon, \qquad 0 < \varepsilon < \varepsilon_{cr} \tag{3.59}$$

$$\sigma = f_{cr} \left(\frac{\varepsilon_{cr}}{\varepsilon}\right)^{0.4}, \quad \varepsilon_{cr} < \varepsilon \tag{3.60}$$

where the cracking stress f_{cr} (= 0.244 ksi) and cracking strain ε_{cr} (= 0.000098) were computed by:

$$f_{cr} = 3.75\sqrt{f_c'\ (psi)} \tag{3.61}$$

$$\varepsilon_{cr} = \frac{f_{cr}}{E_c} \tag{3.62}$$

Figure 3.67 shows the nonlinear constitutive model determined from Equations. (3.55), (3.59), and (3.60). In addition, Figure 3.67 shows that the linear elastic stress-strain curve $\sigma = E_c\varepsilon$ fits the nonlinear model very well within the range of measured strains on the collectors in Phase 1 tests. Hence, for simplicity, the stress of a concrete fiber in the fiber sections for collector member force recovery were determined from the following linear elastic constitutive relation:

$$\sigma_{fib} = E_c\varepsilon_{fib} \tag{3.63}$$

Once the fiber stresses were determined, the resultant axial force, P, and bending moment, M, on a fiber section are calculated by summing up the axial forces and moments produced by all fibers of that section. The associated equations are as follows:

$$P = \sum_{fib=1}^{N_{fib}} \sigma_{fib}A_{fib} \tag{3.64}$$

$$M = \sum_{fib=1}^{N_{fib}} -\sigma_{fib}A_{fib}\,y_{fib} \tag{3.65}$$

where N_{fib} is the total number of fibers of the section. As mentioned earlier, a total of 18 fibers (i.e., N_{fib} = 18) were assigned to each collector fiber section [see Figure 3.62(c) and Figure 3.63(c)]. Fibers 1 through 11 are steel fibers, while Fibers 12 through 18 are concrete fibers. Therefore, for each composite section, the axial force (P_s) and bending moment (M_s) contributed from the steel beam section are computed by:

$$P_s = \sum_{fib=1}^{11} \sigma_{fib} A_{fib} \tag{3.66}$$

$$M_s = \sum_{fib=1}^{11} -\sigma_{fib} A_{fib}\, y_{fib} \tag{3.67}$$

On the other hand, the axial force (P_c) and bending moment (M_c) contributed from the concrete slab are calculated by:

$$P_c = \sum_{fib=12}^{18} \sigma_{fib} A_{fib} \tag{3.68}$$

$$M_c = \sum_{fib=12}^{18} -\sigma_{fib} A_{fib}\, y_{fib} \tag{3.69}$$

Part of this chapter is based on the material published in the 17th World Conference on Earthquake Engineering, titled "Earthquake simulator testing on behavior of seismic collectors in steel buildings" with co-authors Uang C.-M., and Fleischman R.B. (2020). Materials were also submitted for publication in the 12th National Conference on Earthquake Engineering, titled "Shake Table Tests on Seismic Response of Collectors in Steel Buildings" with co-authors Uang C.-M., and Fleischman R.B. (2022). The author of this dissertation serves as the first author of these papers.

Table 3.20 Effective Slab Widths for Collector Member Force Recovery

Dimension	Frame N			Frame S		
	Collector 1	Collector 2	Collectors 3 & 4	Collector 1	Collector 2	Collectors 3 & 4
s_r (in.)	6	6	6	6	6	6
w_r (in.)	2.125	2.125	2.125	2.125	2.125	2.125
b_1 (in.)	1.3125	1.3125	1.3125	1.3125	1.3125	1.3125
$b_{eff,i}$ (in.)	9.7	11.6	7.5	11.1	13.1	7.5
$b_{eff,e}$ (in.)	9.9	10.4	7.5	9.1	10.9	7.5
$b_{eff,ib}$ (in.)	3.4375	3.85	3.4375	0	0	0
$b_{eff,t}$ (in.)	19.6	22	15	20.2	24	15
$b_{eff,b}$ (in.)	13.3375	14.25	10.9375	9.1	10.9	7.5

Table 3.21 Information of Fiber Sections used for 2nd Floor Collectors

(a) North Collector 1 (W14×30)

Fiber No.	y_{fib} (in.)	t_{fib} (in.)	w_{fib} (in.)	A_{fib} (in.^{2})	Material
1	-6.6700	0.3850	6.73000	2.59105	Steel
2	-6.2775	0.4000	0.45725	0.18290	Steel
3	-5.5075	1.1400	0.27000	0.30780	Steel
4	-3.9375	2.0000	0.27000	0.54000	Steel
5	-1.9375	2.0000	0.27000	0.54000	Steel
6	0.0625	2.0000	0.27000	0.54000	Steel
7	2.0625	2.0000	0.27000	0.54000	Steel
8	4.0625	2.0000	0.27000	0.54000	Steel
9	5.6075	1.0900	0.27000	0.29430	Steel
10	6.3525	0.4000	0.45725	0.18290	Steel
11	6.7450	0.3850	6.73000	2.59105	Steel
12	7.1875	0.5000	13.33750	6.66875	Concrete
13	7.6875	0.5000	13.33750	6.66875	Concrete
14	8.1875	0.5000	13.33750	6.66875	Concrete
15	8.6875	0.5000	19.60000	9.80000	Concrete
16	9.1875	0.5000	19.60000	9.80000	Concrete
17	9.6875	0.5000	19.60000	9.80000	Concrete
18	10.1875	0.5000	19.60000	9.80000	Concrete

(b) North Collector 2 (W14×30) except for BW Connection

Fiber No.	y_{fib} (in.)	t_{fib} (in.)	w_{fib} (in.)	A_{fib} (in.^{2})	Material
1	-6.6700	0.3850	6.73000	2.59105	Steel
2	-6.2775	0.4000	0.45725	0.18290	Steel
3	-5.5075	1.1400	0.27000	0.30780	Steel
4	-3.9375	2.0000	0.27000	0.54000	Steel
5	-1.9375	2.0000	0.27000	0.54000	Steel
6	0.0625	2.0000	0.27000	0.54000	Steel
7	2.0625	2.0000	0.27000	0.54000	Steel
8	4.0625	2.0000	0.27000	0.54000	Steel
9	5.6075	1.0900	0.27000	0.29430	Steel
10	6.3525	0.4000	0.45725	0.18290	Steel
11	6.7450	0.3850	6.73000	2.59105	Steel
12	7.1875	0.5000	14.25000	7.12500	Concrete
13	7.6875	0.5000	14.25000	7.12500	Concrete
14	8.1875	0.5000	14.25000	7.12500	Concrete
15	8.6875	0.5000	22.00000	11.00000	Concrete
16	9.1875	0.5000	22.00000	11.00000	Concrete
17	9.6875	0.5000	22.00000	11.00000	Concrete
18	10.1875	0.5000	22.00000	11.00000	Concrete

Table 3.21 Information of Fiber Sections used for 2nd Floor Collectors (continued)

(c) North Collector 2 (W14×30) at BW Connection

Fiber No.	y_{fib} (in.)	t_{fib} (in.)	w_{fib} (in.)	A_{fib} (in.^{2})	Material
1	-6.6700	0.3850	6.73000	2.59105	Steel
2	-6.2775	0.4000	0.45725	0.18290	Steel
3	-5.5388	1.0775	0.27000	0.29093	Steel
4	-4.0000	2.0000	0.27000	0.54000	Steel
5	-2.0000	2.0000	0.27000	0.54000	Steel
6	0.0000	2.0000	0.27000	0.54000	Steel
7	2.0000	2.0000	0.27000	0.54000	Steel
8	4.0000	2.0000	0.27000	0.54000	Steel
9	5.5763	1.1525	0.27000	0.31118	Steel
10	6.3525	0.4000	0.45725	0.18290	Steel
11	6.7450	0.3850	6.73000	2.59105	Steel
12	7.1875	0.5000	14.25000	7.12500	Concrete
13	7.6875	0.5000	14.25000	7.12500	Concrete
14	8.1875	0.5000	14.25000	7.12500	Concrete
15	8.6875	0.5000	22.00000	11.00000	Concrete
16	9.1875	0.5000	22.00000	11.00000	Concrete
17	9.6875	0.5000	22.00000	11.00000	Concrete
18	10.1875	0.5000	22.00000	11.00000	Concrete

(d) North Collectors 3 and 4 (W14×26)

Fiber No.	y_{fib} (in.)	t_{fib} (in.)	w_{fib} (in.)	A_{fib} (in.^{2})	Material
1	-6.7525	0.4200	5.030000	2.1126000	Steel
2	-6.3425	0.4000	0.423125	0.1692500	Steel
3	-5.5713	1.1425	0.255000	0.2913375	Steel
4	-4.0000	2.0000	0.255000	0.5100000	Steel
5	-2.0000	2.0000	0.255000	0.5100000	Steel
6	0.0000	2.0000	0.255000	0.5100000	Steel
7	2.0000	2.0000	0.255000	0.5100000	Steel
8	4.0000	2.0000	0.255000	0.5100000	Steel
9	5.5588	1.1175	0.255000	0.2849625	Steel
10	6.3175	0.4000	0.423125	0.1692500	Steel
11	6.7275	0.4200	5.030000	2.1126000	Steel
12	7.1875	0.5000	10.937500	5.4687500	Concrete
13	7.6875	0.5000	10.937500	5.4687500	Concrete
14	8.1875	0.5000	10.937500	5.4687500	Concrete
15	8.6875	0.5000	15.000000	7.5000000	Concrete
16	9.1875	0.5000	15.000000	7.5000000	Concrete
17	9.6875	0.5000	15.000000	7.5000000	Concrete
18	10.1875	0.5000	15.000000	7.5000000	Concrete

Table 3.21 Information of Fiber Sections used for 2nd Floor Collectors (continued)

(e) South Collector 1 (W14×30)

Fiber No.	y_{fib} (in.)	t_{fib} (in.)	w_{fib} (in.)	A_{fib} (in.^{2})	Material
1	-6.6700	0.3850	6.73000	2.59105	Steel
2	-6.2775	0.4000	0.45725	0.18290	Steel
3	-5.5075	1.1400	0.27000	0.30780	Steel
4	-3.9375	2.0000	0.27000	0.54000	Steel
5	-1.9375	2.0000	0.27000	0.54000	Steel
6	0.0625	2.0000	0.27000	0.54000	Steel
7	2.0625	2.0000	0.27000	0.54000	Steel
8	4.0625	2.0000	0.27000	0.54000	Steel
9	5.6075	1.0900	0.27000	0.29430	Steel
10	6.3525	0.4000	0.45725	0.18290	Steel
11	6.7450	0.3850	6.73000	2.59105	Steel
12	7.1875	0.5000	9.10000	4.55000	Concrete
13	7.6875	0.5000	9.10000	4.55000	Concrete
14	8.1875	0.5000	9.10000	4.55000	Concrete
15	8.6875	0.5000	20.20000	10.10000	Concrete
16	9.1875	0.5000	20.20000	10.10000	Concrete
17	9.6875	0.5000	20.20000	10.10000	Concrete
18	10.1875	0.5000	20.20000	10.10000	Concrete

(f) South Collector 2 (W14×30) except for BW Connection

Fiber No.	y_{fib} (in.)	t_{fib} (in.)	w_{fib} (in.)	A_{fib} (in.^{2})	Material
1	-6.6700	0.3850	6.73000	2.59105	Steel
2	-6.2775	0.4000	0.45725	0.18290	Steel
3	-5.5075	1.1400	0.27000	0.30780	Steel
4	-3.9375	2.0000	0.27000	0.54000	Steel
5	-1.9375	2.0000	0.27000	0.54000	Steel
6	0.0625	2.0000	0.27000	0.54000	Steel
7	2.0625	2.0000	0.27000	0.54000	Steel
8	4.0625	2.0000	0.27000	0.54000	Steel
9	5.6075	1.0900	0.27000	0.29430	Steel
10	6.3525	0.4000	0.45725	0.18290	Steel
11	6.7450	0.3850	6.73000	2.59105	Steel
12	7.1875	0.5000	10.90000	5.45000	Concrete
13	7.6875	0.5000	10.90000	5.45000	Concrete
14	8.1875	0.5000	10.90000	5.45000	Concrete
15	8.6875	0.5000	24.00000	12.00000	Concrete
16	9.1875	0.5000	24.00000	12.00000	Concrete
17	9.6875	0.5000	24.00000	12.00000	Concrete
18	10.1875	0.5000	24.00000	12.00000	Concrete

Table 3.21 Information of Fiber Sections used for 2nd Floor Collectors (continued)

(g) South Collector 2 (W14×30) at BW Connection

Fiber No.	y_{fib} (in.)	t_{fib} (in.)	w_{fib} (in.)	A_{fib} (in.^{2})	Material
1	-6.6700	0.3850	6.73000	2.59105	Steel
2	-6.2775	0.4000	0.45725	0.18290	Steel
3	-5.5388	1.0775	0.27000	0.29093	Steel
4	-4.0000	2.0000	0.27000	0.54000	Steel
5	-2.0000	2.0000	0.27000	0.54000	Steel
6	0.0000	2.0000	0.27000	0.54000	Steel
7	2.0000	2.0000	0.27000	0.54000	Steel
8	4.0000	2.0000	0.27000	0.54000	Steel
9	5.5763	1.1525	0.27000	0.31118	Steel
10	6.3525	0.4000	0.45725	0.18290	Steel
11	6.7450	0.3850	6.73000	2.59105	Steel
12	7.1875	0.5000	10.90000	5.45000	Concrete
13	7.6875	0.5000	10.90000	5.45000	Concrete
14	8.1875	0.5000	10.90000	5.45000	Concrete
15	8.6875	0.5000	24.00000	12.00000	Concrete
16	9.1875	0.5000	24.00000	12.00000	Concrete
17	9.6875	0.5000	24.00000	12.00000	Concrete
18	10.1875	0.5000	24.00000	12.00000	Concrete

(h) South Collectors 3 and 4 (W14×26)

Fiber No.	y_{fib} (in.)	t_{fib} (in.)	w_{fib} (in.)	A_{fib} (in.^{2})	Material
1	-6.7525	0.4200	5.030000	2.1126000	Steel
2	-6.3425	0.4000	0.423125	0.1692500	Steel
3	-5.5713	1.1425	0.255000	0.2913375	Steel
4	-4.0000	2.0000	0.255000	0.5100000	Steel
5	-2.0000	2.0000	0.255000	0.5100000	Steel
6	0.0000	2.0000	0.255000	0.5100000	Steel
7	2.0000	2.0000	0.255000	0.5100000	Steel
8	4.0000	2.0000	0.255000	0.5100000	Steel
9	5.5588	1.1175	0.255000	0.2849625	Steel
10	6.3175	0.4000	0.423125	0.1692500	Steel
11	6.7275	0.4200	5.030000	2.1126000	Steel
12	7.1875	0.5000	7.500000	3.7500000	Concrete
13	7.6875	0.5000	7.500000	3.7500000	Concrete
14	8.1875	0.5000	7.500000	3.7500000	Concrete
15	8.6875	0.5000	15.000000	7.5000000	Concrete
16	9.1875	0.5000	15.000000	7.5000000	Concrete
17	9.6875	0.5000	15.000000	7.5000000	Concrete
18	10.1875	0.5000	15.000000	7.5000000	Concrete

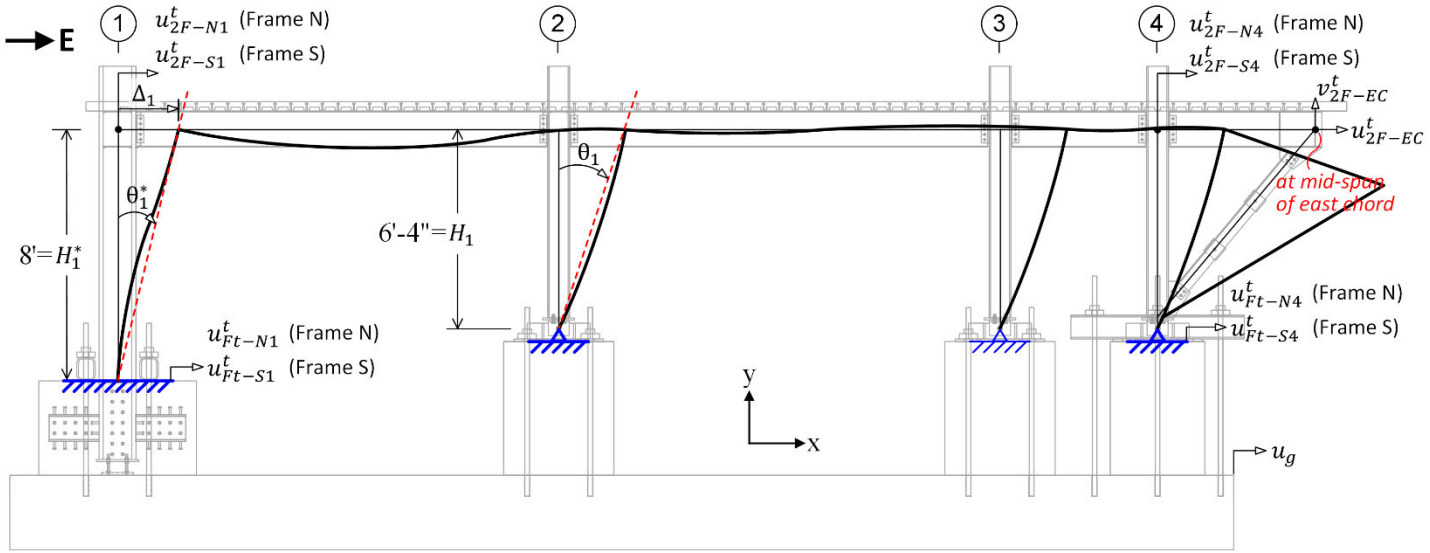

Figure 3.57 Sign Convention for Displacements and Inter-story Drift (Showing Positive Responses)

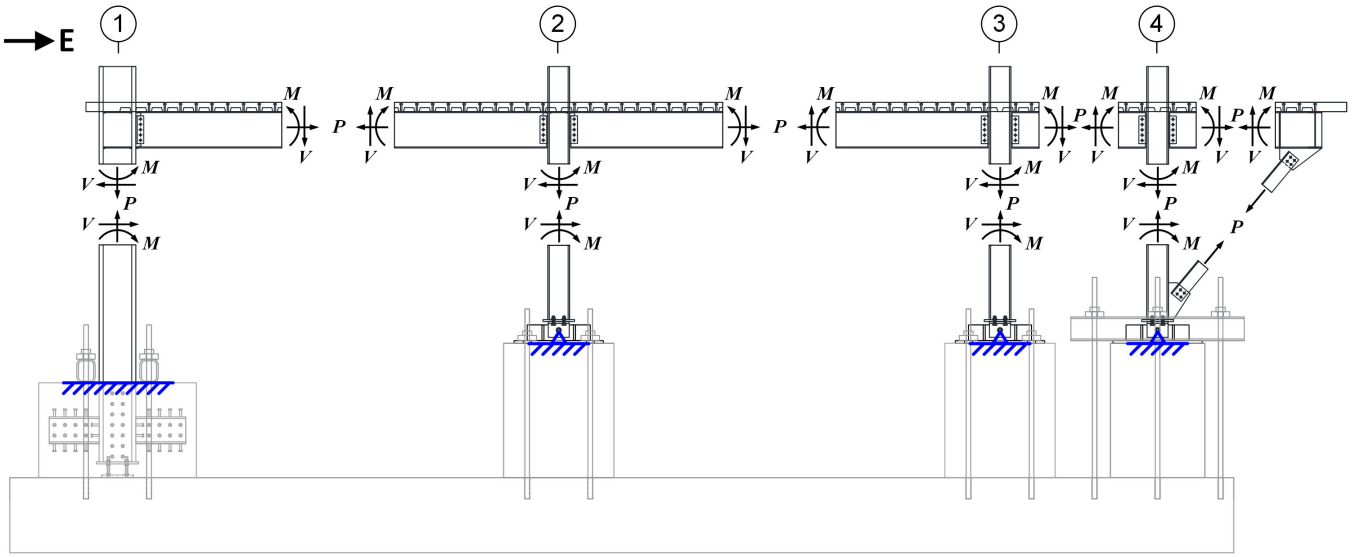

Figure 3.58 Sign Convention for Member Forces (Showing Positive Responses)

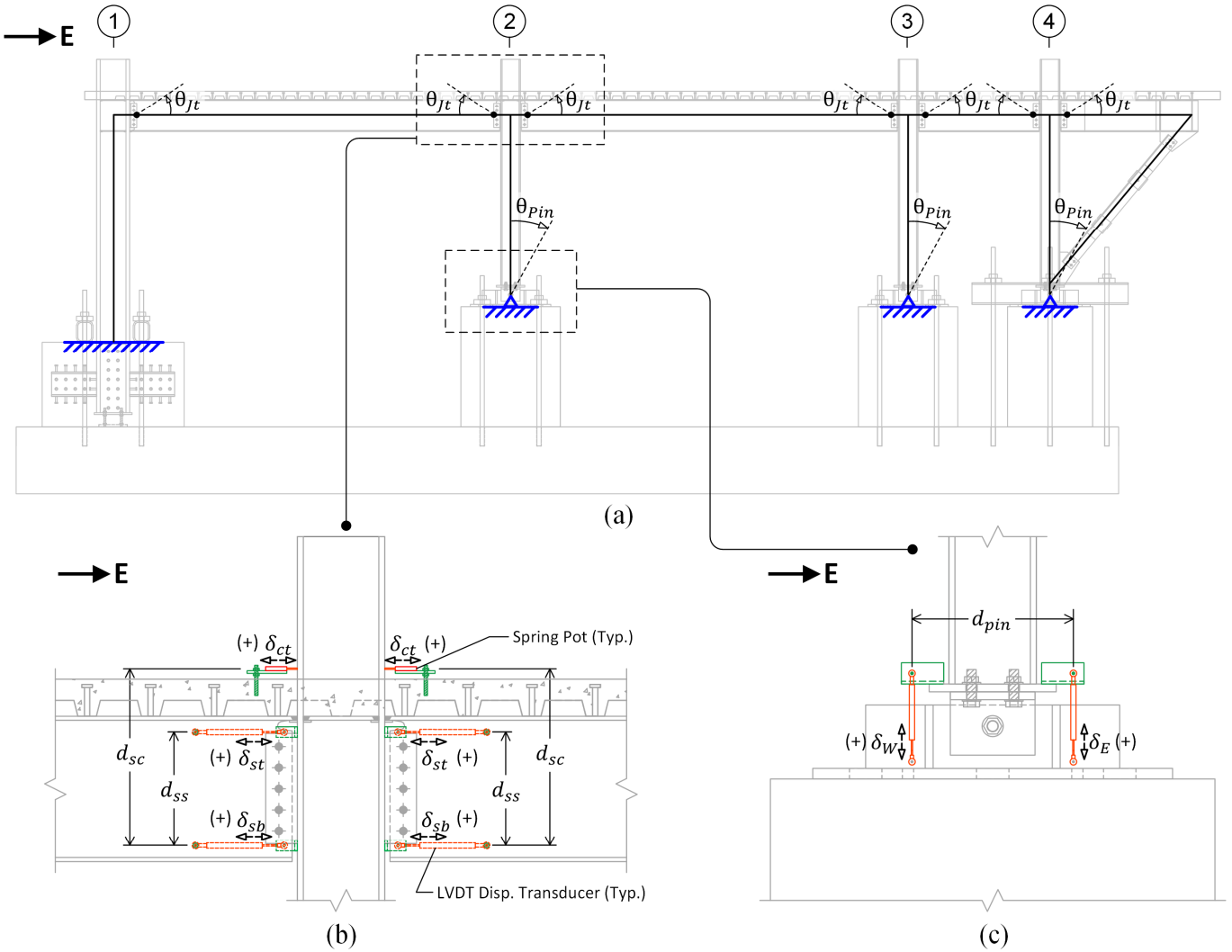

Figure 3.59 (a) Sign Convention for Rotations (Showing Positive Responses) and Measurements of Rotations at (b) Collector Connection and (c) Pin-support

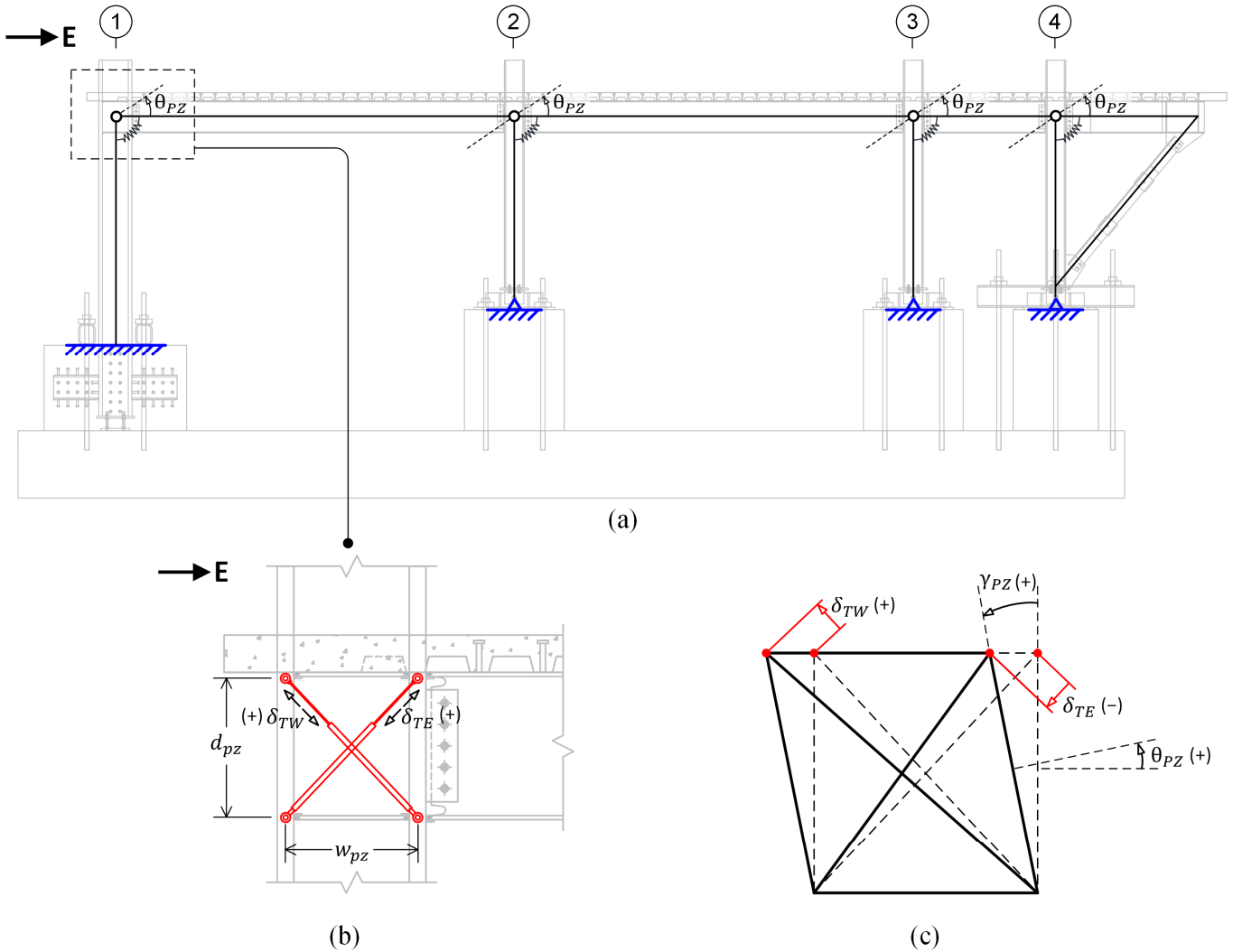

Figure 3.60 Panel Zone: (a) Sign Convention of Rotation (Showing Positive Responses), (b) Measurement of Shear Deformation, and (c) Positive Shear Deformation

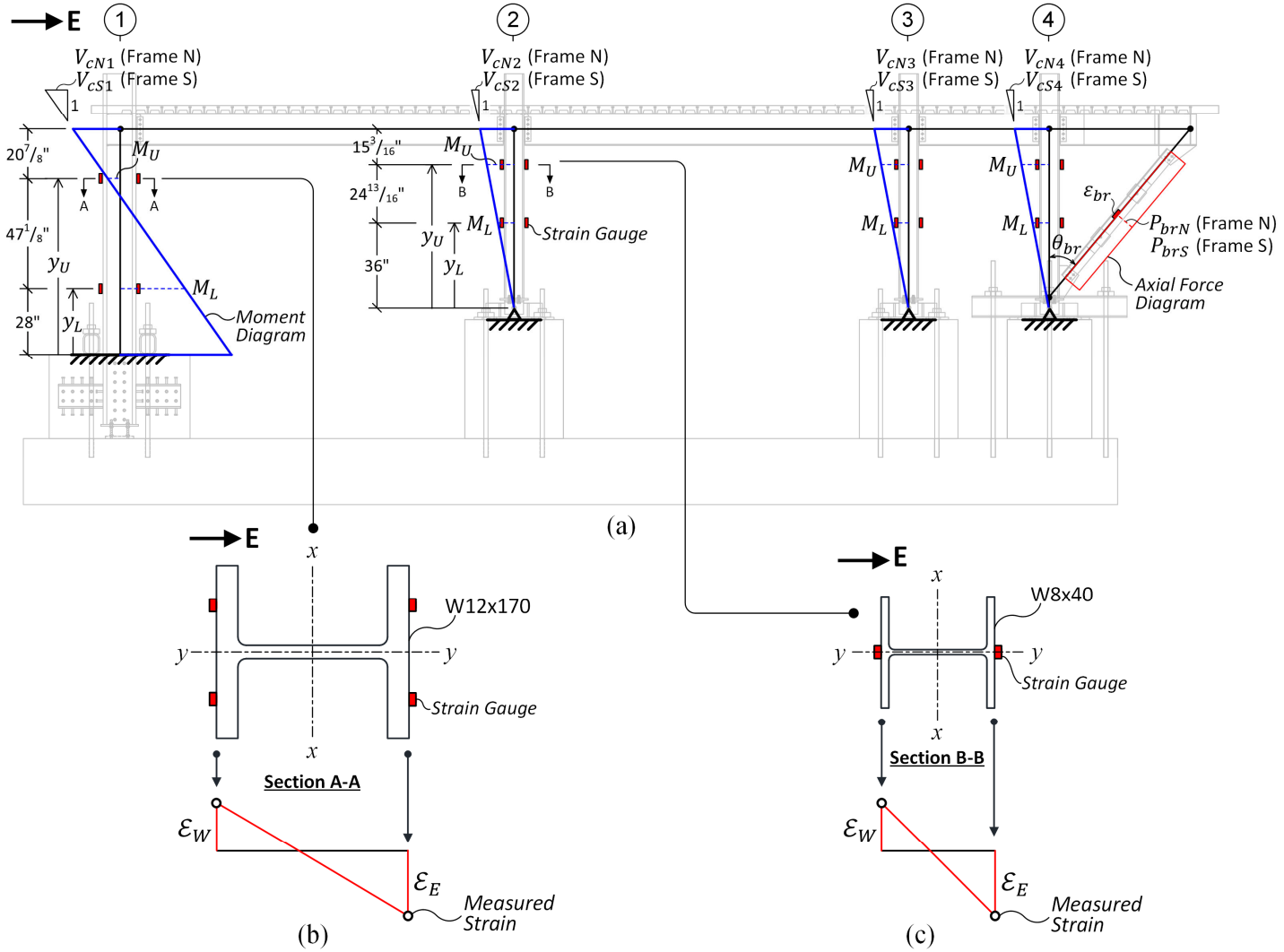

Figure 3.61 (a) Determination of Member Force Diagrams for Base Shear Calculation; and Measured Strain Profile in (b) Cantilever and (c) Gravity Columns

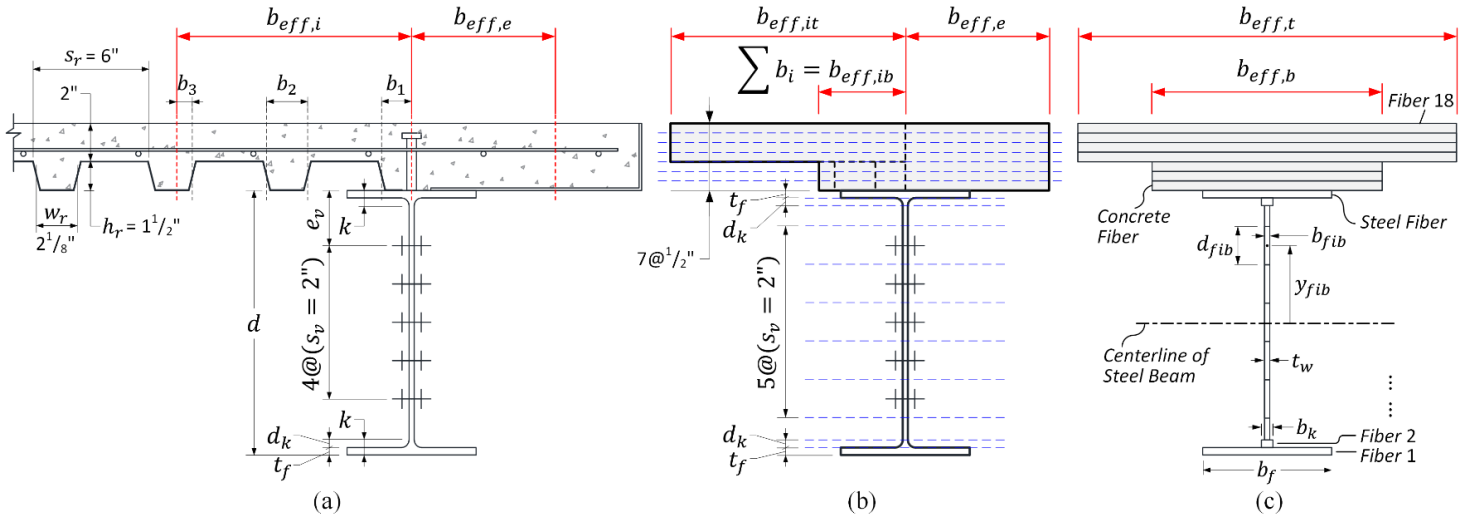

Figure 3.62 Collectors in Frame N: (a) Cross Section Profile, (b) Composite Section Considered, and (c) Fiber Section Used for Member Forces Recovery

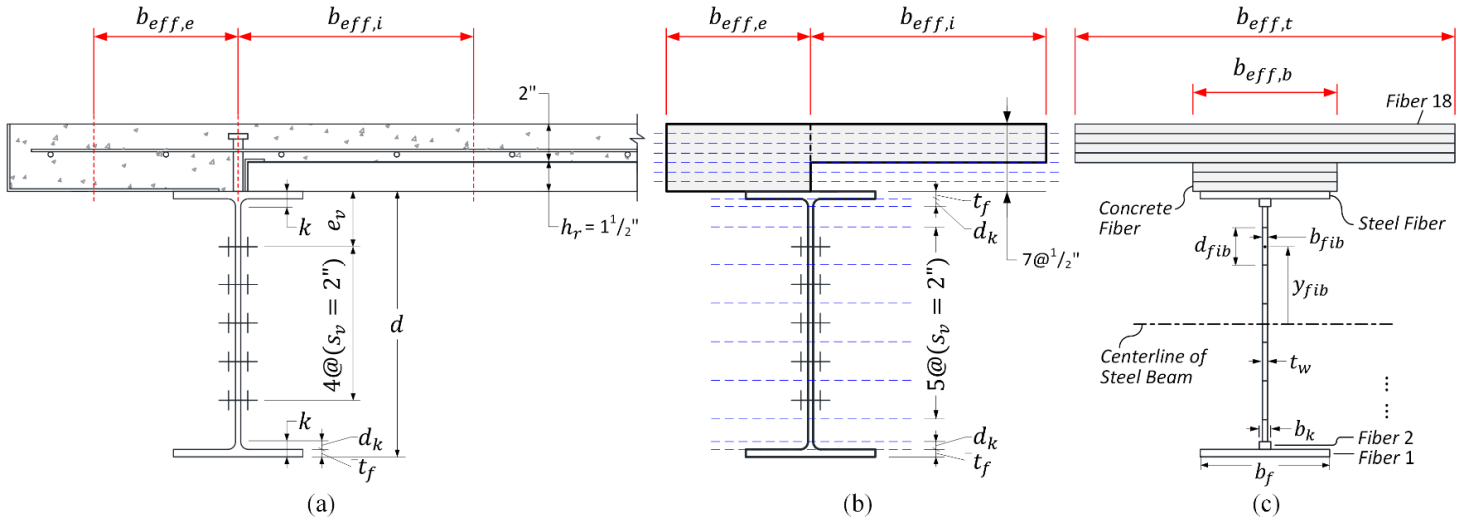

Figure 3.63 Collectors in Frame S: (a) Cross Section Profile, (b) Composite Section Considered, and (c) Fiber Section Used for Member Forces Recovery

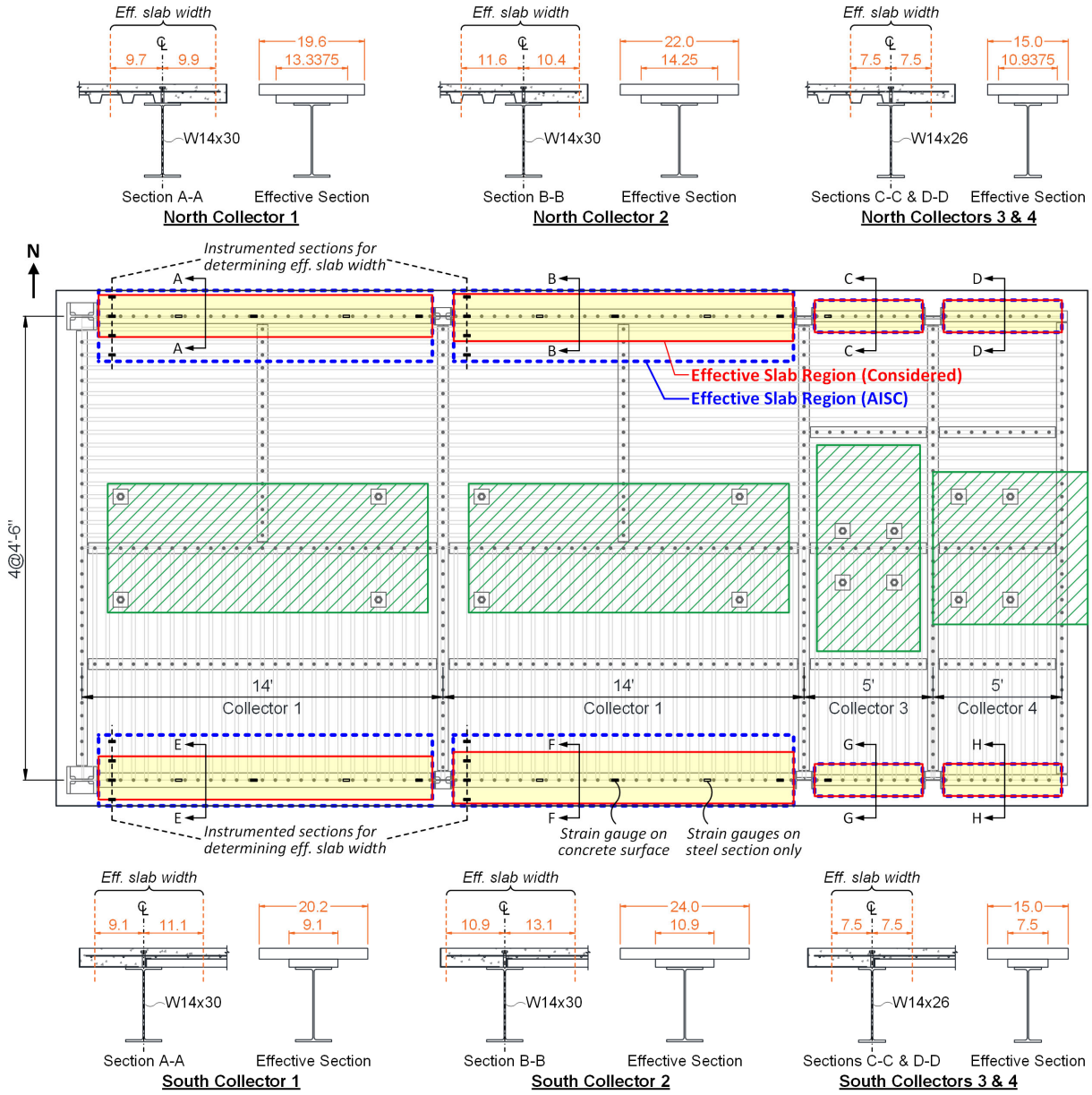

Figure 3.64 Effective Concrete Slab Widths Considered for Collector Member Force Recovery

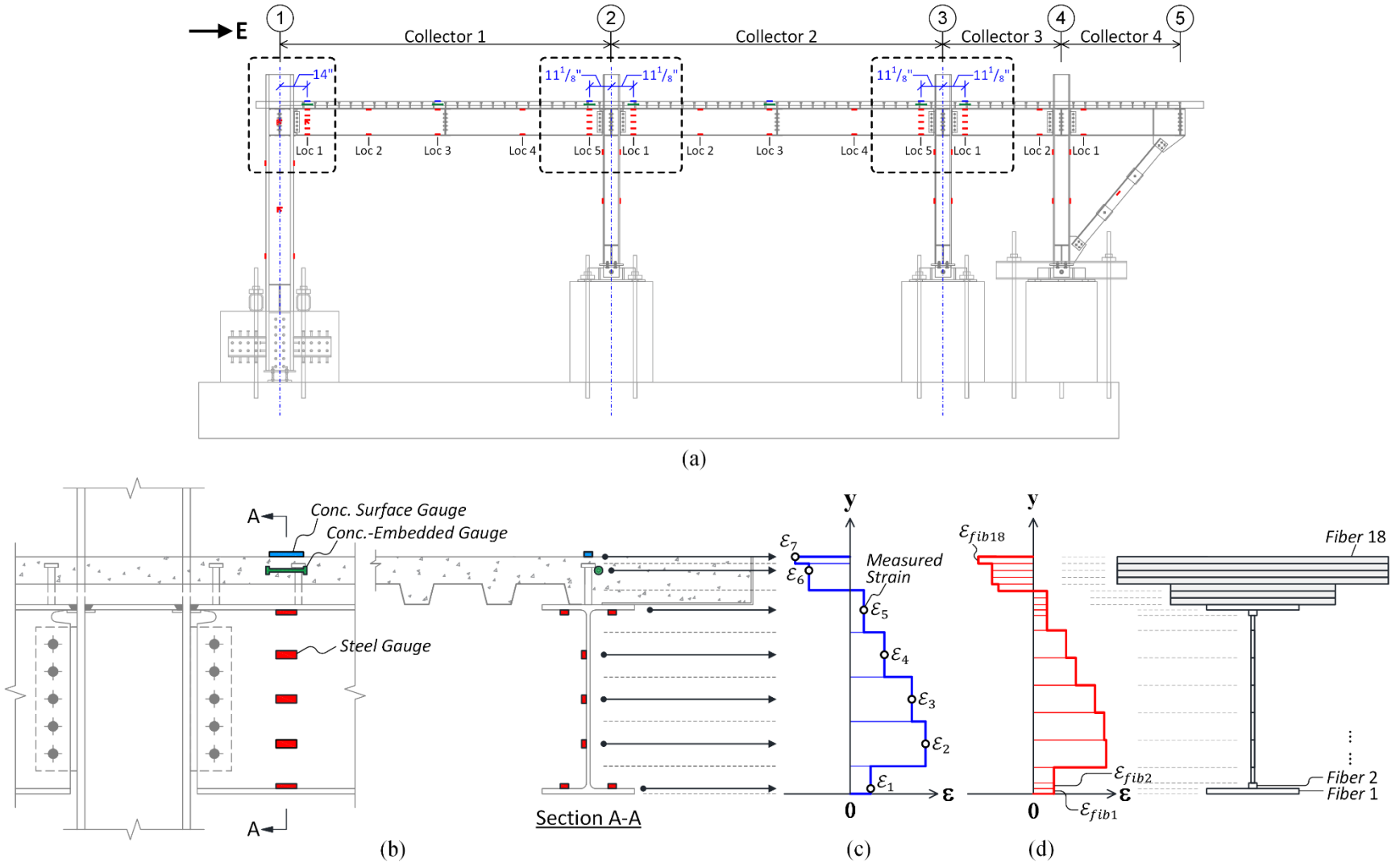

Figure 3.65 (a) Instrumented Sections at Collector Ends and (b) Strain Gauge Layout, (c) Assumed Strain Profile, and (d) Assignment of Strains to Fiber Section

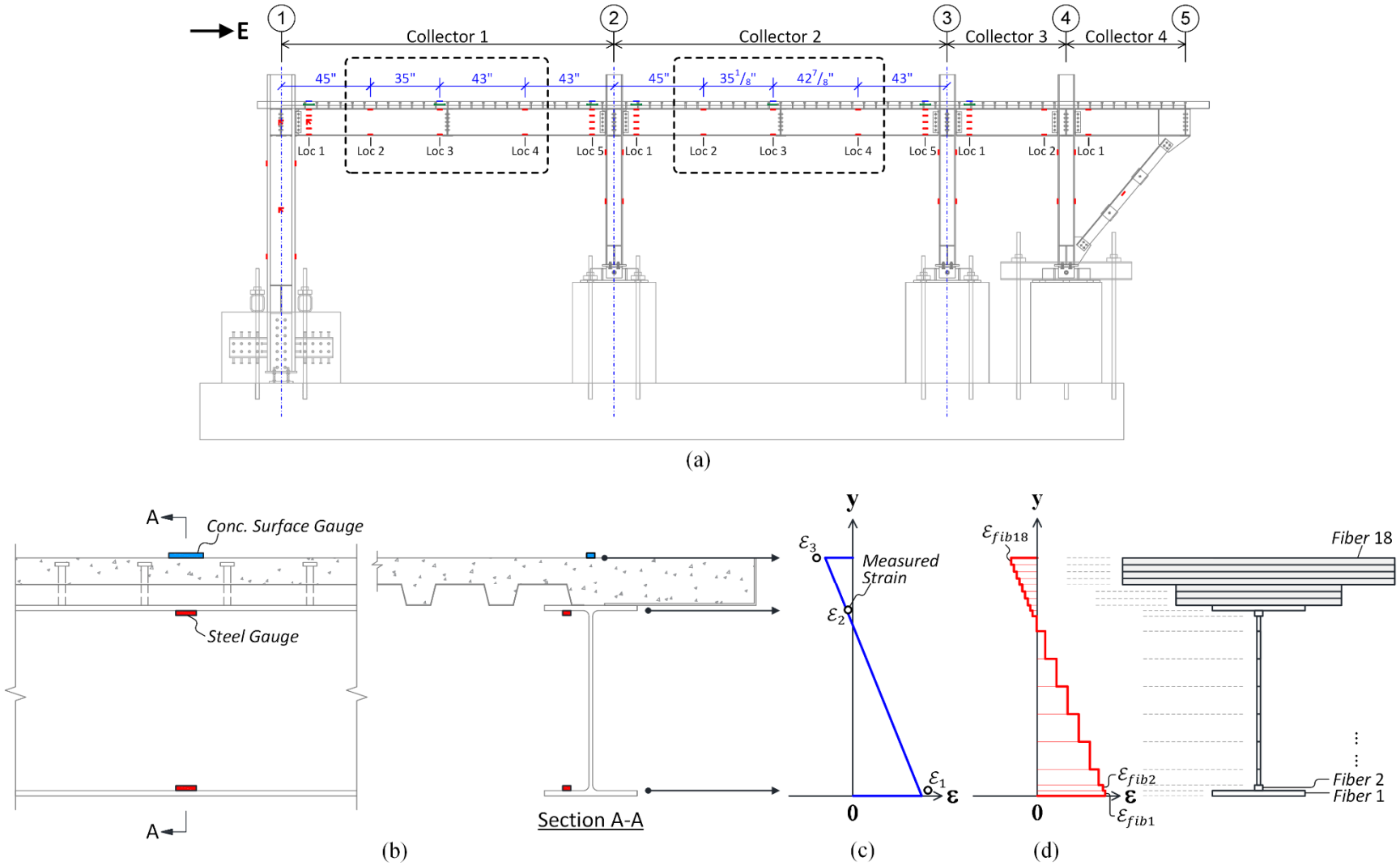

Figure 3.66 (a) Instrumented Sections within Collector Spans and (b) Gauge Layout, (c) Assumed Strain Profile, and (d) Assignment of Strains to Fiber Section

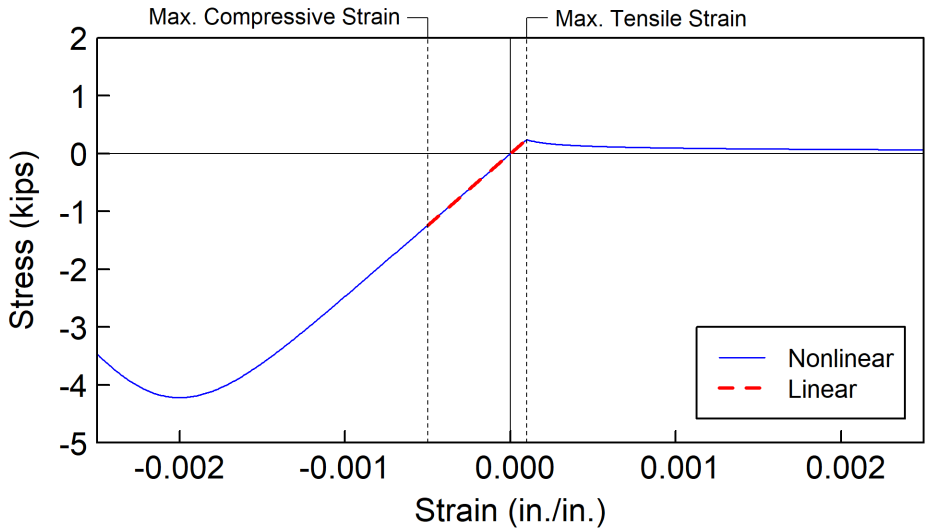

Figure 3.67 Constitutive Models for Concrete Slab

4. PHASE 1 TEST RESULTS

4.1 General Phase 1 Test Results

In Phase 1 testing, three floor acceleration simulation tests, designated as Tests 1-1, 1-2 and 1-3, were conducted to excite the test building to reproduce the target floor accelerations obtained from time history analyses results on the 5th floor of a 12-story prototype building frame subjected to a historical ground motion that was scaled to 20%, 50% and 100% of the design earthquake (DE) levels, respectively. Dynamic characterization tests, including white noise or impulse testing, were performed before and after each shake table test to monitor the variation of dynamic properties of the specimen. Figure 4.1 shows the input table motions for white noise and impulse testing. Figure 4.2 illustrates the variations of measured first-mode frequency and damping ratio of the specimen throughout Phase 1 testing. Table 4.1 summarizes the results of dynamic characterization testing.

As shown in Figure 4.3, Fourier spectra of the white noise test results on the floor acceleration in the longitudinal direction measured by the accelerometer A19, which was placed near the mass center of the floor, was plotted to determine the vibration frequencies. In addition, the time histories of the floor acceleration measured by A19 in impulse testing were plotted as shown in Figure 4.4. The averaged time interval between several successive negative peaks (valleys) of the free vibration after impulse loading was computed to estimate the first-mode period of the specimen. Furthermore, by assuming a logarithmic decrement for the acceleration decay response, the equivalent viscous damping ratio, ξ, was estimated from

$$\xi = \left(\frac{1}{2\pi}\right)\left(\frac{1}{n}\right)\ln\left(\frac{a_1}{a_{n+1}}\right) \tag{4.1}$$

where a_1 is the acceleration response valley amplitude in the first cycle of the free vibration motion, while a_{n+1} is the decayed acceleration amplitude n cycles later.

As shown in Figure 4.2(a), the fundamental frequency remained approximately constant with a very tiny decay during Phase 1 testing. White noise test results show that the first-mode frequency of the specimen before Phase 1 tests was 5.8 Hz and slightly decayed to 5.60 Hz after three main tests had been completed, a variation which was very similar to the impulse test results (see Table 4.1). The measured frequency of the second mode of the specimen, which is related with the vertical vibration of the cantilever slab, was 11.6 Hz before Phase 1 and slightly decreased to 11.2 Hz after Phase 1 testing had been completed. In addition, the measured damping ratio of the specimen varied from 3.03% to 3.50% with an average value of 3.20% throughout Phase 1 testing. As shown in Figure 4.2(b) the variation of damping ratio is not noticeable. In general, the dynamic properties of the test specimen remained approximately constant during Phase 1 testing.

Figure 4.5 through Figure 4.8 show the global responses of the specimen for the three main tests. Table 4.2 tabulates the measured peak responses in floor acceleration and story drift. Figure 4.5 shows the input table accelerations. Figure 4.6 shows the floor acceleration time histories. The peak floor accelerations achieved in Tests 1-1, 1-2, and 1-3 were −0.41 g, −0.93 g, and −1.53 g, respectively. Figure 4.7 shows the time histories of story drift angle. The peak story drift angles achieved in the three tests were +0.11% rad, +0.32% rad, and +0.62% rad, respectively. Figure 4.8 shows the hysteresis responses. The base shear versus story drift relationship basically remained linear throughout Phase 1 tests, suggesting the specimen remained in the elastic range. Since the specimen generally remined linearly elastic, only detailed specimen responses from Test 3-1 are presented in Section 4.2.

Table 4.1 Results of Phase 1 Impulse and White Noise Tests

Test Timing	Impulse Test				White Noise Test				
	Test No.	Fundamental Properties			Test No.	1st Mode		2nd Mode	
		f_1 (Hz)	T_1 (sec)	ξ (%)		f_1 (Hz)	T_1 (sec)	f_2 (Hz)	T_2 (sec)
Before Test 1-1	IM 1-0	5.73	0.174	3.19	WN 1-0	5.80	0.172	11.60	0.0862
After Test 1-1	IM 1-1	5.71	0.175	3.03	–	–	–	–	–
After Test 1-2	IM 1-2	5.64	0.177	3.10	–	–	–	–	–
After Test 1-3	IM 1-3	5.49	0.182	3.50	WN 1-3	5.60	0.179	11.20	0.0893

Table 4.2 Peak Response Quantities of Phase 1 Tests

Test No.	Floor Acceleration (g)		Story Drift (%)	
	Positive	Negative	Positive	Negative
Test 1-1	0.30	-0.41	0.11	-0.08
Test 1-2	0.69	-0.93	0.32	-0.19
Test 1-3	1.13	-1.53	0.62	-0.41

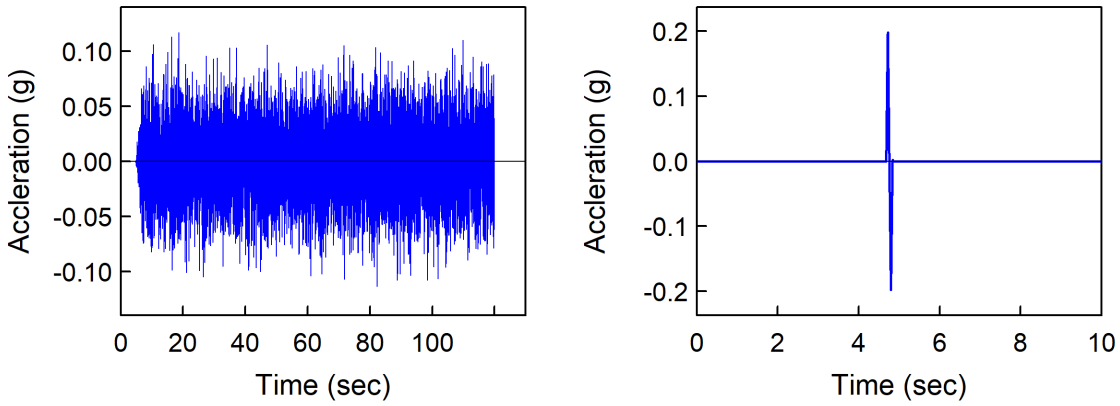

(a) White Noise Test (b) Impulse Test

Figure 4.1 Impute Table Motion for (a) White Noise and (b) Impulse Tests

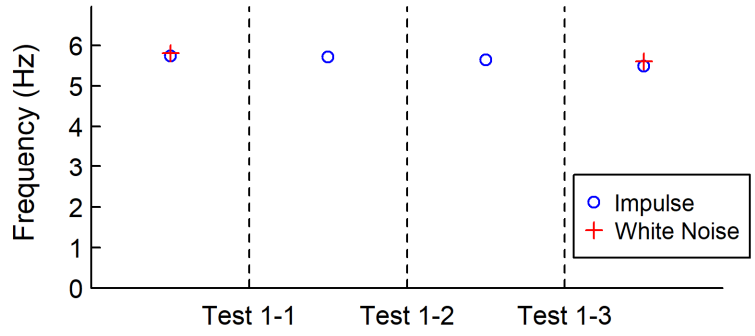

(a)

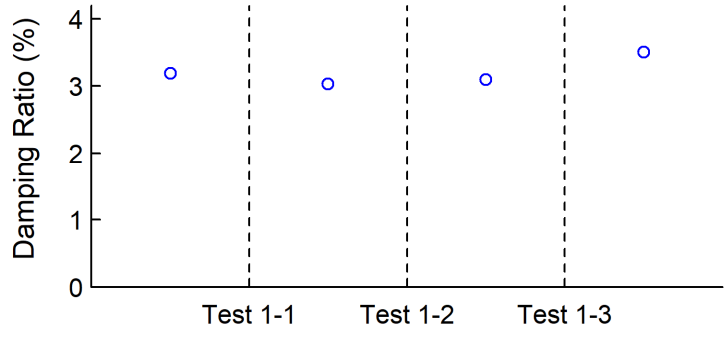

(b)

Figure 4.2 Variations of Measured (a) 1st mode frequency and (b) Damping Ratio throughout Phase-1 Testing

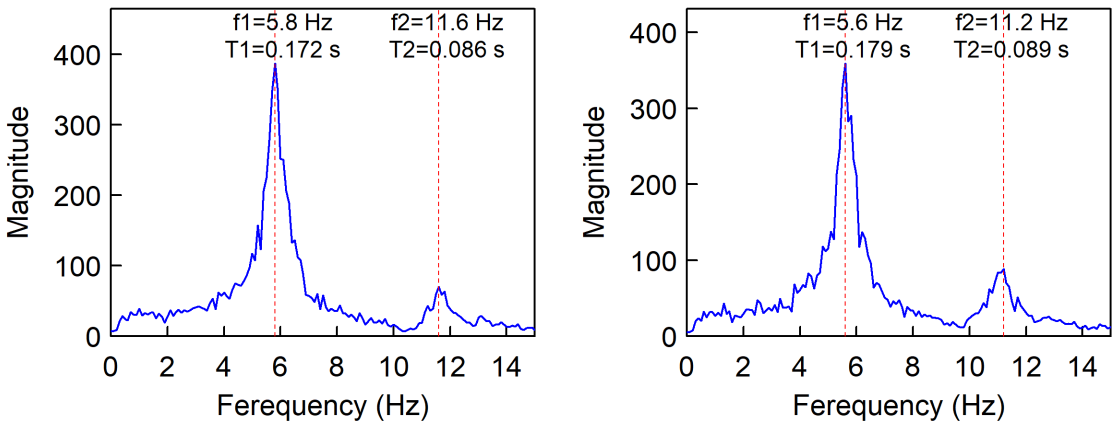

(a) WN 1-0 (b) WN 1-3

Figure 4.3 Phase-1 White Noise Test Results

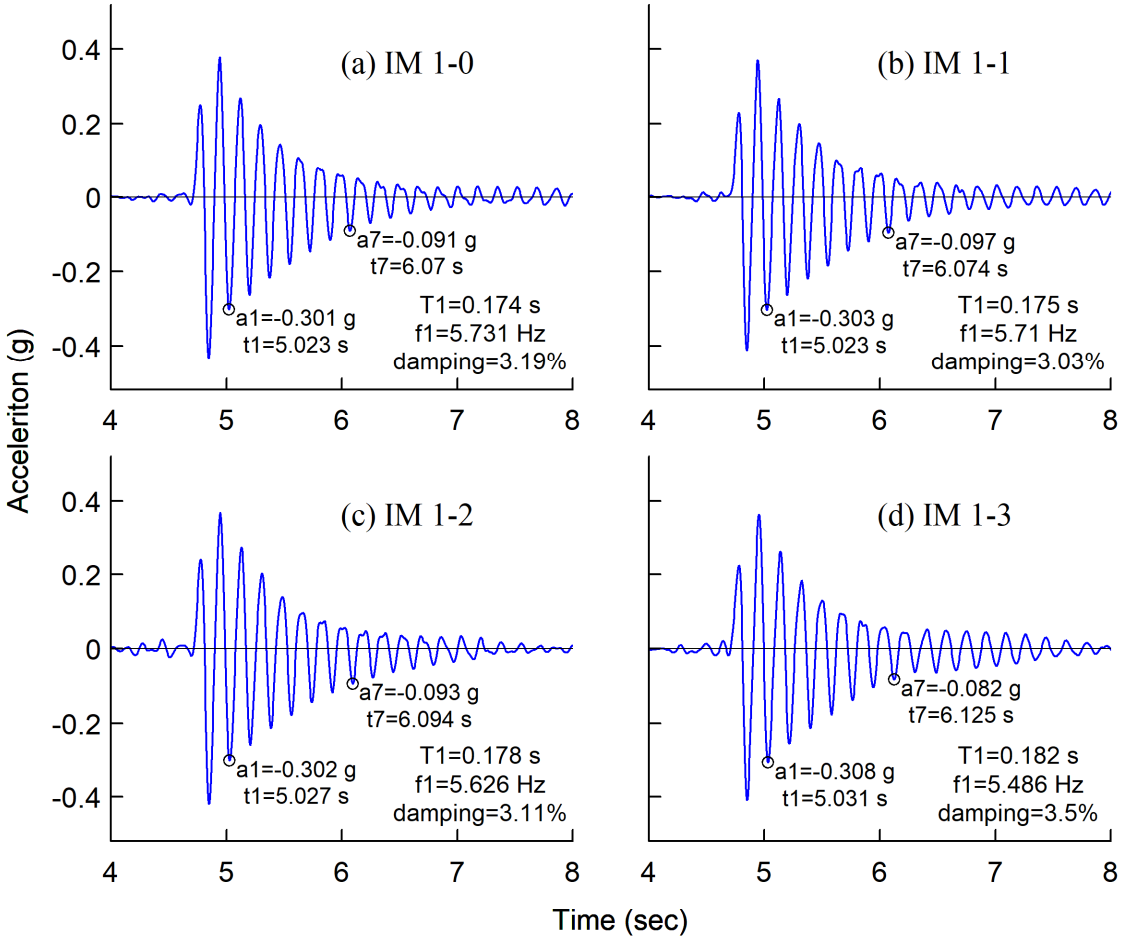

Figure 4.4 Phase-1 Impulse Test Results

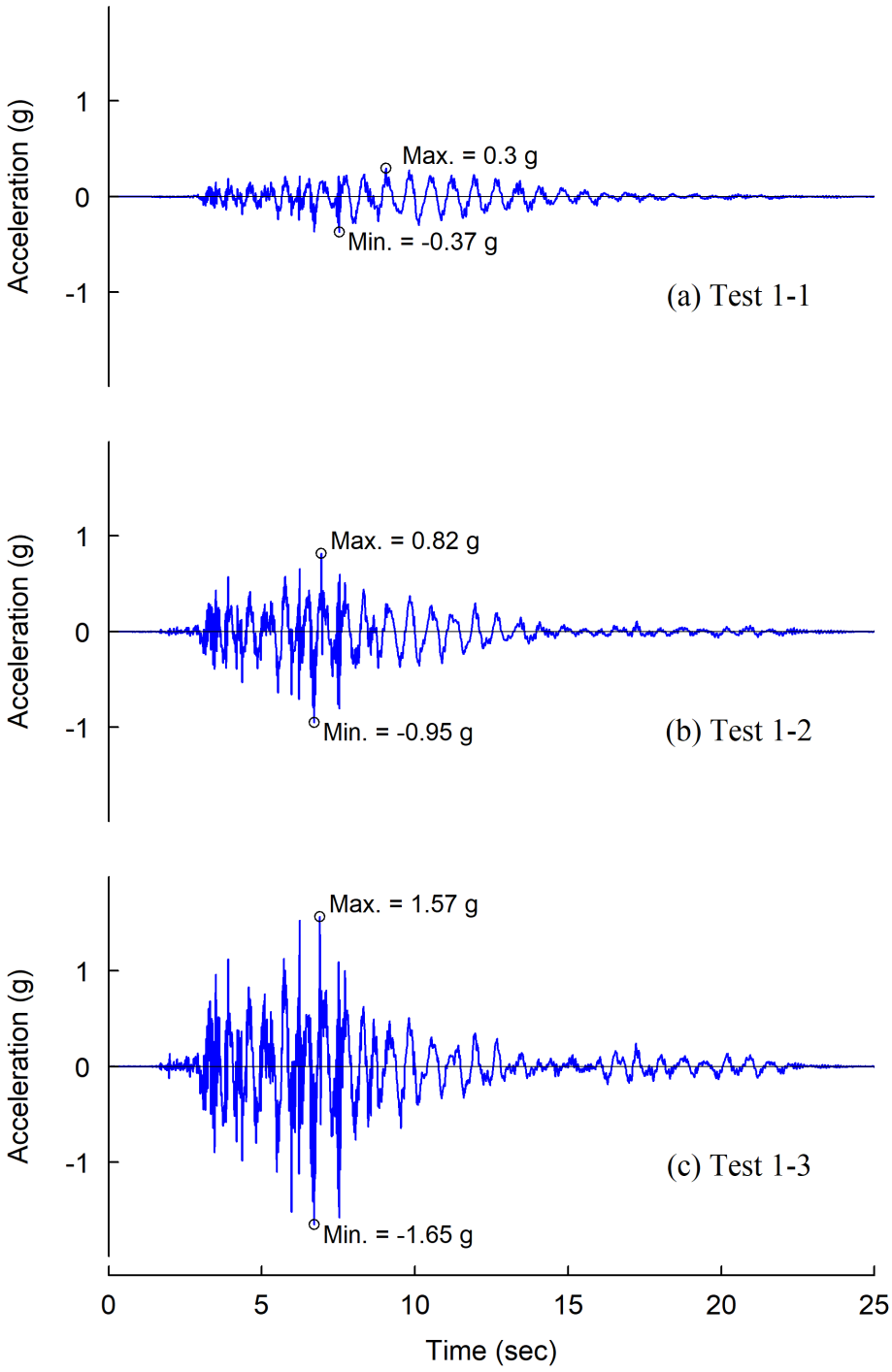

Figure 4.5 Phase 1 Tests: Measured Table Accelerations

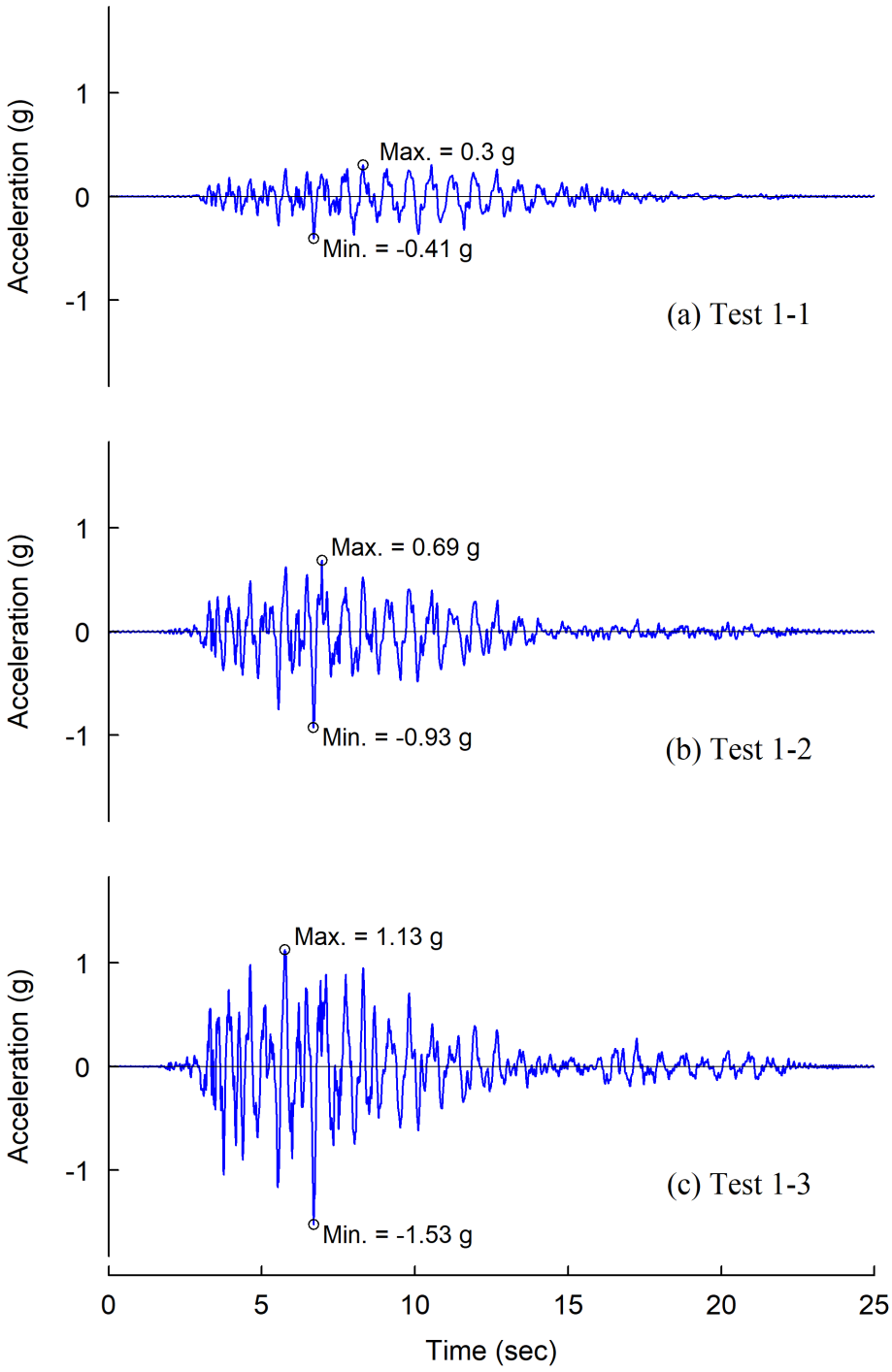

Figure 4.6 Phase 1 Tests: Floor Acceleration Time Histories

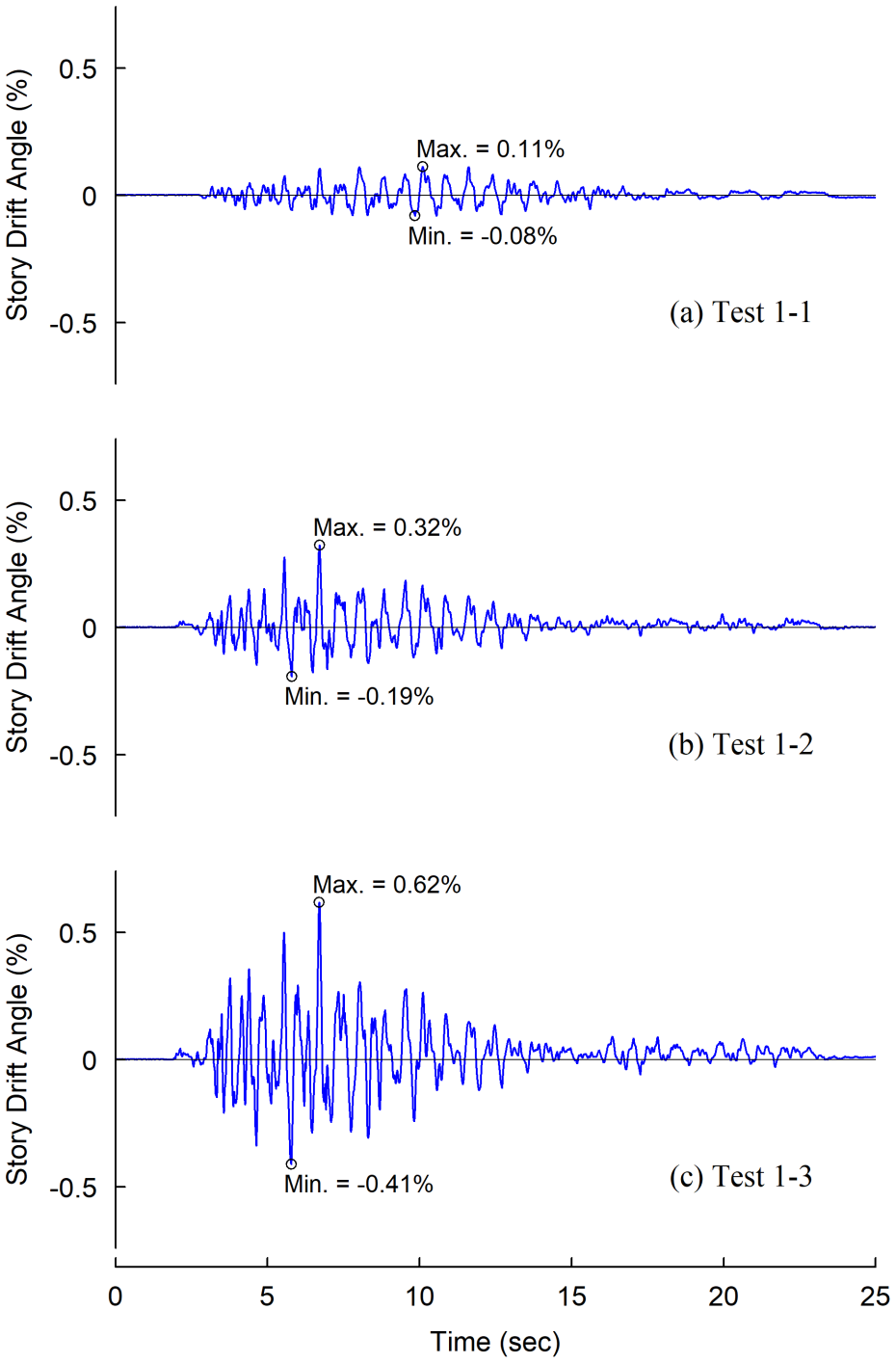

Figure 4.7 Phase 1 Tests: Story Drift Angle Time Histories

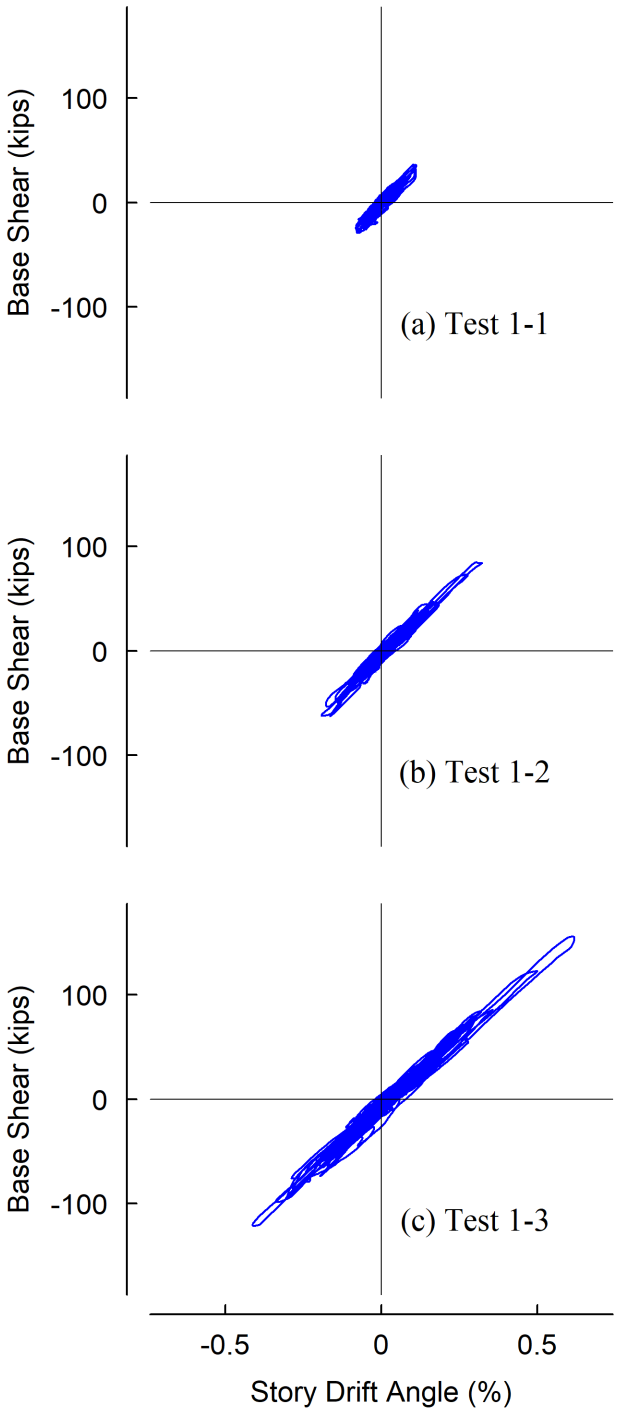

Figure 4.8 Phase 1 Tests: Base Shear versus Story Drift Relationships

4.2 Detailed Results of Test 1-3

4.2.1 Verification of Floor Acceleration Simulation Testing

One of the main objectives of Phase 1 testing is to verify the proposed methodology for floor acceleration simulation testing. Figure 4.9 shows the time history, fast Fourier transform (FFT) and pseudo-acceleration spectrum of the input ground motion employed in the time history analysis on a frame model representing the prototype structure. This input motion was generated by scaling a 30-second duration ground motion record (Beverly Hills-Mulhol station) from the 1994 Northridge earthquake to 100% design earthquake (DE) level [see Figure 4.9(c)]. In addition, modal analysis results showed that vibration periods of the frame model for the first three modes were T_1 = 2.833 sec, T_2 = 1.005 sec, and T_3 = 0.594 sec, respectively, which corresponded to frequencies f_1 = 0.353 Hz, f_2 = 0.995 Hz, and f_3 = 1.684 Hz, respectively. The FFT spectrum [Figure 4.9(b)] indicates that the input ground motion happens to have high frequency contents around the 2nd and 3rd modes of the prototype structure.

Figure 4.10 shows the numerically predicted 5th floor acceleration response of the prototype model, which responds into the inelastic range. Significant spikes in FFT spectrum [Figure 4.10(b)] are very close to the frequencies of the 2nd and 3rd modes, indicating that this acceleration response is mainly contributed from the 2nd-mode vibration, while the amplitude of the 3rd-mode action is also significant. In addition, another two noticeable spikes in the FFT spectrum take place to the right of and slightly away from the frequencies of the 2nd and 3rd modes. These might be caused by the nonlinear responses of the prototype model so that the spikes are not only concentrated at the natural frequencies of the elastic structure.

Based on the similitude law, the time vector of the abovementioned 5th floor acceleration response was scaled by a factor of $\sqrt{0.5}$ to serve as the target floor acceleration for the ½-scale test

specimen. Figure 4.11 shows the time history, FFT and pseudo-acceleration spectrum of this target floor acceleration. The duration of the scaled acceleration time history was squeezed to 21.213 seconds [Figure 4.11(a)]. Note that the scaled periods for the first three modes are T_1^* = 2.003 sec, T_2^* = 0.711 sec, and T_3^* = 0.420 sec, respectively, which corresponded to frequencies f_1^* = 0.499 Hz, f_2^* = 0.141 Hz, and f_3^*= 0.238 Hz, respectively. Consistent to the prototype floor acceleration response, the FFT spectrum of the scaled floor acceleration [Figure 4.11(b)] has significant spikes near the scaled frequencies of the 2nd and 3rd modes (f_2^* and f_3^*).

With the scaled target floor acceleration shown in Figure 4.11 and the dynamic properties (nature frequency and damping ratio) of the specimen estimated from the impulse test prior to the floor acceleration test, the required (i.e., target) input table motion for Test 3-1 was determined by using the proposed methodology described in Chapter 2. Figure 4.12 shows the time history, FFT and pseudo-acceleration spectrum of the target input acceleration together with those of the actual (i.e., measured) table acceleration for Test 1-3. In addition, Figure 4.13 shows the time history, FFT and pseudo-acceleration spectrum for the target and measured floor acceleration of the specimen.

Figure 4.14 shows the comparison between the measured and target input accelerations. Figure 4.14(a) shows that the shake table did not perfectly reproduce the target input acceleration time history. The positive and negative peak acceleration of the measured input motion reached +1.57 g and −1.69 g, both of which were higher than the peak values (+1.33 g and −1.51 g, respectively) of the target input motion. However, as shown in Figure 4.14(b), the relationship of measured versus target responses for the input motion shows a strong linear relationship. The regression gives a slope of 1.154 with an R-squared value of 0.895. It indicates that, the achieved table acceleration overshot the target input motion by approximately 15%. Figure 4.14(c) shows

the comparison of pseudo-acceleration spectra between the measured and target responses of input table acceleration. Basically, the shape of the two spectra was similar. Significant peaks of the two spectra took place at approximately the same periods. However, the amplitudes of three main peaks in the spectrum were higher for the achieved table motion. It is noted that both spectra had a low amplitude at the specimen fundamental period, T_n. Hence, it can be expected that this input motion would not excite significantly the first-mode response of the specimen.

Figure 4.15 shows the comparison between the measured and target floor accelerations of the specimen. As a result of overshooting of the achieved input table acceleration, Figure 4.15(a) shows that the specimen did not perfectly reproduce the target floor acceleration time history. The positive and negative peak acceleration of the measured response reached +1.13 g and −1.53 g, both of which were higher than the peak values (+0.80 g and −1.03 g, respectively) of the target output motion. However, as shown in Figure 4.15(b), the relationship between the measured and target responses still exhibits a positive correlation. The regression gives a slope of 1.139 with an R-squared value of 0.720. This suggests that the magnitude of achieved floor acceleration generally exceeded the target by about 14%, which is similar to the percentage (15%) of overshooting in the table input motion. Figure 4.15(c) shows the spectrum comparison. Again, the shape of the two spectra exhibited a similar pattern. Significant peaks of the two spectra took place at approximately the same periods, indicating that the achieved output acceleration captured the dynamic characteristics of the target response. However, the amplitudes of peaks in the achieved spectrum were higher than those of the target spectrum, which is consistent with the overshooting of the achieved output responses. Further, the spectrum of the achieved response had more peaks than the target spectrum around the fundamental period of the test specimen. This could be attributed to the participation of the first-mode response in the specimen, which may be one of the

causes of lowering the correlation between the achieved and target responses for the output acceleration.

Figure 4.16 shows the spectral amplifications between the measured and target responses for input and output accelerations. These spectral amplifications were made by dividing the pseudo-acceleration spectrum of measured response by the spectrum of target response over the periods. The plots of spectral amplifications reflect the overshooting of the input and output accelerations, respectively. Both spectral amplifications were greater than 1.0 over a wide range of periods. In addition, the shapes of spectral amplifications for both input and output accelerations were very similar, which indicates that the overshooting of the achieved output response was mainly caused by the overshooting of the input table motion. A significant spike with an amplitude of about 2.3 for the output floor acceleration occurs at the specimen fundamental period, which again was due to the participation of the first-mode response.

Figure 4.17 shows the spectral amplifications between the output and input accelerations for target and measured responses. These spectral amplifications were made by dividing the pseudo-acceleration spectrum of output floor acceleration by the spectrum of the input table acceleration over the periods. The spectral amplifications of both target and measured responses were very similar over the entire range. Note that these output/input (O/I) spectral amplification are analogous to the transfer functions of the test specimen. The O/I spectral amplification for the target response was based on the proposed transfer function of Equation (2.7) which incorporated with the experimentally determined dynamic parameters (natural frequency and damping ratio) of the test specimen, while the O/I spectral amplification for the measured accelerations represent the actual transfer function measured during Test 1-3. A good agreement of these two spectral

amplifications suggests that the proposed transfer function captures the actual specimen behavior very well.

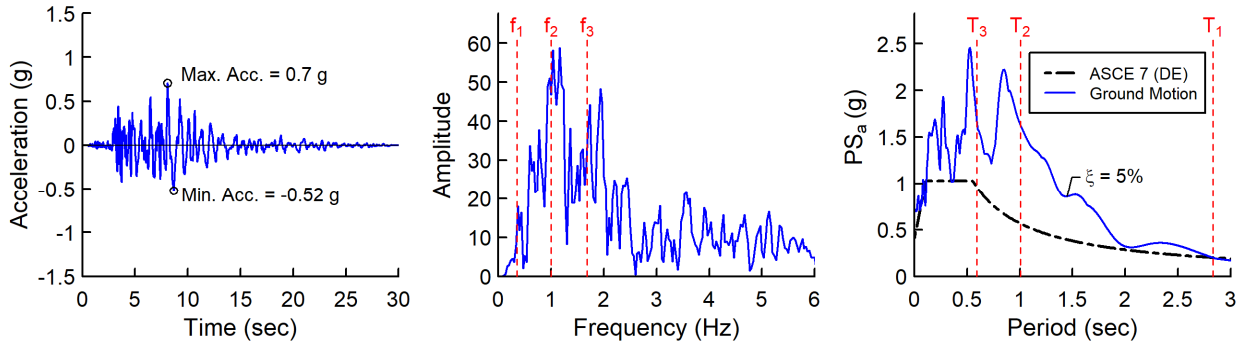

(a) Time History (b) Fast Fourier Ttransform (c) Response Spectrum

Figure 4.9 Ground Motion (100% DE Level) for Analysis on 12F-SDII Building

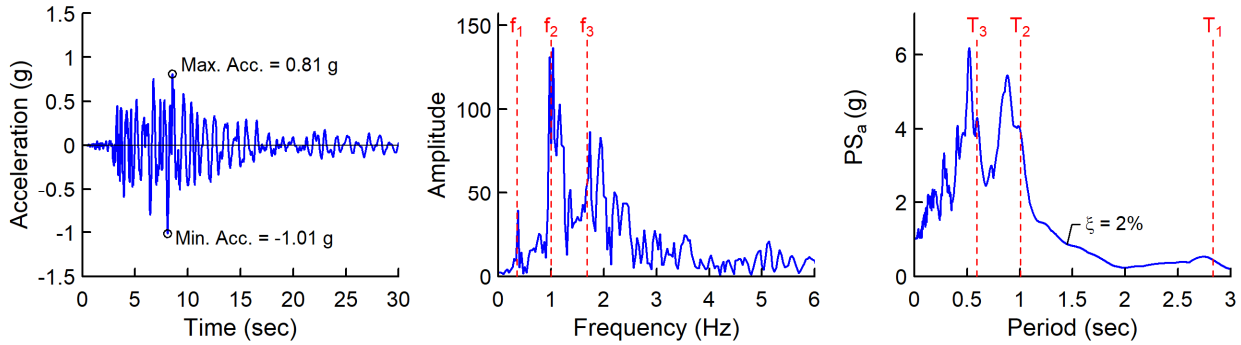

(a) Time History (b) Fast Fourier Ttransform (c) Response Spectrum

Figure 4.10 Predicted 5th Floor Acceleration Responses (100% DE Level) of 12F-SDII Building

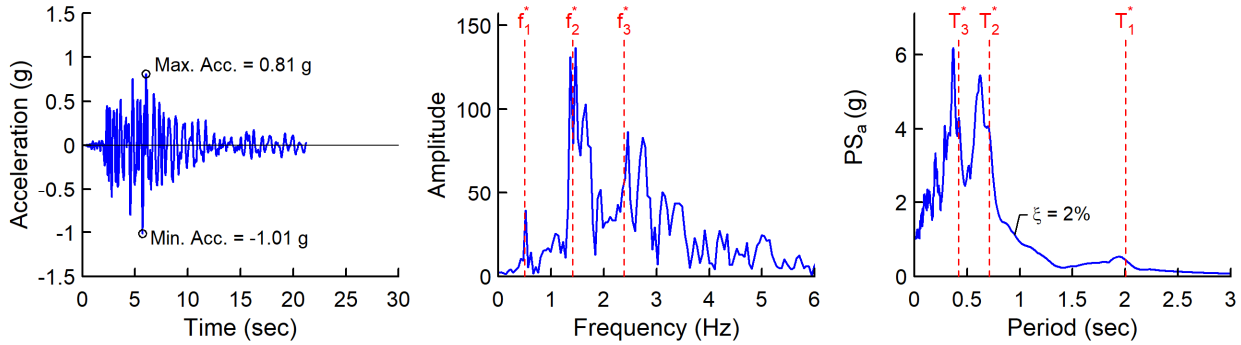

(a) Time History (b) Fast Fourier Ttransform (c) Response Spectrum

Figure 4.11 Scaled 5th Floor Acceleration of 12F-SDII Building (Target Floor Acceleration for Test 1-3 of 0.5-Scale Model)

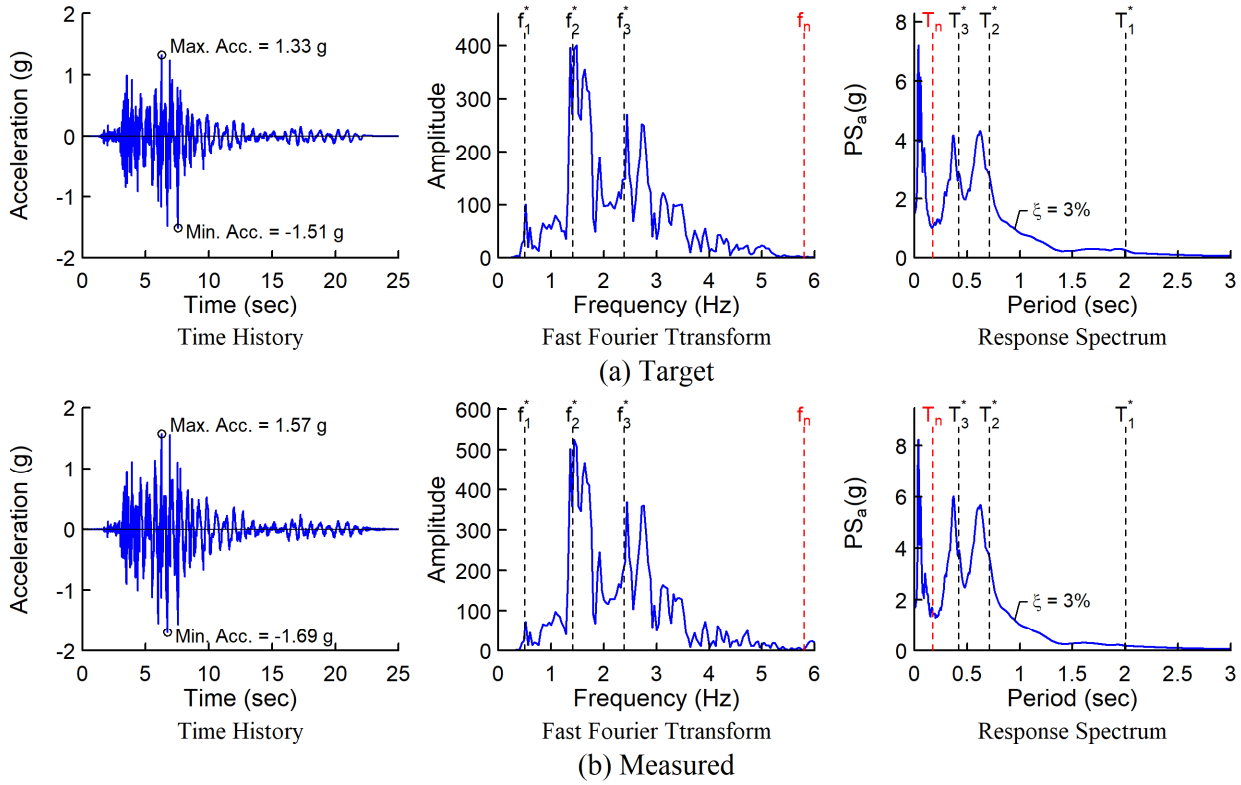

Figure 4.12 Test 1-3: (a) Target and (b) Measured Input Accelerations

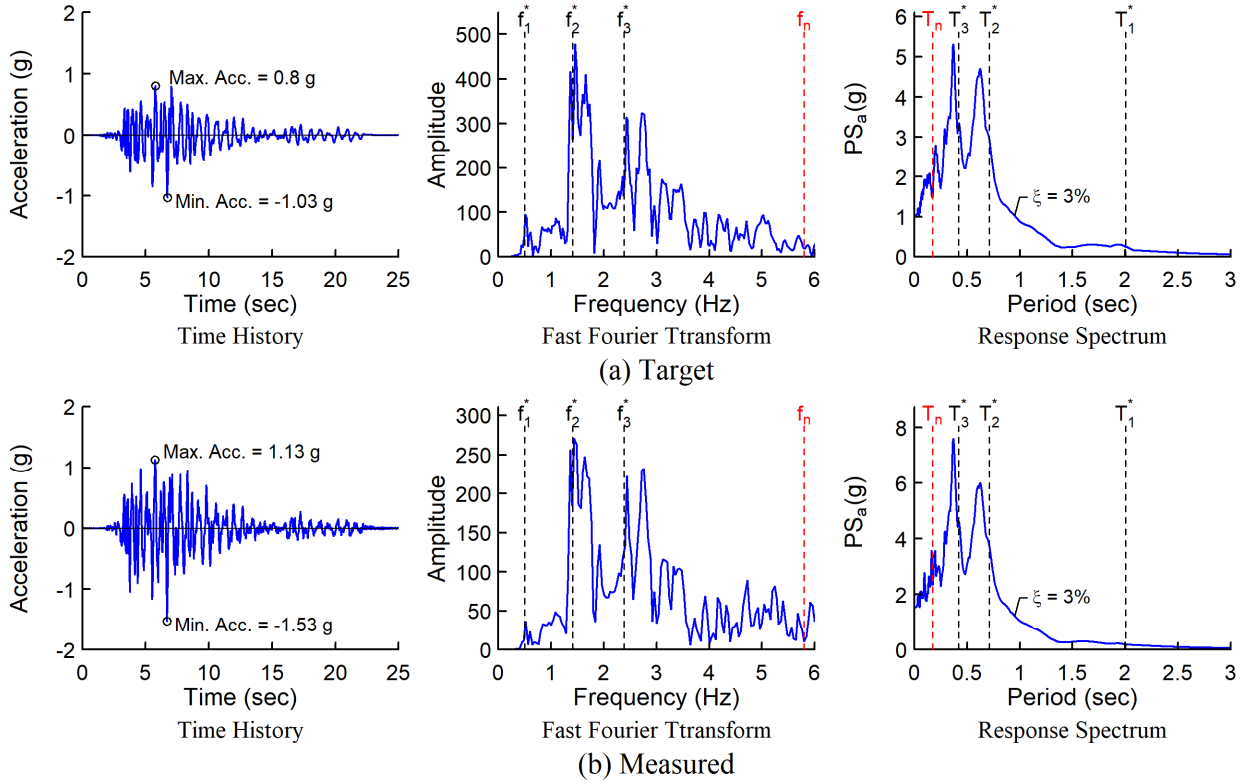

Figure 4.13 Test 1-3: (a) Target and (b) Measured Floor Accelerations

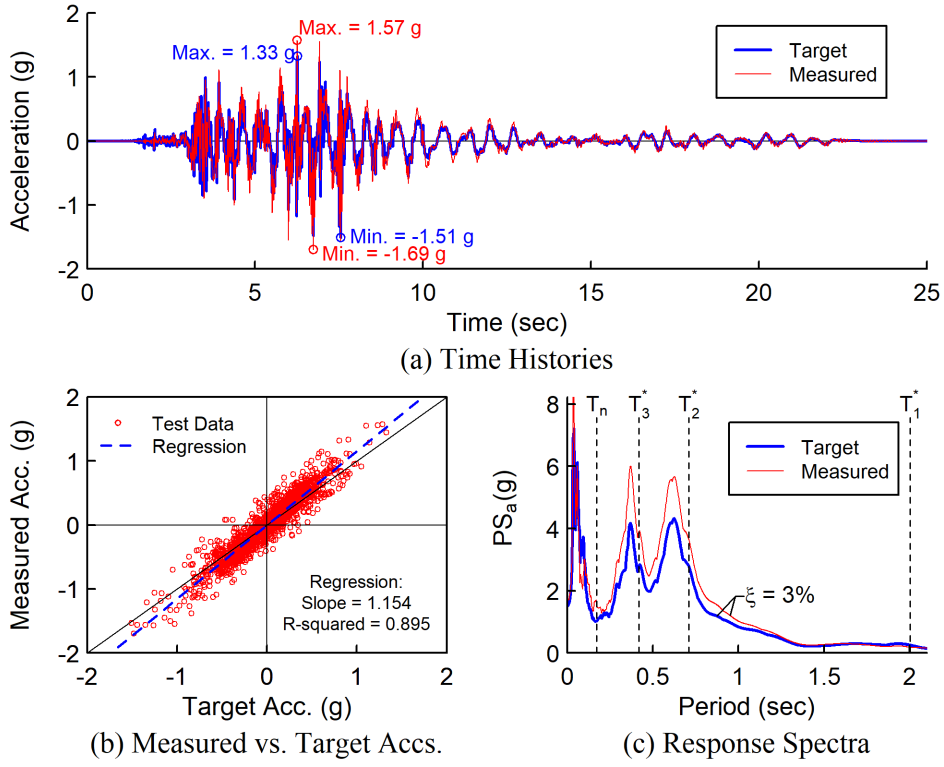

(a) Time Histories

(b) Measured vs. Target Accs.

(c) Response Spectra

Figure 4.14 Test 1-3: Comparison between Measured and Target Input Accelerations

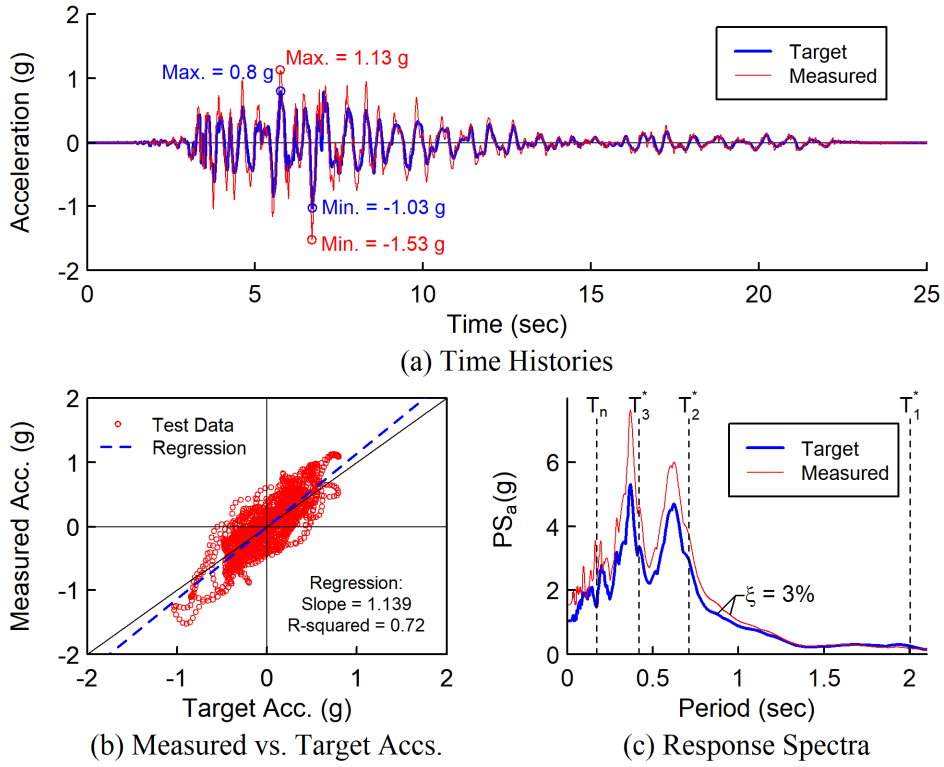

(a) Time Histories

(b) Measured vs. Target Accs.

(c) Response Spectra

Figure 4.15 Test 1-3: Comparison between Measured and Target Floor Accelerations

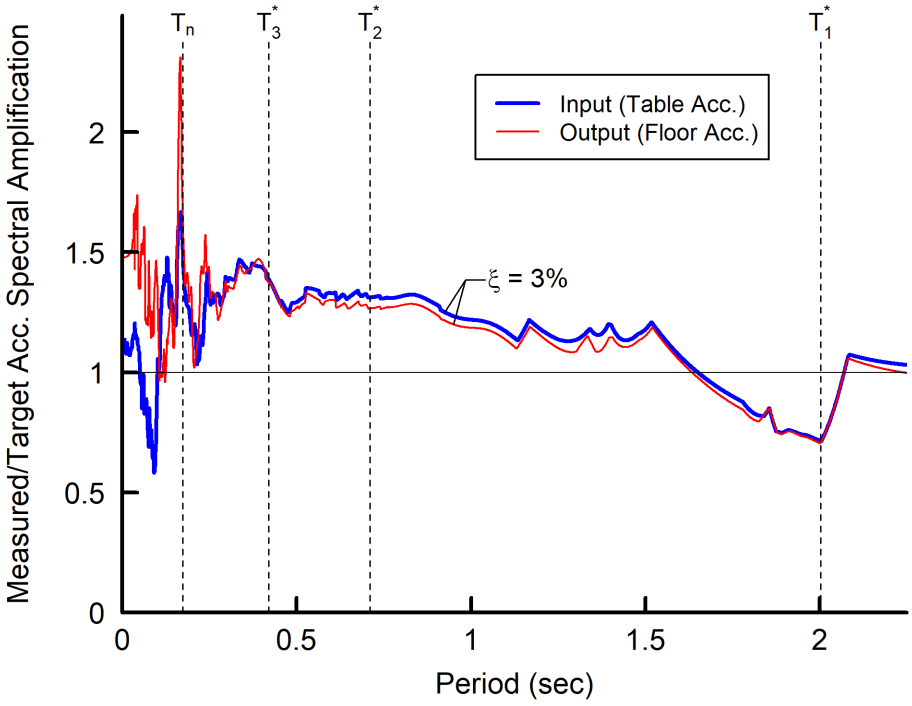

Figure 4.16 Test 1-3: Measured/Target Spectral Amplifications for Input and Output Accelerations

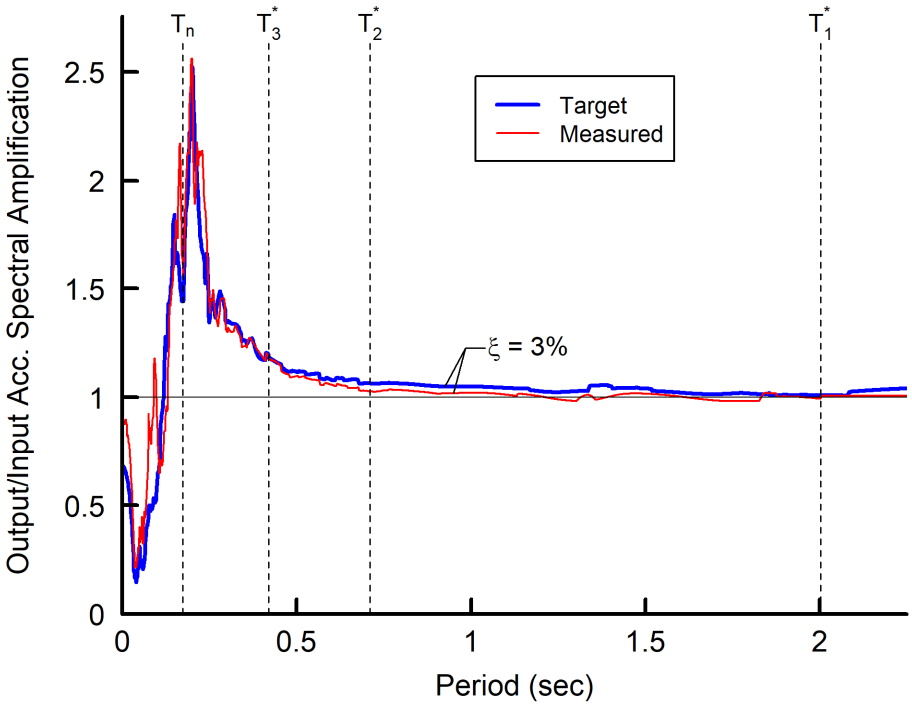

Figure 4.17 Test 1-3: Output/Input Spectral Amplifications for Target and Measured Accelerations

4.2.2 Specimen Global Responses

Figure 4.18 shows the time histories of floor acceleration, story drift angle, and base shear for Test 1-3. The achieved positive and negative peak accelerations were +1.13 g and −1.53 g, while the positive and negative peak story drifts reached +0.61% and −0.42% rad. The time (t = 5.750 sec) at the positive peak acceleration was very close to the time at negative peak story drift (t = 5.777 sec). Likewise, the time (t = 6.695 sec) at the negative peak acceleration was very close to the time at positive peak story drift (t = 6.703 sec). In general, the floor acceleration and story drift were 180 degrees out of phase as the test specimen behaved elastically during the test, which can be evidenced by the linearity of the measured base shear versus story drift relationship shown in Figure 4.20. Since the collectors is the main subject of this study and their force demands are considered more related to the floor accelerations, the detailed responses of the structural members, including the collectors and columns in the test building, at the instant when the specimen reached positive and negative peak accelerations were elaborated in the subsequent sections. In addition, Figure 4.19 shows a good agreement between the measured base shears determined from two methods: one estimated from the measured floor accelerations and the other one computed by using the measured strains on the columns and diagonal braces in the longitudinal direction. A slope of 0.946 from the base shears determined by two methods indicates that the base shear was slightly lower than the total inertial force on the floor diaphragm. These confirmed the reliability of the base shear and column member forces determined from strain gauge readouts.

Figure 4.21 shows the measured slips (relative displacements) between the concrete slab and steel collector beams measured by spring potentiometers installed near several collector-to-column connections. The magnitudes of the slips were much smaller than 0.005 in. This tiny amount of measured displacement may be mainly due to the vibration of the sensors. Hence, test

results show that there was no notable slip between slab and steel collector beams. Figure 4.22 shows the time histories of story shears taken by columns and the diagonal braces in the longitudinal direction of the test building. Figure 4.23 shows the story shears taken by members (columns or diagonal braces) versus total story shear relationships. It can be found that the relationships between the column shear and tory shear were very linear. The slope of the linear regression line of each column shear versus story shear relationship indicate the contribution percentage of the column in taking the story shear. Each cantilever column (on Column Line 1) took approximately 36% of the story shear so that about 72% of story shear was taken by the LFRS of the test building. In addition, from west to east the, each gravity column on the Column Lines 2, 3, 4 took approximately 6%, 5%, and 2% of story shear, respectively. Comparisons of each pair of columns on each of the Column Lines 1, 2, and 3 shows a trend that the story shear taken by the column in the north frame was slightly higher than that taken by the south column. This could be due to the difference in the deck orientation between the north and south halves of floor diaphragm. Note that the metal deck was parallel to the collectors in the north frame while the deck is perpendicular to the collectors in the south frame, which would result in a slightly larger area of concrete slab being mobilized to resist the bending moments in the collectors in the north frame. Thus, the north collectors would have a slightly higher flexural stiffness than the south collectors, which caused the north frame to be slightly stiffer than the south frame and resulted in higher column shears in the north frame. On the other hand, it can be found from Figure 4.23 that the correlation between the story shear and horizontal force taken by each diagonal brace was very weak. This could be explained by the fact that the brace axial forces were mainly induced by the vertical vibrations of the cantilever slab at the east end of the structure instead of the frame sway

action in the longitudinal direction. Thus, for simplicity, the contribution from the braces to resist the story shear is neglected.

Figure 4.24 and Figure 4.25 show the column bending moment diagrams at the positive and negative peak accelerations, respectively. Due to the flexural rigidity of the AFW connections next to the top end of cantilever columns, a noticeable amount of bending moment was induced there, resulting in a double-curvature moment diagram. The inflection point was located at approximately 75% of the column height above the bottom end. In addition, the moment diagrams of the gravity columns indicate that the pin-support worked very well as intended; the bending moments at column bottom end were negligible. By contrast, a noticeable amount of moment developed at the top end of each gravity column, which suggests that the flexural rigidity from the collector-to-column connections should not be neglected for an accurate analysis of the structure. Figure 4.26 and Figure 4.27 show the measured column axial forces. Note that the axial force diagrams were plotted by using the average of the measured axial forces at two instrumented sections along the height of each column, which assumes that the overturning axial force is uniformly distributed. Because the magnitude of the axial forces was very low relative to the yield force, a significant variation between axial forces at two measured sections was found for some columns. In this case, a small error or noise in the strain data could result in a considerable variation in the computed axial force. Although these column axial forces will not be used for further discussions in this research, it was found that a negative frame sway (see Figure 4.26) would induce compressive overturing axial forces in Columns 1 and 3 and tensile axial forces in Columns 2 and 4. On the other hand, a positive frame sway (see Figure 4.27) would introduce tensile axial forces in Columns 1 and 3 and compressive axial forces in Columns 2 and 4.

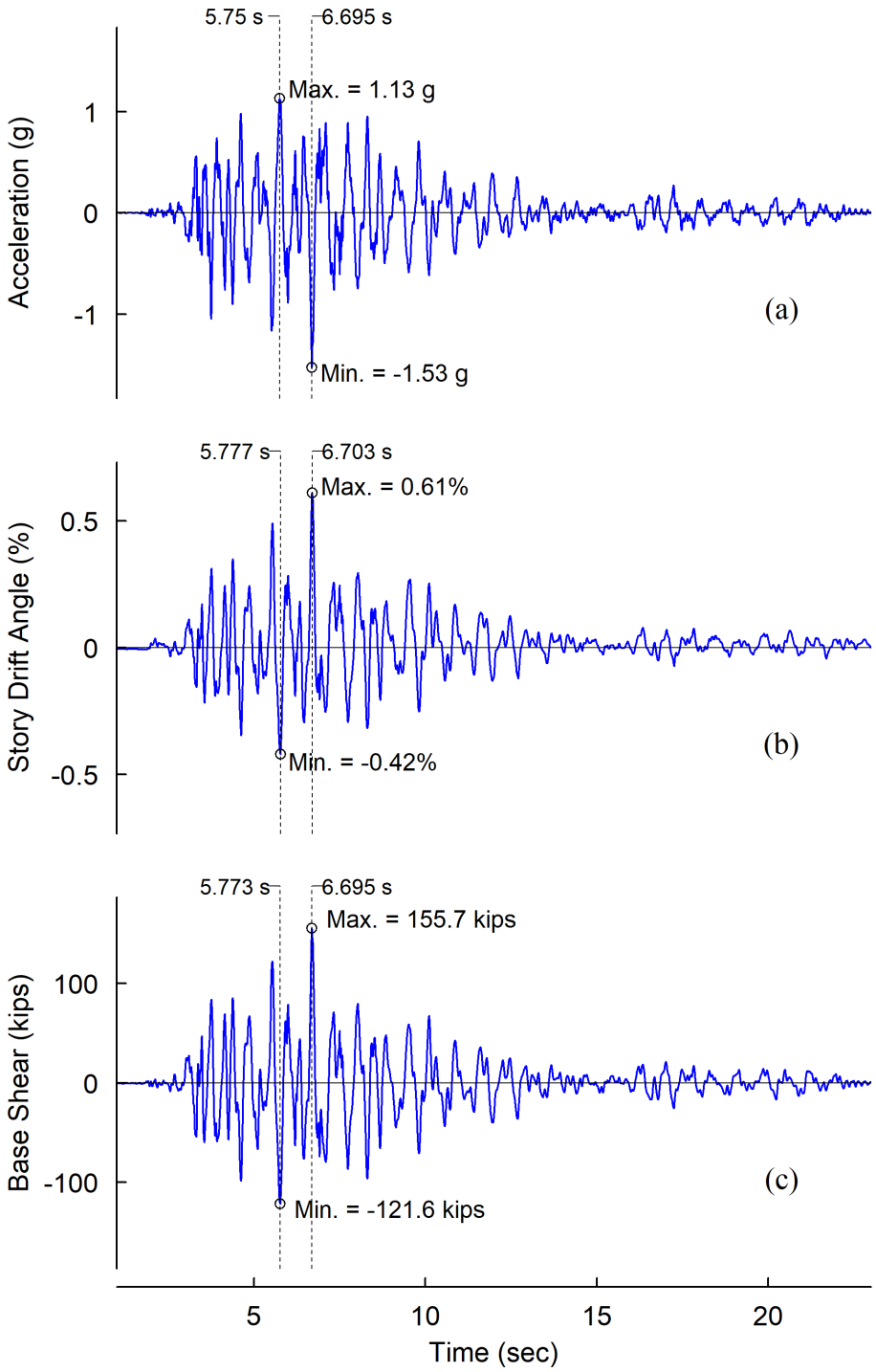

Figure 4.18 Test 1-3: Time Histories of (a) Floor Acceleration, (b) Story Drift Angle, and (c) Base Shear

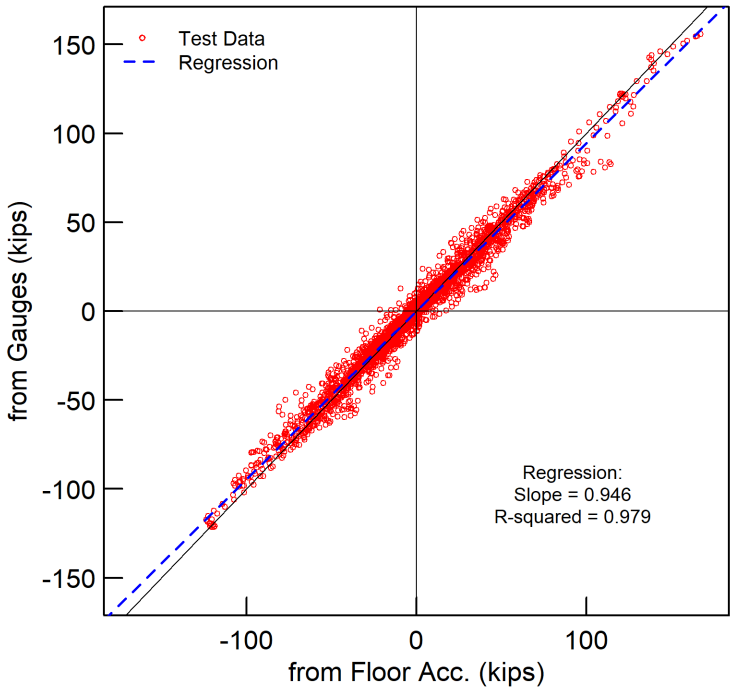

Figure 4.19 Test 1-3: Comparison of Base Shears Determined from Two Methods

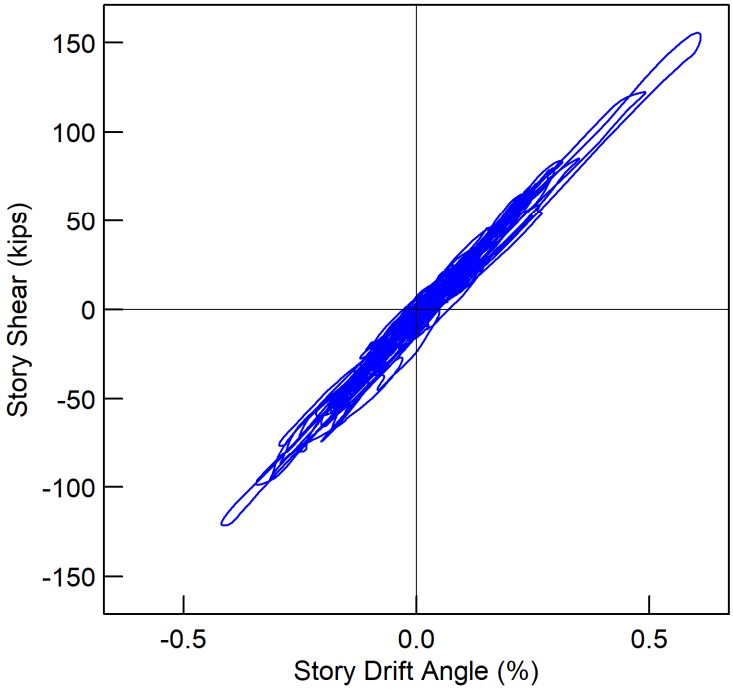

Figure 4.20 Test 1-3: Base Shear versus Story Drift Angle Relationship

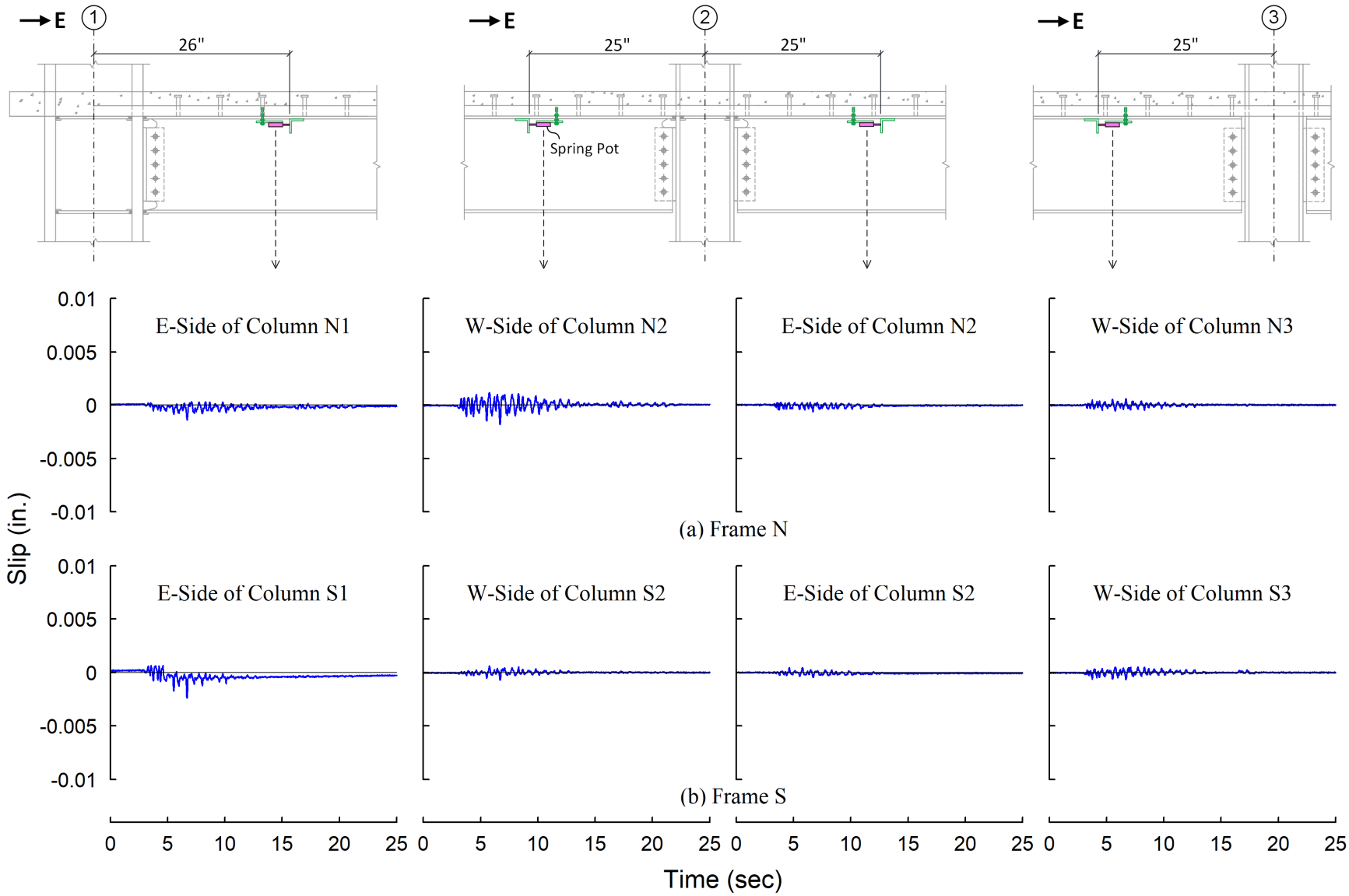

Figure 4.21 Test 1-3: Slips between Concrete Slab and Steel Collector Beams

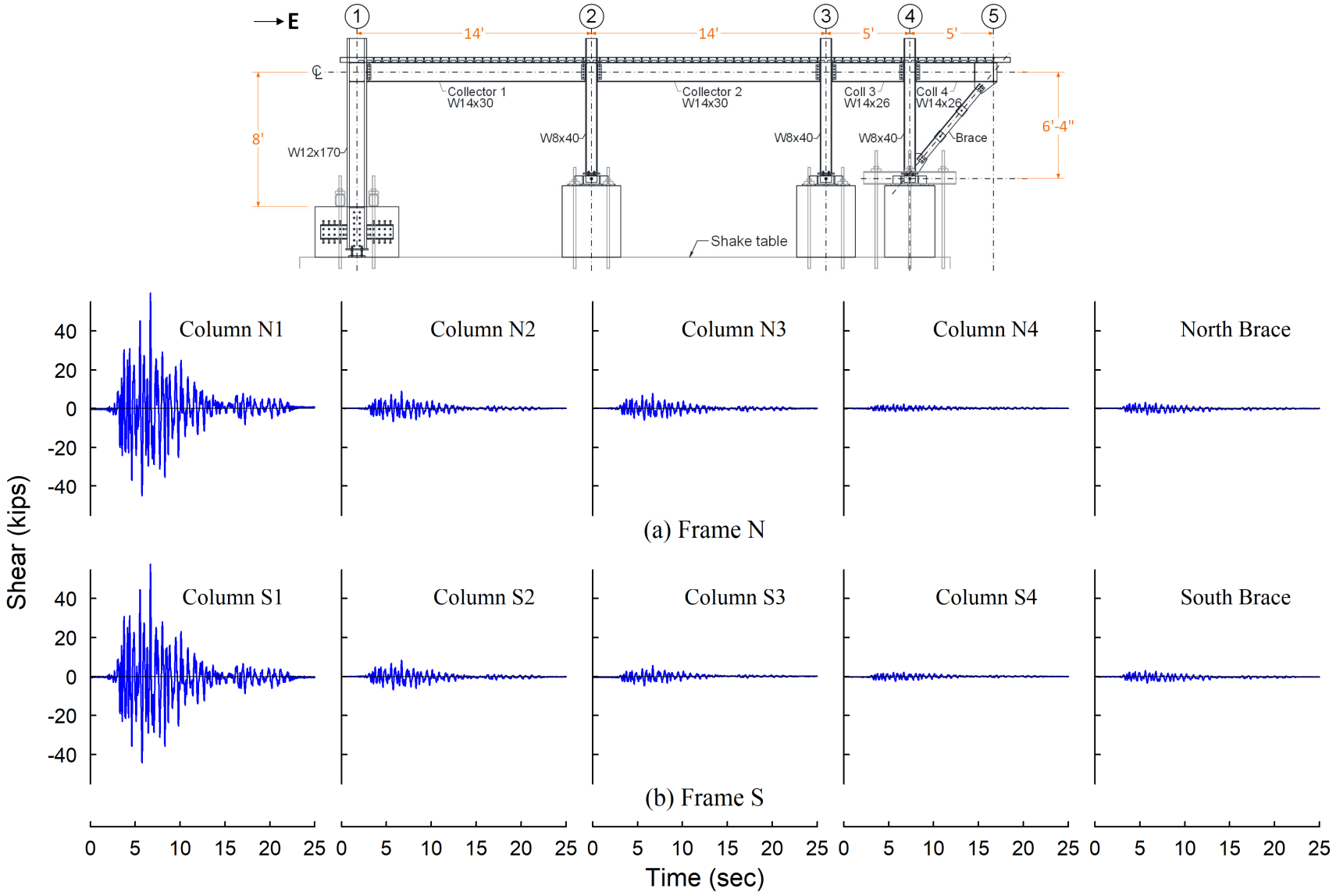

Figure 4.22 Test 1-3: Time Histories of Story Shears Taken by Columns and Diagonal Braces

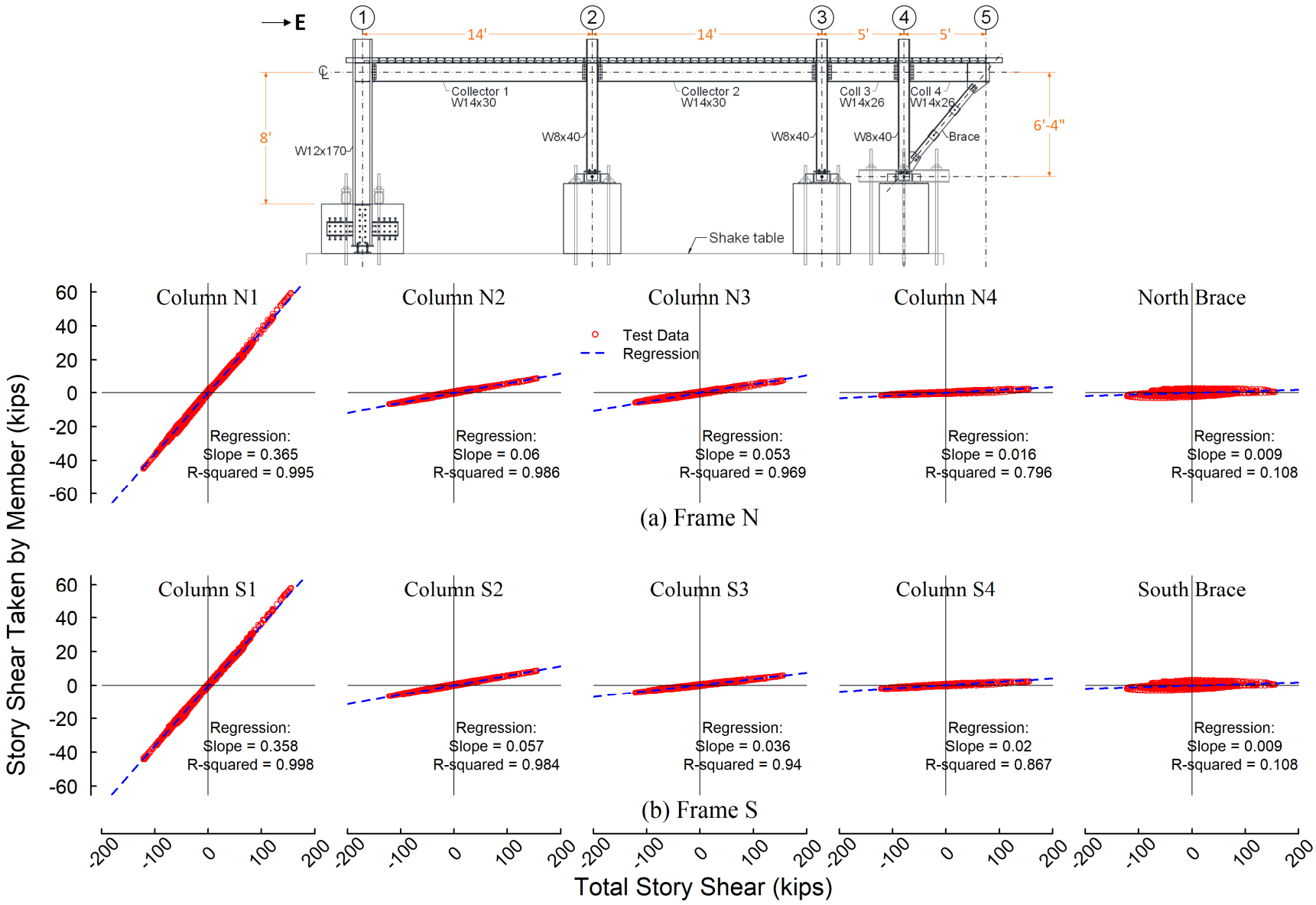

Figure 4.23 Test 1-3: Story Shears Taken by Members versus Total Story Shear Relationships

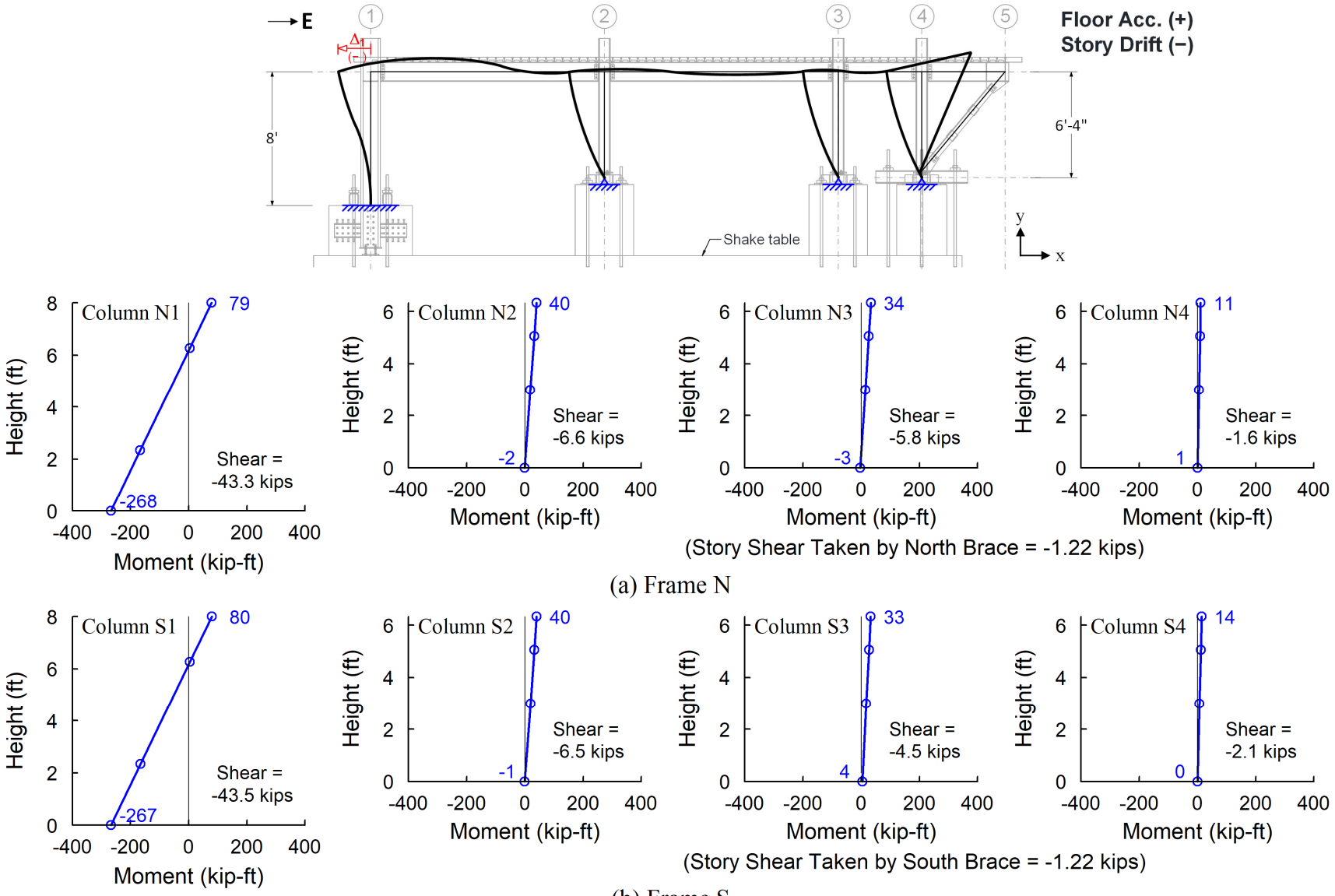

(a) Frame N

(b) Frame S

Figure 4.24 Test 1-3: Bending Moment Diagrams in Columns at Peak Positive Acceleration

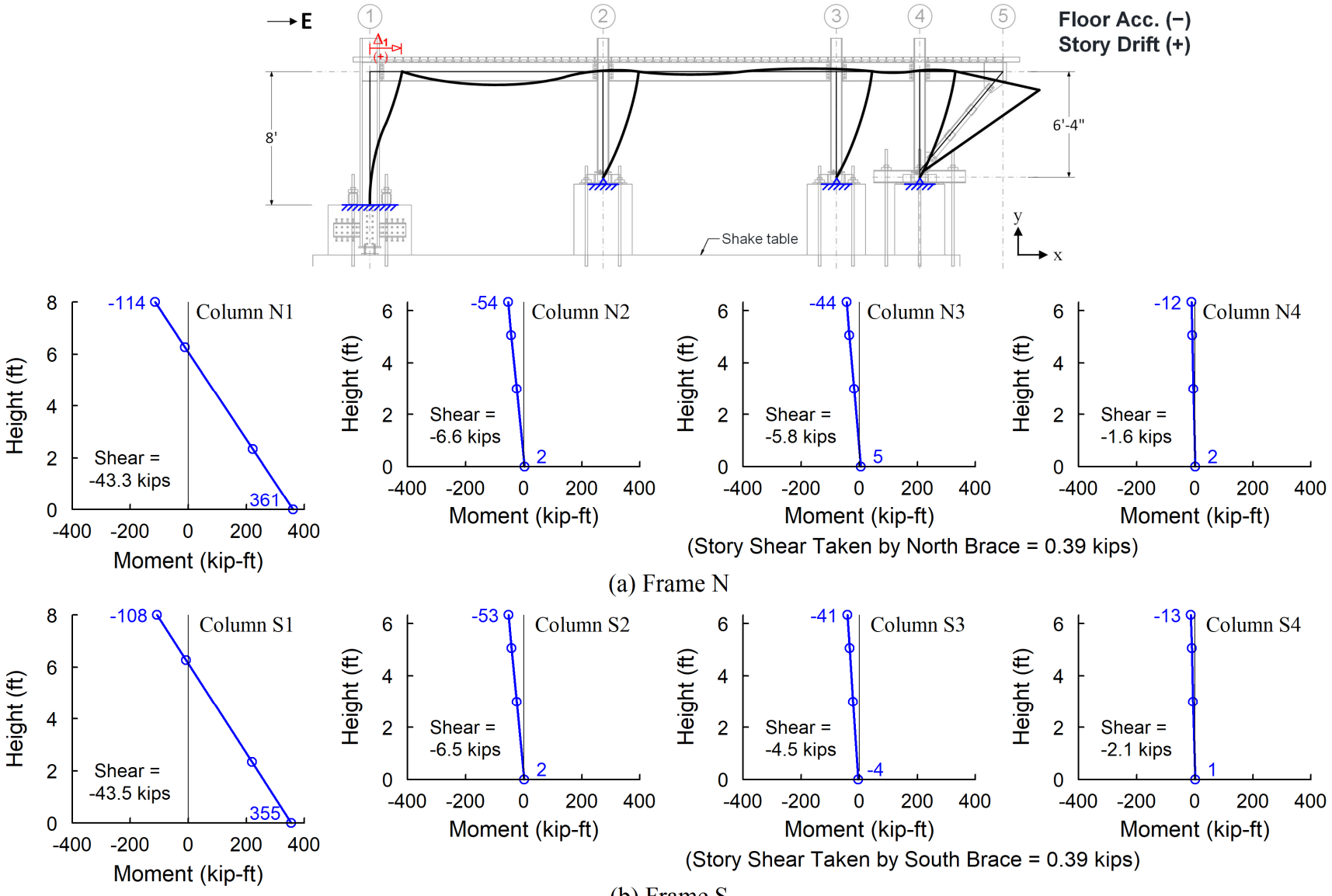

(a) Frame N

(b) Frame S

Figure 4.25 Test 1-3: Bending Moment Diagrams in Columns at Peak Negative Acceleration

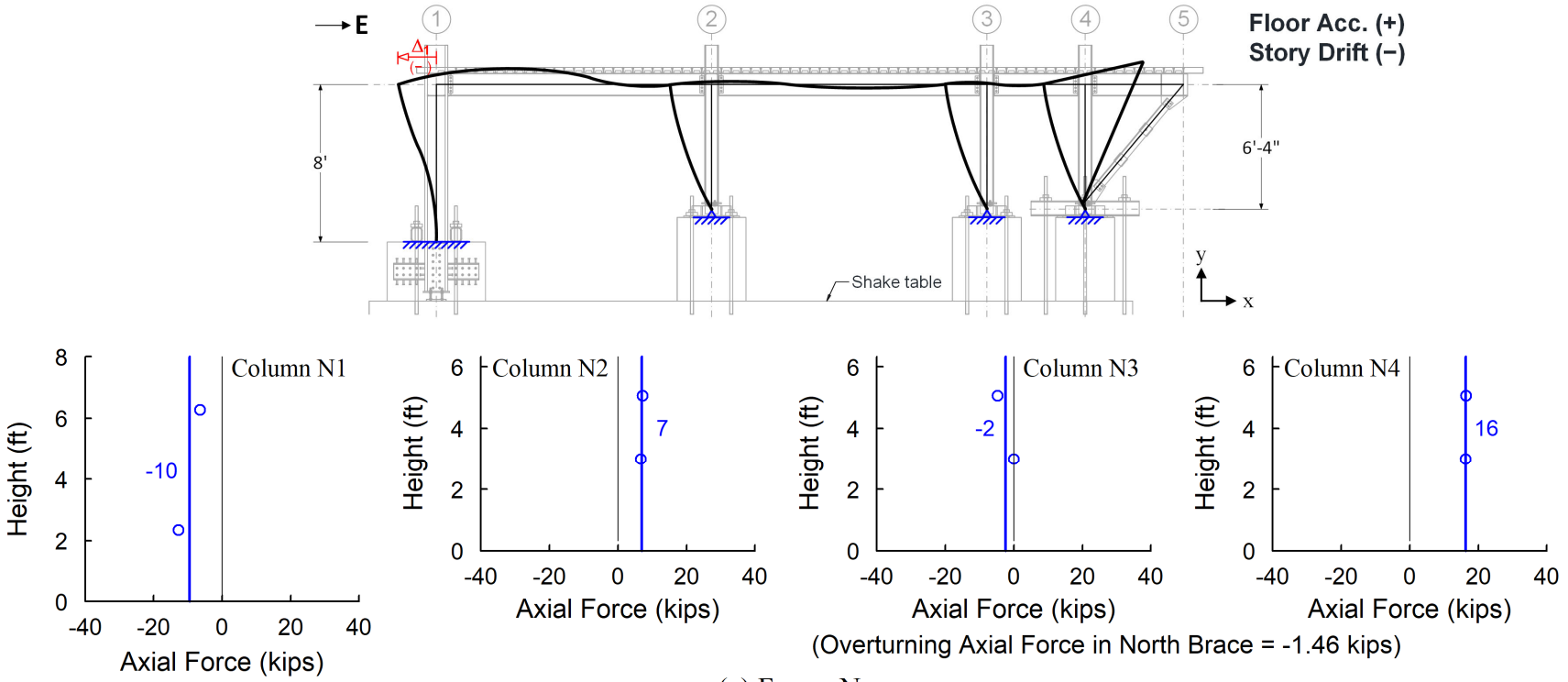

(a) Frame N

(b) Frame S

Figure 4.26 Test 1-3: Axial Force Diagrams in Columns at Peak Positive Acceleration

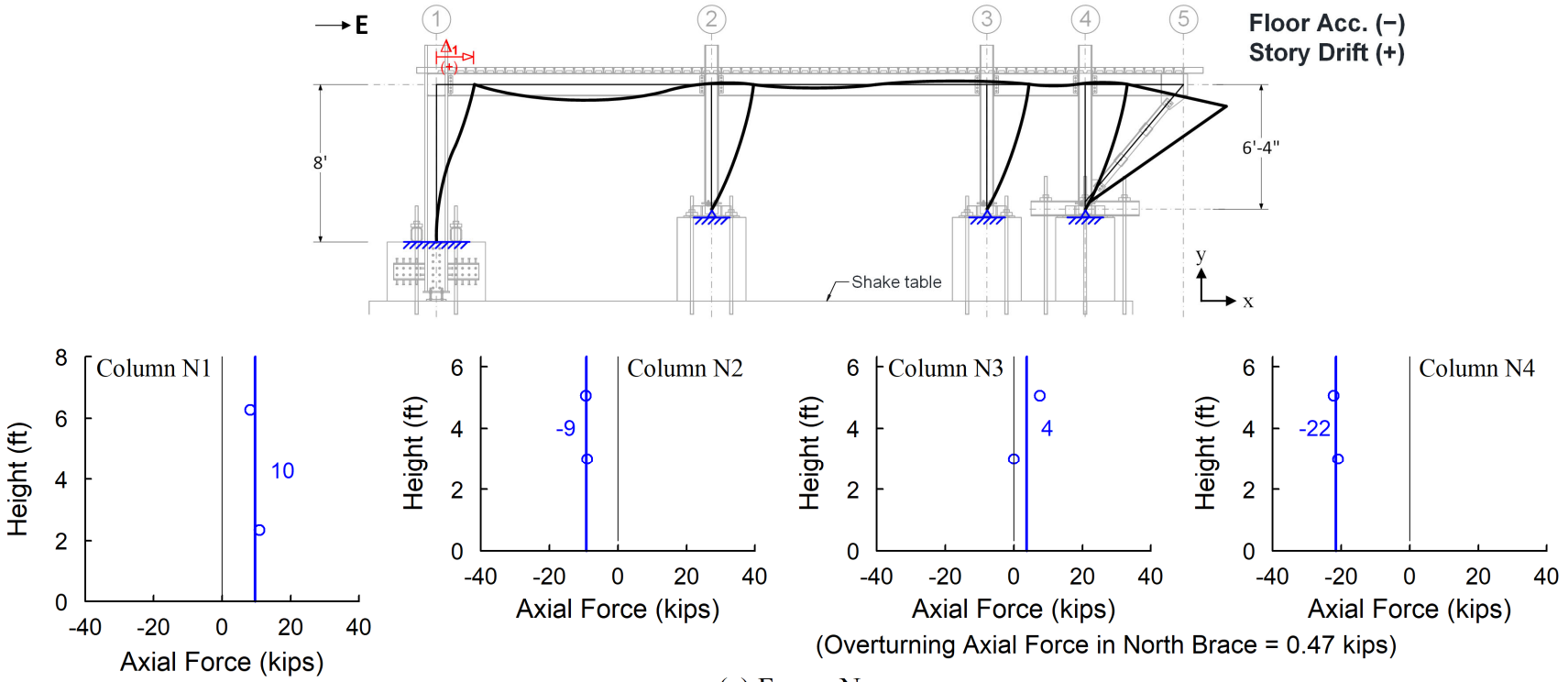

(a) Frame N

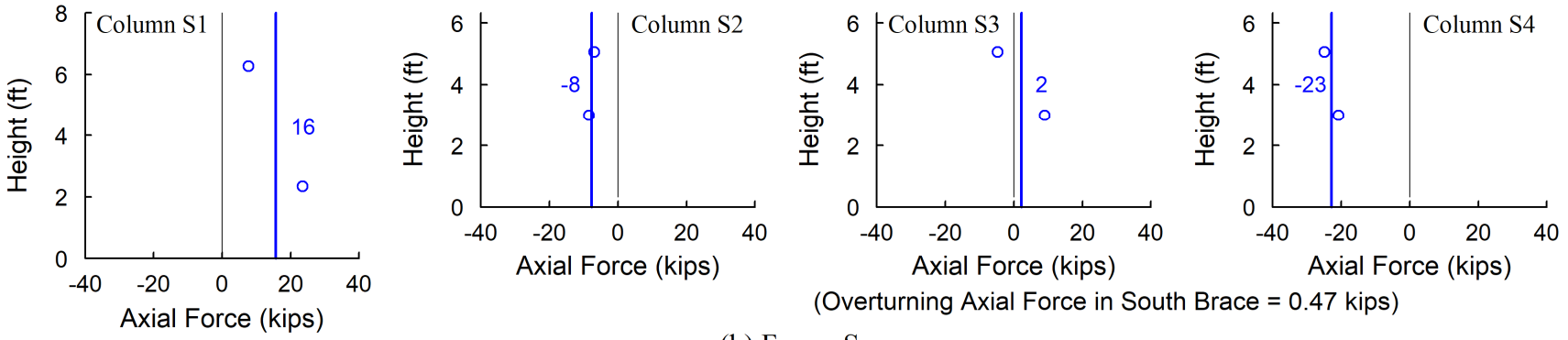

(b) Frame S

Figure 4.27 Test 1-3: Axial Force Diagrams in Columns at Peak Negative Acceleration

4.2.3 Collector Strain and Stress Profiles

Figure 4.28 and Figure 4.29 show the measured strain profiles along the 14-ft long Collectors 1 and 2, respectively. Figure 4.30 shows the measured strain profiles in the 5-ft long Collectors 3 and 4. In each of these figures, both the strain profiles measured at the positive and negative peak accelerations are plotted. It is apparent that, in general, the strain profiles in the collectors were not uniform and a notable strain gradient can be found on most of these measured strain profiles, indicating that the bending action in the collectors is considerable.

As shown in Figure 4.28 and Figure 4.29, for the measured sections near the mid-span (Loc 3) of Collectors 1 and 2, the strain profiles were generally linear over the depth of the composite sections, indicating that Bernoulli beam theory can be applied at these locations for the section force recovery. On the other hand, at most of the measured sections near the ends (Locs 1 and 5), the patten of the strain profiles is complicated, which cannot be simplified as a linear profile. This could be due to the geometric discontinuities at the collector connections. Besides, for the measured sections near the quarter spans (Locs 2 and 4), only the flanges of steel beam were instrumented and the strains in the concrete were not measured. However, considering these sections at quarter spans are far from the collector ends, a linear strain profile can be assumed for the section force recovery.

For the 5-ft long collectors (see Figure 4.30), although three sections (Locs 1 and 2 in Collector 3 and Loc 1 in Collector 4) were instrumented with strain gauges, only Loc 1 in Collector 3 was heavily instrumented. For the sections at Loc 2 in Collector 3 and Loc 1 in Collector 4, strain gauges were only placed on the steel beam flanges. Note that these two locations were near the collector ends, where the pattern of the strain profile are expected to be complicated due to the geometric discontinuities. Hence, the collector strain profiles cannot be recovered by using the

measured strains on steel beam flanges only. Thus, the section force recovery was not carried out for these locations in this research. However, the measured beam flange strains still can reveal some information on the collector response such as (1) the direction of the axial force (tension or compression), and (2) the direction of bending (positive or negative bending).

For comparison purposes, Figure 4.31 plots the measured strain profiles near the collector-to-column connections together. Near the AFW connection next to Column 1 (see the leftmost sub-figures in Figure 4.31), the strain profile was fairly linear along the depth of the composite section at negative peak floor acceleration, at which this collector section was subjected to a positive bending moment and a tensile axial force. This strain pattern indicates that full composite action was mobilized at the collector section near the AFW connection [see Figure 4.32(a) and Figure 4.33(a)] to transmit the combination of tensile axial force and positive bending moment. It should be noted that the concrete slab was in compression, which was mainly due to the bending action, whereas the total axial force on the entire composite section of the collector was tensile. In other words, the bending action caused the resultant axial force taken by the concrete slab to be opposite to the direction of total axial force acting on the entire composite section, suggesting that the concrete slab herein played a counteracting role in transmitting the axial force in the collector. On the other hand, the strain profile near the AFW connection was roughly linear over the depth of steel beam section with negligible tensile strains developed in the concrete slab when the specimen reached the positive peak acceleration, at which this collector section was subjected to a negative bending and a compressive axial force. This strain pattern implies that the negative bending action resulted in a gap between the concrete slab and steel column face such that no significant tensile strains could be developed in the concrete slab near the AFW connection. For

simplicity, it can be considered that the collector end section only used the W-shape steel beam section to transmit the member forces when it was under negative bending.

For discussion purposes, the terms “near side” and “far side” connections are defined for the double-sided TFW (or BW) connection. A double-sided connection has two collectors framing into the same column. The side which is closer to the LFRS is termed “near side”, while the other side is termed “far side”. Thus, for the testing building, as the LFRS (i.e., cantilever columns) was situated at the west end of the structure, the west or east sides of each double-sided TFW (or BW) connection was termed near- or far-side, respectively.

The 2nd and 3rd columns of sub-figures from the left in Figure 4.31 respectively show the strain profiles at the near- and far-side connections on Column Line 2. In addition, the 4th and 5th columns of sub-figures from the left in Figure 4.31 respectively show the strain profiles near the near- and far-side connections on Column Line 3. The common observations from the strain profiles of both types (TFW and BW) of double-sided collector connections are as follows:

1. When the collector sections were subjected to a positive bending, significant compressive strain could be developed in the concrete slab. By contrast, when a collector end resisted a negative bending moment, only very limited tensile strains could be developed in the concrete slab near the collector end. This would be due to a gap formed between the concrete slab and column face when at the collector end. This suggests that, for simplicity, the contribution of concrete slab in transmitting the member forces can be negligible when a collector end is subjected to a negative bending moment.
2. When the test building reached the positive peak acceleration, at which the specimen was subjected to a negative story drift and the composite collectors were supposed to transmit a compressive axial force, the near side of a TFW (or BW) connection was subjected to a positive

bending, while the far side was under negative bending. In this case, the near-side concrete slab was in compression, for which the resultant axial force taken by concrete was considerable and acted in the same direction of the total axial force in the composite collector section. In the meantime, the far-side concrete slab was in tension, for which the resultant axial force in the concrete slab was very low and opposite to the total collector axial force.

3. When the test building achieved the negative peak acceleration, at which the specimen was subjected to a positive story drift and the composite collectors were supposed to transmit a tensile axial force, the near side of a TFW (or BW) connection was subjected to a negative bending, while the far side was under positive bending. In this case, the near-side concrete slab was in tension, for which the resultant axial force in the concrete slab was very low and acted in the same direction of the total axial force in the composite section. In the meantime, the far-side concrete slab was in compression, for which the resultant axial force in the concrete slab was considerable but opposite to the total collector axial force.
4. Based on items 2 and 3, it can be concluded that the concrete slab on the near side of a double-sided collector-to-column connection played a counteracting role in transmitting the collector axial force. By contrast, the concrete slab on the far side played a supporting role in resisting the collector axial force demand.

For the measured strain profiles near the TFW connections (see the 2nd and 3rd columns of sub-figures from the left in Figure 4.31), the strains developed in the bottom steel flanges were very low because that the bottom flanges were not connected to the column. It appears that, when a collector end at a TFW connection was subjected to a positive bending [e.g., the near (west) or far (east) side at the positive or negative peak, respectively], the strain profile was roughly linear over a range from the elevation of bottommost bolt on the steel web to the top face of the concrete

slab. This suggests that, for simplicity, the collector beam end utilized an effective area [see Figure 4.32(b) and Figure 4.33(b)] composed of a T-shaped steel area and an effective concrete slab area to transmit the member forces. Note that the bottom elevation of the T-shaped steel considered was determined by using the bottom edge of the tributary area of the bottommost bolt at the TFW connection. Borrowing the concept of "bolt element" proposed by Liu and Astaneh-Asl (2004), which is used to analyze the moment-rotation relationship for composite shear tab connections, the tributary region of a bolt extends halfway to its adjacent bolts so that the bolt spacing is taken as the depth of the tributary area for each bolt. On the other hand, when a collector beam end at a TFW connection was subjected to a negative bending [e.g., the far (east) or near (west) side at the positive or negative peak, respectively], the strain profile was roughly linear over a range from the elevation of bottommost bolt on the steel web to the steel top flange. This indicates that the collector beam end only relied on the T-shaped steel area to resist member forces.

By comparing the 2nd and 3rd columns of sub-figures from the left in Figure 4.31, it can be found that differences of strain profile pattern between the near-side and far-side collector sections at a double-sided TFW connection. The neutral axis at the near (west) side collector section was located at approximated 3/4 height of the steel beam depth and significant strains developed in the steel top flange, while the neutral axis at the far (east) side collector section was at about the steel top flange. Note that the steel top flange is supposed to be the main role to resist the collector axial force. However, test results indicated that, at a far-side TFW connection, the steel top flange was the place developed the lowest strains in the collector section, while the strains developed around the bottom bolt were significant. This uneven strain distribution would raise concerns that the bolt connections, which play a main role in resisting member forces, would be damaged earlier than the top flange as the flexural and axial force demands acting in the collector increase. Note that

the magnitude of strains developed near the TFW connections in Test 1-3 was below 0.0005 (see Figure 4.31), which is only about 25% of the yield strain. Although the strain profiles measured at this low level of strains could not represent the ultimate states of the collector sections, it is worthwhile to investigate the responses of far-side TFW connection at high strain level.

For the strain profiles near the BW connections (see the 4th and 5th rows of sub-figures from the left in Figure 4.31), the strains developed in both top and bottom flanges were very low as a result of the fact that both steel flanges were not connected to the column. When a collector beam end at a BW connection was subjected to a positive bending [e.g., the near (west) or far (east) side at the positive or negative peak, respectively], by discarding the measured strains on both flanges, there seems to be a roughly linear profile among the remaining five measured strains (including two measured strains in concrete slab and three measured strains on steel web). This suggests that, for simplicity, the collector beam end utilized an effective area [see Figure 4.32(c) and Figure 4.33(c)] composed of part of the steel web and an effective concrete slab area to transmit the member forces. Note that part of steel web considered herein is aligned with the total depth of tributary region of the bolt group on the steel web. On the other hand, when a collector beam end at a BW connection was subjected to negative bending [e.g., the far (east) or near (west) side at the positive or negative peak, respectively], only on the steel beam web were significant strains developed, while both flanges and concrete were about stress free. The strain profile among the three measured strains on the beam web was roughly linear. This indicates that the effective area of the collector section in resisting the member forces can be simplified as part of the steel web aligned with the tributary region of the bolt group on the web of BW connection.

Based on the strains measured at a small number of elevations along the collector depth, Figure 4.34 through Figure 4.36 show the assumed strain profiles, which were employed for

member force recovery, along the entire depth of collector sections. See Section 3.7.6 for the approaches to determine these assumed strain profiles. With these assumed strain profiles, the axial forces and bending moments at the measured sections in the collectors were computed by using the fiber section method described in Section 3.7.6 and illustrated in Figure 3.65 and Figure 3.66. Figure 4.37 though Figure 4.39 demonstrate the strain profiles assigned to the fiber sections, while Figure 4.40 through Figure 4.42 plot the stress profiles assigned to the fiber sections. Figure 4.43 through Figure 4.45 show the distributions of axial forces of fiber sections.

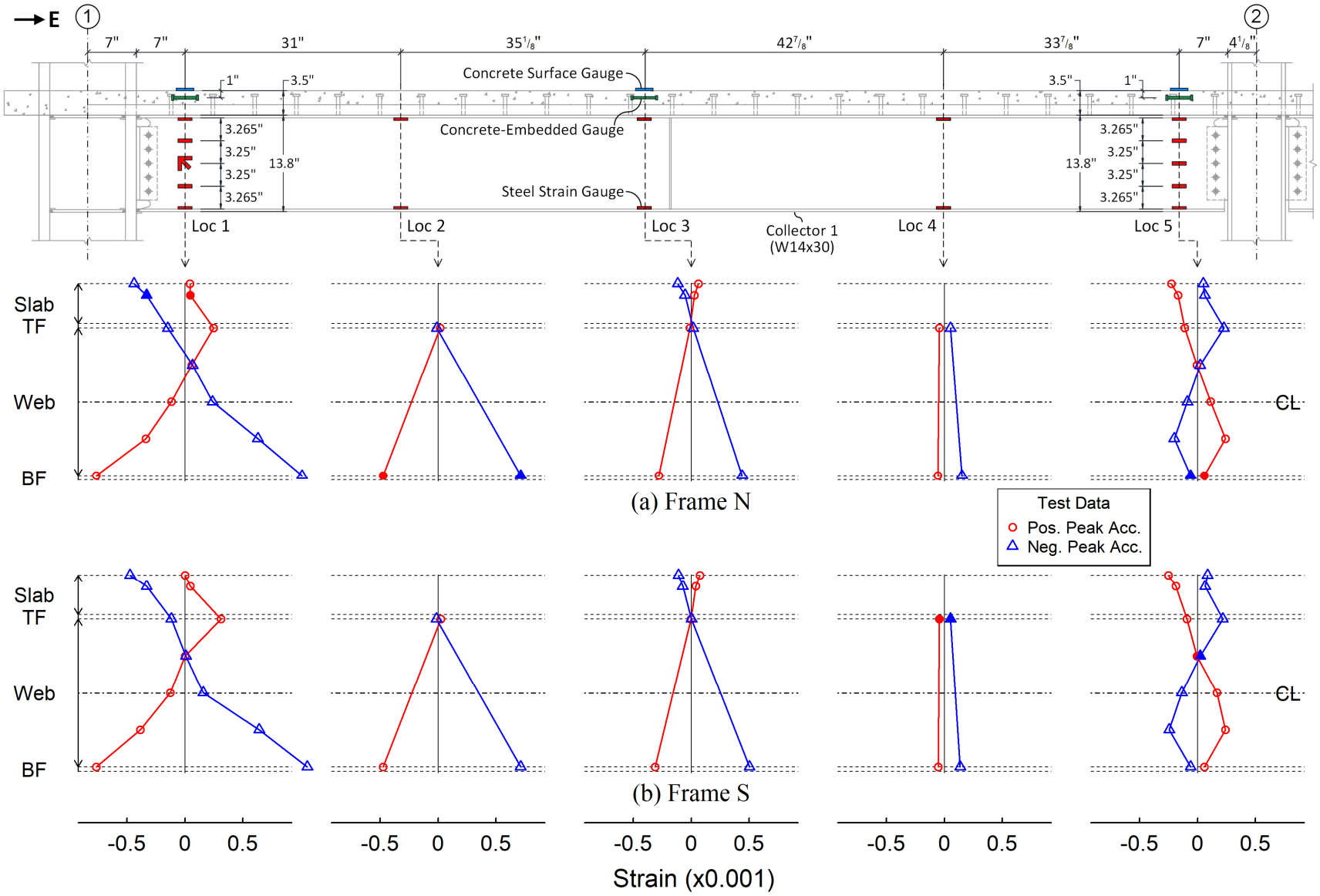

Figure 4.28 Test 1-3: Strain Profiles of Collector 1 (2nd Floor)

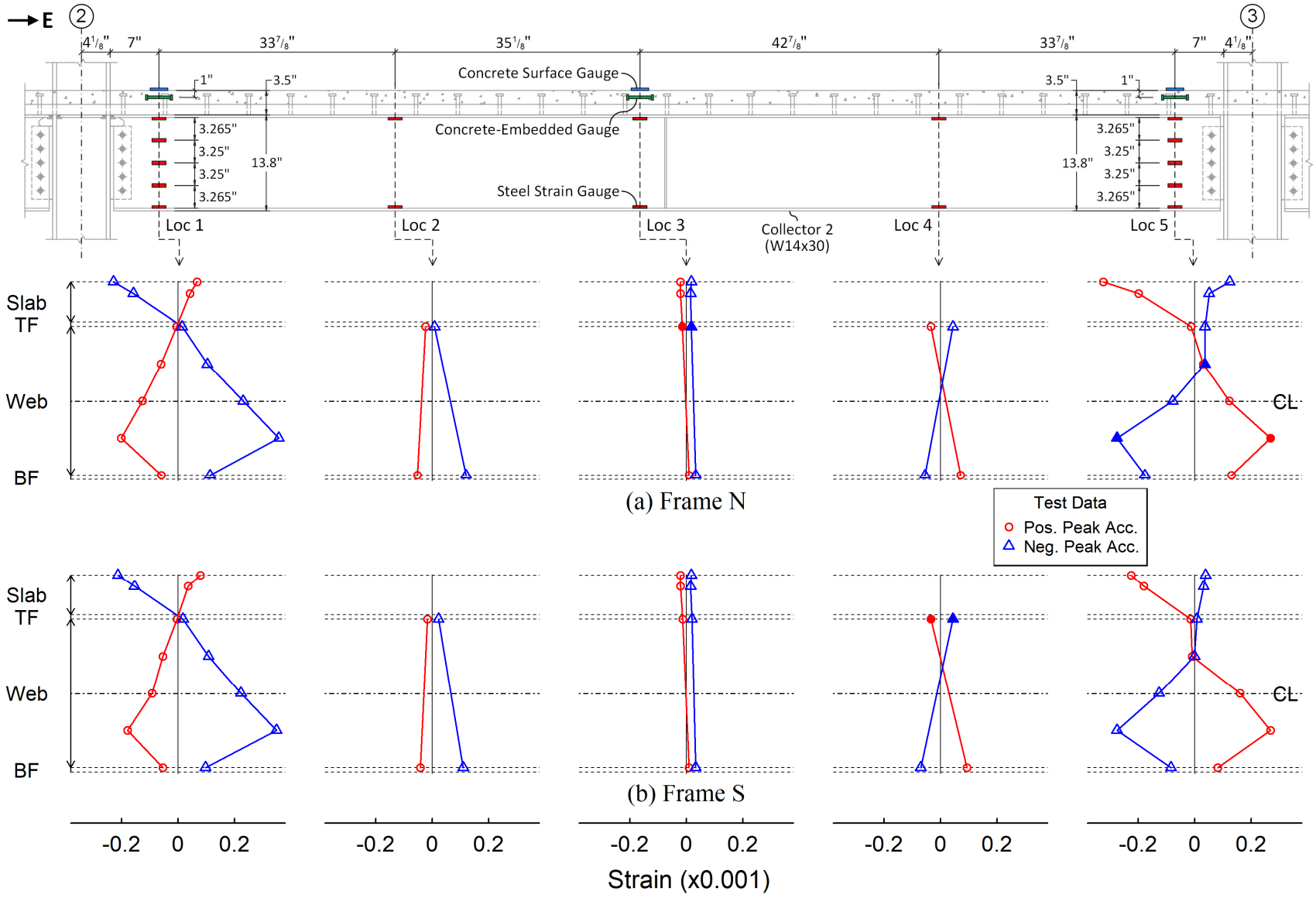

Figure 4.29 Test 1-3: Strain Profiles of Collector 2 (2nd Floor)

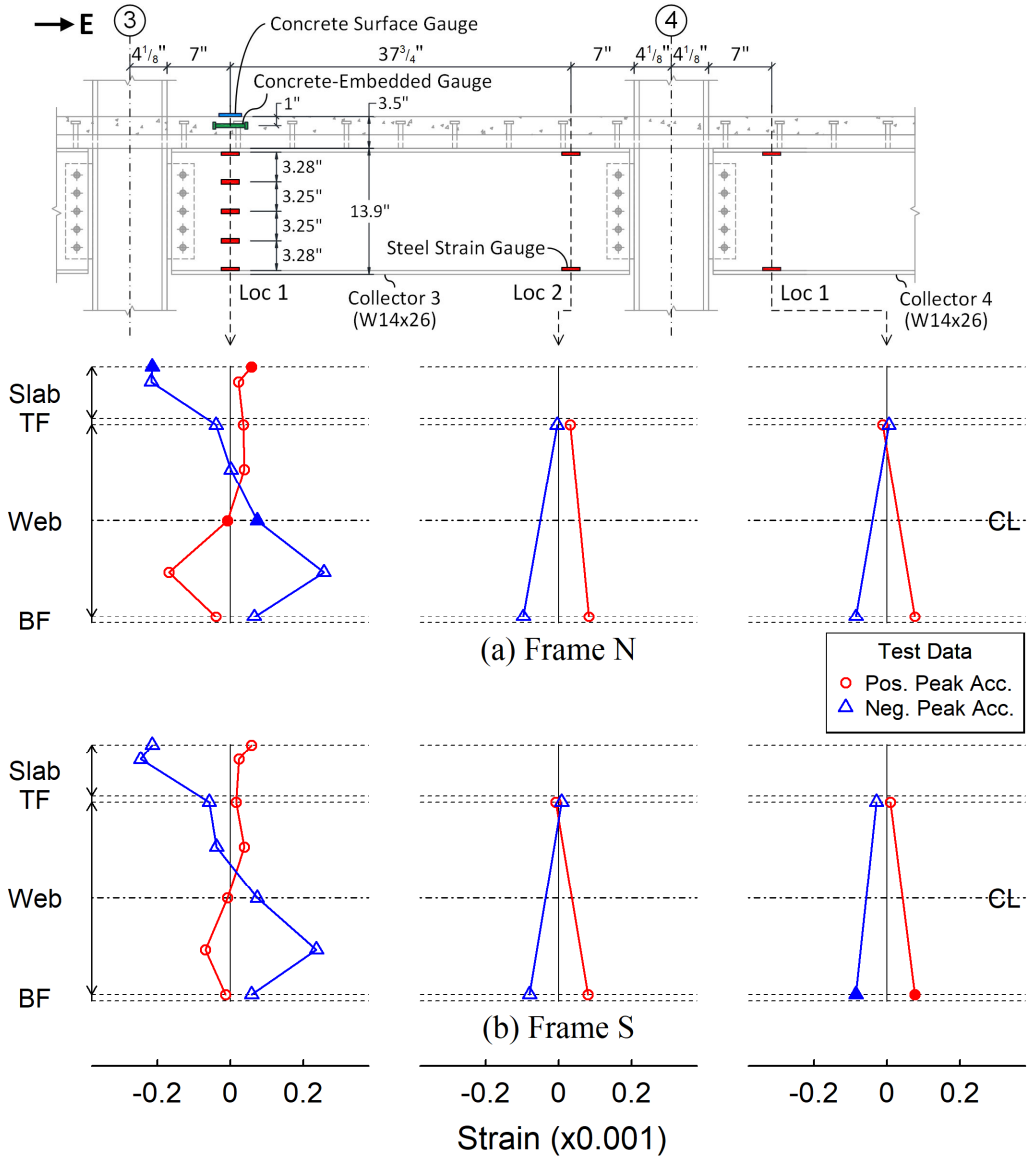

Figure 4.30 Test 1-3: Strain Profiles of Collectors 3 and 4 (2nd Floor)

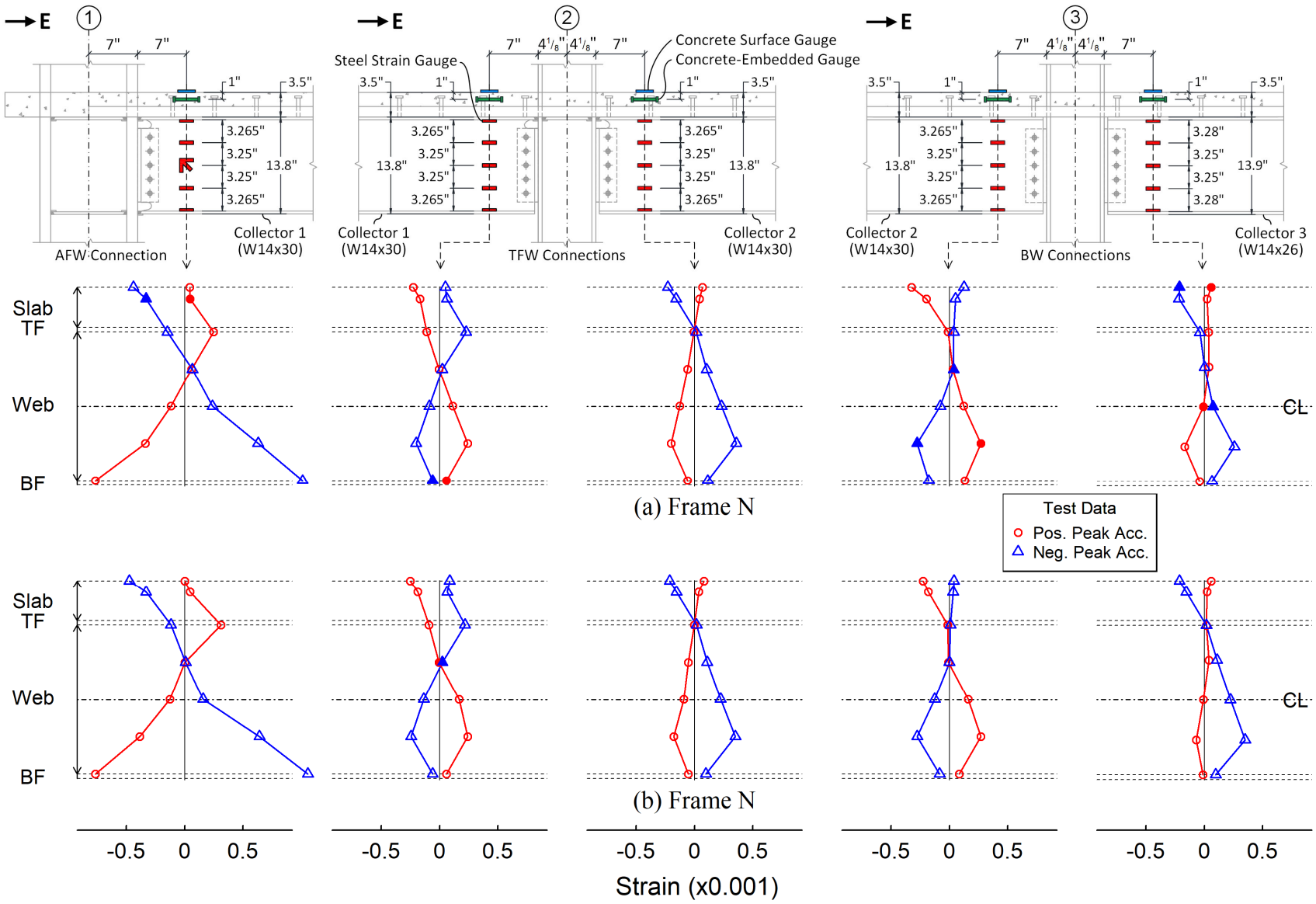

Figure 4.31 Test 1-3: Strain Profiles near Collector-to-Column Connections (2nd Floor)

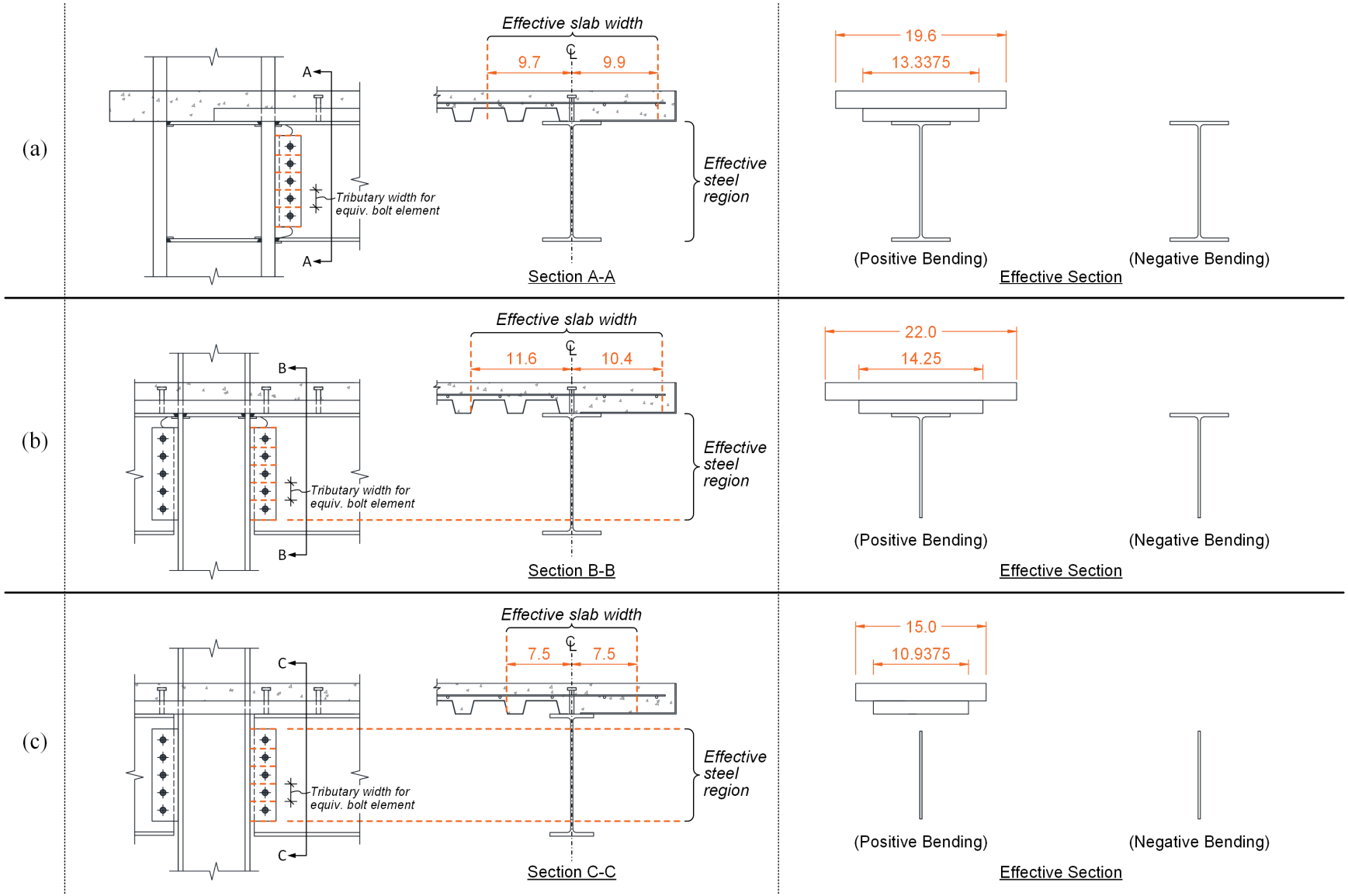

Figure 4.32 Effective Collector Sections near (a) AFW; (b) TFW; and (c) BW Connections (Frame N)

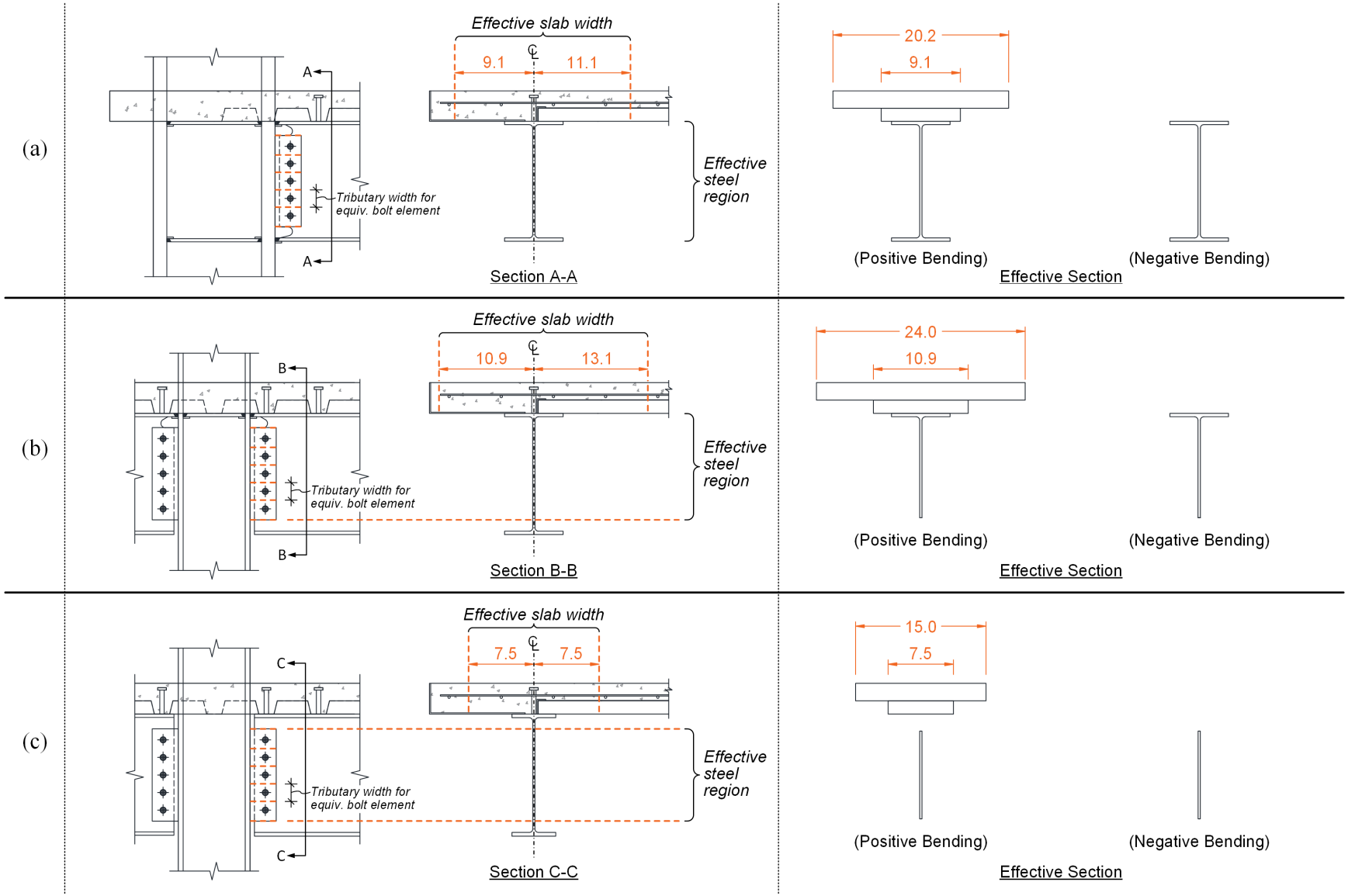

Figure 4.33 Effective Collector Sections near (a) AFW; (b) TFW; and (c) BW Connections (Frame S)

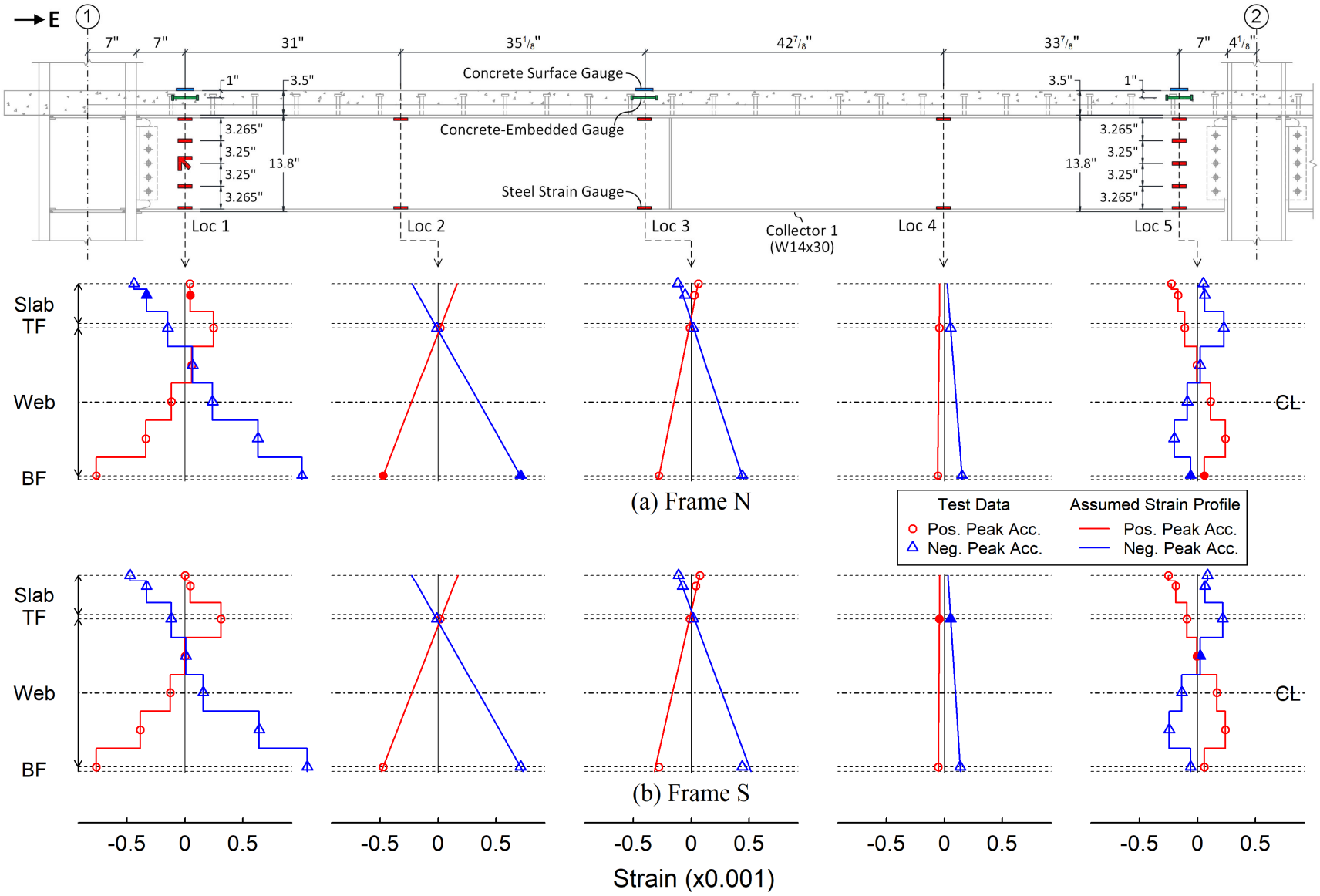

Figure 4.34 Test 1-3: Assumed Strain Profiles for Force Recovery of Collector 1 (2nd Floor)

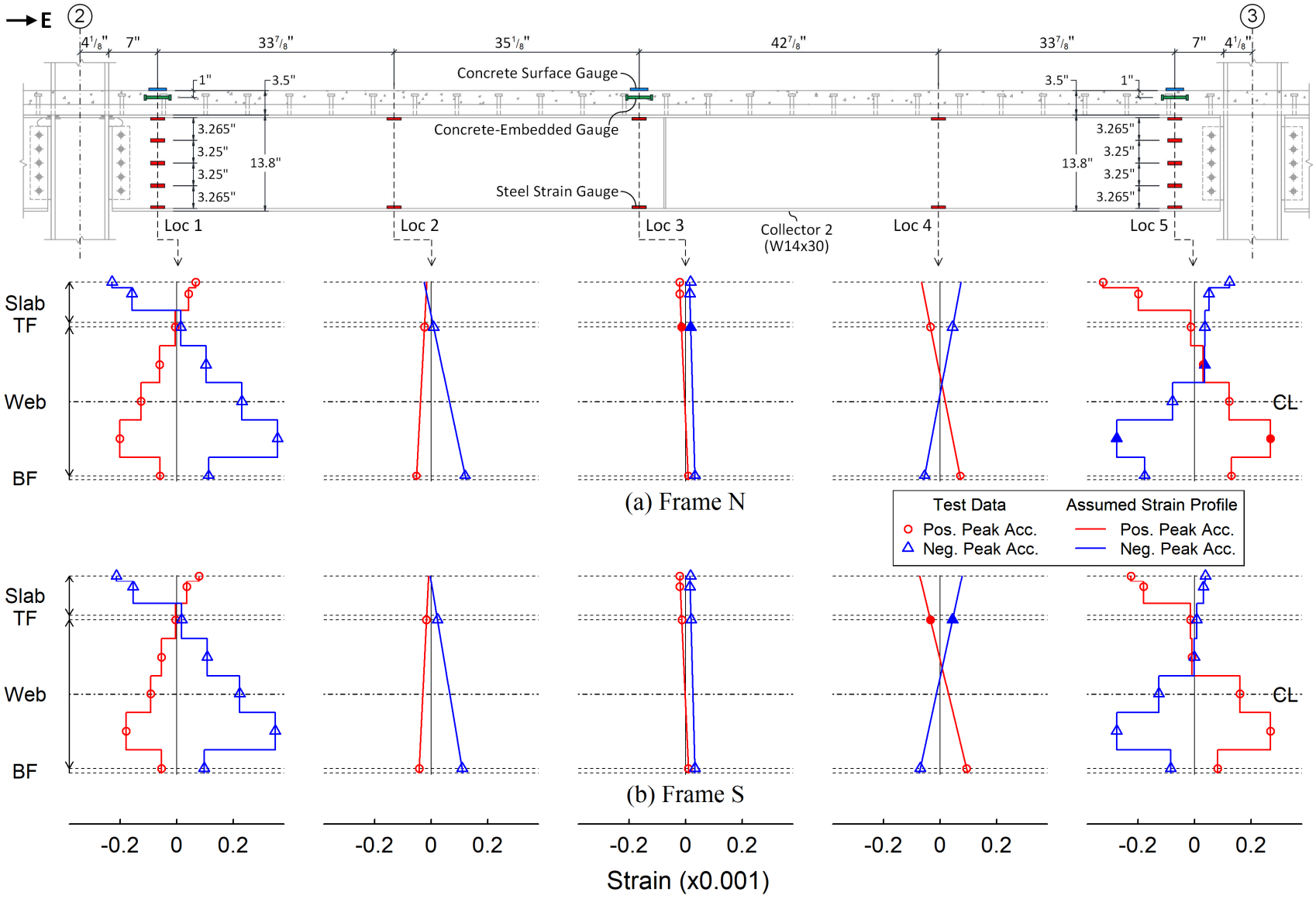

Figure 4.35 Test 1-3: Assumed Strain Profiles for Force Recovery of Collector 2 (2nd Floor)

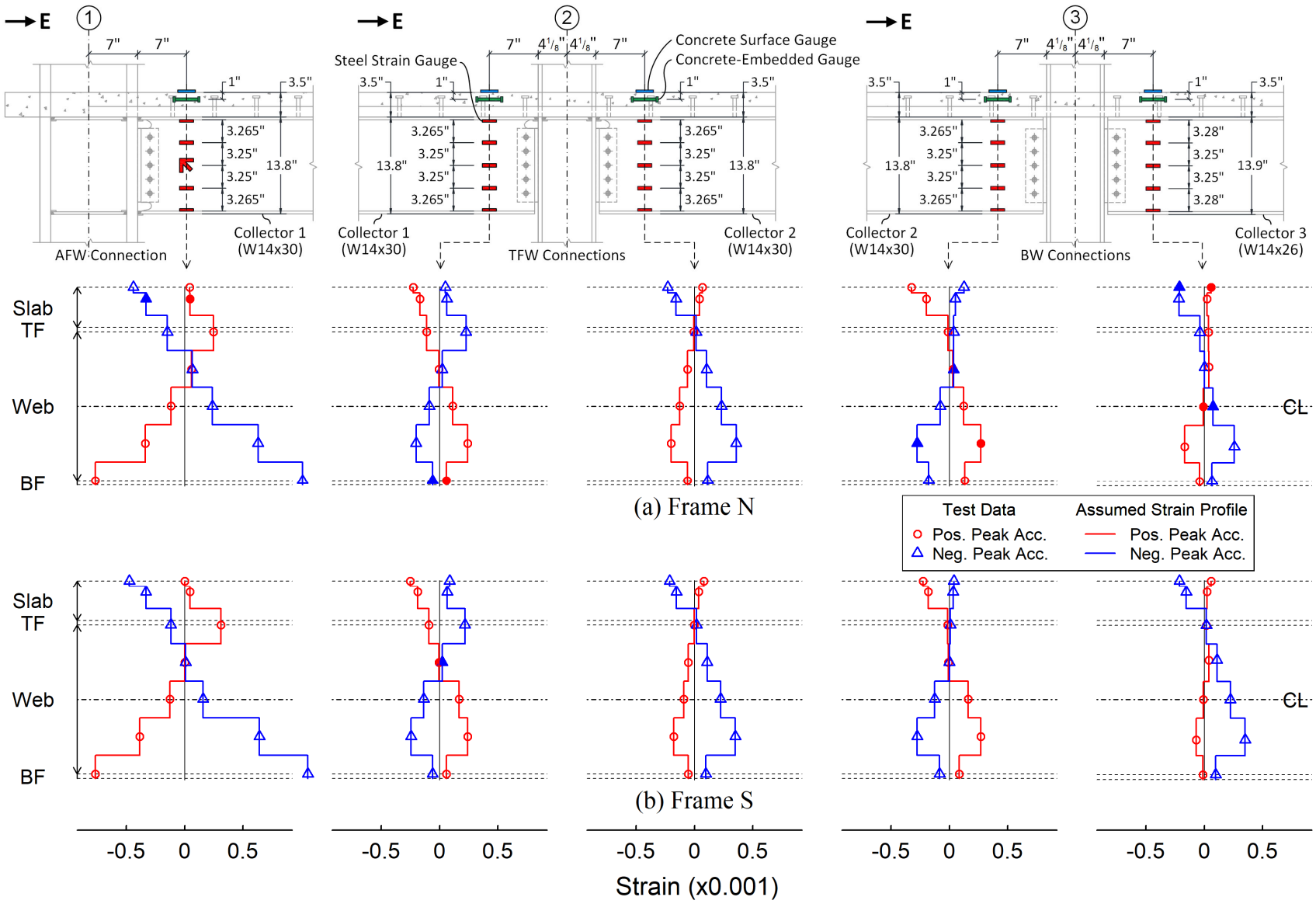

Figure 4.36 Test 1-3: Assumed Strain Profiles for Force Recovery near Collector-to-Column Connections (2nd Floor)

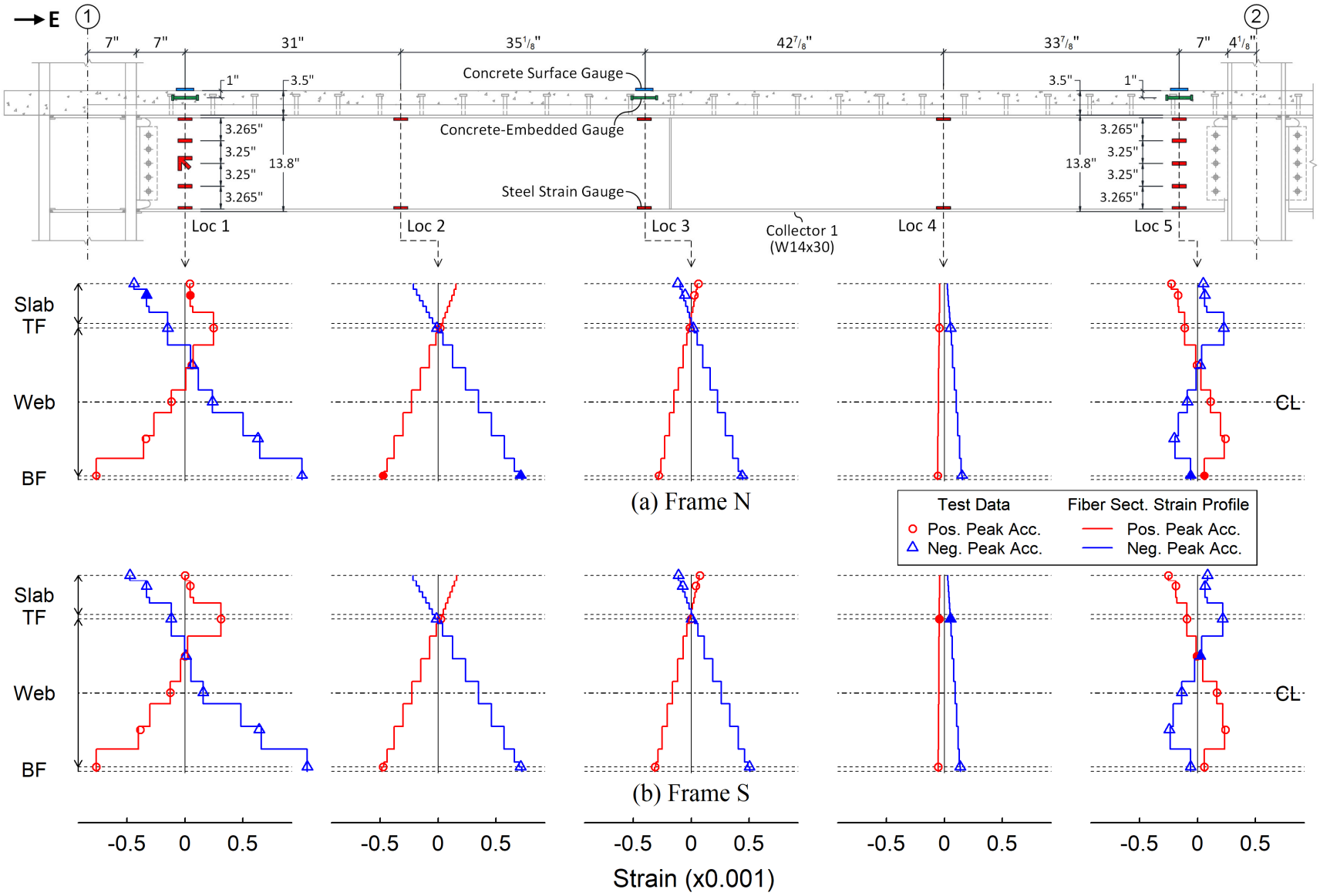

Figure 4.37 Test 1-3: Fiber Section Strain Profiles of Collector 1 (2nd Floor)

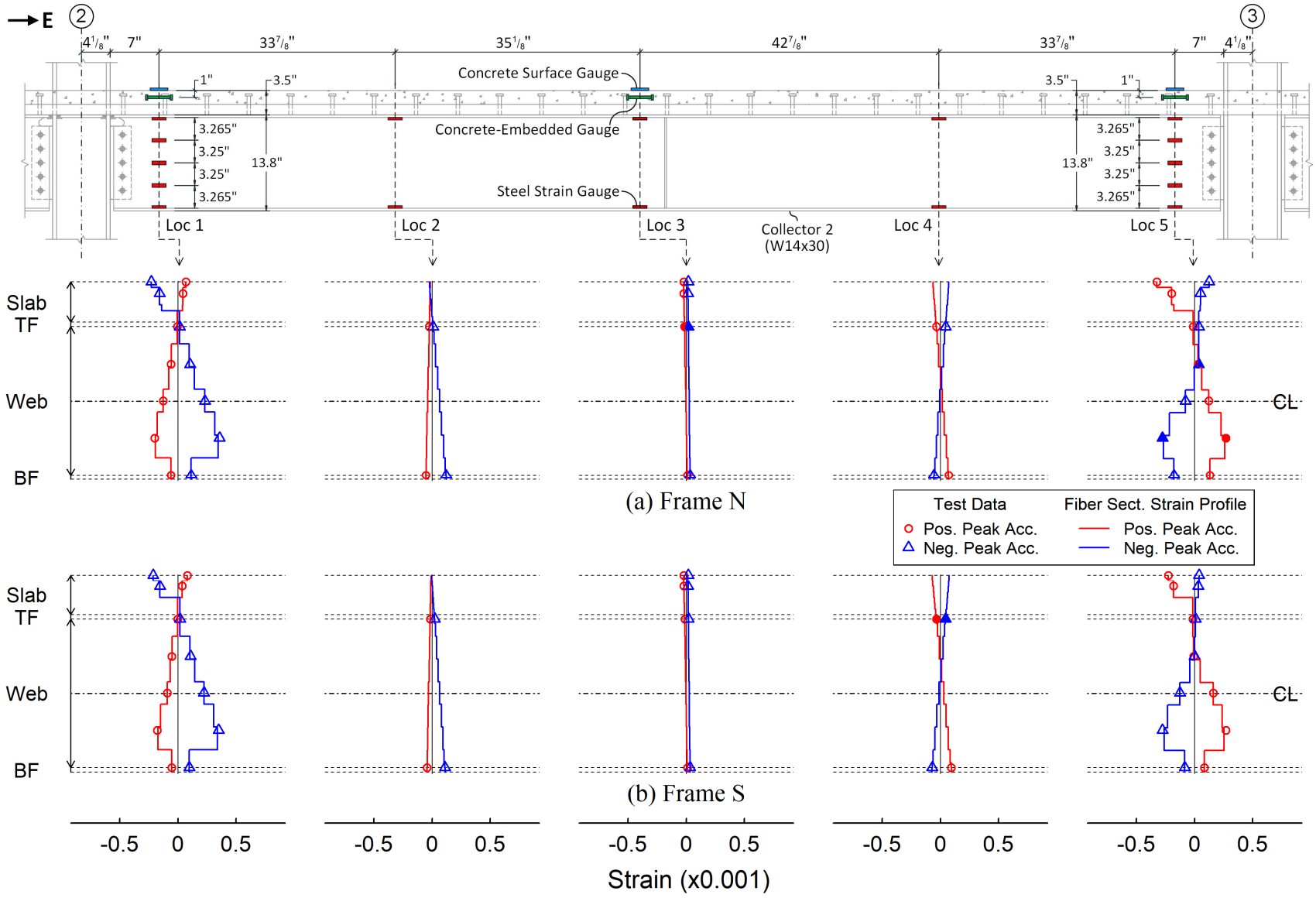

Figure 4.38 Test 1-3: Fiber Section Strain Profiles of Collector 2 (2nd Floor)

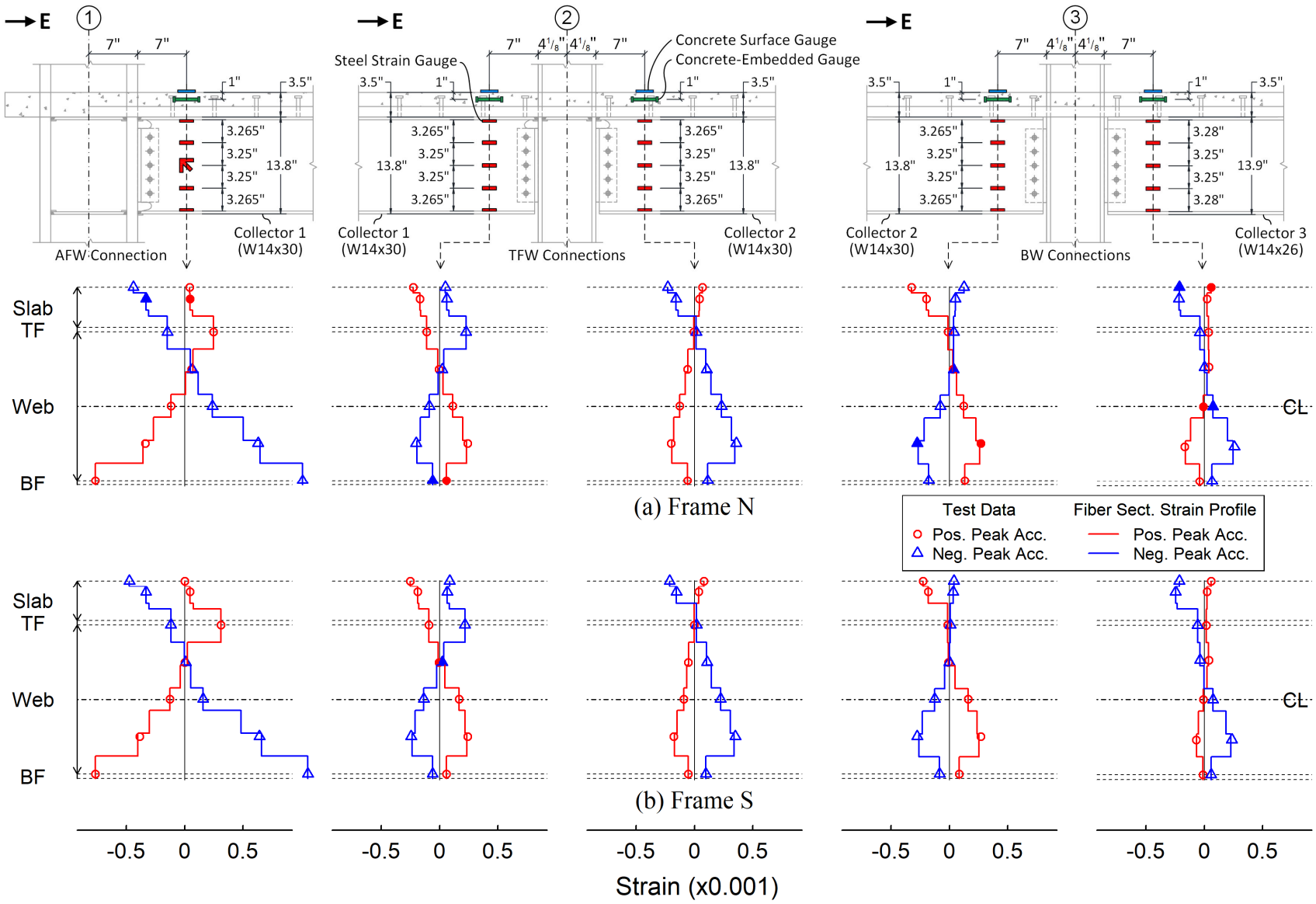

Figure 4.39 Test 1-3: Fiber Section Strain Profiles near Collector-to-Column Connections (2nd Floor)

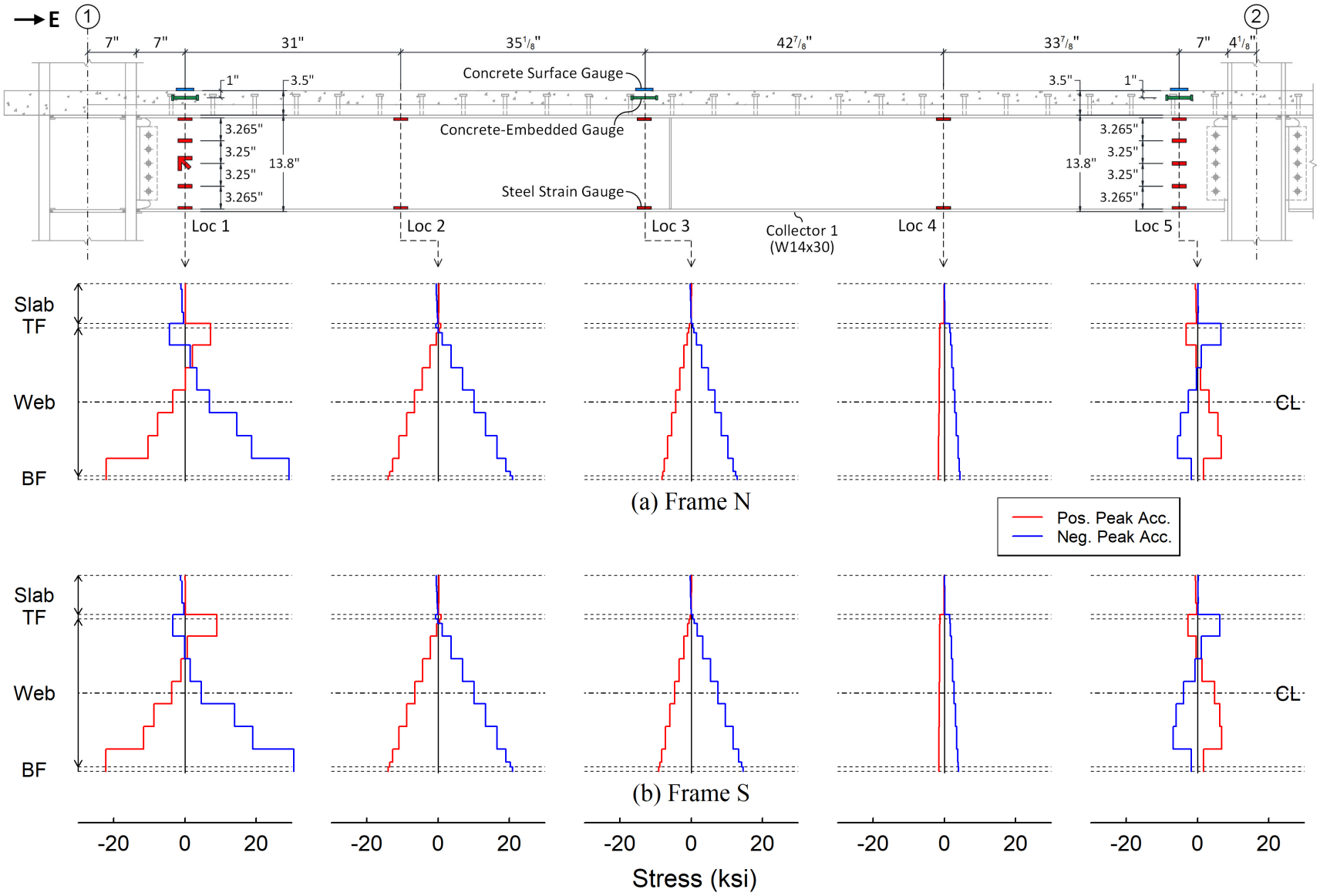

Figure 4.40 Test 1-3: Fiber Section Stress Profiles of Collector 1 (2nd Floor)

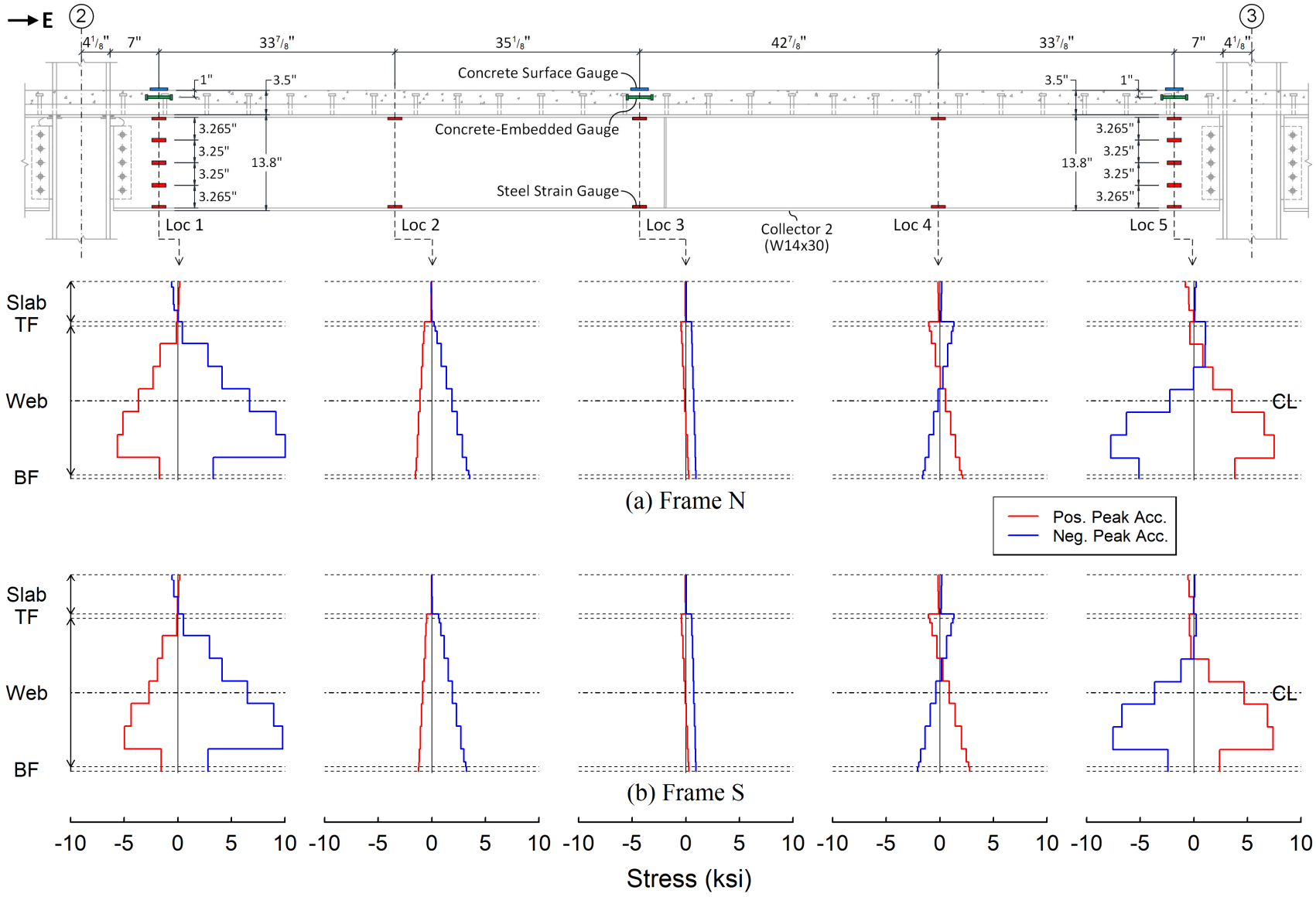

Figure 4.41 Test 1-3: Fiber Section Stress Profiles of Collector 2 (2nd Floor)

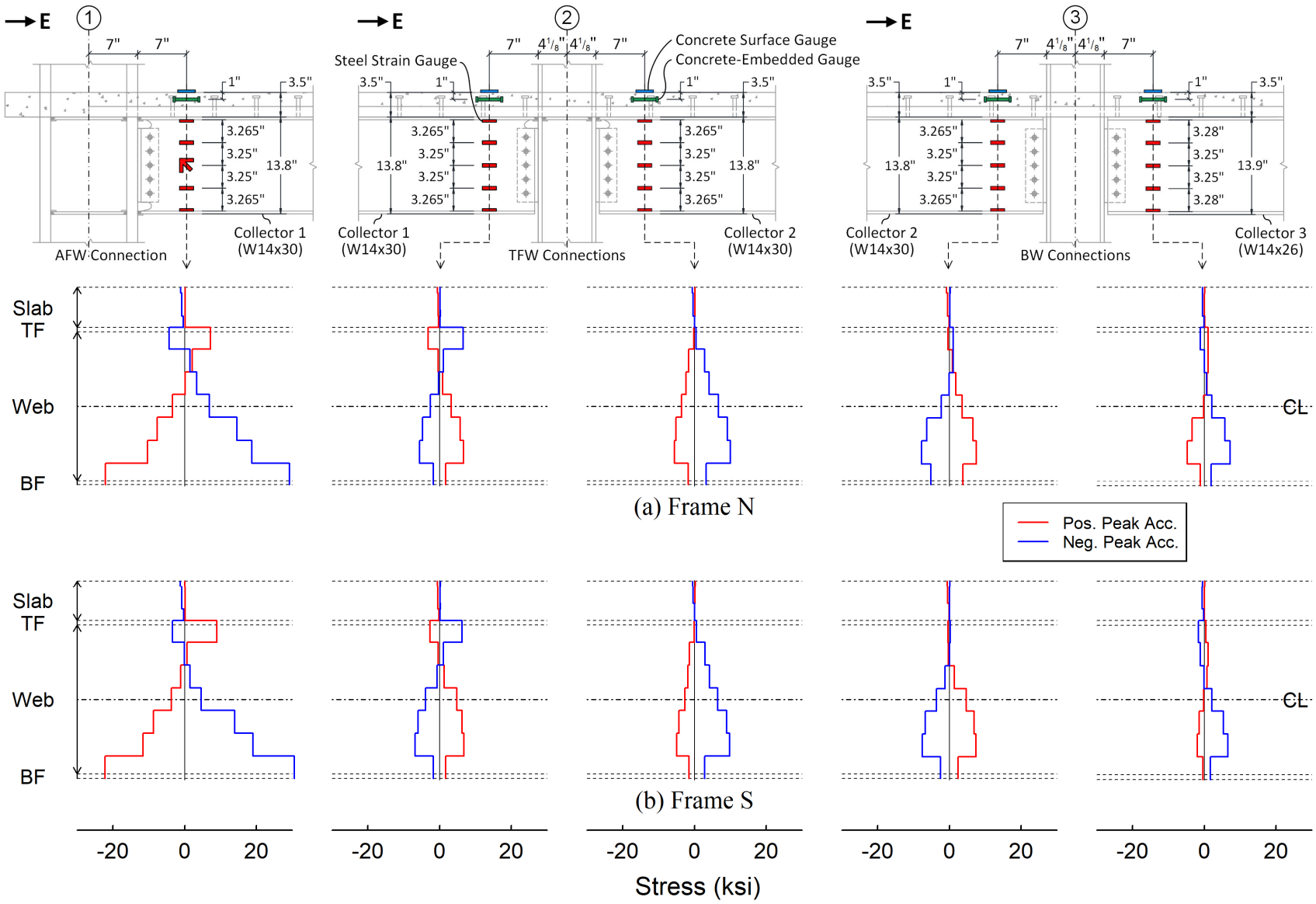

Figure 4.42 Test 1-3: Fiber Section Stress Profiles near Collector-to-Column Connections (2nd Floor)

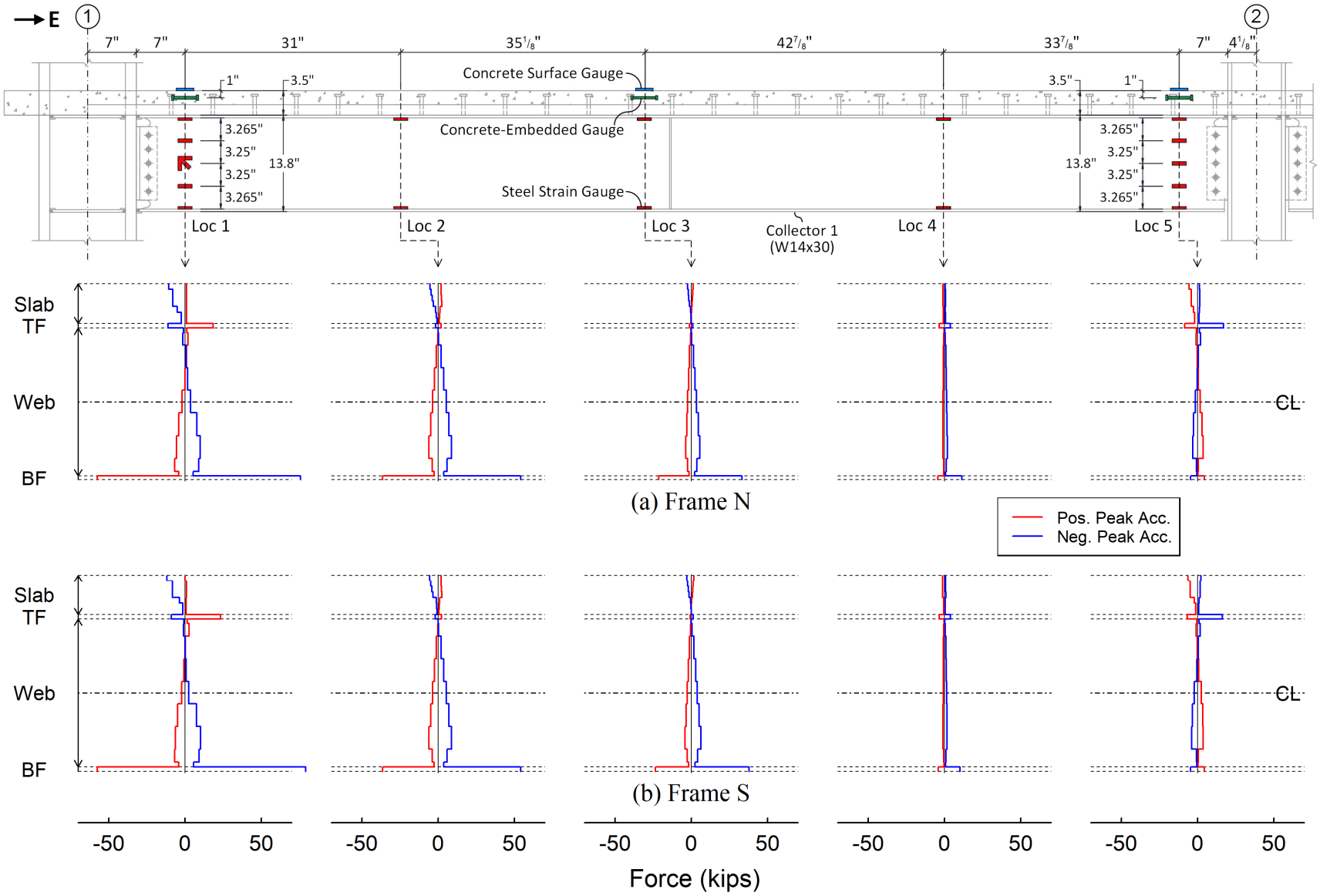

Figure 4.43 Test 1-3: Distribution of Axial Forces in Fibers of Collector 1 (2nd Floor)

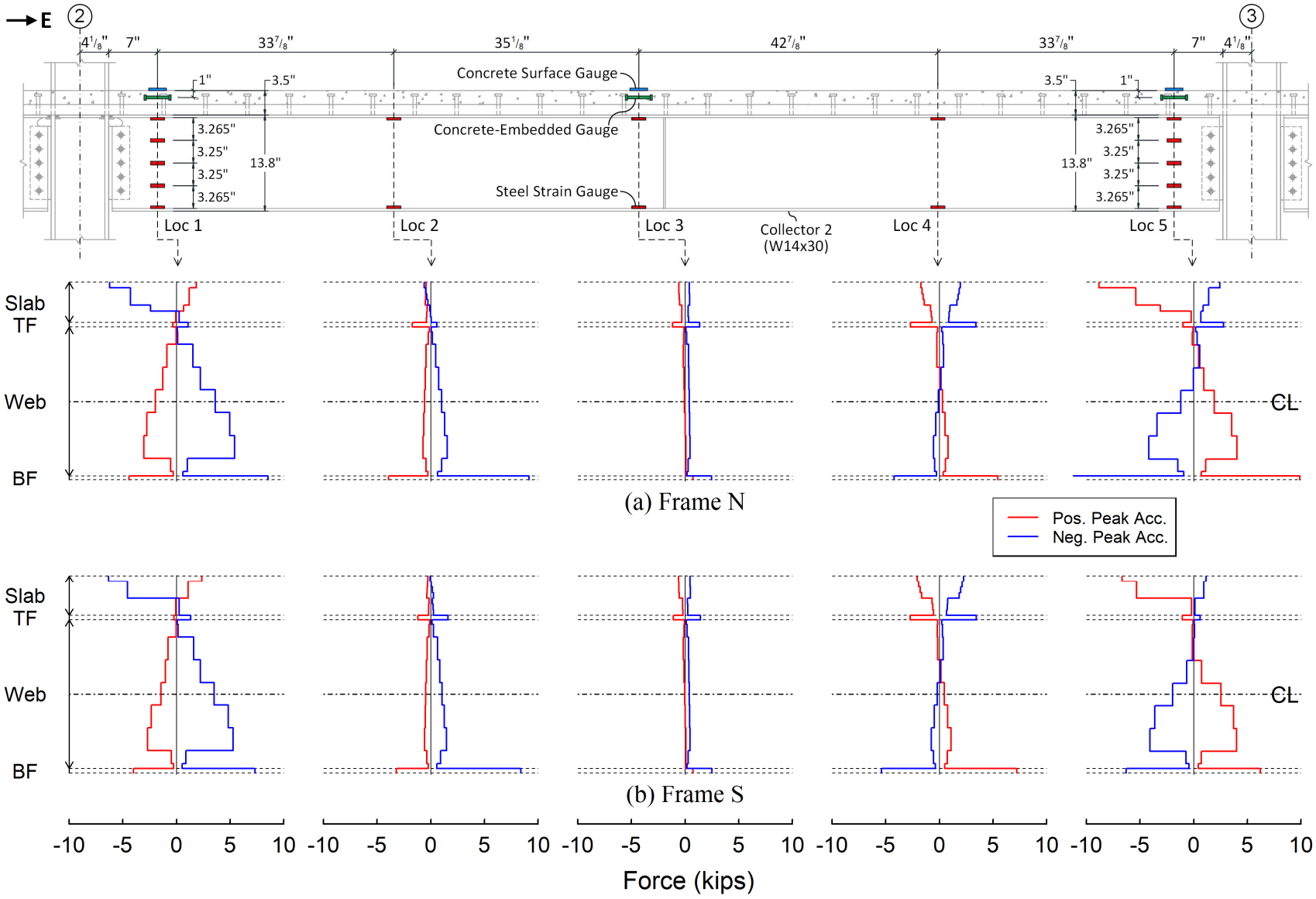

Figure 4.44 Test 1-3: Distribution of Axial Forces in Fibers of Collector 2 (2nd Floor)

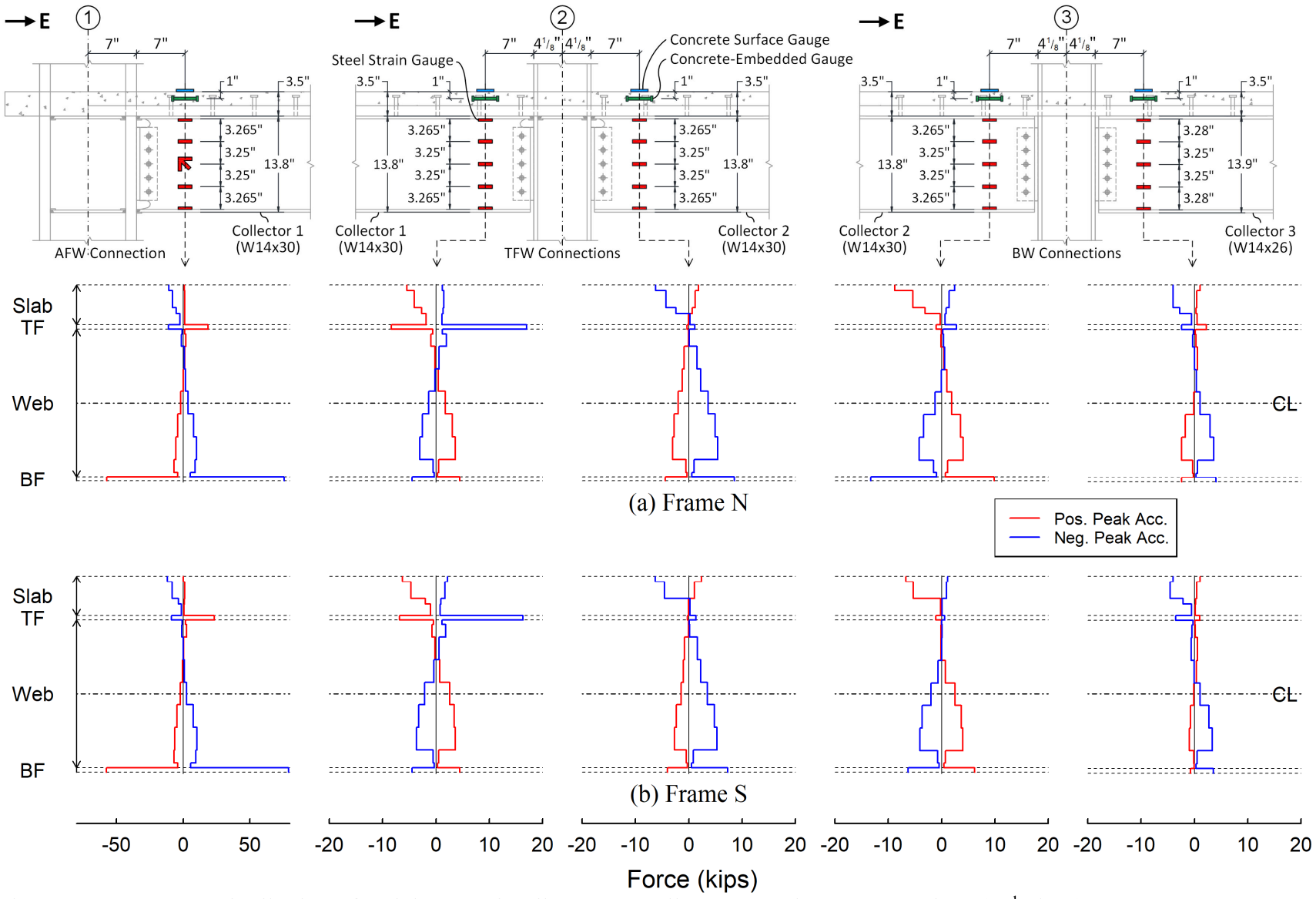

Figure 4.45 Test 1-3: Distribution of Axial Forces in Fibers near Collector-to-Column Connections (2nd Floor)

4.2.4 Collector Member Forces

After the internal axial forces and bending moments in the collector sections instrumented with strain gauges were computed by using the measured strains and fiber section approach, axial force and bending moment diagram along Collectors 1 and 2 can be constructed. Figure 4.46 and Figure 4.47 respectively show the measured axial force and moment diagrams along the collectors at the positive peak acceleration, while Figure 4.48 and Figure 4.49 demonstrate the measured axial force and moment diagrams along the collectors at the negative peak acceleration. Note that the axial force diagrams were plotted by connecting the measured axial force data points along the collectors. On the other hand, the bending moment diagrams in Collectors 1 and 2 were constructed by using the linear regression line among five measured moments along each collector.

In general, the 14-ft long Collectors 1 and 2 were subjected to a compressive axial force at the positive peak acceleration (Figure 4.46), at which the story drift was negative, while the collectors were in tension at the negative peak acceleration (Figure 4.48), at which the story drift was positive. These general directions of the measured collector axial forces agreed with the expected force directions derived from the first-mode deformed shapes of the longitudinal test frame. As shown in Figure 4.46 and Figure 4.48, it is apparent that the magnitude of axial forces increased along the collector lines from the east side, which was on the far side of the LFRS, to the west end, where the LFRS were located, of each collector line. In addition, it is noticeable that the slope of axial force diagram in the Collector 1 beams were obviously higher than that in the Collector 2 beams. This suggests that, along each collector line, there were much more inertial forces dragged into Collector 1 than those collected by Collector 2.

It should be noted that the measured axial forces along Collectors 1 and 2 were not always increasing from the far end to the LFRS as expected. Instead, the collector axial force diagrams

exhibited a slightly “zig-zag” pattern. For example, as shown Figure 4.48, near the west ends of both Collectors 1 and 2, the axial forces measured at the first instrumented section from the west end were slightly lower than the those at the second instrumented section. This could be due to the oversimplification of the assumed effective slab width considered in the collector member force recovery. It is recalled that the collector member forces were calculated based on the assumption that the effective slab width along the entire span of Collectors 1 or 2 was constant and equal to the effective width determined from the test data measured at the west end of the collector. This assumption was made because only at the west end of Collectors 1 or 2 was the concrete slab instrumented multiple strain gauges across a width of the slab such that the effective width could be evaluated. However, several previous studies (Zhu et al. 2015; and Huang et al. 2016) showed that the effective slab width in a composite beam subjected to vertically flexural load would vary along the beam span. Therefore, the effect slab width in a composite collector should not be constant along the entire span and there may be some error in the assumed effective slab for the regions of the collector other than the west end, resulting in some error in the calculated member forces.

Furthermore, some of the measured collector axial forces at the east end of Collector 2 and west end of Collector 3 were opposite to the direction of the axial forces developed in the most part of Collectors 1 and 2 beams. In addition, the measured strain profiles in Collectors 3 and 4 shown in Figure 4.30 indicate that these 5-ft long collectors were in tension and compression at the positive and negative peak accelerations, respectively. These test results showed that the axial forces in Collectors 3 and 4 were very low but acted in an opposite direction to those in Collectors 1 and 2. One possible reason for the opposite direction of axial forces seen in Collectors 3 and 4 was the vertical movement of the cantilever slab at the east end of the test specimen.

Figure 4.47 and Figure 4.49 show that there appears to be a linear moment diagram in double curvature among the measured moments along each span of Collectors 1 or 2. The moment diagrams along Collector 1 beams indicate that the inflection point was located at approximately 2/3 and 3/4 of beam span away from the west end of the collector at the positive (Figure 4.47) and negative (Figure 4.49) peak accelerations, respectively. Consistent with the fact that the inflection point on Collector 1 was always in the east-half span, the magnitude of the bending moment developed at the west end, which used the AFW connection detail, was obviously greater than that developed in the east end, where a TFW connection was employed. This indicates that the rotational rigidity of the AFW connections was significantly larger than that of TFW connections. For the moment diagrams along Collector 2 beams, the inflection point was located at about 30% and 50% of beam span away from the west end of the collector at the positive (Figure 4.47) and negative (Figure 4.49) peak accelerations, respectively. An inflection point located within the east-half span or at about the mid-span of Collector 2 indicates that the rotational rigidity of the TFW connection at the west end was not obviously larger than that of the BW connection at the east end of the collector. When both TFW and BW connections in the same collector use identical bolted connections in the web, it might be expected that the TFW connection is stiffer than the BW connection because the TFW connection can utilize top steel flange to transmit forces. However, test results showed that, when the BW connection of Collector 2 was subjected to a positive bending while the TFW connection was under a negative bending (see Figure 4.47), the magnitude of bending moment developed in the BW connection was greater than that in the TFW connection, suggesting that the rotational rigidity of the BW connection was higher than that of the TFW connection. This could be attributed to the contribution of the concrete slab in transmitting bending

moment at the BW connection subjected to a positive bending. By contrast, the concrete slab at the TFW connection under a negative bending was in tension and transmitted negligible forces.

Figure 4.50 through Figure 4.53 compare the member forces (axial force or bending moment) taken by the entire composite section and bare steel section. At the positive peak acceleration (see Figure 4.50 and Figure 4.51), the specimen deformed shape with a negative story drift suggests the collectors would generally transmit a compressive axial force. In the meantime, near the west end of each Collectors 1 and 2, the collector was under negative bending and the bare steel section resisted a compressive force slightly greater than the total compression force taken by the entire composite section, indicating that the concrete slab played a role slightly counteracting the axial force transmission. By contrast, near the east end of each Collectors 1 or 2, the collector was under positive bending and the entire composite section carried more compression force than the steel part did, suggesting that the action of concrete slab was contributing to the axial force transmission.

On the other hand, at the positive peak acceleration (see Figure 4.52 and Figure 4.53), the deformed shape of the test frame with a positive story drift implies that the collector lines would generally transmit a tensile axial force. Meanwhile, near the west end of each Collectors 1 and 2, the collector was under a positive bending and the bare steel section resisted a tensile axial force noticeably higher than the total tension force taken by the entire composite section, indicating the action of concrete slab herein significantly counteracted the axial force transmission. By contrast, near the east end of each Collectors 1 and 2, the collector was under negative bending and the entire composite section carried slightly more tension force (or less compression force) than the steel part did, suggesting the action of concrete slab herein was slightly contributing to the tension force transmission.

It can be found that the discrepancy between the collector axial forces taking by the bare steel section and entire composite section is more pronounced at the collector ends than that within the bean span. For a composite collector section (especially at the beam end), the combinations of axial forces and bending moments in different directions would cause the concrete slab to play different roles (contributing or counteracting) in transmitting the collector axial force. To summarize the contribution of concrete slab to the collector axial force transmission in a generalized way, the following conditions of four axial force-bending moment (P-M) interaction are considered:

(1) For a collector end subjected to simultaneous tensile axial load and positive bending, the bending action would create considerable compressive stresses in the concrete slab such that the concrete slab would be counteracting the collector axial force transmission.

(2) For a collector end subjected to simultaneous tensile axial load and negative bending, the bending action would result in a very low level of tensile stresses in the concrete slab due to a gap developing between the concrete slab and column face. In this case, the concrete slab would be slightly or negligibly contributing to the collector axial force transmission.

(3) For a collector end subjected to simultaneous compressive axial load and positive bending, the bending action would cause considerable compressive stresses to be developed in the concrete slab such that the concrete slab would be contributing to the collector axial force transmission.

(4) For a collector end subjected to simultaneous compressive axial load and negative bending, the bending action would result in a very low level of tensile stresses developed in the concrete slab so that the concrete slab would be slightly or negligibly counteracting to the collector axial force transmission.

For discussion purposes, between the two ends of a collector, the one more near to the LFRS is termed “near end” of the collector, while the other one is designated “far end”. For the test specimen, at the near ends of Collectors 1 and 2 were the AFW connection and the far-side TFW connection, respectively. At the far end of Collectors 1 and 2 were the near-side TFW connection and near-side BW connections, respectively. Generalized to typical buildings, “within” (i.e., discarding both ends of) a collector line composed of multiple collectors, the far end of a collector is on the near side of a double-sided collector-to-column connection, while at the near end of a collector is a far-side collector connection.

As the test building behaved elastically during Test 1-3, the floor acceleration and the story drift were completely out of phase. As a result of elasticity of the specimen, the near ends of the collectors were only subjected to the P-M interaction conditions (1) and (4), while the far ends of collectors only underwent the P-M interaction conditions (2) and (3). Therefore, during Test 1-3, the concrete slabs at the near ends of collectors were always playing a supporting role to resist the collector axial force demand, while the concrete slab at the far ends of collectors were always counteracting the collector axial force demand.

Note that the current practice for the collector-to-column connection design neglects the concrete slab effects and assumes that the connections at the bare steel section carries the total axial force demand acting on the composite section. This assumption would be acceptable when a collector end is subject to the P-M interaction conditions (2), (3) and (4), for all of which the concrete slab is either contributing or negligibly counteracting to the axial force resistance. However, neglecting concrete slab effect would result in a unconservative design for a collector end connection subjected to the P-M interaction condition (4) (i.e., simultaneous tensile axial force and positive bending). In this case, the action of concrete slab considerably counteracts the

collector axial force transmission, for which the connection at the bare steel sections would be subjected to a tensile axial force noticeably higher than the total axial force demand on the entire composite section. This phenomenon can be exemplified by the responses of the near (west) end of Collector 1 beams, where the AFW connections were located, at the negative peak acceleration in Test 2-3 as shown in Figure 4.52. The steel part of the collector section carried approximately 100 kips of tensile axial force, which was about twice of the total tensile force (about 50 kips) acting on the entire composite section. Hence, it is indicated that, to achieve a safe design for the collector connections, the concrete slab effect should be properly considered.

Figure 4.54(a) and Figure 4.55(a) compare the measured collector axial force (P_{coll}) with the measured column shear (V_c) acting at the AFW connection next to Columns N1 and S1, respectively. Figure 4.56(a) and Figure 4.57(a) compare the measured collector moment (M_{coll}) with the measured column moment (M_c) projected to the centerline beam-to-column intersection at the top ends of Columns N1 and S1, respectively. As illustrated in Figure 3.61, the column shear and moment were calculated based on the readout from the strain gauges on the column flanges. On the other hand, the collector member forces were determined by using the measured strains along the depth of collector section together with an assumed strain profile (see Figure 3.65) and an effective slab width experimentally determined from Test 2A-5 (Figure 8.1). Since there might be some error in the assumed strain profile and experimentally determined effective slab width for the composite collector section, the measured column member forces (V_c and M_c) would be more reliable than the measured collector member forces (P_{coll} and M_{coll}). To achieve the force equilibrium at the beam-to-column intersection of Columns N1 and S1, the magnitudes of V_c and P_{coll} should be about the same because the magnitude of the horizontal forces transmitted from the west chord and floor diaphragm into the column is expected to be small. Similarly, the

magnitude of M_{coll} should be close to that of M_c. Therefore, a proximity of P_{coll} to V_c indicates the reliability of the measurement of P_{coll}. Likewise, a closeness of M_{coll} to M_c suggests the accuracy of the measured values for M_{coll}.

Figure 4.54(a) and Figure 4.56(a) show that P_{coll} followed V_c very well at both AFW connections. The slopes of the regression lines for the P_{coll} versus V_c relationships were 0.978 and 1.084 at Columns N1 and S1, respectively. From Figure 4.55(a) and Figure 4.57(a), it can be found the relationships between M_{coll} and M_c were very linear for both columns. The slopes among the M_{coll} versus M_c relationships were 0.847 and 0.887 at the top ends of Columns N1 and S1, respectively. Form these results, basically, the accuracy of the measured collector member forces (P_{coll} and M_{coll}) are acceptable.

Figure 4.54(b) and Figure 4.55(b) compare the collector axial force taken by the bare steel section, denoted as P_{coll-s}, with the measured column shear (V_c) acting at the AFW connection for the top ends of Columns N1 and S1, respectively. For both columns, the P_{coll-s} versus V_c plot exhibited two different linear relationships among the test data on tension and compression sides of the collector forces, respectively. Both slopes on the tension and compression sides were steeper than the 45-degree between P_{coll-s} versus V_c. In addition, the tension-side slope was steeper than the compression-side slope. This suggests that the concrete slab played a significantly and lightly counteracting role when the collector end transmitted a tensile or compressive axial force, respectively. These caused P_{coll-s} at this collector end to be significantly and slightly higher than P_{coll}, which was close to V_c, when the collector was in tension and compression, respectively.

Figure 4.56(b) and Figure 4.57(b) compare the measured collector moment taken by the steel part, denoted as M_{coll-s}, with M_c at the top ends of Columns N1 and S1, respectively. For both columns, it can be found the relationships between M_{coll-s} and M_c were generally linear. The

slopes among the M_{coll-s} versus M_c relationships were 0.609 and 0.655 at Columns N1 and S1, respectively. Note that these slopes were about 26%~28% flatter than the slopes among M_{coll} versus M_c relationships. This implies that, near the AFW connections, the concrete slab part transmitted about 27% of total bending moment acting on the entire composite collector section.

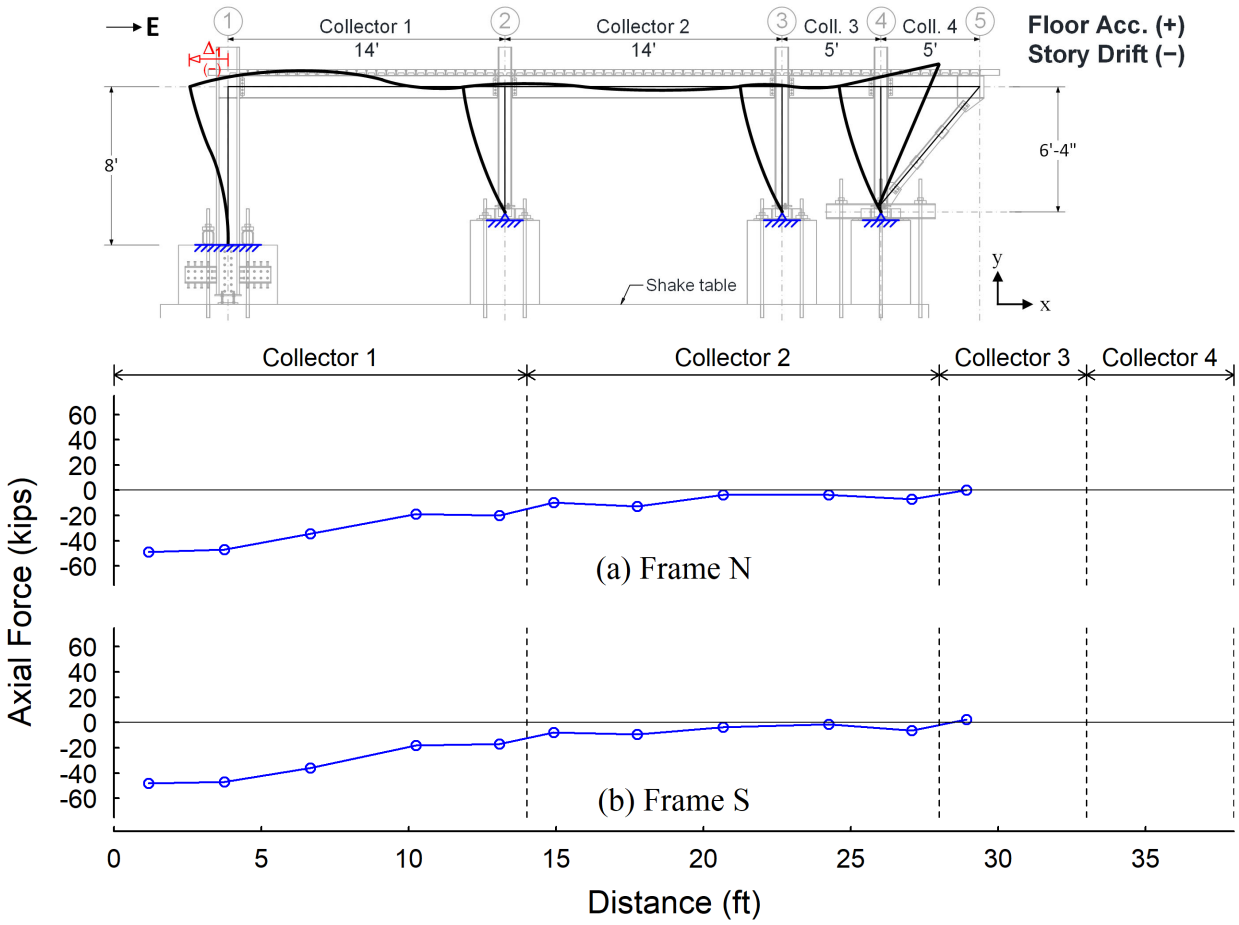

Figure 4.46 Test 1-3: Axial Force Diagrams along Collector Lines at Positive Peak Acceleration

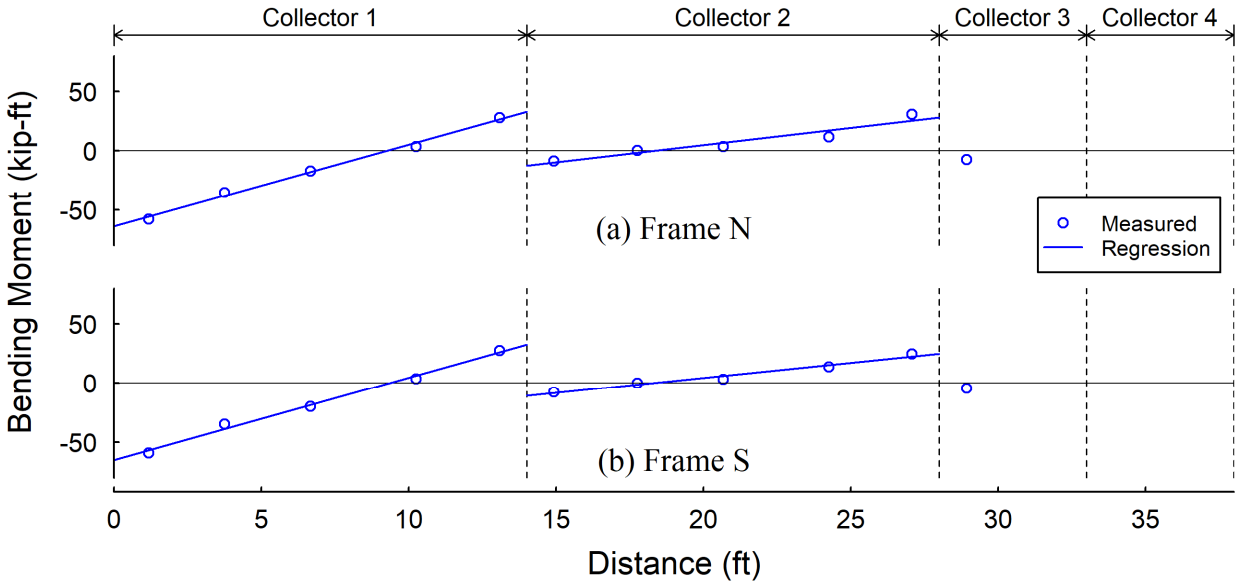

Figure 4.47 Test 1-3: Moment Diagrams along Collector Lines at Positive Peak Acceleration

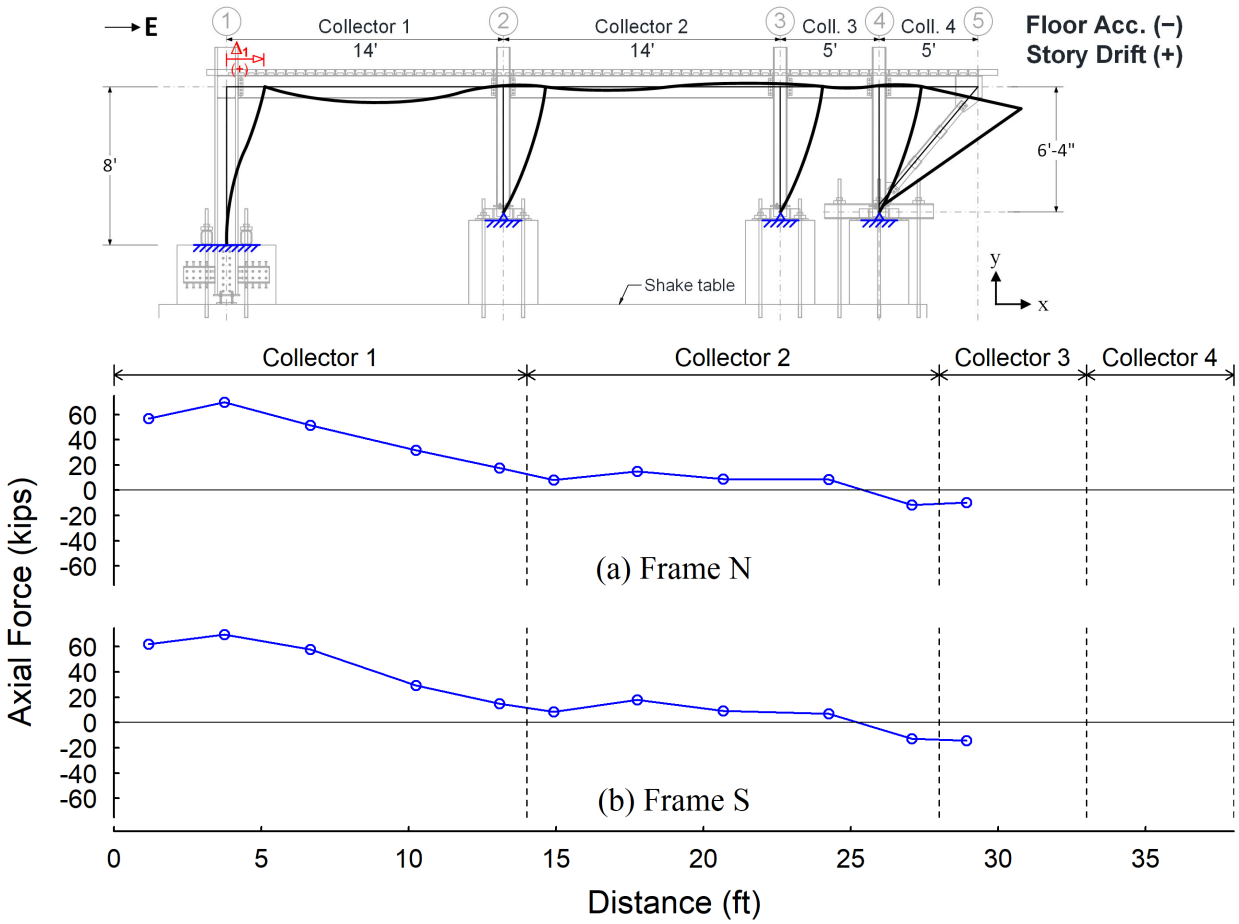

Figure 4.48 Test 1-3: Axial Force Diagrams along Collector Lines at Negative Peak Acceleration

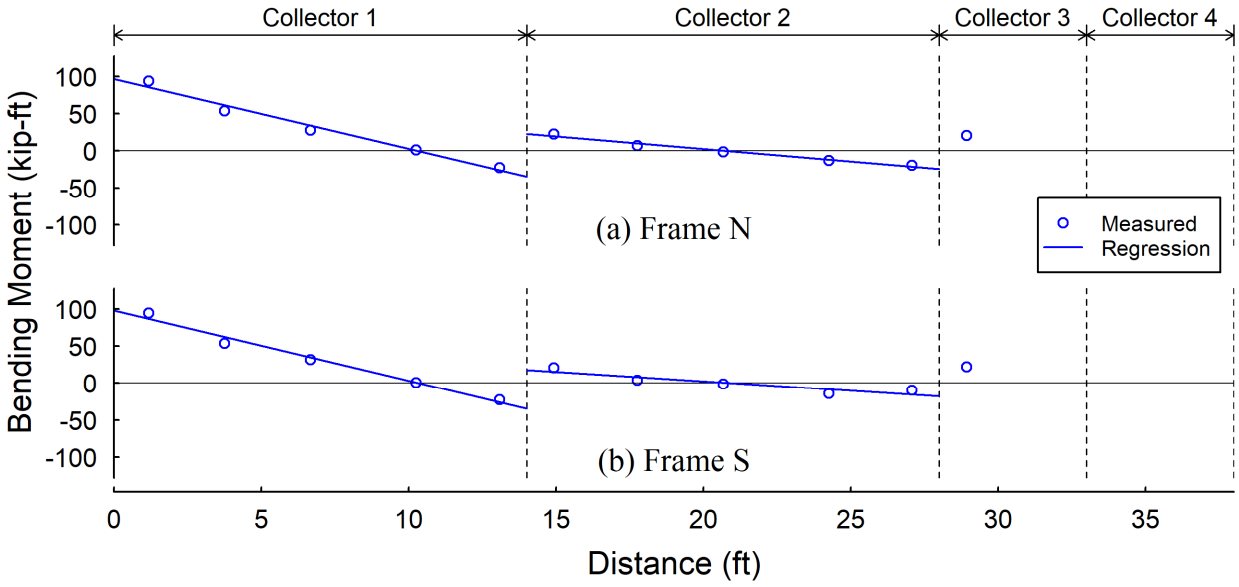

Figure 4.49 Test 1-3: Moment Diagrams along Collector Lines at Negative Peak Acceleration

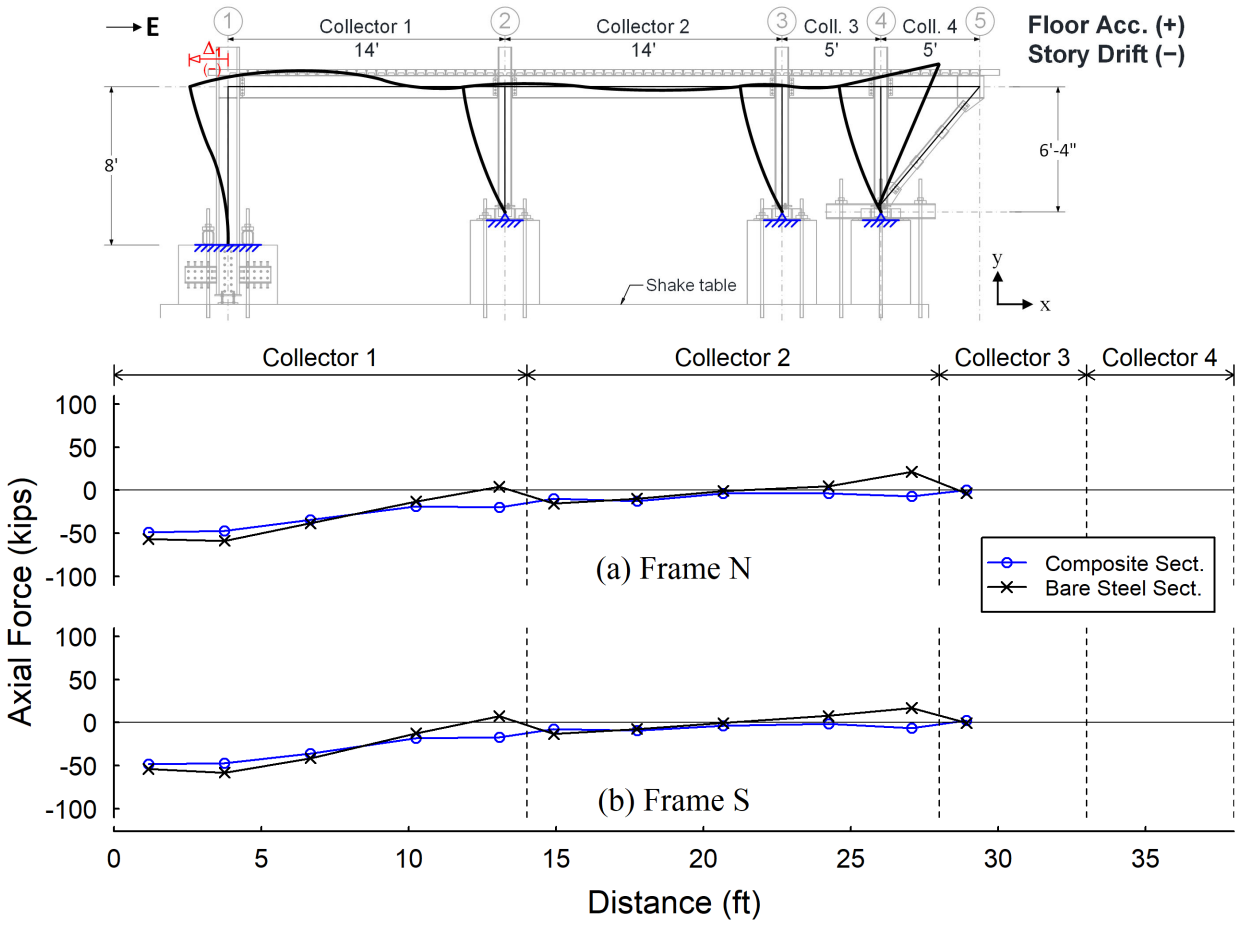

Figure 4.50 Test 1-3: Comparison of Axial Forces Taken by Composite of Bare Steel Sections of Collectors at Positive Peak Acceleration

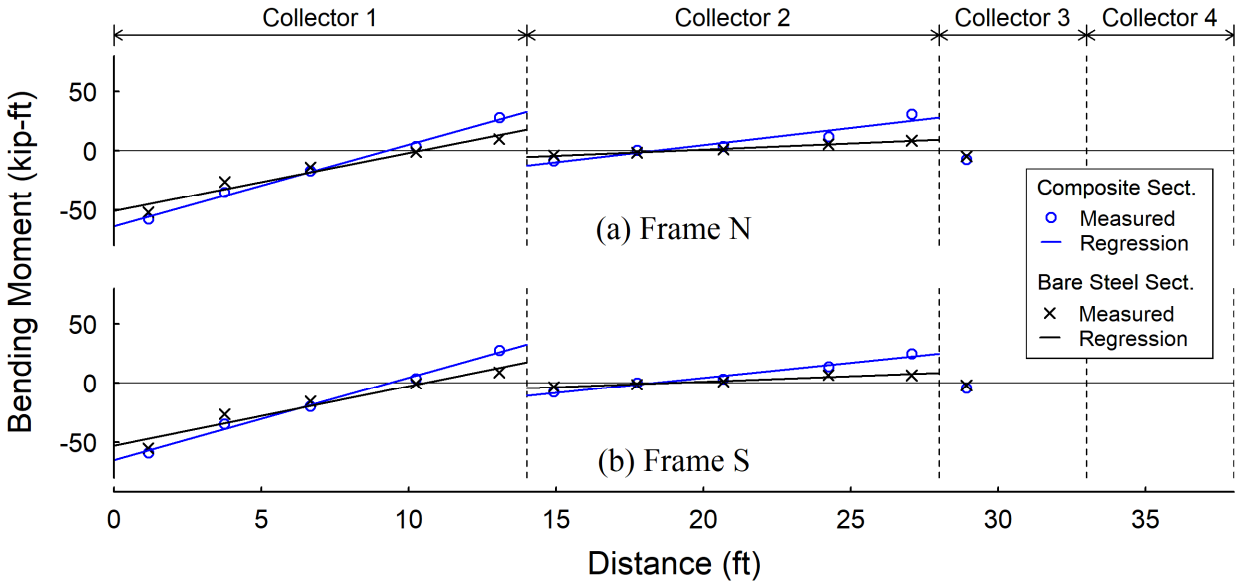

Figure 4.51 Test 1-3: Comparison of Moments Taken by Composite of Bare Steel Sections of Collectors at Positive Peak Acceleration

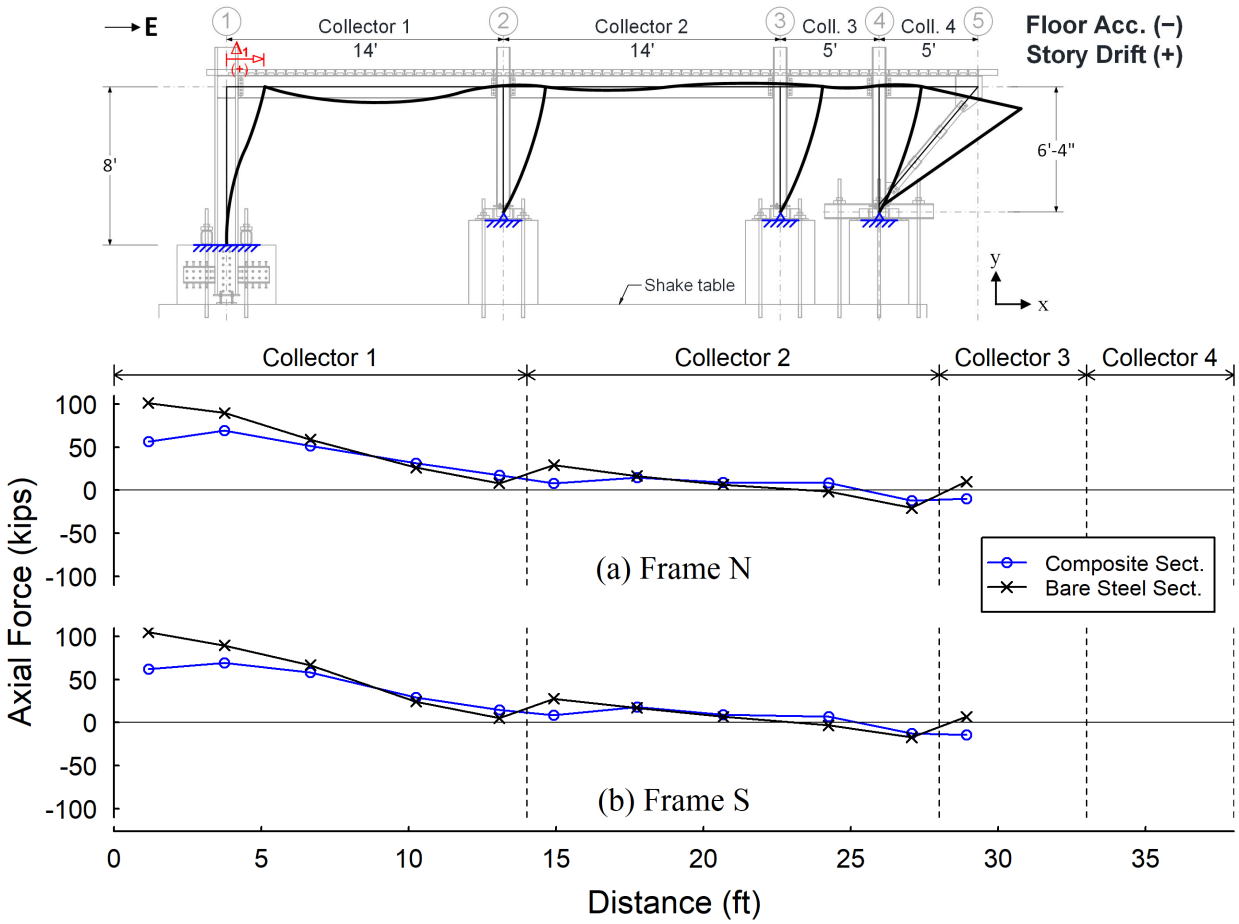

Figure 4.52 Test 1-3: Comparison of Axial Forces Taken by Composite of Bare Steel Sections of Collectors at Negative Peak Acceleration

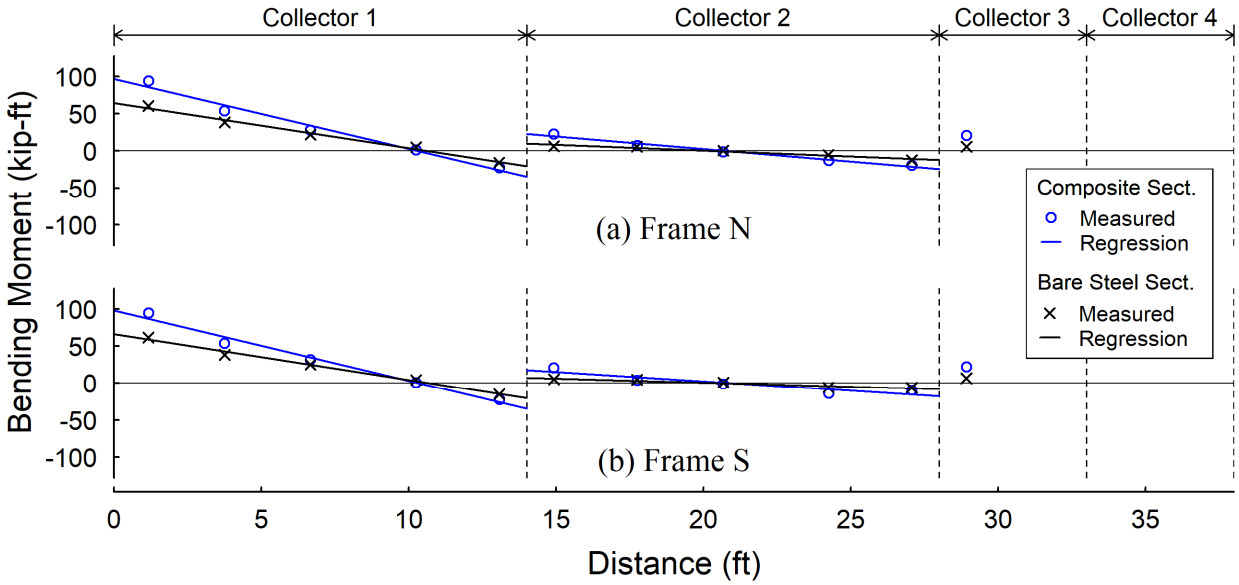

Figure 4.53 Test 1-3: Comparison of Moments Taken by Composite of Bare Steel Sections of Collectors at Negative Peak Acceleration

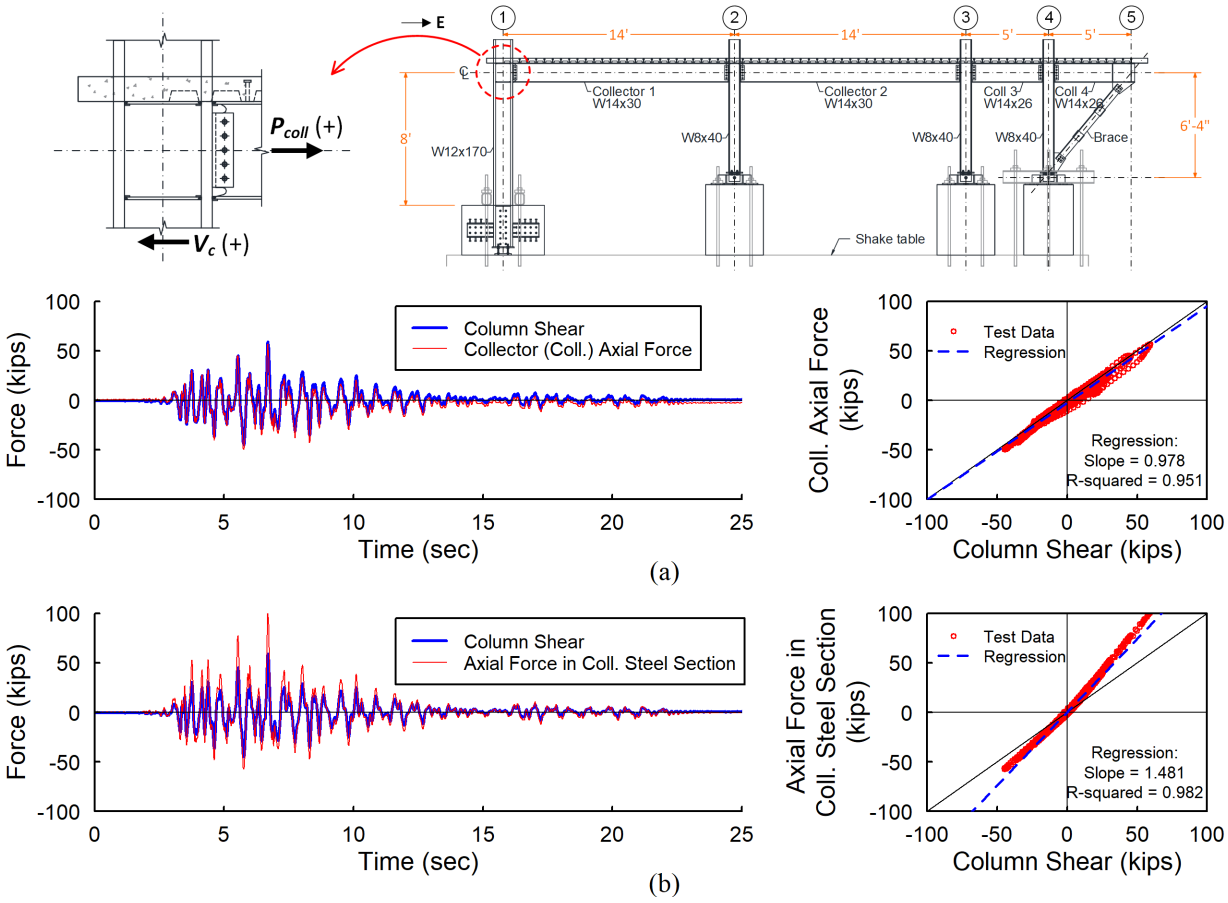

Figure 4.54 Test 1-3: Comparison of Column Shear and Collector Axial Forces Taken by (a) Composite Section and (b) Bare Steel Section near Column N1 Top End

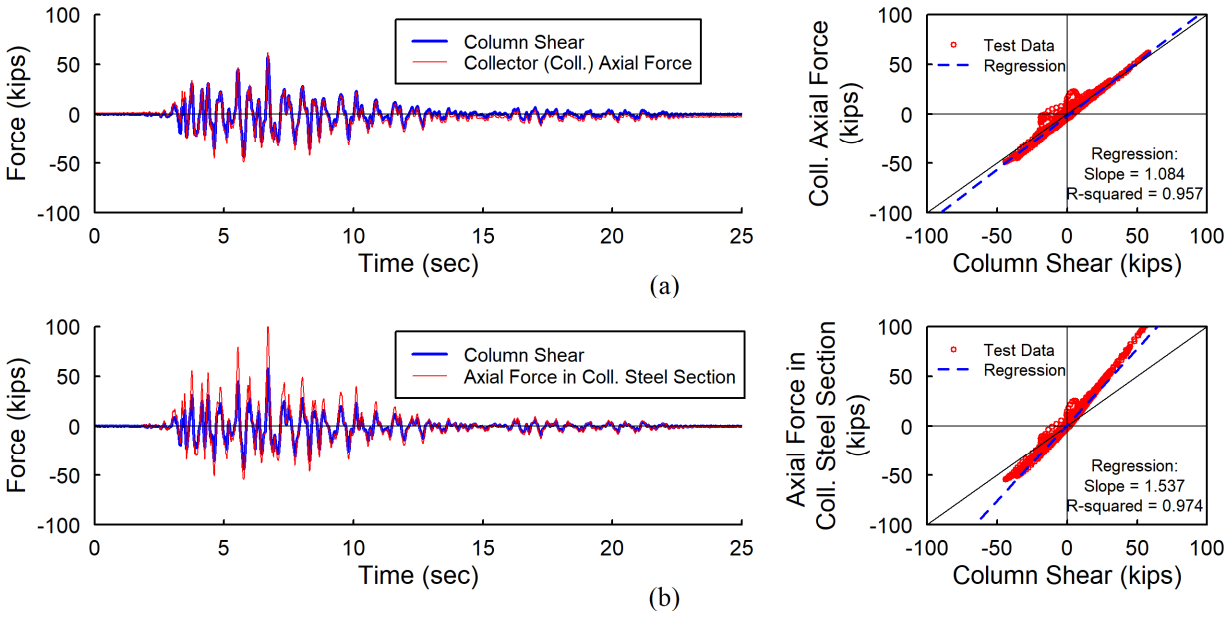

Figure 4.55 Test 1-3: Comparison of Column Shear and Collector Axial Forces Taken by (a) Composite Section and (b) Bare Steel Section near Column S1 Top End

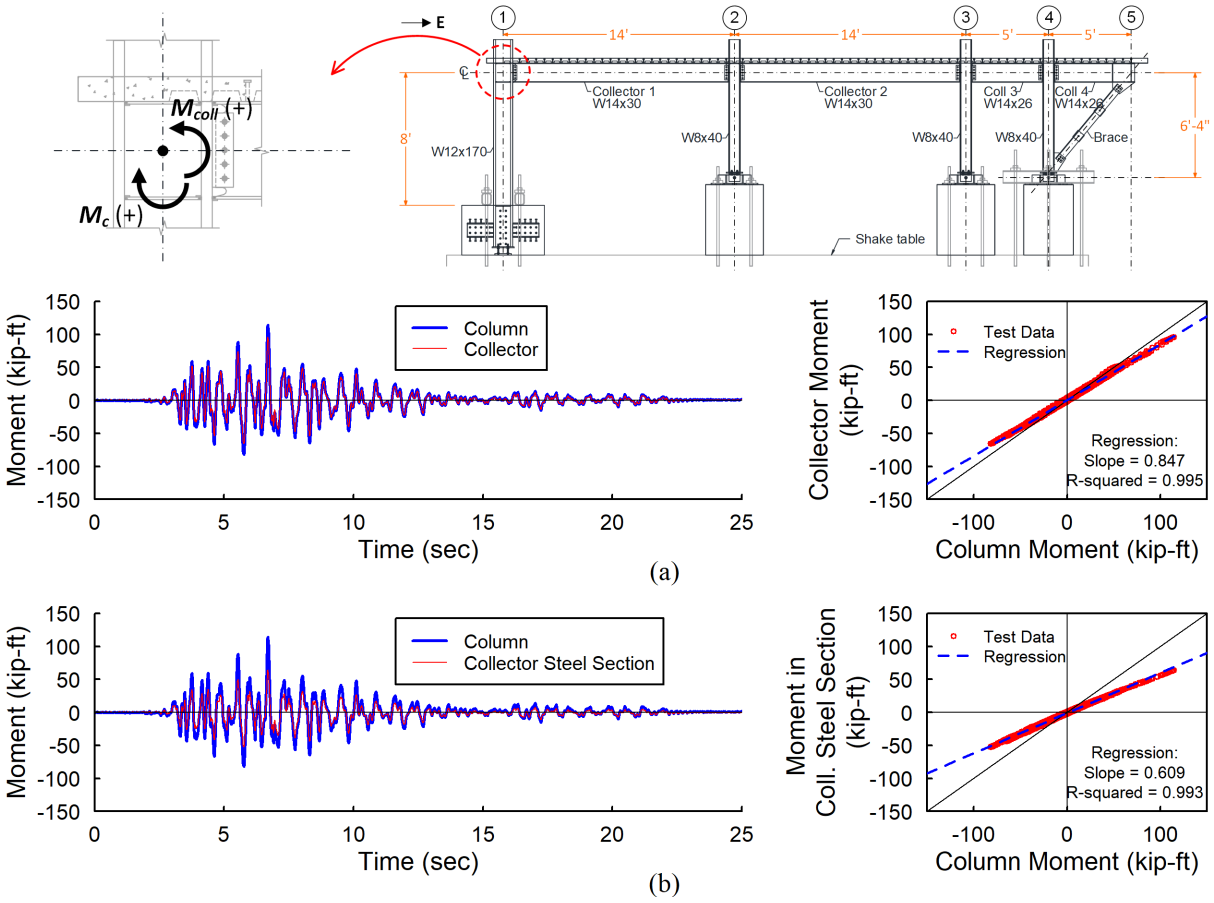

Figure 4.56 Test 1-3: Comparison of Column Moment and Collector Column Taken by (a) Composite Section and (b) Bare Steel Section at Column N1 Top End

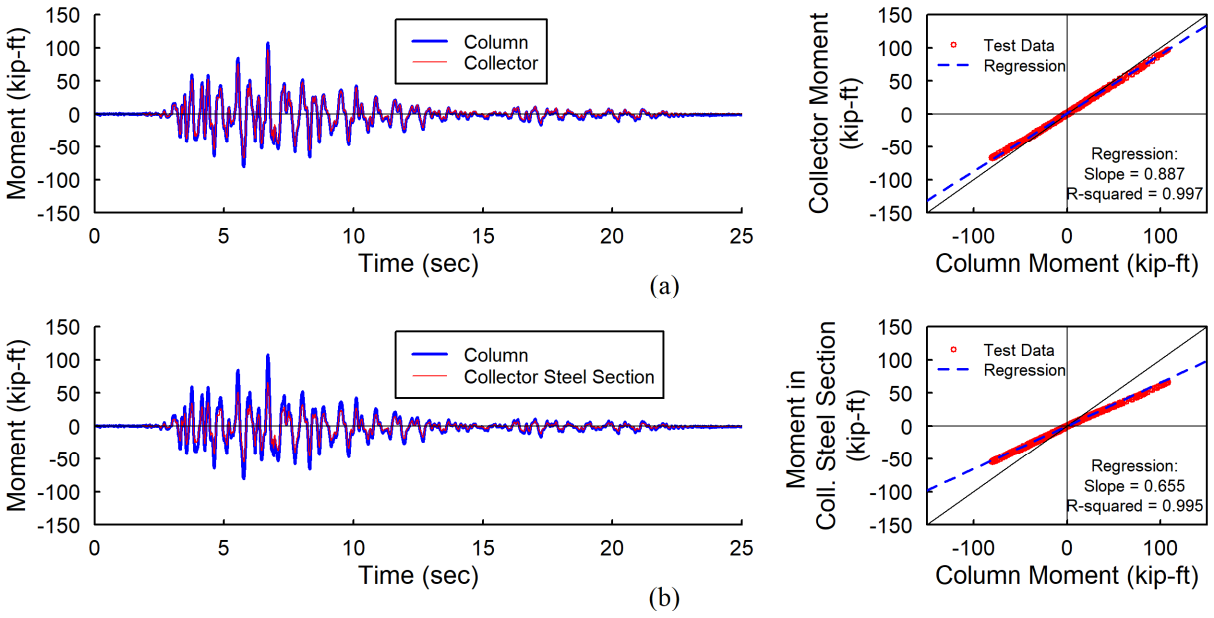

Figure 4.57 Test 1-3: Comparison of Column Moment and Collector Column Taken by (a) Composite Section and (b) Bare Steel Section at Column S1 Top End

4.2.5 Collector-to-Column Connection Responses

As introduced in Section 3.7.3 and illustrate in Figure 3.59, the rotation angles of the collector-to-column connections, denoted as θ_{Jt}, on Column Lines 1, 2, and 3 were measured by using the a series of displacement transducers placed horizontally near the connections. The rotation angle of the collector end connection was estimated by using two methods. Method 1 evaluated the rotation of the entire composite section, θ_{JtC}, by using Eq. (3.35) with the readouts from the two displacement transducers relatively placed on the top of the concrete slab and near the bottom steel flange. Method 2 evaluated the rotation of the bare steel section, θ_{JtS}, by using Eq. (3.34) with the readouts from two displacement transducers relatively near the top and bottom flanges of the steel section.

Figure 4.58 shows the comparison of the measured collector connection rotation angle versus story drift angle relationships between the two methods for each of the instrumented collector connections. Unfortunately, the sensor placed near the bottom steel flange at the east side of Column S1 malfunctioned during Phase 1 test. Thus, the rotation angle at this collector end is not reported. In general, the collector connection rotation angle determined from two methods were similar but slightly different. It appears that the results from the two methods were very similar for negative rotations. For positive rotations, the rotation angles determined from Method 2 were slightly greater than the that obtained from Method 1. Note that, for each collector connection, on the top of concrete slab was placed a spring potentiometer, while two LVDT displacement transducers were used for the steel section. The gauge length of a spring potentiometer was about 4 in., which is shorter than the gauge length (9.5 in.) of LVDT displacement transducer. It should be noted that the displacement measured by the sensors was the resultant displacement due to the combined flexure and axial load accumulated along the gauge

length. Thus, a shorter gauge length would lead to a smaller displacement being measured. This may explain why Method 1, for which the readout from spring potentiometer with a shorter gauge length was used, resulted a smaller rotation angle than that determined from Method 2 for positive rotation. On the other hand, for negative rotation, a gap would appear between the concrete slab and column face. This gap represented the resultant tensile displacements at the top face of slab due to the combined flexure and axial. Since the gap was within the gauge length range of spring potentiometer, the sensor can well capture the resultant displacements at the top face of slab. This explains why the rotation angles obtained from two methods were similar for negative rotation. Considering there may be some issue due to different gauge lengths of the sensors in Method 1, eventually, the connection rotations determined from Method 2, which evaluates the rotation of steel section, are used for the later discussions in this research.

Figure 4.59 shows the measured moment versus rotation (M-θ) relationships for the collector-to-column connections on Column Lines 1, 2, and 3. Note that the sign conventions used herein for the bending moment and rotation are consistent: a positive bending moment (or rotation) means that the beam is concave upward, whereas a negative bending moment (or radiation) means that the beam is concave downward. As shown by the sketches in the top of Figure 4.59, when the specimen was subjected to positive floor acceleration, the test frame underwent negative drift (Case "A" in Figure 4.59). In the meantime, the AFW connections, far-side TFW connections and the far-side BW connections on Column Line 3 were subjected to negative bending, while the near-side TFW connections and near-side BW connections were subjected to positive bending. In addition, it should be noted that, different from the other far-side connections under negative bending, the far-side BW connections on Column Line 4 were subjected to positive bending because of the upward movement of the cantilever slab on the east end of the structure.

On the other hand, when the specimen was subjected to a negative floor acceleration, the test frame underwent a positive drift (Case "B" in Figure 4.59). Meanwhile, the AFW connections, far-side TFW connections and the far-side BW connections on Column Line 3 were subjected to a positive bending, while the near-side TFW and near-side BW connections were subjected to a negative bending. Again, noted that, opposite to the other far-side connections under a positive bending, the far-side BW connections on Column Line 4 were subjected to a negative bending.

As shown in Figure 4.59, for all the instrumented collector-to-column connections, there seem to be two different roughly linear trends respectively among the data in the first (positive bending) and third quadrants (negative bending) of each M-θ plot. The collector connection rotational stiffnesses for positive and negative bending were estimated by using the secant stiffnesses for the data in the first and third quadrants, respectively, of each M-θ plot. Figure 4.60 shows the "zoom-in" version of each measured M-θ relationship to demonstrate the determination of the estimated stiffness. It appears that, for all the collector connections, the secant rotational stiffnesses for positive bending was higher than that for negative bending. This is attributed to the fact that the concrete slab at the connection region resisted significant compressive stresses under positive bending, whereas the slab developed negligible tensile stresses under negative bending.

Form Figure 4.59, it is apparent that the rotational stiffness of AFW connections was significantly higher than those of TFW and BW connections. In general, the difference in the rotational stiffness between TFW and BW connections was insignificant. It seems to be the trend that, for each of the double-side TFW and BW connections, the near side had a rotational stiffness somewhat higher than the far side did for both positive and negative bending. In addition, the near-side connections experienced a greater magnitude of rotations than their corresponding far-side

connections did. Furthermore, the near-side connections exhibited a more pronounced hysteresis and nonlinear response than their corresponding far-side connections did.

4.2.6 Column Panel Zone Responses

As described in Section3.7.3, a pair of LVDT displacement transducers were installed at the column panel zone of each AFW connection to measure the shear deformation of the panel zone. Figure 4.61 shows that the panel zone shear deformation versus story drift angle relationships were very linear for the two AFW connections, suggesting the panel zones responded elastically during Test 1-3. Figure 4.62 shows the moment versus shear deformation (M-γ) relationships for the two panel zones. Note that bending moment at the panel zone was calculated by projecting the moment diagram of Collector 1 to the center of the panel zone. It is apparent that these panel zone M-γ relationships are very linear. Regression analyses were conducted and the slope of the regression line for the M-γ relationship can be taken as the stiffness of a rotational spring representing the panel zone for the modeling of the test specimen.

Part of this chapter is based on the material published in the 17th World Conference on Earthquake Engineering, titled "Earthquake simulator testing on behavior of seismic collectors in steel buildings" with co-authors Uang C.-M., and Fleischman R.B. (2020). Materials were also submitted for publication in the 12th National Conference on Earthquake Engineering, titled "Shake Table Tests on Seismic Response of Collectors in Steel Buildings" with co-authors Uang C.-M., and Fleischman R.B. (2022). The author of this dissertation serves as the first author of these papers.

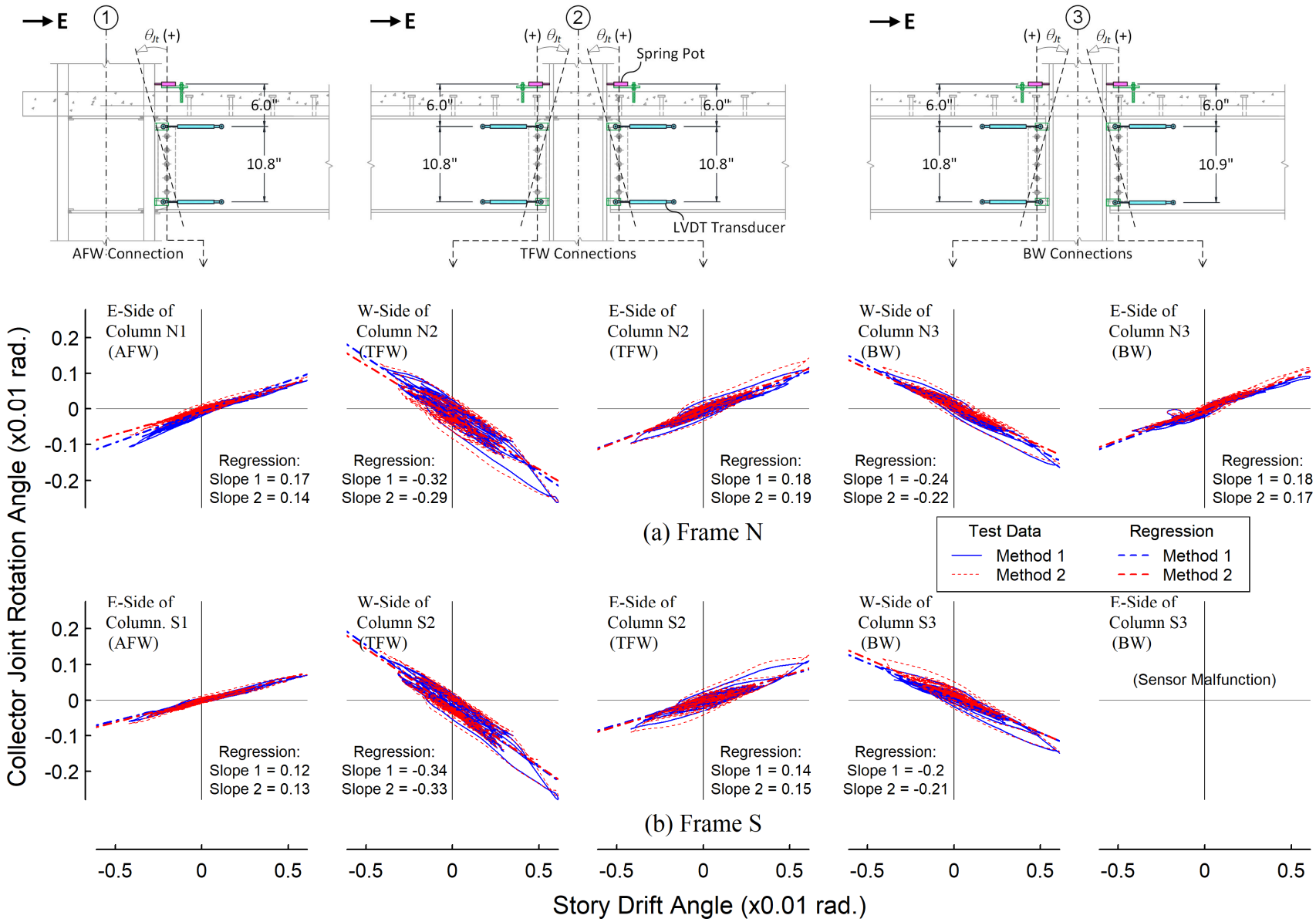

Figure 4.58 Test 1-3: Collector End Rotation versus Story Drift Angle Relationships

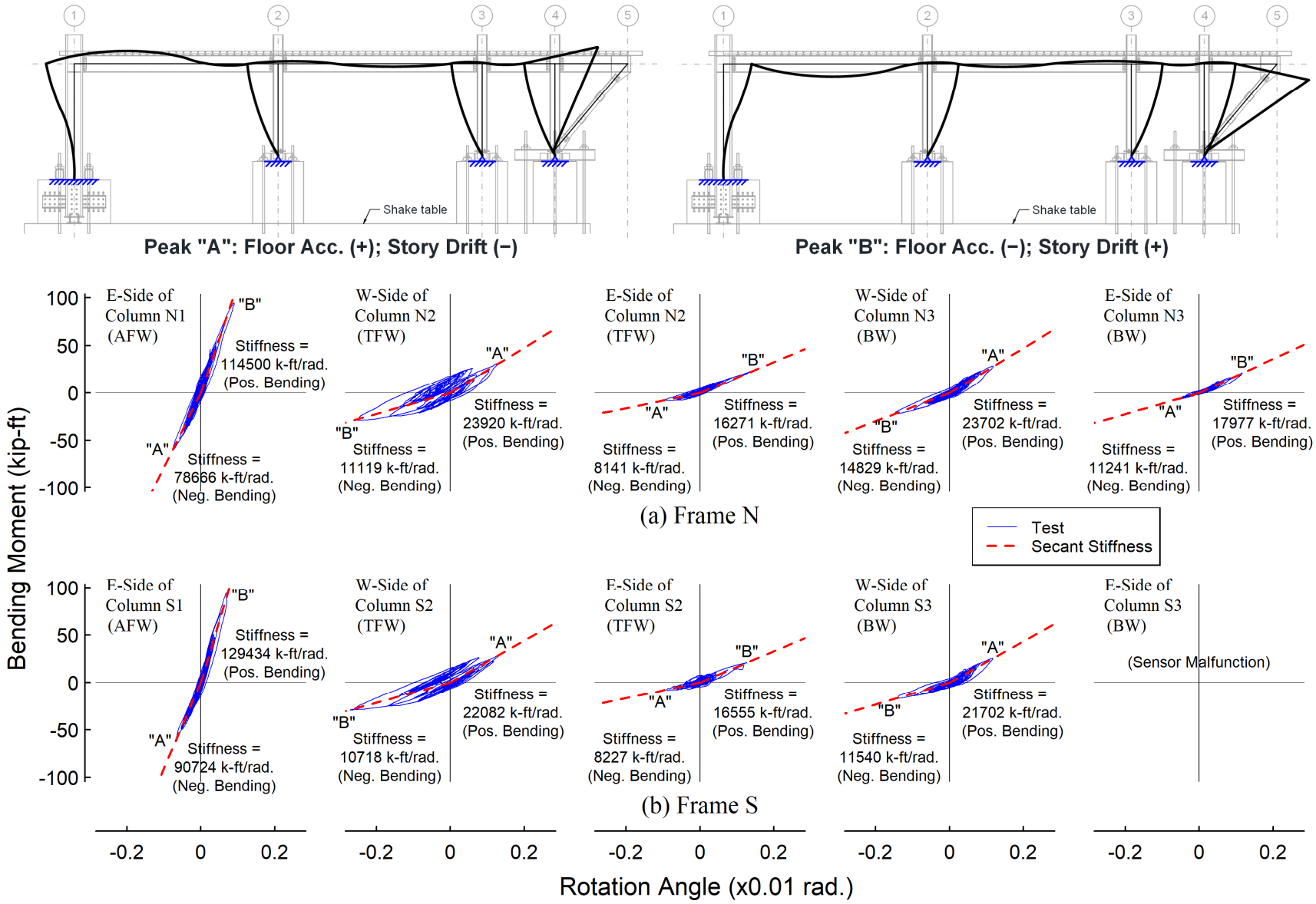

Figure 4.59 Test 1-3: Moment versus Rotation Relationships of Collector-to-Column Connections

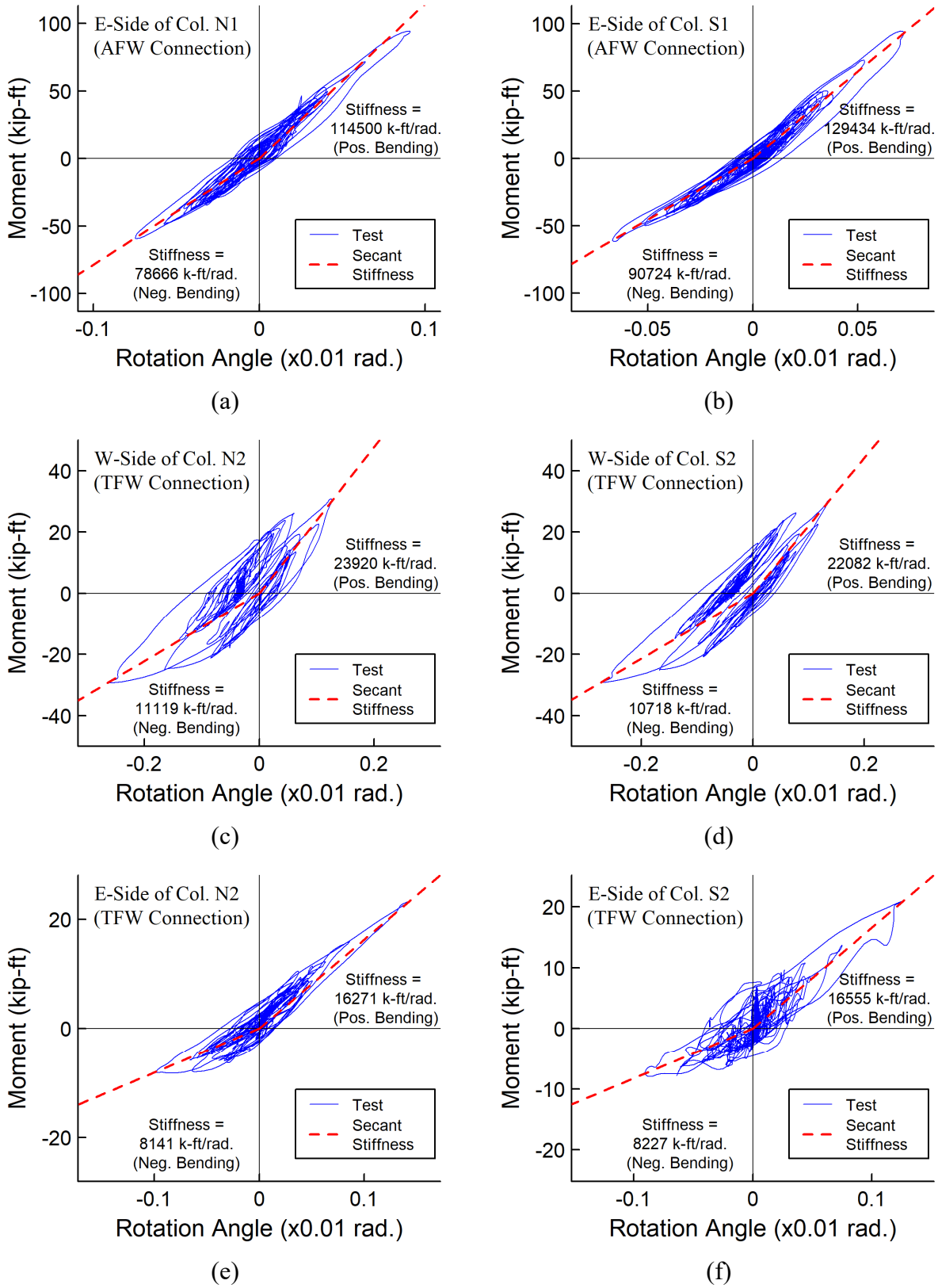

Figure 4.60 Test 1-3: Estimated Stiffnesses for Moment versus Rotation Relationships of Collector-to-Column Connections

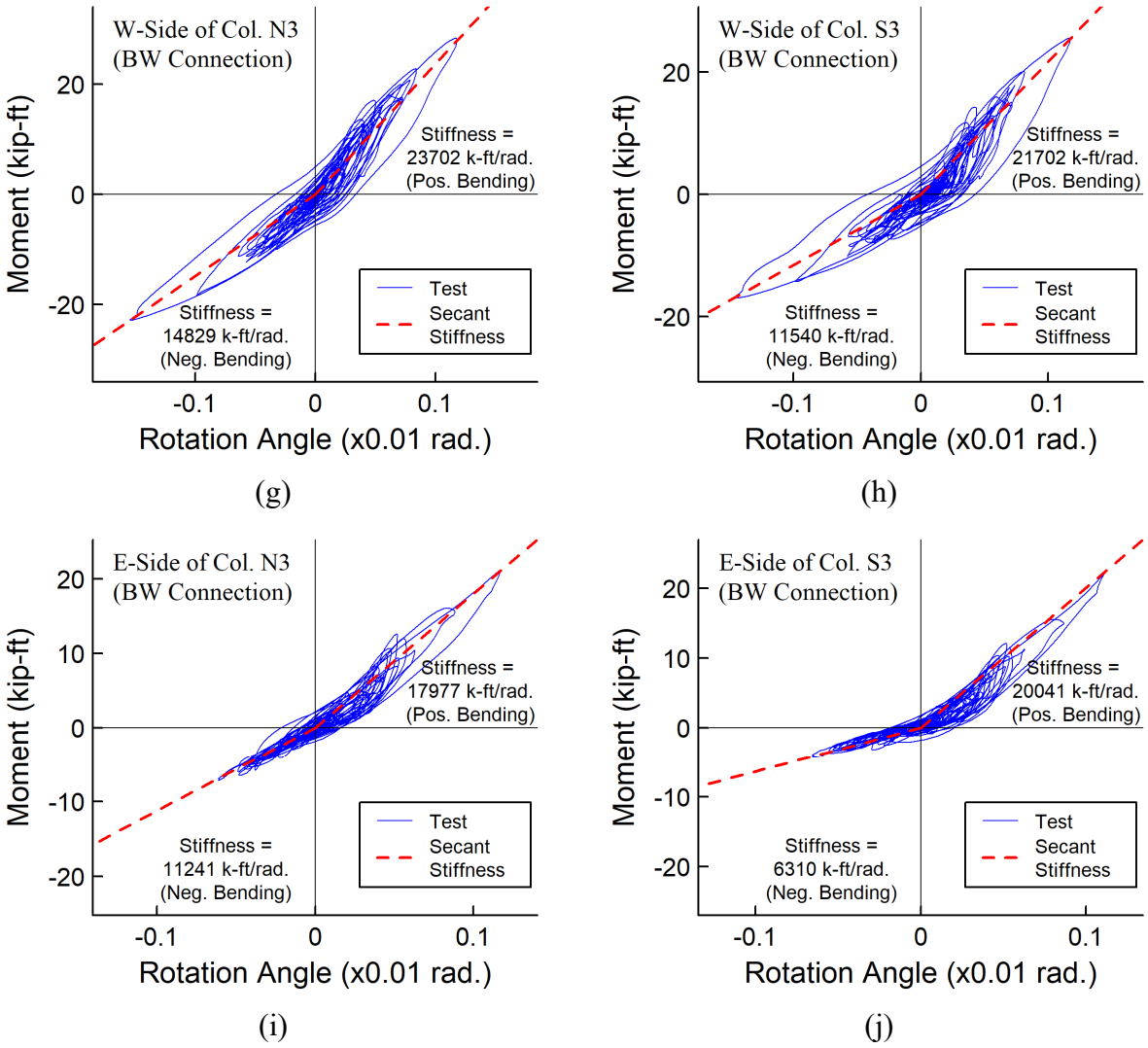

Figure 4.60 Test 1-3: Estimated Stiffnesses for Moment versus Rotation Relationships of Collector-to-Column Connections (continued)

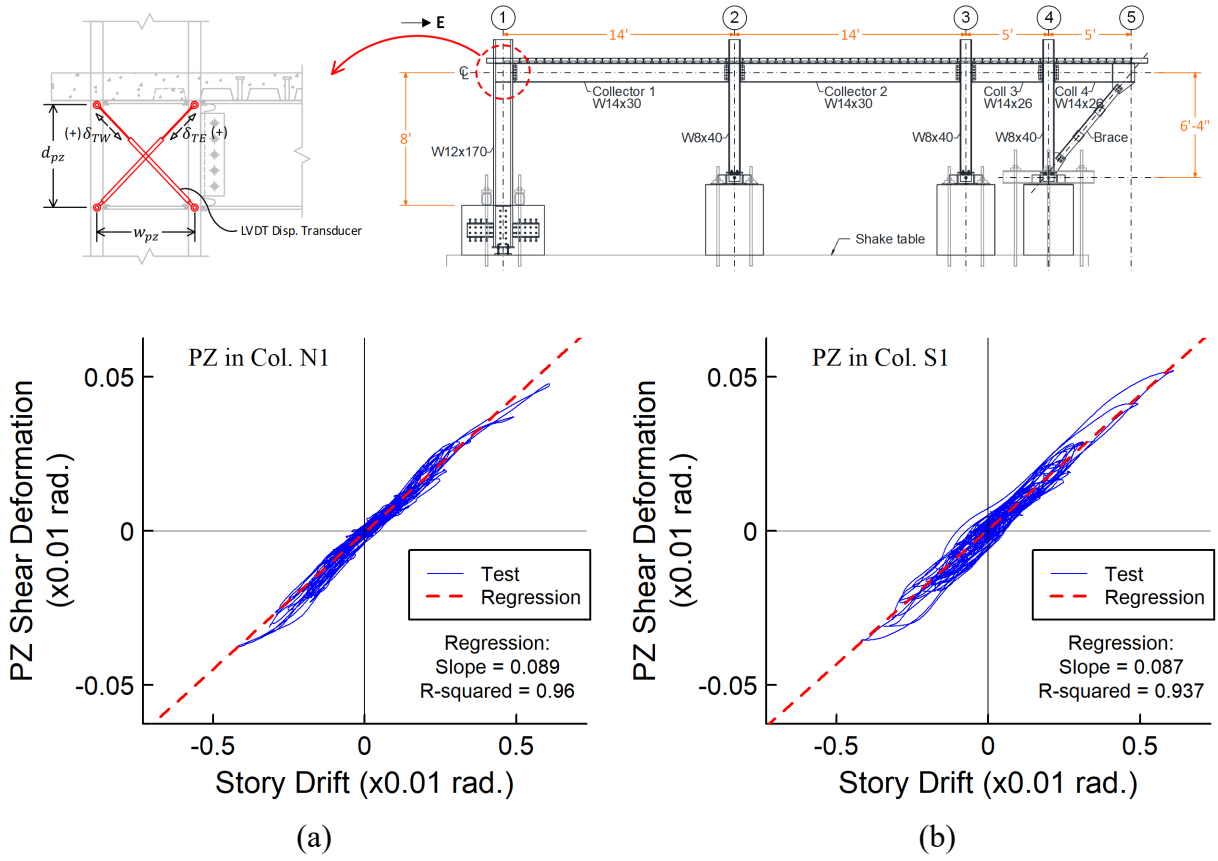

(a) (b)

Figure 4.61 Test 1-3: Panel Zone Shear Deformation versus Story Drift in Columns (a) N1 and (b) S1

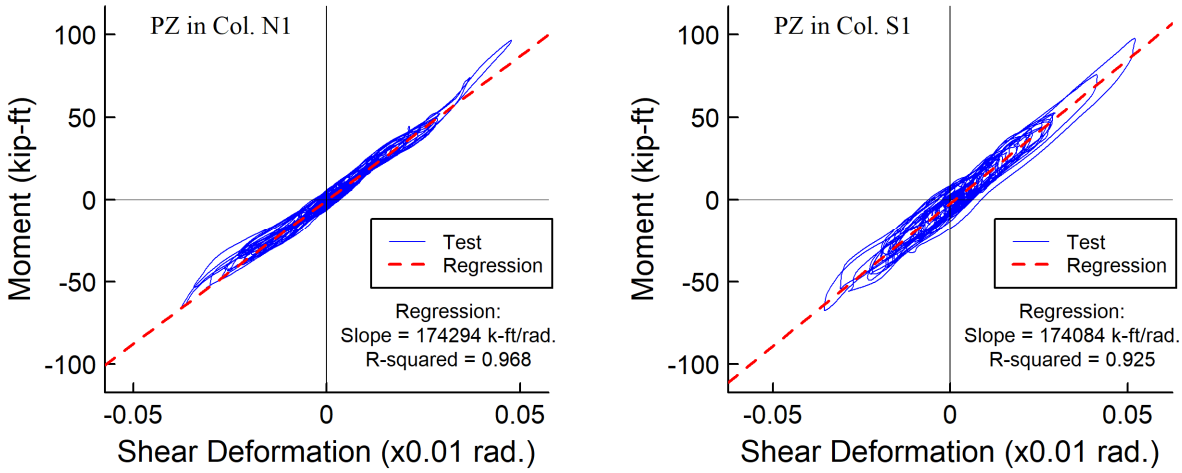

(a) (b)

Figure 4.62 Test 1-3: Moment versus Shear Deformation Relationships of Panel Zones in Columns (a) N1 and (b) S1

5. SIMULATION OF PHASE 1 TESTING AND DESIGN IMPLICATIONS

5.1 General

Phase 1 test results presented in Chapter 4 have provided some insights into the seismic responses of collectors and their connections. However, due to the limitation of the data acquisition system capacity (number of channels), the specimen responses were only measured at a limited number of locations. Since it was difficult to re-construct a thorough picture of the seismic responses of the collectors and the inertial force load path by using the test data only, numerical simulation of Phase 1 testing was conducted to confirm the finding from test results and to explore the specimen responses in a more detailed manner.

A parallel analytical study was also carried out to develop modeling techniques that can be used by researchers and practitioners for seismic analyses of steel building structures with composite collectors. Therefore, instead of using sophisticated finite element modeling with shell and solid elements, frame analyses with beam-column, truss, and joint elements were used for numerical simulation.

5.2 Numerical Modeling of Test Specimen

5.2.1 Description of Specimen Models

As listed in Table 5.1, six three-dimensional (3D) frame models with various detailed modeling settings were developed to simulate the test specimen; the nonlinear structural analysis program PISA3D (Lin et al. 2012) was used for numerical simulation. Two approaches were employed to model the composite floor diaphragm: (1) the Beam-Truss (BT) modeling approach (Lu and Panagiotou 2012), and (2) the proposed “modified strip (MS) model”. In each group of

the BT-series (Figure 5.1) or MS-series (Figure 5.2), three models with varying levels of complexity (Level 0, 1, and 2) for modeling the collector connections.

Table 5.1 Specimen Model Designation

		Complexity of Modeling of TFW and BW Collector Connections		
		Level 0[a]	Level 1[b]	Level 2[c]
Modeling of Composite Floor Diaphragm	Beam-Truss (BT) Model	Model BT-0	Model BT-1	Model BT-2
	Modified Strip (MS) Model	Model MS-0	Model MS-1	Model MS-2

[a]Level 0: Pin-connections at intersections of beam and column centerlines
[b]Level 1: Rotational springs at intersections of beam and column centerlines
[c]Level 2: Scissors model for column panel zone and rotational springs at intersections of beam and column centerlines

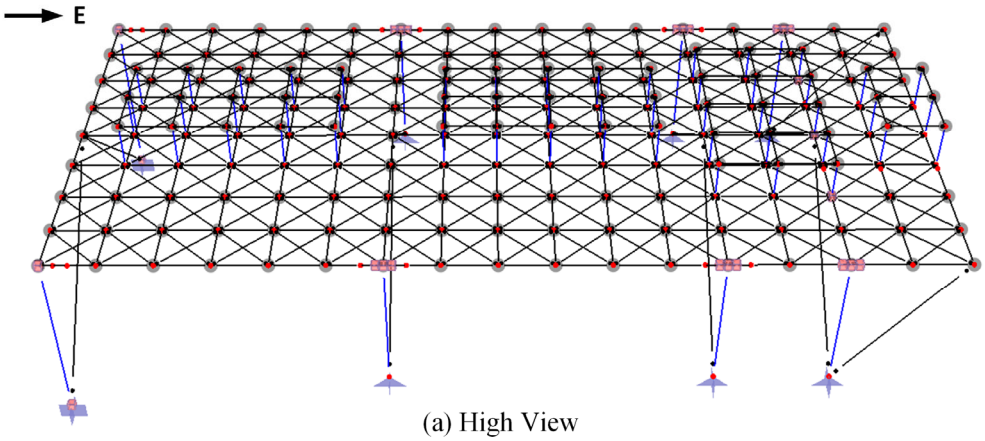

(a) High View

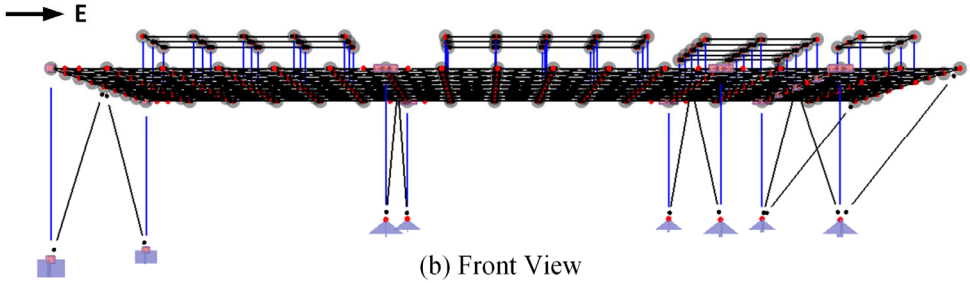

(b) Front View

Figure 5.1 Configuration of BT-Seires Model

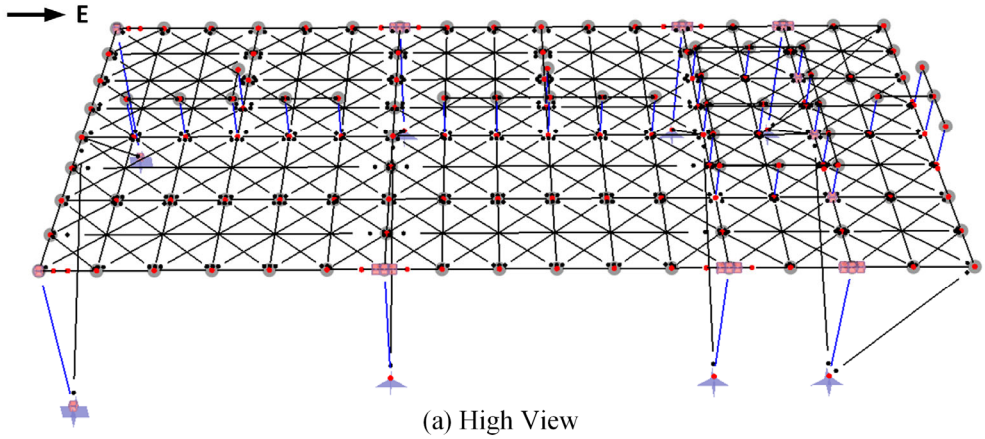

(a) High View

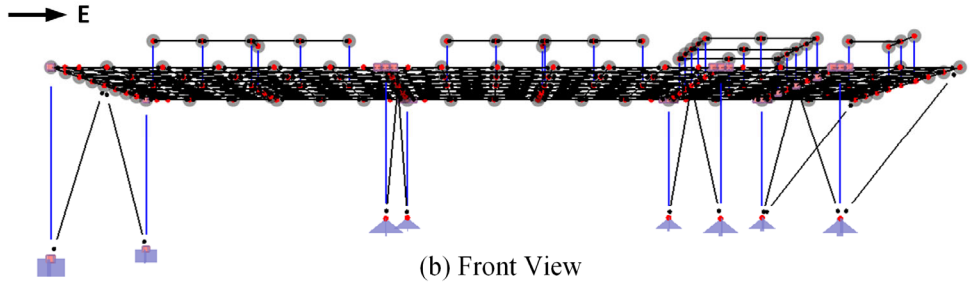

(b) Front View

Figure 5.2 Configuration of MS-Series Model

5.2.2 Modeling of Composite Floor Diaphragm

Two approaches (Beam-Truss model and modified strip model) were used for modeling the composite slab of test specimen. The details of these two approaches are as follows:

Beam-Truss Model

Beam-Truss (BT) model was originally developed by Lu and Panagiotou (2012) was to simulate the nonlinear cyclic response of in-plane shear load-deformation behavior of nonplanar RC shear walls. Since the composite slabs in steel buildings transfer the inertial force mainly through the in-plane shear behavior of the slab, which is analogous to RC shear walls resisting the in-plane shear loading, the BT modeling approach was slightly adapted to represent the composite slab of test specimen.

As shown in Figure 5.3 and Figure 5.4, the floor diaphragm in a BT model was meshed by elastic longitudinal (X-direction) and transverse (Z-direction) beam elements into to many subpanels; each subpanel formed also has with a pair of bi-directional diagonal trusses. The points where at least one longitudinal and one transverse l element intersect with a diagonal truss comprise the nodes of the model. As a results, it requires the creation of many nodes which are not located on the real steel beam locations. In addition, a number of "fictitious" beam elements which do not represent the real steel beams are added into the model to simulate the axial behavior and out-of-plane flexural stiffness of the slab. Figure 5.4-top shows that the fictitious beams are pin-ended in-plane so that they would not provide any flexural rigidity. On the other hand, Figure 5.4-top shows that, in the out-of-plane direction, theses fictitious beams are rigidly connected to their adjacent fictious beams, while pin-connections are used for the joints where the fictious beams meet real beam elements.

Figure 5.5 illustrates the determination of critical section properties for elements in the BT model to simulate the in-plane shear behavior of the composite slab. It assumes that only the part of the concrete slab above the metal deck (with a thickness of t_c) resists the in-plane shear. The tributary width (w_x or w_z) of a fictitious beam or the effective width, b_{eff}, of a diagonal slab truss is defined as a region extending from the element centerline to halfway to its neighboring elements. Thus, the cross-sectional area for a fictious beam or a slab truss is determined by multiplying its tributary width by the concrete slab thickness, t_c.

PISA3D Concrete04 material model was employed for the fictitious beams and diagonal slab trusses. This material model was implemented based on the same constitutive model used for Concte04 in the computer program OpenSees (Mckenna et al. 2000). As shown in Figure 5.5(d), for fictitious beam elements, the material model considering both the compressive and tensile behavior of the concrete is used. On the other hand, the concrete model for the slab truss assumes a zero tensile strength. Because the measured strains of the concrete slab in the test specimen was low, the effect of biaxial strain field on reducing the concrete compressive strength proposed by Lu and Panagiotou was not considered.

Modified Strip Model

The concept of the modified strip model (see Figure 5.6) stems from both the ideas of the BT model and the strip model proposed by Thorburn et al. (1983) for simulating the tension field action of infill panels of a steel plate shear wall. However, different from the conventional strip model, which only uses the inclined trusses for the post-buckling infill plate of the shear wall, the proposed modified strip model not only uses inclined trusses to represent the compression field of the concrete slab in shear but also employs longitudinal and transverse trusses to represent the axial behavior of the slab for both directions. As shown in Figure 5.6 and Figure 5.7, to construct

a modified strip model for a floor diaphragm, the nodes are only assigned along the actual steel beams or at column locations. Inclined trusses together longitudinal and transverse trusses are placed into each panel surrounding by actual steel beams on the floor. The determination of the area and material model for the inclined slab trusses in the modified strip model follow those for diagonal slab trusses in the BT model (see Figure 5.5). Similarly, the input settings for the longitudinal and transverse slab trusses in the modified strip model are the same as those for the fictitious beams in BT model.

It should be noted that the strategy to arrange the layout for the nodes and slab trusses in the BT model is to form a good number of subpanels for a fine mesh of the floor diaphragm, while the layout of a modified strip model is based on the panels surrounding by actual steel beams (collectors and floor beams). Therefore, the BT model requires many "auxiliary nodes" and "short" slab trusses being placed within the region surrounding the actual steel beams to form the subpanels. By contrast, the modified strip model does not need these auxiliary nodes and it utilizes longer slab trusses traversing between nodes on actual beams. As a result, the modified strip model requires a much smaller number of nodes and elements than the BT model does, which can greatly reduce the computational costs.

Figure 5.8 shows the comparison of the nodal mass distributions between two models. The magnitude of the nodal masses can be visualized by comparing the diameter of the circle for each nodal mass to the standard circle for 1 kip shown in the figure. For the BT model [Figure 5.8(a)], use of many auxiliary nodes allows it to simulate the mass distribution in a precise manner. By contrast, the nodal masses in the modified strip model are only assigned along the actual steel beams. Since the test specimen used different floor beam layouts between the north- and south-halves of the slab, the way the gravity loads are distributed to the floor beams is different between

two sides. Hence, a non-symmetric mass distribution pattern is assigned to the nodes in the modified strip model as shown in Figure 5.8(b). However, as the nodal mass distribution follows the same pattern as the distribution of gravity loads to the floor beams, the non-symmetric mass distribution shown in the modified strip model is considered reasonable.

For both the BT and modified strip models, each nodal mass is assigned in three directions (i.e., X-, Y-, and Z-directions). Three dimensional nodal masses were assigned to the auxiliary nodes in the BT model because the fictitious beams were assigned with an out-of-plane flexural stiffness as well such that this model can reflect the out-of-plane vibration modes to pursue a complete modeling of the test specimen. However, if the out-of-plane vibration of the slab is insignificant, the BT model can be simplified as follows to save the computational costs:

- The fictitious beams are replaced by truss elements to represent the axial behavior of the slab.
- The degrees of freedom for three rotational directions and vertical translation (Y-directions) are restrained for the auxiliary nodes.
- Only in-plane nodal masses are assigned to the auxiliary nodes.

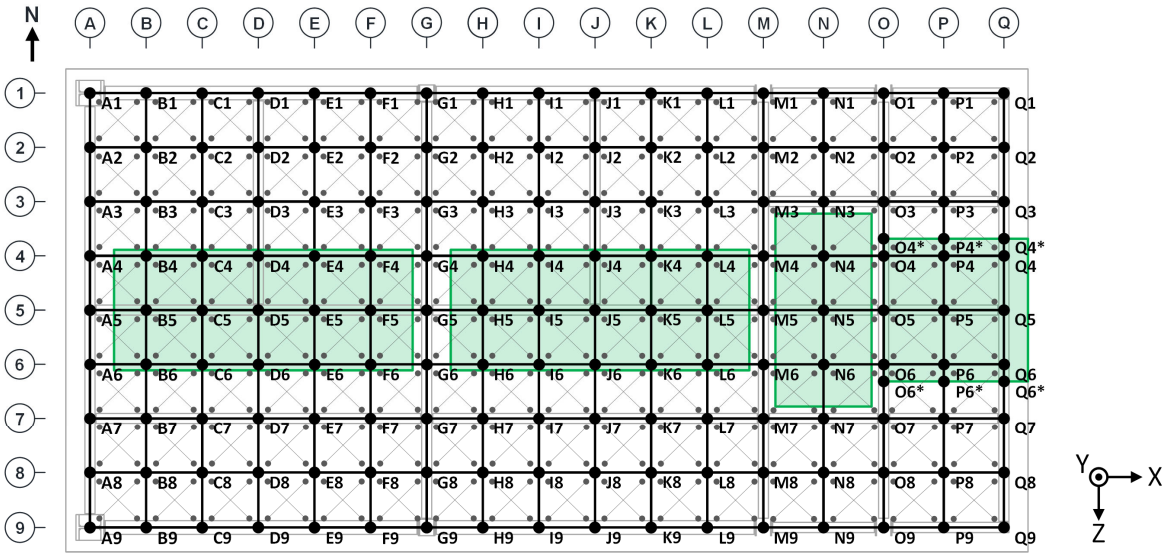

Figure 5.3 Node Layout of Floor Diaghram for BT Model

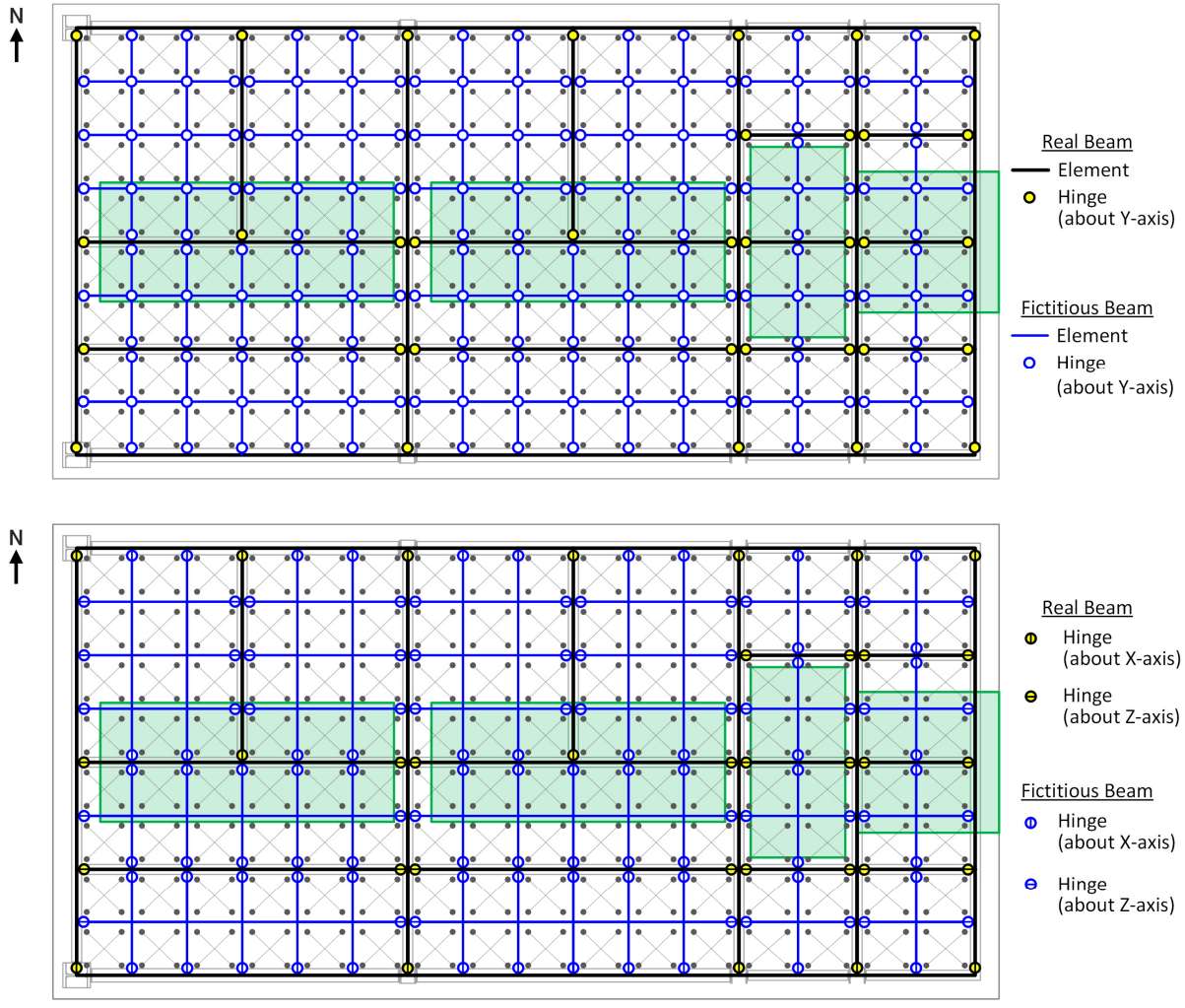

Figure 5.4 Layouts of Floor Beams, Slab Beams and Slab Trusses for BT Model

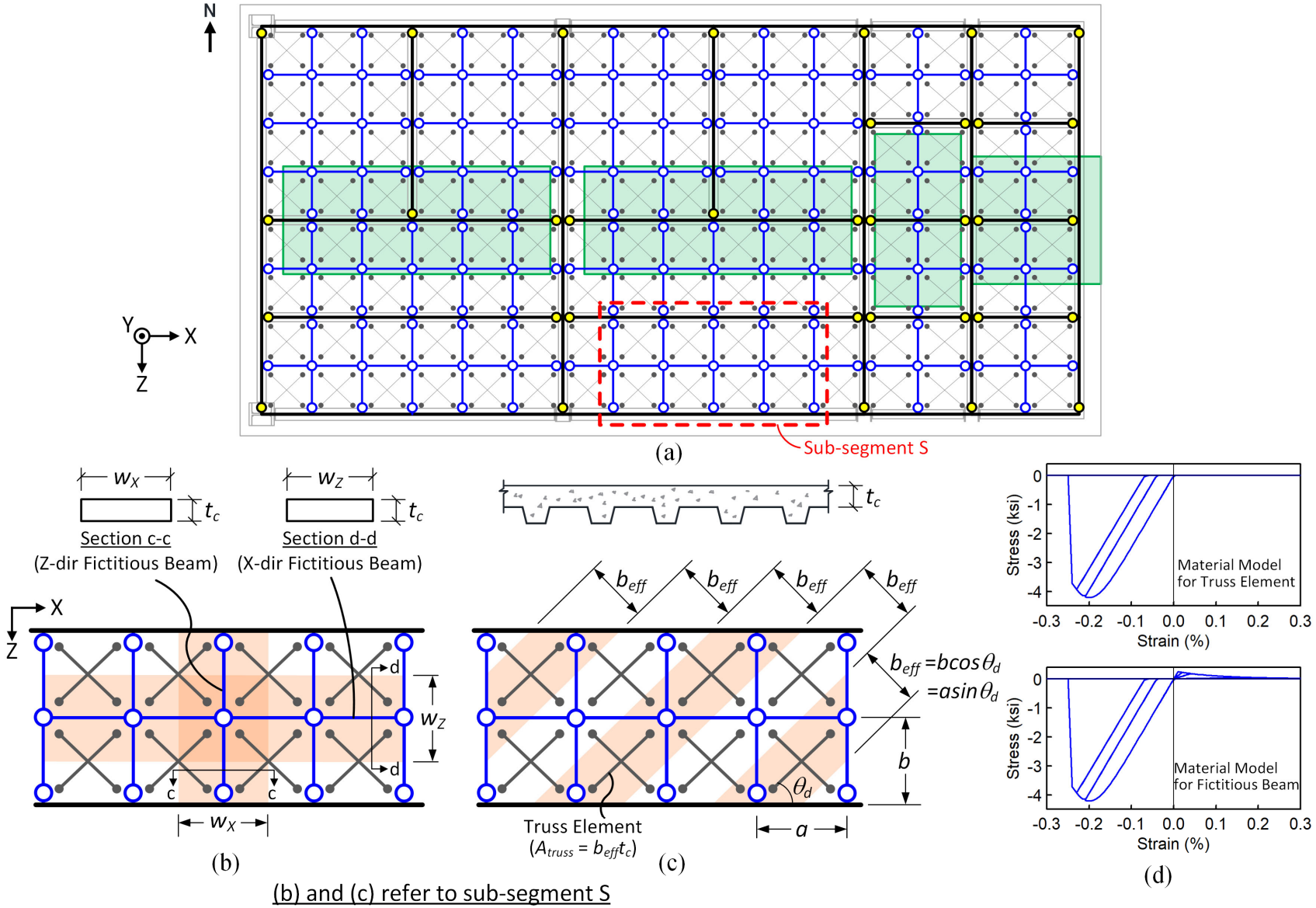

Figure 5.5 Schematic Description of Modeling of Composite Floor Diaphragm (BT Model used as an Example)

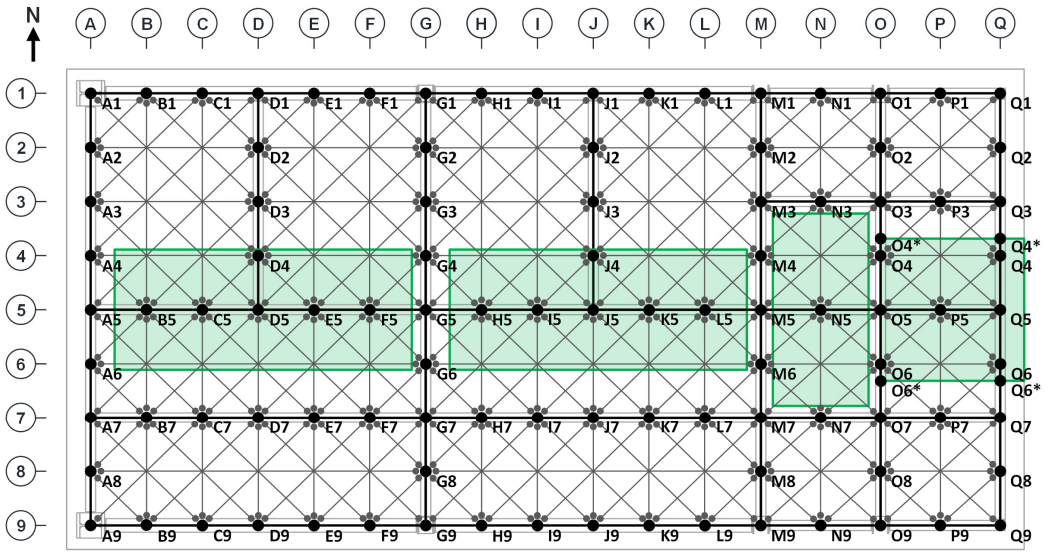

Figure 5.6 Node Layout of Floor Diaghram for Modidied Strip (MS) Model

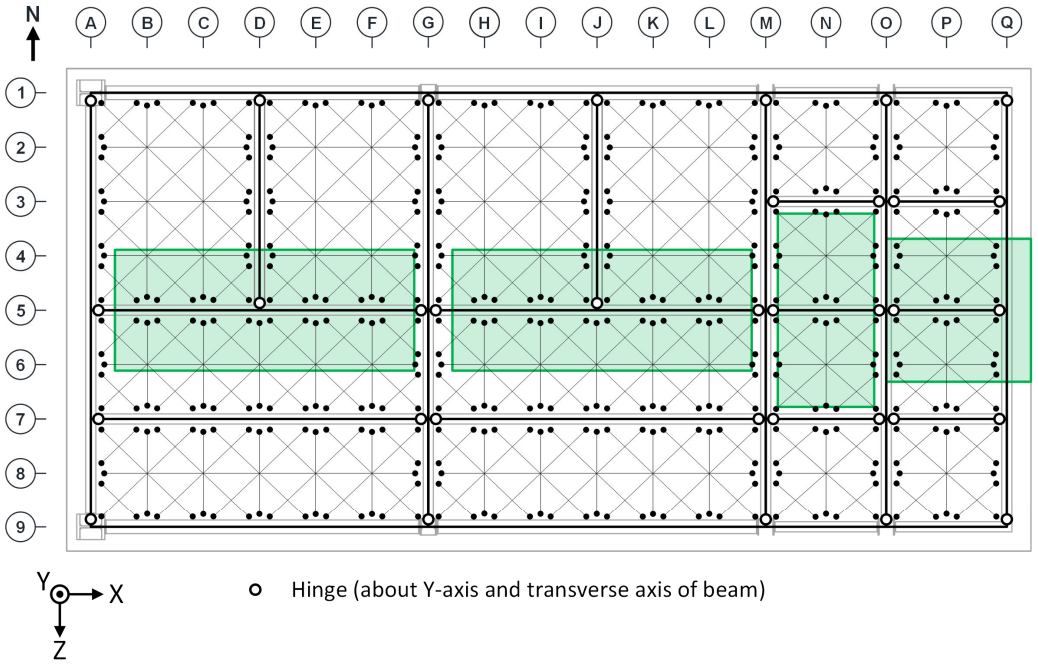

Figure 5.7 Layouts of Floor Beams and Slab Trusses for Modidied Strip (MS) Model

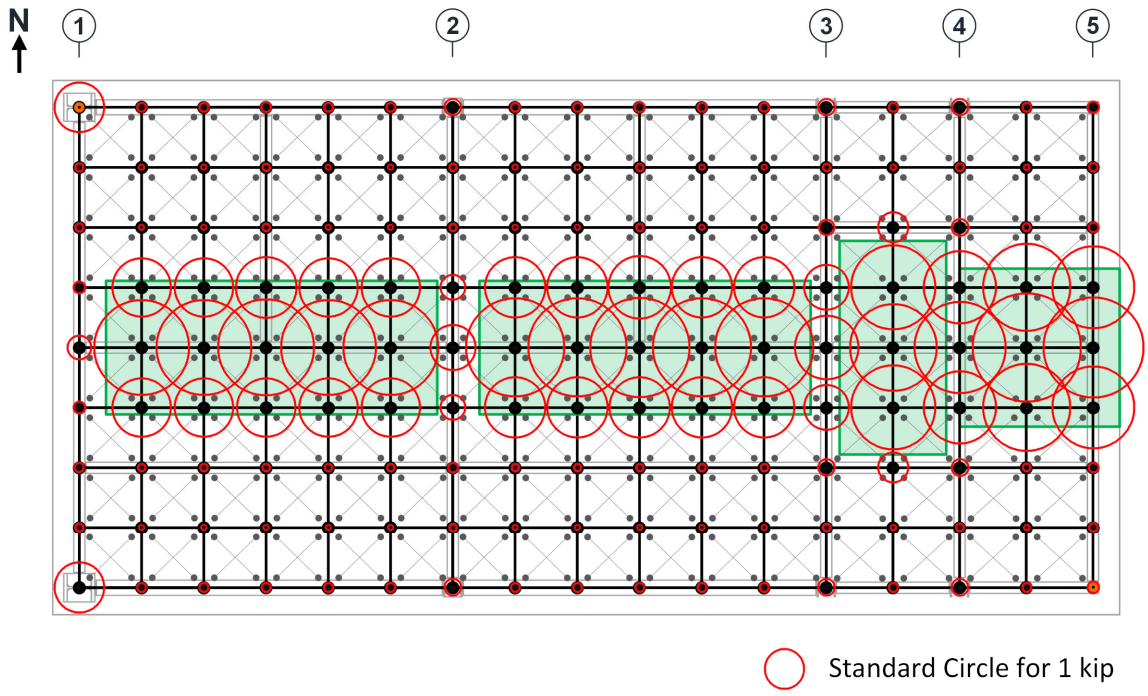

(a) Bema-Truss (BT) Model

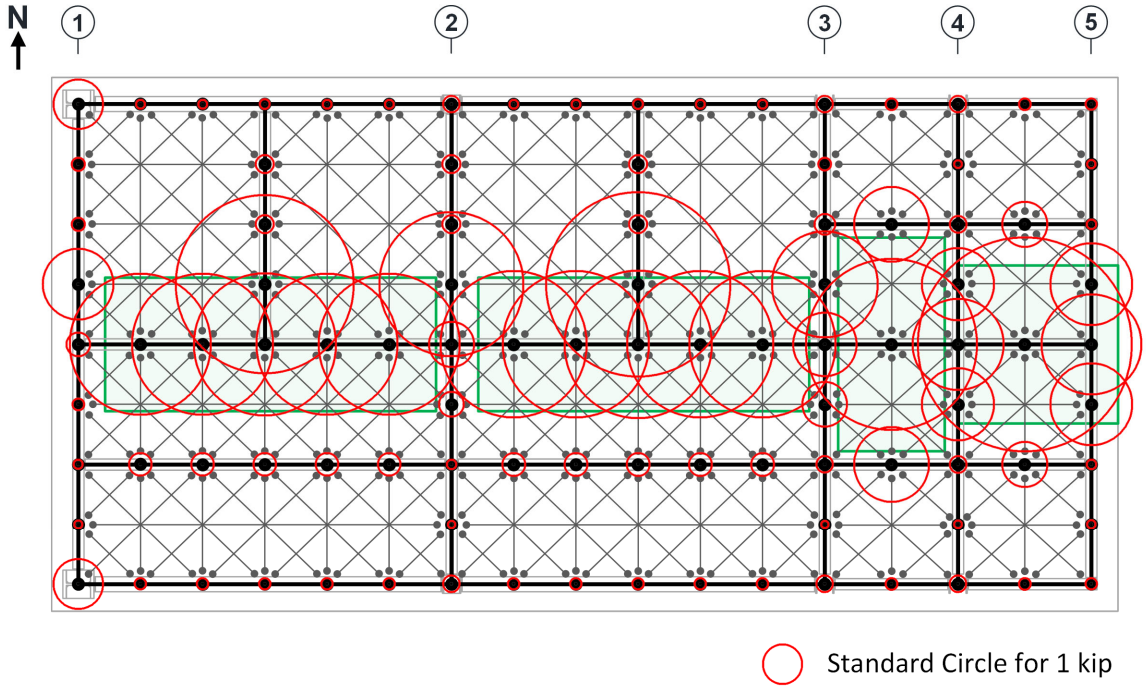

(b) Modified Strip (MS) Model

Figure 5.8 Distributitions of Lumped Nodal Masses in BT Model and MS Model

5.2.3 Modeling of Composite Collectors, Chords, and Floor Beams

The collectors, chords, and floor beams are modeled by using the hinge-model beam-column elements. As the test specimen consisted of a composite floor diaphragm, the collectors, chords, and floor beams acted compositely with the concrete slab. As shown in Figure 4.59, test results on the moment versus rotation responses of the collector connections showed that the composite action from the concrete slab provided a substantial flexural stiffness in positive bending, while the concrete slab contribution to the negative bending stiffness was minimum because no significant tension stress could be developed in the concrete. This leads to a simplification that beam members (collectors, chords, and floor beams) utilized their composite section to resist positive bending, whereas they only relied on the bare steel section to resist negative bending. Figure 4.51 and Figure 4.53 show that, during the shake table testing, the collectors were bent in double curvature, which means that part of the collector resisted positive bending while the rest part was under negative bending. For simplicity, it is assumed that the effective stiffness of the collector beams is the average of the bare steel and composite beam stiffnesses. It is assumed that the shear taken by the concrete slab is negligible such that only the bare steel beam section resists shear. Thus, the cross-sectional properties for the axial and strong-axis flexural actions of the collectors are

$$A_{eff} = \frac{1}{2}\left(A_{comp} + A_s\right) \tag{5.1}$$

$$I_{x,eff} = \frac{1}{2}\left(I_{x,comp} + I_{x,s}\right) \tag{5.2}$$

$$A_{vy,eff} = A_{vy,s} \tag{5.3}$$

where A_{eff}, $I_{x,eff}$, and $A_{vy,eff}$ are the effective (input) cross-sectional area, moment of inertia about strong-axis, and shear area, respectively. A_{comp} and $I_{x,comp}$ are the cross-sectional area and

moment of inertia of the composite section, respectively. These two composite section properties were calculated based on the transformed section with the experimentally determined effective slab widths (see Figure 3.64). Figure 5.9 summarizes the geometries of the collector composite cross sections.

Figure 5.10 and Figure 5.11 show the composite cross sections (with the added mass block sections if it existed) considered for the section properties calculations for longitudinal and transverse floor beams, respectively. The code-prescribed effective slab width (AISC 2016b) is used for the composite sections. The added mass blocks were attached to the concrete slab through post-tension rods in the test frame and the presence of these blocks would increase the stiffness of the floor beams underneath them. For a floor beam with an added mass block above it, the bending stiffness of the block in a transformed-section form was calculated separately, and the total stiffness assigned to that floor beam element was determined from the superposition of the composite beam section stiffness and mass block stiffness. For simplicity and to avoid overestimation of stiffness, the composite action between the floor beam and mass block was ignored.

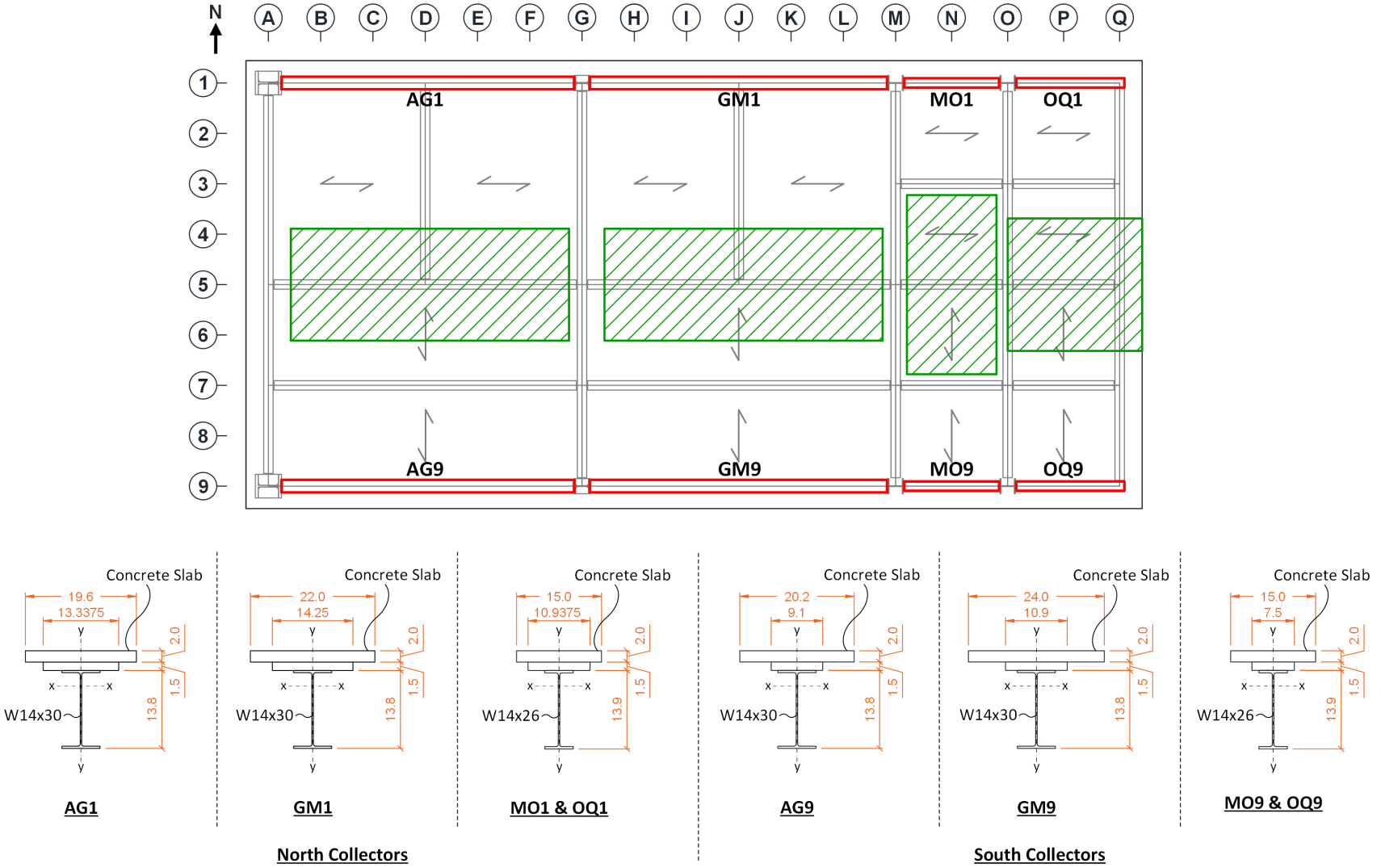

Figure 5.9 Composite Sections for Collector Modeling

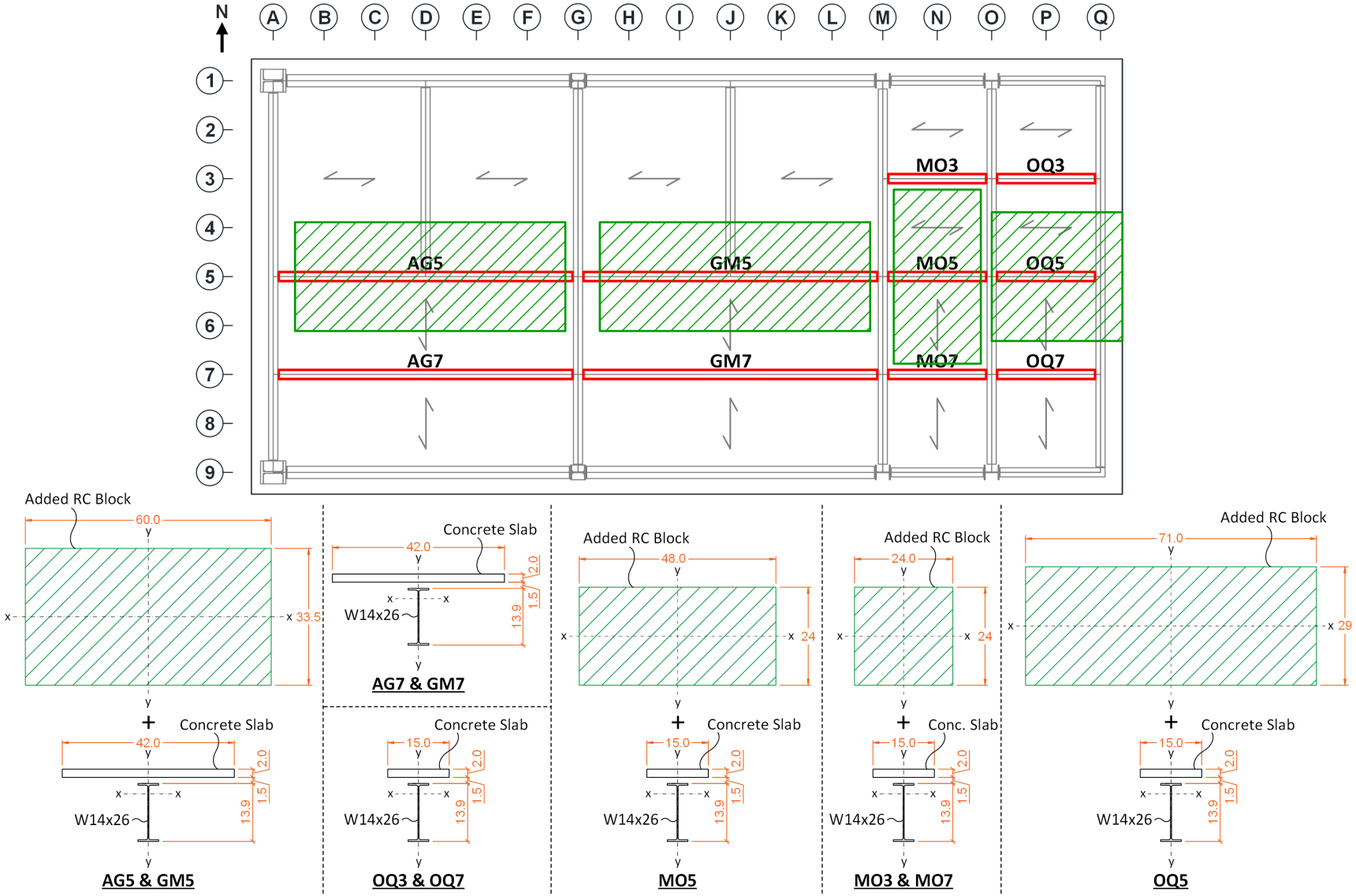

Figure 5.10 Composite Sections for Longitudinal Beam Modeling (with Cross Sections of Added RC Block)

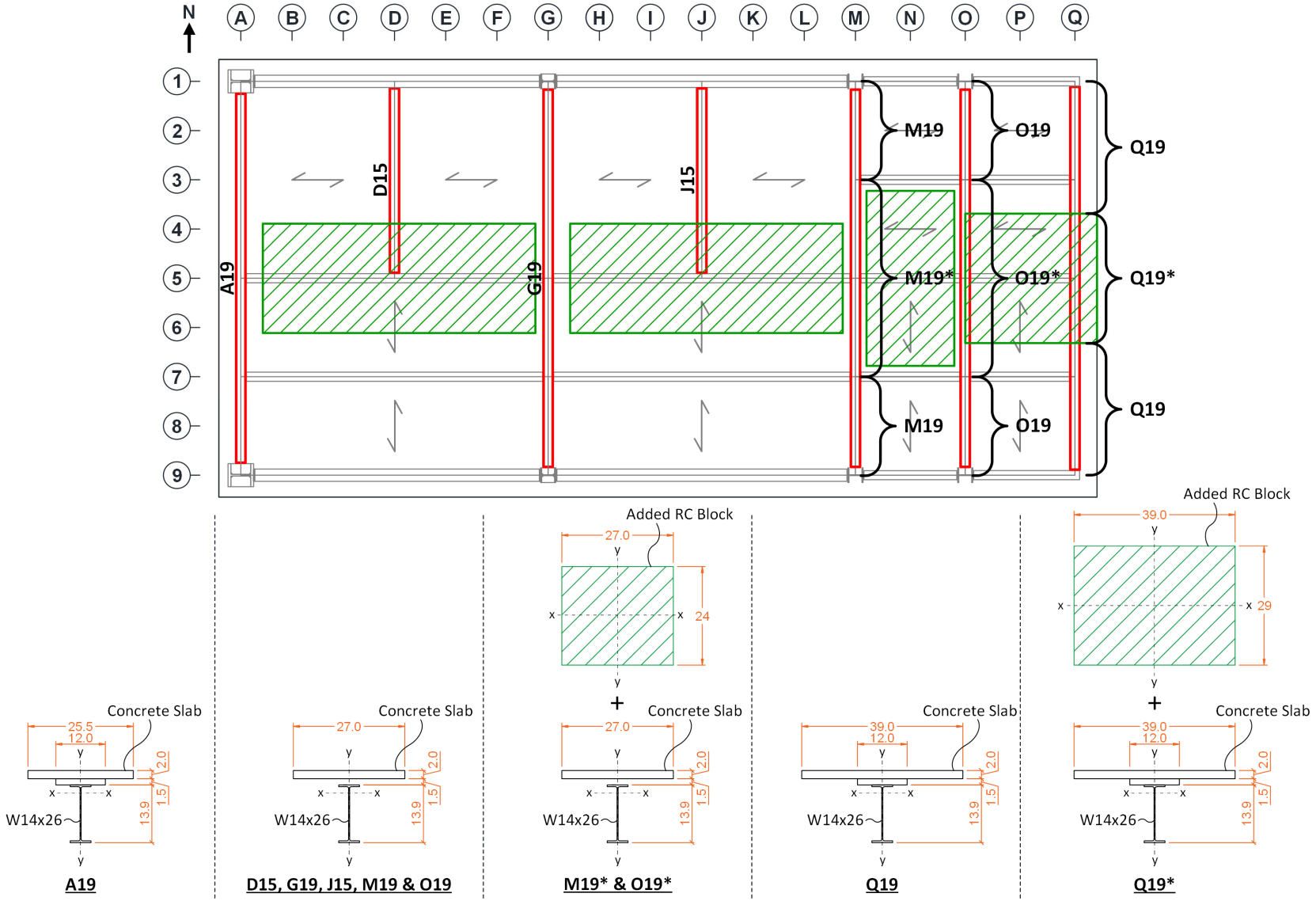

Figure 5.11 Composite Sections Transverse Beam Modeling (with Cross Sections of Added RC Block)

5.2.4 Modeling of Collector-to-Column Connections

Figure 4.59 shows the experimentally determined moment versus rotation responses of collector-to-column connections. Since both steel flanges in the AFW connections were welded to the columns, the AFW connections were modeled as rigid joints. Although the rotational stiffnesses of TFW and BW connections were much lower than that of the AFW connections, these two types of connections still transmitted considerable bending moments. This indicates that TFW and BW connections behaved like semi-rigid connections. In addition, both TFW and BW connections exhibited a nonlinear hysteretic response due to the friction of the bolted connections on the beam web, while the test building remained essentially elastic during Phase 1 testing. This indicates that these two types of connections did not significantly contribute to the overall responses. Hence, a precise simulation of the nonlinear responses for these two collector connections might not be necessary. Instead, a simple model which can capture the general trend of the nonlinear responses at the connections is sufficient for practical applications.

Although TFW and BW connections exhibited a non-symmetric response between positive and negative bending, under cyclic loading the connection on one side of the column was was subjected to positive bending, while the connection on the other side was under negative bending. To simplify the analysis, it is reasonable to model the collector connection by using an elastic rotational spring assigned with a stiffness, $K_{s,avg}$, taken as the average of the secant stiffnesses under positive and negative bending:

$$K_{s,avg} = \frac{1}{2}(K_s^+ + K_s^-) \tag{5.4}$$

To estimate the rotational stiffnesses for the collector connections, this research borrowed the concept of "component-based spring model" proposed by Weigand (2017). Note that the test building essentially stayed within the elastic range during Phase 1 testing and no significant bolt

slippage leading to bolt bearing was observed at the connections. However, the bolt slip in the collector connections did produce nonlinear hysteresis responses. This suggests that the bolts were in a transition stage between "staying still" and "bearing" during the tests. This study used the spring model to estimate the upper-bound and lower-bound stiffnesses for the collector connection moment-rotation behavior. The upper-bound stiffness was derived by assuming the bolts stayed still, while the lower-bound stiffness assumes that the bolts were in bearing at bolt holes throughout Phase 1 testing. For modal analyses, both stiffnesses were used to model the collector connections in the specimen. For the time history analysis simulating Test 1-3, only lower-bound stiffness was used. Table 5.2 and Table 5.3 list the upper-bound and lower-bound stiffnesses for the models. Details of using the spring model approach to estimate the rotational stiffness for collector connections will be presented in Section 5.4.1.

The column panel zone deformation is another source of flexibility for the collector-to-column connection region. Three modeling approaches which can be easily implemented in practice were used. The details of these approaches, representing three levels of modeling complexity (designated as Levels 0, 1, and 2, respectively), are described as follows:

(1) Level 0: The TFW and BW connections are modeled as pin-connections. This approach, which assumes zero stiffness for the collector connections, is commonly used in practice.

(2) Level 1: As shown in Figure 5.12, the TFW and BW connections were modeled by elastic rotational springs. Theses rotational springs were placed at the intersection point between the beam and column centerlines. The column panel zone effect is neglected.

(3) Level 2: As shown in Figure 5.13, the column panel zone is represented by the "scissors model" (Charney and Marshall, 2006), where the beam and column are each modeled as rigid within the panel zone but are allowed to rotate relative to each other to account for the shear

deformation of the panel zone. A rotational spring is placed at the beam-column centerline intersection to connect the rigid elements representing beam and column segments. In addition, the TFW and BW connections were modeled by elastic rotational springs placed at the edge of the panel zone region.

Figure 5.14 shows the panel zone considered for three types of collector connections. The conventional panel zone region for moment frames is used for AFW connections. Concrete slab contributed significantly under positive bending in the TFW and BW connections, and the panel zone might extend upward to the top of the slab. However, the concrete slab contribution is minimum in the negative bending. So far, research on the panel zone modelling for these types of connections is limited. The panel zone regions shown in Figure 5.14 which aligned with the effective area (see Figure 4.32 and Figure 4.33) of the bare steel section near the connection region were used in this research. The rotational stiffness for the panel zone, K_{pz}, was computed as:

$$K_{pz} = G t_{pz} w_{pz} d_{pz} \tag{5.5}$$

where t_{pz}, w_{pz}, and d_{pz} are the thickness, width, and depth of the panel zone, respectively. Table 5.4 summarizes the computed stiffness for panel zone modeling.

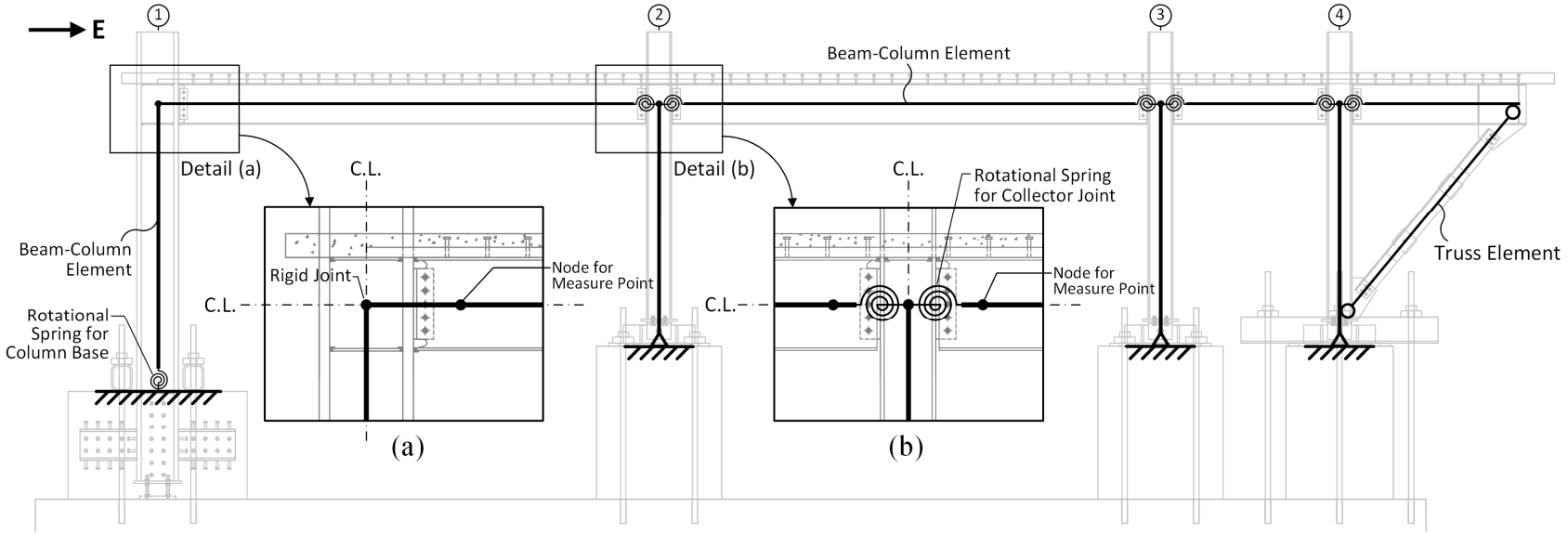

Figure 5.12 Modeling of Logitudinal Frames for Series-1 Models

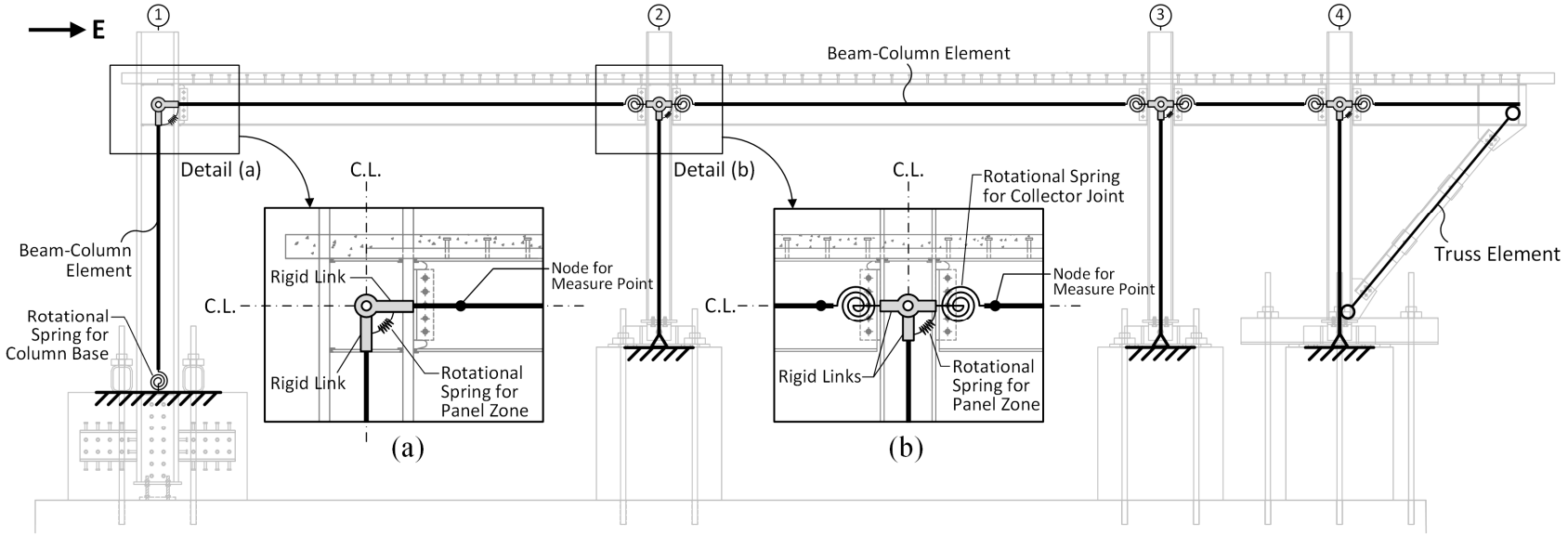

Figure 5.13 Modeling of Logitudinal Frames for Series-2 Models

Table 5.2 Lower-Bound Stiffness for Collector-to-Column Connections

(a) Frame N

			TFW Connections at Column N2		BW Connections at Column N3		BW Connections at Column N4	
			Near-side	Far-side	Near-side	Far-side	Near-side	Far-side
Positive Bending	K_{sj}^{+}	(kip-ft/rad)	33,932	35,156	27,158	24,726	24,726	24,726
Negative Bending	K_{sj}^{-}	(kip-ft/rad)	12,978	12,978	2,097	2,036	2,036	2,036
Averaged Stiffness (Model Input Stiffness)	$K_{sj,avg}$	(kip-ft/rad)	23,455	24,067	14,628	13,381	13,381	13,381

(b) Frame S

Rotational Stiffness			TFW Connections at Column N2		BW Connections at Column N3		BW Connections at Column N4	
			Near-side	Far-side	Near-side	Far-side	Near-side	Far-side
Positive Bending	K_{sj}^{+}	(kip-ft/rad)	34,187	35,992	26,934	24,354	24,354	24,354
Negative Bending	K_{sj}^{-}	(kip-ft/rad)	12,978	12,978	2,097	2,036	2,036	2,036
Averaged Stiffness (Model Input Stiffness)	$K_{sj,avg}$	(kip-ft/rad)	23,583	24,485	14,516	13,195	13,195	13,195

Table 5.3 Upper-Bound Stiffness for Collector-to-Column Connections

(a) Frame N

			TFW Connections at Column N2		BW Connections at Column N3		BW Connections at Column N4	
			Near-side	Far-side	Near-side	Far-side	Near-side	Far-side
Positive Bending	K_{sj}^{+}	(kip-ft/rad)	258,860	266,942	266,535	233,807	233,807	233,807
Negative Bending	K_{sj}^{-}	(kip-ft/rad)	126,914	126,914	37,807	37,807	37,807	37,807
Averaged Stiffness (Model Input Stiffness)	$K_{sj,avg}$	(kip-ft/rad)	192,887	196,928	152,171	135,807	135,807	135,807

(b) Frame S

			TFW Connections at Column N2		BW Connections at Column N3		BW Connections at Column N4	
			Near-side	Far-side	Near-side	Far-side	Near-side	Far-side
Positive Bending	K_{sj}^{+}	(kip-ft/rad)	257,845	270,959	270,877	228,531	228,531	228,531
Negative Bending	K_{sj}^{-}	(kip-ft/rad)	126,914	126,914	37,807	37,807	37,807	37,807
Averaged Stiffness (Model Input Stiffness)	$K_{sj,avg}$	(kip-ft/rad)	192,380	198,937	154,342	133,169	133,169	133,169

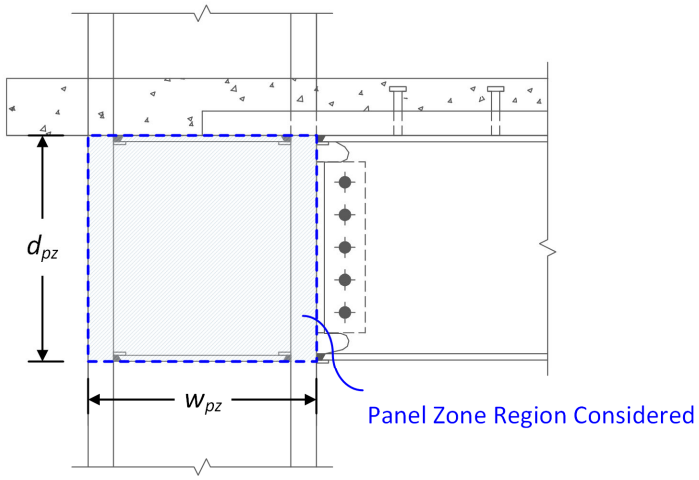

(a) AFW Connection

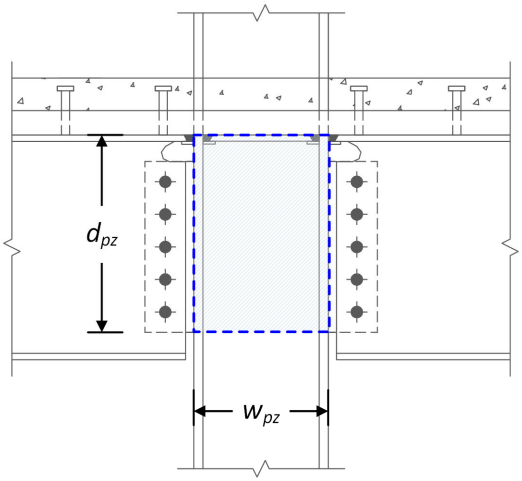

(b) TFW Connection

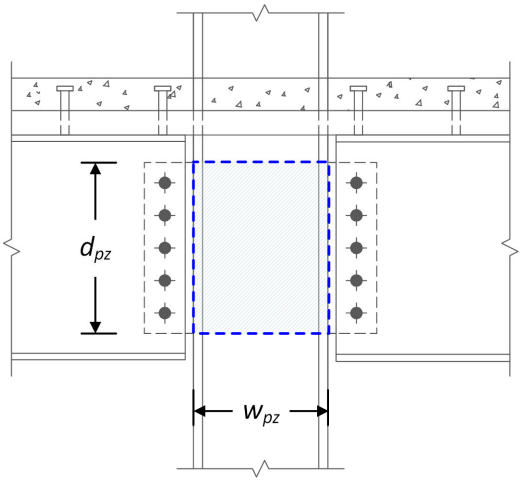

(c) BW Connection

Figure 5.14 Panel Zone for Three Types of Collector Connections

Table 5.4 Stiffness for Column Panel Zone Rotational Springs

		Panel Zone at		
		AFW Connection	TFW Connection	BW Connection
d_{pz}	(in.)	13.8	12.125	10.5
w_{pz}	(in.)	14	8.25	8.25
t_{pz}	(in.)	0.96	0.36	0.36
K_{pz}	(kip-in./rad)	2,068,726	401,664	347,833
	(kip-ft./rad)	172,394	33,472	28,986

5.2.5 Other Modeling Details

Columns in the specimen models were represented by hinge model beam-column elements. As shown in Figure 5.12 and Figure 5.13, an elastic rotational spring was added at the bottom end of each cantilever column at Column Line 1 to account for the deformation taking place at the embedded column base connection in the RC footing, while pin base was assigned to the remaining columns. The double-angle braces in the longitudinal and transverse directions of test building were modeled by using truss elements. In order to compare the simulation results with the measured moment-rotation responses for the collector connections, nodes representing the measuring locations near the collector ends were also added to the model for a direct output of the simulated results.

The reference lines of the beam members (collectors, chord, and floor beams) were set at the elevation of steel beam centerline. For simplicity, the BT model or modified strip model which represent the composite slab floor diaphragm was aligned with beam reference line elevation. The majority of the added mass was placed in the middle portion of the floor diaphragm, and the center of gravity (CG) of the added mass blocks were located considerably above the beam centerline. To achieve an accurate representation of the mass distribution, a series of "added mass nodes" were created at the elevations aligned with CGs of added mass blocks (see Figure 5.1 and Figure 5.2). Each added mass node was connected to a node on the floor diaphragm through a rigid beam element. In addition, longitudinal and transverse truss elements were placed horizontally between the added mass nodes to represent the axial stiffnesses of added mass blocks in the longitudinal and transverse directions, respectively.

5.3 Analysis Results

5.3.1 Modal Analysis Results

Modal analyses were carried out for six specimen models. Table 5.5(a) tabulates the results that used the lower-bound rotational spring stiffnesses to represent the TFW and BW collector connections, while Table 5.5(b) lists the results for upper-bound stiffnesses. In addition, Table 5.5 compares the analytical and experimental determined periods for the first two modes. From Table 5.5, it can be found that Models BT-0 and MS-0, which as a common practice use pins to represent the collector connections would overpredict noticeably the fundamental period. The ratio of the analytical to experimental periods is about 1.23.

The remaining four models, all of which employed rotational springs to simulate the semi-rigid collector connections, satisfactorily predict the periods of the structure. This validates the two proposed approaches (designated as Levels 1 and 2 analyses) for modeling the collector connections. The closeness of the analytical results between models Series-1 and Series 2 models (i.e., BT1 versus BT2; and MS-1 versus MS-2) indicates that the simplification made in Level 1 approach, which places the rotational springs for collector connections at the intersection point of the beam-to-column centerlines, can be used to estimate the combined responses from the collector connections and the adjacent column panel zone.

The four models (BT-1, BT-2, MS-1, and MS-2) with the upper-bound rotational stiffness provides an excellent correlation to the measured fundamental period. By contrast, the lower-bound solution slightly overestimates the fundamental period by about 6%. Note that the measured period was based on the white noise test. However, as presented in Section 5.4.1, a comparison of the experimental moment-rotation responses of collector connections shows that the lower-bound solution provides a better estimation for Test 1-3. Note that the peak floor acceleration from the

white noise test was about 0.15 g, while the peak floor acceleration from Test 1-3 reached 1.65 g. It expected that the upper-bound solution predicts better the specimen response in a white noise test because bolts at collector connections do not slip. On the other hand, the lower-bound solution would provide a better prediction for Test 1-3 because the bolts at collector connections experienced some friction slip during the stronger shaking. Thus, it is difficult to derive a linearly elastic model that applies to all intensity levels of shaking. For a TFW or BW connection, note that the upper-bound stiffness is about eight times that of the lower-bound stiffness for a collector (see Table 5.2 and Table 5.3). However, modal analysis results (Table 5.5) show that the specimen periods predicted by either approach are very similar. This implies that these semi-rigid collector connections did not contribute significantly to the global responses and, as a result, some error in the estimation of connection stiffness is acceptable.

Figure 5.15 shows the first two mode shapes of Model BT-2. Figure 5.15(a) shows the nine degrees of freedom (DOFs) of interest for the mode shapes. The 1st mode is mainly the translation mode in the longitudinal direction. Note that the vertical displacement (DOF 9) at the mid-span of east chord is large than the horizontal displacement (DOF 3). This indicates that the 1st mode was accompanied with a significant vertical movement of the cantilever slab at the east end of the specimen. Figure 5.15(c) shows that the 2nd mode was mainly dominated by the vertical motion of the cantilever portion of the floor diaphragm.

Table 5.5 Modal Analysis Results

(a) with Lower-Bound Rotational Stiffness for Collector-to-Column Connections

			Analysis					
		Experiment	BT-Series Models			MS-Series Models		
			BT-2	BT-1	BT-0	MS-2	MS-1	MS-0
Mode 1	Period (sec)	0.179	0.189	0.190	0.220	0.188	0.189	0.219
	Frequency (Hz)	5.600	5.287	5.263	4.539	5.319	5.294	4.556
	T_{ANA}/T_{EXP}*		1.059	1.064	1.234	1.053	1.058	1.229
Mode 2	Period (sec)	0.089	0.095	0.095	0.096	0.089	0.089	0.089
	Frequency (Hz)	11.20	10.53	10.53	10.43	11.24	11.24	11.18
	T_{ANA}/T_{EXP}*		1.064	1.064	1.073	0.996	0.996	1.002

(b) with Upper-Bound Rotational Stiffness for Collector-to-Column Connections

			Analysis					
		Experiment	BT-Series Models			MS-Series Models		
			BT-2	BT-1	BT-0	MS -2	MS -1	MS-0
Mode 1	Period (sec)	0.179	0.178	0.178	0.220	0.176	0.177	0.219
	Frequency (Hz)	5.600	5.612	5.628	4.539	5.672	5.654	4.556
	T_{ANA}/T_{EXP}*		0.998	0.995	1.234	0.987	0.990	1.229
Mode 2	Period (sec)	0.089	0.095	0.095	0.096	0.089	0.089	0.089
	Frequency (Hz)	11.20	10.56	10.55	10.43	11.26	11.27	11.18
	T_{ANA}/T_{EXP}*		1.061	1.061	1.073	0.994	0.994	1.002

*Experimental period based on white noise test after Test 1-3

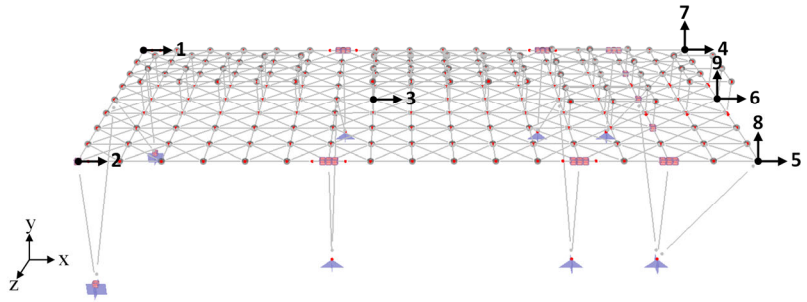

(a) Degrees of Freedom of Interest

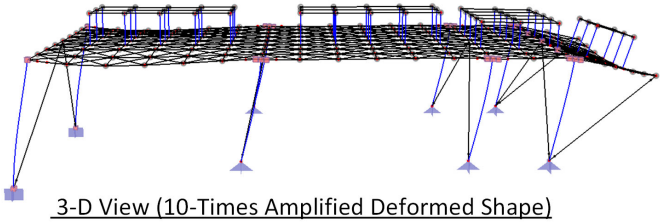

3-D View (10-Times Amplified Deformed Shape)

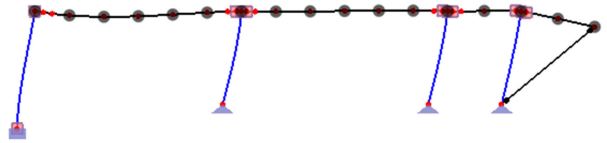

Front View (10-Times Amplified Deformed Shape)

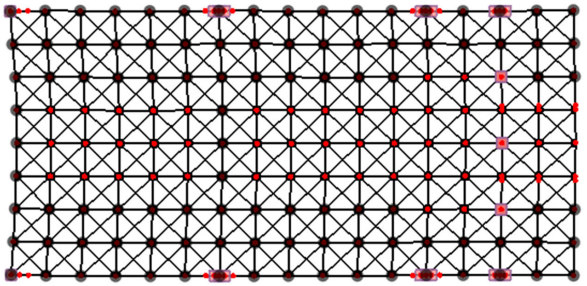

Top View (30-Times Amplified Deformed Shape)

$$\begin{bmatrix} u_1 \\ u_2 \\ u_3 \\ u_4 \\ u_5 \\ u_6 \\ u_7 \\ u_8 \\ u_9 \end{bmatrix} = \begin{bmatrix} 0.888 \\ 0.901 \\ 1.000 \\ 0.968 \\ 0.971 \\ 1.005 \\ -0.776 \\ -0.777 \\ -1.215 \end{bmatrix}$$

(b) 1st Mode

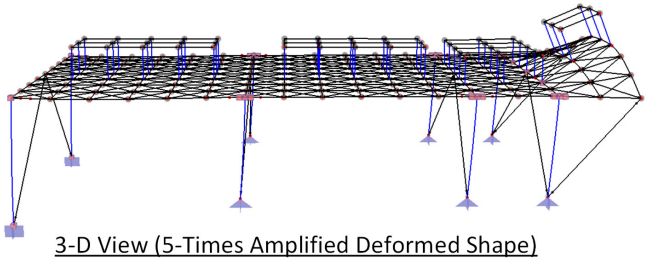

3-D View (5-Times Amplified Deformed Shape)

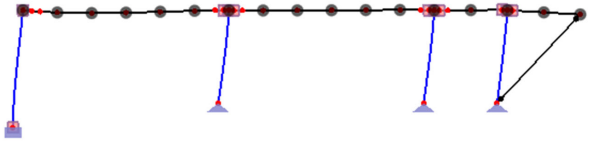

Front View (10-Times Amplified Deformed Shape)

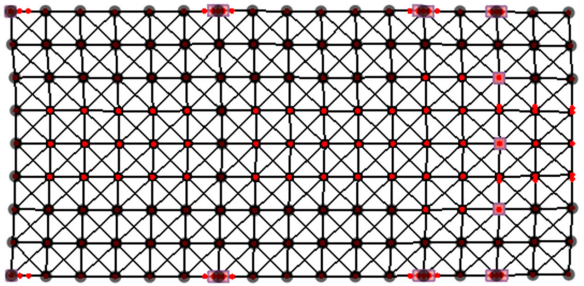

Top View (30-Times Amplified Deformed Shape)

$$\begin{bmatrix} u_1 \\ u_2 \\ u_3 \\ u_4 \\ u_5 \\ u_6 \\ u_7 \\ u_8 \\ u_9 \end{bmatrix} = \begin{bmatrix} 0.152 \\ 0.155 \\ 0.177 \\ 0.145 \\ 0.146 \\ 0.163 \\ -0.063 \\ -0.063 \\ 1.000 \end{bmatrix}$$

(c) 2nd Mode

Figure 5.15 Model BT-2: Mode Shapes

5.3.2 Time History Analysis Results on Global Responses

Time history analyses were conducted to simulate Test 1-3. The measured shake table acceleration was used as the input motion. The Newmark method with the constant average acceleration scheme ($\beta = 1/4$) and with a time step size of 1/512 second was used for integration. Rayleigh damping ratios were assumed as 3% and 4.5% for the 1st and 2nd modes, respectively. The 3% damping for the 1st mode was based on the measured damping from Phase 1 impulse tests. The 4.5% damping for the 2nd mode was used to achieve a good representation of the vertical motion of the cantilever slab in the east end of test specimen, which was based on a parametric study on the 2nd mode damping. Model BT-2 with the lower-bound solution for the rotational springs of the semi-rigid (i.e., TFW or BW) collector connections was used.

Figure 5.16 shows that the analytical floor acceleration follows the experimental results very well but with a slight underestimation on the peak responses in both positive and negative directions. Likewise, Figure 5.17 shows that Model BT-2 predicts the story drift angle response very but slightly underestimates the positive peak response.

Figure 5.18 shows a comparison of the vertical acceleration at the mid-span of east chord. Note that this motion itself is not of main interest in this study. However, the effect of this vertical vibration on the forces in the collectors needs to be clarified first. Figure 5.18(a) and Figure 5.18(d) show that the analytical model fairly captures the test results in the time- and frequency-domains. Although the analytical results overshoot the peak responses [see Figure 5.18(b)] and a plot [Figure 5.18(c)] of analytical versus test responses for this action exhibited a moderately strong, but not perfect, linear relationship (with a R^2 = 0.806), the modeling accuracy for this motion is considered sufficient. This can be further justified by the general resemblance between the analytical and experimental results (see Figure 5.19) on the relationship of vertical acceleration at

mid-span of east chord versus horizontal acceleration near the mass center of floor diaphragm. Both experimental and analytical results show that there is no significant correlation between these two acceleration responses. In addition, Figure 5.19(a) shows that, in the test specimen, the magnitude of the vertical acceleration was relatively small at the instant of peak floor acceleration for both positive and negative directions. As shown in Figure 5.19(b), a similar observation can be made from the analytical result. It suggests that the unintended vertical motion of the cantilever span would not significantly affect the force demands in the collectors at the instant of peak floor accelerations. Therefor, measured responses of the collectors and their connections are not "contaminated" by the vertical vibration of the cantilever slab.

Figure 5.20 shows a comparison of the global response. Both responses show that the specimen responded elastically during Test 1-3. A comparison of the slopes of linear regression lines indicates that the analytical model slightly overestimates the overall lateral stiffness of test frame. Figure 5.21 shows the percentage of story shears resisted by the columns and one diagonal brace. Results from the analytical model correlate well with the numerical simulation.

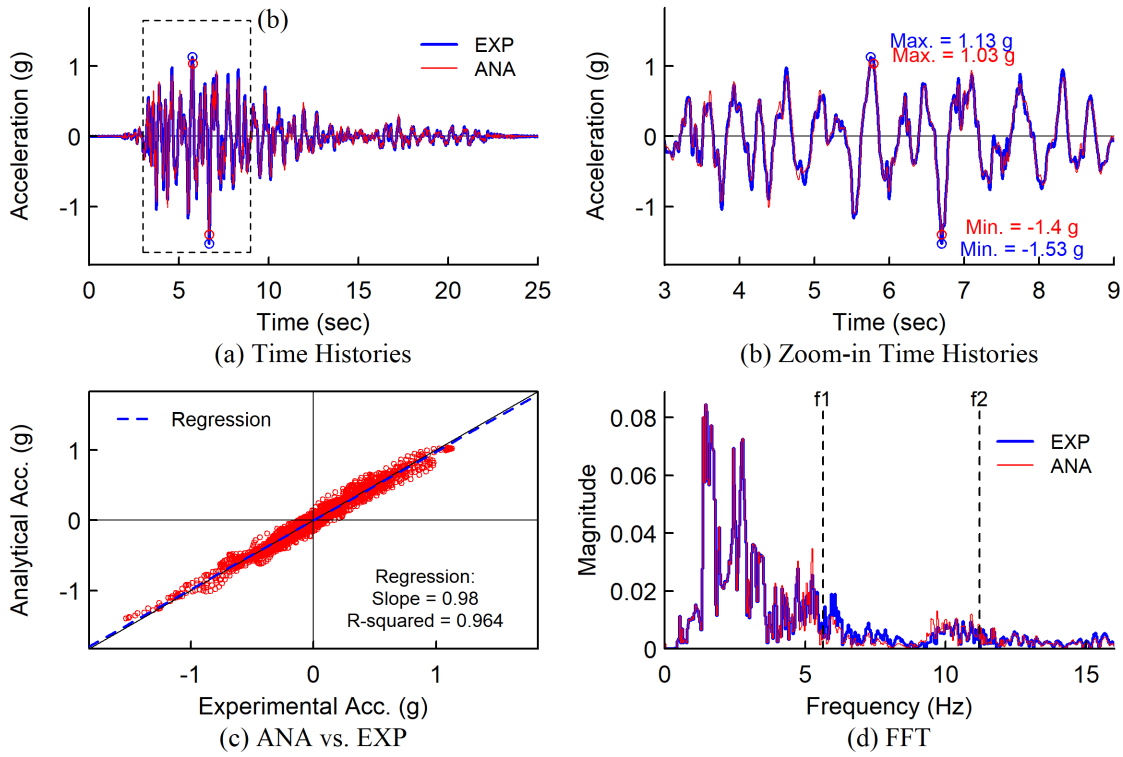

Figure 5.16 Model BT-2: Comparison of Experimental and Analytical Floor Accelerations

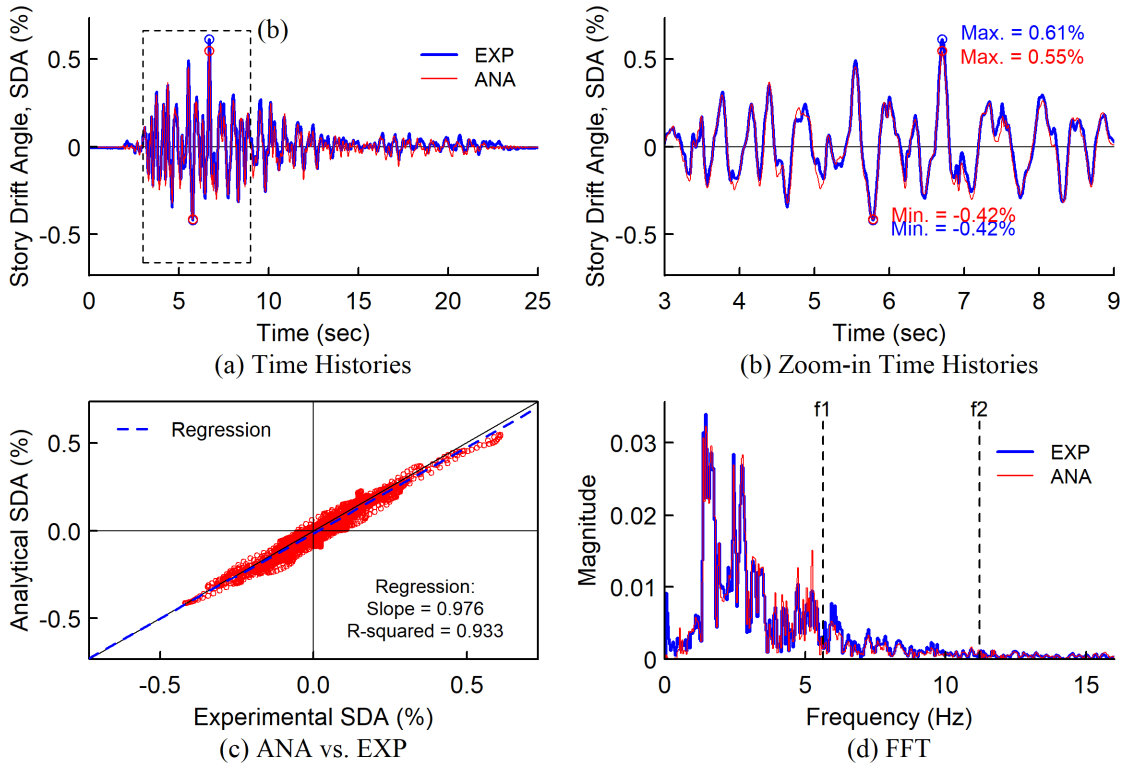

Figure 5.17 Model BT-2: Comparison of Experimental and Analytical Story Drift Angles

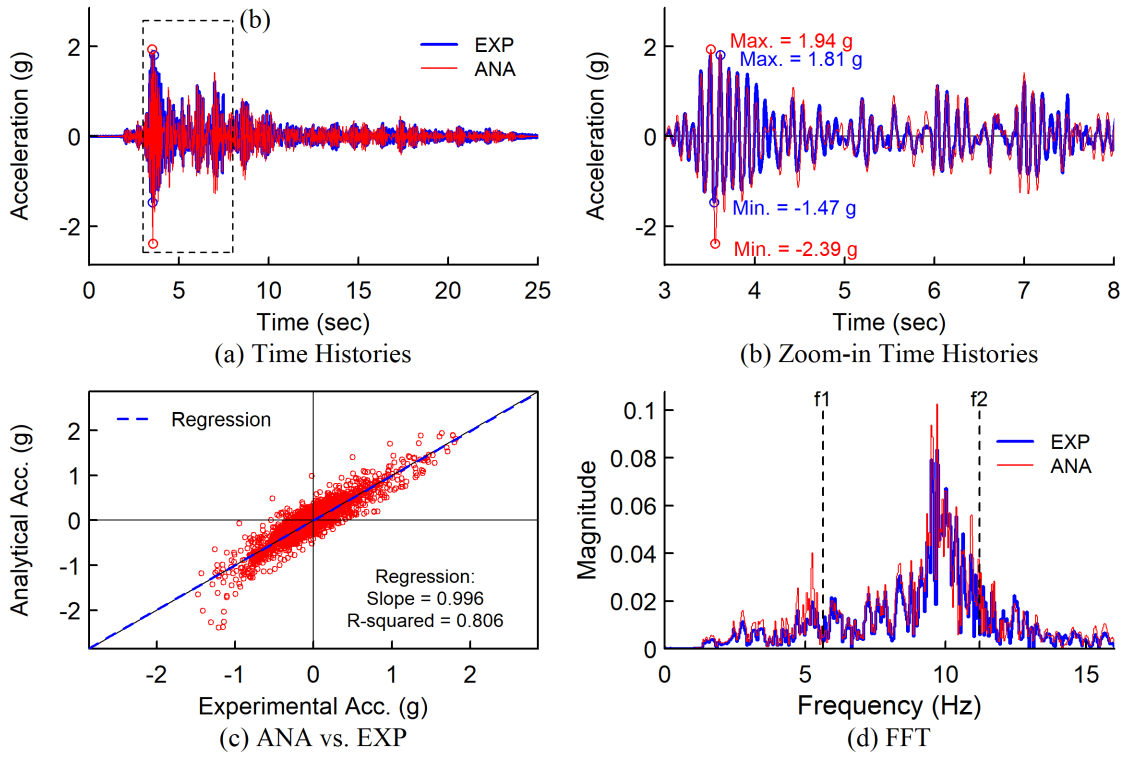

(a) Time Histories (b) Zoom-in Time Histories

(c) ANA vs. EXP (d) FFT

Figure 5.18 Model BT-2: Comparison of Experimental and Analytical Vertical Accelerations at Mid-span of East Chord

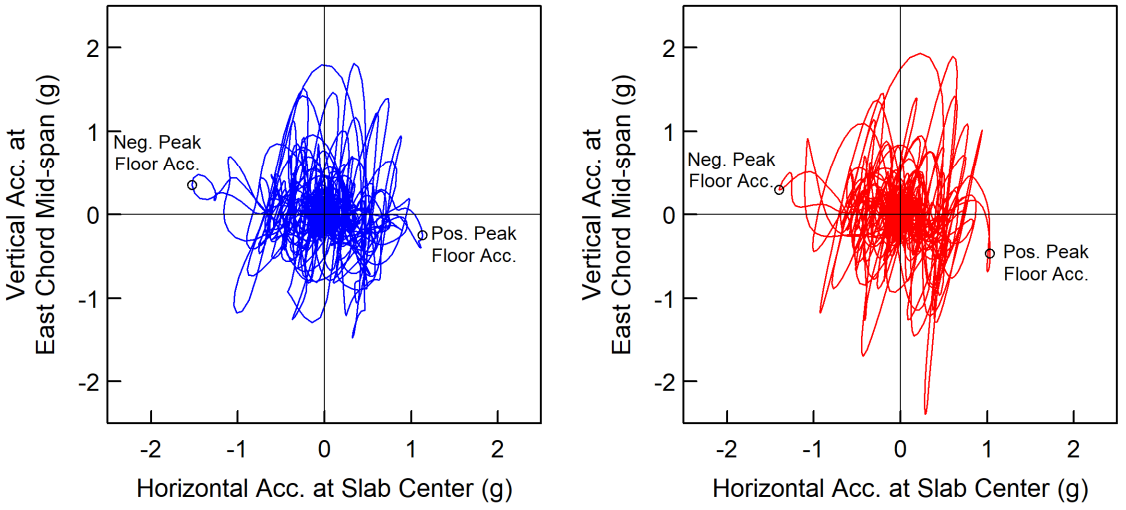

(a) Experiment (b) Analysis

Figure 5.19 Model BT-2: (a) Experimantal and (b) Analytical Reuslts on Vertical Acceleration at East Chord versus Horizontal Floor Acceleration Relationships

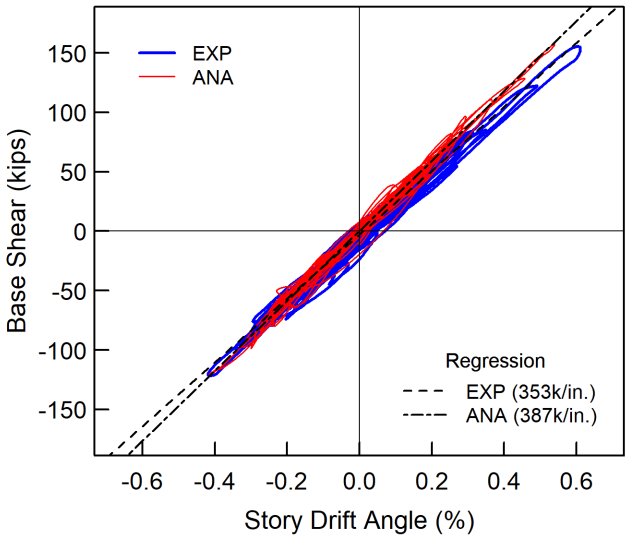

Figure 5.20 Model BT-2: Comparison of Experimental and Analytical Results on Base Shear versus Story Drift Relationships

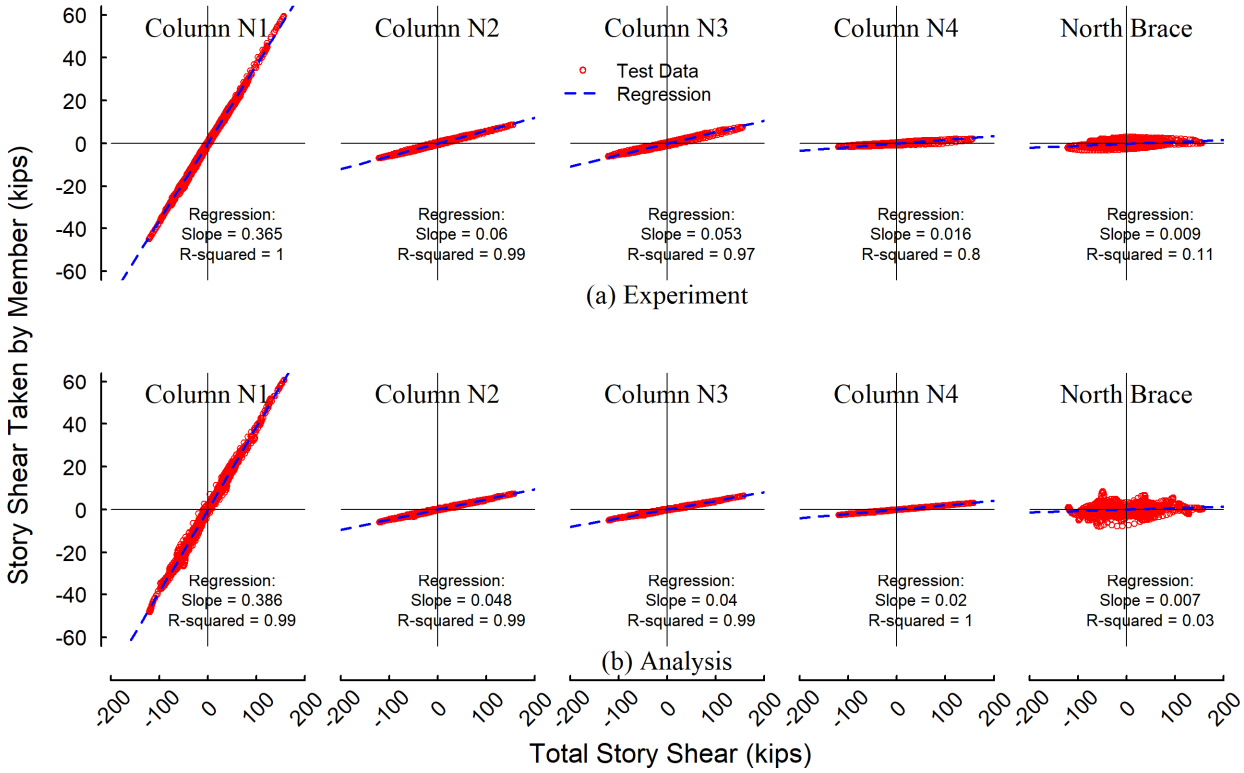

Figure 5.21 Model BT-2: Experimental and Analytical Results on Relationships of Story Shears Taken by Members versus Total Story Shear (Frame N)

5.3.3 Time History Analysis Results on Collector Responses

Figure 5.22 and Figure 5.23 show a comparison of the collector internal forces (axial force and moment) at the instants of positive and negative peak floor accelerations, respectively. The experimental axial force diagrams shown herein were determined based on a varying effective slab width along the collector lines, a topic to be presented in Section 5.4.3. In addition, since the analytical model slightly underestimates the peak floor acceleration responses of the test specimen, the test responses shown in these two figures are not at the exactly peak acceleration points from the test. Instead, at an instant near the actual peak accelerations when the experimental floor acceleration matches the analytical peak acceleration was selected for plotting the experimental collector member forces.

Figure 5.22 and Figure 5.23 show that the trend of analytically predicted collector forces matches that from the experimental results. The experimental data in the span of Collector 2 did show a slightly zigzag pattern. Since the magnitude of axial force in this span was very low and the experimental axial force was computed from the strain gauge data. Noise in the measured strain at such low strain level might have affected the accuracy of the computed axial forces.

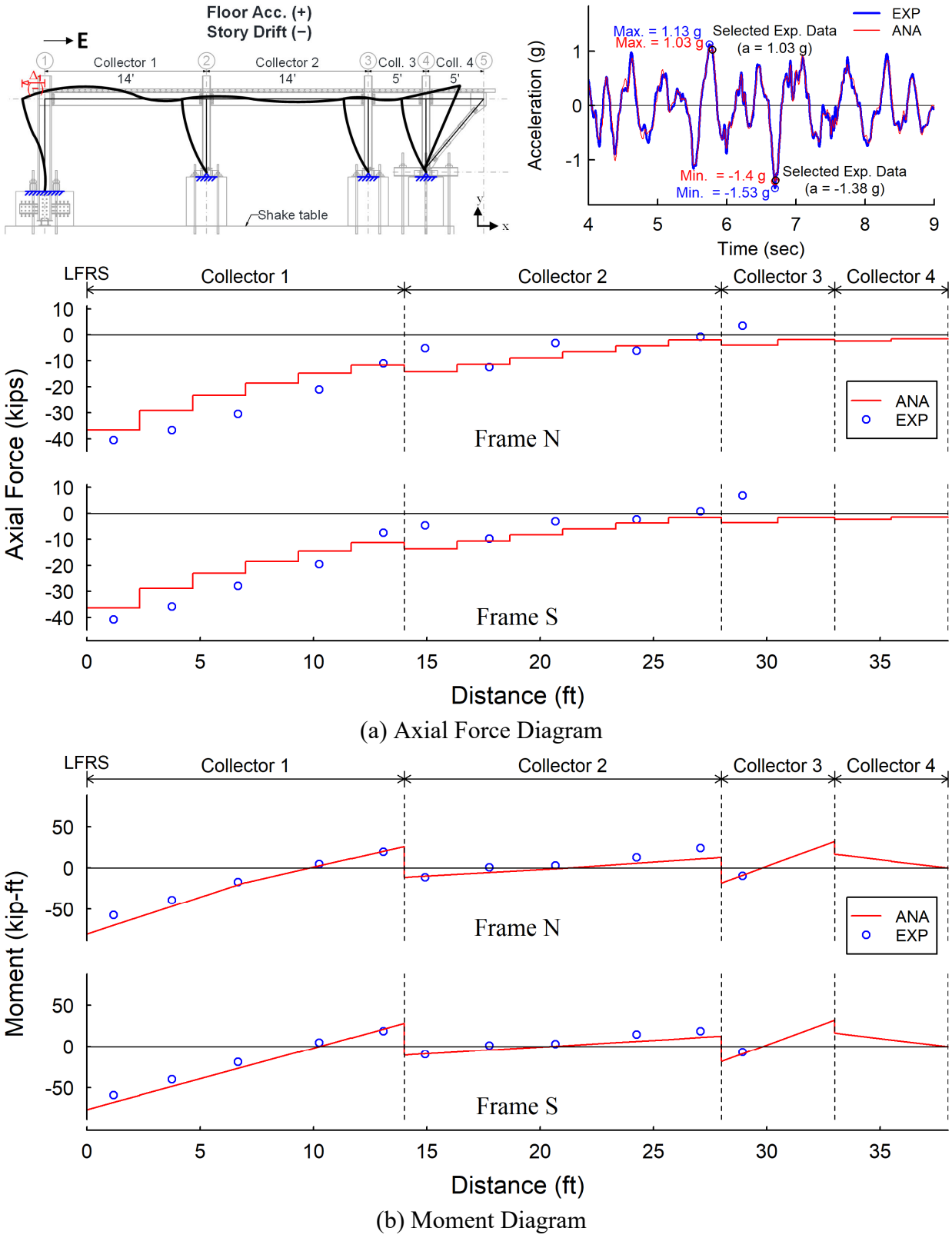

(a) Axial Force Diagram

(b) Moment Diagram

Figure 5.22 Model BT-2: Comparison of Experimental and Analytical Results on Collector Forces (at Positive Peak Acceleration)

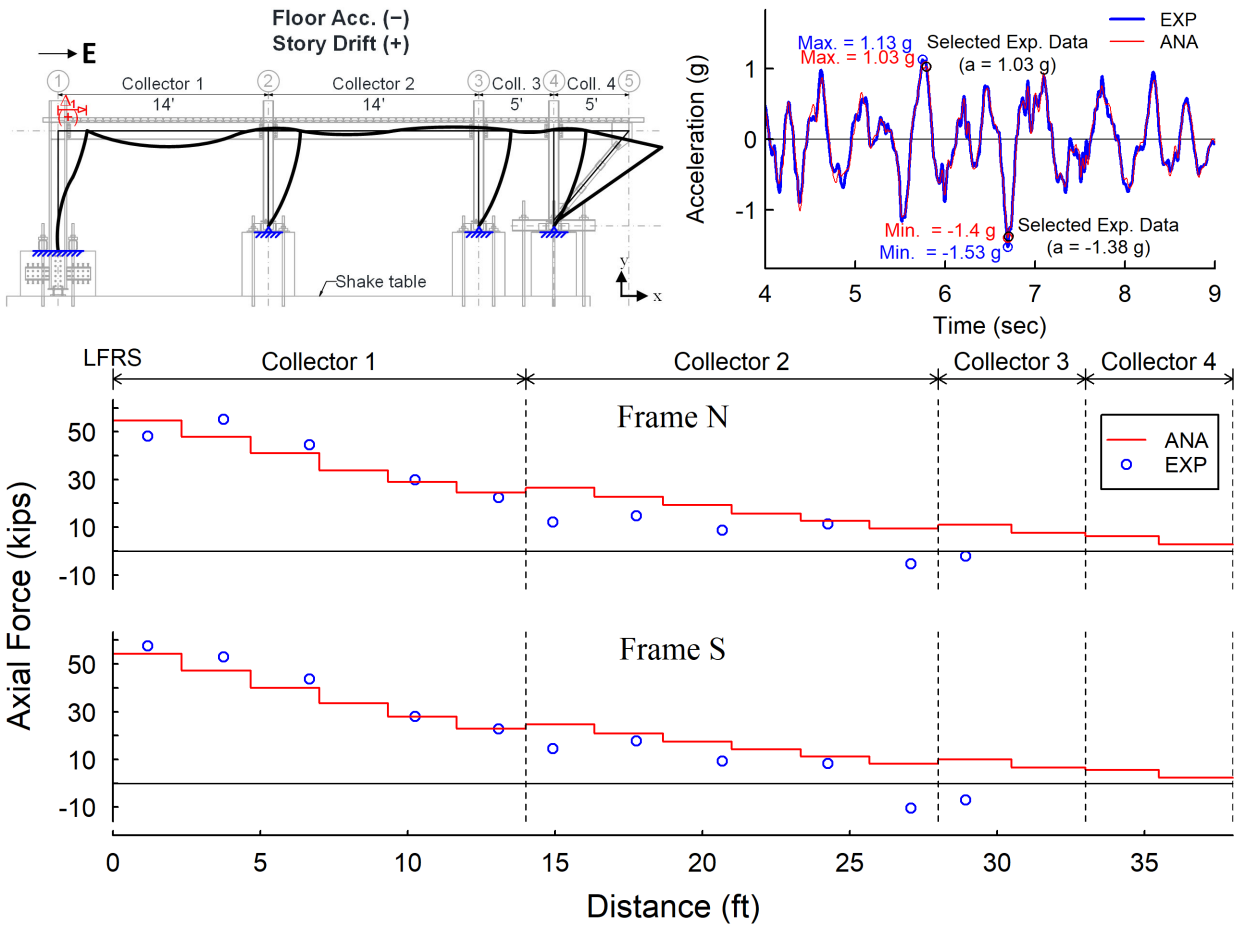

(a) Axial Force Diagram

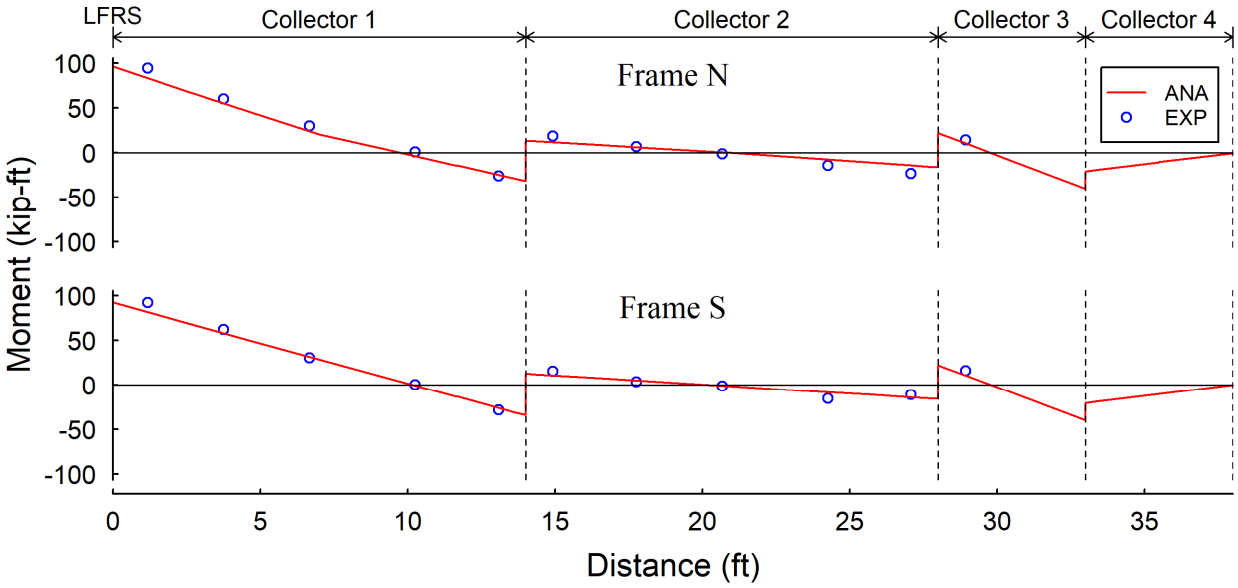

(b) Moment Diagram

Figure 5.23 Model BT-2: Comparison of Experimental and Analytical Results on Collector Forces (at Negative Peak Acceleration)

5.3.4 Time History Analysis Results on Load Path of Diaphragm Force

In this section, some detailed analytical responses from Model BT-2 which could not be determined from test due to the physical limitations of the instrumentation are used to explore the load path in the floor diaphragm.

Figure 5.24(a)-top and Figure 5.24(b)-top show the analytically predicted deformed shape of the floor diaphragm at the instants of positive and negative peak accelerations, respectively. Based on the extent of the deformation of the subpanels, it can be found the highest local shear deformation takes place near the LFRS, while the deformation of the subpanels at the east end of the diaphragm is relatively small. This implies that, when the floor diaphragm is subjected to in-plane inertial forces, LFRSs (i.e., cantilever columns at Northwest and Southwest corners of the test frame) serve as supports to the slab and the east end of the slab is like a free end. High reaction forces provided by the LFRSs were concentrated at the two corners at the west end of the slab, resulting in a stress and deformation concentration of the concrete slab near these two corners.

As shown in Figure 5.24(a)-top, several diagonal slab trusses that are in compression when the floor diaphragm is subjected to a positive acceleration are selected and their axial force-deformation responses for Test 1-3 are presented in Figure 5.24(a)-bottom. Comparing the responses of these compression-only trusses, it can be found that as the truss is located closer to the LFRS, it reaches the higher compressive force. Similarly, as shown in Figure 5.24(b)-top, several trusses that are in compression when the slab is subjected to a negative acceleration are selected and their responses are plotted in Figure 5.24(b)-bottom. The same conclusion regarding the force level and location can be made.

Figure 5.25(a) and (b) show the distribution of shear flow in the slab along the collector lines at the instants of positive and negative peak accelerations, respectively. As illustrated in

Figure 5.25-top, the slab shear flow was determined by using the horizontal component of the axial forces in the diagonal trusses next to the collector lines. (Note that, theoretically, shear forces in the fictitious beams next and perpendicular to the collector lines should be included in the calculation of shear flow. However, the fictitious beam shear is zero because they are pin-ended in the in-plane direction.) In Figure 5.25, a uniform shear flow denoted as "Design" is plotted. This design shear flow is determined by assuming the all the inertial force in the slab region is transmitting to the collector lines through a uniform shear flow along the collector at each side. Thus, the design slab shear flows along the north and south collector lines, respectively denoted as $\overline{v'_N}$ and $\overline{v'_S}$, are

$$\begin{cases} \overline{v'_N} = \overline{w'_N} \cdot \left(\frac{a_{flr}}{g}\right) \\ \overline{v'_S} = \overline{w'_S} \cdot \left(\frac{a_{flr}}{g}\right) \end{cases} \tag{5.6}$$

where $\overline{w'_N}$ and $\overline{w'_S}$ are the averaged linear weights distributed over north and south collector lines, respectively, and a_{flr} is the floor acceleration.

The analysis shows that the distribution of slab shear flow acting along the collector is non-uniform regardless of the direction of floor acceleration (see Figure 5.25). The nearer the LFRS, the higher the shear flow and the faster the shear flow increases. This is consistent with the slab resulting deformation pattern shown in Figure 5.24. Along a collector line, the shear flow, with a magnitude smaller than the design shear flow, increases gradually from the far end (east end) to the LFRS end (west end) over the collector spans 4, 3, and 2, before it increases at a much faster rate and exceeds the design value in the collector span 1. This implies that in the region away from the LFRS, such as in the range of collector spans 2, 3, and 4, a certain portion of the inertial force is transmitted directly in the longitudinal direction before it makes turns and flows into the last collector span (collector 1).

The non-uniform slab shear distribution is also related to the mass layout and the inertial force load path in the floor diaphragm. For the slab shear distribution [Figure 5.25(a)] occurring at the instant of positive peak acceleration, at which time the inertial force acts toward the LFRS (the west) and the collectors are in compression, the highest slab shear flow occurs next to the LFRS and reaches 3.8 kips/ft, which is approximately 2.5 times the design value (about 1.5 kips/ft). On the other hand, at the instant of negative peak acceleration [Figure 5.25(b)], at the instant of negative peak acceleration, the highest slab shear flow reached about 3.2 kips/ft, which was higher than design value (about 2.0 kips/ft) by approximately 60%. It is noted that the percentage increase (about 150%) by which the highest local slab shear exceeds the design value occurring at the positive peak acceleration [Figure 5.25(a)] is noticeably higher than that (about 60%) occurs at the negative peak acceleration [Figure 5.25(b)]. The observation made above indicates that the phenomenon of non-uniform distribution of slab shear flow is more significant when the inertial force acts toward the LFRS. This can be explained by the load path of the inertial force transmission in the floor diaphragm. Figure 5.26 shows the tributary areas of collectors which are determined by simply assuming that the distributed inertial force of the slab is transmitted only through the "diagonal load paths" formed by the compression field of the concrete slab. Based on the simplified load path, when the inertial force acts toward the LFRS [Figure 5.26(a)], the tributary area of Collector 1, which is next to the LFRS, is larger than the floor area in the collector span 1. A good amount of inertial force in the collector span 2 region is transmitted into Collector 1, which would result in a high shear flow along the Collector 1. By contrast, when the inertial force acts away from the LFRS [Figure 5.26(b)], the tributary area of Collector 1 is smaller than the floor area in collector span 1. A part of the inertial force in the collector span 1 region flows into Collector 2, which would lead to a lower shear flow acting along Collector. This explains why

the shear flow next to LFRS is significantly larger than the design value when the inertial force acts toward the LFRS. Note that the load path shown in Figure 5.26 is only one, but not all, source of the inertial force transmission mechanism. For example, a part of the inertial force may be transmitted through the axial action of the slab. If the "diagonal load path" is the only one mechanism for inertial force transmission, the tributary areas shown in Figure 5.26(b) implies that the shear flow acting along Collector 2 will be higher than that along Collector 1 when the inertial force acts away from the LFRS. However, the analysis results [Figure 5.25(b)] show that the shear flow along Collector 1 is higher than that along Collector 2 in this direction of the inertial force. In brief, the non-uniform shear deformation is the governing factor for the non-uniform shear flow along the collectors, the diagonal load path effect is an auxiliary factor which facilitates or mitigates the non-uniform slab shear phenomenon.

Figure 5.27 and Figure 5.28 further assess the non-uniform slab shear in a quantifiable manner. As shown in Figure 5.27-middle, the section cuts along the north and south collector lines are composed of 13 and 11 components, respectively. They include the slabs, chords, and transverse floor beams. Each slab in collector spans 1 and 2 are separated into two halves: west-half (W-half) and east-half (E-half). The bar charts shown in Figure 5.27(a) and (b) visualize the amount of in-plan floor shear transmitted through each component along the north and south collector lines, respectively, at the instant of positive peak acceleration. Only less than 4% of the floor shear is transmitted through the transverse beams (chords and floor beams), suggesting that the amount of inertial force transmitted through the floor beams directly into the columns is negligible. In other words, it is a reasonable assumption that all the inertial forces of the floor diaphragm is transmitted into the collectors through the in-plane slab shear before they are collected and transferred to the LFRS. Along each collector line, the amount of slab shear

transmitted by each slab components increases from the far (i.e., east) end to the LFRS end, which is consistent with the non-uniform shear flow demonstrated in Figure 5.25. Note that the slab component in the last half span of the collector line, which is right next to the LFRS and is denoted as "W-half of Slab 1", carried significantly high slab shear. The analysis shows that approximately 38% of the inertial force is transmitted into the collector line through this short half-span, which only occupies only 18% of the length of the entire collector line. This results in a high local slab shear near the LFRS. Figure 5.28 provides similar information. The same conclusion can be made, i.e., the closer to the LFRS, the higher the slab shear. But the degree of shear concentration next to the LFRS is less in this direction of floor acceleration; about 30% of inertial force is transmitted into the collector line in the last half-span.

The force balance at the AFW connection is analytically investigated as shown in Figure 5.29 and Figure 5.30. As shown in Figure 5.29-top, several elements are connected to the AFW connection: (1) a vertical beam element for the cantilever column, (2) a beam element representing the collector, (3) a beam element representing the west chord, and (4) a diagonal slab truss.

The horizontal force equilibrium in the longitudinal direction of the test building at the AFW connection implies that the cantilever column major-axis shear (V_c) should be balanced by the summation of three components: the collector axial force (P_{coll}), the chord weak-axis shear (V_b), and the longitudinal component of the slab truss axial force (F_{tr}), leading to the following:

$$V_c = P_{coll} + V_b + F_{tr} \tag{5.7}$$

Three sub-figures from left to right in the top row of Figure 5.29 show the relationships between V_c and three components forces from the time history analysis for Test 1-3. First of all, the V_b plot indicates that the contribution from the chord is negligibly small. From the P_{coll} plot, V_c is mostly balanced by P_{coll} when the collector is in tension. By contrast, when the collector is in compression,

only about 75% of the column shear V_c is balanced by the collector axial force P_{coll}; and the remaining (about 25%) column shear is balanced mainly by the force component F_{tr} from the slab truss. The analysis result of a 75% contribution of collector axial force in balancing column shear when the collector is in compression contradicts somehow the experimental results shown in Figure 4.54 and Figure 4.55, for which the collector axial force and column shear were almost balanced in Test 1-3.

This discrepancy between the analytical and experimental results on the force equilibrium at the AFW connection reveals a minor issue of the BT modeling approach. For ease of constructing the BT model, some diagonal trusses at the corner regions of the slab will be directly connected to the nodes at the column locations (see Trusses "xN" and "xS" in Figure 5.29). These corner trusses will transmit the inertial force to the column directly. In fact, a significant portion of the inertial force will be transmitted into the collector first. This effect will show up when the inertial force acts toward the LFRS, leading to an underestimation of the compressive axial force in the collector adjacent to the LFRS. A coarse mesh of the subpanels in the BT model would exacerbate this effect. However, Figure 5.22(a) shows that the model underestimates slightly the compressive axial force in the collector adjacent to the LFRS. The effect of using directly connected diagonal truss members in the corner panels can be reduced by using a mesh size that is sufficiently small.

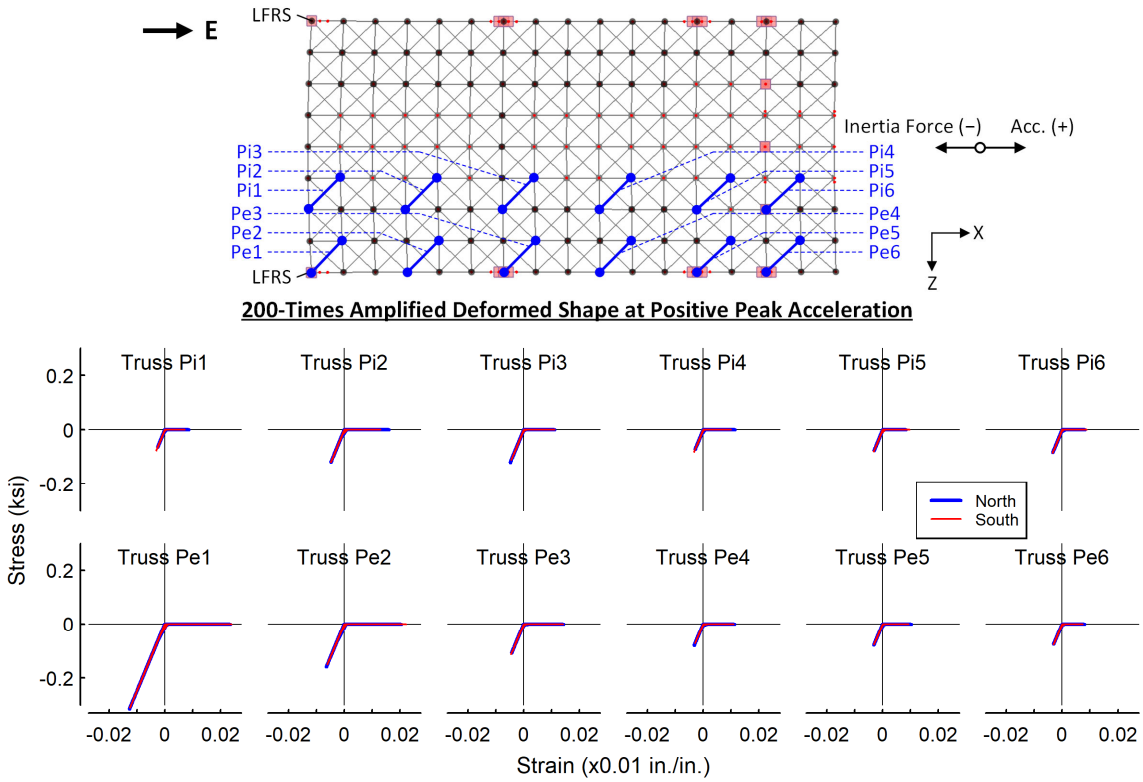

(a) At Positive Peak Acceleration

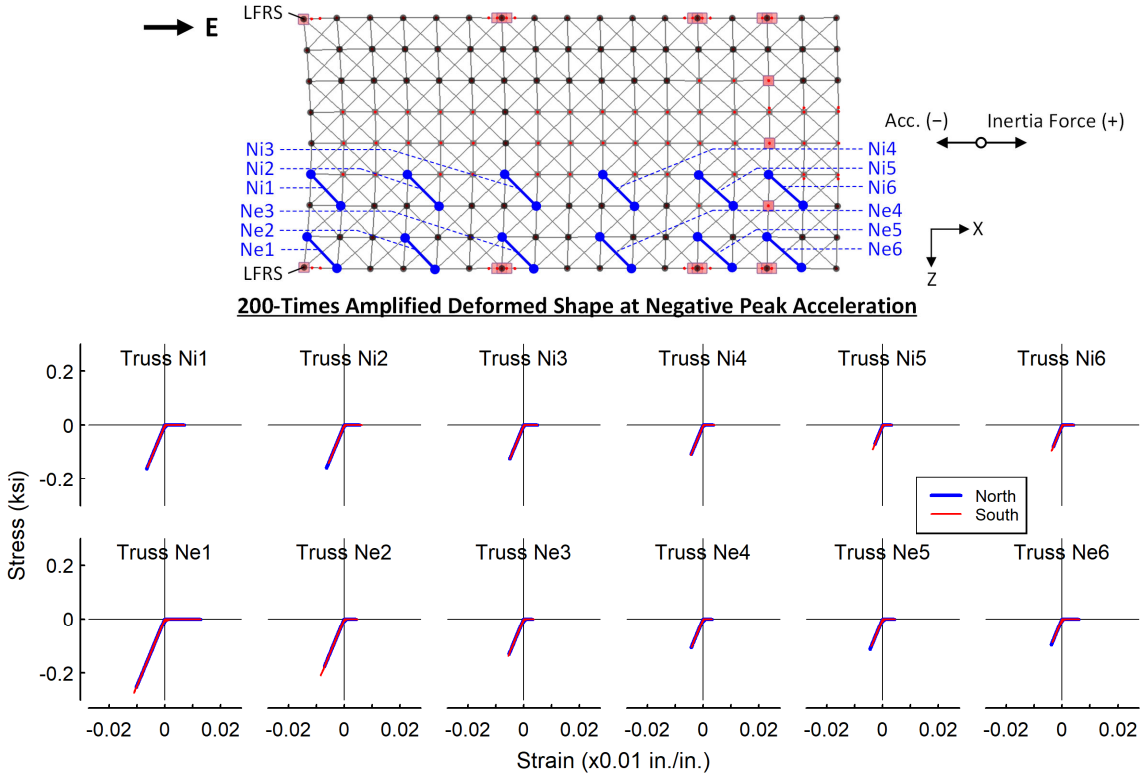

(b) At negative Peak Acceleration

Figure 5.24 Model BT-2: Stress versus Strain Responses of Selected Slab Truss Elements

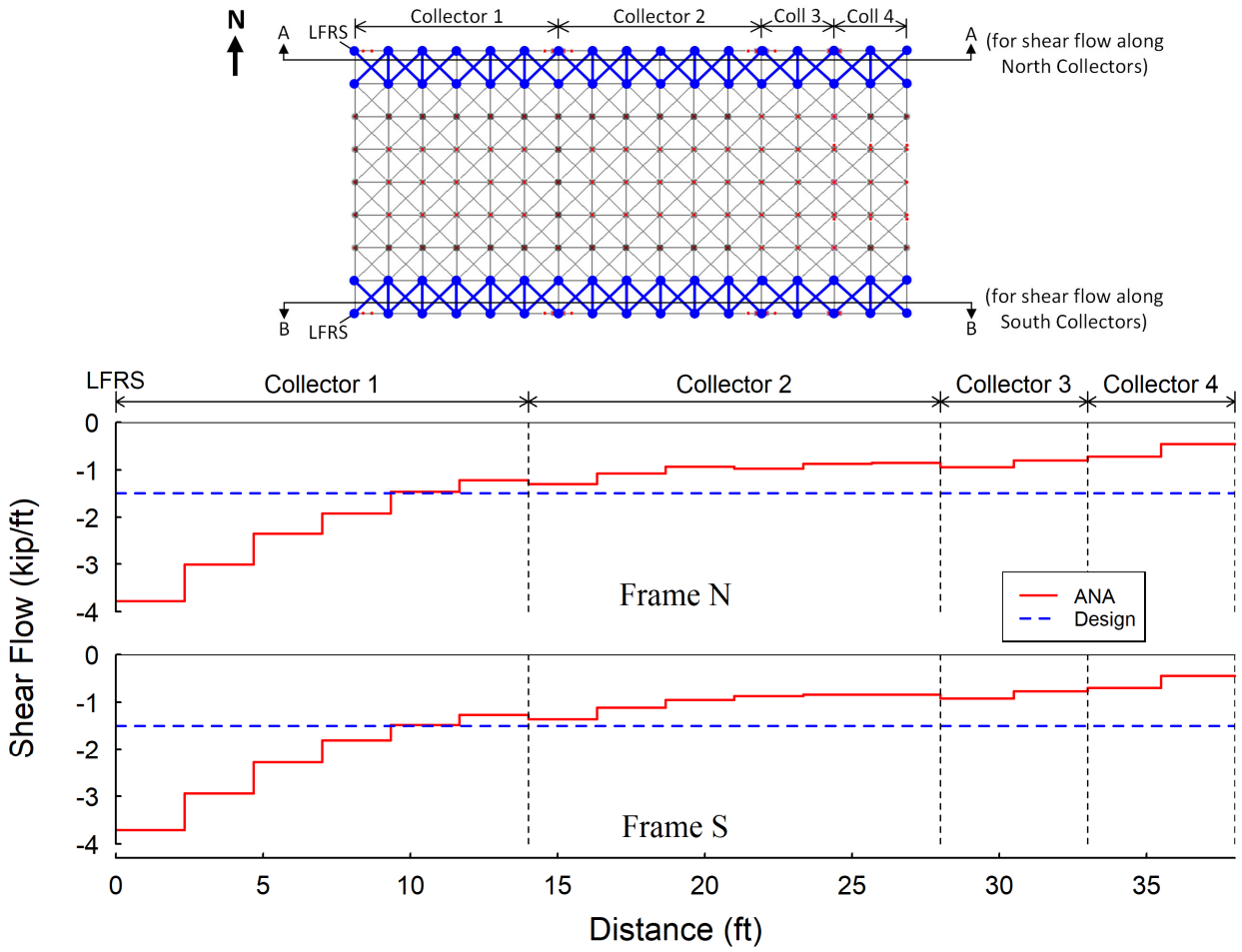

(a) Positive Peak Acceleration

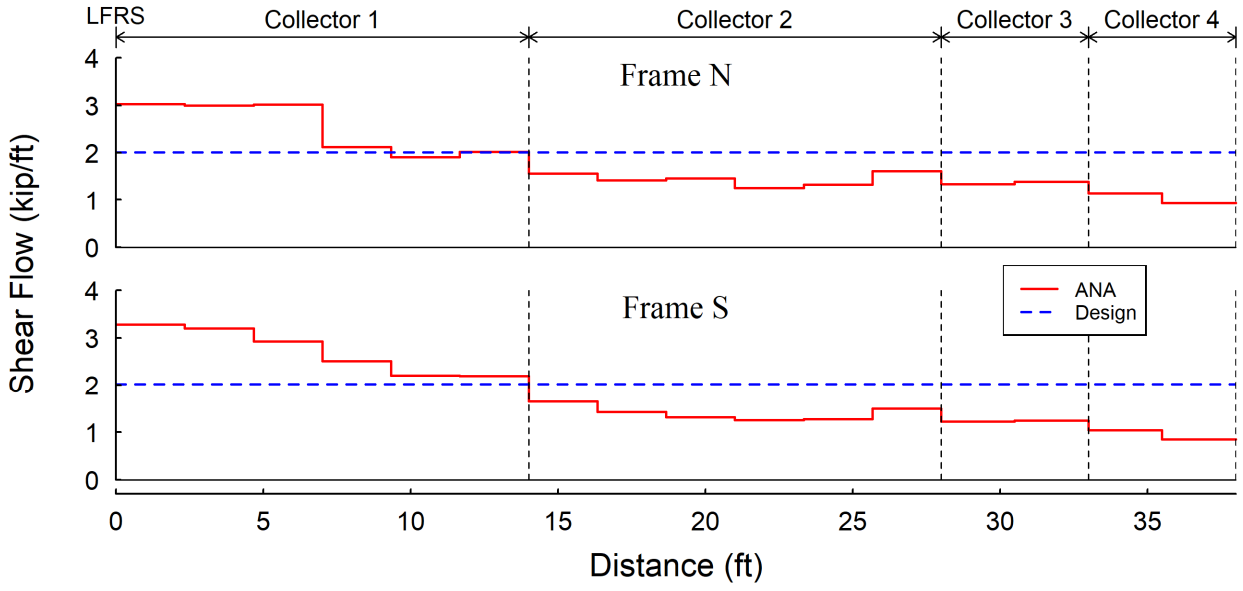

(b) Negative Peak Acceleration

Figure 5.25 Model BT-2: Slab Shear Flows along Collector Lines

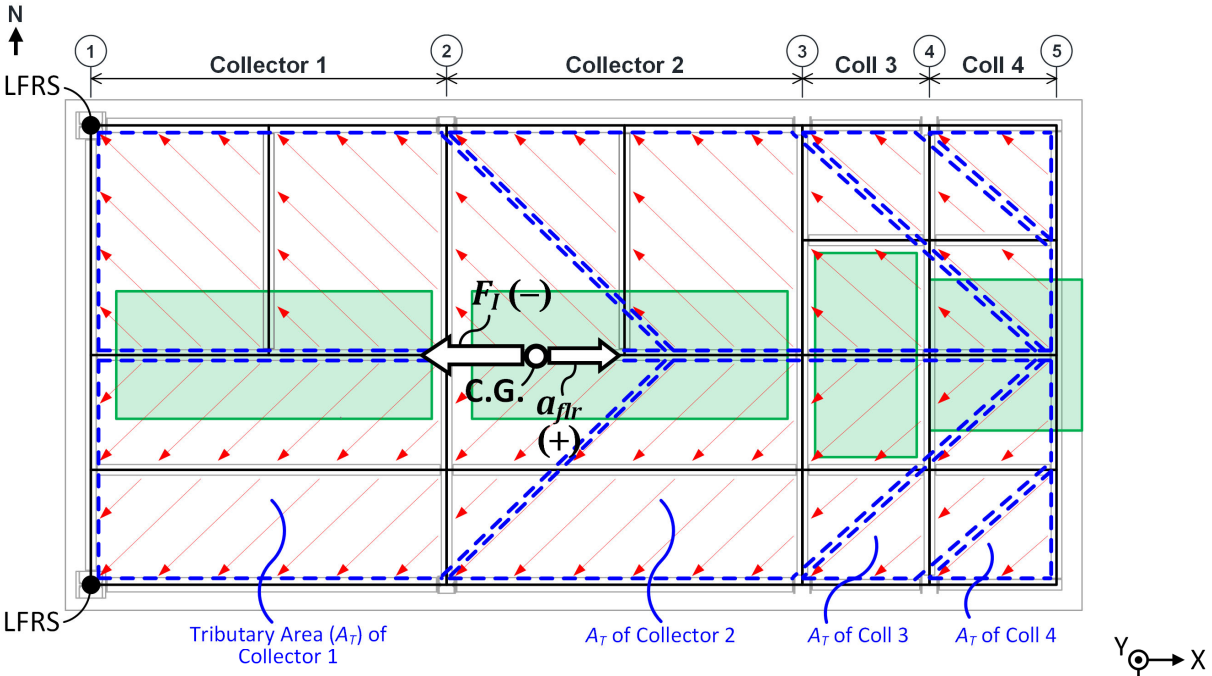

(a) Inertia Force Acting Toward LRFS

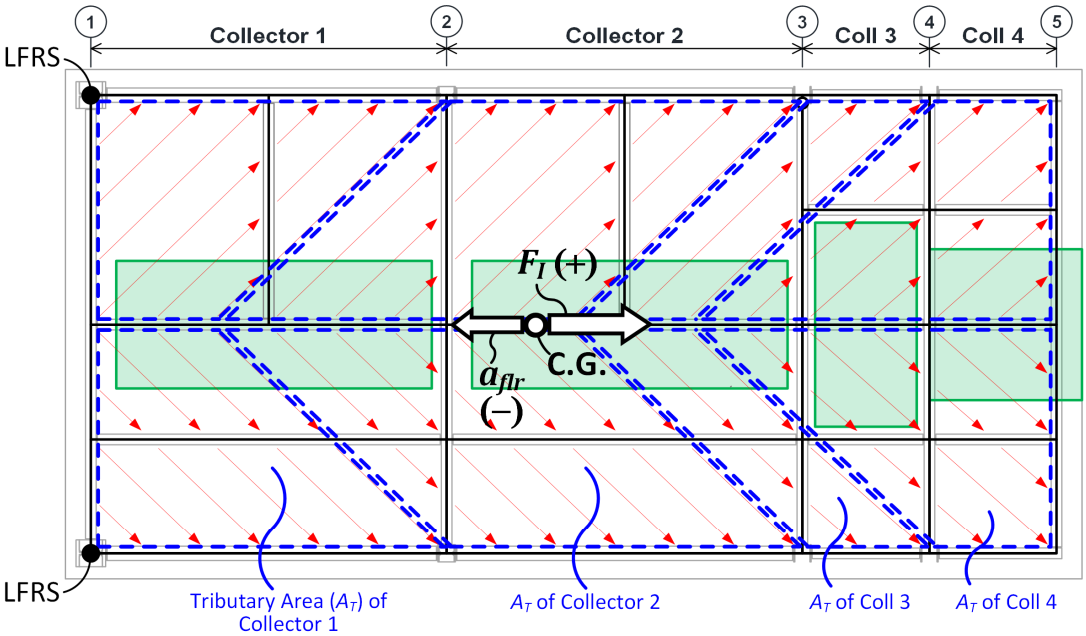

(b) Inertia Force Acting Away From LRFS

Figure 5.26 Tributary Areas for Collectors Assuming Inertial Force Transmitted through Compression Field of Concrete Slab

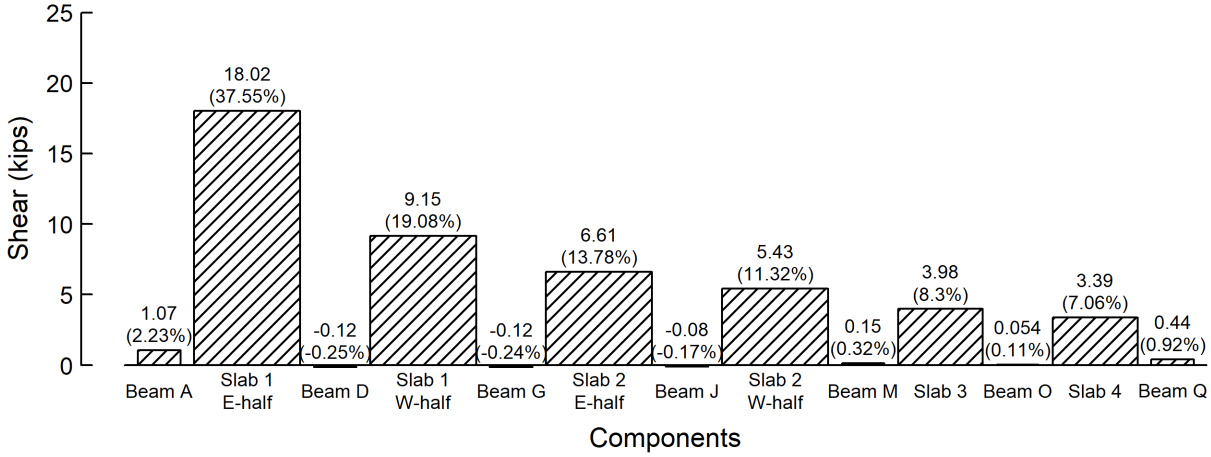

(a) along North Collector Line

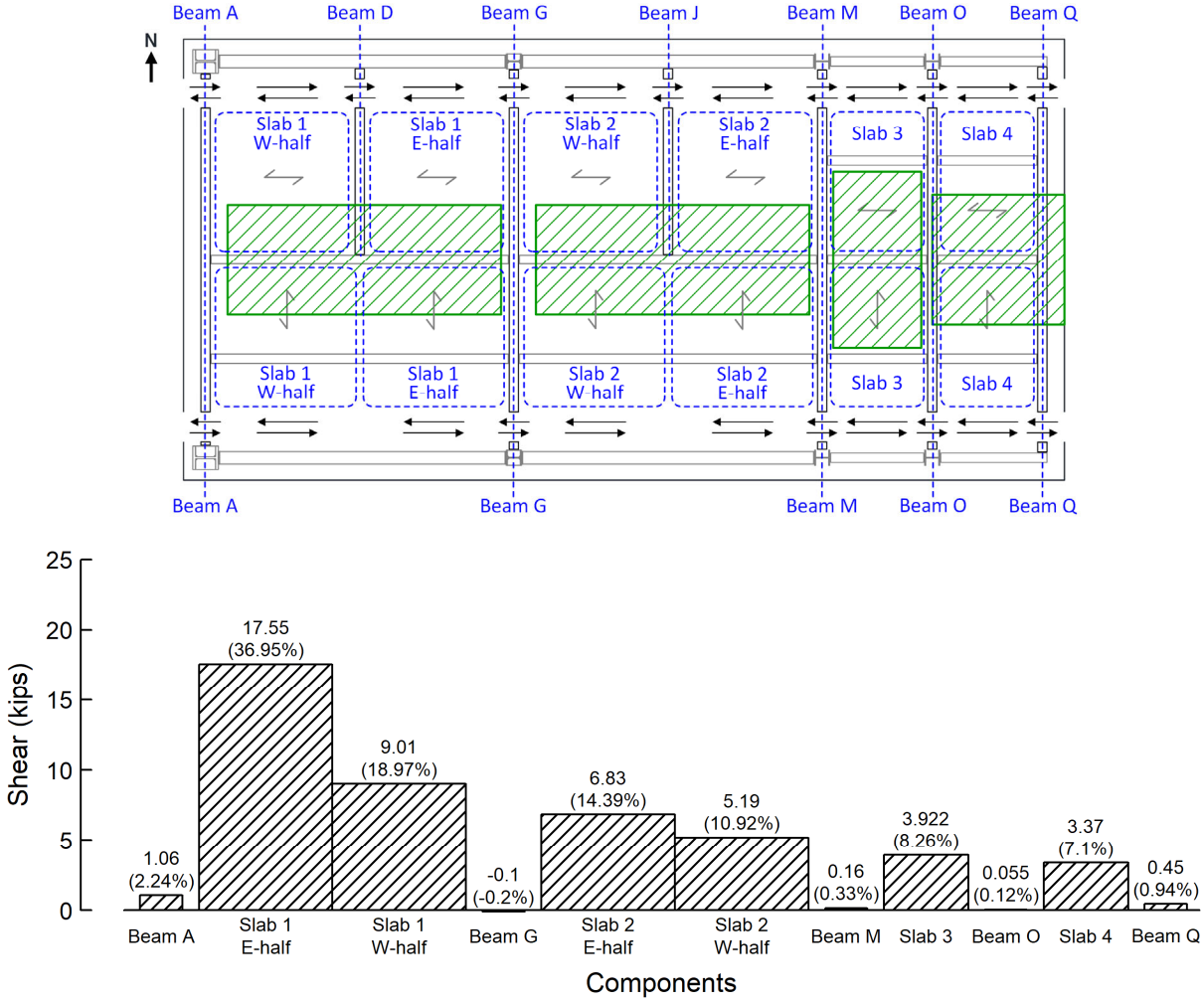

(b) along South Collector Line

Figure 5.27 Model BT-2: Slab Shear Taken by Various Components at Positive Peak Acceleration

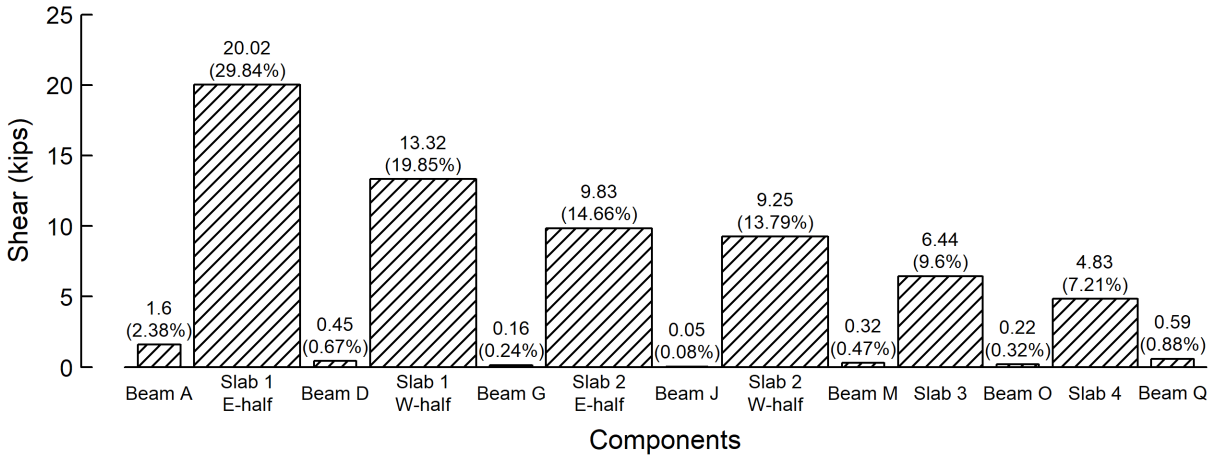

(a) along North Collector Line

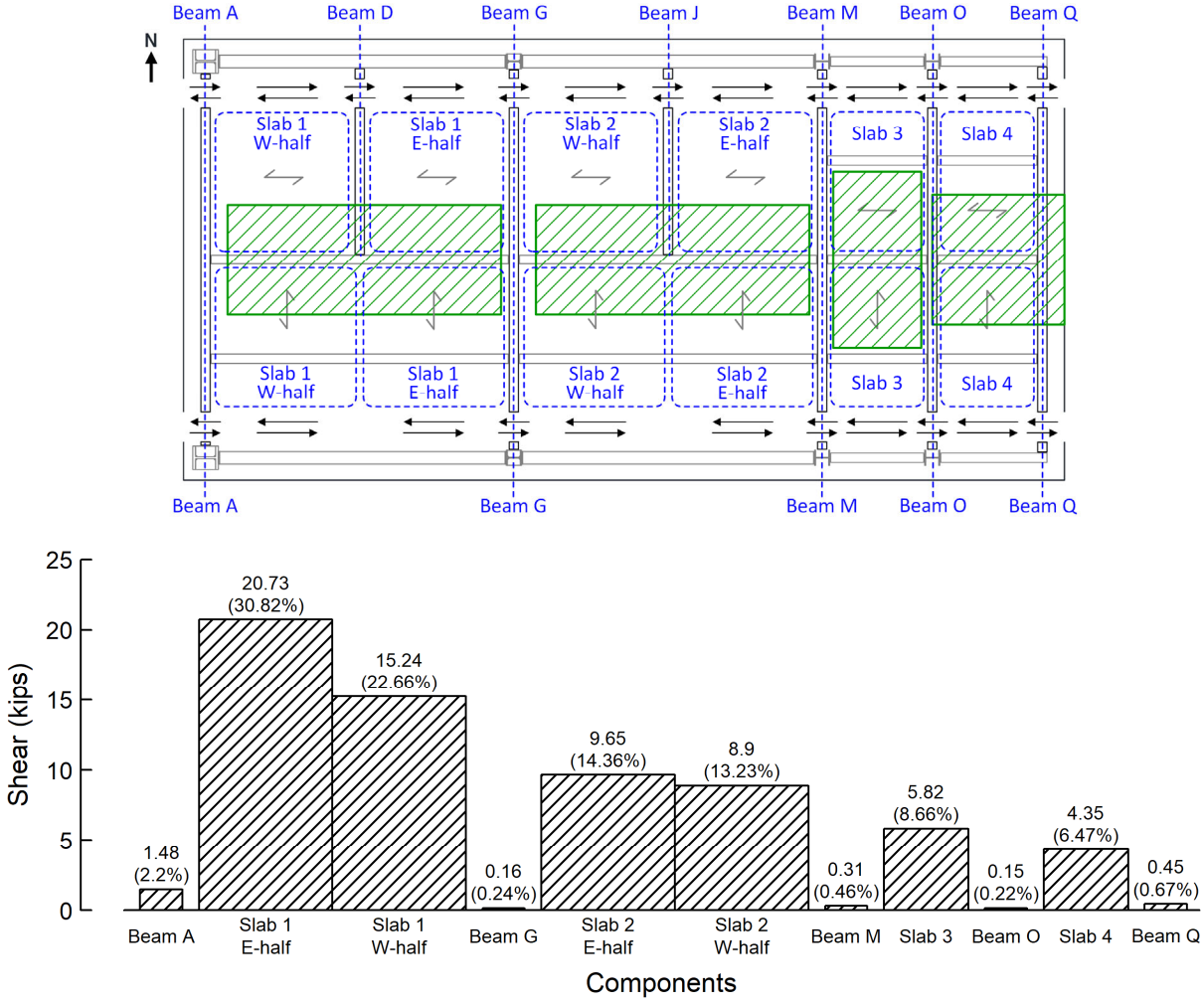

(b) along South Collector Line

Figure 5.28 Model BT-2: Slab Shear Taken by Various Components at Negative Peak Acceleration

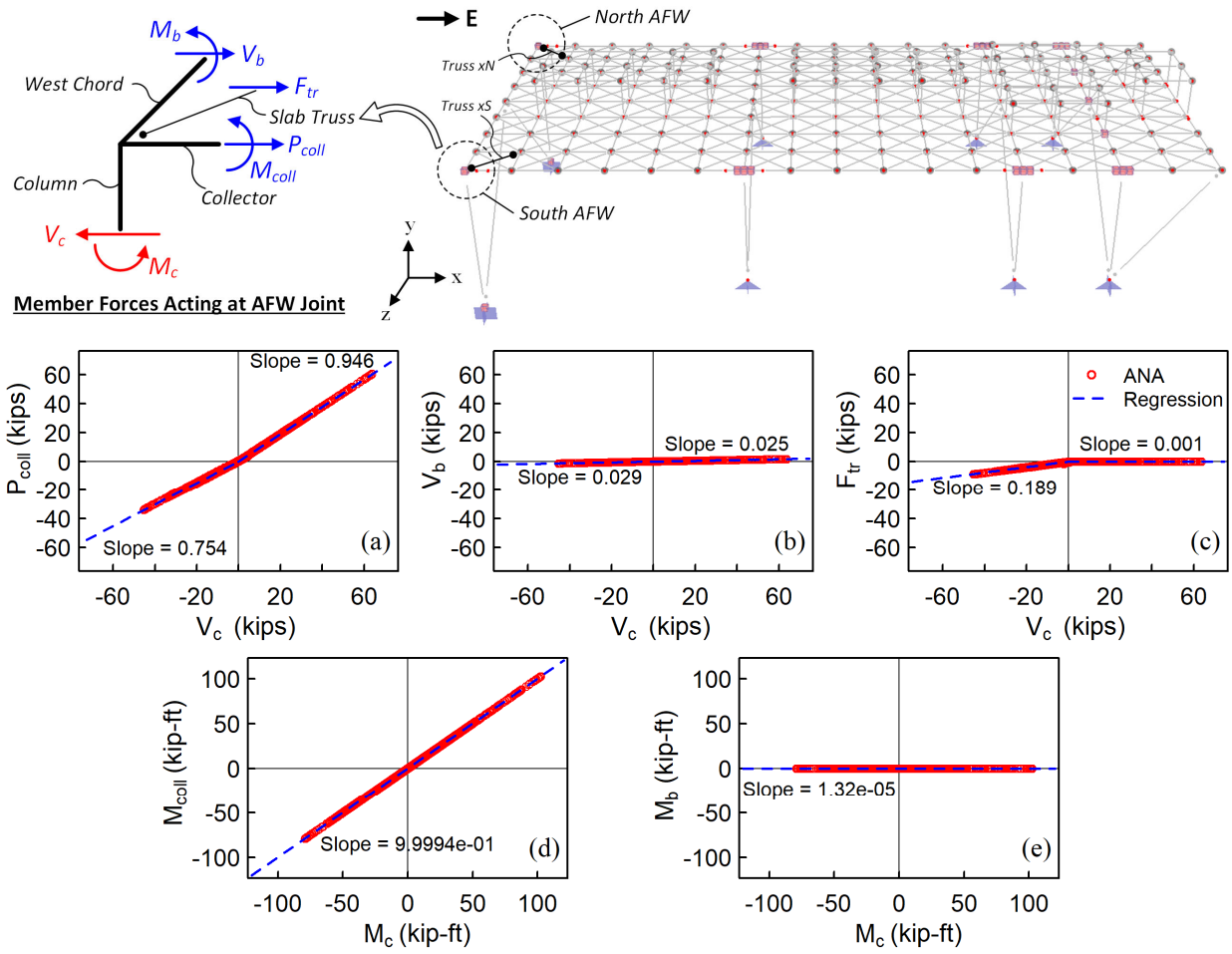

Figure 5.29 Model BT-2: Member Forces Acting at North AFW Connection

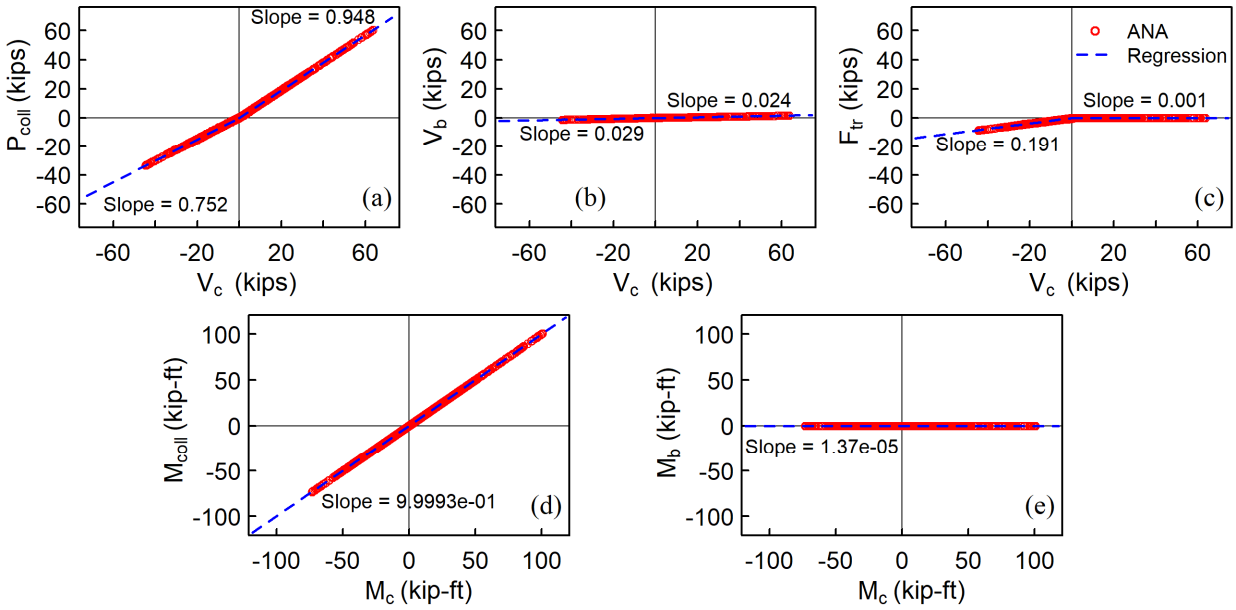

Figure 5.30 Model BT-2: Member Forces Acting at South AFW Connection

5.3.5 Comparisons of Analysis Results from Different Models

As presented in Sections 5.3.2 through 5.3.4, the comparison of analytical and experimental results on various global and local responses have verified the accuracy of Model BT-2, which serves the "benchmark" model for the other five models in Table 5.1 (BT-0, BT-1, MS-0, MS-1, and MS-2). In this section, comparison of analytical results are made among the six models to evaluate the accuracy of (1) the proposed "modified strip (MS) model" to simulate the composite slab in steel buildings, and (2) the proposed simplified approaches for the semi-rigid collector-to-column connections.

Figure 5.31 and Figure 5.32 shows the comparisons of analytical results from each of the six models with the experimental responses on the floor acceleration and story drift anlge, respecively. It is obvious that Models BT-2, BT-1, MS-2, and MS-1 all predict satisfactorily the measured global responses (floor acceleration and story drift). But Models BT-0 and MS-0, both of which ignore the semi-rigid nature of the collector connections, considerably overestimate the floor accleration and story drift responses, and the R^2 values are the lowest.

The prediction of collector axial force is examined in Figure 5.33. It shows that Models BT-2, BT-1, MS-2, and MS-1 well predict the collector axial force diagrams, whereas Models BT-0 and MS-0 noticeably overestimate the magnitude of the collector axial forces. There are two reasons for the overestimation:

(1) The two models with pin instead of semi-rigid connections overestmate the floor accrleration, which is the source of the collector axial force. Larger floor accelerations produce higher collector axial forces.

(2) Use of pin connections to simulate the colector connections will result in zero shear in the gravity columns. Therefore, gravity columns will not "intercept" some inertial forces in the collectors, an issue that will be further discussed in Section 5.4.4.

Figure 5.34 compares the results from Models BT-2 and MS-2 on the slab shear flow along the collector line. Figure 5.34-top shows the concept of section cuts along the collector lines and the elements considered for computing the slab shear flow diagrams for both models. Note that each diagonal slab truss in Model BT-2 spans across a subpanel of slab, which makes all the diagonal trusses being of about the same length. On the other hand, diagonal slab trusses with variable lengths are used to construct the floor diaphragm in Model MS-2. Recall that the proposed modified strip model considers the slab subpanels surrounded by the steel floor beams as the unit subpanels for arranging the slab trusses. Thus, the slab trusses in Model MS-2 "traverse" from one steel beam to another steel beam. Since metal decks are oriented differently between the north and south halves of the floor diaphragm in the test building, the steel floor beam layouts are different between the north and south sides. As a result, the slab truss layouts for both sides are also different in Model MS-2 (see Figure 5.34-top right). Furthermore, due to the difference in arranging slab trusses, the truss layouts are different between Models BT-2 and MS-2.

Figure 5.34 shows that the shear flow distributions obtained from Model MS-2 generally follow the trend of the results from Model BT-2. But some difference does exist between the two models, especially in the region near the LFRS. The shear flow near the LFRS predicted by Model MS-2 is lower than that predicted by Model BT-2. This can be explained by the difference of the slab truss layout. In Model BT-2 (Figure 5.34-top left), the diagonal trusses at the slab corners represent the compression field in a subpanel at the very corner of the slab. By contrast, the diagonal trusses at the slab corners in Model MS-2 (Figure 5.34-top right) span a longer distance.

These long corner trusses represent a slab compression field in a more global sense by assuming that the slab compression fields are developed from steel beams to steel beams. Therefore, these long corner trusses may not be able to represent the stress or deformation concentration at the slab corner in a very accurate manner, especially when a slab corner undergoes a significant localized deformation. The above observation suggests that the proposed modified strip model may lose the accuracy somewhat in modeling floor diaphragms with significant localized deformations. However, Figure 5.31 through Figure 5.33 have shown that Model MS-2 can still achieve a level of accuracy about the same as Model BT-2 in predicting the global responses and collector actions of the test specimen. Notably, Model MS-2 only took about 1/3 of computation time that Model BT-2 spent to complete a time history analysis for simulating Test 1-3. Hence, the "modified strip model" can serve as an alternative approach to model composite floor diaphragms, especially for time history analyses of multi-story steel buildings with floor diaphragms that are expected to experience limited local inelastic responses.

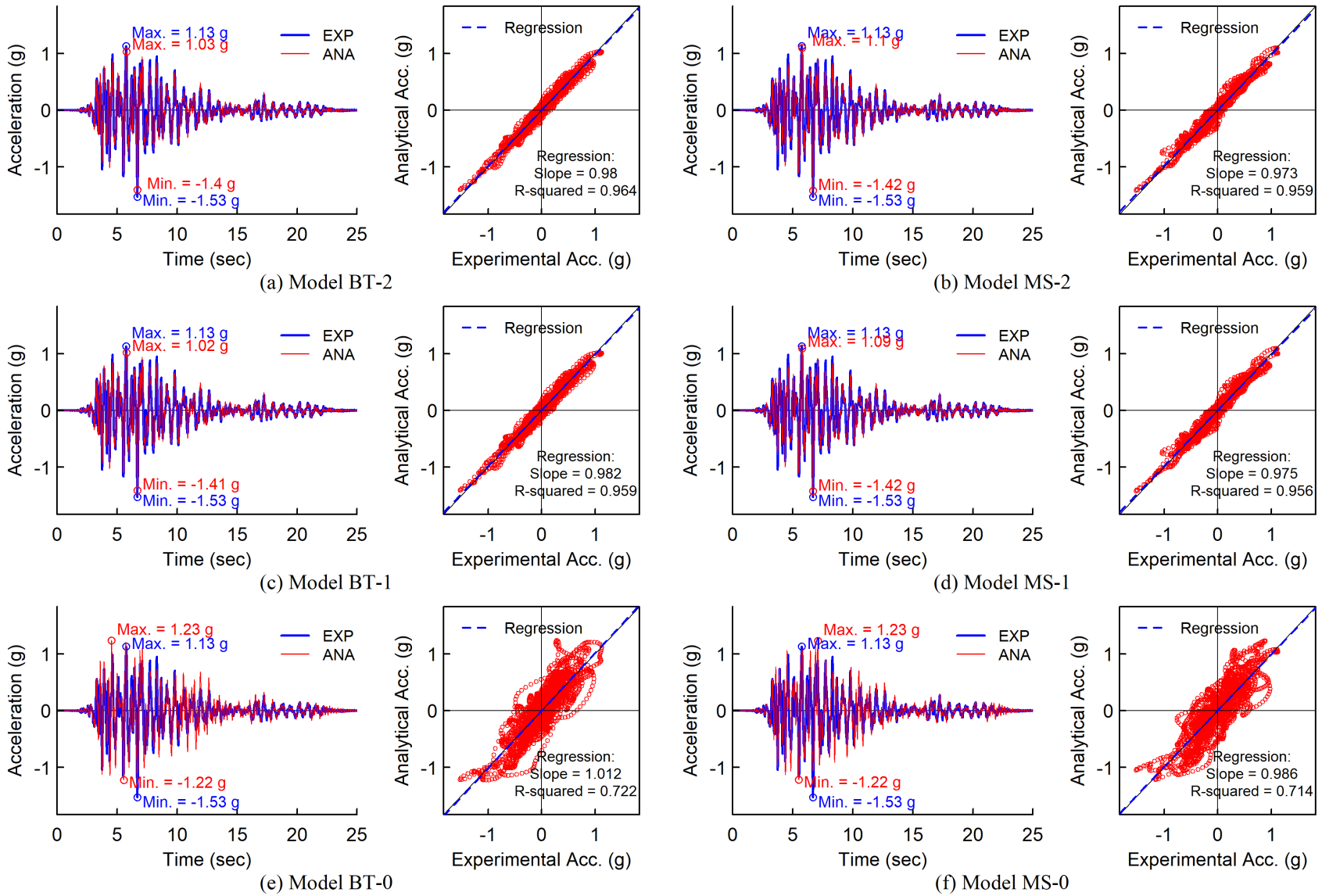

Figure 5.31 Comparison of Analytical Results from Diffrenet Models: Floor Accelerations

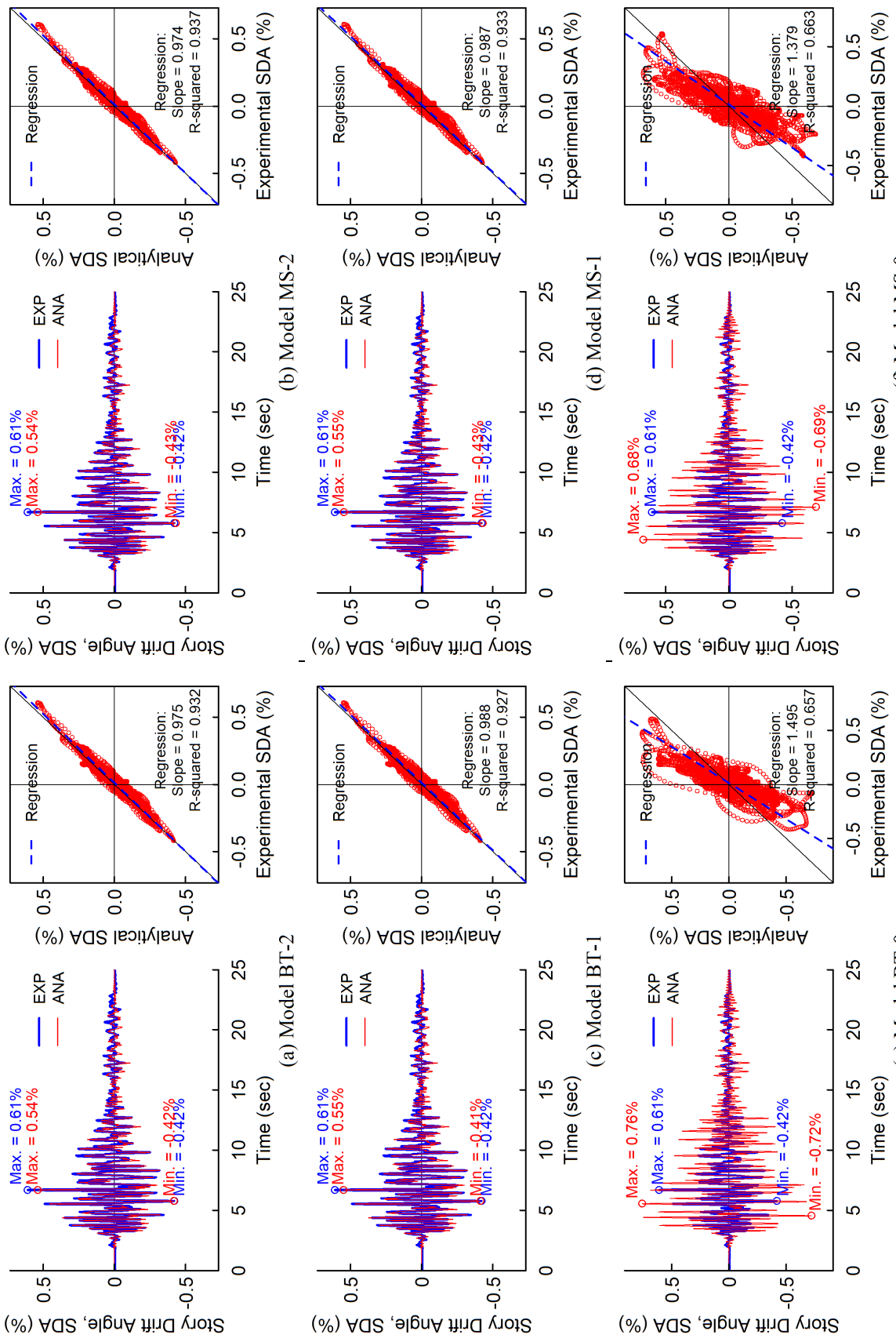

Figure 5.32 Comparison of Analytical Results from Diffrenet Models: Story Drift Angle

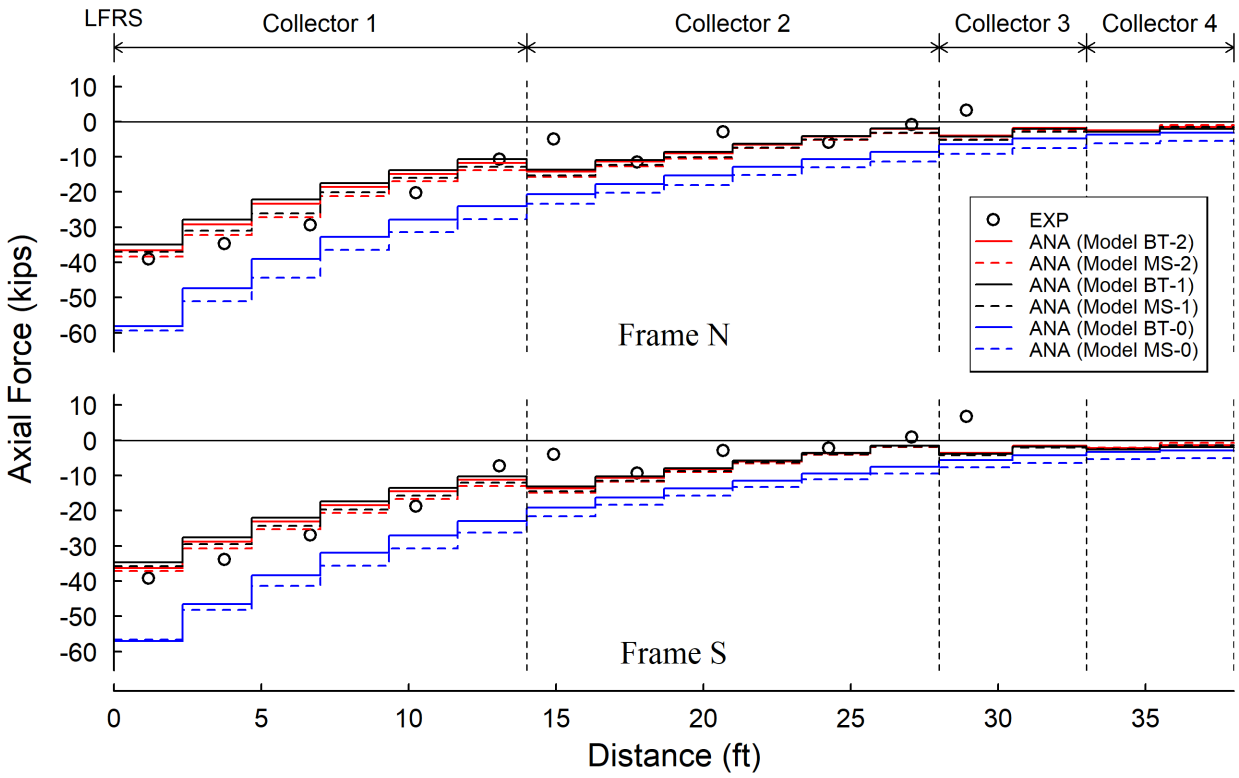

(a) Positive Peak Acceleration

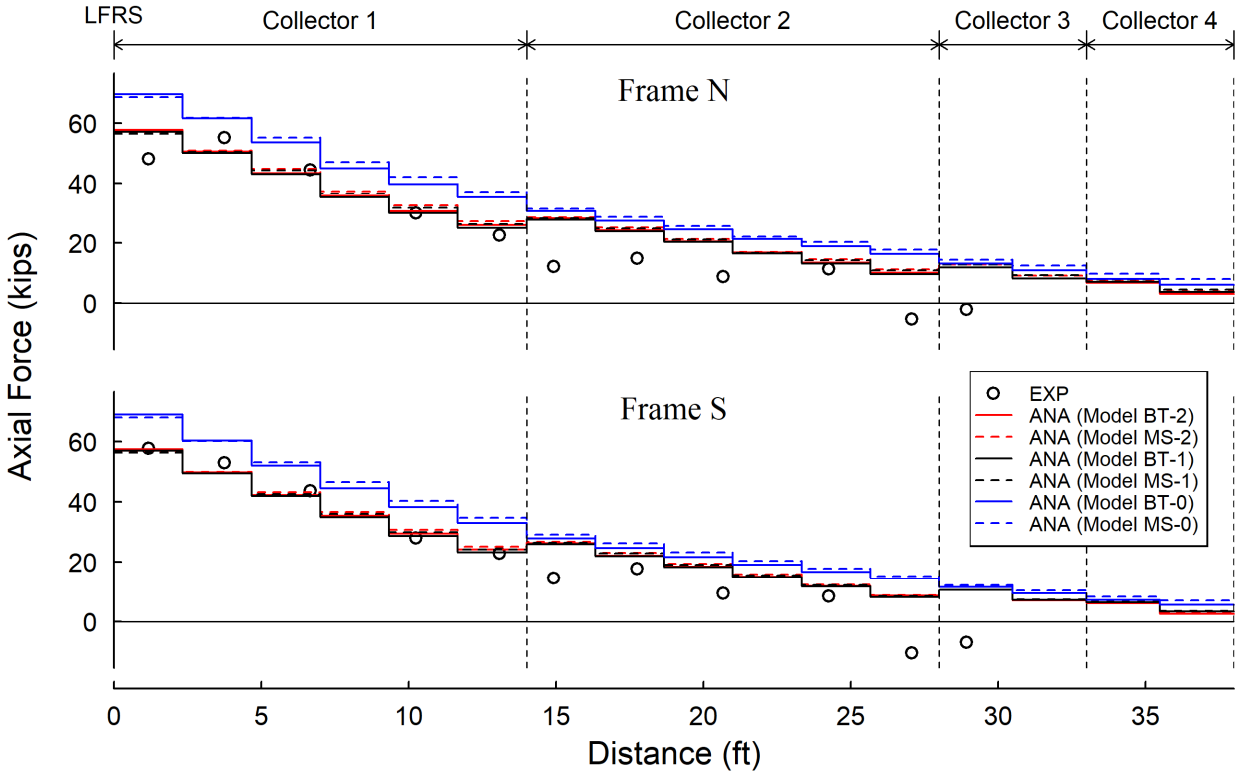

(b) Negative Peak Acceleration

Figure 5.33 Comparison of Analytical Results from Diffrenet Models: Collector Axial Force

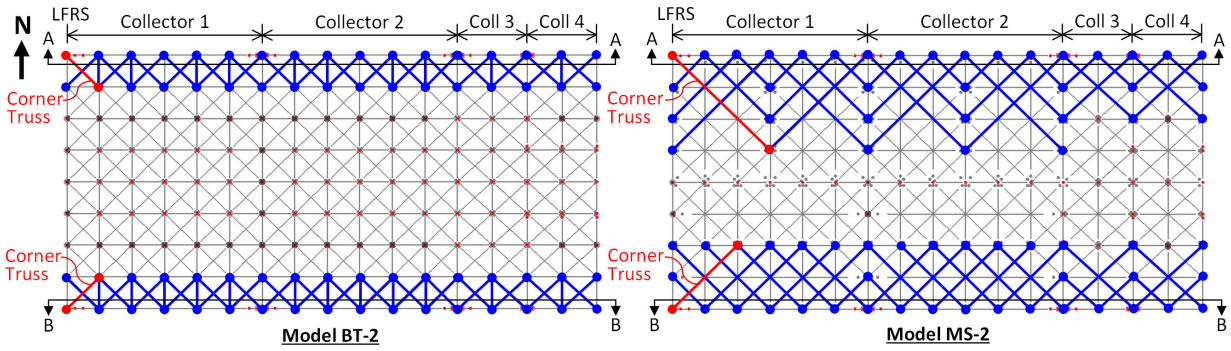

(a) Elements Used for Determining Slab Shear Flow

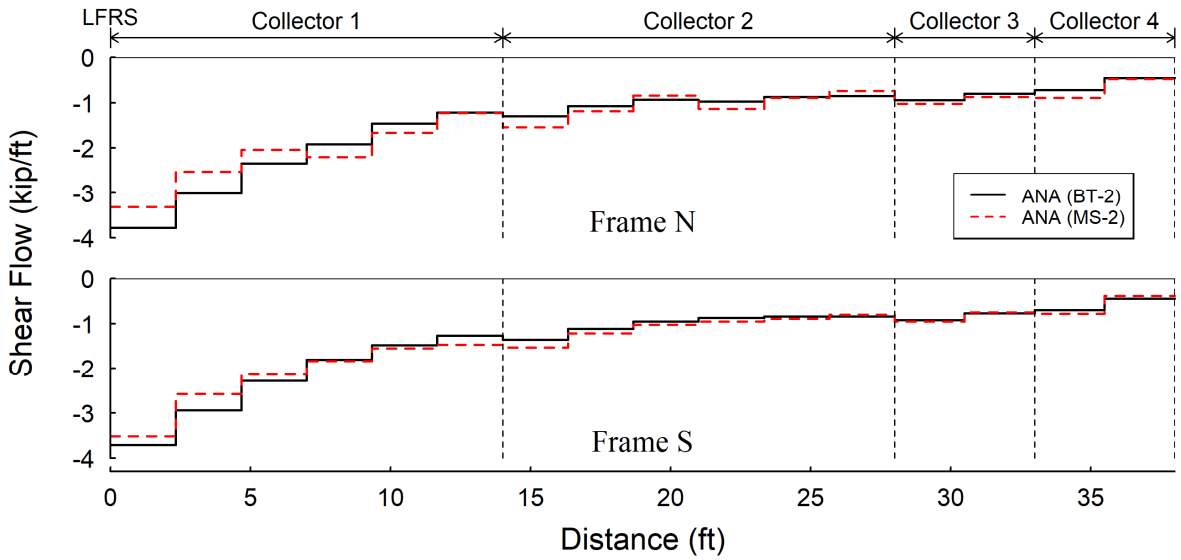

(a) Positive Peak Acceleration

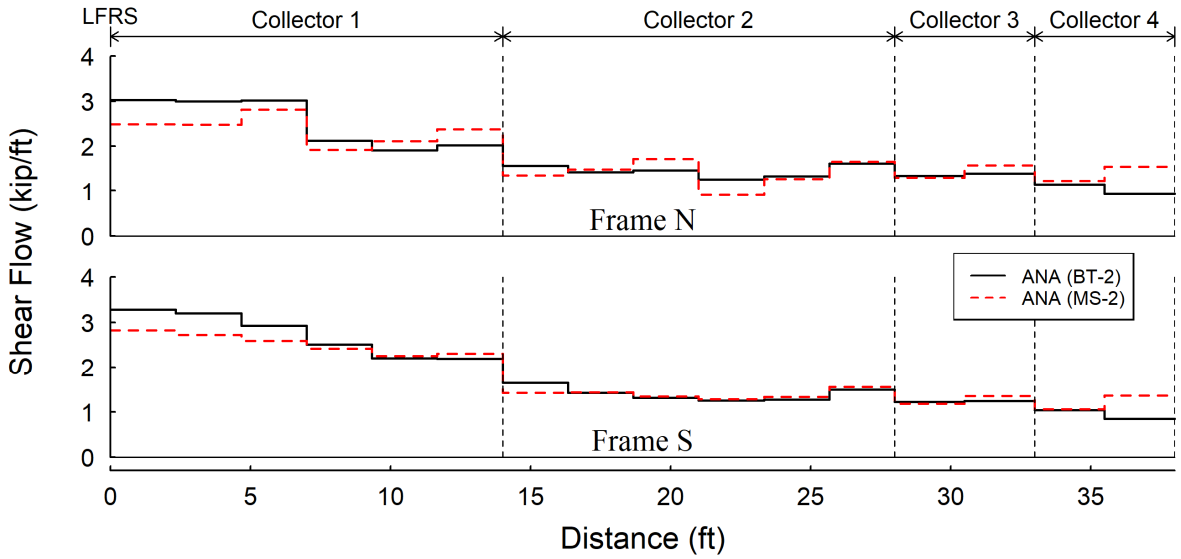

(b) Negative Peak Acceleration

Figure 5.34 Comparison of Analytical Results from Diffrenet Models: Slab Shear Flow along Collector Lines

5.4 Design Implications

5.4.1 Rotational Stiffnesses of Collector-to-Column Connections

Three types of collector-to-column connections (AFW, TFW, and BW details) were used in the test specimen. For a frame analysis on a building structure with collectors, the AFW connection can be modeled as a rigid joint, while the "semi-rigid" TFW and BW connections can be modeled by using rotational springs. However, based on the observations from Phase 1 tests, the modeling of these two semi-rigid connections is challenging in three aspects:

(1) These connections exhibit a nonlinear "hysteresis" behavior even when the imposed rotation angle is small. This results from the slippage of the bolted connections in the web.

(2) The steel collector beams act compositely with the concrete slab. With the participation of concrete slab in resisting bending, the moment-rotation response is markedly "non-symmetric", in which the flexural stiffness and resistance in positive bending is much higher than those in negative bending.

(3) These collector connections are subjected to combined axial force and bending moment.

Hence, it requires sophisticated nonlinear modeling techniques to achieve an accurate representation of these semi-rigid connections. Analytical studies presented in Sections 5.2 and 5.3 showed that the rotational stiffness from these connections was small, although nontrivial, for the test specimen. Therefore, it is judged that a linearly elastic rotational spring which can capture the averaged secant stiffness between positive and negative would be sufficient for seismic design and analysis of collectors. A simple approach for estimating the secant stiffness is proposed in this research and its effectiveness is verified by test results. It is worth noting that, strategically, a method which tends to slightly underestimate, not overestimate, the stiffness of the collector

connections is more desirable as it will not result in an underestimate of the collector force demands for design. This is the basic guideline for the development of the proposed approach.

The concept of "component-based spring model", which was employed by several researchers (Sadek et al. 2008; Koduru and Driver 2014; Weigand 2017) to model axial force-moment interaction of single-plate shear connections, is adopted in this study to develop the approximation method for estimating the rotational stiffness. As shown in Figure 5.35, the connection is discretized into a series of horizontal springs that represents the geometry of the connection, where each component spring represents a component of the connection (e.g., concrete slab, steel flanges, and bolts). These springs are attached to a pair of rigid bars at the edges of the connection, which are permitted to displace and rotate relative to one another. It is assumed that the shear response is rigid in this model.

Although nonlinear springs can be employed to simulate the nonlinear connection response, for simplicity, the proposed method uses elastic springs and neglects the P-M interaction. Note that connection region considered (denoted as L_{jj} in Figure 5.35) ranges from the fixed end of the shear tab to the far-side bolt hole edge on the collector beam web:

$$L_{jj} = L_e^* + \frac{d_{h,BW}}{2} \tag{5.8}$$

where L_e^* is the horizontal distance between the column face and the center of the farthest bolt row (if multiple bolt rows are used) away from the column, and $d_{h,BW}$ is the bolt hole diameter on the collector web.

As the participation of concrete slab in resisting bending only takes place under the positive bending, two sets of component-based spring models are considered; one is for positive bending (Figure 5.35), in which the concrete springs are included, and the other one is for negative bending (Figure 5.36), which ignores the concrete springs. Two layers of concrete slab were considered.

The "top-layer" is the concrete above the corrugated metal deck, while the "bottom-layer" is the concrete below the top of metal deck. The axial spring stiffness, k_{tc}, representing the top-layer concrete is

$$k_{tc} = \frac{E_c b_{eff,t} h_c}{L_{jj}} \tag{5.9}$$

where E_c is the Young's modulus of concrete, $b_{eff,t}$ is the effective slab width at column face, and h_c is the depth of concrete above the deck. Similarly, the axial stiffness, k_{bc}, for the bottom-layer concrete is

$$k_{bc} = \frac{E_c b_{eff,b} h_r}{L_{jj}} \tag{5.10}$$

where $b_{eff,b}$ is the width of the bottom-layer concrete within the range of column face width, and h_r is rib height of the metal deck.

Furthermore, the axial stiffness, k_f, of the steel flange spring is calculated as:

$$k_f = \frac{E_s t_f b_f}{L_{jj}} \tag{5.11}$$

where E_s is the Young's modulus of steel, and b_f and t_f are the width and thickness of flange, respectively.

The determination of spring stiffness, k_{bj}, for a bolted joint can be challenging. As illustrated in Figure 5.37 (Ma and Bocchini 2019), the bolted joint response includes several phases: (1) before slip, (2) joint slippage, (3) bearing loading, (4) bearing stick, and (5) bearing slip. Even though the behavior before slip can be simplified as linear elastic for practical applications, in fact the micro-slip motion (Groper 1985) with a nonlinear behavior also takes place in this phase.

The proposed method uses the secant stiffness to approximate the hysteretic response of the bolted joints, which would lead to an underestimate of the stiffness of collector connections.

Note that the peak rotation response of a collector connection during a design earthquake is expected to be about the same as the response of the beam-to-column connections in the LFRS, which might reach a rotation angle of 0.02 rad or even larger. With this level of rotation response, the bolted joints are expected to enter the bolt bearing phase. The approach to estimate the secant stiffness of a bolted joint entering the bolt-bearing phase is presented in Section 8.2.

Note that the peak rotation angle of collector connections achieved in Test 1-3 was smaller than 0.0025 rad and all the bolted joints did not enter the bolt-bearing phase. This level of response is much smaller than a typical response expected from a design earthquake. As illustrated in Figure 5.38, for estimating an overall stiffness to represent the bolted joint response before it enters the bolt bearing phase, this research uses an upper-bound and a lower-bound stiffnesses to estimate the bolted joint response.

(1) Upper-bound stiffness

By assuming the bolt stays "perfectly still" and does not slip, the deformation of a bolted joint can be characterized as the axial deformation of the shear tab region between the fixed edge and bolt hole. The upper-bound stiffness, k_{bj-UB}, for a bolted joint is estimated by using the axial stiffness, k_{ST}^{a}, of the shear tab:

$$k_{bj-UB} = k_{ST}^{a} = \frac{E_s t_p w_T}{a} \tag{5.12}$$

where a is the clear distance from the column face to the bolt hole edge, t_p is the shear tab thickness, and w_T is the tributary width of the shear tab. Note that the axial stiffness of the shear tab, k_{ST}^{a}, is taken as the initial stiffness [marked as "k_i" in Figure 5.37(a)] in the hysteretic load-deformation model of a bolted joint in several previous studies (Weigand 2017; Ma and Bocchini 2019).

(2) Lower-bound stiffness

Considering the stiffness of a bolted joint before slippage is higher than the stiffness in the bolt bearing phase, the lower-bound stiffness, k_{bj-LB}, for a bolted joint before bolt bearing is estimated as the initial bearing stiffness of the bolted joint under tension, k_{ti}. As illustrated in Figure 5.39, the deformation of a bolted joint in the bolt bearing phase is an aggregate of various deformations at the bolt, shear tab, and collector beam web. Thus, the initial bearing stiffness can be estimated by putting all the stiffnesses representing various deformations in series, which leads to:

$$k_{bj-LB} = k_{ti} = \frac{1}{\frac{1}{k_{ST}^{a}} + \frac{1}{k_{ST}^{br}} + \frac{1}{k_{ST}^{b}} + \frac{1}{k_{ST}^{v}} + \frac{1}{k_{bolt}} + \frac{1}{k_{BW}^{br}} + \frac{1}{k_{BW}^{b}} + \frac{1}{k_{BW}^{v}}} \tag{5.13}$$

Note that k_{ST}^{br} and k_{BW}^{br} account for the bearing deformation at the bolt hole for the shear tab and collector web, respectively. The stiffness for this type of deformation, k^{br}, can be computed as (Rex and Easterling 2003):

$$k^{br} = 120 t_p F_{yp} d_b \tag{5.14}$$

where F_{yp} is yield strength of the connecting plate (shear tab or collector web). d_b is the bolt diameter.

In addition to the bearing deformation at the bolt hole, the connecting plates (shear tab or collector web) would undergo local bending and shearing deformation at the free end of each connecting plate when the bolted joint is in tension. Note k_{ST}^{b} and k_{BW}^{b} in Eq. (5.14) account for the bending deformation near the free-end of the shear tab and collector web, respectively, while k_{ST}^{v} and k_{BW}^{v} account for the bending deformation near the free-end of the shear tab and collector web, respectively. Rex and Easterling (2003) proposed a fixed-end beam model to derive the

bending stiffness, k^b, and shearing stiffness, k^v, for the deformation at the free end of a connecting plate as follows:

$$k^b = 32E_s t_p \left(\frac{L_e}{d_b} - \frac{1}{2}\right)^3 \tag{5.15}$$

$$k^v = 6.67G t_p \left(\frac{L_e}{d_b} - \frac{1}{2}\right) \tag{5.16}$$

where $G = E_s/[2(1+\upsilon)]$ is the shear modulus of the connecting plate (shear tabs or collector web) and υ is the Poisson's ratio. L_e is the distance between the center of bolt hole and the free edge of the plate. Furthermore, the initial stiffness of a bolt force-deformation response is computed by combing two springs representing two different deformations in series as (Weigand 2017):

$$k_{bolt} = \frac{1}{\frac{1}{k_{bolt}^{br}} + \frac{1}{k_{bolt}^{v}}} \tag{5.17}$$

where k_{bolt}^{br} and k_{bolt}^{v} are the bearing and shearing stiffnesses of the bolt, respectively.

The bolt bearing stiffness, k_{bolt}^{br}, is estimated as (Nelson et al. 1983):

$$k_{bolt}^{br} = \frac{1}{1+3\beta_b}\left(\frac{t_p t_w E_{bolt}}{2t_p t_w}\right) \tag{5.18}$$

where t_w is the thickness of the collector web. E_{bolt} is the Young's modulus of the bolt and β_b is a correction factor that accounts for the concentration of bearing forces at the interface between plates for a bolted joint in single shear. β_b is taken as 0.15 for pretension bolts.

In addition, the bolt shearing stiffness is determined by assuming that the bolt acts as a prismatic fixed-ended Timoshenko beam with circular cross section, which leads to:

$$k_{bolt}^{v} = \frac{12E_{bolt}I_{bolt}}{L_{bolt}^3(1+\Phi)} \tag{5.19}$$

where E_{bolt} is the Young's modulus of the bolt, $I_{bolt} = \pi d_b^4/64$ is the moment of inertia of the cross section of the bolt shaft, and $L_{bolt} = t_p + t_w$ is the bolt length considered, which is equal to the clamping thickness of the bolted joint. The term Φ accounts for the relative importance of the shear deformations to the bending deformations in Timoshenko beam theory (Thomas et al. 1973):

$$\Phi = \frac{12E_{bolt}I_{bolt}}{L_{bolt}^2\left(\frac{1}{\kappa G_{bolt}A_{bolt}}\right)} \tag{5.20}$$

where $G_{bolt} = E_{bolt}/[2(1+\upsilon)]$ is the shear modulus of the bolt, and $A_{bolt} = \pi d_b^2/4$ is the area of the bolt shaft, and κ is the shear coefficient for a circular section, which is defined as:

$$\kappa = \frac{1}{\frac{7}{6} + \frac{1}{6}\left(\frac{\upsilon}{1+\upsilon}\right)^2} \tag{5.21}$$

The stiffness, k_{ti}, determined from Eq. (5.13) is for the condition when a bolted joint is in tension. It was taken as the initial stiffness for the bearing loading branch and the unloading stiffness of the bearing slip branch for the tension side of the hysteretic model (Weigand 2017; Ma and Bocchini 2019) [Figure 5.37(a)]. As for the initial bearing stiffness under compression, k_{ci}, it can be computed by Eq. (5.13) with $k_{ST}^b = k_{ST}^v = k_{BW}^b = k_{BW}^v = \infty$ because the bending and shearing deformations at the free edge of the shear tab or collector web are considered negligible when the bolted joint is in compression (see Figure 5.40), resulting in

$$k_{ci} = \frac{1}{\frac{1}{k_{ST}^a} + \frac{1}{k_{ST}^{br}} + \frac{1}{k_{bolt}} + \frac{1}{k_{BW}^{br}}} \tag{5.22}$$

Table 5.6 tabulates the computed initial bearing stiffnesses accounting for various deformations for the bolted joints at the end connections of Collector 1 in the test specimen. It can be found that the terms k_{ST}^{br}, k_{BW}^{br}, and k_{bolt}^{br} are much smaller than the other stiffnesses, indicating the behavior in the bearing-phase would be dominated by the bearing deformation of the bolt shaft or the bearing

deformation at bolt holes. In addition, Table 5.6 lists the total stiffnesses k_i, k_{ti}, and k_{ci}. The values of k_{ti} and k_{ci} are about the same, which suggests that deformations at the free edge of the connecting plates would not be significant. For simplicity, k_{ti} is taken as the lower-bound stiffness for the bolted joint springs.

Table 5.6 Initial Stiffnesses for Various Deformations of a Bolted Joint (for Collector 1)

Bolt Location	Stiffness for Shear Tab Deformations				Stiffness for Collector Beam Web Deformations			Stiffness for Bolt Deformations		Total Stiffness		
	k_{ST}^{a} (k/in.)	k_{ST}^{br} (k/in.)	k_{ST}^{b} (k/in.)	k_{ST}^{v} (k/in.)	k_{BW}^{br} (k/in.)	k_{BW}^{b} (k/in.)	k_{BW}^{v} (k/in.)	k_{bolt}^{br} (k/in.)	k_{bolt}^{v} (k/in.)	k_i (k/in.)	k_{ti} (k/in.)	k_{ci} (k/in.)
Edge	11600	1450	783000	27885	1232	845640	30115	1298	4300	11600	376	386
Interior	10311	1450	783000	27885	1232	845640	30115	1298	4300	10311	374	384

With the stiffnesses for the concrete spring (k_{tc} and k_{bc}), steel flange springs (k_{flg}), and bolted joint springs (k_{bj}), the positive bending stiffness of a collector connection, K_{sj}^{+}, can be computed as follows:

$$K_{sj}^{+} = \sum_{i=1}^{N_c} k_{ci}(y_{ci} - \bar{y}^{+})^2 + \sum_{j=1}^{N_f} k_{fj}\left(y_{fj} - \bar{y}^{+}\right)^2 + \sum_{k=1}^{N_{bj}} k_{bjk}\left(y_{bjk} - \bar{y}^{+}\right)^2 \tag{5.23}$$

where N_c, N_f, N_{bj} are the numbers of springs representing concrete slab, steel flange, and bolted joint, respectively. Note that N_c =2 in this study because two layers of concrete are considered. N_f = 2, 1, and 0 for the AFW, TFW, and BW connections, respectively. N_{bj} = 5 for the collector connections in the test specimen. k_{ci} and y_{ci} are the stiffness and y-coordinate of the *i*-th concrete spring, respectively. The origin of y-axis (vertical axis) can be set at the bottom of the steel beam. k_{fj} and y_{fj} are the stiffness and y-coordinate of the *j*-th steel flange spring, respectively. k_{bjk} and y_{bjk} are the stiffness and y-coordinate of the *k*-th bolted joint spring, respectively. Note that the y-coordinate of the stiffness center for positive bending is

$$\bar{y}^{+} = \frac{\sum_{i=1}^{N_c} k_{ci} y_{ci} + \sum_{j=1}^{N_f} k_{fj} y_{fj} + \sum_{k=1}^{N_{bj}} k_{bjk} y_{bjk}}{\sum_{i=1}^{N_c} k_{ci} + \sum_{j=1}^{N_f} k_{fj} + \sum_{k=1}^{N_{bj}} k_{bjk}} \tag{5.24}$$

For negative bending, the stiffness of a collector connection, K_{sj}^{-}, can be computed as follows:

$$K_{sj}^{-} = \sum_{j=1}^{N_f} k_{fj}\left(y_{fj} - \bar{y}^{-}\right)^2 + \sum_{k=1}^{N_{bj}} k_{bjk}\left(y_{bjk} - \bar{y}^{-}\right)^2 \tag{5.25}$$

The y-coordinate of the stiffness center for negative bending, $\bar{y}^{-}$, is

$$\bar{y}^{-} = \frac{\sum_{j=1}^{N_f} k_{fj} y_{fj} + \sum_{k=1}^{N_{bj}} k_{bjk} y_{bjk}}{\sum_{j=1}^{N_f} k_{fj} + \sum_{k=1}^{N_{bj}} k_{bjk}} \tag{5.26}$$

Figure 5.41-top shows the setup of instrumentation for measuring the moment-rotation responses at the collector connection regions. The rotation of the collector end was measured by a pair of LVDT displacement transducers. The measured rotation was the total rotation of a region including the collector connection (denoted by Segment AB with a length of "L_{jj}") and a short beam segment (denoted by Segment BC with a length of "L_{jb}"). Also, the measured moment for a collector end was computed from the measured strains at a location 7 in. away from the column face, which was about the mid-span of the measured region. Thus, the experimentally determined moment can be used to represent the averaged moment in this region. As these beam segments adjacent to the collector connections remained elastic during Phase 1 testing, the moment-rotation response of the short beam segment can be represented by an elastic rotational spring. The rotational stiffnesses of the short beam segment for positive and negative bending, respectively denoted as K_{sb}^{+} and K_{sb}^{-}, are estimated as:

$$K_{sb}^{+} = \frac{E_s I_{tr}}{L_{jb}} \tag{5.27}$$

$$K_{sb}^{-} = \frac{E_s I_s}{L_{jb}} \tag{5.28}$$

where I_{tr} is the moment of inertia of the transformed section for the "effective" composite beam section next to a collector connection under positive bending. See Figure 5.41 for the effective composite beam sections for each type of collector connections (AFW, TFW, and BW details) under positive bending. Under negative bending, I_s is the moment of inertia of the "effective" steel beam section next to a collector connection; see Figure 5.42 for the effective steel beam sections.

As mentioned earlier, the rotational stiffnesses for a collector connection under positive and negative bending, K_{sj}^{+} and K_{sj}^{-}, were estimated by using the component-based spring model. With the rotational stiffnesses of a collector connection region (K_{sj}^{+} and K_{sj}^{-}) established by using the component-based spring model and those for the adjacent beam segment (K_{sb}^{+} and K_{sb}^{-}), the combined stiffnesses for the measured region can be characterized by combining two rotational springs, which respectively represent the connection region and beam segment, in series (see Figure 5.41 and Figure 5.42):

$$K_{s,total}^{+} = \frac{1}{\frac{1}{K_{sj}^{+}} + \frac{1}{K_{sb}^{+}}} \tag{5.29}$$

$$K_{s,total}^{-} = \frac{1}{\frac{1}{K_{sj}^{-}} + \frac{1}{K_{sb}^{-}}} \tag{5.30}$$

Table 5.7 and Table 5.8 compare the estimated stiffnesses ($K_{s,total}^{+}$ and $K_{s,total}^{-}$) with the measured secant stiffnesses from Test 1-3 (denoted as $K_{s,exp}^{+}$ and $K_{s,exp}^{-}$ for positive and negative bending, respectively). For the AFW connections, the component-based spring model (called the "spring model" later for simplicity) well predicts the rotational stiffness with either the upper- or

lower-bound approaches. This is because the rotation stiffness of this connection type mainly comes from the steel flanges and the contribution from the bolted joints is low.

For both sides of moment-rotation responses of all TFW and BW connections except for negative bending of BW connections, the estimated stiffnesses by using the upper-bound stiffness are about 2 to 3 times the measured stiffness; the ratio of estimated-to-measured stiffnesses, $K_{s,total}/K_{s,exp}$, ranges from 1.79 to 2.84. Recall that the upper-bound stiffness was derived by assuming the bolt stays still without any slippage. These suggest that bolt slip did take place at these collector connections during test even though the achieved rotation angles were small (less than 0.25% rad) in Test 1-3. On the other hand, the spring model with upper-bound stiffness for bolted joints well predicts the negative bending stiffness of the BW connections. The estimated-to-measured ratio ranges from 0.76 to 0.97. This implies that the bolts might have stayed "nearly still" without noticeable slippage when the BW connections were in negative bending during the Test 1-3. It is likely that the BW connections rotated about a location near the center of the bolt group when the connection was subjected to negative bending. Thus, the moment arms between the bolts and rotation center were short, which made the bending strain and stress near the bolted joints very low and could not trigger the bolt slippage.

As shown in Table 5.7 and Table 5.8, for spring model with lower-bound stiffness, the estimated-to-measured stiffness ratio ($K_{s,total}/K_{s,exp}$) range from 0.50 to 0.83 for both directions of responses for all TFW and BW connections, except that the estimated-to-measured ratio drops to about 0.10 for negative bending of BW connections. This indicates that using the spring model equipped with the initial stiffness of bearing-phase bolted joints for the bolted joint springs can provide a fair underestimate of the rotational stiffness of semi-rigid collector connections before the bolted joints get into bearing phase. Note that the analytical study presented in Section 5.3

shows that the contribution from the rotational stiffness of these semi-rigid connections to the global responses of the test building was small but nontrivial. Thus, an underestimate of the rotational stiffness by about 50% is still considered acceptable in practice. In fact, a somewhat underestimate on the rotational stiffness of collector connections would be desirable for the purpose of predicting the collector axial force demand for design, which will be elaborated in Section 5.4.4.

Table 5.7 and Table 5.8 also tabulate the predicted stiffnesses for the semi-rigid collector connections by using two empirical models proposed by Liu and Astaneh-Asl (2000) and FEMA-355D (2000). Note that these two models were developed for single-plate beam-to-column connections in the gravity frames based on the experimental data from quasi-static tests on full-scale beam-to-column subassembly specimens. Thus, their effectiveness and accuracy on the semi-rigid collector connections, which are expected to resist considerable axial force demand, has not been evaluated. The tabulated estimated-to-measured stiffness ratios ($K_{s,total}/K_{s,exp}$) indicate that these two models significantly underestimate the rotational stiffness of the collector connections for Test 1-3.

Figure 5.43 plots the measured moment-rotation responses of the collector connections in Test 1-3 together with the lines representing the estimated stiffnesses obtained from the proposed spring models and the two available empirical models. First, the spring model captures the responses of AFW connections very well. This validates the proposed approach (as illustrated in Figure 5.41 and Figure 5.42). The main purpose of the proposed component-based spring model is to estimate the response of "semi-rigid" collector connections. As shown in Figure 5.43, except for negative bending of BW connections, the moment-rotation responses of TFW and BW connections were more and less within the range between the lower- and upper-bound stiffnesses

computed by the spring model. It appears that, in general, the lower-bound stiffness from the spring model has the best estimate on the collector responses. The upper-bound approach well fits the negative bending response of BW connections. This could be attributed to no noticeable bolt slippage at the BW connections. But the two empirical models significantly underestimate the experimental stiffness. It is worth noting again that the magnitude of achieved rotation angles at the collector connections in Test 1-3 were less than 0.25% rad, which is relatively small for the typical responses that are expected in the design earthquake. Thus, even though the lower-bound stiffness from the spring model provides a good estimation of the collector connection responses in Test 1-3, during which the bolted joints at the collector connections did not get into bearing phase, it is not suitable for real applications. An approach for estimating the secant stiffness of the collector connection for simulation of the response produced by a design earthquake is presented in Section 8.2.

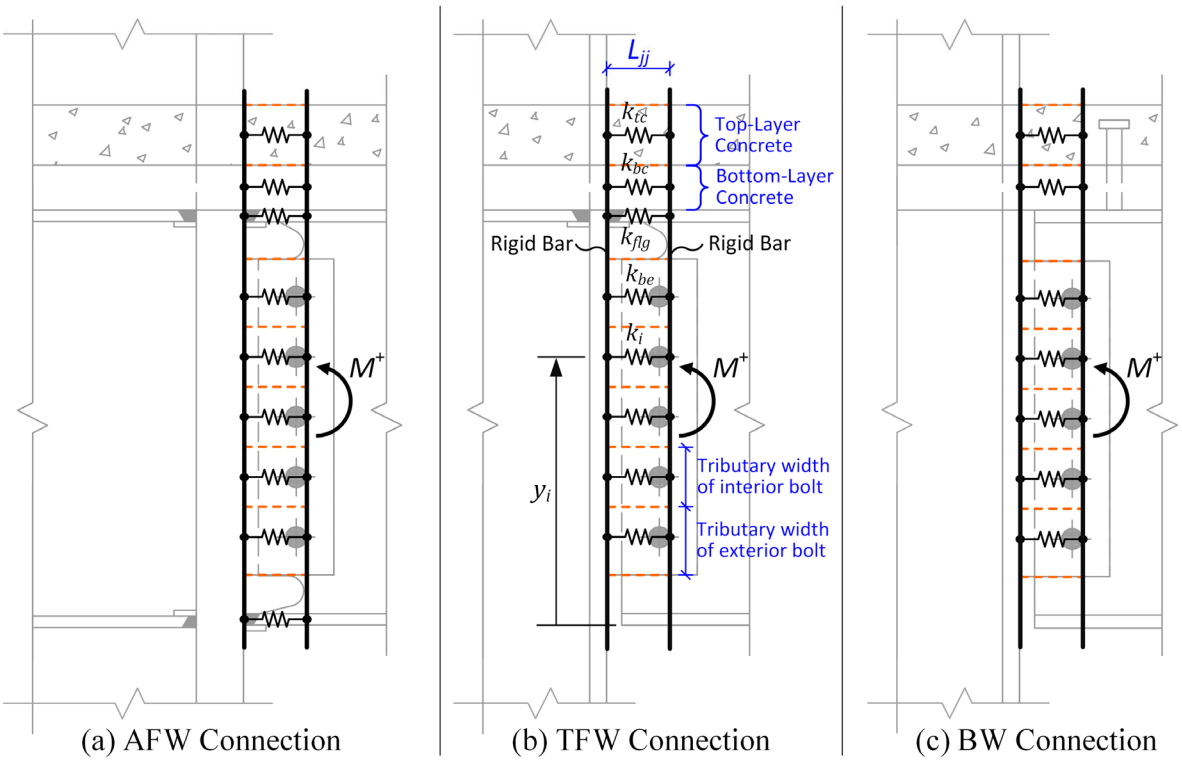

Figure 5.35 Component-Based Spring Models for Collector-to-Column Connections under Positive Bending

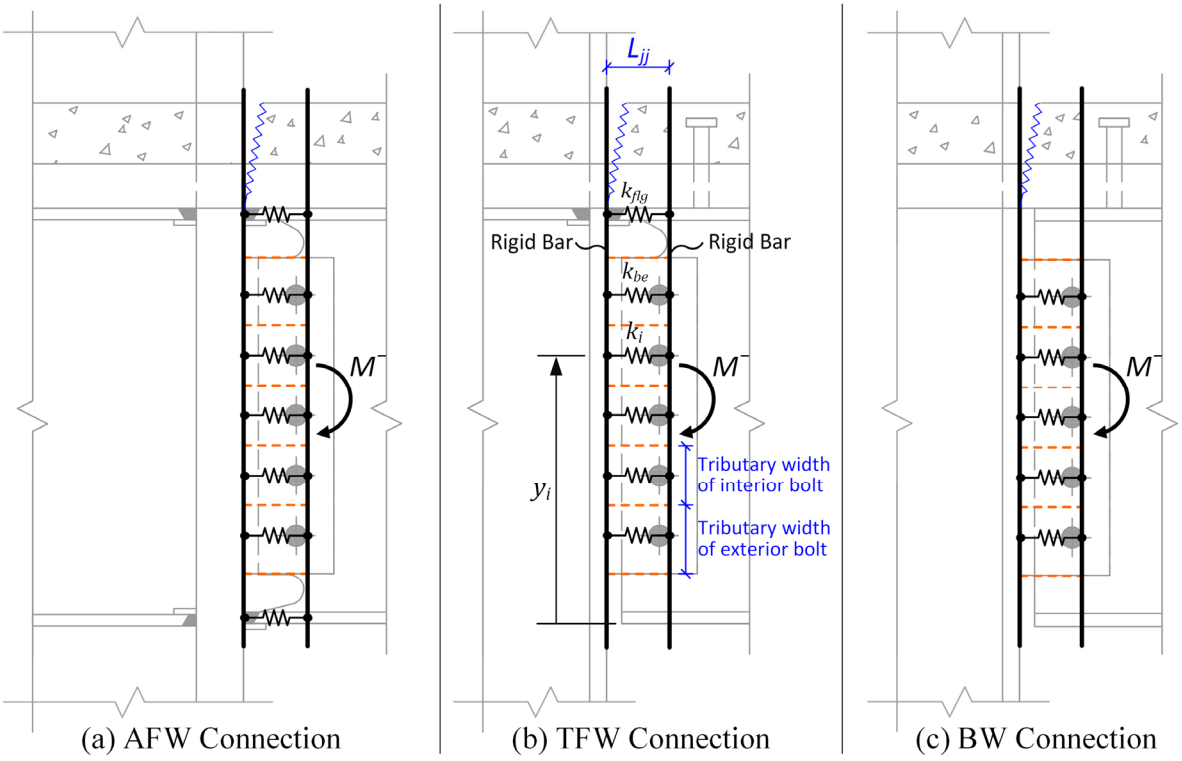

Figure 5.36 Component-Based Spring Models for Collector-to-Column Connections under Negative Bending

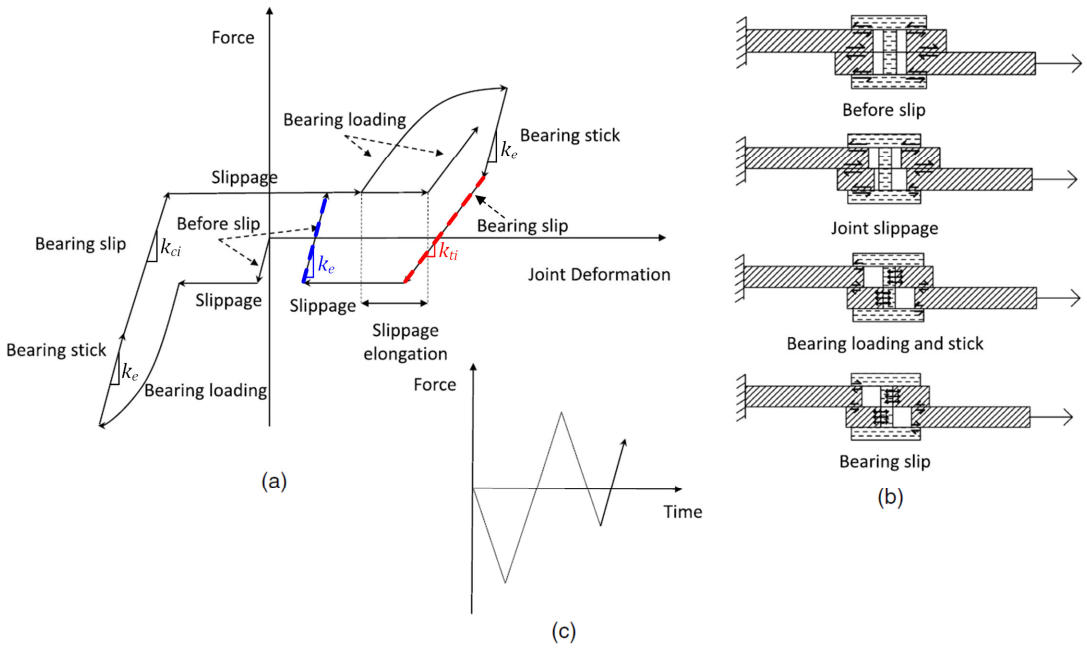

Figure 5.37 (a) Bolted Joint Hysteresis; (b) Free-body Diagrams; and (3) Loading Time History (Ma and Bocchini 2019)

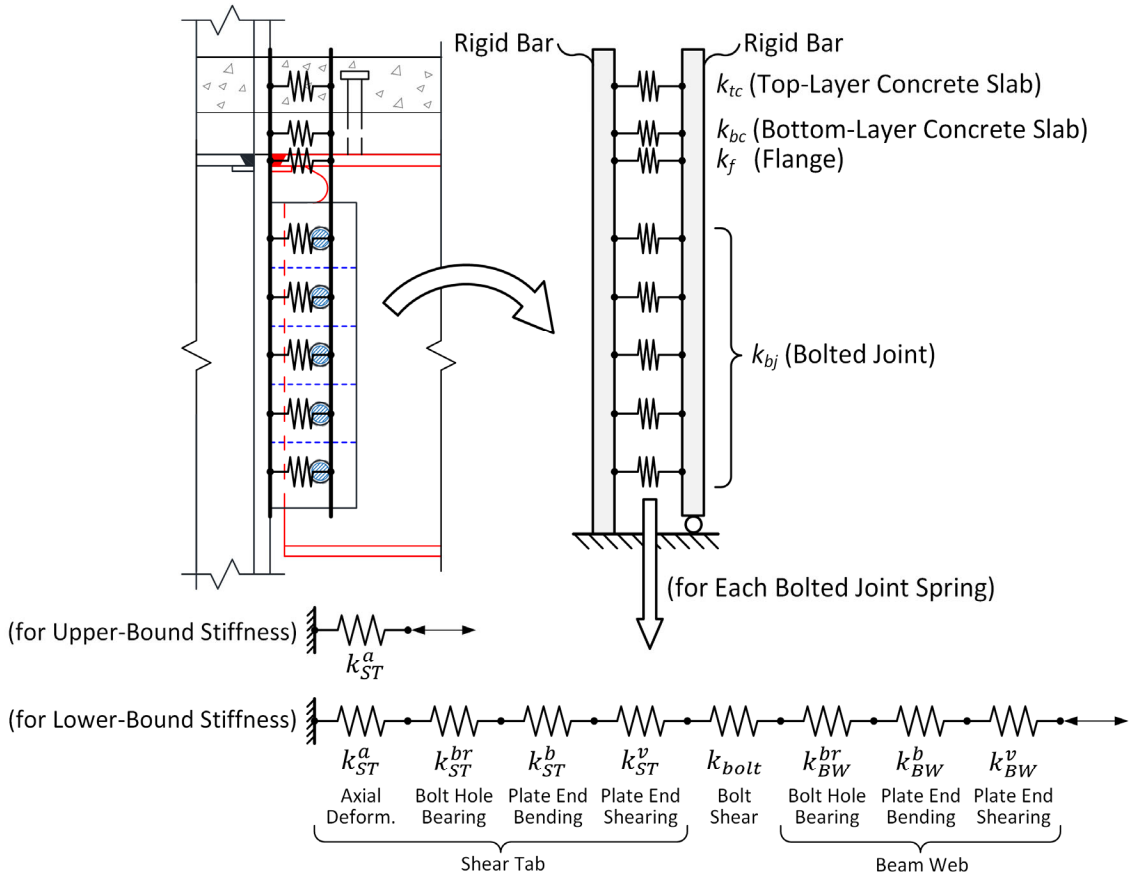

Figure 5.38 Upper-Bound and Lower-Bound Stiffnesses for Bolt Element Spring in Componet-Based Spring Model for Collector-to-Column Connections using

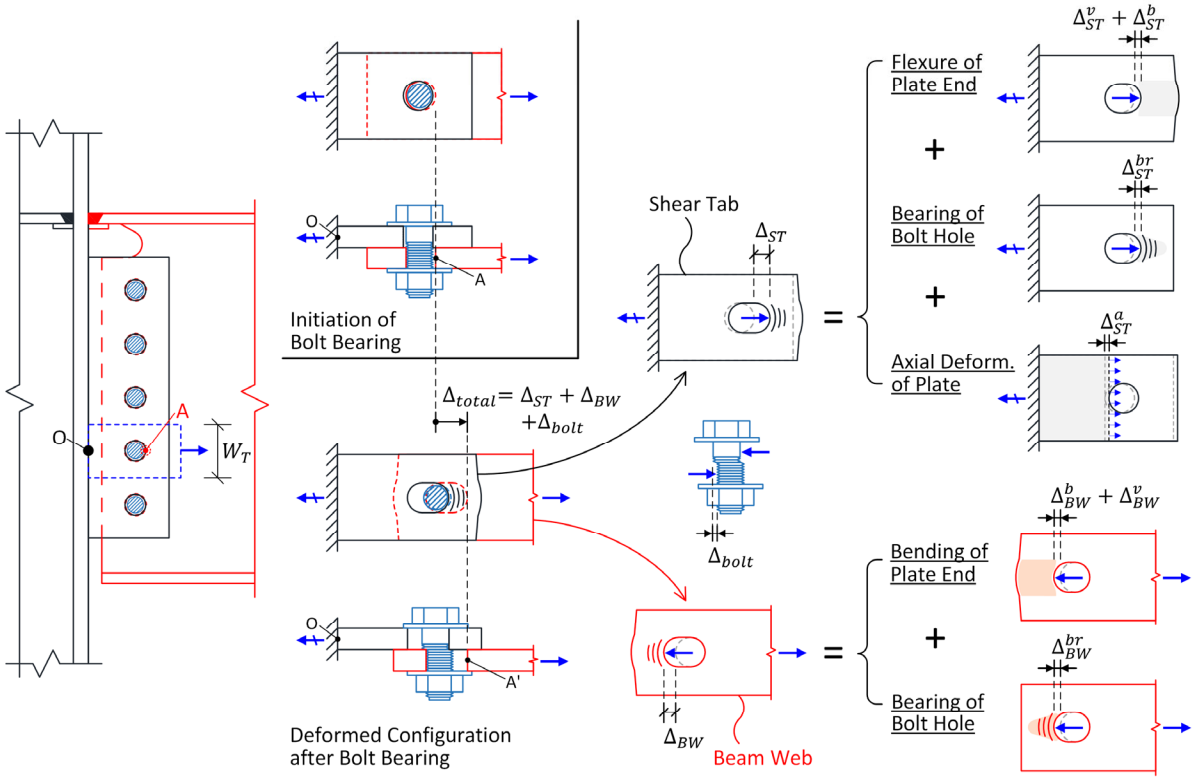

Figure 5.39 Various Deformations of a Bearing-type Shear Tab Bolted Connection in Tension

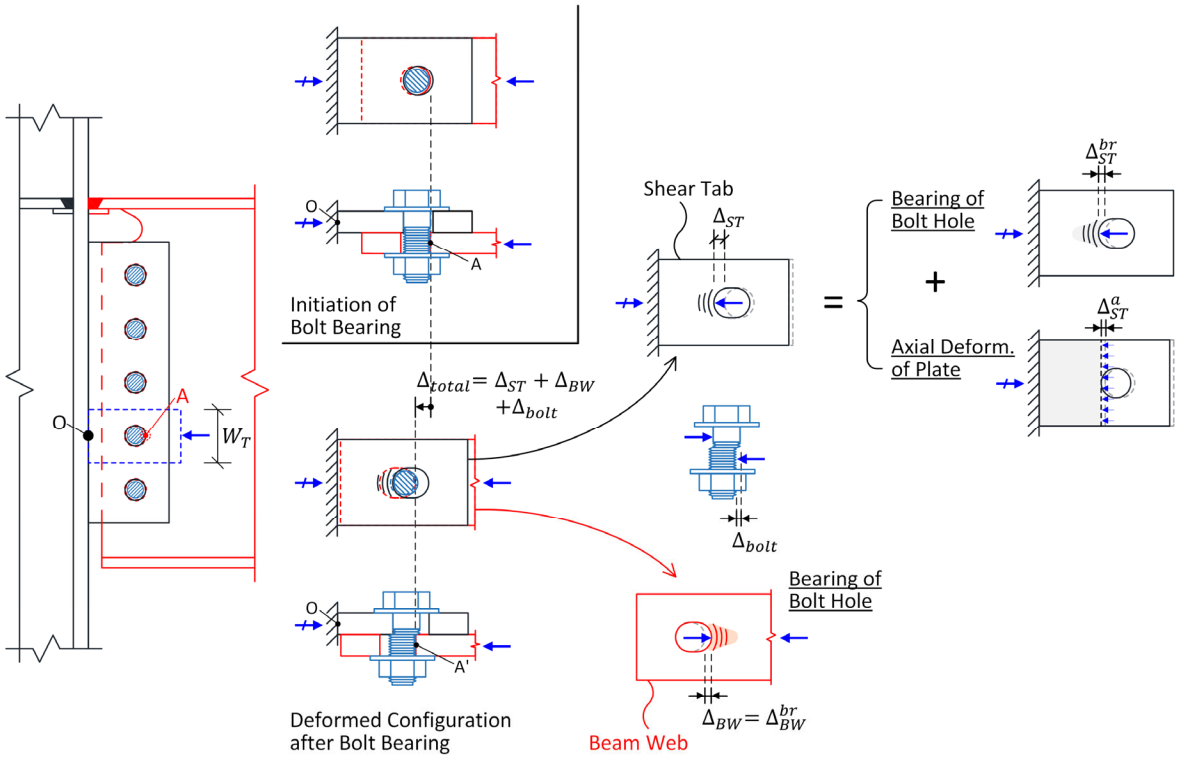

Figure 5.40 Various Deformations a Bearing-type Shear Tab Bolted Connection in Compression

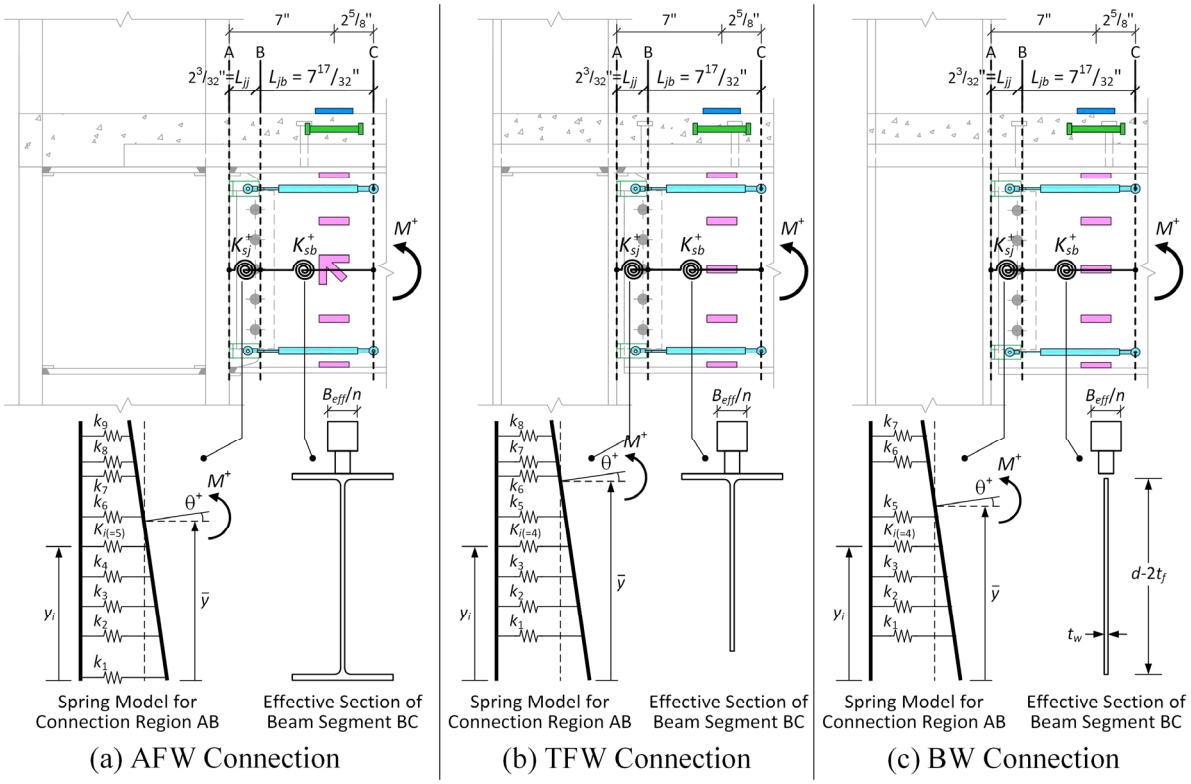

Figure 5.41 Rotational Springs in Series for Estimating Postive Bending Stiffness of Instrumented Regions at Collector Connections

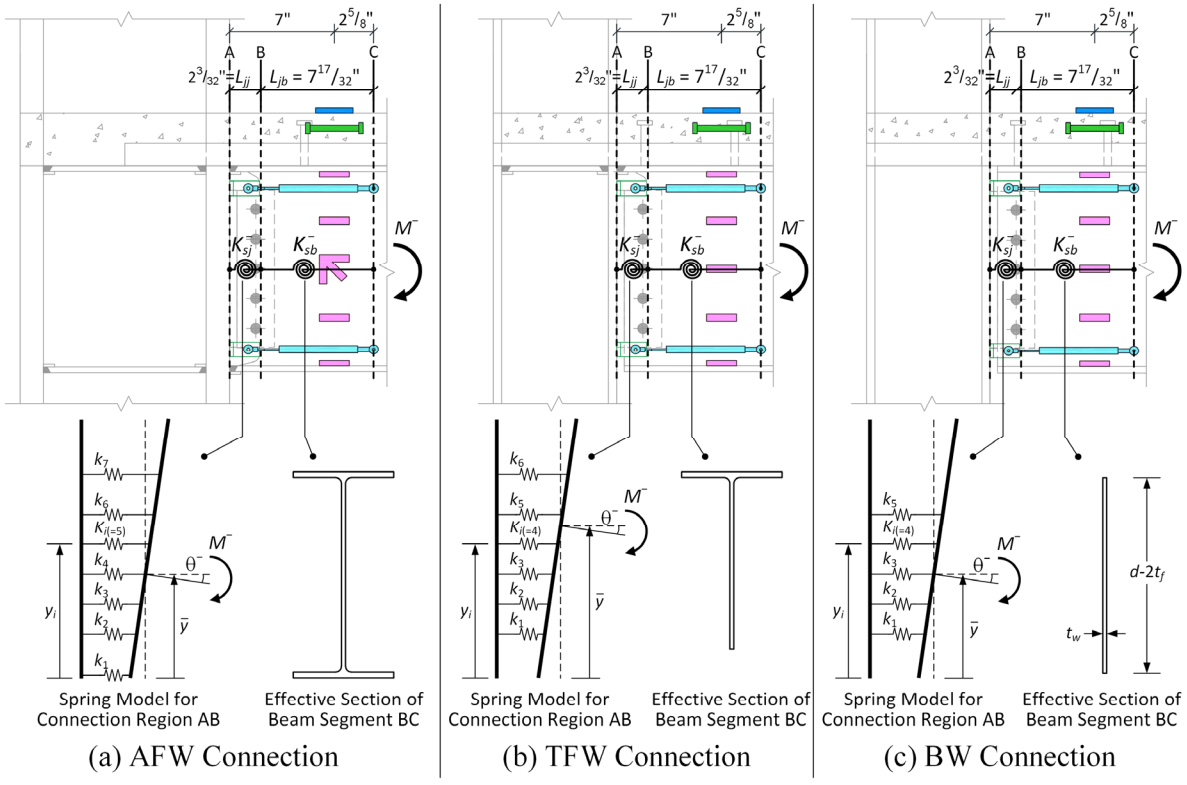

Figure 5.42 Rotational Springs in Series for Estimating Negative Bending Stiffness of Instrumented Regions at Collector Connections

Table 5.7 Comparison of Experimental and Predicted Rotational Stiffnesses for Collector-to-Column Connections in Frame N

Collector-to-Column Connection			AFW Connection		TFW Connection				BW Connection			
					Near-Side		Far-Side		Near-Side		Far-Side	
Bending Direction			Pos.	Neg.	Pos.	Neg.	Pos.	Neg.	Pos.	Neg.	Pos.	Neg.
Experiment	Measured Secant Stiffness	$K_{s,exp}$ (k-ft/rad)	114,500	78,666	23,920	11,119	16,271	8,141	23,702	14,829	17,977	11,241
Prediction	Rotational Stiffness of Beam Segment	K_{sb} (k-ft/rad)	174,983	93,378	55,602	28,713	57,287	28,713	71,623	15,972	61,691	15,189
	K_{sj} Estimated by Lower-Bound Spring Model	K_{sj} (k-ft/rad)	450,705	270,355	17,578	7,879	17,578	7,879	14,360	1,251	14,087	1,223
		$K_{s,total}$ (k-ft/rad)*	126,046	69,406	13,356	6,182	13,451	6,182	11,962	1,160	11,468	1,132
		$K_{s,total}/K_{s,exp}$	1.10	0.88	0.56	0.56	0.83	0.76	0.50	0.08	0.64	0.10
	K_{sj} Estimated by Upper-Bound Spring Model	K_{sj} (k-ft/rad)	519,069	306,912	187,575	118,116	187,575	118,116	161,554	37,807	161,554	37,807
		$K_{s,total}$ (k-ft/rad)*	130,867	71,595	42,889	23,098	43,884	23,098	49,623	11,228	44,643	10,836
		$K_{s,total}/K_{s,exp}$	1.14	0.91	1.79	2.08	2.70	2.84	2.09	0.76	2.48	0.96
	K_{sj} Estimated by Liu & Astaneh-Asl (2000)	K_{sj} (k-ft/rad)	–	–	3,931	2,036	3,931	2,036	3,954	2,036	3,954	2,036
		$K_{s,total}$ (k-ft/rad)*	–	–	3,671	1,901	3,679	1,901	3,747	1,806	3,716	1,795
		$K_{s,total}/K_{s,exp}$	–	–	0.15	0.17	0.23	0.23	0.16	0.12	0.21	0.16
	K_{sj} Estimated by FEMA-355D (2000)	K_{sj} (k-ft/rad)	–	–	10,967	5,600	10,967	5,600	10,967	5,600	10,967	5,600
		$K_{s,total}$ (k-ft/rad)*	–	–	9,160	4,686	9,205	4,686	9,511	4,146	9,312	4,092
		$K_{s,total}/K_{s,exp}$	–	–	0.38	0.42	0.57	0.58	0.40	0.28	0.52	0.36

*$K_{s,total} = 1/(1/K_{sj} + 1/K_{sb})$

Table 5.8 Comparison of Experimental and Predicted Rotational Stiffnesses for Collector-to-Column Connections in Frame S

Collector-to-Column Connection			AFW Connection		TFW Connection				BW Connection			
					Near-Side		Far-Side		Near-Side		Far-Side	
Bending Direction			Pos.	Neg.	Pos.	Neg.	Pos.	Neg.	Pos.	Neg.	Pos.	Neg.
Experiment	Measured Secant Stiffness	$K_{s,exp}$ (k-ft/rad)	129,434	90,724	22,082	10,718	16,555	8,227	21,702	11,540	–	–
Prediction	Rotational Stiffness of Beam Segment	K_{sb} (k-ft/rad)	172,704	93,378	55,444	28,713	58,166	28,713	72,680	15,972	60,398	15,189
	K_{sj} Estimated by Lower-Bound Spring Model	K_{sj} (k-ft/rad)	446,923	270,355	17,568	7,879	17,568	7,879	14,279	1,251	14,003	1,223
		$K_{s,total}$ (k-ft/rad)*	124,568	69,406	13,341	6,182	13,493	6,182	11,934	1,160	11,367	1,132
		$K_{s,total}/K_{s,exp}$	0.96	0.77	0.60	0.58	0.82	0.75	0.55	0.10	-	-
	K_{sj} Estimated by Upper-Bound Spring Model	K_{sj} (k-ft/rad)	513,387	306,912	185,174	118,116	185,174	118,116	157,280	37,807	157,280	37,807
		$K_{s,total}$ (k-ft/rad)*	129,231	71,595	42,668	23,098	44,262	23,098	49,709	11,228	43,640	10,836
		$K_{s,total}/K_{s,exp}$	1.00	0.79	1.93	2.16	2.67	2.81	2.29	0.97	-	-
	K_{sj} Estimated by Liu & Astaneh-Asl (2000)	K_{sj} (k-ft/rad)	–	–	3,931	2,036	3,931	2,036	3,954	2,036	3,954	2,036
		$K_{s,total}$ (k-ft/rad)*	–	–	3,671	1,901	3,682	1,901	3,750	1,806	3,711	1,795
		$K_{s,total}/K_{s,exp}$	–	–	0.17	0.18	0.22	0.23	0.17	0.16	–	–
	K_{sj} Estimated by FEMA-355D (2000)	K_{sj} (k-ft/rad)	–	–	10,967	5,600	10,967	5,600	10,967	5,600	10,967	5,600
		$K_{s,total}$ (k-ft/rad)*	–	–	9,160	4,686	9,205	4,686	9,511	4,146	9,312	4,092
		$K_{s,total}/K_{s,exp}$	–	–	0.41	0.44	0.56	0.57	0.44	0.36	–	–

*$K_{s,total} = 1/(1/K_{sj} + 1/K_{sb})$

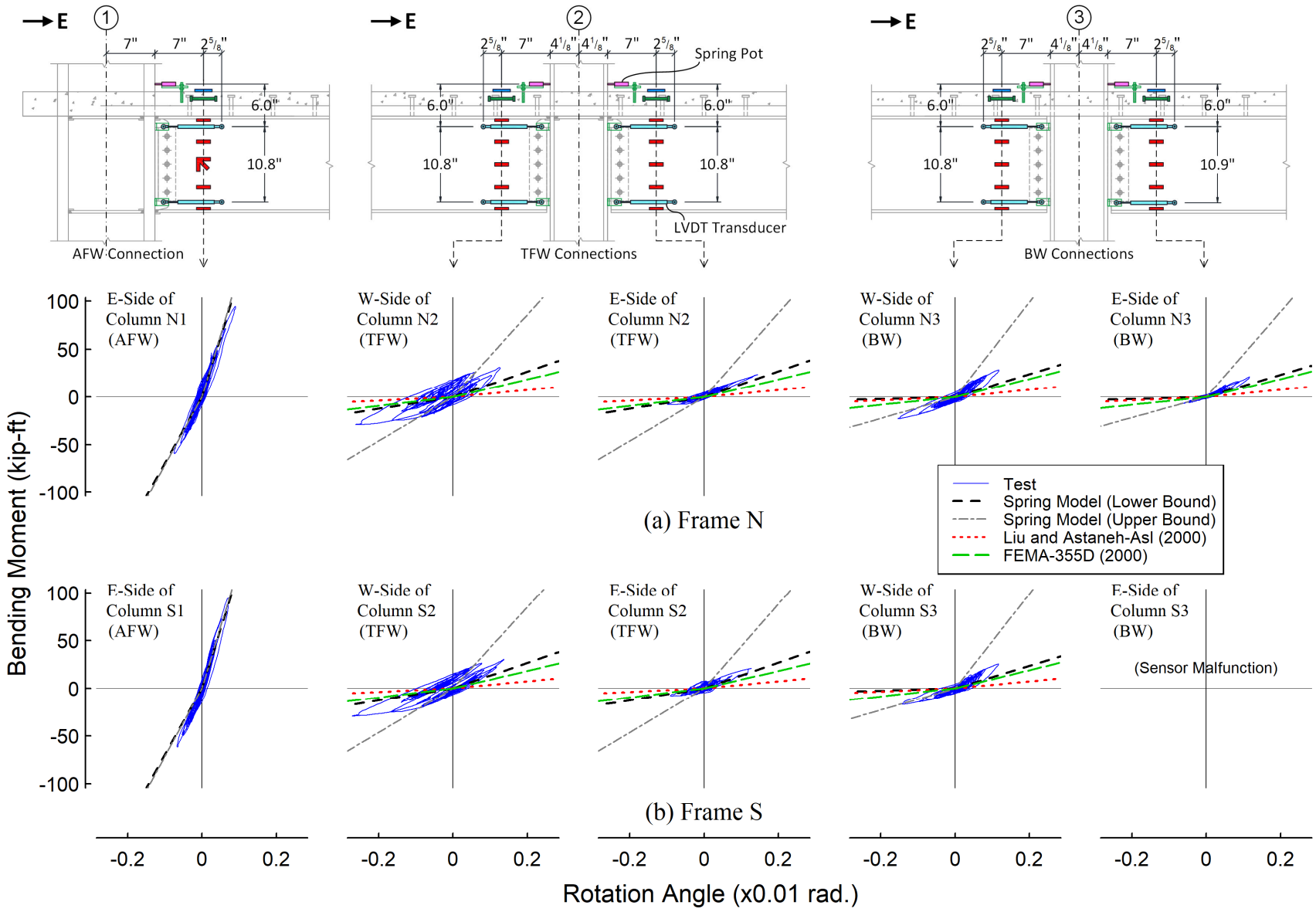

Figure 5.43 Comparison of Experimental and Predicted Moment versus Rotation Relations for Collector Connections (Test 1-3)

5.4.2 Estimation of Lateral Stiffness of Collector-to-Column Subassemblies

The test and analysis results show that the contribution from semi-rigid collector-to-column connections to the global responses of the test building was small but nontrivial. As the semi-rigid collector-to-column connections possessed a mild rotational stiffness, the gravity columns in the test building resisted a mild amount of story shear. It can be envisioned that, although the story shear taken by a single gravity column in a typical building would not be noticeable, the aggregate of story shears taken by all gravity columns would be considerable. Hence, there is a need for an approximation method for engineers to estimate the story shears taken by the gravity columns.

As illustrated in Figure 5.44, a modified portal method is proposed in this study for an approximate lateral load analysis on a plane frame with collectors. The complete procedure of this proposed method for typical buildings will be presented in Section 8.3. This section demonstrates the approximate lateral load analysis on Phase 1 specimen. Based on the Phase 1 test results, the following three assumptions on the inflection point locations can be applied to an approximate analysis on Phase 1 specimen:

1. In Collector 1, which employed a rigid collector-to-column connection (i.e., the AFW connection at the west end) at one end and a semi-rigid connection at the other end (i.e., the TFW connection at the east end), the inflection point is located at 3/4 of beam span away from the rigid joint.
2. In Collector 2, which employed semi-rigid connections at both ends (i.e., the TFW connection at the east end and BW connection at the west end), the inflection point is located at the mid-span because the rotational stiffnesses of these two types of semi-rigid connections are about the same.

3. In Collector 3, which employed BW connections at both ends, the inflection point is located at the mid-span.

With these assumed the inflection point locations, as illustrated in Figure 5.44, each longitudinal frame (i.e., Frame N or Frame S) can be decomposed into four beam-to-column assemblies by cutting the structure at the inflection point locations within the collector beams. It can be assumed that, when the longitudinal frame is subjected to a lateral force, the percentage of the story shear taken by a specific column is proportional to the ratio of the lateral stiffness of the beam-to-column subassembly at that specific column to the total stiffness of the entire frame. Therefore, simplified closed-form equations for estimating the lateral stiffness of those beam-to-column subassemblies shown in Figure 5.44 are derived in this study and presented as follows.

The beam-to-column subassembly at Column 1 is a L-shaped substructure composed of a column rigidly connected with a horizontal beam supported by a roller at the far end. Note that this column severed the LFRS in the test specimen. In addition, to represent the flexibility of the embedded column base connection, a rotational spring was inserted between the column bottom end and fixed base. To derive a closed-form equation for the lateral stiffness of this L-shaped beam-to-column assembly, the frame structure model with four degrees of freedom shown in Figure 5.45 is considered. Assuming the column and beam in this model are axially rigid, the global stiffness matrix, $\boldsymbol{K_{LF}}$, for this structure is established as follows:

$$\boldsymbol{K_{LF}} = \begin{bmatrix} \frac{12EI_c}{H^3} & \frac{6EI_c}{H^2} & 0 & \frac{6EI_c}{H^2} \\ \frac{6EI_c}{H^2} & \frac{4EI_c}{H} + \frac{4EI_b}{L} & \frac{2EI_b}{L} & \frac{2EI_c}{H} \\ 0 & \frac{2EI_b}{L} & \frac{4EI_b}{L} & 0 \\ \frac{6EI_c}{H^2} & \frac{2EI_c}{H} & 0 & \frac{4EI_c}{H} + K_{cb} \end{bmatrix} \tag{5.31}$$

where E is the young's modulus of steel. K_{cb} is the rotational stiffness of the embedded column base connection. H and L are the column height and beam length in this L-shaped frame model, respectively. I_b and I_c are the moments of inertia of beam and column, respectively. Note that, as the beam element represents the composite collector, I_b is taken as the average between the moments of inertia of bare steel section (I_s) and transformed section I_{tr}. That is to say, $I_b = (I_{tr} + I_s)/2$. By conducting static condensation on the global the global stiffness matrix, $\boldsymbol{K_{LF}}$, for only retaining the degree of freedom (DOF) representing the translational displacement of the L-frame (i.e., DOF 1), the closed-form equation for the lateral stiffness of the L-shaped frame model, $k_{F,LF}$, is obtained as follows:

$$k_{F,LF} = \frac{F}{\Delta} = \frac{3EI_c}{H^3}\left[4 - \left[\frac{\frac{4EI_c}{H} + \frac{3EI_b}{L} + K_{cb}}{\frac{EI_c}{H} + \frac{EI_b}{L} + K_{cb}\left[\frac{1}{4}\frac{(I_b/L_b)}{(I_c/L_c)} + \frac{1}{3}\right]}\right]\right] \tag{5.32}$$

To increase the accuracy of the stiffness estimation on this L-shaped substructure. The lateral stiffness regarding the shear deformation of the column, $k_{F,LF}$, is estimated as:

$$k_{F,CV} = \frac{GA_v}{H} \tag{5.33}$$

where $G = 1/[2(1+\upsilon)]$ is the shear modulus of steel. υ is the Poisson's ratio. A_v is the shear area of the steel column. The total lateral stiffness of the L-shaped substructure, which is the LFRS for each longitudinal frame, $k_{F,LFRS}$, is estimated by combining $k_{F,LF}$ and $k_{F,CV}$ in series:

$$k_{F,LFRS} = \frac{1}{\frac{1}{k_{F,LF}} + \frac{1}{k_{F,CV}}} \tag{5.34}$$

As shown in Figure 5.44, the beam-to-column subassemblies at Columns 2 and 3 are a T-shaped beam-to-column assembly which is composed of a pin-supported column and two beams framing to the top end of the column with semi-rigid connections. In addition, the far end of each

beam is assumed to be supported by a roller. Note that this T-shaped beam-to-column assembly represents the interior gravity frame in the topmost story of a typical building. Figure 5.46(a) shows the simplified frame model without considering the column panel zone effect and its deflection shape for deriving the equation for approximating the lateral stiffness of such a T-shaped beam-to-column assembly. The total lateral displacement, Δ_{total}, of this frame model under a lateral force F_H can be computed as the sum of two deflection components, Δ_c and Δ_r, where

Δ_c = lateral deflection caused by flexural deformations in the column

Δ_r = lateral deflection caused by flexural deformations in the beams and rotations at the semi-rigid connections.

These two deflection components can be calculated as:

$$\Delta_c = \left(\frac{H^3}{3EI_c}\right) F_H \tag{5.35}$$

$$\Delta_r = \left(\frac{H}{L_1 + L_2}\right)^2 \left[\frac{L_1^2}{K_{sj1}} + \frac{L_2^2}{K_{sj2}} + \frac{L_1^3}{3EI_{b1}} + \frac{L_2^3}{3EI_{b2}}\right] F_H \tag{5.36}$$

Subsequently, the lateral stiffness of the T-shaped beam-to-column assembly representing the topmost-story interior frame (TIF), $k_{F,TIF}$, can be derived as:

$$\begin{aligned} k_{F,TIF} &= \frac{F_H}{\Delta_{total}} = \frac{F_H}{\Delta_c + \Delta_r} \\ &= \frac{1}{\frac{H^3}{3EI_c} + \left(\frac{H}{L_1 + L_2}\right)^2 \left[\frac{L_1^2}{K_{sj1}} + \frac{L_2^2}{K_{sj2}} + \frac{L_1^3}{3EI_{b1}} + \frac{L_2^3}{3EI_{b2}}\right]} \end{aligned} \tag{5.37}$$

where E is the young's modulus of steel. H and I_c are height and moment of inertia of the column, respectively. L_1 and L_2 are the beam lengths. Note that the moment of inertia of the composite collector beam (I_{b1} or I_{b2}) is taken as the average between the moments of inertia of bare steel section and transformed section. K_{sj1} and K_{sj2} are the rotational stiffnesses of the semi-rigid

connections. It is suggested to use the average between secant stiffnesses in positive and negative bending regimes for the stiffness (K_{sj1} or K_{sj2}) of each semi-rigid connection.

Figure 5.46(b) shows the frame model considering the column panel zone effect and its deflection shape. In this more sophisticated model, in addition to the deflection components Δ_c and Δ_r, the deflection caused by the panel zone deformation, Δ_{pz}, is one of the sources of the total lateral displacement, Δ_{total}. The three deflection components can be calculated as:

$$\Delta_c = \left(\frac{H_c^3}{3EI_c}\right) F_H \tag{5.38}$$

$$\Delta_r = \left(\frac{H}{L_1 + L_2}\right)^2 \left[\frac{L_{c1}^2}{K_{sj1}} + \frac{L_{c2}^2}{K_{sj2}} + \frac{L_{c1}^3}{3EI_{b1}} + \frac{L_{c2}^3}{3EI_{b2}}\right] F_H \tag{5.39}$$

$$\Delta_{pz} = \left(\frac{H \cdot H_c}{K_{pz}}\right) F_H \tag{5.40}$$

where $L_{c1} = L_1 - w_{pz}/2$ and $L_{c2} = L_2 - w_{pz}/2$ are the clear beam lengths outside the panel zone. w_{pz} is the width of panel zone. Usually, w_{pz} is taken as the depth of the column section, d_c. H_c is the clear column height, which is outside the panel zone. It can be estimated as $H_c = H - d_{pz}/2$, where d_{pz} is the depth of panel zone. Figure 5.14 shows the gravity column panel zone regions considered in this study. K_{pz} is the rotational stiffness of the panel zone and computed as:

$$K_{pz} = G d_{pz} w_{pz} t_{pz} = G d_{pz} d_c t_{pz} \tag{5.41}$$

where t_{pz} is thickness of the panel zone.

Subsequently, the closed-form equation for lateral stiffness of the T-shaped beam-to-column assembly representing the TIF, $k_{F,TIF}$, considering the panel zone effect is obtained:

$$k_{F,TIF} = \frac{F_H}{\Delta_{total}} = \frac{F_H}{\Delta_c + \Delta_r + \Delta_{pz}}$$
$$= \frac{1}{\frac{H_c^3}{3EI_c} + \left(\frac{H}{L_1 + L_2}\right)^2 \left[\frac{L_{c1}^2}{K_{sj1}} + \frac{L_{c2}^2}{K_{sj2}} + \frac{L_{c1}^3}{3EI_{b1}} + \frac{L_{c2}^3}{3EI_{b2}}\right] + \frac{H \cdot H_c}{K_{pz}}} \tag{5.42}$$

Looking back to the portal method shown in Figure 5.44-top, the substructure with Column 4 includes the cantilever span with a diagonal truss. For simplicity, this substructure was represented by a L-shaped beam-to-column assembly which composed a pin-supported column and a beam which is framing to the column top end with a semi-rigid connection and supported by a roller at the far end (see Figure 5.44-bottom).

Figure 5.47(a) shows the simplified frame model without considering the column panel zone effect and its deflection shape for deriving the equation for approximating the lateral stiffness, $k_{F,TEF}$, of the L-shaped beam-to-column assembly representing the topmost-story exterior frame (TEF) in a typical building. Based on the same procedure [as shown in Eqs. (5.35) though (5.46)] which was taken for deriving the approximation equations for the stiffness of TIF, the equation for the lateral stiffness $k_{F,TEF}$ without considering panel zone effect is obtained:

$$k_{F,TEF} = \frac{F_H}{\Delta_{total}} = \frac{F_H}{\Delta_c + \Delta_r} = \frac{1}{\frac{H^3}{3EI_c} + \left(\frac{H}{L}\right)^2 \left[\frac{L^2}{K_{sj}} + \frac{L^3}{3EI_b}\right]} \tag{5.43}$$

Similarly, Figure 5.47(b) shows the frame model considering the column panel zone effect and its deflection shape for a TEF. The approximation equation for the lateral stiffness $k_{F,TEF}$ considering panel zone effect is obtained:

$$k_{F,TEF} = \frac{F_H}{\Delta_{total}} = \frac{F_H}{\Delta_c + \Delta_r + \Delta_{pz}} = \frac{1}{\frac{H_c^3}{3EI_c} + \left(\frac{H}{L}\right)^2 \left[\frac{L_c^2}{K_{sj}} + \frac{L_c^3}{3EI_b}\right] + \frac{H \cdot H_c}{K_{pz}}} \tag{5.44}$$

Table 5.8 and Table 5.9 show the calculations of the lateral stiffnesses of the four beam-to-column sub-assemblies in Frames N and S, respectively, by using the proposed approximation equations mentioned above. It is noted that, for computing the lateral stiffnesses of the beam-to-column sub-assemblies with semi-rigid connections, the rotational stiffnesses of the semi-rigid connections considered for listed in were taken as the lower-bound rotational stiffnesses estimated by the spring model described in Section 5.4.1. Table 5.10 tabulates the experimental and estimated stiffnesses for the beam-to-column assemblies by using the proposed approximation equations. As shown in Figure 5.48, the experimental stiffness at a specific beam-to-column subassembly was determined by the slope of the linear regression line for the column shear versus story drift relationship measured in Test 1-3. Note that the diagonal brace in each longitudinal frame resisted a small amount of story shear as well as the column, which means that the brace also contributed slightly to the lateral stiffness of the test frame. However, considering the story shear taken by the brace was small and brace actions were heavily related to the vertical vibration of the cantilever slab, which is not commonly seen in the typical buildings, the lateral stiffness provided by the braces was neglected in computing the total lateral stiffness for the test frame. From Table 5.10, it appears that the estimated stiffness computed by the approximation equation considering panel zone effect is very similar to the estimated stiffness without considering panel zone effect. This justifies the simplified model placing the semi-rigid connections at the intersections of beam-to-column centerlines without representing the panel zone. For the beam-to-column assemblies at the Columns 2 and 3, the estimated stiffnesses are slightly lower than the measured stiffnesses. This validates using the proposed approximation equations incorporated with the mild underestimated rotational stiffness for the semi-rigid collector connections can reach a satisfactory estimation, which intentionally aims at a mild underestimate, of the lateral stiffness

of the interior gravity frame. On the other hand, for the beam-to-column assembly at the Column 4, the proposed approximation equations overestimate the measured stiffness, which may be due to the neglecting of the cantilever slab effect in the approximation equations. The proposed approximation equations for exterior gravity frame will be examined by using Phase 2 test data and presented in Section 8.3.

Table 5.9 Calculation of Lateral Stiffness of Beam-to-Column Sub-Assemblies

(a) Frame N

B-to-C Sub-Assembly at Column N1				B-to-C Sub-Assembly at Column N2				B-to-C Sub-Assembly at Column N3				B-to-C Sub-Assembly at Column N4			
Steel Properties	E =	29000	ksi	Steel Properties	E =	29000	ksi	Steel Properties	E =	29000	ksi	Steel Properties	E =	29000	ksi
	G =	11154	ksi		G =	11154	ksi		G =	11154	ksi		G =	11154	ksi
Beam Properties	L =	126	in.	Beam 1 Properties	L_1 =	42	in.	Beam 1 Properties	L_1 =	84	in.	Beam Properties	L =	30	in.
	I_b =	399	in.^{4}		I_{b1} =	399	in.^{4}		I_{b1} =	427	in.^{4}		I_b =	349	in.^{4}
Column Properties	H =	99.2	in.		d_{b1} =	13.8	in.		d_{b1} =	13.8	in.		d_b =	13.9	in.
	I_c =	1650	in.^{4}		K_{sj1} =	152742	k-in./rad		K_{sj1} =	92763	k-in./rad		K_{sj} =	91860	k-in./rad
	K_{bc} =	5000000	k-in./rad	Beam 2 Properties	L_2 =	84	in.	Beam 2 Properties	L_2 =	30	in.	Column Properties	H =	76	in.
	A_v =	10.44	in.^{2}		I_{b2} =	427	in.^{4}		I_{b2} =	349	in.^{4}		I_c =	146	in.^{4}
	I_b/L =	3.17			d_{b2} =	13.8	in.		d_{b2} =	13.9	in.		d_c =	8.25	in.
	I_c/H =	16.63			K_{sj2} =	152742	k-in./rad		K_{sj2} =	92763	k-in./rad	Panel Zone Properties	t_{pz} =	0.36	in.
	$k_{F,LF}$ =	160.8	kip/in.	Column Properties	H =	76	in.	Column Properties	H =	76	in.		d_{pz} =	10.5	in.
	$k_{F,CV}$ =	1173.9	kip/in.		I_c =	146	in.^{4}		I_c =	146	in.^{4}		w_{pz} =	8.25	in.
	$k_{F,LFRS}$ =	141.4	kip/in.		d_c =	8.25	in.		d_c =	8.25	in.		K_{pz} =	347833	k-in./rad
				Panel Zone Properties	t_{pz} =	0.36	in.	Panel Zone Properties	t_{pz} =	0.36	in.	Clear Distances	L_c =	25.875	in.
					d_{pz} =	12.125	in.		d_{pz} =	10.5	in.		H_c =	69.05	in.
					w_{pz} =	8.25	in.		w_{pz} =	8.25	in.	$k_{F,TEF}$ (w/o PZ) =		9.7	kip/in.
					K_{pz} =	401664	k-in./rad		K_{pz} =	347833	k-in./rad	$k_{F,TEF}$ (with PZ) =		10.9	kip/in.
				Clear Distances	L_{c1} =	37.875	in.	Clear Distances	L_{c1} =	79.875	in.				
					L_{c2} =	79.875	in.		L_{c2} =	25.875	in.				
					H_c =	69.1	in.		H_c =	69.075	in.				
				$k_{F,TIF}$ (w/o PZ) =		16.1	kip/in.	$k_{F,TIF}$ (w/o PZ) =		12.5	kip/in.				
				$k_{F,TIF}$ (with PZ) =		15.8	kip/in.	$k_{F,TIF}$ (with PZ) =		12.3	kip/in.				

Table 5.9 Calculation of Lateral Stiffness of Beam-to-Column Sub-Assemblies (continued)

(b) Frame S

B-to-C Sub-Assembly at Column S1				B-to-C Sub-Assembly at Column S2				B-to-C Sub-Assembly at Column S3				B-to-C Sub-Assembly at Column S4			
Steel Properties	E =	29000	ksi	Steel Properties	E =	29000	ksi	Steel Properties	E =	29000	ksi	Steel Properties	E =	29000	ksi
	G =	11154	ksi		G =	11154	ksi		G =	11154	ksi		G =	11154	ksi
Beam Properties	L =	126	in.	Beam 1 Properties	L_1 =	42	in.	Beam 1 Properties	L_1 =	84	in.	Beam Properties	L =	30	in.
	I_b =	415	in.^{4}		I_{b1} =	415	in.^{4}		I_{b1} =	429	in.^{4}		I_b =	344	in.^{4}
Column Properties	H =	99.2	in.		d_{b1} =	13.8	in.		d_{b1} =	13.8	in.		d_b =	13.9	in.
	I_c =	1650	in.^{4}		K_{sj1} =	152682	k-in./rad		K_{sj1} =	92268	k-in./rad		K_{sj} =	91356	k-in./rad
	K_{bc} =	5000000	k-in./rad	Beam 2 Properties	L_2 =	84	in.	Beam 2 Properties	L_2 =	30	in.	Column Properties	H =	76	in.
	A_v =	10.44	in.^{2}		I_{b2} =	429	in.^{4}		I_{b2} =	344	in.^{4}		I_c =	146	in.^{4}
	I_b/L =	3.29			d_{b2} =	13.8	in.		d_{b2} =	13.9	in.		d_c =	8.25	in.
	I_c/H =	16.63			K_{sj2} =	152682	k-in./rad		K_{sj2} =	92268	k-in./rad	Panel Zone Properties	t_{pz} =	0.36	in.
	$k_{F,LF}$ =	162.4	kip/in.	Column Properties	H =	76	in.	Column Properties	H =	76	in.		d_{pz} =	10.5	in.
	$k_{F,CV}$ =	1173.9	kip/in.		I_c =	146	in.^{4}		I_c =	146	in.^{4}		w_{pz} =	8.25	in.
	$k_{F,LFRS}$ =	142.7	kip/in.		d_c =	8.25	in.		d_c =	8.25	in.		K_{pz} =	347833	k-in./rad
				Panel Zone Properties	t_{pz} =	0.36	in.	Panel Zone Properties	t_{pz} =	0.36	in.	Clear Distances	L_c =	25.875	in.
					d_{pz} =	12.125	in.		d_{pz} =	10.5	in.		H_c =	69.05	in.
					w_{pz} =	8.25	in.		w_{pz} =	8.25	in.	$k_{F,TEF}$ (w/o PZ) =		9.7	kip/in.
					K_{pz} =	401664	k-in./rad		K_{pz} =	347833	k-in./rad	$k_{F,TEF}$ (with PZ) =		10.9	kip/in.
				Clear Distances	L_{c1} =	37.875	in.	Clear Distances	L_{c1} =	79.875	in.				
					L_{c2} =	79.875	in.		L_{c2} =	25.875	in.				
					H_c =	69.1	in.		H_c =	69.075	in.				
				$k_{F,TIF}$ (w/o PZ) =		16.1	kip/in.	$k_{F,TIF}$ (w/o PZ) =		12.4	kip/in.				
				$k_{F,TIF}$ (with PZ) =		15.8	kip/in.	$k_{F,TIF}$ (with PZ) =		12.3	kip/in.				

Table 5.10 Summary of Lateral Stiffness of Beam-to-Column Sub-Assemblies

(a) Frame N

			Stiffness of Beam-to-Column Assembly at				Stiffness of Entire Frame N ($k_{F,total}$)
			Column N1 (k_{F1})	Column N2 (k_{F2})	Column N3 (k_{F3})	Column N4 (k_{F4})	
Experiment	Lateral Stiffness	(kip/in.)	129.4	20.9	18.6	5.6	174.5
	Percentage	(%)	74.2	12.0	10.7	3.2	100
Estimation (w/o Considering PZ Effect)	Lateral Stiffness	(kip/in.)	141.4	16.1	12.5	9.7	189.6
	Percentage	(%)	78.7	9.0	6.9	5.4	100
Estimation (Considering PZ Effect)	Lateral Stiffness	(kip/in.)	141.4	15.8	12.3	10.9	189.1
	Percentage	(%)	78.4	8.8	6.8	6.1	100

(b) Frame S

			Stiffness of Beam-to-Column Assembly				Stiffness of Entire Frame S ($k_{F,total}$)
			Column S1 (k_{F1})	Column S2 (k_{F2})	Column S3 (k_{F3})	Column S4 (k_{F4})	
Experiment	Lateral Stiffness	(kip/in.)	126.6	19.8	12.7	6.8	165.9
	Percentage	(%)	72.6	11.3	7.3	3.9	100
Estimation (w/o Considering PZ Effect)	Lateral Stiffness	(kip/in.)	142.7	16.1	12.4	9.7	190.9
	Percentage	(%)	79.4	9.0	6.9	5.4	100
Estimation (Considering PZ Effect)	Lateral Stiffness	(kip/in.)	142.7	15.8	12.3	10.9	190.3
	Percentage	(%)	79.0	8.8	6.8	6.0	100

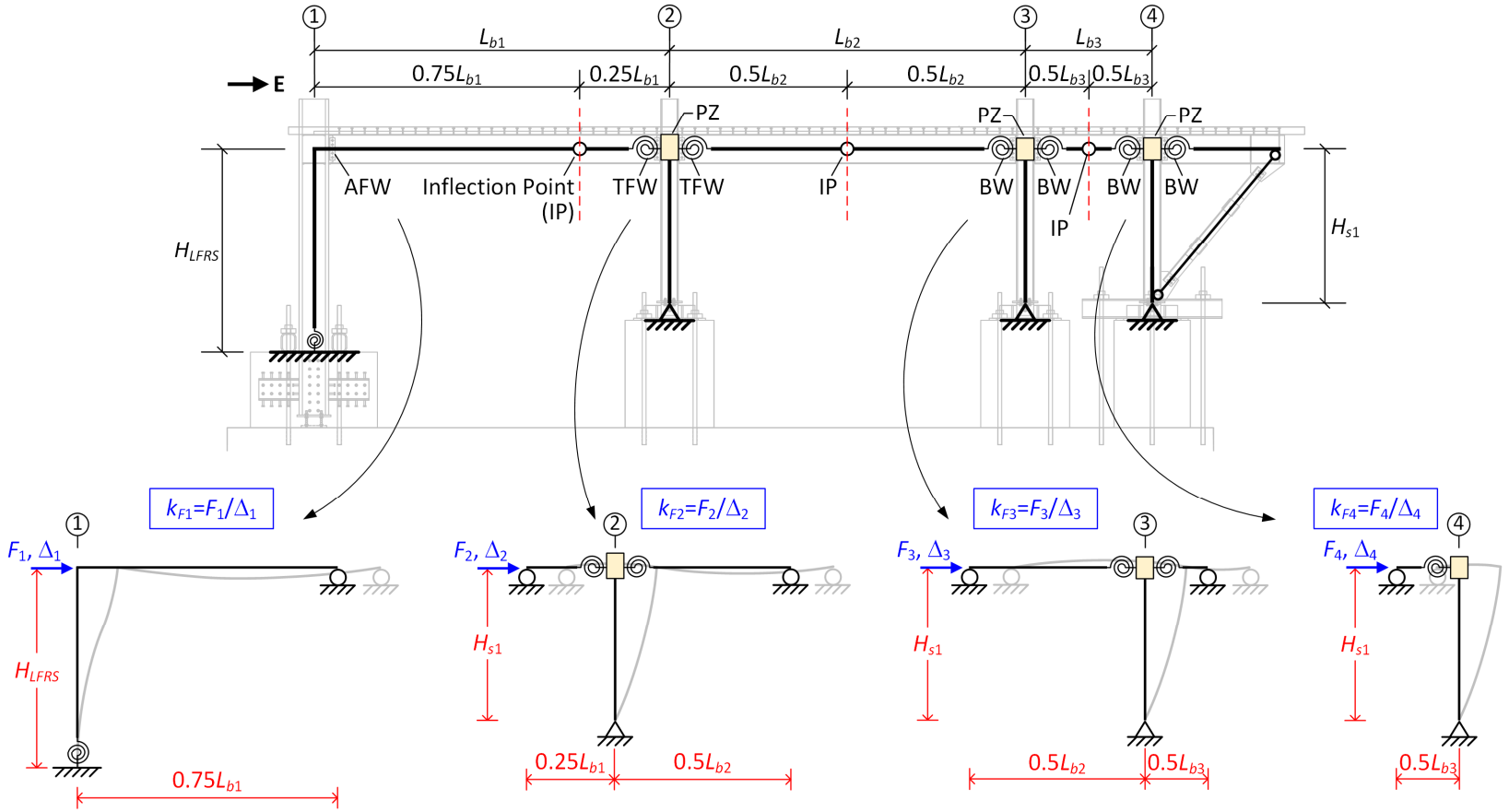

Figure 5.44 Proposed Portal Method for a Frame with Collectors and Beam-to-Column Assemblies for Lateral Stiffness Estimation (Taking Specimen for Example)

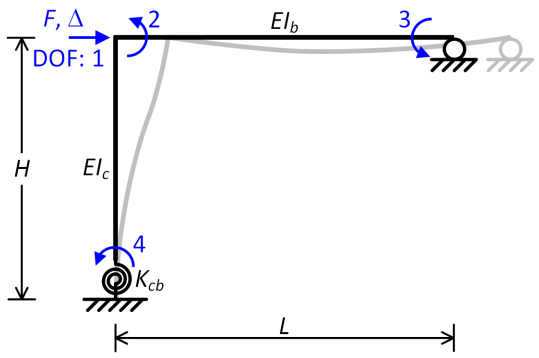

Figure 5.45 L-shaped Frame Model

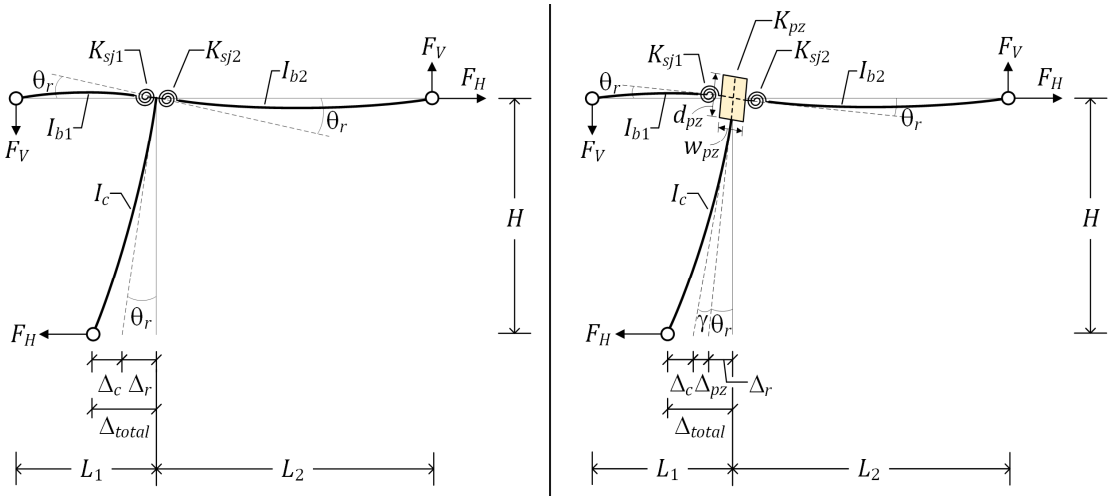

(a) w/o Considering Panel Zone Effect

(b) Considering Panel Zone Effect

Figure 5.46 Lateral Deflection Components of Topmost-Story Interior Beam-to-Column Assembly with Semi-Rigid Connections

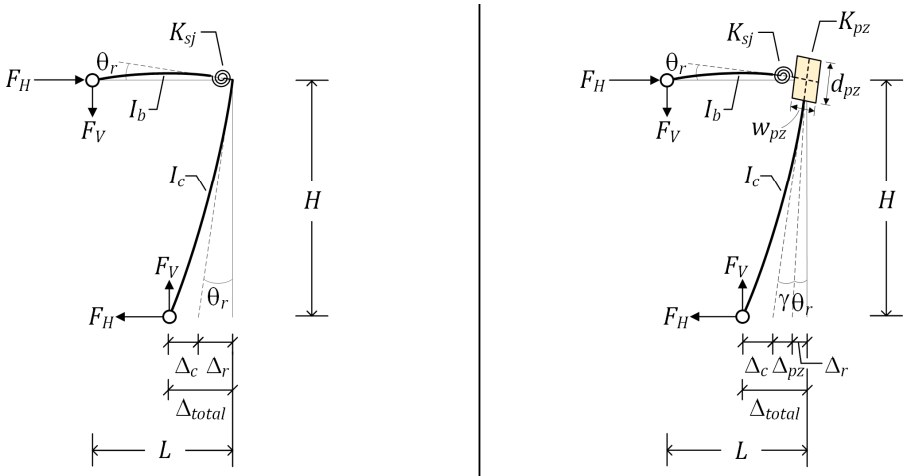

(a) w/o Considering Panel Zone Effect

(b) Considering Panel Zone Effect

Figure 5.47 Lateral Deflection Components of Topmost-Story Exterior Beam-to-Column Assembly with Semi-Rigid Connections

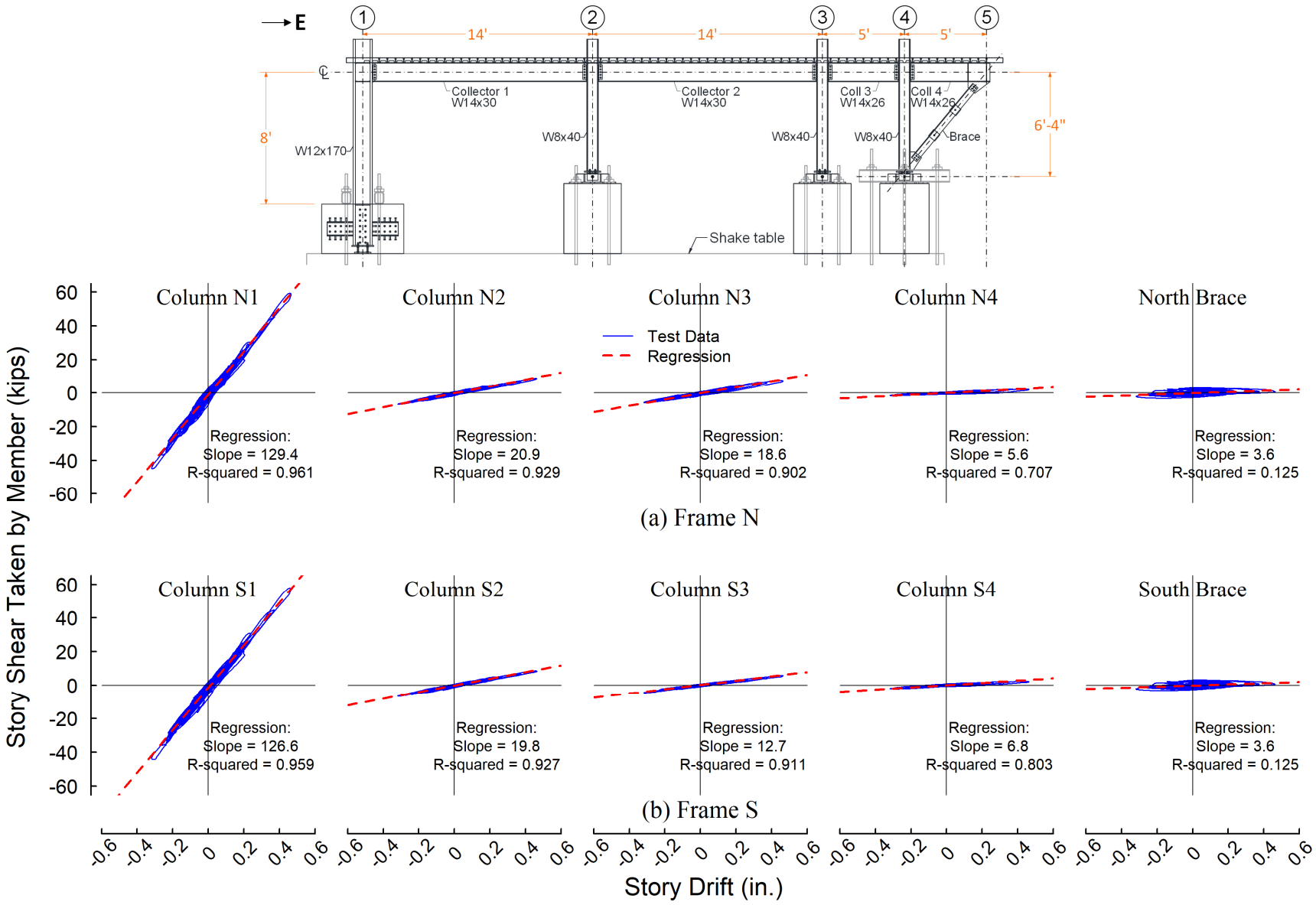

Figure 5.48 Story Shears Taken by Members versus Story Drift Relationships

5.4.3 Effective Slab Width of Composite Collectors

As the collector steel beam acted compositely with the concrete slab to resist the member forces, it requires the knowledge of the effective slab width to conduct the member force recovery for the collectors in the test building. Also, the effective slab width of the collectors is required for the seismic analyses on a frame model representing the collectors by using fiber bema-column elements or beam-column elements with transformed section properties. For Phases 2 and 3 testing, multiple strain gauges were installed on the concrete slab surface near two collector connection regions, which were the AFW connection of Collector 1 and TFW connection of Collector 2, respectively, on each composite collector line in the test building. This allows experimental investigations on the effective slab with at these locations. In this section, a parametric study was conducted to evaluate the accuracy of the effective slab width experimentally determined from Phase 2 Testing.

As shown in Figure 5.30, the results of time history analysis on specimen model BT-2 for simulation of Test 1-3 show that the force equilibrium at the AFW connection, which was adjacent to the top end of the cantilever column, of test specimen was established mainly by the balancing of the member forces between the column and collector. Among all the member forces acting at the AFW connection, the magnitude of slab forces and west chord member forces (weak-axis shear and torsion) acting at the AFW connection were very load compared to the member forces from the column and collector. These indicate that a proper effective slab width used in the test data reduction for the collector would result in a closeness between the measured collector axial force (P_{coll}) and measured column shear (V_c) to achieve the horizontal force equilibrium at the AFW connection, as shown in Figure 5.49-top left. Likewise, a proper effective slab width would lead

to a closeness between the measured collector moment (M_{coll}) and measured column moment (M_c) at the beam-to-column intersection at the AFW connection to establish a moment equilibrium.

As presented in Section 8.1, in this research, the slab effective width at a composite section near each AFW connection was investigated experimentally by using Phase 2 test data. As the collector beams were edge beams in the test building. The effective slab width of a composite section can be separated into two parts: (1) exterior width ($b_{eff,e}$) for the 1-ft overhang slab; and (2) interior width ($b_{eff,i}$) for the interior slab made by corrugated metal deck. Thus, the total effective slab width ($b_{eff,t}$) is the summation of these two parts. As shown in Figure 8.1 and Figure 8.2, the measured strain profile for the exterior slab was determined by using two strain data points with a assumed linear strain profile pattern, which are considered adequate for determining the effective slab width within the 1-ft hangover slab. On the other hand, the measured strain profile for the interior slab was captured by three strain data points. These three measure points only covered a moderate portion of the geometric width of the interior slab. Thus, there might be some uncertainty in the experimentally determined effective width for the interior slab.

Figure 5.49 and Figure 5.50 show the results of a parametric optimization study on the effective slab width to evaluate the reliability of the experimentally determined effective width. Note that the total slab width, $b_{eff,t}$, is the input variable of interest for this study. However, as the experimentally determined slab width for the exterior slab ($b_{eff,e}$) is considered more reliable than that for the interior slab ($b_{eff,i}$), as shown in Figure 5.49-top right, the values of the variable, $b_{eff,t}$, is determined by the summing up the experimentally-determined value for $b_{eff,e}$ and a varying value for $b_{eff,i}$. In addition, the ratios of the collector member forces to column member forces (P_{coll}/V_c and M_{coll}/M_c) at the AFW connection were taken as the output variables for this study. Based on the force equilibrium at AFW connection, the use of a proper value for $b_{eff,t}$ in

computing the collector member forces would make both values of P_{coll}/V_c and M_{coll}/M_c being close to and slightly less than 1.0. This is because there would be some small magnitude of member forces from the west chord and concrete slab acting together with the collector member forces to balance the column member forces at the AFW connection.

Figure 5.49 shows the relationships between the collector/column response ratios (P_{coll}/V_c and M_{coll}/M_c) versus the total effective slab width $b_{eff,t}$ at the instant of negative peak floor acceleration, at which the composite collector section at AFW connection was subjected to a simultaneous tensile axial force and positive bending and the concrete slab there was in compression. It can be found that both P_{coll}/V_c and M_{coll}/M_c values were close to and slightly less than 1.0. for the value of $b_{eff,t}$ ranging from 20 in. to 22 in, indicating the appropriate range for effective width. As marked by the dot lines in Figure 5.49, the experimentally determined values are very close to this range in both Frames N and S. This validates the experimentally determined effective widths at the AFW connections. Furthermore, as marked by the dashed lines in Figure 5.49, it is obvious that the code-prescribed width (AISC 2016c) is notably larger than the range of proper effective width.

Figure 5.50 shows the relationships between the collector/column response ratios (P_{coll}/V_c and M_{coll}/M_c) versus the total effective slab width $b_{eff,t}$ at the instant of negative peak floor, at which the concrete slab there was in tension as the collector end was under negative bending. This parametric study indicates that the appropriate effective slab width was about 42 in. because both P_{coll}/V_c and M_{coll}/M_c ratios were close to and slightly less than 1.0 for this width. This appropriate effective width for negative bending is much wider than the proper width range (21 in.~22 in.) for positive bending. It is also wider than the AISC code-prescribed value. Note that the concrete slab near the collector end could not develop significant tensile strain as a crack

appeared between the concrete slab and the steel column face when the collector end was under negative bending. In addition, the Phase 2 test results (see Figure 8.1) showed that, when the concrete slab was in tension, there was no notable shear-lag phenomenon observed in the measured strain profile along the slab width, which implies that the effective width would be wider than the measured region. This agrees with the results from the parametric study shown in Figure 5.50. Theses suggest that, for the concrete slab at collector ends, the effective width can be taken as 42 in. when the concrete is in tension.

Due to the capacity limit of the data acquisition system, the slab effective width only can be experimentally at two locations (AFW connection of Collector 1 and TFW connection of Collector 2) on composite collector line in the specimen (see Section 8.1 for the associated investigation results). Unfortunately, it is not allowed to obtain the thorough distribution of the effective slab width along the entire collector lines from the test data. For computing the Phase 1 test results on axial force and moment diagrams along the collector lines shown in Figure 4.46 through Figure 4.49, the effective slab width was simply assumed to be "uniform" along each collector at either an experimentally-determined or a code-prescribed width (see Figure 3.64).

In this section, a varying distribution pattern of effective slab width along composite beam span proposed by Zhu et al. (2015) is employed to pursue an improved data reduction on axial force and moment diagrams along the composite collector lines for Phase 1 testing. Figure 5.51 illustrates the piecewise linear distribution pattern of effective slab width proposed by Zhu et al. (2015). Firstly, the whole span of each composite collector beam is separated by end supports and inflection points as a series of equivalence spans. Each equivalence span is further divided into to three equal sub-spans (two end sub-spans and a middle sub-span). It is assumed that the mid-span effective slab width, $b_{eff,u}$, is uniform along the middle sub-span, while the effective width on

each end sub-span is linearly decreasing from the mid-span effective width, $b_{eff,u}$, to the effective width, $b_{eff,s}$, at an end support or an infection point. The mid-span effective width, $b_{eff,u}$, and the effective width at end support, $b_{eff,s}$ are nondimensionalized as the effective width coefficients λ_u and λ_s, respectively by dividing these two widths by the real geometric slab width, b. The formula for computing effective λ_u and λ_s are as follows:

$$\lambda_u = \frac{b_{eff,u}}{b} = 1 - e^{-0.212(b/l_e)^{-1.284}} \tag{5.45}$$

$$\lambda_s = \frac{b_{eff,s}}{b} = 1 - e^{-0.065(b/l_e)^{-1.313}} \tag{5.46}$$

where l_e is the length of an equivalence span. Figure 5.51 shows the distribution pattern of the effective width coefficient in an equivalence span. It should be noted that the European standard Eurocode 4 (CEN 2004) also regulates a similar piecewise linear distribution pattern for effective slab with a wider mid-span effective width and a narrow effective at the beam ends. However, the Eurocode 4 considers that the equivalence span is only related to the geometrical beam span.

Figure 5.52 shows the "varying" distribution of effective slab width along each collector line based on Zhu et al.'s approach. It is noted that, based on the test results, it is assumed that inflection point in Collector 1 is located at ¾ of the beam span away from the west end, where the AFW connection was located. This reflects the fact that the AFW connection (west end) was much stiffer than the TFW connection (east end) in Collector 1. In addition, the inflection point in Collector 2 is assumed to be at the mid-span because test results showed that the rotational stiffness of the TFW connection (west end) was close to that of the BW connection (east end). For comparison, Figure 5.52 also plots the AISC code-prescribed effective width and the "uniform" effective widths based on the measured effective widths at a few measure points. Note that these uniform effective widths were used for the processing the data for the test results shown in Section

4.2. It can be found that the varying effective width distribution has a width close to "measured" effective width at the measure points, which are located near the collector ends. In addition, the varying effective width distribution is close to the code-prescribed width near the mid-span. These somehow validate the use of varying effective width distribution for data processing.

Figure 5.53 through Figure 5.56 show the experimentally determined collector member force diagrams (axial force and bending moment diagrams) obtained by using the "varying" effective slab width distributions for the member force recovery. In addition, the measured collector member force diagrams based on the "uniform" slab width distributions and the analytical member force diagrams obtained from Model BT-2 are plotted in Figure 5.53 through Figure 5.56 for the purpose of comparison. The analytical results provide a reference to evaluate the accuracy of measured responses based on the two effective slab width distributions. From Figure 5.53 and Figure 5.54, it appears that, in general, the collector axial force diagrams based on the varying effective slab width is closer to the analytical results than the axial force diagrams based on the uniform effective slab width. Especially within the half-span adjacent to the LFRS in Collector 1, the magnitude of the axial force obtained from the uniform effective slab width noticeably overshot the analytical results. Note that the bending action in the collector section in this region was considerable because a significant amount of moment was transmitted through the neighboring AFW connection. Thus, the magnitude of strains in concrete slab were relatively high in this region. Furthermore, in this region, the bending action made the direction of the axial stress in the concrete was opposite to the total axial force of the composite section. Thus, an underestimate on the effective slab width would result in an overestimation of the computed collector axial force in this region. This explained why the measured collector axial force based on the uniform effective slab width overshot the analytical results because the uniform effective slab width distribution may be

too narrow to reflect the collector responses for this region. Figure 5.55 and Figure 5.56 show that, between the two slab effective width distributions, using the varying effective width distribution would lead to a better force recovery for the collector moment diagrams. Therefore, the varying slab width distribution is employed for computing the collector member forces in Phase 2 testing. Also, the measured collector member force diagram for Phase 1 testing presented elsewhere (e.g., Sections 5.3 and 5.4.4) in this Chapter are based on the varying slab width distribution.

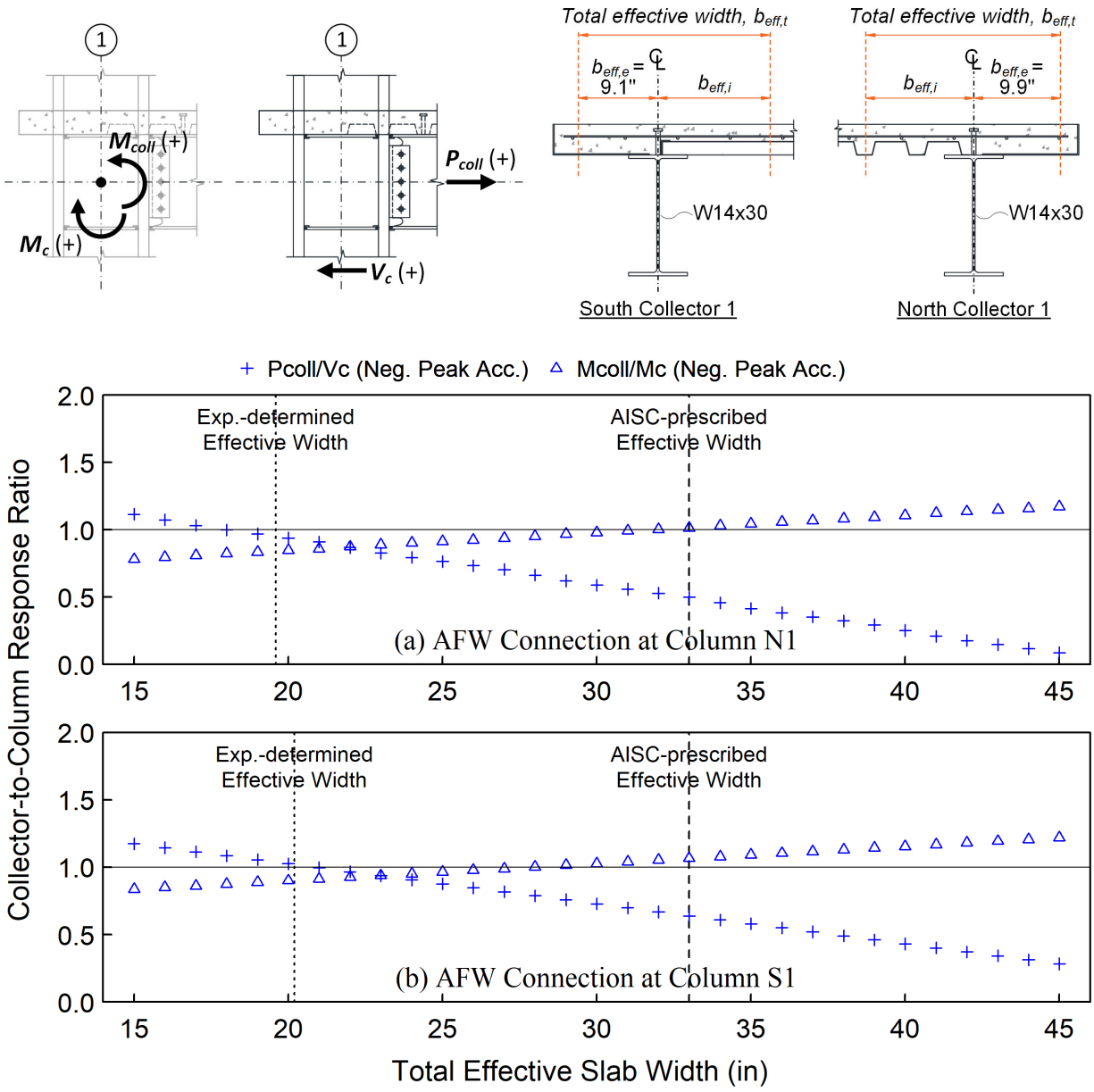

Figure 5.49 Parametric Study on Effective Slab Width in Compression near AFW connections

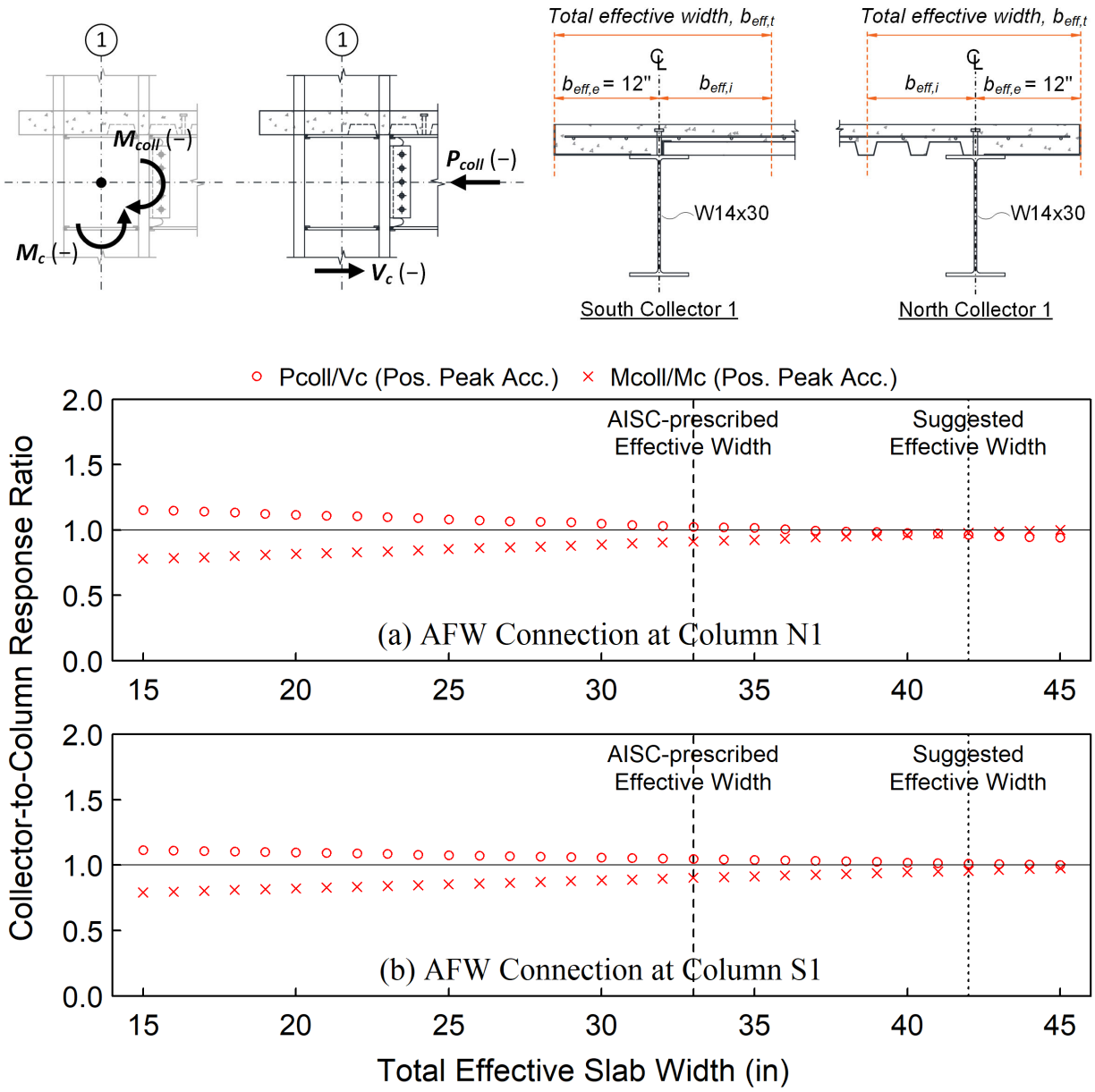

Figure 5.50 Parametric Study on Effective Slab Width in Tension near AFW connections

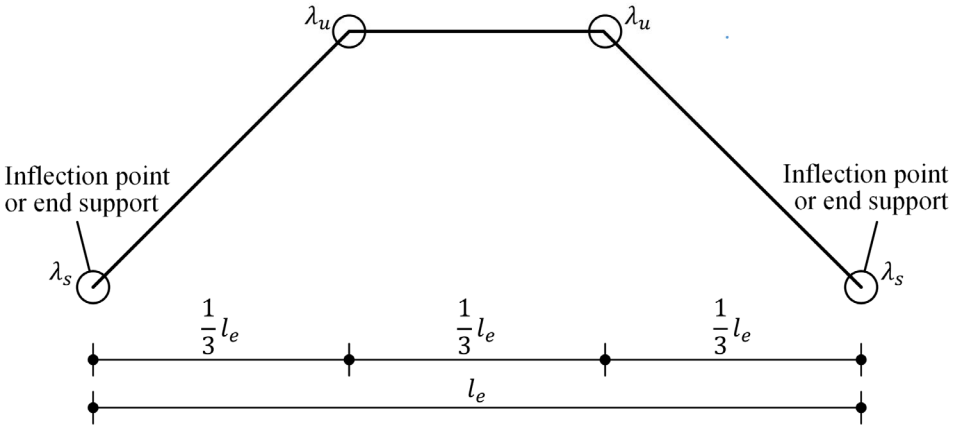

Figure 5.51 Distribution Pattern of Effective Width Coefficients in an Equivalent Span (Zhu et al. 2015)

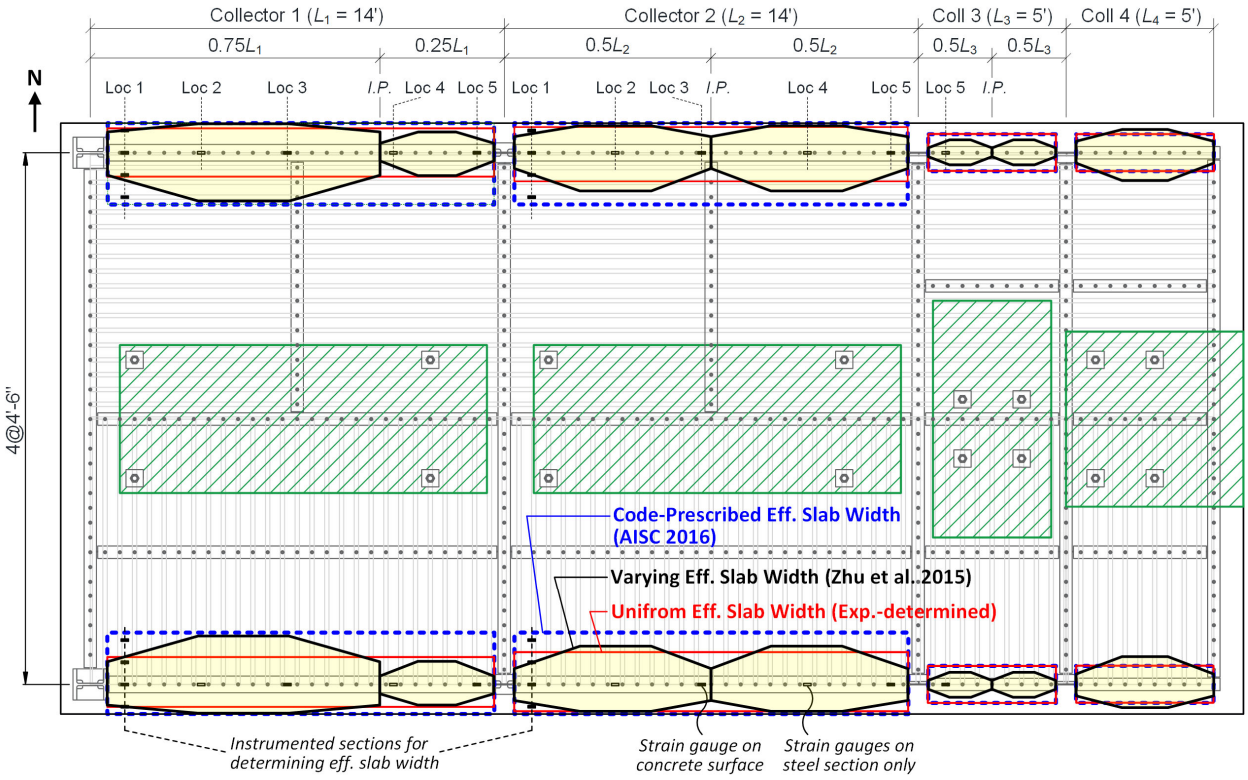

Figure 5.52 Comparison of Constant and Varying Effective Slab Widths along Collector lines

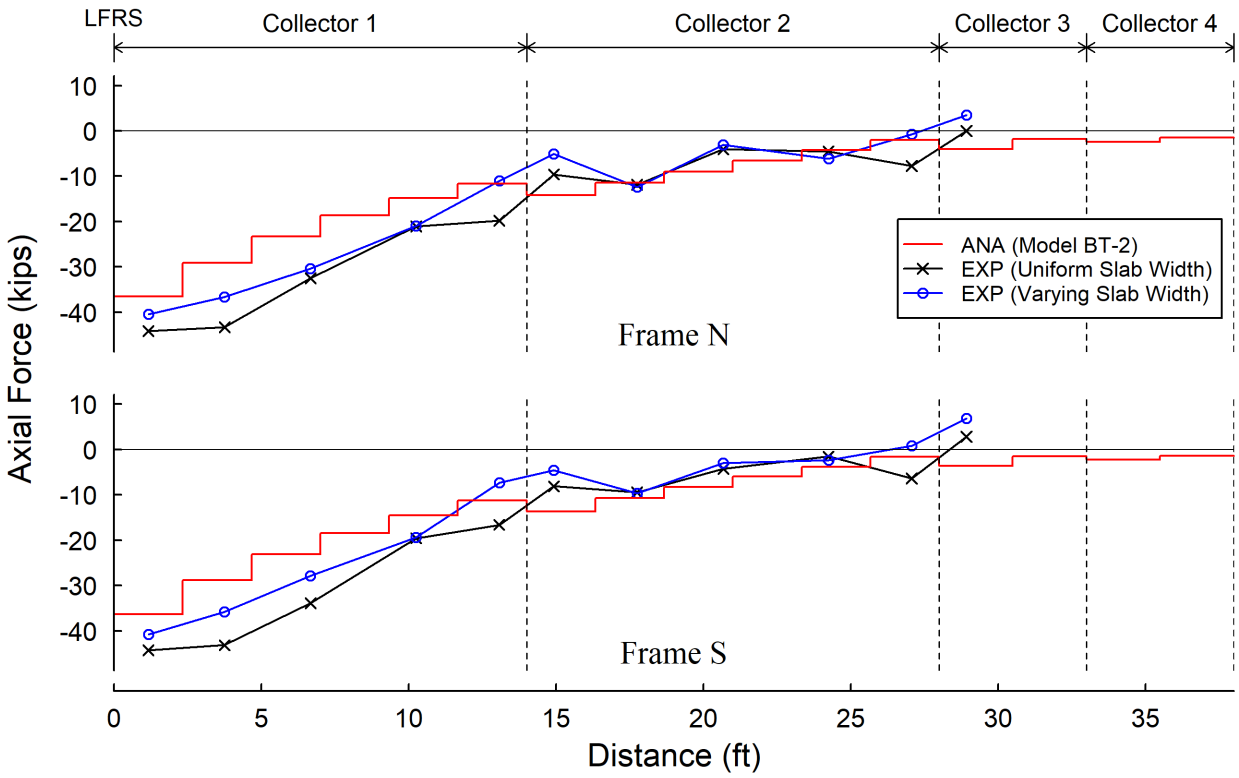

Figure 5.53 Comparison of Collector Axial Forces Obtained from Constant and Varying Effective Slab Widths (at Postive Peak Acceleration)

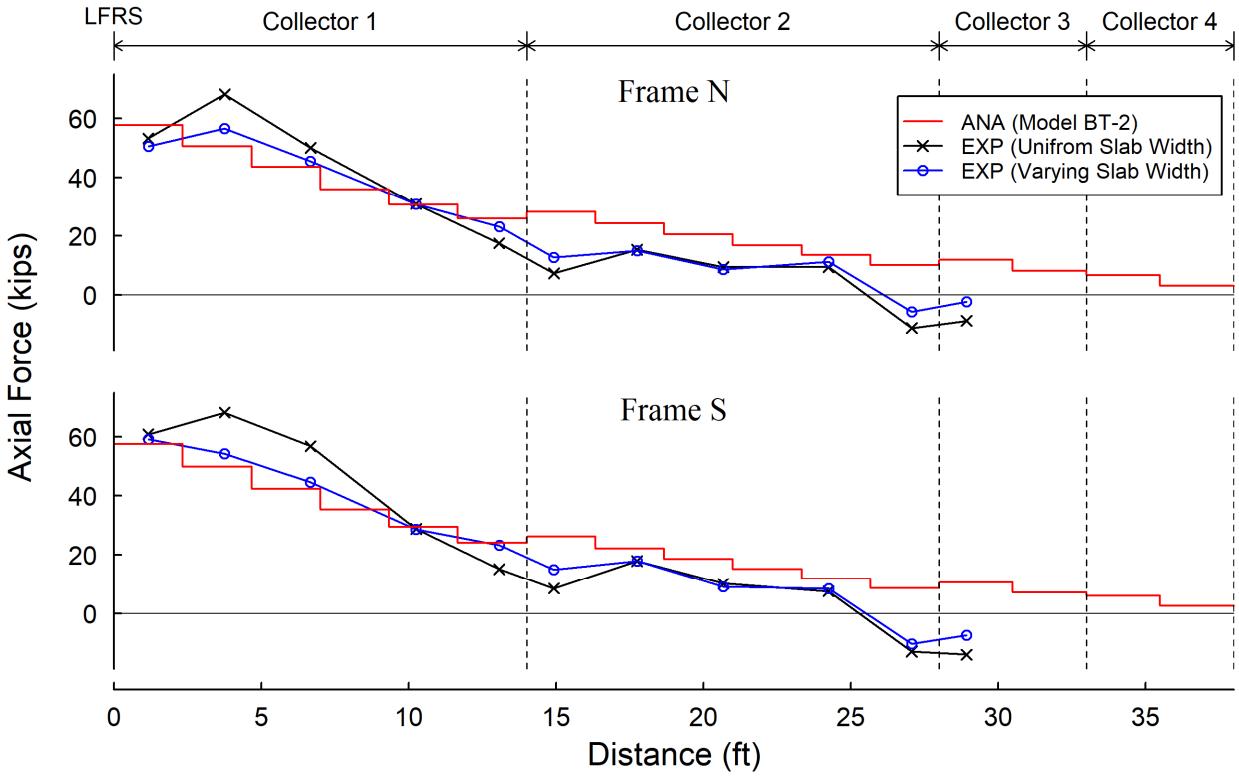

Figure 5.54 Comparison of Collector Axial Forces Obtained from Constant and Varying Effective Slab Widths (at Negative Peak Acceleration)

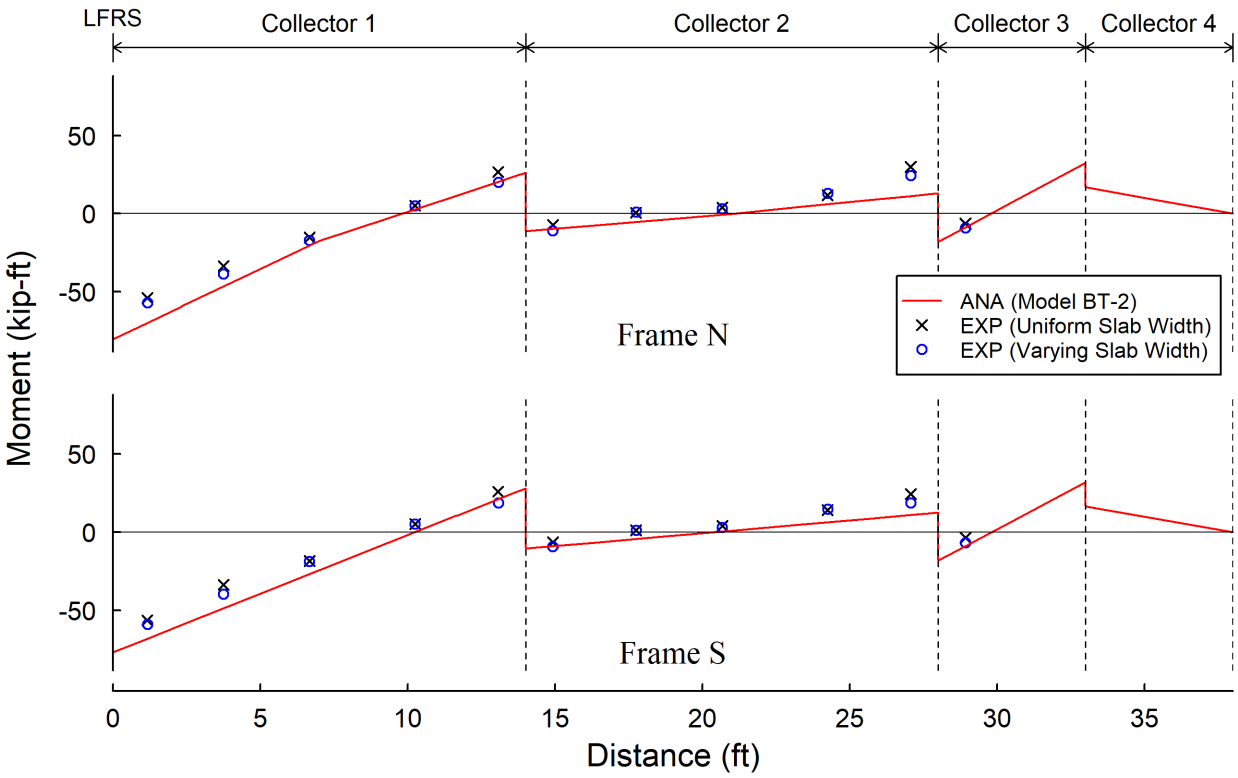

Figure 5.55 Comparison of Collector Bending Moments Obtained from Constant and Varying Effective Slab Widths (at Postive Peak Acceleration)

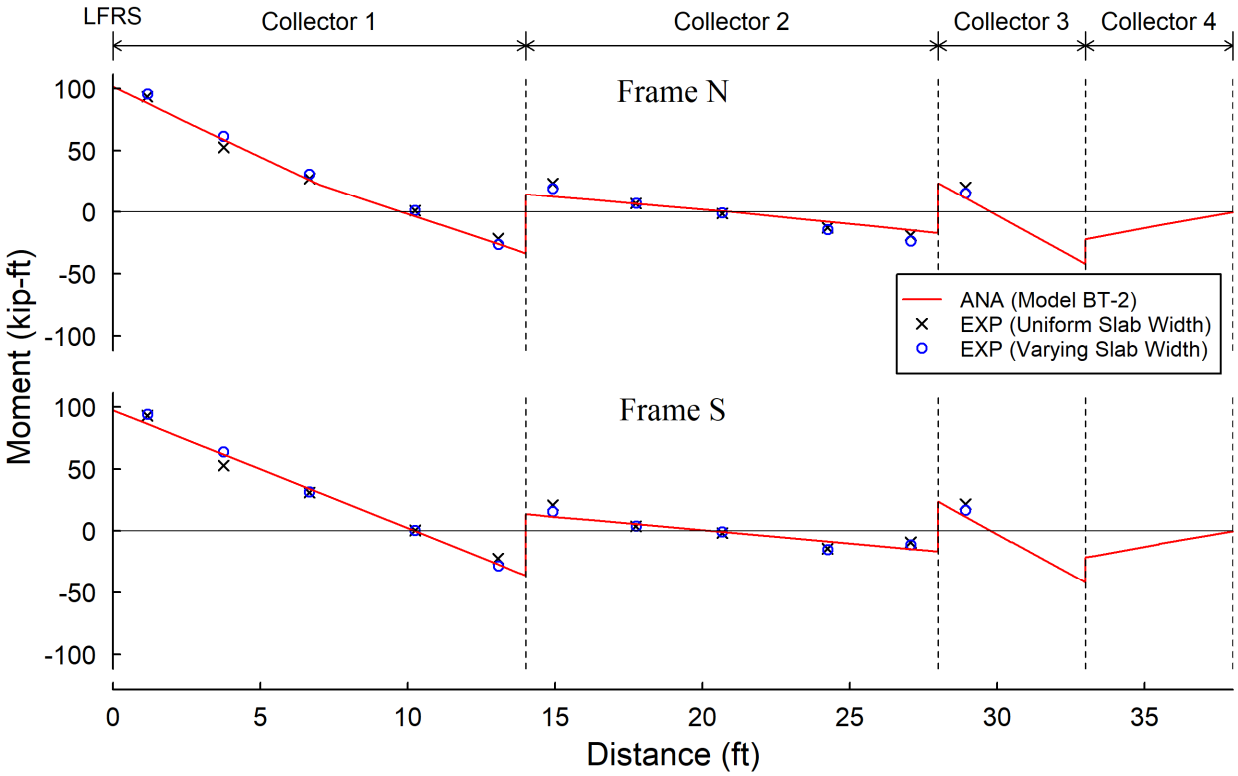

Figure 5.56 Comparison of Collector Bending Moments Obtained from Constant and Varying Effective Slab Widths (at Negative Peak Acceleration)

5.4.4 Estimation of Collector Axial Force Demand

In this section, the effectiveness of the conventional approximate method for estimating the collector axial force demand is examined by comparing with the measured responses in Test 1-3. In addition, an improved approximate approach is proposed in this research and its effectiveness is verified by the test results. Furthermore, an approach using elastic static analyses of planar models is proposed for a more accurate estimation of the collector axial force demands, especially on a building with considerable mass and/or stiffness irregularities on floor plans.

Taking the test specimen for example, Figure 5.57 illustrates the determination of the design slab shear flow acting along the collector lines, which is a necessity for estimating the axial force demand in collectors. As two collector lines were respectively situated along the north and south sides of the floor diaphragm of the test specimen, the total weights applied on or hanged onto the north and south halves of the floor diaphragm were the seismic weights (denoted as W_N' and W_S', respectively) tributary to the north and south collector lines, respectively. Table 3.4 and Table 3.5 show the calculations for W_N' and W_S', respectively. Note that, in this study, the column weights are not included in W_N' and W_S' because it is assumed that the inertial forces generated from column masses would be directly transmitted into the columns instead of being collected by the collectors. Assuming the floor diaphragm is designed for a target floor acceleration, a_{flr}, the design slab shear flows along the north and south collector lines, denoted as $\overline{v_N'}$ and $\overline{v_S'}$, respectively, can be determined from:

$$\overline{v_N'} = \frac{W_N'}{L_{total}}\left(\frac{a_{flr}}{g}\right) \tag{5.47}$$

$$\overline{v_S'} = \frac{W_S'}{L_{total}}\left(\frac{a_{flr}}{g}\right) \tag{5.48}$$

where L_{total} is the length of entire collector line at each side of floor diaphragm. Note that, for simplicity, this design slab shear flow is assumed to be uniformly distributed slab shear flow along each collector line. In practice, based on the design parameters from the modern building code ASCE-7 (ASCE 2016), the target floor acceleration, a_{flr}, for design of collectors can be determined from:

$$a_{flr} = \Omega_0 \left(\frac{F_{px}}{w_{px}} \right) g \tag{5.49}$$

where Ω_0 is the system overstrength factor. F_{px} is the diaphragm design force at level x, which is determined according to ASCE-7 Section 12.10. w_{px} is the weight tributary to the diaphragm at level x. In this research, a_{flr} is taken as the peak (positive or negative) floor acceleration of the test building in order to correspond to the collector axial force responses at the instant of peak floor acceleration.

Figure 5.58(a) illustrates how the conventional method is applied on estimating the collector axial force in test specimen. It is conservatively assumed the gravity columns do not carry any shear force for simplicity. The free-body diagram of the collector line can be simplified as a cantilever beam subjected to a uniform linear load, $\overline{v'}$, in the axial direction of the beam. The LFRS serves as the fixed end of the cantilever beam. The reaction force at the fixed end, R_0, which also represents the lateral force acting on the LFRS, will be the resultant force of the uniform linear load along the entire collector line, which leads to:

$$R_0 = \overline{v'} L_{total} \tag{5.50}$$

This indicates that the conventional method assumes that all the inertial force collected by a collector line will eventually be transmitted to the LFRS at the end of that collector line. As a result, these assumptions made by conventional method leads to a linear axial force diagram along the

entire collector line [see Figure 5.58(c)], for which the axial force increases from zero at the far end to the value of R_0 at the LFRD end.

Note that free-body diagram shown Figure 5.58(a) is directly applied to a collector line, for which only one end of the collector line is connected to an LFRS and the other end is either a free end or connected to a gravity column. However, in the typical buildings, it is commonly seen that a collector line is connected to LFRSs at its both ends. For this case, the conventional method assumes that the entire collector line is subjected to a uniformly distributed axial load, $\overline{v'}$ and a reaction force in a direction opposite to $\overline{v'}$ at each end of the collector line. Note that sum of the two reaction forces, representing the effects of the two LFRSs, is balanced by the resultant force of the uniform linear load. In addition, the magnitude of the two reaction forces is proportional to the stiffness of the corresponding LFRSs.

However, test results show that the gravity columns in test specimen resisted a non-negligible portion of story shear during Test 1-3; and the LFRS (i.e., the cantilever columns at Column Line 1) only took about 73% of story shear. Therefore, this research proposes an improved method for estimating the collector axial force by considering the effects from the gravity columns. As illustrated in Figure 5.58(b), the improved method assumes that a collector line can be represented by a continuous beam element subjected to a uniformly distributed axial load, $\overline{v'}$, and supported by a series of linear springs representing the lateral stiffness of LFRS and gravity columns. As described in Section 5.4.2 and listed in Table 5.10, the lateral stiffnesses of four columns, denoted as k_{F1}, k_{F2}, k_{F3}, and k_{F4}, respectively, in each longitudinal frame of test building were estimated by using the approximate equations for estimating lateral stiffness of beam-to-column sub-assemblies resolved from the longitudinal test frame based on the proposed portal frame method. As the axial stiffnesses of the collectors are much higher the stiffnesses of

these springs representing the effects from LRFS and gravity columns, the spring force acting at Column Line *i* location can be estimated as:

$$R_i = \left(\frac{k_{Fi}}{k_{F,total}}\right)(\overline{v}' L_{total}) \tag{5.51}$$

where $k_{F,total}$ is the total latera stiffness provided by LFRS and gravity columns and computed as:

$$k_{F,total} = \sum_i k_{Fi} \tag{5.52}$$

Subsequently, as shown in Figure 5.58(b)-bottom, free-body diagram of the collector line, which is composed of a continuous beam element subjected to a uniformly distributed axial load, $\overline{v}'$, and spring forces at column locations, can be obtained for computing the axial force diagram along the collector line.

Figure 5.58(c) shows the axial force diagram pattern obtained from the improved method. In general, the axial force on the collector line increase from the far end to the LFRS end. In addition, several sudden small drops in the axial force diagram take place at gravity column locations. This indicates that, once the gravity columns supporting a collector line take shear forces, part of collected inertial force in the collector line will be intercepted by the gravity columns while the collected inertial force, which results in collector axial force, is building up along the collector line and eventually transmitted into the LFRS. As a result of considering the phenomenon of "interception of inertial force by gravity columns", the collector axial force computed from the improved approximation method is lower than that predicted by the conventional method. It can be inferred that, the more the inertial forces intercepted by gravity columns, the less the axial forces induced in the collectors. This indicates that, when the improved approximation method is used, an overestimation of the gravity column shear would result in an underestimation of the collector axial force demand, which is undesirable in the collector design. This also suggests that an

overestimation of the lateral stiffness of the gravity frame, which may be due to an overestimation of the stiffness of the semi-rigid collector connections, is undesirable. Thus, the simplifications made to develop the approximation methods (e.g., approximation methods for estimating the stiffness of collector connections and proposed portal method) in this research shall lead to a slight underestimation of the lateral stiffness of the gravity frames.

Figure 5.59 plots the collector axial forces measured at the instant of positive peak acceleration in Test 1-3 together with two estimated collector axial force diagrams respectively obtained from the conventional approximation method and the proposed improved approximation method. In addition, the collector axial force diagrams obtained from time history analysis on Model BT-2 is also plotted in this figure. Similarly, Figure 5.60 shows the four collector axial force responses respectively obtained from the test data, two approximation methods, and Model BT-2 for the instant of the negative peak acceleration in Test 1-3. It can be found that the conventional approximation method overestimates the axial force throughout the entire collector line. By contrast, the improved approximation method well predicts the collector axial force responses in the region (i.e., the half-span of Collector 1 next to) near the LFRS but mildly overestimates the axial forces for the remaining parts of the collector line. Furthermore, the accuracy of the analytical Model BT-2 in predicting the collector axial forces is better than the two approximation methods.

These suggest that the overestimation of the collector axial forces by the conventional design method is mainly due to two factors: (1) interception of inertial force by gravity columns. (2) non-uniform slab shear flow along the collector line due to the non-uniform in-pane shear deformation of the floor diaphragm. Note that the test results (Figure 4.23) show that about 27% story shear was taken by gravity columns and diagonal braces, which means that about 27% inertial

force was intercepted by these members and only about 73% of the inertial forces was eventually transmitted to the LFRS in the specimen. This indicates that the conventional method, which neglects the interception of inertial force by gravity columns, would apparently overestimate the collector axial force at the LFRS end of a collector line by about 37%. This agrees with the observations from Figure 5.59 and Figure 5.60.

By contrast, the proposed improved method considers the interception of inertial force by gravity columns so that it well predicts the collector axial force at the LFRS end. However, the improved method somewhat overestimates the collector axial force for the remaining part of collector line because it assumes that slab shear flow is uniform along the collector line. Hence, its predicted axial force diagram is increasing from the far end to the LFRD end at a constant rate accompanied with several small sudden drops at the gravity column locations. However, the test results show that the collector axial force from along the collector line was building up in a non-uniform rate. It is apparent that the increase in the collector axial force in Collector 1 was faster that those in the remaining collectors. On the other hand, the dynamic analysis on Model BT-2 can reflect the two factors mentioned above. Thus, the axial force diagrams obtained from Model BT2 matches that measured responses very well.

In overall, test results in this study verify that the proposed improved method provides a satisfactory estimation of the collector axial force for design purpose. Although the assumption of uniform slab shear flow for the improved method would lead to a somewhat overestimation of the collector axial force for the regions other than the LFRS end, this would result in a slightly conservative design, which is acceptable. For the test specimen, in which the distribution of the tributary mass is not perfectly but roughly uniform along the collector line (see Figure 3.25), it was found that the distribution of the slab shear flow was mainly affected by the in-plane deformed

shape of the floor diaphragm. However, the distribution of the slab shear flow is also affected by the distributions of mass and stiffness on the floor diaphragm. Hence, strictly speaking, the assumption of a uniform slab shear flow might not always be conservative. For example, a floor plan layout with heavy masses allocated near the far end, which is far from the LFRS, of a collector line may result in a high slab shear developed near the far end, which would cause the collector axial force near the far end to build up fast.

In addition to the proposed approximation method, which is suitable for estimating the collector axial forces in the typical buildings, designers may consider conducting an elastic static analysis on a planar model representing the floor diaphragm to achieve a precise estimation of collector axial force, especially on the cases where the distribution of mass or stiffness on a floor diaphragm is complicated.

Taking test specimen for example, as shown in Figure 5.61, a planar model, designated Model Planar-BT, using the concept of Beam-Truss (BT) modeling approach (Lu and Panagiotou 2012) to represent the floor diaphragm was developed by using the structural analysis program PISA3D (Lin et al. 2009) for a precise analysis of the collector axial force. Other than the nodes used to represent the real beams, many nodes were created within the space surrounded by the real beams such that the entire slab can be represented by a good number of subpanels. For simplicity, the "fictitious" slab beam elements in the BT model can be replaced by elastic truss elements. To represent the compression field in each slab subpanel, instead of using a pair of bi-directional diagonal slab trusses equipped with nonlinear compression-only material to represent the cyclic reversal of compression field, it is suggested to use a single elastic diagonal truss for the elastic static analysis. In addition, elastic springs were added to the planer model to represent the lateral stiffnesses of the LFRS and gravity column locations for supporting the in-plan deformation of the

floor diaphragm. A nodal force representing the inertial force was assigned to each node for the static analysis. The magnitude of the inertial force acting at node i, f_i, is computed as:

$$f_i = m_i \cdot a_{flr} \tag{5.53}$$

where m_i is the seismic mass assigned to node i. a_{flr} is the target floor acceleration for collector design. For the purpose of comparing analytical and experimental results, a_{flr} was taken as the magnitude of peak floor acceleration in Test 1-3 in this section.

Note that the floor plan of the specimen had non-symmetric distribution of stiff lateral force resisting elements to the center of gravity of the floor. This layout leads to each collector line having a free end at the far end away from the LFRS. In such case, a thorough design process may require two static analyses on two models representing the cases where the inertial force respectively acting toward and away from the LFRS, which cause the collectors in compression and tension, respectively. However, for simplicity, it can be allowed to conduct a single static analysis on a planer model with the diagonal slab trusses and the nodal forces oriented in a manner to represent the case where the floor diaphragm is subjected to inertial forces acting away from the LFRS (as shown in Figure 5.61) for two reasons:

(1) As described in Section 5.3.4, the "non-uniformity" of distribution of the slab shear flows along the collector lines induced by the inertial forces acting away from the LFRS is somewhat less than that triggered by the inertial forces acting toward the LFRS. Note that the a less non-uniform distribution of slab shear flow would cause the collector axial force to build up from the far end to the LFRS end in a faster manner, which would result in a higher collector axial force demand for the regions away from the LFRS end. Hence, a planar model analysis considering the inertial forces acting away from the LRFS would avoid an underestimation of the collector axial force.

(2) For the case where inertial forces acting away from the LRFS, the diagonal slab trusses are oriented in a way that the diagonal truss in the slab subpanel adjacent to the LFRS is not directly connected to the LFRS. In this case, this diagonal truss will bring all its force into the collectors. This also guarantees that contribution of that truss to the collector axial force demand will not be underestimated. By contrast, for the case where inertial forces acting toward the LRFS, the diagonal slab truss in the slab subpanel next to the LFRS will be directly connected to the LFRS. This indicates that the slab truss will bring all its force to the LFRS although there should be a part of slab forces in that subpanel transmitted into the collector, suggesting that the collector axial force near the LFRS may be slightly underestimated.

In addition to a planar model using the BT modeling approach, this study proposes an alternative planar model that employs the proposed modified strip (MS) model to represent a floor diaphragm can be used to conduct a precise estimation of the collector axial forces. As shown in Figure 5.62 , Model Planar-MS, which uses the MS model to represent the floor diaphragm of test building, was constructed by using PISA3D. Recall that, in the MS model, the nodes the nodes are only assigned along the real steel beams. It requires smaller numbers of the nodes and elements than BT model does so that it can lead to a reduced computational cost. As well as Model Planar-BT, the inclined slab trusses and the nodal forces in Model Planar-MS were oriented in a manner to represent inertial force acting away from the LFRS.

Furthermore, the third planar model, designated Model Planar-Panel, was constructed by using PISA3D to represent the floor diaphragm of test specimen. As shown in Figure 5.63, in Model Planar-Panel, each slab subpanel was represented by a PISA3D Panel element, which is a plane stress element and has five in-plan deformation modes including vertical extension, vertical deflection, horizontal extension, horizontal deflection and shear deformation. Note that Model

Planar-Panel is used to mimic the modeling approach which employs membrane or shell elements to model the slab, which can be easily implemented by using the commercially available structural analysis programs, such as ETABS or SAP2000. Lastly, the four planar model, designated Model Planar-BT-0, was constructed for test specimen to represent a simplified situation in which the gravity columns provide zero lateral stiffness to support the floor diaphragm (i.e., the effect of interception of inertial force by gravity columns is neglected). Hence, Models Planar-BT-0 and Planar-BT are identical except that those linear springs representing the gravity columns are removed in Model Planar-BT-0.

Two elastic static analyses were conducted for each of the four planar models representing the floor diaphragm of test specimen. The two analyses for each model consider the target floor acceleration as the peak positive and negative floor acceleration in Test 1-3. Figure 5.64 shows the analytical collector axial force diagrams obtained from the four planar models together with the measured responses for the peak positive accelerations. It can be found that both Models Planar-BT and Planar-MS well predict the axial force in the collector 1 but mildly overestimate the axial force in the remaining collectors (Collectors 2 through 4). The results from these two models are almost the same. Note that, as shown in Figure 5.33 the analytical results from the two 3-dimesional (3-D) models BT-2 and MS-2 match the experimental responses slightly better than the two planar models. The two 3-D models just slightly overestimate the axial force in Collectors 2 through 4. This could be attributed to that the 3-D models include the diagonal braces that supported the cantilever span of the test specimen, while the two planar models neglect the diagonal braces. Thus, the two planar models could not reflect the effect of interception of inertial force by the diagonal braces, resulting in a slightly higher axial force responses in the collectors. However, in overall, the elastic static analyses on the two proposed planar models provide a

satisfactory estimation of the collector axial force response, which is more precise than estimation from the proposed improved approximation method (see Figure 5.59).

Furthermore, the analytical collector axial forces from Model Planar-BT-0 are considerably higher than the measured responses (see Figure 5.64). This indicates that neglecting the effect from the interception of inertial force by the gravity columns would result in a substantial overestimation of the collector axial force. The linear springs representing the lateral stiffness of the gravity columns are required for a planar model to achieve a precise analysis of the collector axial force. Lastly, from Figure 5.64, it is apparent that, the analytical collector axial force from Model-Panel is noticeably smaller than those obtained from the other three planer models. Although it seems that the analytical responses from Model-Panel is close to the measured axial force in collector 2, in general, Model-Panel underestimate the collector axial force responses, which is undesirable for collector design. Therefore, it is not recommended to model the floor diaphragm by using the membrane or shell elements in practice even though this modeling approach can be easily implemented in the commercially available structural analysis programs.

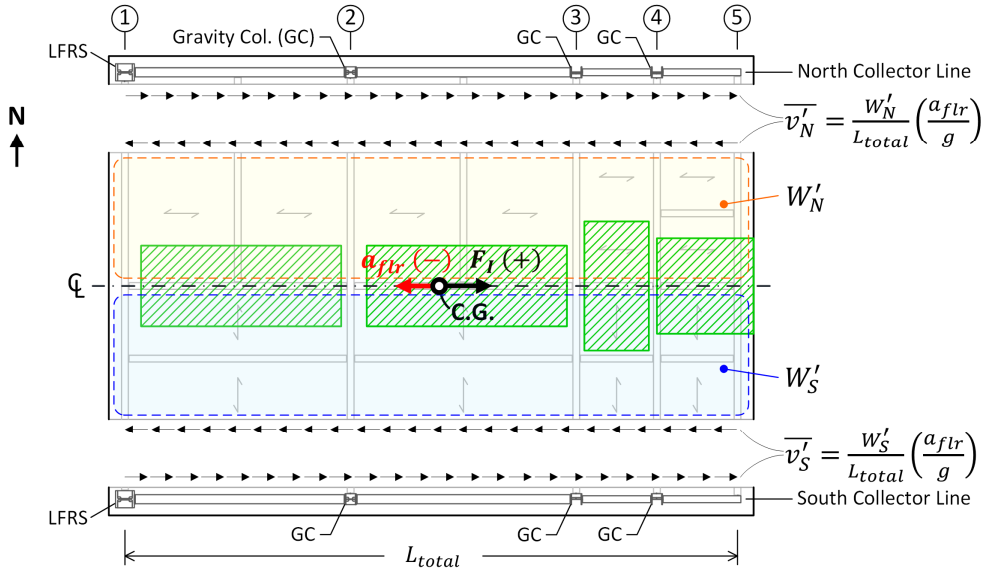

Figure 5.57 Determination of Averaged Slab Shear Flow Acting along Collector Line

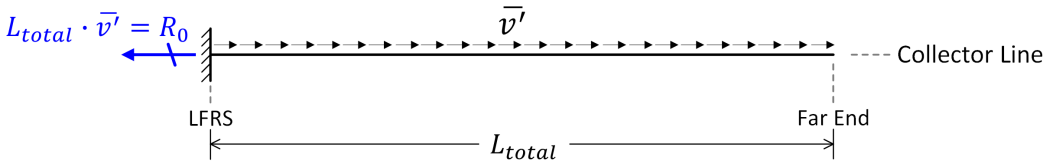

(a) Conventional Method

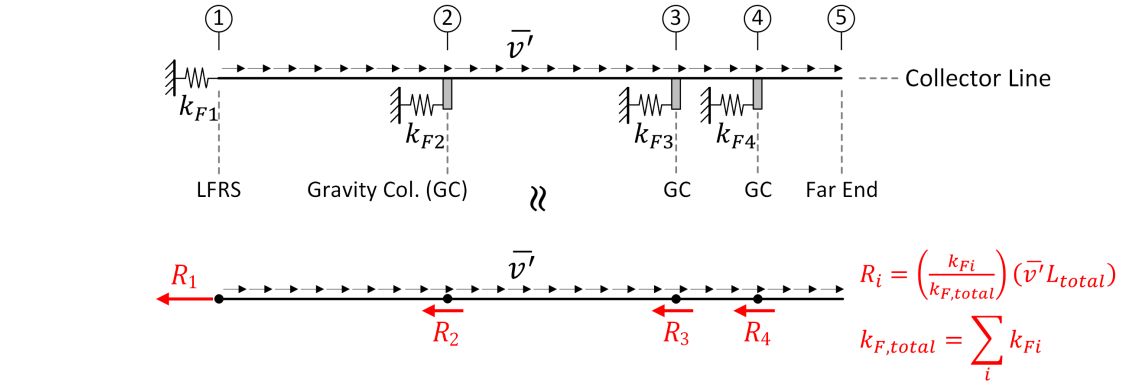

(b) Improved Method

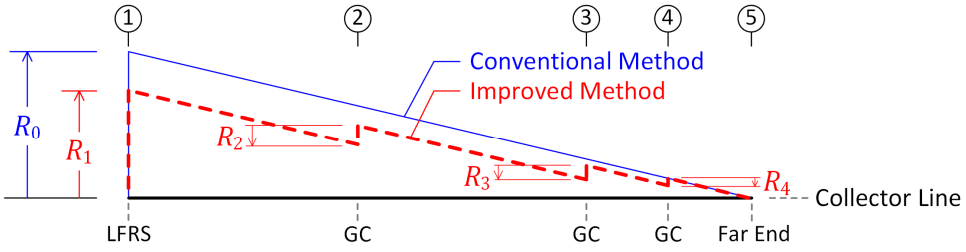

(c) Axial Force Diagram

Figure 5.58 (a) Conventional Method and (b) Proposed Impoved Method for Estimating Collector Axial Force and Associated Axial Force Diagram Patterns

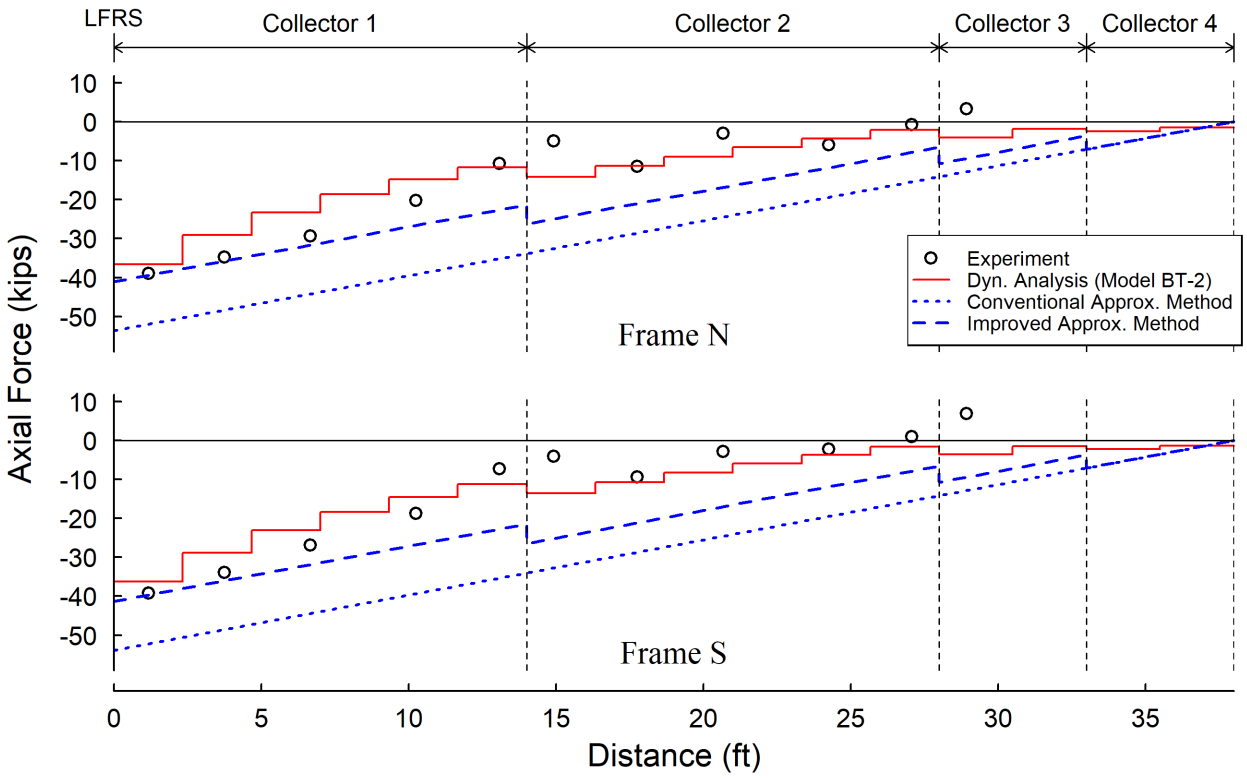

Figure 5.59 Comparison of Collector Axial Forces Obtained from Experiment, Dynamic Analysis and Approximation Methods (at Postive Peak Acceleration)

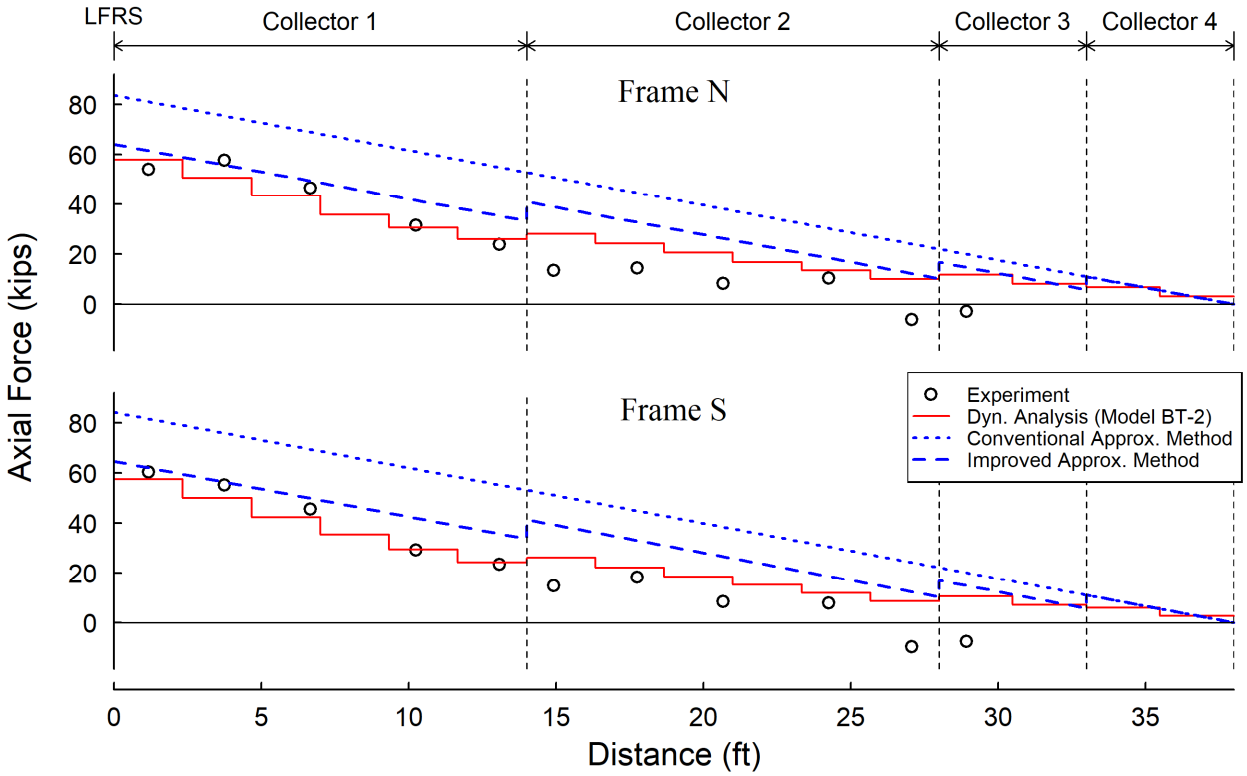

Figure 5.60 Comparison of Collector Axial Forces Obtained from Experiment, Dyanmic Analysis and Approximation Methods (at Negative Peak Acceleration)

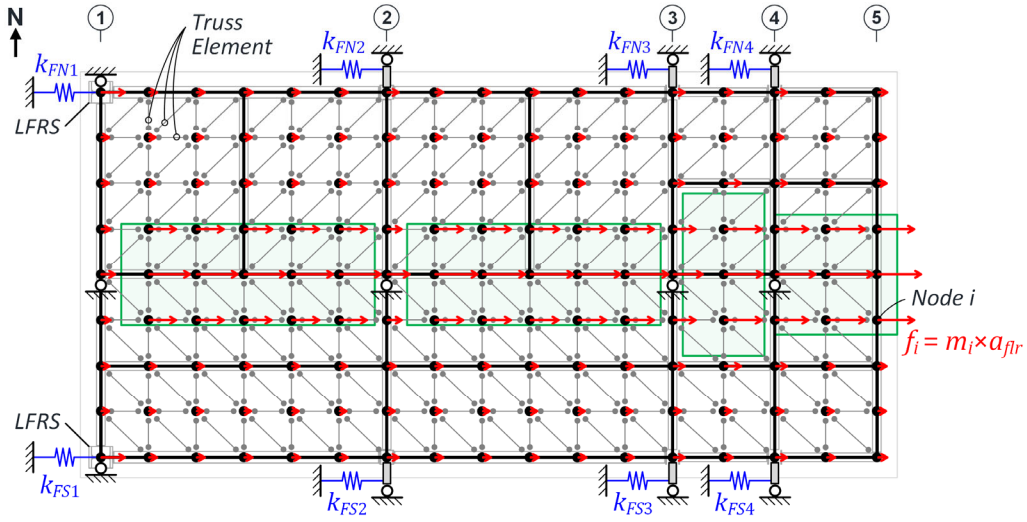

Figure 5.61 Model Planar-BT

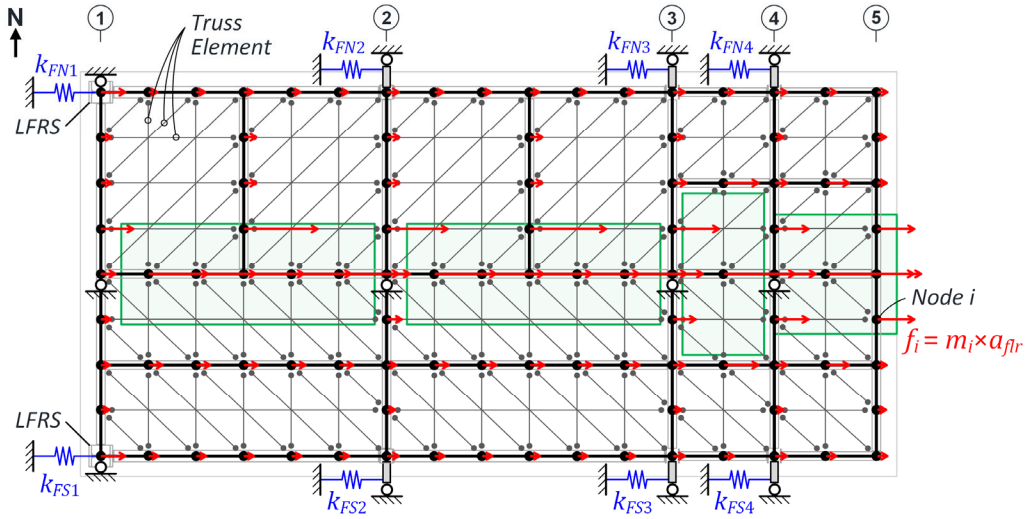

Figure 5.62 Model Planar-MS

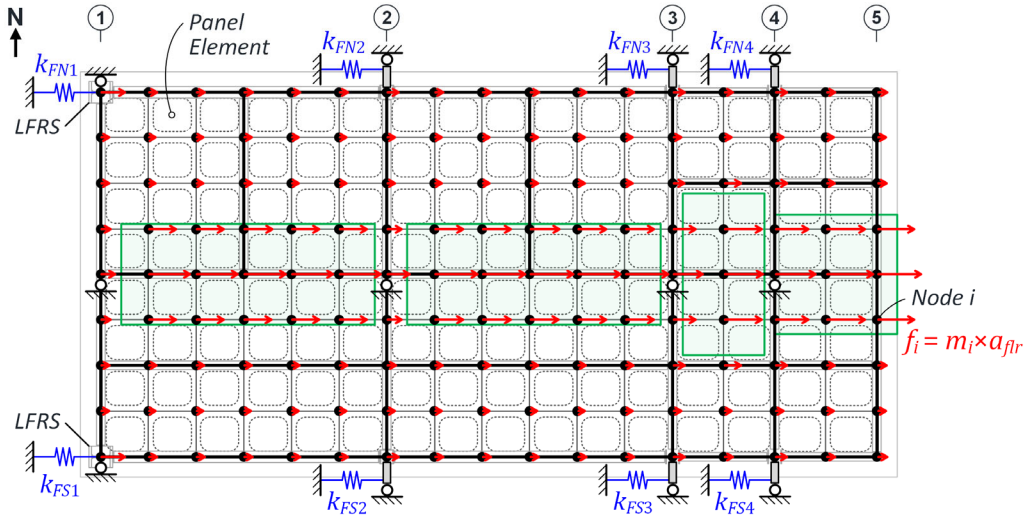

Figure 5.63 Model Planar-Panel

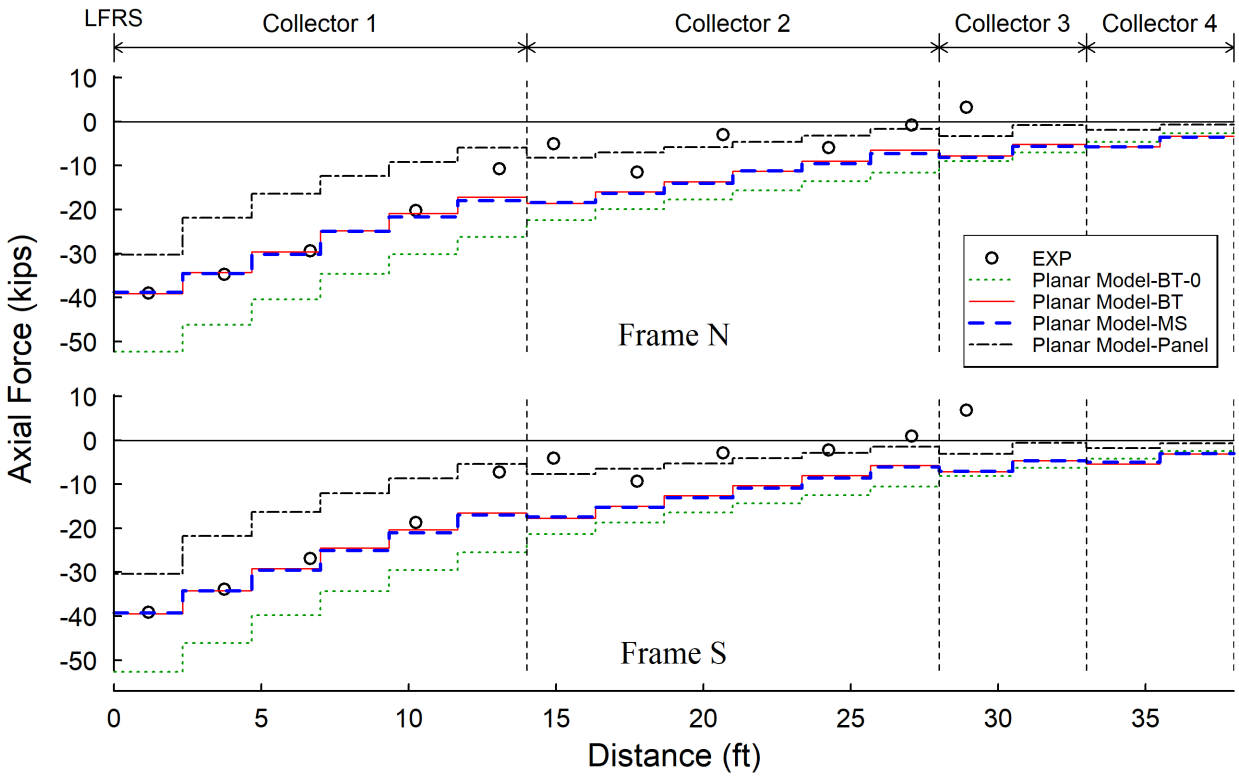

(a) at Postive Peak Acceleration

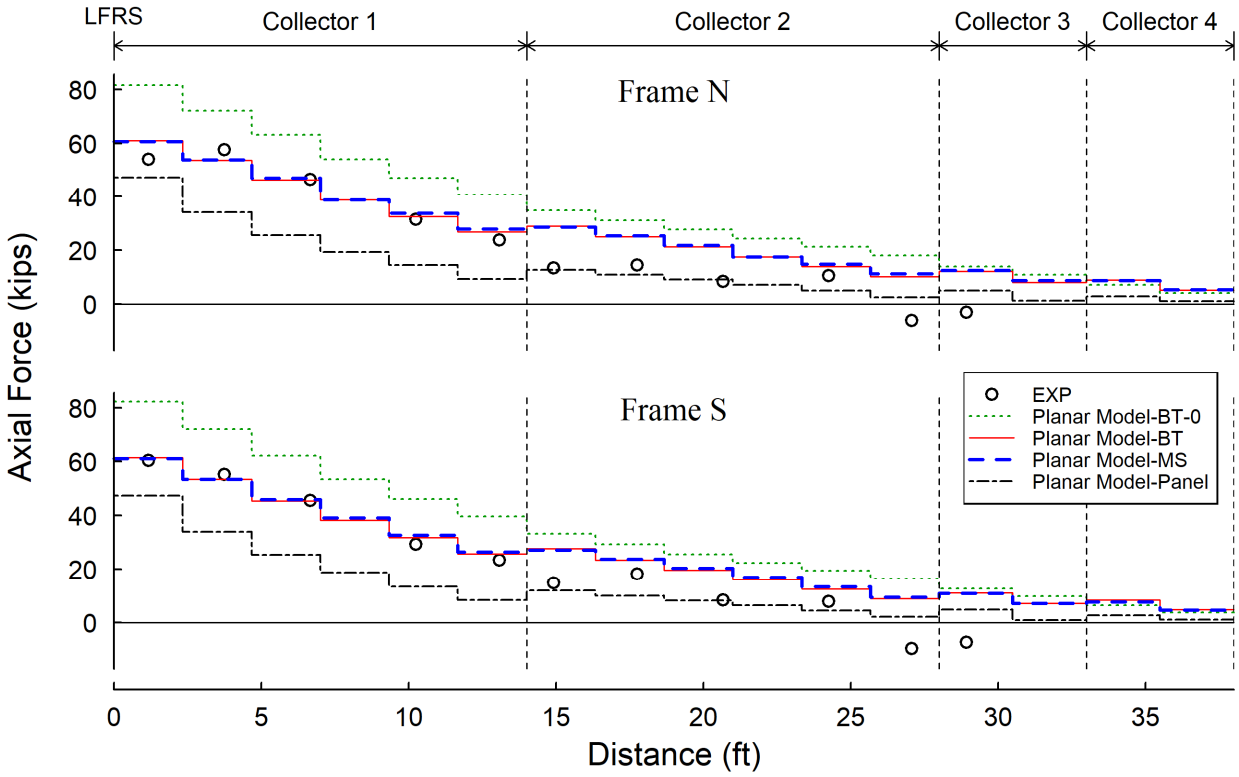

(b) at Negative Peak Acceleration

Figure 5.64 Comparison of Collector Axial Forces Obtained from Experiment and Static Analyses on Planar Model Models

6. PHASE 2 TEST PROGRAM

6.1 General

In Phase 2 test program, a second story with a metal deck roof was added to the Phase 1 test building, and this 2-story building was evaluated by the conventional earthquake simulation testing method. This phase was divided into two parts: Phase 2A tests were conducted for the 2-story test building without the added mass on the roof, which served as an extension of Phase 1 testing to excite the 2nd floor composite diaphragm to a higher floor acceleration response. Phase 2B tests were performed with added roof mass, in which significant inertial forces were generated in both the 2nd floor and roof diaphragms. This chapter describes the testing program including specimen design, test setup, instrumentation plan, and data reduction. The associated test results are presented in Chapter 7, while the implications and interpretations of the test results are presented in Chapter 8.

6.2 Test Specimen and Setup

6.2.1 Test Building

After the Phase 1 tests were completed, the second story of the test specimen was added to make the specimen a two-story test building. Figure 6.1 though Figure 6.7 show the important information of the test building. Design drawings for the test building are provided in Appendix B.

As shown in Figure 6.1(a), the roof plan was 33 feet long and 18 feet wide. In the longitudinal direction, there were two 14-ft long bays and one 5-ft long bay. The second story was 8 feet high with the primary lateral force-resisting columns (on Column Line 1) and the gravity columns (on Column Lines 1, 2, and 3) made by W12×120 and W8×40 columns, respectively (see Figure 6.2).

These 2nd-story columns were spliced on the extension of first-story columns through CJP splices (see Figure 6.7). Note that columns in the Phase 1 test building were designed to extend above the concrete slab by 1-ft to facilitate column splicing. To resist the shaking in the longitudinal direction, the perimeter beams running along Column Lines N and S served as the collectors, while the edge beams at the west and east sides of the floor plan functioned as the diaphragm chords. On each collector line, three collectors from west to east are designated as "Collector 1", "Collector 2", and "Collector 3", respectively. All the collectors, chords, and remaining floor beams were W10×17 shape of A992 steel. In the transverse direction of the specimen, three single-bay chevron braced frames [see Figure 6.2(c)] were employed on Column Lines 1, 2, and 3 to resist the torsional and transverse movements. See Figure 6.8 for the erection of second story frame. All the braces were made with long-leg back-to-back A36 double angle section 2L5×3×$^3/_8$. All the plates, including continuity plates, stiffeners, and gusset plates, were specified to be A572 Gr. 50 steel. All high-strength bolts were specified to be $^5/_8$″-diameter F3125 Gr. F1852 (A325 TC) bolts.

The unfilled bare steel roof diaphragm was made with 20-ga. thick, $1^1/_2$-in. deep Verco PLB-36 decks oriented parallel to the collectors. The north and south edges of the roof diaphragm were aligned with the centerlines of the collector line, while the diaphragm was extended beyond the centerlines of the exterior transverse beams (i.e., chords) by one foot in the longitudinal (West-East) direction. See Figure 6.9 for the installation of roof deck. The deck was attached to the panel supports by using the 36/7 weld pattern, for which an arc spot weld was used for every place where a flute meets the steel beams. The side lap connections between deck panels were made by using punch button connections with a 4-in. spacing.

Similar to the first story, three types of collector-to-column connections were employed. For the roof collector-to-column connections at the primary lateral force-resisting columns (Column

S1 and N1), the all-flange weld (AFW) detail [see Figure 6.3(a)] was used. In addition to the bolted connection between the shear tab and collector web, complete-joint-penetration (CJP) groove welds were used for the top and bottom flanges of the collector. The weld access hole per AWS D1.1/D1.1 (AWS 2015) was employed, and the steel backing was not removed. Note that a cap plate was installed onto the column top end by fillet welds. The collector top flange was welded to the edge of the cap plate, while the collector bottom flange was welded to the column flange. In the column panel zone, continuity plates were installed at the elevations aligned up with the collector bottom flange level. The continuity plates were welded to the column flanges and web by using CJP and double fillet welds, respectively.

For the roof collector-to-column connections at the gravity columns on Column Line 2 (Columns S2 or N2), the top flange weld (TFW) detail [see Figure 6.3(b)] was employed. In addition to the bolted web, only the collector top flange was connected to the column cap plate by using the CJP weld. The welding details used in the AFW connection were also adopted for the TFW connections. Note that the roof TFW connections were made: (1) a weld access hole at collector bottom flange, (2) CJP bevel preparation for the bottom flange, and (3) continuity plates aligned with the collector bottom flange. These three details were made during construction in preparation for the addition of CJP welds at the collector bottom flange level for Phase 3 testing.

For the remaining collector-to-column connections at the gravity columns on Column Lines 3 and 4 (Columns S3, N3, S4, and N4), the bolted-web (BW) shear tab connection detail was used [see Figure 6.3(c) and Figure 6.4]. The shear tabs were welded to the column flange by using double fillet welds. With a $^1/_2$-in. beam setback, three $^5/_8$-in. diameter bolts with a 2-in. spacing and $1^1/_4$-in. -edge distances were used. Note that similar five-bolt shear tab connections were used for the AFW and TFW connections as well. However, the center of the shear tab connection was

aligned with the steel collector center line for BW connections, while the shear tabs in the AFW and TFW connections were located at an elevation with the topmost bolt $2^{7}/_{8}$ in. below the top face of the collector. Also note in Figure 6.3(c), the double-sided BW connections on Column Line 3 were made with details for making the future CJP welds at the collector flanges of the west-side TFW connections in Phase 3 test. For BW connections on Column Line 3 (see Figure 6.4), no continuity plate was installed in the column panel zone.

For the transverse beam-to-column connections, a pair of horizontal stiffeners were welded to the column flanges above and below the extended shear tab. A gap was left between each stiffener and the column web. Figure 6.5 and Figure 6.6 show the details of the transverse beam-to-column connections and the beam-to-beam connections, respectively. For each of these connections, an extended shear tab and with three $^{5}/_{8}$-in. diameter bolts were used.

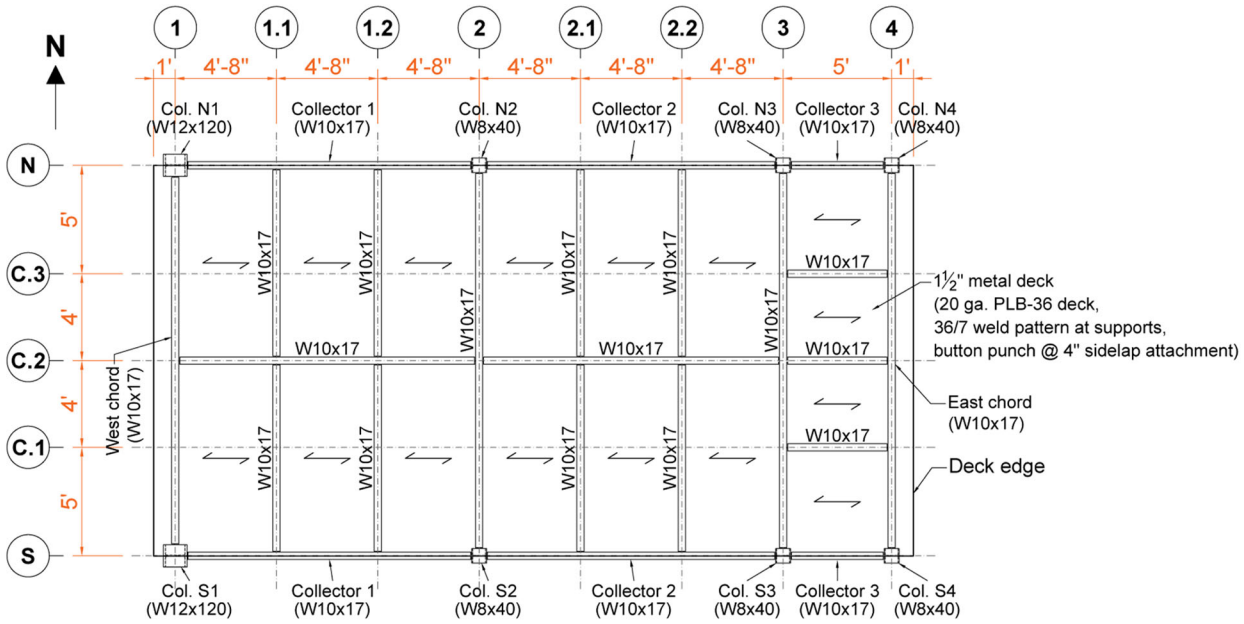

(a) Roof Plan

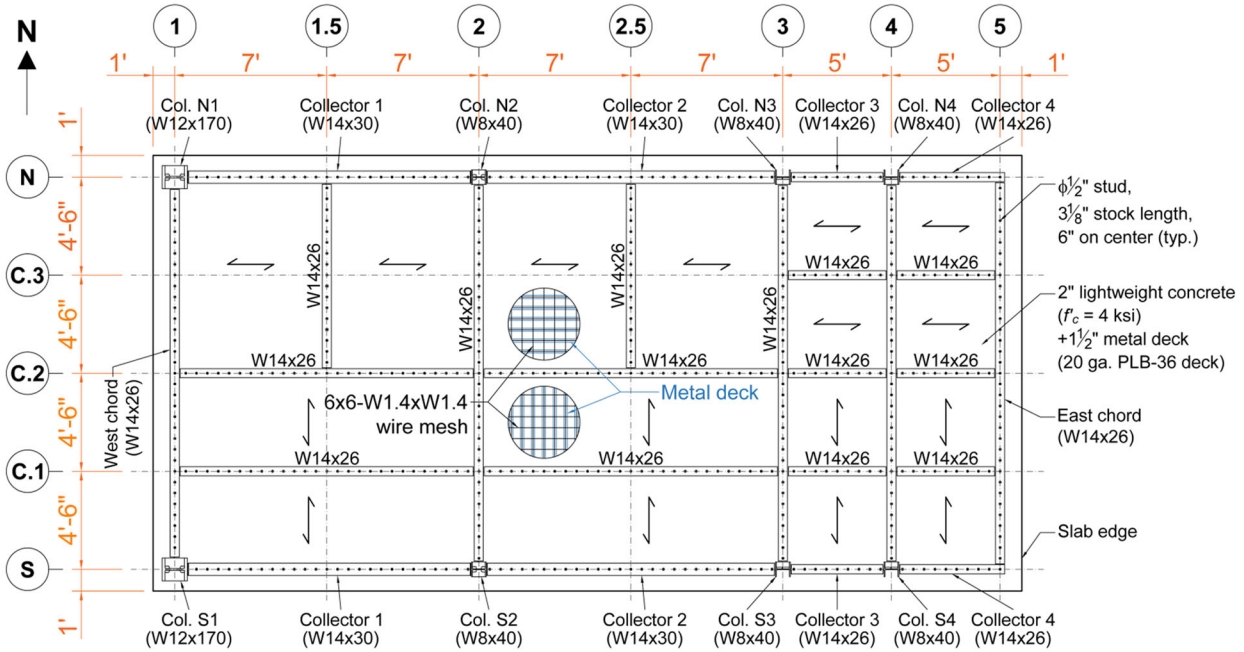

(b) 2nd Floor Plan

Figure 6.1 Phase 2 Test Building: Roof and Floor Plans

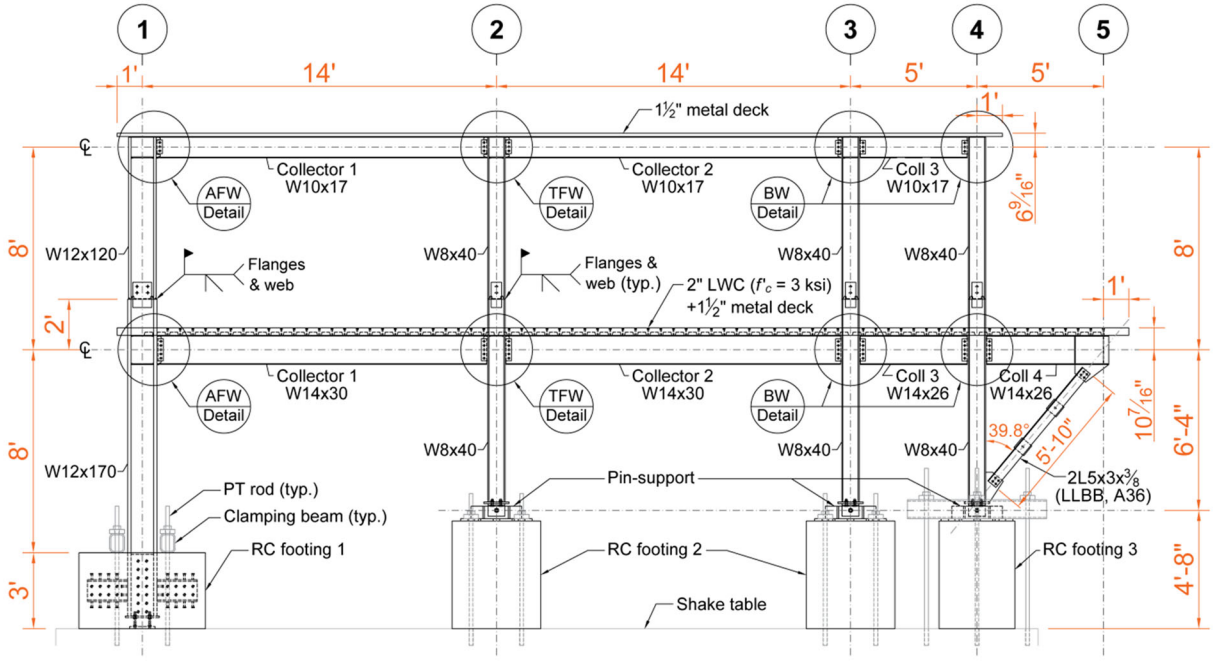

(a) Elevation of Frame S

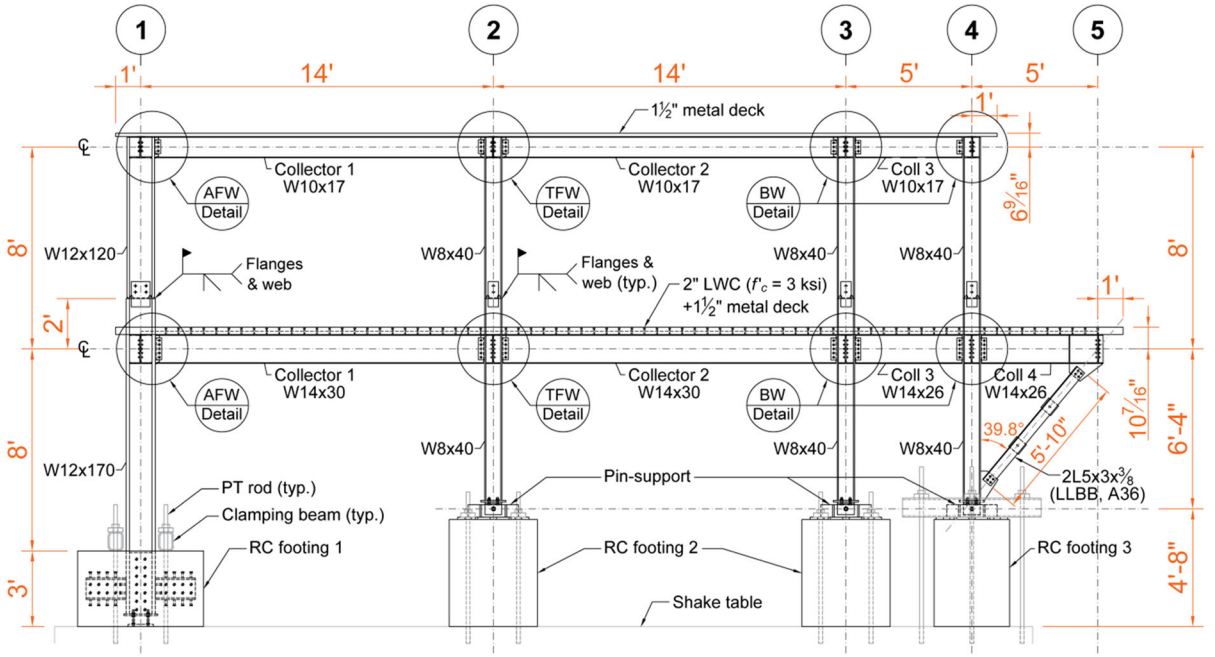

(b) Elevation of Frame N

Figure 6.2 Phase 2 Test Building: Elevations

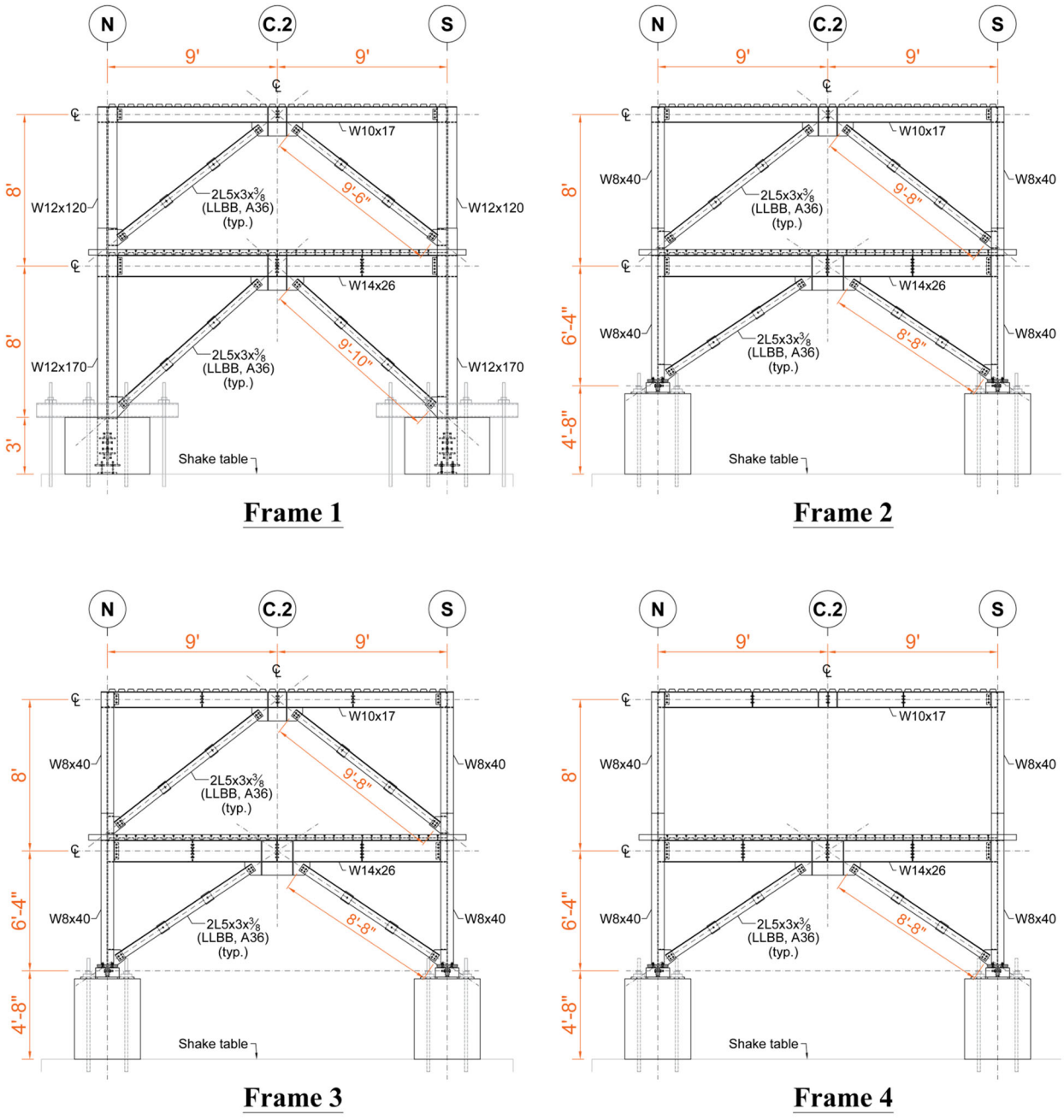

(c) Transverse Frame Elevations

Figure 6.2 Phase 2 Test Building: Elevations (continued)

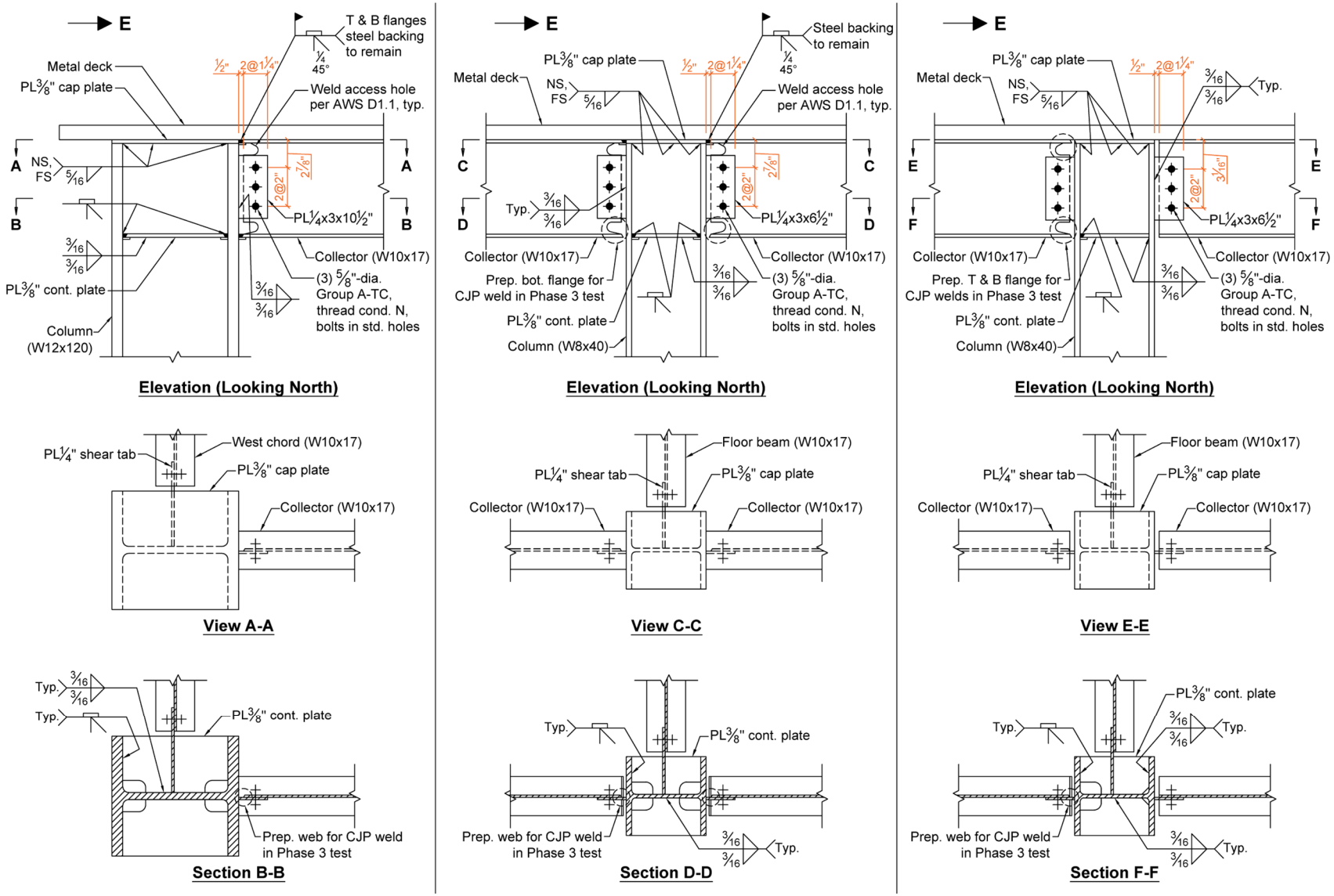

(a) All Flange Weld (AFW) (b) Top Flange Weld (TFW) (c) Bolted Web (BW)

Figure 6.3 Phase 2 Test Building: Roof Collector-to-Column Connections (Frame S)

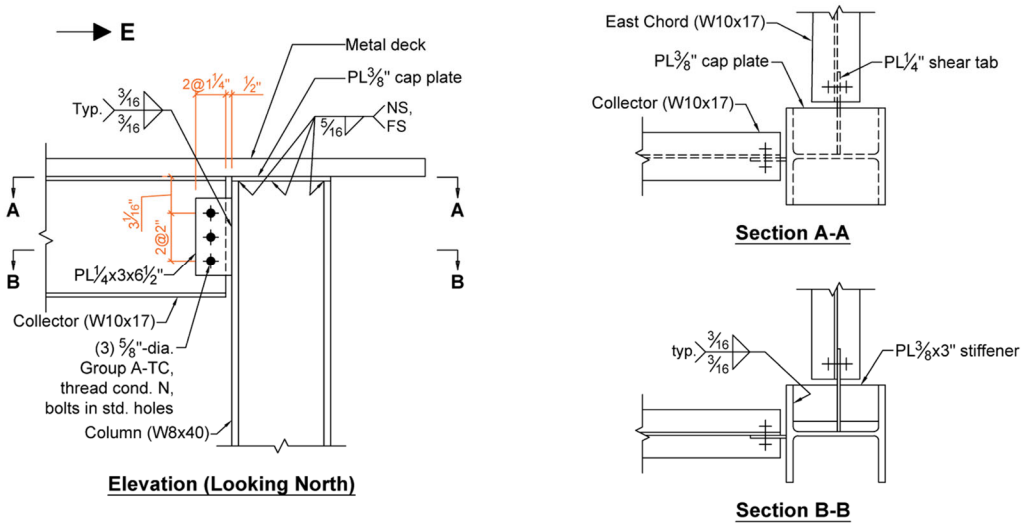

Figure 6.4 Phase 2 Test Building: Roof Collector-to-Column Connections at Column 4

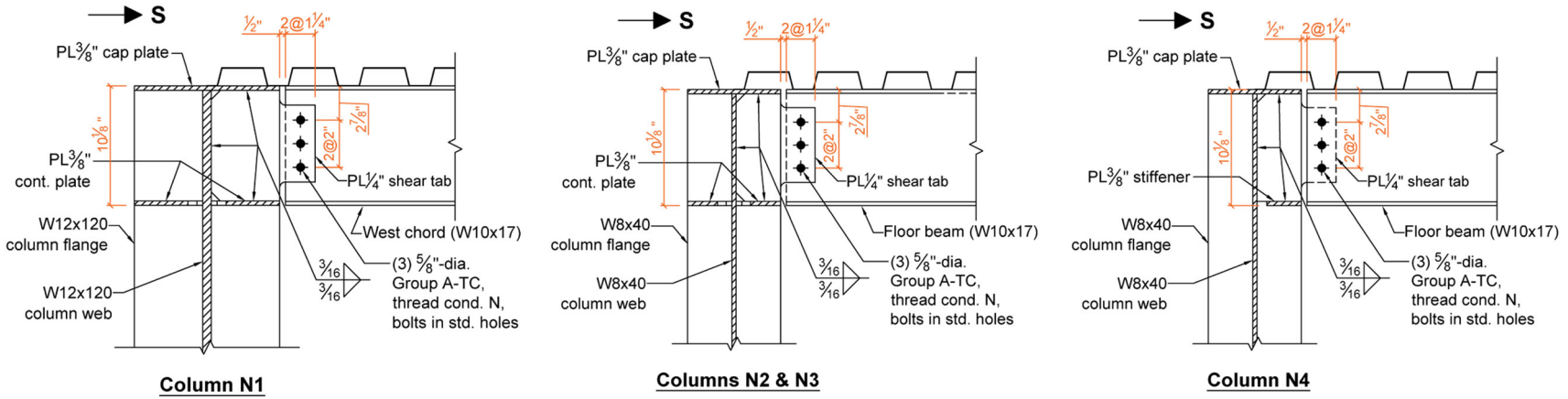

(a) Frame 1 (b) Frame 2 (c) Frames 3 and 4

Figure 6.5 Phase 2 Test Building: Transvers Beam-to-Column Connections

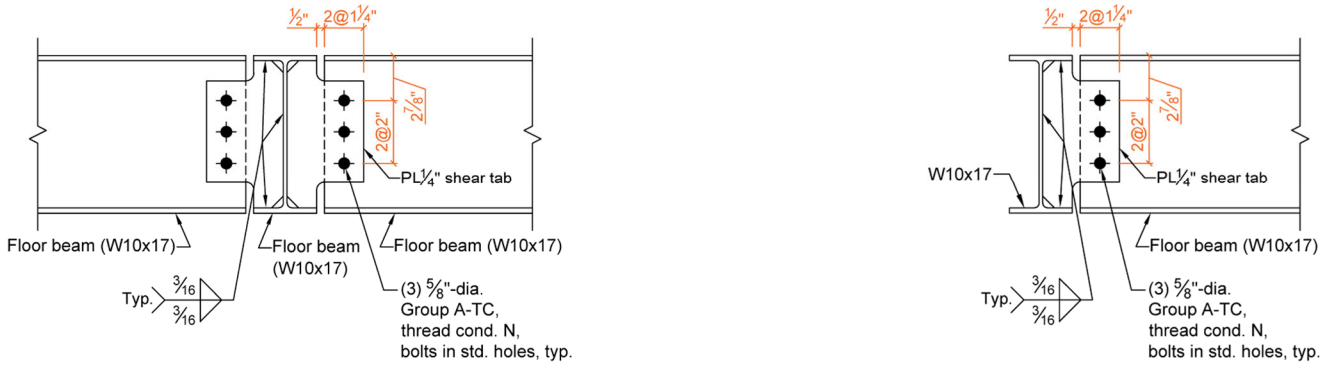

(a) Double-sided (b) Single-sided

Figure 6.6 Phase 2 Test Building: Beam-to-Beam Connections

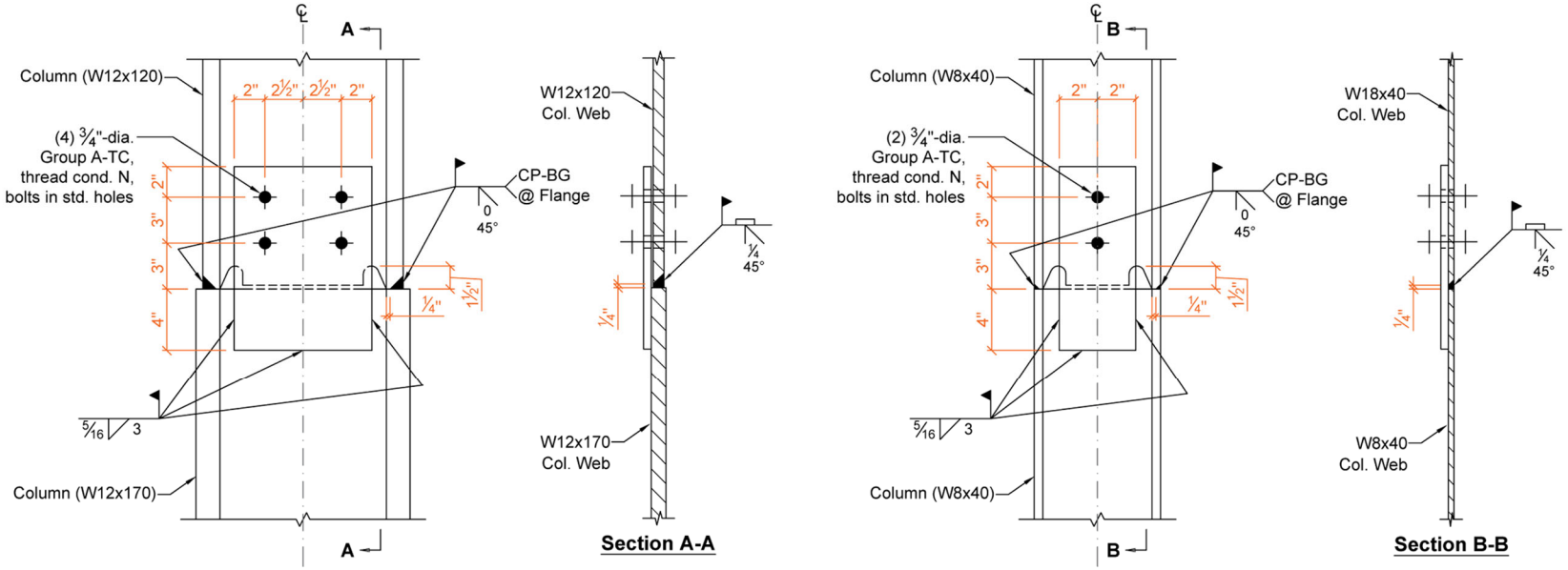

(a) Cantilever Column (b) Gravity Column

Figure 6.7 Phase 2 Test Building: Column Splices

Figure 6.8 Erection of Second Story Frames

Figure 6.9 Installation of Roof Metal Deck

6.2.2 Test Setup

Figure 6.10 and Figure 6.15 show the overview of Phase 2 test setup. Several steel plates, serving as the added mass for Phase 2B testing only, were placed on the roof deck and secured by steel stoppers which were welded to the floor beams before the roof deck was installed. See Figure 6.11 for the layout of the stoppers. The clear distances between stoppers were intentionally designed to be $^1/_4$-in. larger than the associated dimensions of the steel plates such that the steel plates can be smoothly placed between the stoppers. See Figure 6.13 for the placement of the added mass plates. As shown in Figure B.22, four types of stoppers were used. Stoppers 1 and 2 were made by cutting a W12×120 member, while Stoppers 1 and 2 were made from 1-in. thick steel plates. As shown in Figure 6.12 and Figure 6.14, steel shim plates were used to fill the gaps between the stoppers and added mass plates. Some spot welds were placed between the shim plates and added mass plates to minimize the slip of the added mass plates. The total added weights (designated as Added Weights 5, 6, and 7, respectively), including each group of steel plates together with the stoppers, on Spans 1, 2, and 3 were 17.18 kips, 19.58 kips, and 7.592 kips, respectively.

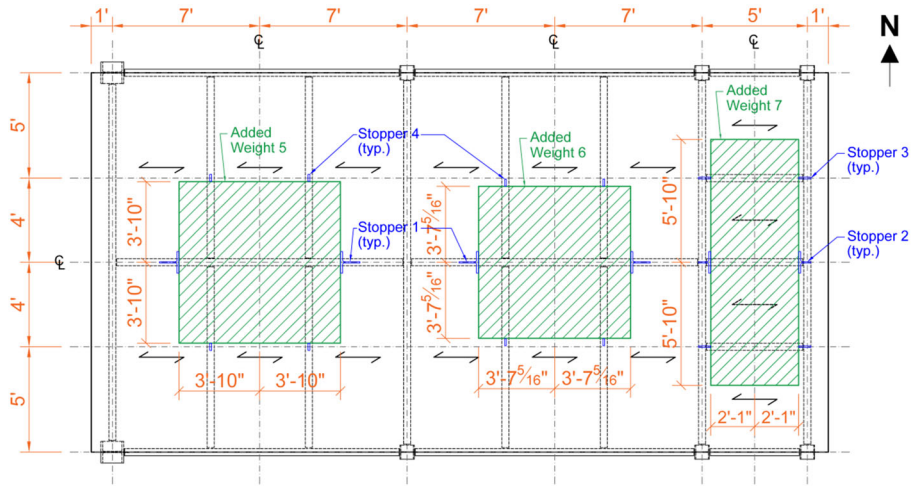

(a) Plan View of Roof Level

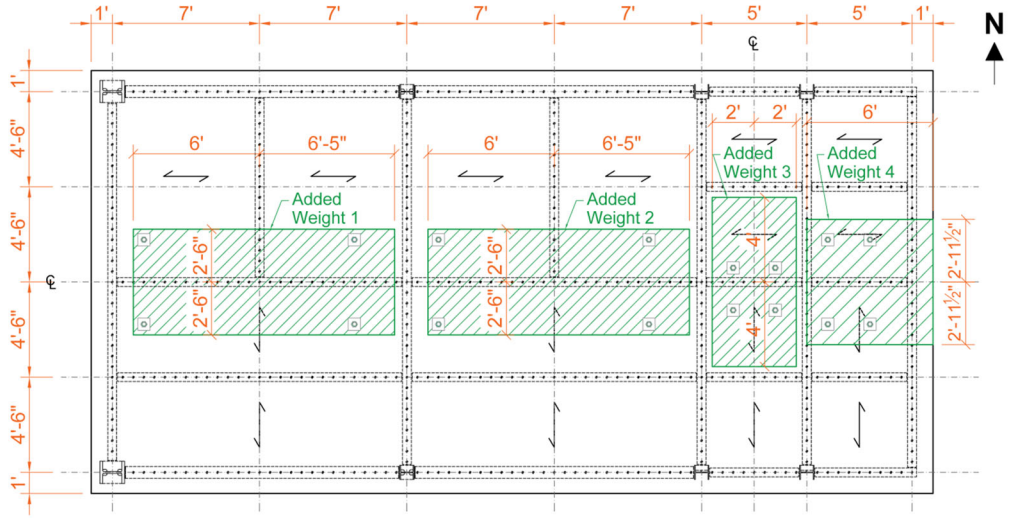

(b) Plan View of 2nd Floor Level

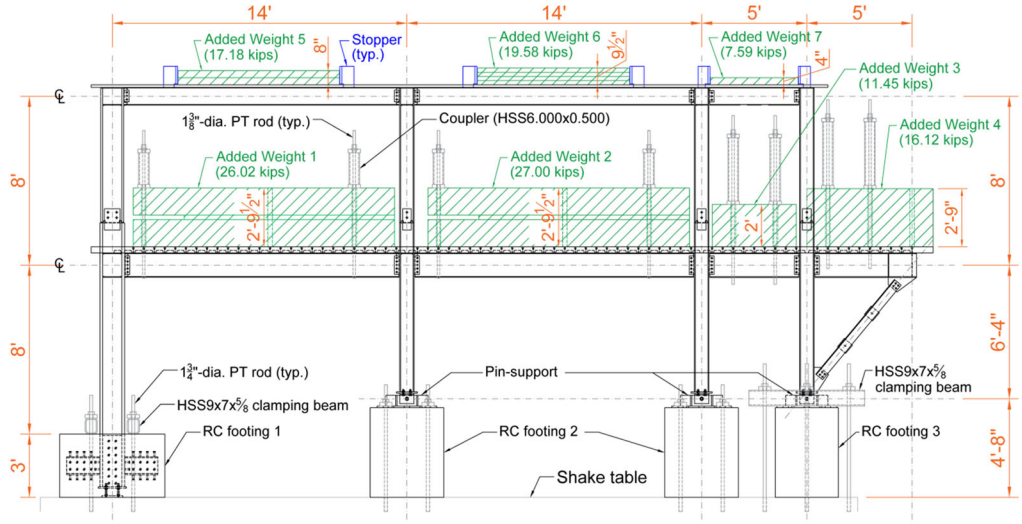

(c) Elevation

Figure 6.10 Phase 2 Test Setup and Added Weight Layout

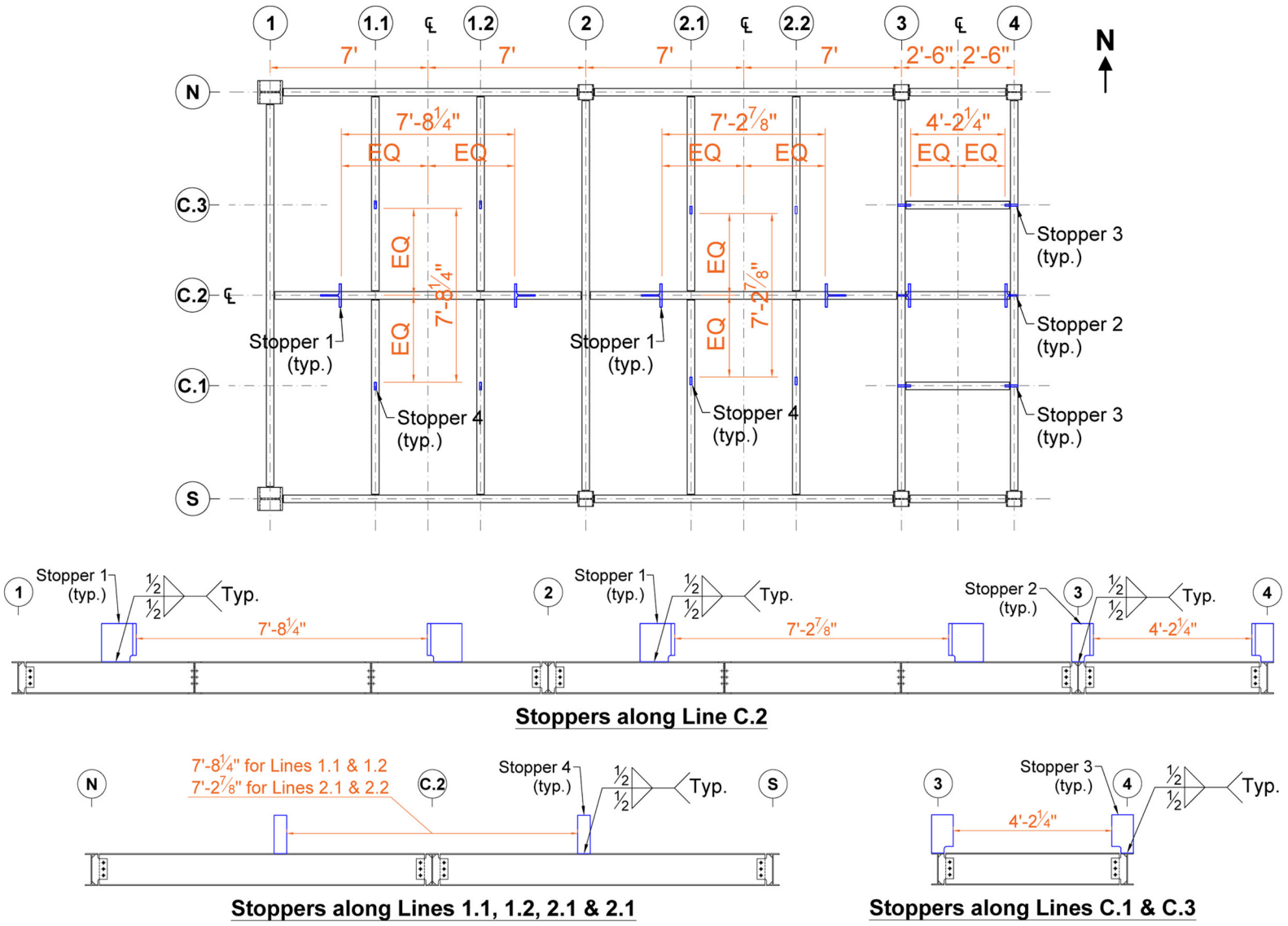

Figure 6.11 Stopper Layout on Roof Level

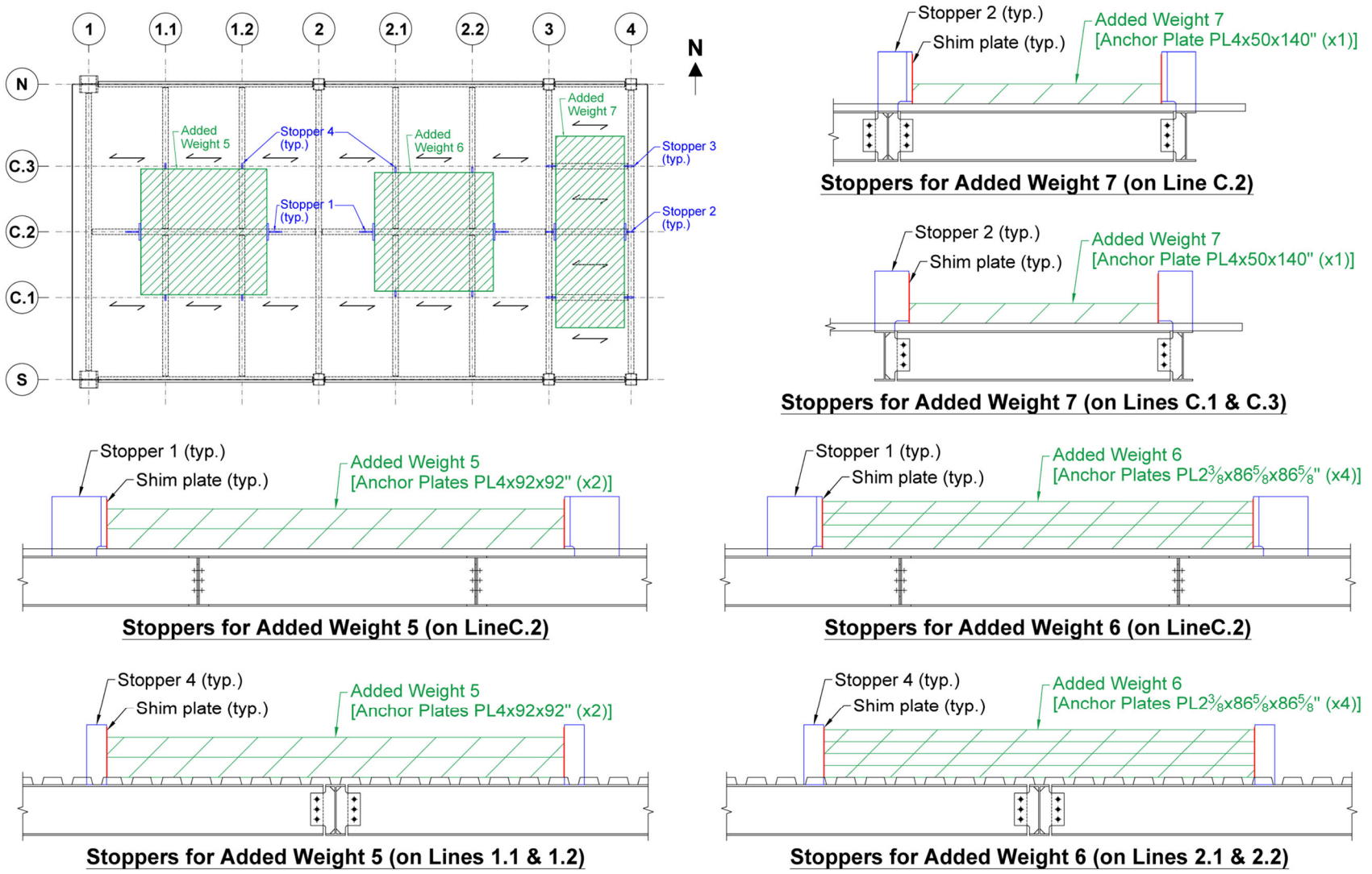

Figure 6.12 Added Weight Installation Details (on Roof Level)

Figure 6.13 Placement of Added Mass Steel Plates

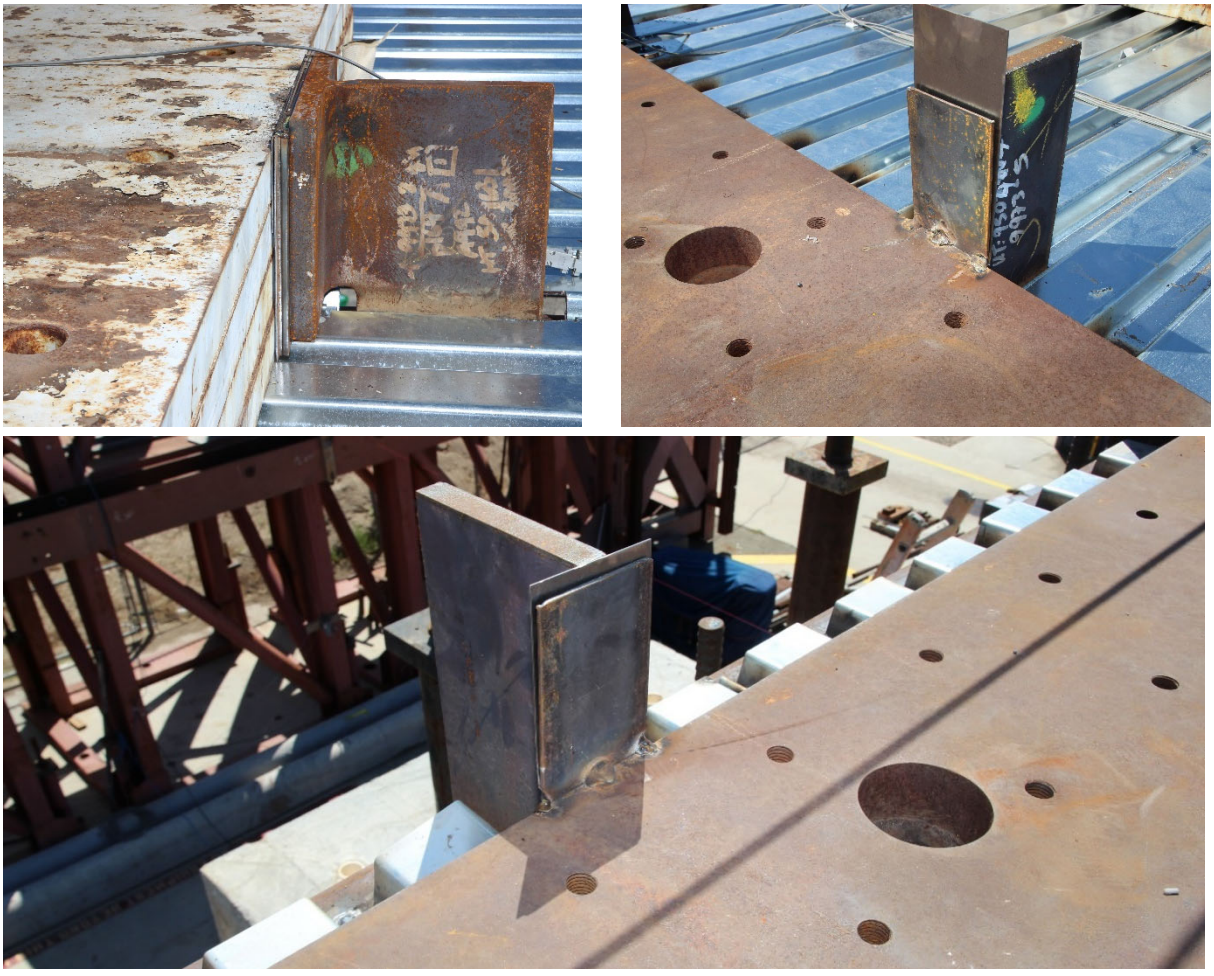

Figure 6.14 Shim Plates between Added Mass Plates and Stoppers

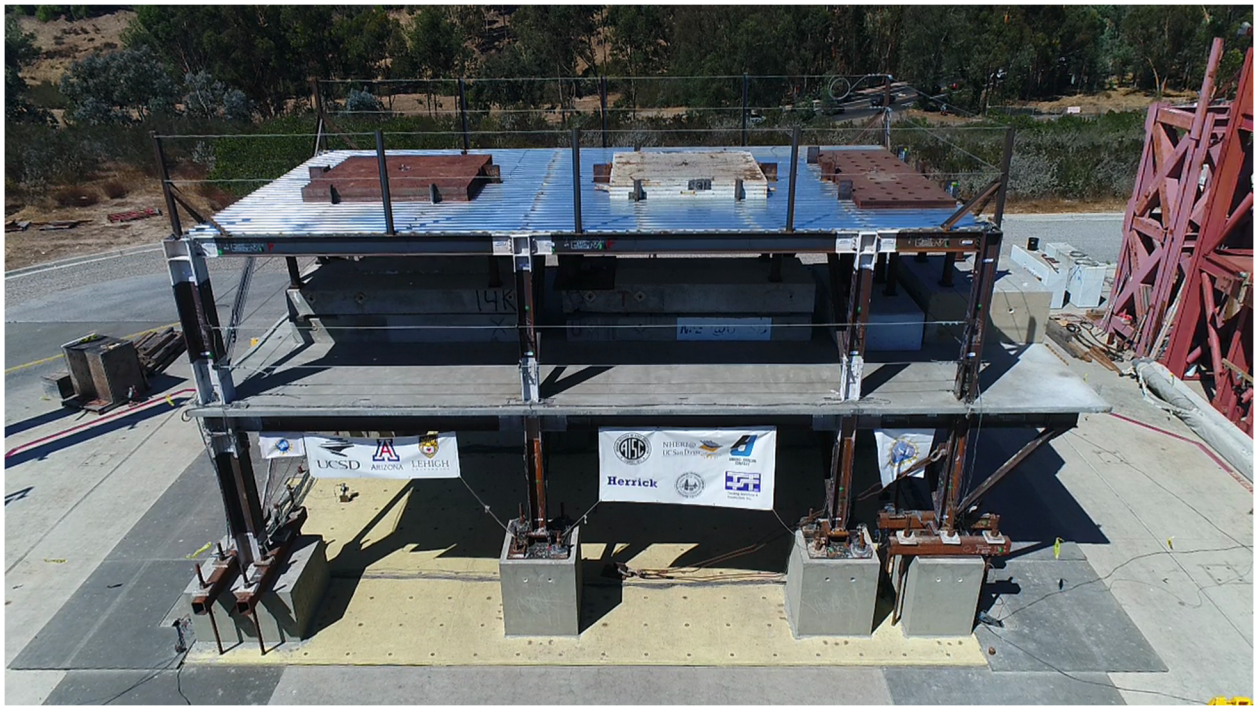

(b) High Angle Front View

(b) Front View (Looking North)

Figure 6.15 Photos of Phase 2B Test Specimen

6.2.3 Seismic Weight Calculations

This section presents the calculation results of the seismic weights tributary to the 2nd floor and roof, denoted as W_{2F} and W_{RF}, respectively, for the Phase 2 test building. In addition, seismic weights tributary to the collectors at 2nd floor and roof levels, denoted as W'_{2F} and W'_{RF}, respectively, are presented. In fact, adding the 2nd story to the test building did not change the seismic wight tributary to the 2nd floor collectors (W'_{2F}). However, it slightly increased the total seismic weight tributary to the 2nd floor (W_{2F}) since the weight of the bottom half of each 2nd-story column and each transverse brace would be lumped to the top end of the adjacent 1st-story column in calculating W_{2F}. Except for this tiny change, the considerations for seismic weight calculations for the 2nd floor of the Phase 1 specimen, as described in Section 3.2.3., can be directly applied to Phase 2 specimen. Thus, this section only presents the calculation of W_{2F} and W'_{2F} through Table 6.1, Table 6.4, Table 6.7, and Table 6.8. The remainder of this section will focus on the calculations of W_{RF} and W'_{RF}.

To illustrate the calculation of seismic weights tributary to the roof diaphragm of the test building, the node and beam designations respectively shown in Figure 6.16 and Figure 6.17 are employed. Figure 6.16 also shows that the weights from the columns, braces, and beam-to-beam connections are treated as nodal weights. The weights of the beams (steel collectors, chord, and floor beams shown in Figure 6.17) are considered as line weights. Figure 6.18 shows that the weights from the roof deck and added weights are simplified as area weights.

Note that total seismic weight tributary to the roof, W_{RF}, is used for seismic force determination in practice. As shown in Figure 6.19, W_{RF} includes the weights from the metal deck, added weights, steel beams, columns, double-angle braces, and the bolts and plates used for the connections. Another seismic weight tributary to the roof collector lines, denoted as W'_{RF}, is used

for determining the collector axial force demand. As shown in Figure 6.20, the weight sources of W'_{RF} are almost the same as those of W_{RF} except that the weights from the 2nd-story columns are not included in W'_{RF} because the inertial forces generated from the masses of steel columns would not be transmitted into the collectors.

Table 6.2 shows the seismic weight calculation from six components. The consideration of each component is summarized below.

(1) Metal deck

According to the product catalog, the unit weight (per unit area) of the deck, denoted as $\overline{w'_0}$, is 2.30 psf. See Table 6.2(a) for the weight calculation of roof deck.

(2) Added weights

As shown in Figure 6.18, three groups of added mass plates, were installed onto the roof deck. Together with the weights of the stoppers used for securing of mass plates to the floor beams, the total weights for the three added weight groups from west to east (denoted as Added Weights 5, 6, and 7 in Figure 6.18) were W_{a5} = 17,180 lbs, W_{a6} = 19,580 lbs, and W_{a7} = 7,592 lbs, respectively. See Table 6.2(c) for the calculations of added weights. Note that Table 6.2(b) shows the added weights for Phase 2A testing; in this case only the weight of the stoppers is considered.

(3) Steel columns

The seismic weight from the steel columns considers the upper half of the 2nd-story columns. It includes the weight from the cap plates, continuity plates and stiffeners in the column panel zones. In addition, the shear tabs and bolts are also considered. See Table 6.2(d) for the calculation of column weights.

(4) Steel beams

The seismic weight tributary to each steel beam (collector, chord, or floor beam) was calculated by multiplying a linear self-weight by the clear beam length. See Table 6.2(e) for the calculation results.

(5) Steel double-angle braces

The seismic weight from the steel double-angle braces considers the self-weight of the braces and the gusset plates connections in the upper half of the 2nd story. For inconvenience, the shear tabs, bolts, and stiffeners on the beams at the brace-to-beam intersections are included as well. See Table 6.2(f) for the calculation results.

(6) Beam-to-beam connections

The seismic weight from the beam-to-beam connections considers the shear tabs and stiffeners at the brace-to-beam connections. See Table 6.2(g) for the calculation results.

Figure 6.18 shows that the seismic weights from the roof deck and added mass can be simplified as a uniform area load applied on the floor. Table 6.3(b) shows the calculations on these area loads. The area loads from the roof deck is w_0' = 2.3 psf. The area loads for three groups of added weights (Added Weights 5, 6, and 7, respectively) are $\overline{w_{a5}}$ = 292.28 psf, $\overline{w_{a6}}$ = 375.74 psf, and $\overline{w_{a7}}$ = 156.18 psf, respectively.

Table 6.5 and Table 6.6 show the summaries of the seismic weight tributary to the roof for Phase 2A and Phase 2B tests, respectively. For Phase 2B test building, the total seismic weight tributary to the roof level is W_{RF} = 52.819 kips. The contributions from the roof deck, added weights, steel beams, double-angle braces, beam-to-beam connections, and steel columns are 2.74%, 83.97%, 7.71%, 1.18%, 0.17%, and 4.23%, respectively. The total seismic weight tributary to roof collector lines is W_{RF}' = 50.583 kips. The contributions from roof deck, added weights, steel

beams, double-angle braces, and beam-to-beam connections are 2.86%, 87.68%, 8.05%, 1.23%, and 0.18%, respectively.

To determine the roof collector axial force demand produced by floor acceleration, it requires the calculation of seismic weight tributary to each collector. Figure 6.20 illustrates that the seismic weight, W'_{Ni} or W'_{Si}, tributary to the *i*-th span of the north or south roof collector line, respectively. Also, the following relationship holds:

$$W'_{RF} = \sum_{i=1}^{3} W'_{Ni} + \sum_{i=1}^{3} W'_{Si} \tag{6.1}$$

For simplicity, it is assumed that seismic weight is uniformly distributed along the collector, so that the linear weight, w'_{Ni} or w'_{Si}, to the *i*-th span of the north or south roof collector line, respectively, can be determined from:

$$\begin{aligned} w'_{Ni} &= W'_{Ni}/L_i \\ w'_{Si} &= W'_{Si}/L_i \end{aligned} \tag{6.2}$$

where L_i is the *i*-th span length.

Table 6.9(a) and (b) show the calculation for seismic weights tributary to the north and south roof collector lines, respectively. Figure 6.21 demonstrates the variation of the linear seismic weight along the collector lines. Figure 6.22 shows that the slab inertial forces, F'_I, that are generated by the floor acceleration, a_{flr}, are transferred into the collectors through the shear forces between the slab and collectors. In practice, it is considered a rational approach to assume that these shear forces are uniformly distributed. Therefore, the slab shear flows, v'_{Ni} and v'_{Si}, which are acting along the *i*-th span of the north and south roof collector lines, respectively, can be determined from

$$v'_{Ni} = w'_{Ni} \times \frac{a_{flr}}{g}$$
$$v'_{Si} = w'_{Si} \times \frac{a_{flr}}{g} \tag{6.3}$$

These shear forces can be used to compute the axial force demand in the collectors.

Table 6.1 Seismic Weights from Various Components Tributary to 2nd Floor of Phase 2 Test Building

(a) Composite Slab

Item	Unit Weight (psf)		Width	Length	Area	Weight
	Concrete	Metal Deck	(ft)	(ft)	(ft^2)	(lbs)
Interior Slab	23.20	2.30	18	38	684	17442
Exterior Slab	32.08	7.18	1	116	116	4554
					Total	21996

(b) Added Weights

Added Weight No.	RC Block	1-3/8"-dia. PT Rod			HSS6.000×0.500			Washer		Bearing Plate 1		Bearing Plate 2		Total Weight
		Unit Wt.	Length	Qty	Unit Wt.	Length	Qty	Each Wt.	Qty	Each Wt.	Qty	Each Wt.	Qty	
	(lbs)	(lb/ft)	(ft)	-	(lbs/ft)	(ft)	-	(lbs)	-	(lbs)	-	(lbs)	-	(lbs)
1	25120	5.56	7	4	29.4	1.5	4	27.08	12	47.04	4	62.38	0	25965
2	26100	5.56	7	4	29.4	1.5	4	27.08	12	47.04	4	62.38	0	26945
3	10170	5.56	8	4	29.4	3	4	27.08	12	47.04	2	62.38	2	11245
4	14840	5.56	8	4	29.4	3	4	27.08	12	47.04	4	62.38	0	15884
													Total	80039

(c) Steel Columns

Node No.	Column 1		Column 2		Cont. Plate		Stiffener		Shear Tab 1		Shear Tab 2		Bolt		Total Weight
	Unit Wt.	Length	Unit Wt.	Length	Each Wt.	Qty.	Each Wt.	Qty.	Each Wt.	Qty.	Each Wt.	Qty.	Each Wt.	Qty.	
	(plf)	(in.)	(plf)	(in.)	(lbs)	-	(lbs)	-	(lbs)	-	(lbs)	-	(lbs)	-	(lbs)
A1	170	72	120	24	6.76	4	0	0	2.24	1	8.30	1	0.353	10	1301
A9	170	72	120	24	6.76	4	0	0	2.24	1	8.30	1	0.353	10	1301
G1	40	52	40	24	2.95	2	2.28	1	2.24	2	6.43	1	0.353	15	278
G9	40	52	40	24	2.95	2	2.28	1	2.24	2	6.43	1	0.353	15	278
M1	40	52	40	24	0	0	2.28	2	2.24	2	6.43	1	0.353	15	274
M9	40	52	40	24	0	0	2.28	2	2.24	2	6.43	1	0.353	15	274
O1	40	52	40	24	0	0	2.28	2	2.24	2	6.43	1	0.353	15	274
O9	40	52	40	24	0	0	2.28	2	2.24	2	6.43	1	0.353	15	274
														Total	4254

Table 6.1 Seismic Weights from Various Components Tributary to 2nd Floor of Phase 2 Test Building(continued)

(d) Steel Beams

Beam Group No.	Beam No.	Beam		Headed Stud Unit Wt.	Length	Each Beam Weight	Qty	Weight
		Shape	Unit Wt.					
			(lb/ft)	(lb/ft)	in.	(lbs)	-	(lbs)
1	AG1, AG9	W14×30	30	0.35	156.875	396.8	2	794
2	GM1, GM9	W14×30	30	0.35	159.250	402.8	2	806
3	MO1, MO9	W14×26	26	0.35	50.750	111.4	2	223
4	OQ1, OQ9	W14×26	26	0.35	57.890	127.1	2	254
5	AG5, AG7, GM5, GM7	W14×26	26	0.35	161.970	355.7	4	1423
6	MO3, MO5, MO7, OQ3, OQ5, OQ7	W14×26	26	0.35	53.970	118.5	6	711
7	A19	W14×26	26	0.35	202.400	444.4	1	444
8	G19, M19, Q19	W14×26	26	0.35	206.930	454.4	3	1363
9	Q19	W14×26	26	0.35	209.970	461.1	1	461
10	D15, J15	W14×26	26	0.35	101.120	222.0	2	444
							Total	6923

(e) Double-Angle Braces Framing to Beams

Node No.	Double-Angle Brace			Gusset Plate		Stitch Plate		Shear Tab		Stiffener 1		Stiffener 2		Bolt 1		Bolt 2		Total Weight
	Area	Half-Length	Qty.	Each Wt.	Qty.	Each Wt.	Qty.	Each Wt.	Qty.	Each Wt.	Qty.	Each Wt.	Qty.	Each Wt.	Qty.	Each Wt.	Qty.	
	(in^2)	(in.)	-	(lbs)	-	(lbs)	-	(lbs)	-	(lbs)	-	(lbs)	-	(lbs)	-	(lbs)	-	(lbs)
A5	5.72	59	2	37.36	1	5.13	1	5.00	1	3.32	4	2.14	4	0.353	5	0.417	10	214
G5	5.72	52	2	47.13	1	5.13	1	5.00	2	3.32	4	2.14	4	0.353	10	0.417	10	196
M5	5.72	52	2	47.13	1	5.13	1	5.00	2	3.32	4	2.14	4	0.353	10	0.417	10	196
O5	5.72	52	2	47.13	1	5.13	1	5.00	2	3.32	4	2.14	4	0.353	10	0.417	10	196
Q1	5.72	35	1	10.91	1	5.13	1	5.00	1	3.32	2	0	0	0.353	5	0.417	5	66
Q9	5.72	35	1	10.91	1	5.13	1	5.00	1	3.32	2	0	0	0.353	5	0.417	5	66
																	Total	933

Table 6.1 Seismic Weights from Various Components Tributary to 2nd Floor of Phase 2 Test Building (continued)

(f) Double-Angle Braces Framing to Columns

Node No.	Double-Angle Brace			Gusset Plate		Stitch Plate		Shear Tab		Stiffener 1		Stiffener 2		Bolt 1		Bolt 2		Total Weight
	Area	Half-Length	Qty.	Each Wt.	Qty.	Each Wt.	Qty.	Each Wt.	Qty.	Each Wt.	Qty.	Each Wt.	Qty.	Each Wt.	Qty.	Each Wt.	Qty.	
	(in^2)	(in.)	-	(lbs)	-	(lbs)	-	(lbs)	-	(lbs)	-	(lbs)	-	(lbs)	-	(lbs)	-	(lbs)
A1	5.72	57	1	13.55	1	5.13	1	0	0	4.65	1	4.3	2	0	0	0.417	5	103
A9	5.72	57	1	13.55	1	5.13	1	0	0	4.65	1	4.3	2	0	0	0.417	5	103
G1	5.72	58	1	12.86	1	5.13	1	0	0	2.28	1	1.83	2	0	0	0.417	5	102
G9	5.72	58	1	12.86	1	5.13	1	0	0	2.28	1	1.83	2	0	0	0.417	5	102
M1	5.72	58	1	12.86	1	5.13	1	0	0	2.28	1	1.83	2	0	0	0.417	5	102
M9	5.72	58	1	12.86	1	5.13	1	0	0	2.28	1	1.83	2	0	0	0.417	5	102
																	Total	613

(g) Beam-to-Beam Connections

Node No.	Shear Tab		Bolt		Total Weight
	Each Wt.	Qty	Each Wt.	Qty	
	(lbs)	-	(lbs)	-	(lbs)
A7	5.00	1	0.353	5	6.77
D1	5.00	1	0.353	5	6.77
D5	5.00	1	0.353	5	6.77
G7	5.00	2	0.353	10	13.53
J1	5.00	1	0.353	5	6.77
J5	5.00	1	0.353	5	6.77
M3	5.00	1	0.353	5	6.77
M7	5.00	2	0.353	10	13.53
O3	5.00	2	0.353	10	13.53
O7	5.00	2	0.353	10	13.53
Q3	5.00	1	0.353	5	6.77
Q5	5.00	1	0.353	5	6.77
Q7	5.00	1	0.353	5	6.77
				Total	115

Table 6.2 Seismic Weights from Various Components Tributary to Roof of Phase 2 Test Building

(a) Roof Deck

Item	Deck Unit Wt.	Width	Length	Area	Weight
	(psf)	(ft)	(ft)	(ft^2)	(lbs)
Roof Deck	2.30	18	35	630	1449
				Total	1449

(b) Added Weights (Phase 2A)

Added Weight No.	Added-on Steel Plate	Stopper 1		Stopper 2		Stopper 3		Stopper 4		Total Weight
		Each Wt.	Qty.	Each Wt.	Qty.	Each Wt.	Qty.	Each Wt.	Qty.	
	(lbs)	(lbs)	-	(lbs)	-	(lbs)	-	(lbs)	-	(lbs)
5	0	62.57	2	52.20	0	21.87	0	13.68	4	180
6	0	62.57	2	52.20	0	21.87	0	13.68	4	180
7	0	62.57	0	52.20	2	21.87	4	13.68	0	192
									Total	552

(c) Added Weights (Phase 2B)

Added Weight No.	Added-on Steel Plate	Stopper 1		Stopper 2		Stopper 3		Stopper 4		Total Weight
		Each Wt.	Qty.	Each Wt.	Qty.	Each Wt.	Qty.	Each Wt.	Qty.	
	(lbs)	(lbs)	-	(lbs)	-	(lbs)	-	(lbs)	-	(lbs)
5	17000	62.57	2	52.20	0	21.87	0	13.68	4	17180
6	19400	62.57	2	52.20	0	21.87	0	13.68	4	19580
7	7400	62.57	0	52.20	2	21.87	4	13.68	0	7592
									Total	44352

Table 6.2 Seismic Weights from Various Components Tributary to Roof of Phase 2 Test Building (continued)

(d) Steel Columns

Node No.	Column		Cont. Plate		Cap Plate		Stiffener		Shear Tab 1		Shear Tab 2		Bolt		Total Weight
	Unit Wt.	Length	Each Wt.	Qty.	Each Wt.	Qty.	Each Wt.	Qty.	Each Wt.	Qty.	Each Wt.	Qty.	Each Wt.	Qty.	
	(plf)	(in.)	(lbs)	-	(lbs)	-	(lbs)	-	(lbs)	-	(lbs)	-	(lbs)	-	(lbs)
A1	120	52.675	6.45	2	17.36	1	0	0	1.39	1	5.89	1	0.353	6	549
A9	120	52.675	6.45	2	17.36	1	0	0	1.39	1	5.89	1	0.353	6	549
G1	40	52.675	2.74	2	7.16	1	0	0	1.39	2	4.59	1	0.353	9	192
G9	40	52.675	2.74	2	7.16	1	0	0	1.39	2	4.59	1	0.353	9	192
M1	40	52.675	2.74	2	7.16	1	0	0	1.39	2	4.59	1	0.353	9	192
M9	40	52.675	2.74	2	7.16	1	0	0	1.39	2	4.59	1	0.353	9	192
O1	40	52.675	0	0	7.16	1	2.28	1	1.39	1	4.59	1	0.353	6	186
O9	40	52.675	0	0	7.16	1	2.28	1	1.39	1	4.59	1	0.353	6	186
														Total	2236

(e) Steel Beams

Beam Group No.	Beam No.	Beam		Length	Each Beam Wrigth	Qty.	Weight
		Shape	Unit Wt.				
			(lb/ft)	in.	(lbs)	-	(lbs)
1	AG1, AG9	W10x17	17	157.325	222.9	2	446
2	GM1, GM9	W10x17	17	159.250	225.6	2	451
3	MO1, MO9	W10x17	17	50.750	71.9	2	144
4	AG5, GM5	W10x17	17	162.990	230.9	2	462
5	MO3′, MO5, MO7′	W10x17	17	54.990	77.9	3	234
6	A19	W10x17	17	202.700	287.2	1	287
7	G19, M19, Q19	W10x17	17	206.930	293.2	3	879
8	C15, E15, I15, K15, C59, E59, I59, K59	W10x17	17	102.990	145.9	8	1167
						Total	4070

Table 6.2 Seismic Weights from Various Components Tributary to Roof of Phase 2 Test Building (continued)

(f) Double-Angle Braces Framing to Beams

Node	Double-Angle Brace			Gusset Plate		Stitch Plate		Shear Tab		Stiffener 1		Stiffener 2		Bolt 1		Bolt 2		Total Weight
	Area	Half-Length	Qty.	Each Wt.	Qty.	Each Wt.	Qty.	Each Wt.	Qty.	Each Wt.	Qty.	Each Wt.	Qty.	Each Wt.	Qty.	Each Wt.	Qty.	
	(in^2)	(in.)	-	(lbs)	-	(lbs)	-	(lbs)	-	(lbs)	-	(lbs)	-	(lbs)	-	(lbs)	-	lbs
A5	5.72	57	2	36.14	1	5.13	1	3.28	1	1.88	4	1.59	4	0.353	3	0.417	10	204
G5	5.72	58	2	36.14	1	5.13	1	3.28	2	1.88	4	1.59	4	0.353	6	0.417	10	208
M5	5.72	58	2	36.14	1	5.13	1	3.28	2	1.88	4	1.59	4	0.353	6	0.417	10	208
																	Total	621

(g) Beam-to-Beam Connections

	Shear Tab		Bolt		Total Weight
	Each Wt.	Qty.	Each Wt.	Qty.	
Node	(lbs)	-	(lbs)	-	(lbs)
C1	3.28	1	0.353	3	4.34
C5	3.28	2	0.353	6	8.68
C9	3.28	1	0.353	3	4.34
E1	3.28	1	0.353	3	4.34
E5	3.28	2	0.353	6	8.68
E9	3.28	1	0.353	3	4.34
I1	3.28	1	0.353	3	4.34
I5	3.28	2	0.353	6	8.68
I9	3.28	1	0.353	3	4.34
K1	3.28	1	0.353	3	4.34
K5	3.28	2	0.353	6	8.68
K9	3.28	1	0.353	3	4.34
M3	3.28	1	0.353	3	4.34
M7	3.28	1	0.353	3	4.34
O3	3.28	1	0.353	3	4.34
O5	3.28	1	0.353	3	4.34
O7	3.28	1	0.353	3	4.34
				Total	91

Table 6.3 Area Loads from Slab, Roof Deck, and Added Weights

(a) 2nd Floor

Item	Area Occupied			Total Weight (lbs)	Area Load, $\overline{w}$ (psf)
	Width (in.)	Length (in.)	Area (ft^2)		
Interior Slab	216	456	684	17442	$\overline{w_0}$ =25.5
Exterior Slab	12	1392	116	4554	$\overline{w_0^*}$ =39.6
Added Weight 1	149	60	62.083	25965	$\overline{w_1}$ = 418.23
Added Weight 2	149	60	62.083	26945	$\overline{w_2}$ = 434.02
Added Weight 3	48	96	32.000	11245	$\overline{w_3}$ = 351.39
Added Weight 4	72	71	35.500	15884	$\overline{w_4}$ = 447.43

(b) Roof (Phase 2B)

Item	Area Occupied			Total Weight (lbs)	Area Load, $\overline{w}$ (psf)
	Width (in.)	Length (in.)	Area (ft^2)		
Roof Deck	216	420	630	1449	$\overline{w_0'}$ =2.3
Added Weight 5	92	92	58.778	17180	$\overline{w_5}$ = 292.28
Added Weight 6	86.625	86.625	52.110	19580	$\overline{w_6}$ = 375.74
Added Weight 7	50	140	48.611	7592	$\overline{w_7}$ = 156.18

Table 6.4 Summary of Seismic Weights Tributary to 2nd Floor of Phase 2 Test Building

(a) for Collector Force Determination

Item	Slab	Added Weight	Steel Beam	Brace Framing to Beam	Beam-to-Beam Connection	Total
Weight (kips)	21.996	80.039	6.923	0.801	0.115	109.873
Mass (kip-sec/$in.^2$)	0.0570	0.2073	0.0179	0.0021	0.0003	0.2846
Percentage (%)	20.02%	72.85%	6.30%	0.73%	0.10%	-

(b) for Seismic Force Determination

Item	Slab	Added Weight	Steel Beam	Brace Framing to Beam	Beam-to-Beam Connection	Steel Column	Brace Framing to Column	Total
Weight (lbs)	21.996	80.039	6.923	0.933	0.115	4.254	0.613	114.873
Mass (lb-sec/$in.^2$)	0.0570	0.2073	0.0179	0.0024	0.0003	0.0110	0.0016	0.2975
Percentage (%)	19.15%	69.68%	6.03%	0.81%	0.10%	3.70%	0.53%	-

Table 6.5 Summary of Seismic Weights Tributary to Roof of Phase 2A Test Building

(a) for Collector Force Determination

Item	Deck	Added Weight (Stoppers Only)	Steel Beam	Brace Framing to Beam	Beam-to-Beam Connection	Total
Weight (kips)	1.449	0.552	4.070	0.621	0.091	6.783
Mass (kips-sec/in.^{2})	0.0038	0.0014	0.0105	0.0016	0.0002	0.0176
Percentage	21.36%	8.13%	60.01%	9.15%	1.34%	-

(b) for Seismic Force Determination

Item	Deck	Added Weight (Stoppers Only)	Steel Beam	Brace Framing to Beam	Beam-to-Beam Connection	Steel Column	Total
Weight (lbs)	1.449	0.552	4.070	0.621	0.091	2.236	9.019
Mass (lb-sec/in.^{2})	0.0038	0.0014	0.0105	0.0016	0.0002	0.0058	0.0234
Percentage (%)	16.07%	6.12%	45.13%	6.88%	1.01%	24.80%	-

Table 6.6 Summary of Seismic Weights Tributary to Roof of Phase 2B Test Building

(a) for Collector Force Determination

Item	Deck	Added Weight	Steel Beam	Brace Framing to Beam	Beam-to-Beam Connection	Total
Weight (kips)	1.449	44.352	4.070	0.621	0.091	50.583
Mass (kips-sec/in.^{2})	0.0038	0.1149	0.0105	0.0016	0.0002	0.1310
Percentage	2.86%	87.68%	8.05%	1.23%	0.18%	-

(b) for Seismic Force Determination

Item	Deck	Added Weight	Steel Beam	Brace Framing to Beam	Beam-to-Beam Connection	Steel Column	Total
Weight (lbs)	1.449	44.352	4.070	0.621	0.091	2.236	52.819
Mass (lb-sec/in.^{2})	0.0038	0.1149	0.0105	0.0016	0.0002	0.0058	0.1368
Percentage (%)	2.74%	83.97%	7.71%	1.18%	0.17%	4.23%	-

Table 6.7 Seismic Weights Tributary to Each Span of North Collector Line at 2nd Floor of Phase 2 Test Building

Span No.	Span length	Interior Slab		Exterior Slab		Added Weight	Steel Beam				Brace	Beam-to-Beam Connection	Total Weight, W'_{Ni}	Linear Weight, w'_{Ni}
							W14×30		W14×26					
		A_T	Unit Wt.	A_T	Unit Wt.		L_T	Unit Wt.	L_T	Unit Wt.				
	(ft)	(ft^2)	(psf)	(ft^2)	(psf)	(lbs)	(in.)	(lb/ft)	(in.)	(lb/ft)	(lbs)	(lbs)	(kips)	(kips/ft)
1	14	126	25.50	24	39.26	12983	335.04	26.35	156.88	30.35	155.83	10.15	18.436	1.3169
2	14	126	25.50	14	39.26	13473	285.57	26.35	159.25	30.35	97.85	16.91	18.380	1.3128
3	5	45	25.50	5	39.26	5622	235.17	26.35	0	30.35	97.85	10.15	7.590	1.5181
4	5	45	25.50	15	39.26	7942	295.56	26.35	0	30.35	48.93	16.91	10.393	2.0786
												Total W'_N =	54.800	kips
												Avg. $\overline{w'_N}$ =	1.4421	kips/ft

Table 6.8 Seismic Weights Tributary to Each Span of South Collector Line at 2nd Floor of Phase 2 Test Building

Span No.	Span length	Interior Slab		Exterior Slab		Added Weight	Steel Beam				Brace	Beam-to-Beam Connection	Total Weight, W'_{Si}	Linear Weight, w'_{Si}
							W14×30		W14×26					
		A_T	Unit Wt.	A_T	Unit Wt.		L_T	Unit Wt.	L_T	Unit Wt.				
	(ft)	(ft^2)	(psf)	(ft^2)	(psf)	(lbs)	(in.)	(lb/ft)	(in.)	(lb/ft)	(lbs)	(lbs)	(kips)	(kips/ft)
1	14	126	25.50	24	39.26	12983	395.89	26.35	156.88	30.35	155.83	16.91	18.577	1.3269
2	14	126	25.50	14	39.26	13473	346.42	26.35	159.25	30.35	97.85	13.53	18.510	1.3221
3	5	45	25.50	5	39.26	5622	235.17	26.35	0	30.35	97.85	13.53	7.594	1.5188
4	5	45	25.50	15	39.26	7942	295.56	26.35	0	30.35	48.93	16.91	10.393	2.0786
												Total W'_S =	55.074	kips
												Avg. $\overline{w'_S}$ =	1.4493	kips/ft

Table 6.9 Seismic Weights Tributary to Each Span of Each Collector Line at Roof of Phase 2 Test Building

(a) Phase 2A

Span No.	Span length	Metal Deck		Added Weight	Steel Beam		Brace	Beam-to-Beam Connection	Total Weight, W'_{Ni} $(= W'_{Si})$	Linear Weight, w'_{Ni} $(= w'_{Si})$
		A_T	Unit Wt.		L_T	Unit Wt.				
	(ft)	(ft^2)	(psf)	(lbs)	(in.)	(lb/ft)	(lbs)	(lbs)	(kips)	(kips/ft)
1	14	135	2.30	90	597.88	17.00	154.11	17.36	1.419	0.0507
2	14	126	2.30	90	550.19	17.00	104.24	19.53	1.283	0.0458
3	5	54	2.30	96	288.43	17.00	52.12	8.68	0.690	0.0690
								Total W'_N $(= W'_S)$ =	3.391	kips
								Avg. $\overline{w'_N}$ $(= \overline{w'_S})$ =	0.103	kip/ft

(b) Phase 2B

Span No.	Span length	Metal Deck		Added Weight	Steel Beam		Brace	Beam-to-Beam Connection	Total Weight, W'_{Ni} $(= W'_{Si})$	Linear Weight, w'_{Ni} $(= w'_{Si})$
		A_T	Unit Wt.		L_T	Unit Wt.				
	(ft)	(ft^2)	(psf)	(lbs)	(in.)	(lb/ft)	(lbs)	(lbs)	(kips)	(kips/ft)
1	14	135	2.30	8590	597.88	17.00	154.11	17.36	9.919	0.7085
2	14	126	2.30	9790	550.19	17.00	104.24	19.53	10.983	0.7845
3	5	54	2.30	3796	288.43	17.00	52.12	8.68	4.390	0.8779
								Total W'_N $(= W'_S)$ =	25.291	kips
								Avg. $\overline{w'_N}$ $(= \overline{w'_S})$ =	0.766	kips/ft

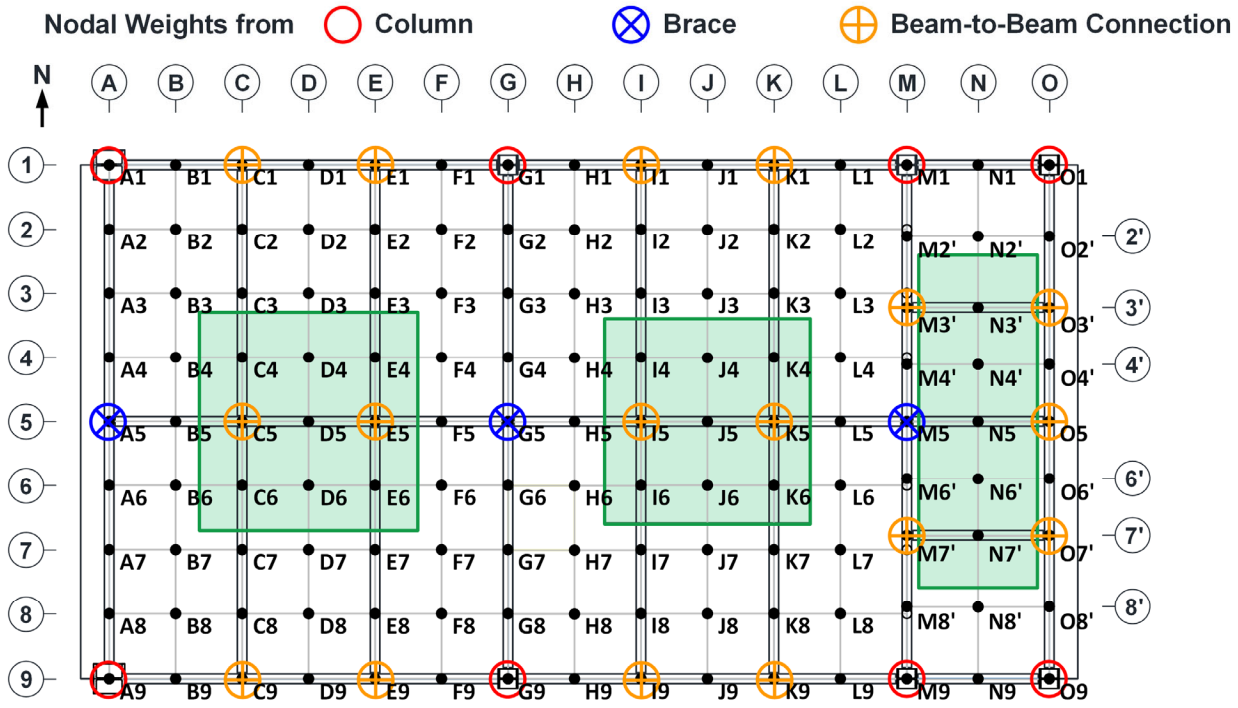

Figure 6.16 Node Designations and Nodal Weights at Roof Level

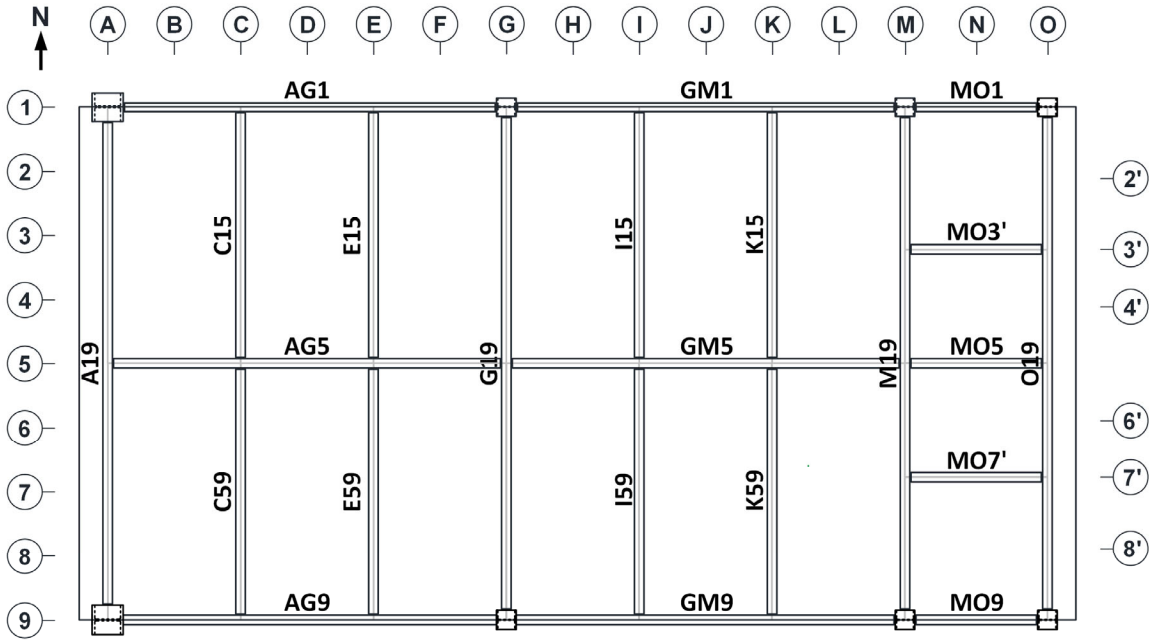

Figure 6.17 Beam Designations at Roof Level

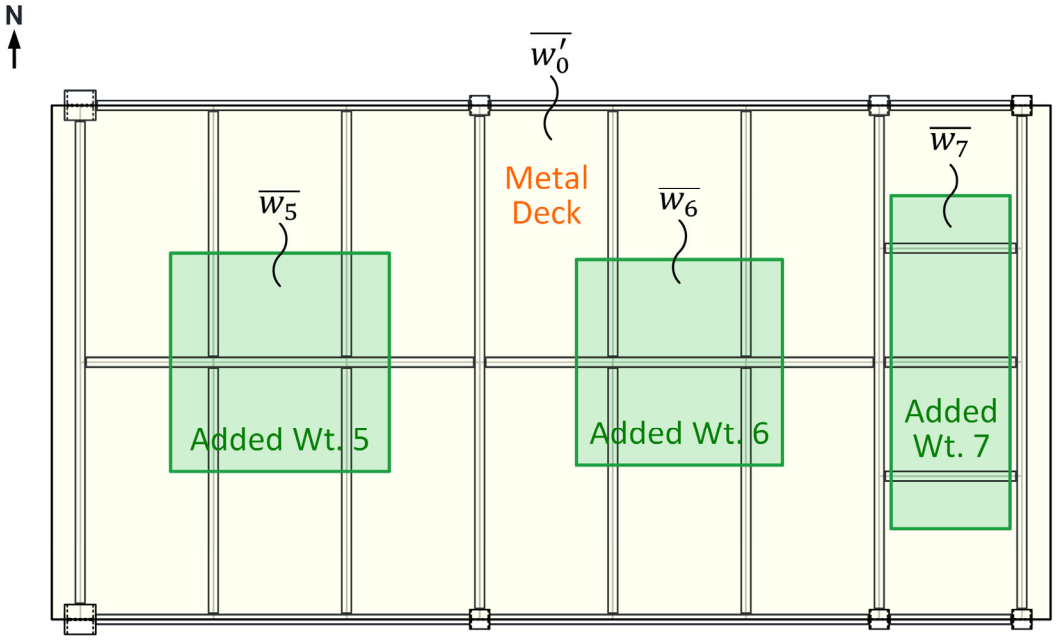

Figure 6.18 Area Weights at Roof Level (Phase 2B)

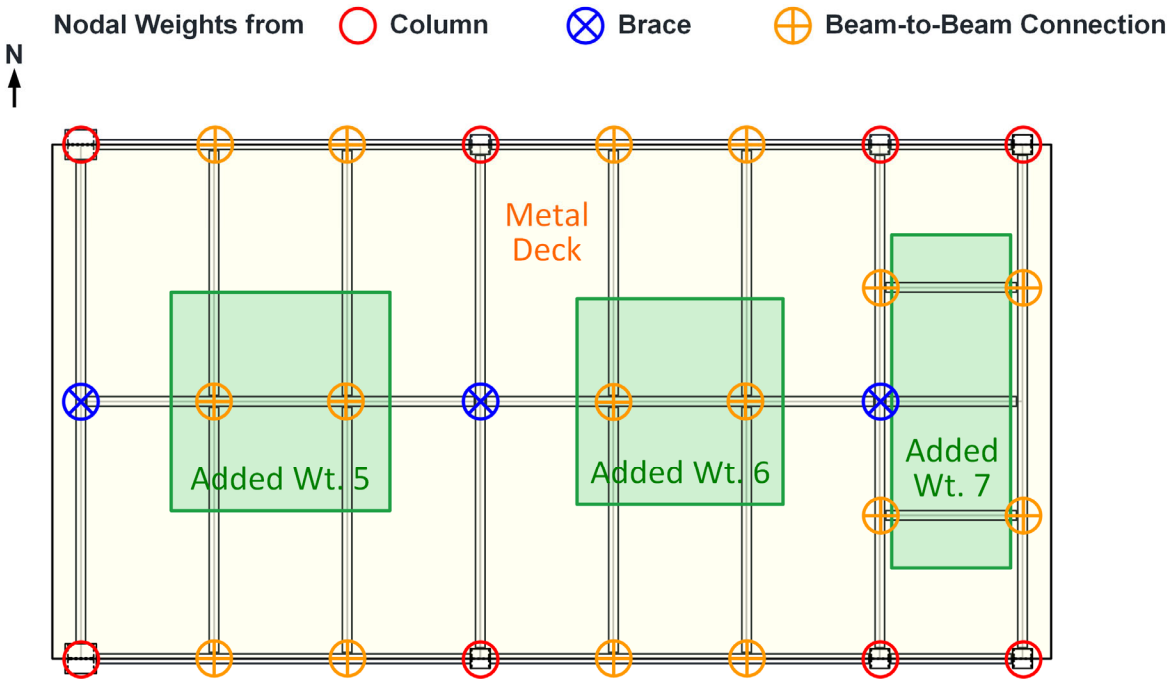

Figure 6.19 Tributary Seismic Weights at Roof Level (Phase 2B)

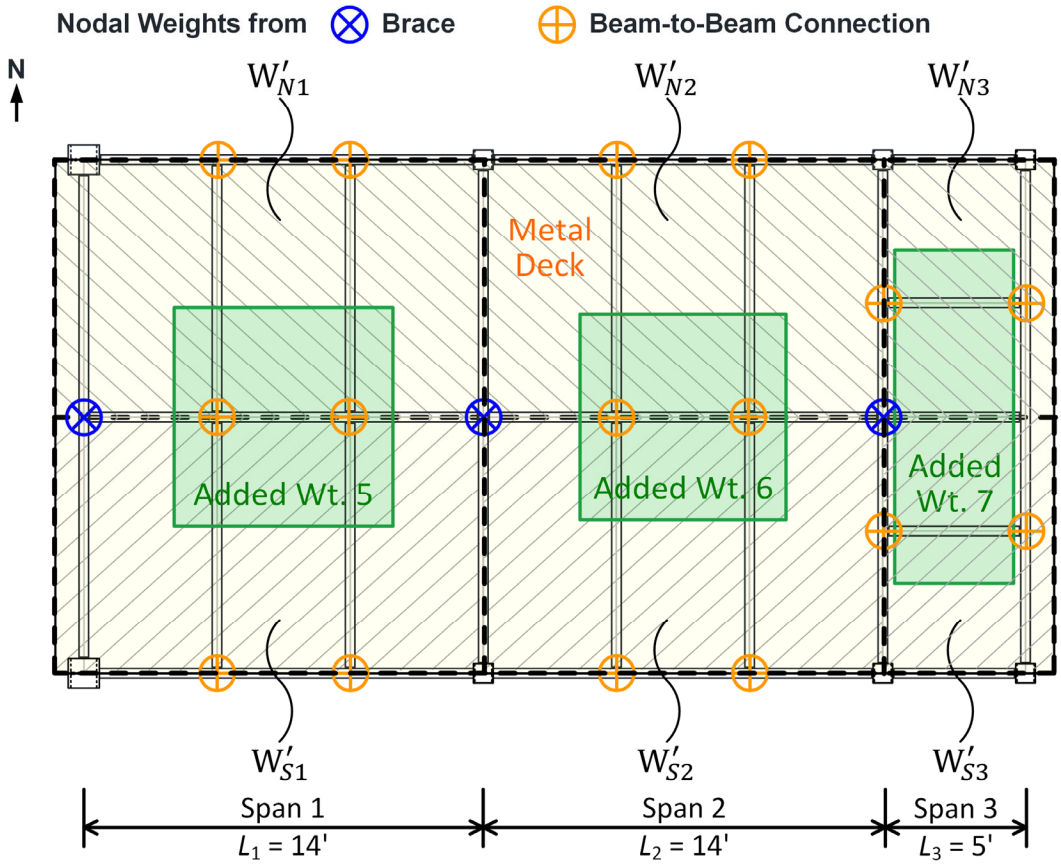

Figure 6.20 Seismic Weights Tributary to Each Span of Roof Collector Lines (Phase 2B)

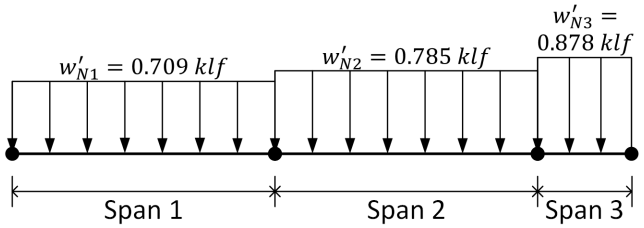

(a)

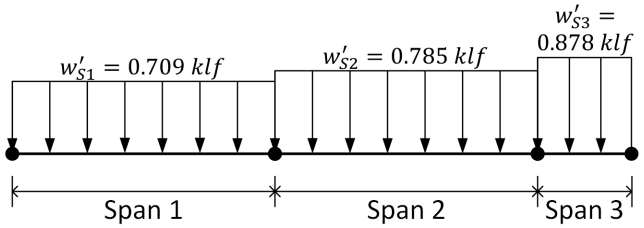

(b)

Figure 6.21 Linear Seismic Weights Tributary to (a) North and (b) South Roof Collector Lines (Phase 2B)

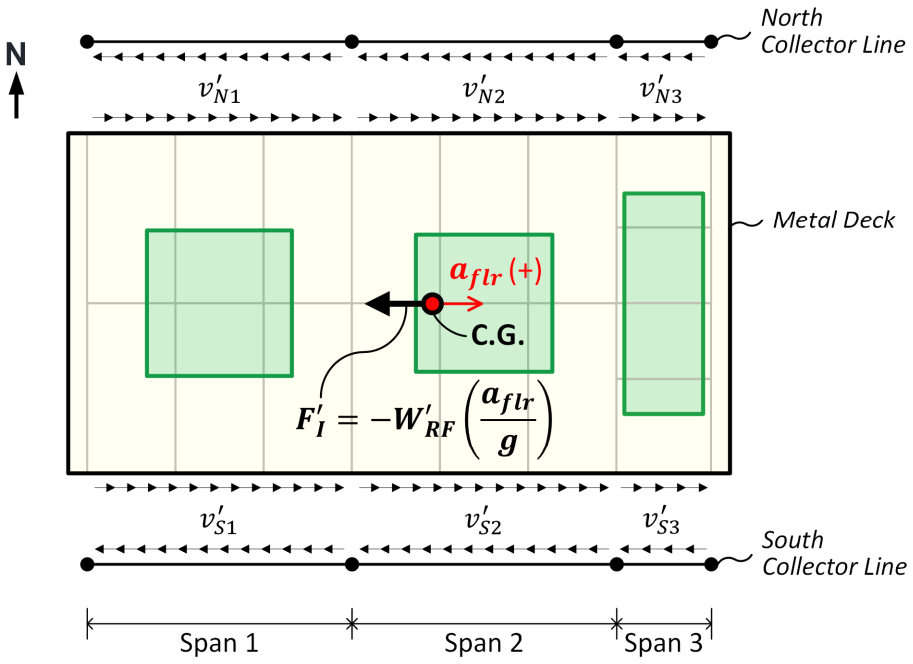

(a)

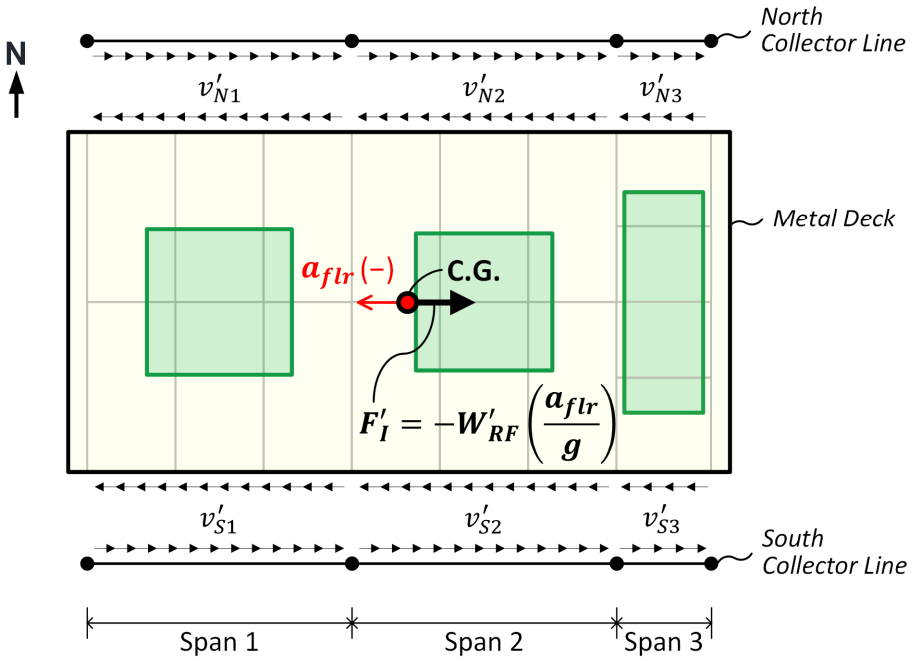

(b)

Figure 6.22 Shear Forces between Slab and Roof Collectors due to (a) Positive and (b) Negative Floor Accelerations

6.3 Instrumentation and Data Filtering

Phase 2 test building was instrumented with a combination of accelerometers, displacement transducers, uniaxial strain gauges, and strain gauge rosettes. Instrumentation plans are shown in Figure 6.23. A total of 420 data channels were used for Phase 2 tests. All sensors were sampled at a rate of 256 Hz throughout each recorded motion. The measured sensor signals were filtered using an 8th order Butterworth low-pass filter with a cutoff frequency of 30 Hz and a zero-phase digital filtering process built into MATLAB (Mathworks 2019). Prior to each test, the gages were biased such that the initial readings of all instruments were zero.

All sensors that had been installed in the Phase 1 specimen (i.e., first story of Phase 2 test building) were used in Phase 2 testing, except that some strain gauges on the transverse braces were intentionally disconnected in Phase 2 testing to release the channels for newly added sensors. This section only introduces the newly added sensors or gauges for Phase 2 testing. As shown in Figure 6.23(b), 12 concrete surface strain gauges were added to the eastside of columns on Column Lines 1 and 2 to investigate the effective slab width of composite collector sections. Figure 6.23(e) shows the newly added steel strain gauges on the west chord and two adjacent floor beams. These gauges were used to measure how much inertial force were transferred to these members.

Figure 6.23(g) and (h) show the strain gauges installed in the 2nd story of Frames N and S, respectively. Uniaxial strain gauges were placed on both flanges at two elevations for each column to recover the member forces so as to construct the moment diagram and axial force diagram. Due to the limitations of the number of channels, for the 2nd story, only the north roof collectors were heavily instrumented. As shown in Figure 6.23(g), the north roof collectors were instrumented at the sections 5½ in. (about half steel beam depth) away from the column faces of the collector connections at Column Lines 1, 2, and 3. For these critical sections, the gauges were placed at five

elevations along the steel collector section depth so that the strain profile of the collector section can be constructed. In addition, strain gauges were placed on the steel flanges at the mid-span and quarter span of each 14-ft long collector (Collectors 1 or 2). Strain gage sections were distributed over the 2nd-story north frame to recover member forces.

Figure 6.23(k) shows the displacement transducers layout for the 2nd story of Frame N. These displacement transducers were used to measure (1) the rotations of the north roof collector connections, (2) the slip of the concrete slab, and (3) shear deformations in the north 2nd story column panel zone. Figure 6.23(n) shows the string potentiometer layout for the roof diaphragm. String potentiometers were placed on the reference columns and a reference frame, which were fixed outside of the shake table, to measure the absolute roof displacements of the test building. Figure 6.23(k) shows the accelerometer layout on the roof diaphragm. Accelerometers were located at the top ends of the 2nd-story columns on Column Lines 1 and 4 to measure accelerations in three orthogonal directions at these locations. In addition, three accelerometers (A32, A33, and A34) were respectively installed on the added steel plates on the roof to monitor the horizontal accelerations of the added masses in the direction of shaking.

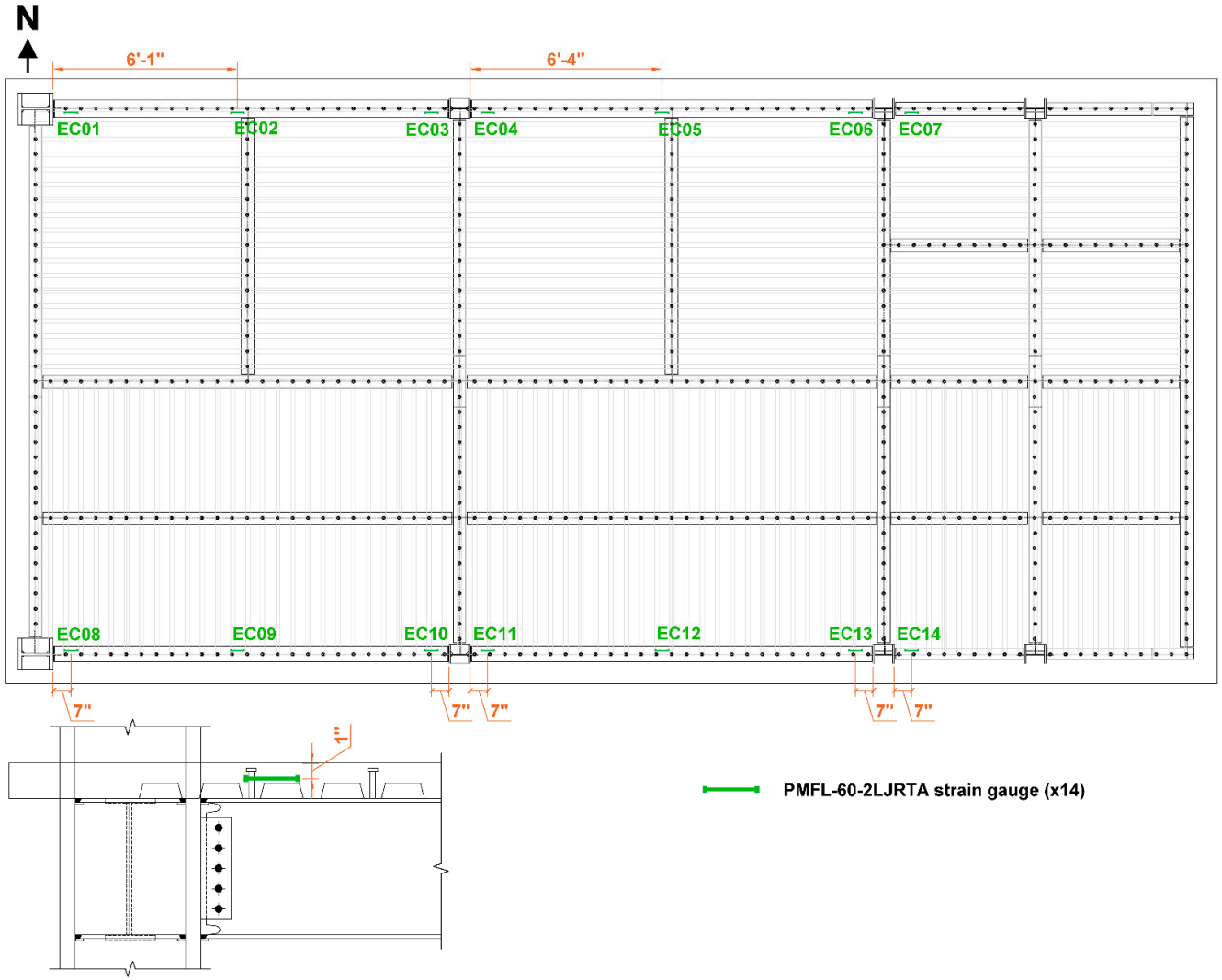

(a) Concrete-embedded Strain Gauges

Figure 6.23 Instrumentation Plan for Phase 2 Test

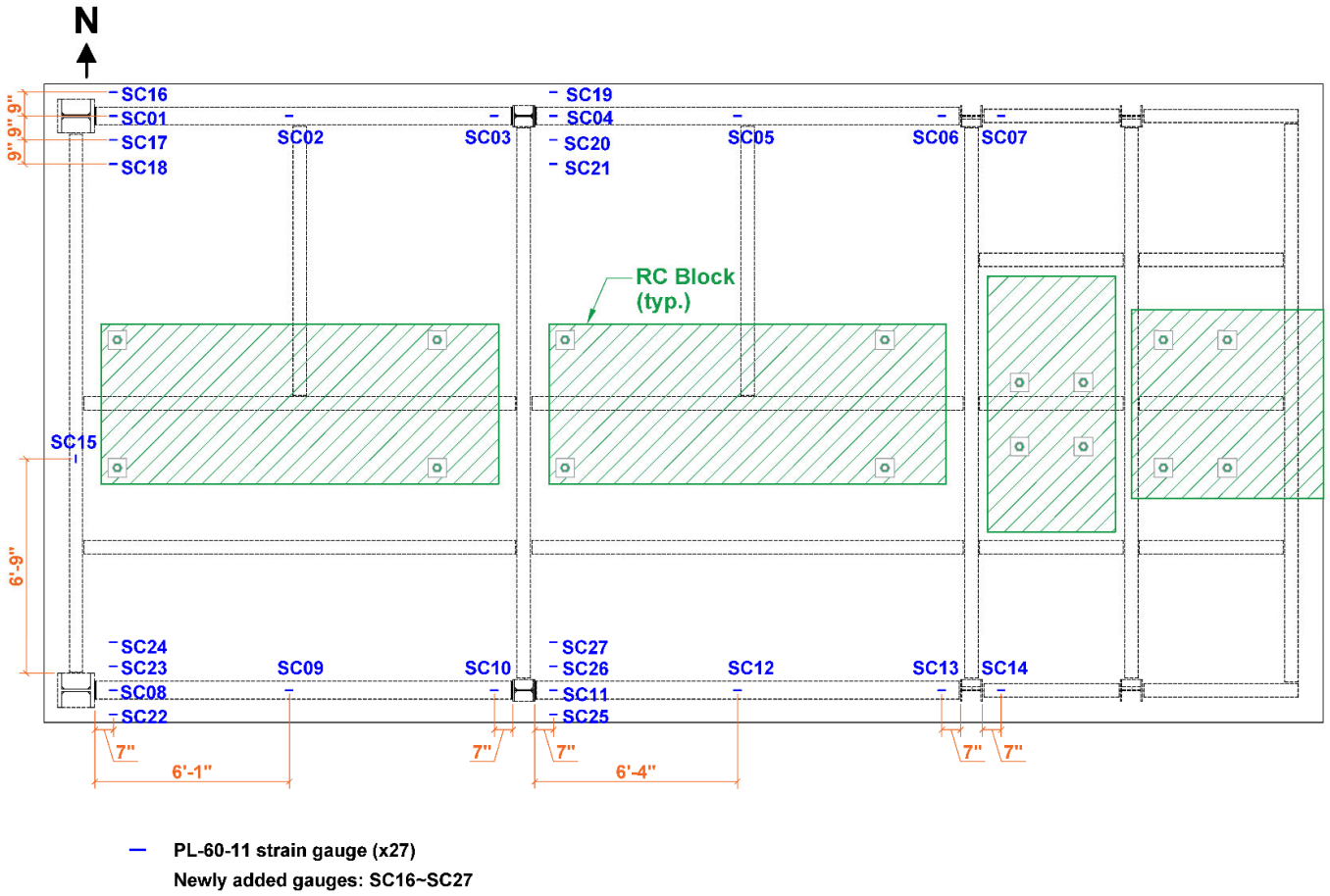

(b) Concrete Surface Strain Gauges

Figure 6.23 Instrumentation Plan for Phase 2 Test (continued)

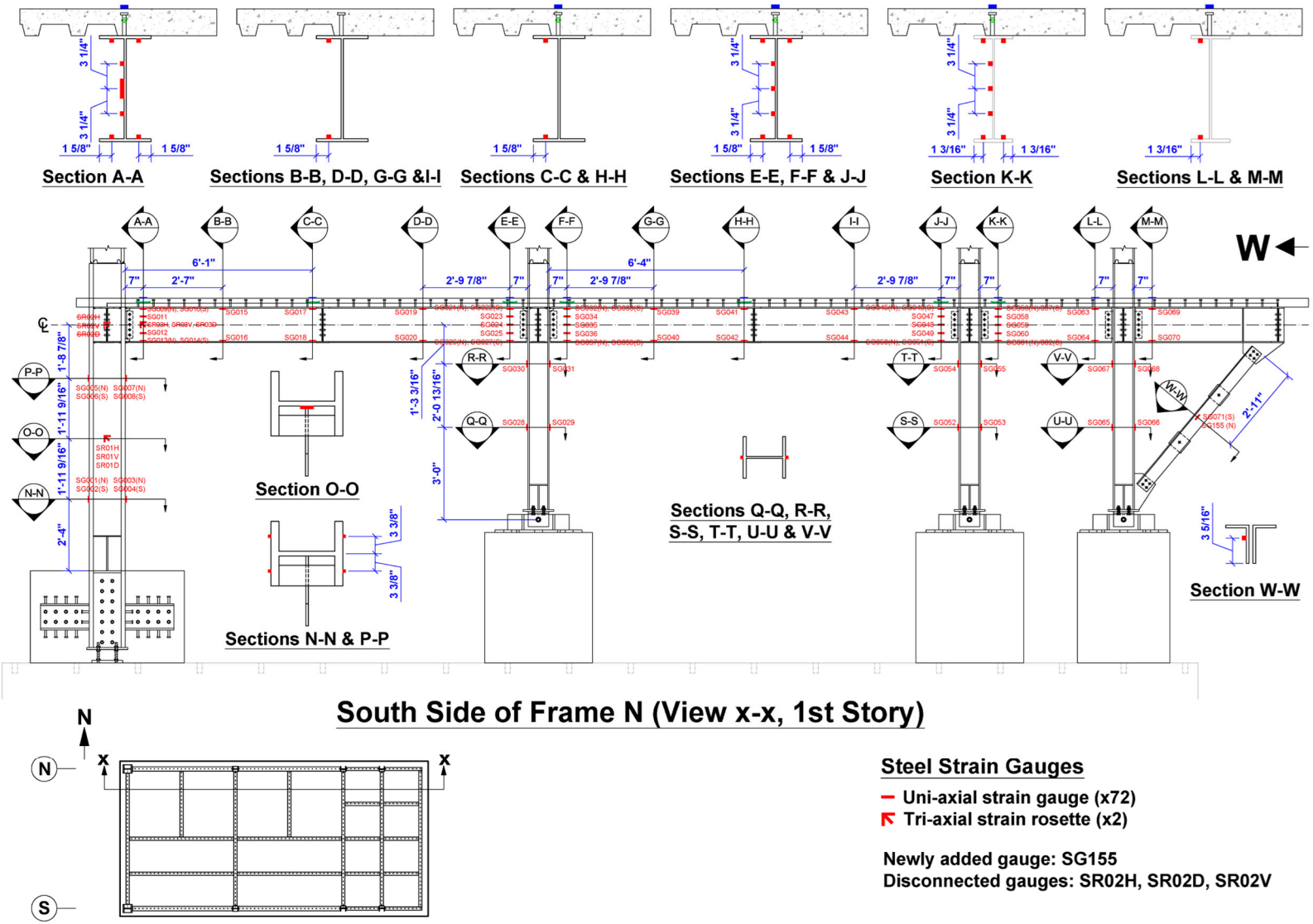

(c) Steel Strain Gauges on Frame N (1st Story)

Figure 6.23 Instrumentation Plan for Phase 2 Test (continued)

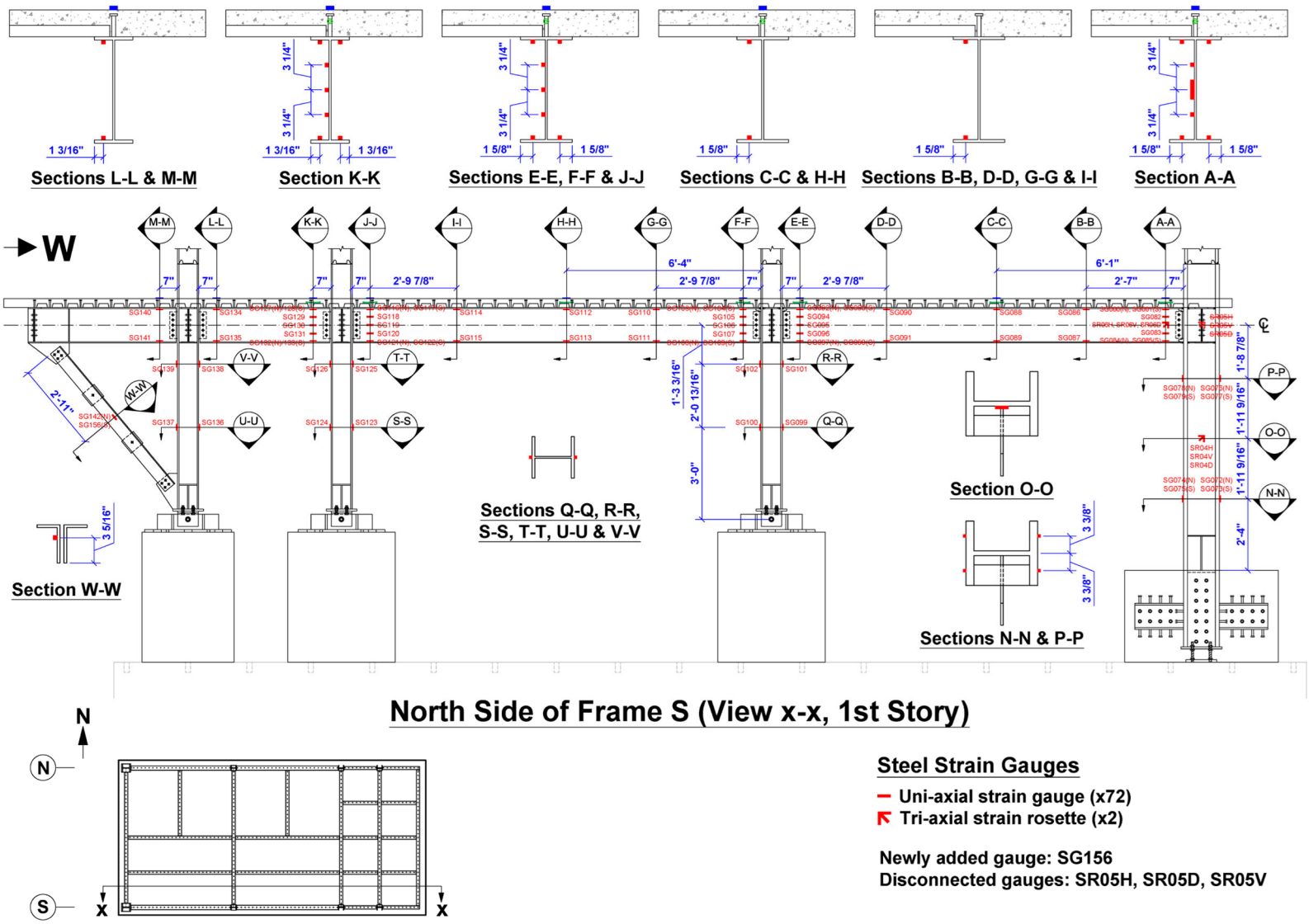

(d) Steel Strain Gauges on Frame S (1st Story)

Figure 6.23 Instrumentation Plan for Phase 2 Test (continued)

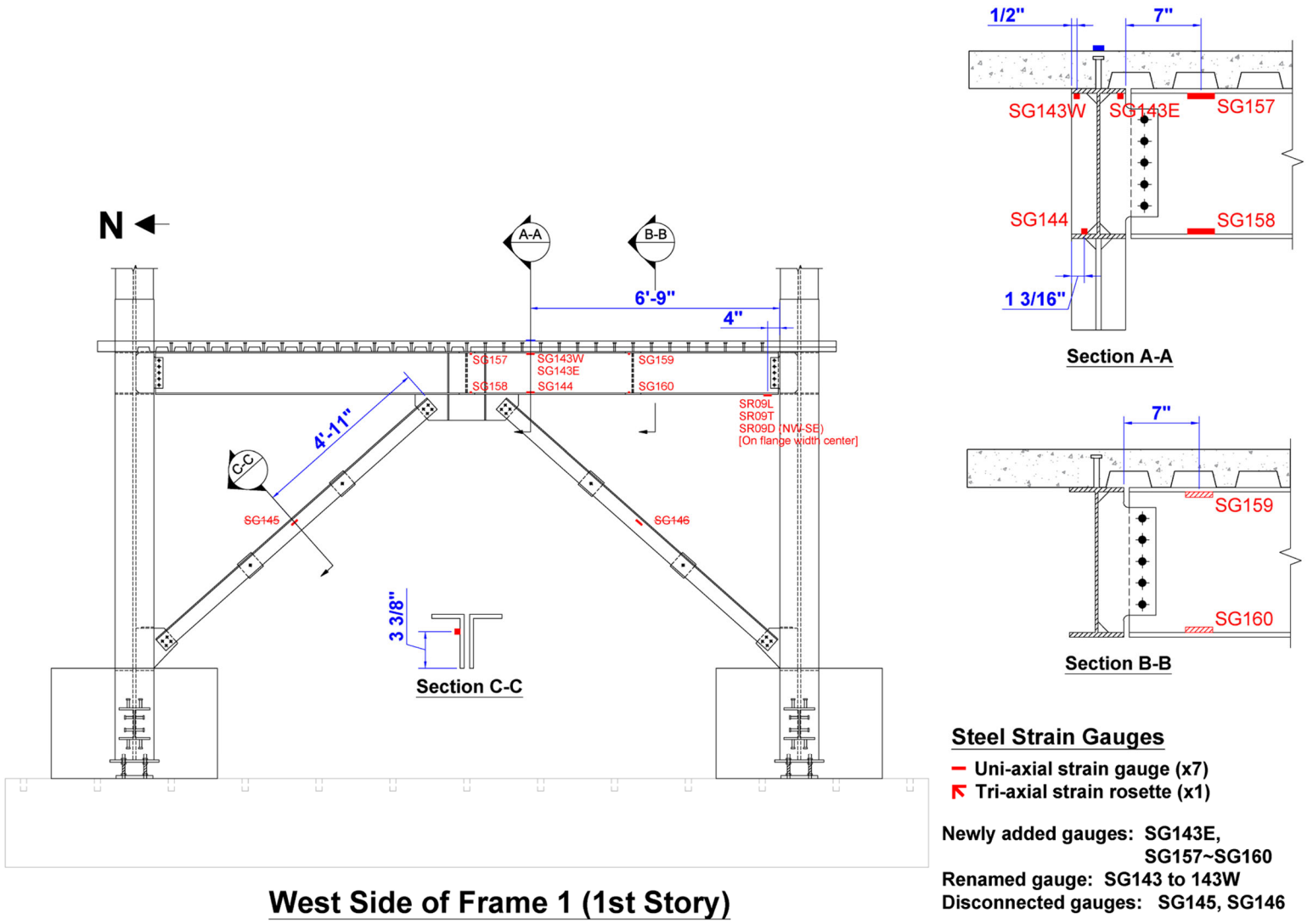

(e) Steel Strain Gauges on Frame 1 (1st Story)

Figure 6.23 Instrumentation Plan for Phase 2 Test (continued)

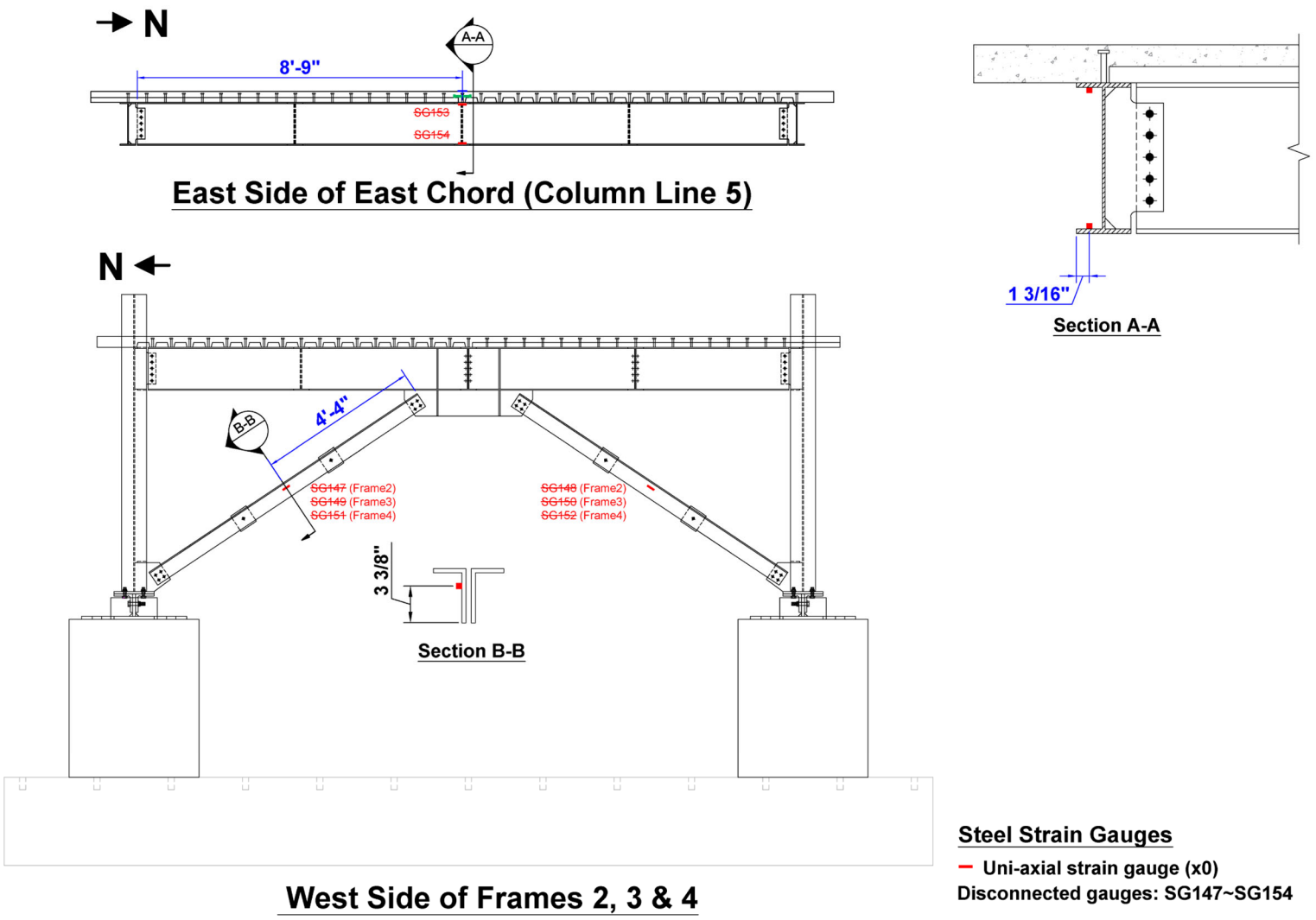

(f) Steel Strain Gauges on 2nd Floor East Chord and Frames 2, 3, and 4 (1st Story)

Figure 6.23 Instrumentation Plan for Phase 2 Test (continued)

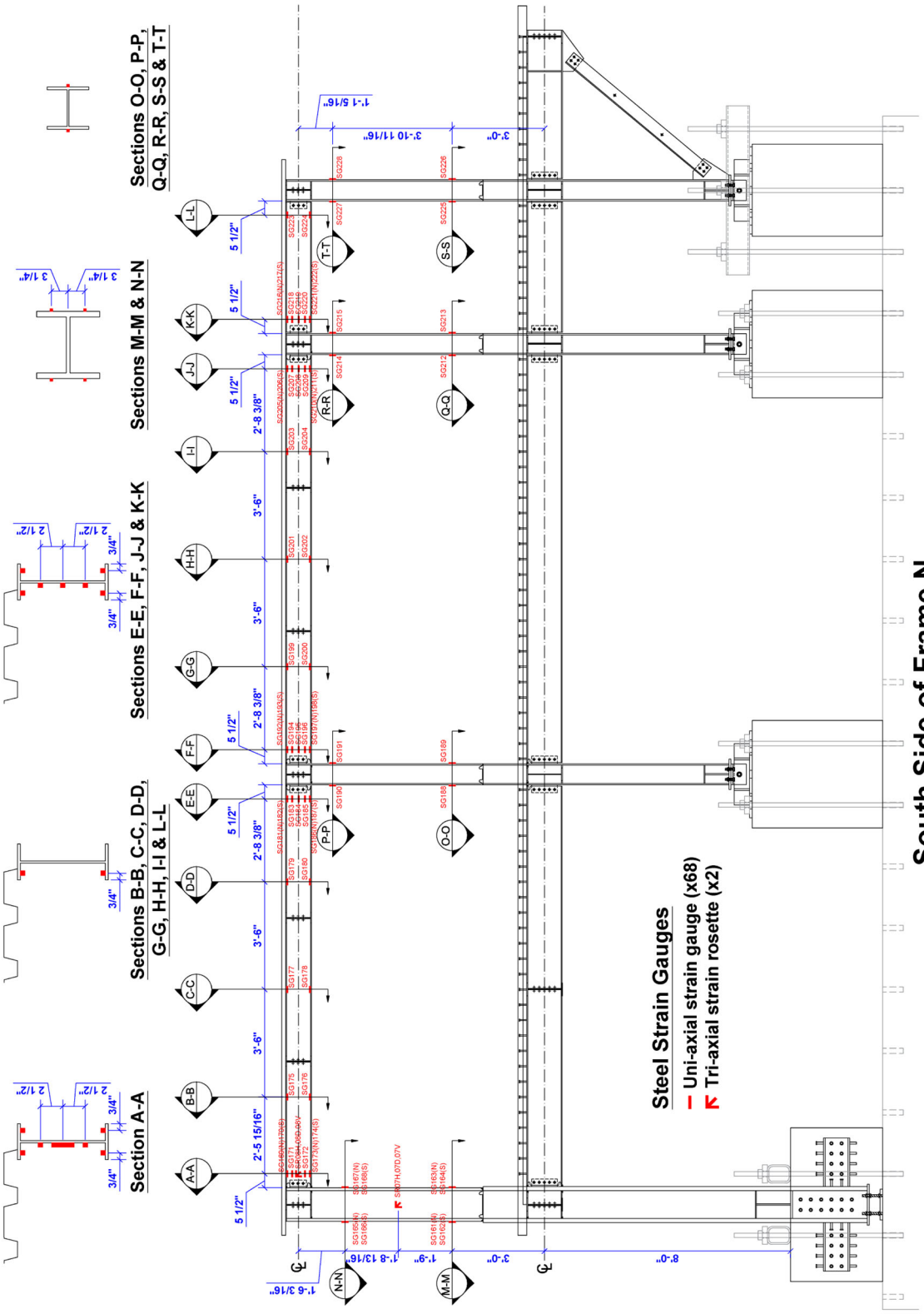

(g) Steel Strain Gauges on Frame N (2nd Story)

Figure 6.23 Instrumentation Plan for Phase 2 Test (continued)

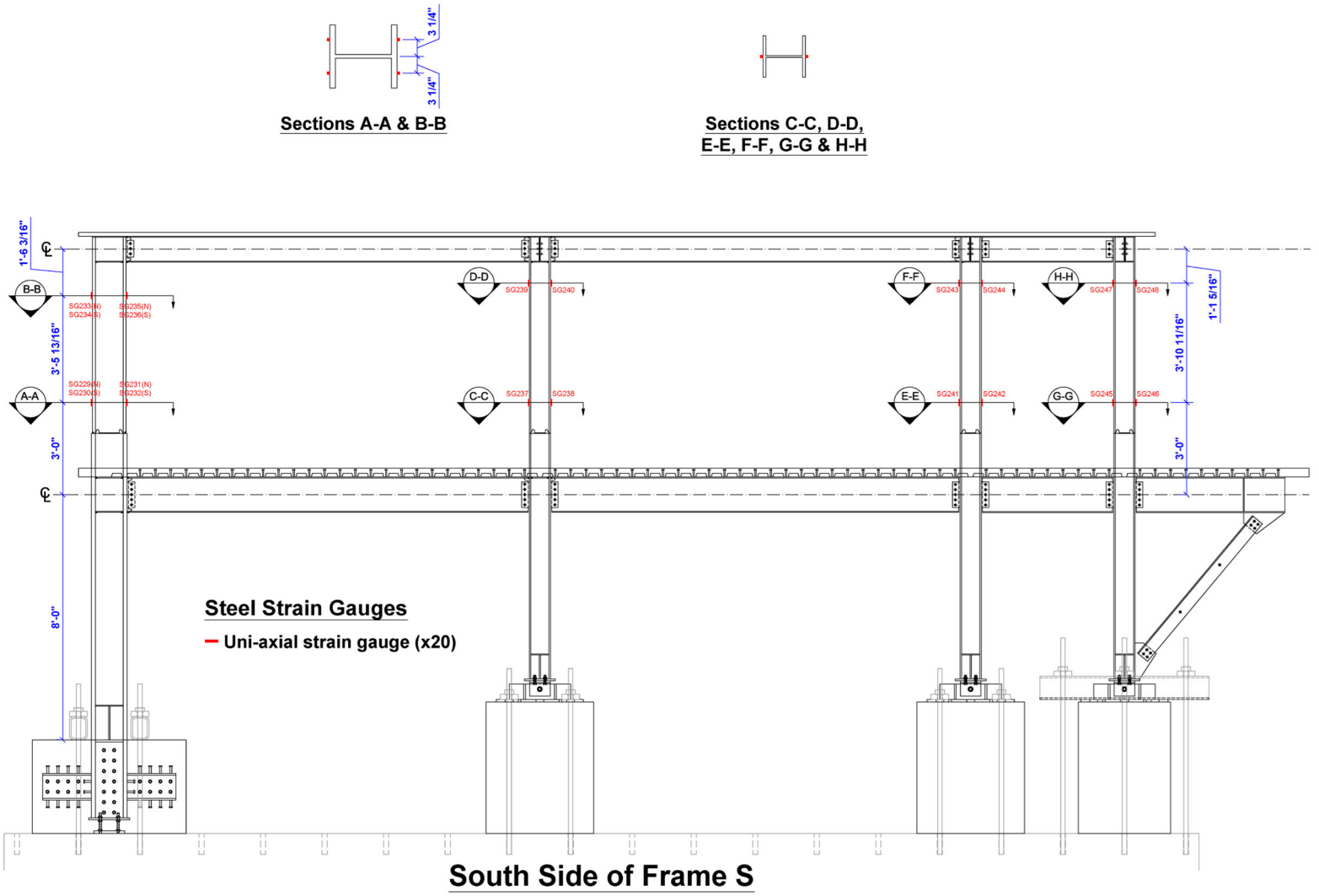

(h) Steel Strain Gauges on Frame S (2nd Story)

Figure 6.23 Instrumentation Plan for Phase 2 Test (continued)

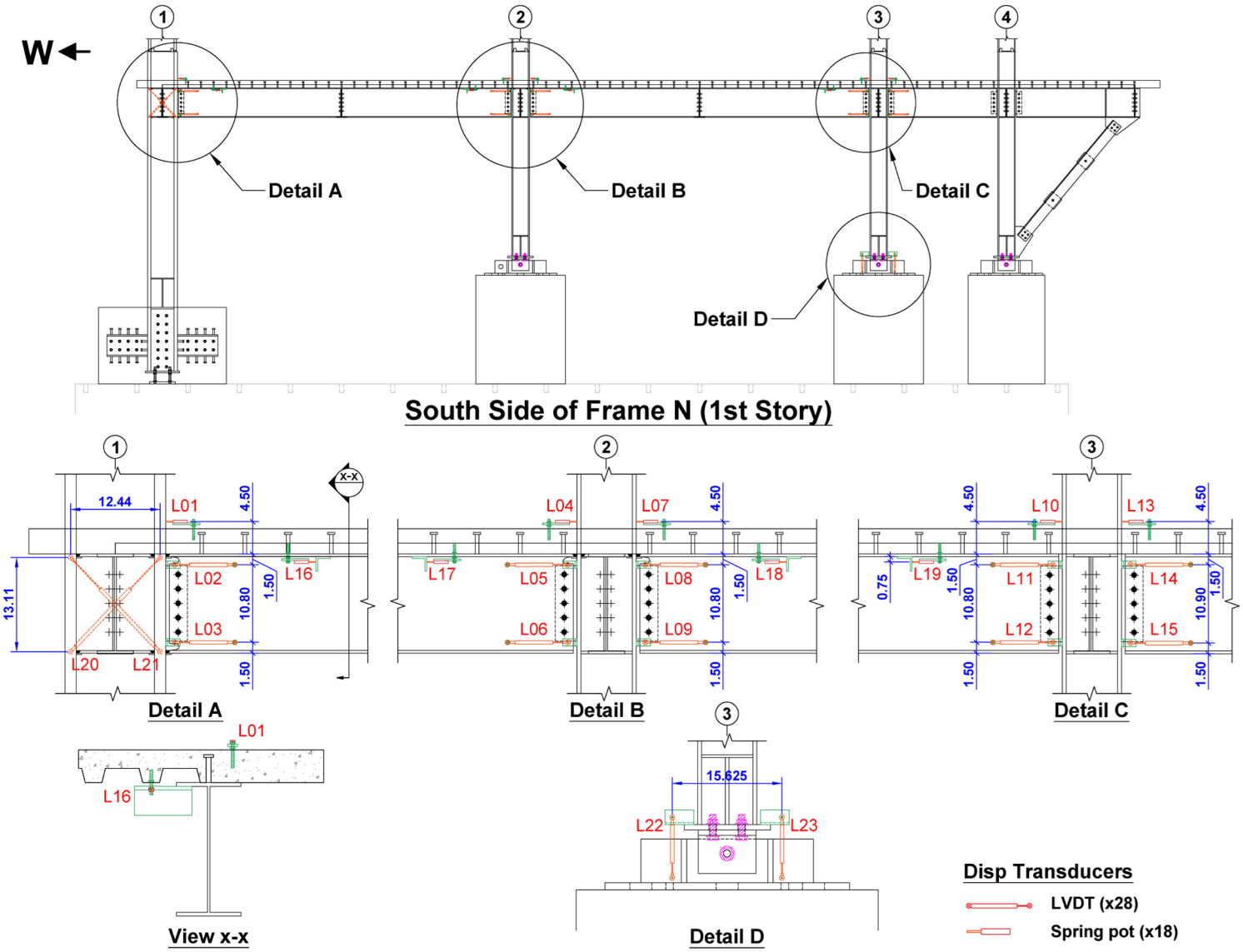

(i) Displacement Transducers on Frame N (1st Story)

Figure 6.23 Instrumentation Plan for Phase 2 Test (continued)

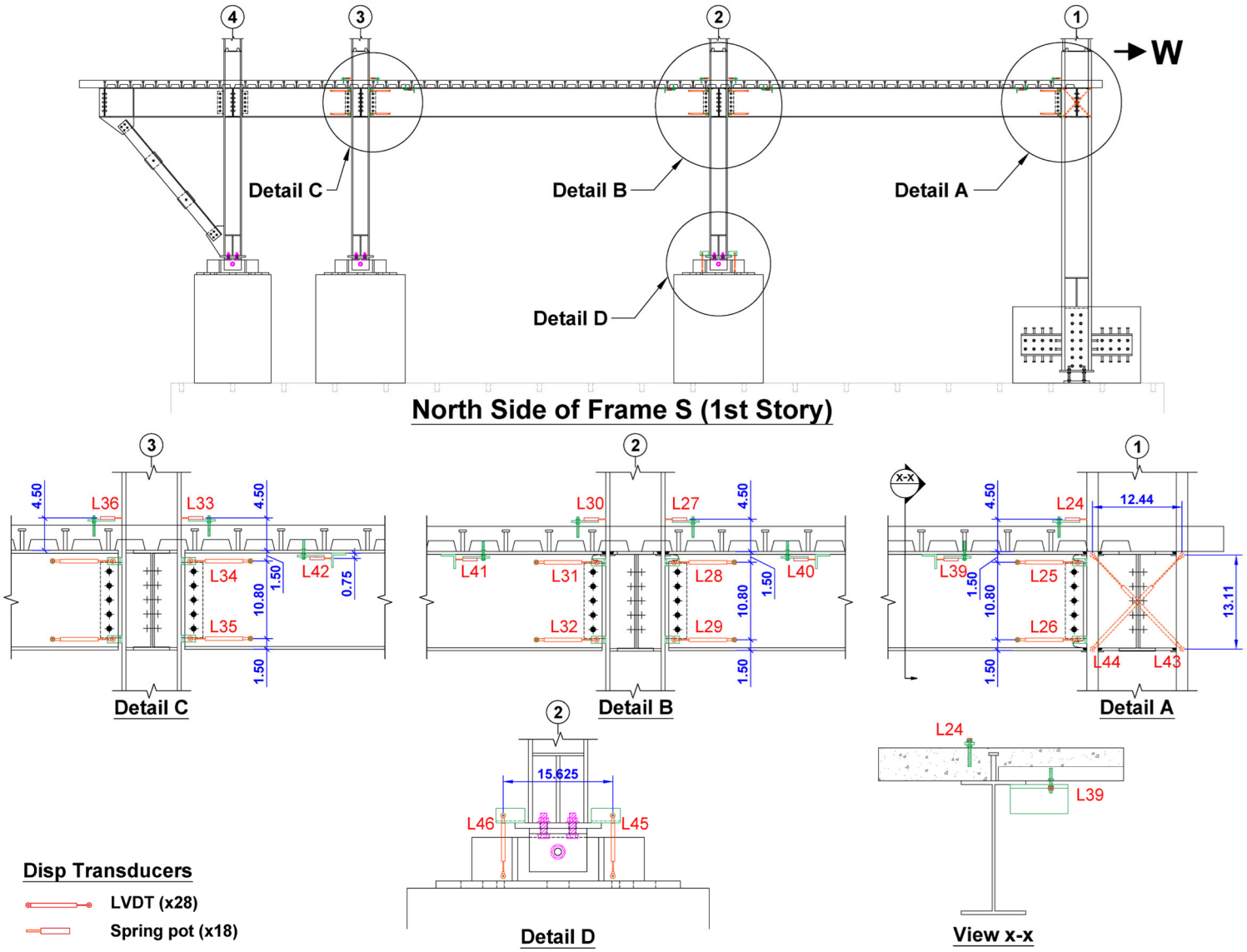

(j) Displacement Transducers on Frame S (1st Story)

Figure 6.23 Instrumentation Plan for Phase 2 Test (continued)

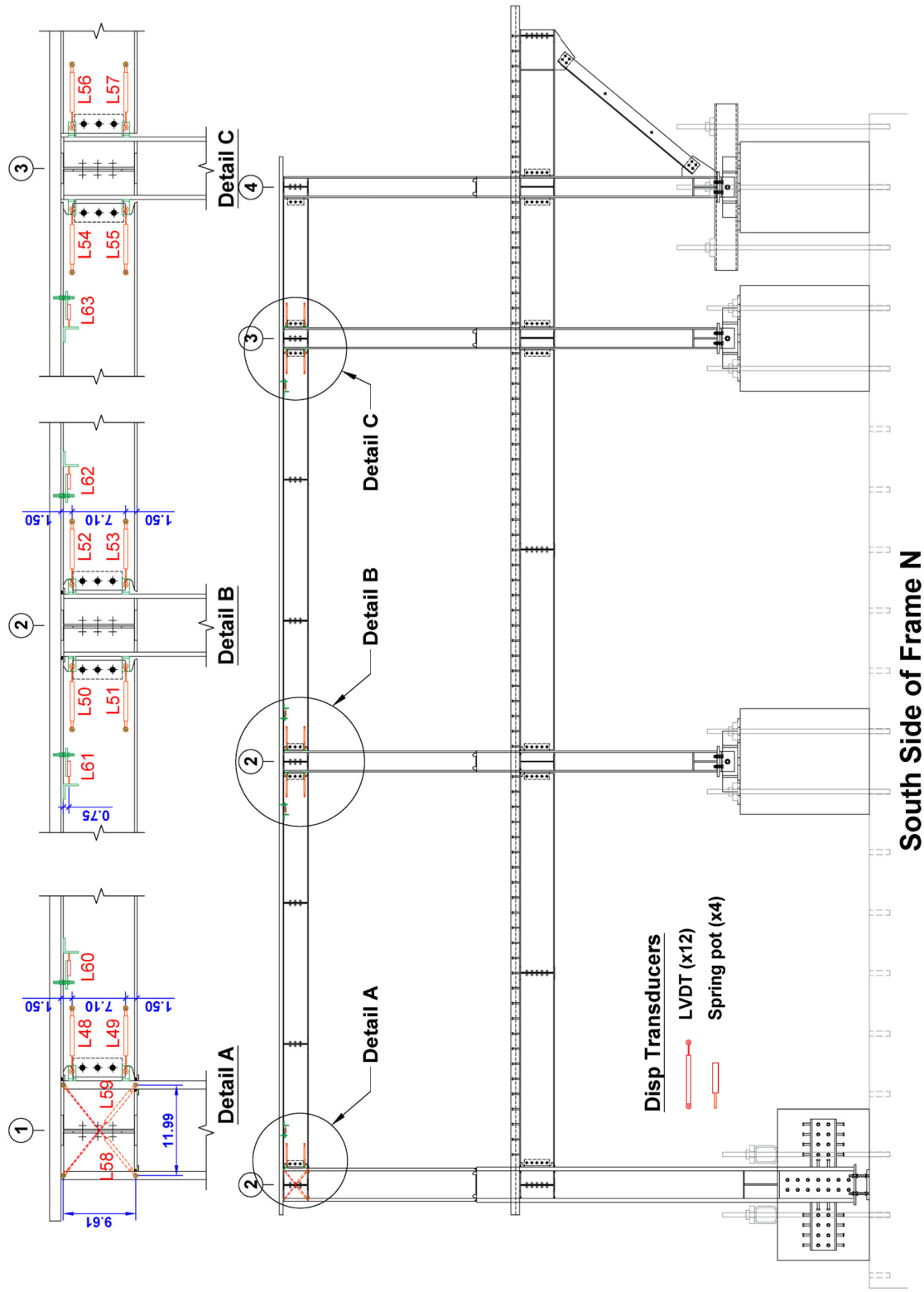

(k) Displacement Transducers in 2nd Story

Figure 6.23 Instrumentation Plan for Phase 2 Test (continued)

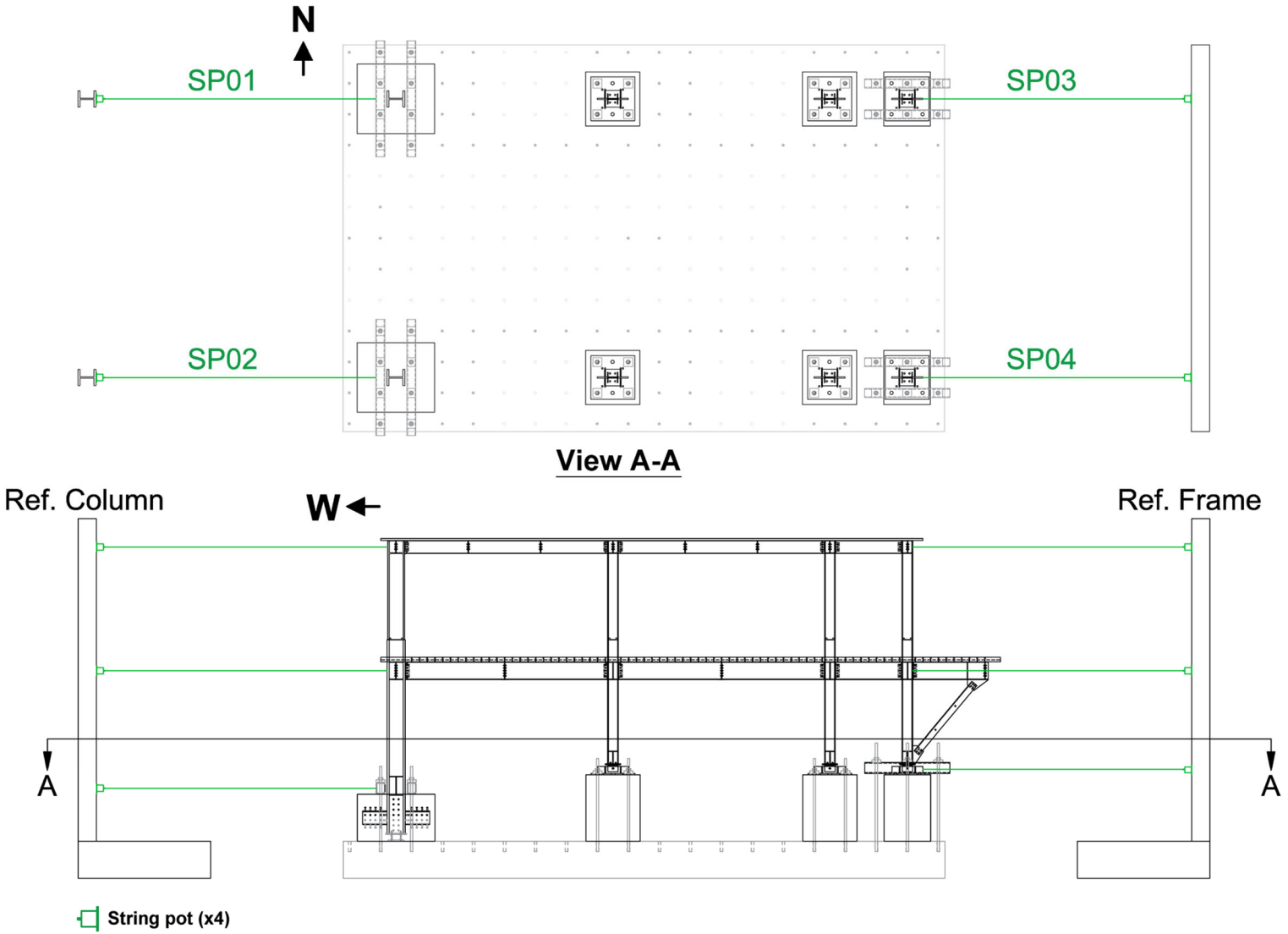

(l) Spring Pots on Footing Level

Figure 6.23 Instrumentation Plan for Phase 2 Test (continued)

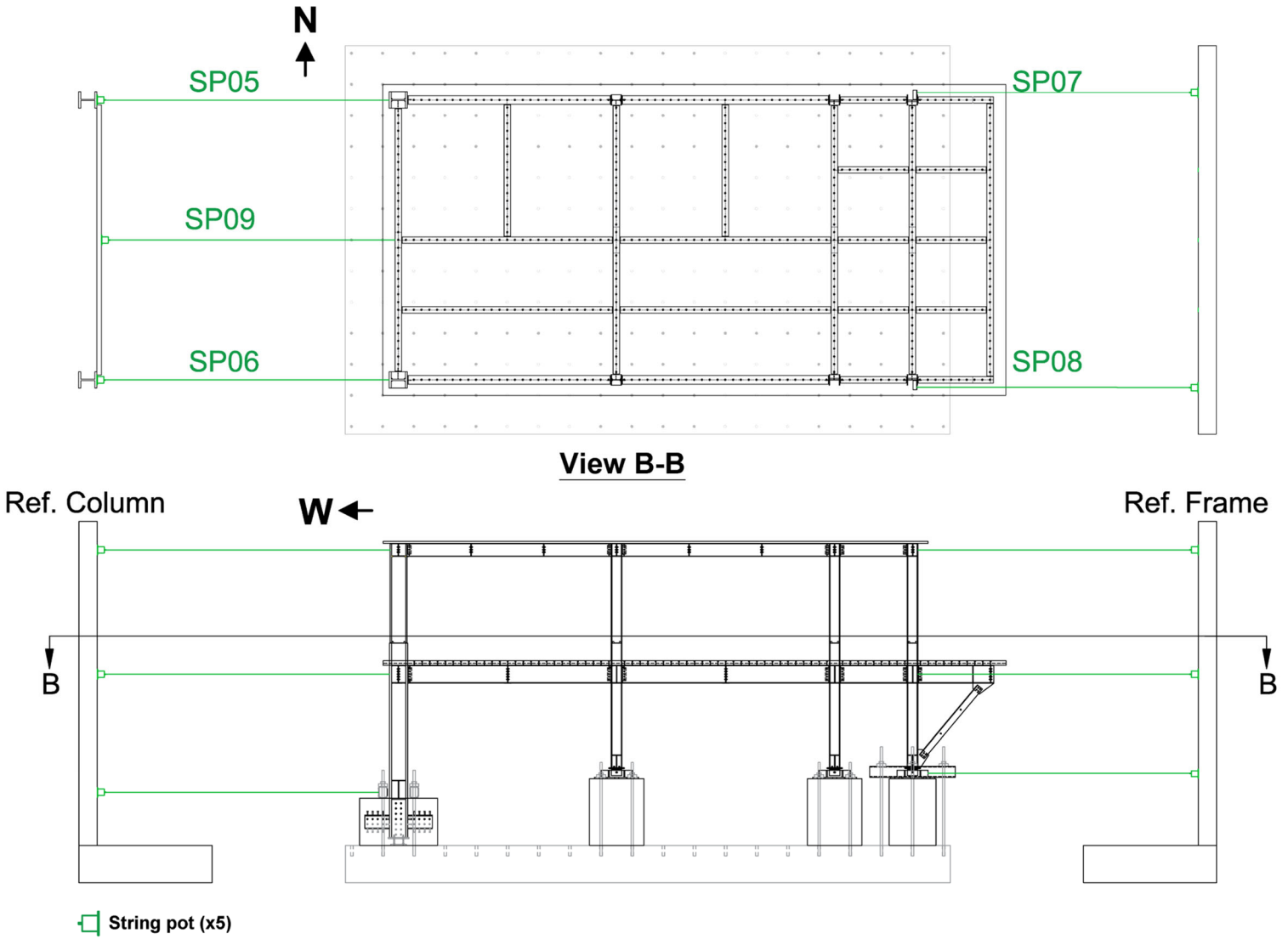

(m) Spring Pots on 2nd Floor Level

Figure 6.23 Instrumentation Plan for Phase 2 Test (continued)

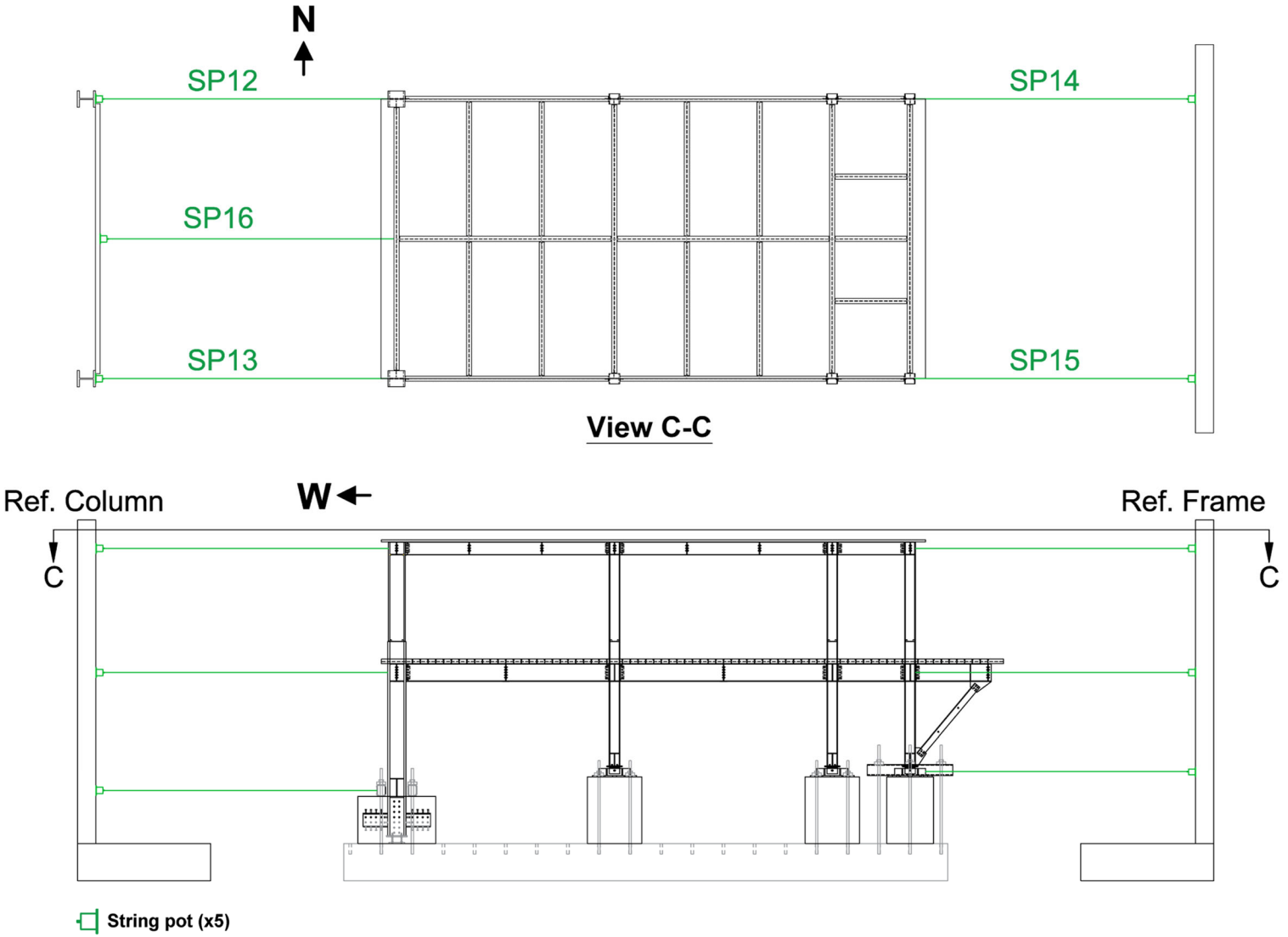

(n) Spring Pots on Roof Level

Figure 6.23 Instrumentation Plan for Phase 2 Test (continued)

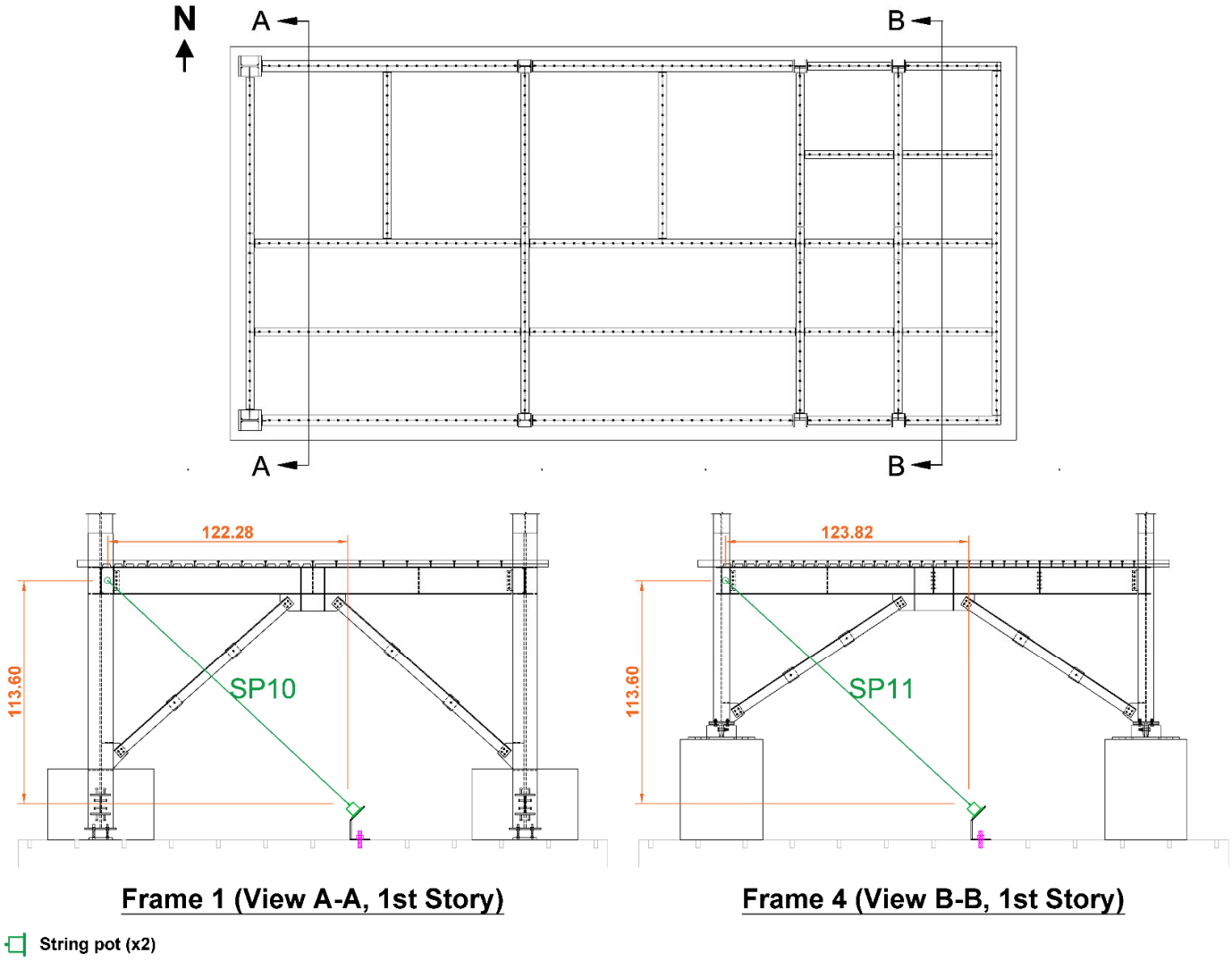

(o) Diagonal String Pots for Measuring Transverse Displacement (1st Story)

Figure 6.23 Instrumentation Plan for Phase 2 Test (continued)

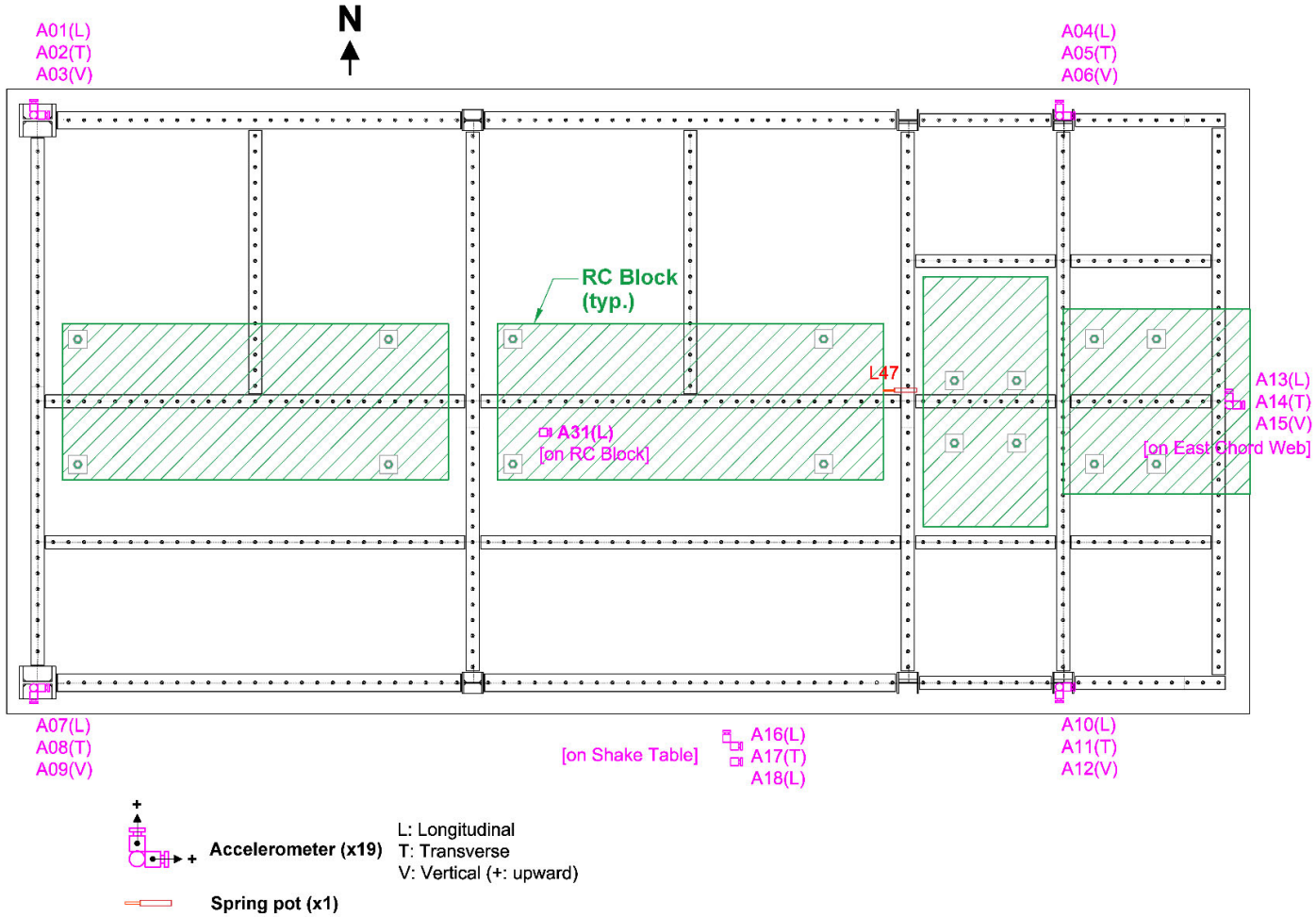

(p) Accelerometers and the Spring Pot for Monitoring Slippage of Added RC Block on 2nd Floor Level

Figure 6.23 Instrumentation Plan for Phase 2 Test (continued)

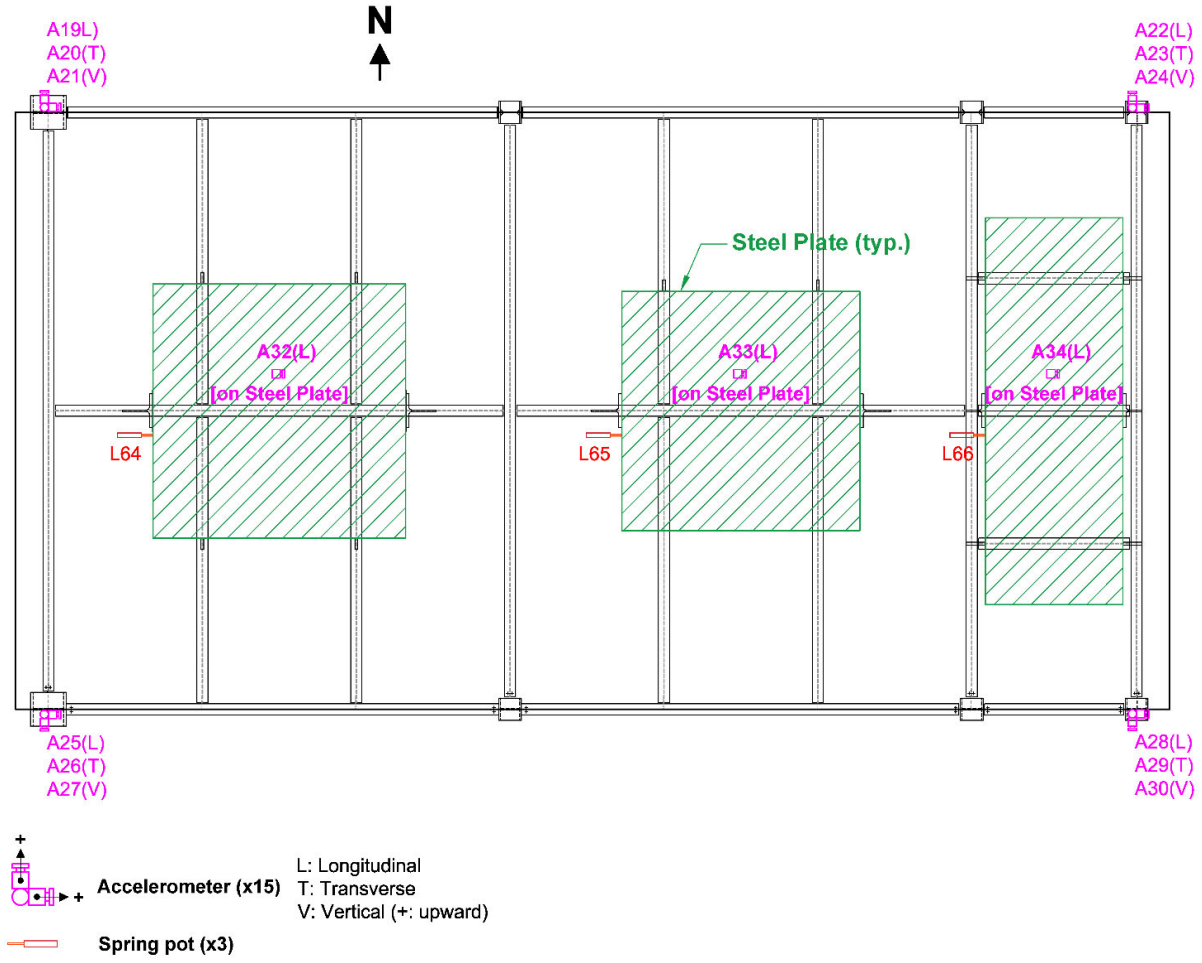

(q) Accelerometers and the Spring Pots for Monitoring Slippage of Added Steel Plates on Roof Level

Figure 6.23 Instrumentation Plan for Phase 2 Test (continued)

6.4 Material Properties

A992 steel was specified for all the beams and columns in the 2nd story of the test building, A572 Gr. 50 steel was specified for the plates, including shear tabs, continuity plates, gusset plates, and stiffeners. A36 steel was specified for the double-angle braces added in the 2nd story. The specified grades and material properties based on tensile coupon tests are summarized in Table 6.10. Tensile test results in the form of stress-strain curves are shown in Figure 6.24.

The specified concrete compressive strengths, f_c', for the 2nd floor slab, cantilever column footings, gravity column footings were 4 ksi, 8 ksi, and 5 ksi, respectively. Table 6.11 shows the results of the concrete cylinder tests that were conducted on the first day Phase 2B testing. A3125 Gr. F1852 (Group A) high-strength bolts were specified for the collector-to-column connections, transverse beam-to-column connections, beam-to-beam connections, and gusset plate connections.

Table 6.10 Steel Tensile Coupon Test Results

Component	Steel Type	Nominal Thickness (in.)	Measured Thickness (in.)	F_y (ksi)	F_u (ksi)	Elong.[a] (%)
W12×120 Column Flange	A992	1.110	1.110	59.19	72.72	43.8
W12×120 Column Web	A992	0.710	0.692	53.61	69.61	44.8
W8×40 Column Flange	A992	0.560	0.549	53.03	72.27	39.3
W8×40 Column Web	A992	0.360	0.369	57.31	72.15	36.6
W10×17 Collector Flange-1	A992	0.330	0.314	53.27	67.07	37.5
W10×17 Collector Flange-2	A992	0.330	0.301	53.28	66.01	38.4
W10×17 Collector Web-1	A992	0.240	0.248	55.06	67.09	37.3
W10×17 Collector Web-2	A992	0.240	0.245	56.19	68.14	38.1
Shear Tab (PL1/4")	A572 Gr. 50	0.250	0.252	69.07	76.30	28.6
a) Elongation values are based on test results of coupons with 2 in. gage length						

Table 6.11 Concrete Cylinder Test Results

Component	Age (Days)	f_c' of Each Cylinder (ksi)		Average f_c' (ksi)
Gravity Column Footings -Truck #1	91	#1:	5.733	5.872
		#2:	6.100	
		#3:	5.783	
Gravity Column Footings -Truck #2	91	#1:	5.874	5.880
		#2:	5.911	
		#3:	5.854	
Cantilever Column Footings	76	#1:	9.063	8.467
		#2:	7.713	
		#3:	8.624	
2nd Floor Slab	38	#1:	4.446	4.716
		#2:	5.015	
		#3:	4.687	

Test Date: 9/12/2019

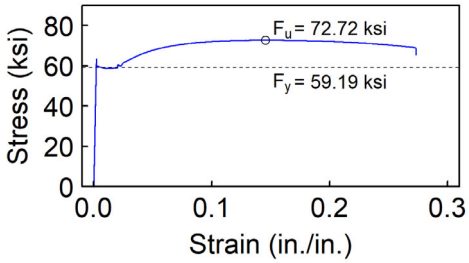

(a) W12x120 Column Flange

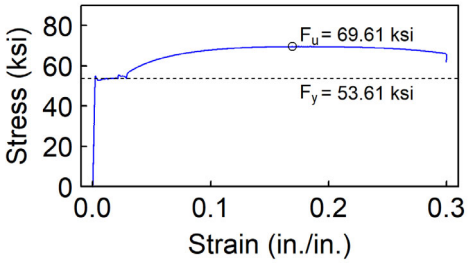

(b) W12x120 Column Web

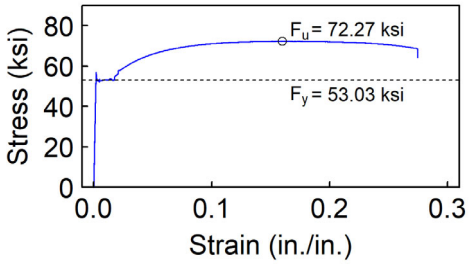

(c) W8x40 Column Flange

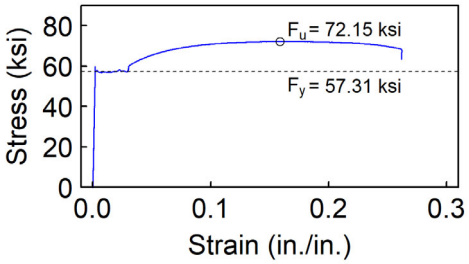

(d) W8x40 Column Web

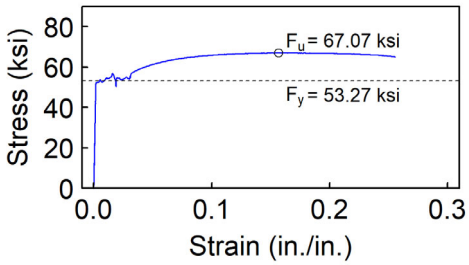

(e) W10x17 Collector Flange-1

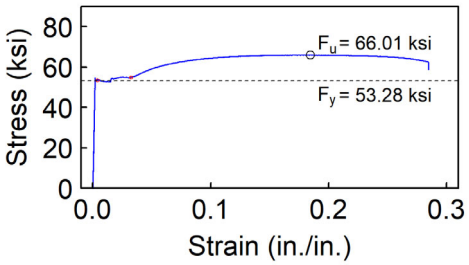

(f) W10x17 Collector Flange-2

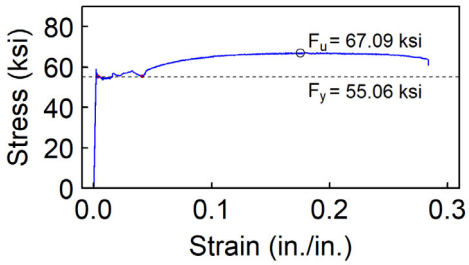

(g) W10x17 Collector Web-1

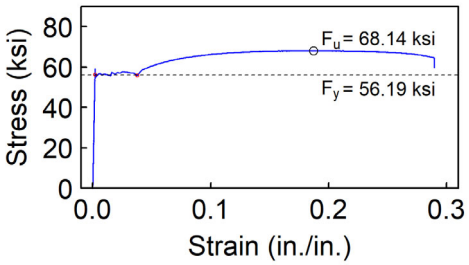

(h) W10x17 Collector Web-2

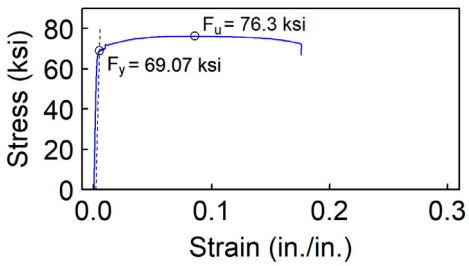

(i) Shear Tab for Roof Collector

Figure 6.24 Steel Tensile Coupon Stress-Strain Curves

6.5 Testing Protocol

Table 6.12 and Table 6.13 show the test matrices for Phases 2A and 2B testing, respectively. Each phase included five earthquake simulation tests. The input table motions were generated by scaling a ground motion record (Beverly Hills-Mulhol station) from the 1994 Northridge earthquake to different intensity levels. Since the test building was a 1/2-scale specimen, the time of the original ground motion was scaled by a factor of $\sqrt{0.5}$. Subsequently, the acceleration response of the time-scaled ground motion was scaled to the target intensities by using the $S_a(T_1)$ method (Shome and Cornell 1998) such that the 5% damped spectral acceleration of the time-scaled ground motion matched the target design response spectrum for design earthquake (DE), which was constructed with S_{DS} = 1.030 and S_{D1} = 0.569 per ASCE 7 (ASCE 2016), at the experimentally determined fundamental period of the test building. Dynamic characterization tests were performed by using a both 2-munite long white noise motion with a peak ground acceleration (PGA) at 0.1 g and a short-duration impulse motion with a PGA of 0.2 g to assess the variation of the dynamic characteristics (natural periods and damping) of the specimen.

In Phase 2A (see Table 6.12), the five earthquake simulation tests (designations as Test 2A-1 through Test 2A-5, respectively) were performed for three intensity levels: 50% DE, 100% DE, and 200% DE. Note that a test denoted with "Direct" means the input motion was directly from the above-mentioned scaled ground motion, while a test denoted with "Inverted" means the input motion was multiplied by −1.0. Reversing the sign of some input motions was intended to achieve both high tension and compression axial forces in the collectors. In Phase 2B (see Table 6.13), the five earthquake tests (designations as Test 2B-1 through Test 2B-5) were conducted at three intensity levels: 50% DE, 100% DE, and 125% DE. Some tests were repeated (e.g., both Tests 2A-2 and 2A-4 were 100% DE).

Table 6.12 Phase 2A Test Matrix

Test No.	Description	Test Date
WN 2A-0	White Noise Test	9/9/2019
IM 2A-0	Impulse Test	9/9/2019
2A-1	Earthquake Simulation Test (50% DE, Direct)	9/9/2019
IM 2A-1	Impulse Test	9/9/2019
2A-2	Earthquake Simulation Test (100% DE, Direct)	9/9/2019
IM 2A-2	Impulse Test	9/9/2019
2A-3	Earthquake Simulation Test (200% DE, Inverted)	9/9/2019
WN 2A-3	White Noise Test	9/9/2019
IM 2A-3	Impulse Test	9/9/2019
2A-4	Earthquake Simulation Test (100% DE, Direct)	9/10/2019
IM 2A-4	Impulse Test	9/10/2019
2A-5	Earthquake Simulation Test (200% DE, Inverted)	9/10/2019
IM 2A-5	Impulse Test	9/10/2019
WN 2A-5	White Noise Test	9/10/2019

Table 6.13 Phase 2B Test Matrix

Test No.	Description	Test Date
WN 2B-0	White Noise Test	9/12/2019
IM 2B-0	Impulse Test	9/12/2019
2B-1	Earthquake Simulation Test (50% DE, Direct)	9/12/2019
WN 2B-1	White Noise Test	9/12/2019
IM 2B-1	Impulse Test	9/12/2019
2B-2	Earthquake Simulation Test (100% DE, Direct)	9/12/2019
WN 2B-2	White Noise Test	9/12/2019
IM 2B-2	Impulse Test	9/12/2019
2B-3	Earthquake Simulation Test (100% DE, Inverted)	9/12/2019
WN 2B-3	White Noise Test	9/12/2019
IM 2B-3	Impulse Test	9/12/2019
2B-4	Earthquake Simulation Test (100% DE, Direct)	9/13/2019
WN 2B-4	White Noise Test	9/13/2019
IM 2B-4	Impulse Test	9/13/2019
2B-5	Earthquake Simulation Test (125% DE, Inverted)	9/13/2019
WN 2B-5	White Noise Test	9/13/2019
IM 2B-5	Impulse Test	9/13/2019

6.6 Data Reduction

6.6.1 General

Most of the data reduction approaches used for Phase 1 testing (see Section 3.7) were used in Phase 2 testing. This section describes the changes made and new procedures.

6.6.2 Floor and Roof Acceleration Determination

As shown in Figure 6.25, seven accelerometers were installed at the roof level. Test results showed that there were some slight differences among the measured accelerations from these sensors. Therefore, the weighted average of these measured accelerations is used to represent the roof acceleration, a_{rf}, as follows:

$$a_{rf} = \left(\frac{\sum_{i=1}^{7} W_{Ti} a_i}{\sum_{i=1}^{7} W_{Ti}} \right)_{RF} \tag{6.4}$$

where a_i is the acceleration measured from the *i*-th accelerometer on the roof level, and W_{Ti} is the weight tributary to *i*-th accelerometer. See Figure 6.25 for the region tributary to each acceleration and the associated value for W_{Ti}.

Similar to the roof level, six accelerometers were installed on the 2nd floor, as shown in Figure 6.26. The averaged 2nd floor acceleration can be estimated as:

$$a_{flr} = \left(\frac{\sum_{i=1}^{6} W_{Ti} a_i}{\sum_{i=1}^{6} W_{Ti}} \right)_{F2} \tag{6.5}$$

where a_i is the acceleration measured from the *i*-th accelerometer on the 2nd floor. W_{Ti} is the weight tributary to *i*-th accelerometer. See Figure 6.26 the region tributary to each accelerometer on the 2nd floor and the associated value for W_{Ti}. However, for simplicity, the readout of the accelerometer installed on the added mass block was taken as the 2nd floor acceleration response presented in Section 7.

6.6.3 Story Shear Calculation

Two methods were used to derive the story shear from the instrumentation. The first estimation of story shear was made by using the accelerometer data. For the two-story Phase 2 test building, the 2nd story shear, $V_{a2}(t)$, was estimated as the total inertial force generated by the mass tributary to the roof level with a reversed sign, leading to:

$$V_{a2}(t) = -\left[\frac{W_{RF}}{g}\right] a_{rf}(t) \tag{6.6}$$

where W_{RF} is the total weight tributary to the roof, and $a_{rf}(t)$ is the roof acceleration from Eq. (6.4). In addition, the 1st story shear, $V_{a1}(t)$, was estimated as the summation of the inertial forces at the roof level and the 2nd floor with a reversed sign as follows:

$$V_{a1}(t) = -\left[\frac{W_{RF}}{g}\right] a_{rf}(t) - \left[\frac{W_{2F}}{g}\right] a_{flr}(t) \tag{6.7}$$

where W_{2F} is the total weight tributary to the 2nd floor, while $a_{flr}(t)$ is the 2nd floor acceleration.

The second method for calculating the base shear was to sum up the experimentally determined story shear resisted by columns and diagonal braces in the longitudinal frames. Figure 3.61 shows that the member force recovery for the 1st-story columns and diagonal braces were based on the measurements of the strain gauges on these members. Also see Section 3.7.4 for the details of these member force recovery. The same approach was also applied to the 2nd story columns. The time history of the 1st story shear (i.e., base shear) taken by Frame N, $V_{b1N}(t)$, was computed as:

$$V_{b1N}(t) = \sum_{i=1}^{4} V_{c1Ni}(t) + P_{brN}(t)\sin\theta \tag{6.8}$$

where V_{c1N1} through V_{c1N4} represent the measured column shear forces for the 1st-story Columns N1 to N4, respectively, P_{brN} is the measured axial force of the 1st-story north diagonal brace, and

θ is the inclination angle between the brace and the vertical. Likewise, the time history of the 1st story shear taken by Frame S, $V_{bS}(t)$, was computed as:

$$V_{b1S}(t) = \sum_{i=1}^{4} V_{c1Si}(t) + P_{brS}(t)\sin\theta \tag{6.9}$$

where V_{c1S1} to V_{c1S4} represent the measured column shear forces for 1st-story Columns S1 to S4, respectively, and P_{brS} is the measured axial force of the south brace. Then, the total base shear of the test building, $V_b(t)$, was determined by summing up the story shears resisted by Frames N and S:

$$V_{b1}(t) = V_{b1N}(t) + V_{b1S}(t) \tag{6.10}$$

Similarly, the time history of the 2nd story shear taken by Frame N, $V_{b2N}(t)$, was computed as:

$$V_{b2N}(t) = \sum_{i=1}^{4} V_{c2Ni}(t) \tag{6.11}$$

where V_{c2N1} through V_{c2N4} represent the measured column shear forces for 2nd-story Columns N1 to N4, respectively. Likewise, the time history of the 2nd-story shear taken by Frame S, $V_{b2S}(t)$, was computed as:

$$V_{b2S}(t) = \sum_{i=1}^{4} V_{c2Si}(t) \tag{6.12}$$

where V_{c2S1} to V_{c2S4} represent the measured column shear forces for 2nd-story Columns S1 to S4, respectively. Then, the total 2nd-story shear of the test building, $V_{b2}(t)$, was determined by summing up the 2nd-story shears taken by Frames N and S:

$$V_{b2}(t) = V_{b2N}(t) + V_{b2S}(t) \tag{6.13}$$

Both methods were applied to Phase 2 specimen for every test in this phase. It was found that both methods resulted in close story shears. Because the story shears determined from strain

gauges (V_{b1} and V_{b2}) were found to result in a smoother curve (less "noisy") and its theoretical advantage over the story shear determined from the accelerometers (V_{a1} and V_{b2}), Eqs. (6.8) through (6.13) were used as the primary method for story shear determination in this research.

6.6.4 Member Force Recovery for Collectors

The fiber section approach was used in Phase 1 testing (see Section 3.7.6) was employed to compute member internal forces for the 2nd floor composite collector and roof bare steel collectors. For the fiber section approach to the composite collectors, a minor change made to Phase 2 testing was the effective slab width used for the concrete fibers. Based on the implications learned the from Phase 1 testing as described in Section 5.4.3, the distribution of the effective slab width along a beam span as proposed by Zhu et al. (2015) was used to determine the width of the concrete fibers at the sections where no surface concrete strain gages were installed to experimentally determine the effective slab width. For the four measured collector sections near the AFW and east-side TFW connections at the 2nd floor, where the concrete slabs were heavily instrumented and the experimentally determined effective slab widths are available, the averaged measured effective slab widths presented in Table 8.1 were used to define the fiber sections. On the other hand, fiber sections defined for the measured sections in the roof bare steel collectors were similar to the layout of the steel fibers for composite collector section as shown in Figure 3.62(c). Eleven layers of steel fibers were used for the roof bare steel collectors. See Table 6.14 for the detailed information about fiber sections.

It is noted that, for Phase 2 testing, the Giuffré-Menegotto-Pinto (GMP) constitutive law (Menegotto and Pinto 1973) was employed for computing the steel fiber stresses because all the collector bottom flanges near the AFW connections (for both 2nd floor and roof level) had yielded. See Figure 6.27(a) and Figure 6.28(b) for the measured strain histories of the bottom flanges near

the AFW connections at the 2nd floor and roof level, respectively, for Test 2B-5. The peak strain responses exceeded the yield strain, ε_y. In addition, Figure 6.27(a) and Figure 6.28(b) compare the stress-strain hysteresis response predicted by the GMP model based on the measured strain time histories with the monotonic stress-strain curves measured from tensile coupon. These predicted hysteresis responses matched well the experimental monotonic stress-strain curves, justifying the use of the GMP model and the associated model parameters.

Figure 6.29(a) shows the responses of two concrete strain gages that the highest response magnitude in Test 2B-5. The data from gauge SC20 provided a peak measured tensile strain denoted as, ε_{max}, while gauge SC20 provided a peak measured compressive strain denoted as, ε_{min}. Figure 6.29(b) shows the monotonic nonlinear constitutive model adopted for the concrete fibers. The compressive branch is predicted by the models proposed by Popovics (1973) and Mander et al. (1988) as shown in Eq. (3.55) through (3.58), while the tensile branch is determined from the model proposed by Belarbi and Hsu (1994), as shown in Eqs. (3.59) through (3.62). The peak measured tensile and compressive strains in Test 2B-5 are also marked in Figure 6.29. It can be found that, for the compressive side, the concrete had not reached crushing in Test 2B-5. Therefore, a linear stress-strain relationship can be assumed for the concrete fibers when the when the fiber strain is compressive. On the hand, for the tensile side, the measured peak tensile strain, ε_{max}, exceeded the cracking strain, resulting in a nonlinear response. However, as the tensile stress developed in the concrete was much smaller than the compressive stress, the contribution from the concrete fibers in tension is low. This justifies the use of the monotonic stress-strain relationship determined by Eqs. (3.55) through (3.62) for concrete fibers in the member force recovery of composite collectors.

Part of this chapter is based on the material published in the 17th World Conference on Earthquake Engineering, titled "Earthquake simulator testing on behavior of seismic collectors in steel buildings" with co-authors Uang C.-M., and Fleischman R.B. (2020). Materials were also submitted for publication in the 12th National Conference on Earthquake Engineering, titled "Shake Table Tests on Seismic Response of Collectors in Steel Buildings" with co-authors Uang C.-M., and Fleischman R.B. (2022). The author of this dissertation serves as the first author of these papers.

Table 6.14 Information of Fiber Sections used for 2nd Floor Collectors

(a) Collectors 1 and 2 except for BW Connection (W10×17)

Fiber No.	y_{fib} (in.)	t_{fib} (in.)	w_{fib} (in.)	A_{fib} (in.^{2})	Material
1	-4.8850	0.3300	4.01000	1.3233	Steel
2	-4.5700	0.3000	0.36967	0.1109	Steel
3	-4.0213	0.7975	0.24000	0.1914	Steel
4	-3.2238	0.7975	0.24000	0.1914	Steel
5	-1.8250	2.0000	0.24000	0.4800	Steel
6	0.1750	2.0000	0.24000	0.4800	Steel
7	2.1750	2.0000	0.24000	0.4800	Steel
8	3.4863	0.6225	0.24000	0.1494	Steel
9	4.1088	0.6225	0.24000	0.1494	Steel
10	4.5700	0.3000	0.36967	0.1109	Steel
11	4.8850	0.3300	4.01000	1.3233	Steel

(b) Collector 3 and BW Connection in Collector 2 (W10×17)

Fiber No.	y_{fib} (in.)	t_{fib} (in.)	w_{fib} (in.)	A_{fib} (in.^{2})	Material
1	-4.8850	0.3300	4.01000	1.3233	Steel
2	-4.5700	0.3000	0.36967	0.1109	Steel
3	-4.0650	0.7100	0.24000	0.1704	Steel
4	-3.3550	0.7100	0.24000	0.1704	Steel
5	-2.0000	2.0000	0.24000	0.4800	Steel
6	0.0000	2.0000	0.24000	0.4800	Steel
7	2.0000	2.0000	0.24000	0.4800	Steel
8	3.3550	0.7100	0.24000	0.1704	Steel
9	4.0650	0.7100	0.24000	0.1704	Steel
10	4.5700	0.3000	0.36967	0.1109	Steel
11	4.8850	0.3300	4.01000	1.3233	Steel

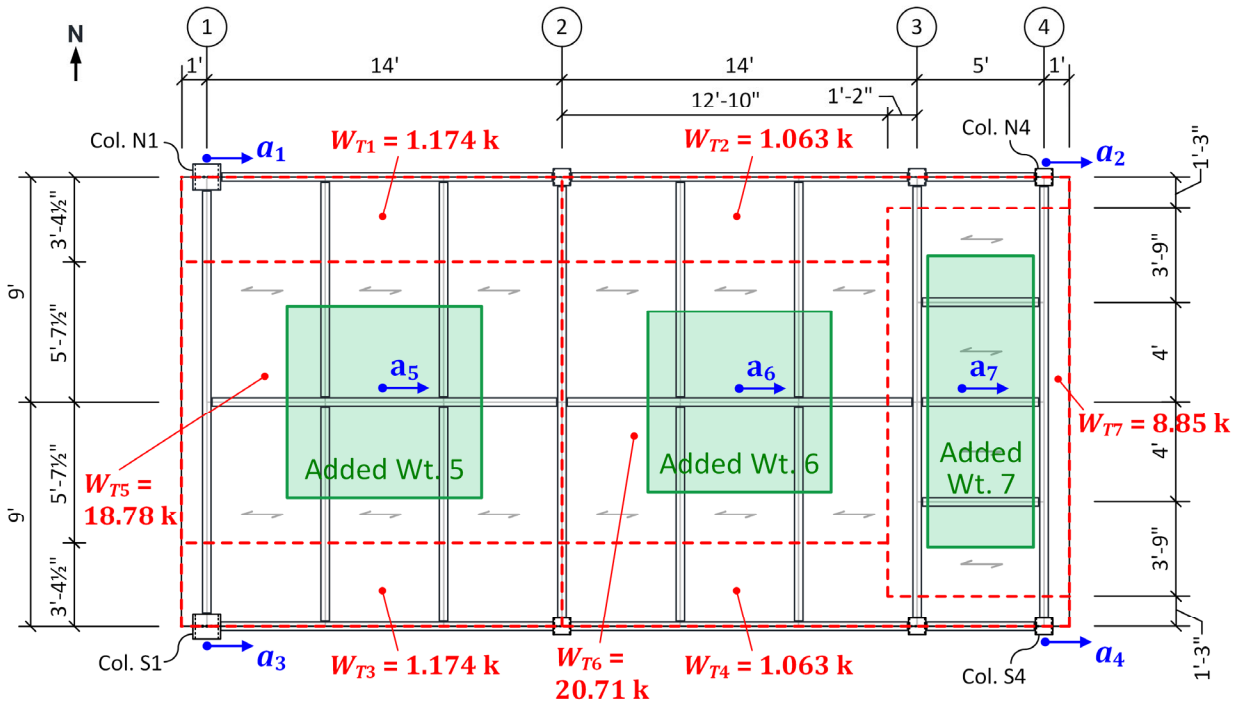

Figure 6.25 Seven Measured Roof Accelerations and Associated Tributary Area and Weights

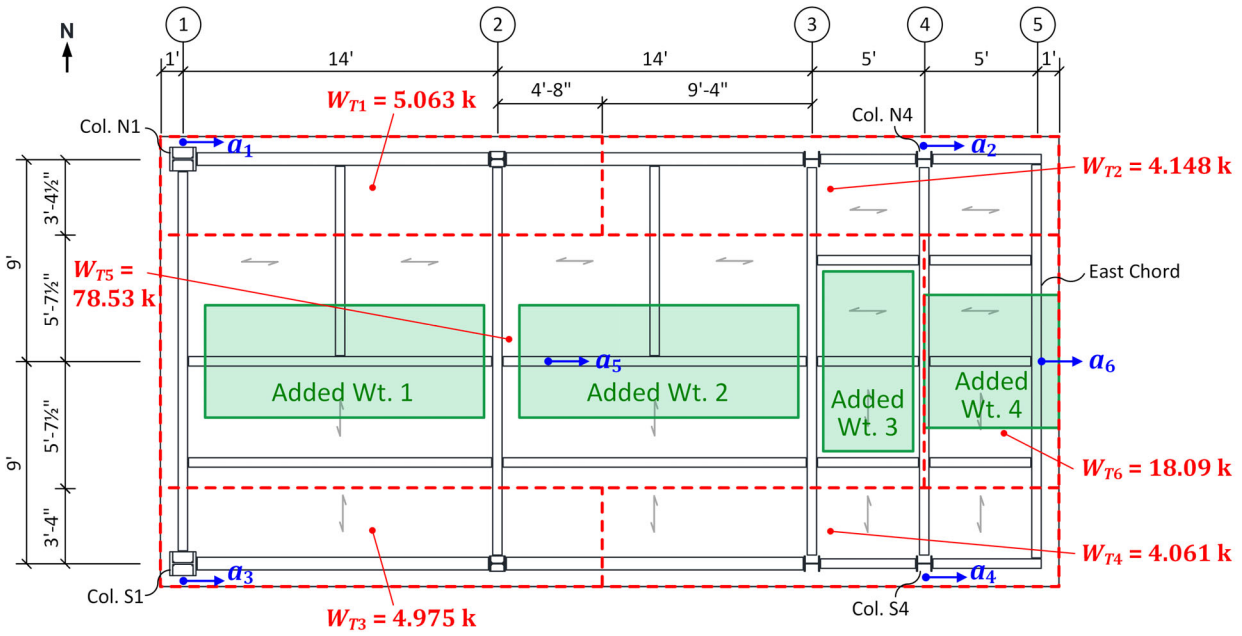

Figure 6.26 Six Measured 2nd Floor Accelerations and Associated Tributary Area and Weights

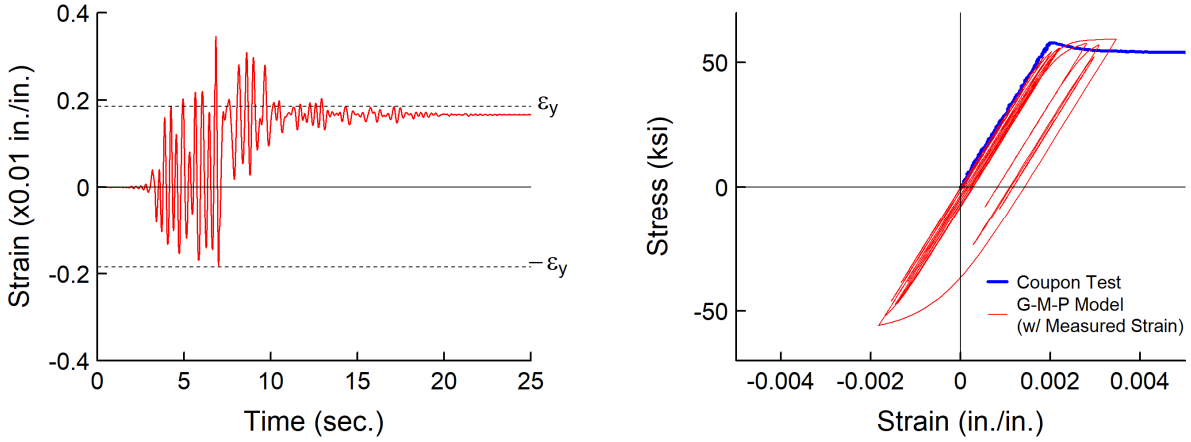

(a) (b)

Figure 6.27 (a) Measured Strain Response Near 2nd Floor AFW Connection and (b) Hysteretic Responses Predicted by Giuffré-Menegotto-Pinto (GMP) Model

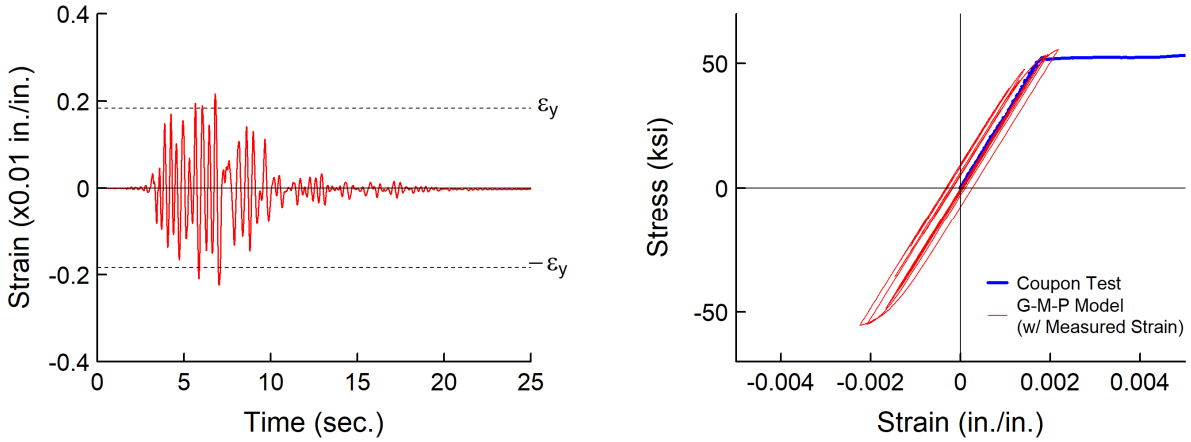

(a) (b)

Figure 6.28 (a) Measured Strain Response Near Roof AFW Connection and (b) Hysteretic Responses Predicted by Giuffré-Menegotto-Pinto (GMP) Model

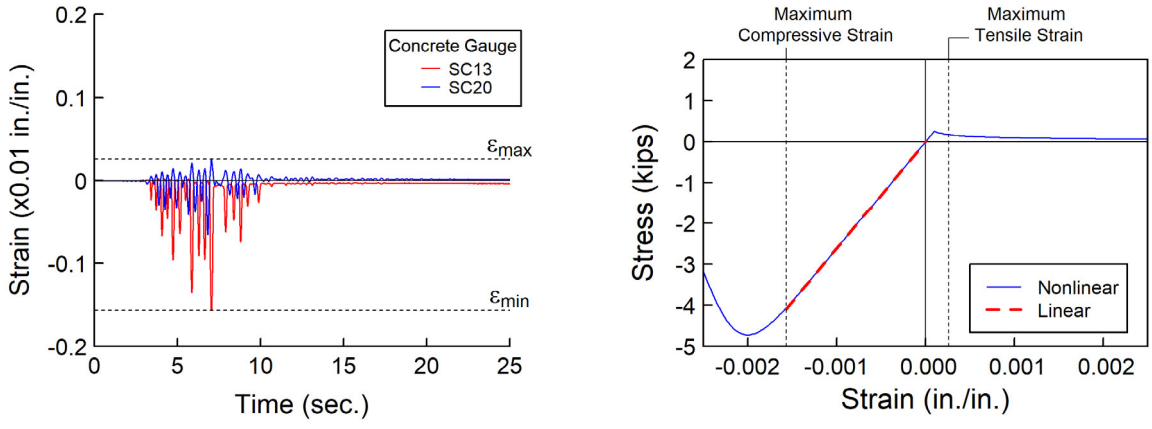

(a) (b)

Figure 6.29 (a) Measured Strain Responses on Concrete Slab and (b) Constitutive Models Used for Predicting Associated Stress Response

7. PHASE 2 TEST RESULTS

7.1 General

An overview of test results for Phase 2A and Phase 2B testing is provided in Sections 7.2 and 7.3, respectively. A detailed presentation of the test results of one significant test (Test 2B-5) is provided in Section 7.4.

7.2 Overview of Phase 2A Test Results

In Phase 2A, five earthquake simulation tests designated as Tests 2A-1 through 2A-5, were conducted at the intensity levels of 50% DE, 100% DE, 200% DE, 100% DE, and 200% DE, respectively. Dynamic characterization tests, including white noise or impulse testing, were performed before and after each floor acceleration test to monitor the dynamic properties of the specimen. Figure 7.1 shows the input table motions for white noise and impulse testing. Figure 7.2 illustrates the variations of the measured first-mode frequency and equivalent viscous damping ratio of the specimen in Phase 2A testing. Table 7.1 summarizes the dynamic characterization testing results. As shown in Figure 7.3, Fourier spectra of the white noise test results on the 2nd floor acceleration are plotted to determine the vibration frequencies. In addition, the 2nd floor acceleration time histories in impulse testing were plotted as shown in Figure 7.4. The averaged time interval between several successive negative peaks (valleys) of the free vibration response after the impulse loading was used to estimate the first-mode period of the specimen. The damping ratio, ξ, was estimated based on the decay response of the free vibration motion by using Eq. (4.1).

As shown in Figure 7.2(a) and Table 7.1, the fundamental frequency remained approximately constant with a very tiny decay during Phase 2A testing. White noise test results showed that the first-mode frequency of the specimen remained about 5.30 Hz, while the impulse

test results showed that the 1st mode frequency slightly decreased from 5.37 Hz to 5.26 Hz. The measured frequency of the second mode of the specimen, which is related with the vertical vibration of the cantilever slab, was 11.3 Hz before Phase 2A and slightly decreased to 10.9 Hz after Phase 2A testing was completed. In addition, the measured damping ratio varied from 3.07% to 3.47% with an average value of 3.21% in Phase 2A testing. Figure 7.2(b) shows that the variation of damping ratio is not significant. In general, the test specimen maintained approximately constant dynamic properties.

Figure 7.5 through Figure 7.11 show the specimen global responses for the five main tests in Phase 2A. Figure 7.5 shows the table input accelerations and the associated response spectra. Table 7.2 tabulates the measured peak responses in floor accelerations and story drifts. Figure 7.7 shows the time histories of the roof and 2nd floor accelerations. In Phase 2A testing, the positive and negative peak roof accelerations reached +2.51 g, and −3.28 g, respectively. The positive and negative peak 2nd floor accelerations were +1.24 g and −1.99 g, respectively. Figure 7.8 shows the story drift angle time histories. The reached positive and negative peak 2nd-story drift angles were +0.77 %, and −0.39 % rad, respectively. The positive and negative peak 1st-story drift angles were +1.19%, and −0.54% rad, respectively. Figure 7.9 shows the story shear time histories. Figure 7.10 shows a good agreement between the measured story shears determined from two methods: one was estimated from measured floor acceleration, while the other one was computed by using the measured strains on the columns and diagonal braces in the longitudinal direction. It confirms the reliability of the story shear and column member forces determined from strain gauge readouts. Figure 7.11 shows the story hysteresis responses for five main tests. The first story exhibited very limited inelastic behavior in Tests 2A-3 and 2A-5. After Test 2A testing was completed, minor yielding was observed on the bottom flanges at the 2nd floor AFW connections (see Figure 7.12).

Table 7.1 Phase 2A Impulse and White Noise Test Results

Test	Impulse Test				White Noise Test								
	Test No.	Fundamental Properties			Test No.	1st Mode		2nd Mode		3rd Mode		4th Mode	
		f_1 (Hz)	T_1 (sec)	ξ (%)		f_1 (Hz)	T_1 (sec)	f_2 (Hz)	T_2 (sec)	f_3 (Hz)	T_3 (sec)	f_4 (Hz)	T_4 (sec)
Before Test 2A-1	IM 2A-0	5.37	0.186	3.15	WN 2A-0	5.30	0.189	11.30	0.088	16.00	0.0625	19.50	0.0513
After Test 2A-1	IM 2A-1	5.35	0.187	3.18	–	–	–	–	–	–	–	–	–
After Test 2A-2	IM 2A-2	5.31	0.188	3.47	–	–	–	–	–	–	–	–	–
After Test 2A-3	IM 2A-3	5.28	0.189	3.07	WN 2A-3	5.30	0.189	11.10	0.090	16.00	0.0625	19.20	0.0521
After Test 2A-4	IM 2A-4	5.22	0.191	3.17	–	–	–	–	–	–	–	–	–
After Test 2A-5	IM 2A-5	5.26	0.190	3.24	WN 2A-5	5.30	0.189	10.90	0.092	16.00	0.0625	19.10	0.0524

Table 7.2 Peak Response Quantities of Phase 2A Tests

Test No.	Floor Acceleration (g)				Story Drift Angle (% rad)			
	2nd Floor		Roof		1st Story		2nd Story	
	Positive	Negative	Positive	Negative	Positive	Negative	Positive	Negative
Test 2A-1	0.56	-0.33	0.85	-0.52	0.13	-0.21	0.10	-0.18
Test 2A-2	1.16	-0.62	1.78	-1.11	0.29	-0.48	0.19	-0.38
Test 2A-3	1.24	-1.97	2.42	-3.28	1.12	-0.54	0.74	-0.39
Test 2A-4	1.07	-0.57	1.84	-1.10	0.38	-0.38	0.29	-0.30
Test 2A-5	1.24	-1.99	2.51	-2.97	1.19	-0.45	0.77	-0.33

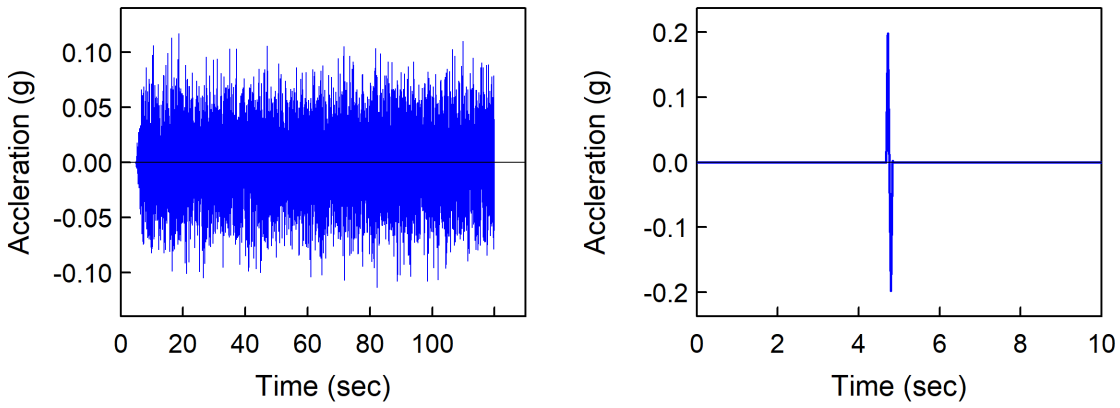

(a) White Noise Test (b) Impulse Test

Figure 7.1 Impute Table Motion for (a) White Noise and (b) Impulse Tests in Phase 2

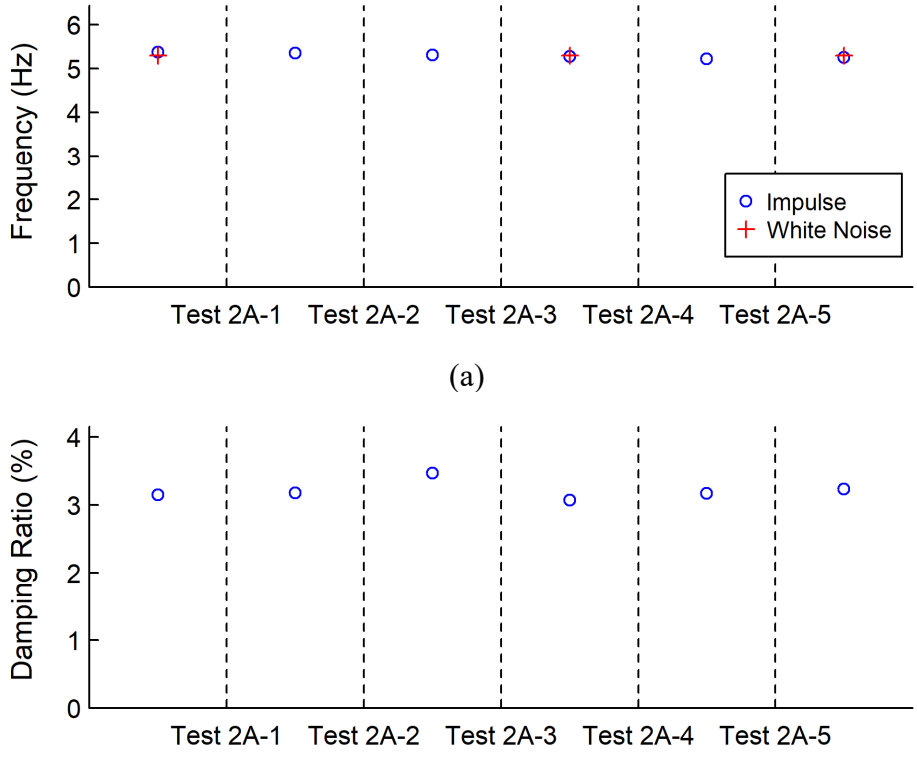

(a)

(b)

Figure 7.2 Variations of Measured (a) 1st Mode Frequency and (b) Damping Ratio in Phase 2A Testing

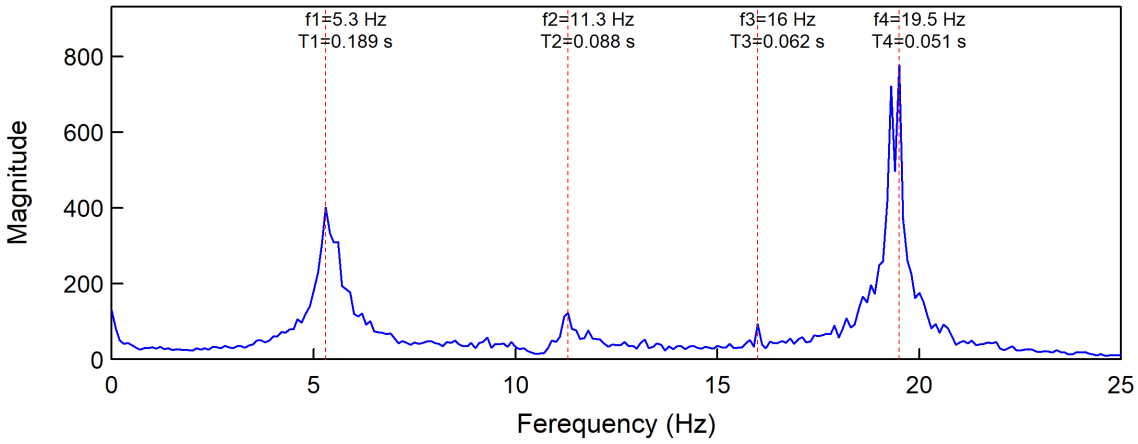

(a) Test WN 2A-0

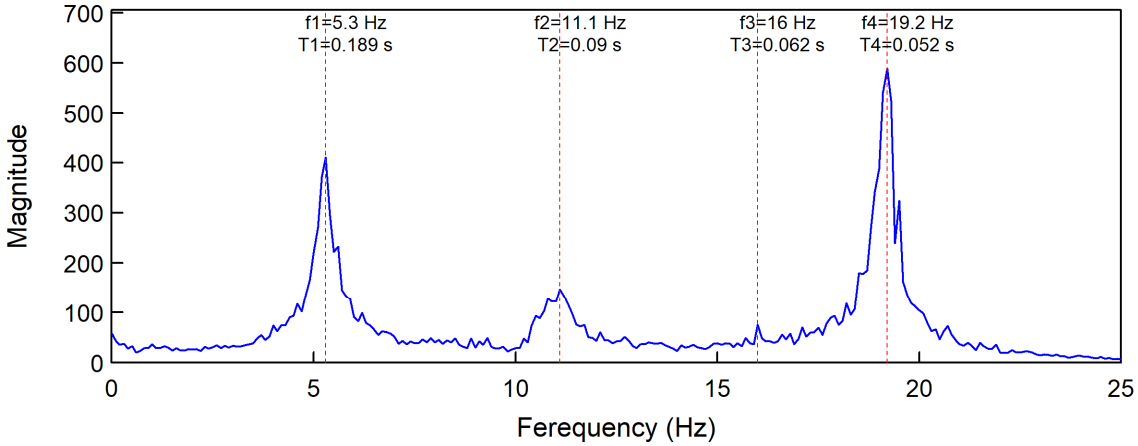

(b) Test WN 2A-2

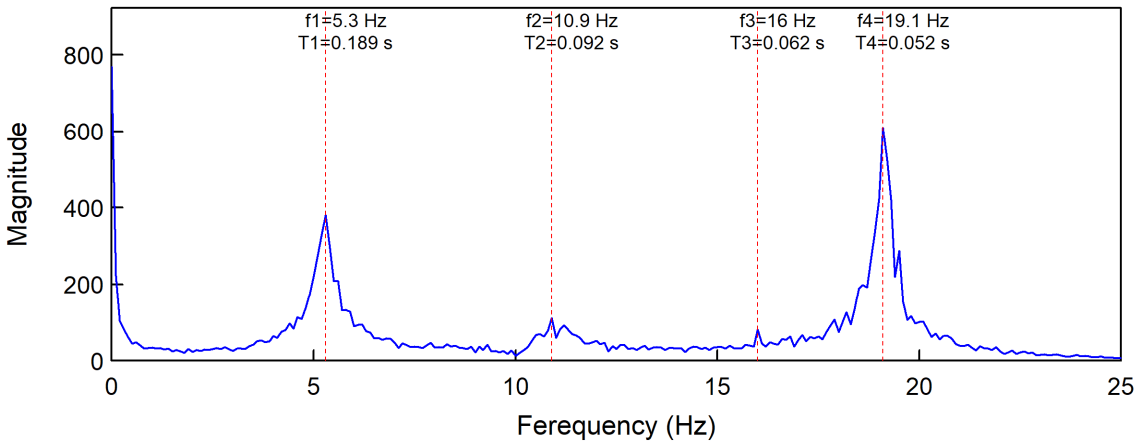

(c) Test WN 2A-5

Figure 7.3 Phase 2A White Noise Test Results

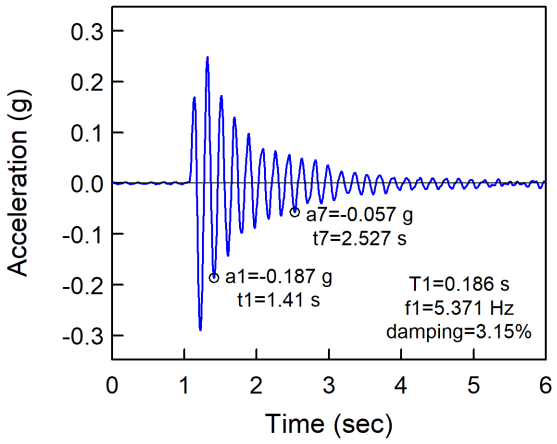

(a) Test IM 2A-0

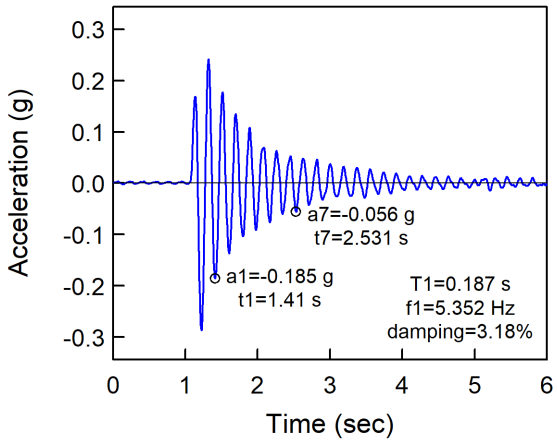

(b) Test IM 2A-1

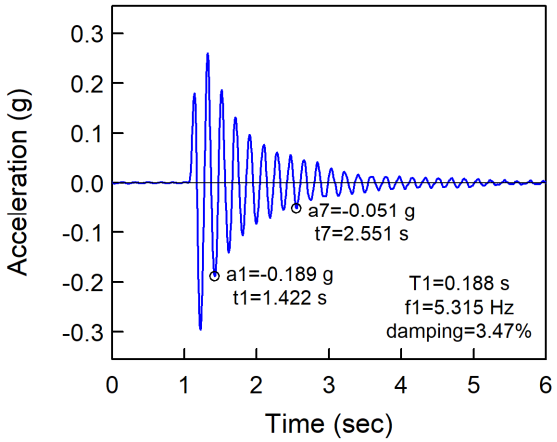

(c) Test IM 2A-2

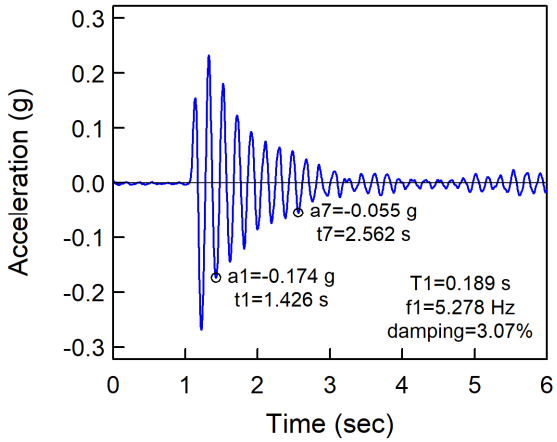

(d) Test IM 2A-3

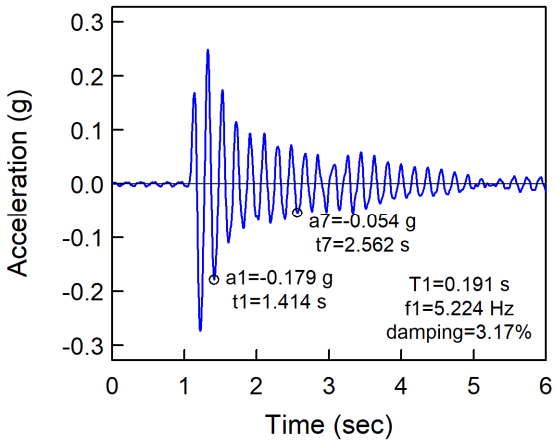

(e) Test IM 2A-4

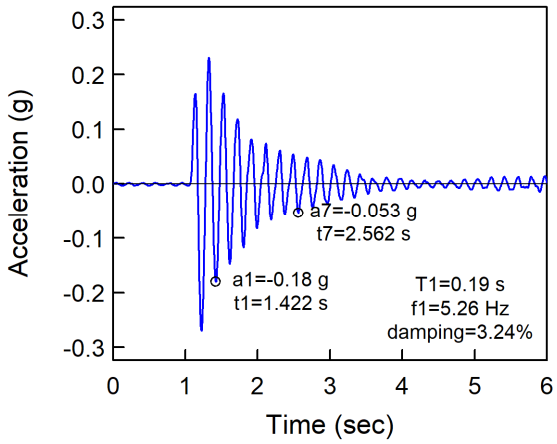

(f) Test IM 2A-5

Figure 7.4 Phase 2A Impulse Test Results

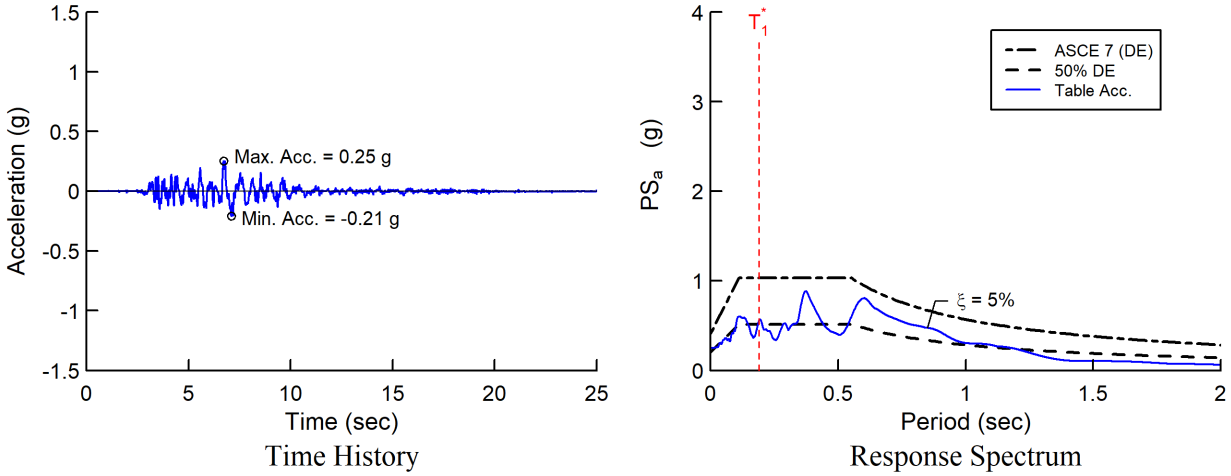

(a) Test 2A-1 (Target Intensity: 50% DE)

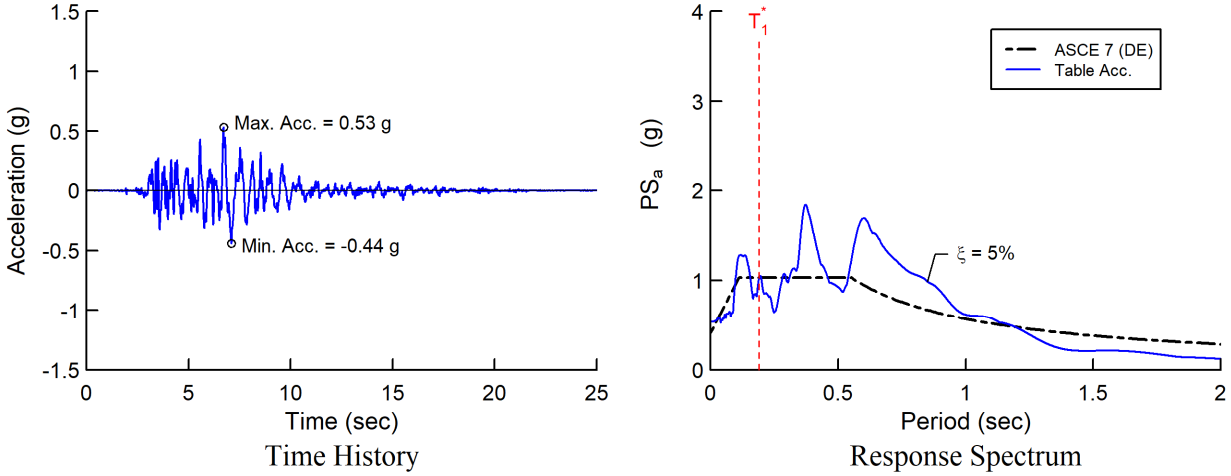

(b) Test 2A-2 (Target Intensity: 100% DE)

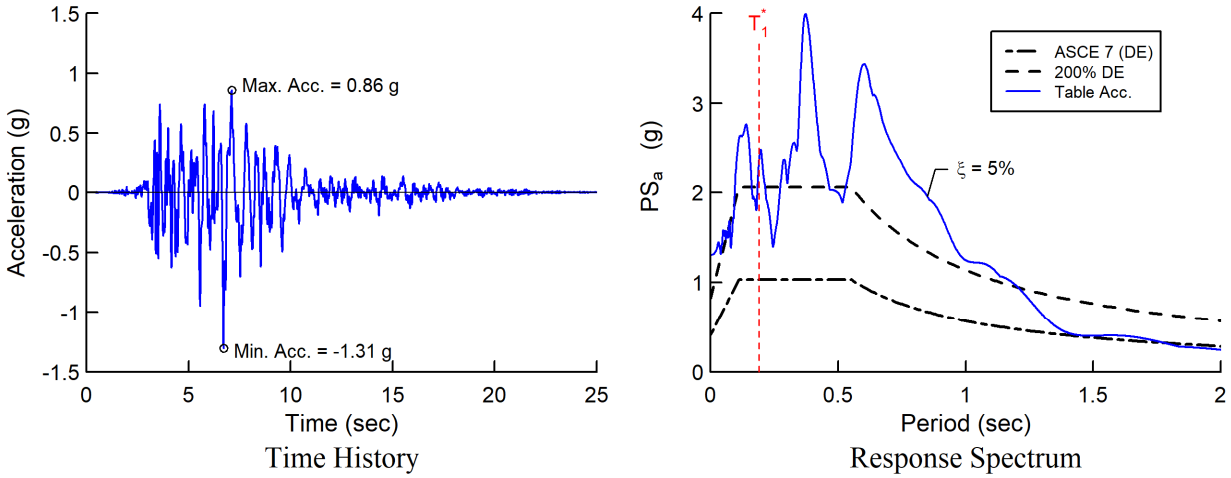

(c) Test 2A-3 (Target Intensity: 200% DE)

Figure 7.5 Measured Table Accelerations and Response Spectra for Phase 2A Tests

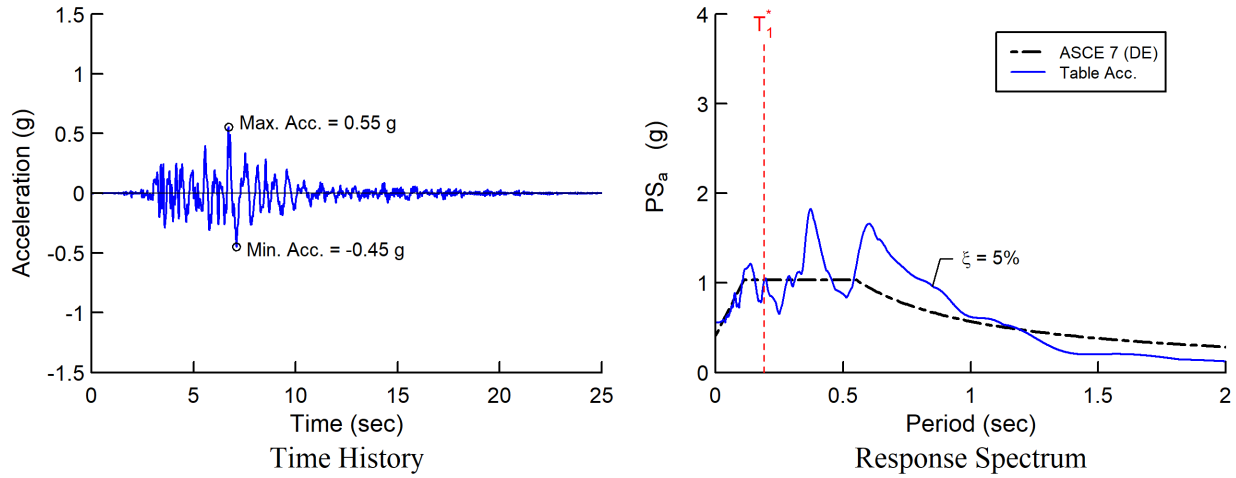

(d) Test 2A-4 (Target Intensity: 100% DE)

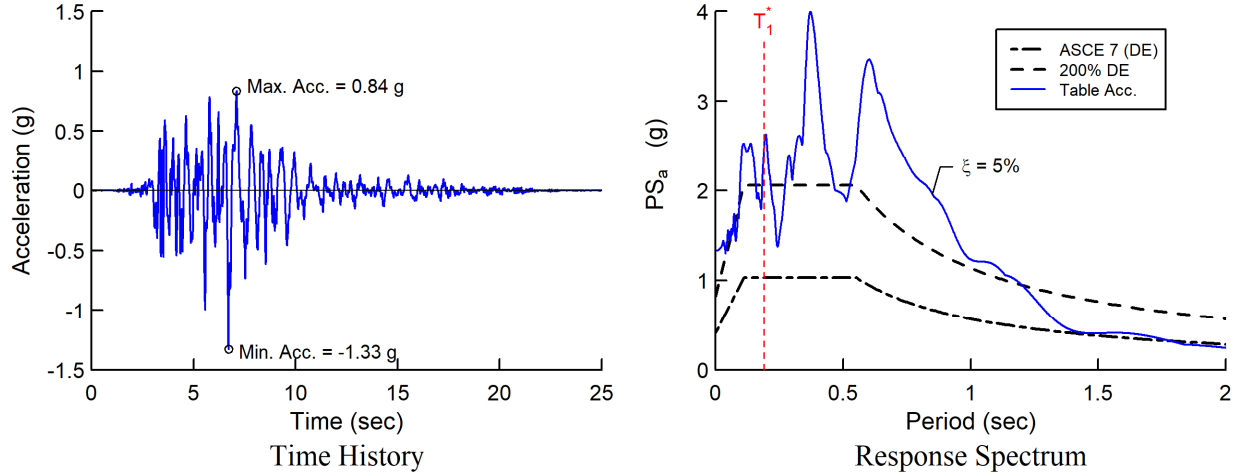

(e) Test 2A-5 (Target Intensity: 200% DE)

Figure 7.5 Measured Table Accelerations and Response Spectra for Phase 2A Tests (continued)

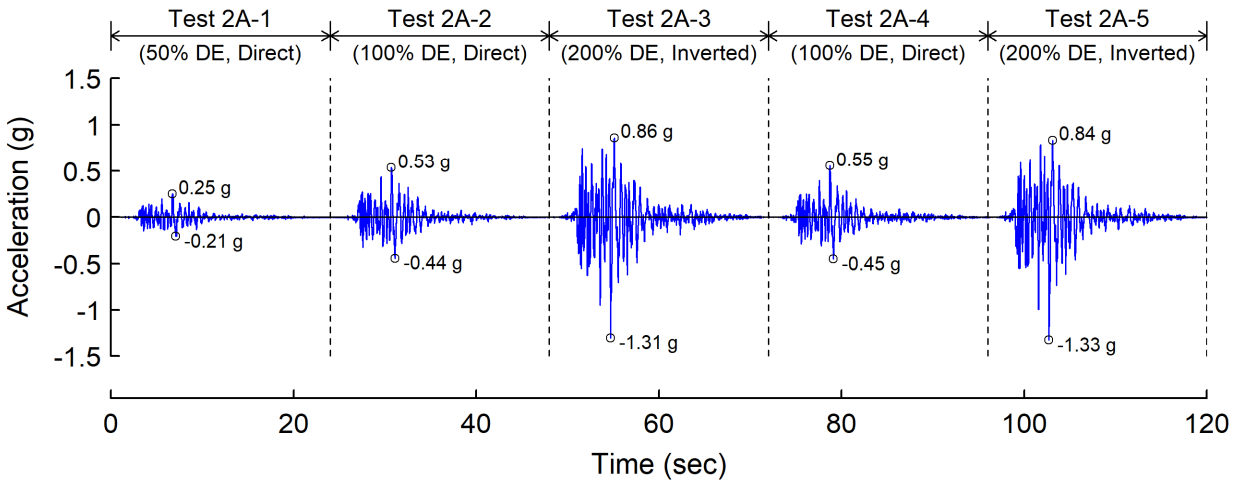

Figure 7.6 Measured Table Acceleration for Phase 2A Testing

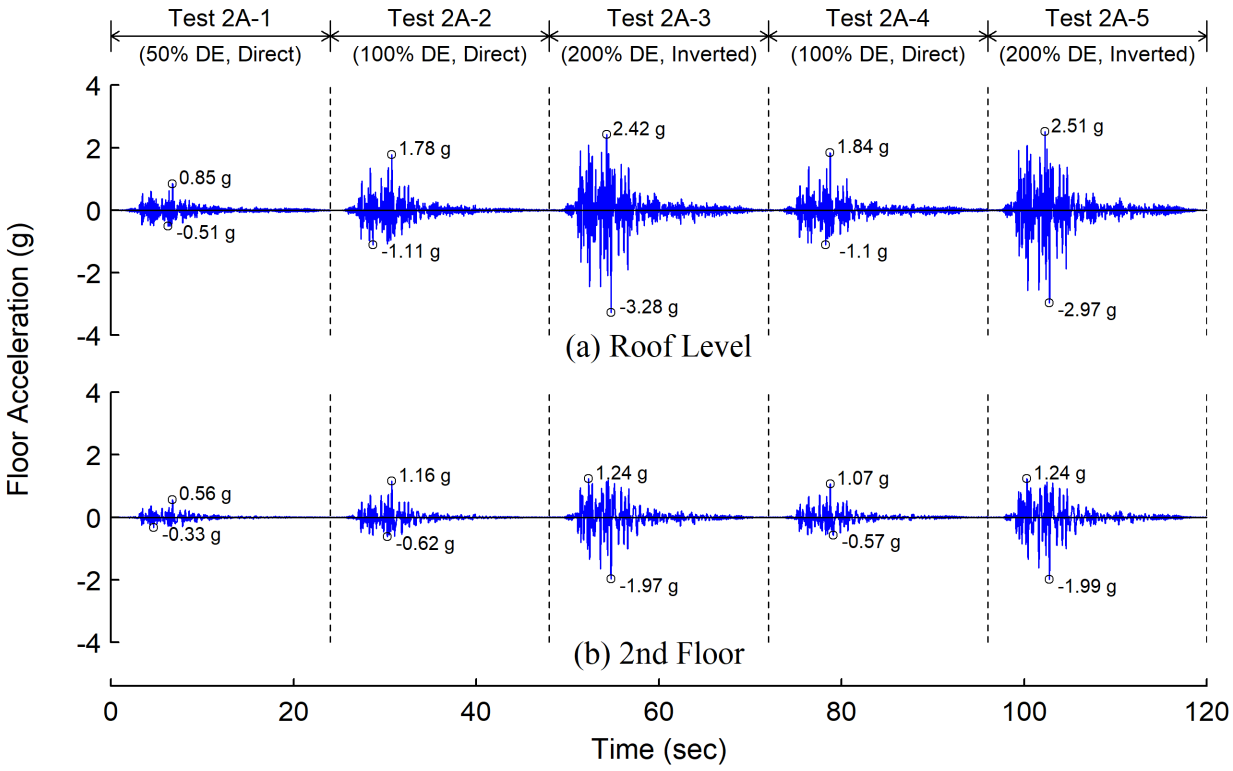

Figure 7.7 Floor Acceleration Responses for Phase 2A Testing

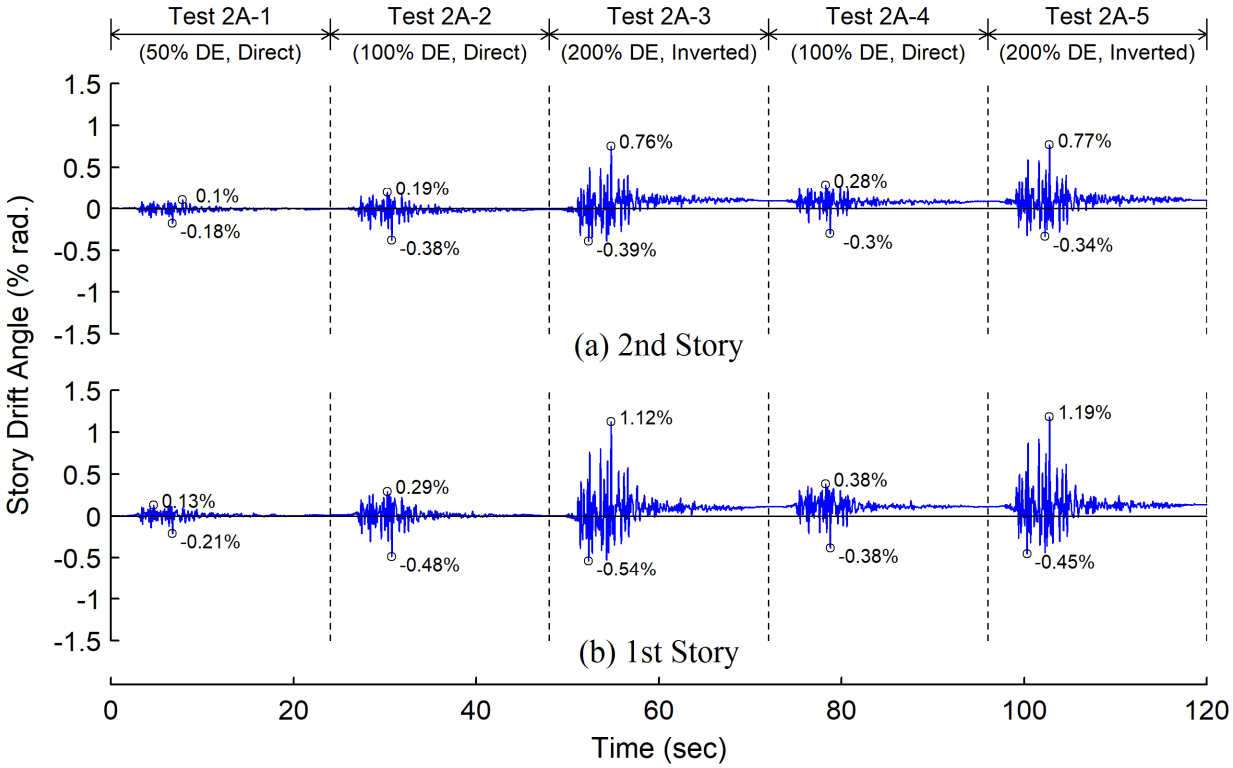

Figure 7.8 Story Drift Angle Responses for Phase 2A Testing

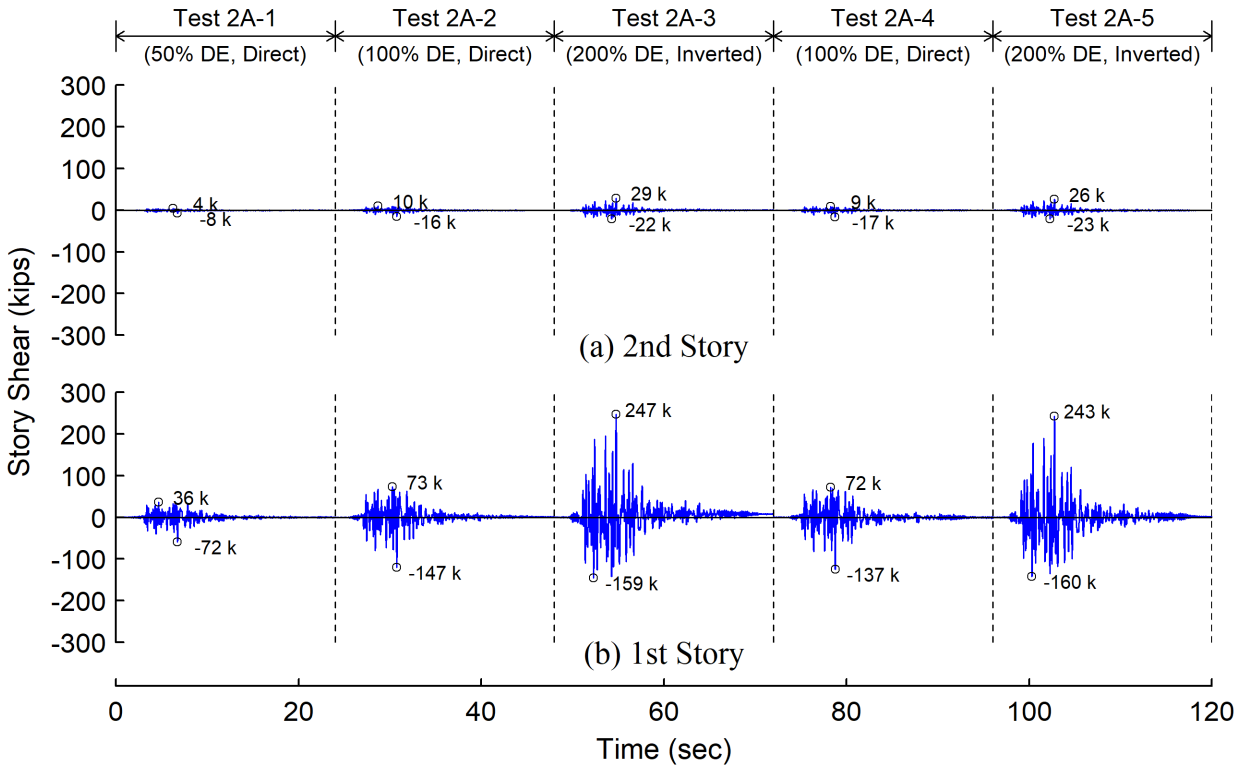

Figure 7.9 Story Shear Responses for Phase 2A Testing

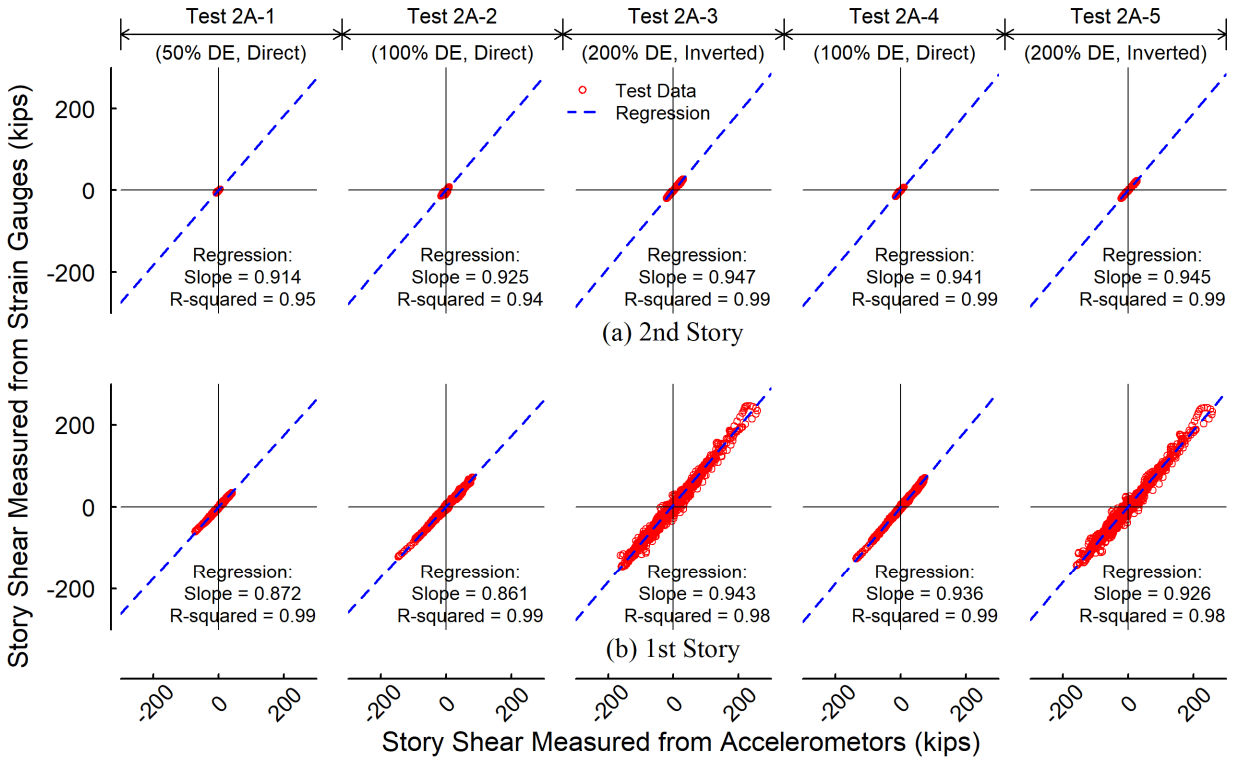

Figure 7.10 Comparison of Story Shear Measured from Two Methods for Phase 2A Tests

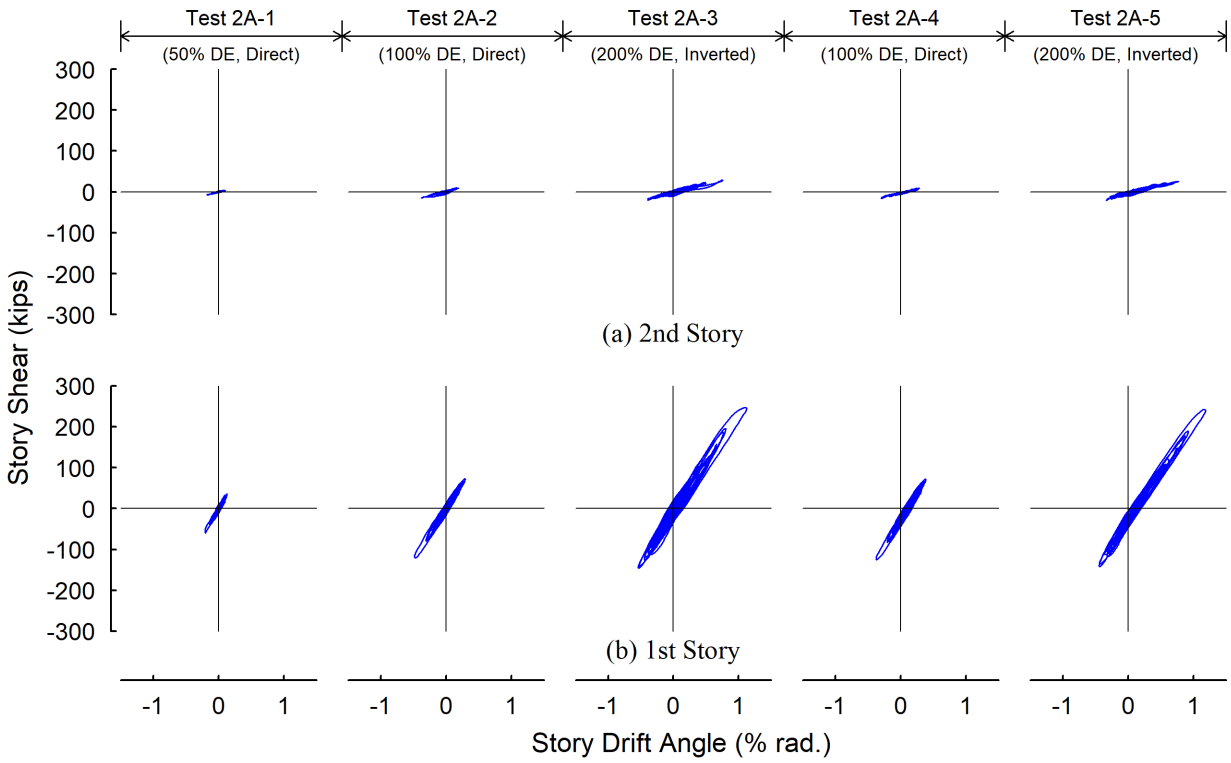

Figure 7.11 Story Shear versus Story Drift Angle Responses for Phase 2A Tests

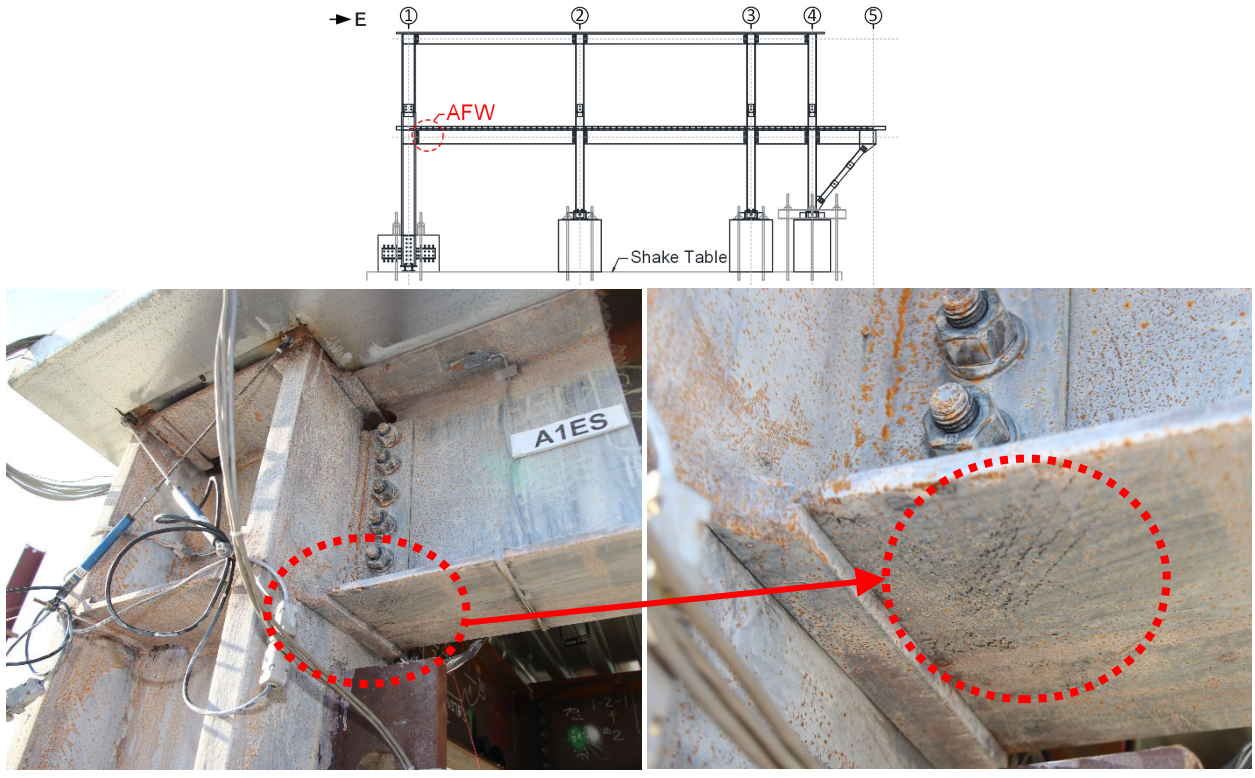

Figure 7.12 Yielding of Bottom Flange at 2nd Floor AFW Connections (after Phase 2A Testing)

7.3 Overview of Phase 2B Test Results

7.3.1 Specimen Global Responses

In Phase 2B, five earthquake simulation tests, designated Tests 2B-1 through 2B-5, were conducted at the intensity levels of 50% DE, 100% DE, 100% DE, 100% DE, and 125% DE, respectively. Figure 7.13 illustrates the variations of the measured first-mode frequency and damping ratio of the specimen in Phase 2B tests. Table 7.3 summarizes the results of dynamic characterization testing. As shown in Figure 7.14, Fourier spectra of the white noise test results on the roof acceleration are plotted to determine the vibration frequencies. In addition, the 2nd floor acceleration time histories measured in the impulse testing are plotted as shown in Figure 7.15. The fundamental period and damping ratio of the specimen were determined based on the free vibration after impulse loading.

As shown in Figure 7.13(a) and Table 7.3, the fundamental frequency remained about constant with a very tiny decay during Phase 2B testing. White noise test results showed that the first-mode frequency of the specimen remained about 3.60 Hz from the beginning to the end of Test 2B-4 but slightly dropped to 3.43 Hz after Test 2B-5. Similarly, the impulse test results show that the 1st-mode frequency slightly decreased from 3.67 Hz to 3.48 Hz. The second mode frequency was 9.27 Hz before Phase 2B and slightly decreased to 8.79 Hz after Phase 2B testing was completed. In addition, the measured damping ratio varied from 3.12% to 3.50% with an average value of 3.36% in Phase 2B testing. Figure 7.13(b) shows that the variation of damping ratio is not significant. In general, the test specimen maintained approximately constant dynamic properties in Tests 2B-1 through 2B-4. A small drop of the fundamental frequency was observed after Test 2B-5. This could be due to local buckling of the collector bottom flanges at the 2nd floor AFW connections during Test 2B-5.

Figure 7.16 through Figure 7.22 show the specimen global responses for the five main tests in Phase 2B. Figure 7.16 shows the table input accelerations and the associated response spectra. Table 7.4 tabulates the measured peak responses in floor accelerations and story drifts for Phase 2B tests. Figure 7.18 shows the time histories of the roof and 2nd floor accelerations. In Phase 2B testing the reached positive and negative peak roof accelerations were +2.71 g and −3.03 g, respectively. The positive and negative peak 2nd floor accelerations were +1.64 g and −1.43 g, respectively. Figure 7.19 shows the time histories of story drift angles. The positive and negative peak 2nd-story drift angles reached −1.79%, and −1.81% rad, respectively. The positive and negative peak 1st-story drift were +1.75%, and −1.64% rad, respectively. Figure 7.20 shows the story shear time histories. Figure 7.21 shows a good agreement between the measured story shears determined from two methods. It confirms the reliability of the story shear and column member forces determined from strain gauge readouts. Figure 7.22 shows the story hysteresis responses for five main tests. Both stories experienced mild to moderate inelastic actions in Tests 2B-2 through 2B-5.

Table 7.3 Phase 2B Impulse and White Noise Test Results

Test Timing	Impulse Test					White Noise Test						
	Test No.	Fundamental Properties				Test No.	1st Mode		2nd Mode		3rd Mode	
		f_1 (Hz)	T_1 (sec)	ξ (%)			f_1 (Hz)	T_1 (sec)	f_2 (Hz)	T_2 (sec)	f_3 (Hz)	T_3 (sec)
Before Test 2B-1	IM 2B-0	3.67	0.273	3.27		WN 2B-0	3.60	0.278	9.27	0.108	12.93	0.0773
After Test 2B-1	IM 2B-1	3.61	0.277	3.37		WN 2B-1	3.60	0.278	9.27	0.108	12.73	0.0785
After Test 2B-2	IM 2B-2	3.54	0.283	3.12		WN 2B-2	3.60	0.278	8.93	0.112	12.73	0.0785
After Test 2B-3	IM 2B-3	3.51	0.285	3.50		WN 2B-3	3.60	0.278	8.93	0.112	12.73	0.0785
After Test 2B-4	IM 2B-4	3.51	0.285	3.47		WN 2B-4	3.61	0.277	8.90	0.112	12.71	0.0787
After Test 2B-5	IM 2B-5	3.48	0.288	3.40		WN 2B-5	3.43	0.292	8.79	0.114	12.71	0.0787

Table 7.4 Peak Response Quantities of Phase 2B Tests

Test No.	Floor Acceleration (g)				Story Drift Angle (% rad)			
	2nd Floor		Roof		1st Story		2nd Story	
	Positive	Negative	Positive	Negative	Positive	Negative	Positive	Negative
Test 2B-1	0.57	-0.45	1.00	-0.68	0.34	-0.44	0.32	-0.52
Test 2B-2	1.28	-1.07	2.44	-1.75	0.84	-1.22	0.84	-1.37
Test 2B-3	0.97	-1.43	1.76	-2.65	1.31	-1.00	1.33	-1.12
Test 2B-4	1.13	-1.35	2.31	-2.35	1.34	-1.23	1.27	-1.36
Test 2B-5	1.64	-1.38	2.71	-3.03	1.75	-1.64	1.79	-1.81

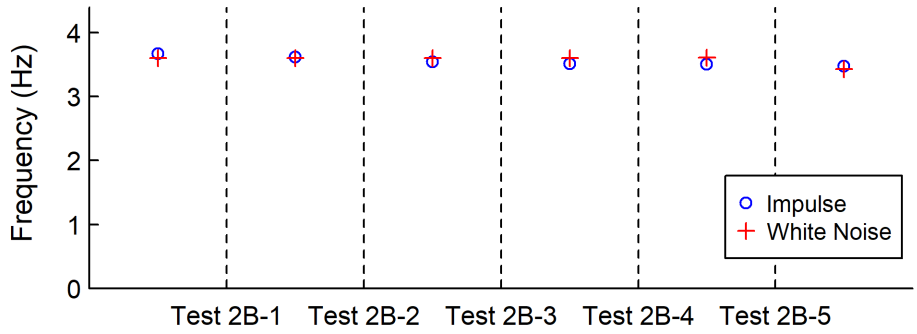

(a)

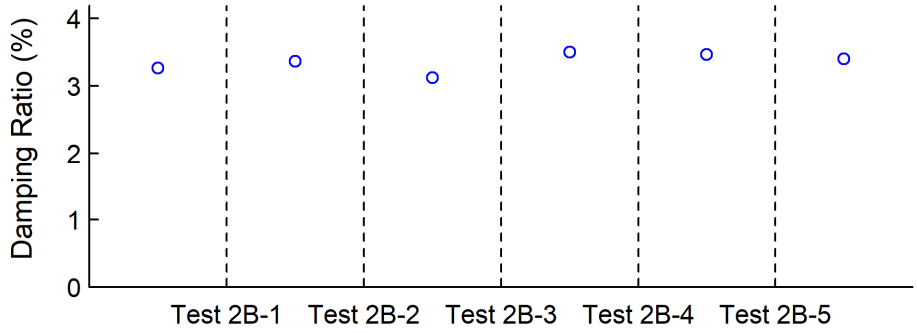

(b)

Figure 7.13 Variations of Measured (a) 1st Mode f=Frequency and (b) Damping Ratio in Phase 2B Testing

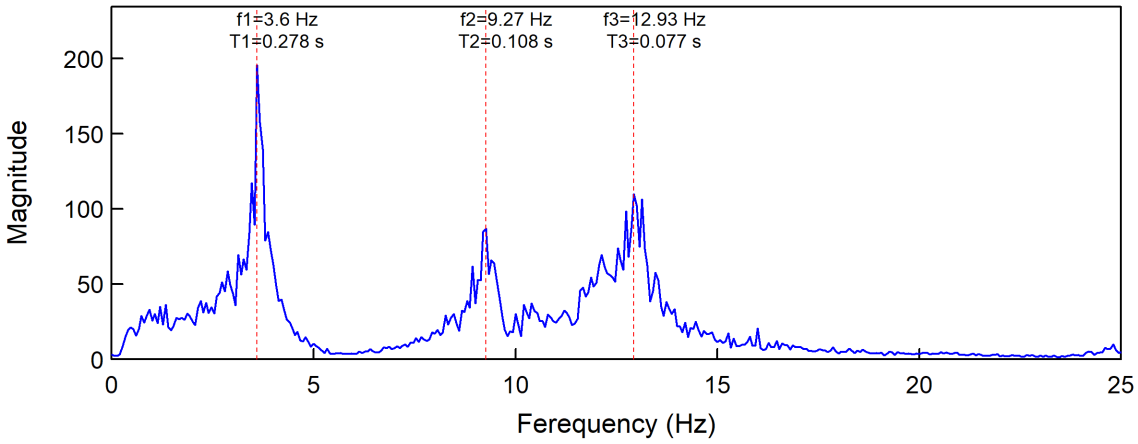

(a) Test WN 2B-0

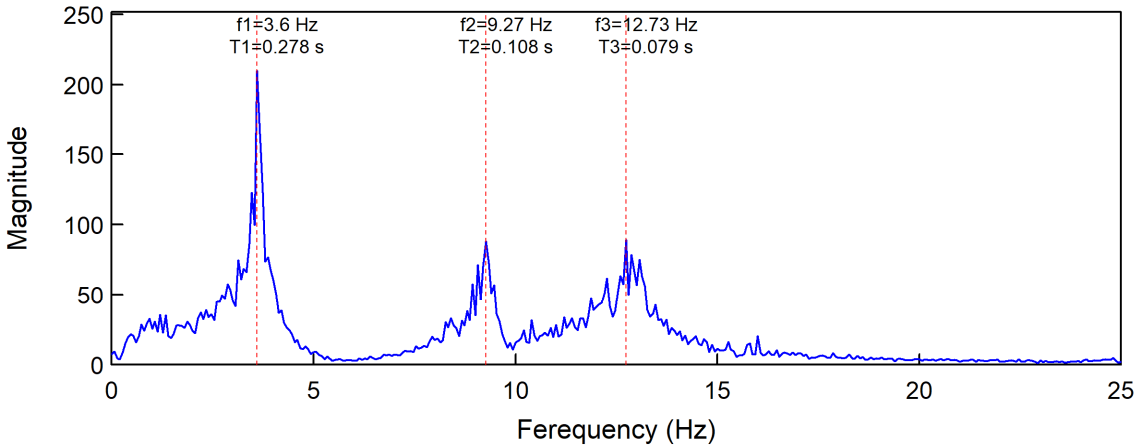

(b) Test WN 2B-1

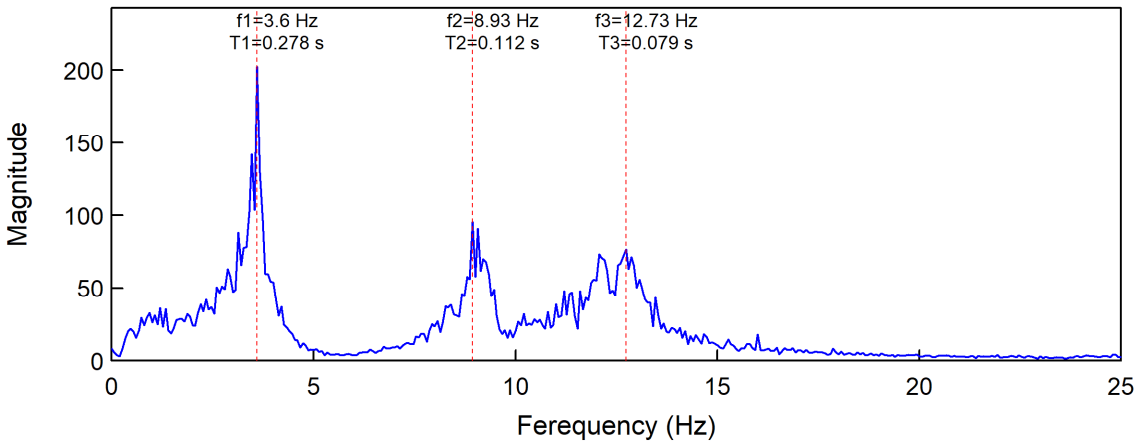

(c) Test WN 2B-2

Figure 7.14 Phase 2B White Noise Test Results

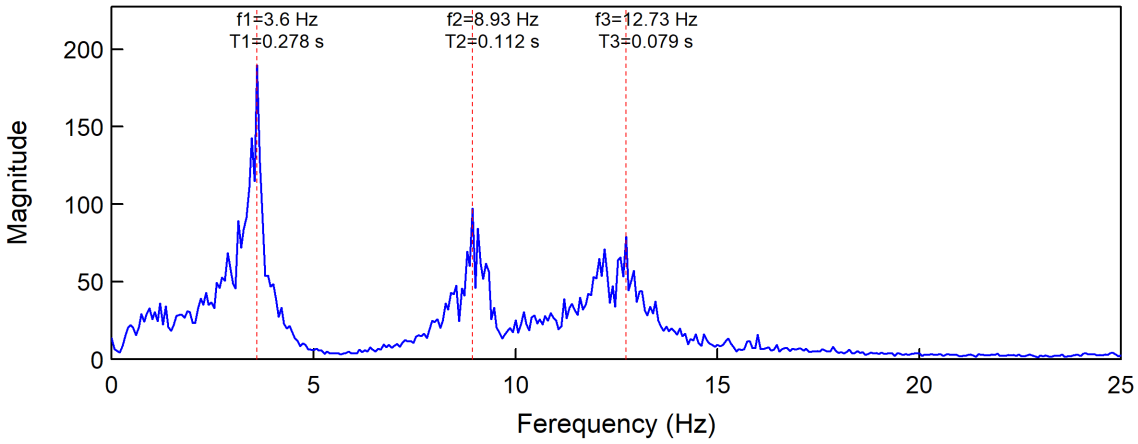

(d) Test WN 2B-3

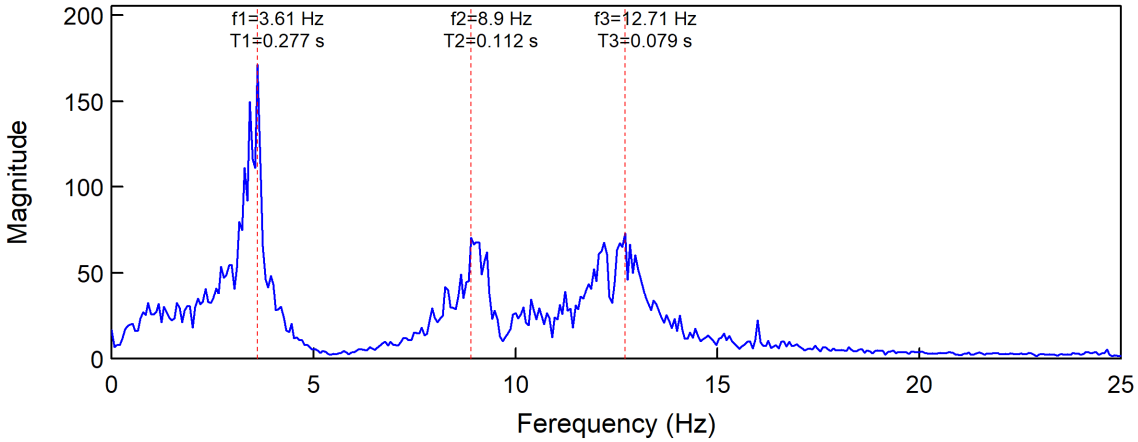

(e) Test WN 2B-4

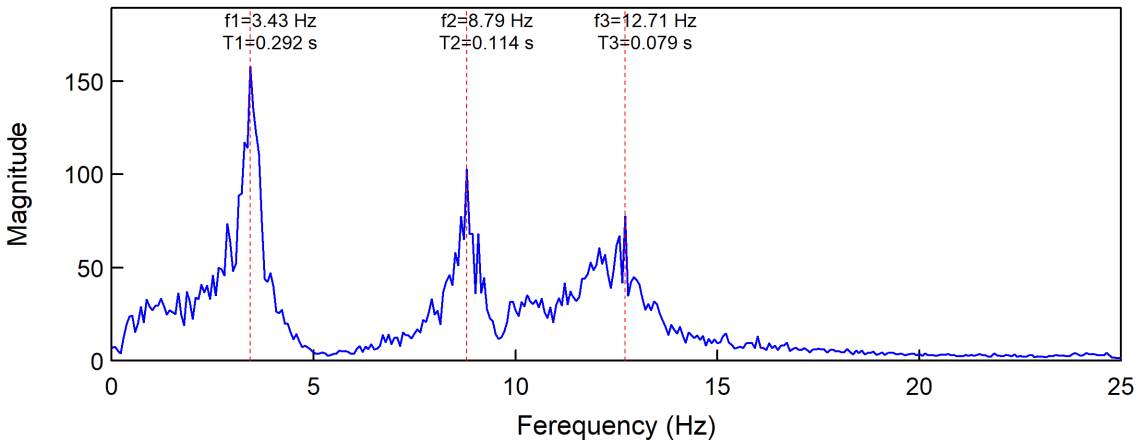

(f) Test WN 2B-5

Figure 7.14 Phase 2B White Noise Test Results (continued)

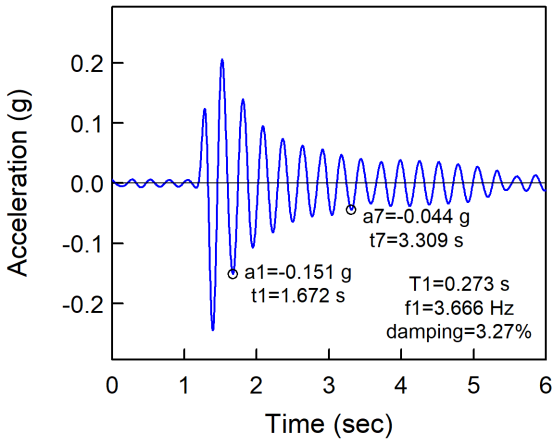

(a) Test IM 2B-0

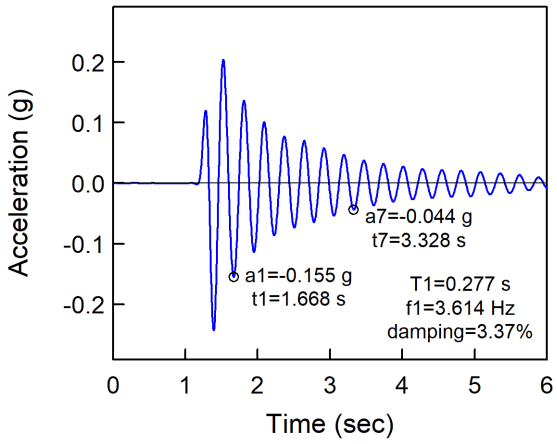

(b) Test IM 2B-1

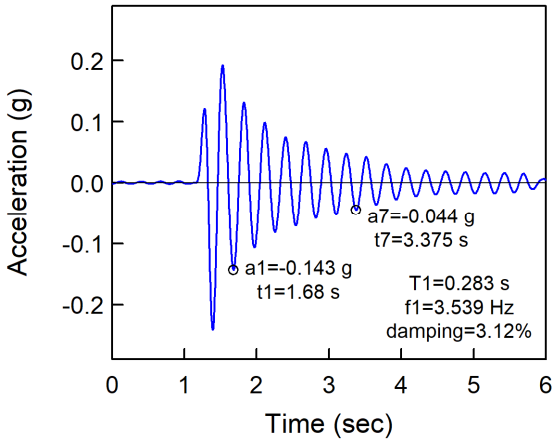

(c) Test IM 2B-2

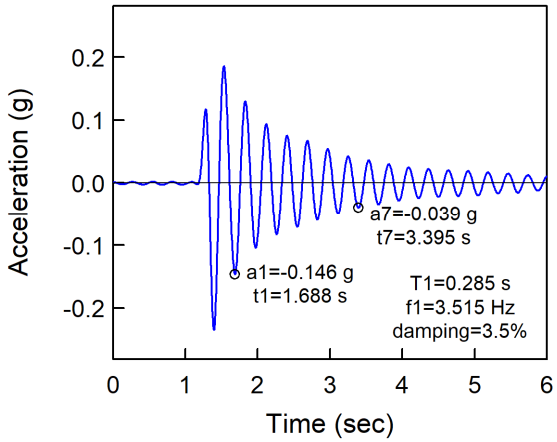

(d) Test IM 2B-3

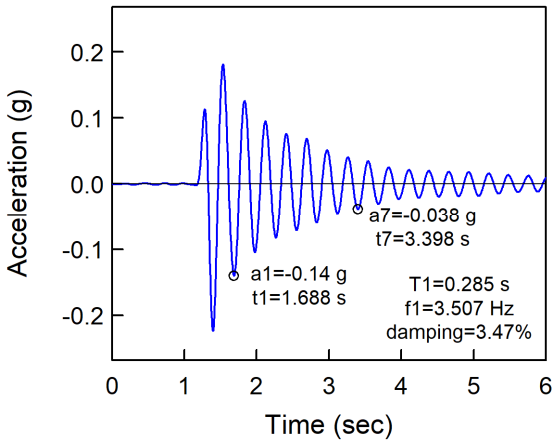

(e) Test IM 2B-4

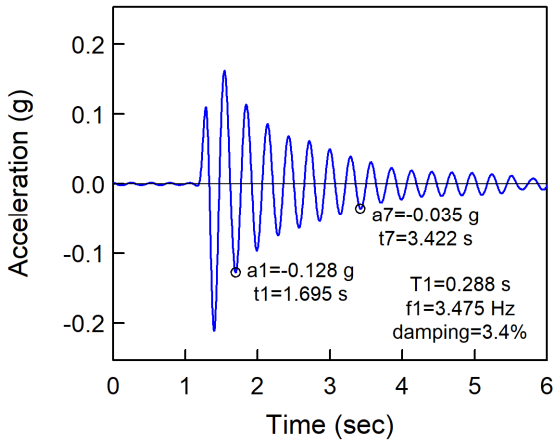

(f) Test IM 2B-5

Figure 7.15 Phase 2B Impulse Test Results

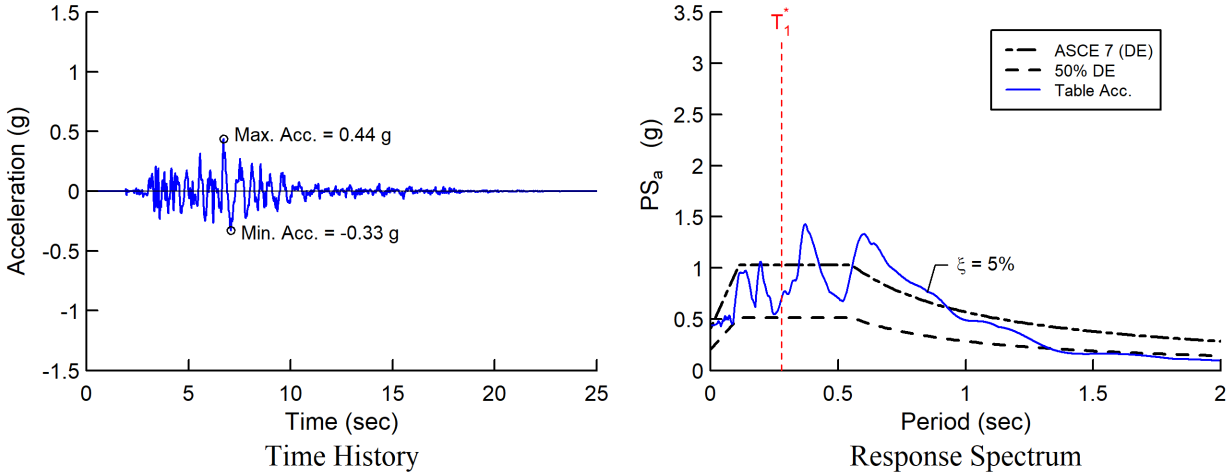

(a) Test 2B-1 (Target Intensity: 50% DE)

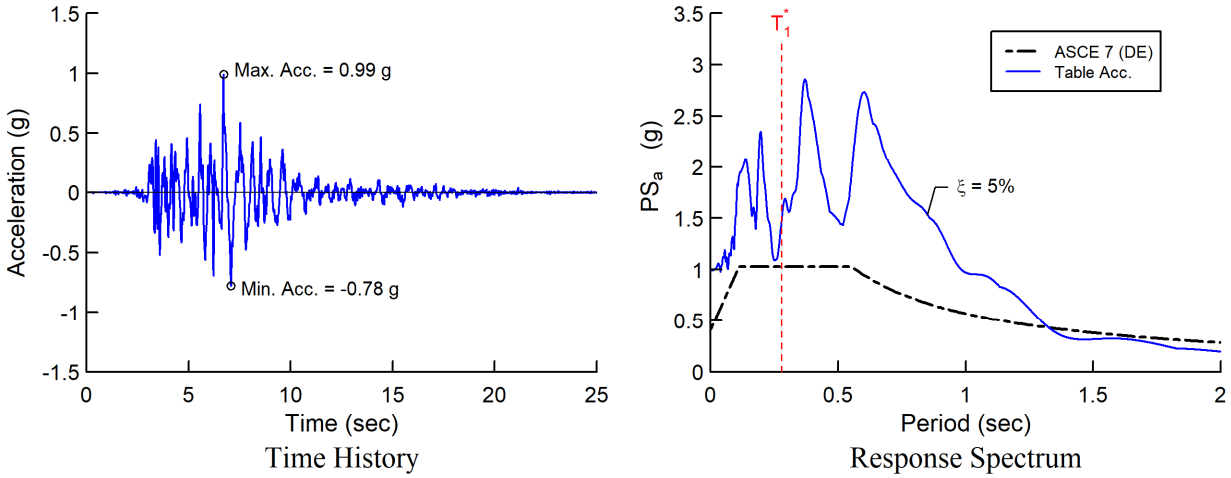

(b) Test 2B-2 (Target Intensity: 100% DE)

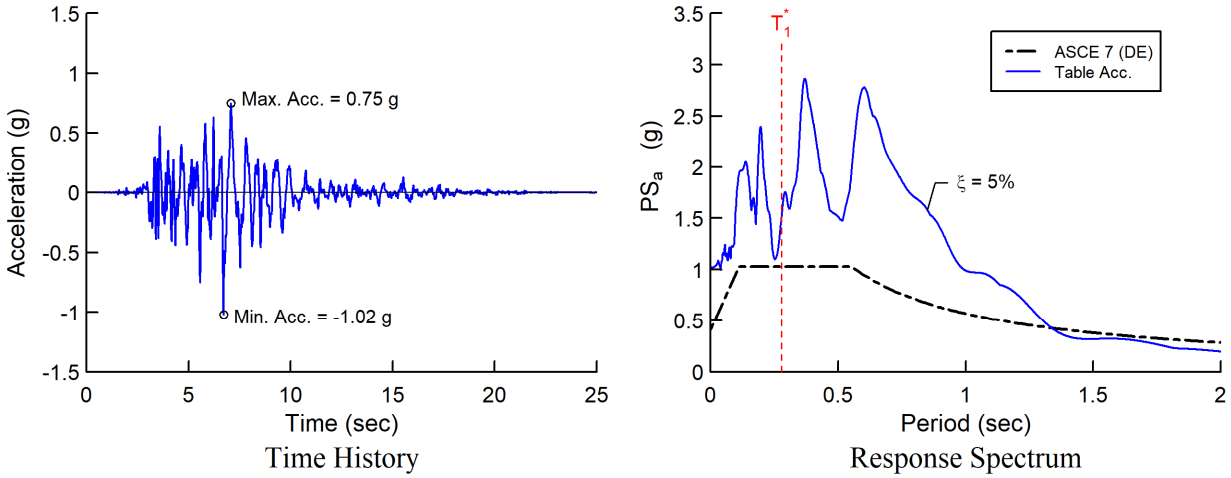

(c) Test 2B-3 (Target Intensity: 100% DE)

Figure 7.16 Measured Table Accelerations and Response Spectra for Phase 2B Tests

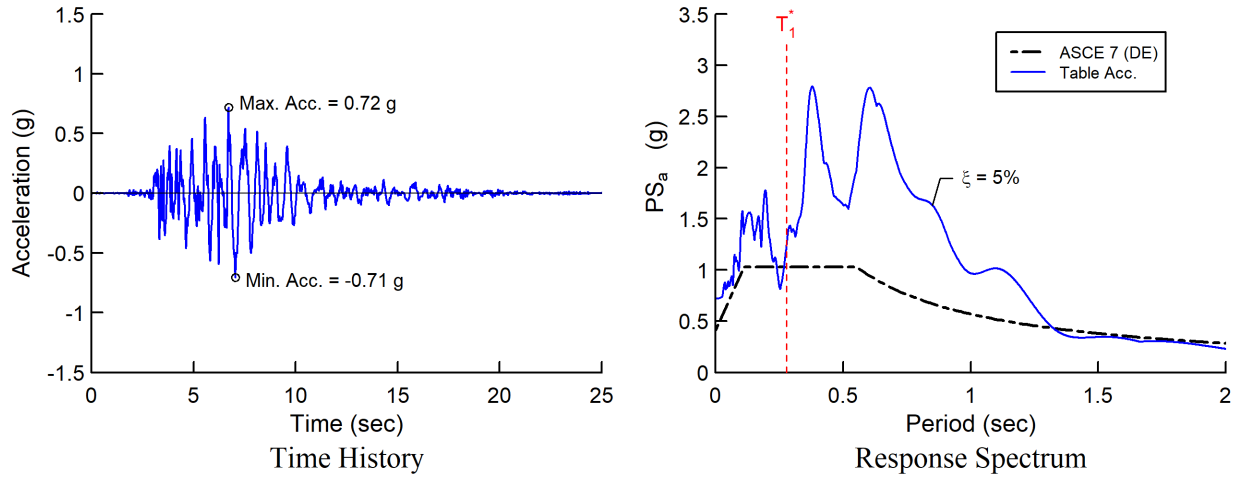

(d) Test 2B-4 (Target Intensity: 100% DE)

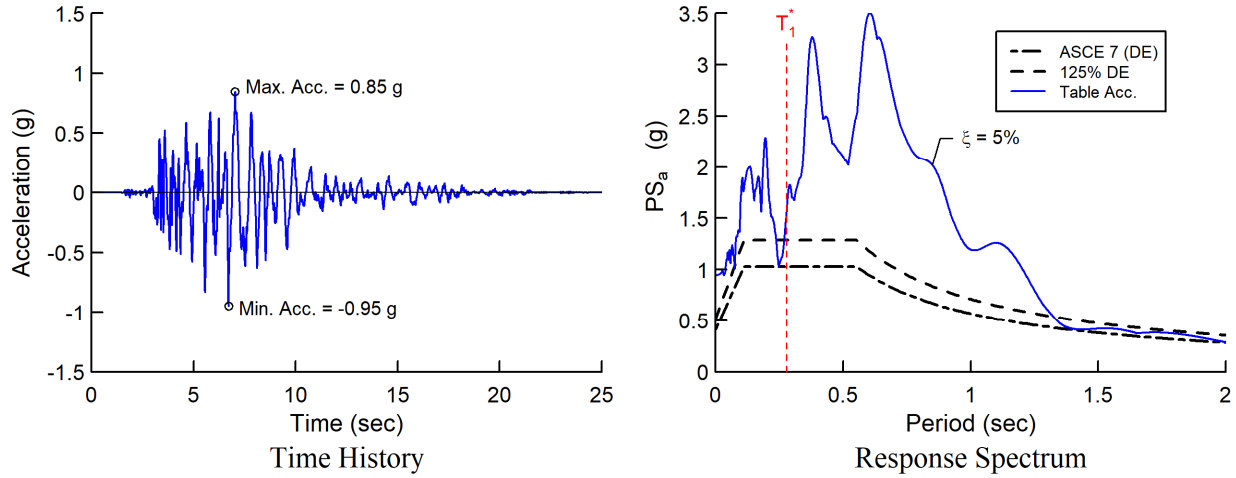

(e) Test 2B-5 (Target Intensity: 125% DE)

Figure 7.16 Measured Table Accelerations and Response Spectra for Phase 2B Tests (continued)

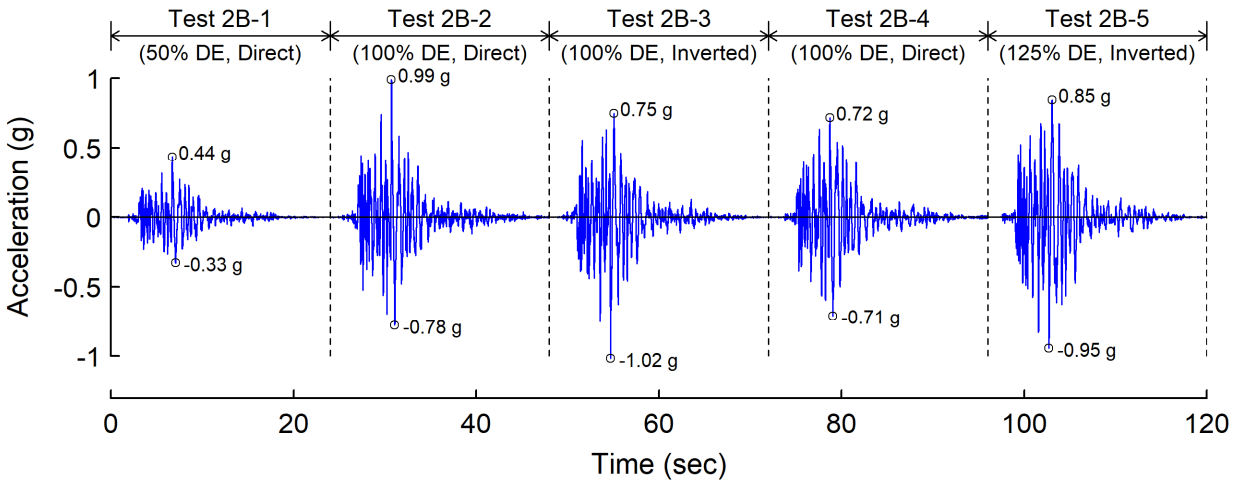

Figure 7.17 Measured Table Acceleration for Phase 2B Testing

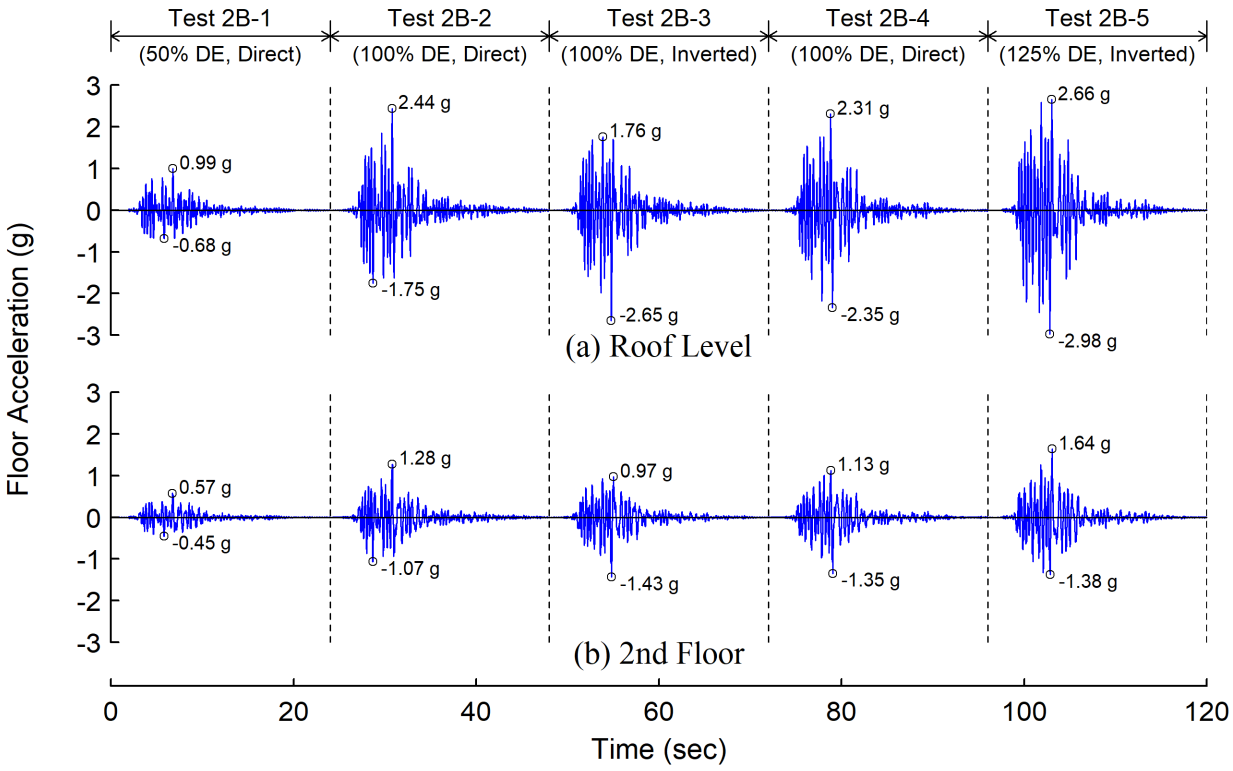

Figure 7.18 Floor Acceleration Responses for Phase 2B Testing

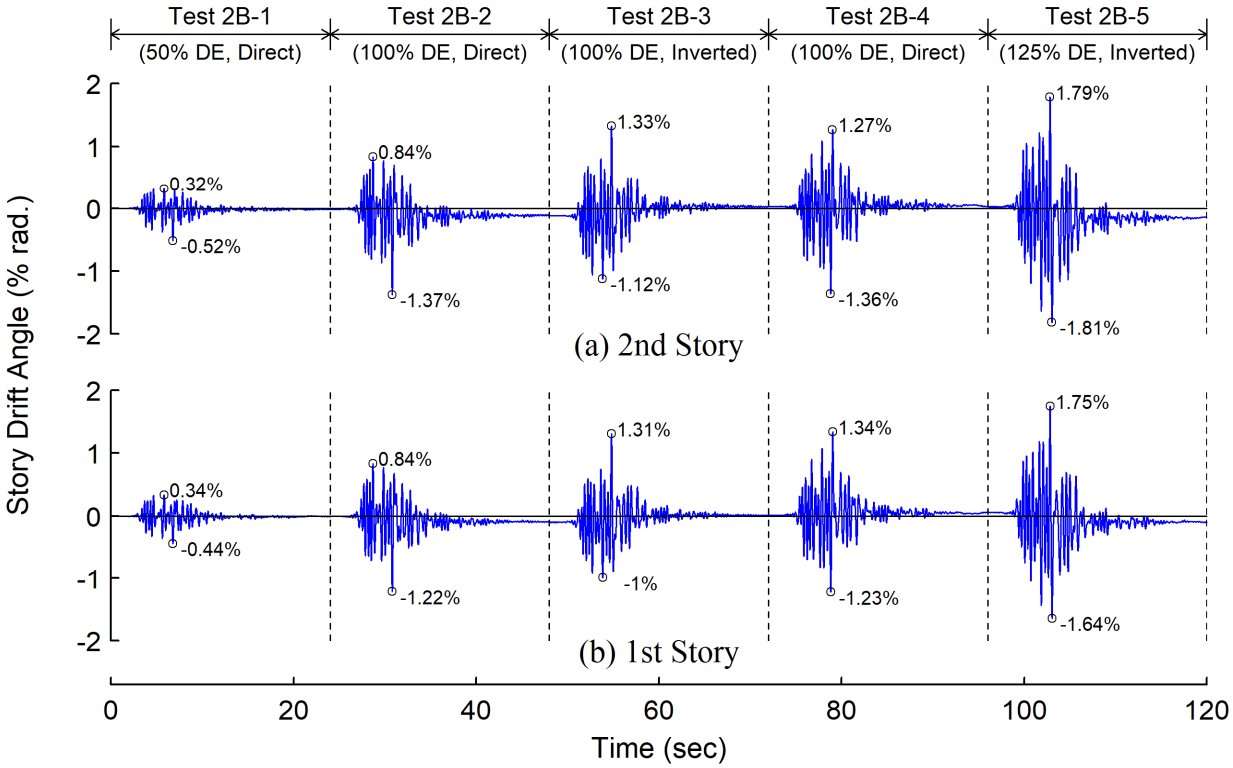

Figure 7.19 Story Drift Angle Responses for Phase 2B Testing

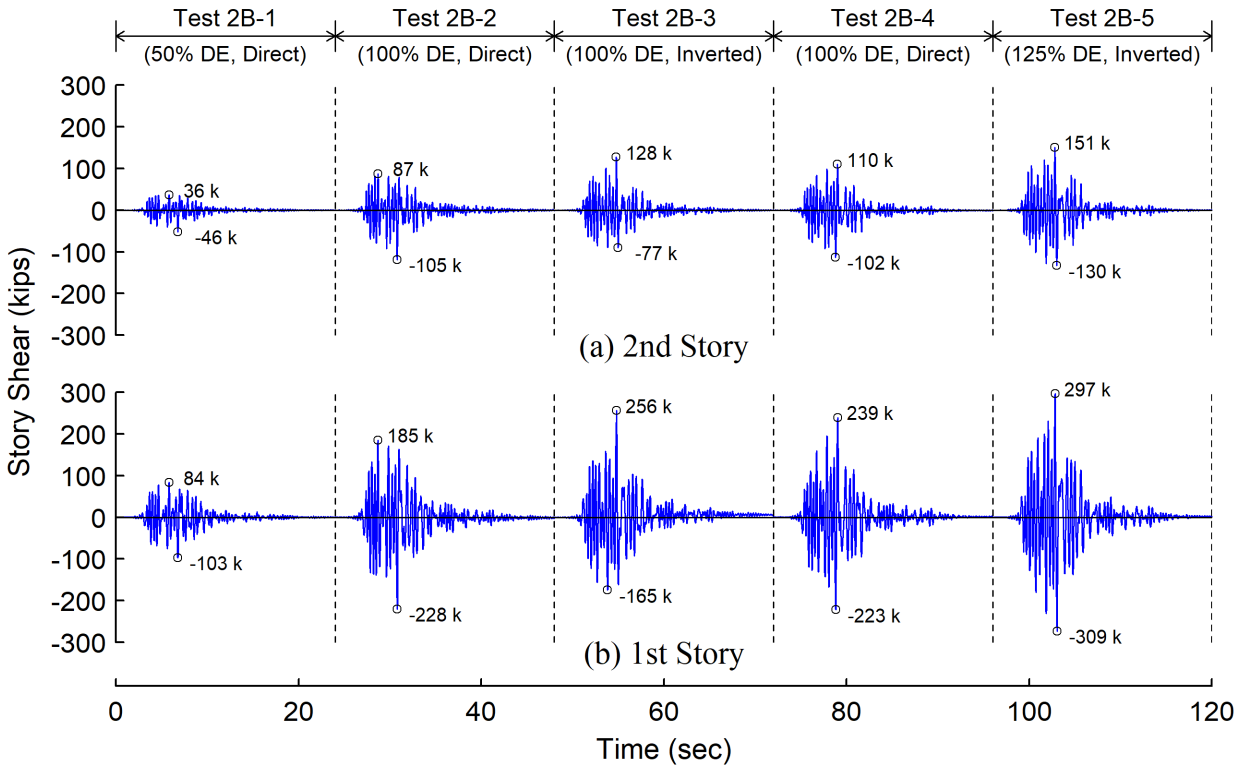

Figure 7.20 Story Shear Responses for Phase 2B Testing

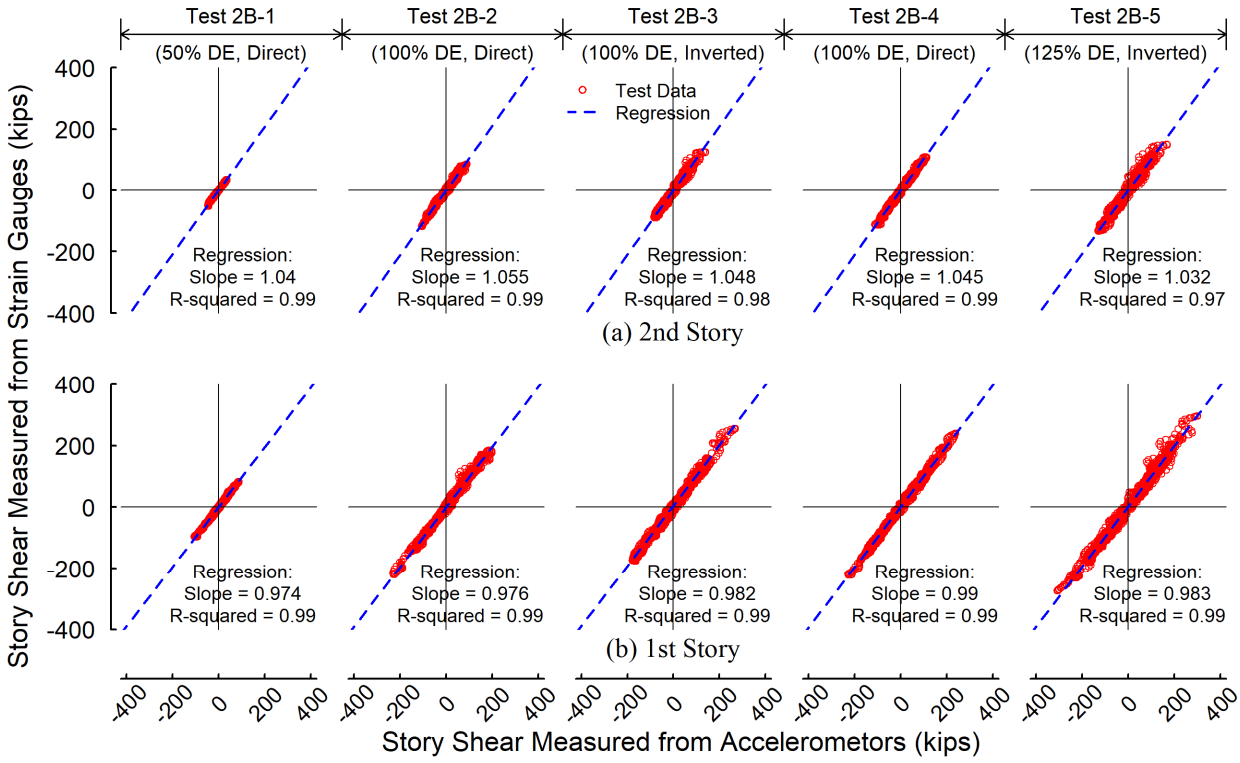

Figure 7.21 Comparison of Story Shear Measured from Two Methods for Phase 2B Tests

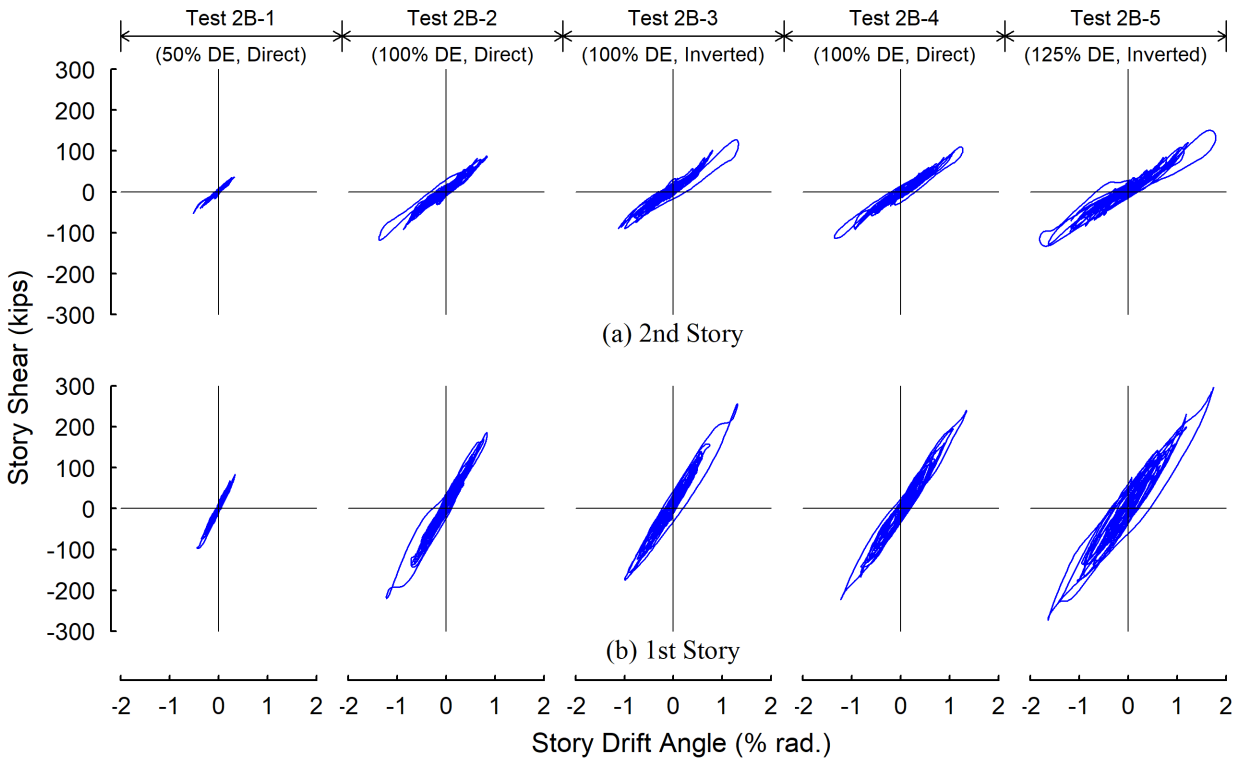

Figure 7.22 Story Shear versus Story Drift Angle Responses for Phase 2B Tests

7.3.2 Specimen Conditions after Test 2B-3

After Test 2B-3, a visual inspection of the entire test building was conducted. Most of this inspection relied on observing the flaking or cracking of the whitewash on the steel members. Slight yielding of collector bottom flange was detected at the roof AFW connections (Figure 7.23). As shown in Figure 7.24 and Figure 7.25, the scratching of whitewash on the collector web along the vertical edge of the bottom corner of the shear tab implies bolt slippage at the roof TFW connections. Moderate yielding of the collector bottom flange was observed at the 2nd floor AFW connections (Figure 7.26). Figure 7.27 and Figure 7.28 show that the bolt slippage occurred at the 2nd floor TFW connections. Figure 7.29 and Figure 7.30 respectively show slight whitewash flaking in the column panel zones at the 2nd floor TFW and BW connections, suggesting high stress flowing through these regions.

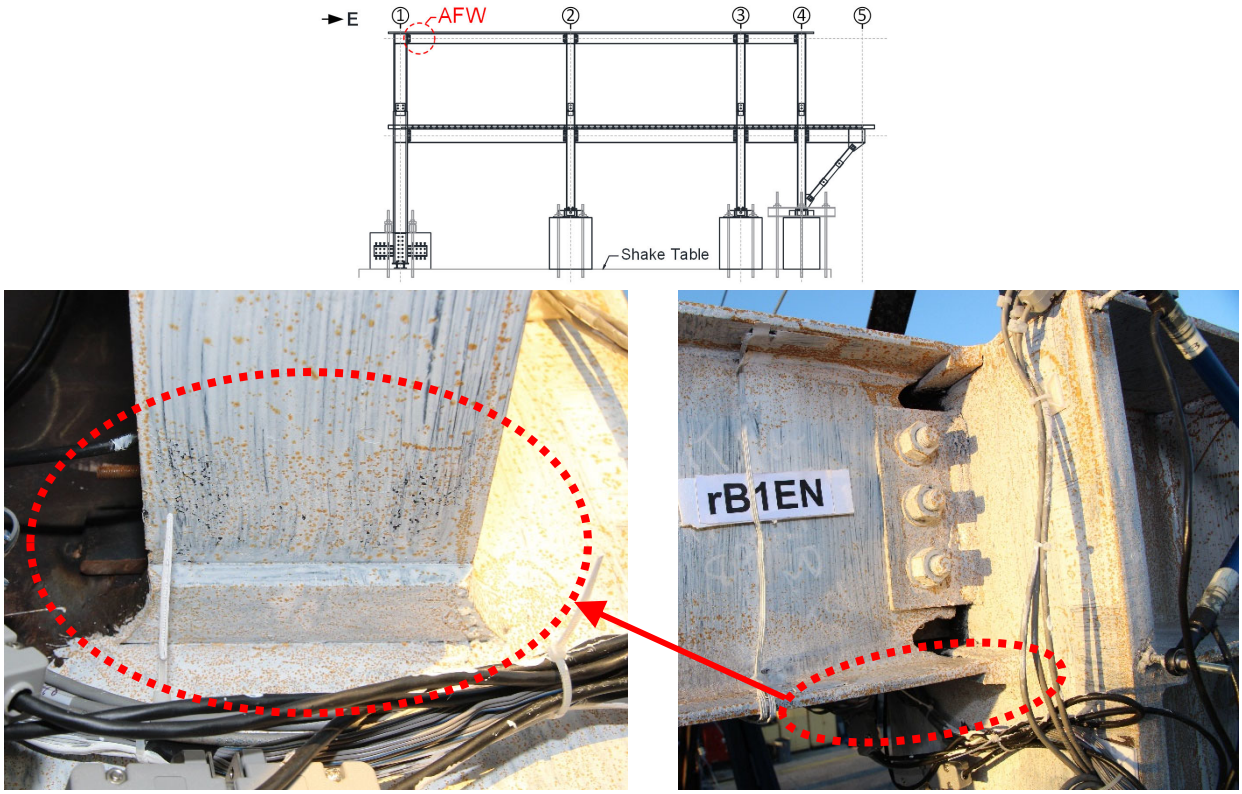

Figure 7.23 After Test 2B-3: Slight Yielding of Bottom Flange at Roof AFW Connections

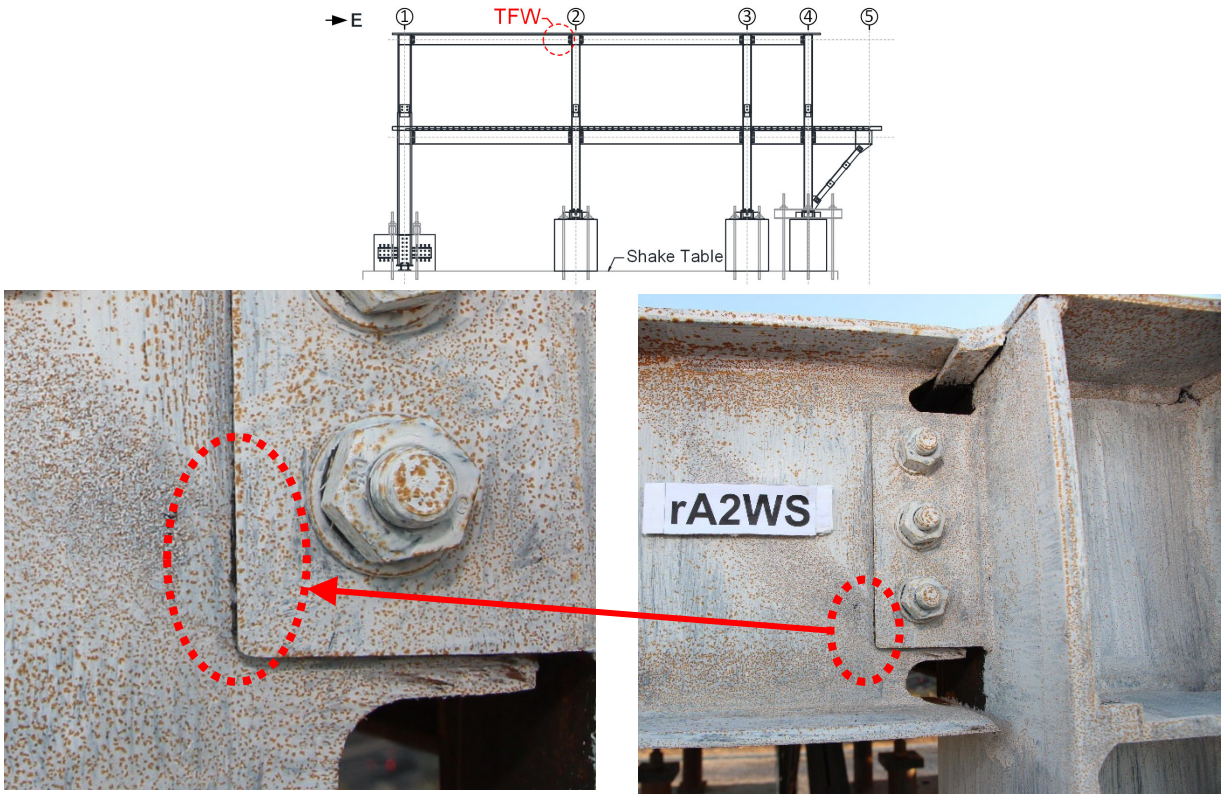

Figure 7.24 After Test 2B-3: Bolt Slippage at Roof West-Side TFW Connections

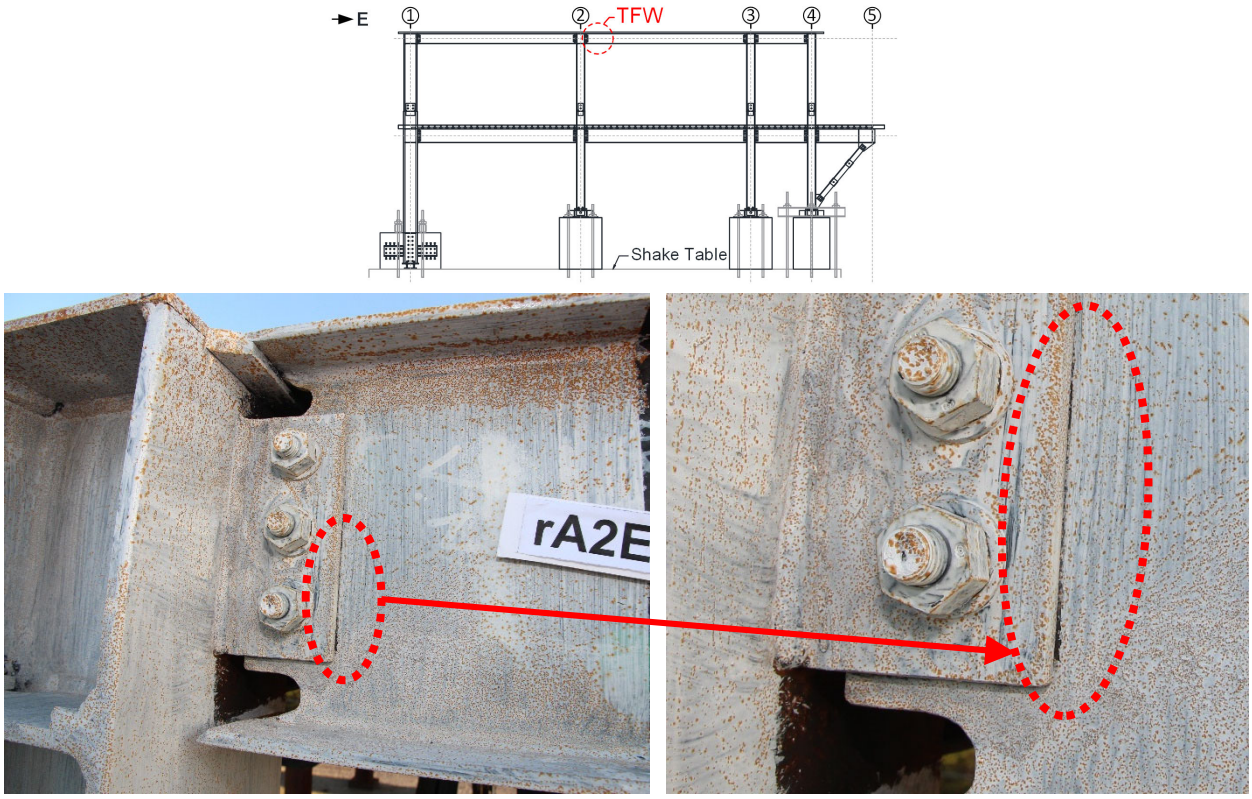

Figure 7.25 After Test 2B-3: Bolt Slippage at Roof East-Side TFW Connections

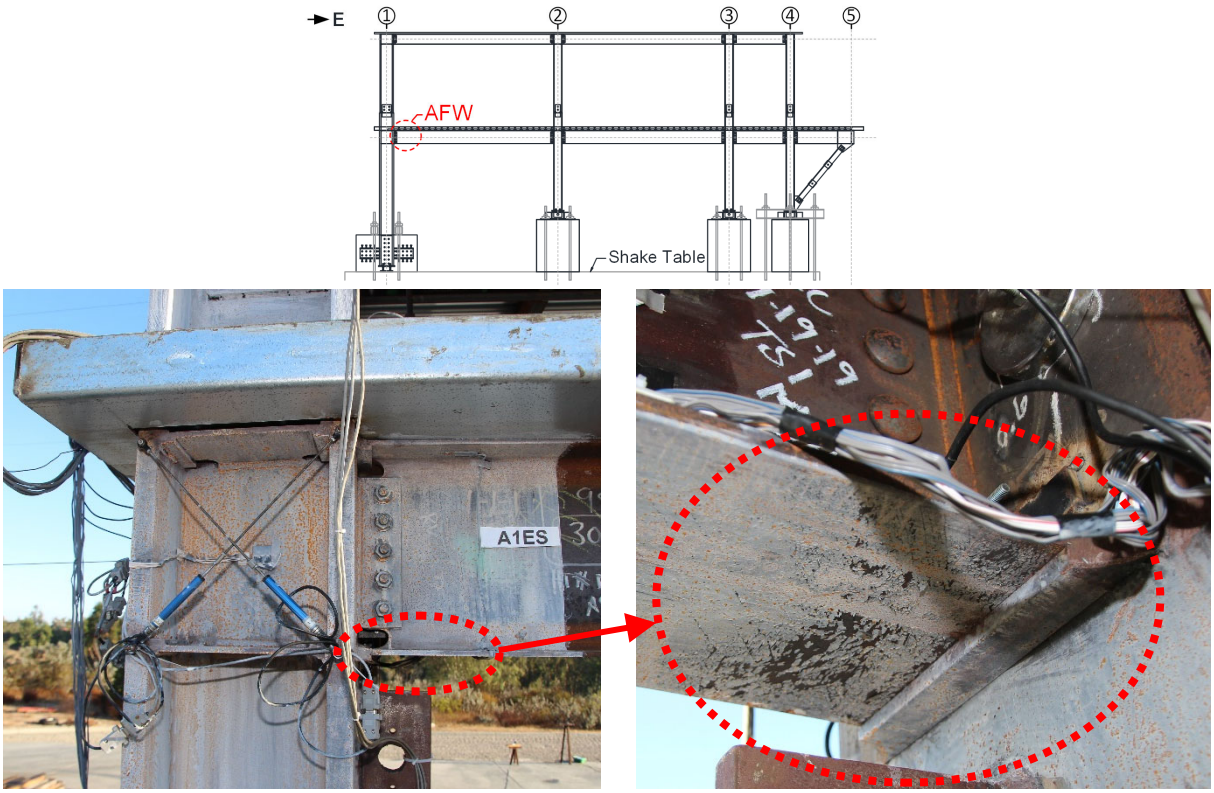

Figure 7.26 After Test 2B-3: Yielding of Bottom Flange at 2nd Floor AFW Connections

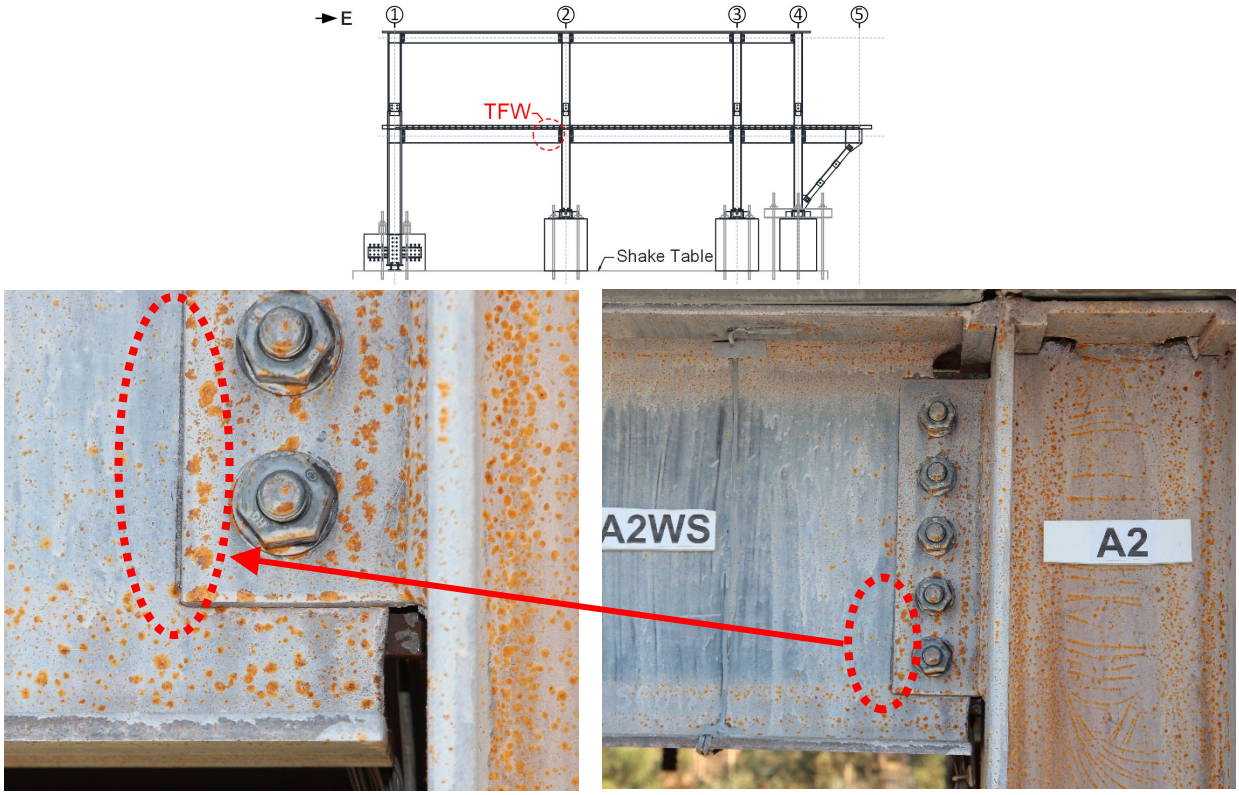

Figure 7.27 After Test 2B-3: Bolt Slippage at 2nd Floor West-Side TFW Connections

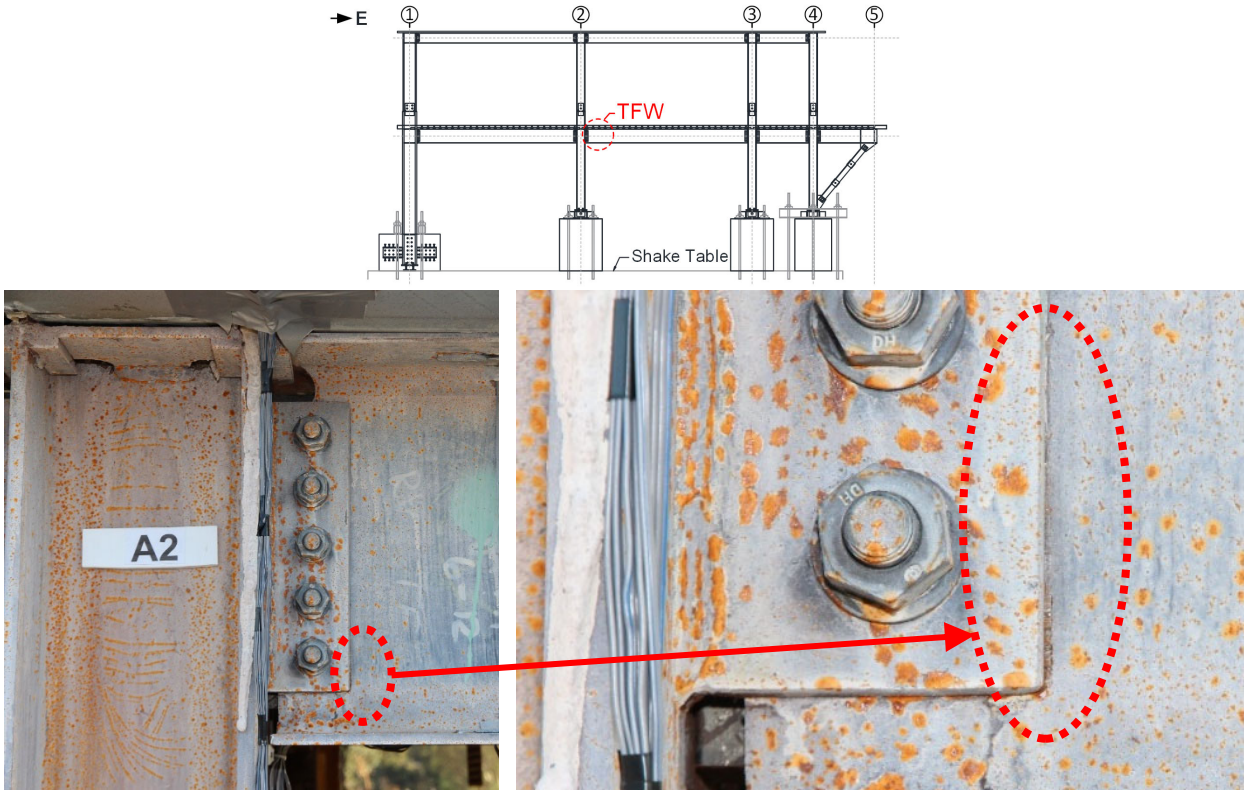

Figure 7.28 After Test 2B-3: Bolt Slippage at 2nd Floor East-Side TFW Connections

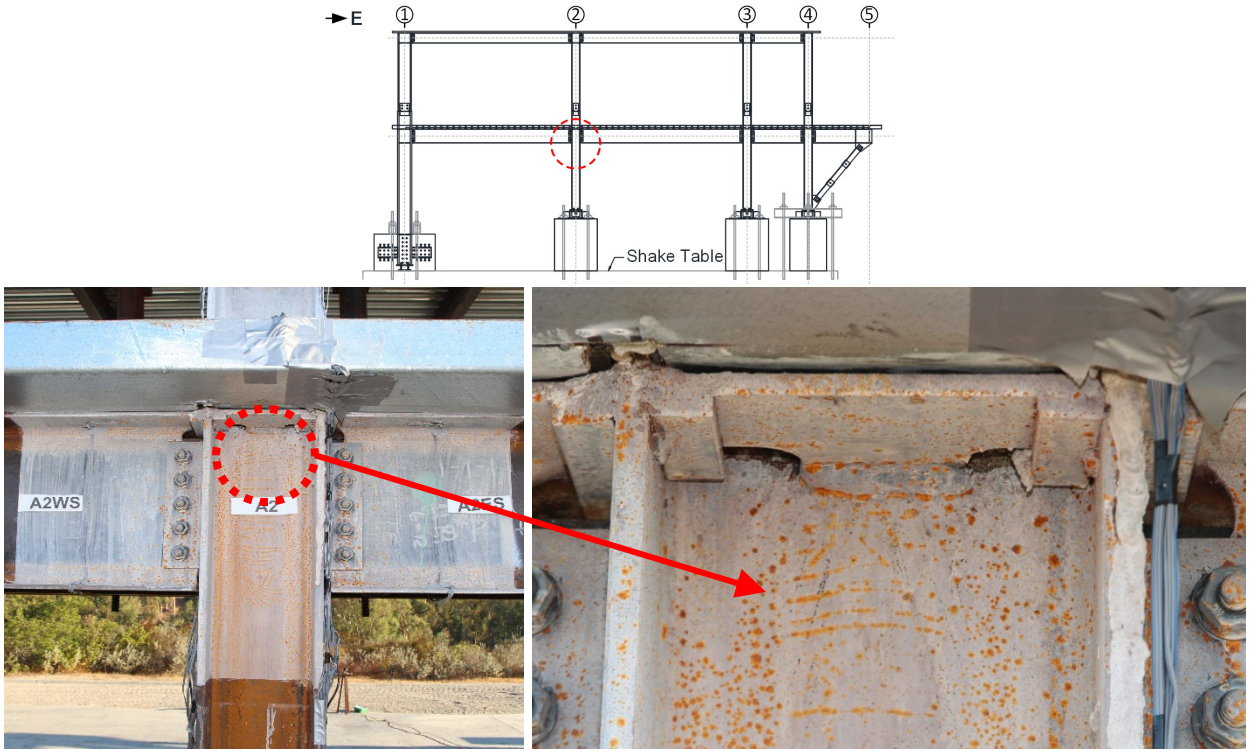

Figure 7.29 After Test 2B-3: Minor Flaking of Whitewash in Column Panel Zone of 2nd Floor TFW Connections

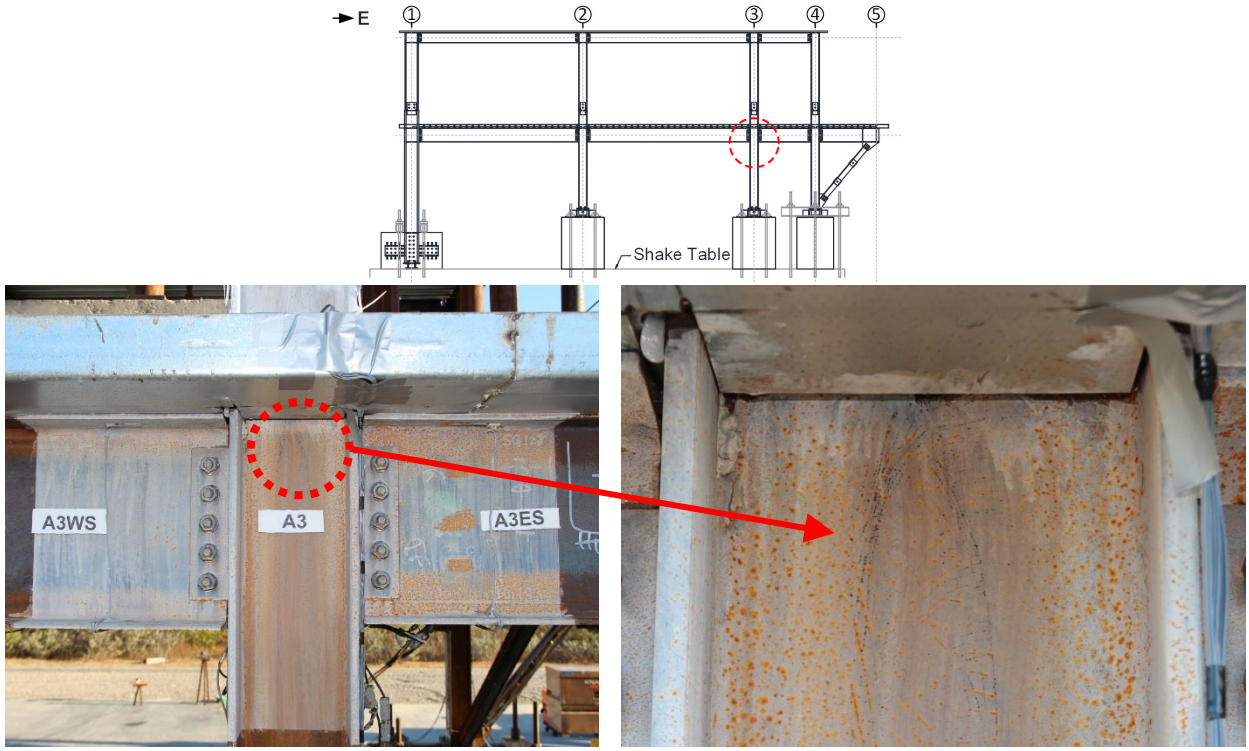

Figure 7.30 After Test 2B-3: Minor Flaking of Whitewash in Column Panel Zone of 2nd Floor BW Connections

7.3.3 Specimen Conditions after Test 2B-5

Mild yielding of collector bottom flange was detected at the roof AFW connections (Figure 7.31). At the roof west-side TFW connection (Figure 7.32), the scratching of whitewash on the collector web along the entire vertical edge of the shear tab indicates that the peak horizontal bolt slips were nearly uniform among the bolted joints on the collector web. This implies that relative axial displacement between the collector web and shear tab may be considerable. At the roof east-side TFW connections (Figure 7.33), the scratching of whitewash on the collector web occurred along the vertical edge of the bottom corner of the shear tab, indicating the rotation of these collector connections. At roof west-side BW connections (Figure 7.34), the whitewash scratching on the collector web took place along the vertical edges of both the top and bottom corners of the shear tab, indicating the rotation of these collector connections.

Figure 7.35 and Figure 7.36 show that significant yielding and minor local bucking of the collector bottom flanges occurred at the 2nd floor AFW connections. Also, slight yielding of the collector top flanges was detected at these AFW connections. For the 2nd floor TFW connections, as shown in Figure 7.37 and Figure 7.38, the whitewash scratching on the collector web along the edge of shear tab had a width of about 1/8 in. near the bottom corner of the shear tab. This width of whitewash scratching indicated that the rotation of these collector connections caused the bottom bolts to slip into bearing. For the 2nd floor west-side TFW connections (Figure 7.39), the whitewash scratching on the collector web along the shear tab edge had a width of about 1/8 in. and 1/16 in. near the bottom and top corners of the shear tab, respectively. It indicates that considerable rotations took place at these connections, which caused both the top and bottom bolts at theses connections to experience noticeable slips. It also suggests that the bottom bolts at these connections might have slipped into bearing during the testing. Figure 7.40 and Figure 7.41

respectively show slight whitewash flaking in the column panel zones at the 2nd floor TFW and BW connections, suggesting high stress flows passing through these regions. Figure 7.42 shows that no noticeable yielding was detected at the bottom ends of the lateral force-resisting columns. A few of thin cracks were observed on the concrete footing, suggesting that minor deformation may have taken place at the embedded column base connections. Figure 7.43 shows slight cracking of the concrete slab at the steel column faces of the 2nd floor BW collector connections.

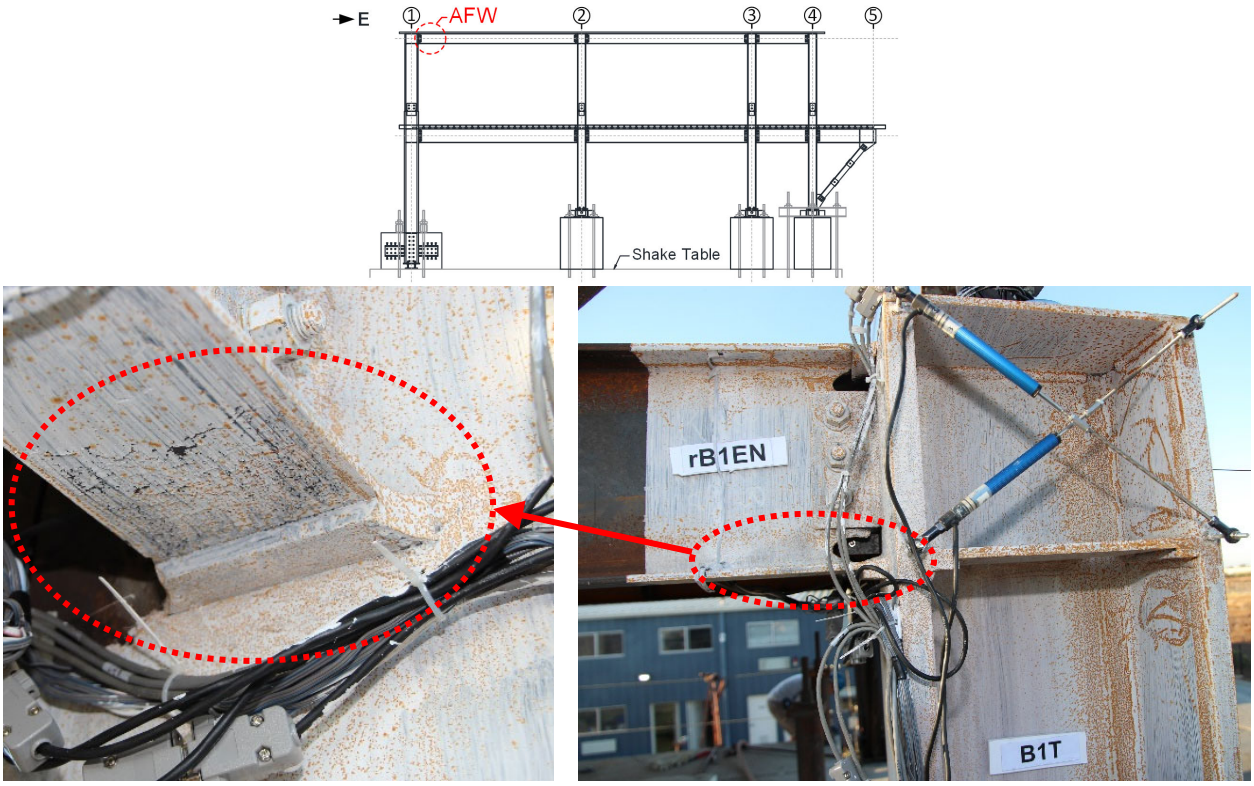

Figure 7.31 After Test 2B-5: Mild Yielding of Bottom Flange at Roof AFW Connections

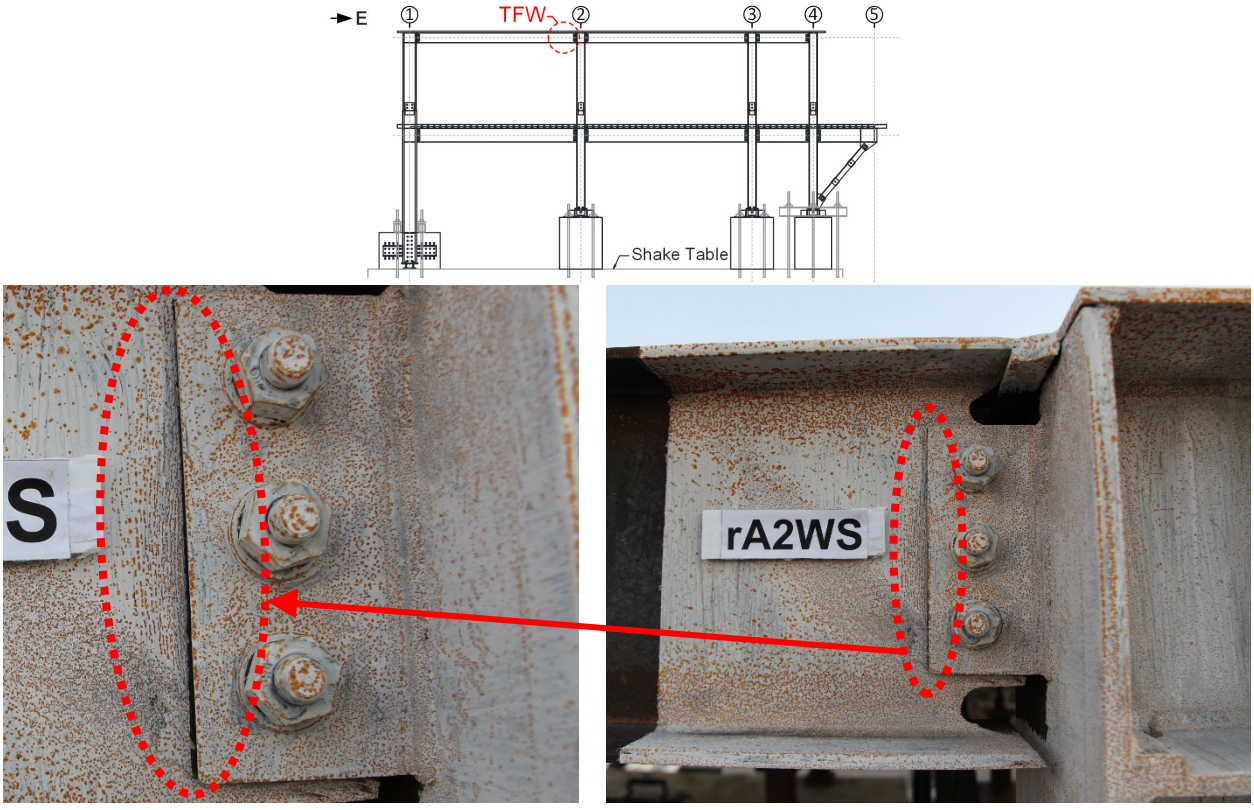

Figure 7.32 After Test 2B-5 Bolt Slippage at Roof West-Side TFW Connections

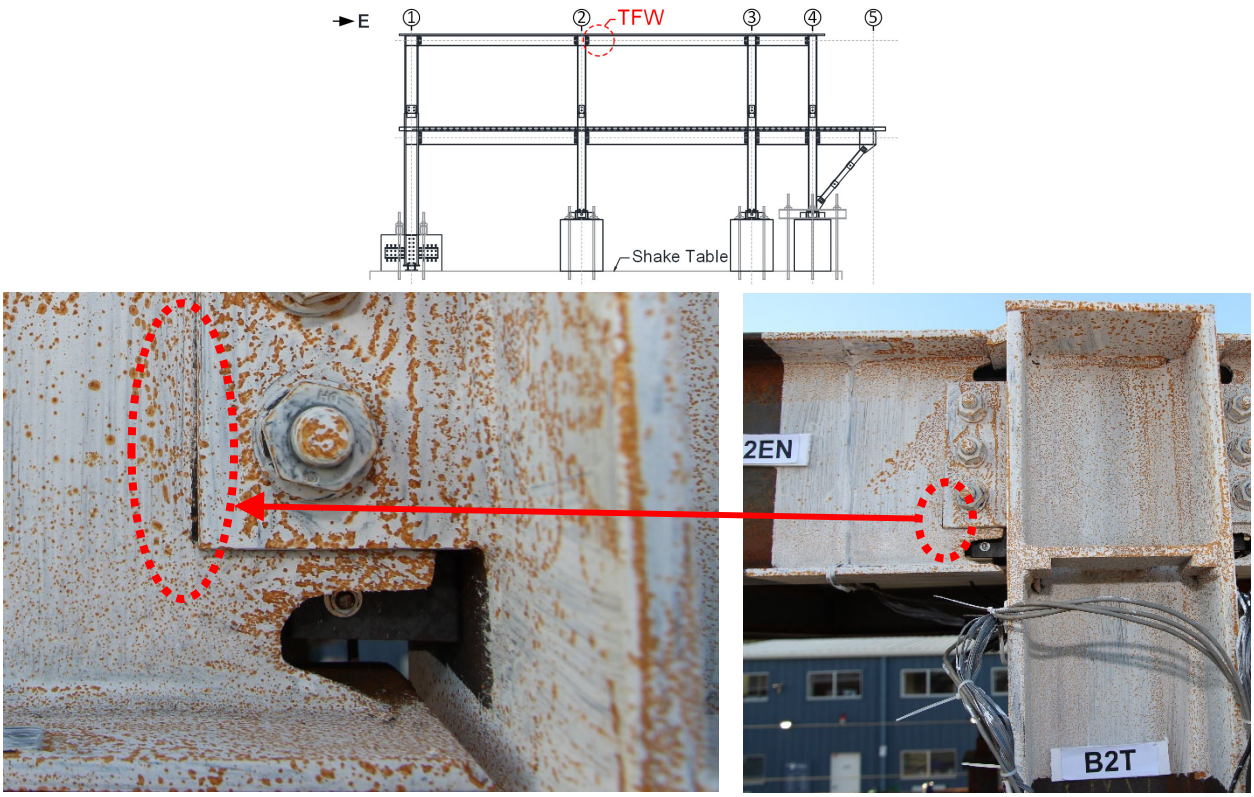

Figure 7.33 After Test 2B-5: Bolt Slippage at Roof East-Side TFW Connections

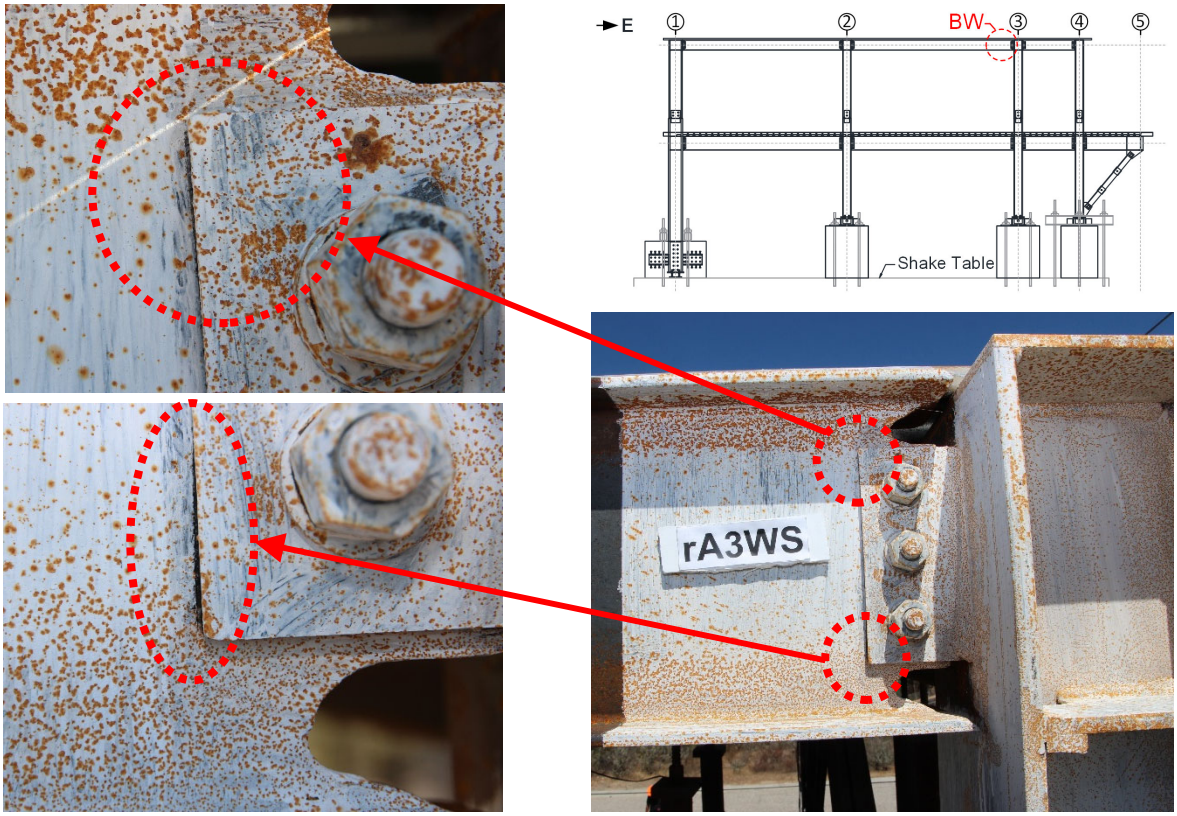

Figure 7.34 After Test 2B-5: Bolt Slippage at Roof West-Side BW Connections

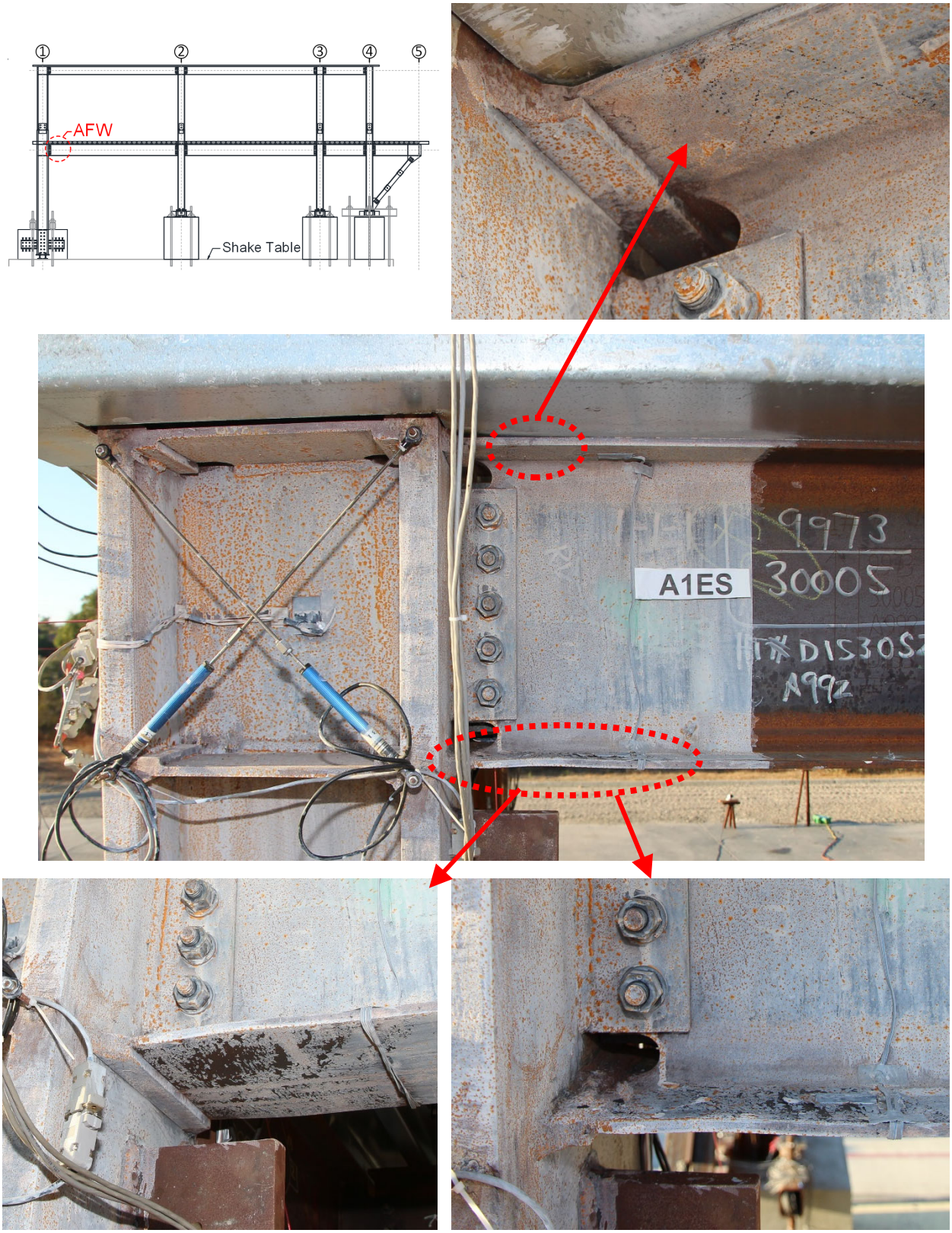

Figure 7.35 After Test 2B-5: Yielding and Local Buckling of Bottom Flange at 2nd Floor AFW Connection in South Frame

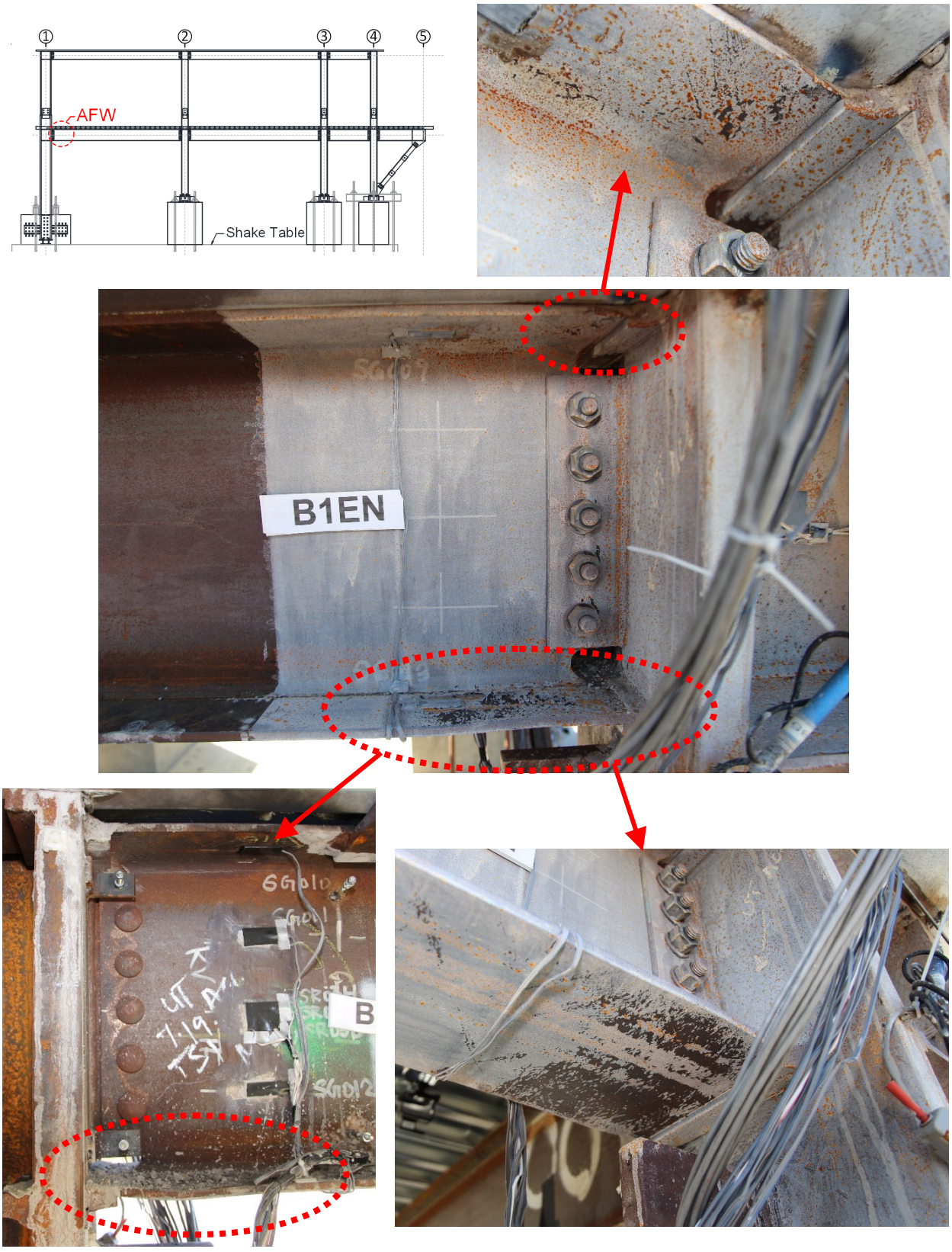

Figure 7.36 After Test 2B-5: Yielding and Local Buckling of Bottom Flange at 2nd Floor AFW Connection in North Frame

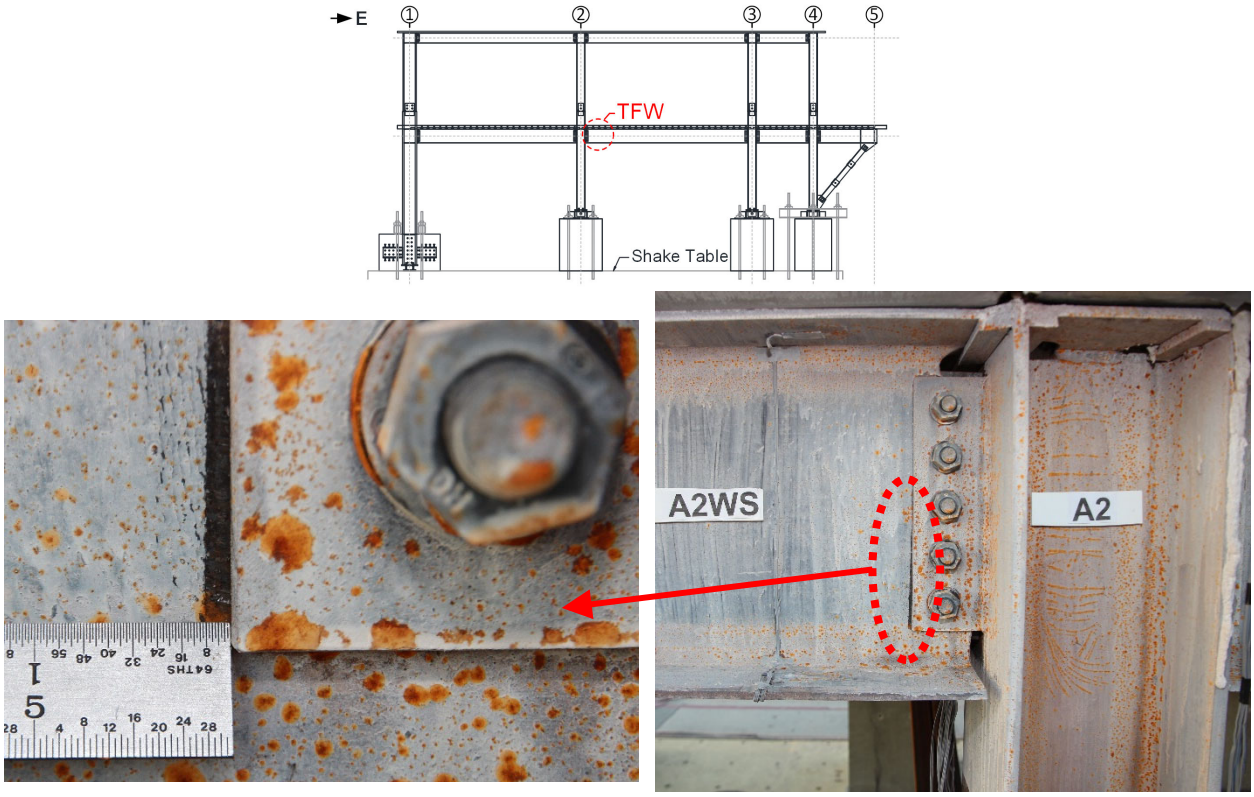

Figure 7.37 After Test 2B-5: Bolt Slippage at 2nd Floor West-Side TFW Connections

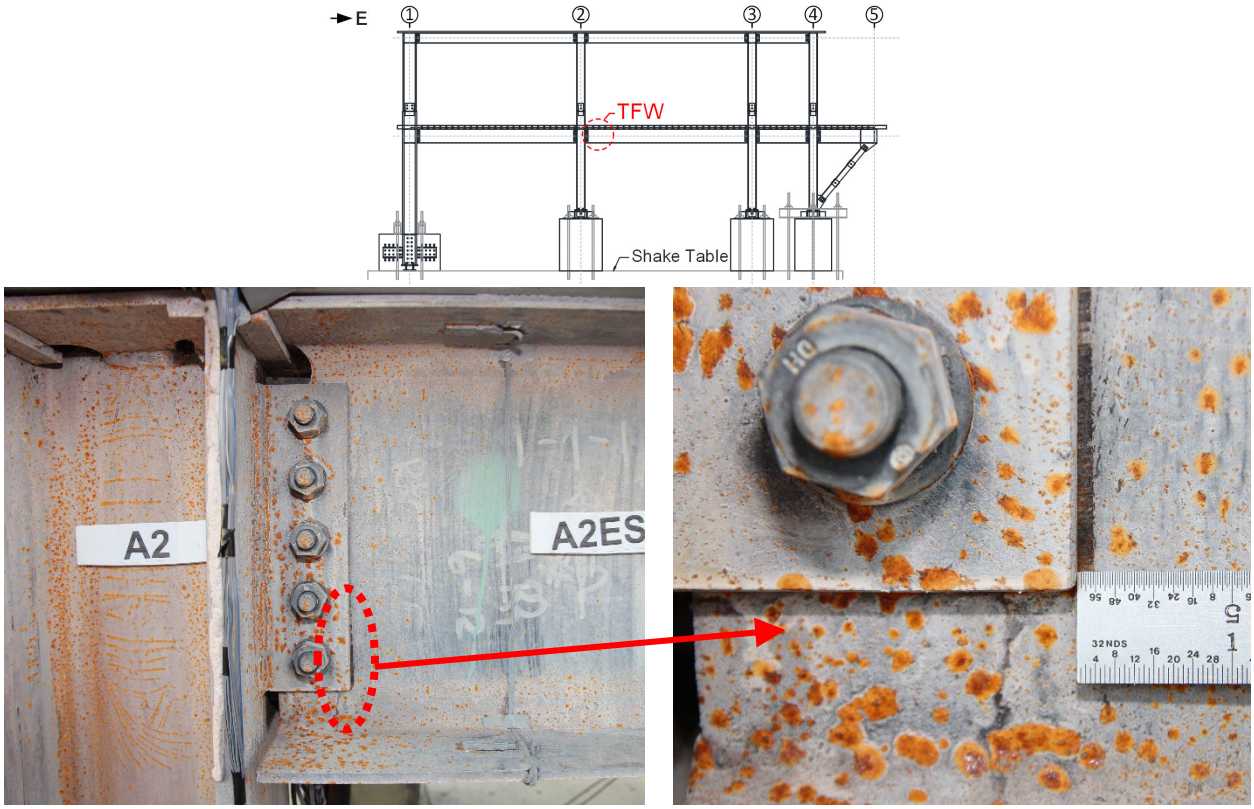

Figure 7.38 After Test 2B-5: Bolt Slippage at 2nd Floor East-Side TFW Connections

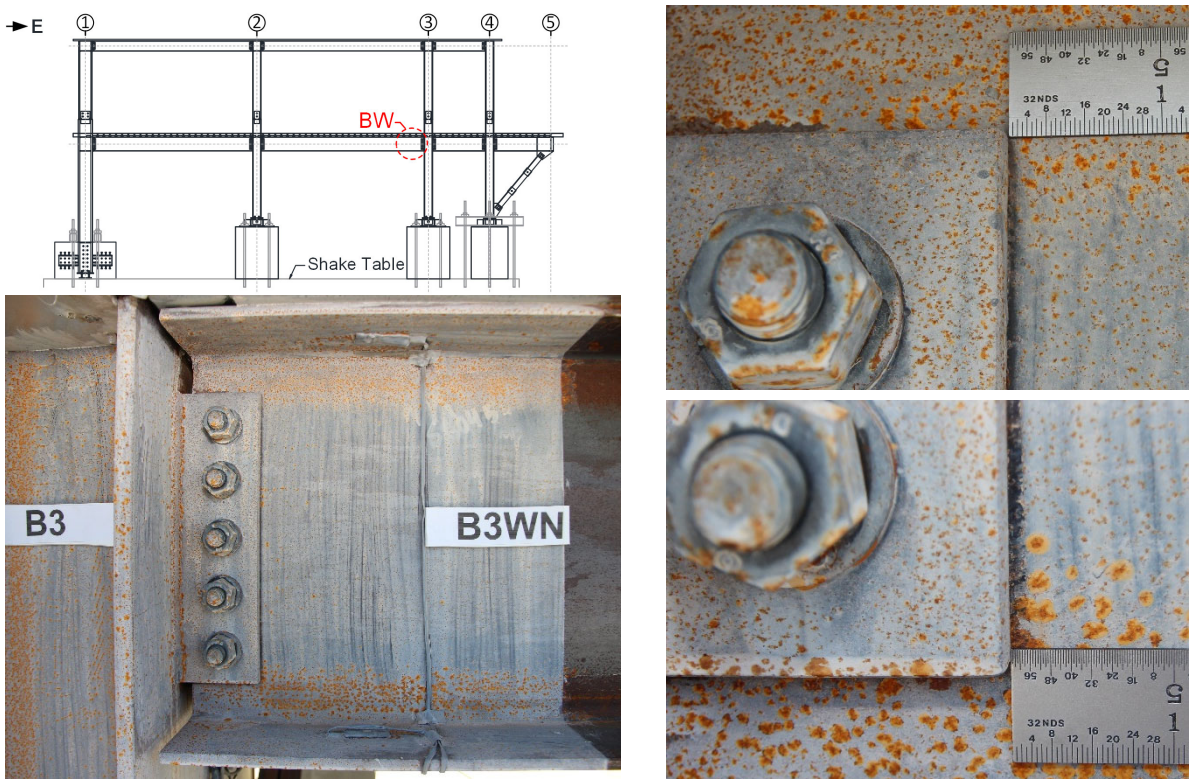

Figure 7.39 After Test 2B-5: Bolt Slippage at 2nd Floor West-Side BW Connections

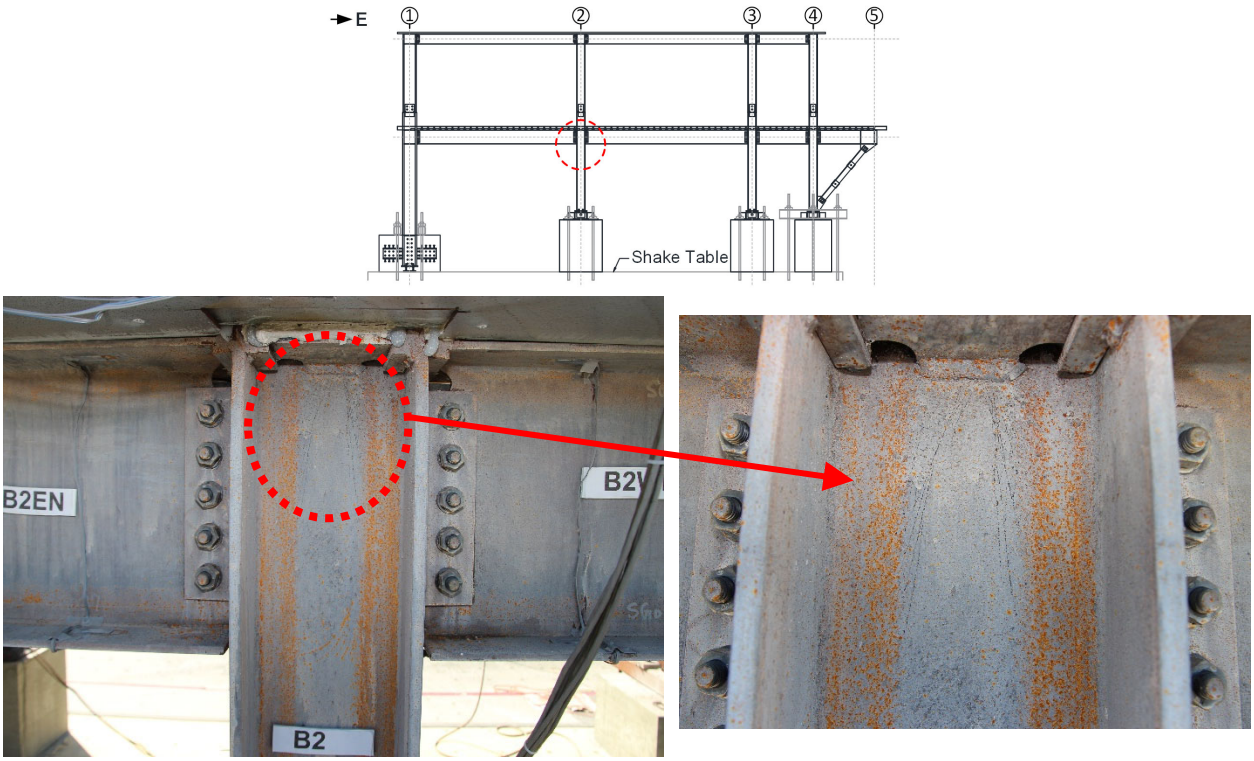

Figure 7.40 After Test 2B-5: Minor Flaking of Whitewash in Column Panel Zone of 2nd Floor TFW Connections

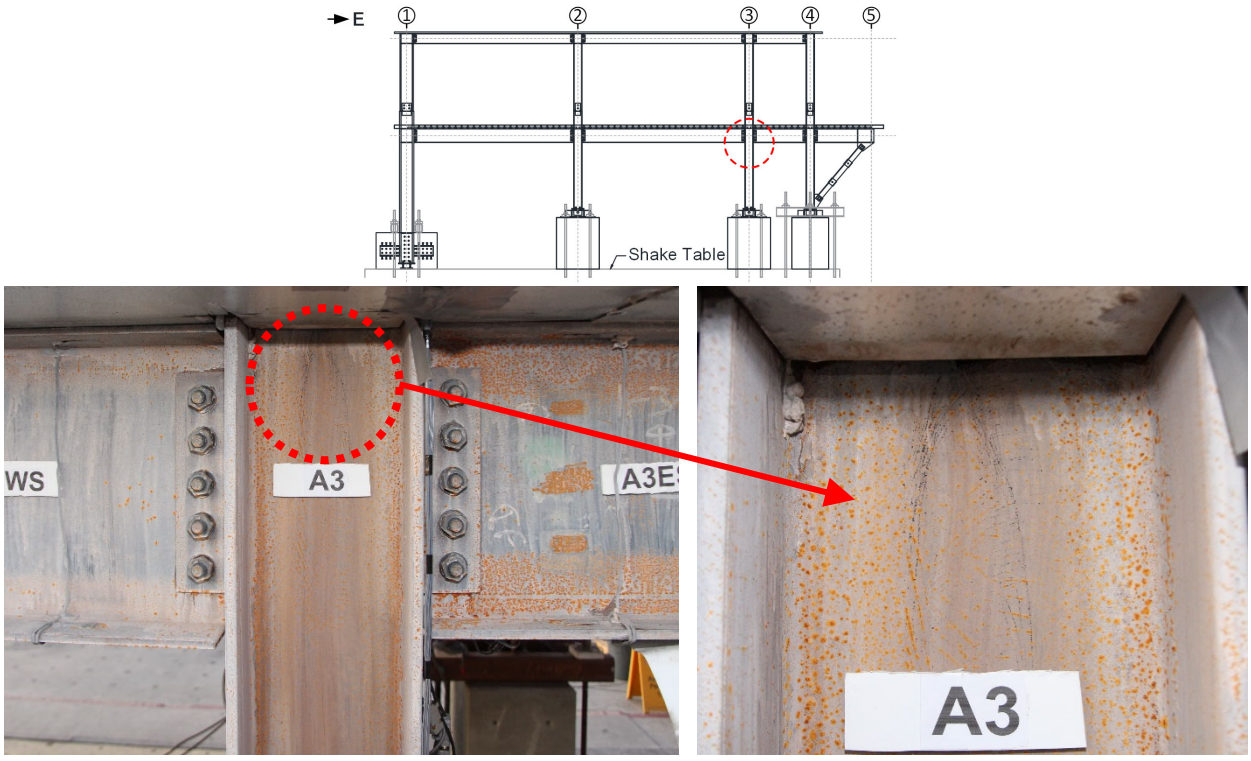

Figure 7.41 After Test 2B-5: Minor Flaking of Whitewash in Column Panel Zone of 2nd Floor BW Connections

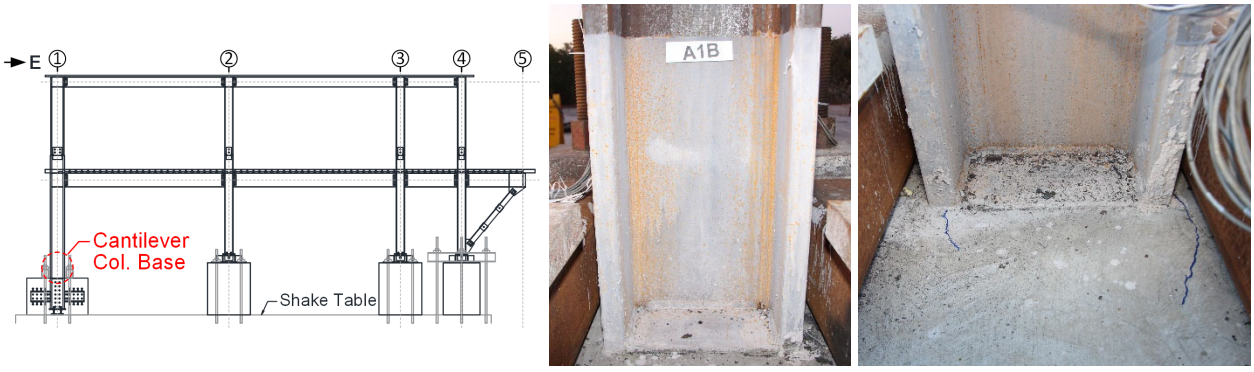

Figure 7.42 After Test 2B-5: Condition of Bottom End of Lateral Force-Resisting Column

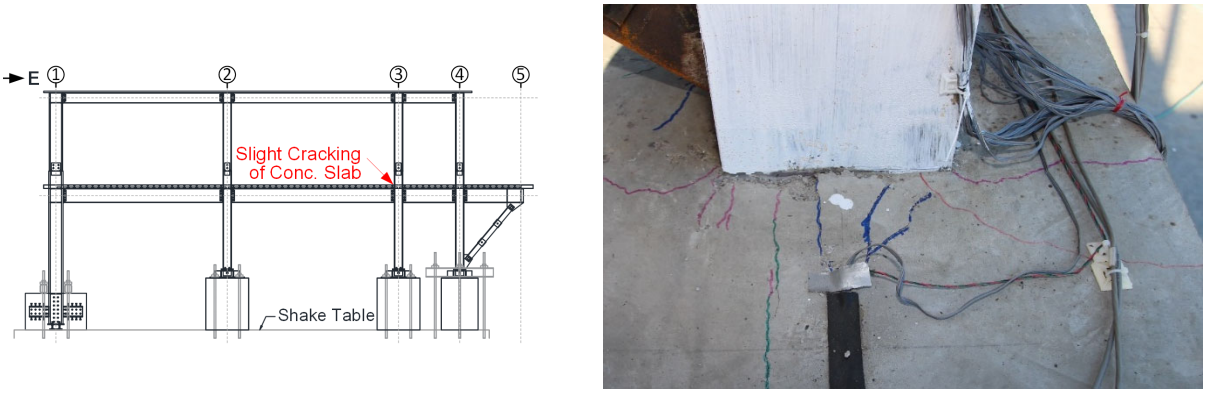

Figure 7.43 After Test 2B-5: Cracking of Slab near Column Face at 2nd Floor BW Connections

7.4 Detailed Results for Test 2B-5

7.4.1 Specimen Global Responses

Figure 7.44(a) and (b) shows the roof and 2nd floor acceleration time histories, respectively. The positive and negative peak roof accelerations were +2.71 g and −3.03 g, respectively, while positive and negative peak 2nd floor accelerations were +1.64 g and −1.38 g, respectively. The positive peak accelerations of the roof and 2nd floor reached at about the same time (6.004 s and 6.055 s, respectively). Likewise, the negative peak accelerations of the roof and 2nd floor occurred at about the same time (5.801 s and 5.832 s, respectively). Figure 7.45 shows that the positive and negative peak 2nd-story drift angles were +1.79 % and −1.81 % rad, respectively, while positive and negative peak 1st-story drift angles were +1.75 % and −1.64 % rad, respectively. The positive peak story drifts in the 1st and 2nd stories reached at about the same time (6.031 s and 6.047 s, respectively). Likewise, the negative peak story drifts in the 1st and 2nd stories reached at roughly the same time (5.820 s and 5.824 s, respectively). In general, the peak positive floor accelerations and negative story drifts occurred at the same time. The peak negative floor accelerations and positive story drifts were reached at round the same time. Since the collectors is the main subject of this study and their force demands are considered more related to the floor accelerations, detailed responses of the structural members, including the collectors and columns in the test building, at the instants when the specimen reached positive and negative peak accelerations were elaborated in the subsequent sections.

Figure 7.46(a) and (b) show the 2nd story and 1st-story hysteretic responses, respectively. The two stories experienced moderate inelastic responses. Figure 7.47 shows a good agreement between the measured story shears determined from two methods for the two stories.

Figure 7.48 shows the measured roof accelerations at seven locations. It can be found that roof accelerations at the four instrumented column locations (Columns N1, N4, S1, and S4) were very similar. By contrast, from the linear regression results shown in Figure 7.49 and the peak response values shown in Figure 7.48, it seems to indicate that the accelerations at the three added masses were slightly higher than those at the column locations. Also, a mild variation between the accelerations at the added masses and column locations was also observed. For example, the R-squared value of the linear regression between the accelerations at middle added mass and Column N1 was about 0.88 [see Figure 7.49(a)]. The variation in acceleration also existed between the added masses, which can be exemplified by an R-squared value of about 0.88 from the linear regression between accelerations at west and middle added masses [see Figure 7.49(i)]. These variations could be due to the small slippage of added masses. Therefore, the roof acceleration was determined by a weight average of these measured accelerations.

Figure 7.50 shows the measured 2nd floor accelerations at six locations, including four column locations, middle-west added mass, and east chord. From the linear regression results shown in Figure 7.51, it seems to indicate that the accelerations among these instrumented locations were very similar. However, some minor variation in acceleration response between the east chord and other places occurred near the positive peak acceleration responses [see the top right corners of Figure 7.51 (f) and (g)]. This could be due to the 2nd mode action of the test specimen, which was dominated by the vertical vibration of the cantilever span at the 2nd floor. In addition, as shown in Figure 7.50, the magnitude of negative peak acceleration of the added masses was somewhat smaller than those at other places. It could be due to the random noise. Thus, instead of the measured acceleration at the added mass, the weighted average of the measured

accelerations at the various locations on the 2nd floor was used to represent the 2nd floor acceleration.

Figure 7.52 and Figure 7.53 show the column bending moment diagrams at the positive and negative peak accelerations, respectively. The following observations can be:

(1) The inflection point in the 1st-story lateral force-resisting columns (Columns N1 and S1) was very close to the top end of the columns.

(2) The inflection point in the 2nd-story lateral force-resisting columns (Columns N1 and S1) was slightly above the mid-height of the columns.

(3) For each gravity column, the magnitude of the shear forces in the 1st and 2nd story columns were about the same.

(4) In the 2nd-story gravity columns, the inflection point was slightly above the mid-height of the columns.

Figure 7.54 and Figure 7.55 show the column axial forces at the positive and negative peak accelerations, respectively. In general, the level of overturning axial forces in was very low when compared to the axial strength of the columns.

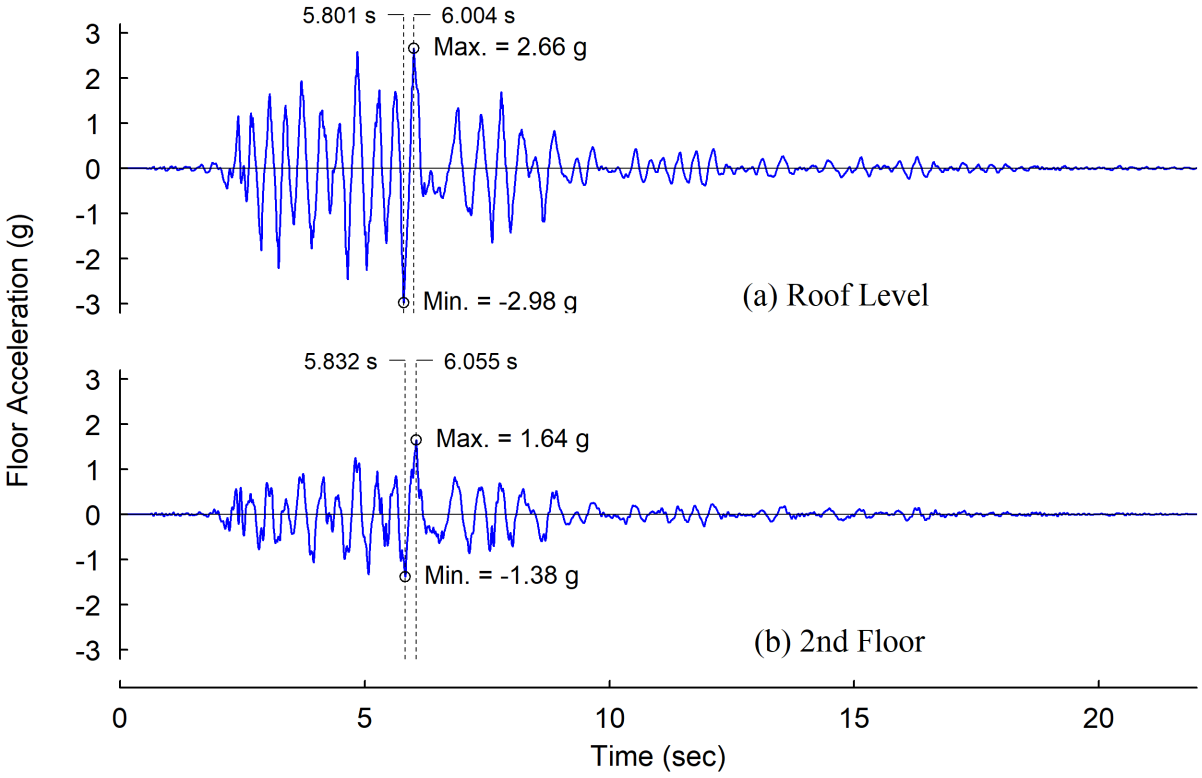

Figure 7.44 Test 2B-5: Floor Acceleration Reponses

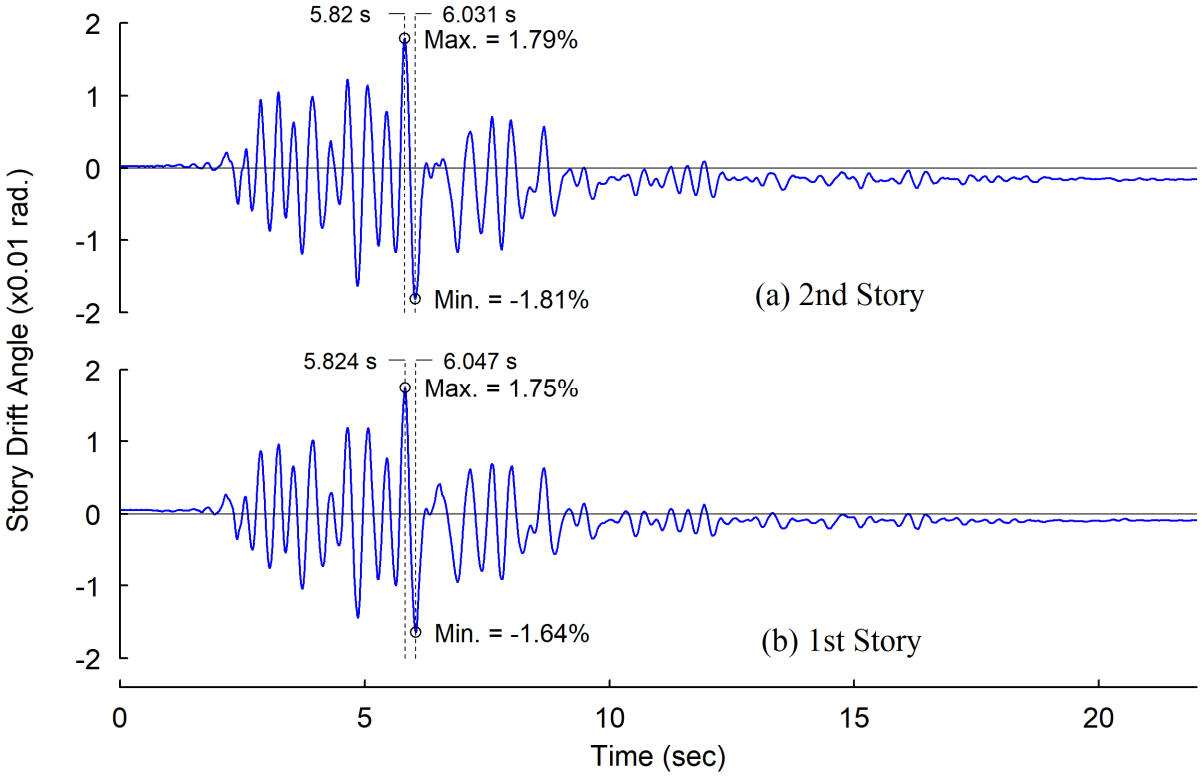

Figure 7.45 Test 2B-5: Story Drift Angle Reponses

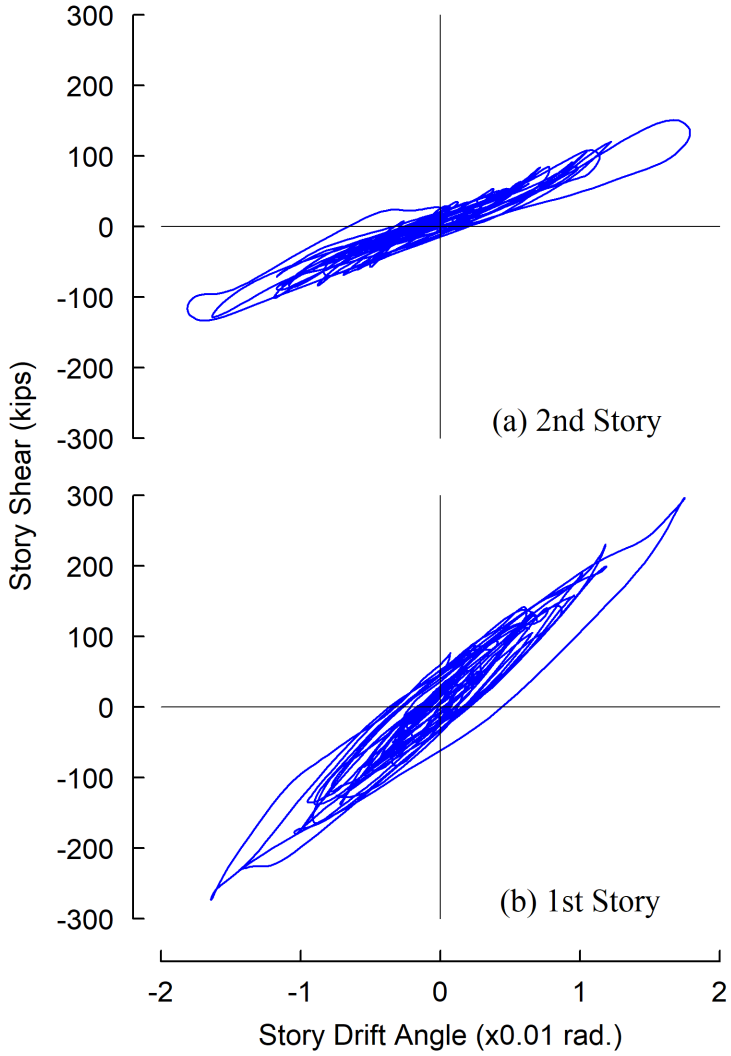

Figure 7.46 Test 2B-5: Hysteresis Responses

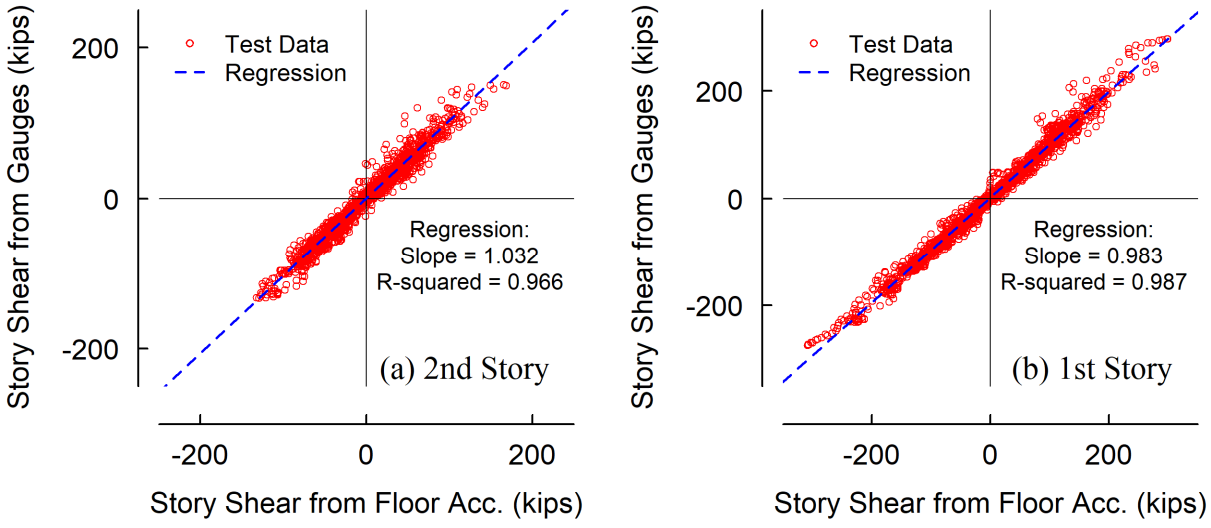

Figure 7.47 Test 2B-5: Comparison of Story Shears Measured from Two Methods

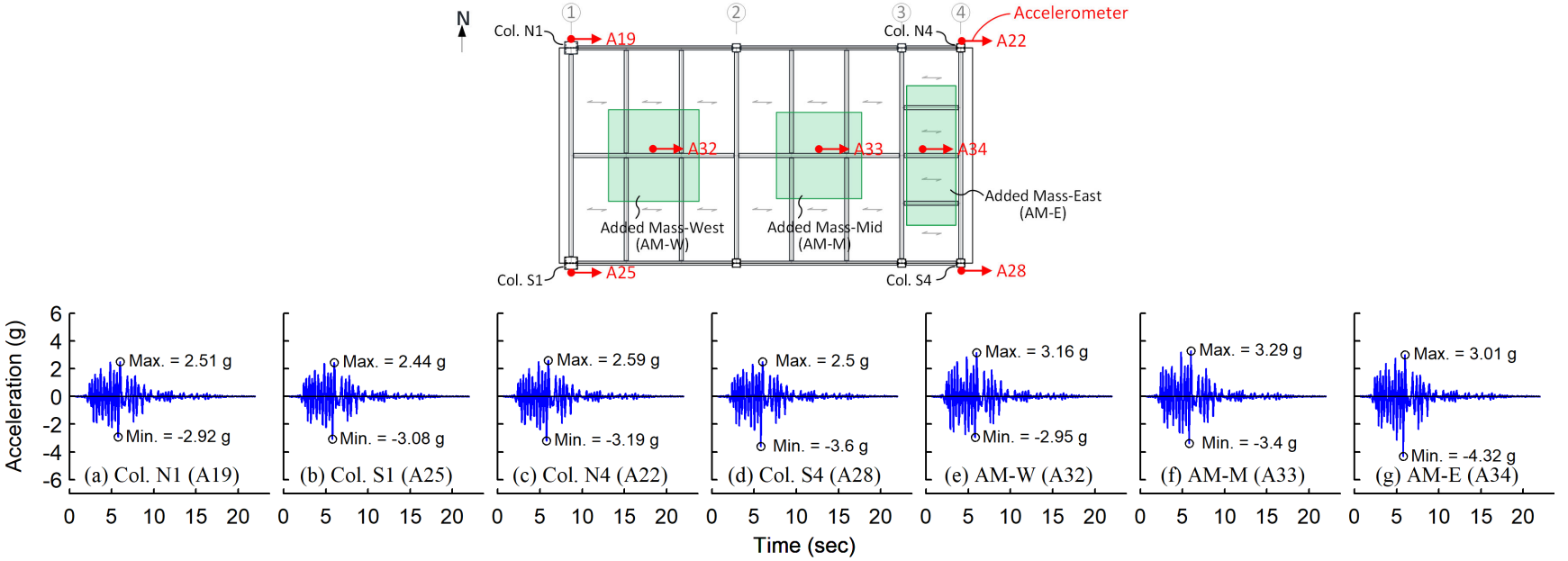

Figure 7.48 Test 2B-5: Measured Roof Accelerations at Various Locations

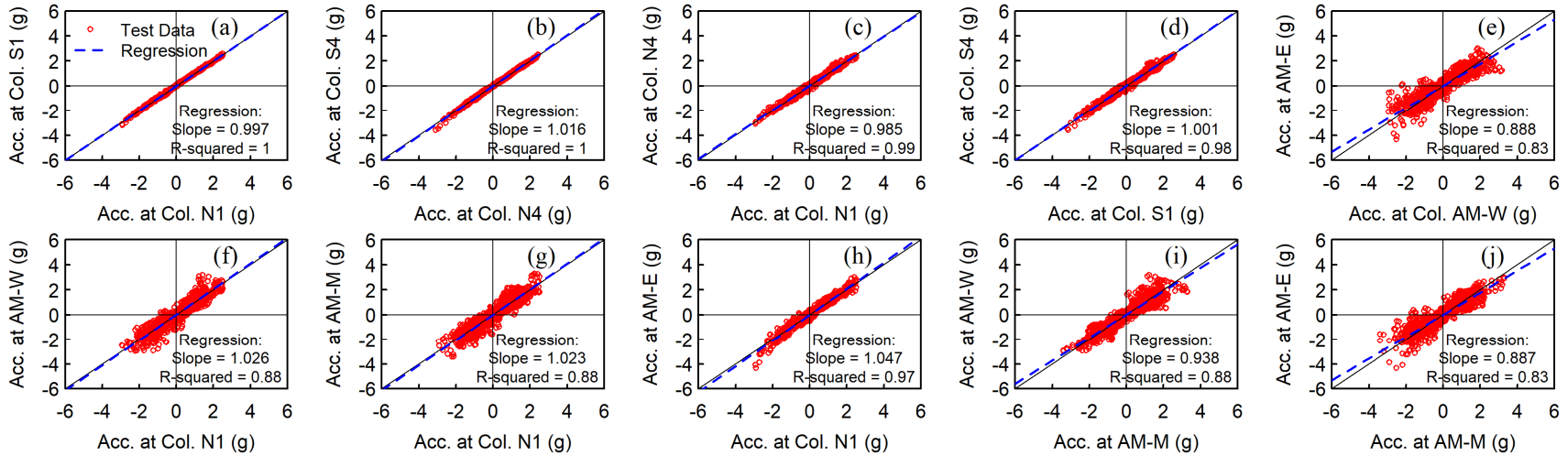

Figure 7.49 Test 2B-5: Comparison of Roof Accelerations Measured at Various Locations

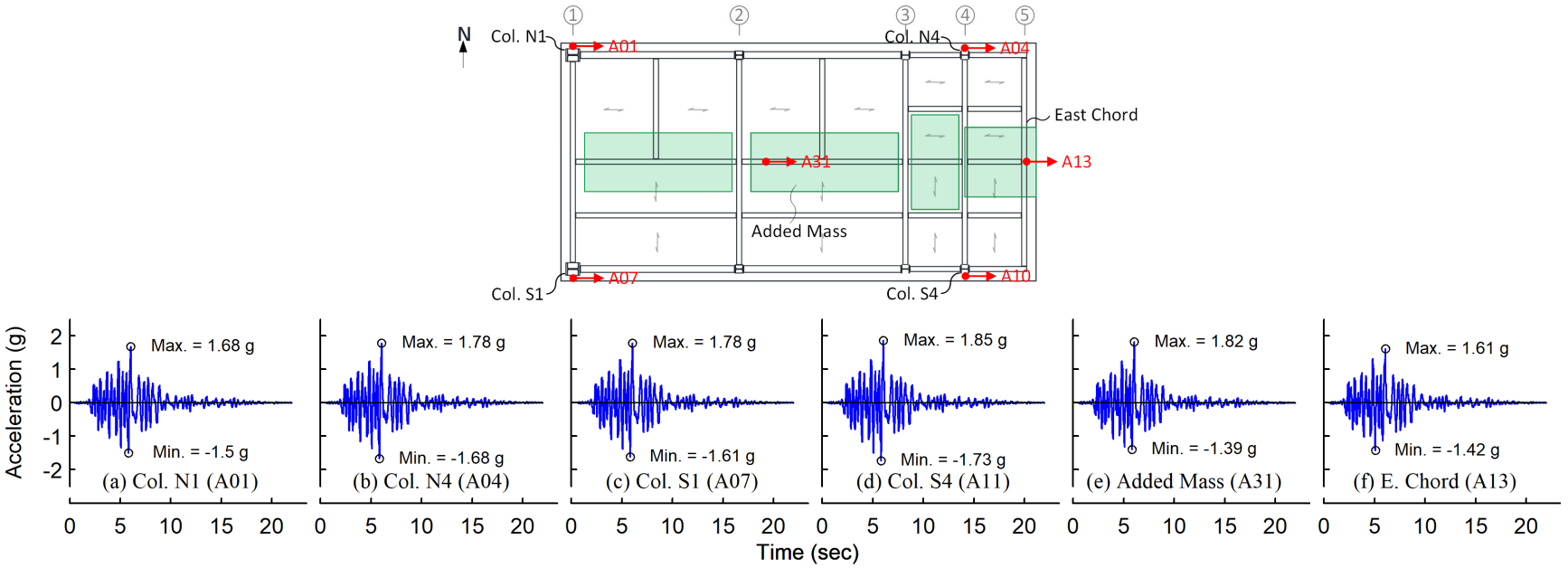

Figure 7.50 Test 2B-5: Measured 2nd Floor Accelerations at Various Locations

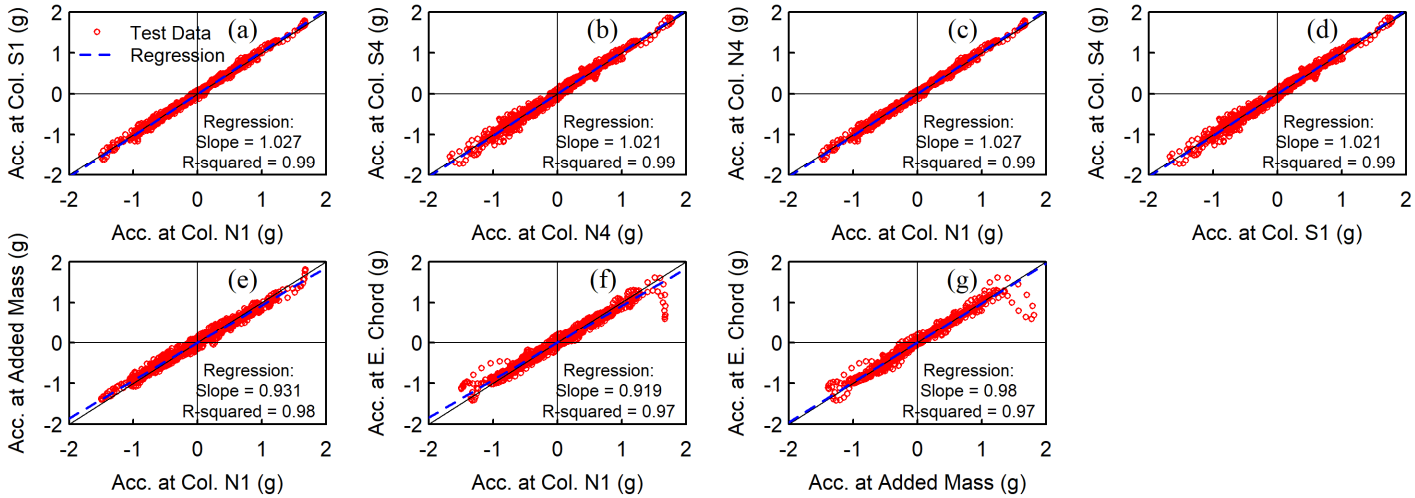

Figure 7.51 Test 2B-5: Comparison of 2nd Floor Accelerations Measured at Various Locations

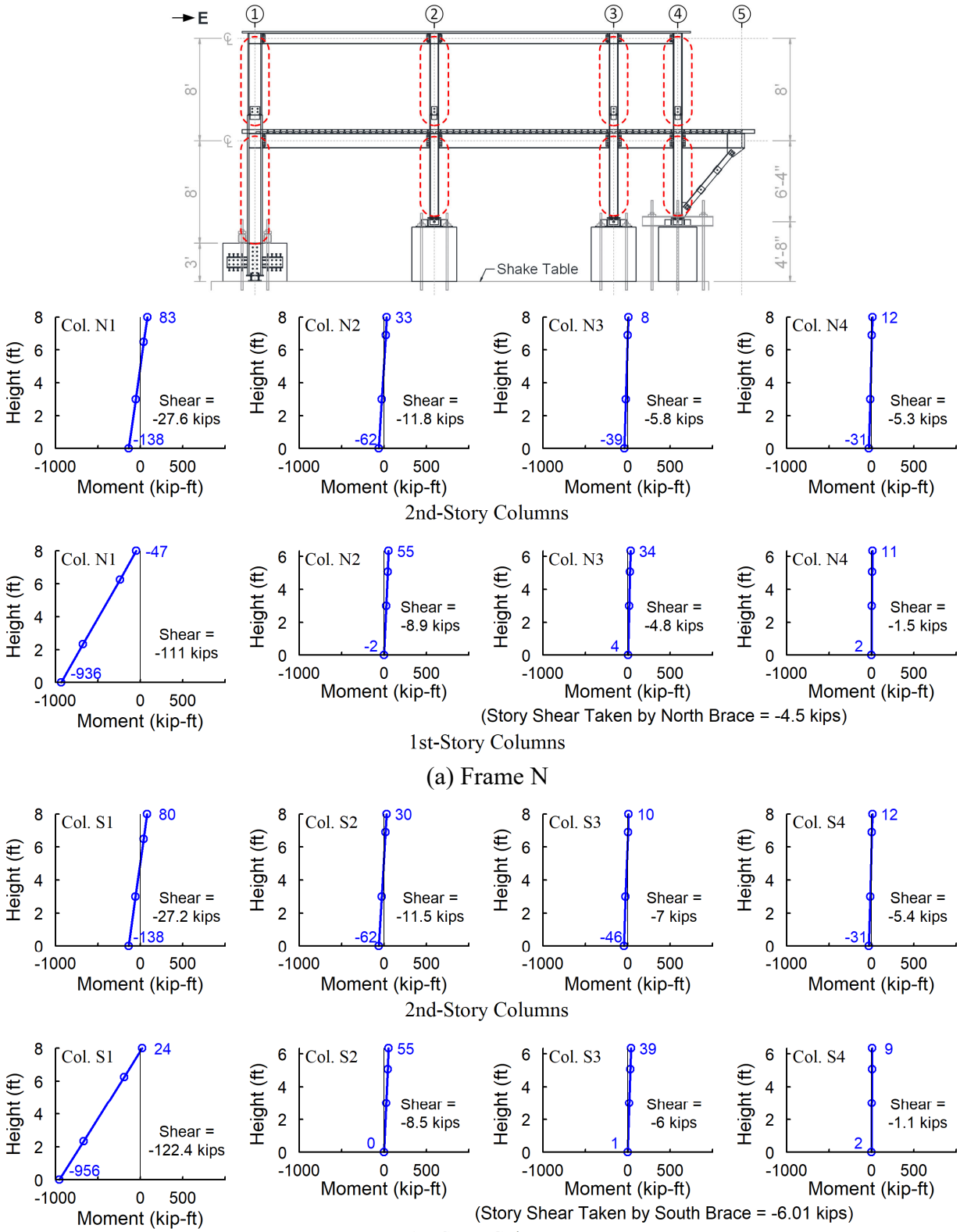

Figure 7.52 Test 2B-5: Column Bending Moment Diagrams at Peak Positive Acceleration

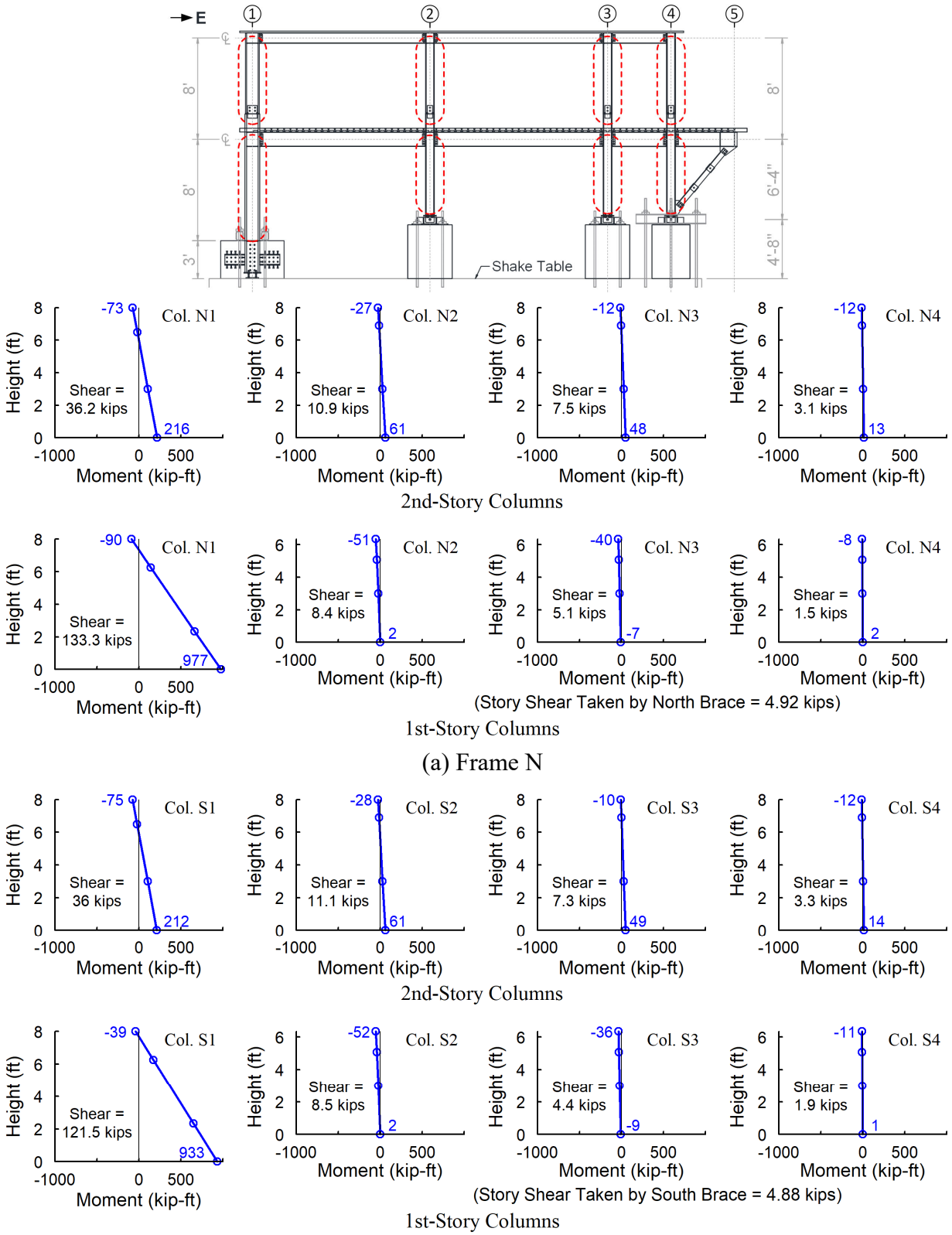

Figure 7.53 Test 2B-5: Column Bending Moment Diagrams at Peak Negative Acceleration

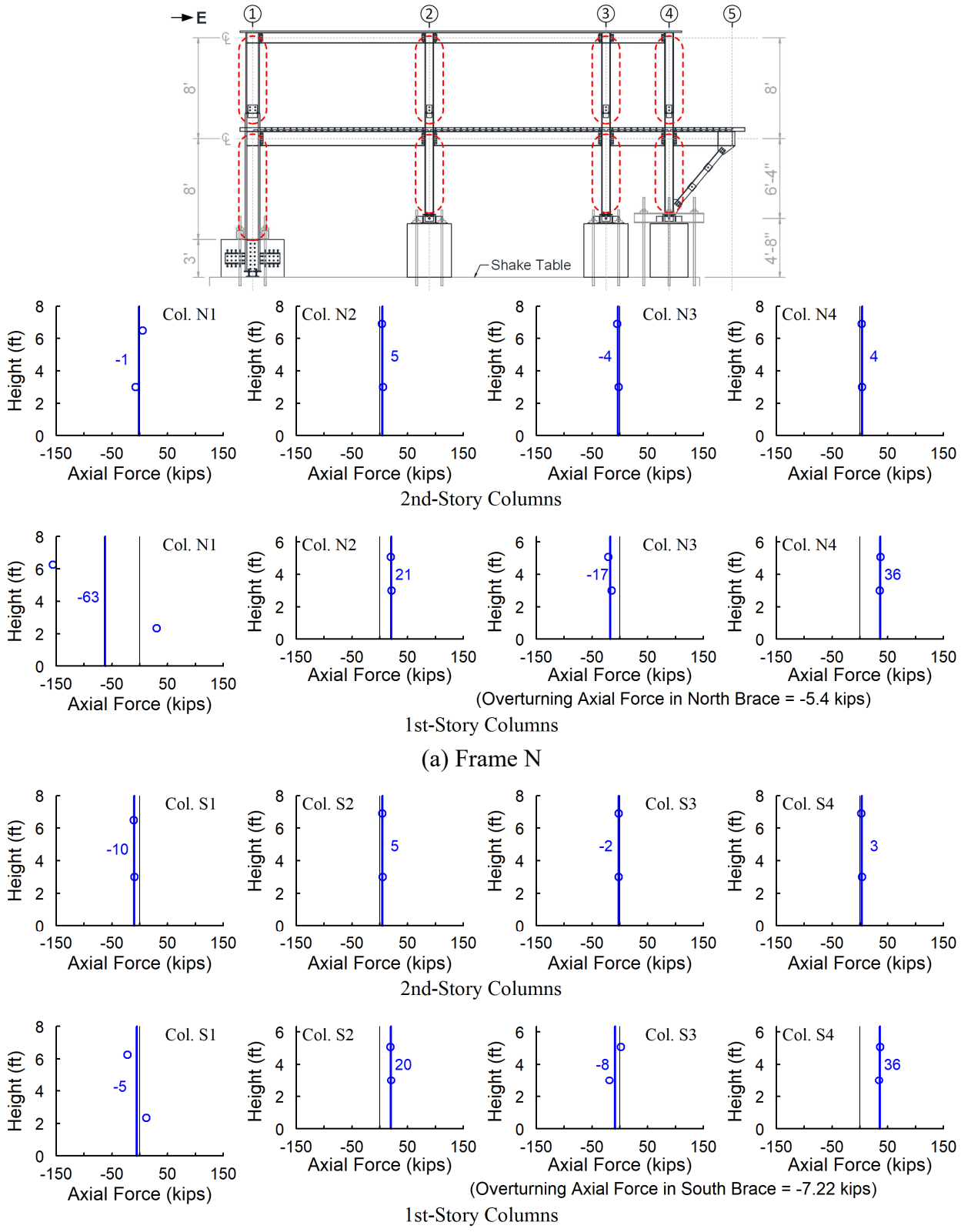

Figure 7.54 Test 2B-5: Column Axial Force Diagrams at Peak Positive Acceleration

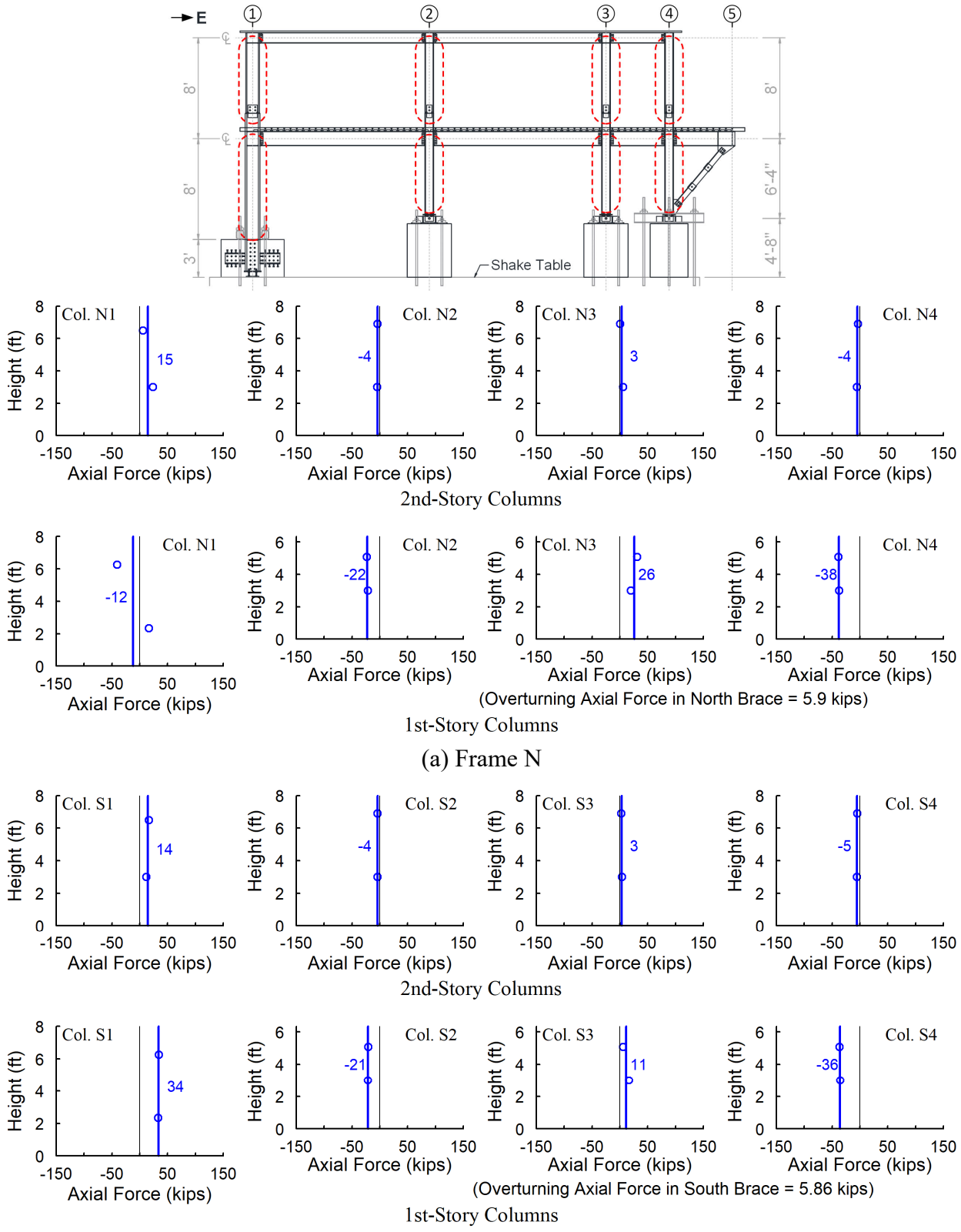

(a) Frame N

(b) Frame S

Figure 7.55 Test 2B-5: Column Axial Force Diagrams at Peak Negative Acceleration

7.4.2 Collector Strain and Stress Profiles

Figure 7.56 and Figure 7.57 show the measured strain profiles along the Collectors 1 beams at the roof and 2nd floor levels, respectively. Figure 7.58 and Figure 7.59 show the measured strain profiles along the Collectors 2 beams at the roof and 2nd floor levels, respectively. In each of these figures, both the strain profiles measured at the positive and negative accelerations are plotted. In general, the strain profiles in the collectors are not uniformly distributed and a notable strain gradient can be found on most of the measured strain profiles, indicating that the bending action in the collectors is considerable. Recall that it is common to assume in design that the collector is axially loaded by the seismic forces.

Figure 7.60 and Figure 7.61 show the measured strain profiles near the collector-to-column connections at the roof and 2nd floor levels, respectively. Near the north roof bare steel AFW connection (see the leftmost sub-figure in Figure 7.60), the strain profiles were roughly linear at both positive and negative peak roof accelerations, indicating that this connection acted like a moment connection. A significant slope of these roughly linear strain profiles suggests that this connection was subjected to significant bending moments. However, the neutral axis of each strain profile was located above the centroid of the beam section, suggesting that the beam section was under combined axial forces and bending moments.

Near the 2nd floor composite AFW connections (see the leftmost sub-figures Figure 7.61), the strain profile was roughly linear along the depth of the steel beam section with negligible tensile strains developed in the concrete slab at the positive peak floor acceleration, at which this collector section was subjected to negative bending and with a compressive axial force. This strain pattern implies that the negative bending action resulted in a gap between the concrete slab and steel column face such that no significant tensile strains could be developed in the concrete slab near

the AFW connection. It can be considered that the collector end section only relied on the steel beam section to transmit the member forces when it was under negative bending. On the other hand, the strain profile was roughly linear across the entire depth of the composite section at the negative peak floor acceleration, at which this collector section was subjected to a positive bending moment and a tensile axial force. This strain pattern indicates that the AFW connection utilized the fully composite action to transmit the collector member forces when the connection was under positive bending. It should be noted that the concrete slab was in compression mainly due to the bending, which was opposite to a total tensile axial force on the entire composite section of the collector. In this case, the steel section played a "main" role in transmitting the collector axial force, while the concrete slab played a "counteracting" role.

Near the west-side roof bare steel TFW connections (see the second left sub-figure in Figure 7.60), the top flange was in compression while relatively uniform and small tensile strains developed in the web next to the bolted joints at the positive peak roof acceleration, at which this collector section was subjected to positive bending and a compressive axial force. The uniform strain distribution developed in the central portion of the web implies that these bolted joints might have gotten into the inelastic range (such as slip or bolt bearing). In this direction of combined forces, the top flange played a "main" role in transmitting the collector axial force, while the bolted joints in the web played a "counteracting" role. On the other hand, the strain profile at the negative peak roof acceleration shows that the top flange was in tension while relatively uniform and small compressive strains developed in the web. This suggests that, when the bare steel TFW connection was under simultaneous tension and negative bending, the top flange played the "main" role in transmitting the collector axial force, while the forces in developed the web bolted joints counteracted the collector axial force delivery.

Near the west-side 2nd floor composite TFW connections (see the second left sub-figures in Figure 7.61), the strain profile at the positive peak floor acceleration showed that significant compressive strains developed in the concrete slab, while small tensile strains developed in the web. In the meantime, the strain developed in the top flange was low. This suggests that, for a composite TFW connection under simultaneous compression and positive bending, the concrete slab played the "main" role in transmitting the collector axial force, while the web bolted joints play a "counteracting" role and the contribution from top flange might be low. On the other hand, the strain profile at the negative peak floor acceleration showed significant tensile strains in the top flange, with relatively small compressive strains in the collector web and negligible tensile strains in the concrete slab. It suggests that, for a composite TFW connection under simultaneous tension and negative bending, the top flange played a "main" role in delivering the collector axial force, while the web bolted joints played a "counteracting" role and the concrete slab effect was negligible.

Near the east-side roof bare steel TFW connections (see the central sub-figure in Figure 7.60), the top flange was in tension with a strain magnitude close to that of the compressive strains developed in the web at the positive peak roof acceleration, at which this collector section was subjected to a negative bending and a compressive axial force. In this direction of combined forces, the web bolted joints played a "main" role in conveying the collector axial force, while the top flange played a "counteracting" role. On the other hand, the top flange was in compression with a strain magnitude close to that of the tensile strains developed on the web at the negative peak roof acceleration. In this direction of combined forces, again, the web bolted joints played a "main" role in transmitting the collector axial force, while the top flange played a "counteracting" role.

Near the east-side 2nd floor composite TFW connections (see the central sub-figures in Figure 7.61), the strain profile at the positive peak floor acceleration shows that relatively uniform compressive strains developed in the collector web, while tensile strains developed in the top flange and concrete slab was very low. This suggests that, for a composite TFW connection under simultaneous compression and negative bending, the bolted joint played a "main" role in transmitting the collector axial load, while the concrete slab effect was negligible and the contribution from the top flange might be low. On the other hand, the strain profile at the negative peak floor acceleration shows that significant compressive strains developed in the concrete slab, while relatively uniform and small tensile strains developed in the top flange and web of the steel section. This suggests that, for a composite TFW connection under simultaneous tension and positive bending, the top flange and web bolted jointed played a "main" role in conveying the collector axial force, while the concrete slab joints played a "counteracting" role. Since it requires to mobilize both top flange and bolted joints to convey the collector axial force while the concrete slab develop a significant force opposite to the effects of the top flange and bolted joints. Among all combinations of combined axial and bending forces, simultaneous tension and positive bending tends to induce the highest tensile axial force demand to the steel connection, which includes the top flange weld and web bolted joints, of a composite TFW connection.

Near the roof bare steel BW connections (see the rightmost two sub-figures in Figure 7.60), at both positive and negative peak roof accelerations, the region of the collector web next to the bolted joints developed relatively linear strain profiles while both flanges were about stress free, indicating that web bolted joints resisted all the member force demand. For the west-side BW connection, the neutral axis of the strain profiles was slightly above the centroid of the steel beam section, indicating a moderate axial force demand. For the east-side BW connection, the neutral

axis of the strain profiles was around the centroid of the steel beam section, indicating that axial force demand was low.

Near the west-side 2nd floor composite BW connections (see the second right sub-figures in Figure 7.61), the strain profile at the positive peak floor acceleration shows that significant compressive strains developed in the concrete slab, while small tensile strains were developed in the web. This suggests that, for a composite BW connection under the simultaneous compression and positive bending, the concrete slab played a "main" role in conveying the collector axial force, while the web bolted joints played a "counteracting" role. On the other hand, the strain profile at the negative peak floor acceleration showed that only the collector web developed noticeable compressive strain in a relatively linear profile, while the strains in concrete and flanges were negligible. This suggests that, for a composite BW connection under the negative bending, the web bolted joints conveyed all the collector member force as if the composite BW connections behaved like a bare steel BW section.

Near the east-side 2nd floor composite BW connections (see the rightmost sub-figures in Figure 7.61), the strain profile at the positive peak floor acceleration shows that only the collector web developed noticeable compression strains in a relatively linear profile, while tensile strains developed in the top flange and concrete slab were negligible. This suggests that, for a composite BW connection under negative bending, the web bolted joints conveyed all the collector member force as if the composite BW connections became a bare steel BW section. On the other hand, the strain profile at the negative peak floor acceleration shows that significant compressive strains developed in the concrete slab, while small tensile strains were developed on the web. This suggests that, for a composite BW connection under simultaneous tension and positive bending,

the web bolted joints played a “main” role in conveying the collector axial force, while the concrete slab played a “counteracting” role.

Based on the measured strains in the collectors as shown in Figure 7.60 and Figure 7.61, the fiber section approach was used to compute the collector internal force. Figure 7.62 and Figure 7.63 show the fiber section strain profiles along the Collectors 1 beams at the roof and 2nd floor levels, respectively. Figure 7.64 and Figure 7.65 show the fiber section strain profiles along the Collectors 2 beams at the roof and 2nd floor levels, respectively. Figure 7.66 and Figure 7.67 show the fiber section strain profiles near the collector-to-column connections at the roof and 2nd floor levels, respectively. Figure 7.68 and Figure 7.69 show the fiber section stress profiles near the collector-to-column connections at the roof and 2nd floor levels, respectively. Figure 7.70 and Figure 7.71 show the fiber axial force profiles near the collector-to-column connections at the roof and 2nd floor levels, respectively.

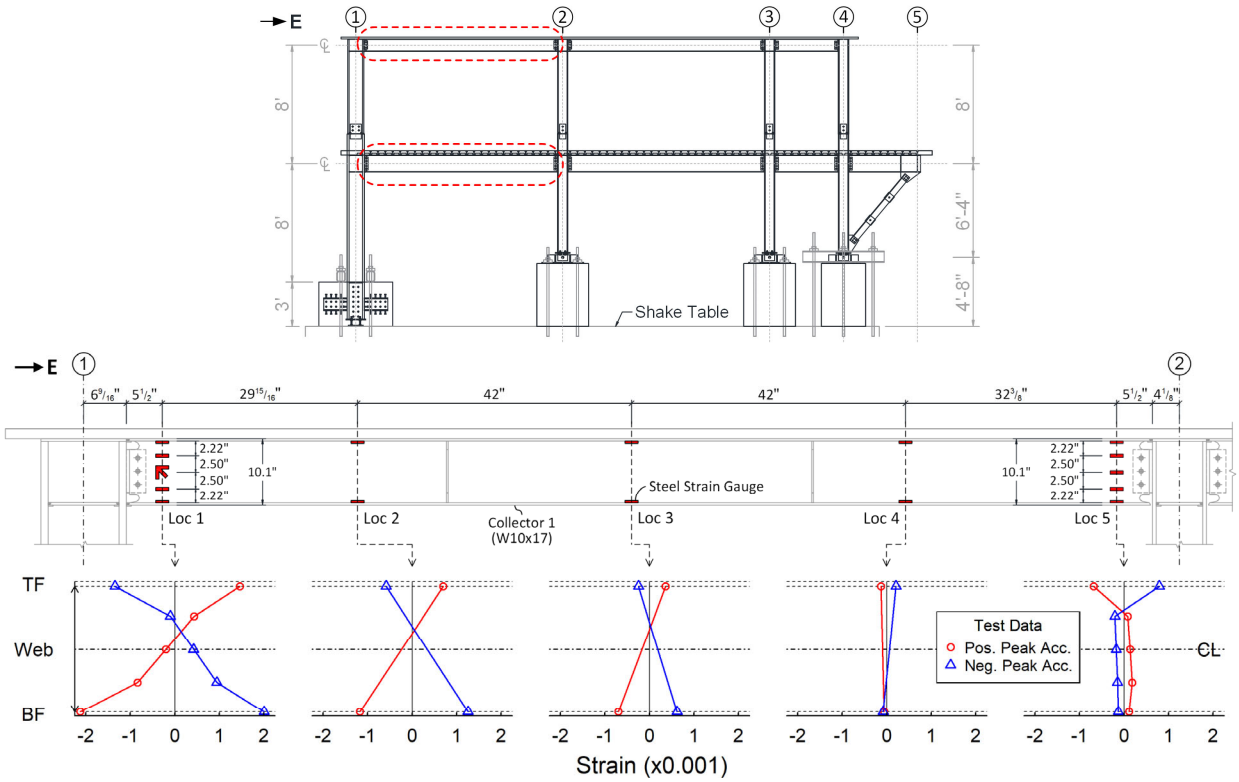

Figure 7.56 Test 2B-5: Strain Profiles of North Roof Collector 1

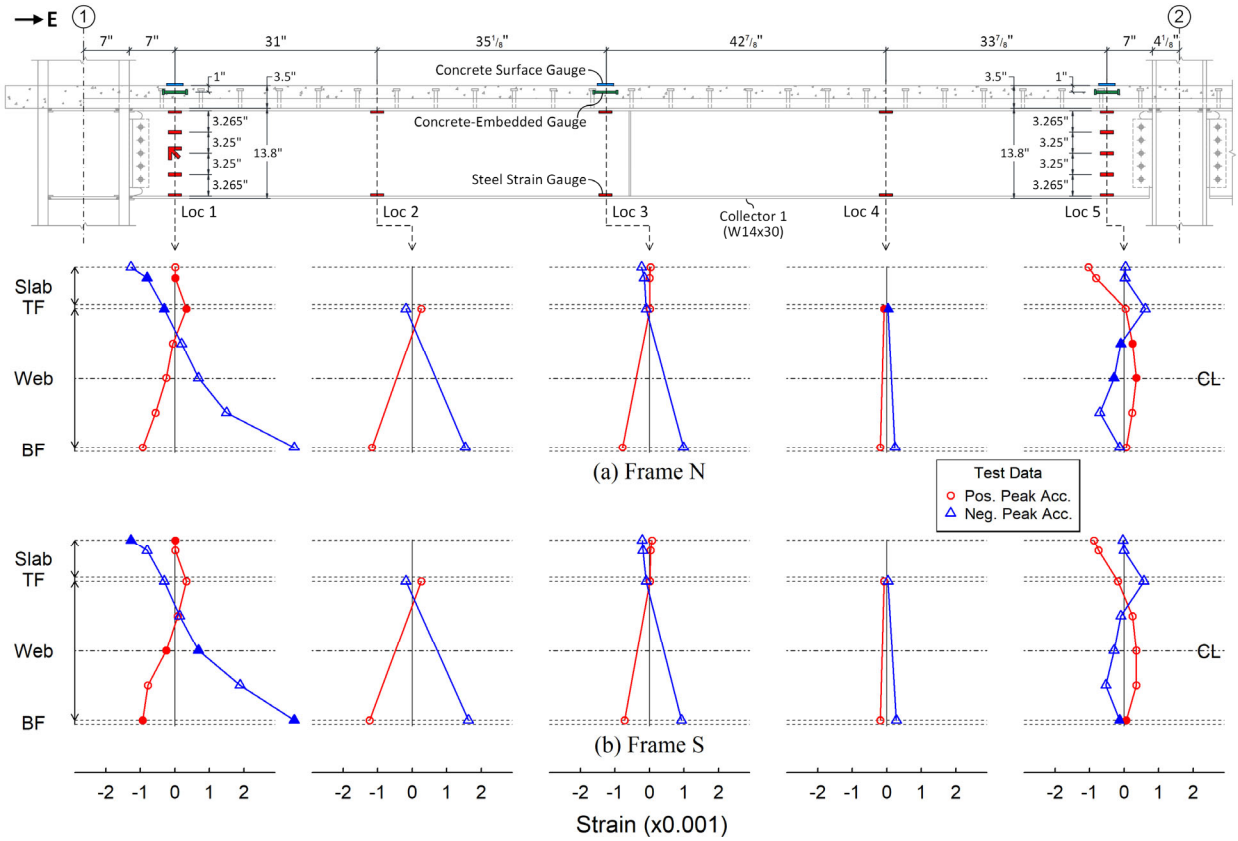

Figure 7.57 Test 2B-5: Strain Profiles of 2nd Floor Collector 1 Beams

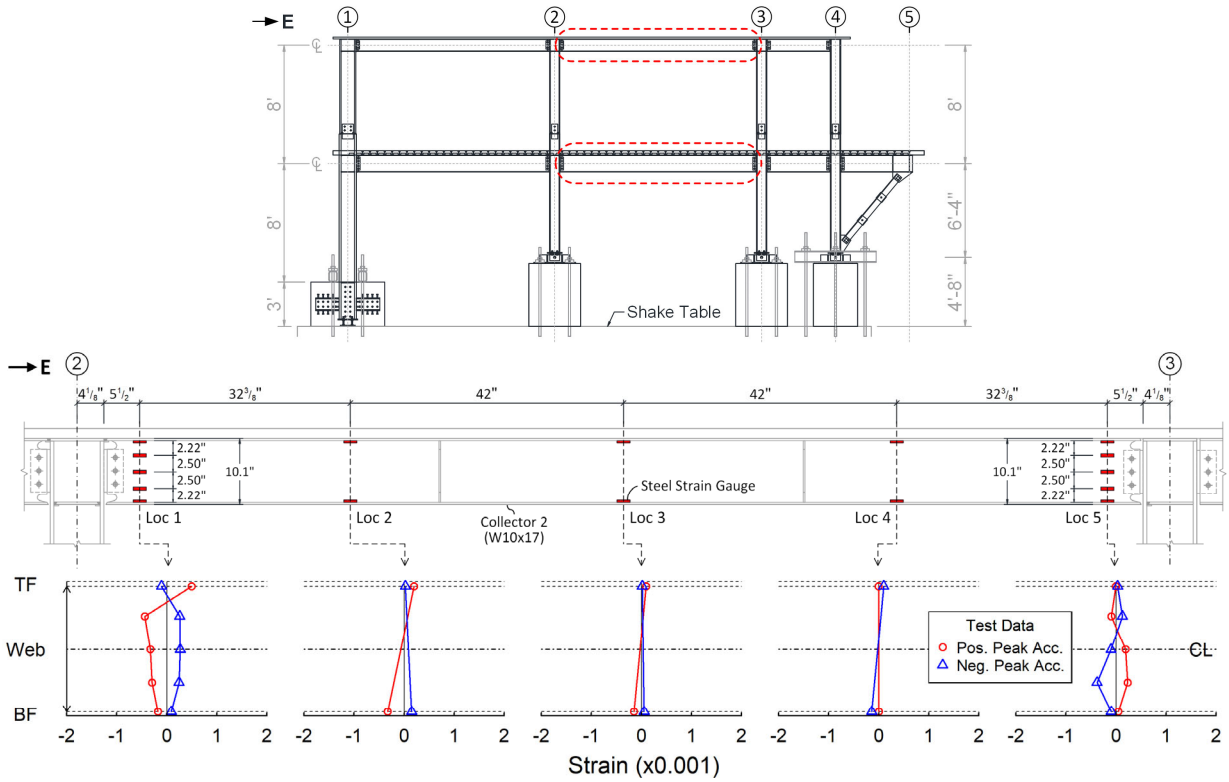

Figure 7.58 Test 2B-5: Strain Profiles of North Roof Collector 2

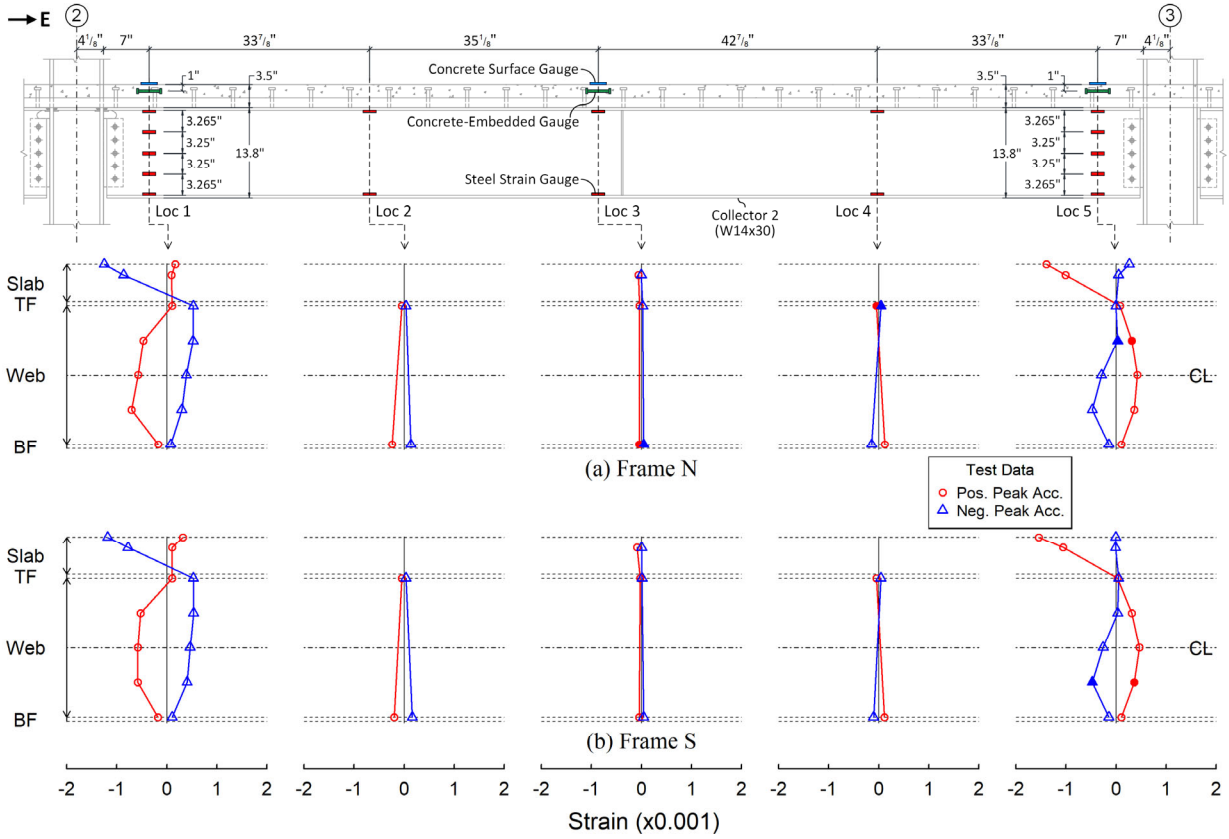

Figure 7.59 Test 2B-5: Strain Profiles of 2nd Floor Collector 2

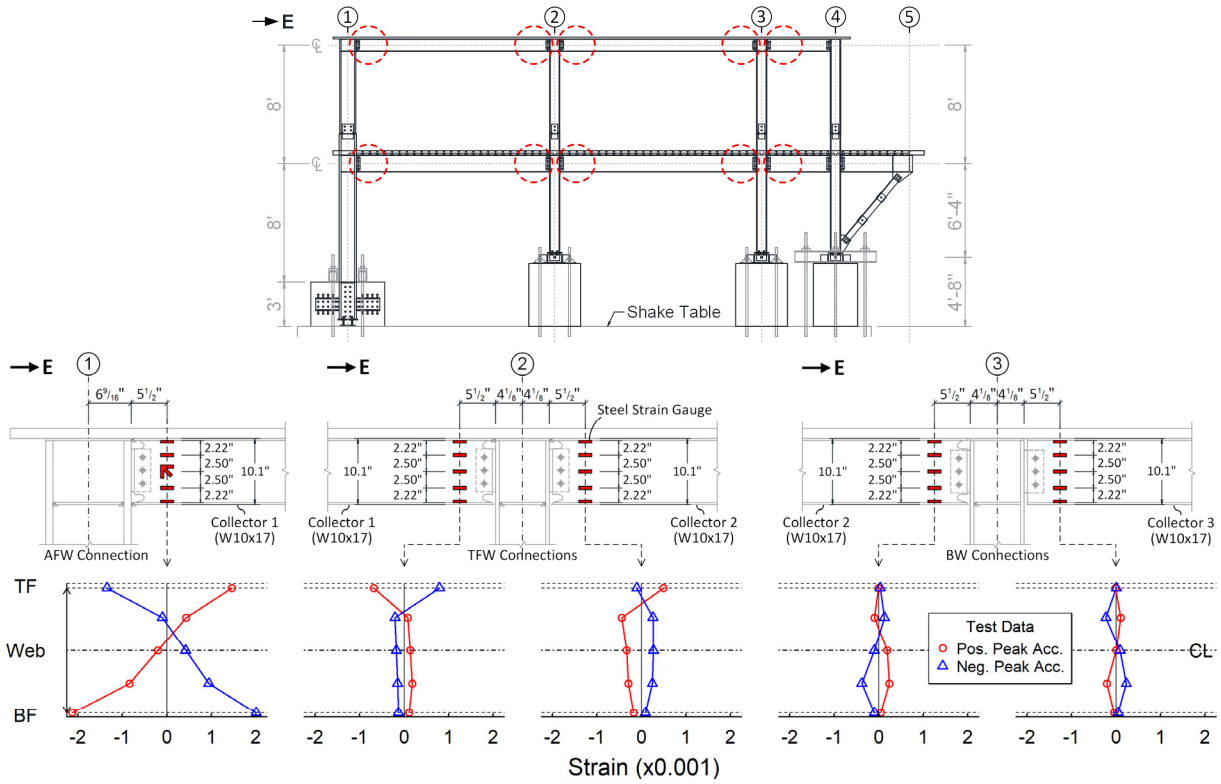

Figure 7.60 Test 2B-5: Strain Profiles near North Roof Collector Connections

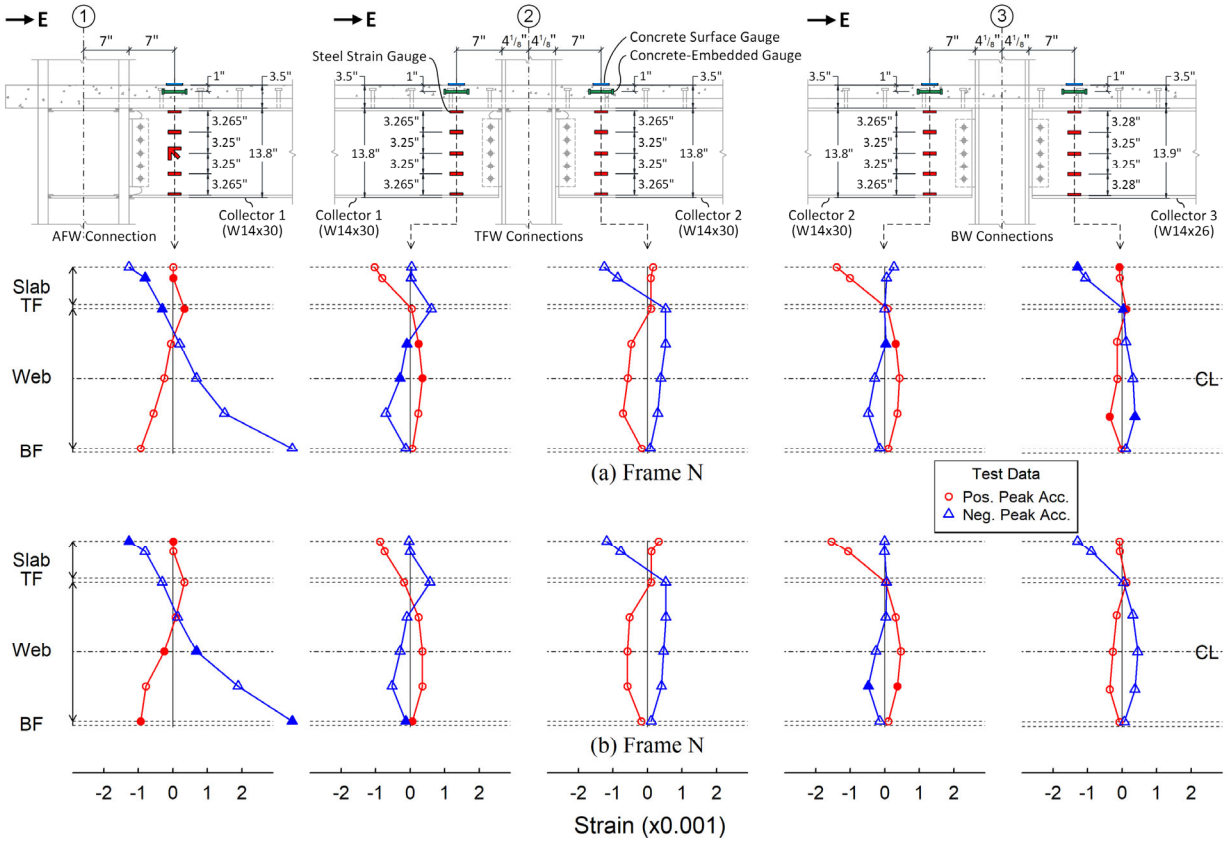

Figure 7.61 Test 2B-5: Strain Profiles near 2nd Floor Collector Connections

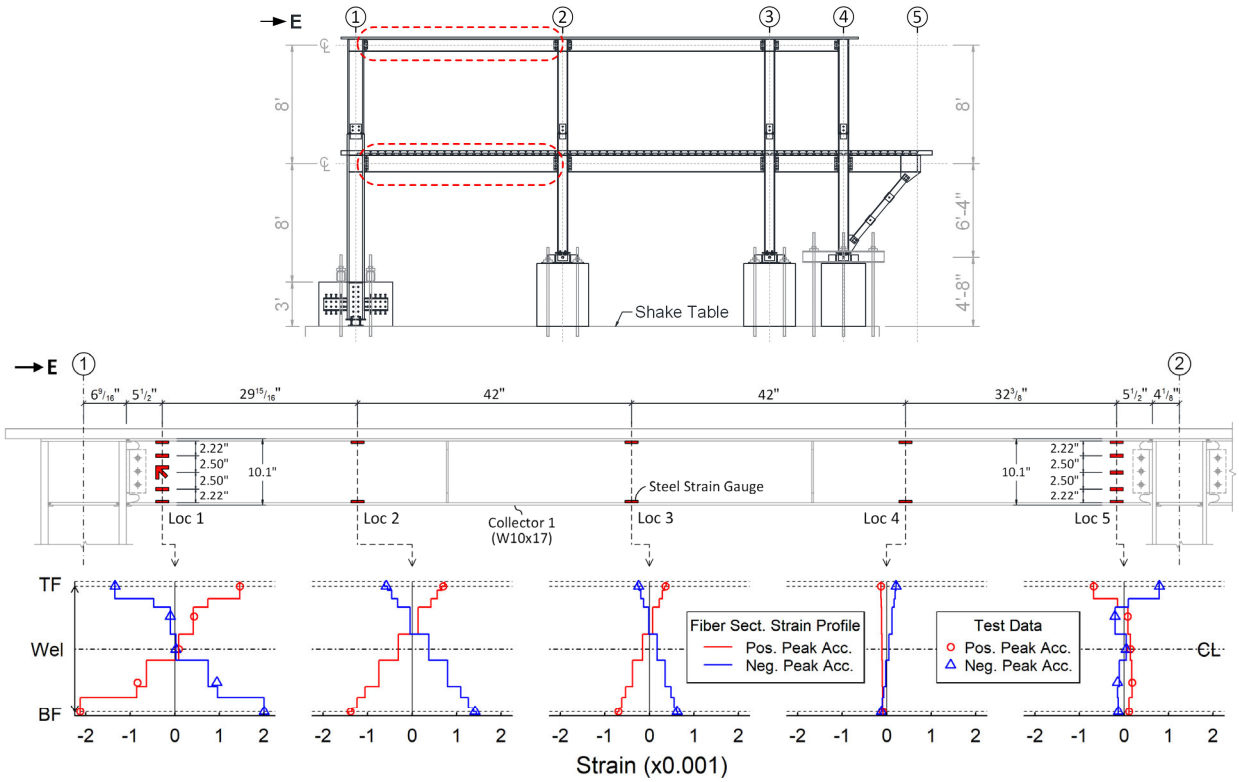

Figure 7.62 Test 2B-5: Fiber Section Strain Profiles of North Roof Collector 1

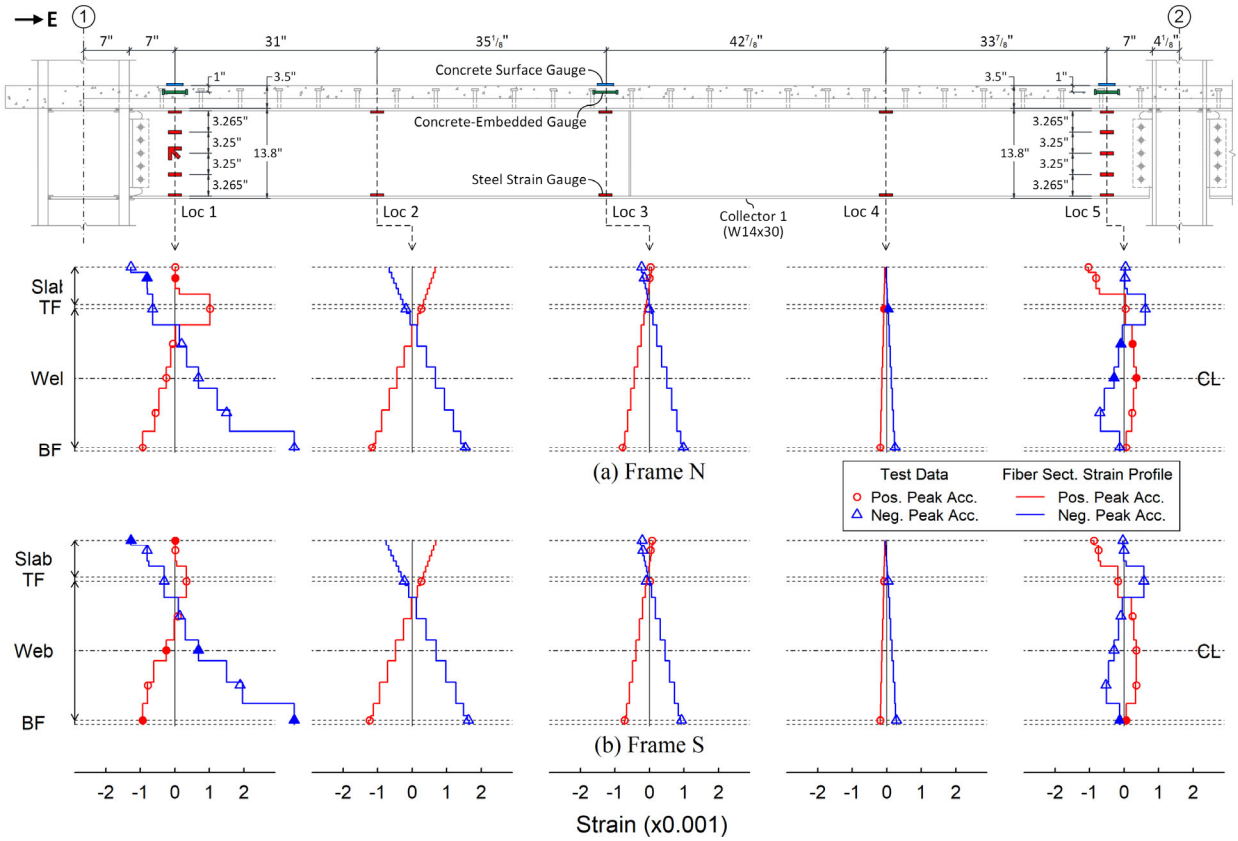

Figure 7.63 Test 2B-5: Fiber Section Strain Profiles of 2nd Floor Collector 1

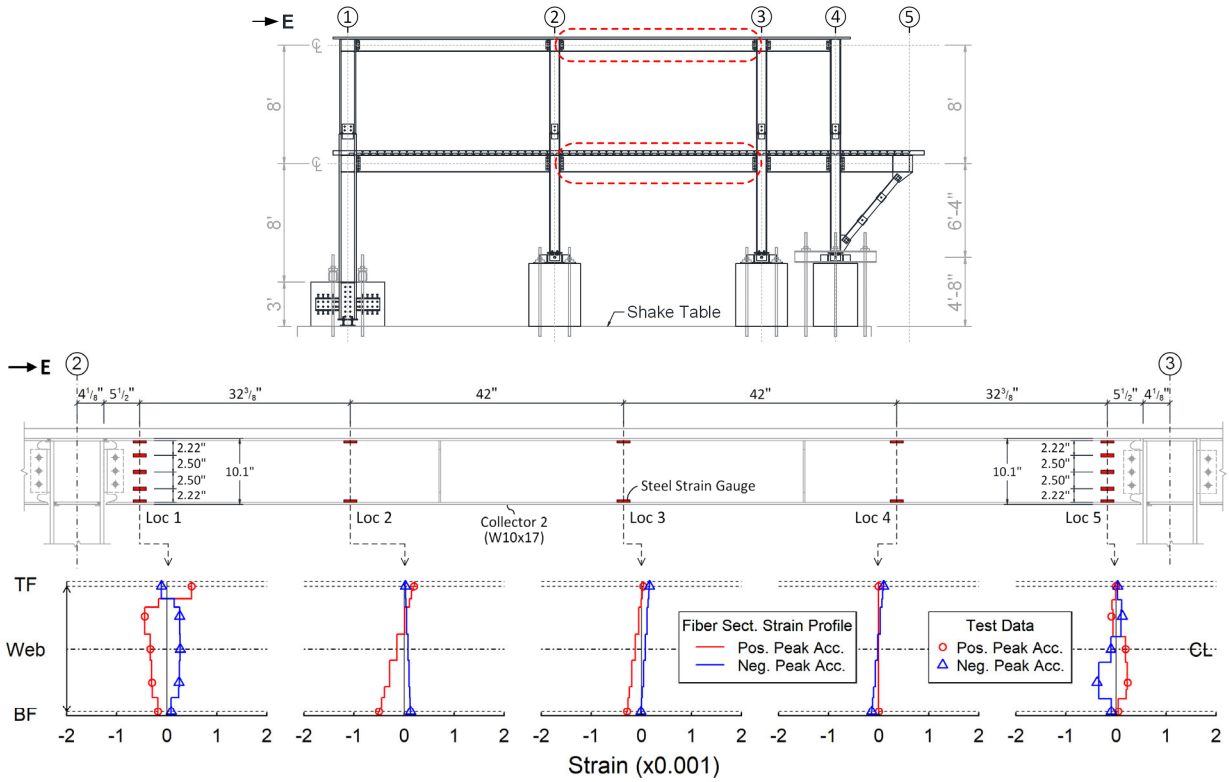

Figure 7.64 Test 2B-5: Fiber Section Strain Profiles of North Roof Collector 2

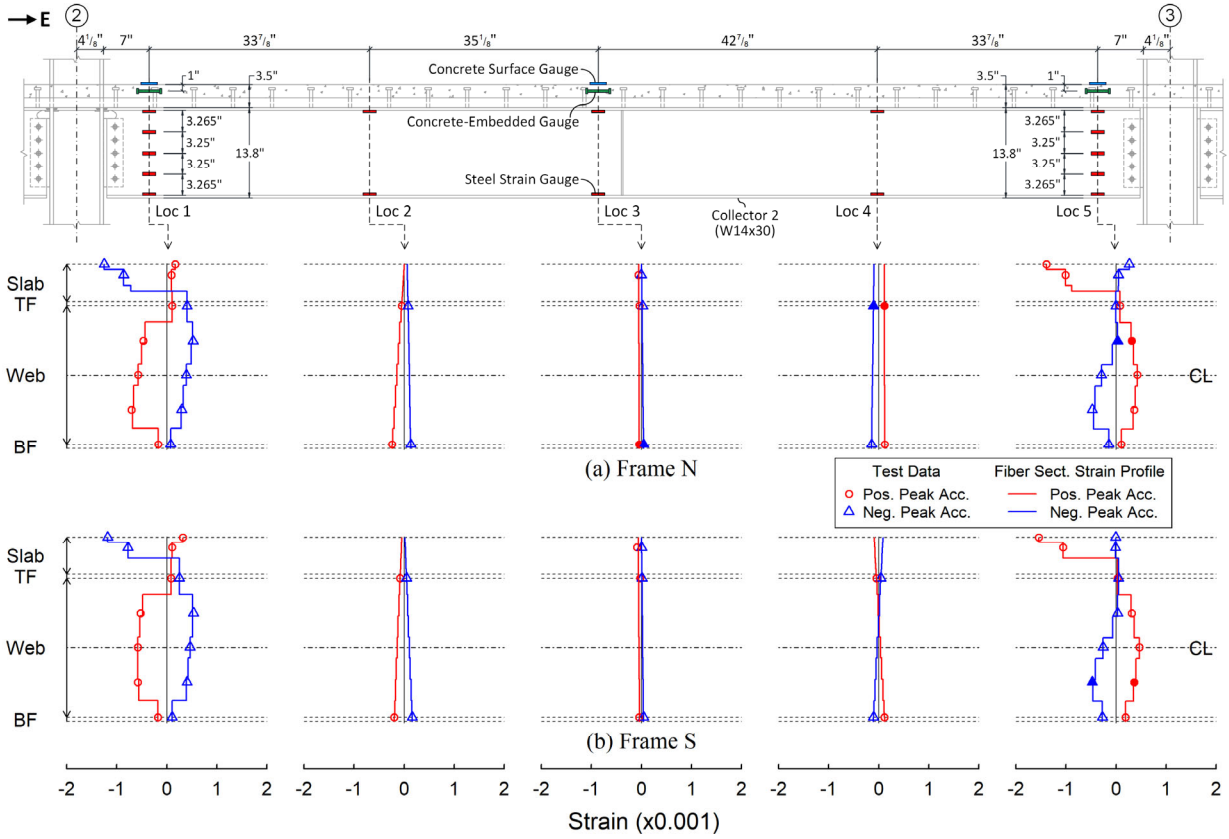

Figure 7.65 Test 2B-5: Fiber Section Strain Profiles of 2nd Floor Collector 2

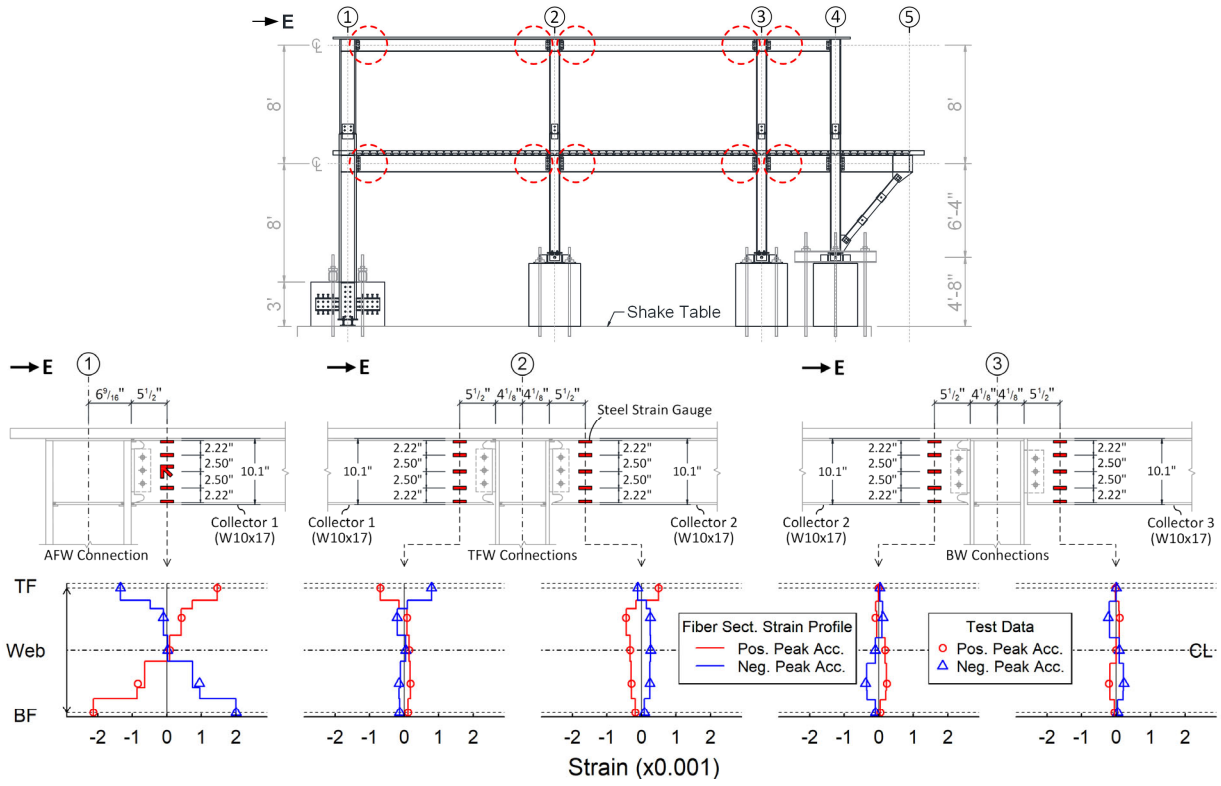

Figure 7.66 Test 2B-5: Fiber Section Strain Profiles of Roof Collector Connections

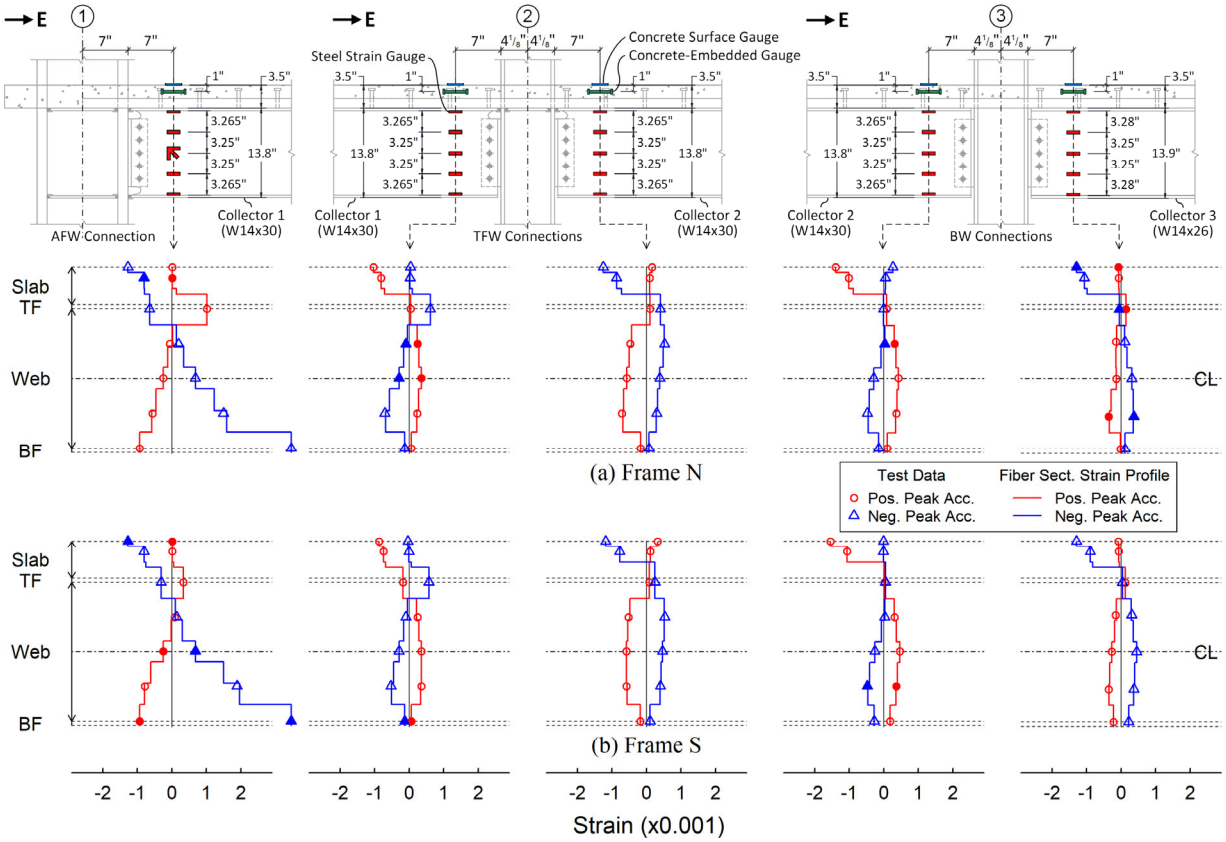

Figure 7.67 Test 2B-5: Fiber Section Strain Profiles of 2nd Floor Collector Connections

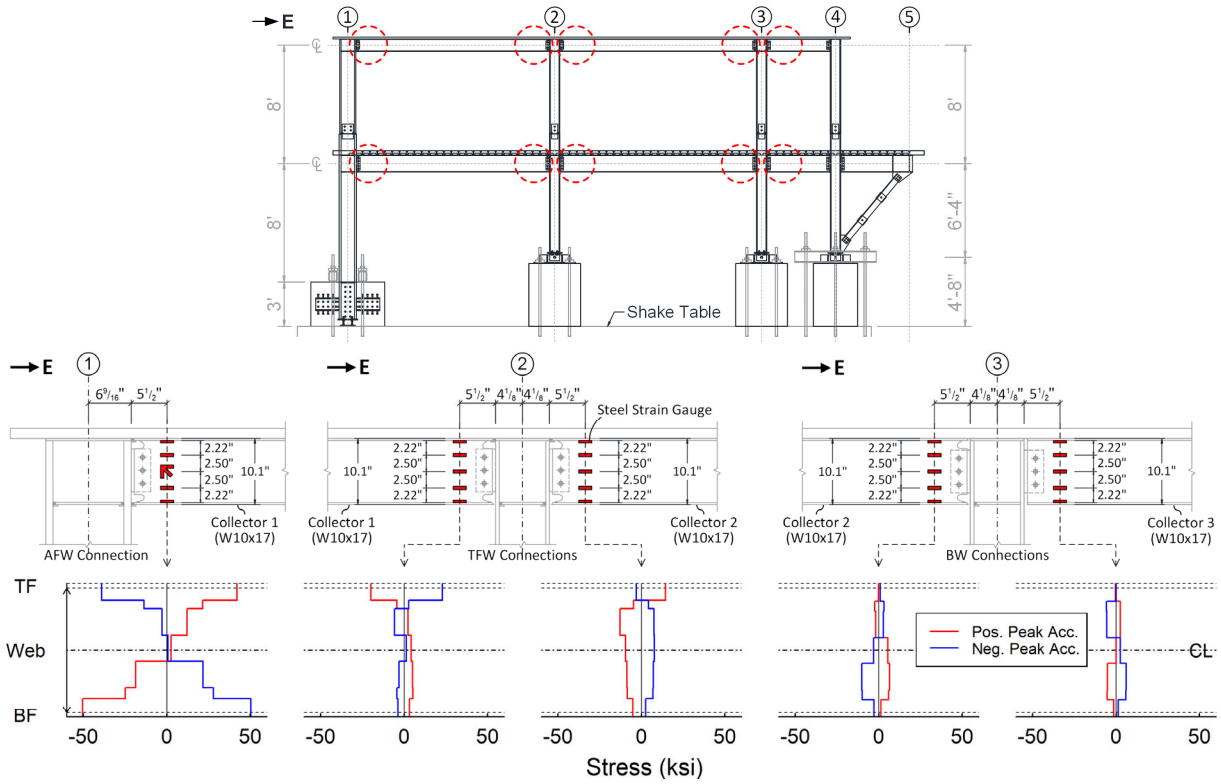

Figure 7.68 Test 2B-5: Fiber Section Stress Profiles of Roof Collector Connections

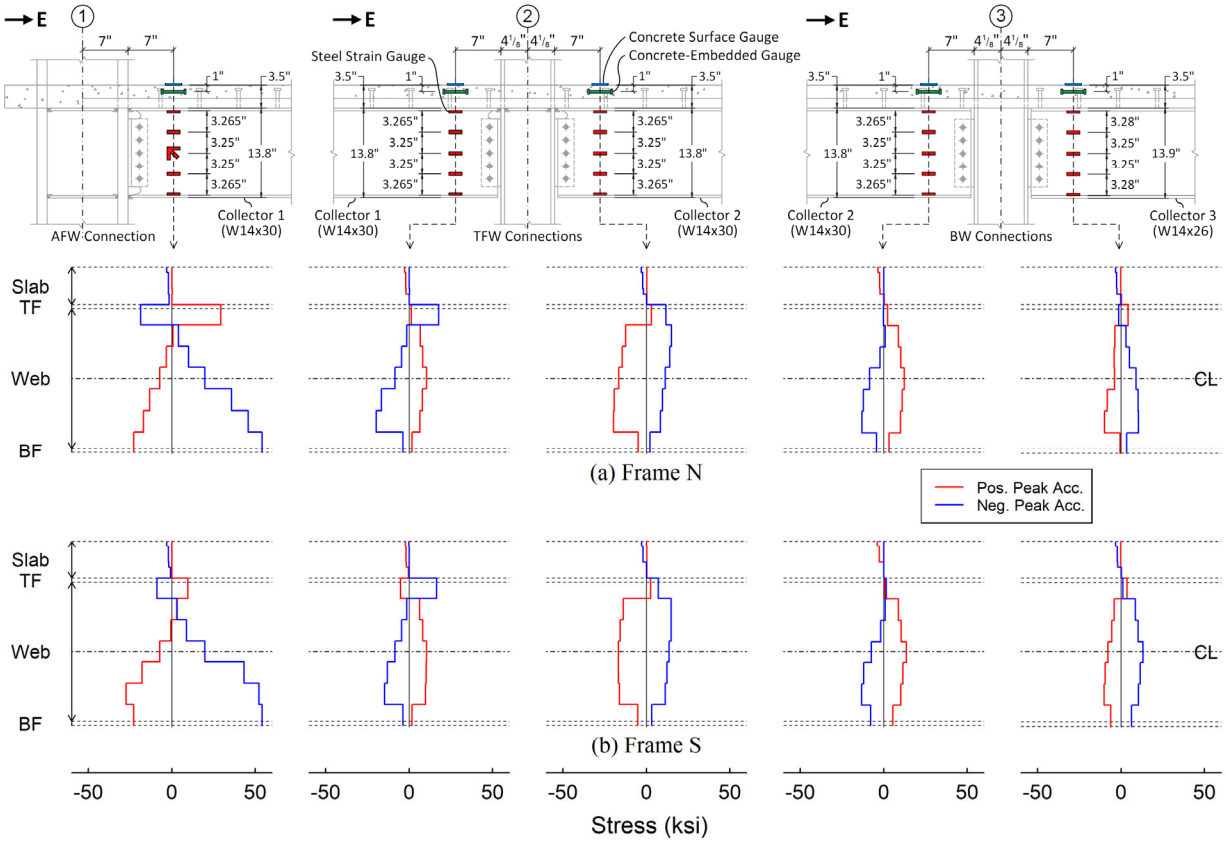

Figure 7.69 Test 2B-5: Fiber Section Stress Profiles of 2nd Floor Collector Connections

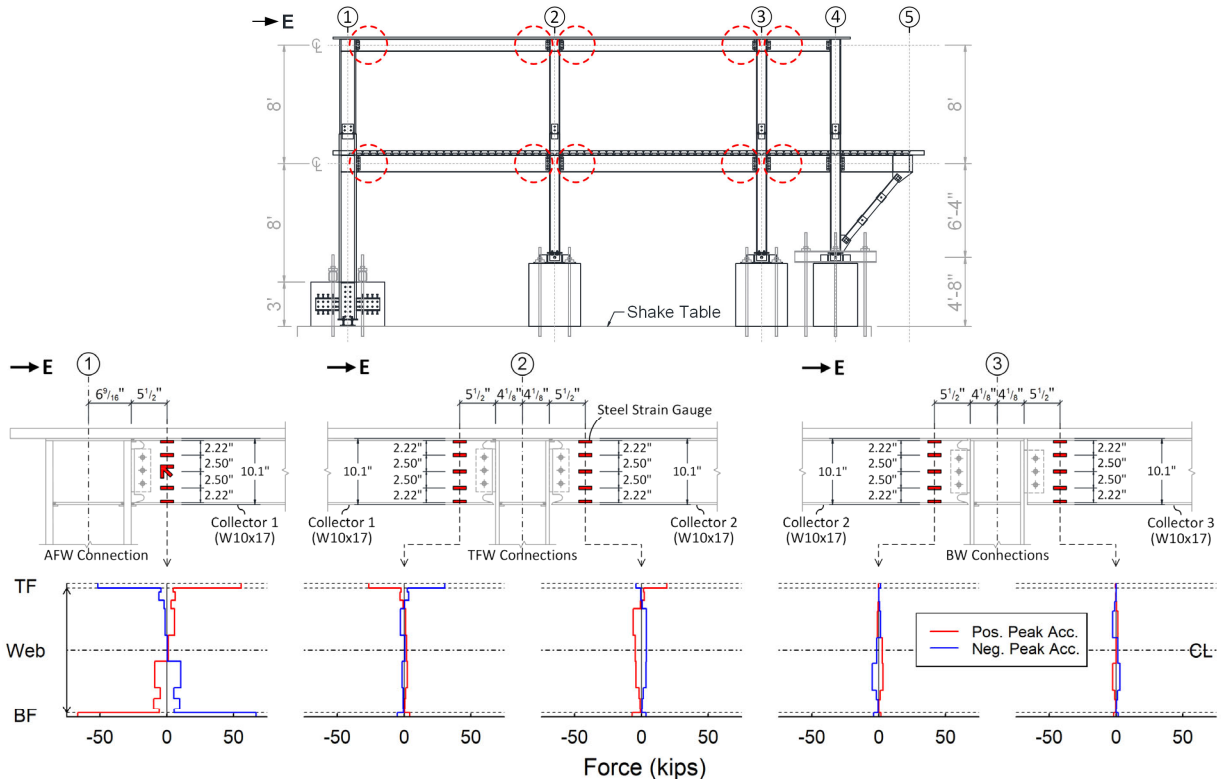

Figure 7.70 Test 2B-5: Fiber Axial Force Profiles of Roof Collector Connections

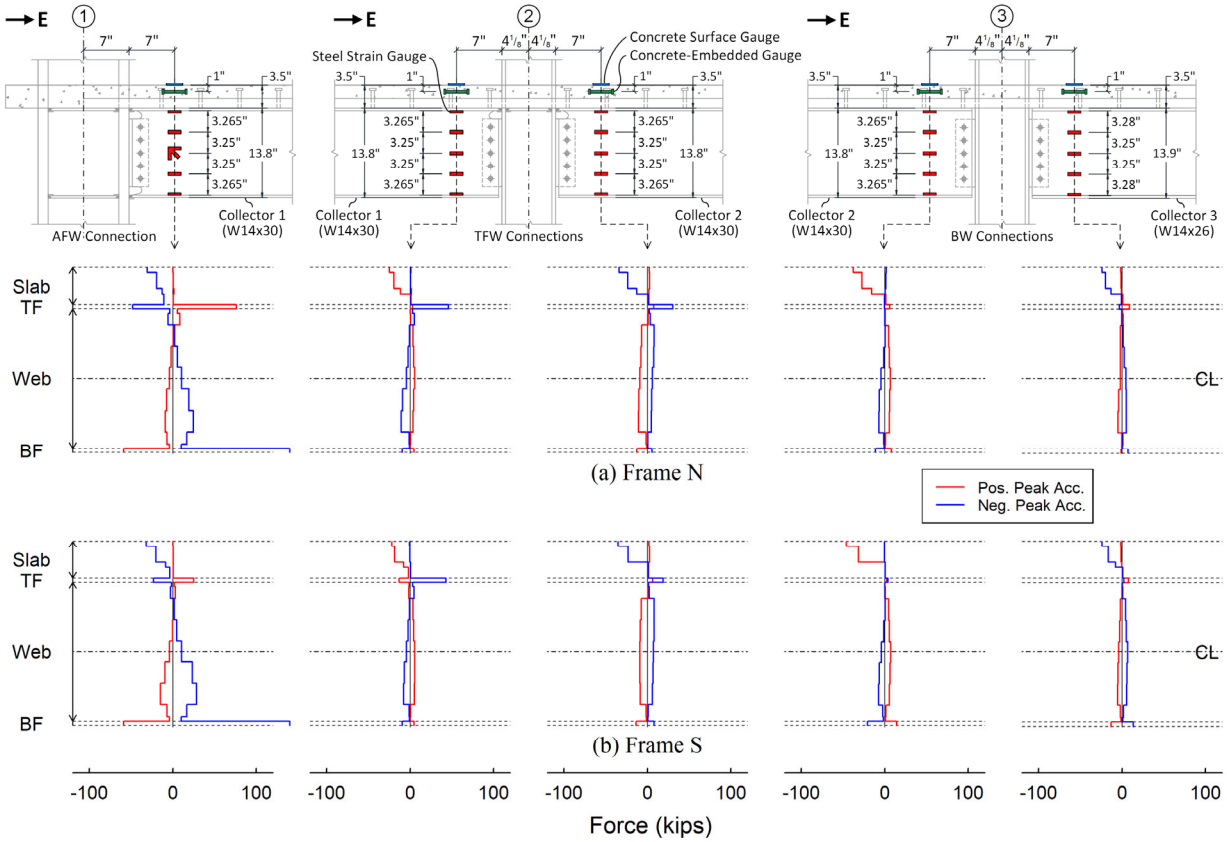

Figure 7.71 Test 2B-5: Fiber Axial Force Profiles of 2nd Floor Collector Connections

7.4.3 Collector Member Forces

After the axial forces and bending moments at the instrumented collector sections were computed, the axial force and bending moment diagram along the collector lines can be constructed. Figure 7.72 and Figure 7.73 show the axial force diagrams at the positive peak floor accelerations for the collector lines at roof and 2nd floor levels, respectively. Figure 7.74 and Figure 7.75 show the bending moment diagrams at the positive peak floor accelerations for the collector lines at roof and 2nd floor levels, respectively. Figure 7.76 and Figure 7.77 show the measured axial force diagrams at the negative peak floor accelerations for the collector lines at roof and 2nd floor levels, respectively. Figure 7.78 and Figure 7.79 show the measured bending moment diagrams at the negative peak floor accelerations for the collector lines at roof and 2nd floor levels, respectively. Note that the axial force diagrams were plotted by connecting the axial force data points along the collectors. On the other hand, the bending moment diagrams in Collectors 1 and 2 were constructed by using a linear regression line among five calculated moments along each collector.

Looking at the total axial force in the composite section of 2nd floor collectors and the total axial force of the bare steel roof collector shown in Figure 7.72 and Figure 7.73, the 14-ft long Collectors 1 and 2 at both levels were mainly in compression at the positive peak acceleration, at which them the inertial force in the floor was acting towards the LFRS. On the other hand, as shown in Figure 7.76 and Figure 7.77, Collectors 1 and 2 members at both levels were mainly in tension at the negative peak acceleration, at which time the inertial force in the floor was acting away from the LFRS. It is apparent that the magnitude of axial forces increased along the collector lines from the far end to the LFRS end. In addition, the slope of axial force diagram in the Collector

1 was obviously higher than that in the Collector 2. This suggests that, along each collector line, more inertial forces were dragged into Collector 1 than those collected by Collector 2.

In addition to the measured total axial forces acting on the composite sections of the 2nd floor collectors, Figure 7.73 and Figure 7.77 also plot the measured axial forces taken by the bare steel sections of these composite collectors at the instants of positive and negative peak 2nd floor accelerations, respectively. Along a composite collector line, the difference between the total axial force on a composite collector section and the axial force taken by the bare steel section only was significant at places where the composite collector was subjected to a considerable positive bending moment.

At the instant of the positive peak acceleration, the east ends of 2nd floor Collectors 1 and 2 were subjected to a significant positive bending moment (Figure 7.75) in addition to a compressive axial force demand (Figure 7.73). At these two locations, the axial force on the bare steel section was in tension, implying that axial force in the concrete slab was compressive with a magnitude even larger than the total compressive axial force acting on the entire composite section. It is indicated that, the concrete slab played the main role in transmitting the collector axial force, while the steel section played a "counteracting" role. In this case, the magnitude of the tensile axial force on the steel section could be noticeable as exampled by the response at the east end of Collector 2 shown in Figure 7.73, where the magnitude of tensile axial force on the bare steel section was about the same as that of the total axial force on the composite section.

On the other hand, at the instant of the negative peak acceleration, near the east ends of 2nd floor Collectors 1, 2 and 3, the composite sections there were subjected to a significant positive bending moment (Figure 7.79) in addition to an axial force demand (Figure 7.77). At these three locations, the axial force on the bare steel section was in tension with a magnitude significantly

larger than the total axial force acting on the entire composite section. This phenomenon can be explained by the strain profiles (Figure 7.61) at these locations that the bare steel section played the main role in conveying the collector axial force, while the concrete slab played a "counteracting" role in the delivery of collector axial force. Thus, as a significant compressive force developed in the concrete slabs at these ends under positive bending, the steel collector beam sections there were burdened by these concrete forces, resulting in a high resultant axial force demand on the steel section. This phenomenon would bring up a serious issue on the design of collector connection, which will be elaborated in Section 8.4.2.

As shown in Figure 7.74, Figure 7.75, Figure 7.78 and Figure 7.79, there appears to be a linear moment diagram in double curvature along each span of Collectors 1 or 2 for both the roof and 2nd floor levels. As shown in Figure 7.75 and Figure 7.79, the moment diagrams of composite sections along the 2nd floor Collector 1 beams indicate that the inflection point was located at approximately 2/3 and 3/4 of the beam span away from the west end of the collector at the positive (Figure 7.75) and negative (Figure 7.79) peak accelerations, respectively. The fact that the inflection point of Collector 1 was always in the east-half span is due to the unequal rotational stiffness at two ends of the collector. (Note that the AFW connection detail was employed at the west end of Collector 1, while the TFW detail was used at the east end.) Thus, the west end was much stiffer than the east end, resulting in a higher moment demand at the west end. For the composite section moment diagrams along Collector 2 beams, the inflection point was located at about 40% and 60% of the beam span away from the west end of the collector at the positive (Figure 7.75) and negative (Figure 7.79) peak accelerations, respectively. An inflection point located within the east-half span or at about the mid-span of Collector 2 indicates that the rotational

stiffness of the TFW connection at the west end, despite having the top flange welded, was not obviously larger than that of the BW connection at the east end.

As shown in Figure 7.74 and Figure 7.78, moment diagrams of roof bare steel Collector 1 indicate that the inflection point was located at approximately 3/4 of the beam span away from the west end of the collector at both positive (Figure 7.74) and negative (Figure 7.78) peak accelerations, respectively. For the moment diagrams along the roof bare steel Collector 2, the inflection point was located at about 80% and 40% of the beam span away from the west end at the positive (Figure 7.74) and negative (Figure 7.78) peak accelerations, respectively. It appears to suggest that the locations of inflection point in a bare steel collector with semi-rigid collector connections would vary a lot between two swaying directions of the structure.

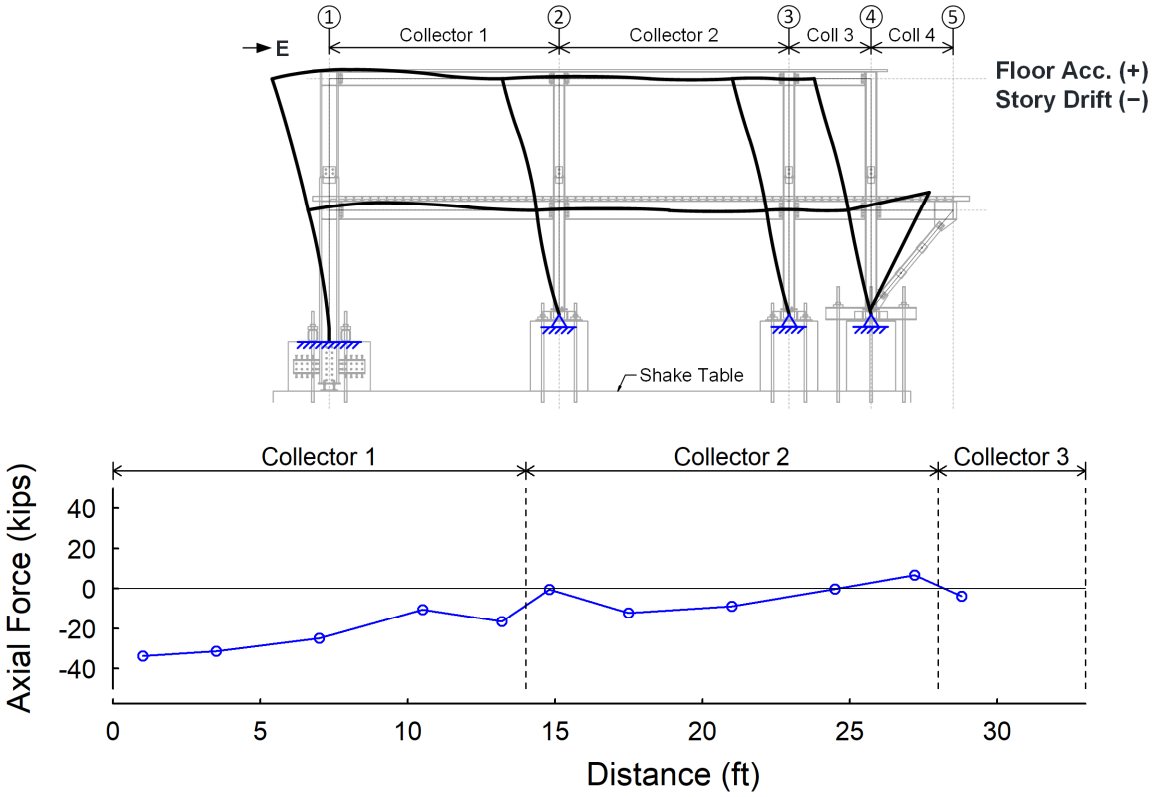

Figure 7.72 Test 2B-5: Axial Force Diagram along North Roof Collector Line at Positive Peak Floor Acceleration

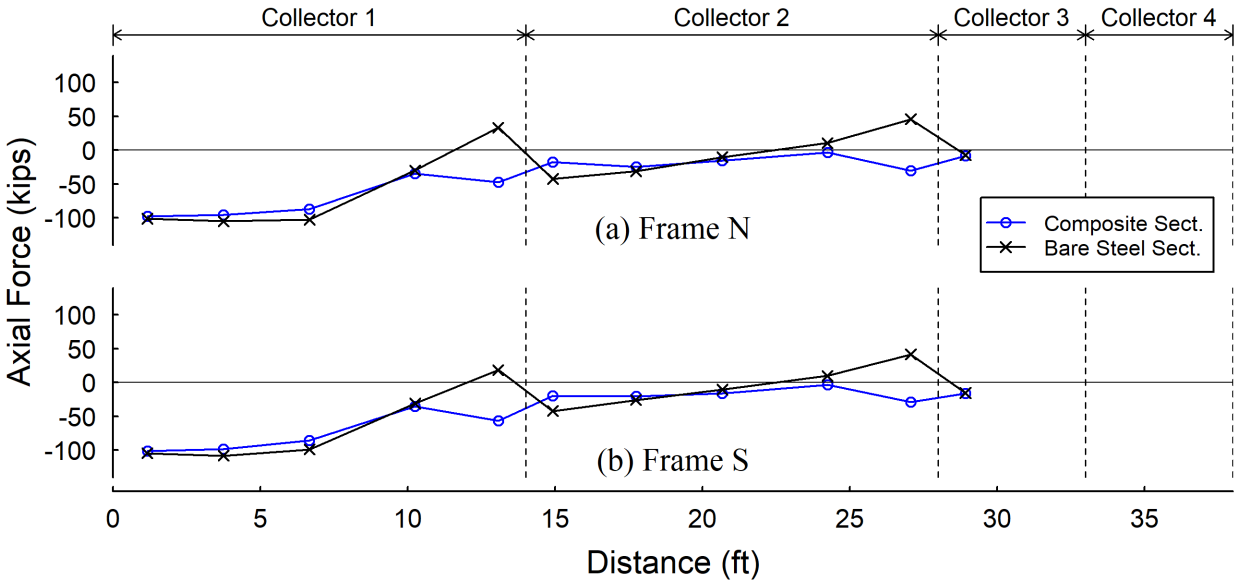

Figure 7.73 Test 2B-5: Axial Force Diagram along 2nd Floor Collector Lines at Positive Peak Floor Acceleration

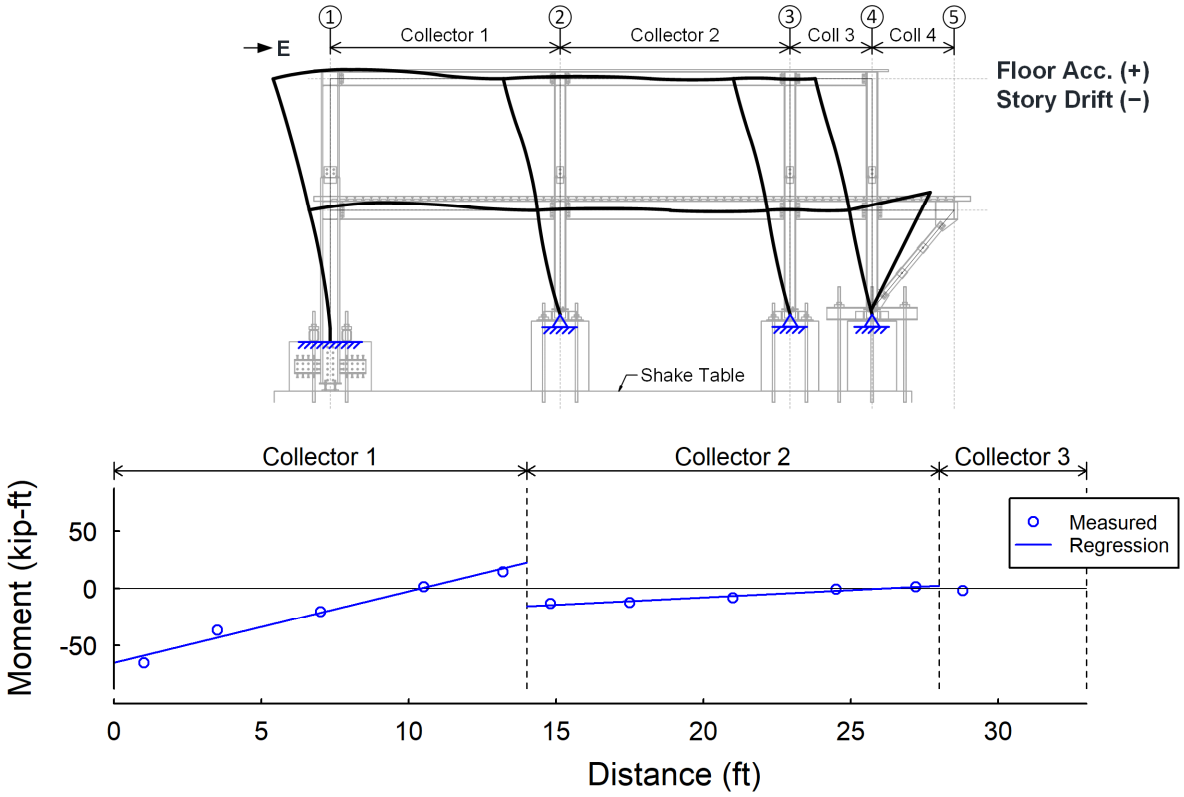

Figure 7.74 Test 2B-5: Moment Diagram along North Roof Collector Line at Positive Peak Floor Acceleration

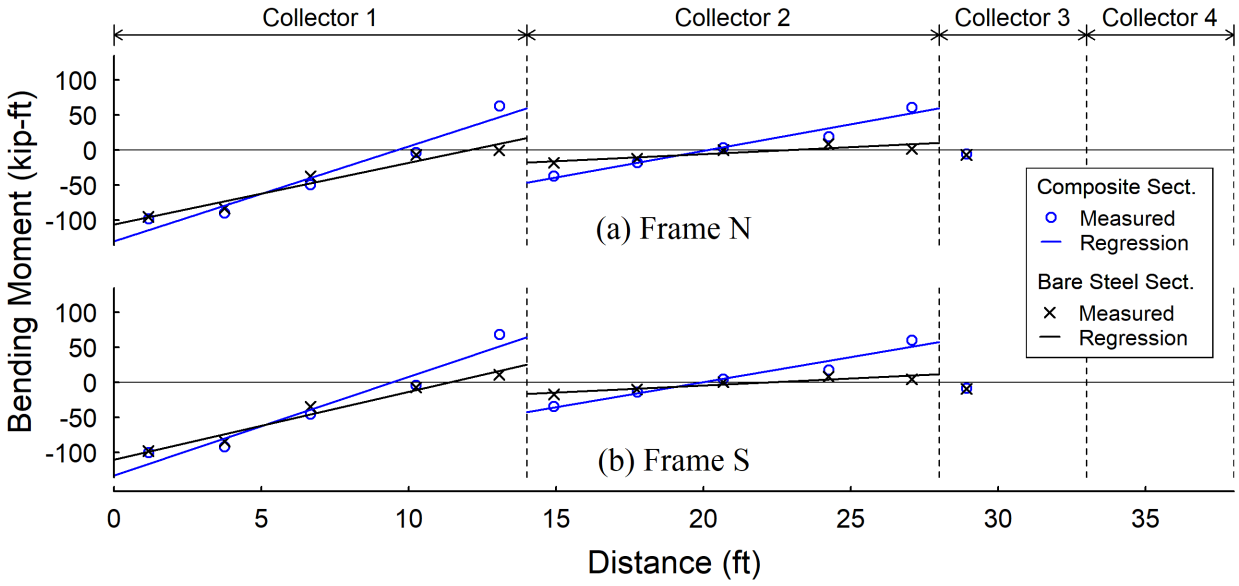

Figure 7.75 Test 2B-5: Moment Diagram along 2nd Floor Collector Lines at Positive Peak Floor Acceleration

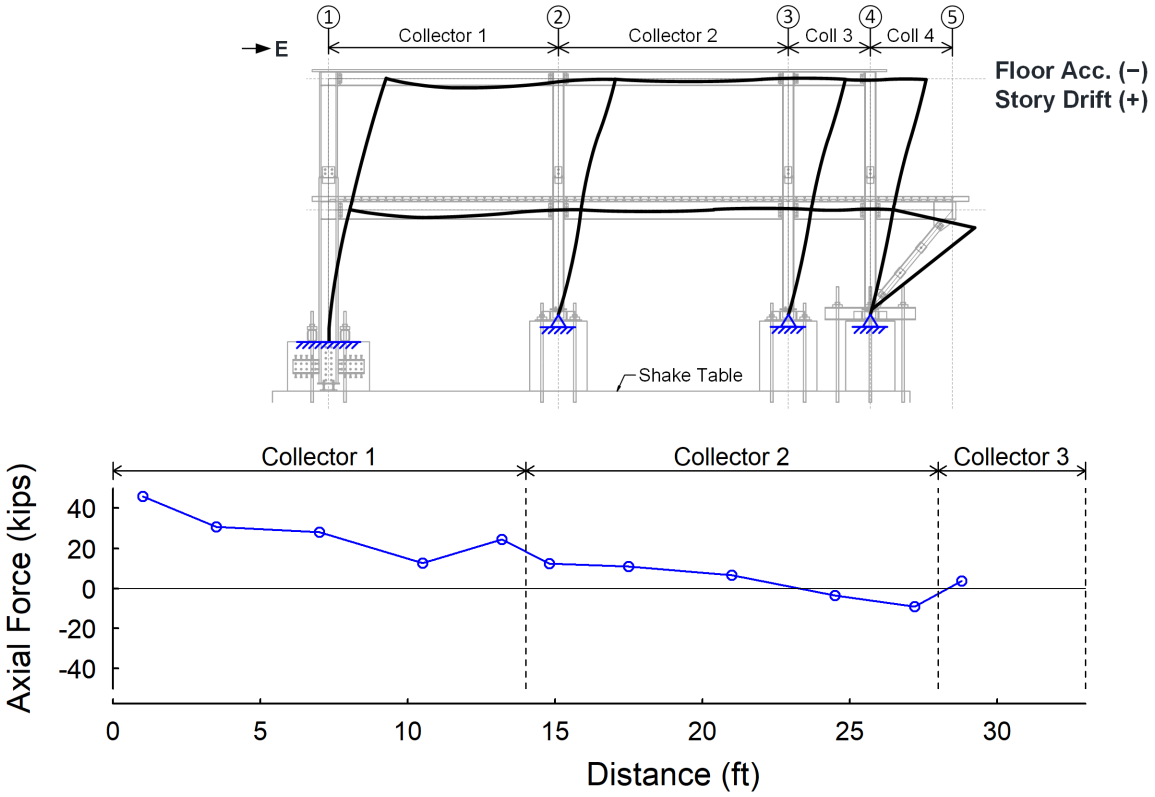

Figure 7.76 Test 2B-5: Axial Force Diagram along North Roof Collector Line at Negative Peak Floor Acceleration

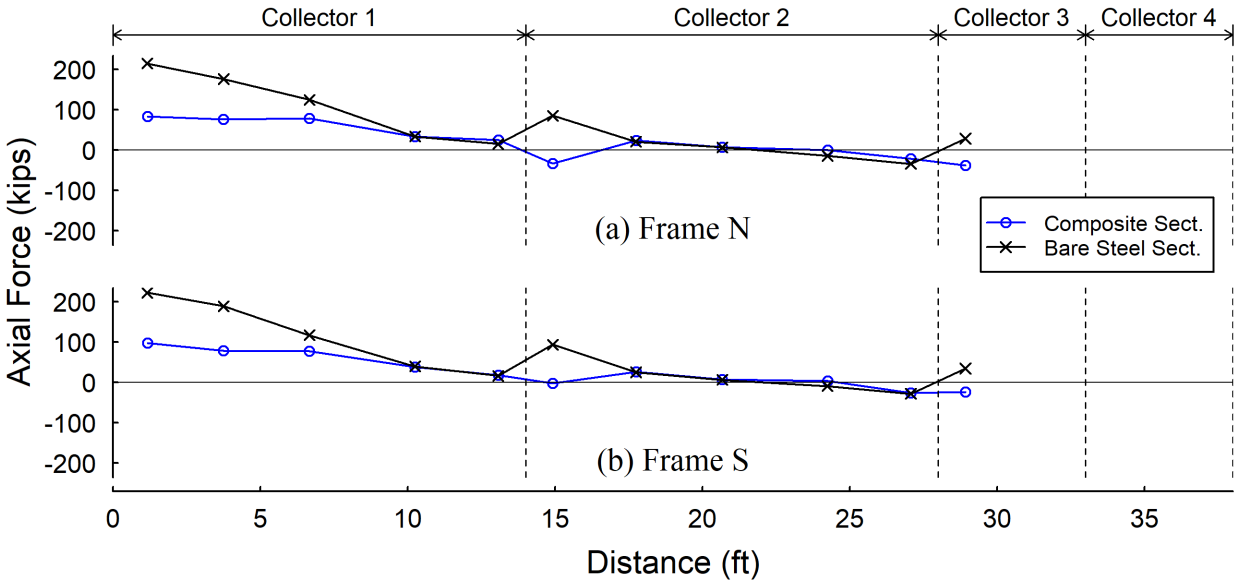

Figure 7.77 Test 2B-5: Axial Force Diagram along 2nd Floor Collector Lines at Negative Peak Floor Acceleration

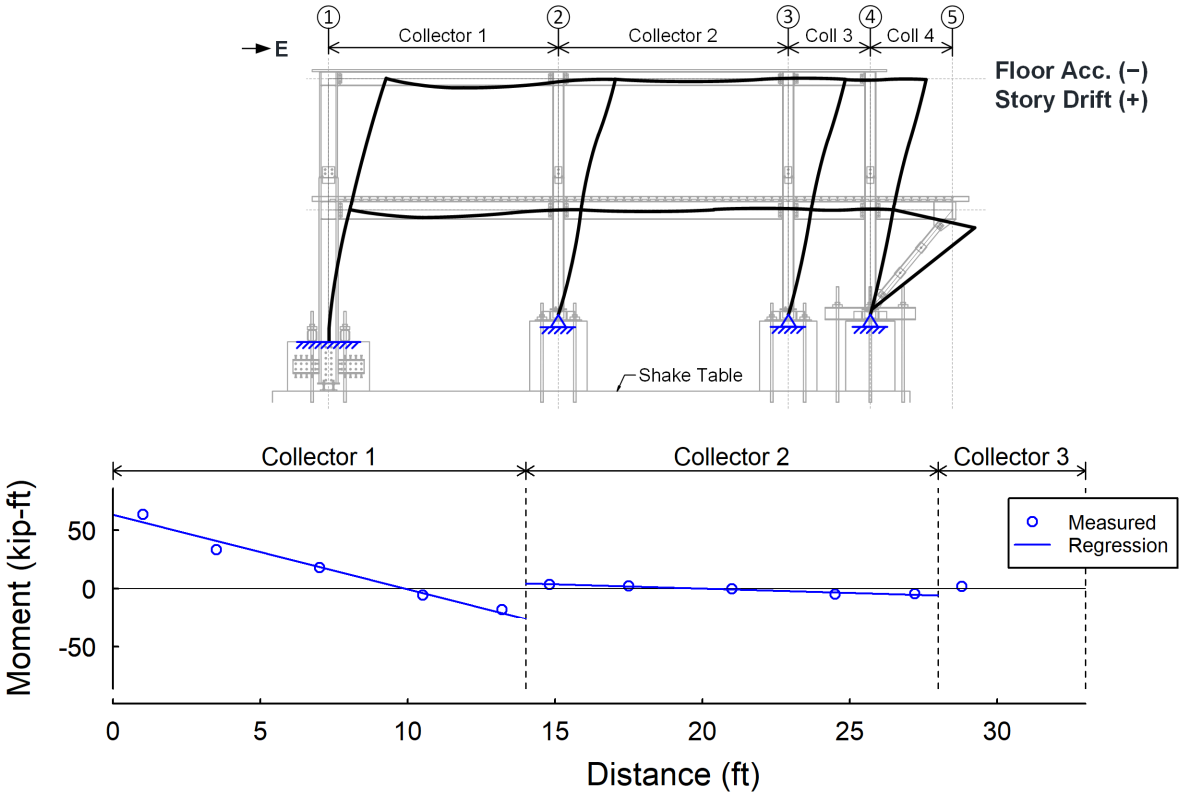

Figure 7.78 Test 2B-5: Moment Diagram along North Roof Collector Line at Negative Peak Floor Acceleration

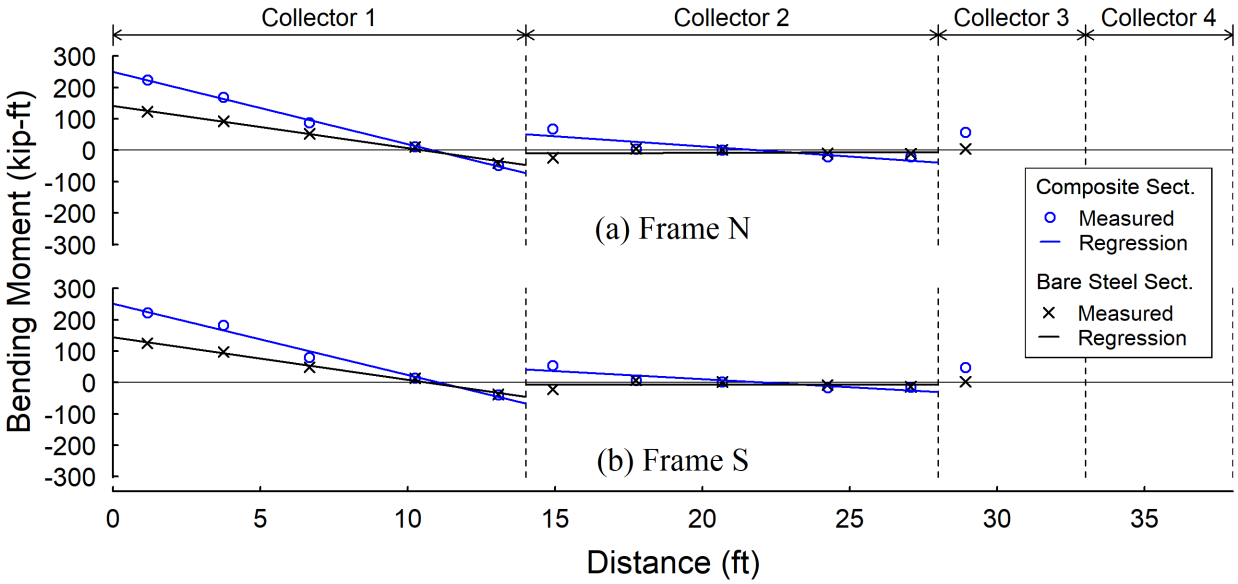

Figure 7.79 Test 2B-5: Moment Diagram along 2nd Floor Collector Lines at Negative Peak Floor Acceleration

7.4.4 Collector-to-Column Connection Responses

Figure 7.80 and Figure 7.81 show the measured moment-rotation (M-θ) relationships for the collector-to-column connections at the roof and 2nd floor levels. Note that the sign conventions used herein for the bending moment and rotation are consistent: a positive bending moment (or rotation) represents that the beam is concave upward, whereas a negative bending moment (or radiation) means that the beam concave downward. As shown by the sketches in the top of Figure 7.80, when the specimen was subjected to a positive floor acceleration, the test frame underwent a negative drift (Peak "A" in Figure 7.80). In the meantime, the AFW connections, east-side TFW connections, and the east-side BW connections on were subjected to a negative bending, while the west-side TFW connections and west-side BW connections were subjected to a positive bending.

On the other hand, when the specimen was subjected to a negative floor acceleration, the test frame underwent a positive drift (Peak "B" in Figure 7.80). Meanwhile, the AFW connections, east-side TFW connections, and the east-side BW connections were subjected to a positive bending, while the west-side TFW and west-side BW connections were subjected to a negative bending.

As shown in Figure 7.80 for the bare steel collector connections, it is apparent that the magnitude bending moments produced in the AFW connection was significantly higher than those in TFW and BW connections. The pattern of hysteresis loops of the AFW connection indicated it behaved like a moment connection and got into somewhat inelastic range during Test 2B-5. Comparing the bare steel TFW and BW connections, between which the main difference lies in use of top flange weld, it can be found that the magnitude of moments produced in the TFW connections were moderately higher those in the BW connections. Due to the bolt slippage, apparent plateaus can be observed in the moment-rotation responses for both TFW and BW. It can

be observed that of the hysteresis loops of TFW connections "redeveloped" the stiffness after the responses had entered a plateau, which indicates some bolted joints got into bearing status.

As shown in Figure 7.81 for the composite collector connections, it is apparent that the magnitude bending moments produced in the AFW connection was significantly higher than those in TFW and BW connections. Both TFW and BW connections exhibited an obvious the "unsymmetric" response, for which the magnitude of the moments produced by positive bending was noticeably higher that that by negative bending. This indicates the concrete slab contributed significantly to producing the positive bending moments for these two types of semi-rigid connection. It can be found that, on the positive bending side (i.e., the first quadrant of a M-θ plot), the responses of TFW and BW connections were similar. This indicates that the force transmitted through the top flange weld would not significantly produce positive moment to the composite section. By contrast, on the negative bending side (i.e., the third quadrant of a M-θ plot), the magnitude of negative moments generated in the TFW connections was mildly larger than that in the BW connection because the composite connections under the negative bending would behave like a bare steel connection.

For all measured M-θ plot for TFW and BW connections, the secant stiffnesses of the positive and negative bending regimes were taken to serve as the representative stiffnesses for the two bending directions. Figure 7.82 through Figure 7.85 show the "zoom-in" version of each measured M-θ relationship to demonstrate the determination of secant stiffness in a clearer manner.

Figure 7.86 plots the measured moment-rotation response together with the measured axial force-moment (P-M) relationship for the north roof bare steel AFW connection. In the P-M plot [Figure 7.86(b)], two P-M interaction curves were plotted as well. The P-M interaction curve for initial yield was determined from the following equation:

$$\frac{P}{P_y} + \frac{M}{M_y} = 1 \tag{7.1}$$

where yielding axial strength $P_y = A_g F_y$ and yielding moment $M_y = S_x F_y$. Note that A_g and S_x are the gross area and strong-axis section modulus of the steel collector section, respectively. F_y is taken as the measured yield stress of the collector from the coupon test. In addition, the P-M interaction curve for plastic hinge was determined from the following equation (AISC 2016c):

$$\frac{P}{P_y} + \frac{8}{9}\frac{M}{M_p} = 1 \quad \text{for} \quad \frac{P}{P_y} \geq 0.2 \tag{7.2}$$

$$\frac{1}{2}\frac{P}{P_y} + \frac{M}{M_y} = 1 \quad \text{for} \quad \frac{P}{P_y} < 0.2 \tag{7.3}$$

where plastic moment $M_p = Z_x F_y$. Note that Z_x is the strong-axis plastic modulus of the steel collector section. It can be found that the roof bare steel AFW connection reached initial yield surface [see Figure 7.86(b)] during Test 2B-5. This agrees with the mild whitewash flaking on the collector bottom flange observed after the testing as shown in Figure 7.87.

Figure 7.88(b) and Figure 7.90(b) show the measured axial force-moment (P-M) relationships the steel section of the 2nd floor composite AFW connections in Frames N and S, respectively. It can be found that the steel sections of these AFW connections reached the P-M interaction representing a "plastic hinge". This somehow matched the significantly whitewash flaking on the collector bottom flanges observed after the testing as shown in Figure 7.89 and Figure 7.91 for north and south AFW connections, respectively. In addition, a drop of negative bending moment capacity was observed in the hysteresis loops of these two composite AFW connection. The drop of the negative moment capacity corresponded to the local bucking of the collector bottom flange, which also were observed after the testing (see Figure 7.89 and Figure 7.91).

Part of this chapter is based on the material published in the 17th World Conference on Earthquake Engineering, titled “Earthquake simulator testing on behavior of seismic collectors in steel buildings” with co-authors Uang C.-M., and Fleischman R.B. (2020). Materials were also submitted for publication in the 12th National Conference on Earthquake Engineering, titled “Shake Table Tests on Seismic Response of Collectors in Steel Buildings” with co-authors Uang C.-M., and Fleischman R.B. (2022). The author of this dissertation serves as the first author of these papers.

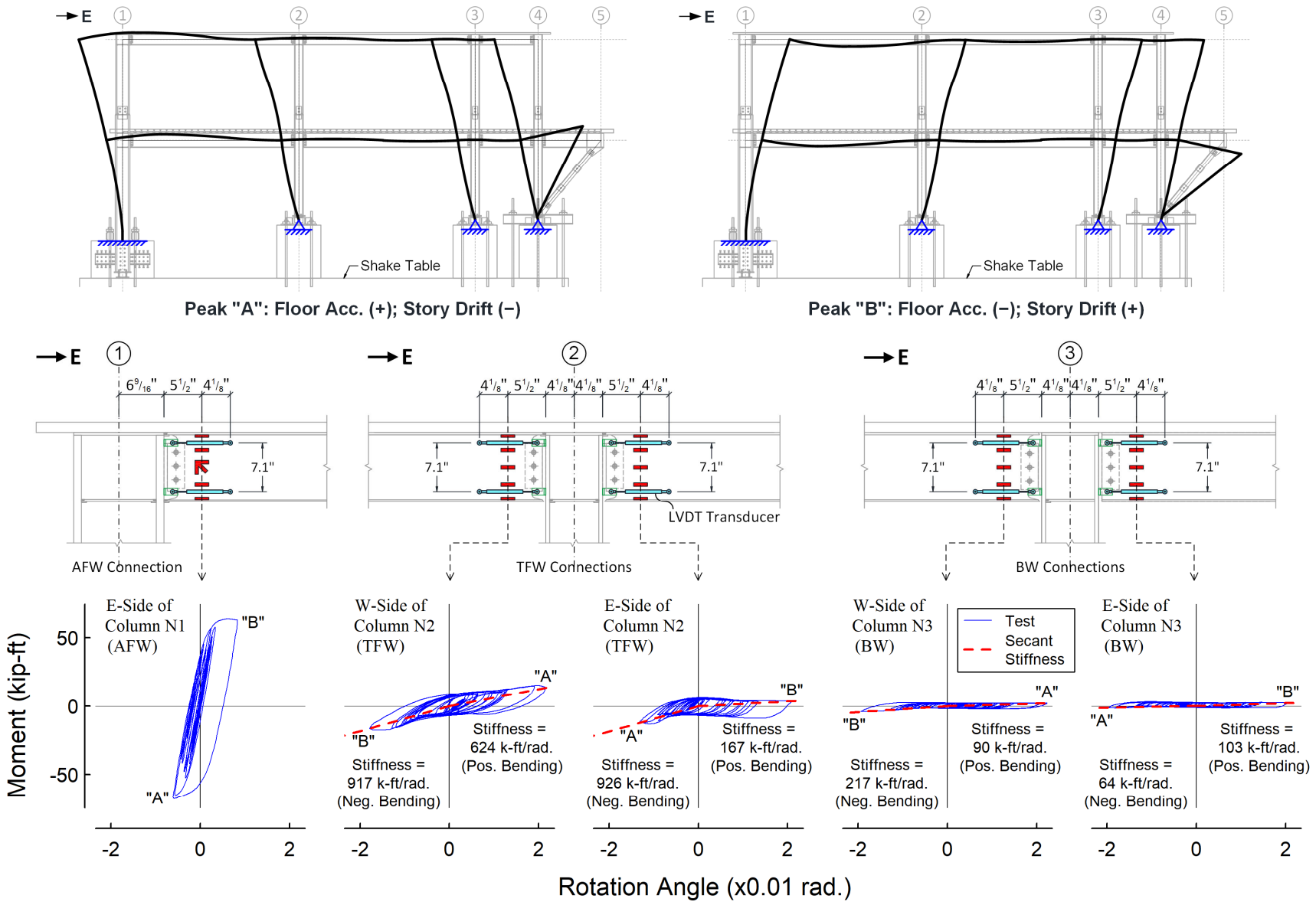

Figure 7.80 Test 2B-5: Moment versus Rotation Responses of 2nd Floor Collector Connections

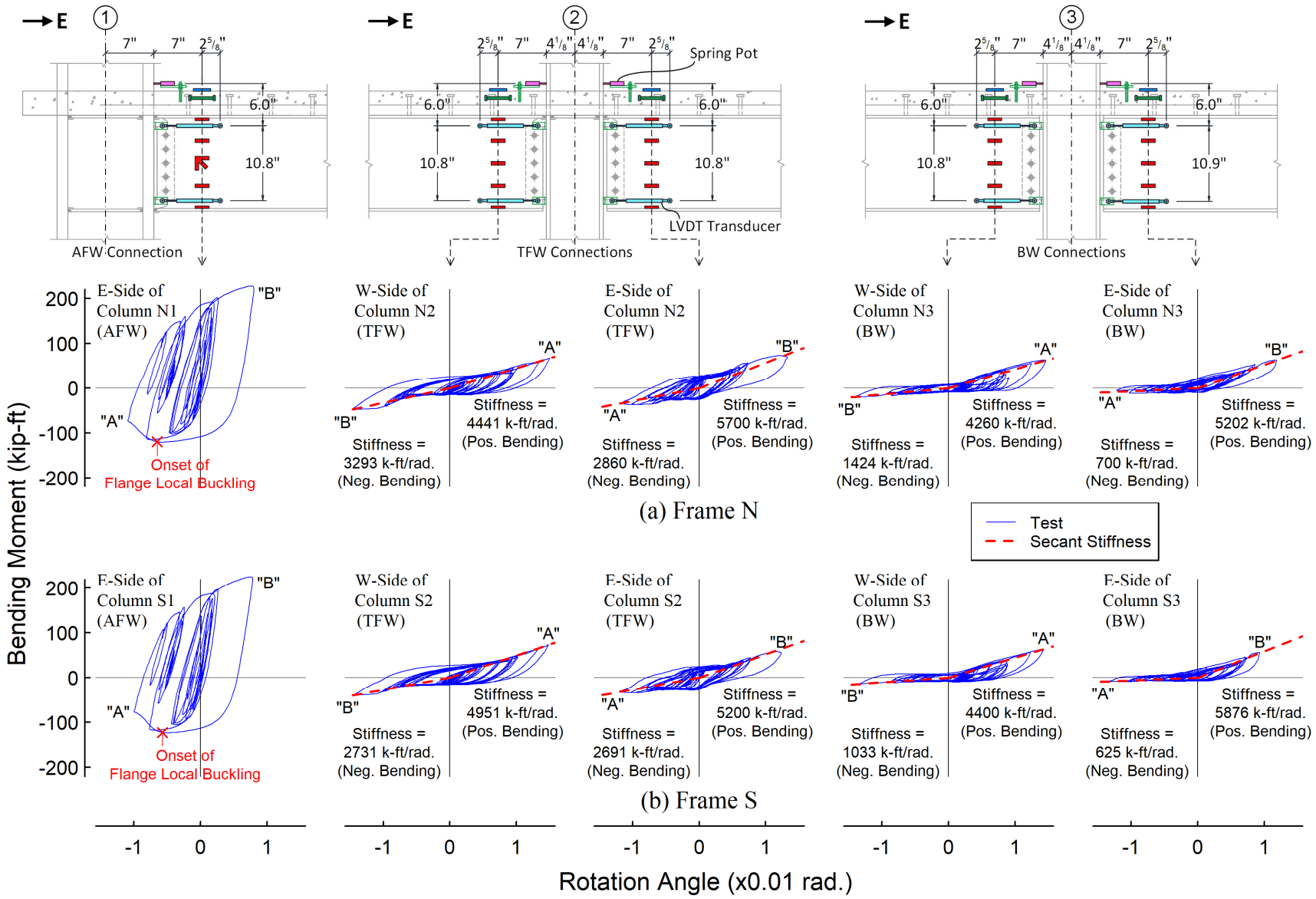

Figure 7.81 Test 2B-5: Moment versus Rotation Responses of Roof Collector Connections

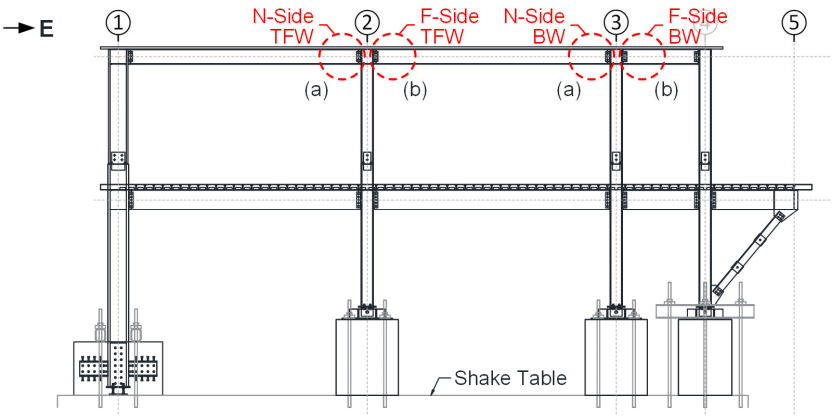

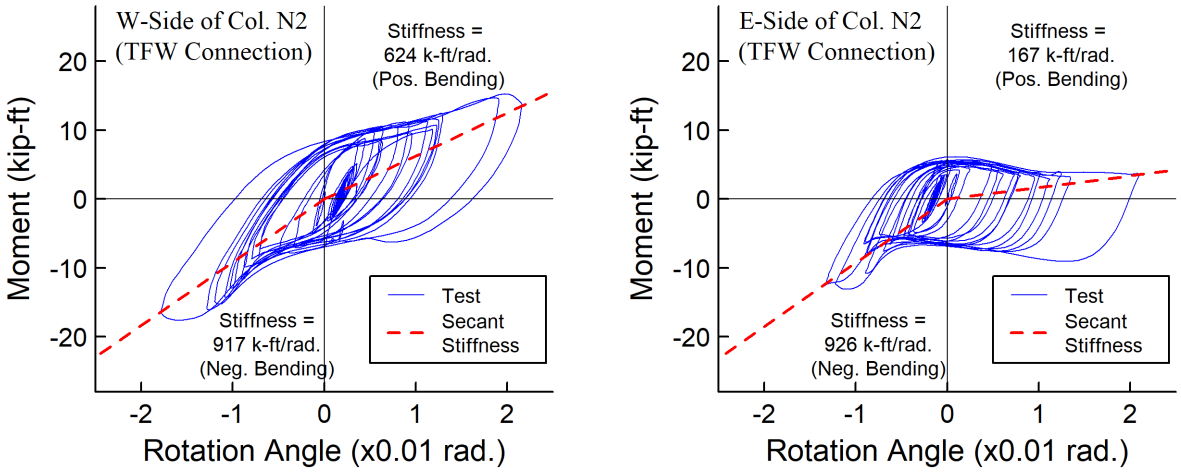

(a) Near-Side TFW Connection (b) Far-Side TWF Connection

Figure 7.82 Test 2B-5: Determination of Secant Stiffnesses for Moment versus Rotation Relationships of Roof TFW Collector-to-Column Connections

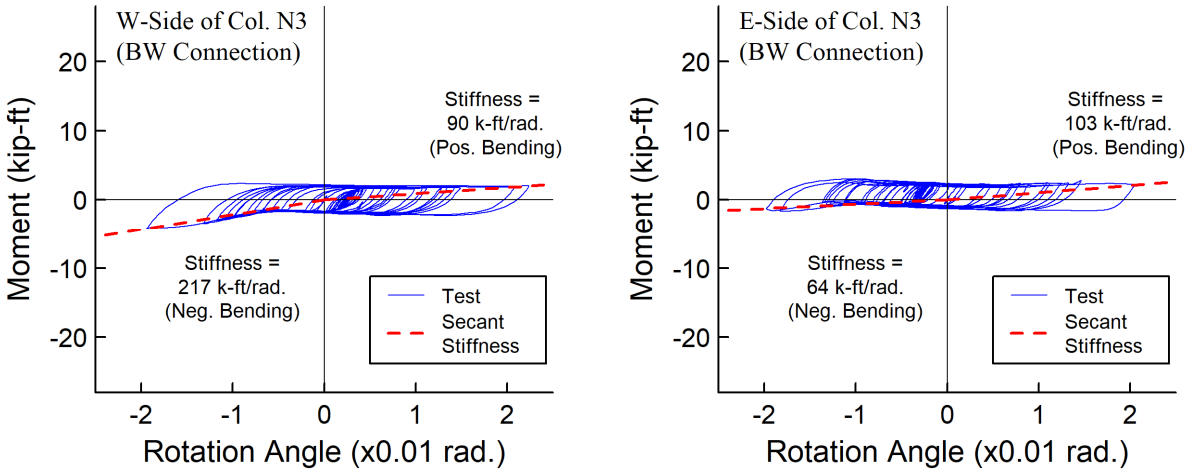

(a) Near-Side BW Connection (b) Far-Side BW Connection

Figure 7.83 Test 2B-5: Determination of Secant Stiffnesses for Moment versus Rotation Relationships of Roof BW Collector-to-Column Connections

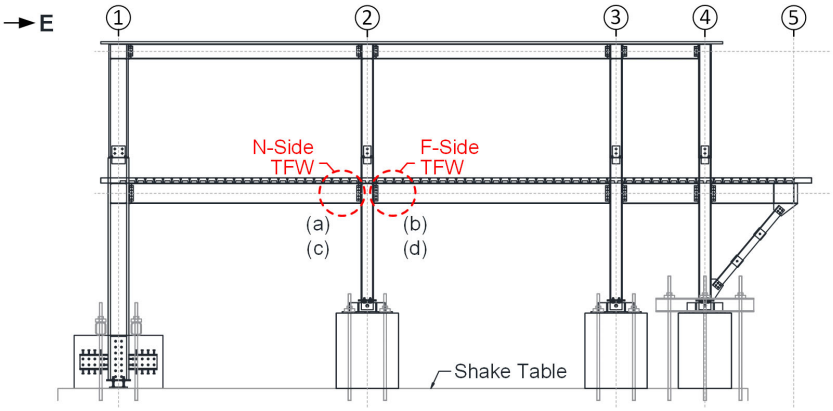

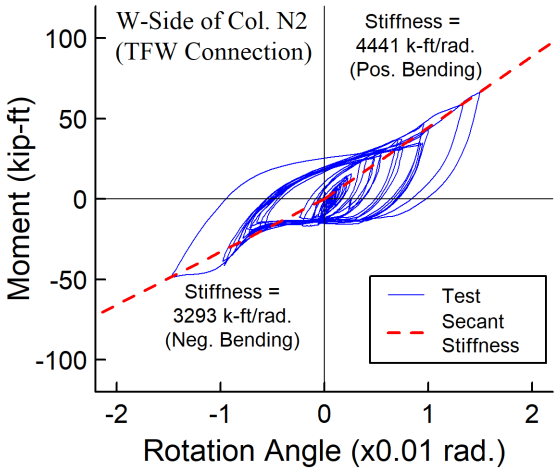

(a) North Near-Side TFW Connection

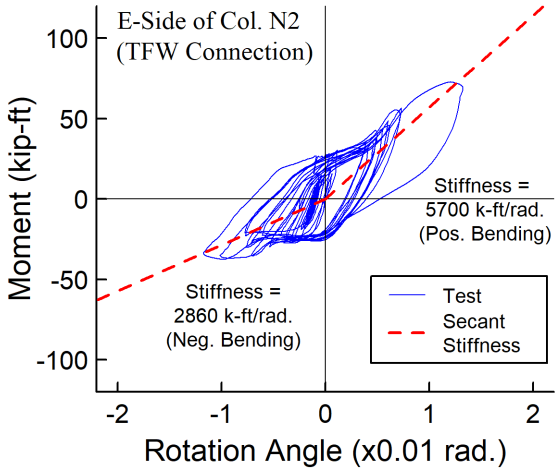

(b) North Far-Side TFW Connection

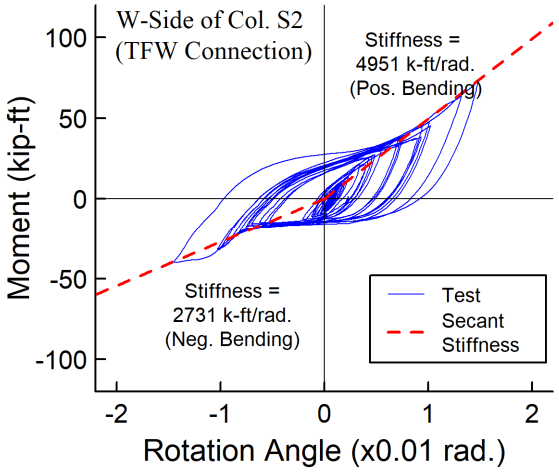

(c) South Near-Side TFW Connection

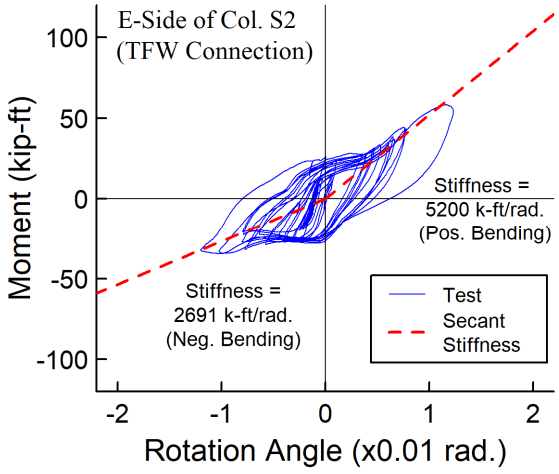

(d) South Far-Side TFW Connection

Figure 7.84 Test 2B-5: Determination of Secant Stiffnesses for Moment versus Rotation Relationships of 2nd Floor TFW Collector-to-Column Connections

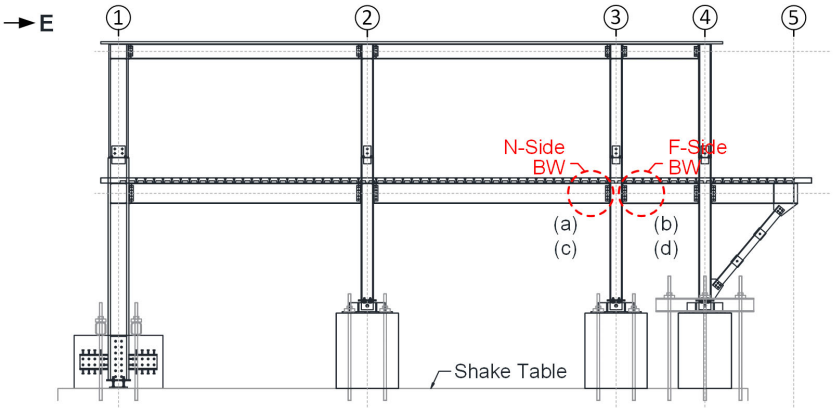

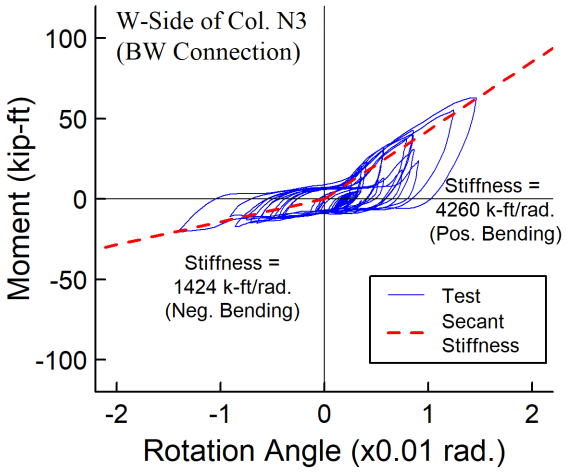

(a) North Near-Side TFW Connection

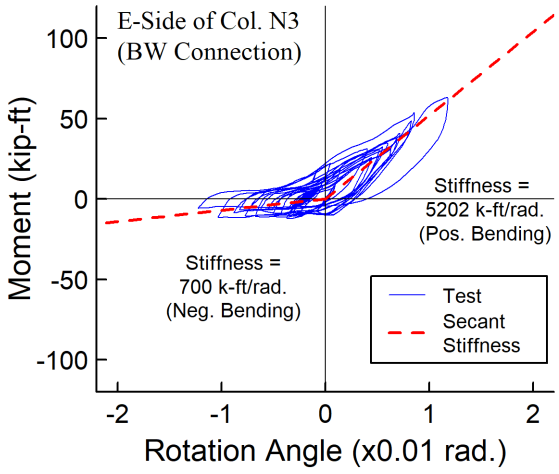

(b) North Far-Side TFW Connection

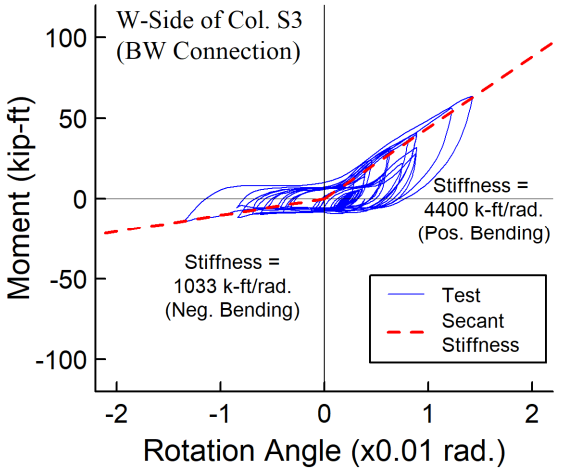

(c) South Far-Side TFW Connection

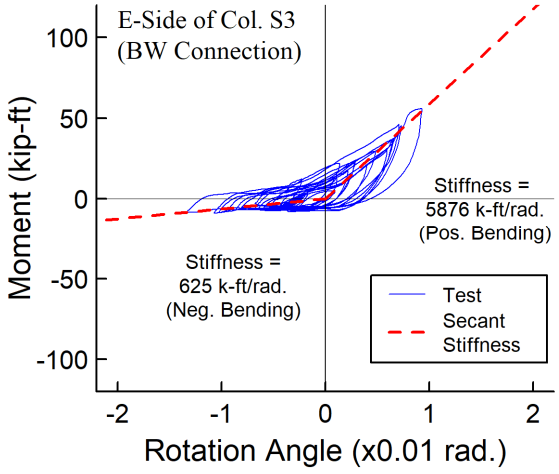

(d) South Near-Side TFW Connection

Figure 7.85 Test 2B-5: Determination of Secant Stiffnesses for Moment versus Rotation Relationships of 2nd Floor BW Collector-to-Column Connections

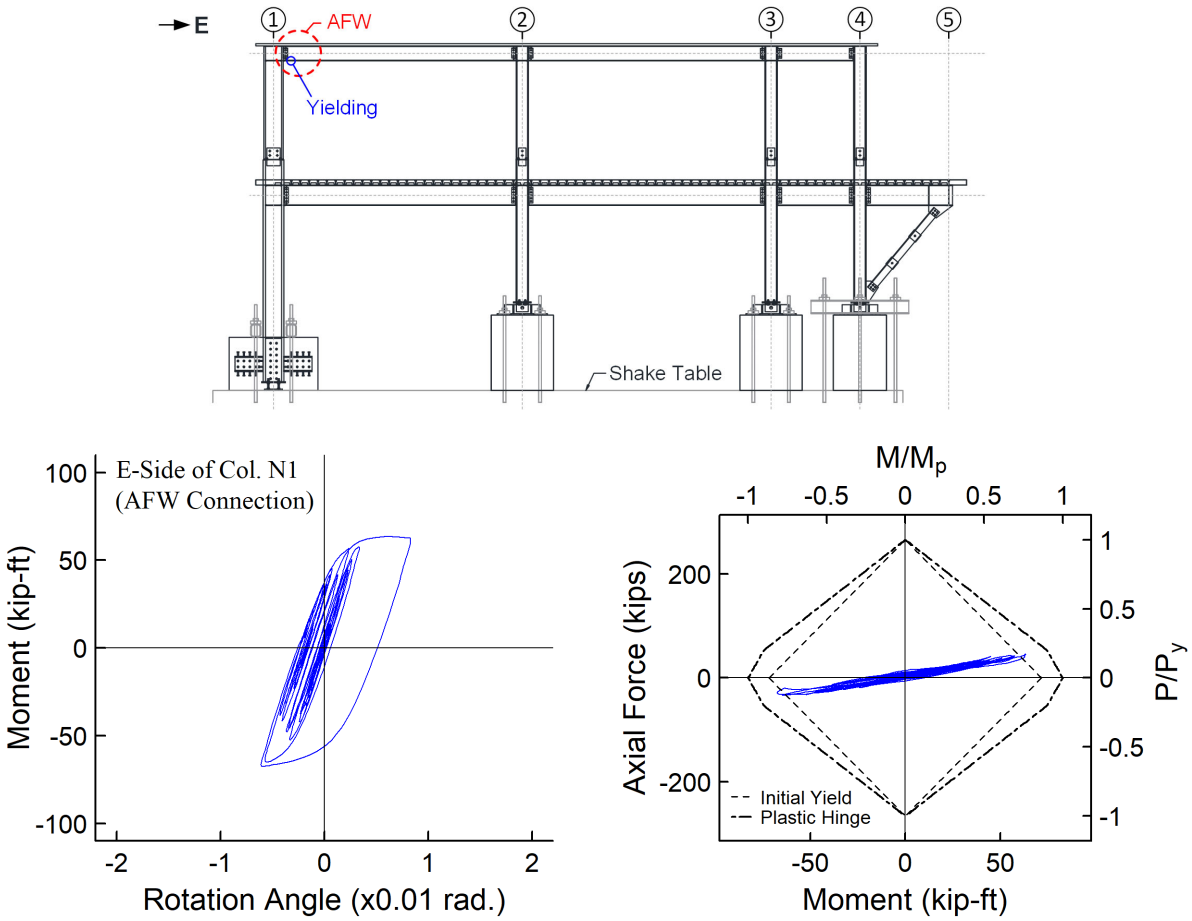

Figure 7.86 Test 2B-5: (a) Moment versus Rotation Relationship and (b) P-M Interaction of North Roof AFW Collector Connections

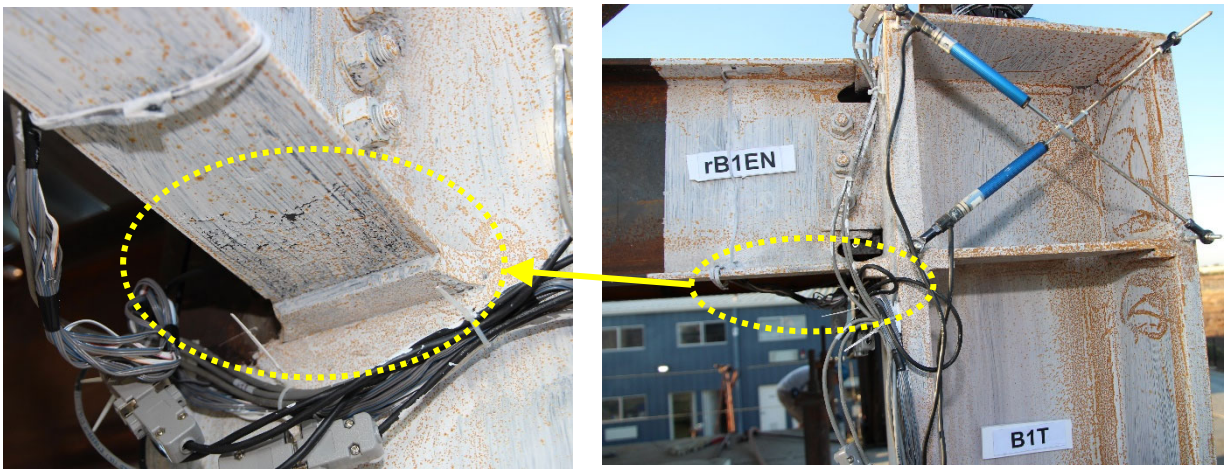

Figure 7.87 After Test 2B-5: Yielding of Bottom Flange at North Roof AFW Collector-to-Column Connection

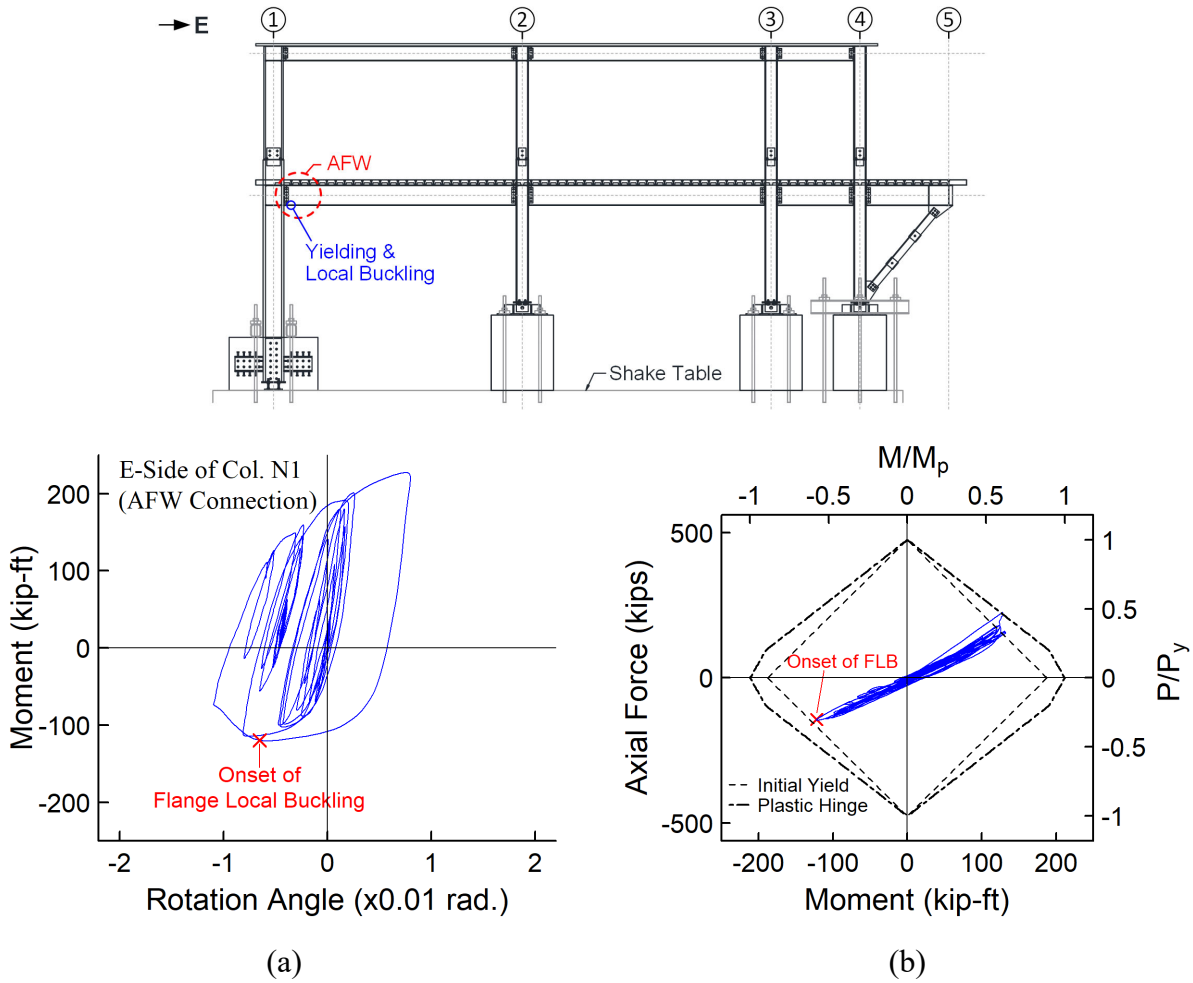

Figure 7.88 Test 2B-5: (a) Moment-Rotation Relationship of Composite Section and (b) P-M Interaction of Steel Section of North 2nd Floor AFW Connection

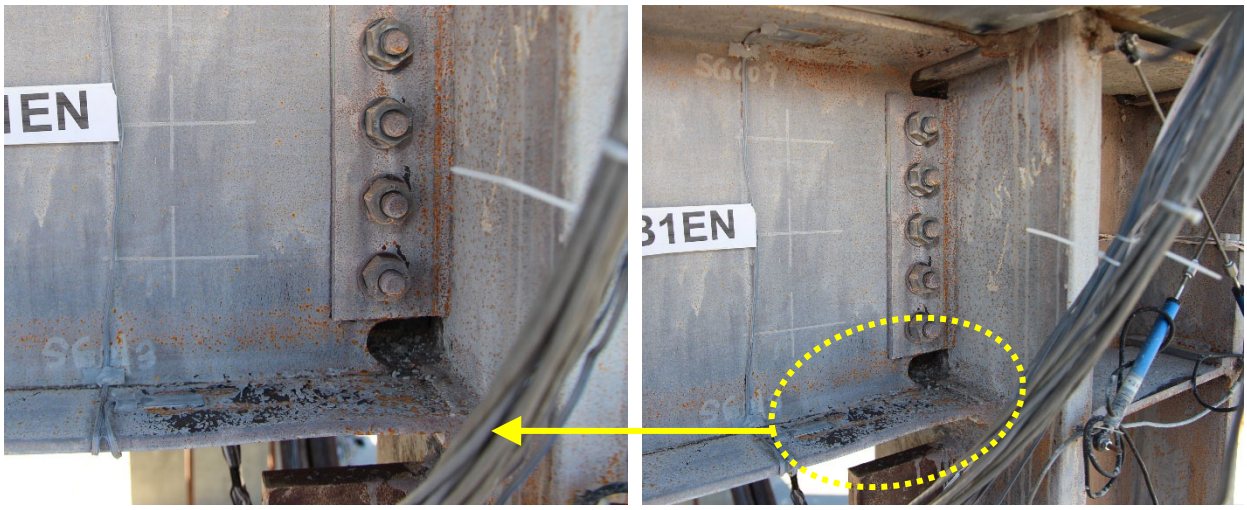

Figure 7.89 After Test 2B-5: Yielding and Local Buckling of Bottom Flange at North 2nd Floor AFW Collector-to-Column Connection

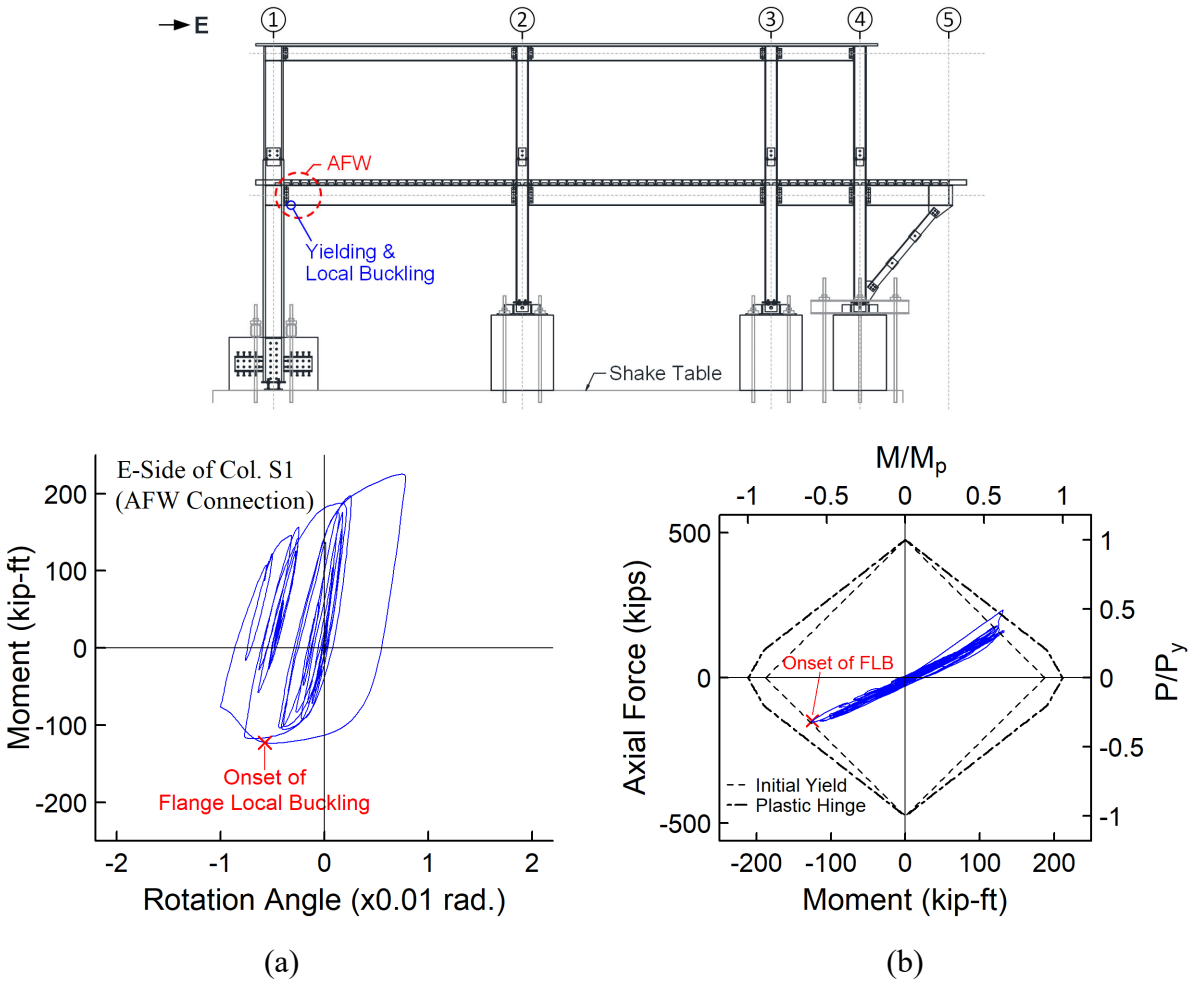

Figure 7.90 Test 2B-5: (a) Moment-Rotation Relationships of Composite Section and (b) P-M Interaction of Steel Section of South 2nd Floor AFW Connection

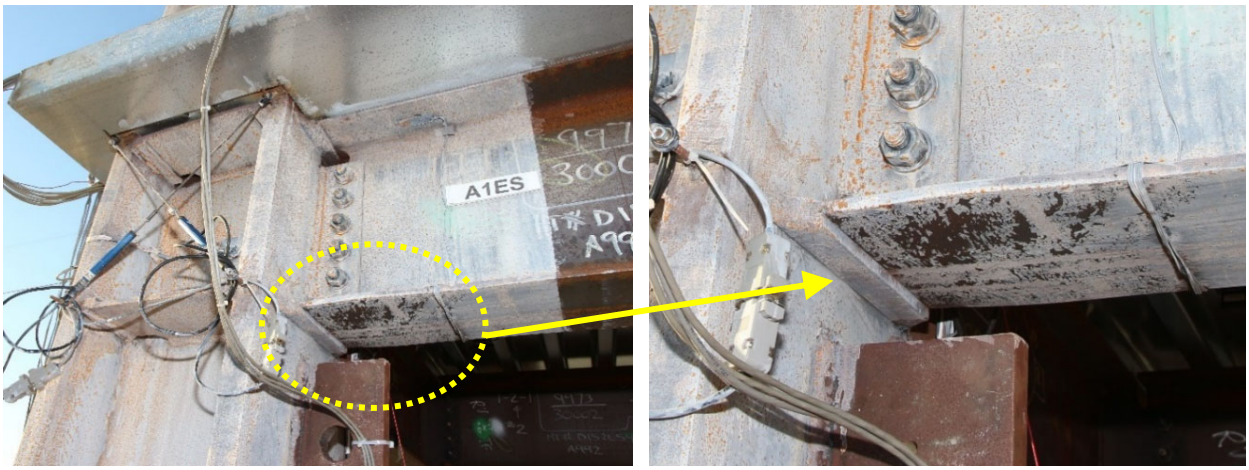

Figure 7.91 After Test 2B-5: Yielding and Local Buckling of Bottom Flange at South 2nd Floor AFW Collector-to-Column Connection

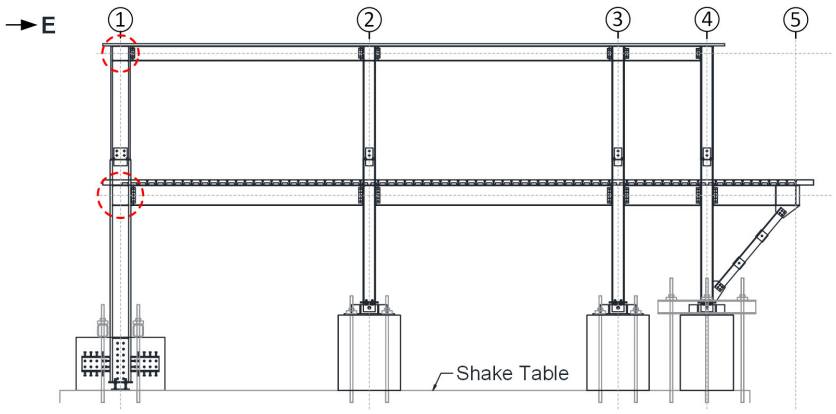

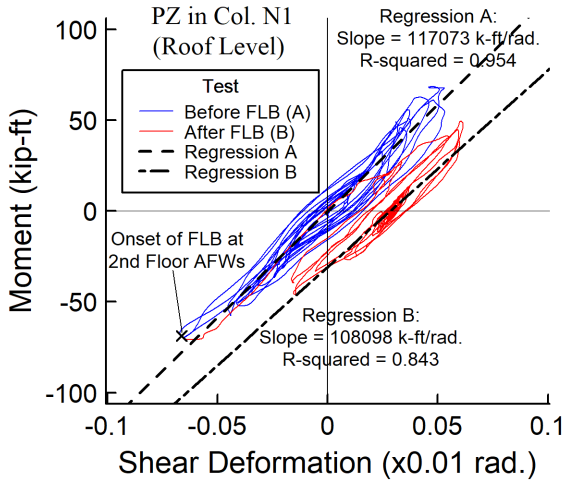

(a)

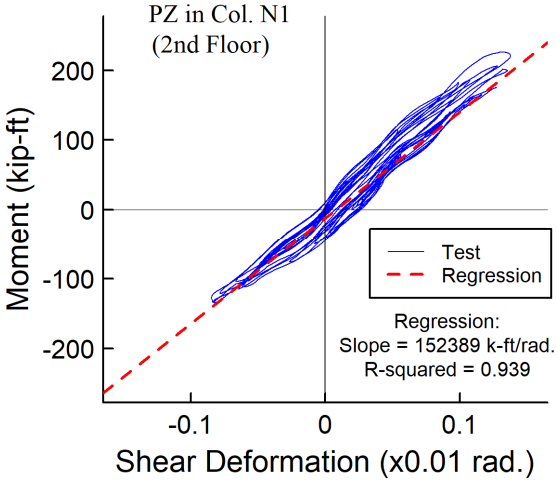

(b)

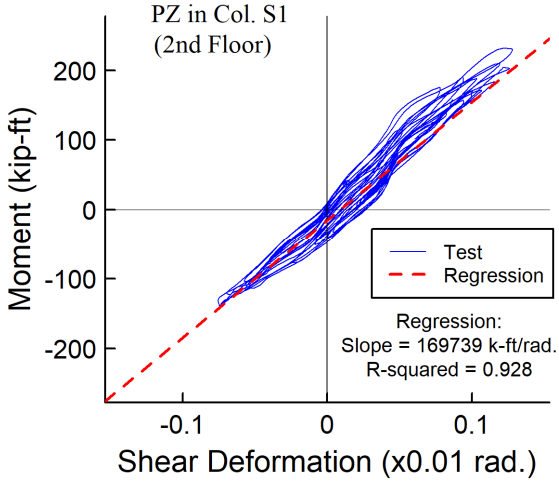

(c)

Figure 7.92 Test 2B-5: Column Panel Zone Moment versus Shear Deformation Responses

8. DESIGN IMPLICATIONS FROM PHASE 2 TESTING

8.1 Effective Slab Width of Composite Collectors

The effective slab width of composite collectors is required for the experimental data processing on the member force recovery for collectors and seismic analyses on frame models using line elements to represent collectors. Therefore, in Phase 2 testing, four concrete surface strain gauges were placed near each AFW collector-to-column connection (Figure 8.1-top) on the 2nd floor of the test specimen such that the strain profile along the slab width could be measured. Similarly, four concrete surface strain gauges were installed near each east-side composite TFW collector (Figure 8.3-top). For each measured region with four concrete gauges, one gauge (denoted as gauge "b" as shown Figure 8.1-top) was placed aligned with the centerline of steel collector. In addition, one gauge (denoted as gauge "a") was placed on the exterior slab (i.e., 1-ft hangover slab) at 9 in. from the collector centerline. Lastly, two gauges (denoted as gauge "c" and "d", respectively) were placed on the interior slab at distances of 9 in. and 18 in., respectively, from the steel beam centerline.

Figure 8.1 and Figure 8.2 show the measured concrete slab strains near the AFW connections at the instants of peak floor accelerations in Tests 2A-5 and 2B-5, respectively, while Figure 8.3 and Figure 8.4 show the measured concrete slab strains near the TFW connections at the peak corresponding floor accelerations. For all measured regions, the concrete strains were generally in tension with a very small magnitude at the instant of positive peak accelerations, at which sections the collector were in negative bending. As the measured tensile strains were very low, the signal noise would be noticeable compared to the measured values. In addition, the contribution from the concrete slab to the member forces is low when a composite beam section

is under negative bending. Thus, the strain data measured at positive peak accelerations were not used to investigate the effective slab.

On other hand, as shown in Figure 8.1 through Figure 8.4, significant compressive strains were developed on the concrete slabs at negative peak acceleration, at which the measured collector sections were in positive bending. In this case, for all measured regions, an apparent pattern that strains on the concrete slab decreased with the increasing distance from the steel collector centerline can be observed in all measured regions. The measured strain profiles were constructed by assumed a piecewise linear distribution between the measured points. For the slab overhang, the strain profile outside gauge "a" was determined by linearly extrapolating the strain data measured from gauges "a" and "b" to the edge of the slab. The strain profile beyond gauge "d" was determined by linearly extrapolating the strain data measured from gauges "c" and "d". Subsequently, the effective widths on each side of the steel collector centerline ($b_{eff,e}$ and $b_{eff,i}$, respectively) were determined separately by using the equal area principle such that a uniform strain equal to the maximum strain across the effective width creates the same total effect as that caused by the actual measured strain distribution. Table 8.1 tabulates the results of experimentally determined effective slab widths. Figure 8.1 through Figure 8.4 also plot the range of the measured effective width in comparison with that of the code-prescribed effective width from the AISC specification (AISC 2016c), which is determined from the least among the following three dimensions on each side of the collector centerline:

(1) one-eighth of the beam-span, center-to-center of supports;

(2) one-half of the distance to centerline of the adjacent beam; and

(3) the distance to the edge of the slab of the beam-span.

It can be found that measured effective slab widths $b_{eff,i}$ are noticeably narrower than the code-prescribed widths. For each type of collector connections (AFW or TFW details), the measured effective slab widths for the north and south sides frames were about the same. Note that the metal decks in the north and south halves of the floor diaphragm were respectively oriented parallel and perpendicular to the collector beams. It may suggest that the deck orientation would not noticeably affect the slab width. In addition, there is no noticeable difference between the measured effective width near the AFW connections and east-side TFW connections.

Table 8.1 Experimentally Determined Slab Effective Widths

		AFW Connection		East-Side TFW Connection	
		$b_{eff,i}$ (in.)	$b_{eff,e}$ (in.)	$b_{eff,i}$ (in.)	$b_{eff,e}$ (in.)
AISC-Prescribed Values		21	12	21	12
Test 2A-5	North-Side (Deck Parallel)	9.7	9.9	11.6	10.4
	South-Side (Deck Perpendicular)	11.1	9.1	13.1	10.9
Test 2B-5	North-Side (Deck Parallel)	11.8	10.6	10.3	8.5
	South-Side (Deck Perpendicular)	13.5	10.8	10.9	8.7
Average		11.5	10.1	11.5	9.6
C.O.V.		13.7%	7.6%	10.5%	12.5%

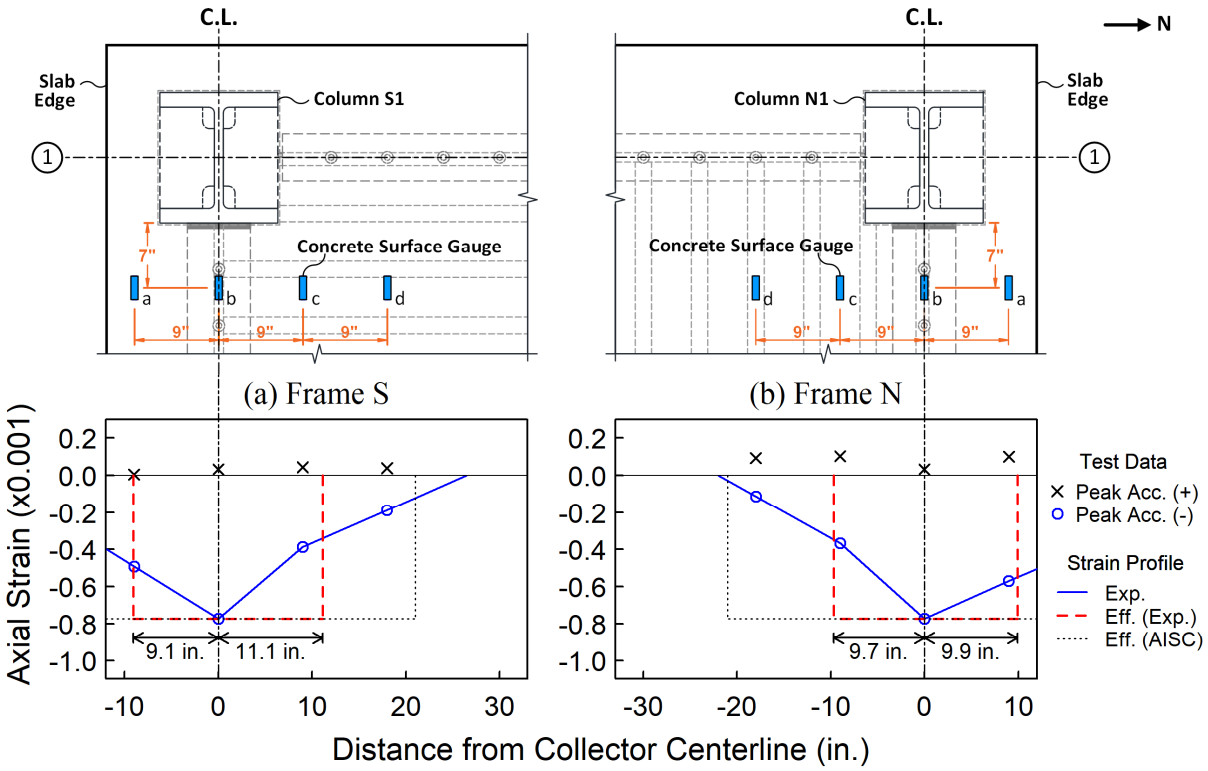

Figure 8.1 Measured Slab Strains near 2nd Floor AFW Connections (Test 2A-5)

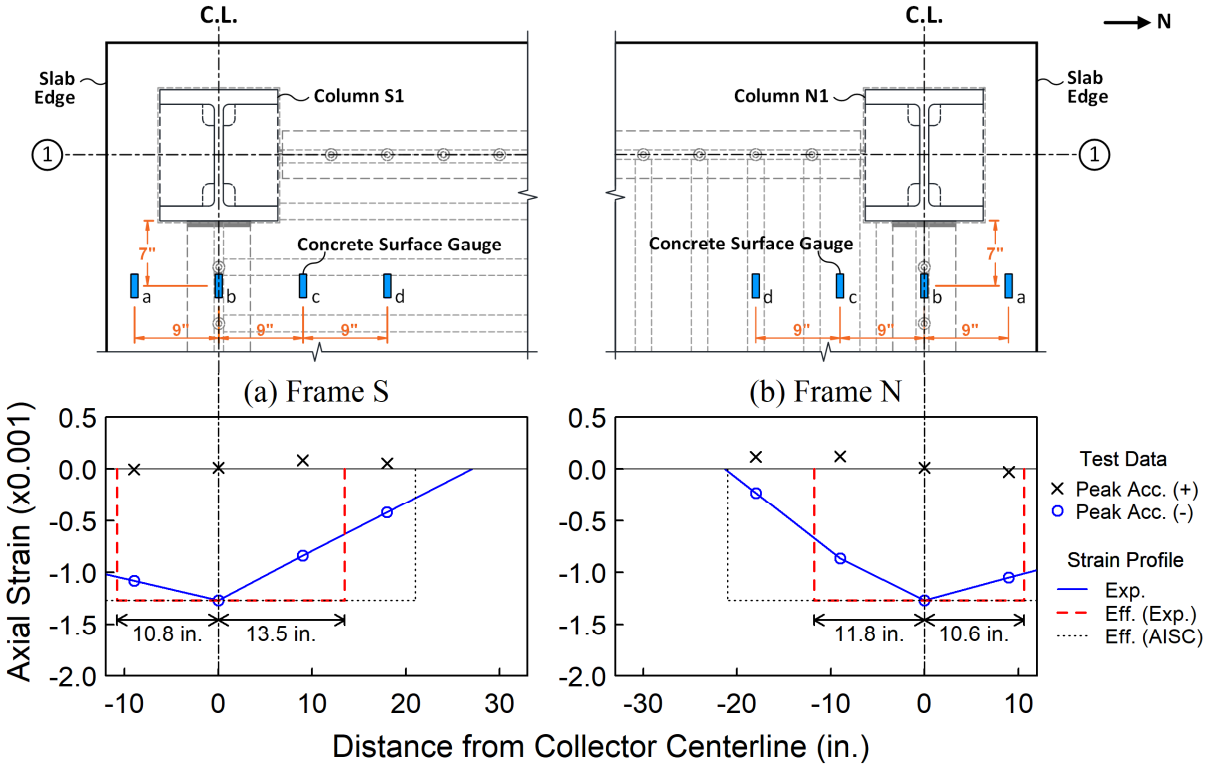

Figure 8.2 Measured Slab Strains near 2nd Floor AFW Connections (Test 2B-5)

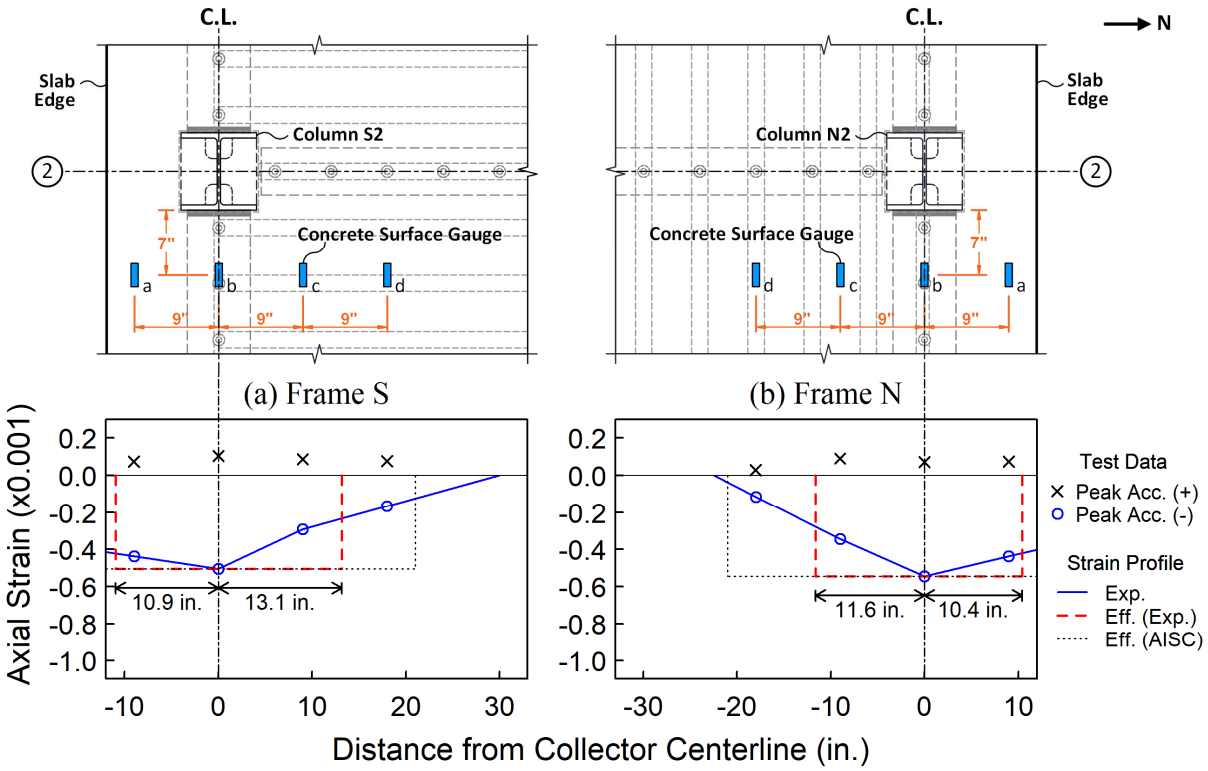

Figure 8.3 Measured Slab Strains near 2nd Floor TFW Connections (Test 2A-5)

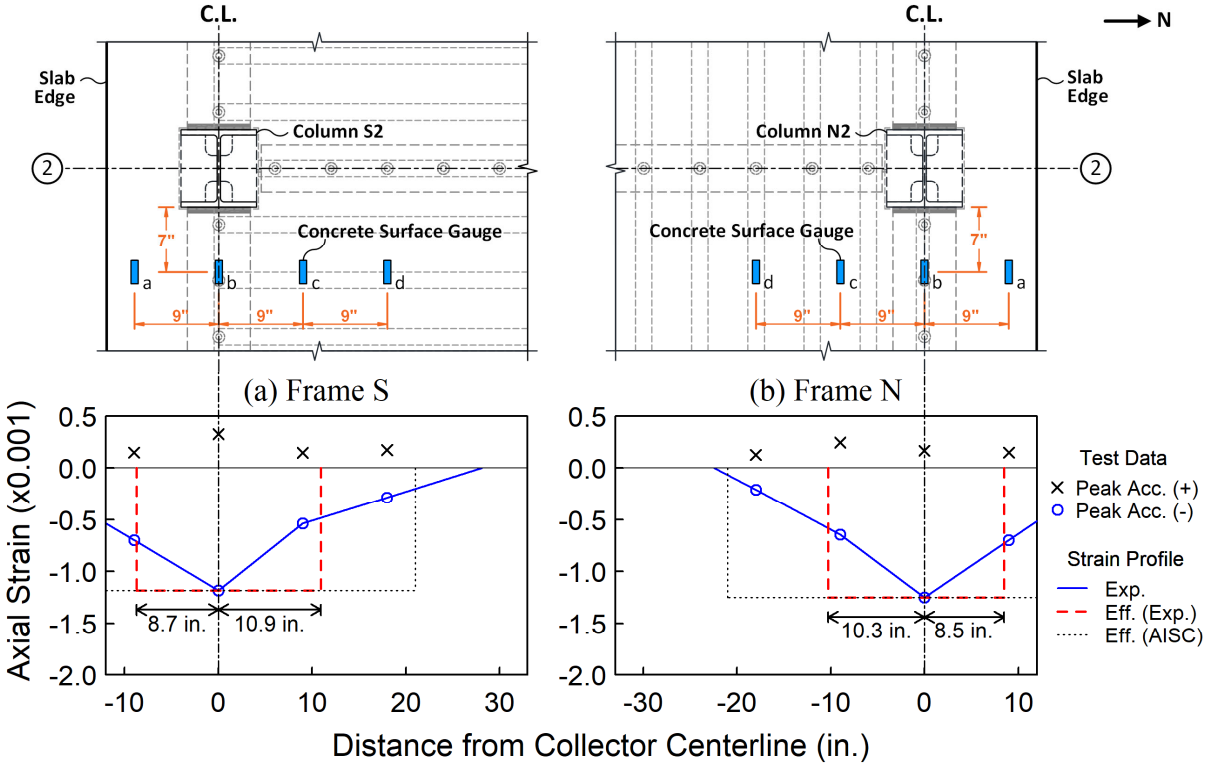

Figure 8.4 Measured Slab Strains near 2nd Floor TFW Connections (Test 2B-5)

8.2 Rotational Stiffness of Collector-to-Column Semi-Rigid Connections

8.2.1 Introduction

Experimental and analytical results from Phase 1 testing indicate that, although the rotational stiffness of a collector-to-column semi-rigid connection (TFW or BW) seems to be negligible, the combined effect of all these connections on the lateral stiffness of the test building is non-trivial. There is a need for a predictive model for the moment-rotation responses of semi-rigid connections in order to provide to an accurate estimation of the seismic force demands for collector design. However, the responses of the semi-rigid connections exhibit a nonlinear hysteresis behavior even at a very small deformation level because of the nonlinearity from bolt slip and the effects of concrete slab. An approximation method for estimating the rotational stiffness of the semi-rigid collector connections is resented below and its effectiveness is verified by using the Phase 2 test results.

8.2.2 Moment-Rotation Responses of Semi-Rigid Collector-to-Column Connections

Figure 8.5 shows the moment-rotation responses of four selected collector connections measured in Test 2B-5. These four connections respectively represent four types of collector-to-column connections: (1) bare steel TFW connection; (2) bare steel BW connection; (3) composite TFW connection; and (4) composite BW connection. Note that the two bare steel TWF and BW connections employed the same size collector beams (W10×17) and a very similar bolt layout in the web connection. The only difference between was whether the top flange was welded to the column flange or not. Comparing the hysteresis loops between these two bare steel collector connections, it can be found that the strength of the TWF connection [Figure 8.5(a)] is noticeably larger than that of the BW connection [Figure 8.5(b)], suggesting that the a good amount of bending moment in the TFW connection was produced due to the presence of the top flange weld.

For these two bare steel connections, the flat plateaus in the hysteresis loops were produced by bolt slip. In the negative bending of TWF connection [the 3rd quadrant of Figure 8.5(a)], it is apparent that the stiffness and strength of the connection hardened when the connection rotation angle exceeded 0.75% rad. This post-plateau hardening phenomenon was caused by bearing of the bolts against the connecting plates. Similarly, a slight post-plateau hardening can be observed in the BW connection [Figure 8.5(b)]. For both bare steel connections, the responses in positive and negative bending actions are similar in general.

Like the bare steel counterpart, the two composite TWF and BW connections employed the similar collector beams (W14×30 versus W14×26) and bolt layouts. The top flange weld made the difference between these two connections. As shown in Figure 8.5(c) and (d), both composite collector connections exhibited an unsymmetric responses under the positive and negative bending actions. For each connection, the stiffness and strength under positive bending (the 1st quadrant) was noticeably higher than those under negative bending (the 3rd quadrant), which was due to the participation of concrete slab in producing the moment. Under negative bending, the contribution from the concrete in resisting the moments is negligible. But concrete slab contributed significantly under positive bending and the slab effect also affected the load path and internal force distribution within the composite connections.

Since the positive bending responses of these two composite connections were similar, it suggests that, in the TFW connection, the force transmitted through the top flange did not produce a significant increase of moment in positive bending. This also implies that the pivot of the rotation along the depth of collector section would be near the top flange. On the other hand, the stiffness and strength of the TFW connection under negative bending [Figure 8.5(c)] were moderately higher than those of the BW connection [Figure 8.5(d)], suggesting that the top flange in the TFW

connection was mobilized under negative bending and it increased the stiffness and strength significantly. In general, the difference in the moment-rotation response between the composite TFW and BW connections with a similar bolted web configuration is not significant, although the BW connection had a mildly lower stiffness and strength in the negative bending. This implicates that adding a top-flange-only weld to a composite BW collector connection would not extensively increase the bending stiffness of the connection.

Furthermore, note that these two composite connections relied almost exclusively on their bare steel sections to resist the moment when they were subjected to negative bending. The negative bending response of the composite TFW connection [Figure 8.5(c)] exhibited a significant post-plateau hardening phenomenon due to the bolt-bearing. By contrast, this hardening was relatively mild, and it initiated at a larger deformation level in the composite BW connection [Figure 8.5(d)]. This is similar to that observed in the comparison between the bare steel TFW and BW connections. The fact that TFW connection exhibited a stronger and earlier post-plateau hardening than the BW connection can be explained by the location of rotation pivot of the collector section. As the top flange serves as the stiff point in the bare steel TFW connection, the rotation pivot of the section is around the top flange. By contrast, the rotation pivot of the bare steel BW connection should be near the center of the bolt group. Thus, the moment arm between the rotation pivot and exterior bolt (i.e., the bottommost bolt) in the TFW connection was much longer than that in the BW connection. This means, under the same magnitude of imposed rotation angle, the outermost bolt in the TFW connection would undergo a larger displacement than that in the BW connection. Therefore, the bolts in the TFW connection be in bearing would get into earlier than those in the BW connection, which resulted in a stronger and earlier post-plateau hardening in the TFW connection.

8.2.3 Proposed Approximation Method

Considering the semi-rigid and highly nonlinear nature of the collector connections, this research aims to evaluate the secant stiffness of the moment-rotation responses as illustrated in Figure 8.5. For the composite collector connections [Figure 8.5(c) and (d)], test results showed unsymmetric response in positive and negative bending. The secant stiffnesses for positive and negative bending, denoted as K_{sj}^{+} and K_{sj}^{-}, respectively, are first evaluated. Then, the average secant stiffness, $\overline{K_{sj}} = \left(K_{sj}^{+} + K_{sj}^{-}\right)/2$ is used to represent the overall rotational stiffness of the connection. For the bare steel collector connections [Figure 8.5(a) and (b)], however, test results showed that the difference in the response between positive and negative bending was insignificant. Hence, only one secant stiffness, K_{sj}^{*}, is needed to model the connection.

Since the secant stiffness decreases with an increase of the rotation, for design purposes the proposed secant stiffness was calibrated to the response level at the design earthquake. For simplicity, it is assumed that the axial force in the collector dose not affect the rotational characteristics of the connections. As illustrated in the Figure 8.6, the concept of "component-based spring model" (Sadek et al. 2008; Koduru and Driver 2014; Weigand 2017) is adopted herein to evaluate the rotational stiffness of the connections. The collector connection is discretized into a series of horizontal springs, where each spring represents a component of the connection (e.g., concrete slab, steel flange, and bolts). These springs are attached to a pair of rigid bars at the edges of the connection, which are permitted to rotate and displace horizontally relative to each another. It is assumed that the shear response is rigid at the in the connection. The behavior of the connection is aggregated from the behavior of individual components from which it is comprised.

Note that, during Test 2B-5, the peak 1st and 2nd inter-story drift angles of the test specimen reached 1.74% and 1.81% rads, respectively. Based on the experience from extensive experimental

and analytical study on various types of building structure systems, this level of story drifts is close to a moderate response of a building structure under the design earthquake. Test results showed that the nonlinearity of the semi-rigid collector connection response came from the bolted joints and concrete slab, while the steel top flanges in the TFW connections remained elastic. Thus, in the proposed spring models (see Figure 8.6), the stiffness of the spring representing the steel flange, k_f, is determined from the elastic properties of the flange. The nonlinearity of the concrete slab responses is embodied in the unsymmetric behavior between tension and compression. Figure 6.29 shows that, on the compression side, the concrete had not reached the crushing strain and the compressive response can be simplified as linearly elastic. On the tension side, the strength developed in the concrete can be negligible. For positive bending [Figure 8.6(a)-top], the concrete slab is divided into two layers (i.e., the concrete slabs above and below the top of the meatal deck) and each layer of concrete is modeled by a linear spring with a stiffness (k_{tc} or k_{bc}) determined based on the initial stiffness of the concrete. The concrete springs are removed under negative bending [Figure 8.6(a)-bottom]. Lastly, to address the nonlinearity of the bolted joint response, which comes from bolt slip and bolt bearing, each bolt is modelled as a linear spring assigned with a secant stiffness (k_{bj}). For design purposes, the estimated secant stiffness of the bolted joint should correspond to the peak rotation response of the collector connection under the design earthquake. Details for determining the stiffness of each component are described as follows.

Collector Flange

The connection region considered (denoted as L_{jj} in Figure 8.6) runs from the column face to the far-side bolt hole edge on the collector web, which leads to:

$$L_{jj} = L_e^* + \frac{d_{h,BW}}{2} \tag{8.1}$$

where L_e^* the horizontal distance between the column face and the centerline of the farthest bolt row (if multiple bolt rows are used). $d_{h,BW}$ is the bolt hole diameter on the collector web. With the range of the connection region defined, the axial stiffness, k_f, of the steel flange is

$$k_f = \frac{E_s t_f b_f}{L_{jj}} \tag{8.2}$$

where E_s is the Young's modulus of steel, and b_f and t_f are the width and thickness of the flange.

Concrete Slab

The axial stiffness, k_{tc}, for the top-layer concrete slab is

$$k_{tc} = \frac{E_c b_{eff,t} h_c}{L_{jj}} \tag{8.3}$$

where E_c is the Young's modulus of concrete, $b_{eff,t}$ is the width of the column face for the effective slab width considered herein, and h_c is the depth of concrete slab above the metal deck. Similarly, the stiffness, k_{bc}, for the bottom-layer concrete slab s

$$k_{bc} = \frac{E_c b_{eff,b} h_r}{L_{jj}} \tag{8.4}$$

where $b_{eff,b}$ is the width of the bottom-layer concrete within the range of column face width, and h_r is the rib height of the metal deck. For simplicity, the bottom-layer concrete spring can be ignored, which would result in a conservative estimation (underestimation) of the rotational stiffness of the connection.

Concrete Web

As shown in Figure 8.6, every bolted joint is given the same stiffness, k_{bj}, which in turn is determined from the secant stiffness of the bottommost bolted joint of the bolt group on the. When a collector connection is subjected to a rotation angle, the bottommost bolt would undergo the

largest displacement and contribute the most to the rotational stiffness of the connection. Thus, assigning the secant stiffness from this bolted joint to the remaining bolts would lead to an underestimation of the stiffness of these bolts. This underestimation is preferable as it would, to some extent, compensate the neglect of the axial force effect on the rotational stiffness of the collector connection.

To determine k_{bj} for the bottommost bolted joint, a target displacement, Δ_t, for the bolt produced by design rotation angle of the collector connection, θ_t, is needed. In practice, the design rotation angle can be taken as the design story drift angle of the frame:

$$\theta_t = C_d \theta_e / I_e \tag{8.5}$$

where C_d and I_e are the code-prescribed deflection amplification factor and seismic importance factor, respectively (ASCE 2016). θ_e is the story drift angle produced by the code-prescribed design earthquake forces. To verify the proposed method with the test results, however, θ_t is taken as the measured peak story drift angle from the test specimen. With the target rotation angle, θ_t, , Figure 8.7 and Figure 8.8 illustrate the proposed approach for approximating the target displacement of the bottommost bolt, Δ_t, in the TFW and BW connections, respectively. As shown in Figure 8.7, for both composite and bare steel TFW connections, it is assumed that the rotation pivots at the top steel flange regardless the directions of the applied bending moments. In addition, for a composite BW connection [Figure 8.8(a)], it is assumed that rotation pivots at the top of the metal deck when the connection is under positive bending, while the rotation pivots at the center of the bolt group when the collector is under negative bending. Lastly, for a bare steel connection [Figure 8.8(a)], the rotation pivots at the center of the bolt group for both positive and negative bending. These assumed pivot point locations are based on observations from the test results but with some simplification leading to a slight overestimation of the moment arm between the pivot

point and the outermost bolt. Define the distances from the assumed pivot point to the outermost bolt as d^+ and d^- for positive and negative bending, respectively, the target displacements of this bolt are the following for the composite connections.

$$\Delta_t^+ = \theta_t \cdot d^+ \tag{8.6}$$

$$\Delta_t^- = \theta_t \cdot d^- \tag{8.7}$$

For bare steel connections, the pivot distance (or arm) d^* is used for both positive and negative bending, and the corresponding target displacement is

$$\Delta_t^* = \theta_t \cdot d^* \tag{8.8}$$

Given the target displacement, the next step is to determine the secant stiffness of the bolted joint (k_{bj}^+, k_{bj}^-, or k_{bj}^*) corresponding to the target displacement (Δ_t^+, Δ_t^-, or Δ_t^*). As illustrated in Figure 8.9, the bolt load-deformation relationship model proposed by Reynolds et al. (2021) is employed in this research to determine the secant stiffness of a bolted joint. Per Reynolds et al.'s model, the predicted backbone curve for the load-deformation response of a single fully-pretensioned bolted joint can be divided into three stages: (1) before slip, (2) slip stage, and (3) bearing stage, which can be described by the following force-displacement relationships:

$$R = R_{ult}(1 - e^{-\mu\Delta})^{\lambda} \qquad \text{when } 0 < \Delta \leq \Delta_s \tag{8.9}$$

$$R = R_s \qquad \text{when } \Delta_s < \Delta \leq \Delta_s + \Delta_{sd} \tag{8.10}$$

$$R = R_{ult}\left[1 - e^{-\mu(\Delta - \Delta_{sd})}\right]^{\lambda} \qquad \text{when } \Delta_s + \Delta_{sd} < \Delta \tag{8.11}$$

where R is the shear force resisted by the bolted joint, Δ is the total deformation of the bolted joint, including shear, bearing, and bending deformation of the bolt, bolt slip, and bearing deformation of the connecting plates. μ and λ are empirically determined regression parameters, taken as 0.394/mm (10/in.) and 0.55, respectively (Crawford and Kulak 1971). R_{ult} is the bearing strength

of the bolted joint, which is taken as the least nominal strength among the bolt bearing strength and the bearing and tearout strengths at boles on the connecting plates. R_s is the slip resistance of the bolt and can be determined as:

$$R_s = \mu_s D_u T_b \tag{8.12}$$

where μ_s is the mean slip coefficient for the faying surface. D_u (= 1.13) is the multiplier reflecting the ratio of the mean installed bolt pretension to the specified minimum bolt pretension, T_b. Note that Δ_{sd} in Figure 8.9 is the distance that must be traversed by bolt before coming into bearing, which can be taken as the difference between the bolt hole diameter and bolt nominal diameter. Δ_s is the deformation of the bolted joint at which slip of the bolt initiates and can be computed as:

$$\Delta_s = -\frac{1}{\mu}\ln\left[1 - \left(\frac{R_s}{R_{ult}}\right)^{1/\lambda}\right] \tag{8.13}$$

With the stiffnesses for the concrete springs (k_{tc} and k_{bc}), steel flange spring (k_{flg}) and bolted joint springs (k_{bj}), the rotational stiffnesses of the proposed spring models shown in Figure 8.6 can be computed. By summing up the rotational stiffness produced by each spring in the spring model representing a composite connection under positive bending [Figure 8.6(a)-top], the equation for computing the positive bending stiffness of a composite collector connection, K_{sj}^{+}, is

$$K_{sj}^{+} = \sum_{i=1}^{N_c} k_{ci}(y_{ci} - \bar{y}^{+})^2 + \sum_{j=1}^{N_f} k_{fj}\left(y_{fj} - \bar{y}^{+}\right)^2 + \sum_{k=1}^{N_{bj}} k_{bj}^{+}\left(y_{bjk} - \bar{y}^{+}\right)^2 \tag{8.14}$$

where N_c, N_f, N_{bj} are the numbers of springs representing concrete slab, steel flange, and bolted joint, respectively. Note that N_c = 2 in this section because two layers of concrete are considered. N_f = 1 and 0 for the TFW and BW connections, respectively. N_{bj} = 5 for the collector connections in test specimen. k_{ci} and y_{ci} are the stiffness and y-coordinate of the *i*-th concrete spring, respectively. The origin of y-axis (vertical axis) can be arbitrarily set at the bottom of the steel

beam. k_{fj} and y_{fj} are the stiffness and y-coordinate of the *j*-th steel flange spring, respectively. Recall that k_{bj}^{+} is taken as the estimated secant stiffness of the exterior bolted joint in the collector connection under the positive bending and this stiffness is assigned to all the bolted joint springs. k_{bj}^{+} and y_{bjk} are the stiffness and y-coordinate of the *k*-th bolted joint spring. The center of rigidity of all springs under positive bending, $\bar{y}^{+}$, is determined from:

$$\bar{y}^{+} = \frac{\sum_{i=1}^{N_c} k_{ci} y_{ci} + \sum_{j=1}^{N_f} k_{fj} y_{fj} + \sum_{k=1}^{N_{bj}} k_{bj}^{+} y_{bjk}}{\sum_{i=1}^{N_c} k_{ci} + \sum_{j=1}^{N_f} k_{fj} + N_{bj} k_{bj}^{+}} \tag{8.15}$$

Similarly, the rotational stiffness of the composite connection under negative bending is computed as [Figure 8.6(a)-bottom]:

$$K_{sj}^{-} = \sum_{j=1}^{N_f} k_{fj}\left(y_{fj} - \bar{y}^{-}\right)^2 + \sum_{k=1}^{N_{bj}} k_{bj}^{-}\left(y_{bjk} - \bar{y}^{-}\right)^2 \tag{8.16}$$

The y-coordinate of the rigidity center is

$$\bar{y}^{-} = \frac{\sum_{j=1}^{N_f} k_{fj} y_{fj} + \sum_{k=1}^{N_{bj}} k_{bj}^{-} y_{bjk}}{\sum_{j=1}^{N_f} k_{fj} + N_{bj} k_{bj}^{-}} \tag{8.17}$$

The average secant stiffness, $\overline{K_{sj}}$, of the composite collector connection is taken as the following for frame analysis and collector design:

$$\overline{K_{sj}} = \left(K_{sj}^{+} + K_{sj}^{-}\right)/2 \tag{8.18}$$

For a bare steel collector connection, the rotational stiffness, K_{sj}^{*}, is used to characterize the rotational response under both positive and negative bending. The following equation is used to compute the radiational stiffness of the connection shown in Figure 8.6(b):

$$K_{sj}^{*} = \sum_{j=1}^{N_f} k_{fj}\left(y_{fj} - \bar{y}^{*}\right)^2 + \sum_{k=1}^{N_{bj}} k_{bj}^{*}\left(y_{bjk} - \bar{y}^{*}\right)^2 \tag{8.19}$$

The y-coordinate of the rigidity center, $\bar{y}^*$, is

$$\bar{y}^* = \frac{\sum_{j=1}^{N_f} k_{fj} y_{fj} + \sum_{k=1}^{N_{bj}} k_{bj}^* y_{bjk}}{\sum_{j=1}^{N_f} k_{fj} + N_{bj} k_{bj}^*} \tag{8.20}$$

8.2.4 Experimental Verification of Proposed Method

The effectiveness of the proposed method to estimate the rotational stiffness of collector connections was evaluated by correlating the measured responses from Test 2B-5. However, as shown in Figure 5.41-top, the measured rotation by a pair of LVDT displacement transducers at collector end was the total rotation in a region including the collector connection (denoted by Segment AB with a length "L_{jj}") and a short collector segment (denoted by Segment BC with a length "L_{jb}"). Also, the moment was computed from the measured strains at a location 7 in. away from the column face. Thus, this moment can be used to represent the averaged moment in this region and the secant stiffness obtained from the moment-rotation response can be considered as the combined stiffness with the collector connection (Segment AB) and short collector segment (Segment BC) in series. That is, the effect of the short collector segment needs to be considered before a meaningful correlation can be made. As the collector segments adjacent to the semi-rigid collector connections remained elastic during Test 2B-5, the short collector segment can be represented by an elastic rotational spring. The positive and negative stiffnesses of the short collector segment in a composite collector are estimated as:

$$K_{sb}^{+} = \frac{E_s I_{tr}}{L_{jb}} \tag{8.21}$$

$$K_{sb}^{-} = \frac{E_s I_s}{L_{jb}} \tag{8.22}$$

where I_{tr} is the moment of inertia of the transformed section for the "effective" composite beam section next to the collector connection. See Figure 5.41 for the effective composite beam sections

next to three types of collector connections (TFW and BW details) under positive bending. On the other hand, I_s is the moment of inertia of the "effective" steel beam section (see Figure 5.42) next to the collector connection under negative bending. Similarly, the rotational stiffness of the short collector segment next a bare steel collector connection is:

$$K_{sb}^{*} = \frac{E_s I_s}{L_{jb}} \tag{8.23}$$

Subsequently, the combined flexural stiffnesses of a composite collector connection are:

$$K_{s,total}^{+} = \frac{1}{\frac{1}{K_{sj}^{+}} + \frac{1}{K_{sb}^{+}}} \tag{8.24}$$

$$K_{s,total}^{-} = \frac{1}{\frac{1}{K_{sj}^{-}} + \frac{1}{K_{sb}^{-}}} \tag{8.25}$$

The average stiffness $\overline{K}_{s,total} = \left(K_{s,total}^{+} + K_{s,total}^{-}\right)/2$ is then used to compare with the average secant stiffness from Test 2B-5. Similarly, the combined flexural stiffness of a bare steel collector connection is:

$$K_{s,total}^{*} = \frac{1}{\frac{1}{K_{sj}^{*}} + \frac{1}{K_{sb}^{*}}} \tag{8.26}$$

Table 8.2 and Table 8.3 show the comparisons among the predicted stiffnesses ($K_{s,total}^{+}$, $K_{s,total}^{-}$, and $\overline{K}_{s,total}$) by the proposed method and the experimentally determined secant stiffnesses from Test 2B-5 (denoted as $K_{s,exp}^{+}$, $K_{s,exp}^{-}$ and $\overline{K}_{s,exp}$ for positive bending, negative bending, and average stiffnesses, respectively) for the composite collector connections at the 2nd floor of the test building. Table 8.4 shows the similar comparisons for the roof bare steel collector connections. These tables also list the collector connection stiffness predicted by using models proposed by Liu and Astaneh-Asl (2004) and FEMA-355D (2000). Note that these two models were developed for

single-plate bolted web beam-to-column connections in the gravity frames based on quasi-static tests of full-scale beam-to-column subassembly specimens. For Liu and Astaneh-Asl's model, the secant stiffnesses corresponding to the peak story drift angles in Test 2B-5 were determined from their proposed moment-rotation backbone curves. On the other hand, the stiffnesses computed by the FEMA-355D equations, which are intended for estimating the initial stiffness of the single-plate connections, are directly compared with the test results. To demonstrate the results graphically, Figure 8.10 shows the measured moment-rotation responses of the 2nd floor composite semi-rigid collector connections in Test 2B-5 together with the straight lines representing the predicted stiffnesses obtained from the proposed method and the two currently available models. Figure 8.11 shows the similar comparison between for the roof bare steel collector connections.

From Table 8.2 through Table 8.4, it can be found that the ratio of prediction-to-test stiffnesses, $\overline{K}_{s,total}/\overline{K}_{s,exp}$, ranges from 0.60 to 1.39 with a mean value of 0.96 and a coefficient of variation (COV) of 31%. On the other hand, the Liu and Astaneh-Asl's model provides a prediction-to-test ratio ranging from 0.26 to 2.33 with a mean value of 0.64 and a COV of 93%. The ratio based on FEMA-355D model ranges from 1.63 to 14.98 with mean value of 3.63 and a COV of 110%. Note that mean value of the prediction-to-test ratios based on the proposed method is very closed to 1.0 and the COV is smaller than those obtained by the two available models. The appropriateness of the proposed method for frame analysis to predict the collector seismic force demand will be further verified in Sections 8.3 and 8.4.

It appears from Figure 8.10 and Figure 8.11 that the FEMA-355D model significantly overestimates the secant stiffnesses of collector connections. On the other hand, Liu and Astaneh-Asl's model noticeably underestimates the collector connection stiffness in many cases. However, Liu and Astaneh-Asl's model provides a good estimation for some situations, such as negative

bending of the composite BW connections and both directions of bending in the bare steel BW connections. Among the three methods, the proposed method provides the best prediction in an overall sense. But it does lead to a modest overestimation or underestimation in some situations. As shown in Table 8.2 through Table 8.4, the prediction-to-test ratio for the positive and negative bending stiffnesses ranges from 0.21 to 2.98 for the proposed method. It appears that, for the composite TFW connections, the proposed method tends to overestimate the positive bending stiffness but underestimate the negative bending stiffness. For the composite BW connections, the proposed approximation method would underestimate the stiffnesses for both directions of bending. For the bare steel collector connections, no trend on overestimation or underestimation was observed from the proposed method.

It will be shown in the next section that, for the purpose of evaluating the required axial force in the collectors for design, it is desirable (i.e., conservative in design) that a lower-bound estimate of the collector connection flexural stiffness be made. However, test results showed that the proposed method may overestimates the collector connection stiffness for some cases, which may be due to assumptions like neglecting the effect of axial load in the proposed method.

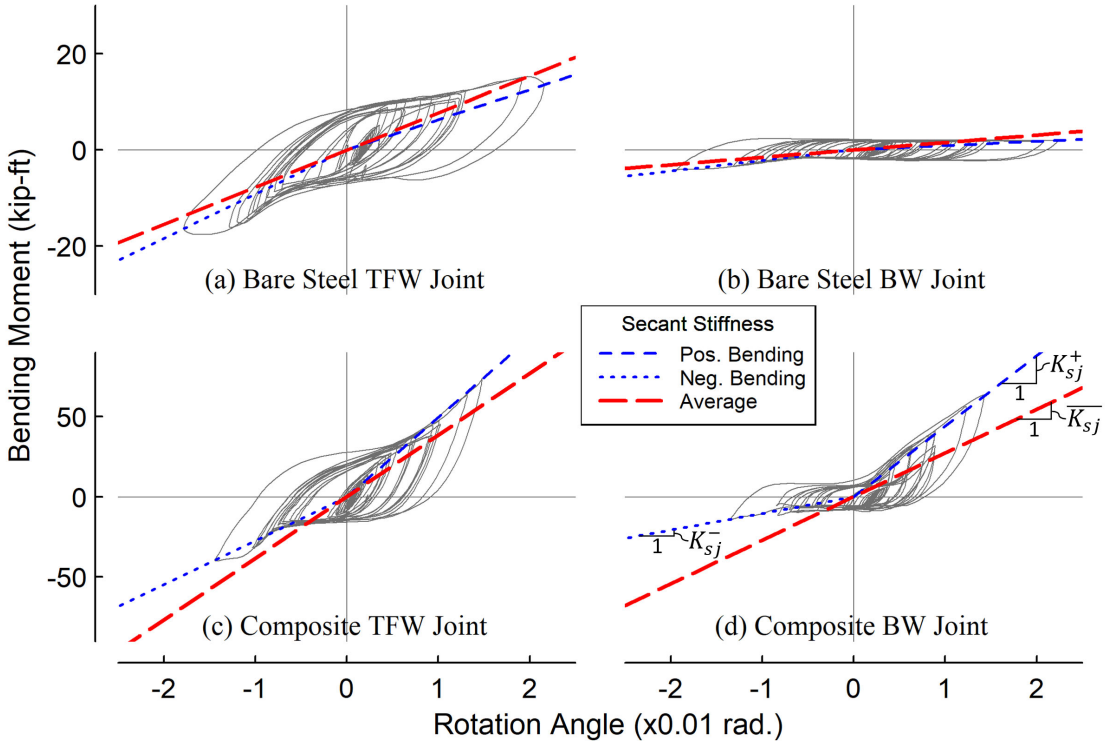

Figure 8.5 Secant Stiffnesses for Semi-Rigid Collector-to-Column Connections

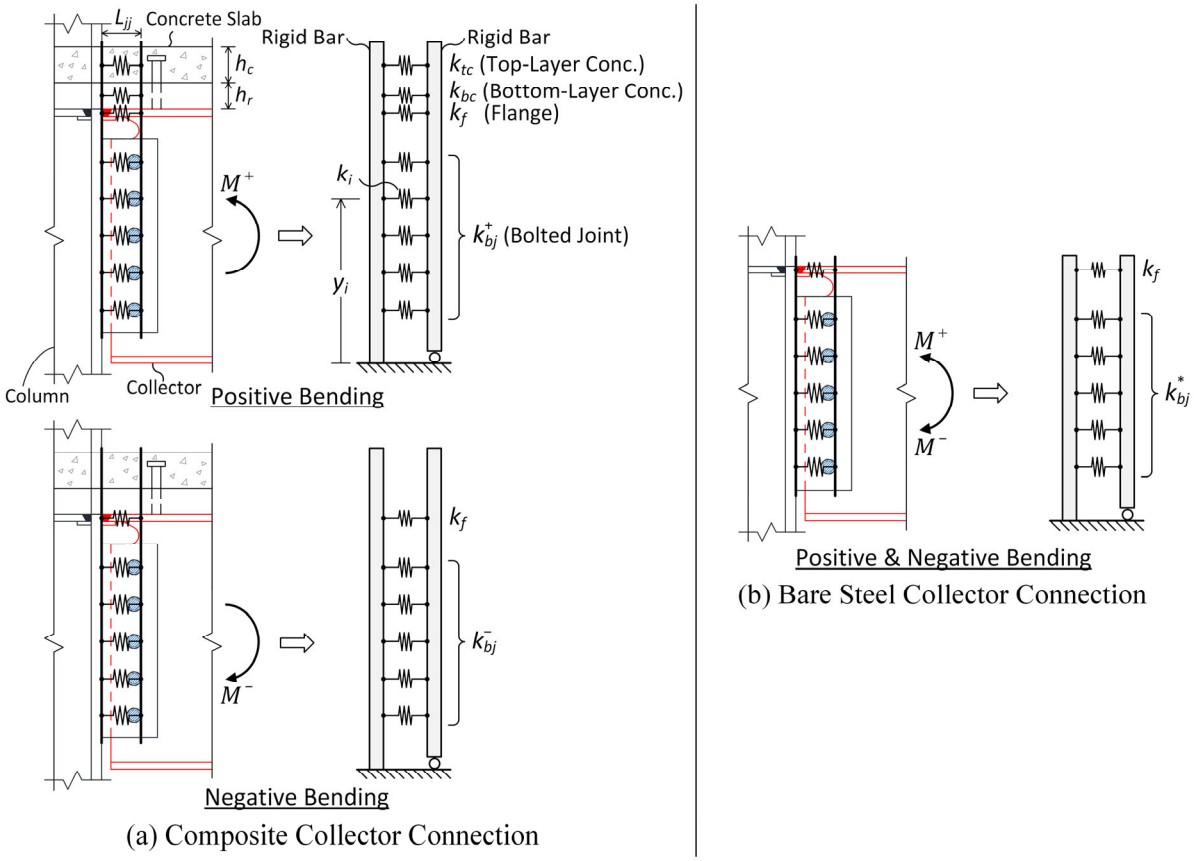

Figure 8.6 Spring Models for (a) Composite and (b) Bare Steel Collector Connections

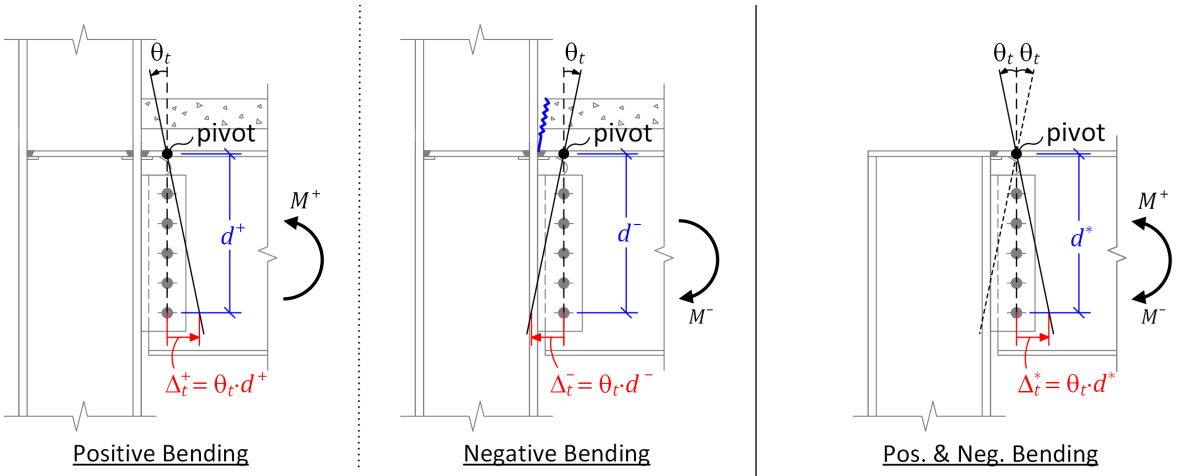

(a) Composite TFW Connection (b) Bare Steel TFW Connection

Figure 8.7 Approximation of Target Displacement of Bolted Joints in TFW Connections

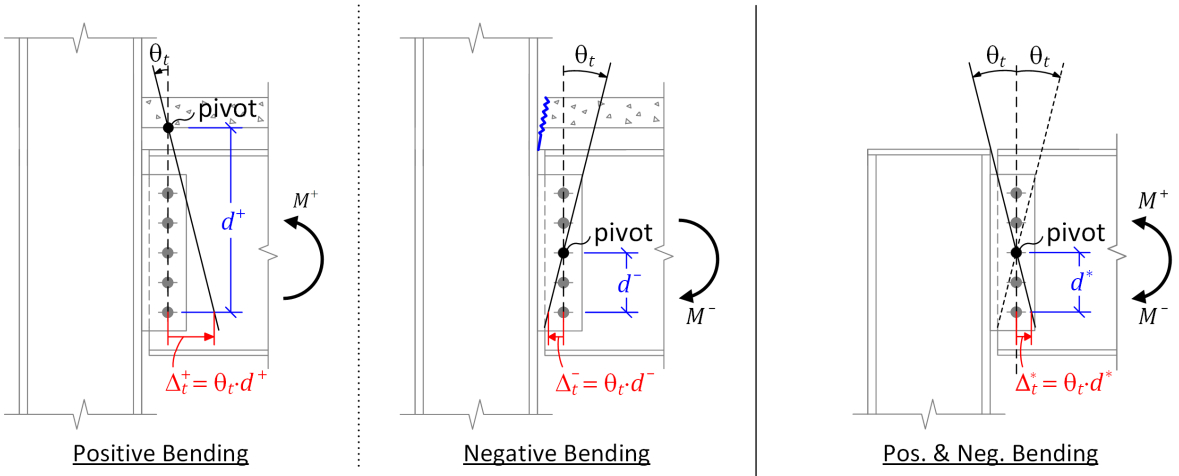

(a) Composite BW Connection (b) Bare Steel BW Connection

Figure 8.8 Approximation of Target Displacement of Bolted Joints in BW Connections

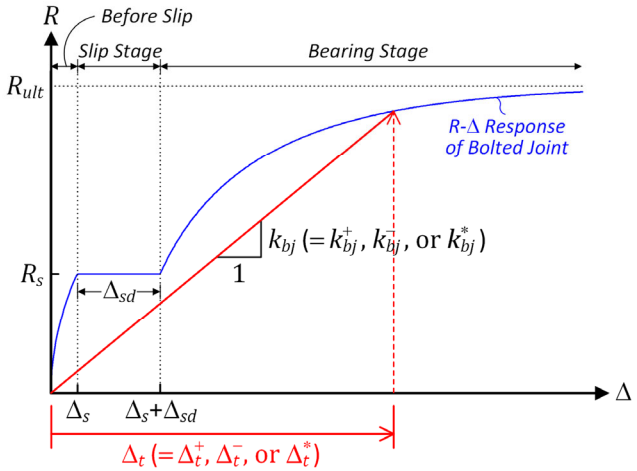

Figure 8.9 Determination of Secant Stiffness of Bolted Joint

Table 8.2 Comparison of Experimental and Predicted Stiffnesses for 2nd Floor Collector-to-Column Connections in Frame N

Collector-to-Column Connection			TFW Connection						BW Connection					
			W-Side			E-Side			W-Side			E-Side		
Bending Direction			Pos.	Neg.	Avg.	Pos.	Neg.	Avg.	Pos.	Neg.	Avg.	Pos.	Neg.	Avg.
Experiment	Secant Stiffness	$K_{s,exp}$ (k-ft/rad)	4441	3293	3867	5700	2860	4280	4260	1424	2842	5202	700	2951
Prediction	Rotational Stiffness of Collector Segment	K_{sb} (k-ft/rad)	56451	28713	–	58152	28713	–	72879	15972	–	62914	15189	–
	K_{sj} per the Proposed Method	K_{sj} (k-ft/rad)	9811	1589	–	9811	1589	–	4099	308	–	4099	308	–
		$K_{s,total}$ (k-ft/rad)	8358	1506	4932	8395	1506	4950	3881	302	2091	3848	302	2075
		$K_{s,total}/K_{s,exp}$	1.88	0.46	1.28	1.47	0.53	1.16	0.91	0.21	0.74	0.74	0.43	0.70
	K_{sj} per Liu & Astaneh-Asl (2004)	K_{sj} (k-ft/rad)	2149	829	-	2076	829	-	1959	829	-	1959	829	-
		$K_{s,total}$ (k-ft/rad)	2070	890	1480	2006	890	1448	1976	890	1433	1976	890	1433
		$K_{s,total}/K_{s,exp}$	0.47	0.27	0.38	0.35	0.31	0.34	0.46	0.63	0.50	0.38	1.27	0.49
	K_{sj} per FEMA-355D (2000)	K_{sj} (k-ft/rad)	10967	5600	–	10967	5600	–	10967	5600	–	10967	5600	–
		$K_{s,total}$ (k-ft/rad)	9183	4686	6935	9227	4686	6956	9533	4146	6839	9339	4092	6715
		$K_{s,total}/K_{s,exp}$	2.07	1.42	1.79	1.62	1.64	1.63	2.24	2.91	2.41	1.80	5.85	2.28

$K_{s,total} = 1/(1/K_{sj} + 1/K_{sb})$

Table 8.3 Comparison of Experimental and Predicted Stiffnesses for 2nd Floor Collector-to-Column Connections in Frame S

Collector-to-Column Connection			TFW Connection						BW Connection					
			W-Side			E-Side			W-Side			E-Side		
Bending Direction			Pos.	Neg.	Avg.	Pos.	Neg.	Avg.	Pos.	Neg.	Avg.	Pos.	Neg.	Avg.
Experiment	Secant Stiffness	$K_{s,exp}$ (k-ft/rad)	4951	2731	3841	5200	2691	3945.5	4400	1033	2716.5	5876	625	3250.5
Prediction	Rotational Stiffness of Collector Segment	K_{sb} (k-ft/rad)	56314	28713	–	59058	28713	–	73964	15972	–	61654	15189	–
	K_{sj} per the Proposed Method	K_{sj} (k-ft/rad)	9811	1589	–	9811	1589	–	3843	308	–	3843	308	–
		$K_{s,total}$ (k-ft/rad)	8355	1506	4931	8413	1506	4960	3653	302	1978	3618	302	1960
		$K_{s,total}/K_{s,exp}$	1.69	0.55	1.28	1.62	0.56	1.26	0.83	0.29	0.73	0.62	0.48	0.60
	K_{sj} per Liu & Astaneh-Asl (2004)	K_{sj} (k-ft/rad)	2149	829	-	2076	829	-	1959	829	-	1959	829	-
		$K_{s,total}$ (k-ft/rad)	2070	890	1480	2006	890	1448	1976	890	1433	1976	890	1433
		$K_{s,total}/K_{s,exp}$	0.42	0.33	0.39	0.39	0.33	0.37	0.45	0.86	0.53	0.34	1.42	0.44
	K_{sj} per FEMA-355D (2000)	K_{sj} (k-ft/rad)	10967	5600	–	10967	5600	–	10967	5600	–	10967	5600	–
		$K_{s,total}$ (k-ft/rad)	9183	4686	6935	9227	4686	6956	9533	4146	6839	9339	4092	6715
		$K_{s,total}/K_{s,exp}$	1.85	1.72	1.81	1.77	1.74	1.76	2.17	4.01	2.52	1.59	6.55	2.07

$K_{s,total} = 1/(1/K_{sj} + 1/K_{sb})$

Table 8.4 Comparison of Experimental and Predicted Stiffnesses for Roof Collector-to-Column Connections in Frame N

Collector-to-Column Connection			TFW Connection						BW Connection					
			W-Side			E-Side			W-Side			E-Side		
Bending Direction			Pos.	Neg.	Avg.	Pos.	Neg.	Avg.	Pos.	Neg.	Avg.	Pos.	Neg.	Avg.
Experiment	Secant Stiffness	$K_{s,exp}$ (k-ft/rad)	624	917	770.5	167	926	546.5	90	217	153.5	103	64	83.5
Prediction	Rotational Stiffness of Collector Segment	K_{sb} (k-ft/rad)	7201	7201	-	7201	7201	-	5339	5339	-	5339	5339	-
	K_{sj} per the Proposed Method	K_{sj} (k-ft/rad)	534	534	-	534	534	-	118.6	118.6	-	118.6	118.6	-
		$K_{s,total}$ (k-ft/rad)	497	497	497	497	497	497	116	116	116	116	116	116
		$K_{s,total}/K_{s,exp}$	0.80	0.54	0.65	2.98	0.54	0.91	1.29	0.53	0.76	1.13	1.81	1.39
	K_{sj} per Liu & Astaneh-Asl (2004)	K_{sj} (k-ft/rad)	202	202	-	202	202	-	202	202	-	202	202	-
		$K_{s,total}$ (k-ft/rad)	196	196	196	196	196	196	195	195	195	195	195	195
		$K_{s,total}/K_{s,exp}$	0.31	0.21	0.26	1.18	0.21	0.36	2.16	0.90	1.27	1.89	3.04	2.33
	K_{sj} per FEMA-355D (2000)	K_{sj} (k-ft/rad)	1633	1633	-	1633	1633	-	1633	1633	-	1633	1633	-
		$K_{s,total}$ (k-ft/rad)	1331	1331	1331	1331	1331	1331	1251	1251	1251	1251	1251	1251
		$K_{s,total}/K_{s,exp}$	2.13	1.45	1.73	7.97	1.44	2.44	13.89	5.76	8.15	12.14	19.54	14.98

$K_{s,total} = 1/(1/K_{sj} + 1/K_{sb})$

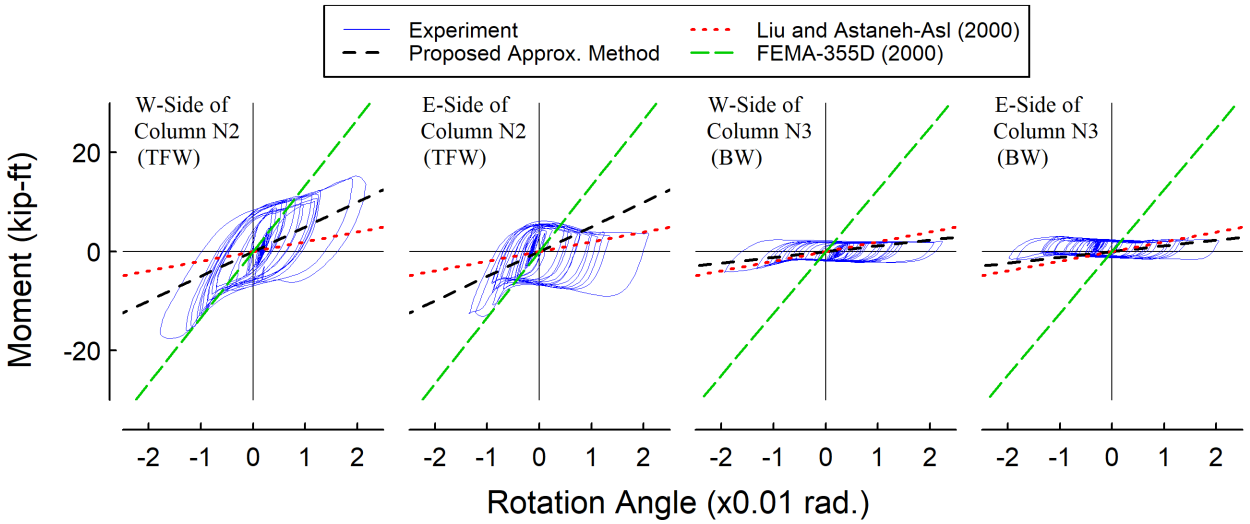

Figure 8.10 Comparison of Experimental and Predicted Moment-Rotation Relations for North Roof Collector Connections (Test 2B-5)

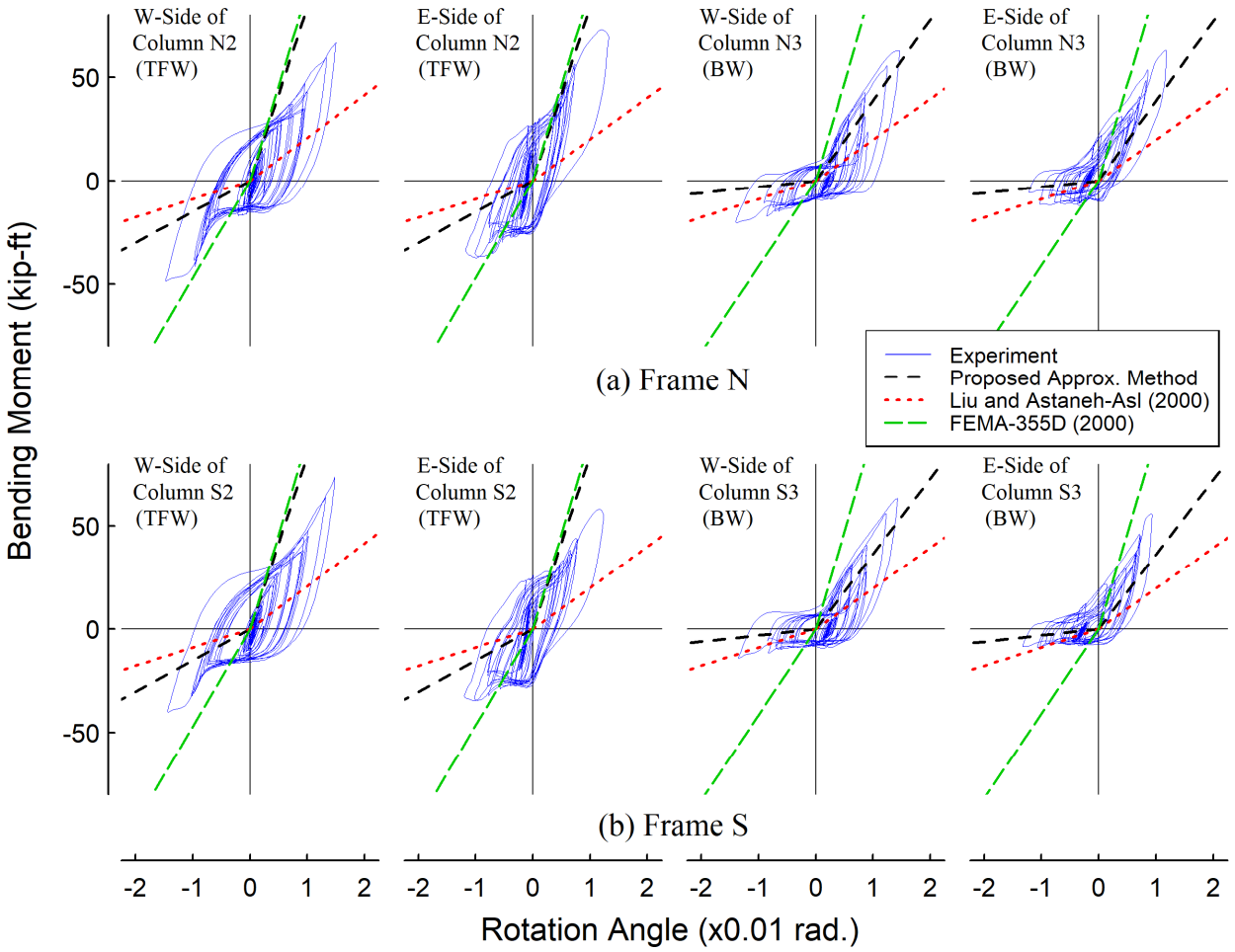

Figure 8.11 Comparison of Experimental and Predicted Moment-Rotation Relations for 2nd Floor Collector Connections (Test 2B-5)

8.3 Approximate Lateral Load Analysis of Topmost-Story Gravity Frame with Collectors

8.3.1 Proposed Lateral Load Analysis Method

As described in Sections 5.4.4 and 8.4, test results showed that, in the topmost story of a typical building, gravity columns supporting the roof collectors would participate in resisting part of the collected inertial forces in the collectors, while the collectors are collecting inertial forces on the roof diaphragm. Inertial force intercepted by each top-story gravity column is eventually turned into a shear force in that column. Taking this phenomenon into account would improve the accuracy for evaluating the collector axial force demand. To this end, an approximate lateral load analysis method is proposed.

As illustrated in Figure 8.12, a modified portal method is proposed. Based on the test results, the following two assumptions on the location of inflection points in the top-story of a plane frame under lateral forces are made:

1. The inflection point in the top-story column is at the mid-height of the column.
2. Location of the inflection point in a collector depends on the end condition of the collector as shown in Figure 8.13. For a collector with rigid connections (e.g., AFW connections) at both ends, the inflection point is at the mid-span of the collector [Figure 8.13(a)]. For a collector with a rigid connection at one end and a semi-rigid connection (e.g., TFW or BW connection) at the other end, the inflection point is at quarter span from the semi-rigid connection [Figure 8.13(b)]. For a collector with semi-rigid connections at both ends, the inflection point is at the mid-span [Figure 8.13(c)].

With these assumed inflection point locations, as illustrated in Figure 8.12, the topmost-story gravity frame can be decomposed into several collector-to-gravity column subassemblies by cutting the structure at theses inflection point locations. The closed-form solutions for the lateral

stiffnesses of each subassembly are presented in Section 8.3.2. As illustrated in Figure 8.14, with the calculated lateral stiffnesses (K_{F1} through K_{F3} for the example frame in Figure 8.12) of the collector-to-column subassemblies together with an estimated lateral stiffness for the LFRS (K_{F0}) in the top-most story, an approximate lateral load analysis then can be conducted. The topmost story is simplified as a roof collector line supported by several springs representing the LRFS and gravity columns and axially loaded by an external force equal to the total roof lateral force, F_t (i.e., the total story shear in the topmost story of a plane frame). The reaction force in a spring represents the story shear taken by the associated vertical element (LFRS or gravity column). For simplicity, the story shears resisted by the LFRS and gravity columns are proportional to their respective stiffnesses:

$$R_i = \left(\frac{k_{Fi}}{\sum_i k_{Fi}}\right) F_t \tag{8.27}$$

where R_i is the reaction force acting on the i-th spring.

Note that, each collector-to-column subassembly taken out from the plane frame represents a "half-story" substructure. To be compared with lateral stiffnesses obtained from collector-to-column subassemblies, the lateral stiffness of LFRS, K_{F0}, should also be taken as the "half-story" stiffness of LFRS. In real applications, this can be approximated by doubling the lateral stiffness of the full-height topmost story in the LFRS. In addition, although the roof collector connection adjacent to the LFRS may also provide some provide some lateral stiffness, this contribution is neglected because it is expected to be much smaller than the stiffness of the LFRS itself.

8.3.2 Derivation of Lateral Stiffnesses of Collector-to-Column Subassemblies

Based on the geometry and the type of collector connection, the topmost-story collector-to-column subassemblies can be categorized into four cases (see Figure 8.15 through Figure 8.18): (1) interior beam-to-column subassembly with semi-rigid connections; (2) exterior beam-to-column subassembly with semi-rigid connections; (3) interior beam-to-column subassembly with rigid joints; and (4) exterior beam-to-column subassembly with rigid connections. Furthermore, for each type of beam-to-column subassembly, two simplified frame models are considered to develop the approximate equations. The first model neglects the column panel zone effect, while the second model takes the panel zone effect into account.

Case 1: Interior Subassembly with Semi-Rigid Connections

Figure 8.15(a) shows the simplified frame model neglecting the panel zone effect and its deflection shape for an interior topmost-story beam-to-column subassembly with semi-rigid connections. The total lateral displacement, Δ_{total}, of this model under a lateral force F_H can be computed as the summation of two deflection components, Δ_c and Δ_r, where

Δ_c = lateral deflection caused by flexural deformations in the column, and

Δ_r = lateral deflection caused by flexural deformations in the beams and rotations at the semi-rigid connections.

These two components are calculated as:

$$\Delta_c = \left(\frac{H^3}{3EI_c}\right) F_H \tag{8.28}$$

$$\Delta_r = \left(\frac{H}{L_1 + L_2}\right)^2 \left[\frac{L_1^2}{K_{sj1}} + \frac{L_2^2}{K_{sj2}} + \frac{L_1^3}{3EI_{b1}} + \frac{L_2^3}{3EI_{b2}}\right] F_H \tag{8.29}$$

The lateral stiffness of the beam-to-column subassembly representing a topmost-story interior frame (TIF), $k_{F,TIF}$, can be derived as follows:

$$k_{F,TIF} = \frac{F_H}{\Delta_{total}} = \frac{F_H}{\Delta_c + \Delta_r} = \frac{1}{\frac{H^3}{3EI_c} + \left(\frac{H}{L_1 + L_2}\right)^2 \left[\frac{L_1^2}{K_{sj1}} + \frac{L_2^2}{K_{sj2}} + \frac{L_1^3}{3EI_{b1}} + \frac{L_2^3}{3EI_{b2}}\right]} \tag{8.30}$$

where H and I_c are height and moment of inertia of the column in the subassembly, respectively. L_1 and L_2 are the beam lengths. Note that the moment of inertia of the composite collector beam (I_{b1} or I_{b2}) is taken as the average between the moments of inertia of bare steel section and transformed section. K_{sj1} and K_{sj2} are the rotational stiffnesses of the semi-rigid connections. It is suggested to use the average value between of the secant stiffnesses in positive and negative bending for K_{sj1} and K_{sj2}.

Figure 8.15(b) shows the frame model considering the column panel zone effect In this model, in addition to the deflection components Δ_c and Δ_r, the deflection caused by the panel zone deformation, Δ_{pz}, also contributes to the total lateral displacement, Δ_{total}. The three deflection components can be calculated as:

$$\Delta_c = \left(\frac{H_c^3}{3EI_c}\right) F_H \tag{8.31}$$

$$\Delta_r = \left(\frac{H}{L_1 + L_2}\right)^2 \left[\frac{L_{c1}^2}{K_{sj1}} + \frac{L_{c2}^2}{K_{sj2}} + \frac{L_{c1}^3}{3EI_{b1}} + \frac{L_{c2}^3}{3EI_{b2}}\right] F_H \tag{8.32}$$

$$\Delta_{pz} = \left(\frac{H \cdot H_c}{K_{pz}}\right) F_H \tag{8.33}$$

where $L_{c1} = L_1 - w_{pz}/2$ and $L_{c2} = L_2 - w_{pz}/2$ are the clear beam lengths. w_{pz} is the width of panel zone. Usually, w_{pz} is taken as the depth of the column section, d_c. H_c is the clear column height, which equals $H - d_{pz}/2$ with d_{pz} being the depth of the panel zone. Figure 5.14 shows the gravity column panel zone regions considered in this study. K_{pz} is the rotational stiffness of the panel zone:

$$K_{pz} = G d_{pz} w_{pz} t_{pz} = G d_{pz} d_c t_{pz} \tag{8.34}$$

where t_{pz} is the thickness of the panel zone.

Then, the lateral stiffness of a beam-to-column assembly representing a TIF, $k_{F,TIF}$, with semi-rigid connections is

$$\begin{aligned} k_{F,TIF} &= \frac{F_H}{\Delta_{total}} = \frac{F_H}{\Delta_c + \Delta_r + \Delta_{pz}} \\ &= \frac{1}{\frac{H_c^3}{3EI_c} + \left(\frac{H}{L_1 + L_2}\right)^2 \left[\frac{L_{c1}^2}{K_{sj1}} + \frac{L_{c2}^2}{K_{sj2}} + \frac{L_{c1}^3}{3EI_{b1}} + \frac{L_{c2}^3}{3EI_{b2}}\right] + \frac{H \cdot H_c}{K_{pz}}} \end{aligned} \tag{8.35}$$

Case 2: Exterior Subassembly with Semi-Rigid Connections

Figure 8.16(a) shows the frame model neglecting the column panel zone effect for an L-shaped beam-to-column subassembly with semi-rigid connections. This L-shaped beam-to-column subassembly represents the topmost-story exterior frame (TEF) in a typical building. Following the similar procedure, the following lateral stiffness, $k_{F,TEF}$, for a topmost-story exterior beam-to-column subassembly with a semi-rigid connection is obtained:

$$k_{F,TEF} = \frac{F_H}{\Delta_{total}} = \frac{F_H}{\Delta_c + \Delta_r} = \frac{1}{\frac{H^3}{3EI_c} + \left(\frac{H}{L}\right)^2 \left[\frac{L^2}{K_{sj}} + \frac{L^3}{3EI_b}\right]} \tag{8.36}$$

Figure 8.16(b) shows the model that considers the column panel zone effect. The lateral stiffness, $k_{F,TEF}$, is

$$k_{F,TEF} = \frac{F_H}{\Delta_{total}} = \frac{F_H}{\Delta_c + \Delta_r + \Delta_{pz}} = \frac{1}{\frac{H_c^3}{3EI_c} + \left(\frac{H}{L}\right)^2 \left[\frac{L_c^2}{K_{sj}} + \frac{L_c^3}{3EI_b}\right] + \frac{H \cdot H_c}{K_{pz}}} \tag{8.37}$$

Case 3: Interior Subassembly with Rigid Connections

Based on the frame model shown in Figure 8.17(a), the lateral stiffness of an interior topmost-story beam-to-column subassembly with rigid connections is obtained:

$$k_{F,TIF} = \frac{F_H}{\Delta_{total}} = \frac{F_H}{\Delta_c + \Delta_r} = \frac{1}{\frac{H^3}{3EI_c} + \left(\frac{H}{L_1 + L_2}\right)^2 \left[\frac{L_1^3}{3EI_{b1}} + \frac{L_2^3}{3EI_{b2}}\right]} \tag{8.38}$$

Derived from the frame model shown in Figure 8.17(b), the lateral stiffness of an interior topmost-story beam-to-column subassembly with rigid connections becomes

$$k_{F,TIF} = \frac{F_H}{\Delta_{total}} = \frac{F_H}{\Delta_c + \Delta_r + \Delta_{pz}} = \frac{1}{\frac{H_c^3}{3EI_c} + \left(\frac{H}{L_1 + L_2}\right)^2 \left[\frac{L_{c1}^3}{3EI_{b1}} + \frac{L_{c2}^3}{3EI_{b2}}\right] + \frac{H \cdot H_c}{K_{pz}}} \tag{8.39}$$

Case 4: Exterior Subassembly with Rigid Connections

The frame model shown in Figure 8.18(a) leads to the following lateral stiffness for an exterior topmost-story beam-to-column subassembly with a rigid connection:

$$k_{F,TEF} = \frac{F_H}{\Delta_{total}} = \frac{F_H}{\Delta_c + \Delta_r} = \frac{1}{\frac{H^3}{3EI_c} + \left(\frac{H}{L}\right)^2 \left[\frac{L^3}{3EI_b}\right]} \tag{8.40}$$

Lastly, derived from the frame model shown in Figure 8.18(b), the lateral stiffness of an exterior topmost-story beam-to-column subassembly with a rigid connection is

$$k_{F,TEF} = \frac{F_H}{\Delta_{total}} = \frac{F_H}{\Delta_c + \Delta_r + \Delta_{pz}} = \frac{1}{\frac{H_c^3}{3EI_c} + \left(\frac{H}{L}\right)^2 \left[\frac{L_c^3}{3EI_b}\right] + \frac{H \cdot H_c}{K_{pz}}} \tag{8.41}$$

8.3.3 Experimental Verification of Proposed Lateral Load Analysis Method

The effectiveness of the proposed approximation lateral load analysis for the topmost-story gravity frame is evaluated by using the Test 2B-5 results. Figure 8.19-top shows the assumed inflection point locations in the collectors and columns in the 2nd story. Note that the inflection point in the 2nd-story Column 1, which served as the LFRS of the test frame, is assumed to be the mid-height of the column. The upper story can be decomposed into four beam-to-column subassemblies by cutting the structure at the assumed inflection point locations. The L-shaped beam-to-column subassembly at Column Line 1 (see Figure 8.19-bottom left) represents the substructure combining the LFRS and the adjacent AFW collector connection. Instead of using the proposed approximate equation [i.e., Eqs. (8.40) or (8.41)], for this correlation study, the lateral stiffness of this L-shaped substructure, k_{F1}, was derived by the following equation, which is derived by conducting a static condensation on the global stiffness matrix of an L-shaped frame model:

$$k_{F1} = \frac{12EI_c}{H^3}\left[1 - \frac{\frac{I_c}{H} + \frac{3}{4}\left(\frac{I_b}{L}\right)}{\frac{I_c}{H} + \frac{I_b}{L}}\right] \tag{8.42}$$

where H and L are column height and beam span of this L-shaped substructure, respectively. I_c and I_b are the moments of inertia of the column and beam in this L-shaped substructure.

The estimated lateral stiffnesses for the three collector-to-column subassemblies at Column Lines 2, 3, and 4, denoted as k_{F2}, k_{F3}, and k_{F4}, respectively, were computed by the proposed equations presented in Section 8.3.2. Two sets of lateral stiffnesses for these collector-to-column subassemblies were computed by using two sets of rotational stiffnesses for the semi-rigid (TFW and BW) collector connections. The first set is taken as the average secant stiffnesses measured in Test 2B-5, and the second set is estimated by the proposed method described in Section 8.2. Table

8.5 and Table 8.6 list the lateral stiffnesses of the beam-to-column subassemblies by using the two sets of data.

Figure 8.20 and Figure 8.21 show the measured story shear resisted by members (columns or longitudinal braces) versus story drift for the 2nd and 1st stories, respectively, of the test building in Test 2B-5. The column shear versus story drift relationships in the 2nd story gravity columns (i.e., Columns 2, 3, and 4) exhibited a considerably nonlinear hysteretic behavior. The main source of this nonlinear responses was from the semi-rigid collector connections. On the other hand, Figure 8.22 and Figure 8.23 show the measured story shear taken by members versus total story shear for the 2nd and 1st stories, respectively, of the test building. These relationships are roughly linear for all the members. The slope of the regression line represents the percentage of the total story shear taken by that column. Although the test specimen deformed into the inelastic range in Test 2B-5, this indicates that the distribution of the story shears taken by LFRS and gravity columns remained the same throughout the testing. These test results also imply that the story shears taken by the LFRS and gravity columns would be roughly proportional to the "initial" stiffnesses of the LFRS and the corresponding collector-to-gravity column subassemblies. Note that the proposed analysis method for the collector connection stiffness is with respect to the "secant" stiffness, which is lower than the "initial" stiffness. Thus, it can be expected that a lateral load analysis using the secant stiffnesses would lead to an underestimation of the gravity column shears.

Based on the slopes of the measured column shear versus total story shear relationships (Figure 8.22), in each longitudinal frame (Frames N or S), the 2nd story Columns 1, 2, 3, and 4 respectively took approximately 59%, 21%, 12%, and 8% of the 2nd story shear. Table 8.7 compares these test results with those obtained from the proposed lateral load analysis. It was

found that the results from the lateral load analyses with and without considering the effect of panel zones are very similar. In addition, the predicted gravity column shears resulted from the use of collector connection rotational stiffnesses based on the proposed method are slightly lower than those estimated by using the experimental secant stiffness of the roof collector connections. Based on the proposed lateral load analysis together with the proposed collector connection stiffnesses, the 2nd story Columns 1, 2, 3, and 4 are predicted to resist about 79%, 15%, 3.5%, and 2.5% of the 2nd story shear, respectively. Therefore, the proposed lateral load analysis modestly underestimates the gravity column shears. This will result in an overestimation of the required collector axial force, which is conservative from the design perspective.

Table 8.5 Lateral Stiffness of 2nd Story Collector-to-Column Subassemblies Based on Experimental Secant Stiffnesses of Collector Connections

Subassembly at Column 1				Subassembly at Column 2				Subassembly at Column 3				Subassembly at Column 4			
Steel Properties	E =	29000	ksi	Steel Properties	E =	29000	ksi	Steel Properties	E =	29000	ksi	Steel Properties	E =	29000	ksi
	G =	11154	ksi		G =	11154	ksi		G =	11154	ksi		G =	11154	ksi
Beam Properties	L =	126	in.	Beam 1 Properties	L_1 =	42	in.	Beam 1 Properties	L_1 =	84	in.	Beam Properties	L =	30	in.
	I_b =	81.9	in.^{4}		I_{b1} =	81.9	in.^{4}		I_{b1} =	81.9	in.^{4}		I_b =	81.9	in.^{4}
Column Properties	H =	48	in.		d_{b1} =	10.1	in.		d_{b1} =	10.1	in.		d_b =	10.1	in.
	I_c =	1070	in.^{4}		K_{sj1} =	8571	k-in./rad		K_{sj1} =	1433	k-in./rad		K_{sj} =	1433	k-in./rad
	A_v =	9.23	in.^{2}	Beam 2 Properties	L_2 =	84	in.	Beam 2 Properties	L_2 =	30	in.	Column Properties	H =	48	in.
$k_{F,LFRS}$ =		23.8	kip/in.		I_{b2} =	81.9	in.^{4}		I_{b2} =	81.9	in.^{4}		I_c =	146	in.^{4}
					d_{b2} =	10.1	in.		d_{b2} =	10.1	in.		d_c =	8.25	in.
					K_{sj2} =	8571	k-in./rad		K_{sj2} =	1433	k-in./rad	Panel Zone Properties	t_{pz} =	0.36	in.
				Column Properties	H =	48	in.	Column Properties	H =	48	in.		d_{pz} =	6.5	in.
					I_c =	146	in.^{4}		I_c =	146	in.^{4}		w_{pz} =	8.25	in.
					d_c =	8.25	in.		d_c =	8.25	in.		K_{pz} =	215325	k-in./rad
				Panel Zone Properties	t_{pz} =	0.36	in.	Panel Zone Properties	t_{pz} =	0.36	in.	Clear Distances	L_c =	25.875	in.
					d_{pz} =	8.125	in.		d_{pz} =	6.5	in.		H_c =	42.95	in.
					w_{pz} =	8.25	in.		w_{pz} =	8.25	in.	$k_{F,ERF}$ (w/o PZ) =		0.61	kip/in
					K_{pz} =	269156	k-in./rad		K_{pz} =	215325	k-in./rad	$k_{F,ERF}$ (with PZ) =		0.82	kip/in
				Clear Distances	L_{c1} =	37.875	in.	Clear Distances	L_{c1} =	79.875	in.				
					L_{c2} =	79.875	in.		L_{c2} =	25.875	in.				
					H_c =	42.95	in.		H_c =	42.95	in.				
				$k_{F,IRF}$ (w/o PZ) =		5.83	kip/in.	$k_{F,IRF}$ (w/o PZ) =		0.99	kip/in.				
				$k_{F,IRF}$ (with PZ) =		6.34	kip/in.	$k_{F,IRF}$ (with PZ) =		1.11	kip/in.				

Table 8.6 Lateral Stiffness of 2nd Story Collector-to-Column Subassemblies Based on Collector Connection Stiffness from the Proposed Method

B-to-C Subassembly at Column 1				B-to-C Subassembly at Column 2				B-to-C Subassembly at Column 3				B-to-C Subassembly at Column 4			
Steel Properties	E =	29000	ksi	Steel Properties	E =	29000	ksi	Steel Properties	E =	29000	ksi	Steel Properties	E =	29000	ksi
	G =	11154	ksi		G =	11154	ksi		G =	11154	ksi		G =	11154	ksi
Beam Properties	L =	126	in.	Beam 1 Properties	L_1 =	42	in.	Beam 1 Properties	L_1 =	84	in.	Beam Properties	L =	30	in.
	I_b =	81.9	in.^{4}		I_{b1} =	81.9	in.^{4}		I_{b1} =	81.9	in.^{4}		I_b =	81.9	in.^{4}
Column Properties	H =	48	in.		d_{b1} =	10.1	in.		d_{b1} =	10.1	in.		d_b =	10.1	in.
	I_c =	1070	in.^{4}		K_{sj1} =	5964	k-in./rad		K_{sj1} =	1392	k-in./rad		K_{sj} =	1392	k-in./rad
	A_v =	9.23	in.^{2}	Beam 2 Properties	L_2 =	84	in.	Beam 2 Properties	L_2 =	30	in.	Column Properties	H =	48	in.
$k_{F,LFRS}$ =		23.8	kip/in.		I_{b2} =	81.9	in.^{4}		I_{b2} =	81.9	in.^{4}		I_c =	146	in.^{4}
					d_{b2} =	10.1	in.		d_{b2} =	10.1	in.		d_c =	8.25	in.
					K_{sj2} =	5964	k-in./rad		K_{sj2} =	1392	k-in./rad	Panel Zone Properties	t_{pz} =	0.36	in.
				Column Properties	H =	48	in.	Column Properties	H =	48	in.		d_{pz} =	6.5	in.
					I_c =	146	in.^{4}		I_c =	146	in.^{4}		w_{pz} =	8.25	in.
					d_c =	8.25	in.		d_c =	8.25	in.		K_{pz} =	215325	k-in./rad
				Panel Zone Properties	t_{pz} =	0.36	in.	Panel Zone Properties	t_{pz} =	0.36	in.	Clear Distances	L_c =	25.875	in.
					d_{pz} =	8.125	in.		d_{pz} =	6.5	in.		H_c =	42.95	in.
					w_{pz} =	8.25	in.		w_{pz} =	8.25	in.	$k_{F,ERF}$ (w/o PZ) =		0.60	kip/in
					K_{pz} =	269156	k-in./rad		K_{pz} =	215325	k-in./rad	$k_{F,ERF}$ (with PZ) =		0.80	kip/in
				Clear Distances	L_{c1} =	37.875	in.	Clear Distances	L_{c1} =	79.875	in.				
					L_{c2} =	79.875	in.		L_{c2} =	25.875	in.				
					H_c =	42.95	in.		H_c =	42.95	in.				
				$k_{F,IRF}$ (w/o PZ) =		4.22	kip/in.	$k_{F,IRF}$ (w/o PZ) =		0.96	kip/in.				
				$k_{F,IRF}$ (with PZ) =		4.64	kip/in.	$k_{F,IRF}$ (with PZ) =		1.08	kip/in.				

Table 8.7 Percentage of Story Shear Resisted by Columns in 2nd Story

					Column N1	Column N2	Column N3	Column N4
Experiment			Percentage of Story Shear Taken by Columns in Frame N	(%)	59.1	21.4	11.4	8.0
			Percentage of Story Shear Taken by Columns in Frame S	(%)	59.5	20.8	12.6	8.4
Lateral Load Analysis	Experimental Collector Connection Rotational Stiffness	w/o Considering PZ Effect	Lateral Stiffness of Beam-to-Column Sub-Assemblies	(kip/in.)	23.8	5.83	0.99	0.61
			Percentage of Story Shear Taken by Columns in Each Frame	(%)	76.2	18.6	3.2	2.0
		Considering PZ Effect	Lateral Stiffness of Beam-to-Column Sub-Assemblies	(kip/in.)	23.8	6.34	1.11	0.82
			Percentage of Story Shear Taken by Columns in Each Frame	(%)	74.2	19.7	3.5	2.6
	Predicated Collector Connection Rotational Stiffness from the Proposed Method	w/o Considering PZ Effect	Lateral Stiffness of Beam-to-Column Sub-Assemblies	(kip/in.)	23.8	4.22	0.96	0.60
			Percentage of Story Shear Taken by Columns in Each Frame	(%)	80.5	14.2	3.3	2.0
		Considering PZ Effect	Lateral Stiffness of Beam-to-Column Sub-Assemblies	(kip/in.)	23.8	4.64	1.08	0.80
			Percentage of Story Shear Taken by Columns in Each Frame	(%)	78.5	15.3	3.6	2.6

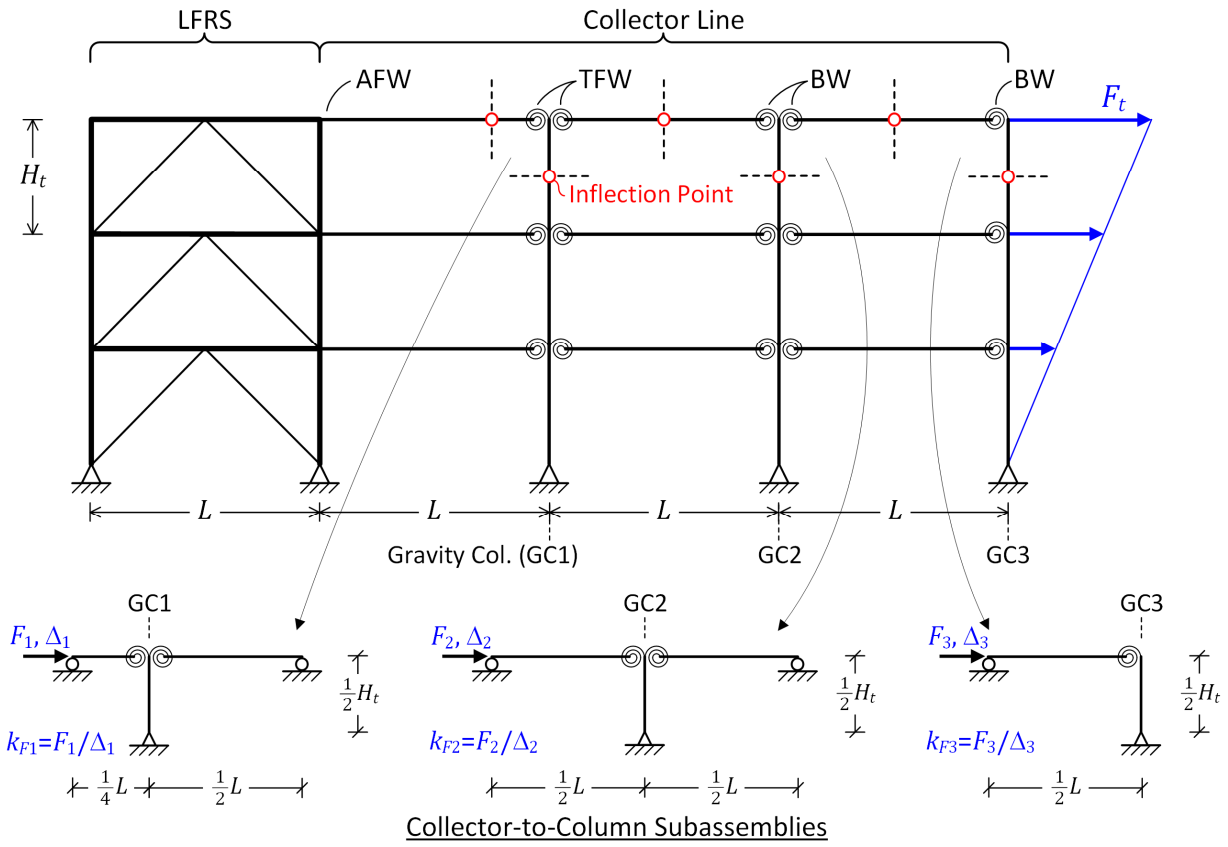

Figure 8.12 Proposed Portal Method for Topmost-Story Gravity Frame with Collectors

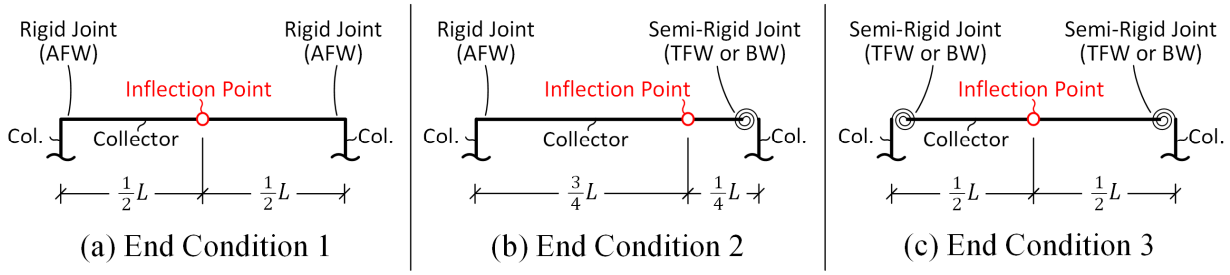

Figure 8.13 Assumed Collector Inflection Point Location Based on Connection Types

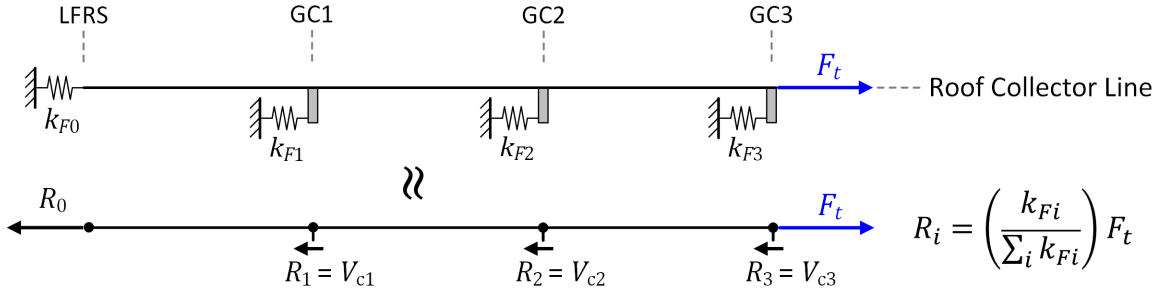

Figure 8.14 Proposed Lateral Load Analysis of Topmost-Story Gravity Frame with Collectors

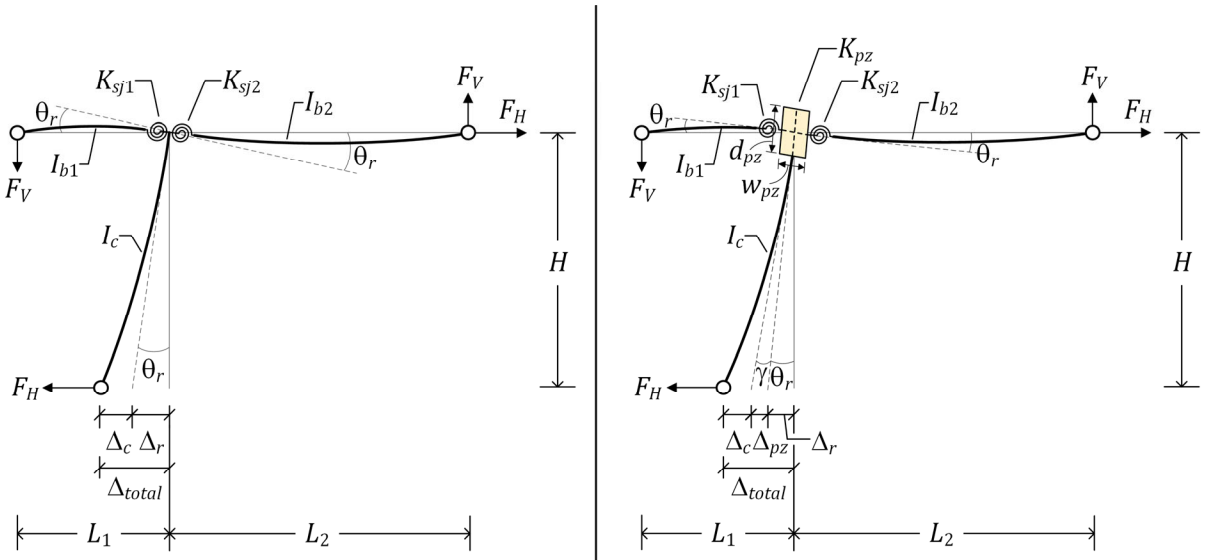

(a) w/o Considering Panel Zone Effect (b) Considering Panel Zone Effect

Figure 8.15 Deformation Configurations of Topmost-Story Interior Beam-to-Column Subassembly with Semi-Rigid Connections

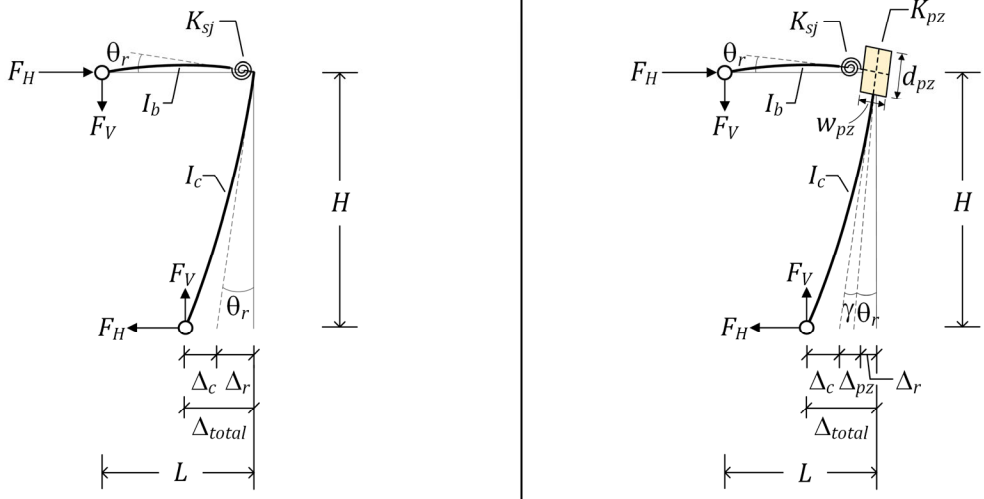

(a) w/o Considering Panel Zone Effect (b) Considering Panel Zone Effect

Figure 8.16 Deformation Configurations of Topmost-Story Exterior Beam-to-Column Subassembly with Semi-Rigid Connections

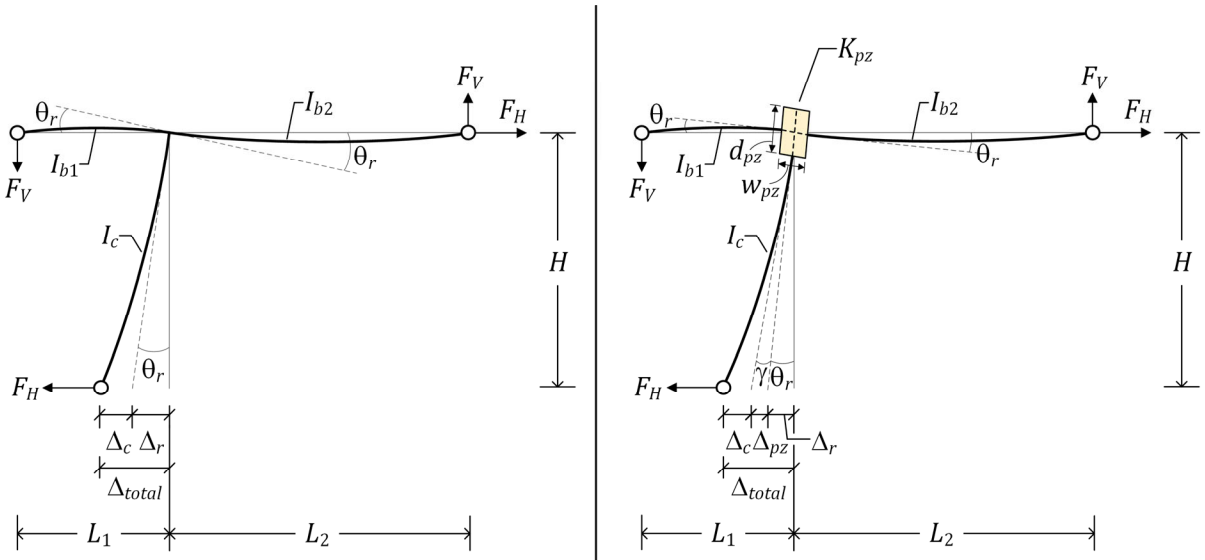

(a) w/o Considering Panel Zone Effect (b) Considering Panel Zone Effect

Figure 8.17 Deformation Configurations of Topmost-Story Interior Beam-to-Column Subassembly with Rigid Connections

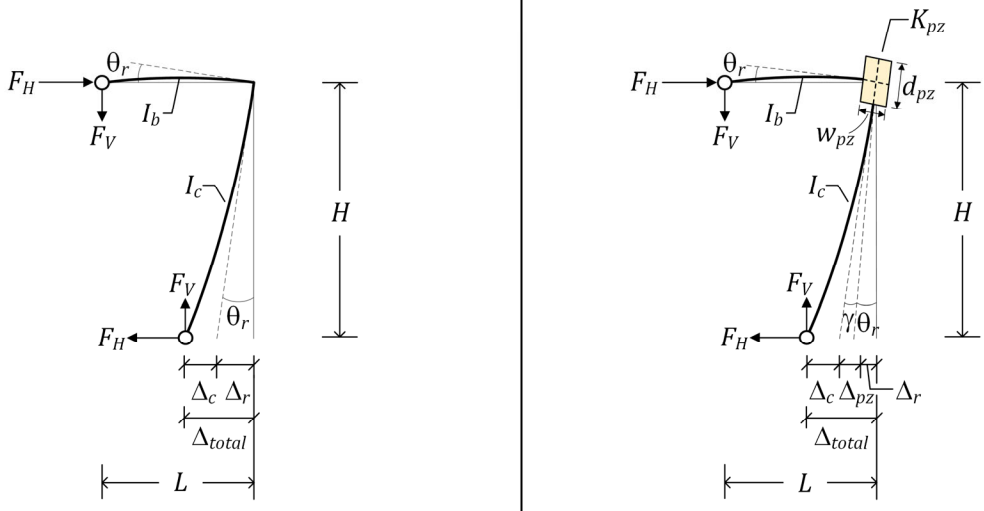

(a) w/o Considering Panel Zone Effect (b) Considering Panel Zone Effect

Figure 8.18 Deformation Configurations of Topmost-Story Exterior Beam-to-Column Subassembly with Rigid Connections

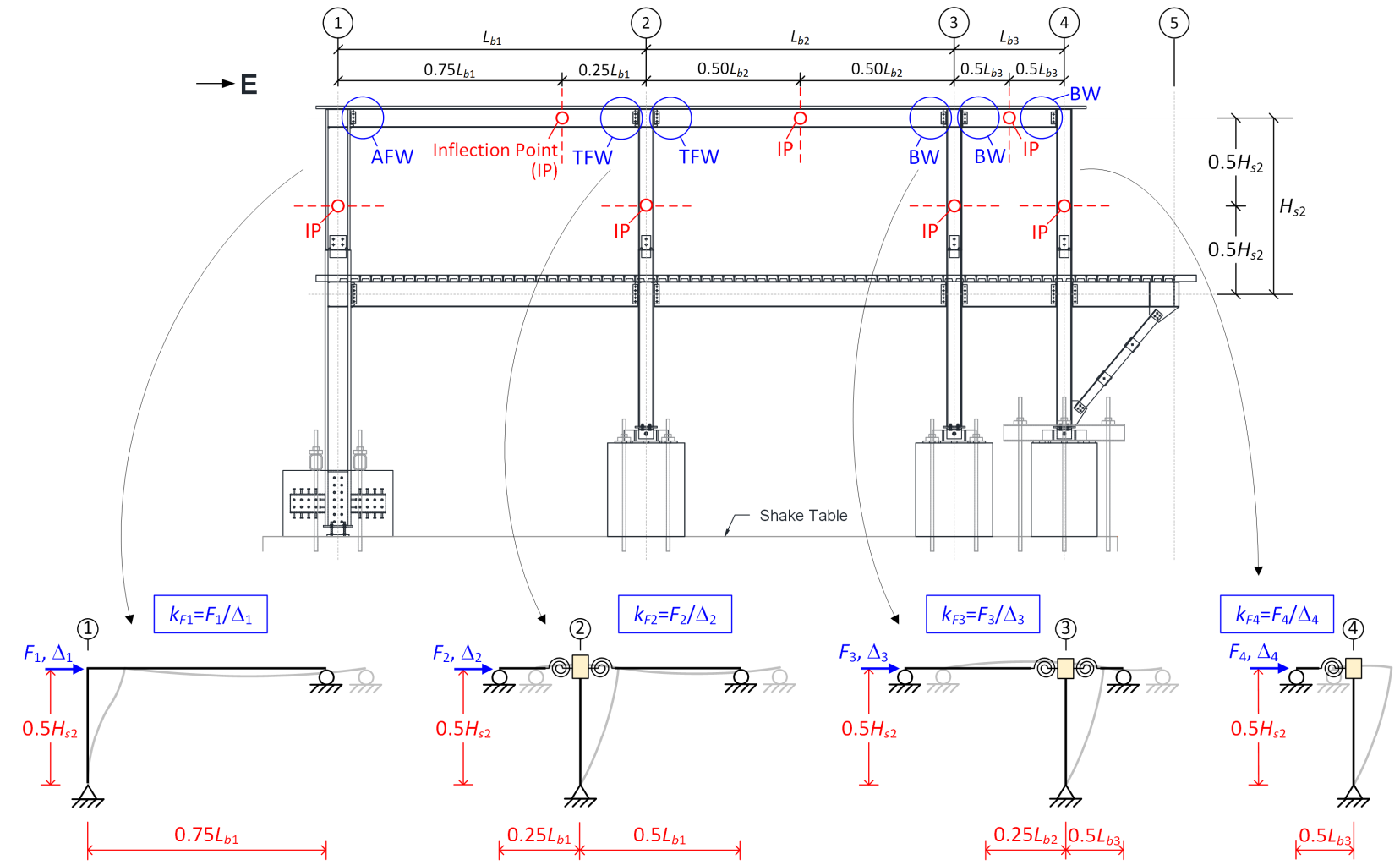

Beam-to-Column Sub-assemblies

Figure 8.19 Proposed Portal Method for Determining Beam-to-Column Assemblies for Estimating Lateral Stiffness of 2nd-Story Gravity Columns

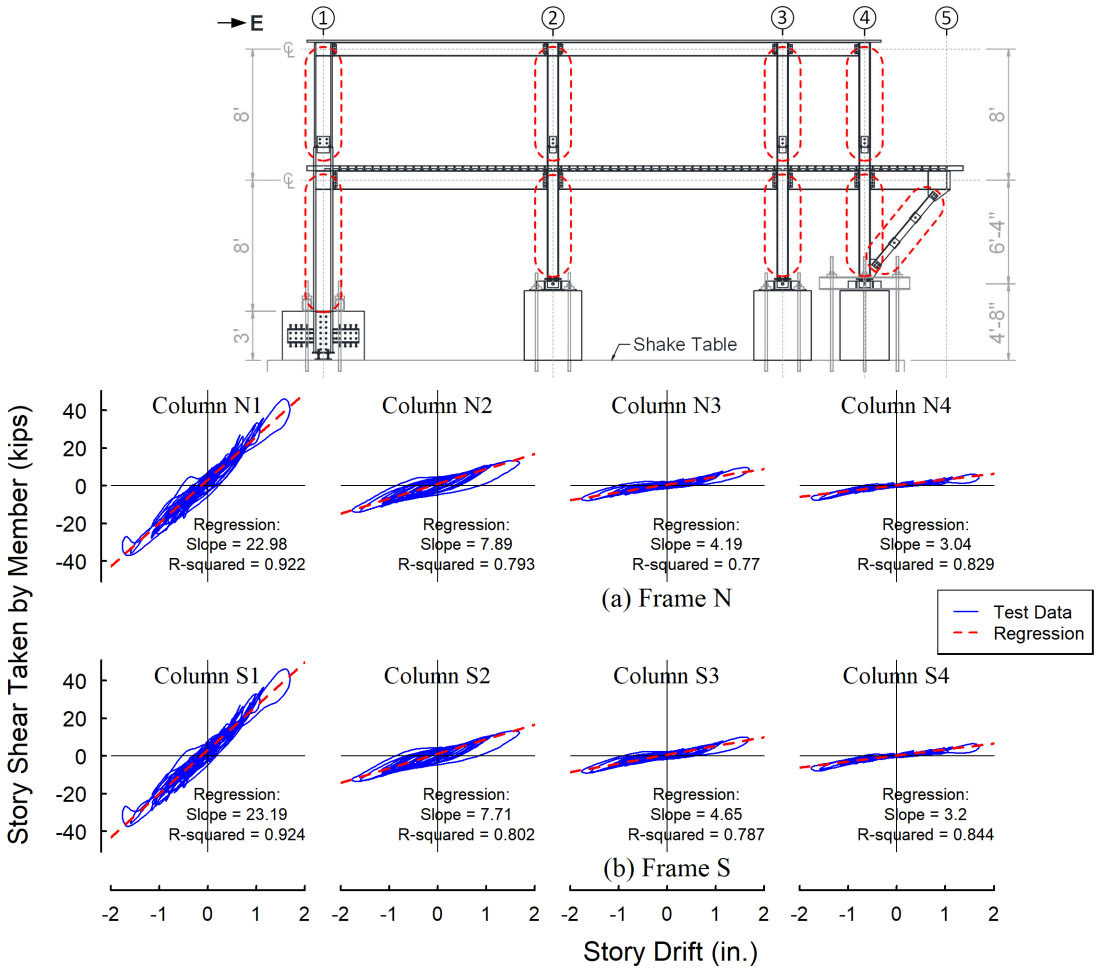

Figure 8.20 Test 2B-5: Story Shear Resisted by Members versus Story Drift for 2nd Story Columns

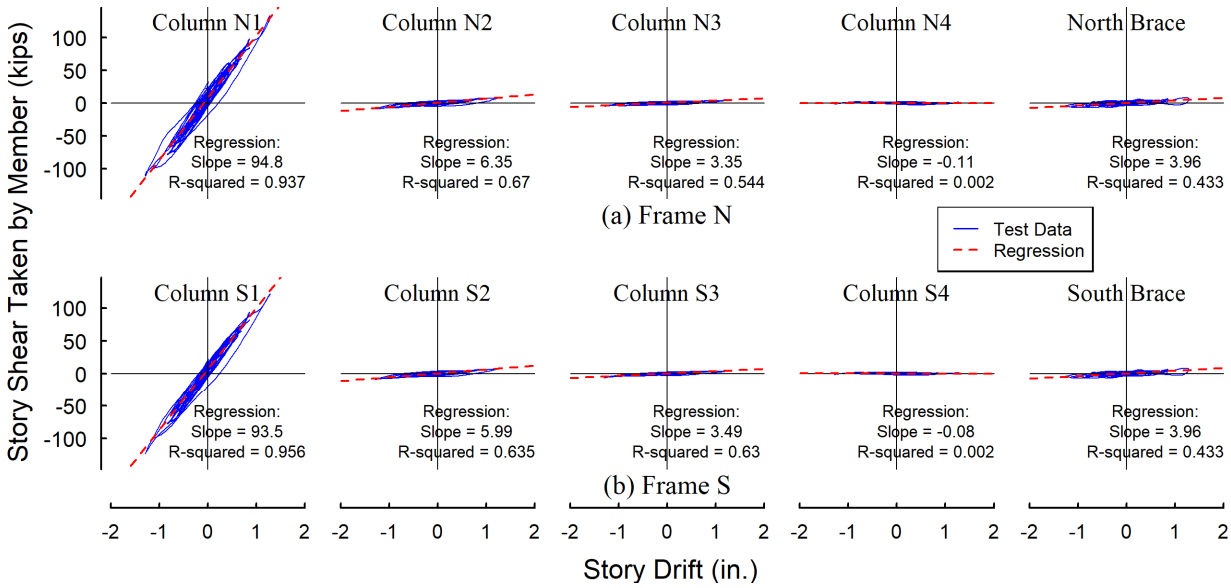

Figure 8.21 Test 2B-5: Story Shear Resisted by Members versus Story Drift for 1st Story Columns and Braces

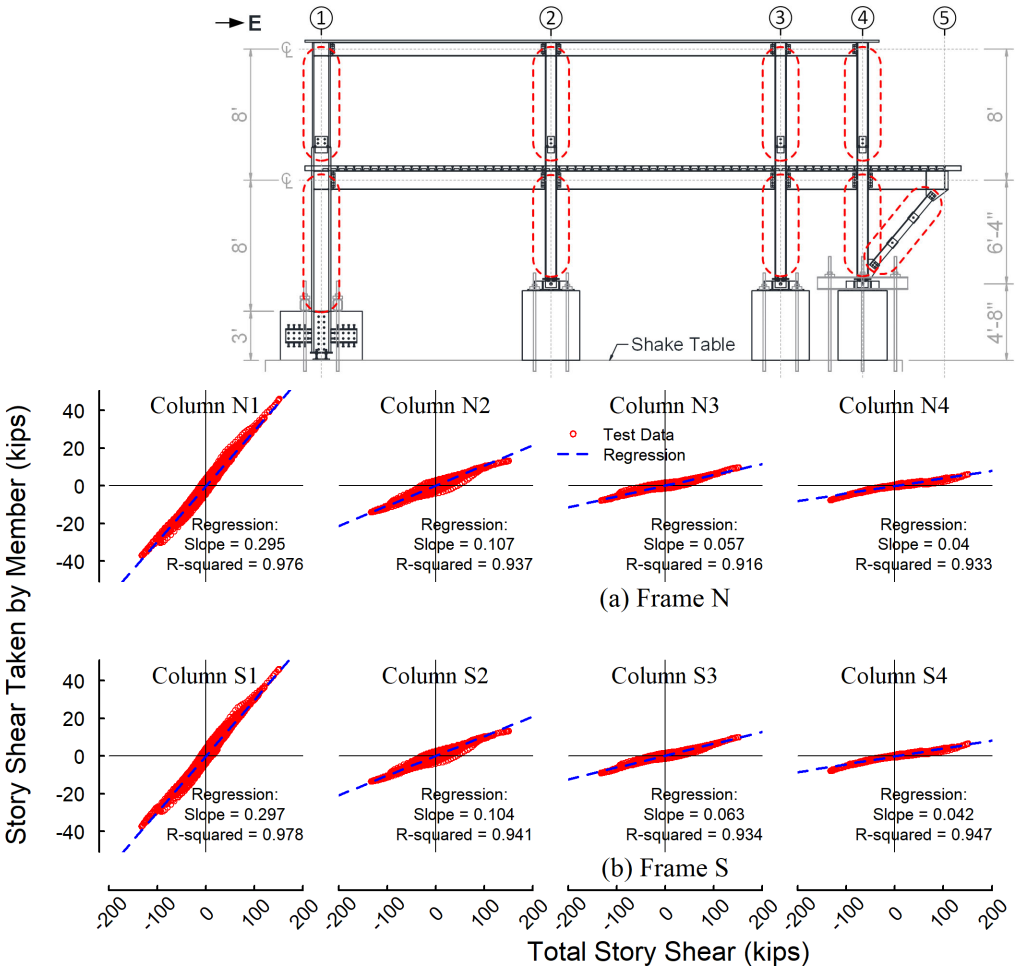

Figure 8.22 Test 2B-5: Story Shear Resisted by Members versus Total Story Shear for 2nd Story Columns

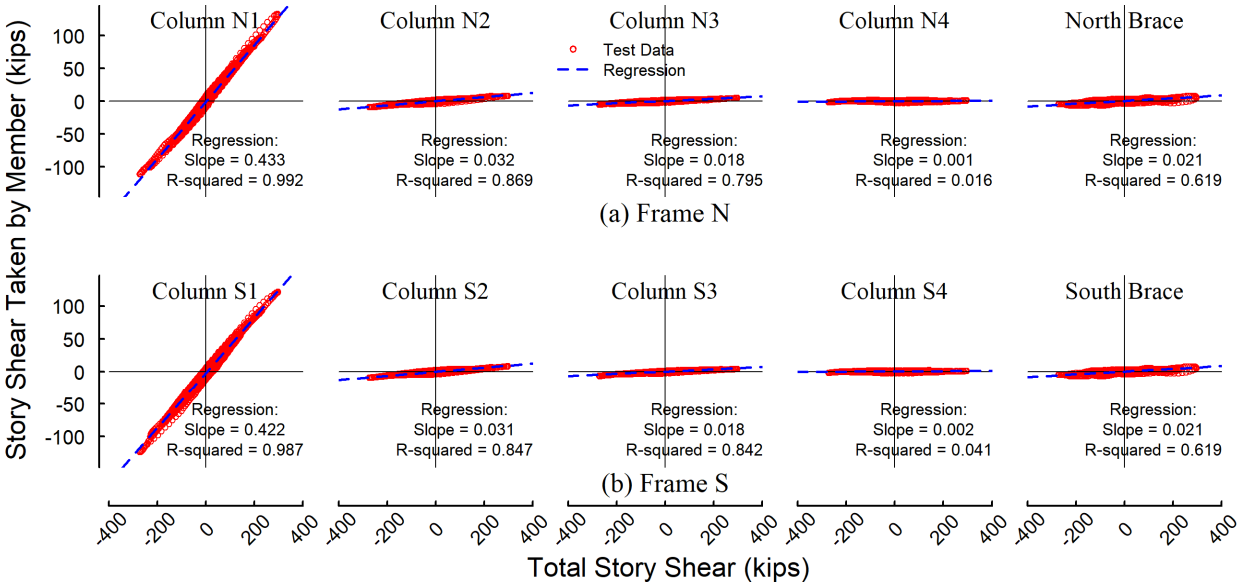

Figure 8.23 Test 2B-5: Story Shear Resisted by Members versus Total Story Shear for 1st Story Columns and Braces

8.4 Recommendations on Collector and Collector Connection Design

8.4.1 Required Collector Axial Force

In this section, the conventional method for estimating the collector seismic axial force demand is examined by comparing it with the measured responses from Test 2B-5. In addition, an improved approximate approach for the roof collectors is proposed and its effectiveness is verified by the test results.

Figure 5.58 illustrates how the conventional and improved approximation methods are applied to estimate the axial forces in the 2nd floor composite collectors in the test building. Figure 8.24 illustrates how both methods are applied to collectors at the roof level in the test specimen. As shown in Figure 8.24(a), the conventional method simply assumes that the inertia forces are transmitted into the collectors through a uniform slab shear flow, $\bar{v}'$, along the entire collector line and all the inertial forces collected by the collectors are eventually delivered to the LFRS at the end of the collector line. The uniform slab shear flow, $\bar{v}'$, is determined from:

$$\bar{v}' = \frac{W'}{L_{total}}\left(\frac{a_{flr}}{g}\right) \tag{8.43}$$

where W' is the total seismic weight tributary to the collector line, L_{total} is the total length of the collector line, and a_{flr} is the floor acceleration. For a collector line with one end connected to the LFRS and one end free, the conventional method assumes that the LFRS will resist the sum of the inertial forces tributary to the collector line, $R_0 = \bar{v}' L_{total}$. As a result, the conventional method predicts a linear axial force diagram along the entire collector line [as shown by the solid line in Figure 8.24(c)], for which the axial force increases from zero at the far end to R_0 at the LFRD end.

On the other hand, as shown in Figure 8.24(b), the proposed improved method also assumes that inertial forces are transmitted into the collectors through a uniform slab shear flow like the

conventional method. However, the improved method considers that part of the collected inertial forces in a roof collector line would be "intercepted" by the gravity columns along the collector line in the form of column shears. It is assumed that the inertial forces are distributed to the LFRS and gravity columns along the collector line in proportion to their relative lateral stiffnesses. By using the proposed lateral load analysis described in Section 8.3.3 that also incorporates with the proposed collector connection rotational stiffness, the lateral stiffnesses (denoted as k_{F1}, k_{F2}, k_{F3}, and k_{F4}, respectively) provided by the four columns in 2nd along each roof collector line, can be estimated. Then, the column shear at Column Line i, R_i, is estimated as:

$$R_i = \left(\frac{k_{Fi}}{k_{F,total}}\right)(\bar{v}' L_{total}) \tag{8.44}$$

where $k_{F,total}$ is the total lateral stiffness provided by LFRS (Column 1) and gravity columns (Columns 2, 3, and 4):

$$k_{F,total} = \sum_i k_{Fi} \tag{8.45}$$

The axial force diagram along a collector line obtained from the improved method is illustrated by the dashed line in Figure 8.24(c). In general, the axial force on the collector line increase from the far end to the LFRS end. In addition, a drop of axial force takes place at individual column locations. Therefore, the collector axial force computed from the improved method is lower than that predicted by the conventional method.

Figure 8.25 and Figure 8.27 plot the predicted roof collector axial force diagrams computed by the approximation methods together with the measured collector axial forces at the instants of positive and negative peak roof accelerations in Test 2B-5, respectively. In each figure, three predicted axial force diagrams are plotted:

(1) the first one was predicted by the conventional method.

(2) the second one was predicted by the proposed improved method which was carried out by using the “estimated column shears” determined from the proposed lateral load analysis.

(3) the third one was predicted by the improved method that incorporated the “measured column shears”, which was determined by the measured relative stiffnesses of the columns.

Note that the second one represents a prediction by the improved method which is conducted by using the “intentionally underestimated gravity column shears”, while the third one represents a prediction by the improved method which is carried out by using the “actual gravity column shears”. From both Figure 8.25 and Figure 8.27, it can be found that the predicted axial force diagram by the improved method with the measured column shears matches well the measured axial forces in Collector 1 but slightly overestimates the measured axial forces in Collector 2. This indicates the axial force demand of the roof collector adjoining to the LFRS can be well predicted by the improved method if the inertial forces intercepted by the gravity columns are well captured. The slight overestimation of axial force for Collector 2 could be attributed to the fact that the inertia forces were transmitted into the collectors through a non-uniform slab shear flow along the collector line instead of a uniform slab shear flow as is assumed by the improved method. This nonuniform slab shear flow caused the axial force in the collector adjacent to the LFRS to build up in a pace faster than assumed, while the build-up of the axial forces in the remaining collectors was slower than that expected by the uniform slab shear assumption. Note that it is difficult to develop a universal mathematical model for the nonuniform distribution of slab shear flow along a collector line because the slab shear distribution is related to the layout of the floor plan, which varies from case to case. Therefore, the assumption of uniform slab shear is considered acceptable for estimating the collector axial force. In addition, it appears that the

assumption of uniform slab shear tends to result in an overestimate of axial force in the collectors away from the LFRS, which is on the safe side for collector design.

In addition, as shown in Figure 8.25 and Figure 8.27, the prediction by the improved method incorporated with the "estimated column shears" slightly overestimates the axial force in the roof Collector 1 and modestly overestimates the axial force in the roof Collector 2. Note that the proposed method on the collector connection stiffness aims to predict the secant stiffness, which tends to underestimate the actual stiffness of the collector connection. In addition, the proposed portal method for the lateral load analysis is also developed to avoid an overestimation of the lateral stiffness of the gravity columns. As a results, the proposed lateral load analysis intentionally underestimates the gravity column shears, which leads to a minor to moderate overestimation of axial forces in the roof collectors as demonstrated in Figure 8.25 and Figure 8.27. This suggests that the proposed methods would lead to a modestly conservative design of the collector.

Moreover, from Figure 8.25 and Figure 8.27, it is apparent that the conventional method noticeably overestimates the roof collector axial forces. This suggests that the effect of the interception of inertia force by the gravity columns on the resultant collector axial forces is considerable for the roof level. Taking the test specimen for example, the 2nd story gravity columns intercepted about 40% of the roof inertial forces so that only about 60% of inertial forces collected by each collector line were transmitted to the collector end adjacent to the LFRS. By contrast, the conventional method assumes that all the inertial forces collected by each collector line would be delivered to the collector end next to the LFRS. Thus, the conventional method overestimates the axial force at that collector end by approximately 67%. It is indicated that, to achieve a precise

estimation of the axial force demands in the roof collectors, the effect of the interception of inertia force by the gravity columns needs to be considered.

Figure 8.26 and Figure 8.28 plot the predicted 2nd floor collector axial force diagrams computed by the conventional method together with the measured collector axial forces at the instants of positive and negative peak 2nd floor accelerations in Test 2B-5, respectively. It can be found that the approximation method well predicts the resultant axial forces on the composite collector sections for the half-span of collector just next to the LFRS (i.e., the west-half span of Collector 1), while it modestly overestimates the axial forces on the composite collector sections for the remaining region of each collector line. The good agreement of the prediction and the measured composite collector axial force for the collector region next to the LFRS indicates that almost all the inertial forces collected by each collector line were delivered to the collector end next to the LFRS as assumed by the conventional method. This also implies that the phenomenon of interception of inertial forces by the gravity columns was insignificant for the 2nd floor collector lines. This could be attributed to that, at each collector-to-gravity column connection, the column shears acting at the column from the upper and lower stories were of about the same magnitude but opposite in sign to each other, which was observed in Test 2B-5 as shown in Figure 7.52 and Figure 7.53. In other words, the effects of the upper- and lower-story gravity columns on intercepting the inertial forces cancelled out each other. Thus, the conventional method for approximating the collector axial force, which neglects the gravity column effects, is suitable for this case. On the other hand, the conventional method modestly overestimates the composite collector axial forces for the regions away from the LFRS. This is because the collector lines were subjected to a nonuniform slab shear flow, in contrary to the assumption of a uniform slab shear in the conventional method. However, the modest overestimation of the axial force demand for

part of the collector line from the conventional method is considered acceptable as it ensures that the collector design is on the safe side.

It is worth noting the phenomenon that the inertial forces in the composite slab were intercepted by the gravity columns supporting the collector lines was noticeable when the composite slab served as the roof diaphragm in the single-story Phase 1 specimen. By contrast, this phenomenon was negligible when the composite slab served as an intermediate floor in Phase 2 testing. Based on the test results, it can be inferred that the interception of inertial forces by gravity columns would be insignificant for the intermediate floors (i.e., typical floors except for the roof) in a typical building. In addition, it is a common practice to use the same collector or gravity beam design for all floors in a typical building, which would tend to result in a negligible difference in shear force between any two adjacent gravity columns above and below a floor when the building is subjected to lateral forces [see Figure 8.29(a)]. This also justifies that considering the interception of inertial forces by gravity columns is unnecessary for typical floors.

In summary, based on the results from Phases 1 and 2 testing, as illustrated in Figure 8.29, the design recommendations for estimating the collector axial force demands in a typical multi-story building are as follows:

(1) For typical floors [see Figure 8.29(b)], the collector axial forces can be estimated by using the conventional method, which neglects the effects from gravity columns. This method would predict well the collector axial forces in the region near LFRS but would somewhat overestimate the collector axial forces for the regions away from LFRS.

(2) For the roof level [see Figure 8.29(c)], the collector axial forces can be estimated by using the proposed improved method, which takes the interception of inertial forces by gravity columns into account.

(3) Using the proposed improved method to calculate the required roof collector axial forces requires an estimation of the shear forces taken by the top-story gravity columns. The estimation of gravity column shears can be caried out by using the proposed lateral load analysis procedure, which includes a portal method for decomposing a top-story gravity frame with collectors into collector-to-column subassemblies and approximate equations for estimating the lateral stiffnesses of these subassemblies, incorporated with the proposed method for estimating the rotational stiffnesses of semi-rigid collector connections. It is expected that the whole set of proposed methods would lead to a minor-to-modest overestimation of the axial force demands in the roof collectors.

8.4.2 Design of Composite Collector-to-Column Connections

In addition to the measured total axial forces acting on the composite sections of the 2nd floor collectors, Figure 8.26 and Figure 8.28 also plot the measured resultant axial forces taken by the bare steel sections of these composite collectors at the instants of positive and negative peak 2nd floor accelerations in Test 2B-5, respectively. It can be found that, along a composite collector line, the difference between the total axial force on a composite collector section and the resultant axial force taken by the bare steel section of the composite section was significant at the places where the composite collector was subjected to a considerable positive bending moment.

At the instant of the positive peak acceleration (Figure 8.26), the inertial force acted toward the LFRS, which induced a compressive axial force to the composite collectors. At that time, near the east ends of 2nd floor Collectors 1 and 2 (near the measure points “e” and “j”, respectively, shown in Figure 8.26), the collectors were subjected to a significant positive bending moment in addition to the compressive axial force demand. At these two locations, the resultant axial force on the bare steel section was in tension, implying that resultant axial force in the concrete slab was

compressive with a magnitude even larger than the total compressive axial force acting on the entire composite section. It is indicated that, when a composite collector section is subjected to a simultaneous compressive axial force and positive bending moment, the concrete slab plays the main role in conveying the collector axial force, while the steel section plays a "counteracting" role in the delivery of collector axial force. In this case, the magnitude of the tensile axial force on the steel section could be noticeable as exampled by the response at the east end of Collector 2 (i.e., measure point "j") shown in Figure 8.26, where the magnitude of tensile axial force on the bare steel section was about the same as that of the total axial force on the composite section. However, this situation is not considered critical for the collector-to-column connection design because the worst-case scenario for the collector connection design would take place at the collector ends subjected to simultaneous tensile axial force and positive bending moment, which will be presented later.

On the other hand, at the instant of the negative peak acceleration (Figure 8.28), the inertial force acted away from the LFRS, which tended to induce a tensile total axial force to the composite collectors. At that time, near the east ends of 2nd floor Collectors 1, 2 and 3 (near the measure points "a", "f", and "k", respectively, shown in Figure 8.28), the composite sections there were subjected to a significant positive bending moment in addition to the axial force demand. At these three locations, the resultant axial force on the bare steel section was in tension with a magnitude significantly larger than the total axial force acting on the entire composite section. In addition, the resultant tensile axial forces on the bare steel sections at these collector ends were significantly larger than the axial force demand predicted by the conventional method. This phenomenon can be explained by the measured stress profile patterns and the associated force equilibriums near theses collector ends. As shown in Figure 8.30, regardless of the types of steel connections

employed at a composite collector end, the force equilibrium there under a simultaneous combination of axial load and positive bending moment can be expressed as:

$$P_u = T_s - C_c \tag{8.46}$$

where P_u is the total axial force demand on the composite section, T_s is the resultant tensile axial force acting on the bare steel section, and C_c is the resultant compressive axial force acting on concrete slab. Eq. (8.46) implies that, when P_u is in tension, the bare steel section plays the main role in conveying the collector axial force, while the concrete slab plays a "counteracting" role in the delivery of collector axial force. Furthermore, Eq. (8.46) can be rewritten as:

$$T_s = P_u + C_c \tag{8.47}$$

This implies that the bare steel section not only takes the total axial force on the composite section, P_u, but also carries an extra force, C_c, to balance the force coming from concrete slab, which is analogous to the "prying action". Note that this "prying action-like" behavior triggered by positive bending moments would cause the bare steel section of a composite collector to be subjected to a resultant tensile force even larger than the total tensile force on the entire composite section.

The prying action-like phenomenon mentioned above, when not properly considered, can be a concern for the design of collector-to-column connections. Recalled that the common practice is to design the connections (i.e., AFW, TFW or BW connections) in a composite construction for the total axial force demand, P_u. This design philosophy assumes that (1) there is no bending moment at the collector end, and (2) no compressive force due to the flexural action will develop in the concrete slab. However, test results in this study indicates that the unintended bending moment at the composite collector end would occur, causing the collector connection to experience a tension force demand much larger than the demand used in.

Although shake table tests conducted in this study only drove the composite AFW connections to reach a limit state of flange local bucking, by extrapolating from the measured stress profiles (see Figure 8.30) and basing the experience learned from past experimental researches on gravity frames (Liu and Astaneh-Asl 2000; 2004), it is recommended that the composite collector connections shall be designed for the suggested limit states illustrated in Figure 8.31. It is assumed that, in this "worst-case scenario", the plastic neutral axis is located between the steel beam section and the concrete slab above the metal deck; and the concrete slab develops the maximum compressive force, while all the bolted and welded joints in the steel section reach their governing tensile strength. Therefore, the steel collector connection shall be designed to sustain axial force demand, $P_{u,s}$, equal to the axial force demand for the entire composite section, P_u, combined with an extra force, C_c, which comes from the concrete slab due to the "prying action-like" behavior (Figure 8.32). This gives:

$$P_{u,s} = P_u + C_c \tag{8.48}$$

Note that axial force, P_u, is determined from the proposed analysis procedure described in Section 8.4.1. The force term C_c is computed as (Liu and Astaneh-Asl 2000):

$$C_c = 0.85 f_c' b_{eff} a \tag{8.49}$$

where f_c' is the compressive strength of the concrete, b_{eff} is the width of the column face bearing against the concrete, and a is effective depth of the concrete slab. It is suggested that $a = h_c$ for the deck parallel to the collector, while $a = 0.6h_c$ for the deck perpendicular to the collector, where h_c is the thickness of concrete slab above the meatal deck.

For a complete design procedure, the shear demand, V_u, at the collector connection also needs to be considered. It is a common practice to only consider the gravity-induced shear force, V_g, for V_u. However, from the slope of measured the bending moment diagrams in the collectors

(as shown in Figure 7.79), it is indicated that the seismic-induced shear forces, V_e, in the collectors, especially for a collector with at least one AFW connection, may not be negligible because the rotational stiffnesses of collector connections are non-trivial. Further investigations are needed for developing an estimation of V_e at the limit state of the collector connection because V_e may be related to the bending strength of collector connections. However, it can be expected that V_e would not be a crucial term for collector design because it is expected to be relatively small compared to the collector axial force demand (P_u or $P_{u,s}$) in typical buildings. Moreover, as the simultaneous tensile axial force and positive bending moment is identified as the critical case for design of a composite collector connection, it is worthy noting that the directions of V_g and V_e will be opposite at the collector end subjected to positive bending due to the frame sway action. This suggests that, for the design of composite collector connections, the effects from V_g and V_e are not additive. This also means that the common practice that neglects V_e would be conservative and reasonable unless the magnitude of V_e is more than twice that of V_g. Hence, it is suggested to follow the current practice to assume $V_u = V_g$, before a precise estimation of V_e is developed. Thus, the resultant force demand for a composite collector connection is

$$R_u = \sqrt{{P_{u,s}}^2 + {V_u}^2} \tag{8.50}$$

Then, the general design criterion for three types of steel collector connections (AFW, TFW and TW details) in a composite collector connection can be expressed as:

$$\phi R_n = n_f \phi R_{n,f} + \phi R_{n,w} \geq R_u \tag{8.51}$$

where ϕR_n = total design strength of the connection. $\phi R_{n,w}$ = design strength of web bolted connection. $\phi R_{n,f}$ = design strength of the flange weld, and n_f is the number of welded flanges. Note that n_f = 2, 1, and 0 for the AFW, TFW and BW connections, respectively. Instead of using

ϕ = 0.75 per AISC 360, it is suggested that ϕ_n (= 0.90) as defined in AISC 358 (AISC 2016a) for nonductile limit states be used.

Other than designing the steel collector connections for a target force to account for the C_c force in the concrete slab, an alternative approach is to provide a gap between the column and concrete slab to "eliminate" the force C_c. This can be achieved, for example, by inserting a compressible foam-like material in front of the column face, an approach that is required for a number of prequalified moment connections in AISC 358 (AISC 2016a). Once the isolation is achieved, composite collector connections can be designed as bare steel collector connections.

8.4.3 Detailed Design Requirements

In designing a collector-to-column connections, a common practice is to treat it as a connection that is capable of transmitting the required collector axial force. The collector is treated as a force-controlled element, and no additional requirement is specified in AISC 341 (AISC 2016b). However, shake table test results indicated that all collector connections (including AFW, TFW, and BW details) were subjected to considerable bending moment in addition to the axial forces. It can be expected that, as a building is laterally swaying back and forth during an earthquake, the collector connections are subjected to rotational demands corresponding to the lateral drift of the building. Hence, the collector connection design should be design for the combined axial and flexural demands. There is a need for future research to investigate the axial force-bending moment (P-M) interaction for the collector-to-column connections.

With both flanges welded to the column and a shear tab bolted connection on the web at the collector end, the AFW connection acts like a moment connection. This connection is very similar to the typical pre-Northridge steel moment connections, for which the ductility capacity is inadequate. Although notch-tough electrodes are required after the 1994 Northridge Earthquake,

the ductility of the AFW connection to serve as a moment connection is still questionable because the bolted web has been shown to be ineffective in participating in moment resistance (FEMA 2000). Not to mention that the AFW connections are subjected to combined axial and flexural demands. Future research is needed to investigate this issue. In Test 2B-5, significant yielding of the bottom flange (Figure 7.91) was observed at the 2nd floor composite AFW connections, while the maximum axial force demand on the steel connection $P_{u,s}$ only reached about 70% axial force design strength, ϕR_n, of the collector connection. In addition, mild yielding of the bottom flange (Figure 7.87) was detected at the bare steel AFW connections on the roof while the collector connection reached a demand-to-capacity ratio ($P_u/\phi R_n$) only about 32%. These suggest that the combined axial and bending actions on an AFW connection would cause one flange to get into yield earlier than the entire collector connection reaches the expected limit state. It requires an adequate ductility for the welded joint to prevent a premature damage. Therefore, it is prudent that some detailing requirements for Ordinary Moment Frame (OMF) connections be used. This includes the removal of the steel backing at the bottom flange level.

Minor local bucking of the bottom flange (Figure 7.91) was observed at the 2nd floor composite AFW connections in Test 2B-5. It is considered as a premature damage because it took place before the AFW connections developed the expected strength. In addition, flange local buckling took place during the AFW connections were subjected to an approximately ±1.0% rad cycle of rotation (Figure 7.81). Local buckling occurring at this level of rotation would result in a limited rotational capacity of the AFW connection for seismic applications.

As shown in Table 8.8, the seismic compactness of the collector sections employed for AFW connections in the test building are evaluated based on the limiting slenderness ratios prescribed in the upcoming AISC seismic provisions (AISC 2022). Per the newest code

requirements, for the width-to-thickness ratio of the flange ($b_f/2t_f$) in a wide-flange beam, the "highly ductile" and "moderately ductile" limiting ratios, denoted as λ_{hd} and λ_{md}, respectively, are computed as:

$$\lambda_{hd} = 0.30\sqrt{\frac{E}{F_{ya}}} \tag{8.52}$$

$$\lambda_{md} = 0.38\sqrt{\frac{E}{F_{ya}}} \tag{8.53}$$

where F_{ya} is the measured yield stress, replacing the expected yield strength, R_yF_y, in the code formula. In addition, for the width-to-thickness ratio of the web (h/t_w) in a wide-flange flexural member in compression, λ_{hd} and λ_{md} are computed as:

$$\lambda_{hd} = 2.5(1 - C_a)^{2.3}\sqrt{\frac{E}{F_{ya}}} \tag{8.54}$$

$$\lambda_{md} = 5.4(1 - C_a)^{2.3}\sqrt{\frac{E}{F_{ya}}} \tag{8.55}$$

where $C_a = P_u/(A_gF_{ya})$. P_u is taken as the measured maximum compressive axial force induced on the steel section at the composite or bare steel AFW connection in Test 2B-5. As the compactness check results listed in Table 8.8, for the collector section (W14×30) used for the 2nd floor AFW connection, both flange and web are moderately ductile elements. Note that its flange width-to-thickness ratio is very close to λ_{md}, which means the flange just meets the moderate ductile requirement. However, the flange local bucking occurring in Test 2B-5 seem to indicate that the moderately ductile requirement is not adequate for AFW connections. It is recommended that the highly ductile requirements should be applied to the collectors with AFW connections.

Table 8.8 Compactness Check for Collectors with AFW Connections

(a) Flange

Location	Collector Section	$b_f/(2t_f)$	F_{ya} (kips)	λ_{hd}	λ_{md}
2nd Floor AFW Connection	W14×30	8.74	53.67	7.0	8.8
Roof AFW Connection	W10×17	6.08	53.28	7.0	8.9

(b) Web

Location	Collector Section	h/t_w	F_{ya} (kips)	A_g (in.^{2})	P_u (kips)	C_a	λ_{hd}	λ_{md}
2nd Floor AFW Connection	W14×30	45.4	55.45	8.85	100	0.204	33.9	73.1
Roof AFW Connection	W10×17	36.9	55.63	4.99	31	0.112	43.5	93.9

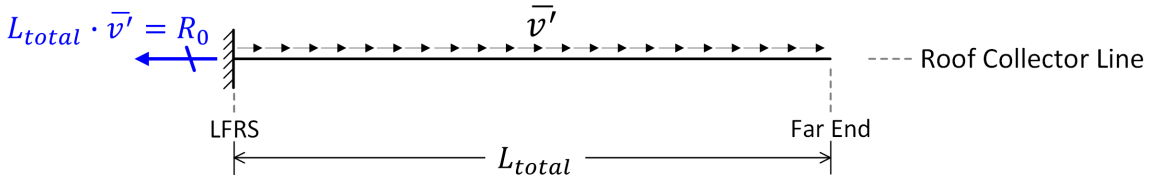

(a) Conventional Method

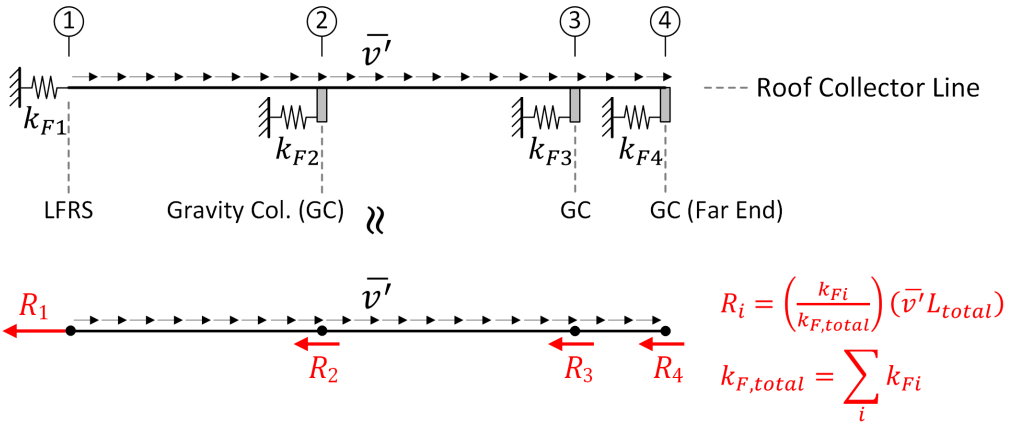

(b) Improved Method

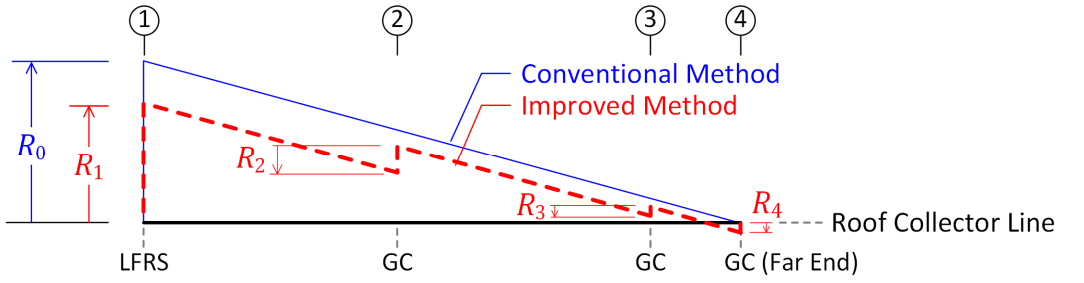

(c) Axial Force Diagram

Figure 8.24 (a) Conventional and (b) Impoved Methods for Estimating Roof Collector Axial Force in Specimen and Associated Axial Force Diagram Patterns

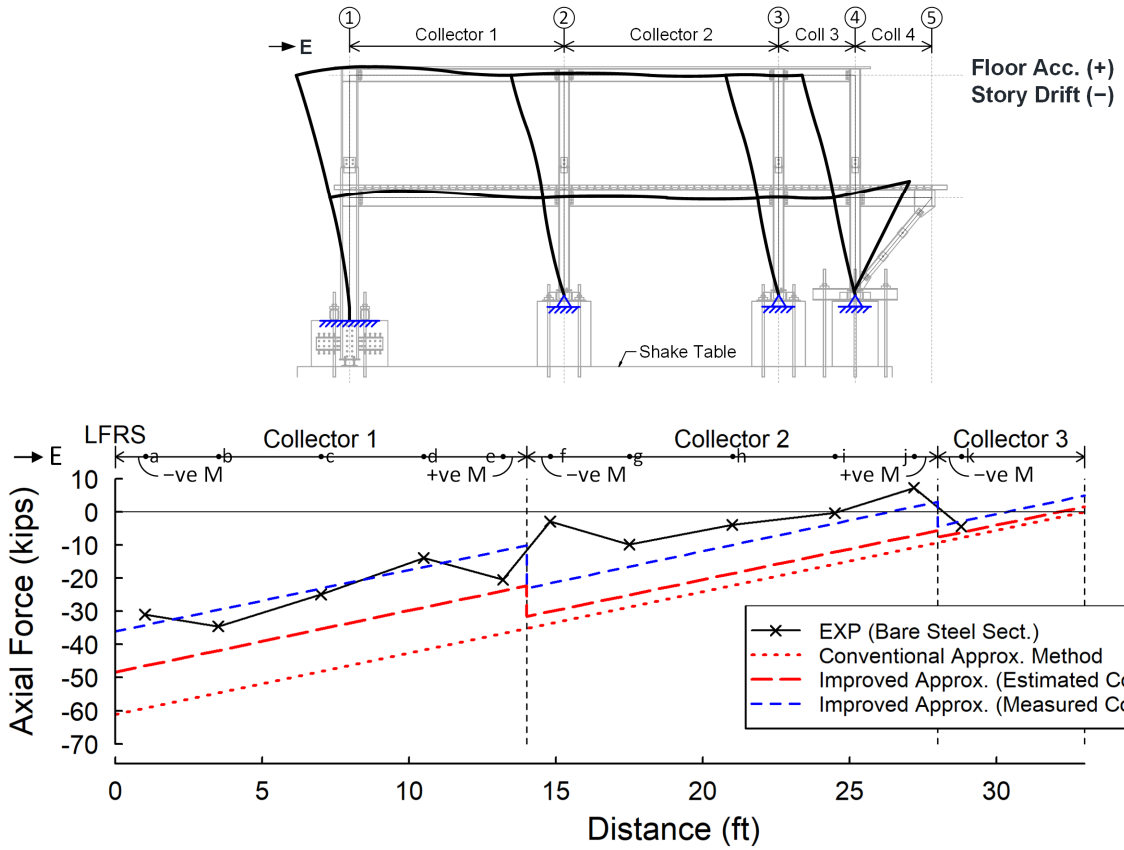

Figure 8.25 Comparison of Roof Collector Axial Forces Obtained from Experiment and Simplified Models (at Positive Peak Acceleration)

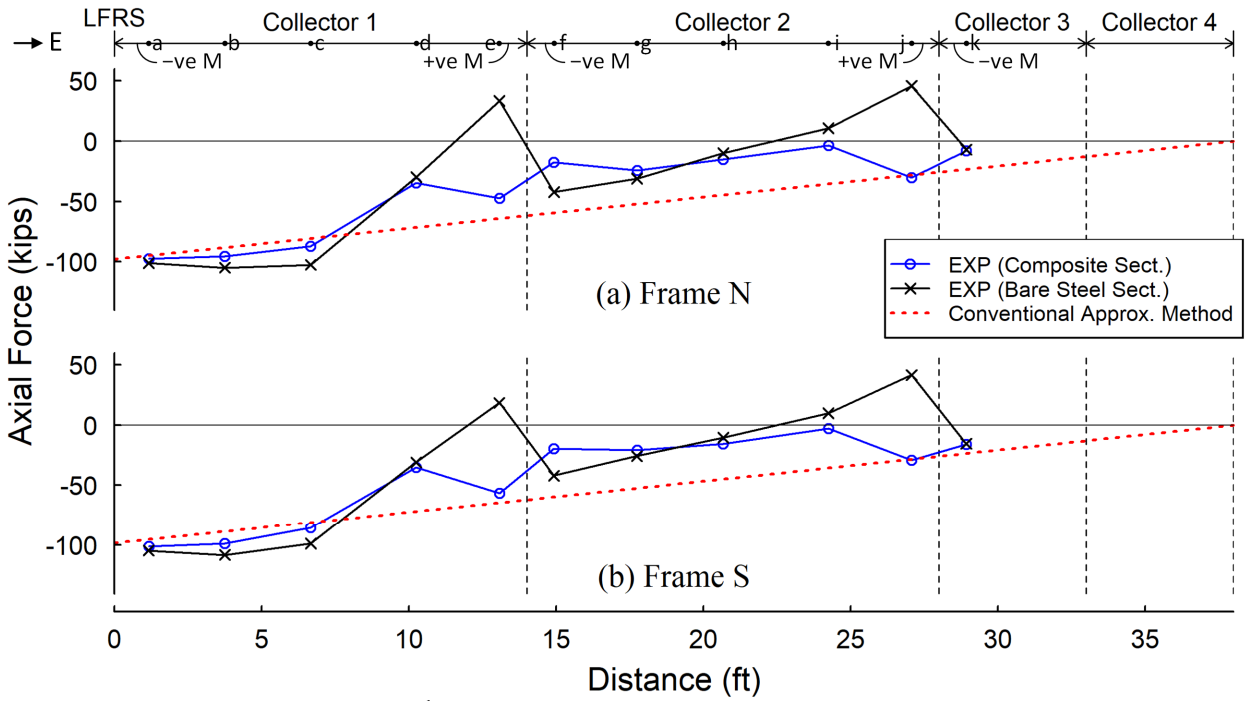

Figure 8.26 Comparison of 2nd Floor Collector Axial Forces Obtained from Experiment and Simplified Models (at Positive Peak Acceleration)

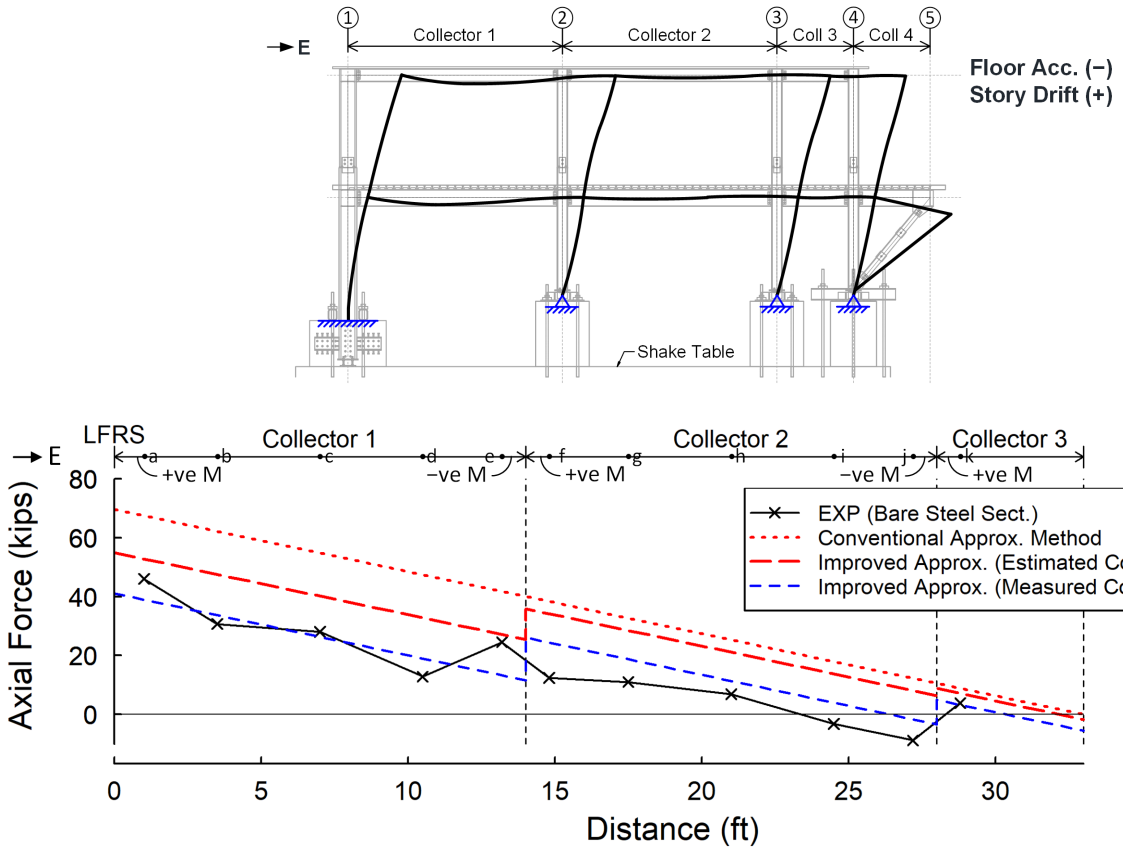

Figure 8.27 Comparison of Roof Collector Axial Forces Obtained from Experiment and Simplified Models (at Negative Peak Acceleration)

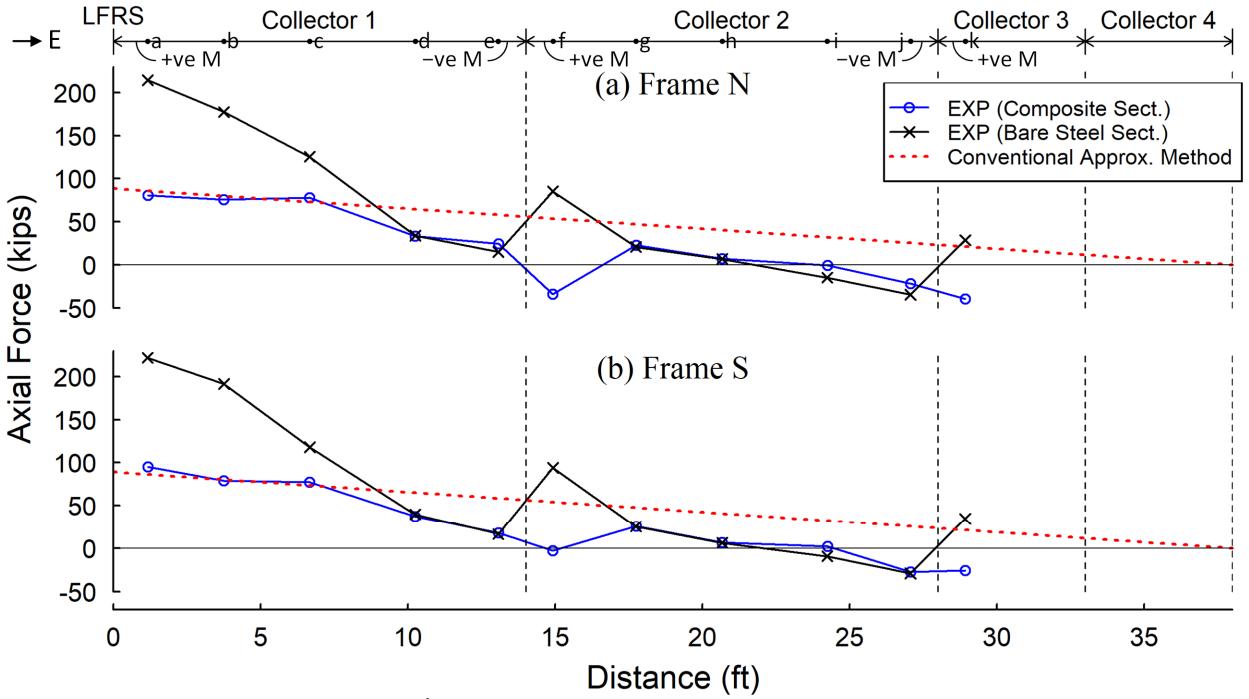

Figure 8.28 Comparison of 2nd Floor Collector Axial Forces Obtained from Experiment and Simplified Models (at Negative Peak Acceleration)

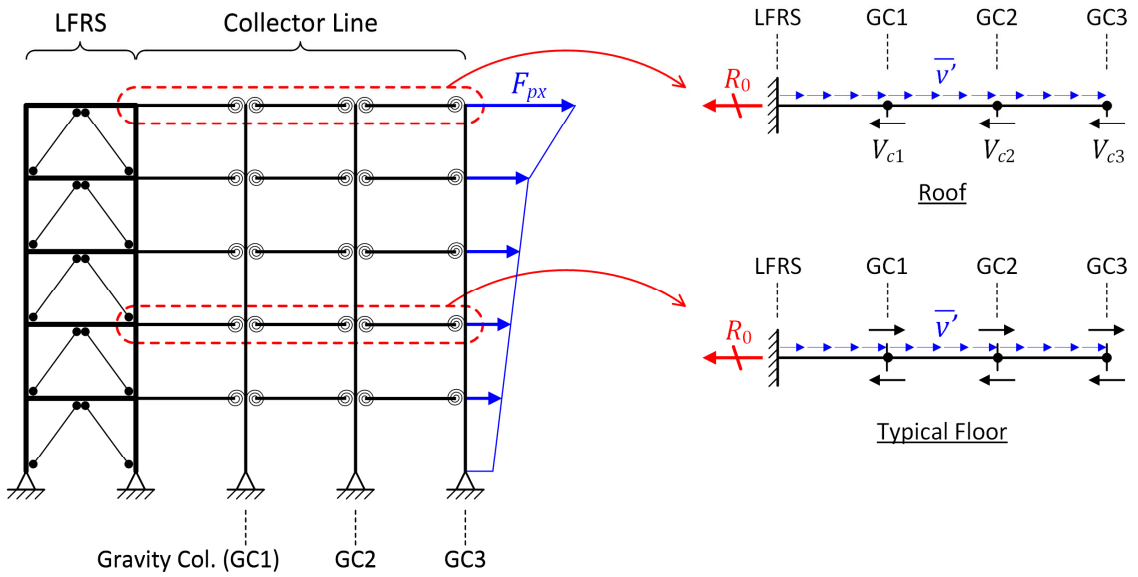

(a) Collector Lines in Multi-Story Buildings

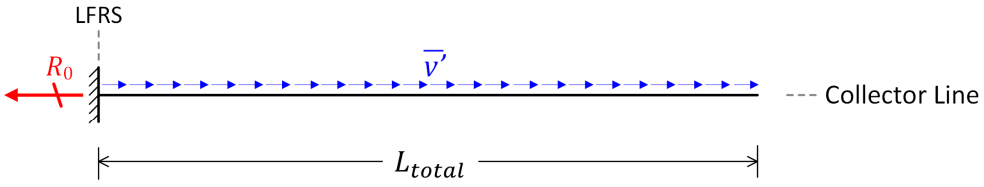

(b) Conventional Approximation Method for Typical Floor

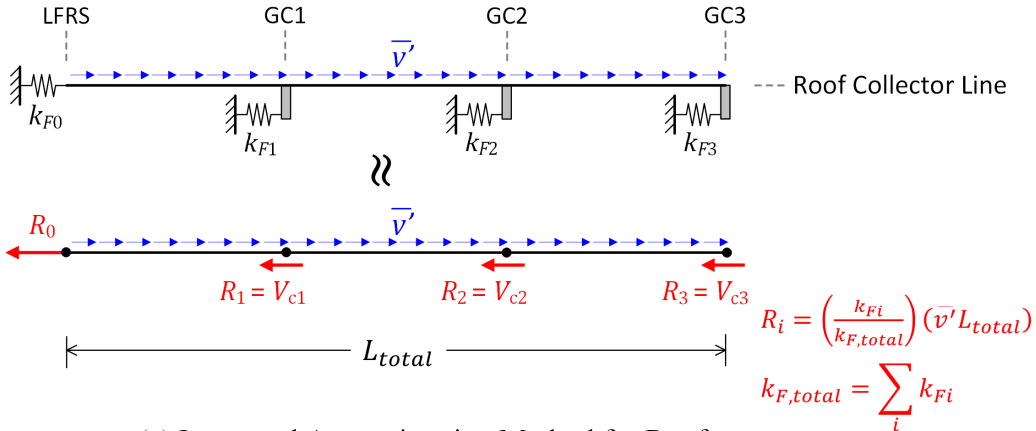

(c) Improved Approximation Method for Roof

Figure 8.29 Design Reccomendations on Estimating Collector Axial Force Demands in Multi-Story Buildigns

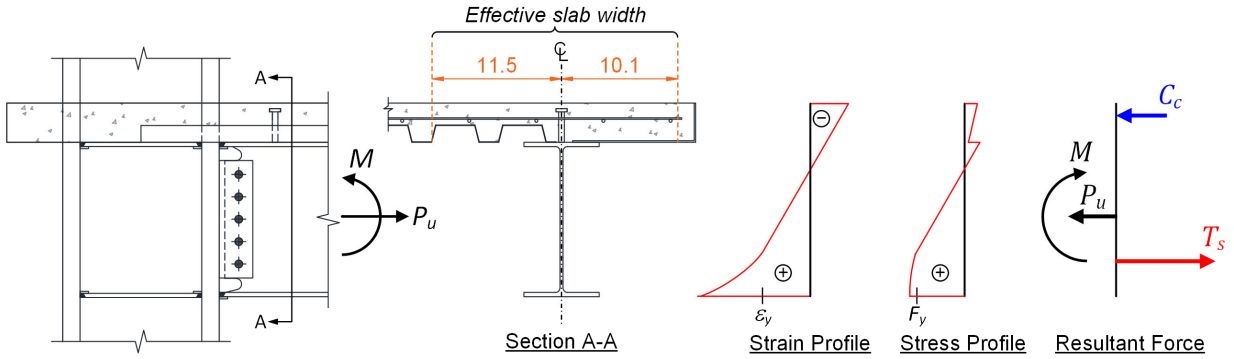

(a) AFW Collector-to-Column Connection

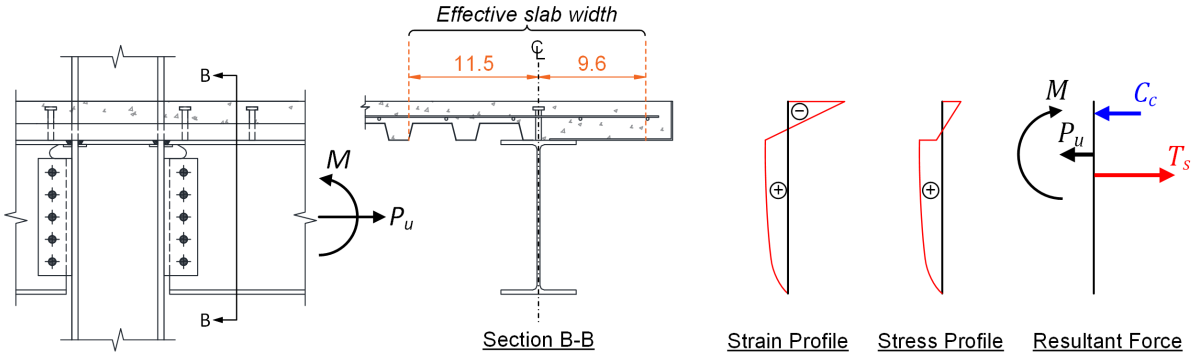

(b) TFW Collector-to-Column Connection

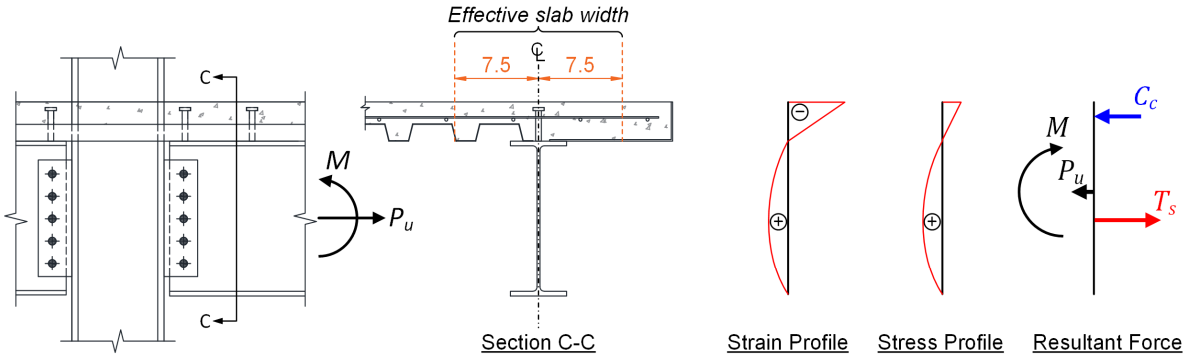

(c) BW Collector-to-Column Connection

Figure 8.30 Strain and Stress Profiles near Composite Collector Connections Subjected to Simutaneous Tensile Axial Force and Postive Bending Moment

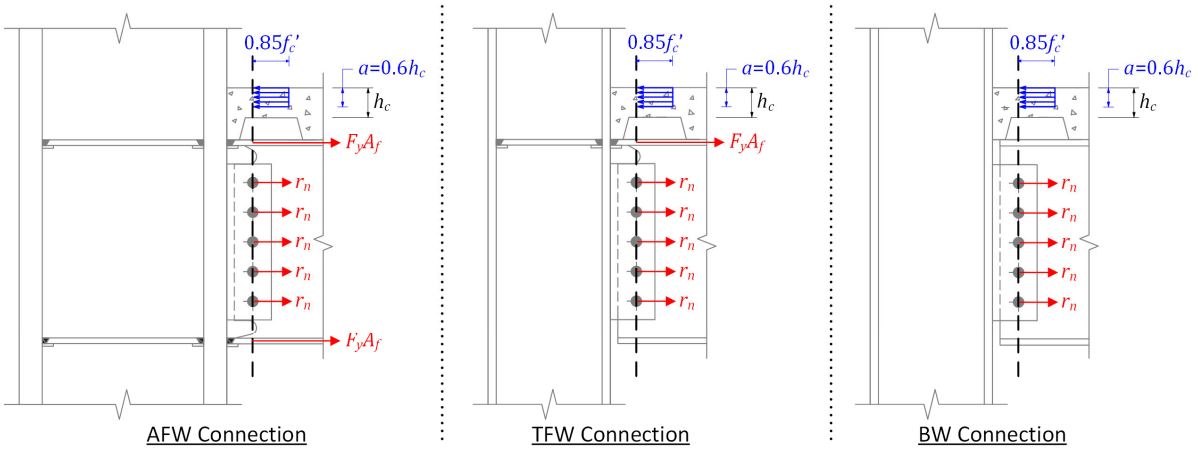

(a) Deck Perpendicular to Collector

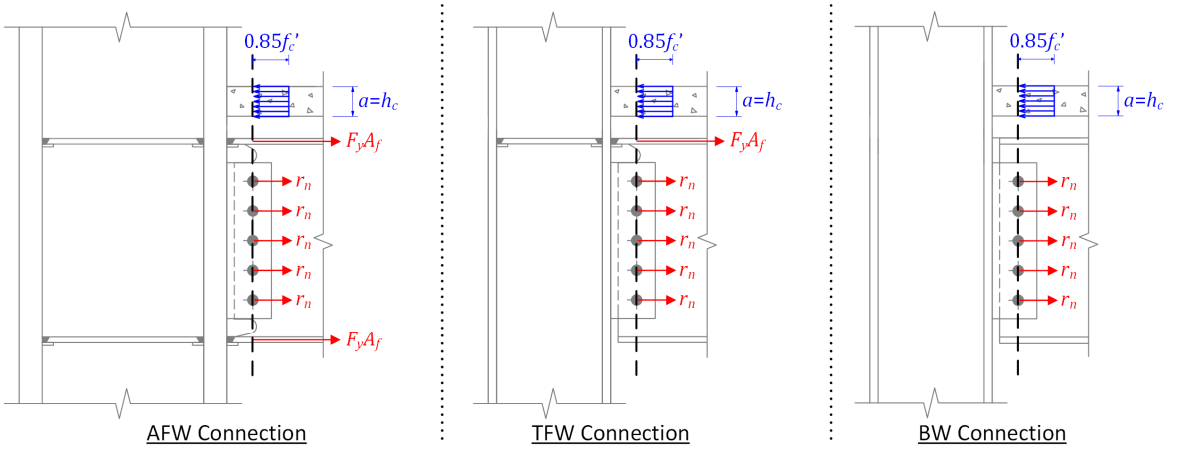

(b) Deck Parallel to Collector

Figure 8.31 Limit States Considered for Design of Various Types of Collector Connections

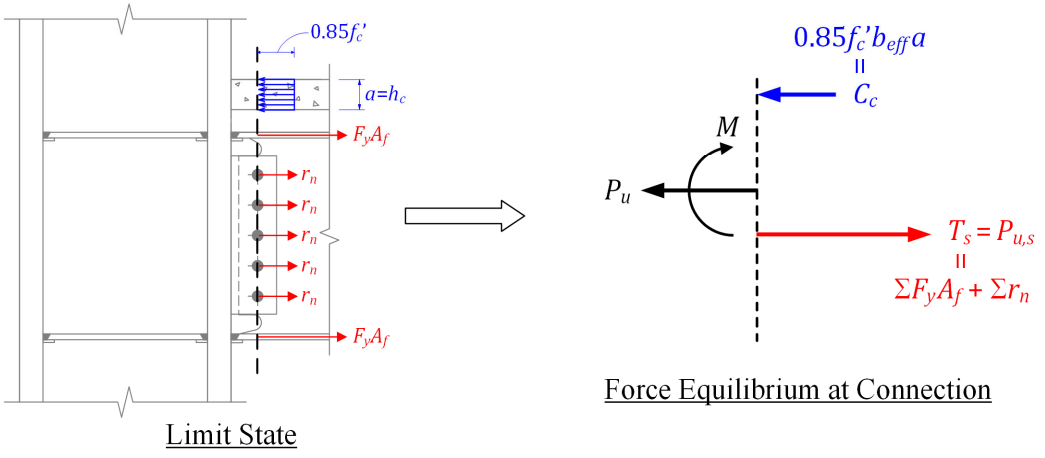

Figure 8.32 Force Equilibrium of Collector Connection at Limit State

9. PHASE 3 TESTING

9.1 General

In Phase 3 test program, a pair of buckling-restrained braces (BRBs) were added to the second story of the test building to modify the building dynamic characteristics and the collector seismic load path. This "braced frame phase" test building was tested at the NHERI@UCSD LHPOST by using the conventional earthquake simulation testing method. This chapter describes the testing program and test results .

9.2 Test Specimen and Setup

Two buckling-restrained braces (BRBs), designated as Braces S1 and N1, were respectively installed into the south and north sides in the second story of the test building (see Figure 9.1). In addition, another two identical BRBs were fabricated together with the first pair of BRBs (i.e., S1 and N1) and tested individually to provide a reference to calibrate the axial forces of the first pair of BRBs during shake table tests. These four BRBs consisted of an A36 flat steel core plate with a cross-sectional area of 0.75 $in.^2$ encased in a grout-filled square casing made from HSS7×7×0.25 and had an expected yield strength of 33 kips. See Figure 9.2 for the overall brace geometry.

To install the BRBs, 1/2-in. thick gusset plates were field welded to the test building, and the BRBs were connected to gusset plates with 7/8-in. diameter F3125 Gr. F2280 tension-control bolts with standard holes on the brace end and oversized holes on the gusset plates. As required by AISC Seismic Provisions (AISC 2016b), the beam-to-column connections at the brace ends shall be designed to resist 1.1 times the lesser of the expected plastic moment of the beam and the sum of the expected column flexural strengths. To satisfy this requirement, modifications to some collector end connections were made. Figure 9.3 shows the details of the top gusset connection.

The collector-to-column connection used for Phase 2 testing was a top-flange weld (TFW) connection, in which only the top flange of the collector was connected to the column using a CJP groove weld with steel backing bar not removed. For Phase 3 testing, two welds were added to this connection to increase its flexural resistance: (1) the edge of the bottom flange of the collector was beveled before CJP welding with a steel backing left in place was employed to connect the flange to the column, (2) the edge of the collector web was beveled and then a CJP weld was added between the beam web and column flange.

Figure 9.4(a) shows the details of the bottom gusset connection. The collector-to-column connection was an all-flange weld (AFW) connection in both Phases 1 and 2 testing, in which the top and bottom flanges of the collector were connected to the column using CJP welds with steel backing at both flange levels not removed, but the beam web was bolted through a shear tab to the column flange. For Phase 3 testing, a CJP weld between the collector web and column flange was added [see Figure 9.4(b)] with the edge of collector web being beveled first. As shown in Figure 9.5, a small portion of the second-floor concrete slab was cut out such that the gusset plate could be field welded to the test building. Non-shrinkage cement mortar was then used to fill the cutout.

The installation of BRBs and the associated modifications of collector connections made the only difference of the test building between Phase 2B and Phase 3. All the Phase 2B test setup, including the way specimen was mounted on the shake table and the attachment of added masses on the 2nd floor slab and roof deck, remained in Phase 3. See Figure 9.6 and Figure 9.7 for Phase 3 test setup.

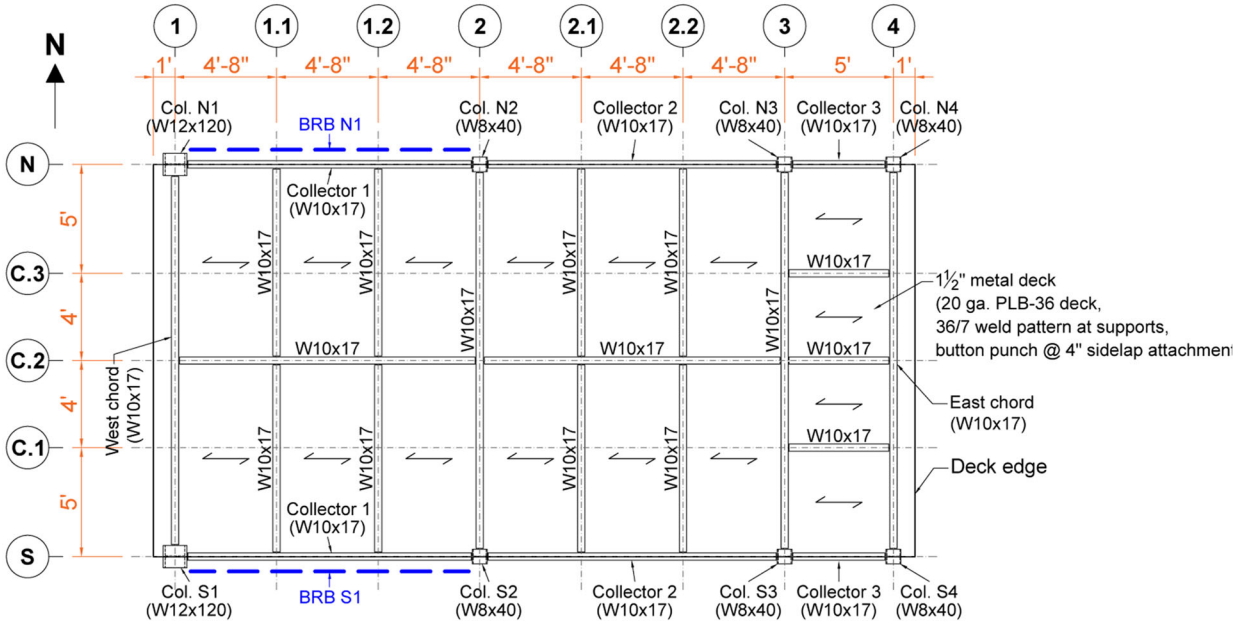

(a) Roof Plan

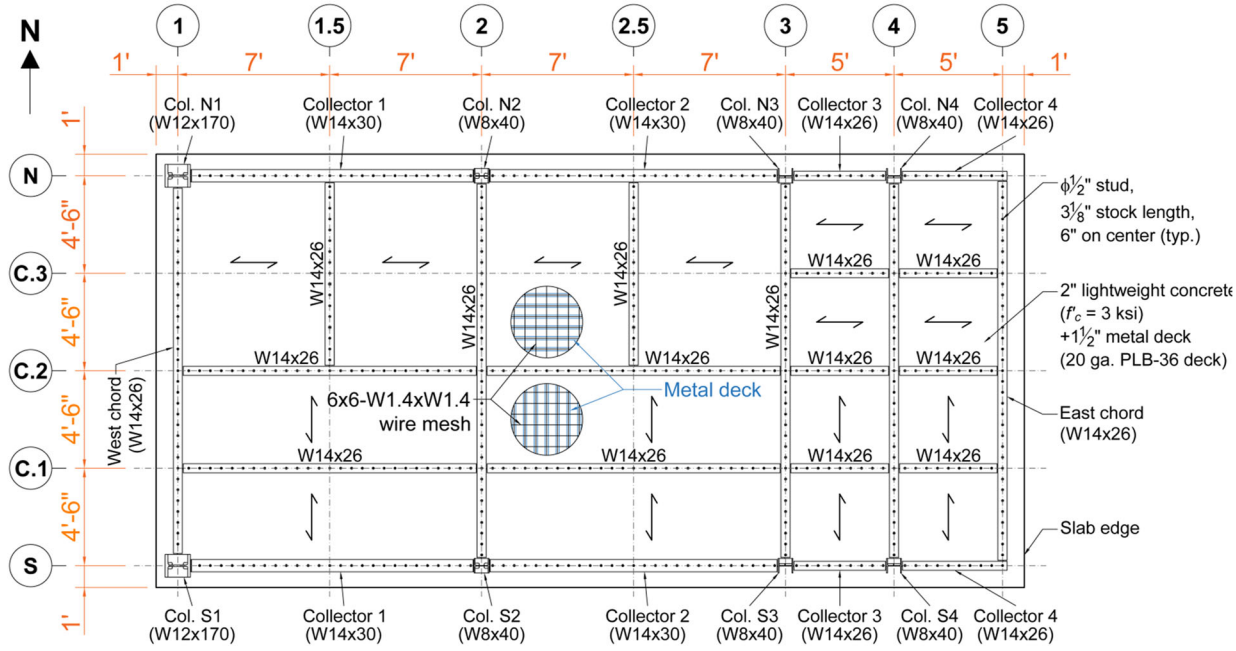

(b) 2nd Floor Plan

Figure 9.1 Phase 3 Test Building: Overview

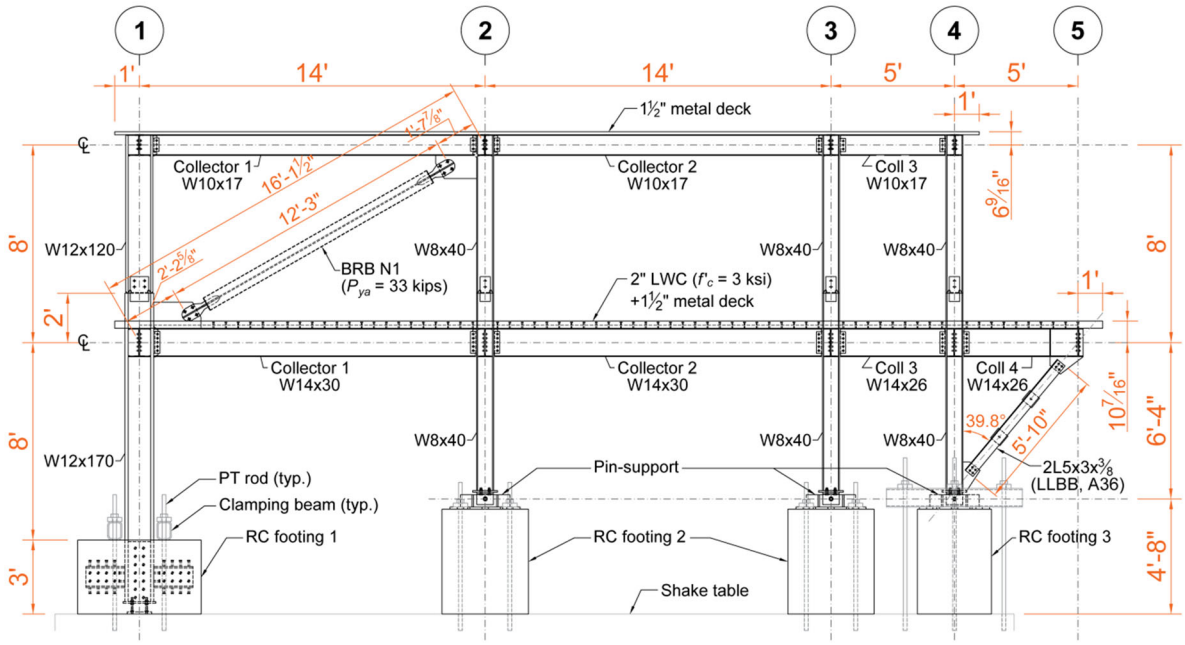

(c) Elevation of Frame S

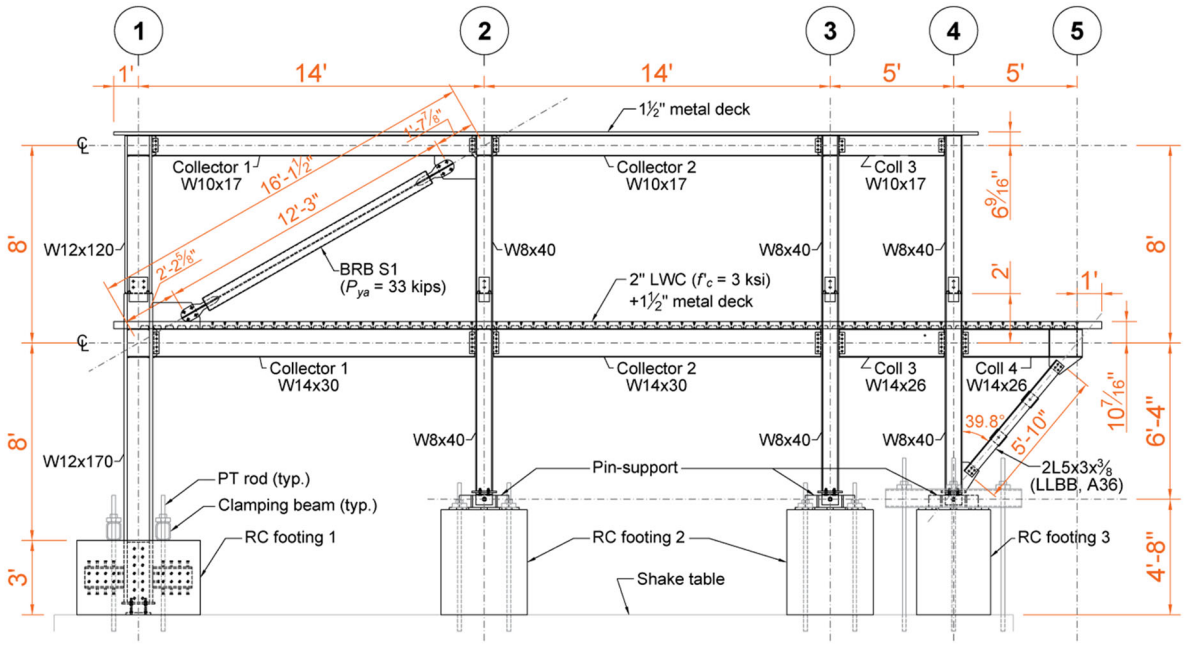

(d) Elevation of Frame N

Figure 9.1 Phase 3 Test Building: Overview (continued)

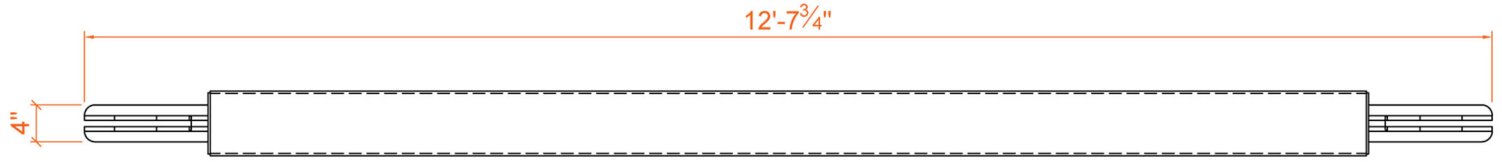

(a) Plan View

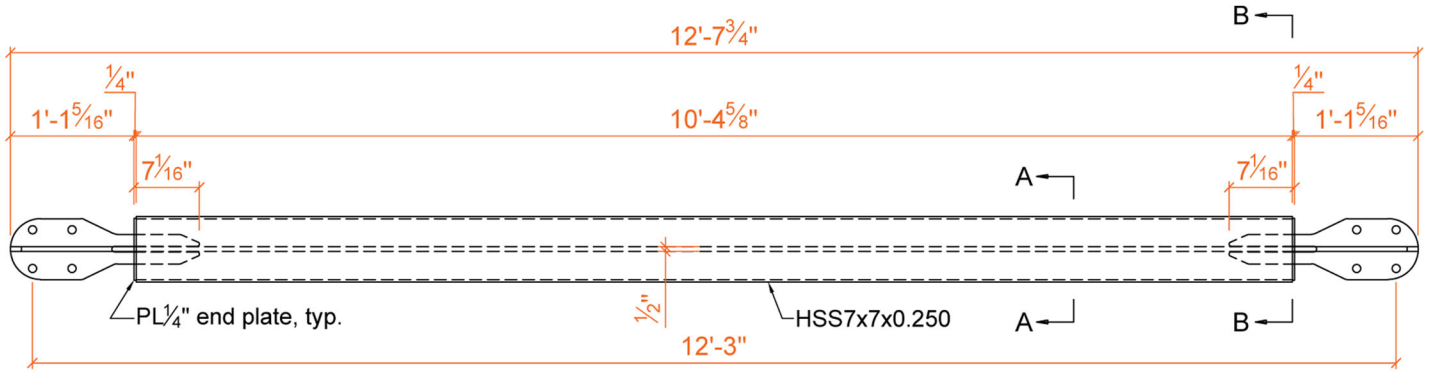

(b) Elevation View

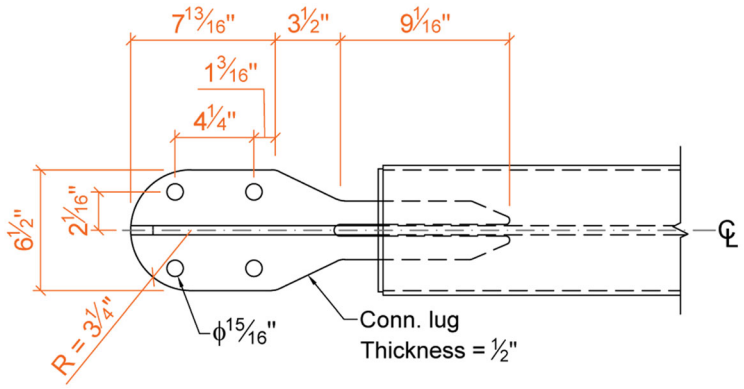

(c) End Detail

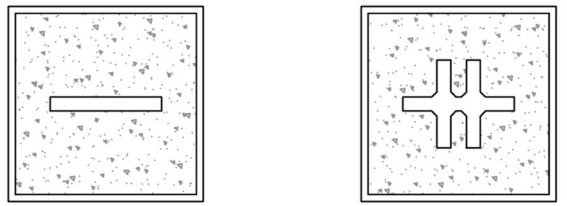

(d) Cross Sections

Figure 9.2 Buckling-Restrained Brace Detail

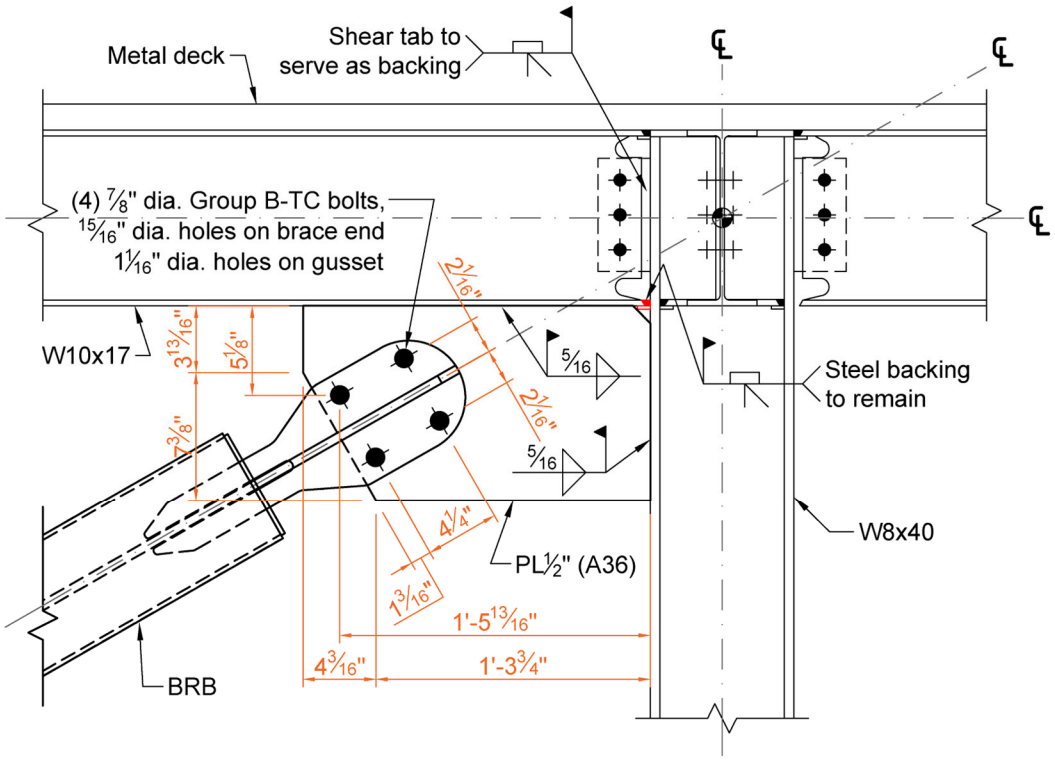

(a) Connection Detail

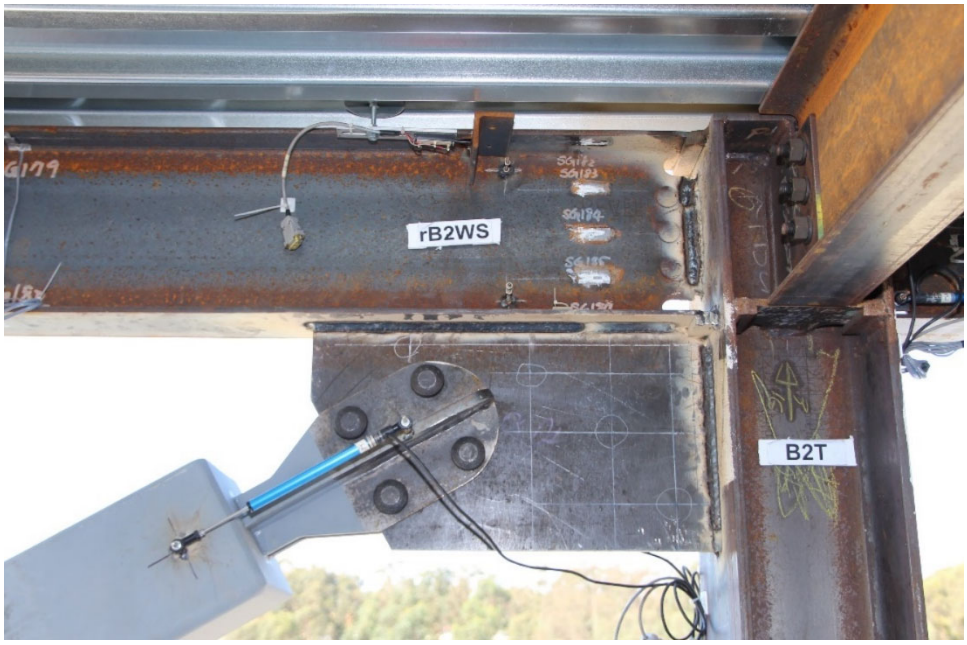

(b) Gusset Connection and Modified Collector-to-Column Connection

Figure 9.3 Top-End BRB Gusset Connection Detail (Second Story of Frame N)

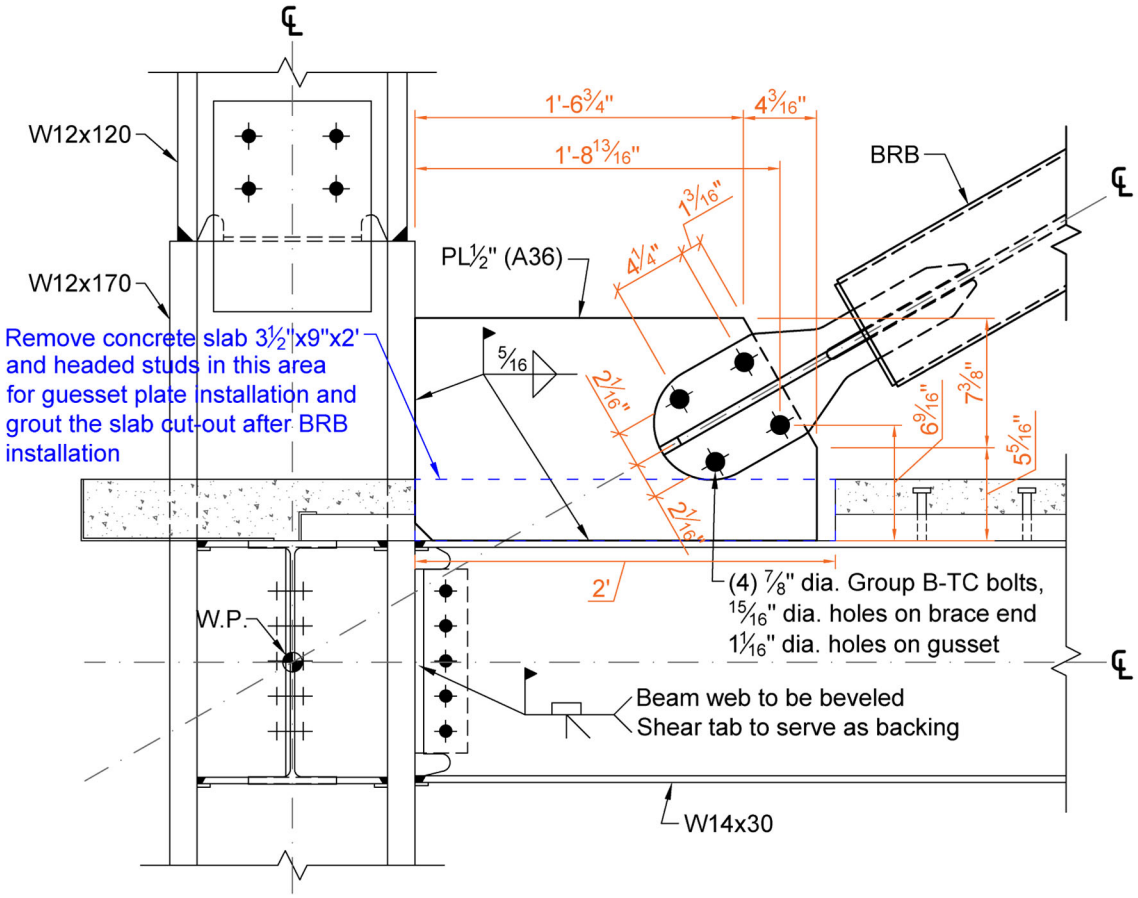

(a) Connection Detail

(b) Modified Collector-to-Column Connection

Figure 9.4 Bottom-End BRB Gusset Connection Detail (Second Story of Frame N)

(a) before Grouting

(b) after Grouting

Figure 9.5 Bottom-End BRB Gusset Connection (Second Story of North Frame)

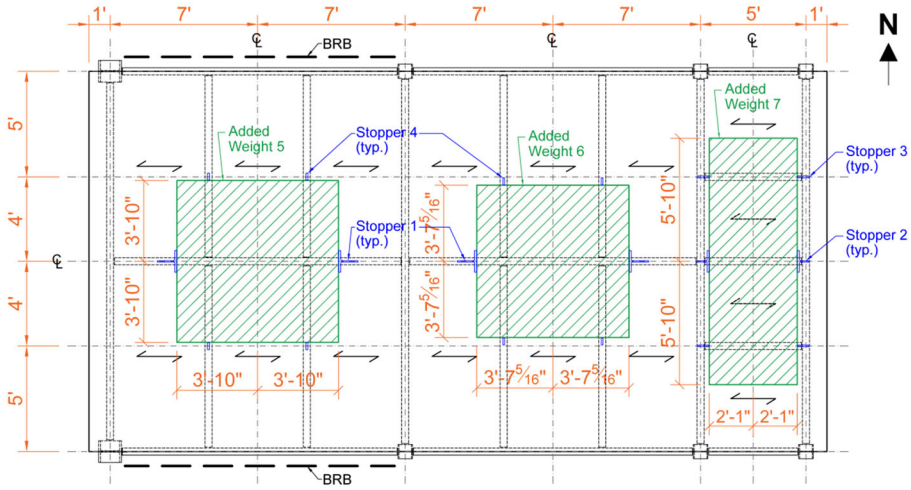

(a) Plan View of Roof Level

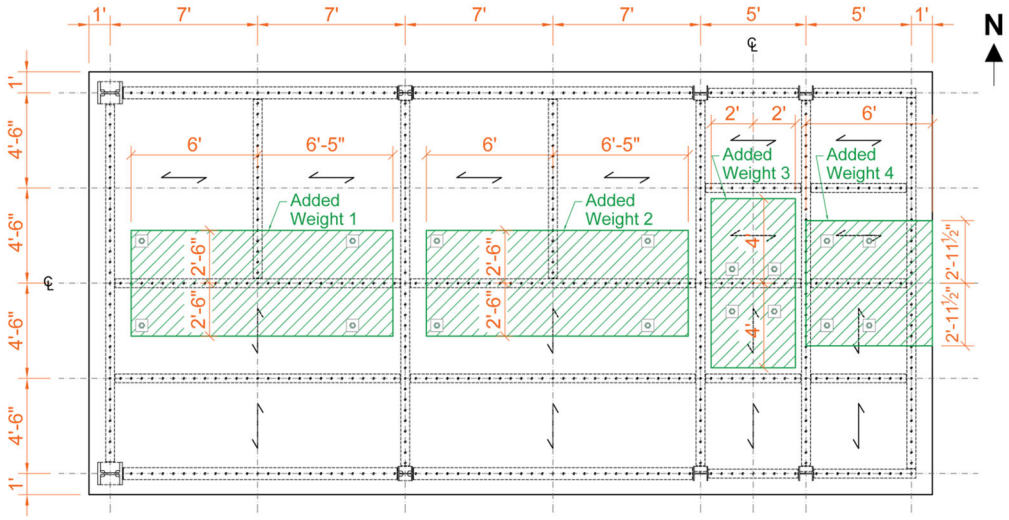

(b) Plan View of 2nd Floor Level

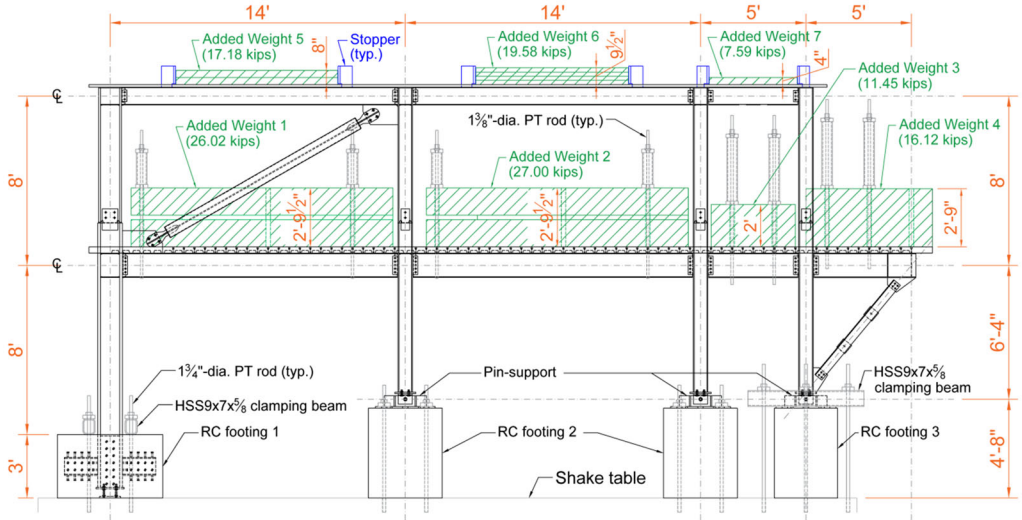

(c) Elevation View

Figure 9.6 Phase 3 Test Setup and Added Weight Layout

(a) Front View (Looking North)

(b) High Angle Front View

Figure 9.7 Photos of Test Building

9.3 Instrumentation and Data Filtering

Phase 3 test building was thoroughly instrumented with a combination of accelerometers, displacement transducers, uniaxial electrical resistance strain gauges, and strain gauge rosettes. Instrumentation plans are shown in Figure 9.8. A total of 420 separate data channels were used for Phase 3 Tests. The policies for filtering and biasing the raw data follows that used in Phases 1 and 2 testing.

About 90% of the sensors which had been installed in Phase 2 specimen were re-used in Phase 3 testing. There were 39 sensors were removed or disconnected for accommodating newly added instruments in Phase 3. These removed and disconnected sensors are denoted in Figure 9.8. Newly added sensors follow. A pair of LVDT displacement transducers were installed at each brace end between the outer casing and the elastic segment of the steel core to measure the brace axial deformation [see Figure 9.8(m)]. A pair of uni-axial strain gauges were placed on the stiffener of each lug at the top end of the brace [SG257 to SG260 in Figure 9.8(i)]. Figure 9.8(i) also shows that the top gusset plate in the north frame was heavily instrumented with strain gauges and strain rosettes.

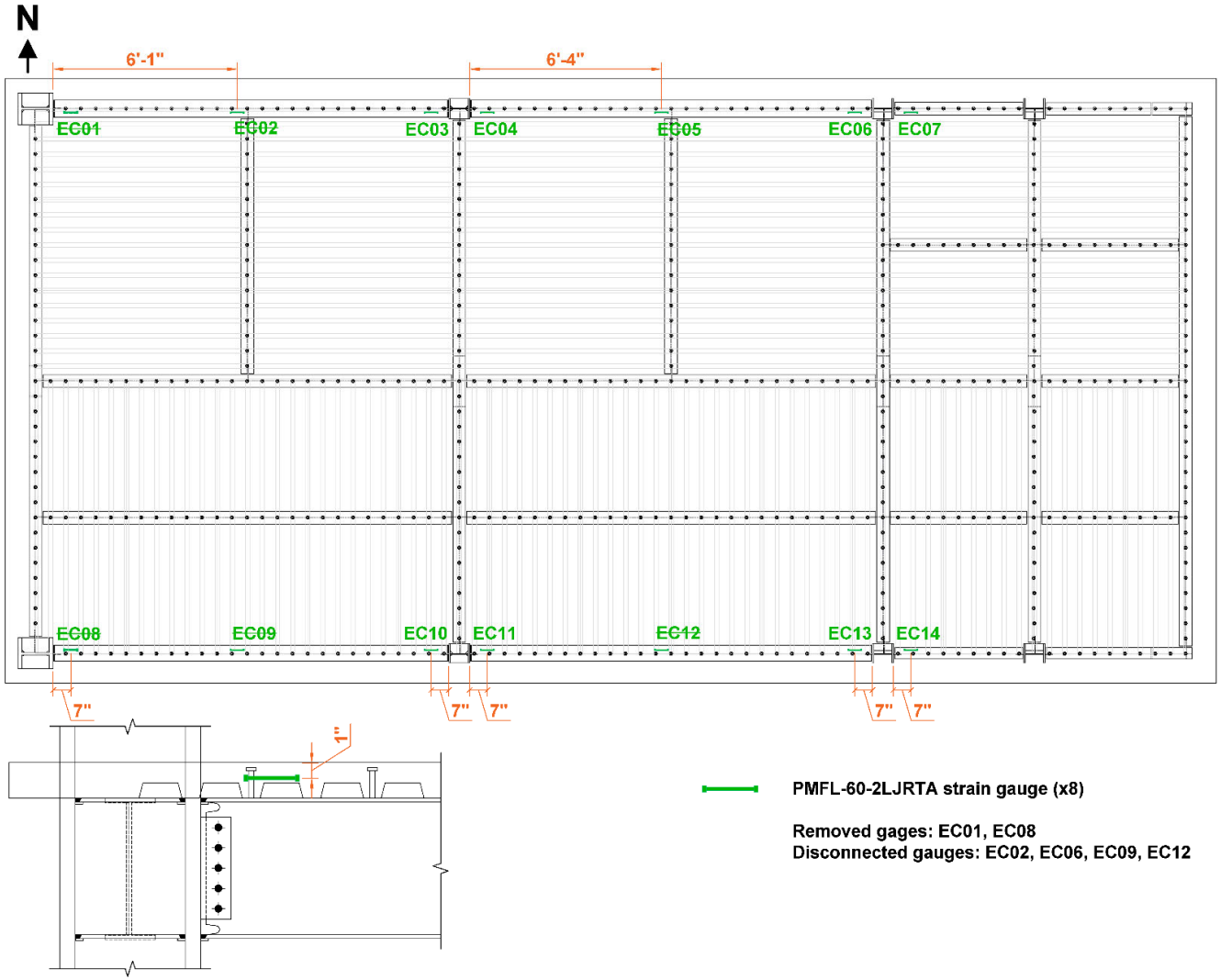

(a) Concrete-embedded Strain Gauges

Figure 9.8 Instrumentation Plan for Phase 3 Test

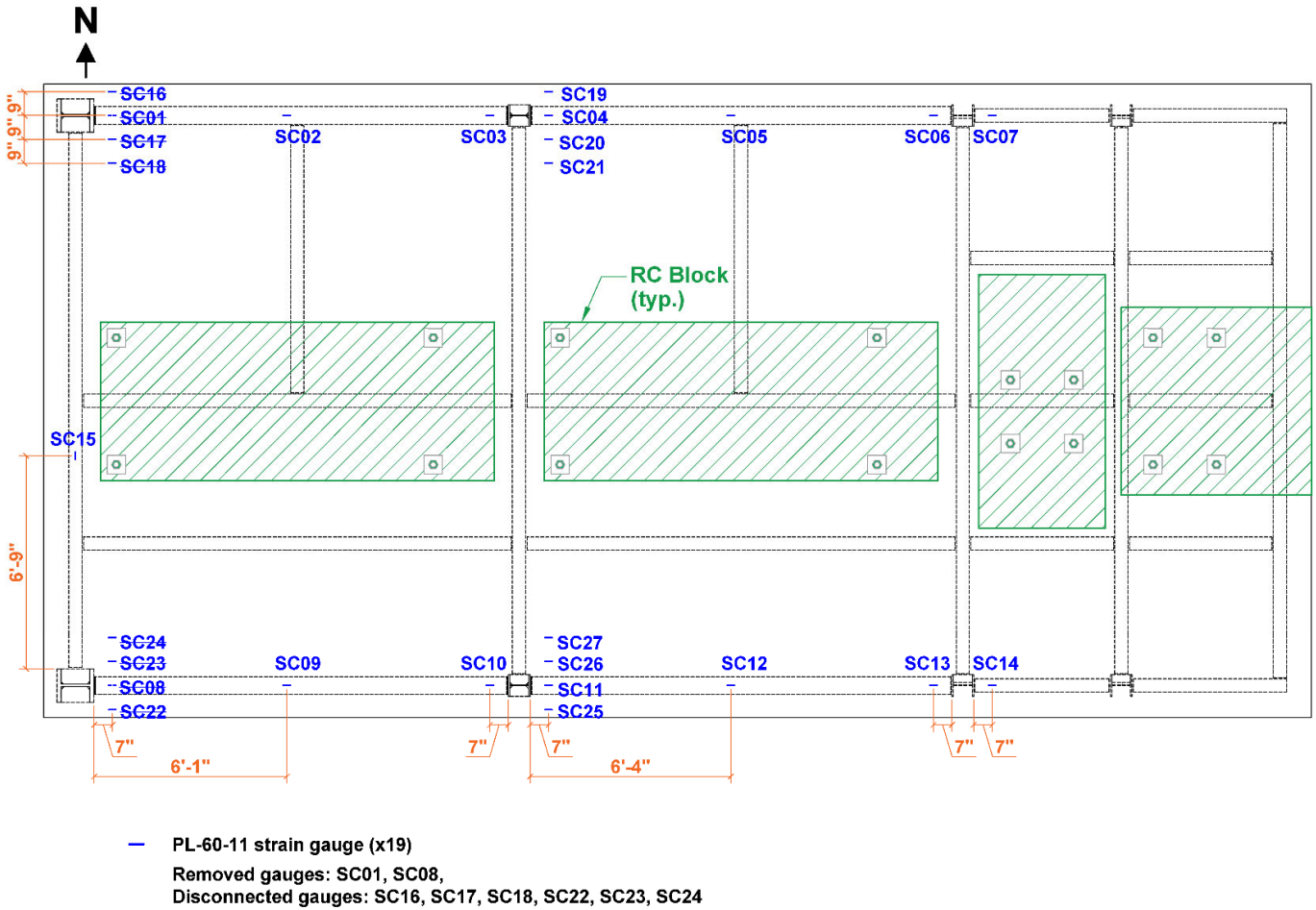

(b) Concrete Surface Strain Gauges

Figure 9.8 Instrumentation Plan for Phase 3 Test (continued)

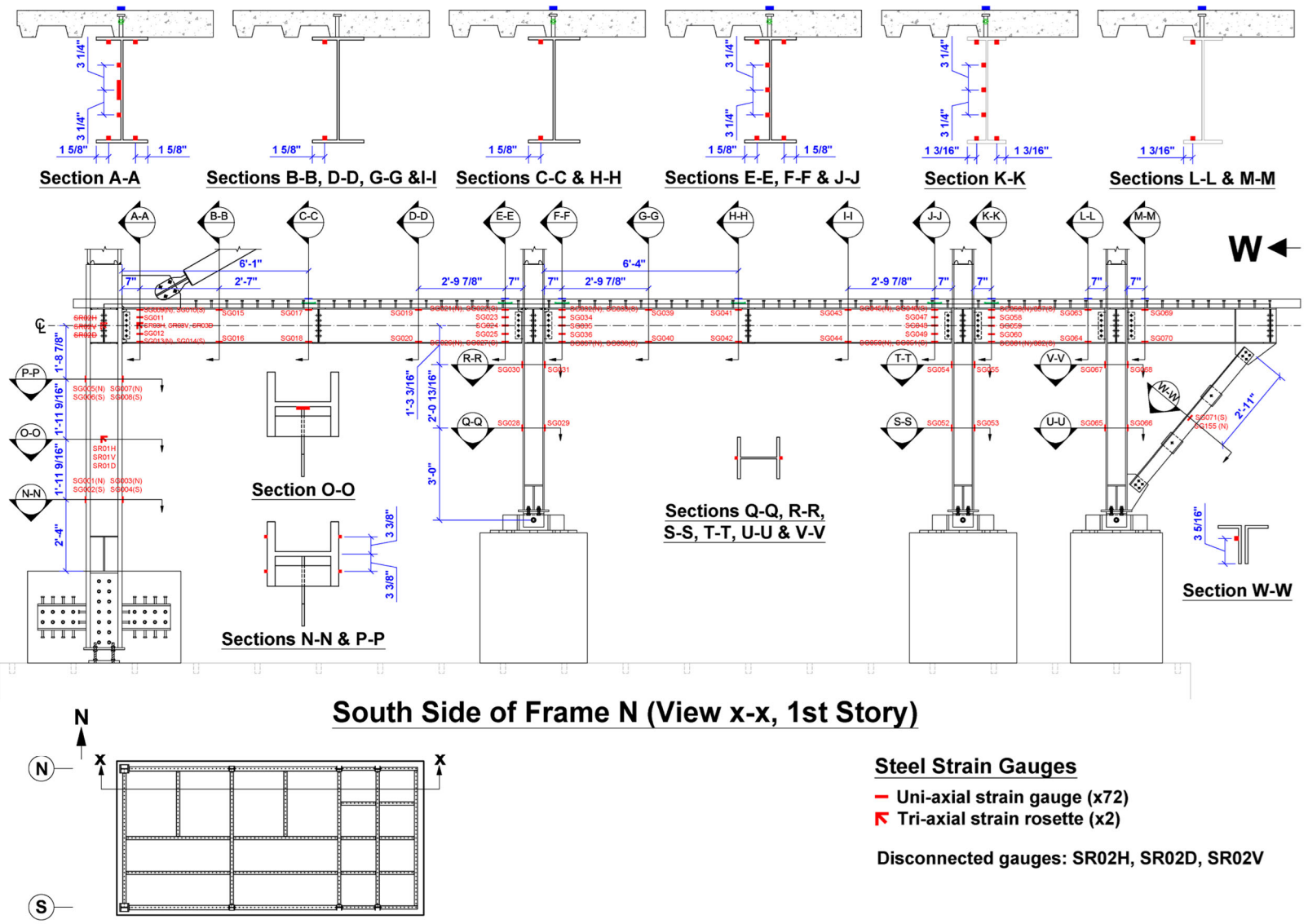

(c) Steel Strain Gauges on Frame N (1st Story)

Figure 9.8 Instrumentation Plan for Phase 3 Test (continued)

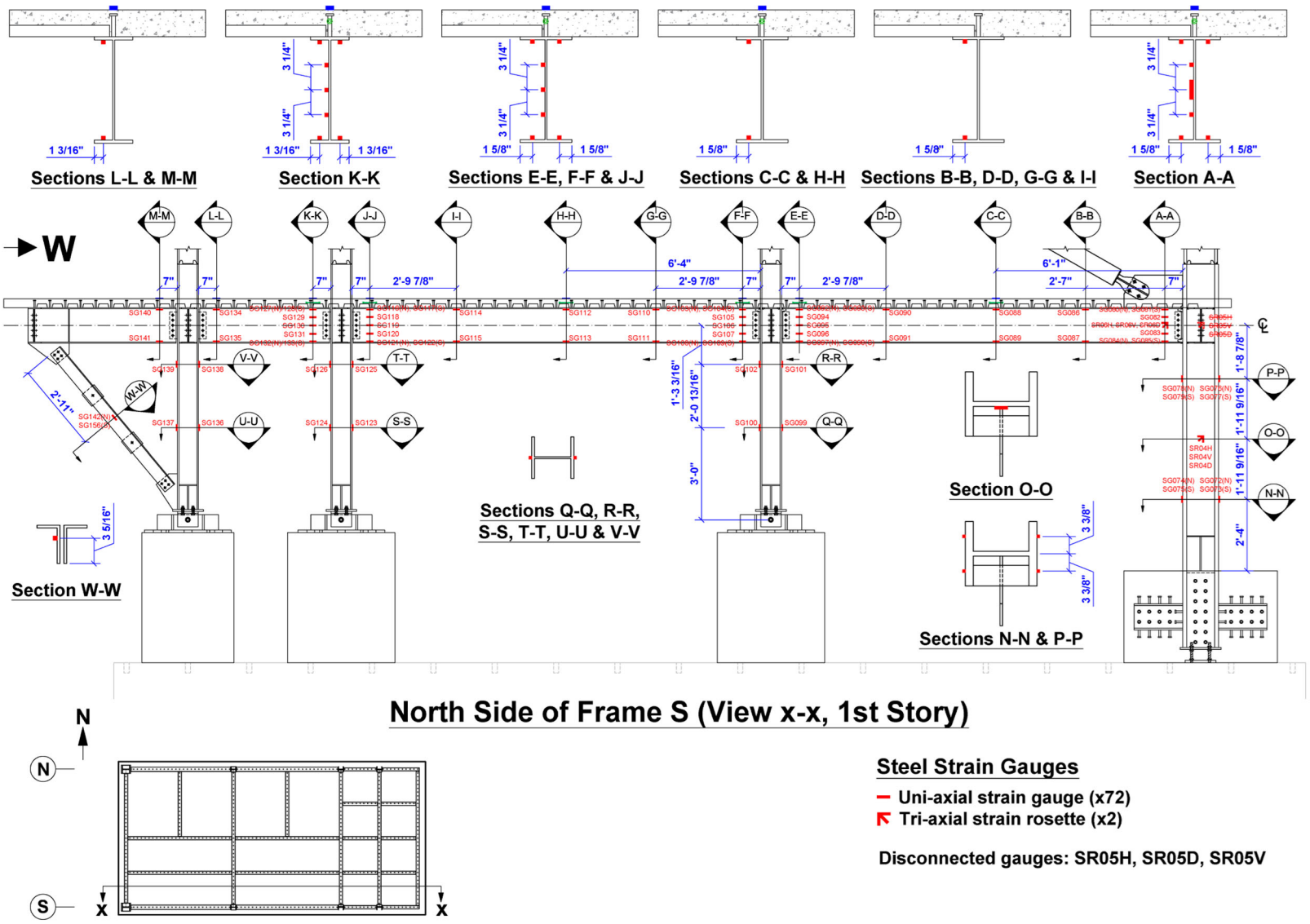

(d) Steel Strain Gauges on Frame S (1st Story)

Figure 9.8 Instrumentation Plan for Phase 3 Test (continued)

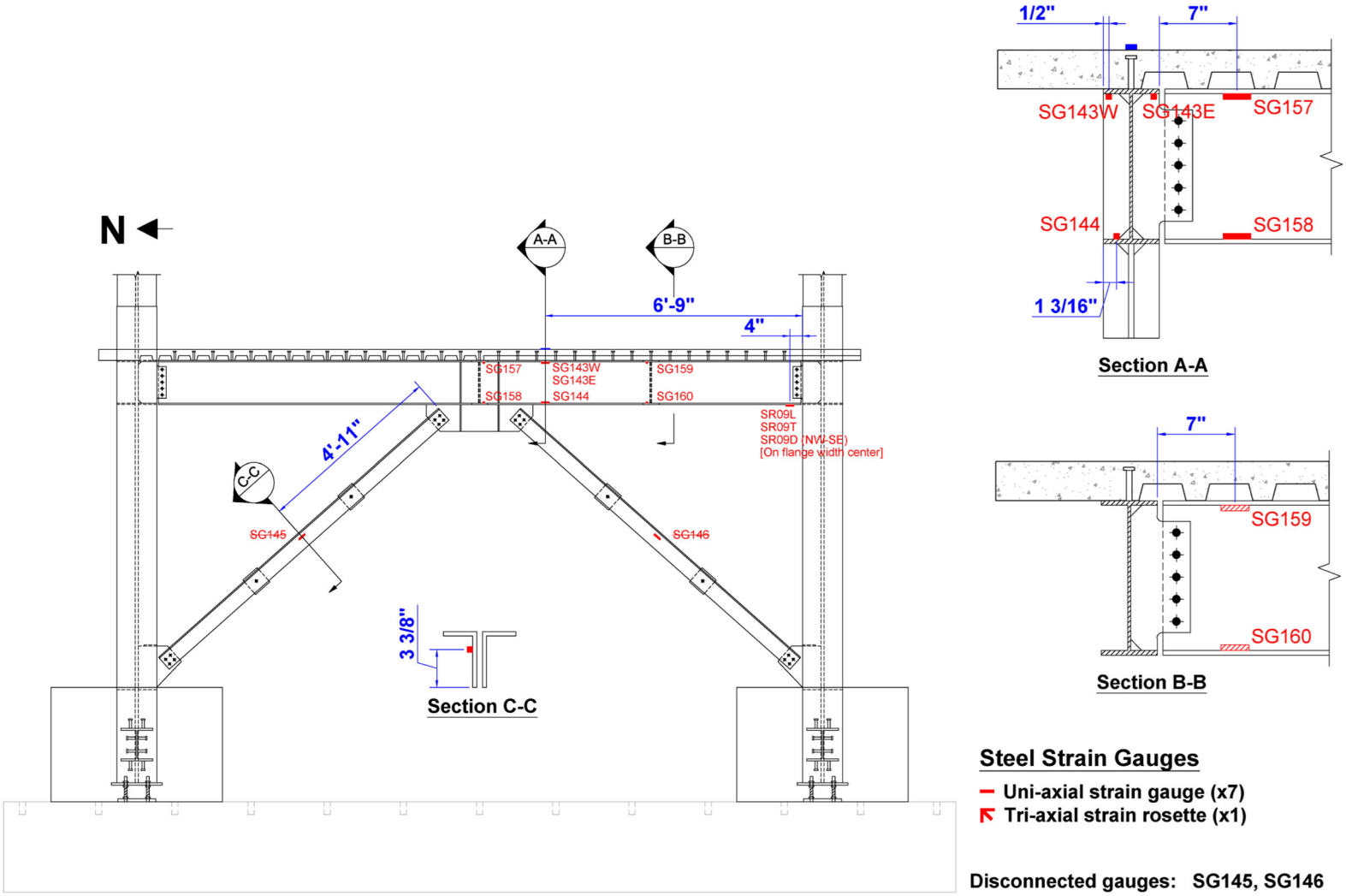

(e) Steel Strain Gauges on Frame 1 (1st Story)

Figure 9.8 Instrumentation Plan for Phase 3 Test (continued)

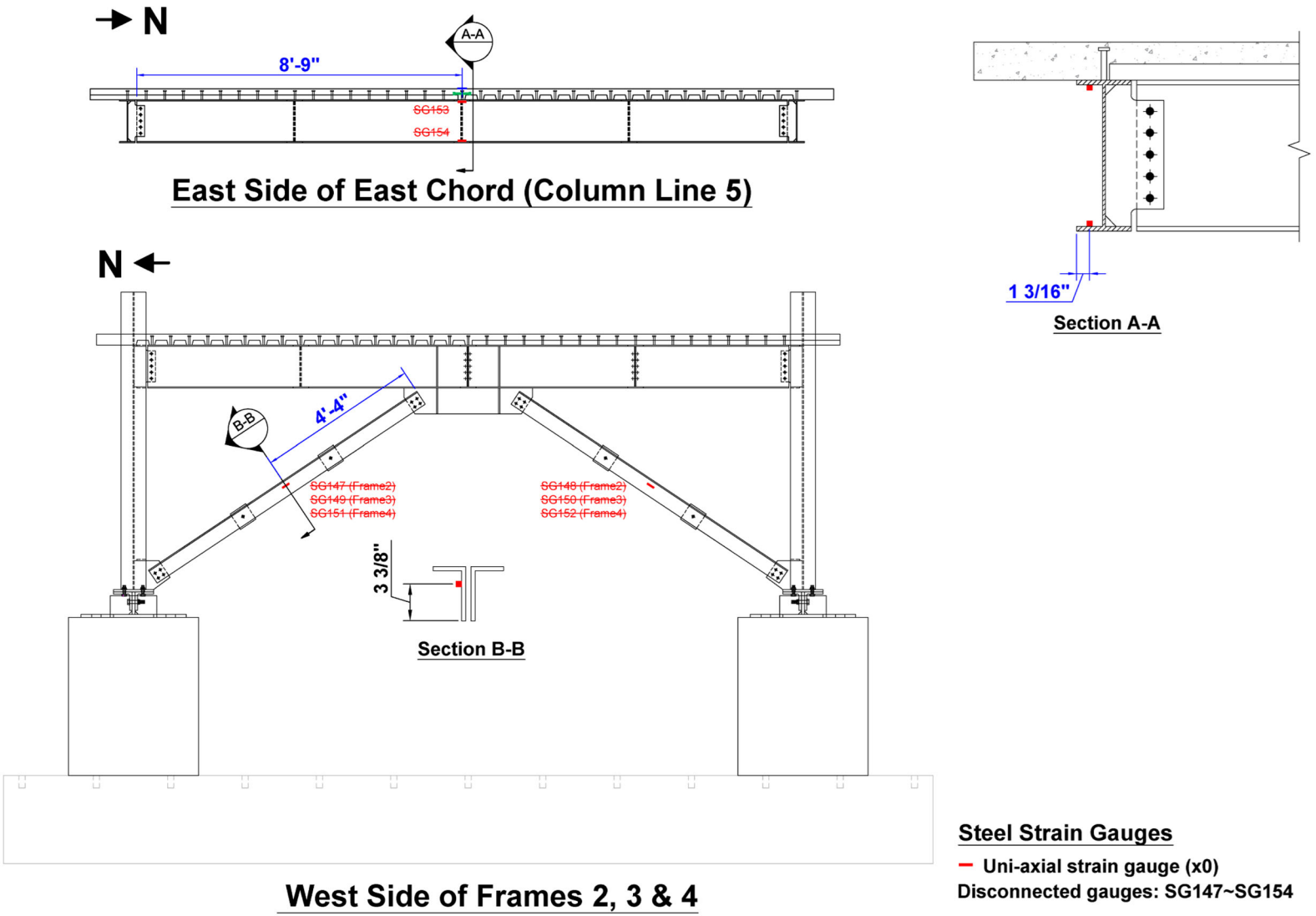

(f) Steel Strain Gauges on 2nd Floor East Chord and Frames 2, 3, and 4 (1st Story)

Figure 9.8 Instrumentation Plan for Phase 3 Test (continued)

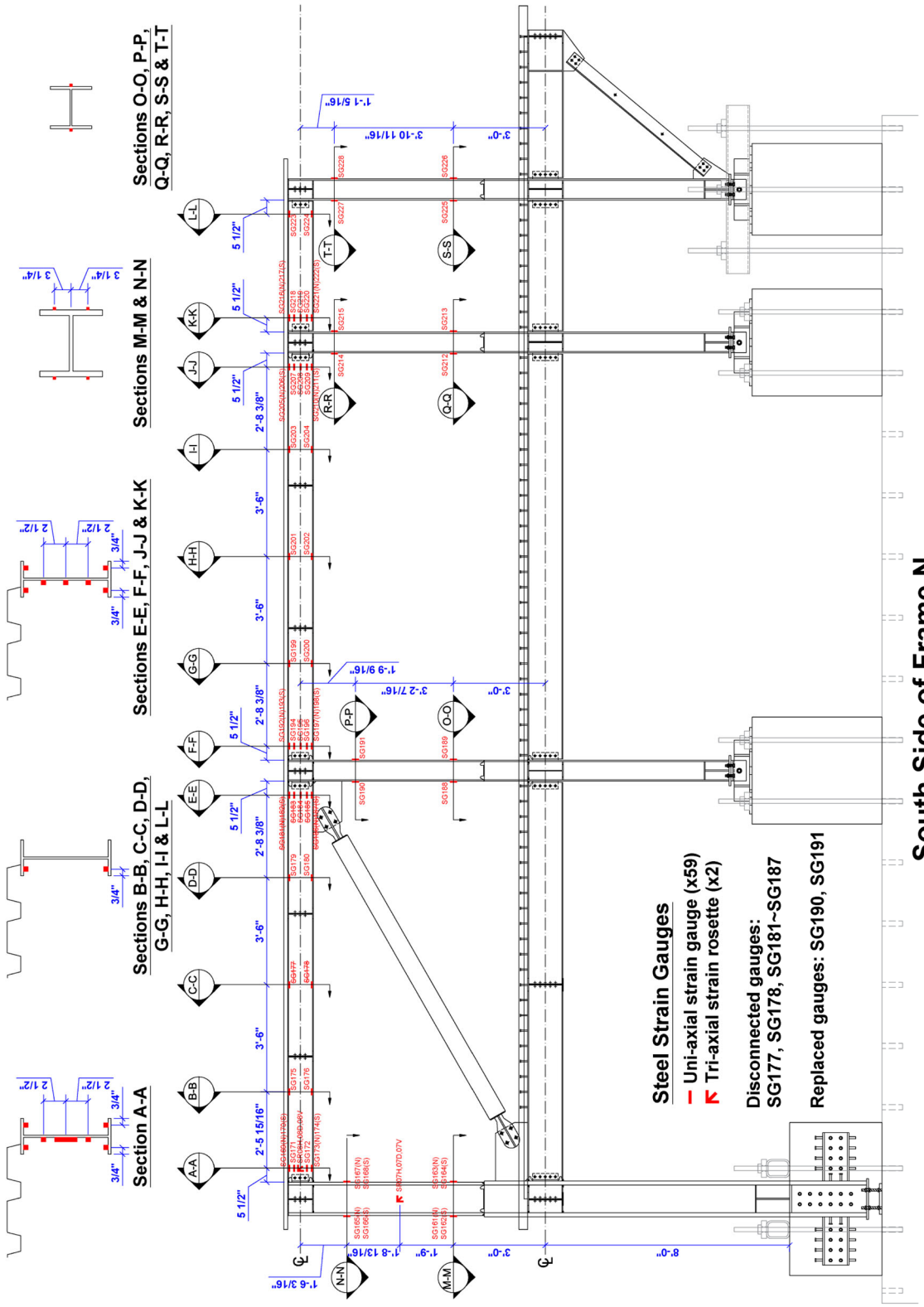

(g) Steel Strain Gauges on Frame N (2nd Story)

Figure 9.8 Instrumentation Plan for Phase 3 Test (continued)

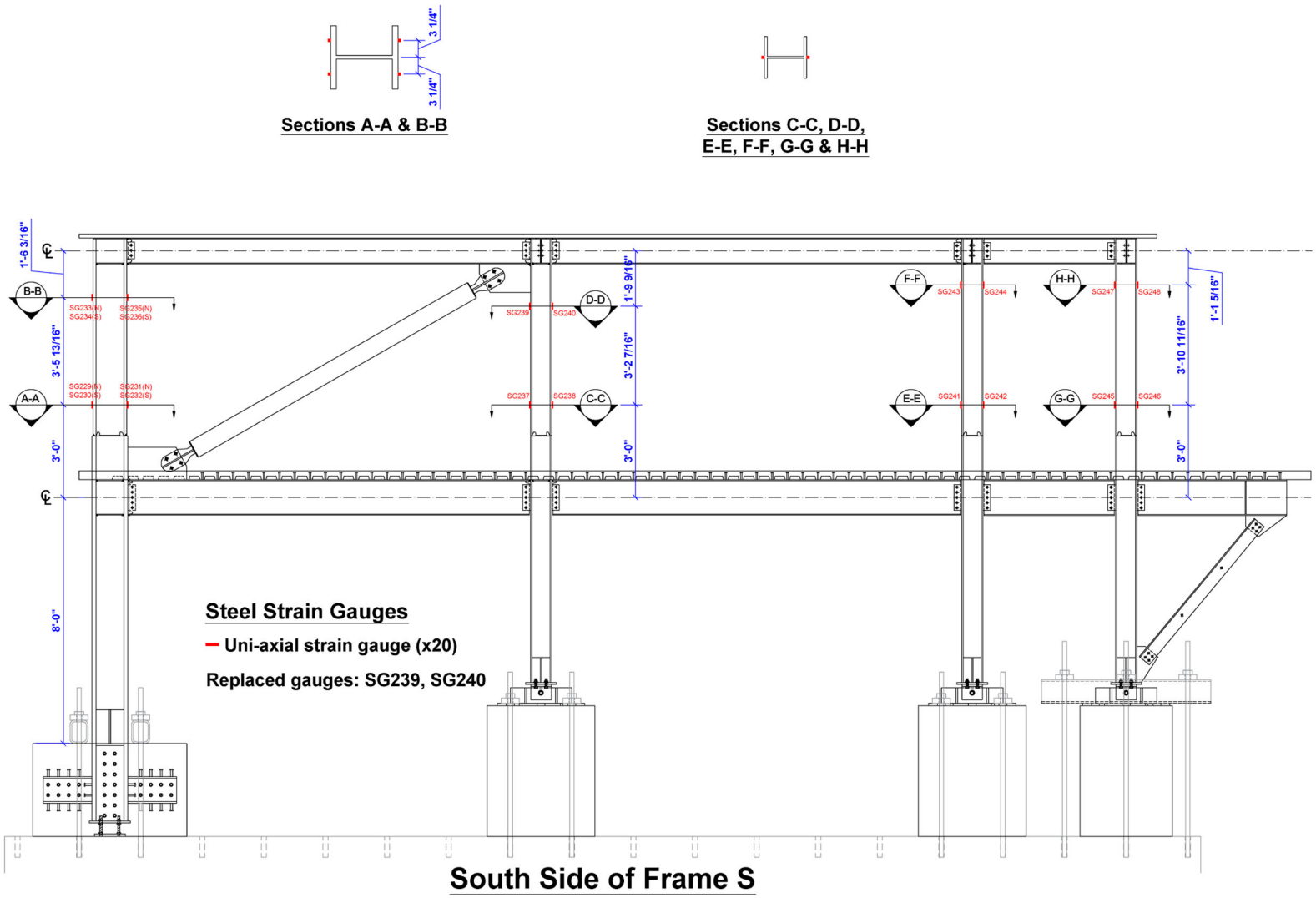

(h) Steel Strain Gauges on Frame S (2nd Story)

Figure 9.8 Instrumentation Plan for Phase 3 Test (continued)

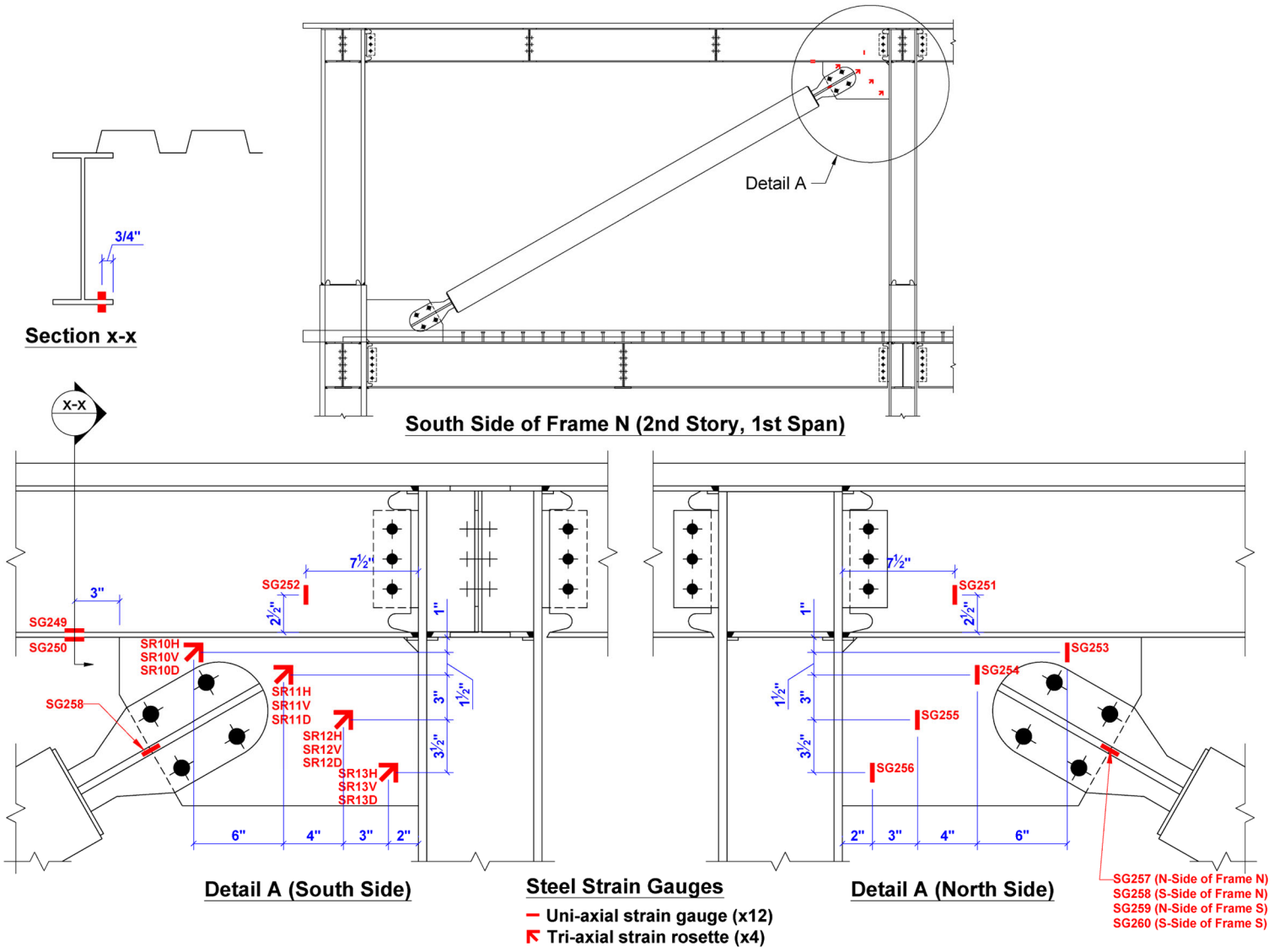

(i) Steel Strain Gauges on BRBs and Top Gusset Plate in Frame S

Figure 9.8 Instrumentation Plan for Phase 3 Test (continued)

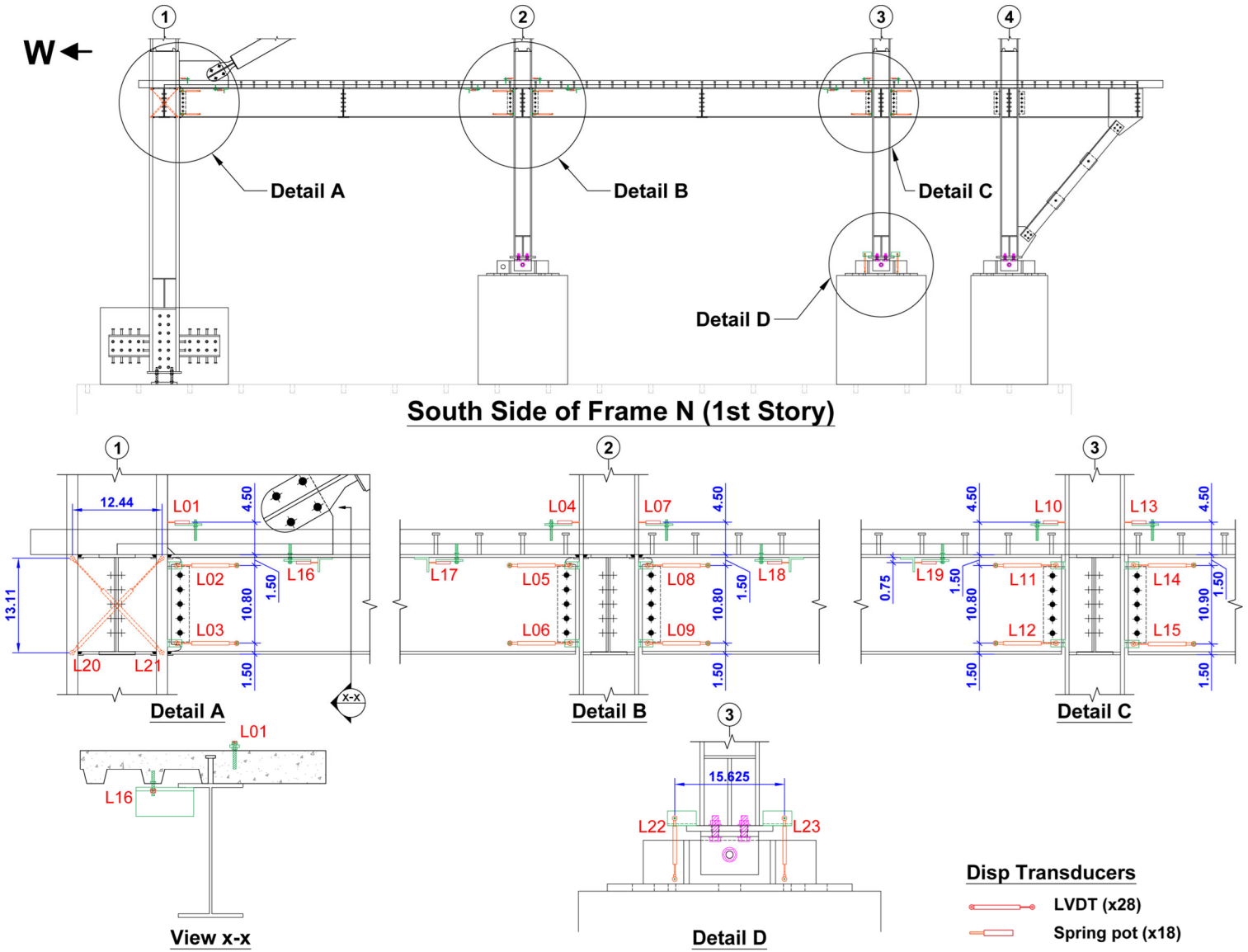

(j) Displacement Transducers on Frame N (1st Story)

Figure 9.8 Instrumentation Plan for Phase 3 Test (continued)

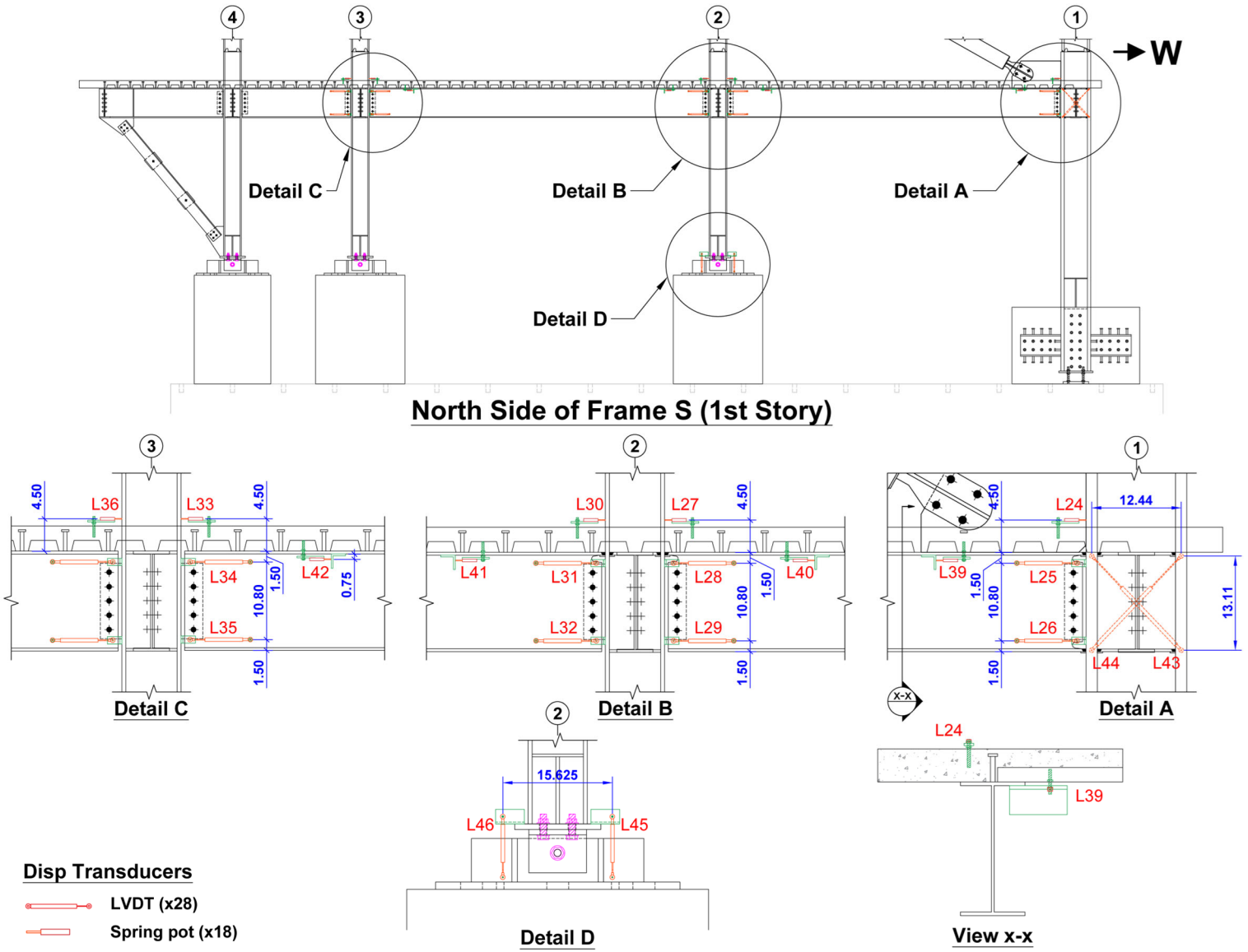

(k) Displacement Transducers on Frame S (1st Story)

Figure 9.8 Instrumentation Plan for Phase 3 Test (continued)

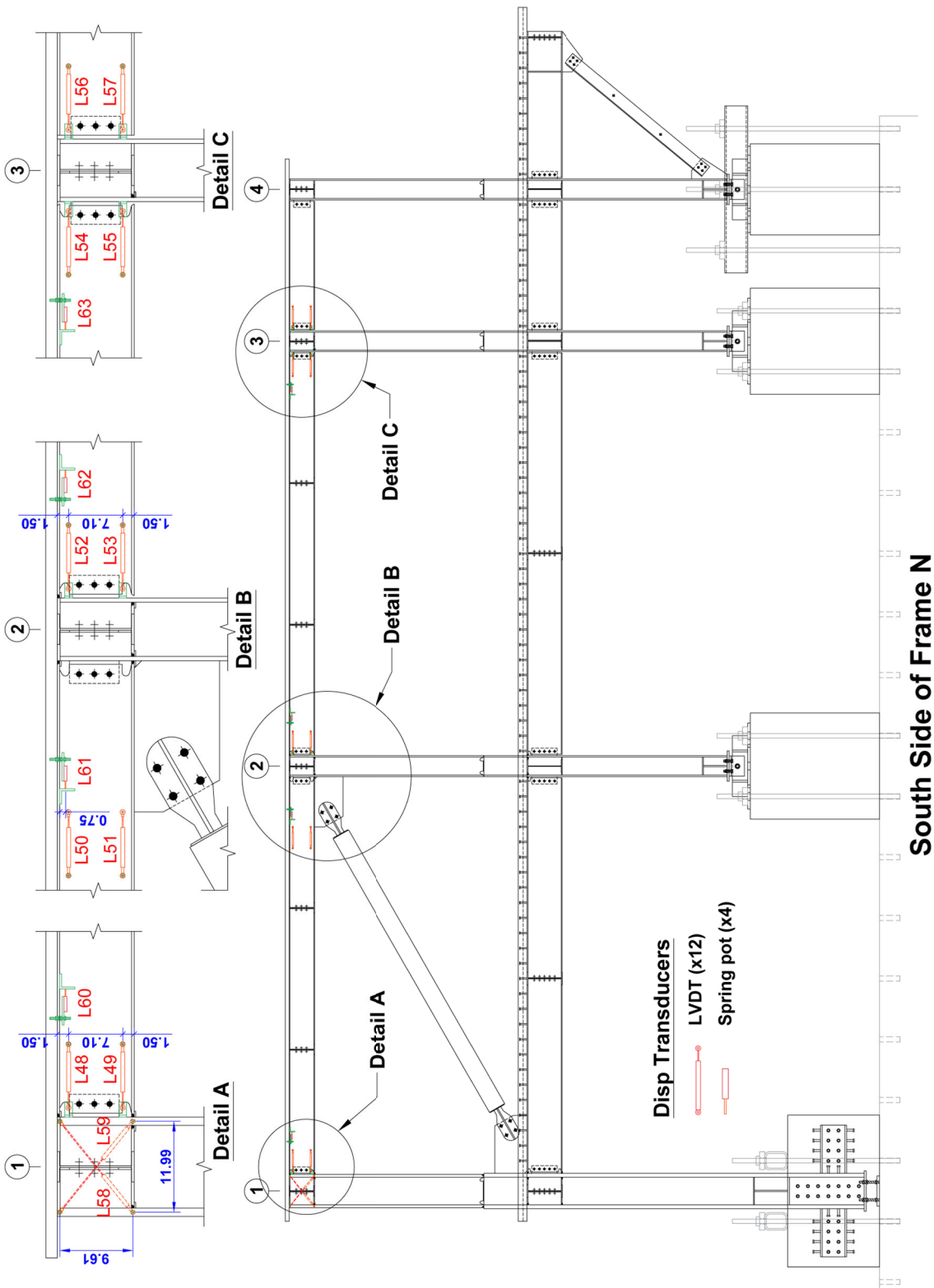

(l) Displacement Transducers in 2nd Story

Figure 9.8 Instrumentation Plan for Phase 3 Test (continued)

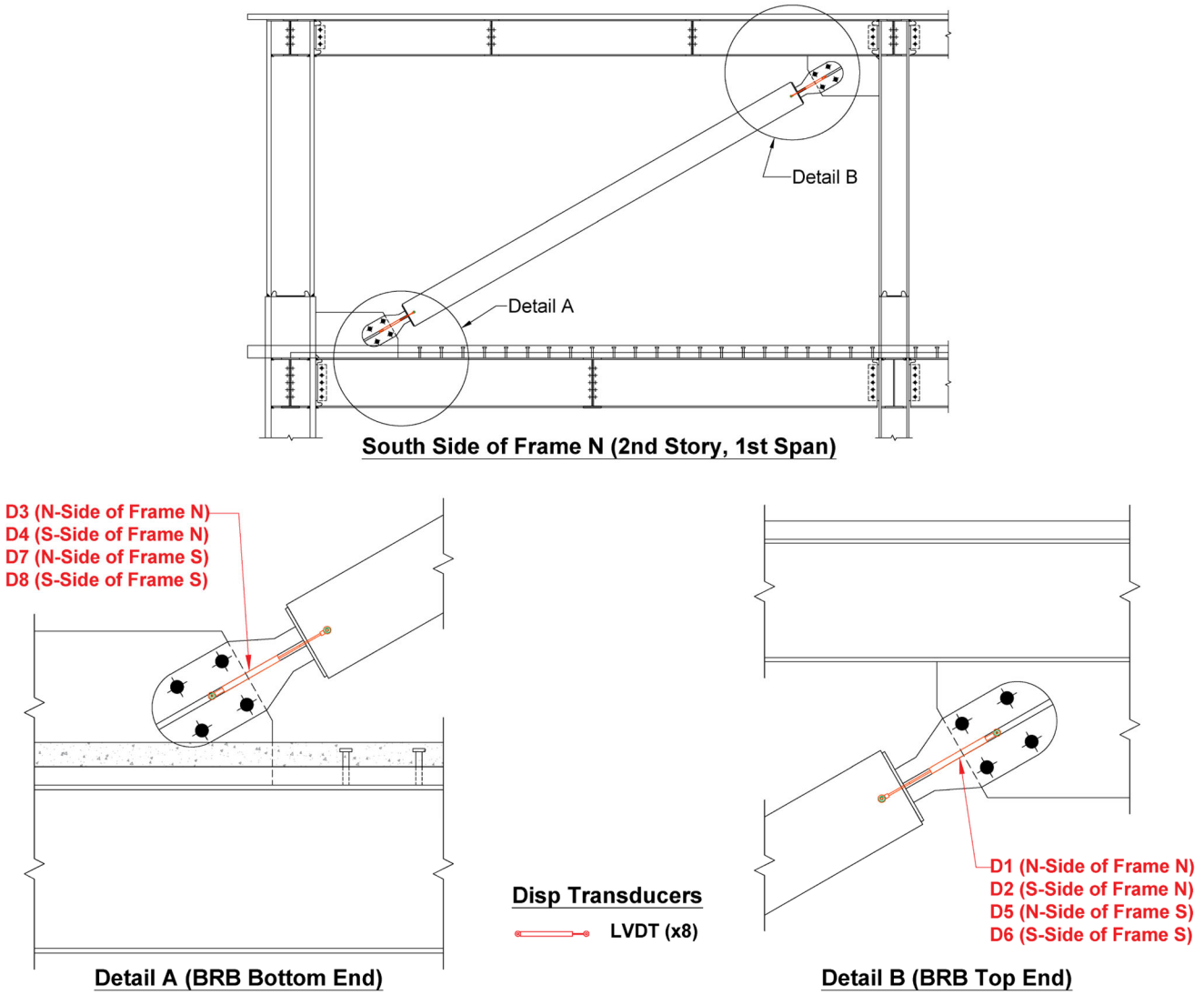

(m) Displacement Transducers on BRBs

Figure 9.8 Instrumentation Plan for Phase 3 Test (continued)

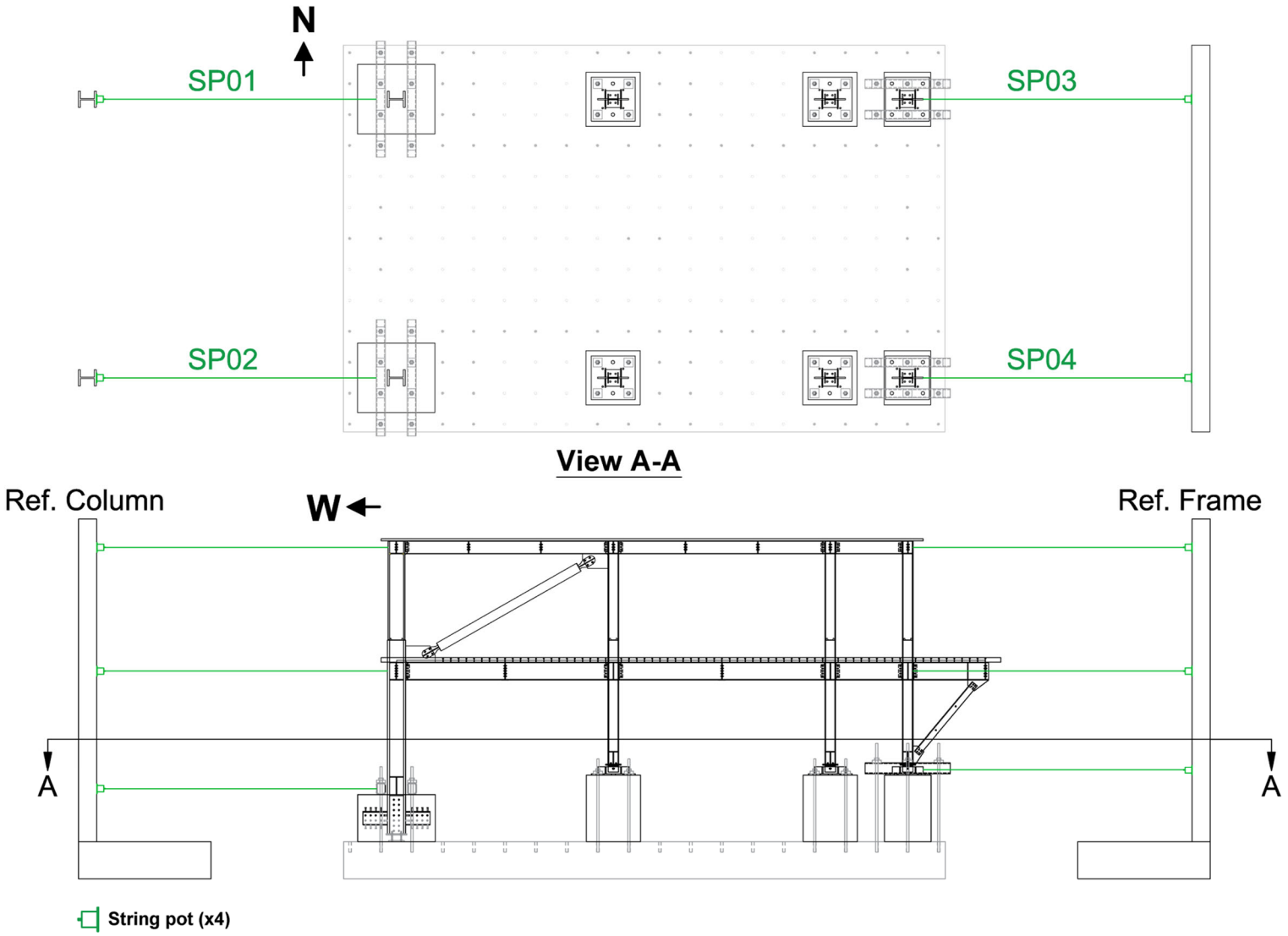

(n) Spring Pots on Footing Level

Figure 9.8 Instrumentation Plan for Phase 3 Test (continued)

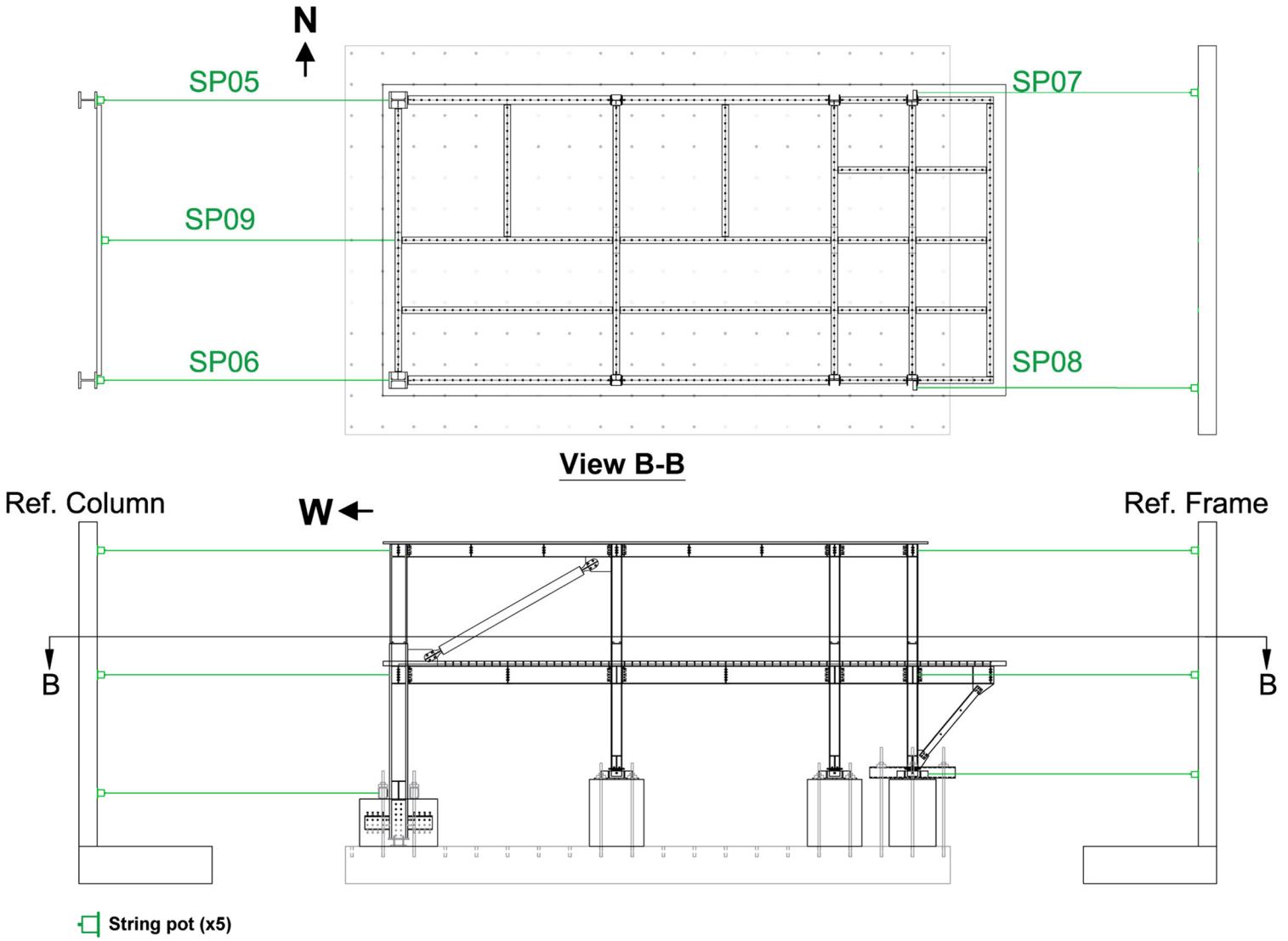

(o) Spring Pots on 2nd Floor Level

Figure 9.8 Instrumentation Plan for Phase 3 Test (continued)

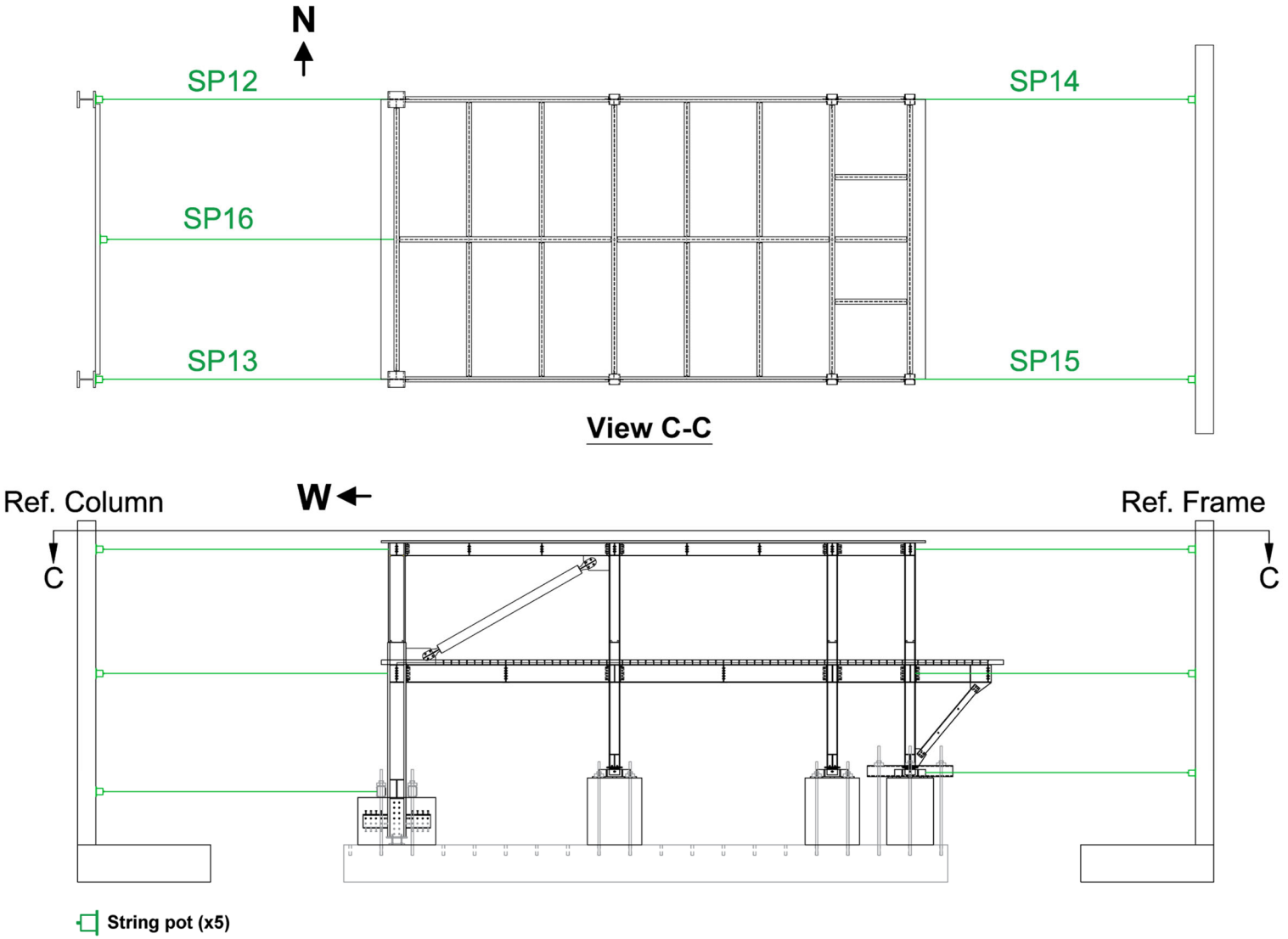

(p) Spring Pots on Roof Level

Figure 9.8 Instrumentation Plan for Phase 3 Test (continued)

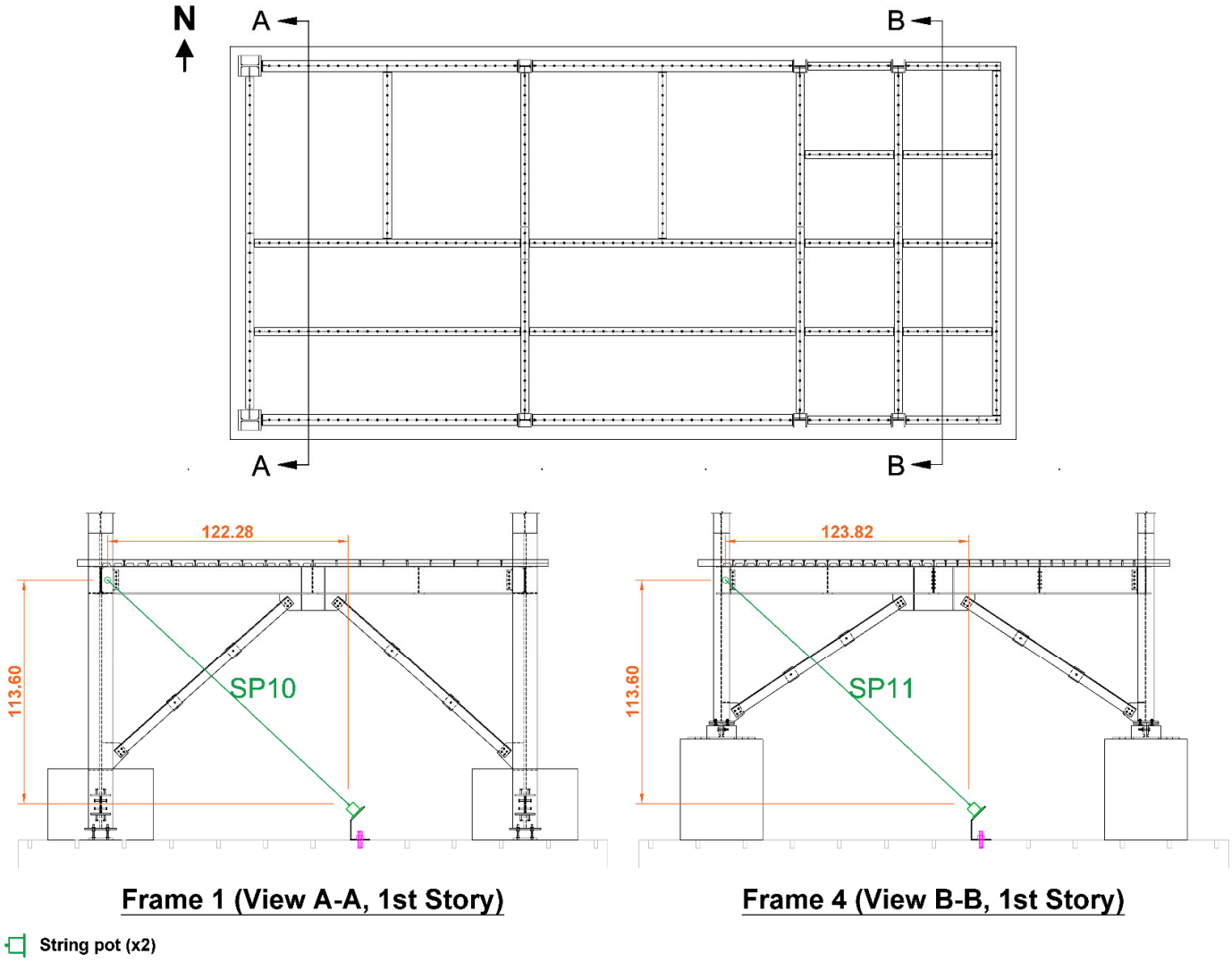

(q) Diagonal String Pots for Measuring Transverse Displacement (1st Story)

Figure 9.8 Instrumentation Plan for Phase 3 Test (continued)

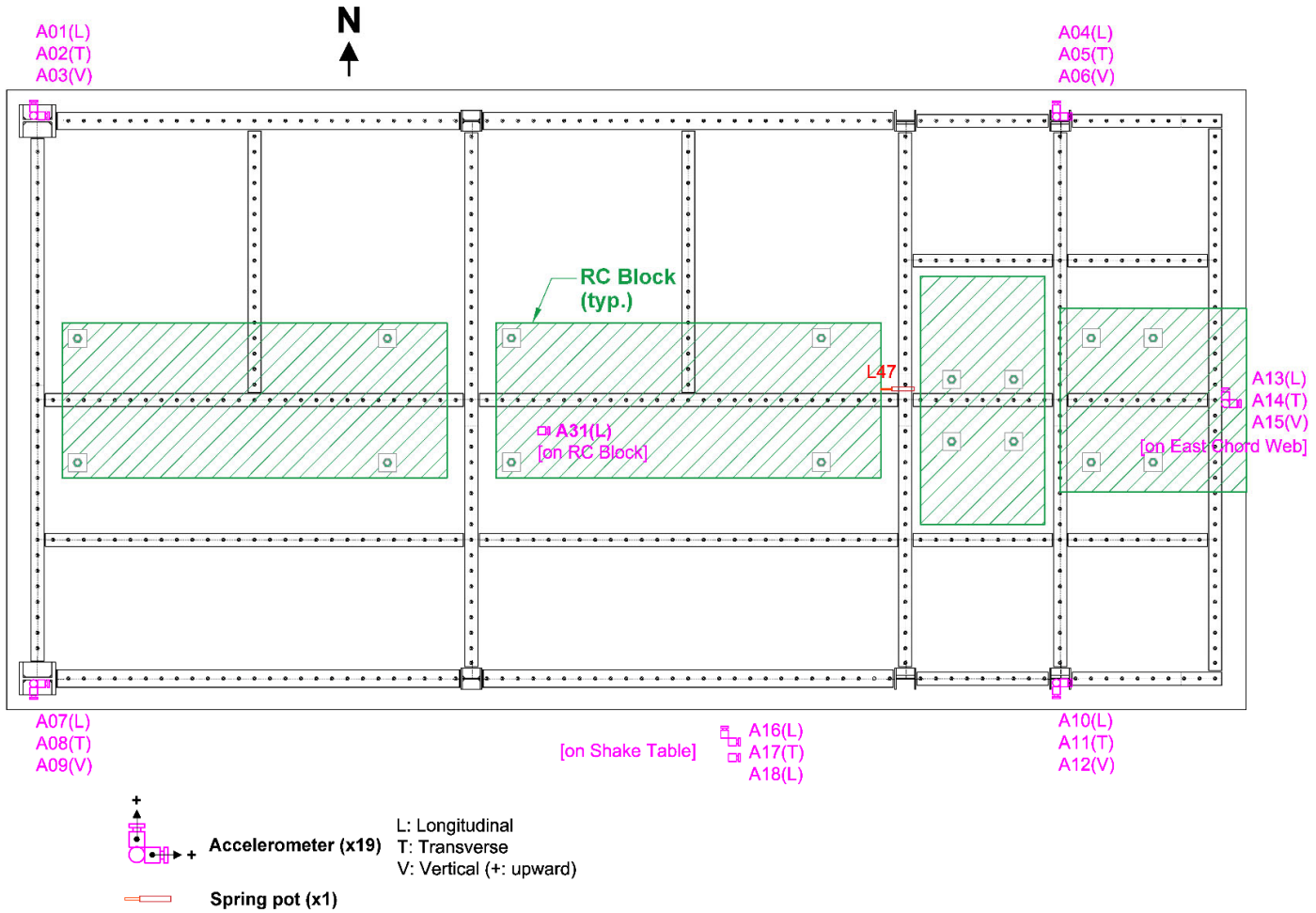

(r) Accelerometers and the Spring Pot for Monitoring Slippage of Added RC Block on 2nd Floor Level

Figure 9.8 Instrumentation Plan for Phase 3 Test (continued)

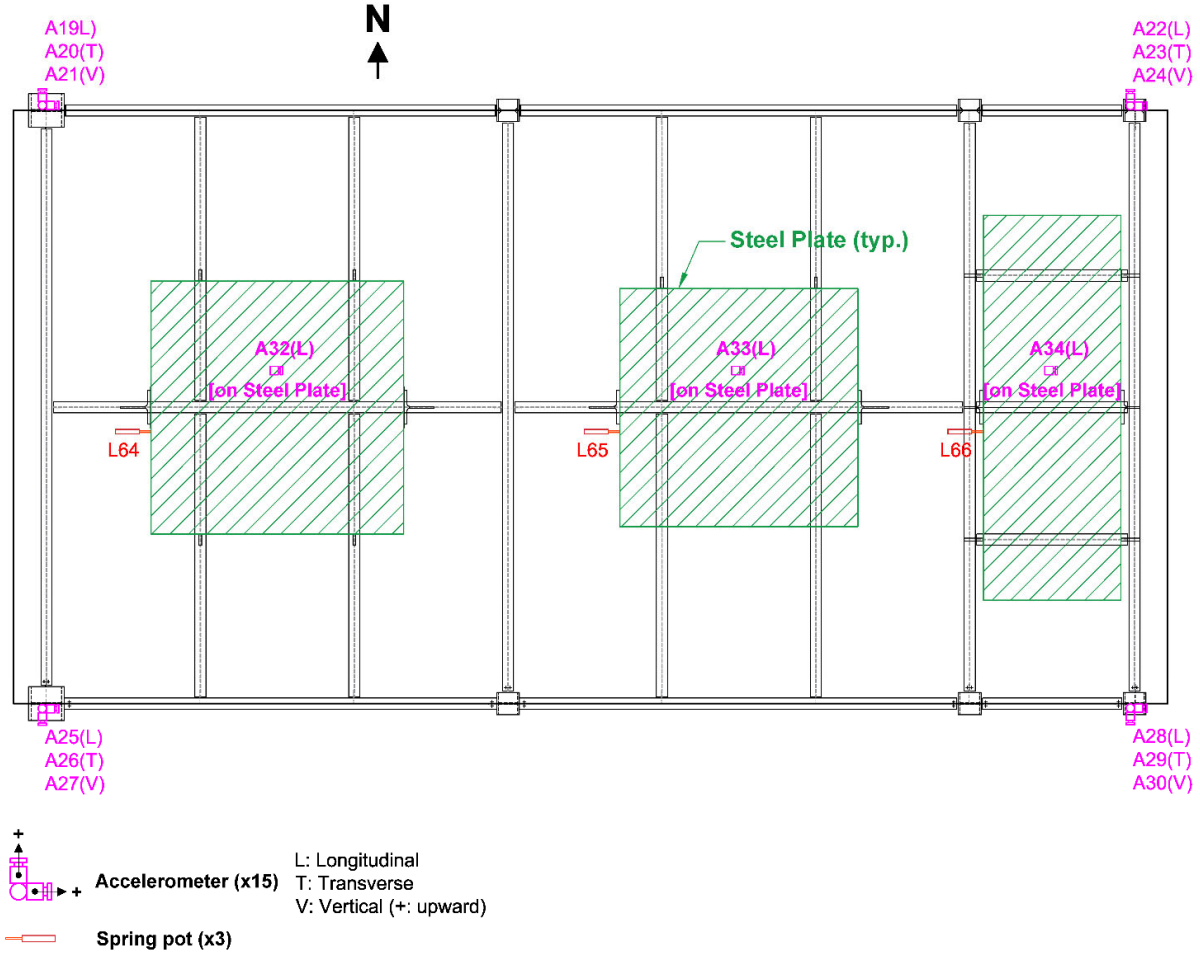

(s) Accelerometers and the Spring Pots for Monitoring Slippage of Added Steel Plates on Roof Level

Figure 9.8 Instrumentation Plan for Phase 3 Test (continued)

9.4 Material Properties

The steel cores and HSS casings were manufactured with ASTM A36 plate and A53 Gr. B steel, respectively. Measured steel properties from the mill reports and tensile coupon tests of the steel core plate materials are summarized in Table 9.1. Based on measured yield stress, F_{ya}, the material overstrength factor, R_y, the actual brace yield force, P_{ya}, and brace deformation at first significant yield, Δ_{by}, are listed in Table 9.2.

The specified concrete compressive strengths, f'_c, for the 2nd floor slab, cantilever column footings, gravity column footings were 4 ksi, 8 ksi, and 5 ksi, respectively. Table 9.3 shows the results of the concrete cylinder tests that were conducted around test days of Phase 3 testing.

Table 9.1 Mechanical Properties of BRB Core Plate

Mill Test Report Average					Tensile Coupon Average				
Heat No.	F_{ya} (ksi)	F_{ua} (ksi)	$\frac{F_{ua}}{F_{ya}}$	Elong.[a] (%)	Plate No.	F_{ya} (ksi)	F_{ua} (ksi)	$\frac{F_{ua}}{F_{ya}}$	Elong.[a] (%)
N19450	42.5	64.0	1.51	30.0 (8")	4751	43.4	63.2	1.46	39.5 (2")

a) Value in parenthesis indicates gage length of sample

Table 9.2 Yield Force and Deformation of BRB

A_{sc} (in.²)	F_{yn} (ksi)	$P_{yn}{}^{a}$ (kips)	$P_{ya}{}^{b}$ (kips)	$R_y{}^{c}$	$\Delta_{by}{}^{d}$ (in.)
0.75	36	27	33	1.20	0.112

a) $P_{yn} = A_{sc}F_{yn}$, where F_{yn} is the nominal yield stress
b) $P_{ya} = A_{sc}F_{ya}$
c) $R_y = F_{ya}/F_{yn}$
d) $\Delta_{by} = P_{ya}L_y/(EA_{sc})$

Table 9.3 Cylinder Test Results of Concrete for Phase 3 Testing

(a) Test Date: 9/18/2019

Component	Age (Days)	f_c' of Each Cylinder (ksi)		Average f_c' (ksi)
2nd Floor Slab	44	#1:	4.593	4.800
		#2:	5.199	
		#3:	4.609	

(b) Test Date: 9/20/2019

Component	Age (Days)	f_c' of Each Cylinder (ksi)		Average f_c' (ksi)
Cantilever Column Footings	84	#1:	8.532	7.838
		#2:	7.145	
2nd Floor Slab	46	#1:	4.854	4.844
		#2:	4.657	
		#3:	5.022	

9.5 Testing Protocol

Table 9.4 shows the test matrix. Phases 3 testing were composed of seven main tests, which were the conventional earthquake simulation tests. The input table motions were generated by scaling a ground motion record (Beverly Hills-Mulhol station) from the 1994 Northridge earthquake to different intensities. The acceleration response of the time-scaled ground motion was scaled to the target intensities by using the $S_a(T_1)$ method (Shome and Cornell 1998). In Phase 3 (see Table 9.4), the seven earthquake simulation tests (designations as Test 3-1 through Test 3-7, respectively) were performed at four intensity levels: 50% Design Earthquake (DE), 100% DE, 150% DE, and 200% DE.

Table 9.4 Phase 3 Test Matrix

Test No.	Description	Test Date
WN 3-0	White Noise Test	9/18/2019
IM 3-0	Impulse Test	9/18/2019
3-1	Earthquake Simulation Test (50% DE, Direct)	9/18/2019
WN 3-1	White Noise Test	9/18/2019
IM3-1	Impulse Test	9/18/2019
3-2	Earthquake Simulation Test (100% DE, Direct)	9/18/2019
WN 3-2	White Noise Test	9/18/2019
IM 3-2	Impulse Test	9/18/2019
3-3	Earthquake Simulation Test (100% DE, Inverted)	9/18/2019
WN 3-3	White Noise Test	9/18/2019
IM 3-3	Impulse Test	9/18/2019
3-4	Earthquake Simulation Test (150% DE, Direct)	9/18/2019
WN 3-4	White Noise Test	9/18/2019
IM 3-4	Impulse Test	9/18/2019
3-5	Earthquake Simulation Test (150% DE, Inverted)	9/19/2019
WN 3-5	White Noise Test	9/19/2019
IM 3-5	Impulse Test	9/19/2019
3-6	Earthquake Simulation Test (200% DE, Direct)	9/19/2019
WN 3-6	White Noise Test	9/19/2019
IM 3-6	Impulse Test	9/19/2019
3-7	Earthquake Simulation Test (200% DE, Inverted)	9/19/2019
WN 3-7	White Noise Test	9/19/2019
IM 3-7	Impulse Test	9/19/2019

9.6 Data Reduction

Most of the data reduction approaches that had been used in Phase 2 testing were used in Phase 3 testing. This section described the changes made and the newly added items for the data reduction.

9.6.1 BRB Responses

The BRB deformation, Δ_b, was determined from the sum of the measured displacements at both brace ends [see Figure 9.8(m)], which were the average of those measured by a pair of LVDT displacement transducers at each brace end. The brace axial core strain was calculated per Eq. (9.1).

$$\varepsilon = \frac{\Delta_b}{L_y} \tag{9.1}$$

where L_y equals the length of the steel core plate in the yielding zone as shown in Table 9.2. The brace axial deformation is also normalized by the yield deformation. Note that Δ_b includes some minor elastic deformation outside the yielding length, L_y. See Appendix E for the details of the axial force determination for the shake table tests.

9.6.2 Story Shear Calculation

Two methods were used to derive the story shear from the instrumentation. The first estimation of story shear was made by using the accelerometer data. The associated data reduction approach used in Phase 2 testing were used for Phase 3 testing. See Eqs. (6.6) and (6.7) for the determinations of the 2nd-story shear (V_{a2}) and 1st-story shear (V_{a1}), respectively, by using the accelerometer data.

The second method of calculating the base shear was to sum up the measured story shear taken by columns and diagonal braces in the longitudinal frames. The time history of the 1st story shear (i.e., base shear) taken by Frame N, $V_{b1N}(t)$, was calculated as:

$$V_{b1N}(t) = \sum_{i=1}^{4} V_{c1Ni}\,(t) + P_{brN}(t) \cdot \sin\theta_{br} \tag{9.2}$$

where V_{c1N1} through V_{c1N4} represent the measured column shear forces for the 1st-story Columns N1 to N4, respectively. P_{brN} is the experimentally determined axial force of the 1st-story north diagonal brace, and θ_{br} is the inclination angle between the brace and the vertical. Likewise, the time history of the 1st story shear taken by Frame S, $V_{bS}(t)$, was computed as:

$$V_{b1S}(t) = \sum_{i=1}^{4} V_{c1Si}\,(t) + P_{brS}(t) \cdot \sin\theta_{br} \tag{9.3}$$

where V_{c1S1} to V_{c1S4} represent the measured column shear forces for the 1st-story Columns S1 to S4, respectively. P_{brS} is the measured axial force of the south brace. Then, the total base shear, $V_b(t)$, was determined by summing up the story shears taken by Frames N and S:

$$V_{b1}(t) = V_{b1N}(t) + V_{b1S}(t) \tag{9.4}$$

Similarly, the 2nd story shears taken by Frames N and S, V_{b2N} and V_{b2S},was calculated similarly:

$$V_{b2N}(t) = \sum_{i=1}^{4} V_{c2Ni}\,(t) + P_{BRBN}(t) \cdot \sin(\theta_{BRB}) \tag{9.5}$$

$$V_{b2S}(t) = \sum_{i=1}^{4} V_{c2Si}\,(t) + P_{BRBS}(t) \cdot \sin(\theta_{BRB}) \tag{9.6}$$

where V_{c2N1} through V_{c2N4} represent the measured column shear forces for 2nd-story Columns N1 to N4, respectively. V_{c2S1} through V_{c2S4} are for the measured 2nd column shear forces in Frame S. P_{BRBN} and P_{BRBS} is the measured axial forces of north and south BRBs, respectively. θ_{BRB} is the angle between the BRB and the vertical. The total 2nd-story shear $V_{b2}(t)$, was computed as:

$$V_{b2}(t) = V_{b2N}(t) + V_{b2S}(t) \tag{9.7}$$

9.7 Test Results

9.7.1 Overview of Phase 3 Test Results

Dynamic characterization tests, including white noise or impulse testing, were performed before and after each of the seven earthquake simulation tests to monitor the dynamic properties of the specimen. Figure 9.9 shows the variations of the measured first-mode frequency and damping ratio. Table 9.5 summarizes the results of dynamic characterization testing. As shown in Table 9.6, Fourier spectra of the 2nd floor acceleration from the white noise tests were plotted to determine the vibration frequencies. In addition, the 2nd floor acceleration time histories from impulse testing were plotted as shown in Figure 9.11. The associated experimentally determined first-mode period and damping ratio, ξ, are denoted in Figure 9.11 as well.

As shown in Figure 9.9(a) and Table 9.5, the fundamental frequency remained approximately constant with a slight decay from Tests 3-1 through 3-6. The fundamental frequency dropped drastically because the side lap connections of roof metal deck diaphragm were fractured during Test 3-7. The impulse test results showed that the 1st mode frequency (f_1) slightly decreased from 4.80 Hz to 4.45 Hz from Test 3-1 through Test 3-6. After Test 3-7, f_1 dropped to 1.56 Hz. The 2nd mode frequency (f_2), which is related with the vertical vibration of the cantilever slab, was 13.73 Hz before Phase 3 testing and was decreased slightly to 12.61 Hz after Test 3-6. After Test 3-7, f_2 decreased to 6.06 Hz. In addition, the measured damping ratio varied from 4.22% to 5.46% with an average value of 4.69% from Tests 3-1 through 3-6. Figure 9.9(b) shows that the variation of damping ratio is not significant from Tests 3-1 through 3-6.

Figure 9.12 through Figure 9.17 show the specimen global responses for the seven main tests. Figure 9.12 shows the input table accelerations and the associated response spectra. Table 9.6 tabulates the peak responses of the floor accelerations and story drifts. Figure 9.14 shows the

time histories of the roof and 2nd floor accelerations. In Phase 3 testing, the reached positive and negative peak roof accelerations were +3.42 g and −2.93 g, respectively. The peak positive and negative reached 2nd floor accelerations were +2.01 g and −2.56 g, respectively. The reached positive and negative peak 2nd-story drift angles were 1.19% and −1.16 % rad, respectively. The peak positive and negative 1st-story drift angles reached 1.49% and −1.34 % rad, respectively Figure 9.16 shows the time histories of story shears. Figure 9.17 shows the story hysteresis responses of seven main tests. The test building exhibited moderate inelastic behavior from Tests 3-4 through 3-7. Some side lap connections of roof deck fractured in Test 3-7. After that, the roof deck diagram lost its function to transfer the inertial force. Instead, the inertial forces were transmitted to the LFRS through the roof floor beams. Thus, transverse roof beams (running in north-south direction) were subjected to substantial minor-axis flexural forces (bending moments and shears), resulting in yielding and excessive deflection of these roof beams. As the roof deck diaphragm had been damaged, Phase 3 testing was concluded after the last white noise and impulse tests following Test 3-7.

9.7.2 Specimen Condition after Phase 3 Testing

After Phase 3 testing, noticeable damages of the test building included the damage of the roof diaphragm and excessive residual deformations in roof beams. Figure 9.18 shows the top view of the damaged roof deck diaphragm. The roof diaphragm was composed of six rows of deck panels (denoted as Panel Rows 1 through 6 in Figure 9.18) oriented parallel to the longitudinal direction of the building. Button punch side lap connections at a spacing of 4 in. were used to connect the deck panels together. As shown in Figure 9.18, there were five rows of side lap connections (denoted as Sidelap Conn. 1 through 5) on the diaphragm. During Test 3-7, the entire rows of side lap connections along the two exterior side lap lines (Sidelap Conn. 1 and 5) were

fractured. The fracture of the button punch side lap connections resulted in the separation of the female and male plies at the side lap connections and the friction between the male and female plies. The horizontal relative motion of the crimped (male) and female plies caused the opening-up in the female ply. The vertical relative motion between the male and female plies caused the male ply to hit the female ply. The impact of the hitting fractured the arc spot welds (see Figure 9.18) neighboring the damaged side lap connection lines (Sidelap Conn. 1 and 5). See Figure 9.19 for the fractured side lap connections. Figure 9.20 shows the damaged arc spot welds. Figure 9.21 through Figure 9.24 show the excessive residual deformations in the roof chords and roof beams.

9.8 Parallel Research After Phase 3 Testing

After Phase 3 tests, the two BRBs were removed from the test building and stored with another pair of un-tested identical braces for about seven and half months to allow the first two braces to strain age. Component testing of these four isolated braces to failure was then performed by using the Caltrans Seismic Response Modification Device (SRMD) Testing Facility to investigate the strain aging effect on the seismic responses of BRBs. All braces were subjected to a three-stage testing program including simulated earthquake and cyclic loading tests. Test results showed that strain aging would markedly elevate the yield strength of the brace. However, the magnitude of isotropic hardening in the strain-aged braces was less than that in the non-aged braces resulting in nearly identical strain hardened strengths. Test results also indicated that strain aging tends to reduce the low-cycle fatigue life of BRBs. See reference (Li and Uang, 2020) for the details of the parallel study.

Table 9.5 Phase 3 Impulse and White Noise Test Results

Test Timing	Impulse Test				White Noise Test						
	Test No.	Fundamental Properties			Test No.	1st Mode		2nd Mode		3rd Mode	
		f_1 (Hz)	T_1 (sec)	ξ (%)		f_1 (Hz)	T_1 (sec)	f_2 (Hz)	T_2 (sec)	f_3 (Hz)	T_3 (sec)
Before Test 3-1	IM 3-0	4.80	0.208	4.69	WN 3-0	4.85	0.206	13.73	0.073	16.0	0.0625
After Test 3-1	IM 3-1	4.68	0.214	4.78	WN 3-1	4.55	0.220	13.05	0.077	16.0	0.0625
After Test 3-2	IM 3-2	4.68	0.214	4.30	WN 3-2	4.55	0.220	13.05	0.077	16.0	0.0625
After Test 3-3	IM 3-3	4.67	0.214	4.22	WN 3-3	4.55	0.220	13.25	0.075	16.0	0.0625
After Test 3-4	IM 3-4	4.76	0.210	4.75	WN 3-4	4.55	0.220	12.70	0.079	16.0	0.0625
After Test 3-5	IM 3-5	4.49	0.223	4.62	WN 3-5	4.55	0.220	13.05	0.077	16.0	0.0625
After Test 3-6	IM 3-6	4.45	0.225	5.46	WN 3-6	4.44	0.225	12.61	0.079	16.0	0.0625
After Test 3-7	IM 3-7	1.51	0.662	21.99	WN 3-7	1.56	0.643	6.06	0.165	10.6	0.0942

Table 9.6 Peak Response Quantities for Phase 3 Tests

Test No.	Floor Acceleration (g)				Story Drift Angle (% rad)			
	2nd Floor		Roof		1st Story		2nd Story	
	Positive	Negative	Positive	Negative	Positive	Negative	Positive	Negative
Test 3-1	0.41	-0.33	0.64	-0.48	0.19	-0.23	0.08	-0.13
Test 3-2	0.94	-0.63	1.38	-0.84	0.40	-0.51	0.14	-0.35
Test 3-3	0.62	-0.95	0.87	-1.36	0.56	-0.33	0.35	-0.15
Test 3-4	1.40	-1.02	2.36	-1.41	0.55	-0.86	0.33	-0.73
Test 3-5	0.94	-1.44	1.35	-2.40	0.99	-0.52	0.77	-0.32
Test 3-6	2.01	-1.49	3.42	-2.40	1.02	-1.34	0.78	-1.16
Test 3-7	1.85	-2.56	2.69	-2.93	1.49	-1.31	1.19	-1.04

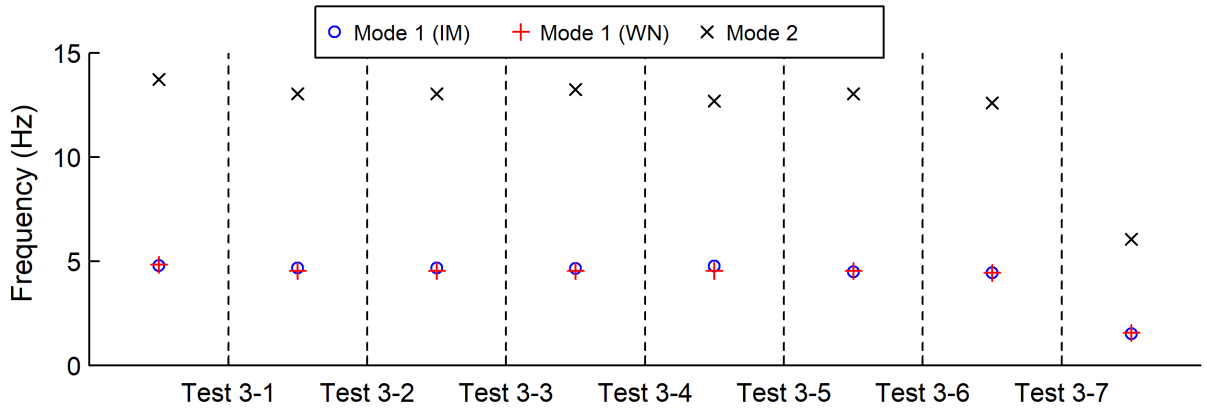

(a)

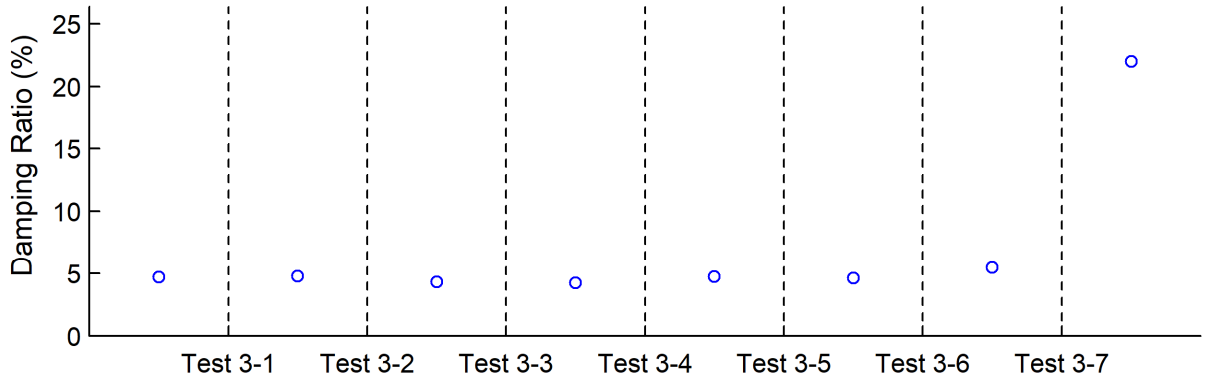

(b)

Figure 9.9 Variations of Measured (a) frequencies for 1st and 2nd Modes and (b) Damping Ratio in Phase 3 Testing

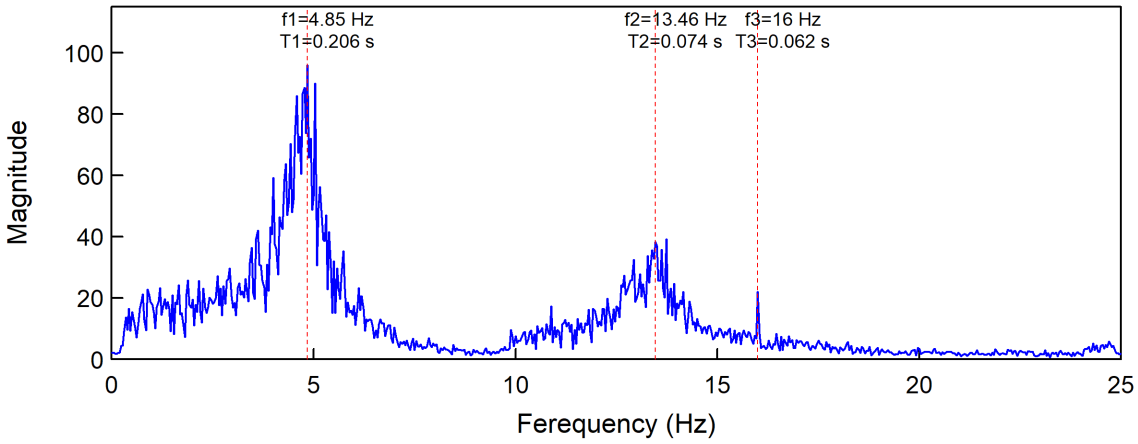

(a) Test WN 3-0

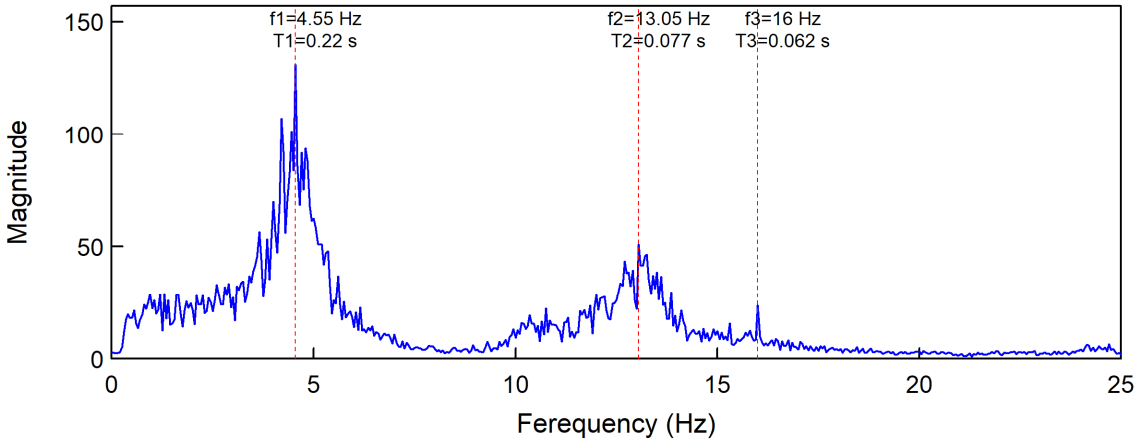

(b) Test WN 3-1

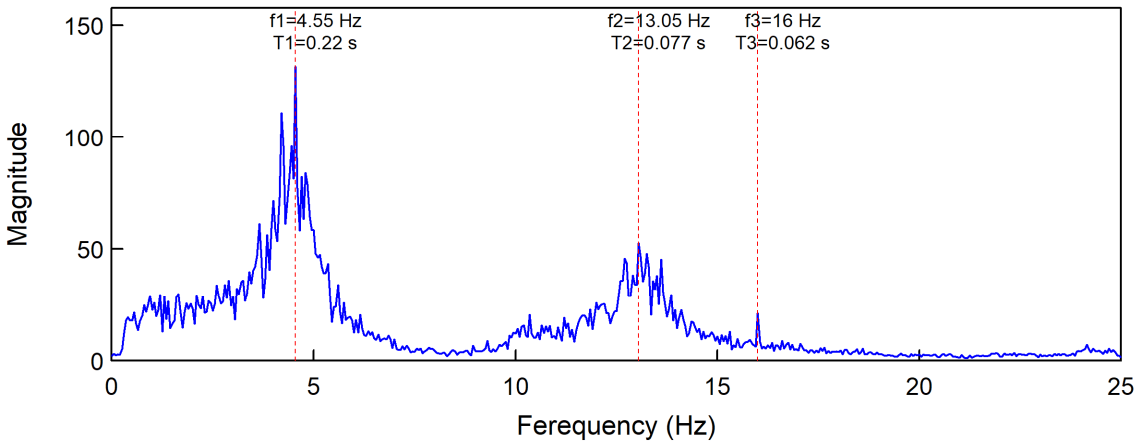

(c) Test WN 3-2

Figure 9.10 Phase 3 White Noise Test Results

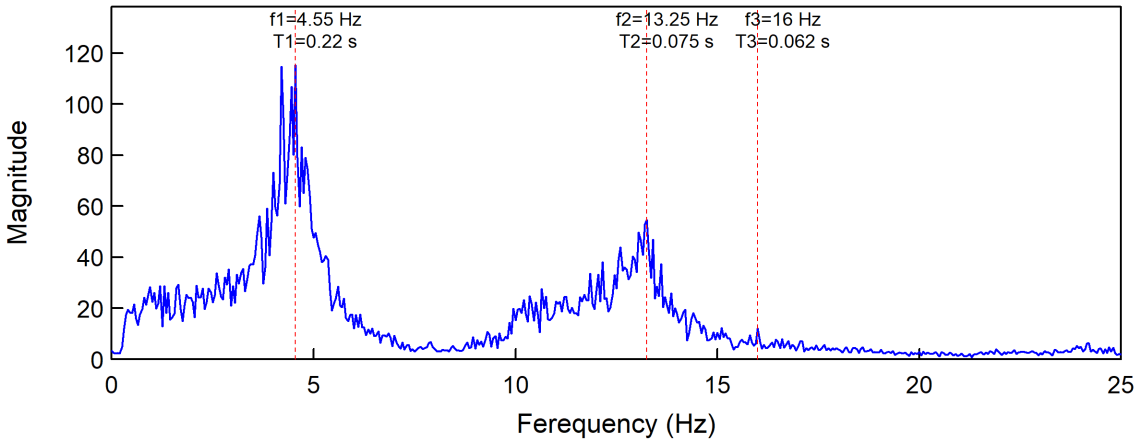

(d) Test WN 3-3

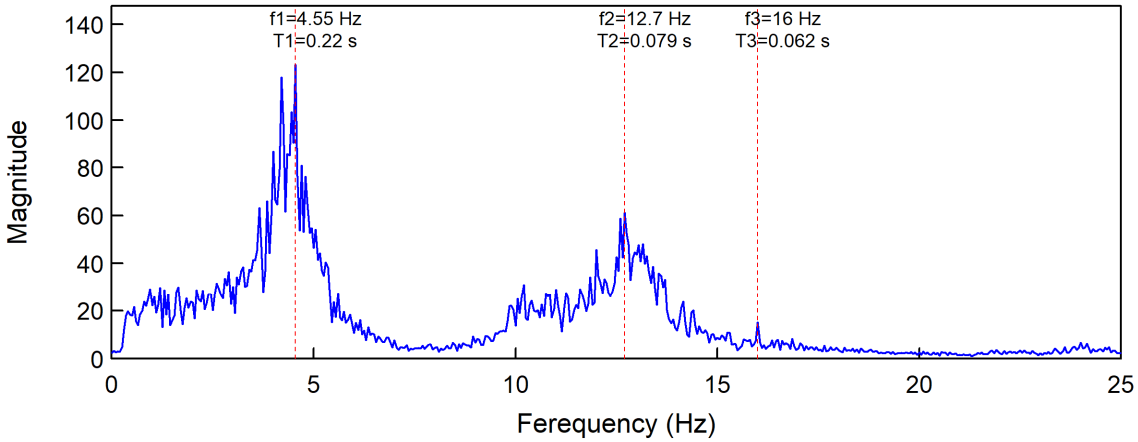

(e) Test WN 3-4

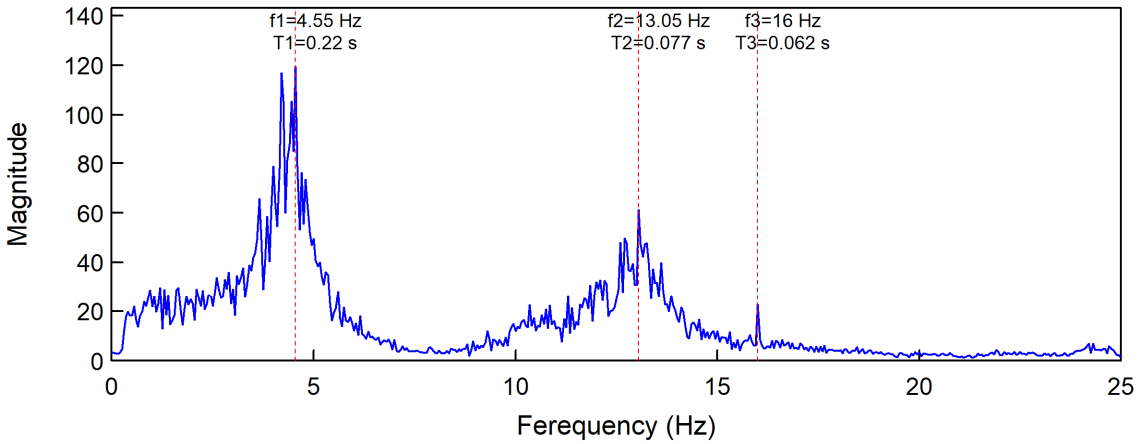

(f) Test WN 3-5

Figure 9.10 Phase 3 White Noise Test Results (continued)

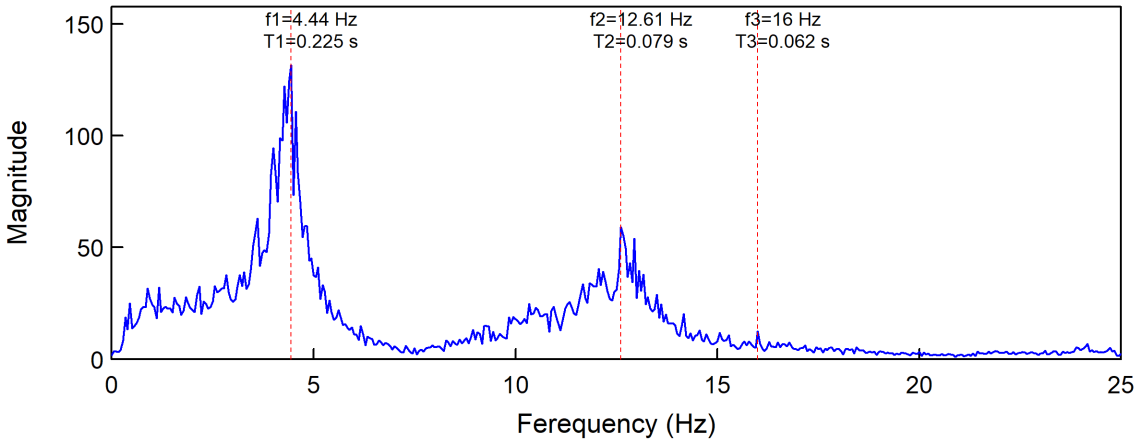

(e) Test WN 3-6

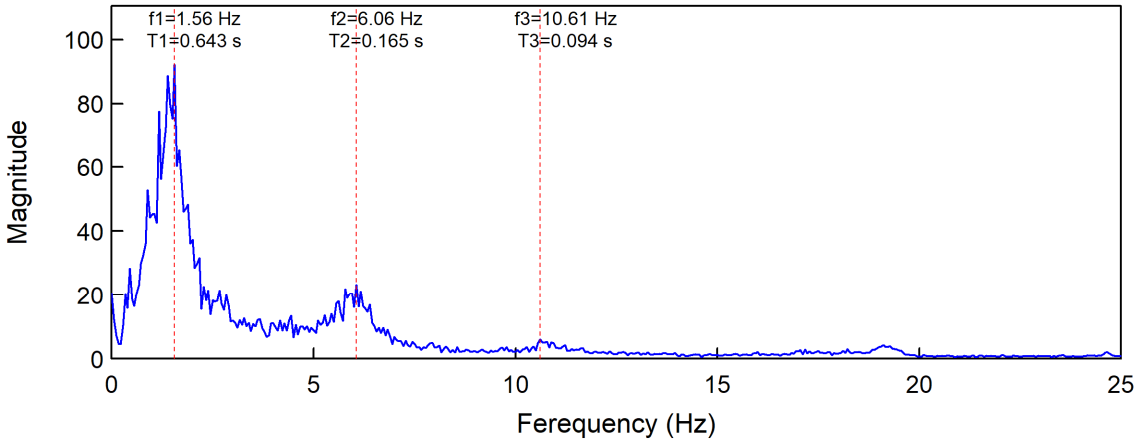

(f) Test WN 3-7

Figure 9.10 Phase 3 White Noise Test Results (continued)

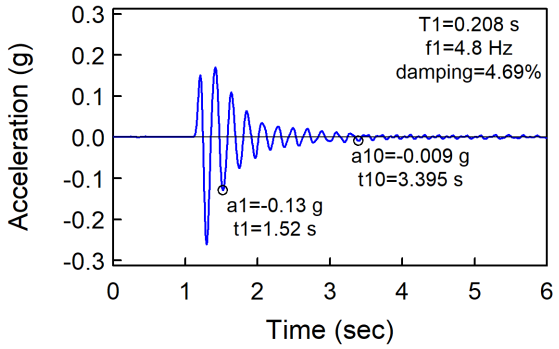

(a) Test IM 3-0

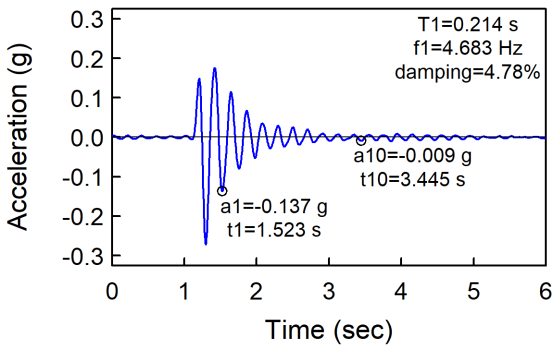

(b) Test IM 3-1

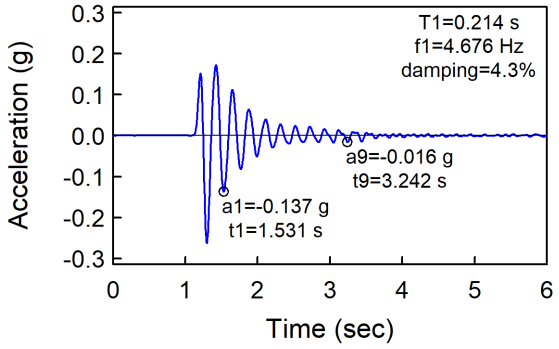

(c) Test IM 3-2

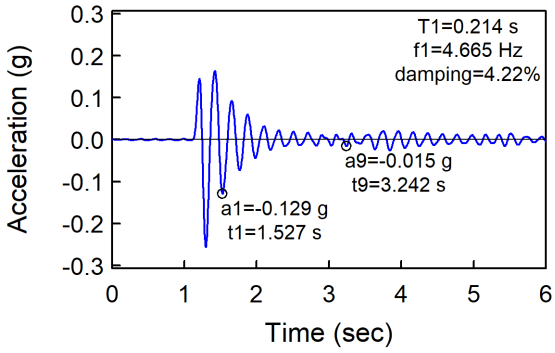

(d) Test IM 3-3

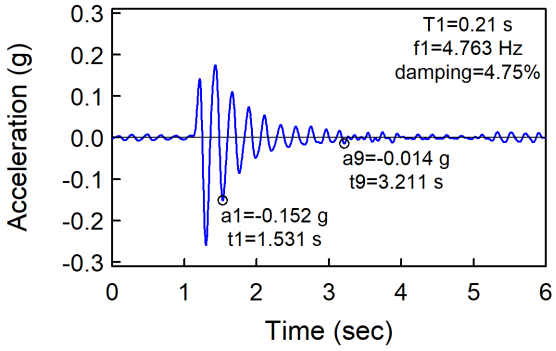

(e) Test IM 3-4

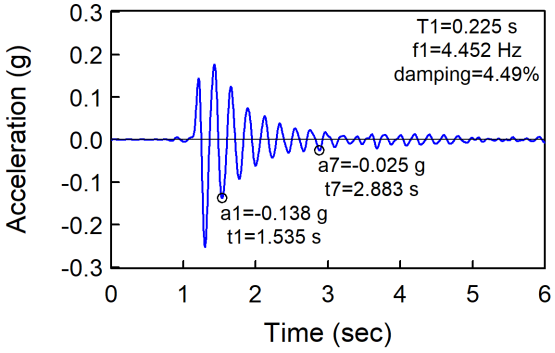

(f) Test IM 3-5

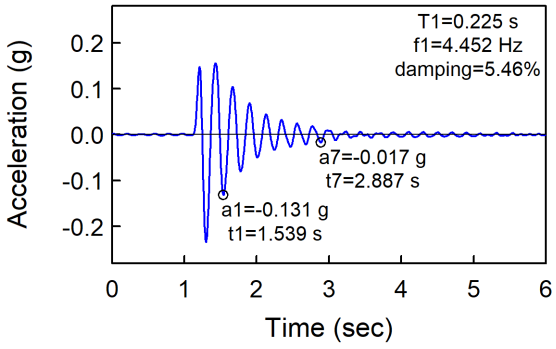

(g) Test IM 3-6

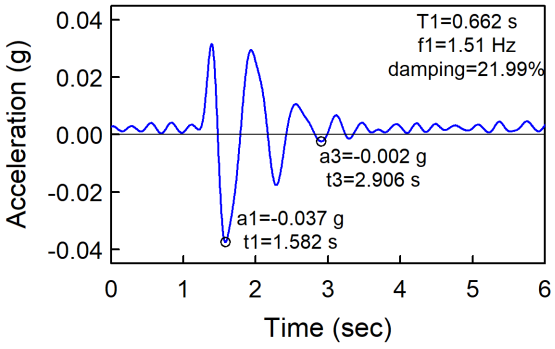

(h) Test IM 3-7

Figure 9.11 Phase 3 Impulse Test Results

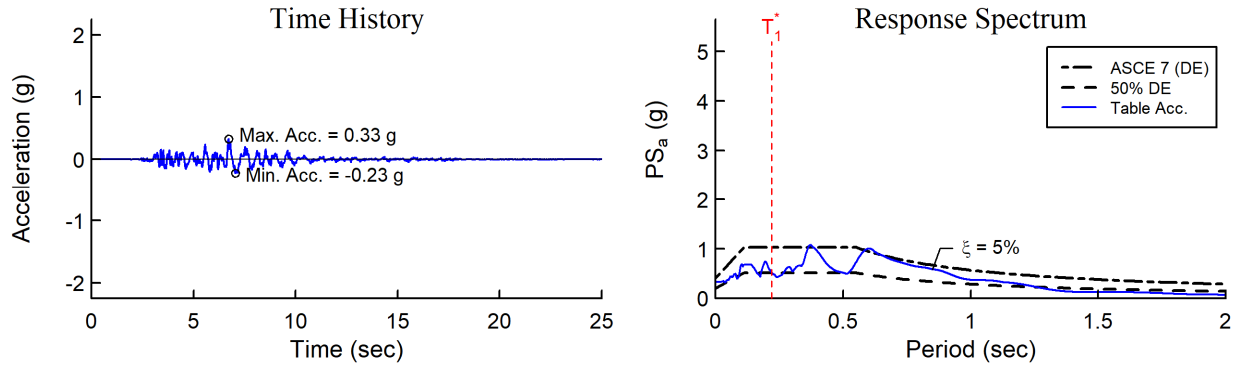

(a) Test 3-1 (Target Intensity: 50% DE)

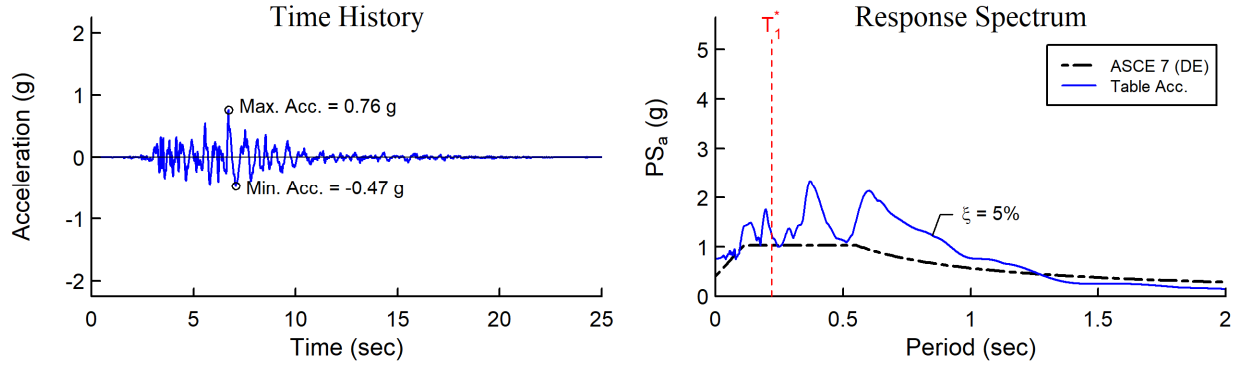

(b) Test 3-2 (Target Intensity: 100% DE)

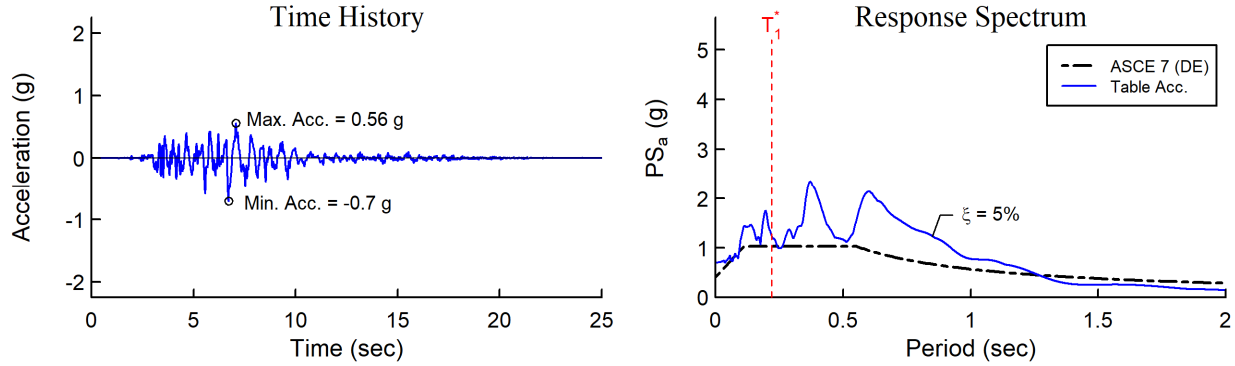

(c) Test 3-3 (Target Intensity: 100% DE)

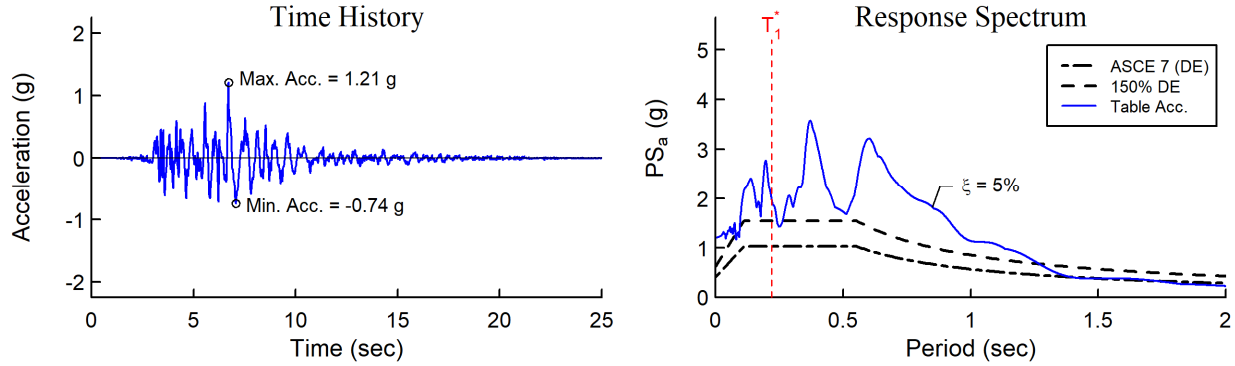

(d) Test 3-4 (Target Intensity: 150% DE)

Figure 9.12 Measured Table Accelerations and Response Spectra for Phase 3 Tests

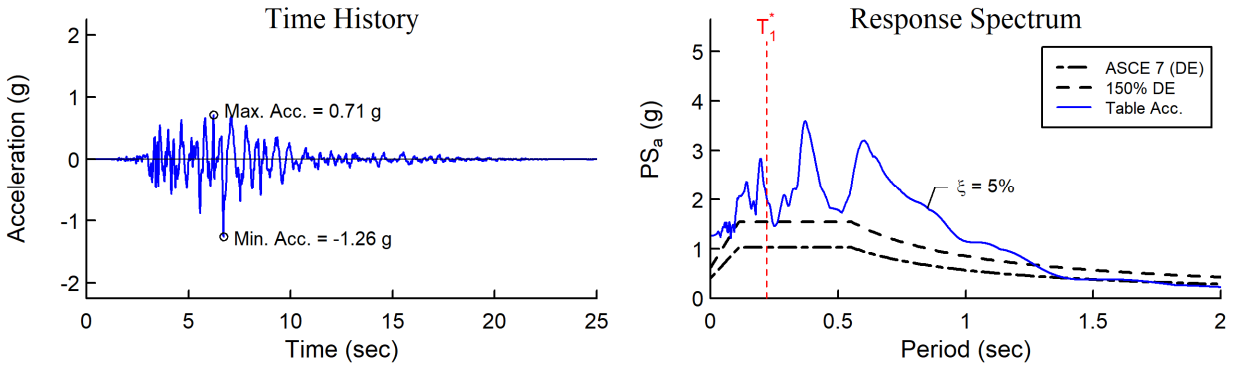

(e) Test 3-5 (Target Intensity: 150% DE;)

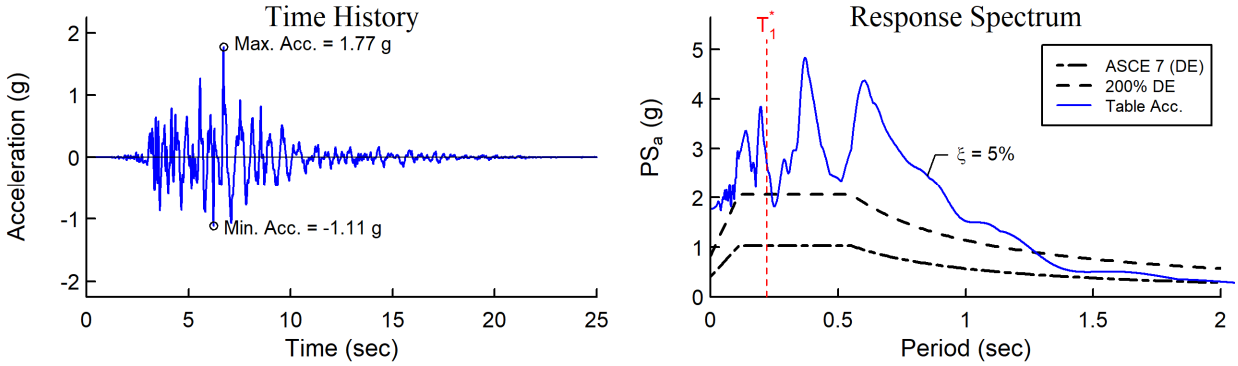

(f) Test 3-6 (Target Intensity: 200% DE)

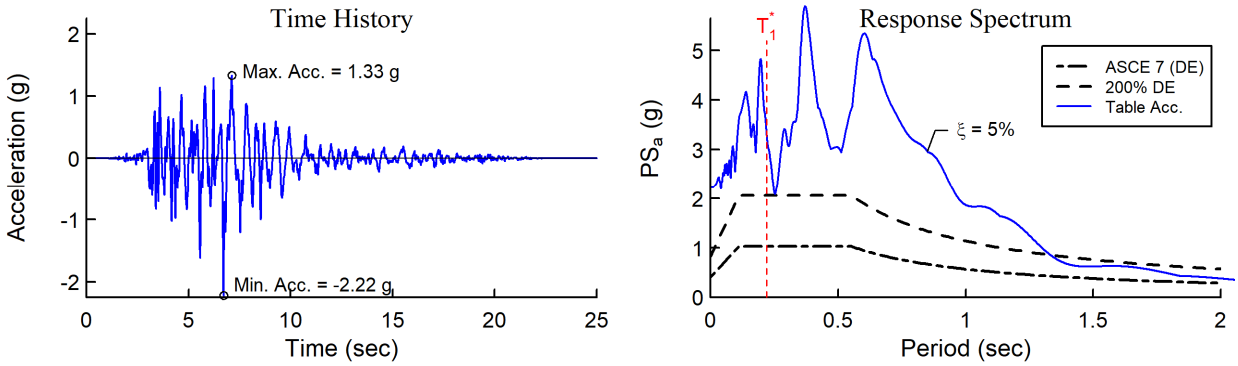

(g) Test 3-7 (Target Intensity: 200% DE)

Figure 9.12 Measured Table Accelerations and Response Spectra for Phase 3 Tests (continued)

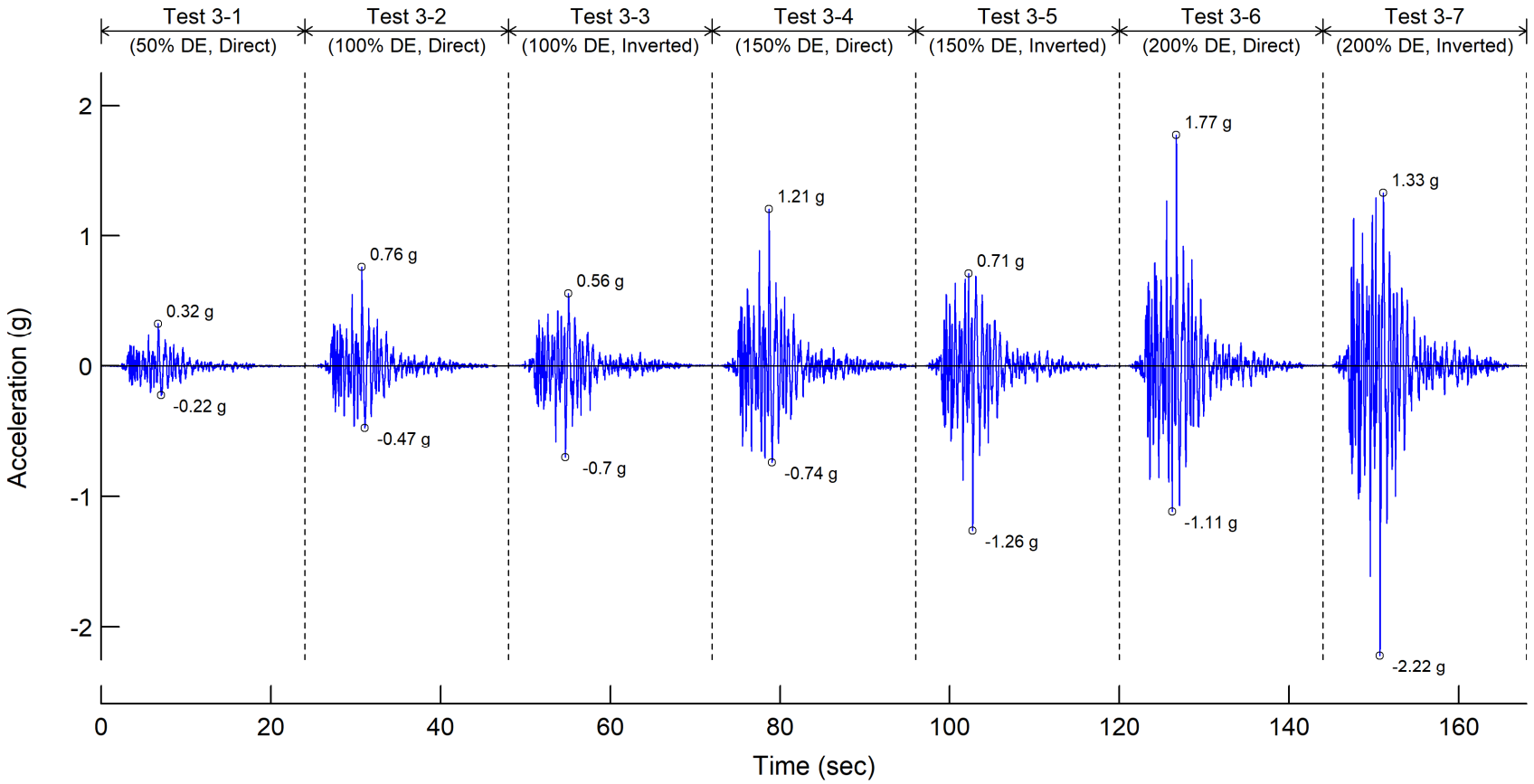

Figure 9.13 Measured Table Acceleration for Phase 3 Testing

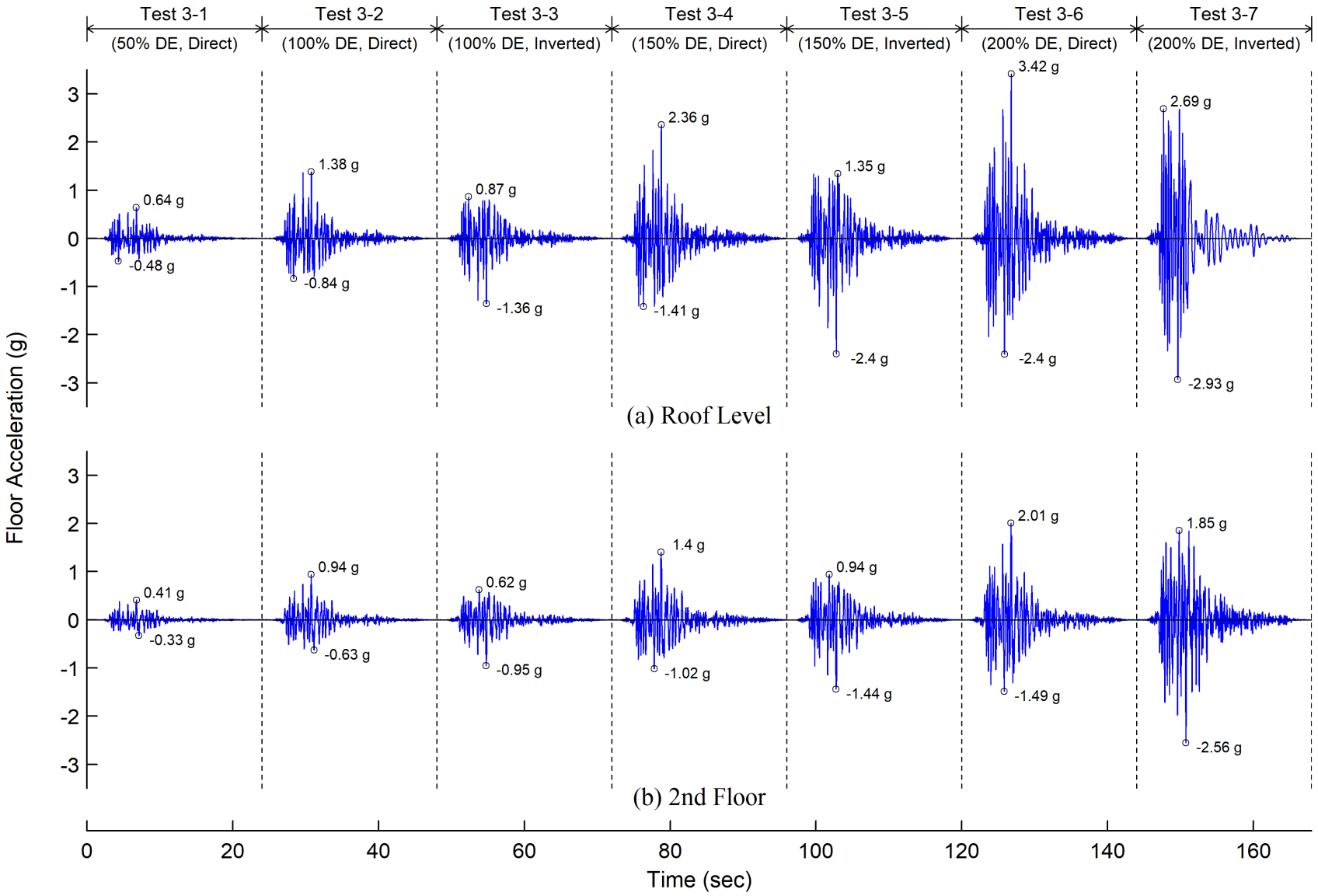

Figure 9.14 Floor Acceleration Responses for Phase 3 Testing

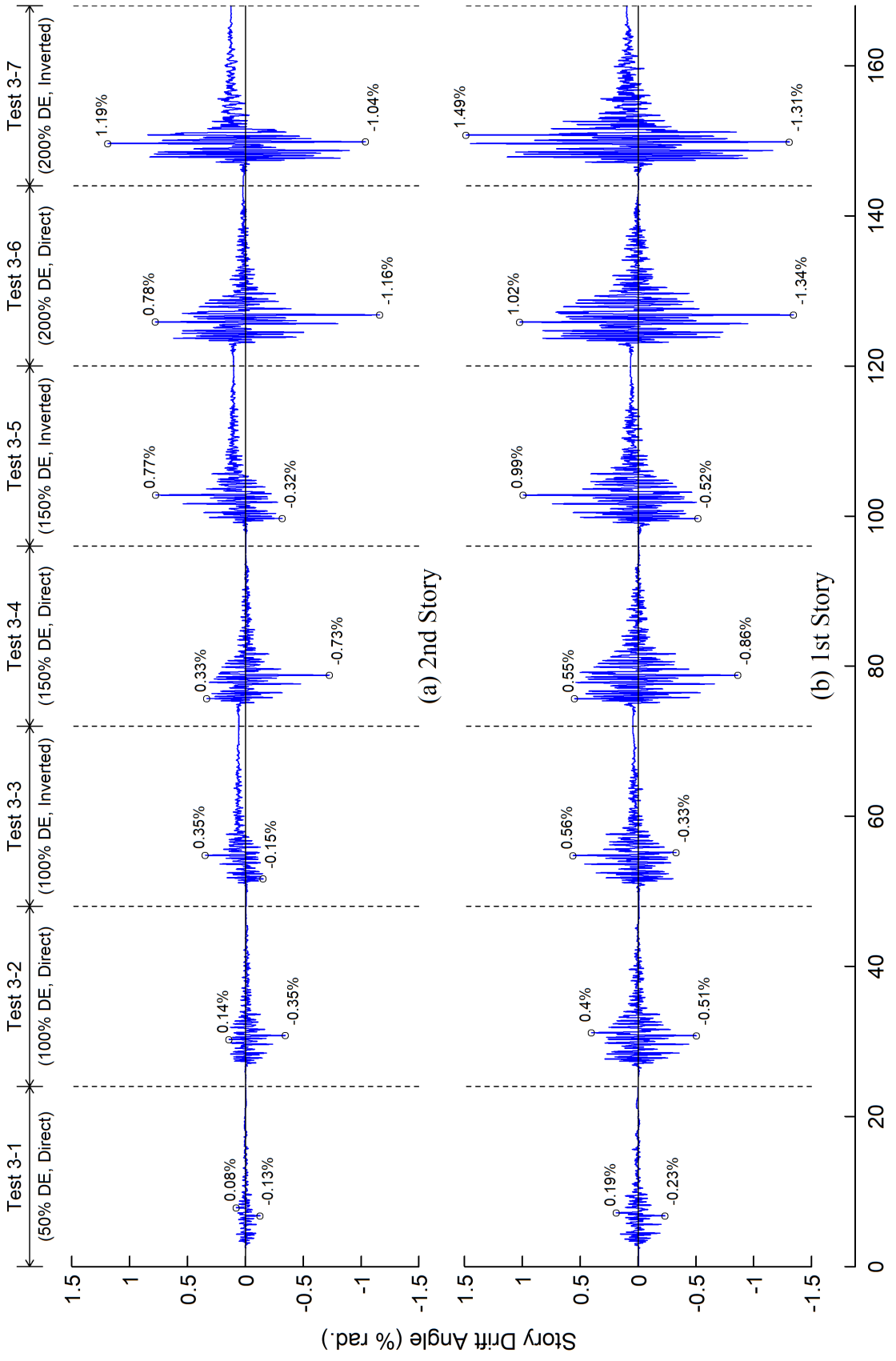

Figure 9.15 Story Drift Angle Responses for Phase 3 Testing

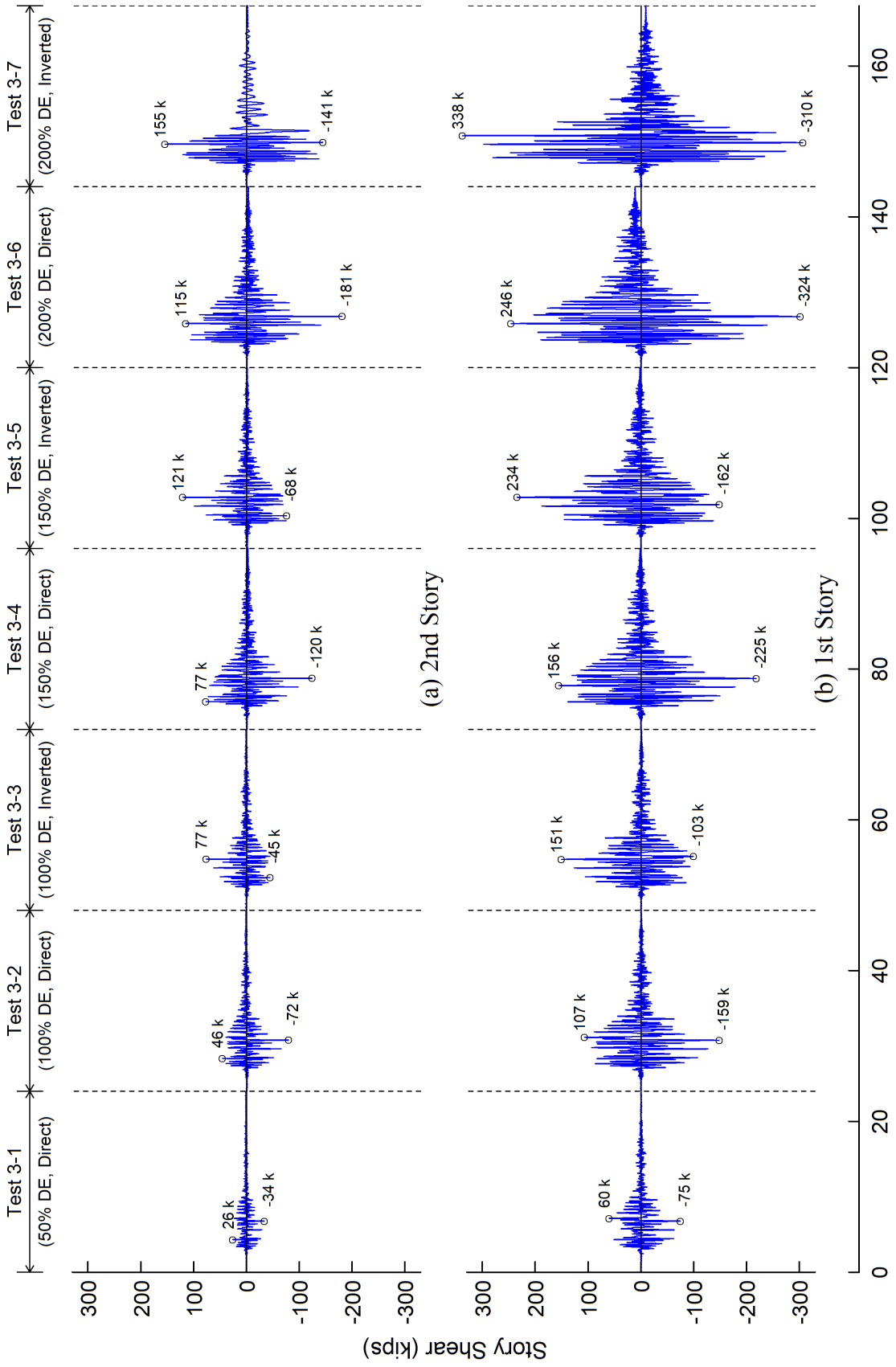

Figure 9.16 Story Shear Responses for Phase 3 Testing

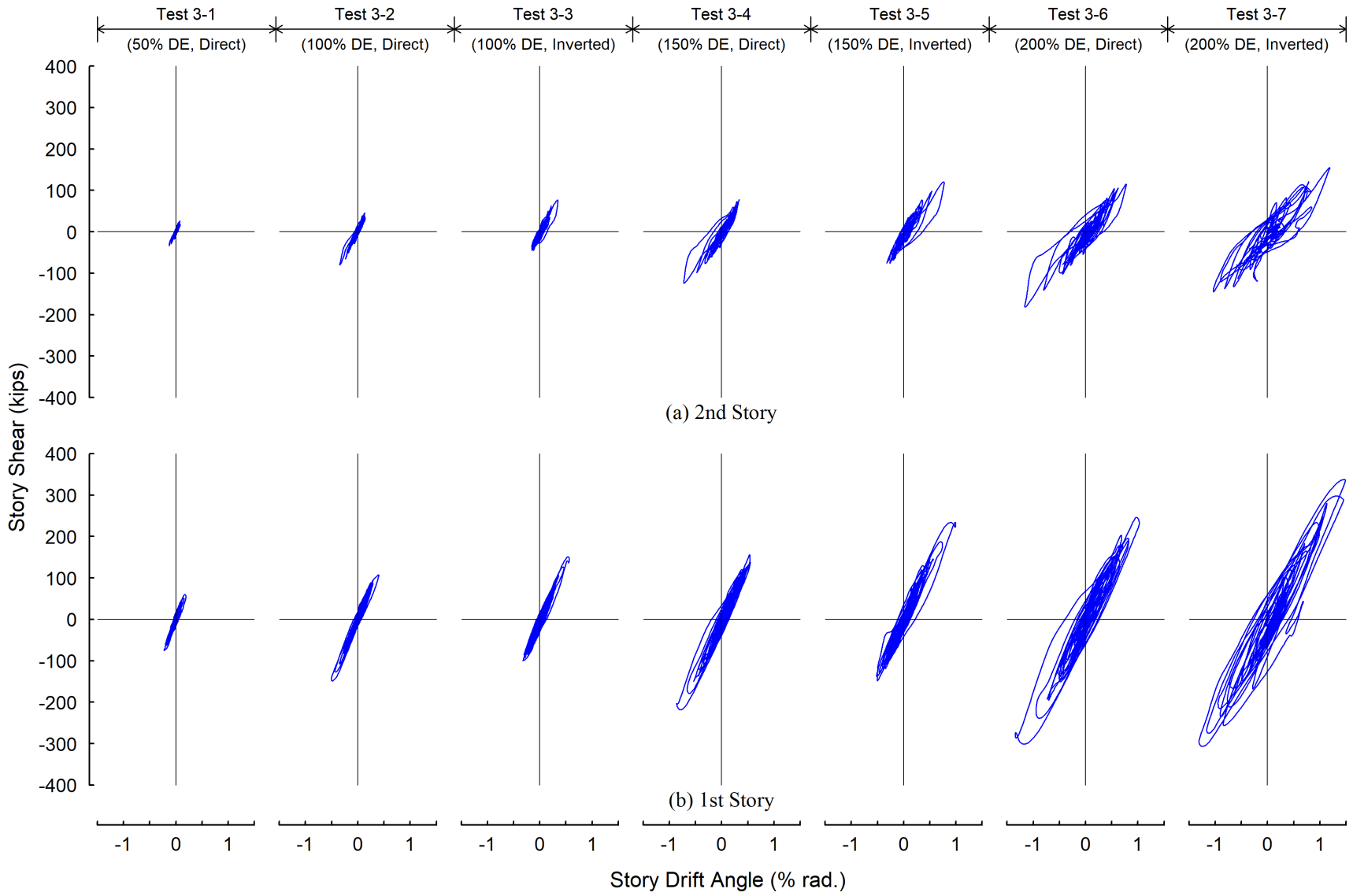

Figure 9.17 Story Shear versus Story Drift Angle Responses for Phase 3 Tests

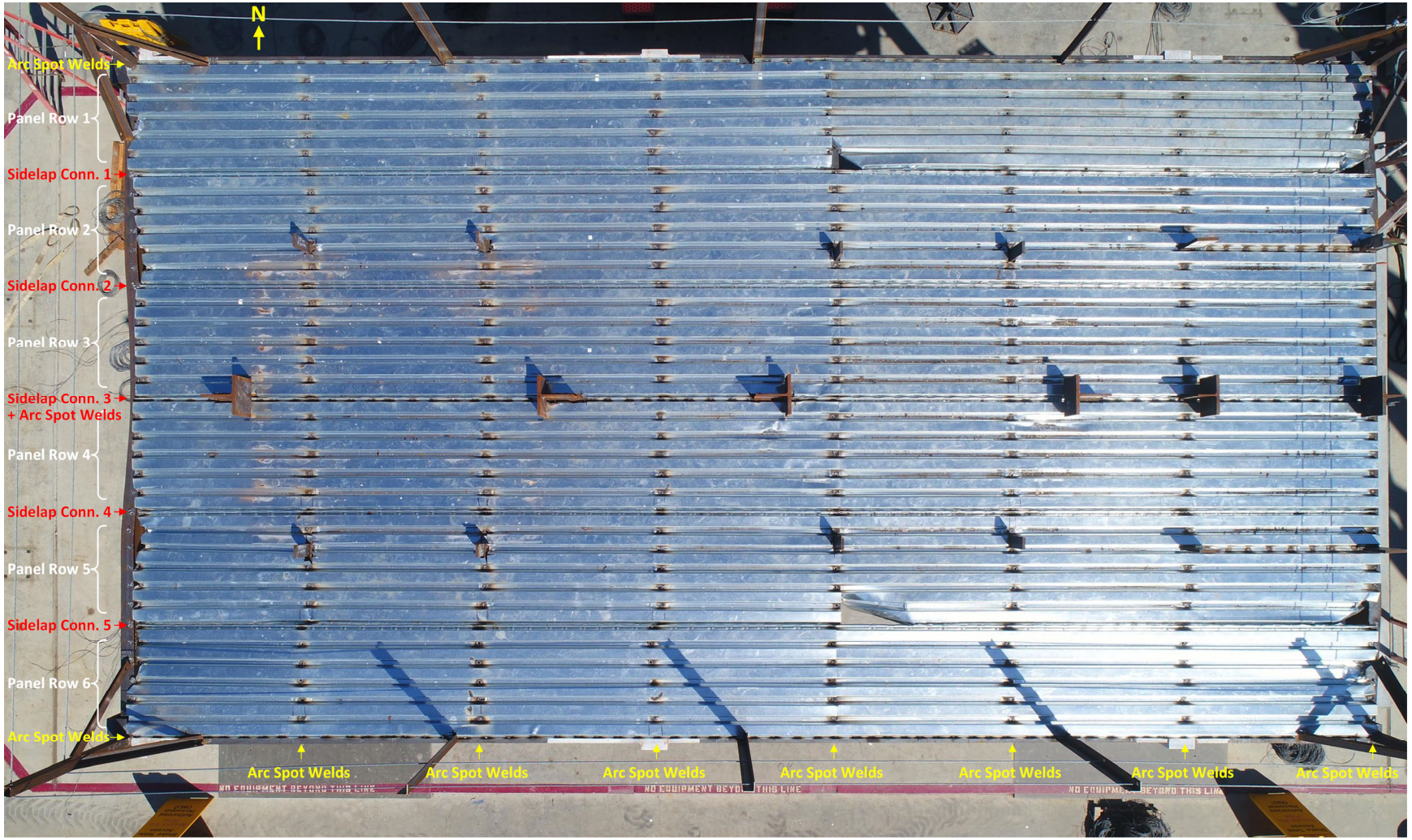

Figure 9.18 Top View of Damaged Roof Deck

(a) near Southwest Corner

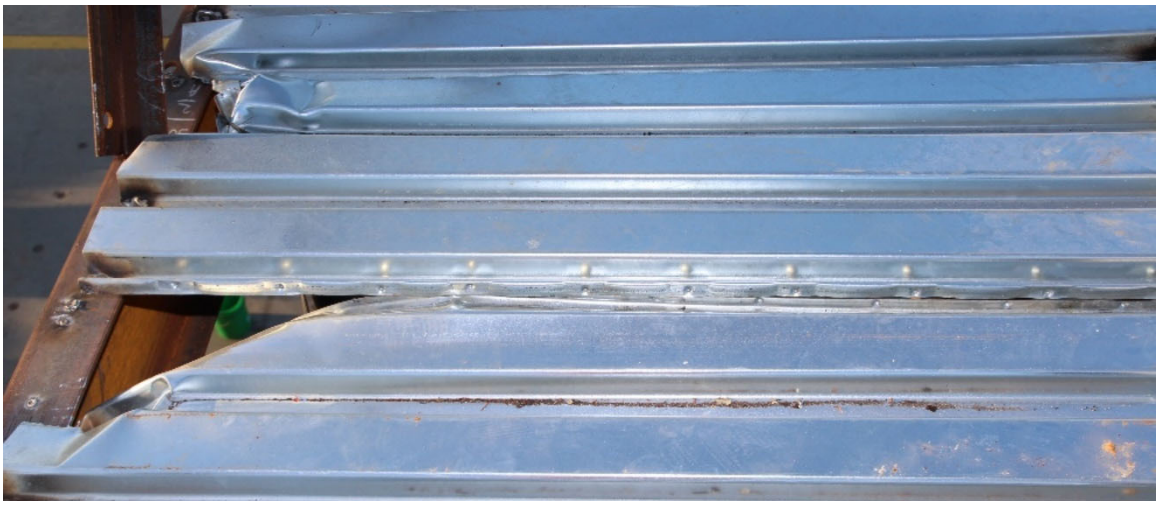

(b) near Southeast Corner

(c) Middle Portion of South Side Lap Connection

Figure 9.19 Damage of Side Lap Connection

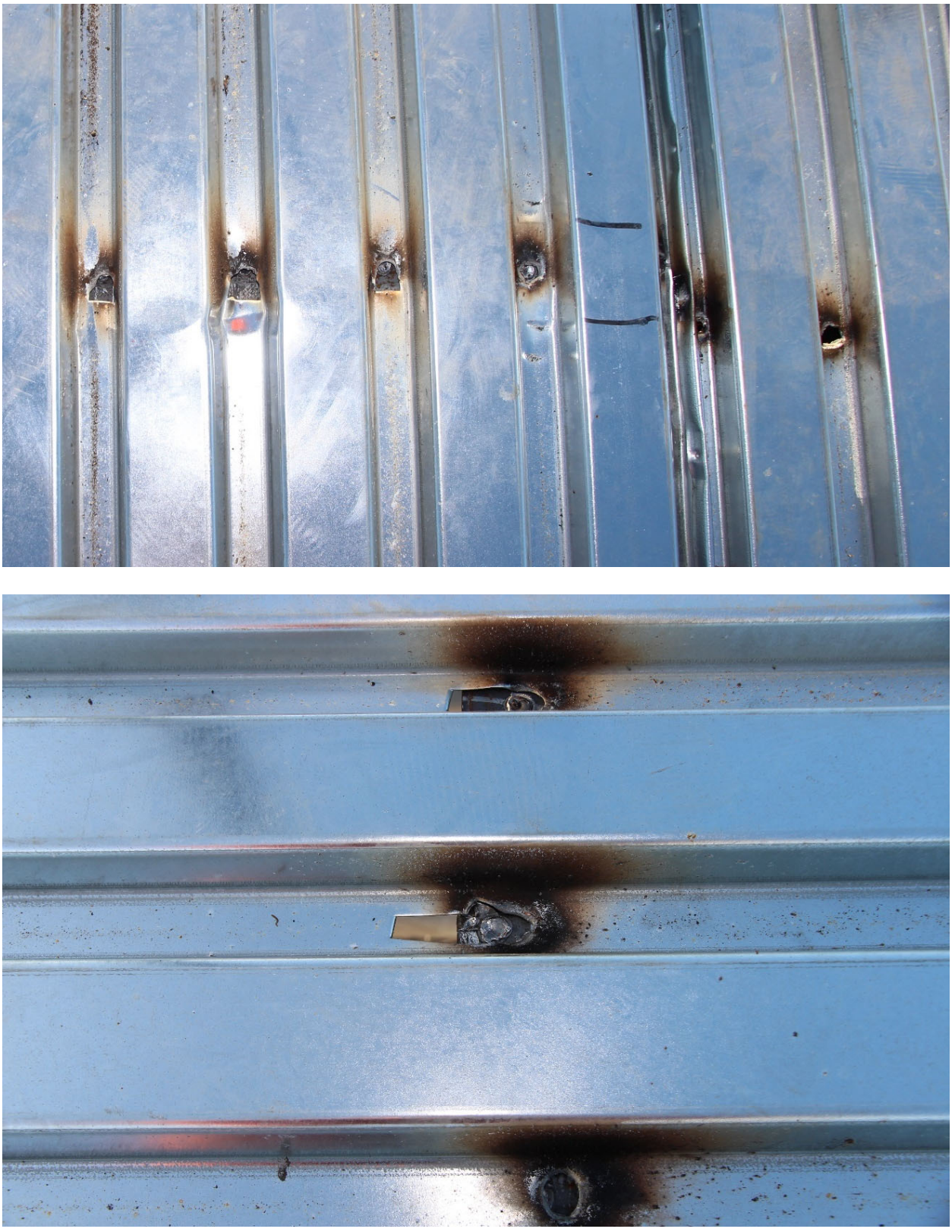

Figure 9.20 Damage of Arc Spot Welds

Figure 9.21 Residual Deformation of Roof East Chord

Figure 9.22 Residual Deformation of Roof West Chord

Figure 9.23 Residual Deformation of Roof West Chord

Figure 9.24 Residual Deformation of Roof Beams (after Deck Removed)

10. SUMMARY AND CONCLUSIONS

10.1 Summary

Collectors are structural components that play a critical role to transmit inertia forces in the floor diaphragms to the seismic force-resisting system (SFRS) in a building structure. Yet little research has focused on collectors and their connections, and both the seismic behavior and demands on these elements are not well understood. In this research, a three-phase shake table test program were conducted on a half-scale, two-story multi-bay steel building by using the NHERI@UCSD large high performance outdoor shake table (LHPOST). The test building included a composite floor diaphragm at the second floor and a bare metal deck diaphragm at the roof level; the collectors were located on the perimeter of the test building. In addition, three commonly used collector connections, the all-flange weld (AFW), top flange weld (TFW), and bolted web (BW) details, were employed in the test building. The main objectives of this research project include: (1) investigating on the collector load paths in the floor and roof diaphragms under inertial force mechanisms, (2) examining the seismic behavior and performance of steel collectors and collector-to-column connections, (3) evaluating the adequacy current design practice of seismic steel collectors and connections, (4) developing approximate methods for estimating collector force demands, and (5) making recommendations on design of collectors and their connections.

Phase 1 tests were performed on the “single-story phase” of the test building, in which only the first story of the test building with a composite slab was designed and constructed. An innovative testing methodology was developed and employed such that the floor absolute acceleration time histories of any floor in a multi-story building could be simulated by this single-story specimen through a transfer function approach. Three floor acceleration simulation tests were

conducted to excite the test building to reproduce the target floor accelerations obtained from time history analyses on the 5th floor of a 12-story prototype building frame model subjected to a historical ground motion scaled to 20%, 50% and 100% design earthquake (DE) levels, respectively. The achieved peak floor acceleration was 1.53 g. The reached peak story drift was 0.62% rad. The test specimen exhibited nearly elastic response as intended. It shows that the achieved specimen floor acceleration somewhat exceeded the target acceleration, which was caused by the overshoot of the table input acceleration. However, the shapes of the response spectra of the achieved and target specimen floor accelerations were similar. In general, the target floor acceleration response was reproduced in the test specimen, which confirms the effectiveness of the proposed test methodology.

A series of analytical studies by using the line element frame models were conducted for numerical simulation of Phase 1 testing. The combined experimental and numerical simulation results were used to investigate the collector load path and seismic behavior of collectors. Test results showed that the gravity columns "intercepted" a part of inertial forces collected in the collectors such that the LFRS did not receive the total inertial forces in the floor as expected by the conventional design method. In addition, analytical results show that the distribution of the slab shear flows along the collector lines was nonuniform due to the nonuniform in-plane shear deformation of the floor diaphragm. Thus, the rate of accumulation of the collector axial force along the collector line was nonuniform as well. This phenomenon implies that the assumption of uniform slab shear flow in practical design may overestimate the rate of the collector axial force increases along these collectors away from the LFRS.

Phase 1 test and analytical results also indicated that the AFW collector connections behaved like a moment connection, while TFW and BW connections acted as semi-rigid

connections. The effect of the rotational stiffness of the semi-rigid collector connections was small but non-trivial to the global response of the test specimen. Note that rotations of the collector connections in Phase 1 tests only triggered the bolted joints in the connections to slip but not reach the bolt bearing status. For estimating the rotational stiffness of semi-rigid collector connections under this level of rotation, the component-based spring model concept which incorporated the initial bearing stiffness for the bolted joints as proposed by previous research was used. In addition, a lateral load analysis method which considered the rotational stiffness of the collector connections was proposed. The predicted collector axial force demand from this proposed analysis method removes some conservatism in the conventional method.

An analytical study was carried out to develop practical modeling techniques to predict load path in the composite floor diaphragm and collectors. The studies showed that the Beam-Truss model proposed by Lu and Panagiotou (2012) and the proposed Modified Strip model are both reliable, but the latter was much more efficient for numerical simulation.

Phase 2 tests were conducted after the second story with a bare steel roof deck was added to the test building. Three commonly used collector connections were again employed at the roof level. The two-story structure was treated as a building and tested with the conventional earthquake simulation testing by using scaled historic ground motion as input motion. The entire Phase 2 testing was divided into two parts: Phase 2A tests were conducted for the 2-story test building without the added mass on the roof, which served as an extension of Phase 1 testing to excite the 2nd floor diaphragm to experience a higher floor acceleration. Phase 2B tests were performed on the specimen with added roof mass, in which significant inertial forces were generated in both the 2nd floor and roof diaphragms. In Phase 2A, five earthquake simulation tests were conducted at three intensity levels from 50% DE to 200% DE, and the peak roof and 2nd floor accelerations

reached 3.28 g and 2.04 g, respectively. The peak 2nd- and 1st-story drift angles reached 0.77% and +1.19% rad, respectively. The specimen experienced slight inelasticity in Phase 2A testing. Very limited yielding was observed in the bottom flanges at the 2nd floor AFW connections. In Phase 2B, five earthquake simulation tests were conducted at three intensity levels from 50% DE to 125% DE. The peak roof and 2nd floor accelerations reached 3.03 g and 1.82 g, respectively. The peak 2nd- and 1st-story drift angles reached 1.81% and +1.75% rad, respectively. The specimen exhibited mild to moderate inelastic response. Significant yielding and local bucking of the steel collector bottom flange took place at the 2nd floor composite AFW collector connections.

Phase 2 test results showed that the moment-rotation responses of composite semi-rigid (TFW and BW) collector connections were markedly unsymmetric because the concrete slab only contributed to resisting moment under positive bending, while the response of bare steel semi-rigid collectors did not vary that much between positive and negative bending. The peak rotation angles reached in these semi-rigid collector connections at roof and 2nd floor levels were about 2.0% and 1.5% rad, respectively. This level of deformation was considered representative of moderate responses under the design level earthquake. A procedure was proposed to estimate the secant stiffnesses of composite and bare steel collector connections. This procedure employs the component-based spring model concept together with the secant stiffness for bolted connections estimated from a model proposed by Reynolds et al. (2021). An experimental verification showed that the proposed method satisfactorily predicts the secant stiffness of the semi-rigid collector connections.

Phase 2 test results also showed the effect of the rotational stiffness of collector connections to “intercept” floor inertia forces through shear in gravity columns in the topmost story of test building. This phenomenon is insignificant in the bottom story due to the cancellation effect of the

column shears above and below the floor. Hence, the conventional design method, which neglects the gravity column effects, is suitable for estimating the collector axial force demand for typical floors. An experimental verification showed that the proposed modeling and analysis mentioned above provides a better prediction on the roof collector axial forces than the conventional design method.

Test results also showed that, when a composite collector was under the simultaneous tensile axial force and bending moment, the unintended bending moment demand would cause the resultant axial force on the steel section to be even larger than the total axial force on the composite section. This suggests that the current practice may significantly underestimate the axial force demand on steel collector connections because of the "prying action-like" phenomenon occurring at the ends of composite collectors. To address this issue, this research proposes design recommendations on estimating the axial force demand for collector connection design and some detailed design requirements to prevent premature local buckling of the collector under combine axial and flexural forces.

In Phase 3 testing, a pair of buckling-restrained braces (BRBs) were added to the 2nd story of the test building to modify the building dynamic characteristics and the collector seismic load path. Earthquake simulation testing by using scaled historic ground motions were conducted in this phase until the failure of the side lap of connections of the bare steel roof deck occurred. The test data of this phase provide useful information for the future research on the seismic collector and steel roof deck.

10.2 Conclusions

Based on the results from both shake table tests and the associated analytical studies, the following conclusions can be made:

(1) The proposed testing method that used a transfer function approach to excite an elastic one-story test building to reproduce the target absolute acceleration response of any floor of a multistory building that was expected to experience nonlinear response was shown to be effective. Although the measured floor accelerations were higher than the target responses due to the overshooting of the table input motion, the expected frequency content which reflected the higher mode effects of the multistory prototype building was well reproduced.

(2) The axial force diagram along a collector line would be affected by two factors: one is the interception of inertial forces by gravity columns, and the other one is the distribution of the slab shear flow, through which the inertial forces in the floor are transferred to the collectors, along the collector line. Flexural rigidity of the collector connections at the roof level helped in reducing the seismic force demand in the collectors and their connections at that level. The results from Phases 1 and 2 testing indicated that approximately 30% to 40% of inertial forces at the roof level were transferred through the gravity columns in the test building. Thus, neglect this effect would result in rather overestimation of the axial force in the roof collector next to the LFRS.

(3) The slab shear flow distribution is dependent on the distributions of stiffness and mass on the floor diaphragm. Along a collector line, the nearer the LFRS, the higher the slab shear flow. Therefore, the assumption of a uniform slab shear along a collector line, as is commonly done in practice, would lead to an overestimation of the axial forces in the collectors in the bays not adjoining to the LFRS.

(4) Analytical studies showed that the Beam-Truss model proposed by Lu and Panagiotou (2012) and the proposed Modified Strip model are both reliable in simulating the composite floor diaphragm and collector actions, but the latter was much more efficient for numerical simulation. Take the numerical simulation of Test 1-3, the proposed Modified Strip model only took less than half of computational time required by the Beam-Truss model. An approach using elastic analysis on a planar Modified Strip model is proposed to precisely analyze the nonuniform slab shear flow distribution and collector axial force distribution. This approach could be used for the design of floor or roof diaphragm and collectors on a highly irregular floor plan.

(5) Experimental and analytical results showed that the effect of the rotational stiffness of the semi-rigid collector connections was small but non-trivial to the global response of the test specimen. A procedure, employs the component-based spring model concept together with the secant stiffness for bolted connections, was proposed to estimate the secant stiffnesses of composite and bare steel semi-rigid collector connections. An experimental verification using Phase 2B-5 test results showed that the proposed method provides a satisfactory prediction in an overall sense. for the purpose of evaluating the required axial force in the collectors for design, it is desirable (i.e., conservative in design) that a lower-bound estimate of the collector connection flexural stiffness be made. However, test results showed that the proposed method may overestimates the collector connection stiffness for some cases, which may be due to assumptions like neglecting the effect of axial load in the proposed method.

(6) An improved analysis method for estimating the roof collector axial force forces that considers flexural rigidity of the collector connections is proposed in this research. This

procedure includes a portal frame method for lateral load analysis on the topmost-story gravity frame with collectors. Closed-form solutions for the lateral stiffness of various types of collector-to-gravity column subassemblies are developed to facilitate the lateral load analysis. A comparison between the predicted and measured axial force diagrams shows that the proposed analysis method incorporated with the collector connection secant stiffness, provides a better prediction of the roof collector axial forces. For example, results from Test 2B-5 showed that the conventional method overestimated the collector axial force at the end next to the LFRS by about 75%, while such overestimated was reduced to 38% based on the proposed improve method. In contrast to the roof level, Phase 2 test results also showed that the phenomenon of interception of inertial force by gravity column was insignificant in the bottom story due to the cancellation effect of the column shears above and below the floor. This suggests that that the conventional design method is still suitable for estimating the axial force demand for collector in typical floors.

(7) Test results show that, when a composite collector is under the simultaneous tensile axial forces and positive bending moment, this unintended bending moment demand due to the flexural rigidity of the collector connections would result in a "prying action-like" phenomenon causing the bare steel section of a composite collector to be subjected to a resultant tensile force even larger than the total tensile force on the entire composite section. This brings up a concern that the current practice may significantly underestimate the force demand in design of collector connections. To address with this issue, it is recommended that the axial force demand for designing steel collector connections should consider an extra term $C_c = 0.85 f_c' b_{eff} a$, which is the maximum possible axial force that the concrete slab can develop.

(8) Alternatively, it is also recommended to separate the concrete slab and steel column face by an open gap or by use of compressible foam-like material to “eliminate” the “prying action-like” behavior. Once the seismic isolation is achieved, the composite collector connections can be designed as a bare steel collector connection.

(9) As the significant yielding and local buckling of the collector bottom flange at the 2nd floor composite AFW connections in the test building during Test 2B-5. It is indicated that the combined axial and bending demands on a AFW connection would cause its one flange to get into yield earlier than the entire collector connection reaches the expected limit state. It requires an adequate ductility for the welded joint to prevent a premature damage. Therefore, it is prudent that some detailing requirements for Ordinary Moment Frame (OMF) connections be used. This includes the removal of the steel backing at the bottom flange level. Also, to prevent premature local bucking, it is recommended that the highly ductile requirements should be specified for the collector beams used for AFW connections.

Appendix A. Design Drawings for Phase 1 Test Specimen and Setup

This Appendix provides the complete design drawings for fabrication of Phase 1 test specimen and setup. Table A.1 lists the brief description of drawings.

Table A.1 List of Drawings for Phase 1 Testing

DWG No.	Content
S00	Test Setup
S01	Test Building Floor Plan
S02	Core Drilling Holes on Concrete Slab
S03	Frame S Elevation
S04	Frame N Elevation
S05	Frame 1 Elevation
S06	Frames 2, 3, and 4 Elevation
S07	Longitudinal Floor Beams
S08	Transverse Floor Beams
S09	All Flange Weld (AFW) Collector-to-Column Connection
S10	Top Flange Weld (TFW) Collector-to-Column Connection
S11	Bolted Web (BW) Collector-to-Column Connection
S12	Beam-to-Beam Connection
S13	Gusset Plate Connections for Longitudinal Double-Angle Brace
S14	Bottom Gusset Plate Connection in Frame 1
S15	Top Gusset Plate Connection in Frame 1
S16	Bottom Gusset Plate Connection in Frames 2, 3, and 4
S17	Top Gusset Plate Connection in Frames 2, 3, and 4
S18	Pin-Support for Gravity Columns in Frames 2 and 3
S19	Pin-Support for Gravity Columns in Frame 4
S20	Pin-Support Components and Gravity Column Base Plate

Table A.1 List of Design Drawings for Phase 1 Testing (continued)

DWG No.	Description
S21	Details of Double-Angle Braces
S22	Embedded Column Base Connection
S23	Cantilever Column Bottom End Details
S24	Clamping Beams
S25	Added-on Mass Layout
S26	Added-on Mass Blocks Attachment Details
S27	Slab Edge Form Layout
C01	RC Footing 1 for Columns S1 and N1
C02	RC Footing 2 for Columns S2, S3, N2 and N3
C03	RC Footing 3 for Columns S4 and N4
C04	Rebar Schedule-Page 1
C05	Rebar Schedule-Page 2
C06	Rebar Schedule-Page 3
C07	Rebar Schedule-Page 4

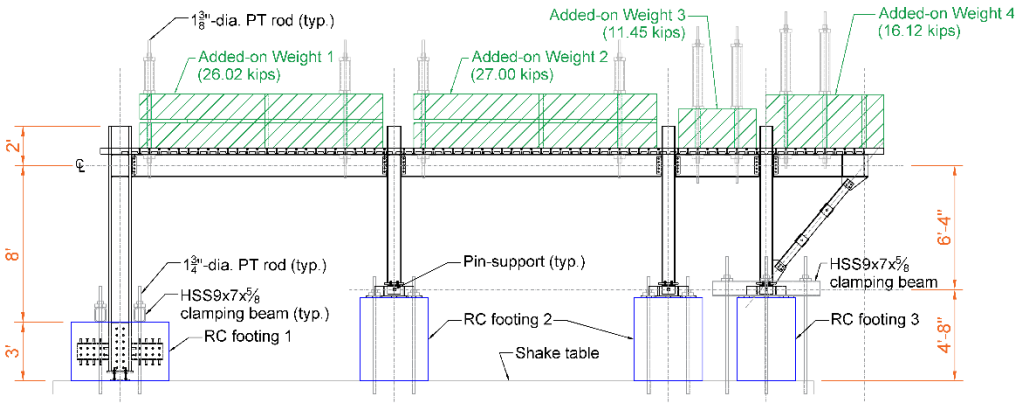

Elevation

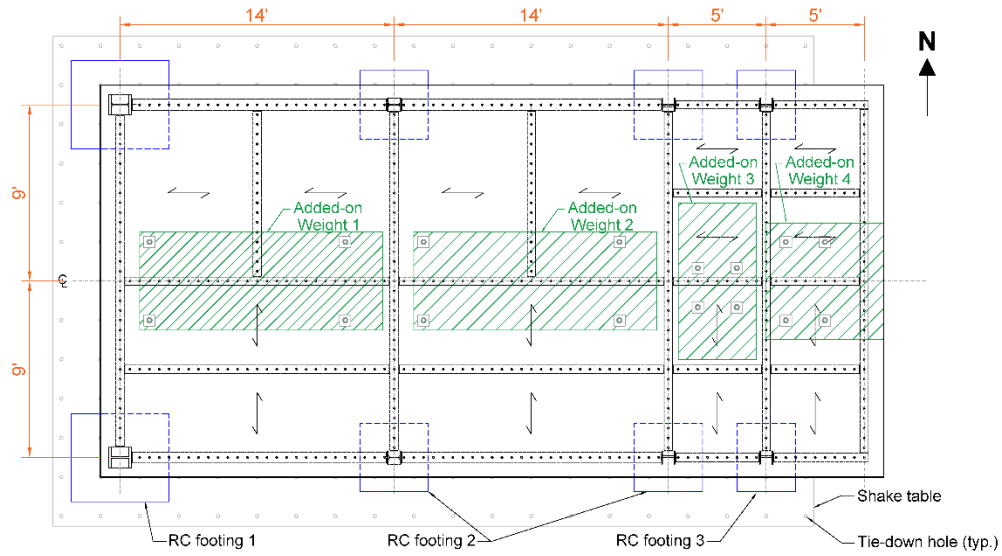

Test Building Floor Plan

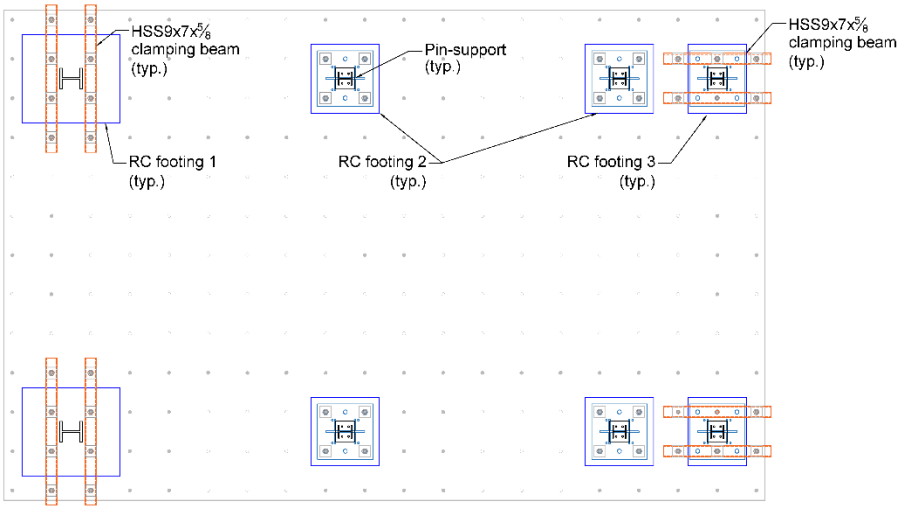

Plan View of RC Footings on Shake Table

Figure A.1 Test Setup (DWG S00)

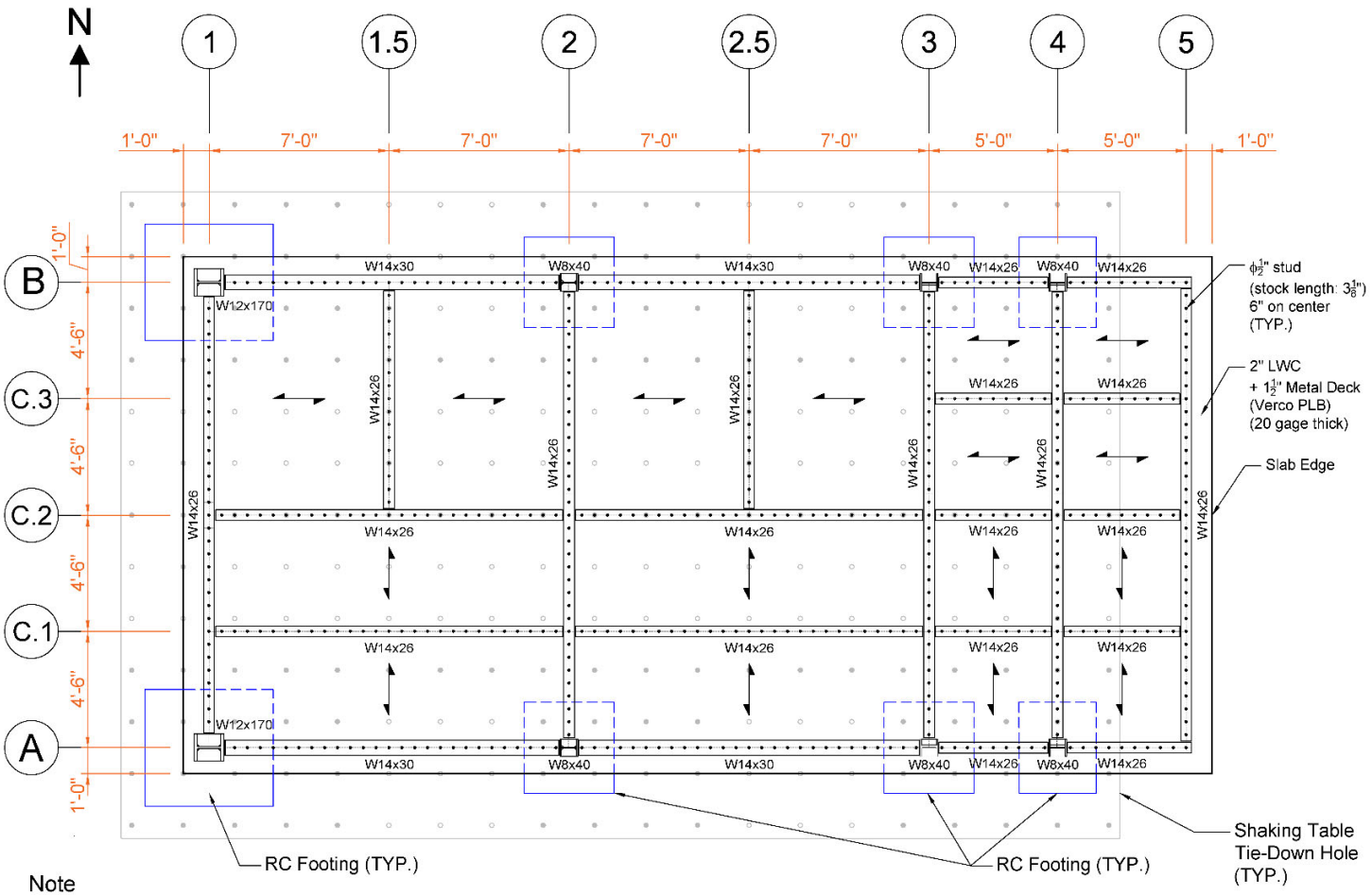

Note

1. Use A992 steel for W shapes and A36 steel for angles
2. Use A572 Gr. 50 steel for all plates
3. Concrete slab: f'_c = 4 ksi
4. All bolts to be fully pretensioned
5. Use E70 electrode

Figure A.2 Test Building Floor Plan (DWG S01)

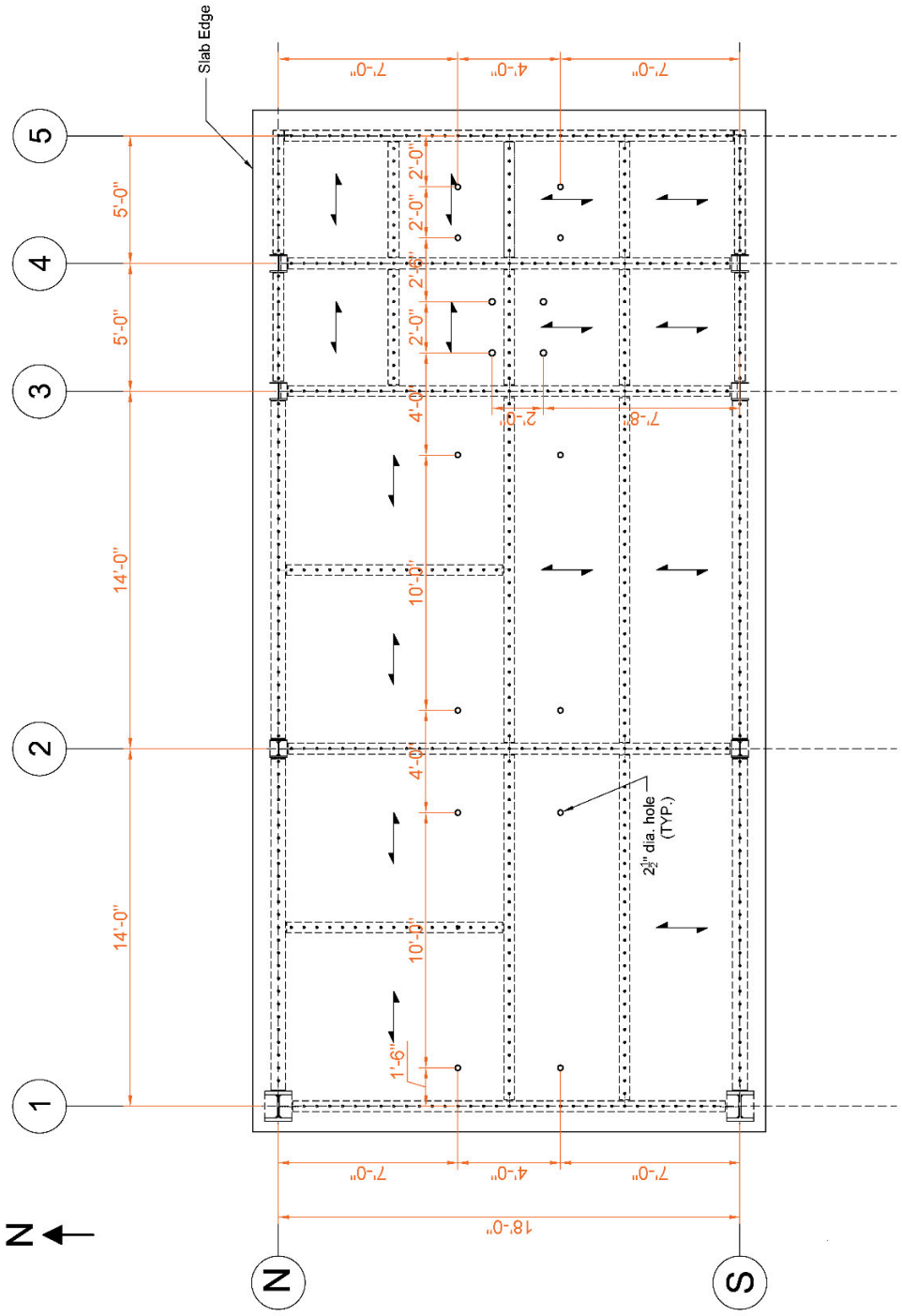

Figure A.3 Core Drilling Holes on Concrete Slab (DWG S02)

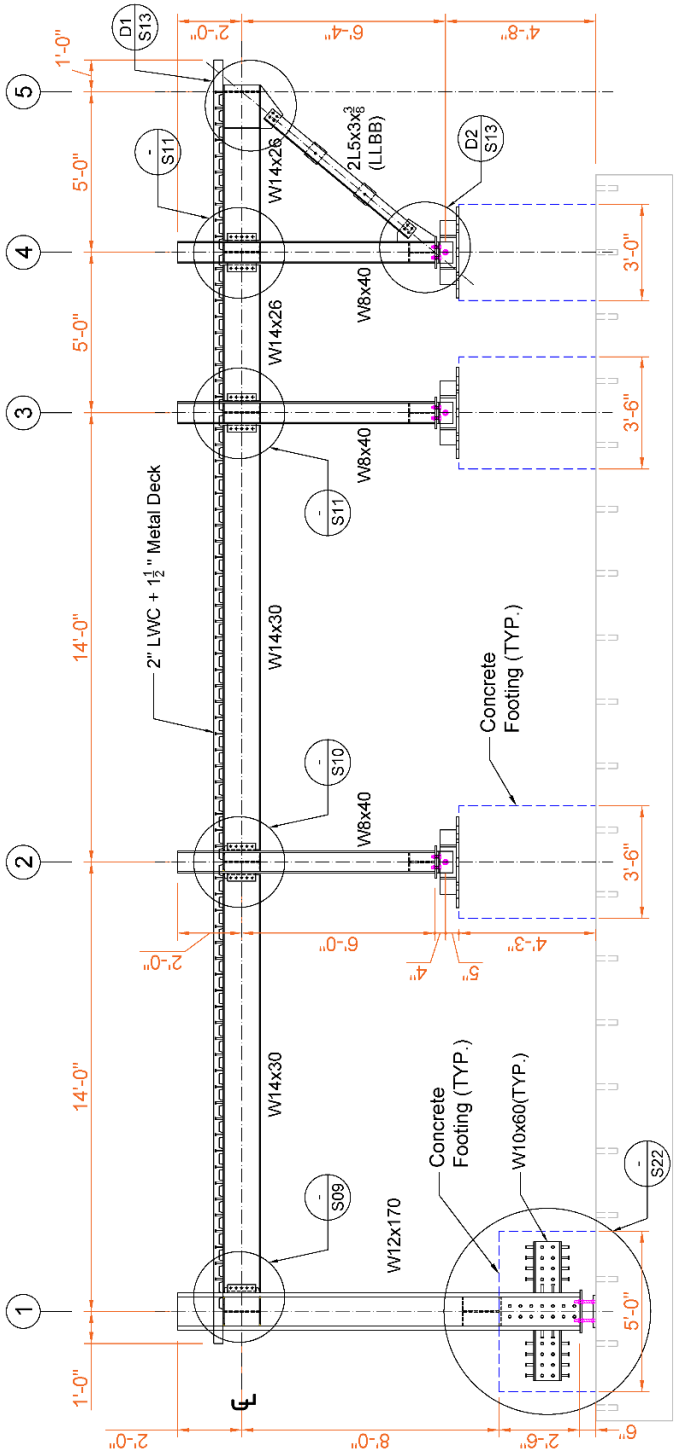

Figure A.4 Frame S Elevation (DWG S03)

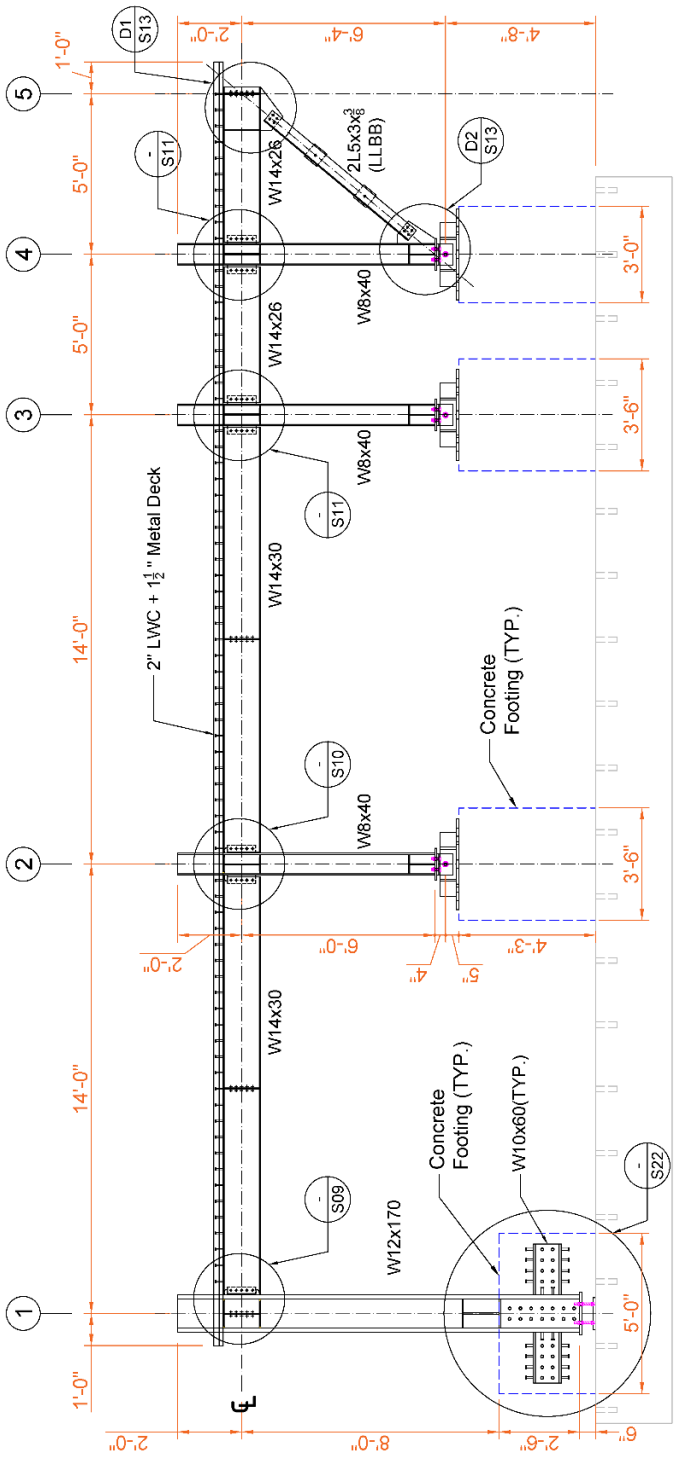

Figure A.5 Frame N Elevation (DWG S04)

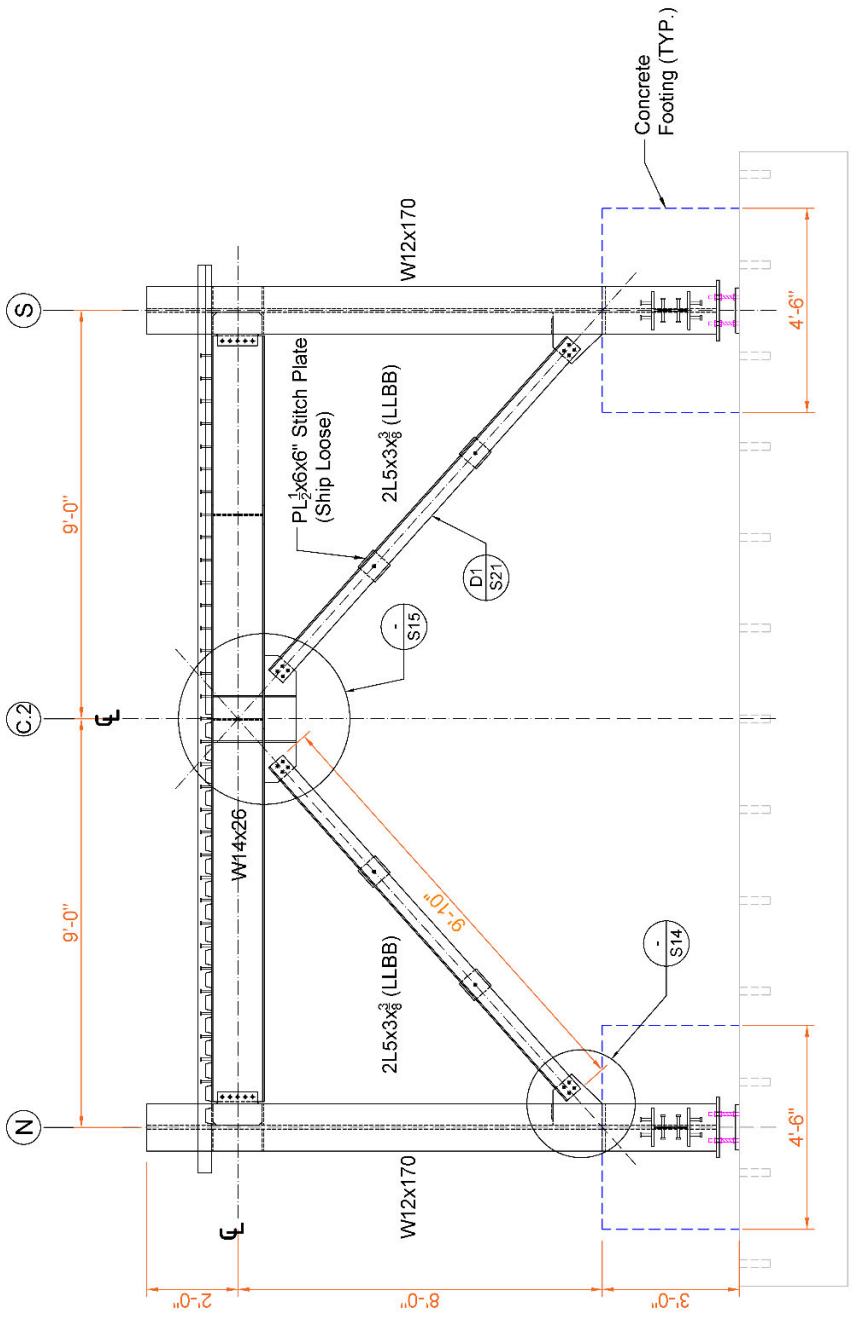

Figure A.6 Frame 1 Elevation (DWG S05)

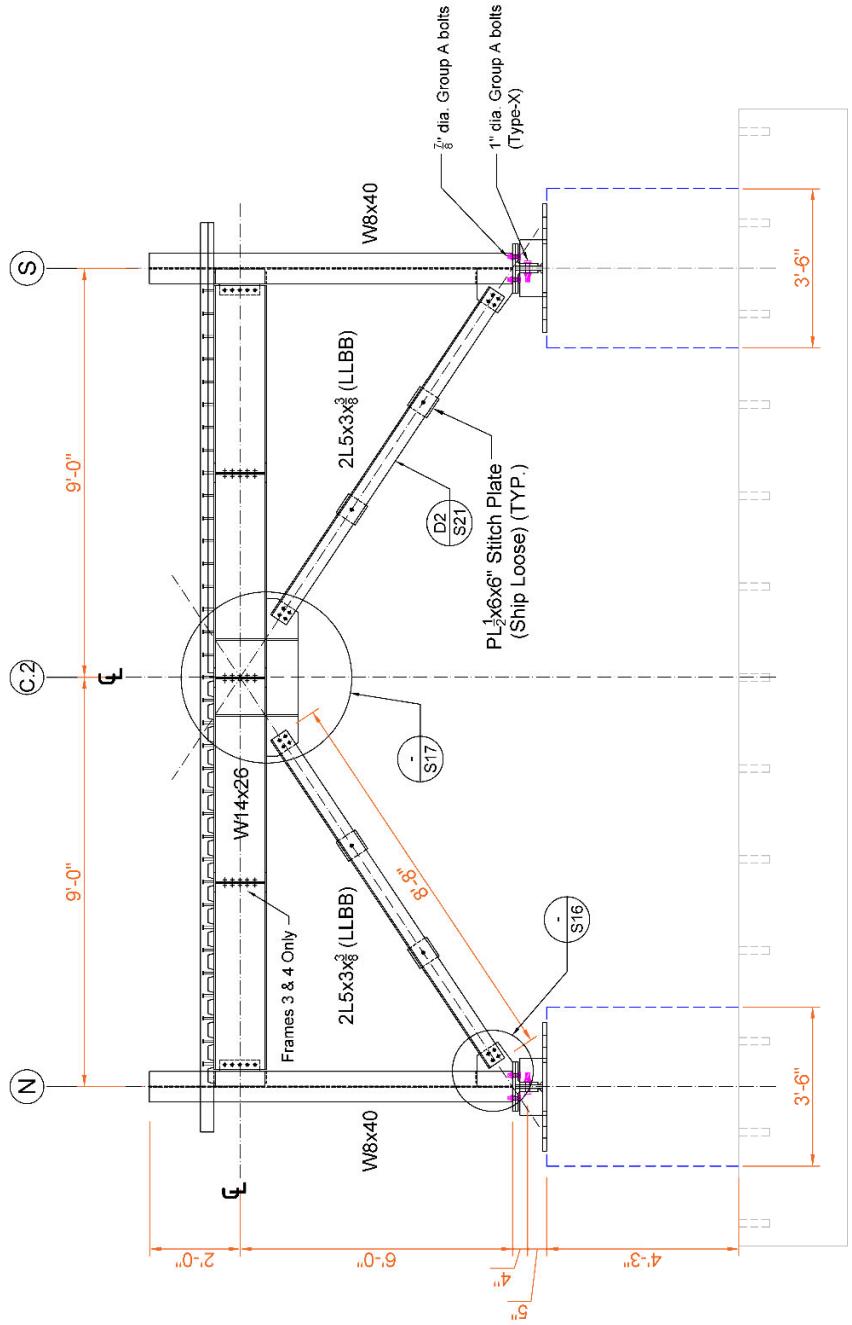

Figure A.7 Frames 2, 3, and 4 Elevation (DWG S06)

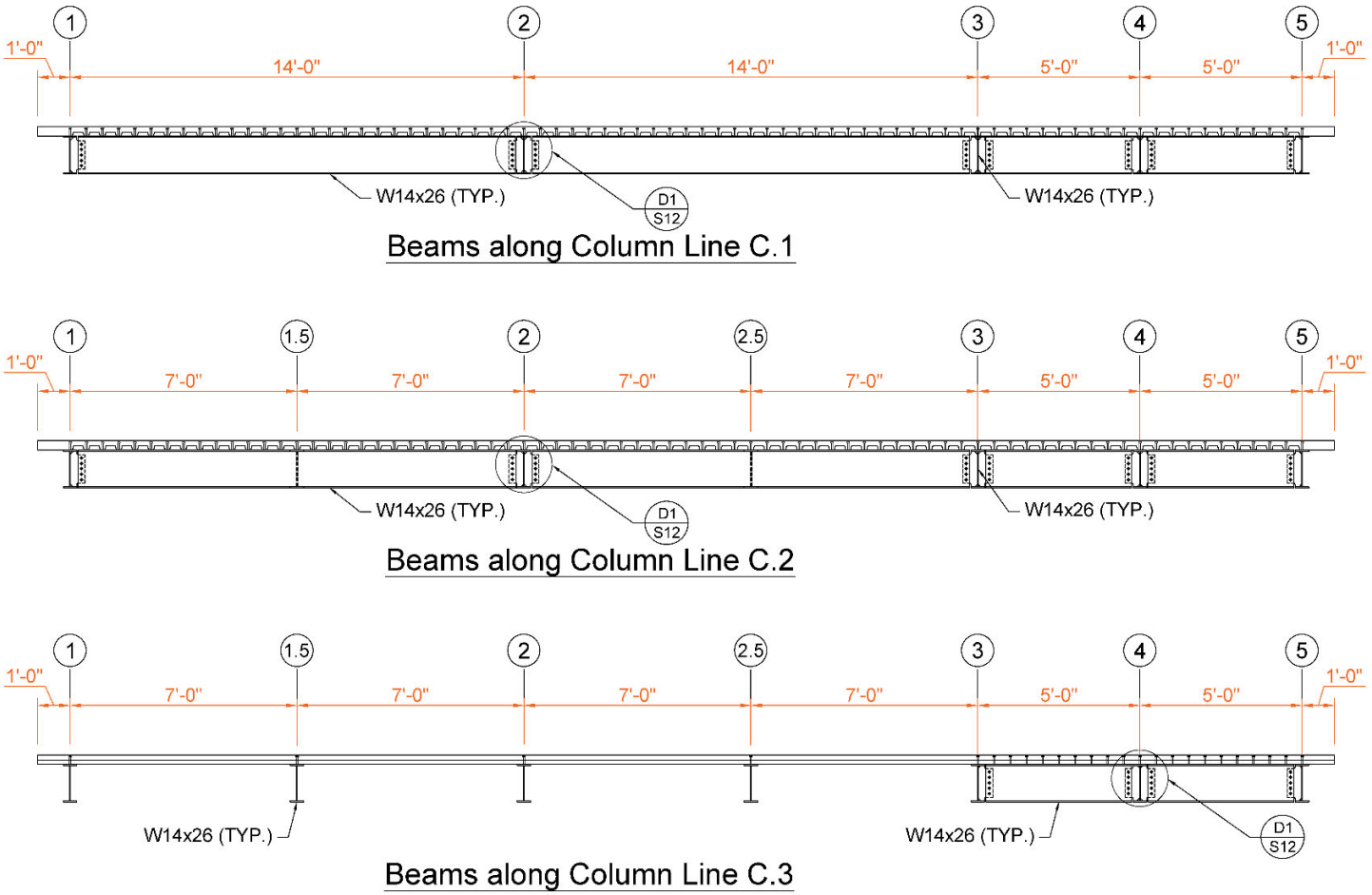

Figure A.8 Longitudinal Floor Beams (DWG S07)

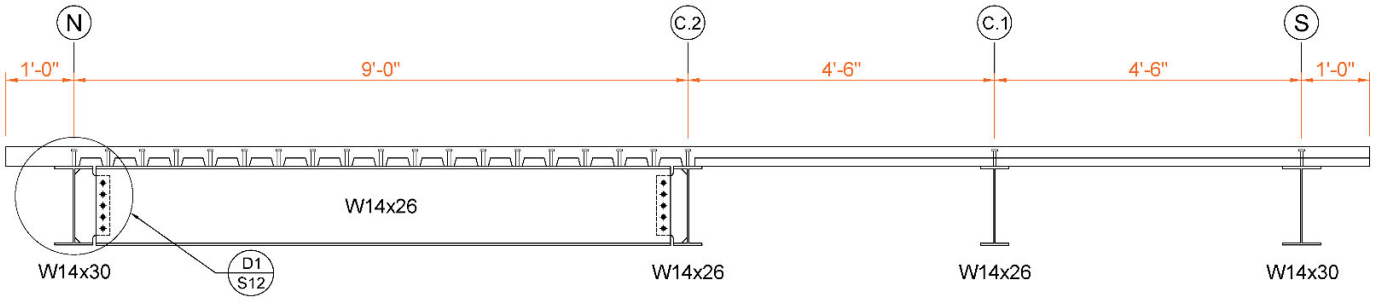

Beams along Column Lines 1.5 and 2.5

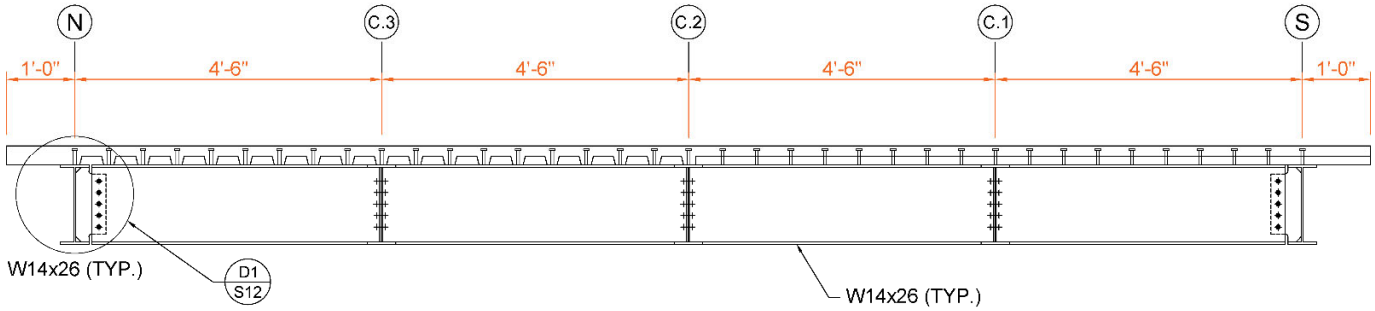

Beams along Column Line 5

Figure A.9 Transverse Floor Beams (DWG S08)

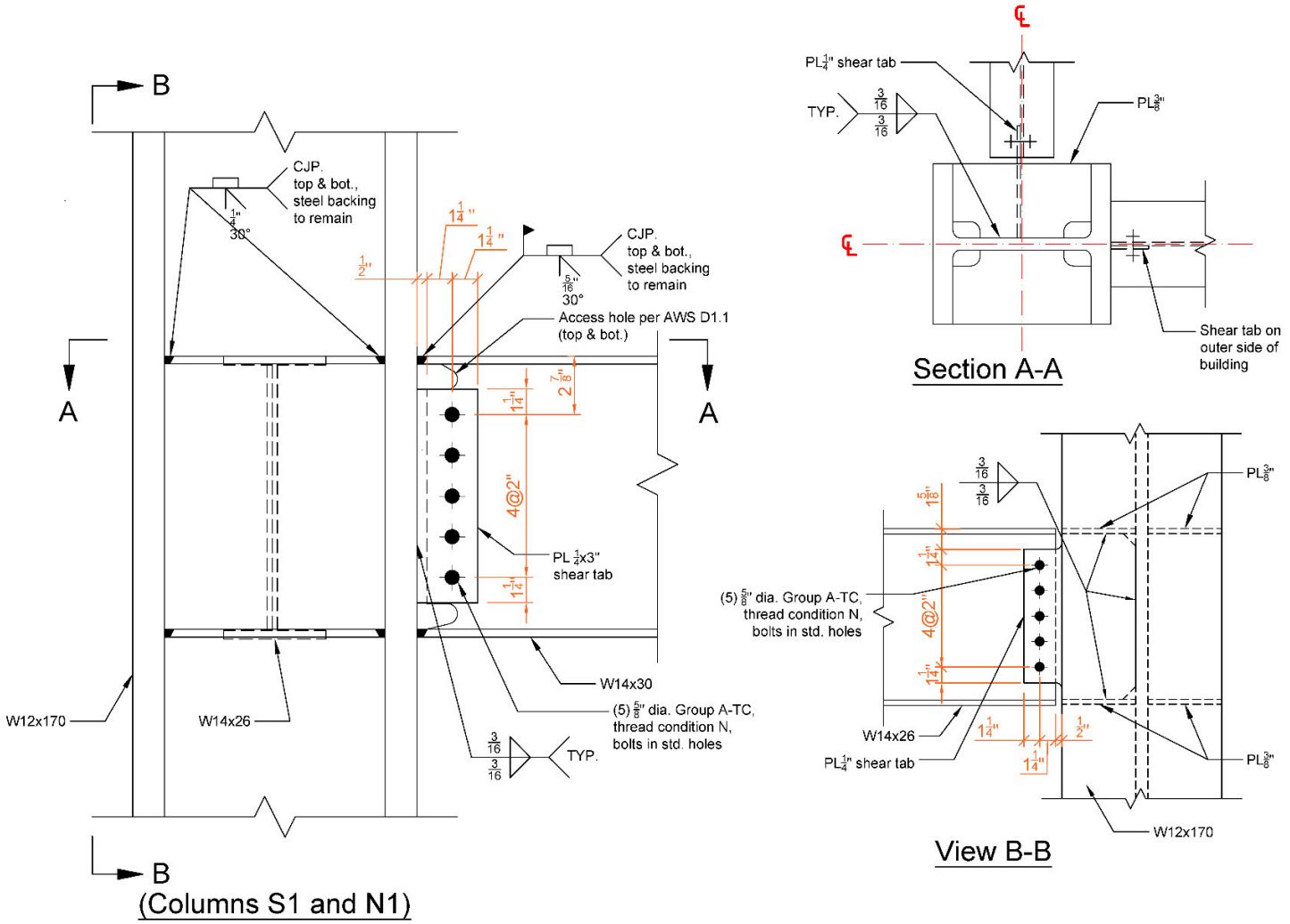

Figure A.10 All Flange Weld (AFW) Collector-to-Column Connection (DWG S09)

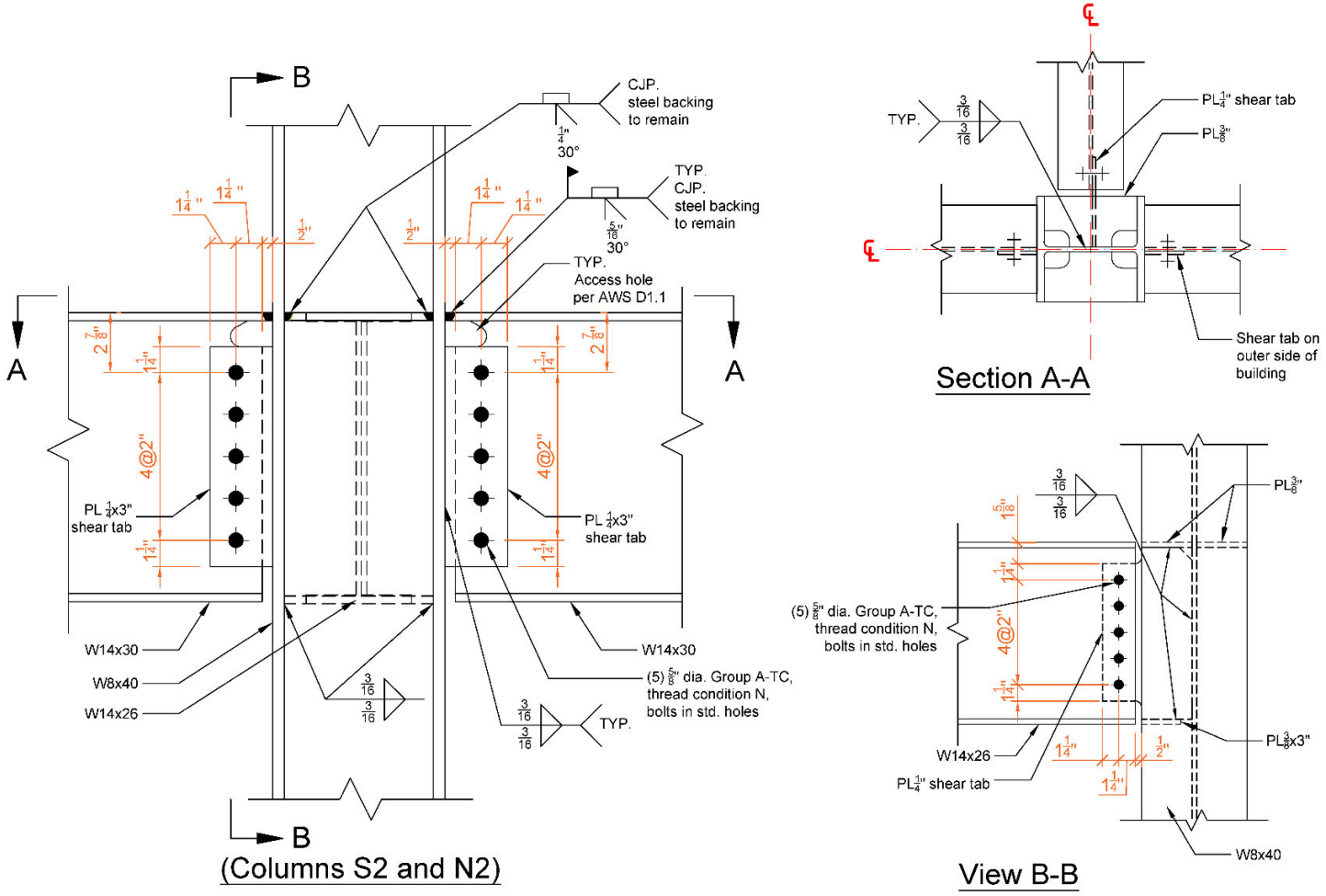

Figure A.11 Top Flange Weld (TFW) Collector-to-Column Connection (DWG S10)

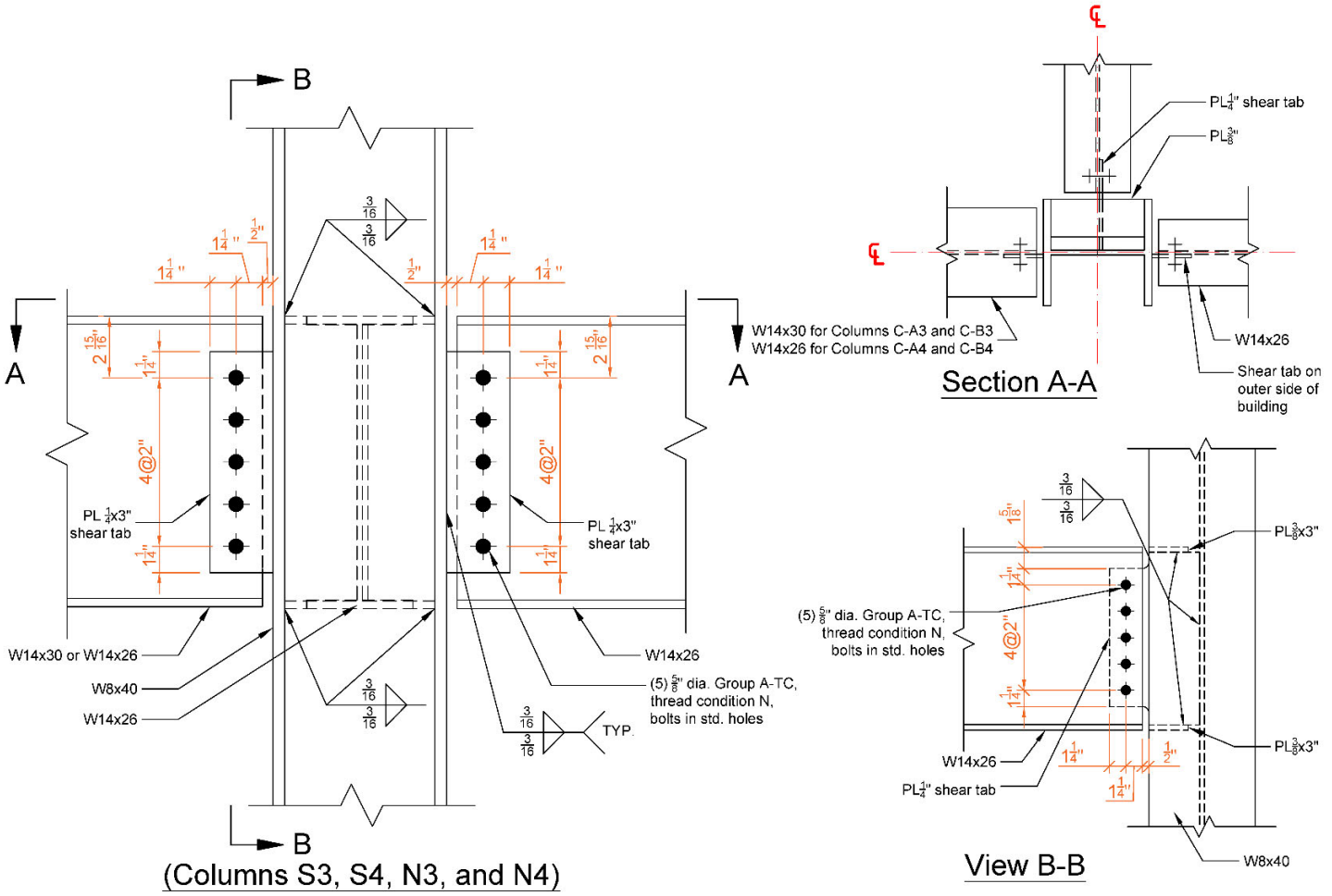

Figure A.12 Bolted Web (BW) Collector-to-Column Connection (DWG S11)

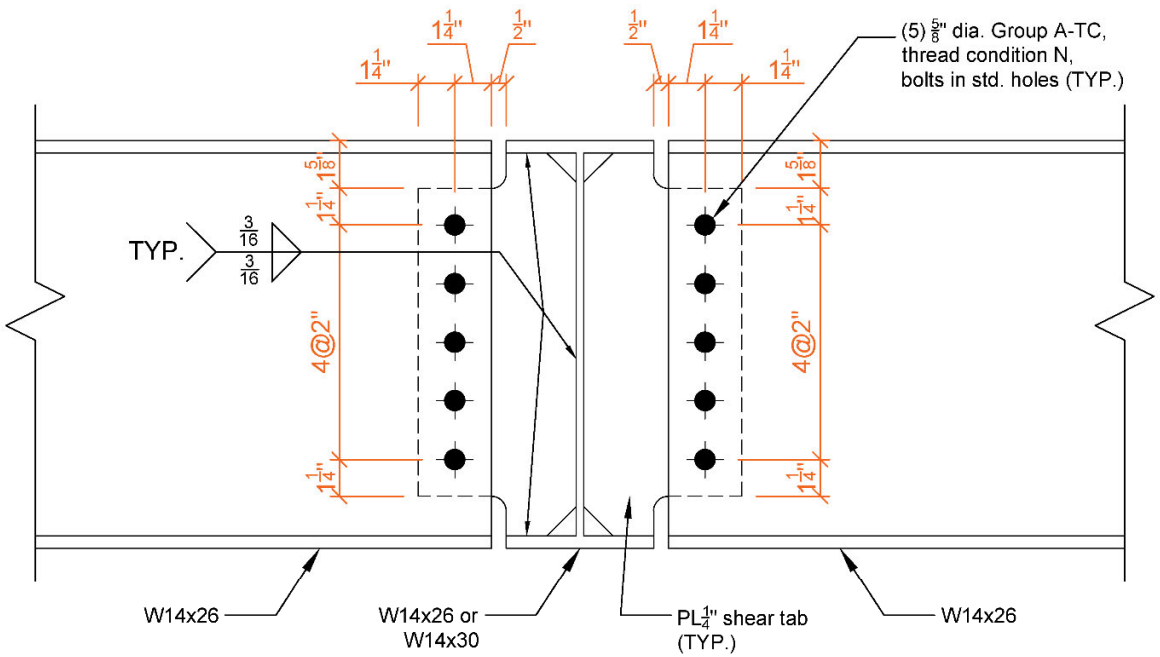

D1 Beam-to-Beam Single- or Double-Sided Connection

Figure A.13 Beam-to-Beam Connection (DWG S12)

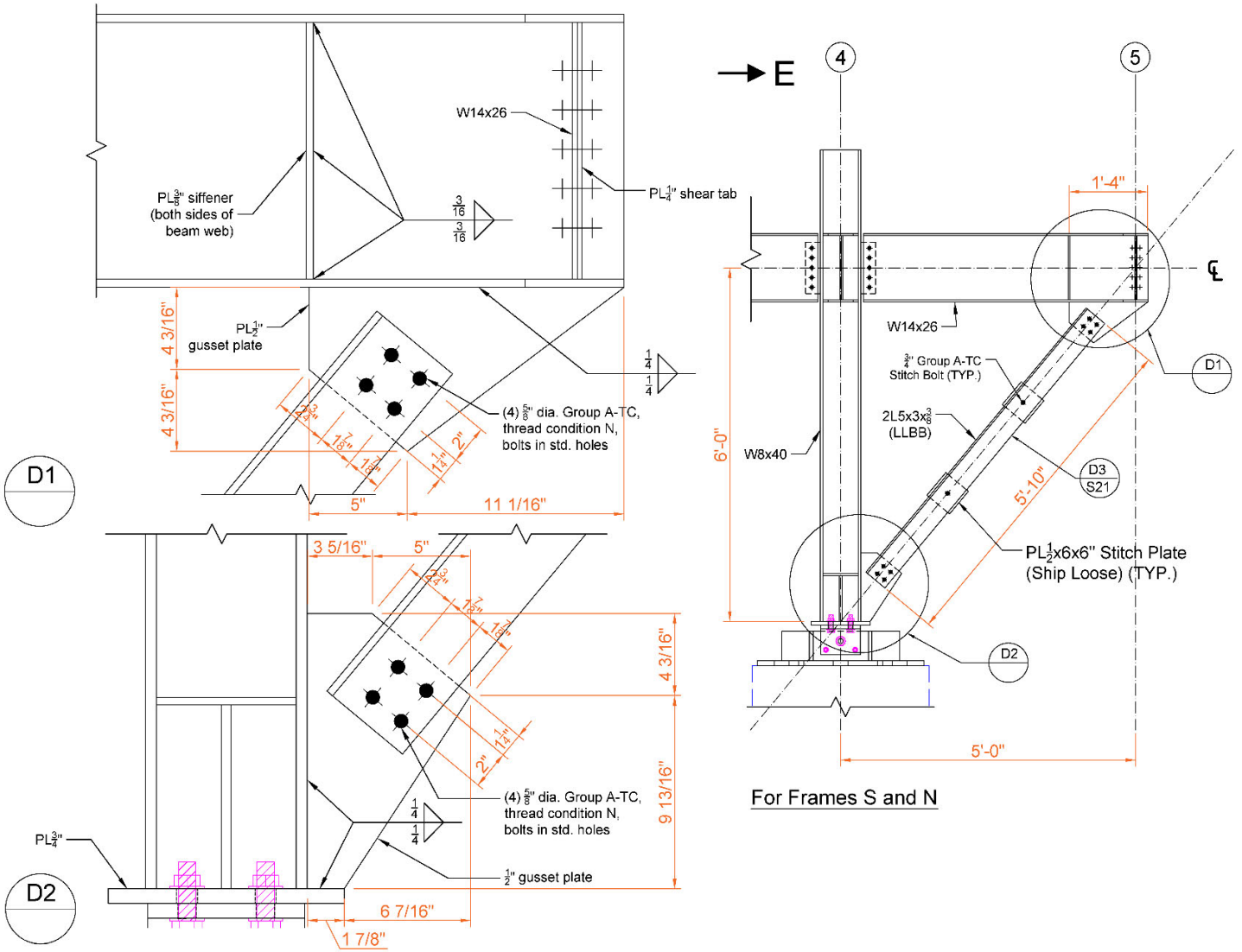

Figure A.14 Gusset Plate Connections for Longitudinal Double-Angle Brace (DWG S13)

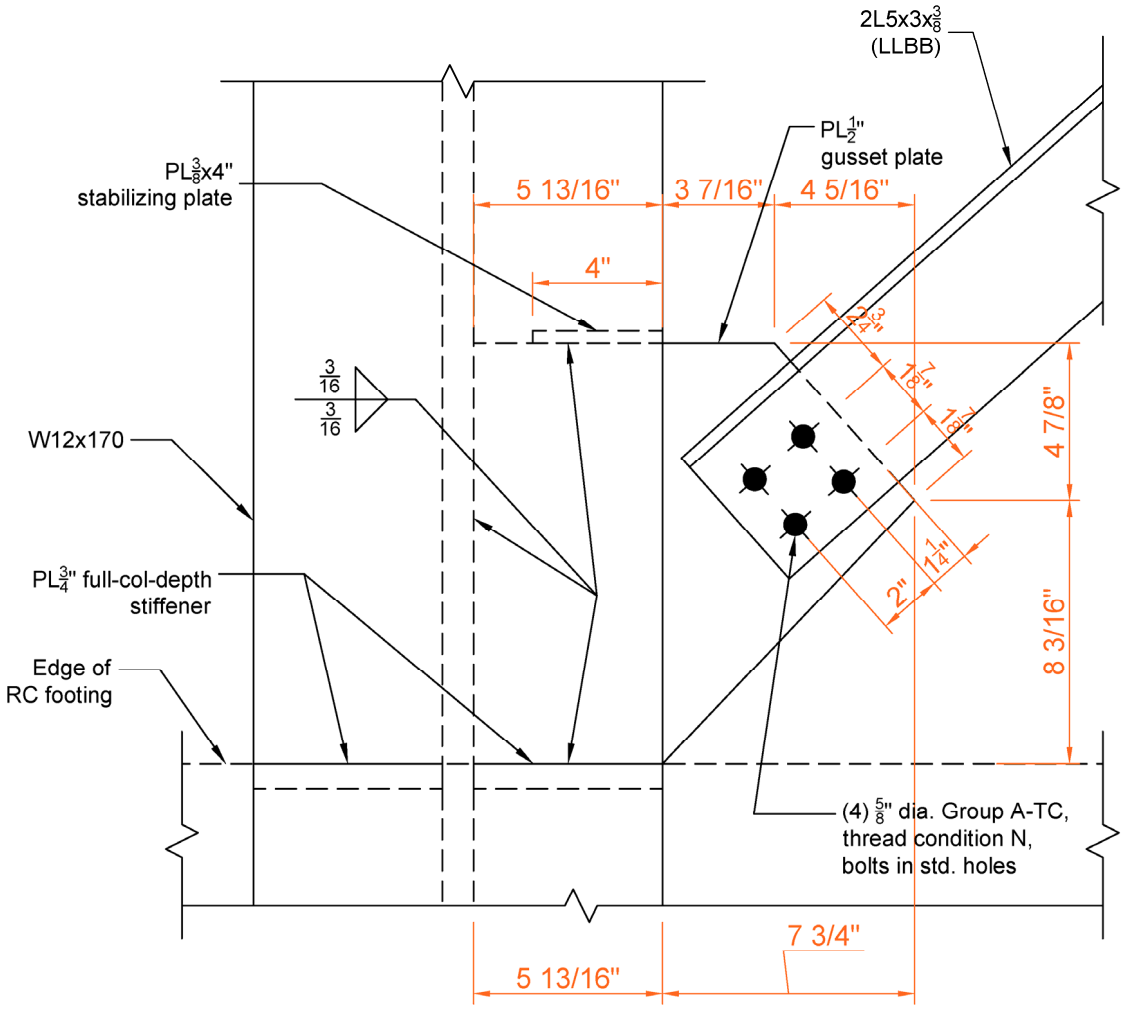

Figure A.15 Bottom Gusset Plate Connection in Frame 1 (DWG S14)

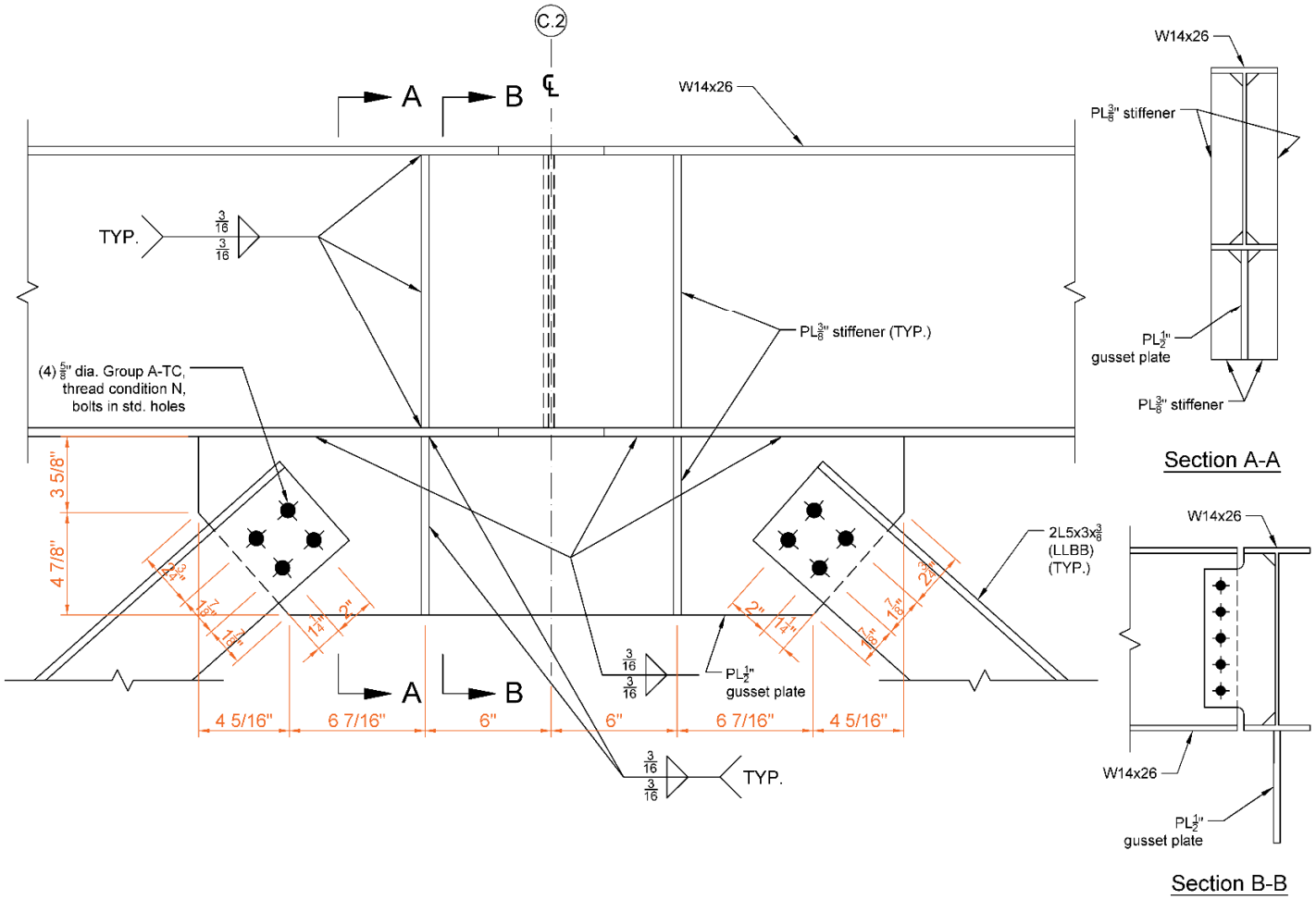

Figure A.16 Top Gusset Plate Connection in Frame 1 (DWG S15)

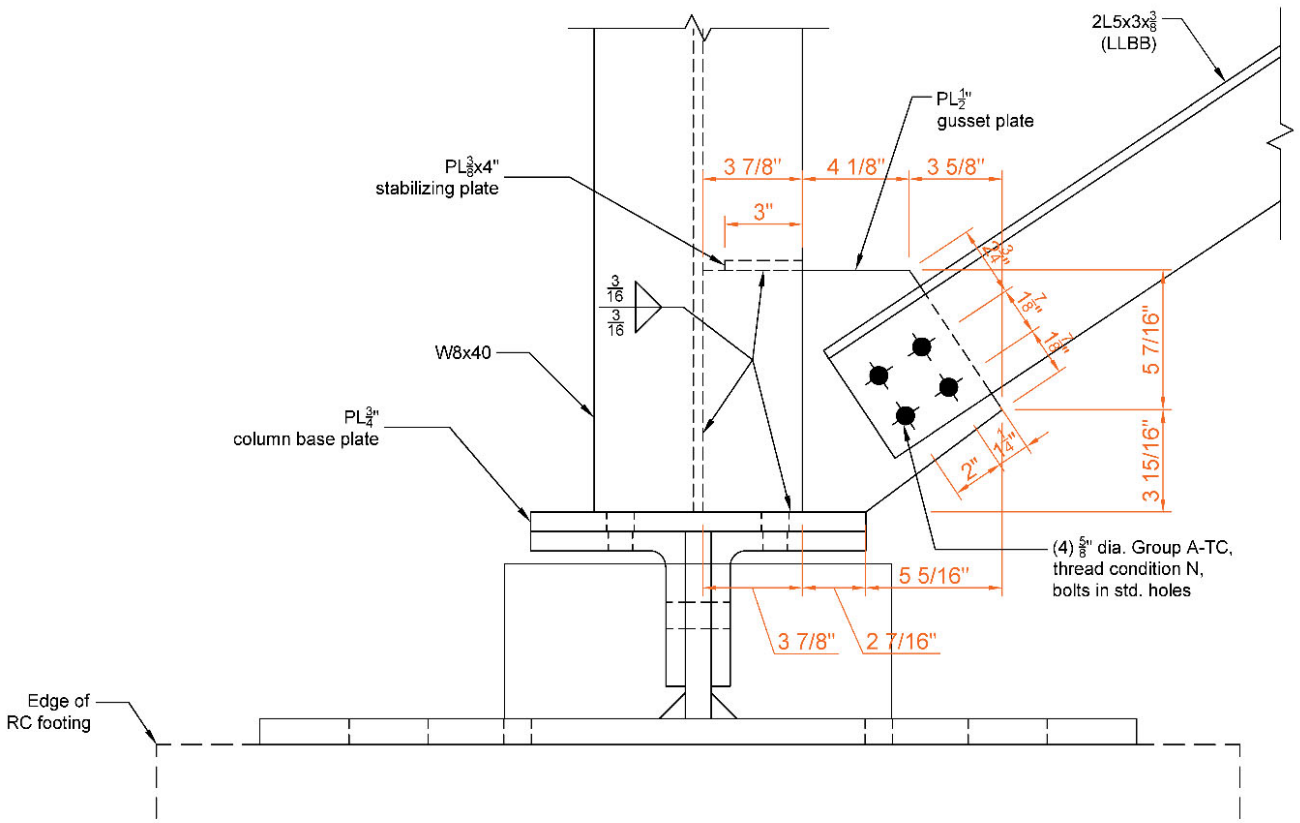

Figure A.17 Bottom Gusset Plate Connection in Frames 2, 3, and 4 (DWG S16)

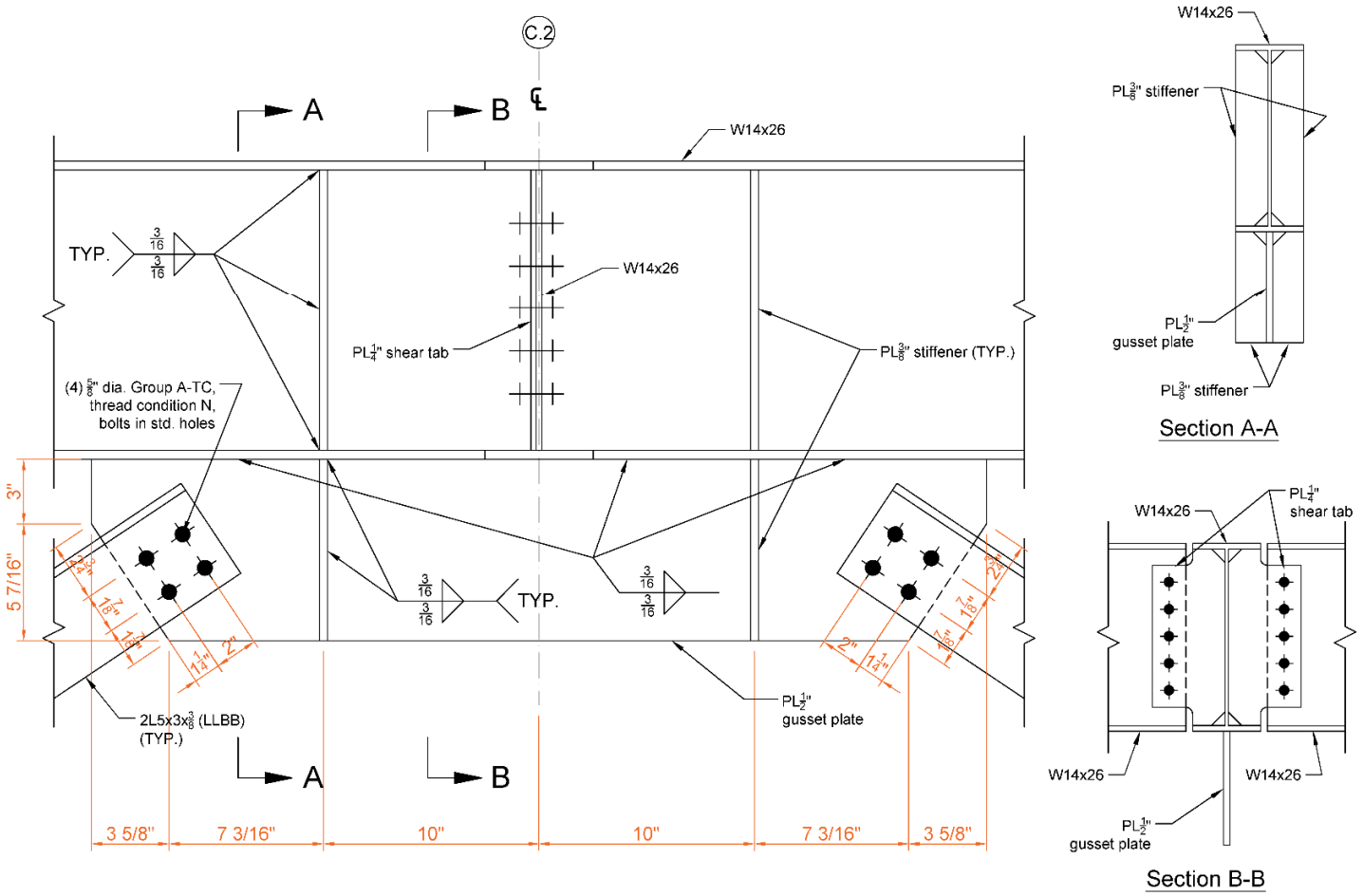

Figure A.18 Top Gusset Plate Connection in Frames 2, 3, and 4 (DWG S17)

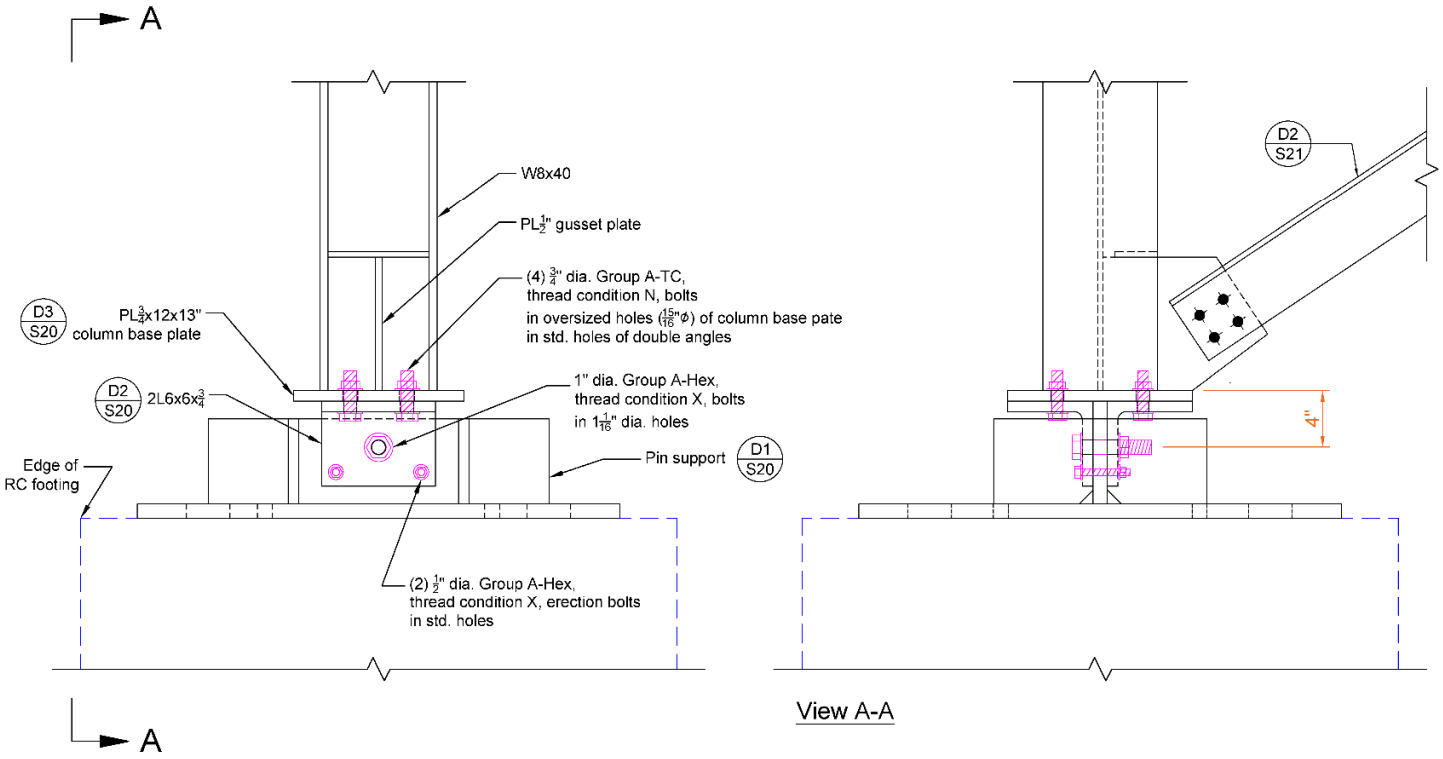

Figure A.19 Pin-Support for Gravity Columns in Frames 2 and 3 (DWG S18)

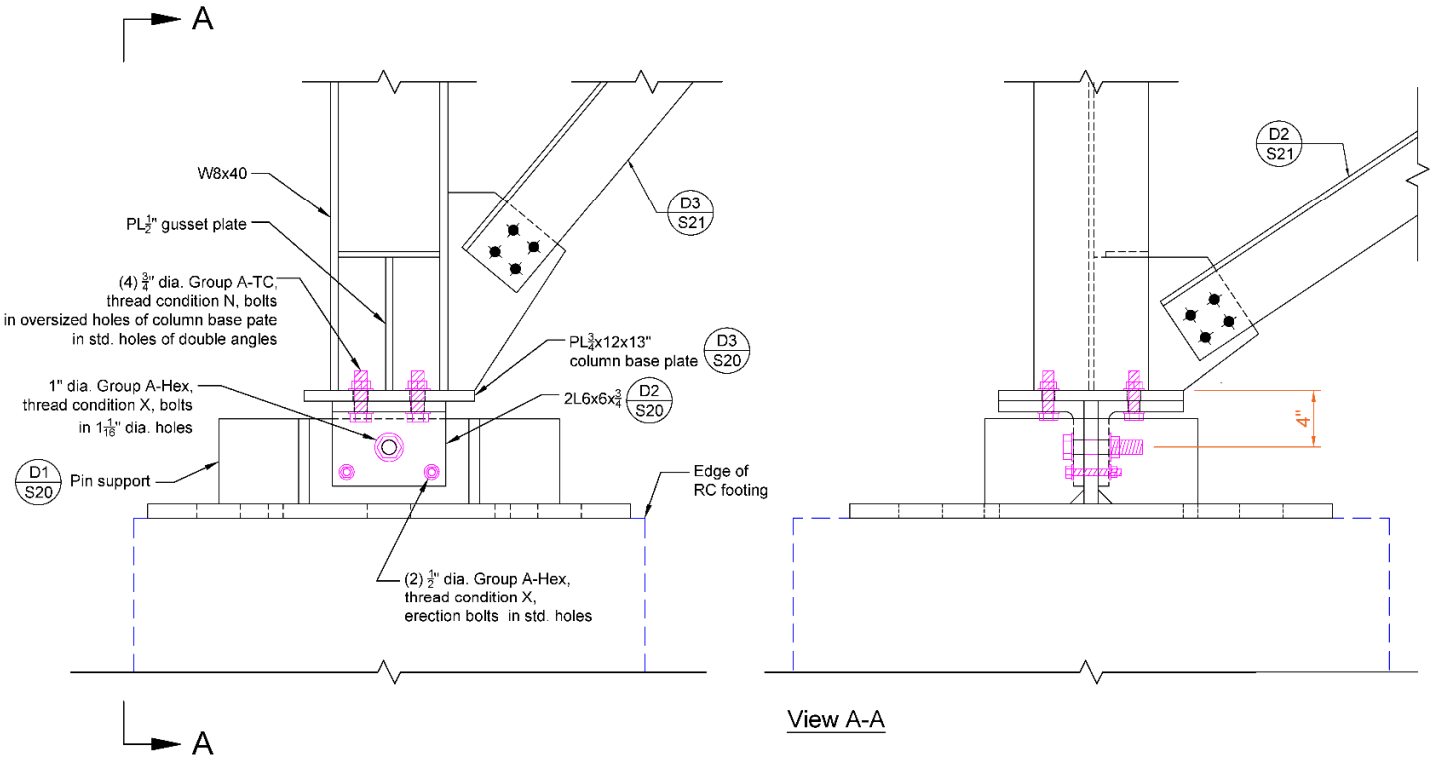

Figure A.20 Pin-Support for Gravity Columns in Frame 4 (DWG S19)

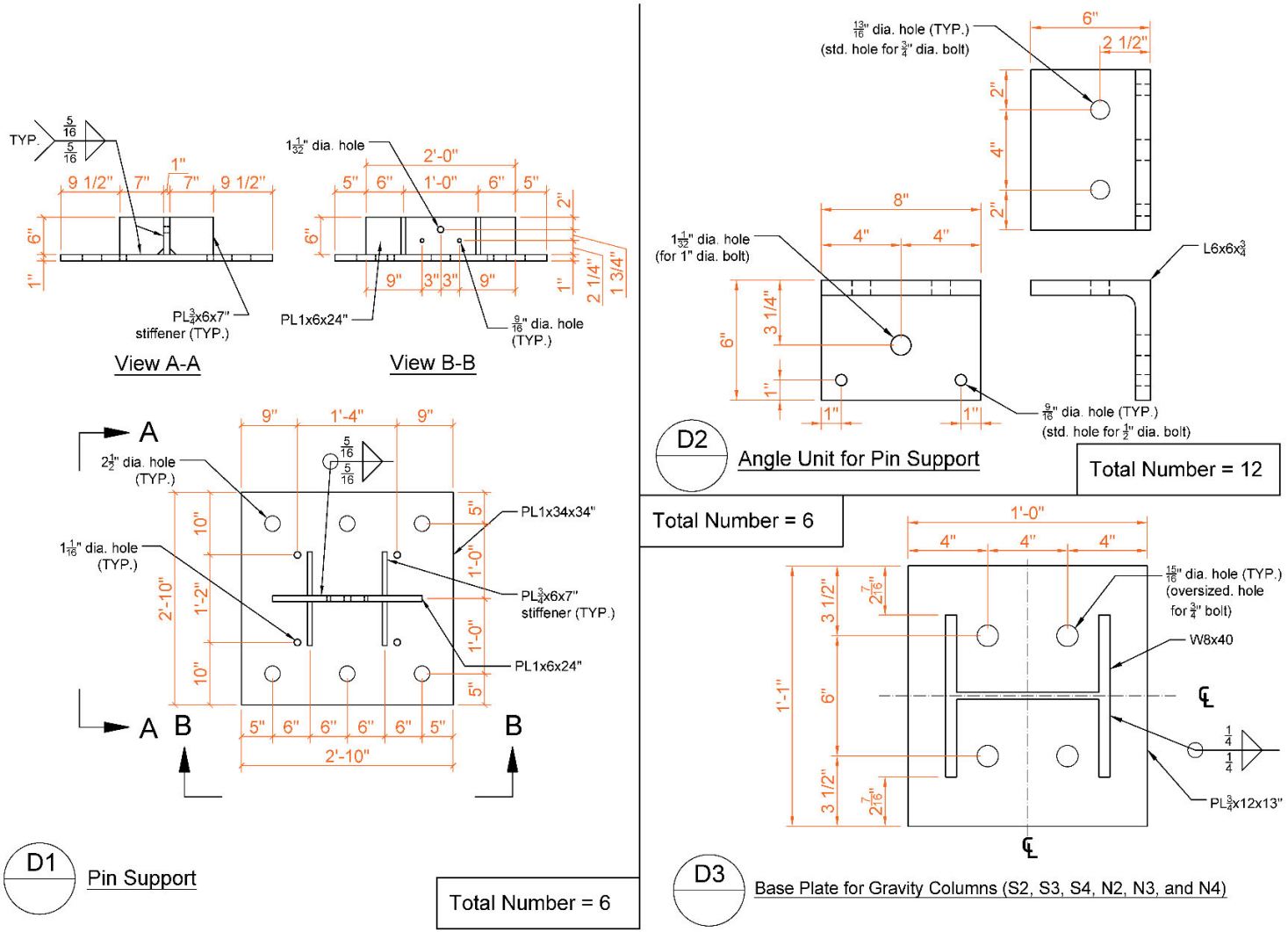

Figure A.21 Pin-Support Components and Gravity Column Base Plate (DWG S20)

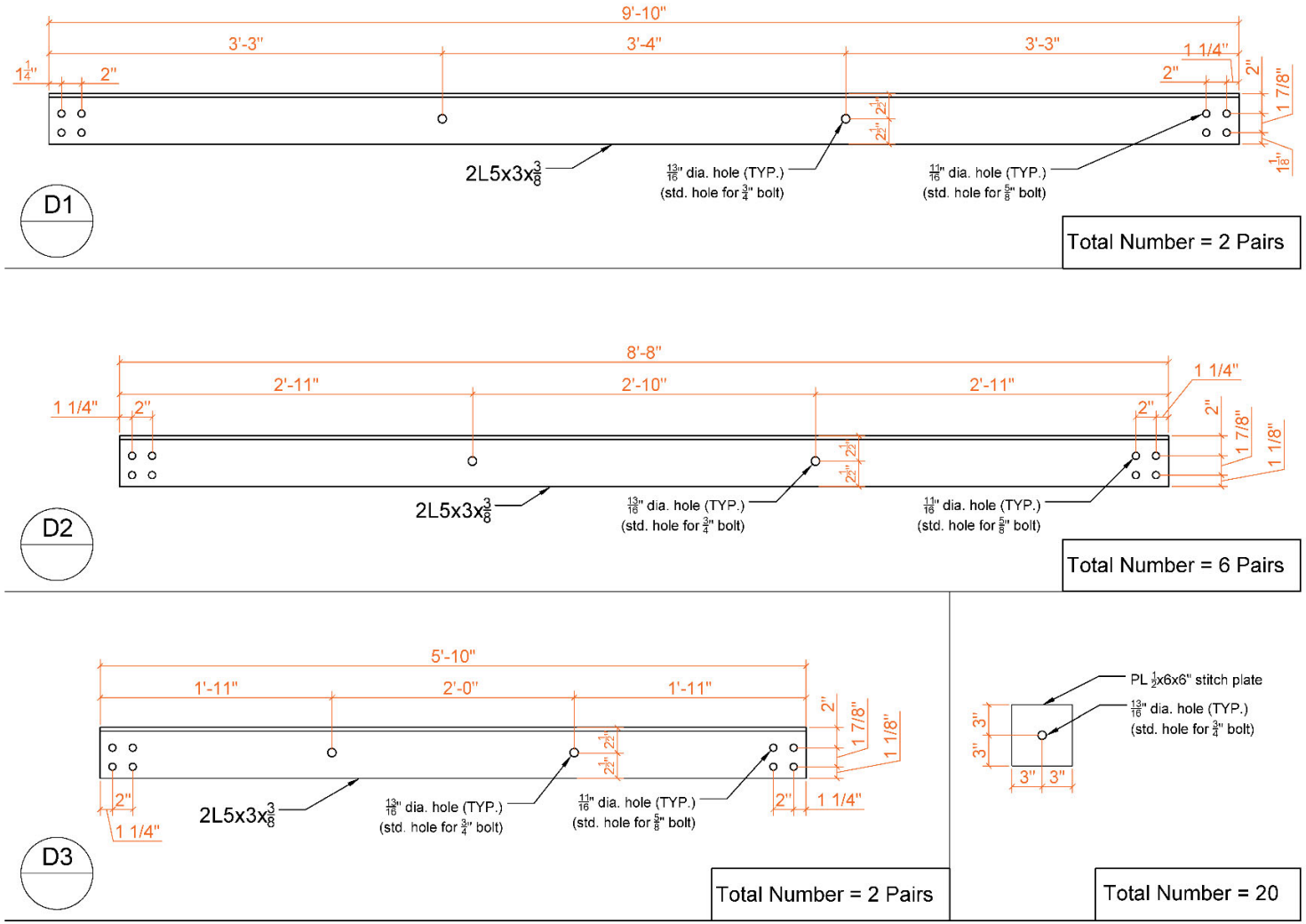

Figure A.22 Details of Double-Angle Braces (DWG S21)

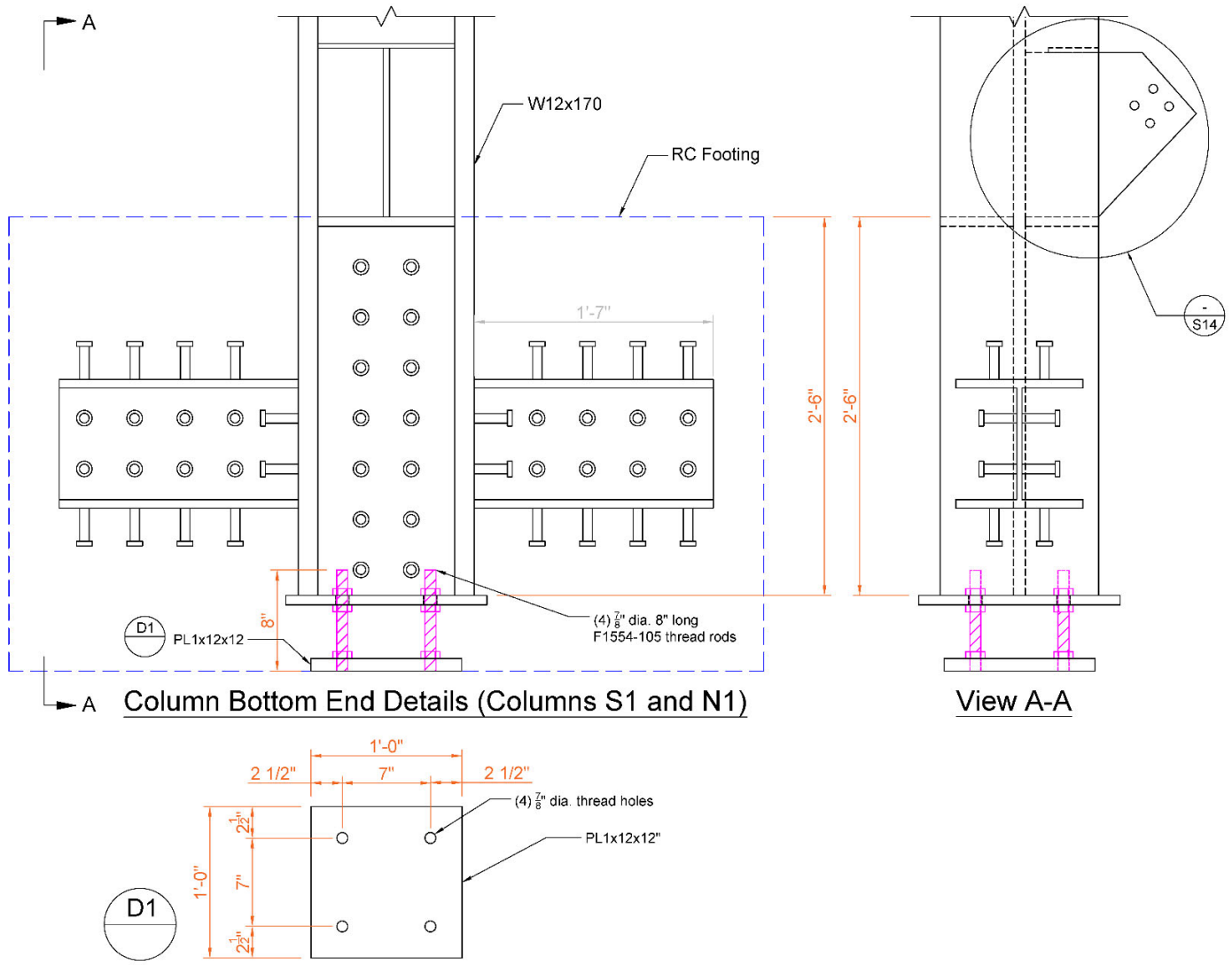

Figure A.23 Embedded Column Base Connection (DWG S22)

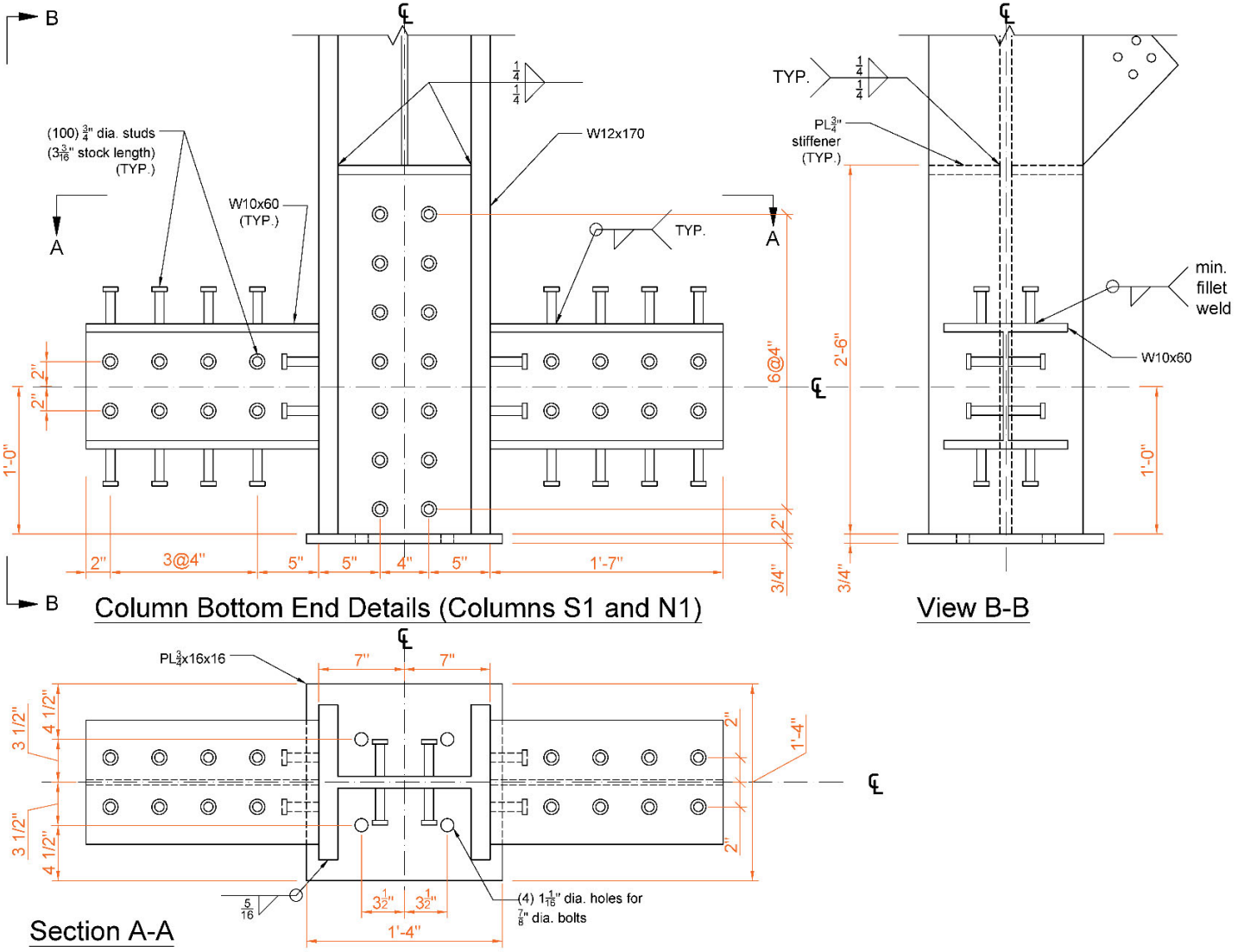

Figure A.24 Cantilever Column Bottom End Details (DWG S23)

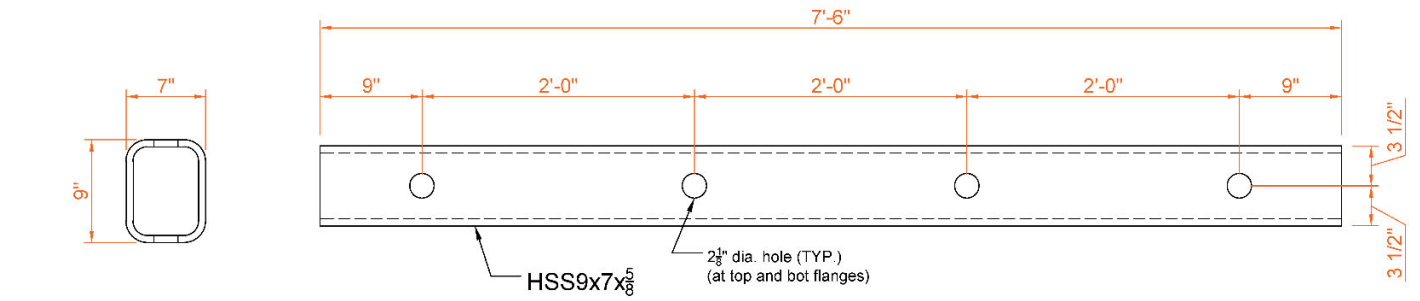

D1 Footing Clamp Beam for Columns S1 and N1

Total Number = 4

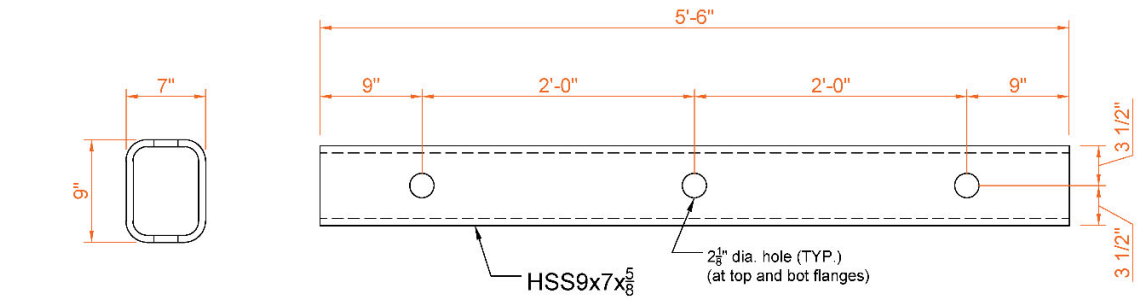

D2 Footing Clamp Beam for Columns S4 and N4

Total Number = 4

Figure A.25 Clamping Beams (DWG S24)

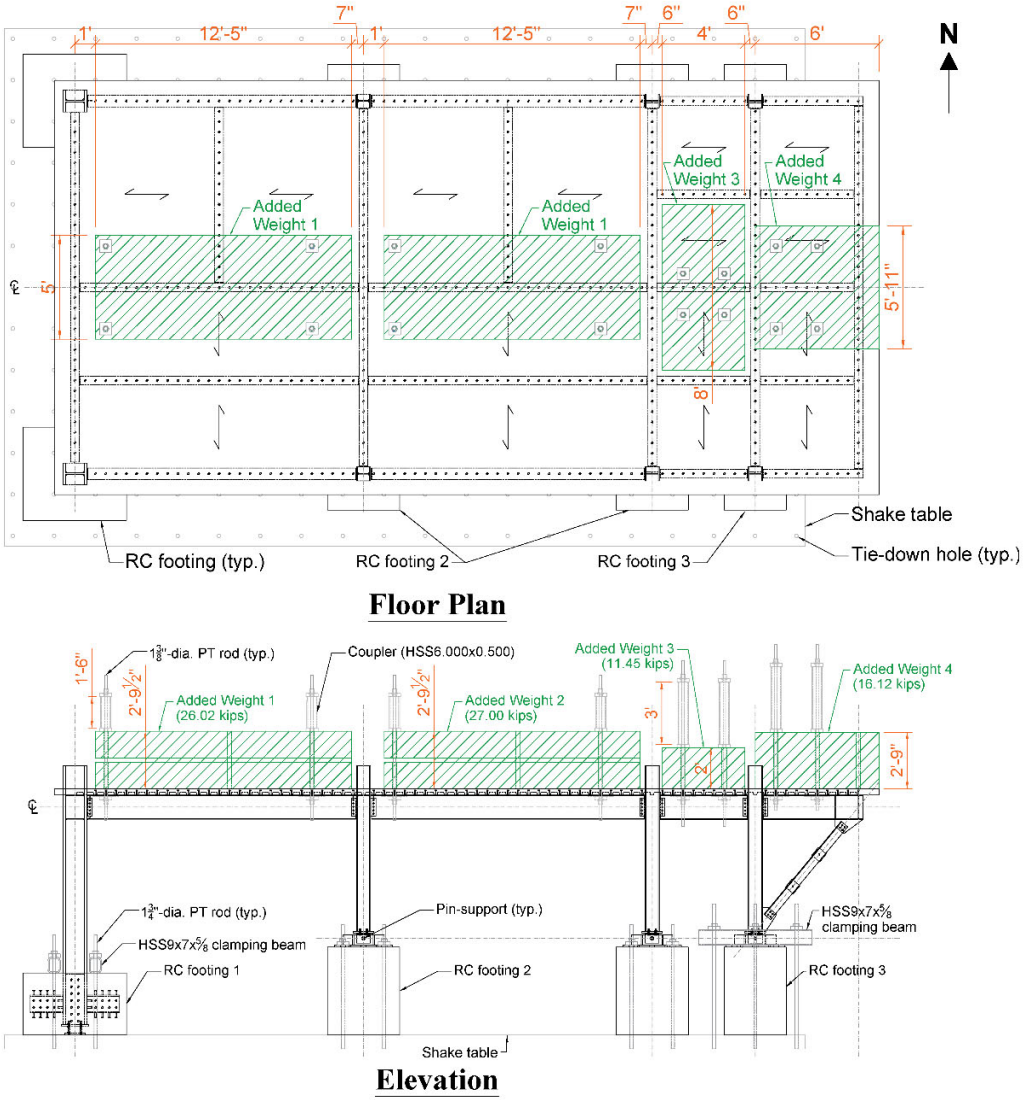

Figure A.26 Added-on Mass Blocks Attachment Details (DWG S25)

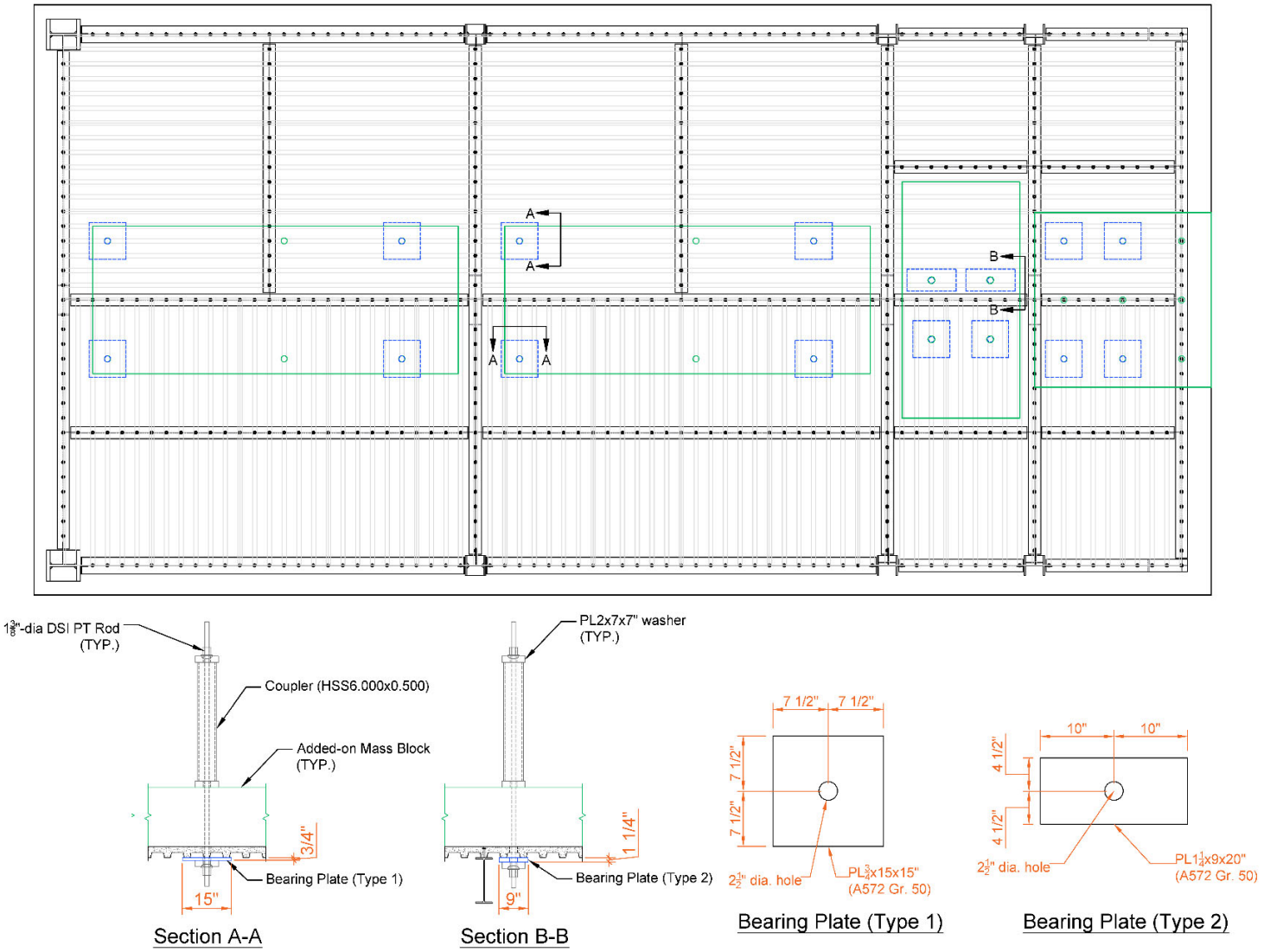

Figure A.27 Details for Clamping Added-on Mass Blocks (DWG S26)

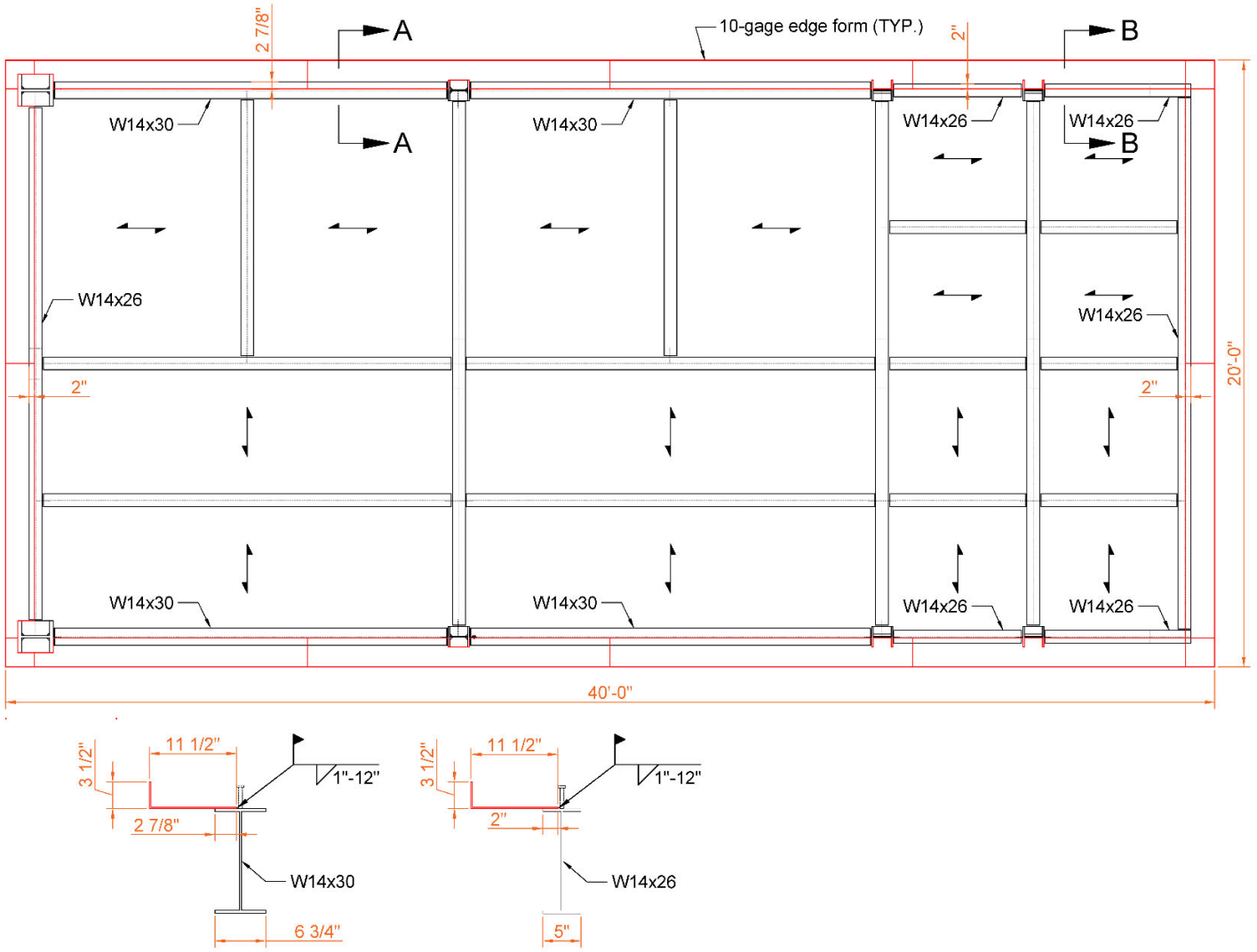

Figure A.28 Slab Edge Form Layout (DWG S27)

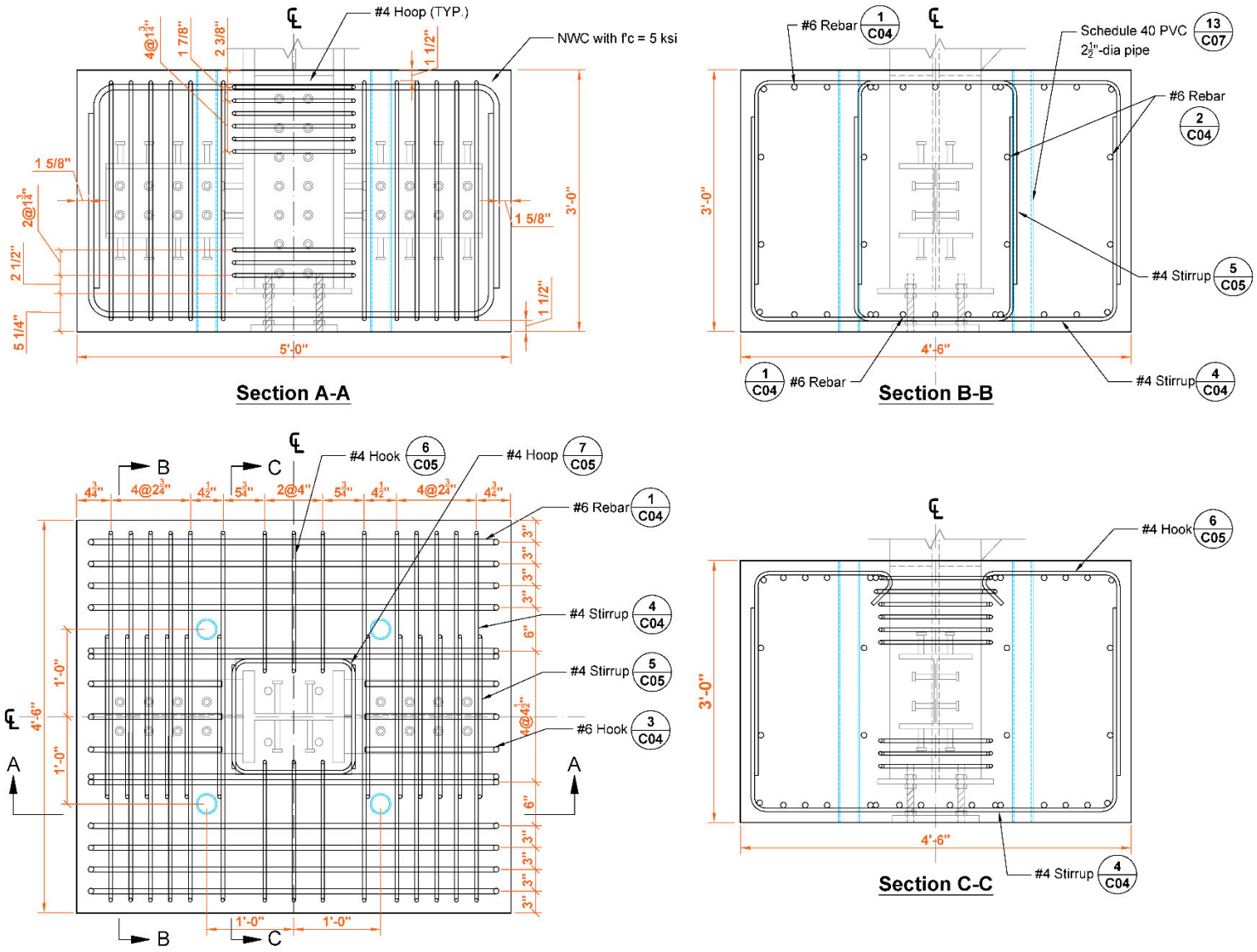

Figure A.29 RC Footing 1 for Columns S1 and N1 (DWG C01)

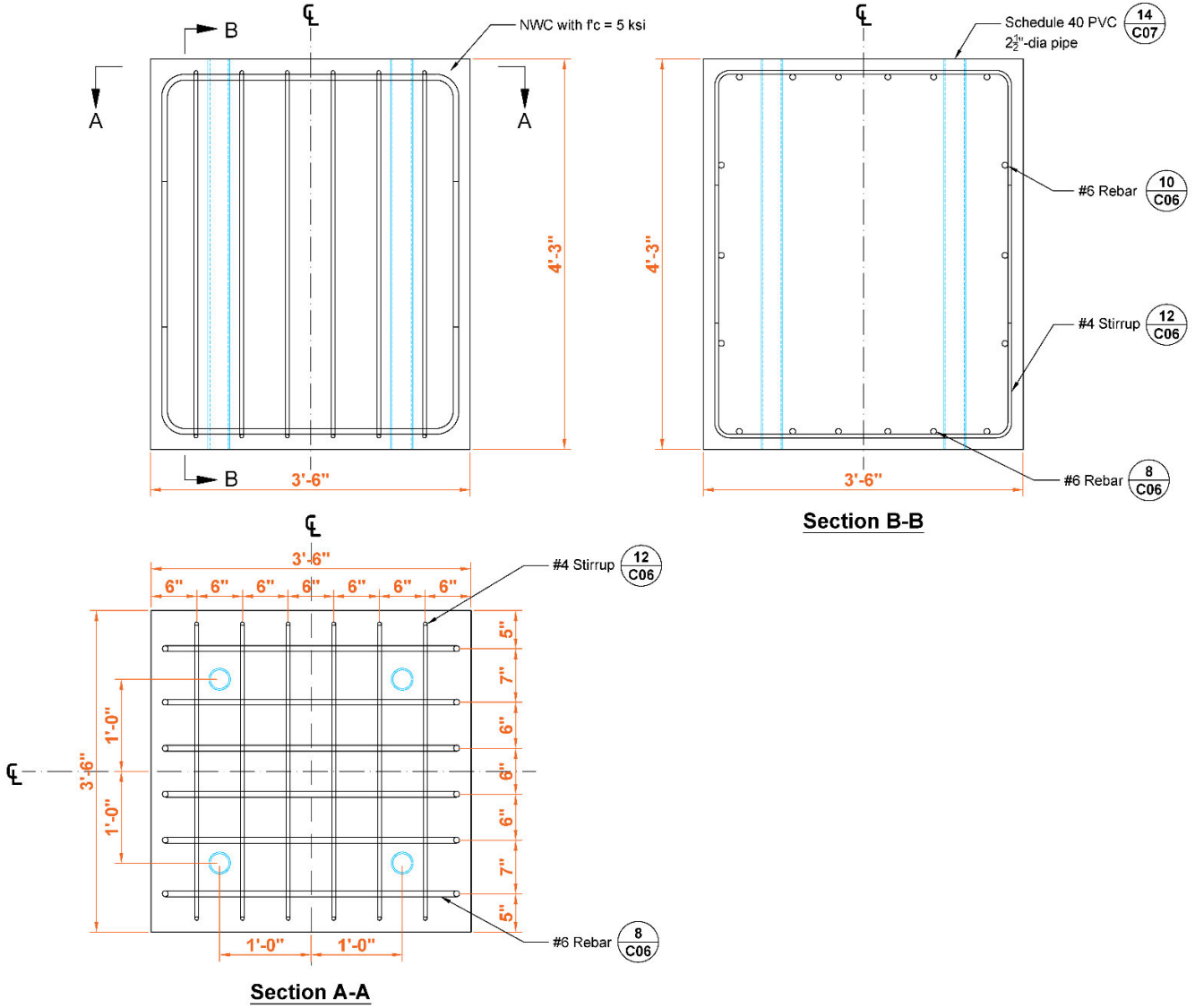

Figure A.30 RC Footing 2 for Columns S2, S3, N2 and N3 (DWG C02)

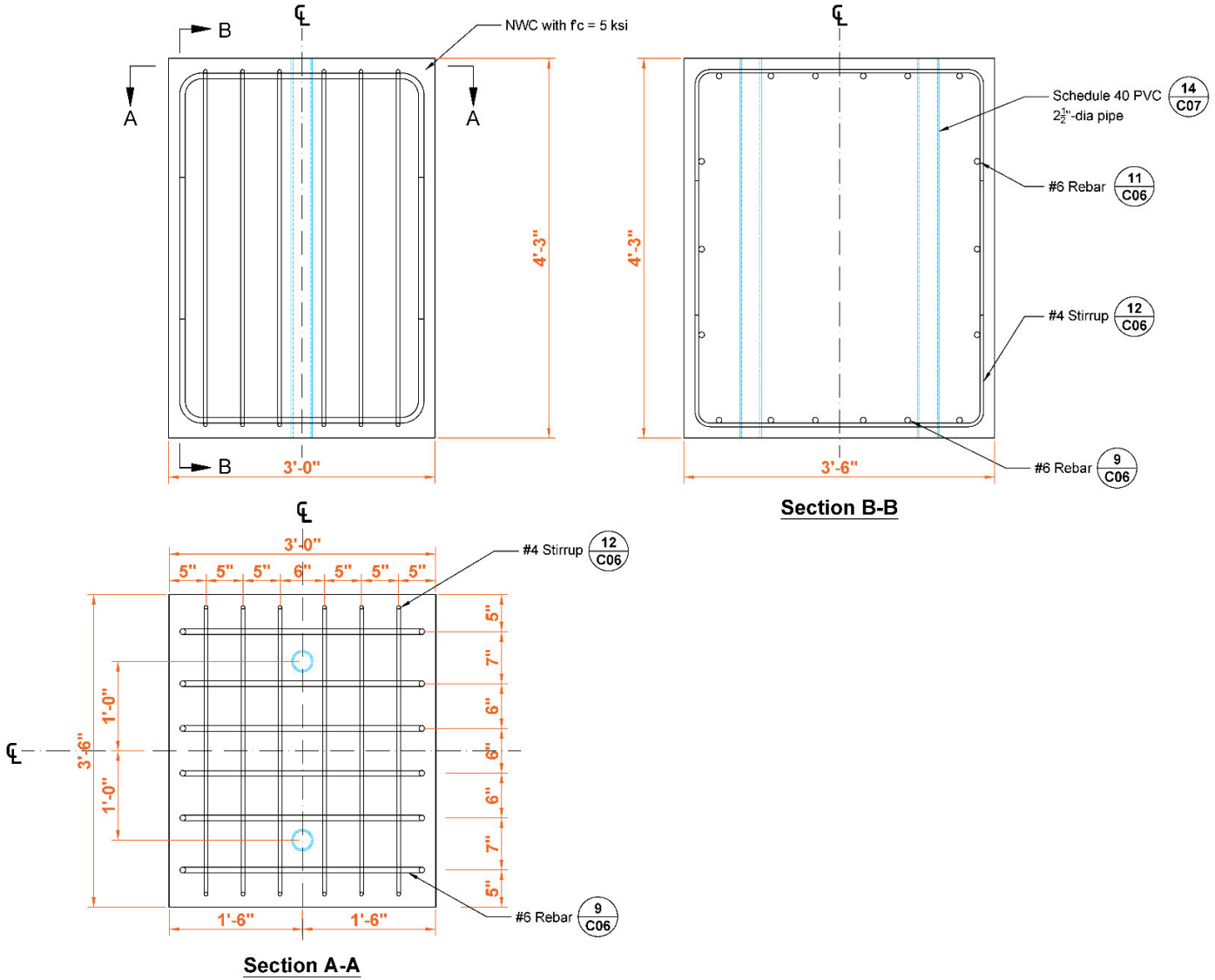

Figure A.31 RC Footing 3 for Columns S4 and N4 (DWG C03)

Item	Bar Size	Material	Length	Number	Shape
1	#6	ASTM A706 GR 60	9'-4"	54	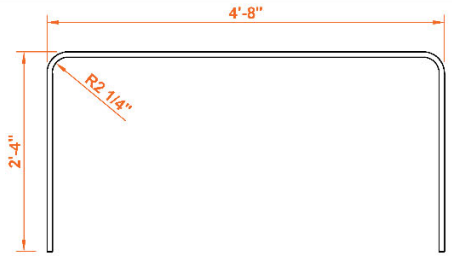
2	#6	ASTM A706 GR 60	4'-8"	16	
3	#6	ASTM A706 GR 60	3'-10½"	12	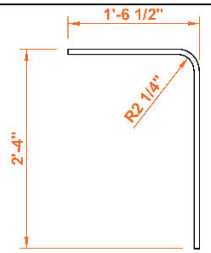
4	#4	ASTM A706 GR 60	8'-10½"	54	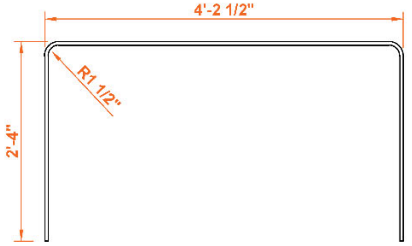

Figure A.32 Rebar Schedule-Page 1 (DWG C04)

Item	Bar Size	Material	Length	Number	Shape
5	#4	ASTM A706 GR 60	6'-6"	48	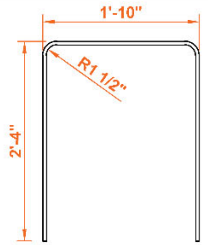
6	#4	ASTM A706 GR 60	7'-11½"	12	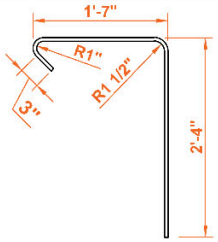
7	#4	ASTM A706 GR 60	3'-11"	36	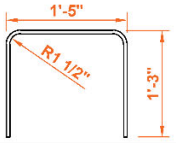
8	#6	ASTM A706 GR 60	8'-9"	48	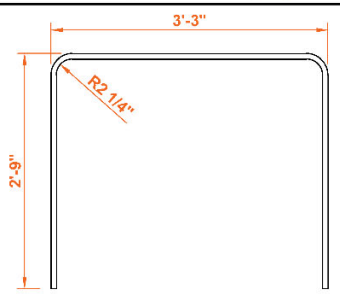

Figure A.33 Rebar Schedule-Page 2 (DWG C05)

Item	Bar Size	Material	Length	Number	Shape
9	#6	ASTM A706 GR 60	8'-3"	24	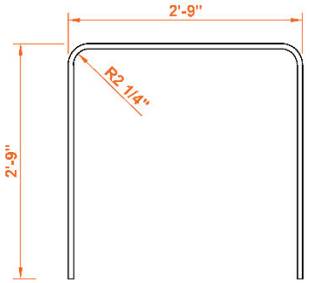
10	#6	ASTM A706 GR 60	3'-3"	24	
11	#6	ASTM A706 GR 60	2'-9"	12	
12	#4	ASTM A706 GR 60	8'-9"	72	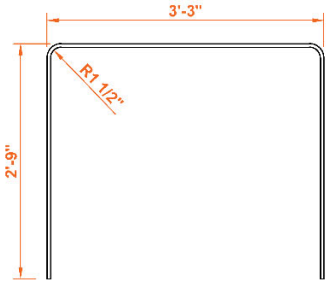

Figure A.34 Rebar Schedule-Page 3 (DWG C06)

Appendix B. Design Drawings for Phase 2 Test Specimen and Setup

This Appendix provides the complete design drawings for fabrication of Phase 2 test specimen and setup. Table B.1 lists the brief description of drawings.

Table B.1 List of Drawings for Phase 2 Testing

Drawing No.	Content
NS00	Test Setup
NS01	Test Building Roof Plan
NS02	Frame S Elevation
NS03	Frame N Elevation
NS04	Frame 1 Elevation
NS05	Frame 2 Elevation
NS06	Frame 3 Elevation
NS07	Frame 4 Elevation
NS08	Roof Beams
NS09	All Flange Weld (AFW) Collector-to-Column Connection
NS10	Top Flange Weld (TFW) Collector-to-Column Connection
NS11	Bolted Web (BW) Collector-to-Column Connection at Column Line 3
NS12	Bolted Web (BW) Collector-to-Column Connection at Column Line 4
NS13	Roof Beam-to-Beam Connection
NS14	Top Gusset Plate Connection in 2nd Story of Frame 1
NS15	Bottom Gusset Plate Connection in 2nd Story of Frame 1
NS16	Top Gusset Plate Connection in 2nd Story of Frames 2 and 3
NS17	Bottom Gusset Plate Connection in 2nd Story of Frames 2 and 3
NS18	Details of Double-Angle Braces in 2nd Story
NS19	Plan View of Stopper Layouts
NS20	Side View of Stopper Layouts
NS21	Details of Stoppers
NS22	Roof Added-on Mass Layouts

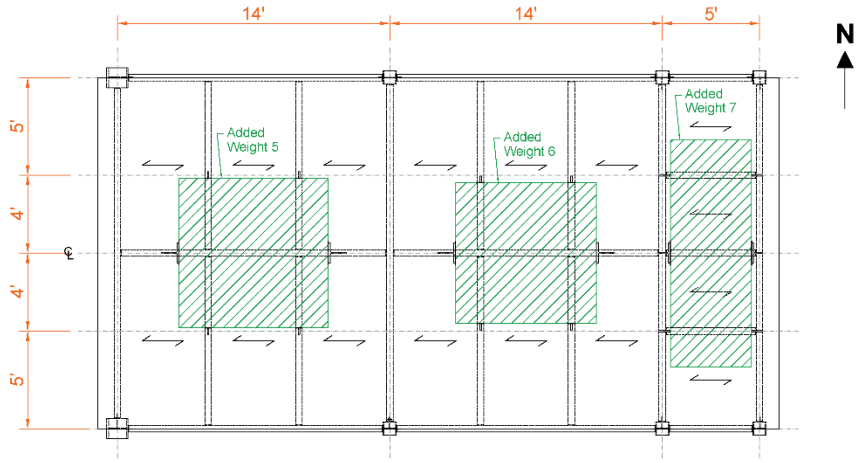

Roof Plan

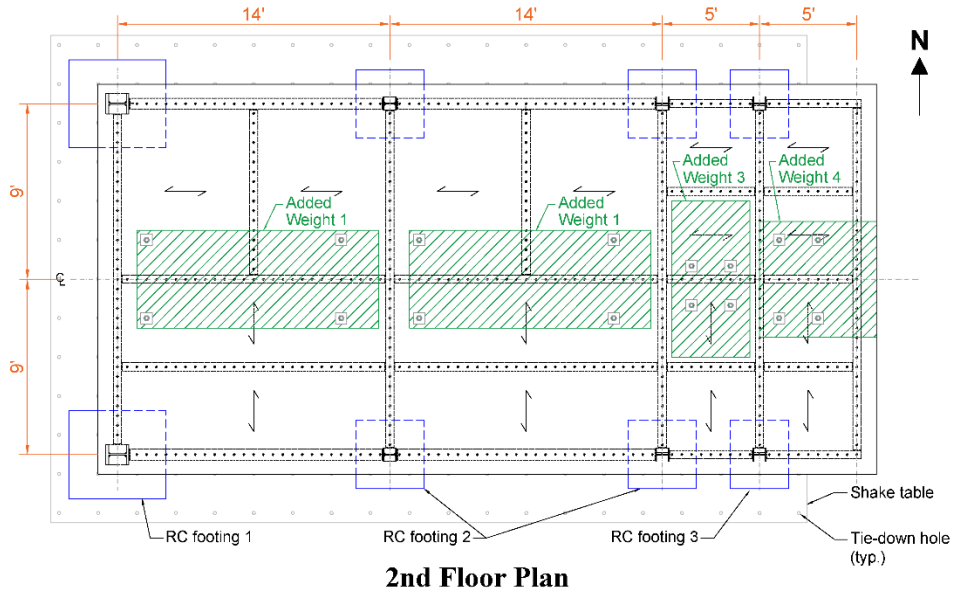

2nd Floor Plan

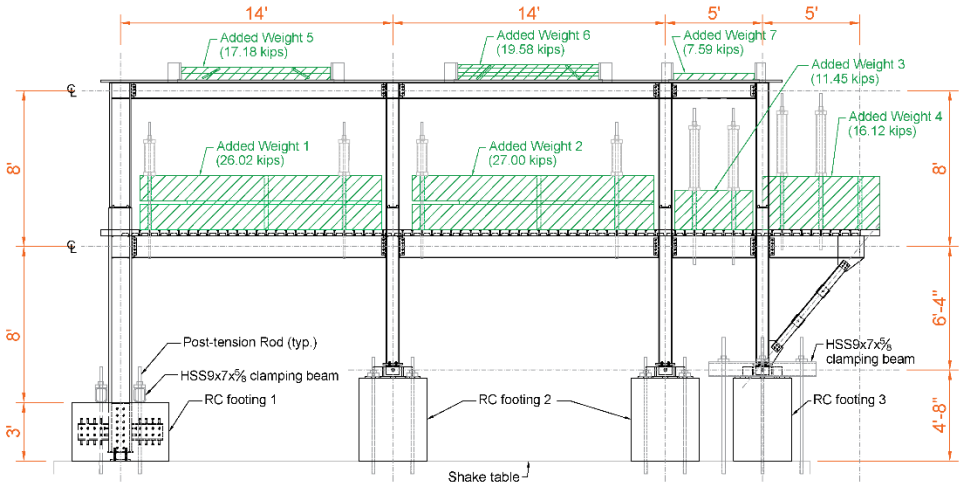

Elevation

Figure B.1 Test Setup (DWG NS00)

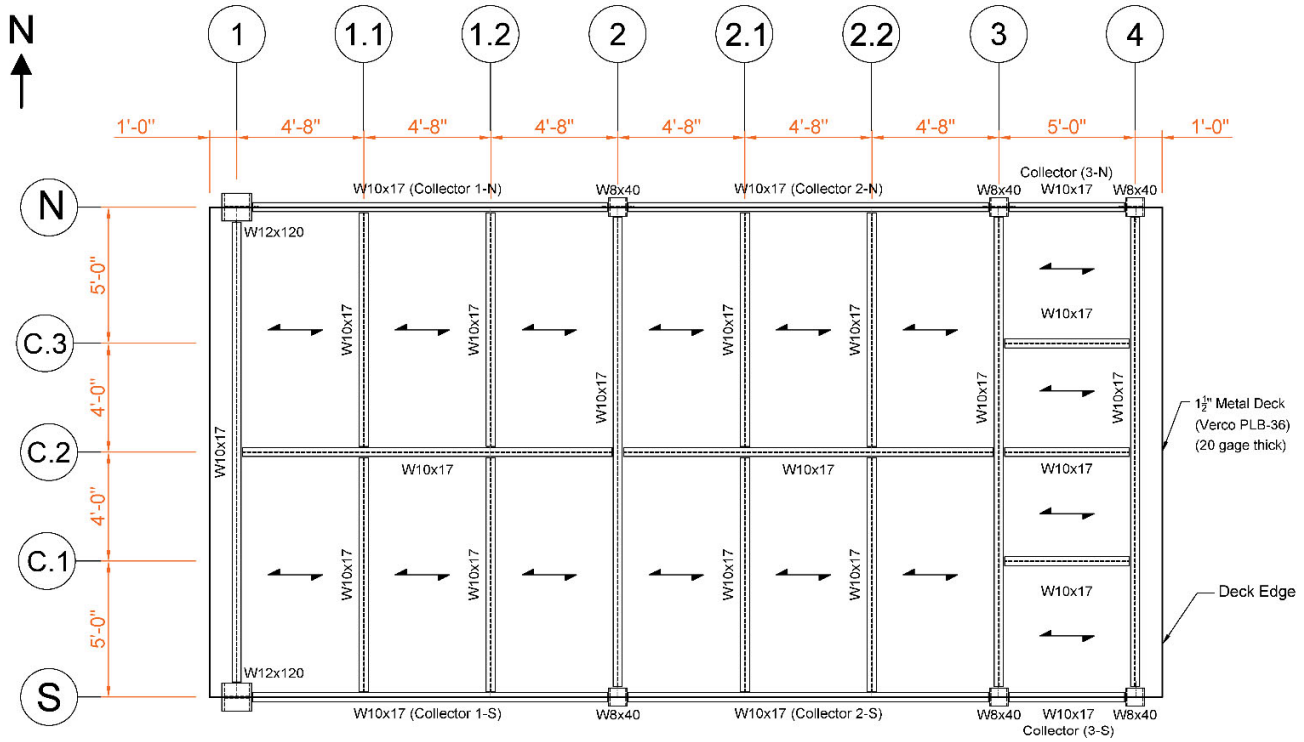

Roof Deck Details

1. Verco PLB-36, $1\frac{1}{2}$" deep, 20-gage thick metal deck
2. 36/7 weld pattern at supports
3. Sidelaps connected with PunchLok II Tool with VSC2 @ 4" attachment

Notes

1. Use A992 steel for W shapes and A36 steel for angles
2. Use A572 Gr. 50 steel for all plates
3. All bolts to be fully pretensioned
4. Use E70 electrode

Figure B.2 Test Building Roof Plan (DWG NS01)

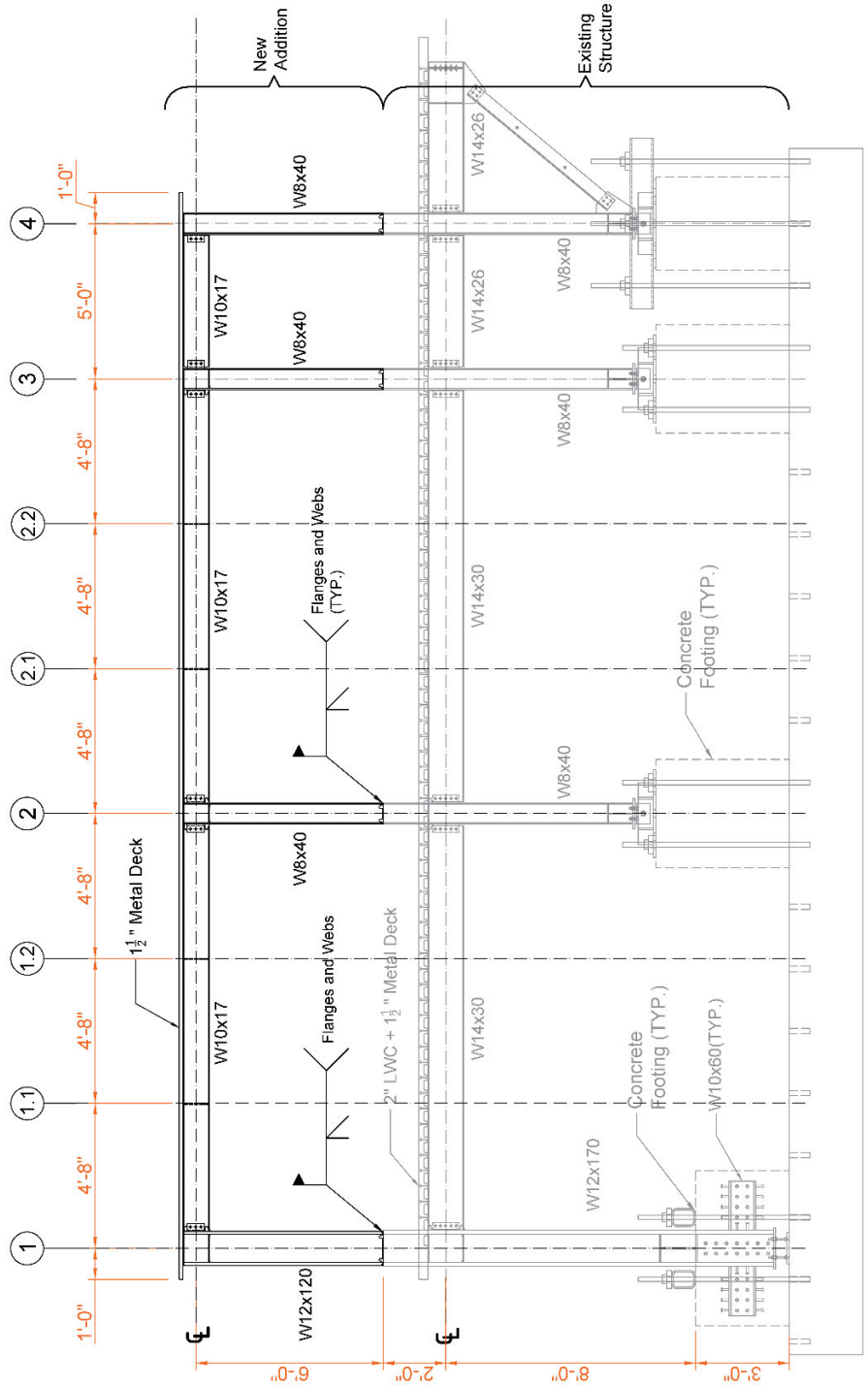

Figure B.3 Frame S Elevation (DWG NS02)

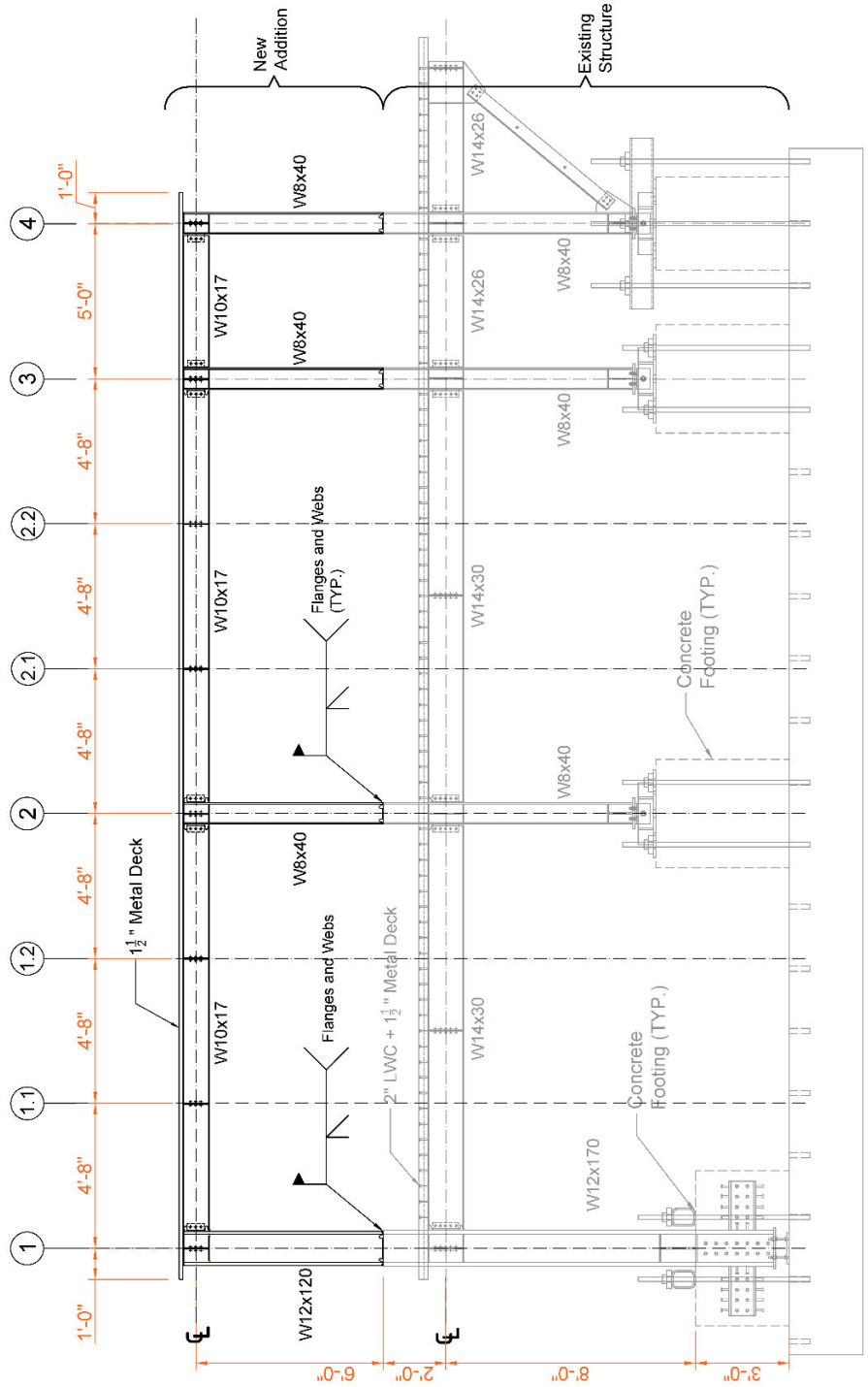

Figure B.4 Frame N Elevation (DWG NS03)

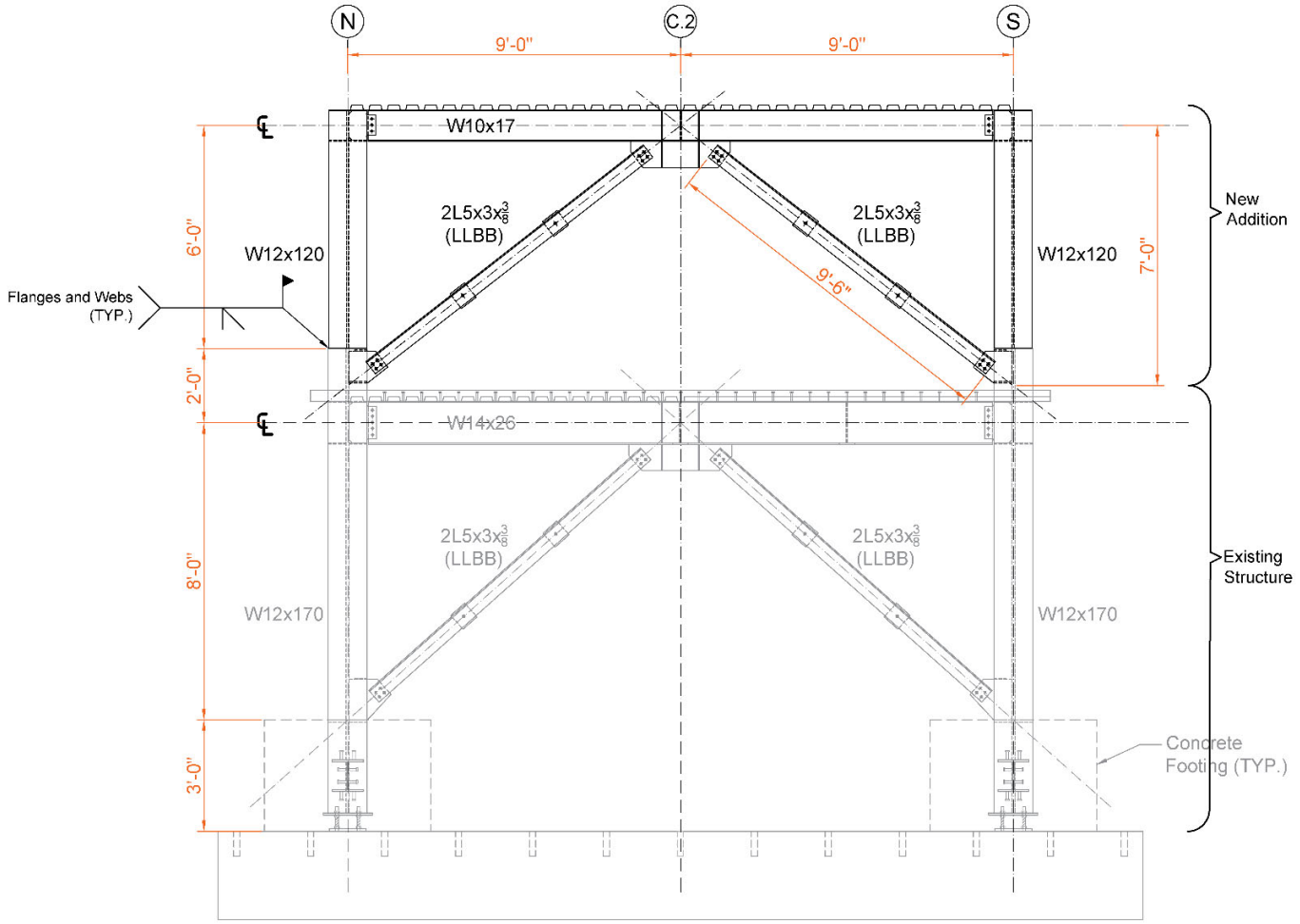

Figure B.5 Frame 1 Elevation (DWG NS04)

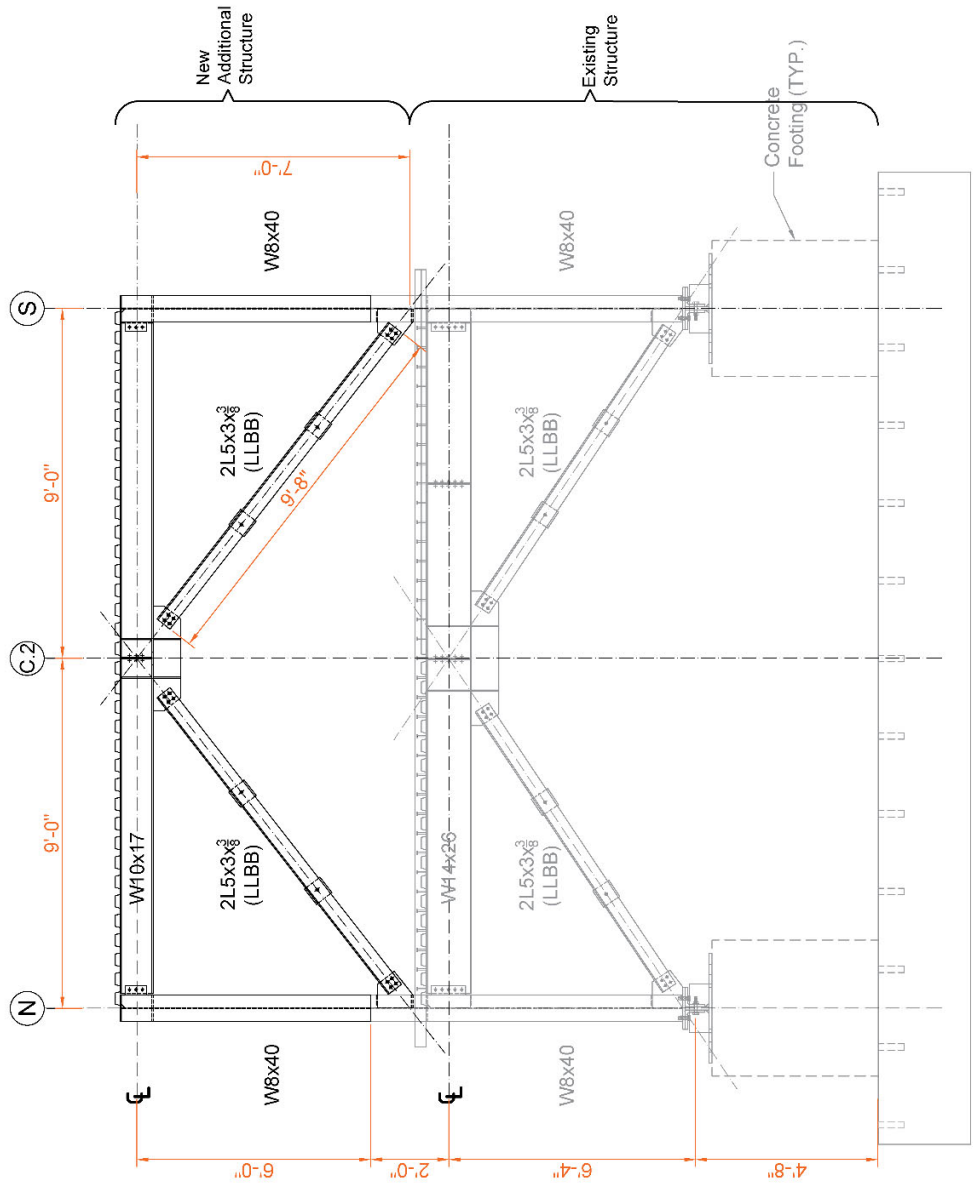

Figure B.6 Frame 2 Elevation (DWG NS05)

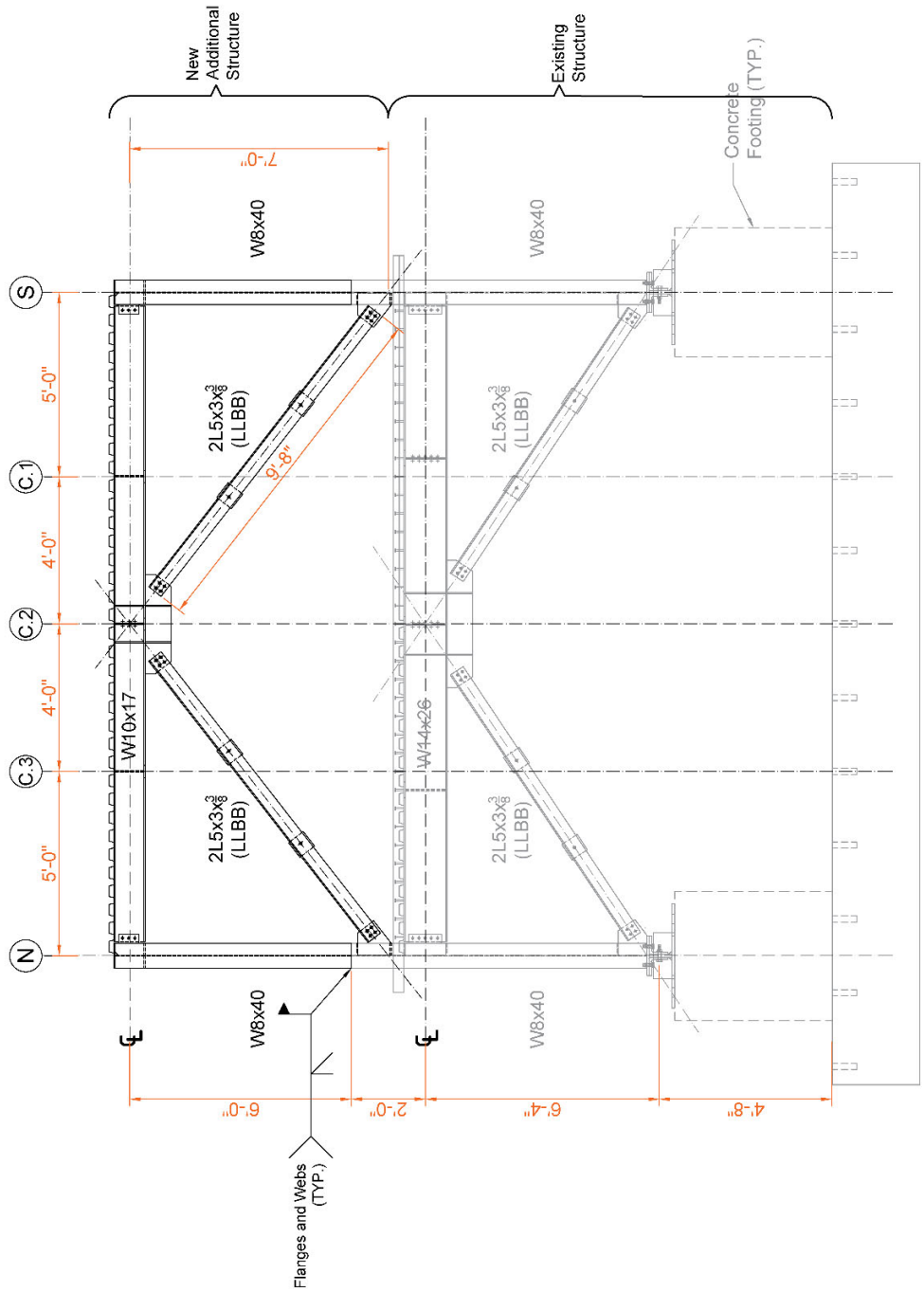

Figure B.7 Frame 3 Elevation (DWG NS06)

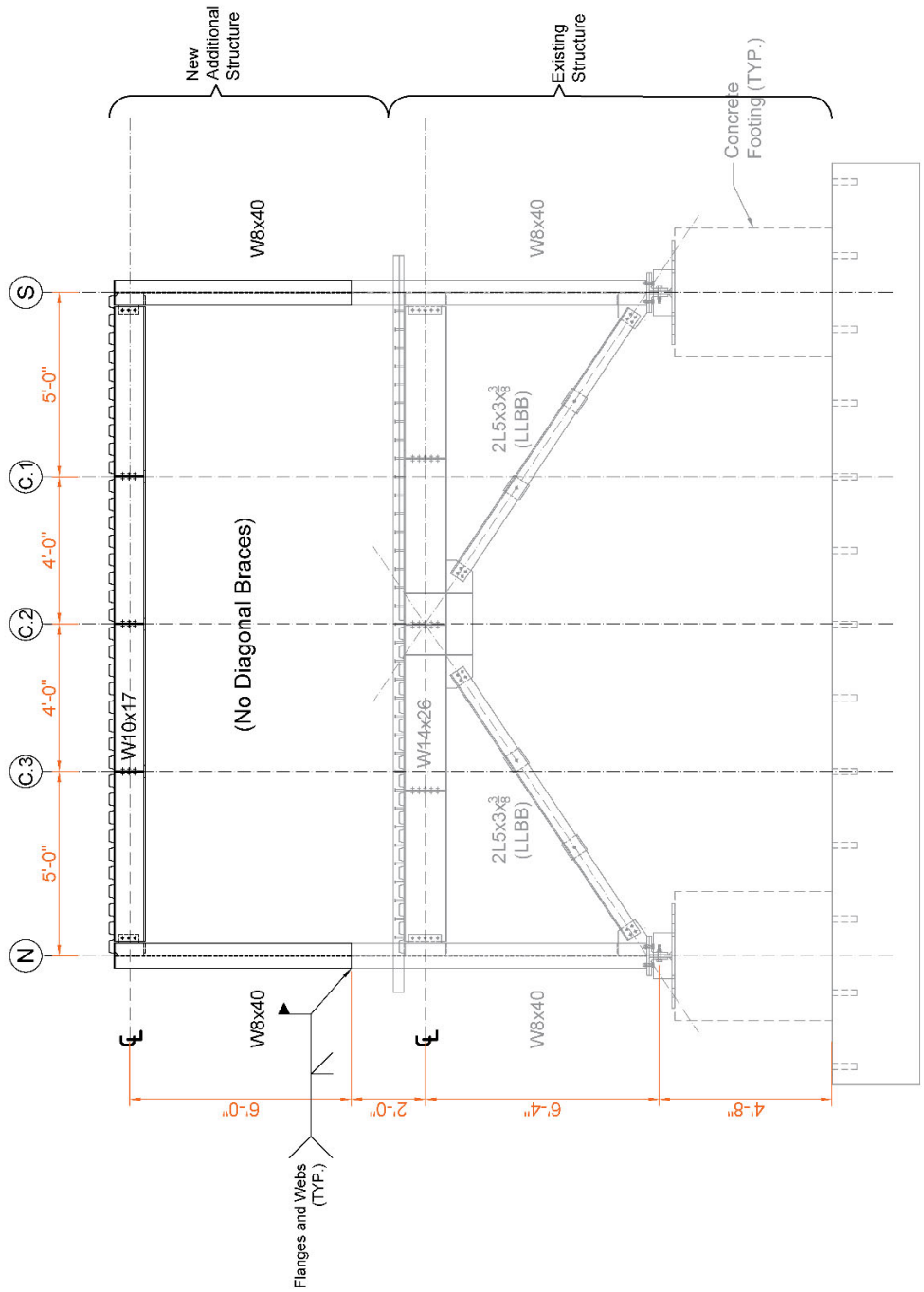

Figure B.8 Frame 4 Elevation (DWG NS07)

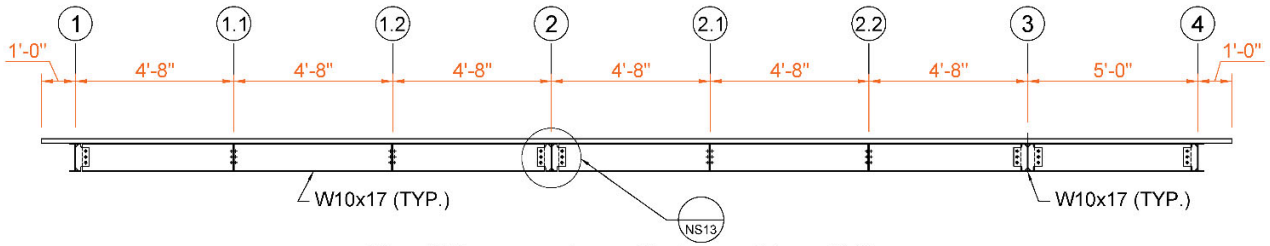

Roof Beams along Column Line C.2

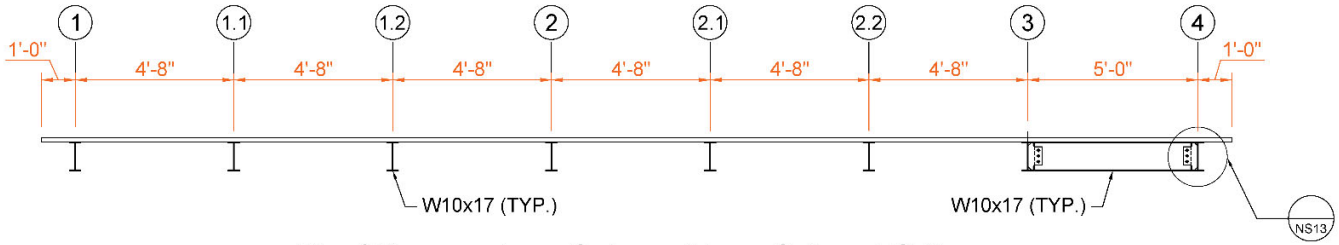

Roof Beams along Column Lines C.1 and C.2

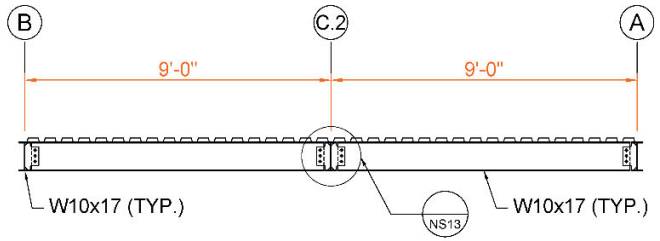

Roof Beams along Column Lines 1.1, 1.2, 2.1 and 2.2

Figure B.9 Roof Beams (DWG NS08)

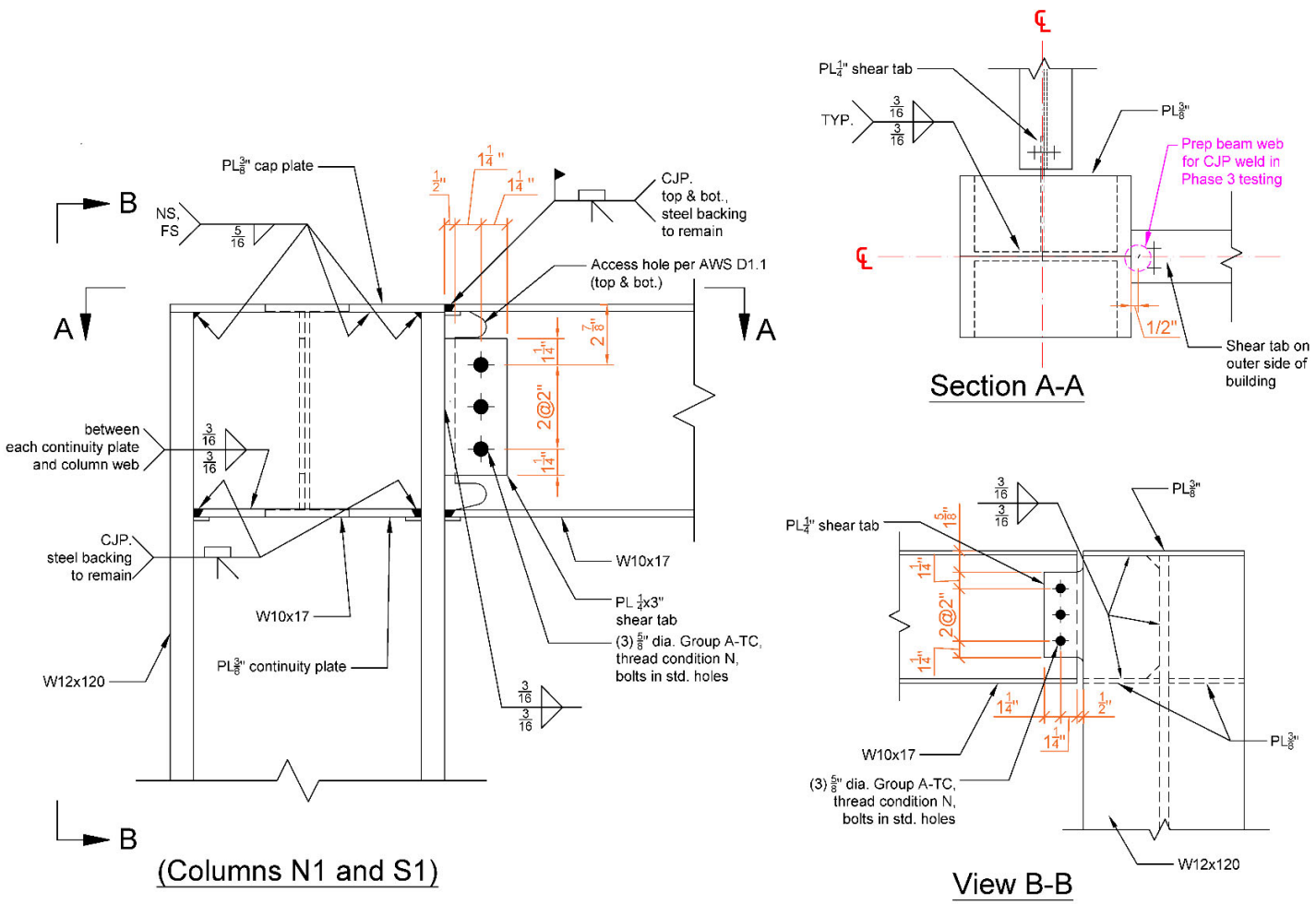

Figure B.10 All Flange Weld (AFW) Collector-to-Column Connection (DWG NS09)

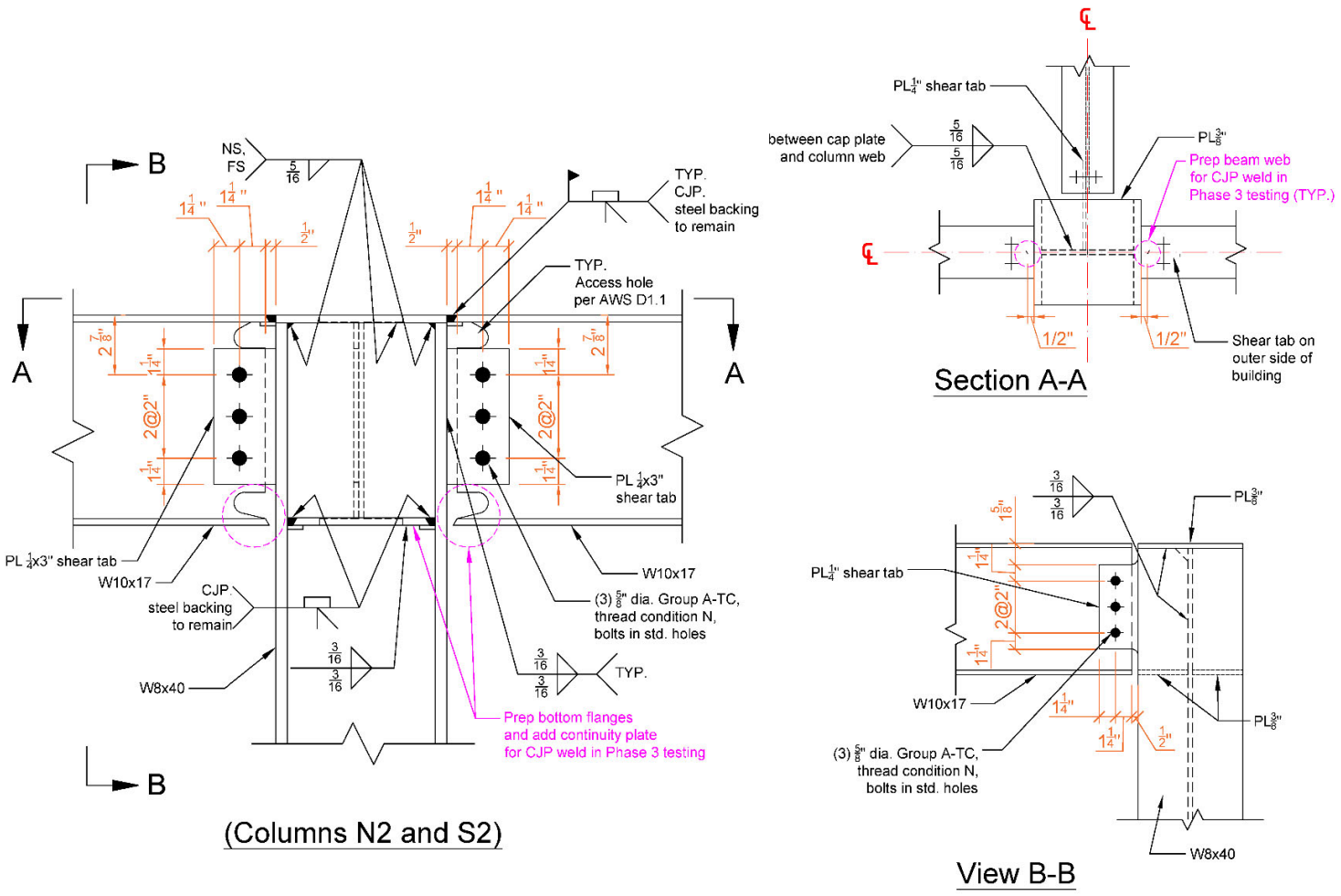

Figure B.11 Top Flange Weld (TFW) Collector-to-Column Connection (DWG NS10)

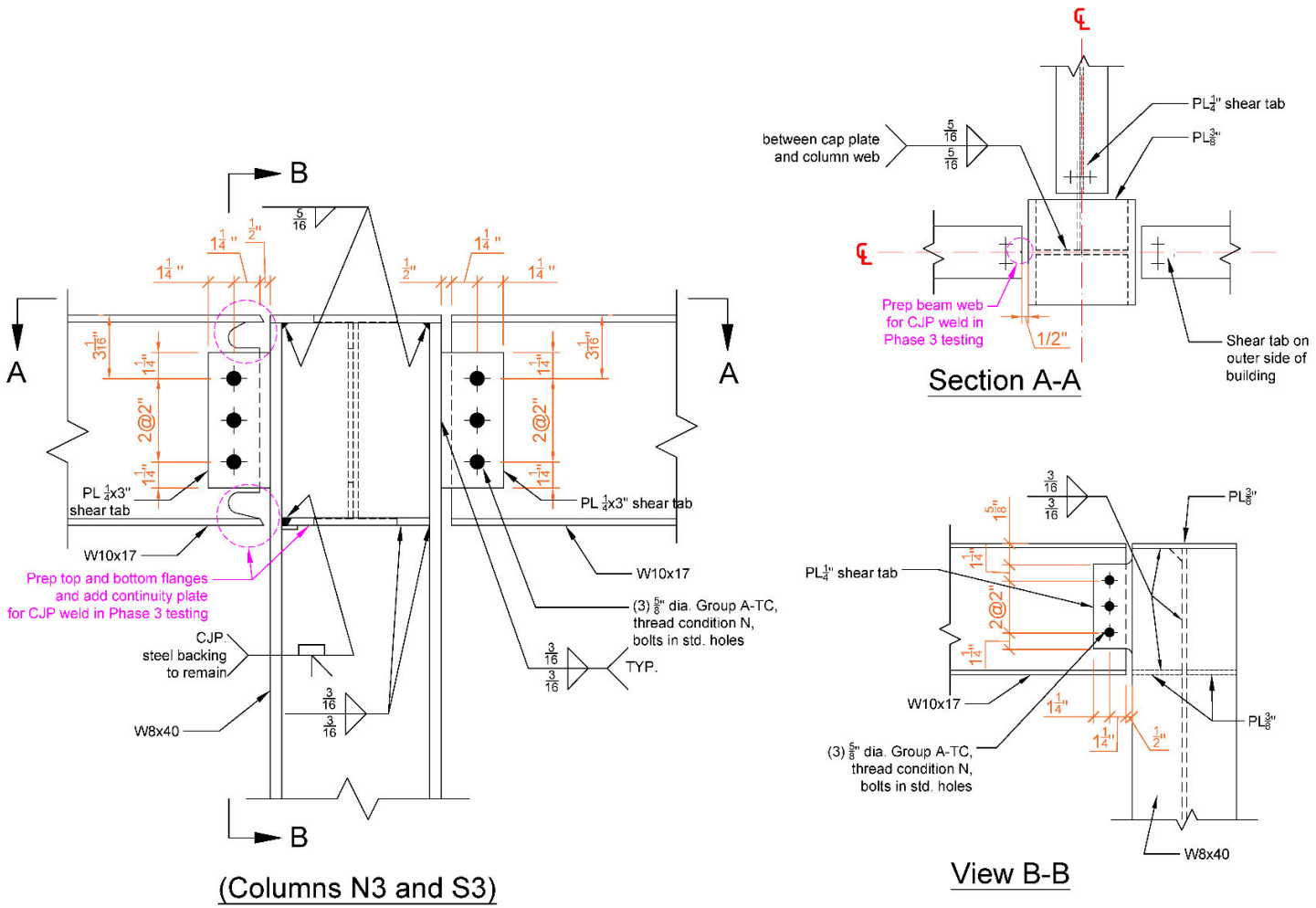

Figure B.12 Bolted Web (BW) Collector-to-Column Connection at Column Line 3 (DWG NS11)

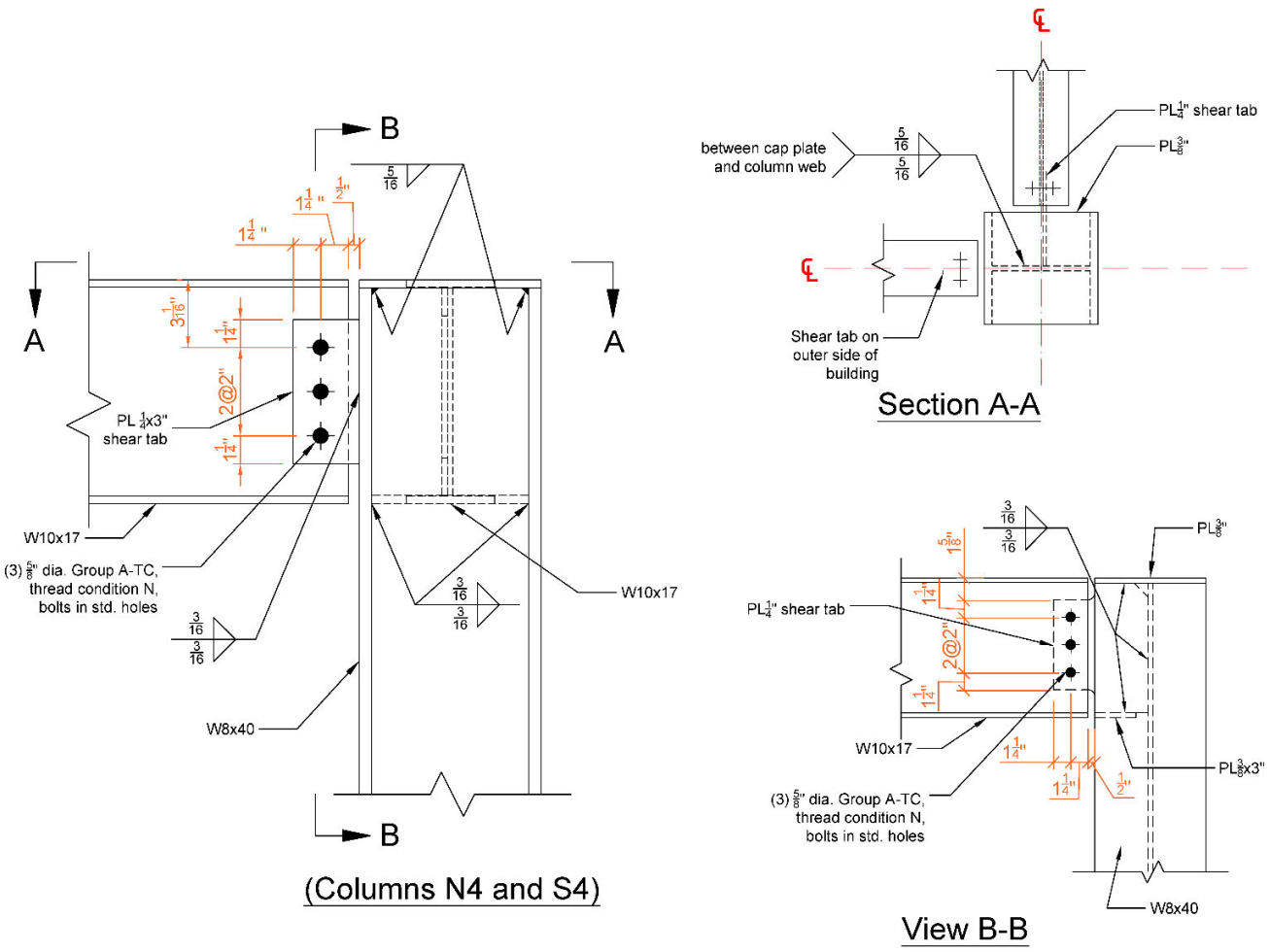

Figure B.13 Bolted Web (BW) Collector-to-Column Connection at Column Line 4 (DWG NS12)

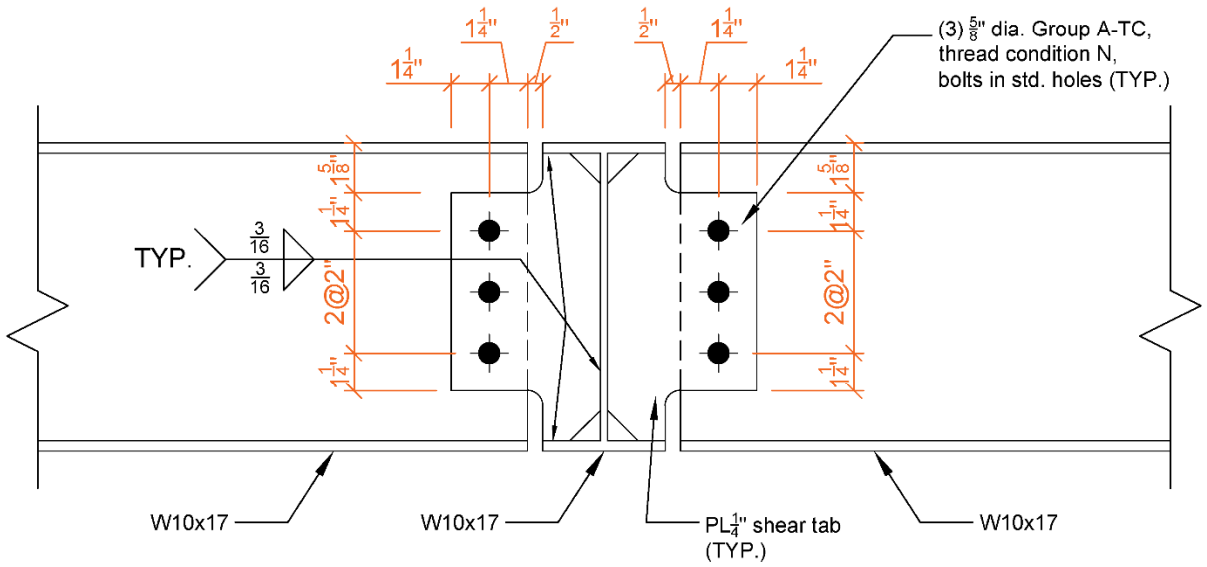

Roof Beam-to-Beam Single- or Double-Sided Connection

Figure B.14 Roof Beam-to-Beam Connection (DWG NS13)

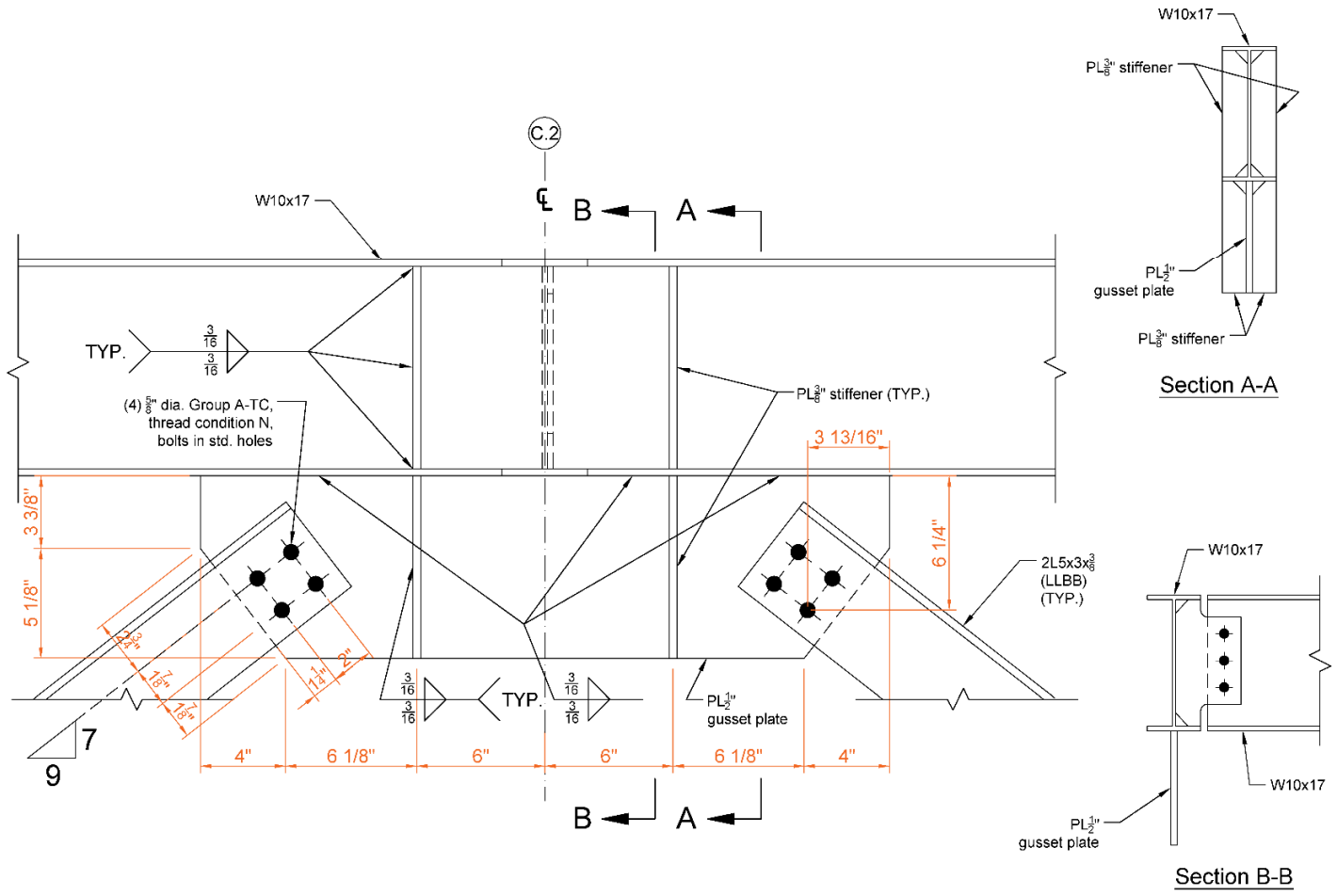

Figure B.15 Top Gusset Plate Connection in 2nd Story of Frame 1 (DWG NS14)

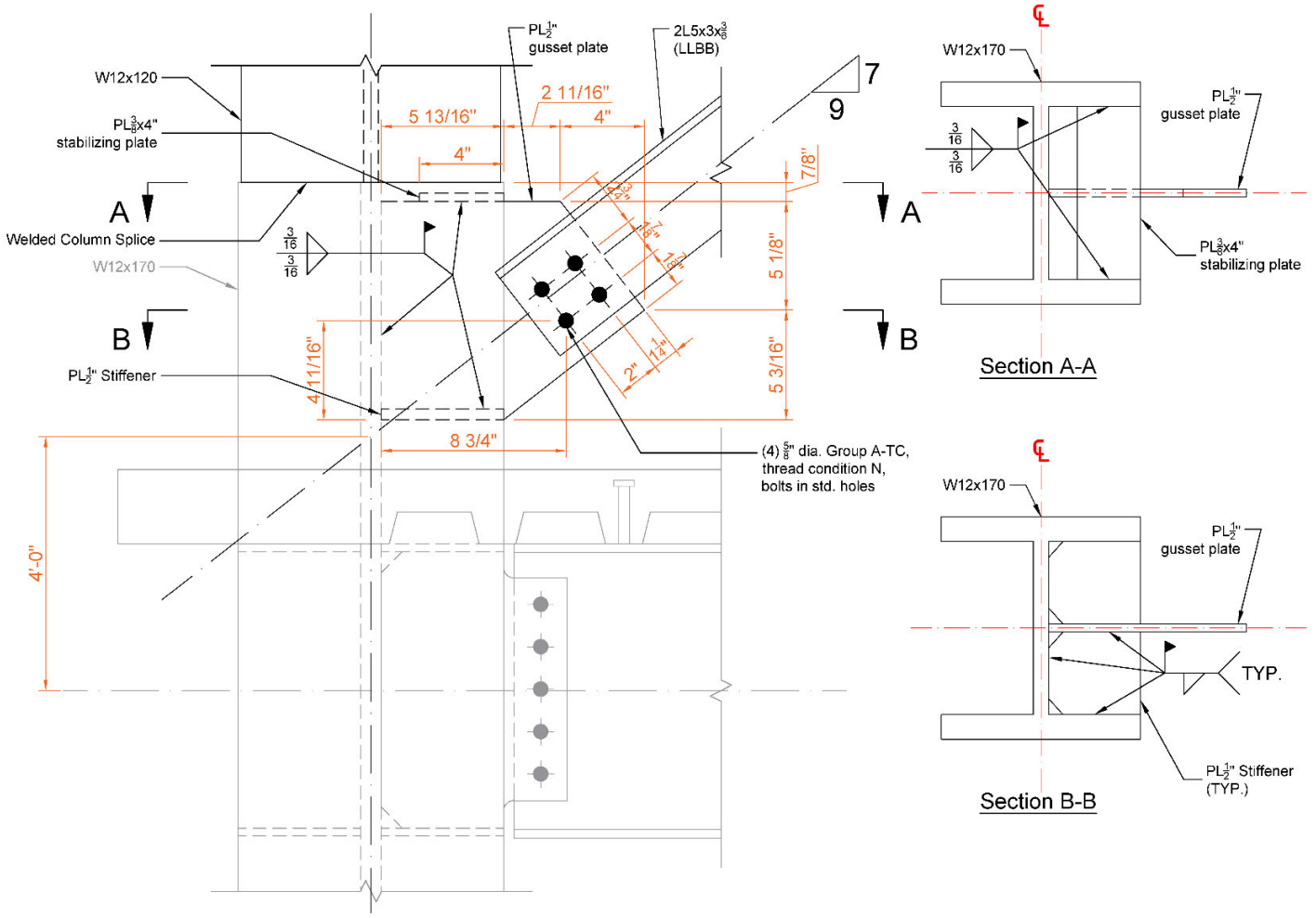

Figure B.16 Bottom Gusset Plate Connection in 2nd Story of Frame 1 (DWG NS15)

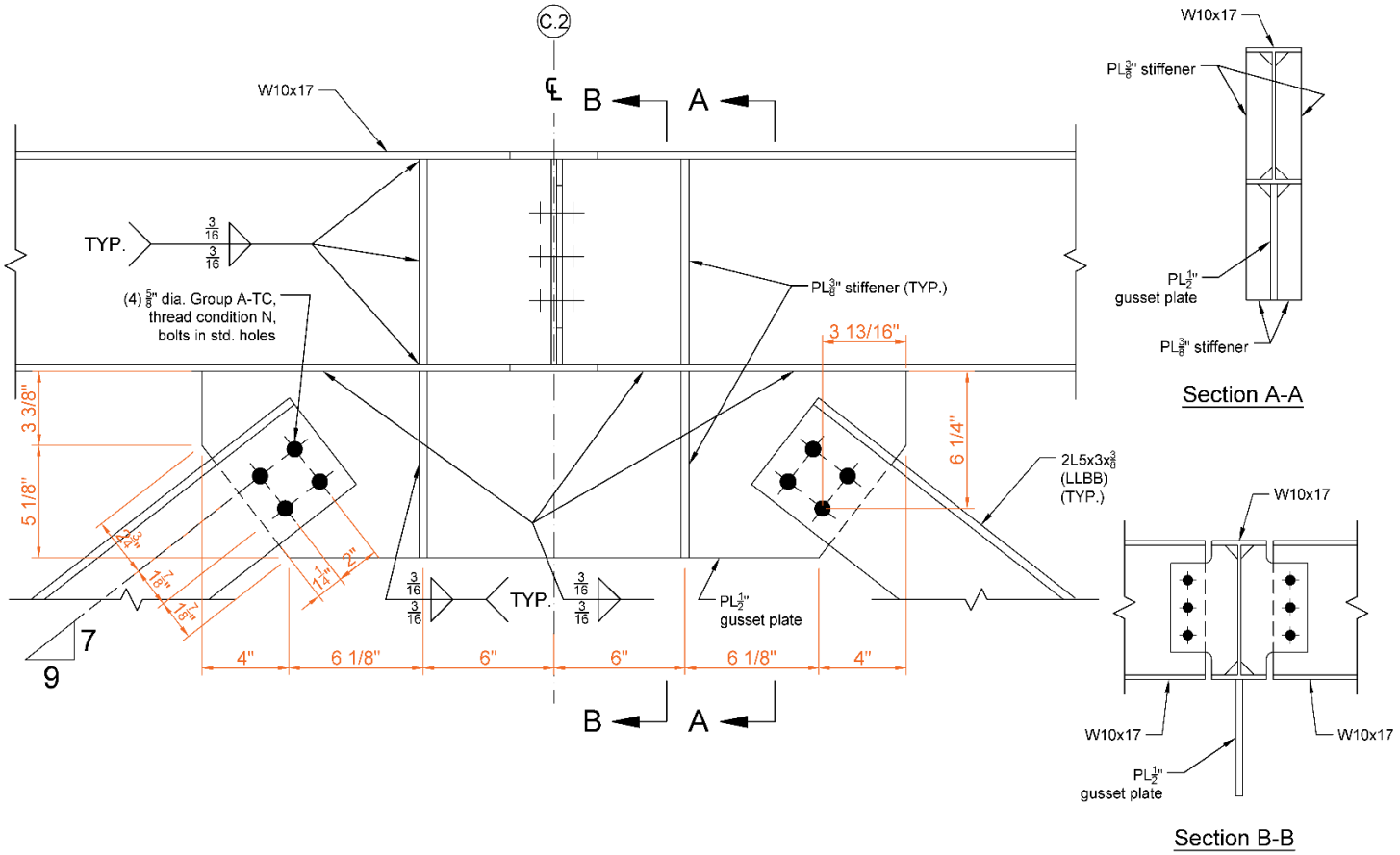

Figure B.17 Top Gusset Plate Connection in 2nd Story of Frames 2 and 3 (DWG NS16)

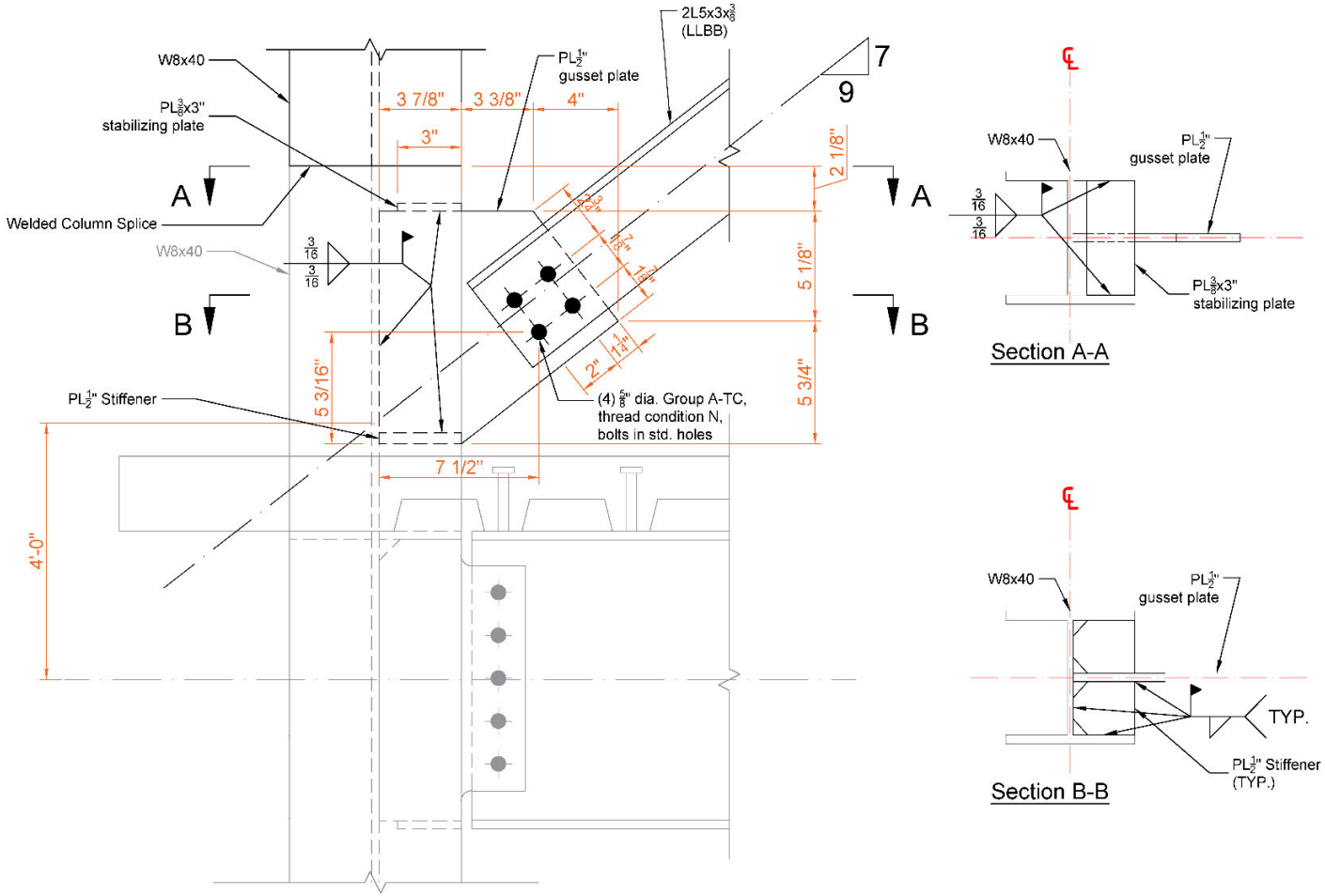

Figure B.18 Bottom Gusset Plate Connection in 2nd Story of Frames 2 and 3 (DWG NS17)

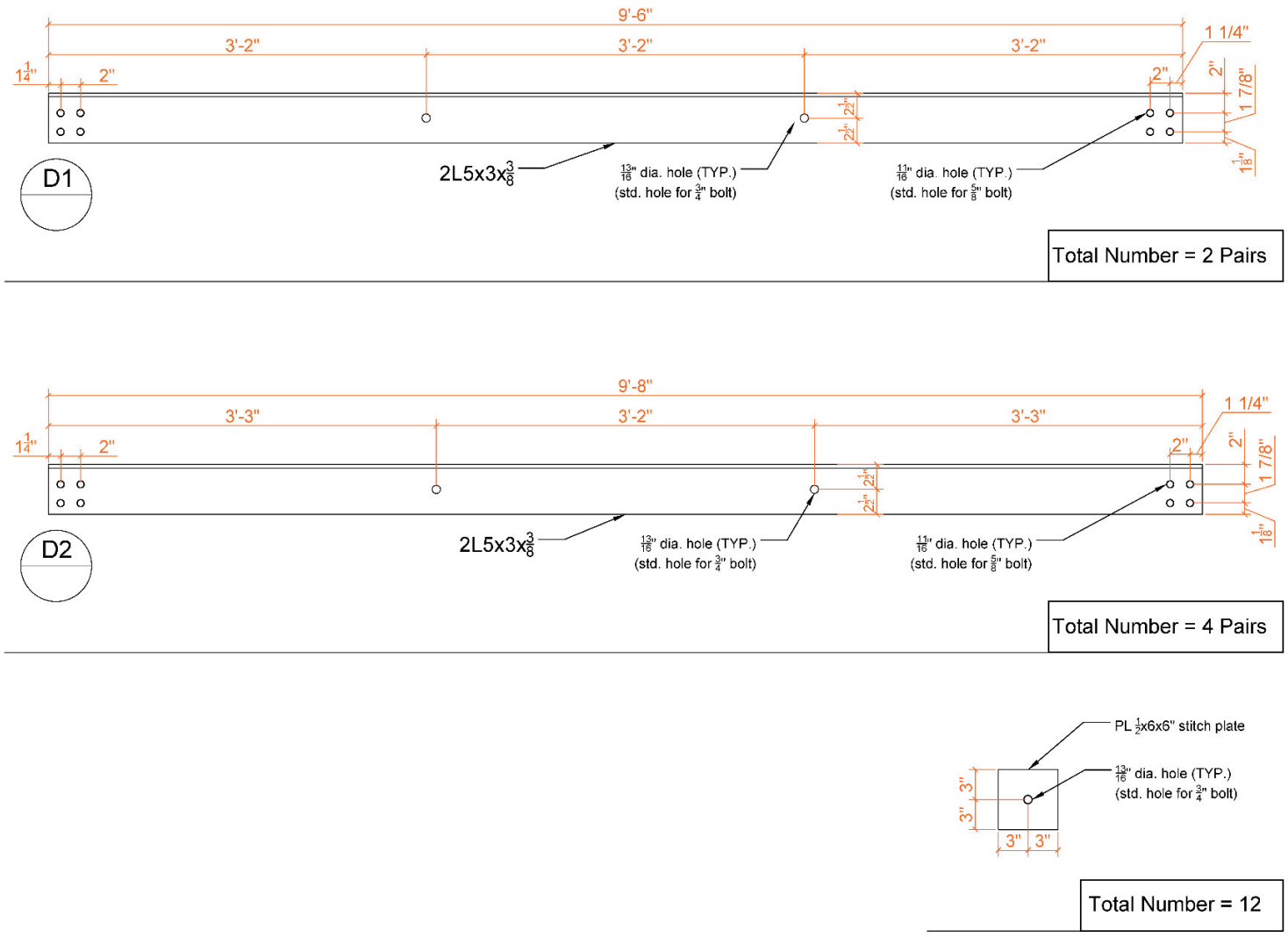

Figure B.19 Details of Double-Angle Braces in 2nd Story (DWG NS18)

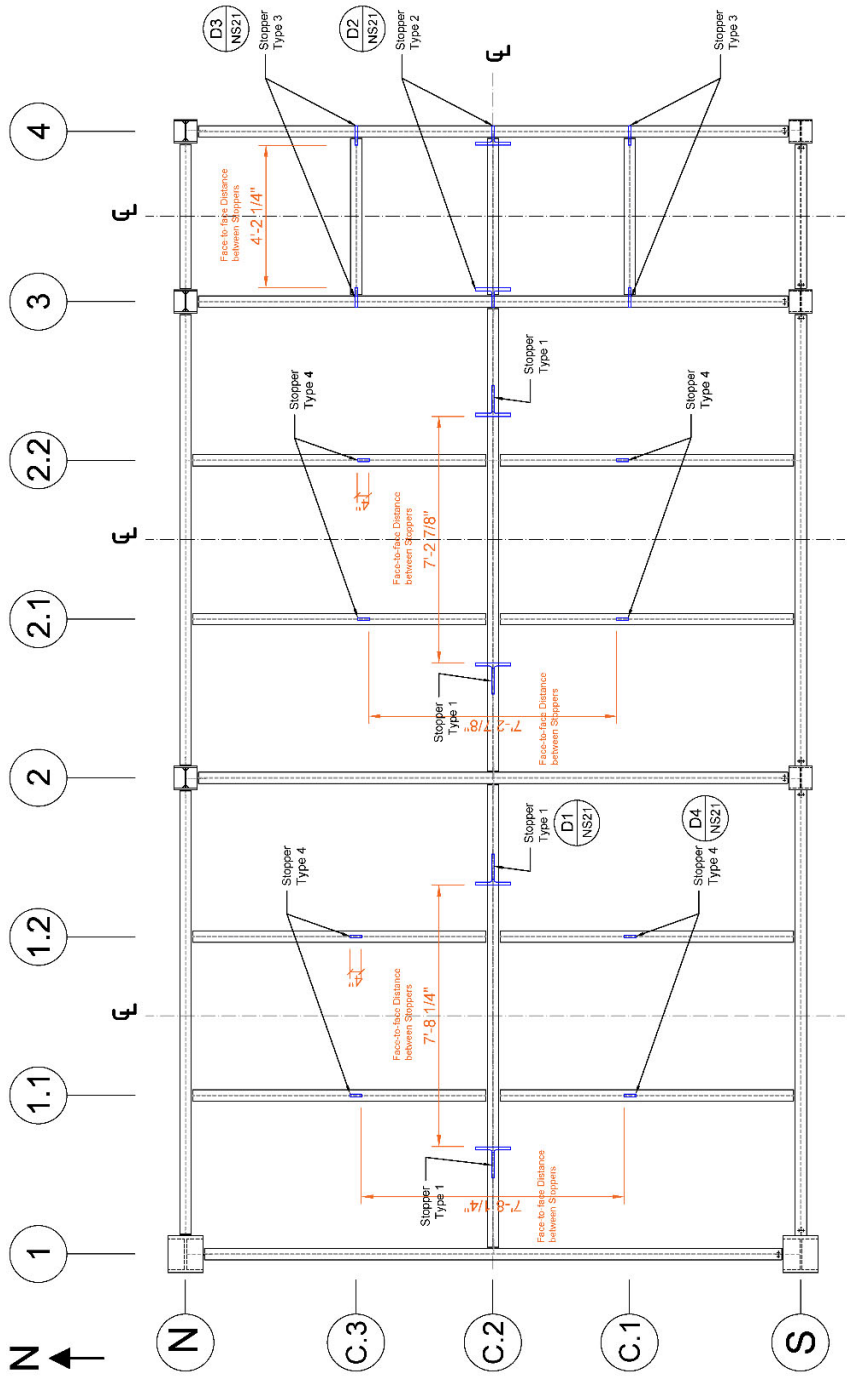

Figure B.20 Plan View of Stopper Layouts (DWG NS19)

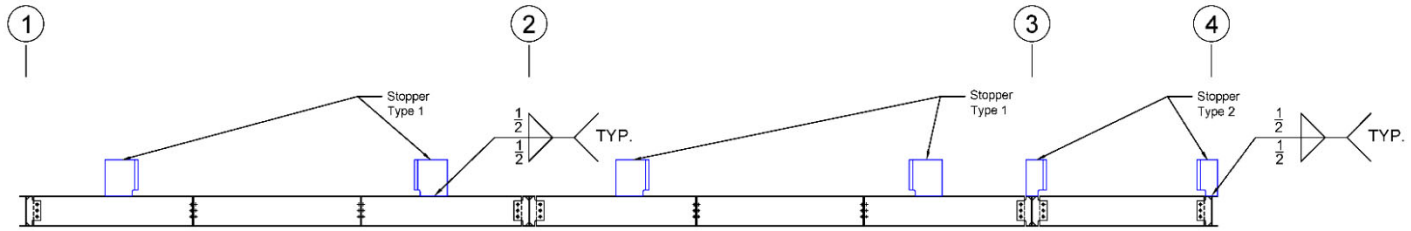

Stoppers along Column Line C.2

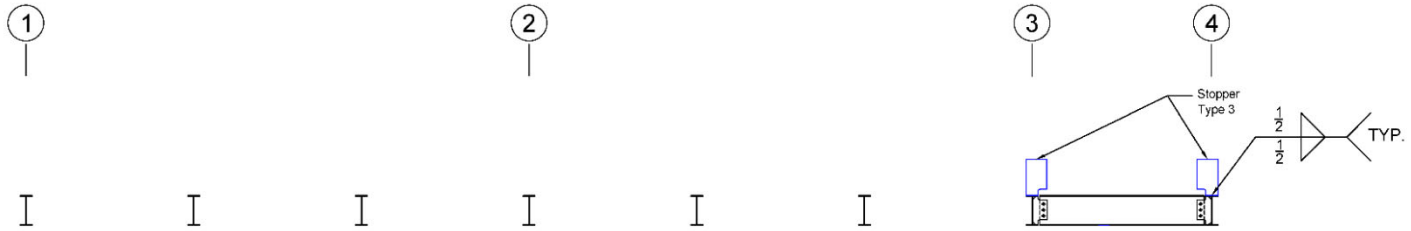

Stoppers along Column Lines C.1 and C.3

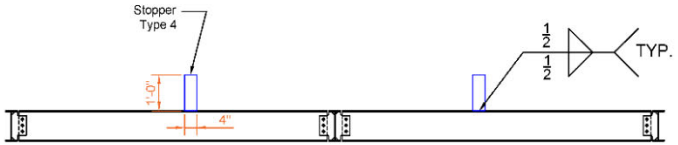

Stoppers along Column Lines 1.1, 1.2, 2.1 and 2.2

Figure B.21 Side View of Stopper Layouts (DWG NS20)

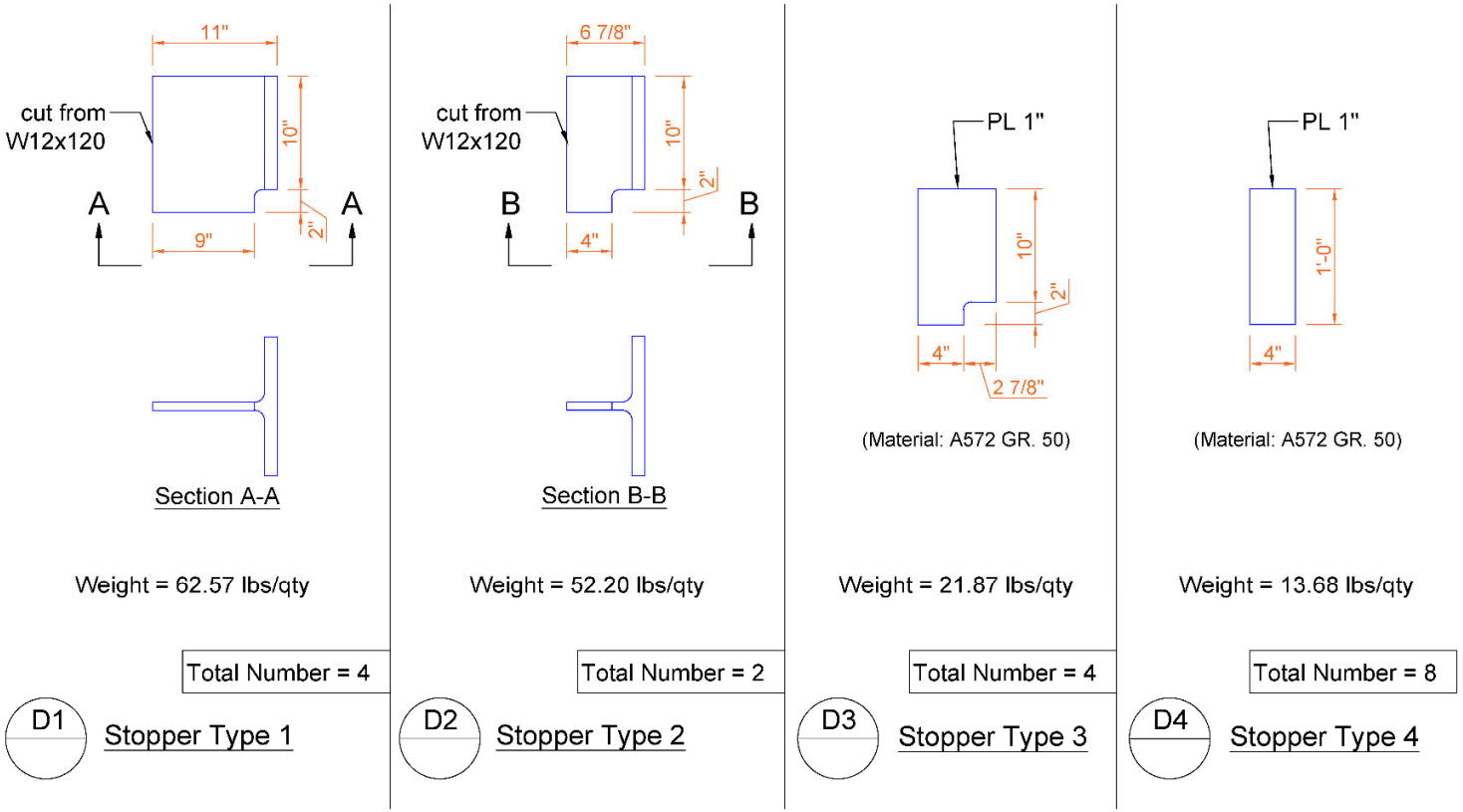

Figure B.22 Details of Stoppers (DWG NS21)

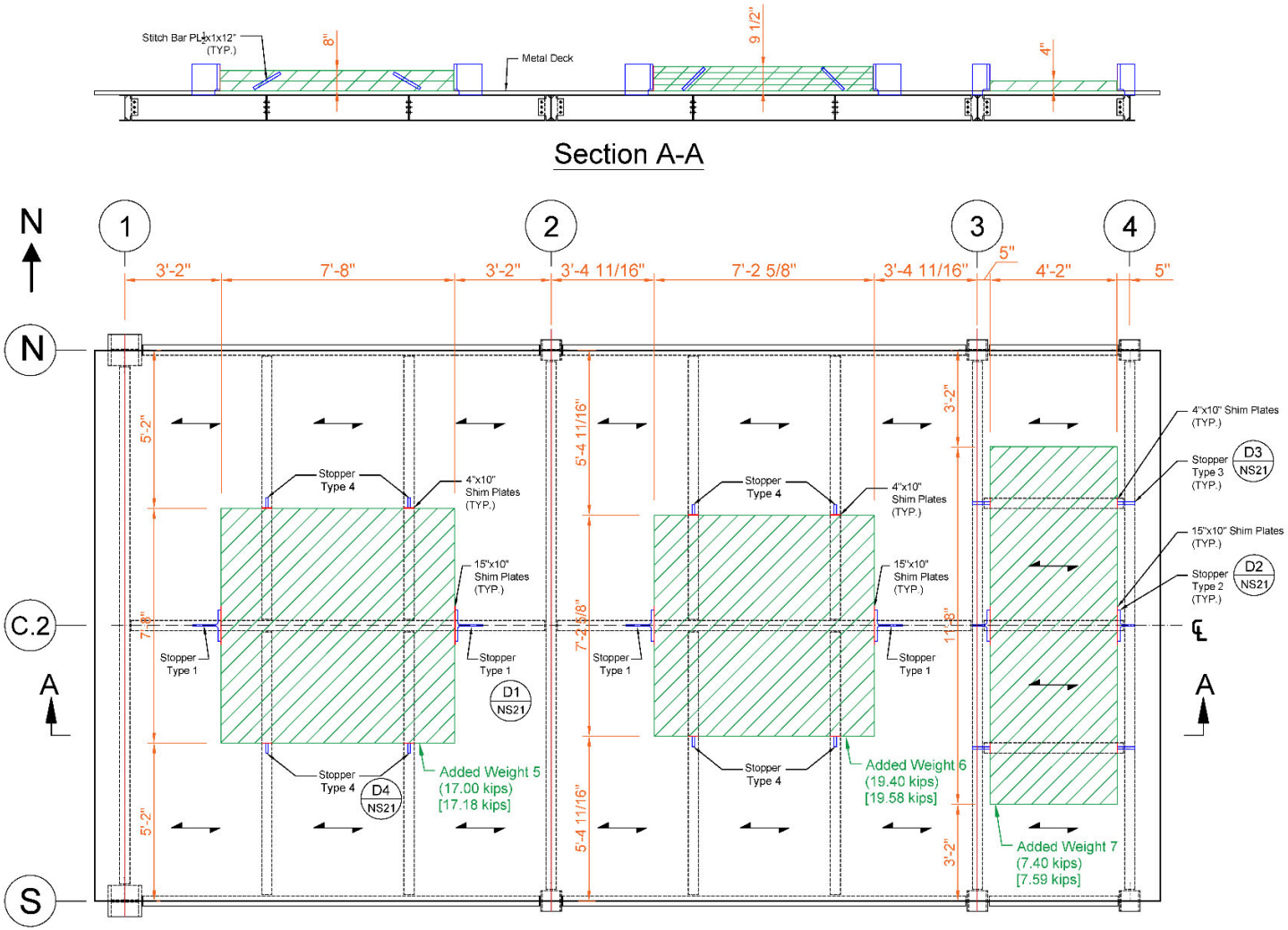

Note: Weight values in parenthese are for steel plates only; while values in brackets are for combination of steel plates and stoppers

Figure B.23 Roof Added-on Mass Layouts (DWG NS22)

Appendix C. Calculations for Numerical Model Settings

This Appendix provides the calculations for numerical model settings. Figure C.1 and Figure C.2 show the nodes defined on the 2nd floor and roof levels, respectively, of analytical specimen models. Table C.1 and Table C.2 show the calculations of nodal masses/weights for the 2nd floor of Phases 1 and 2 specimen models, respectively. Table C.3 and Table C.4 show the calculations of nodal masses/weights for the roof level of Phases 2A and 2B specimen models, respectively. Table C.5 shows the calculations of section properties for the beam elements representing the 2nd floor composite collectors. Table C.6 shows the calculations of section properties for the beam elements representing chord elements and floor beams on the 2nd floor.

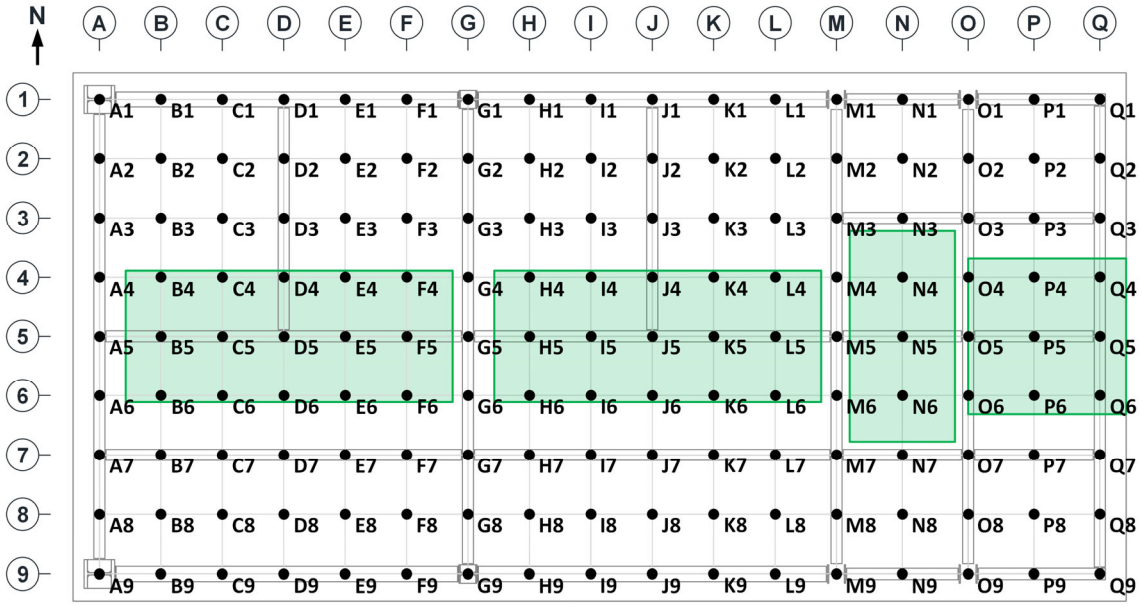

Figure C.1 Nodes on 2nd Floor and Corresponding Designations

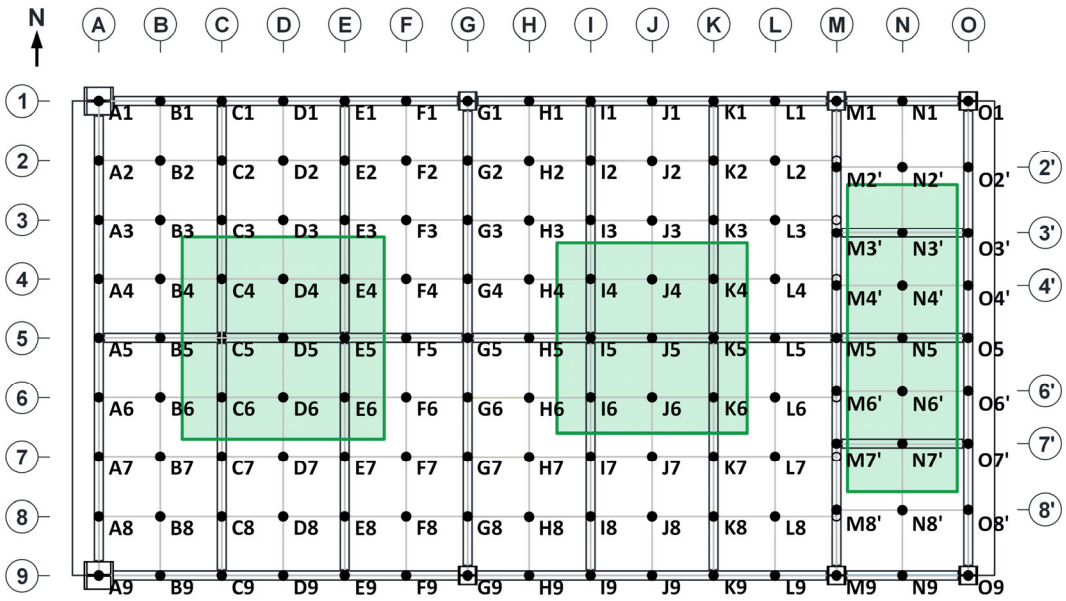

Figure C.2 Nodes on Roof Level and Corresponding Designations

Table C.1 Nodal Weights and Masses on 2nd Floor of Phase 1 Specimen Model

Node	Source of Weight and Mass															Total Nodal Weight	Total Nodal Mass
	Interior Slab		Exterior Slab		Added Weight				Steel Beam				Brace Framing to Beam	Beam-to-Beam Joints	Column		
					Item 1		Item 2		Item 1		Item 2						
	A_T	Unit Wt.	A_T	Unit Wt.	A_T	Unit Wt.	A_T	Unit Wt.	L_T	Unit Wt.	L_T	Unit Wt.					
	(ft^2)	(psf)	(ft^2)	(psf)	(ft^2)	(psf)	(ft^2)	(psf)	(in.)	(lb/ft)	(in.)	(lb/ft)	(lbs)	(lbs)	(lbs)	(kips)	(kip-sec/$in.^2$)
A1	1.313	25.50	3.292	39.26	0.00	0	0.00	0	6.70	26.35	7.00	30.35	0	0	1061.11	1.2562	3.254E-03
A2	2.625	25.50	2.250	39.26	0.00	0	0.00	0	27.00	26.35	0.00	30.35	0	0	0	0.2146	5.557E-04
A3	2.625	25.50	2.250	39.26	0.00	0	0.00	0	27.00	26.35	0.00	30.35	0	0	0	0.2146	5.557E-04
A4	2.625	25.50	2.250	39.26	0.23	418.2	0.00	0	27.00	26.35	0.00	30.35	0	0	0	0.3104	8.040E-04
A5	2.625	25.50	2.250	39.26	0.38	418.2	0.00	0	37.99	26.35	0.00	30.35	213.81	0	0	0.6093	1.578E-03
A6	2.625	25.50	2.250	39.26	0.23	418.2	0.00	0	27.00	26.35	0.00	30.35	0	0	0	0.3104	8.040E-04
A7	2.625	25.50	2.250	39.26	0.00	0	0.00	0	37.99	26.35	0.00	30.35	0	6.77	0	0.2454	6.357E-04
A8	2.625	25.50	2.250	39.26	0.00	0	0.00	0	27.00	26.35	0.00	30.35	0	0	0	0.2146	5.557E-04
A9	1.313	25.50	3.292	39.26	0.00	0	0.00	0	6.70	26.35	7.00	30.35	0	0	1061.11	1.2562	3.254E-03
B1	2.625	25.50	2.333	39.26	0.00	0	0.00	0	0.00	26.35	28.00	30.35	0	0	0	0.2294	5.941E-04
B2	5.250	25.50	0.000	39.26	0.00	0	0.00	0	0.00	26.35	0.00	30.35	0	0	0	0.1339	3.467E-04
B3	5.250	25.50	0.000	39.26	0.00	0	0.00	0	0.00	26.35	0.00	30.35	0	0	0	0.1339	3.467E-04
B4	5.250	25.50	0.000	39.26	3.21	418.2	0.00	0	0.00	26.35	0.00	30.35	0	0	0	1.4757	3.822E-03
B5	5.250	25.50	0.000	39.26	5.25	418.2	0.00	0	28.00	26.35	0.00	30.35	0	0	0	2.3911	6.193E-03
B6	5.250	25.50	0.000	39.26	3.21	418.2	0.00	0	0.00	26.35	0.00	30.35	0	0	0	1.4757	3.822E-03
B7	5.250	25.50	0.000	39.26	0.00	0	0.00	0	28.00	26.35	0.00	30.35	0	0	0	0.1954	5.060E-04
B8	5.250	25.50	0.000	39.26	0.00	0	0.00	0	0.00	26.35	0.00	30.35	0	0	0	0.1339	3.467E-04
B9	2.625	25.50	2.333	39.26	0.00	0	0.00	0	0.00	26.35	28.00	30.35	0	0	0	0.2294	5.941E-04
C1	2.625	25.50	2.333	39.26	0.00	0	0.00	0	0.00	26.35	28.00	30.35	0	0	0	0.2294	5.941E-04
C2	5.250	25.50	0.000	39.26	0.00	0	0.00	0	0.00	26.35	0.00	30.35	0	0	0	0.1339	3.467E-04
C3	5.250	25.50	0.000	39.26	0.00	0	0.00	0	0.00	26.35	0.00	30.35	0	0	0	0.1339	3.467E-04
C4	5.250	25.50	0.000	39.26	3.21	418.2	0.00	0	0.00	26.35	0.00	30.35	0	0	0	1.4757	3.822E-03
C5	5.250	25.50	0.000	39.26	5.25	418.2	0.00	0	28.00	26.35	0.00	30.35	0	0	0	2.3911	6.193E-03
C6	5.250	25.50	0.000	39.26	3.21	418.2	0.00	0	0.00	26.35	0.00	30.35	0	0	0	1.4757	3.822E-03
C7	5.250	25.50	0.000	39.26	0.00	0	0.00	0	28.00	26.35	0.00	30.35	0	0	0	0.1954	5.060E-04
C8	5.250	25.50	0.000	39.26	0.00	0	0.00	0	0.00	26.35	0.00	30.35	0	0	0	0.1339	3.467E-04
C9	2.625	25.50	2.333	39.26	0.00	0	0.00	0	0.00	26.35	28.00	30.35	0	0	0	0.2294	5.941E-04

Table C.1 Nodal Weights and Masses on 2nd Floor of Phase 1 Specimen Model (continued)

Node	Source of Weight and Mass															Total Nodal Weight	Total Nodal Mass
	Interior Slab		Exterior Slab		Added Weight				Steel Beam				Brace Framing to Beam	Beam-to-Beam Joints	Column		
					Item 1		Item 2		Item 1		Item 2						
	A_T	Unit Wt.	A_T	Unit Wt.	A_T	Unit Wt.	A_T	Unit Wt.	L_T	Unit Wt.	L_T	Unit Wt.					
	(ft^2)	(psf)	(ft^2)	(psf)	(ft^2)	(psf)	(ft^2)	(psf)	(in.)	(lb/ft)	(in.)	(lb/ft)	(lbs)	(lbs)	(lbs)	(kips)	(kip-sec/$in.^2$)
D1	2.625	25.50	2.333	39.26	0.00	0	0.00	0	9.64	26.35	28.00	30.35	0	6.77	0	0.2573	6.664E-04
D2	5.250	25.50	0.000	39.26	0.00	0	0.00	0	27.00	26.35	0.00	30.35	0	0	0	0.1932	5.003E-04
D3	5.250	25.50	0.000	39.26	0.00	0	0.00	0	27.00	26.35	0.00	30.35	0	0	0	0.1932	5.003E-04
D4	5.250	25.50	0.000	39.26	3.21	418.2	0.00	0	27.00	26.35	0.00	30.35	0	0	0	1.5350	3.976E-03
D5	5.250	25.50	0.000	39.26	5.25	418.2	0.00	0	38.49	26.35	0.00	30.35	0	6.77	0	2.4209	6.270E-03
D6	5.250	25.50	0.000	39.26	3.21	418.2	0.00	0	0.00	26.35	0.00	30.35	0	0	0	1.4757	3.822E-03
D7	5.250	25.50	0.000	39.26	0.00	0	0.00	0	28.00	26.35	0.00	30.35	0	0	0	0.1954	5.060E-04
D8	5.250	25.50	0.000	39.26	0.00	0	0.00	0	0.00	26.35	0.00	30.35	0	0	0	0.1339	3.467E-04
D9	2.625	25.50	2.333	39.26	0.00	0	0.00	0	0.00	26.35	28.00	30.35	0	0	0	0.2294	5.941E-04
E1	2.625	25.50	2.333	39.26	0.00	0	0.00	0	0.00	26.35	28.00	30.35	0	0	0	0.2294	5.941E-04
E2	5.250	25.50	0.000	39.26	0.00	0	0.00	0	0.00	26.35	0.00	30.35	0	0	0	0.1339	3.467E-04
E3	5.250	25.50	0.000	39.26	0.00	0	0.00	0	0.00	26.35	0.00	30.35	0	0	0	0.1339	3.467E-04
E4	5.250	25.50	0.000	39.26	3.21	418.2	0.00	0	0.00	26.35	0.00	30.35	0	0	0	1.4757	3.822E-03
E5	5.250	25.50	0.000	39.26	5.25	418.2	0.00	0	28.00	26.35	0.00	30.35	0	0	0	2.3911	6.193E-03
E6	5.250	25.50	0.000	39.26	3.21	418.2	0.00	0	0.00	26.35	0.00	30.35	0	0	0	1.4757	3.822E-03
E7	5.250	25.50	0.000	39.26	0.00	0	0.00	0	28.00	26.35	0.00	30.35	0	0	0	0.1954	5.060E-04
E8	5.250	25.50	0.000	39.26	0.00	0	0.00	0	0.00	26.35	0.00	30.35	0	0	0	0.1339	3.467E-04
E9	2.625	25.50	2.333	39.26	0.00	0	0.00	0	0.00	26.35	28.00	30.35	0	0	0	0.2294	5.941E-04
F1	2.625	25.50	2.333	39.26	0.00	0	0.00	0	9.64	26.35	28.00	30.35	0	6.77	0	0.2573	6.664E-04
F2	5.250	25.50	0.000	39.26	0.00	0	0.00	0	27.00	26.35	0.00	30.35	0	0	0	0.1932	5.003E-04
F3	5.250	25.50	0.000	39.26	0.00	0	0.00	0	27.00	26.35	0.00	30.35	0	0	0	0.1932	5.003E-04
F4	5.250	25.50	0.000	39.26	3.21	418.2	0.00	0	27.00	26.35	0.00	30.35	0	0	0	1.5350	3.976E-03
F5	5.250	25.50	0.000	39.26	5.25	418.2	0.00	0	38.49	26.35	0.00	30.35	0	6.77	0	2.4209	6.270E-03
F6	5.250	25.50	0.000	39.26	3.21	418.2	0.00	0	0.00	26.35	0.00	30.35	0	0	0	1.4757	3.822E-03
F7	5.250	25.50	0.000	39.26	0.00	0	0.00	0	28.00	26.35	0.00	30.35	0	0	0	0.1954	5.060E-04
F8	5.250	25.50	0.000	39.26	0.00	0	0.00	0	0.00	26.35	0.00	30.35	0	0	0	0.1339	3.467E-04
F9	2.625	25.50	2.333	39.26	0.00	0	0.00	0	0.00	26.35	28.00	30.35	0	0	0	0.2294	5.941E-04

Table C.1 Nodal Weights and Masses on 2nd Floor of Phase 1 Specimen Model (continued)

Node	Source of Weight and Mass															Total Nodal Weight	Total Nodal Mass
	Interior Slab		Exterior Slab		Added Weight				Steel Beam				Brace Framing to Beam	Beam-to-Beam Joints	Column		
					Item 1		Item 2		Item 1		Item 2						
	A_T	Unit Wt.	A_T	Unit Wt.	A_T	Unit Wt.	A_T	Unit Wt.	L_T	Unit Wt.	L_T	Unit Wt.					
	(ft^2)	(psf)	(ft^2)	(psf)	(ft^2)	(psf)	(ft^2)	(psf)	(in.)	(lb/ft)	(in.)	(lb/ft)	(lbs)	(lbs)	(lbs)	(kips)	(kip-sec/$in.^2$)
G1	2.625	25.50	2.333	39.26	0.00	0	0.00	0	8.97	26.35	19.75	30.35	0	0	197.72	0.4259	1.103E-03
G2	5.250	25.50	0.000	39.26	0.00	0	0.00	0	27.00	26.35	0.00	30.35	0	0	0	0.1932	5.003E-04
G3	5.250	25.50	0.000	39.26	0.00	0	0.00	0	27.00	26.35	0.00	30.35	0	0	0	0.1932	5.003E-04
G4	5.250	25.50	0.000	39.26	0.80	418.2	0.23	434.0	27.00	26.35	0.00	30.35	0	0	0	0.6281	1.627E-03
G5	5.250	25.50	0.000	39.26	1.31	418.2	0.38	434.0	48.97	26.35	0.00	30.35	195.70	0	0	1.1488	2.975E-03
G6	5.250	25.50	0.000	39.26	0.80	418.2	0.23	434.0	27.00	26.35	0.00	30.35	0	0	0	0.6281	1.627E-03
G7	5.250	25.50	0.000	39.26	0.00	0	0.00	0	48.97	26.35	0.00	30.35	0	13.53	0	0.2549	6.603E-04
G8	5.250	25.50	0.000	39.26	0.00	0	0.00	0	27.00	26.35	0.00	30.35	0	0	0	0.1932	5.003E-04
G9	2.625	25.50	2.333	39.26	0.00	0	0.00	0	8.97	26.35	19.75	30.35	0	0	197.72	0.4259	1.103E-03
H1	2.625	25.50	2.333	39.26	0.00	0	0.00	0	0.00	26.35	28.00	30.35	0	0	0	0.2294	5.941E-04
H2	5.250	25.50	0.000	39.26	0.00	0	0.00	0	0.00	26.35	0.00	30.35	0	0	0	0.1339	3.467E-04
H3	5.250	25.50	0.000	39.26	0.00	0	0.00	0	0.00	26.35	0.00	30.35	0	0	0	0.1339	3.467E-04
H4	5.250	25.50	0.000	39.26	3.21	434.0	0.00	0	0.00	26.35	0.00	30.35	0	0	0	1.5263	3.953E-03
H5	5.250	25.50	0.000	39.26	5.25	434.0	0.00	0	28.00	26.35	0.00	30.35	0	0	0	2.4739	6.408E-03
H6	5.250	25.50	0.000	39.26	3.21	434.0	0.00	0	0.00	26.35	0.00	30.35	0	0	0	1.5263	3.953E-03
H7	5.250	25.50	0.000	39.26	0.00	0	0.00	0	28.00	26.35	0.00	30.35	0	0	0	0.1954	5.060E-04
H8	5.250	25.50	0.000	39.26	0.00	0	0.00	0	0.00	26.35	0.00	30.35	0	0	0	0.1339	3.467E-04
H9	2.625	25.50	2.333	39.26	0.00	0	0.00	0	0.00	26.35	28.00	30.35	0	0	0	0.2294	5.941E-04
I1	2.625	25.50	2.333	39.26	0.00	0	0.00	0	0.00	26.35	28.00	30.35	0	0	0	0.2294	5.941E-04
I2	5.250	25.50	0.000	39.26	0.00	0	0.00	0	0.00	26.35	0.00	30.35	0	0	0	0.1339	3.467E-04
I3	5.250	25.50	0.000	39.26	0.00	0	0.00	0	0.00	26.35	0.00	30.35	0	0	0	0.1339	3.467E-04
I4	5.250	25.50	0.000	39.26	3.21	434.0	0.00	0	0.00	26.35	0.00	30.35	0	0	0	1.5263	3.953E-03
I5	5.250	25.50	0.000	39.26	5.25	434.0	0.00	0	28.00	26.35	0.00	30.35	0	0	0	2.4739	6.408E-03
I6	5.250	25.50	0.000	39.26	3.21	434.0	0.00	0	0.00	26.35	0.00	30.35	0	0	0	1.5263	3.953E-03
I7	5.250	25.50	0.000	39.26	0.00	0	0.00	0	28.00	26.35	0.00	30.35	0	0	0	0.1954	5.060E-04
I8	5.250	25.50	0.000	39.26	0.00	0	0.00	0	0.00	26.35	0.00	30.35	0	0	0	0.1339	3.467E-04
I9	2.625	25.50	2.333	39.26	0.00	0	0.00	0	0.00	26.35	28.00	30.35	0	0	0	0.2294	5.941E-04

Table C.1 Nodal Weights and Masses on 2nd Floor of Phase 1 Specimen Model (continued)

Node	Source of Weight and Mass															Total Nodal Weight	Total Nodal Mass
	Interior Slab		Exterior Slab		Added Weight				Steel Beam				Brace Framing to Beam	Beam-to-Beam Joints	Column		
					Item 1		Item 2		Item 1		Item 2						
	A_T	Unit Wt.	A_T	Unit Wt.	A_T	Unit Wt.	A_T	Unit Wt.	L_T	Unit Wt.	L_T	Unit Wt.					
	(ft^2)	(psf)	(ft^2)	(psf)	(ft^2)	(psf)	(ft^2)	(psf)	(in.)	(lb/ft)	(in.)	(lb/ft)	(lbs)	(lbs)	(lbs)	(kips)	(kip-sec/$in.^2$)
J1	2.625	25.50	2.333	39.26	0.00	0	0.00	0	9.64	26.35	28.00	30.35	0	6.77	0	0.2573	6.664E-04
J2	5.250	25.50	0.000	39.26	0.00	0	0.00	0	27.00	26.35	0.00	30.35	0	0	0	0.1932	5.003E-04
J3	5.250	25.50	0.000	39.26	0.00	0	0.00	0	27.00	26.35	0.00	30.35	0	0	0	0.1932	5.003E-04
J4	5.250	25.50	0.000	39.26	3.21	434.0	0.00	0	27.00	26.35	0.00	30.35	0	0	0	1.5856	4.107E-03
J5	5.250	25.50	0.000	39.26	5.25	434.0	0.00	0	38.49	26.35	0.00	30.35	0	6.77	0	2.5037	6.485E-03
J6	5.250	25.50	0.000	39.26	3.21	434.0	0.00	0	0.00	26.35	0.00	30.35	0	0	0	1.5263	3.953E-03
J7	5.250	25.50	0.000	39.26	0.00	0	0.00	0	28.00	26.35	0.00	30.35	0	0	0	0.1954	5.060E-04
J8	5.250	25.50	0.000	39.26	0.00	0	0.00	0	0.00	26.35	0.00	30.35	0	0	0	0.1339	3.467E-04
J9	2.625	25.50	2.333	39.26	0.00	0	0.00	0	0.00	26.35	28.00	30.35	0	0	0	0.2294	5.941E-04
K1	2.625	25.50	2.333	39.26	0.00	0	0.00	0	0.00	26.35	28.00	30.35	0	0	0	0.2294	5.941E-04
K2	5.250	25.50	0.000	39.26	0.00	0	0.00	0	0.00	26.35	0.00	30.35	0	0	0	0.1339	3.467E-04
K3	5.250	25.50	0.000	39.26	0.00	0	0.00	0	0.00	26.35	0.00	30.35	0	0	0	0.1339	3.467E-04
K4	5.250	25.50	0.000	39.26	3.21	434.0	0.00	0	0.00	26.35	0.00	30.35	0	0	0	1.5263	3.953E-03
K5	5.250	25.50	0.000	39.26	5.25	434.0	0.00	0	28.00	26.35	0.00	30.35	0	0	0	2.4739	6.408E-03
K6	5.250	25.50	0.000	39.26	3.21	434.0	0.00	0	0.00	26.35	0.00	30.35	0	0	0	1.5263	3.953E-03
K7	5.250	25.50	0.000	39.26	0.00	0	0.00	0	28.00	26.35	0.00	30.35	0	0	0	0.1954	5.060E-04
K8	5.250	25.50	0.000	39.26	0.00	0	0.00	0	0.00	26.35	0.00	30.35	0	0	0	0.1339	3.467E-04
K9	2.625	25.50	2.333	39.26	0.00	0	0.00	0	0.00	26.35	28.00	30.35	0	0	0	0.2294	5.941E-04
L1	2.625	25.50	2.333	39.26	0.00	0	0.00	0	0.00	26.35	28.00	30.35	0	0	0	0.2294	5.941E-04
L2	5.250	25.50	0.000	39.26	0.00	0	0.00	0	0.00	26.35	0.00	30.35	0	0	0	0.1339	3.467E-04
L3	5.250	25.50	0.000	39.26	0.00	0	0.00	0	0.00	26.35	0.00	30.35	0	0	0	0.1339	3.467E-04
L4	5.250	25.50	0.000	39.26	3.21	434.0	0.00	0	0.00	26.35	0.00	30.35	0	0	0	1.5263	3.953E-03
L5	5.250	25.50	0.000	39.26	5.25	434.0	0.00	0	28.00	26.35	0.00	30.35	0	0	0	2.4739	6.408E-03
L6	5.250	25.50	0.000	39.26	3.21	434.0	0.00	0	0.00	26.35	0.00	30.35	0	0	0	1.5263	3.953E-03
L7	5.250	25.50	0.000	39.26	0.00	0	0.00	0	28.00	26.35	0.00	30.35	0	0	0	0.1954	5.060E-04
L8	5.250	25.50	0.000	39.26	0.00	0	0.00	0	0.00	26.35	0.00	30.35	0	0	0	0.1339	3.467E-04
L9	2.625	25.50	2.333	39.26	0.00	0	0.00	0	0.00	26.35	28.00	30.35	0	0	0	0.2294	5.941E-04

Table C.1 Nodal Weights and Masses on 2nd Floor of Phase 1 Specimen Model (continued)

Node	Source of Weight and Mass															Total Nodal Weight	Total Nodal Mass
	Interior Slab		Exterior Slab		Added Weight				Steel Beam				Brace Framing to Beam	Beam-to-Beam Joints	Column		
					Item 1		Item 2		Item 1		Item 2						
	A_T	Unit Wt.	A_T	Unit Wt.	A_T	Unit Wt.	A_T	Unit Wt.	L_T	Unit Wt.	L_T	Unit Wt.					
	(ft^2)	(psf)	(ft^2)	(psf)	(ft^2)	(psf)	(ft^2)	(psf)	(in.)	(lb/ft)	(in.)	(lb/ft)	(lbs)	(lbs)	(lbs)	(kips)	(kip-sec/$in.^2$)
M1	2.719	25.50	2.417	39.26	0.00	0	0.00	0	19.34	26.35	9.38	30.35	0	0	194.10	0.4245	1.099E-03
M2	5.438	25.50	0.000	39.26	0.00	0	0.00	0	27.00	26.35	0.00	30.35	0	0	0	0.1979	5.127E-04
M3	5.438	25.50	0.000	39.26	0.00	0	0.47	351.4	38.99	26.35	0.00	30.35	0	6.77	0	0.3957	1.025E-03
M4	5.438	25.50	0.000	39.26	0.80	434.0	1.69	351.4	27.00	26.35	0.00	30.35	0	0	0	1.1390	2.950E-03
M5	5.438	25.50	0.000	39.26	1.31	434.0	1.69	351.4	49.97	26.35	0.00	30.35	195.70	0	0	1.6067	4.161E-03
M6	5.438	25.50	0.000	39.26	0.80	434.0	1.69	351.4	27.00	26.35	0.00	30.35	0	0	0	1.1390	2.950E-03
M7	5.438	25.50	0.000	39.26	0.00	0	0.47	351.4	49.97	26.35	0.00	30.35	0	13.53	0	0.4266	1.105E-03
M8	5.438	25.50	0.000	39.26	0.00	0	0.00	0	27.00	26.35	0.00	30.35	0	0	0	0.1979	5.127E-04
M9	2.719	25.50	2.417	39.26	0.00	0	0.00	0	19.34	26.35	9.38	30.35	0	0	194.10	0.4245	1.099E-03
N1	2.813	25.50	2.500	39.26	0.00	0	0.00	0	30.00	26.35	0.00	30.35	0	0	0	0.2357	6.106E-04
N2	5.625	25.50	0.000	39.26	0.00	0	0.00	0	0.00	26.35	0.00	30.35	0	0	0	0.1434	3.715E-04
N3	5.625	25.50	0.000	39.26	1.56	351.4	0.00	0	30.00	26.35	0.00	30.35	0	0	0	0.7584	1.964E-03
N4	5.625	25.50	0.000	39.26	5.63	351.4	0.00	0	0.00	26.35	0.00	30.35	0	0	0	2.1200	5.491E-03
N5	5.625	25.50	0.000	39.26	5.63	351.4	0.00	0	30.00	26.35	0.00	30.35	0	0	0	2.1859	5.662E-03
N6	5.625	25.50	0.000	39.26	5.63	351.4	0.00	0	0.00	26.35	0.00	30.35	0	0	0	2.1200	5.491E-03
N7	5.625	25.50	0.000	39.26	1.56	351.4	0.00	0	30.00	26.35	0.00	30.35	0	0	0	0.7584	1.964E-03
N8	5.625	25.50	0.000	39.26	0.00	0	0.00	0	0.00	26.35	0.00	30.35	0	0	0	0.1434	3.715E-04
N9	2.813	25.50	2.500	39.26	0.00	0	0.00	0	30.00	26.35	0.00	30.35	0	0	0	0.2357	6.106E-04
O1	2.813	25.50	2.500	39.26	0.00	0	0.00	0	29.72	26.35	0.00	30.35	0	0	194.10	0.4292	1.112E-03
O2	5.625	25.50	0.000	39.26	0.00	0	0.00	0	27.00	26.35	0.00	30.35	0	0	0	0.2027	5.251E-04
O3	5.625	25.50	0.000	39.26	0.47	351.4	0.00	0	50.97	26.35	0.00	30.35	0	13.53	0	0.4336	1.123E-03
O4	5.625	25.50	0.000	39.26	1.69	351.4	2.29	447.4	27.00	26.35	0.00	30.35	0	0	0	1.8211	4.717E-03
O5	5.625	25.50	0.000	39.26	1.69	351.4	2.81	447.4	50.97	26.35	0.00	30.35	195.70	0	0	2.3024	5.963E-03
O6	5.625	25.50	0.000	39.26	1.69	351.4	2.29	447.4	27.00	26.35	0.00	30.35	0	0	0	1.8211	4.717E-03
O7	5.625	25.50	0.000	39.26	0.47	351.4	0.00	0	50.97	26.35	0.00	30.35	0	13.53	0	0.4336	1.123E-03
O8	5.625	25.50	0.000	39.26	0.00	0	0.00	0	27.00	26.35	0.00	30.35	0	0	0	0.2027	5.251E-04
O9	2.813	25.50	2.500	39.26	0.00	0	0.00	0	29.72	26.35	0.00	30.35	0	0	194.10	0.4292	1.112E-03

Table C.1 Nodal Weights and Masses on 2nd Floor of Phase 1 Specimen Model (continued)

Node	Source of Weight and Mass															Total Nodal Weight	Total Nodal Mass
	Interior Slab		Exterior Slab		Added Weight				Steel Beam				Brace Framing to Beam	Beam-to-Beam Joints	Column		
					Item 1		Item 2		Item 1		Item 2						
	A_T	Unit Wt.	A_T	Unit Wt.	A_T	Unit Wt.	A_T	Unit Wt.	L_T	Unit Wt.	L_T	Unit Wt.					
	(ft^2)	(psf)	(ft^2)	(psf)	(ft^2)	(psf)	(ft^2)	(psf)	(in.)	(lb/ft)	(in.)	(lb/ft)	(lbs)	(lbs)	(lbs)	(kips)	(kip-sec/$in.^2$)
P1	2.813	25.50	2.500	39.26	0.00	0	0.00	0	30.00	26.35	0.00	30.35	0	0	0	0.2357	6.106E-04
P2	5.625	25.50	0.000	39.26	0.00	0	0.00	0	0.00	26.35	0.00	30.35	0	0	0	0.1434	3.715E-04
P3	5.625	25.50	0.000	39.26	0.00	0	0.00	0	30.00	26.35	0.00	30.35	0	0	0	0.2093	5.421E-04
P4	5.625	25.50	0.000	39.26	4.58	447.4	0.00	0	0.00	26.35	0.00	30.35	0	0	0	2.1942	5.683E-03
P5	5.625	25.50	0.000	39.26	5.63	447.4	0.00	0	30.00	26.35	0.00	30.35	0	0	0	2.7261	7.061E-03
P6	5.625	25.50	0.000	39.26	4.58	447.4	0.00	0	0.00	26.35	0.00	30.35	0	0	0	2.1942	5.683E-03
P7	5.625	25.50	0.000	39.26	0.00	0	0.00	0	30.00	26.35	0.00	30.35	0	0	0	0.2093	5.421E-04
P8	5.625	25.50	0.000	39.26	0.00	0	0.00	0	0.00	26.35	0.00	30.35	0	0	0	0.1434	3.715E-04
P9	2.813	25.50	2.500	39.26	0.00	0	0.00	0	30.00	26.35	0.00	30.35	0	0	0	0.2357	6.106E-04
Q1	1.406	25.50	3.375	39.26	0.00	0	0.00	0	28.00	26.35	0.00	30.35	66.04	0	0	0.2959	7.664E-04
Q2	2.813	25.50	2.250	39.26	0.00	0	0.00	0	27.00	26.35	0.00	30.35	0	0	0	0.2193	5.681E-04
Q3	2.813	25.50	2.250	39.26	0.00	0	0.00	0	38.99	26.35	0.00	30.35	0	6.77	0	0.2524	6.538E-04
Q4	2.813	25.50	2.250	39.26	4.13	447.4	0.00	0	27.00	26.35	0.00	30.35	0	0	0	2.0650	5.349E-03
Q5	2.813	25.50	2.250	39.26	5.06	447.4	0.00	0	38.99	26.35	0.00	30.35	0	6.77	0	2.5175	6.521E-03
Q6	2.813	25.50	2.250	39.26	4.13	447.4	0.00	0	27.00	26.35	0.00	30.35	0	0	0	2.0650	5.349E-03
Q7	2.813	25.50	2.250	39.26	0.00	0	0.00	0	38.99	26.35	0.00	30.35	0	6.77	0	0.2524	6.538E-04
Q8	2.813	25.50	2.250	39.26	0.00	0	0.00	0	27.00	26.35	0.00	30.35	0	0	0	0.2193	5.681E-04
Q9	1.406	25.50	3.375	39.26	0.00	0	0.00	0	28.00	26.35	0.00	30.35	66.04	0	0	0.2959	7.664E-04

Table C.2 Nodal Weights and Masses on 2nd Floor of Phase 2 Specimen Model

Node	Source of Weight and Mass															Total Nodal Weight	Total Nodal Mass
	Interior Slab		Exterior Slab		Added Weight				Steel Beam				Brace Framing to Beam	Beam-to-Beam Joints	Column		
					Item 1		Item 2		Item 1		Item 2						
	A_T	Unit Wt.	A_T	Unit Wt.	A_T	Unit Wt.	A_T	Unit Wt.	L_T	Unit Wt.	L_T	Unit Wt.					
	(ft^2)	(psf)	(ft^2)	(psf)	(ft^2)	(psf)	(ft^2)	(psf)	(in.)	(lb/ft)	(in.)	(lb/ft)	(lbs)	(lbs)	(lbs)	(kips)	(kip-sec/$in.^2$)
A1	1.313	25.50	3.292	39.26	0.000	0	0.000	0	6.70	26.35	7.00	30.35	0	0	1403.73	1.5988	4.141E-03
A2	2.625	25.50	2.250	39.26	0.000	0	0.000	0	27.00	26.35	0.00	30.35	0	0	0	0.2146	5.557E-04
A3	2.625	25.50	2.250	39.26	0.000	0	0.000	0	27.00	26.35	0.00	30.35	0	0	0	0.2146	5.557E-04
A4	2.625	25.50	2.250	39.26	0.229	418.2	0.000	0	27.00	26.35	0.00	30.35	0	0	0	0.3104	8.040E-04
A5	2.625	25.50	2.250	39.26	0.375	418.2	0.000	0	37.99	26.35	0.00	30.35	213.81	0	0	0.6093	1.578E-03
A6	2.625	25.50	2.250	39.26	0.229	418.2	0.000	0	27.00	26.35	0.00	30.35	0	0	0	0.3104	8.040E-04
A7	2.625	25.50	2.250	39.26	0.000	0	0.000	0	37.99	26.35	0.00	30.35	0	6.77	0	0.2454	6.357E-04
A8	2.625	25.50	2.250	39.26	0.000	0	0.000	0	27.00	26.35	0.00	30.35	0	0	0	0.2146	5.557E-04
A9	1.313	25.50	3.292	39.26	0.000	0	0.000	0	6.70	26.35	7.00	30.35	0	0	1403.73	1.5988	4.141E-03
B1	2.625	25.50	2.333	39.26	0.000	0	0.000	0	0.00	26.35	28.00	30.35	0	0	0	0.2294	5.941E-04
B2	5.250	25.50	0.000	39.26	0.000	0	0.000	0	0.00	26.35	0.00	30.35	0	0	0	0.1339	3.467E-04
B3	5.250	25.50	0.000	39.26	0.000	0	0.000	0	0.00	26.35	0.00	30.35	0	0	0	0.1339	3.467E-04
B4	5.250	25.50	0.000	39.26	3.208	418.2	0.000	0	0.00	26.35	0.00	30.35	0	0	0	1.4757	3.822E-03
B5	5.250	25.50	0.000	39.26	5.250	418.2	0.000	0	28.00	26.35	0.00	30.35	0	0	0	2.3911	6.193E-03
B6	5.250	25.50	0.000	39.26	3.208	418.2	0.000	0	0.00	26.35	0.00	30.35	0	0	0	1.4757	3.822E-03
B7	5.250	25.50	0.000	39.26	0.000	0	0.000	0	28.00	26.35	0.00	30.35	0	0	0	0.1954	5.060E-04
B8	5.250	25.50	0.000	39.26	0.000	0	0.000	0	0.00	26.35	0.00	30.35	0	0	0	0.1339	3.467E-04
B9	2.625	25.50	2.333	39.26	0.000	0	0.000	0	0.00	26.35	28.00	30.35	0	0	0	0.2294	5.941E-04
C1	2.625	25.50	2.333	39.26	0.000	0	0.000	0	0.00	26.35	28.00	30.35	0	0	0	0.2294	5.941E-04
C2	5.250	25.50	0.000	39.26	0.000	0	0.000	0	0.00	26.35	0.00	30.35	0	0	0	0.1339	3.467E-04
C3	5.250	25.50	0.000	39.26	0.000	0	0.000	0	0.00	26.35	0.00	30.35	0	0	0	0.1339	3.467E-04
C4	5.250	25.50	0.000	39.26	3.208	418.2	0.000	0	0.00	26.35	0.00	30.35	0	0	0	1.4757	3.822E-03
C5	5.250	25.50	0.000	39.26	5.250	418.2	0.000	0	28.00	26.35	0.00	30.35	0	0	0	2.3911	6.193E-03
C6	5.250	25.50	0.000	39.26	3.208	418.2	0.000	0	0.00	26.35	0.00	30.35	0	0	0	1.4757	3.822E-03
C7	5.250	25.50	0.000	39.26	0.000	0	0.000	0	28.00	26.35	0.00	30.35	0	0	0	0.1954	5.060E-04
C8	5.250	25.50	0.000	39.26	0.000	0	0.000	0	0.00	26.35	0.00	30.35	0	0	0	0.1339	3.467E-04
C9	2.625	25.50	2.333	39.26	0.000	0	0.000	0	0.00	26.35	28.00	30.35	0	0	0	0.2294	5.941E-04

Table C.2 Nodal Weights and Masses on 2nd Floor of Phase 2 Specimen Model (continued)

Node	Source of Weight and Mass															Total Nodal Weight	Total Nodal Mass
	Interior Slab		Exterior Slab		Added Weight				Steel Beam				Brace Framing to Beam	Beam-to-Beam Joints	Column		
					Item 1		Item 2		Item 1		Item 2						
	A_T	Unit Wt.	A_T	Unit Wt.	A_T	Unit Wt.	A_T	Unit Wt.	L_T	Unit Wt.	L_T	Unit Wt.					
	(ft^2)	(psf)	(ft^2)	(psf)	(ft^2)	(psf)	(ft^2)	(psf)	(in.)	(lb/ft)	(in.)	(lb/ft)	(lbs)	(lbs)	(lbs)	(kips)	(kip-sec/$in.^2$)
D1	2.625	25.50	2.333	39.26	0.000	0	0.000	0	9.64	26.35	28.00	30.35	0	6.77	0	0.2573	6.664E-04
D2	5.250	25.50	0.000	39.26	0.000	0	0.000	0	27.00	26.35	0.00	30.35	0	0	0	0.1932	5.003E-04
D3	5.250	25.50	0.000	39.26	0.000	0	0.000	0	27.00	26.35	0.00	30.35	0	0	0	0.1932	5.003E-04
D4	5.250	25.50	0.000	39.26	3.208	418.2	0.000	0	27.00	26.35	0.00	30.35	0	0	0	1.5350	3.976E-03
D5	5.250	25.50	0.000	39.26	5.250	418.2	0.000	0	38.49	26.35	0.00	30.35	0	6.77	0	2.4209	6.270E-03
D6	5.250	25.50	0.000	39.26	3.208	418.2	0.000	0	0.00	26.35	0.00	30.35	0	0	0	1.4757	3.822E-03
D7	5.250	25.50	0.000	39.26	0.000	0	0.000	0	28.00	26.35	0.00	30.35	0	0	0	0.1954	5.060E-04
D8	5.250	25.50	0.000	39.26	0.000	0	0.000	0	0.00	26.35	0.00	30.35	0	0	0	0.1339	3.467E-04
D9	2.625	25.50	2.333	39.26	0.000	0	0.000	0	0.00	26.35	28.00	30.35	0	0	0	0.2294	5.941E-04
E1	2.625	25.50	2.333	39.26	0.000	0	0.000	0	0.00	26.35	28.00	30.35	0	0	0	0.2294	5.941E-04
E2	5.250	25.50	0.000	39.26	0.000	0	0.000	0	0.00	26.35	0.00	30.35	0	0	0	0.1339	3.467E-04
E3	5.250	25.50	0.000	39.26	0.000	0	0.000	0	0.00	26.35	0.00	30.35	0	0	0	0.1339	3.467E-04
E4	5.250	25.50	0.000	39.26	3.208	418.2	0.000	0	0.00	26.35	0.00	30.35	0	0	0	1.4757	3.822E-03
E5	5.250	25.50	0.000	39.26	5.250	418.2	0.000	0	28.00	26.35	0.00	30.35	0	0	0	2.3911	6.193E-03
E6	5.250	25.50	0.000	39.26	3.208	418.2	0.000	0	0.00	26.35	0.00	30.35	0	0	0	1.4757	3.822E-03
E7	5.250	25.50	0.000	39.26	0.000	0	0.000	0	28.00	26.35	0.00	30.35	0	0	0	0.1954	5.060E-04
E8	5.250	25.50	0.000	39.26	0.000	0	0.000	0	0.00	26.35	0.00	30.35	0	0	0	0.1339	3.467E-04
E9	2.625	25.50	2.333	39.26	0.000	0	0.000	0	0.00	26.35	28.00	30.35	0	0	0	0.2294	5.941E-04
F1	2.625	25.50	2.333	39.26	0.000	0	0.000	0	0.00	26.35	28.00	30.35	0	0	0	0.2294	5.941E-04
F2	5.250	25.50	0.000	39.26	0.000	0	0.000	0	0.00	26.35	0.00	30.35	0	0	0	0.1339	3.467E-04
F3	5.250	25.50	0.000	39.26	0.000	0	0.000	0	0.00	26.35	0.00	30.35	0	0	0	0.1339	3.467E-04
F4	5.250	25.50	0.000	39.26	3.208	418.2	0.000	0	0.00	26.35	0.00	30.35	0	0	0	1.4757	3.822E-03
F5	5.250	25.50	0.000	39.26	5.250	418.2	0.000	0	28.00	26.35	0.00	30.35	0	0	0	2.3911	6.193E-03
F6	5.250	25.50	0.000	39.26	3.208	418.2	0.000	0	0.00	26.35	0.00	30.35	0	0	0	1.4757	3.822E-03
F7	5.250	25.50	0.000	39.26	0.000	0	0.000	0	28.00	26.35	0.00	30.35	0	0	0	0.1954	5.060E-04
F8	5.250	25.50	0.000	39.26	0.000	0	0.000	0	0.00	26.35	0.00	30.35	0	0	0	0.1339	3.467E-04
F9	2.625	25.50	2.333	39.26	0.000	0	0.000	0	0.00	26.35	28.00	30.35	0	0	0	0.2294	5.941E-04

Table C.2 Nodal Weights and Masses on 2nd Floor of Phase 2 Specimen Model (continued)

Node	Source of Weight and Mass															Total Nodal Weight	Total Nodal Mass
	Interior Slab		Exterior Slab		Added Weight				Steel Beam				Brace Framing to Beam	Beam-to-Beam Joints	Column		
					Item 1		Item 2		Item 1		Item 2						
	A_T	Unit Wt.	A_T	Unit Wt.	A_T	Unit Wt.	A_T	Unit Wt.	L_T	Unit Wt.	L_T	Unit Wt.					
	(ft^2)	(psf)	(ft^2)	(psf)	(ft^2)	(psf)	(ft^2)	(psf)	(in.)	(lb/ft)	(in.)	(lb/ft)	(lbs)	(lbs)	(lbs)	(kips)	(kip-sec/$in.^2$)
G1	2.625	25.50	2.333	39.26	0.000	0	0.000	0	8.97	26.35	19.75	30.35	0	0	379.68	0.6079	1.574E-03
G2	5.250	25.50	0.000	39.26	0.000	0	0.000	0	27.00	26.35	0.00	30.35	0	0	0	0.1932	5.003E-04
G3	5.250	25.50	0.000	39.26	0.000	0	0.000	0	27.00	26.35	0.00	30.35	0	0	0	0.1932	5.003E-04
G4	5.250	25.50	0.000	39.26	0.802	418.2	0.229	434.0	27.00	26.35	0.00	30.35	0	0	0	0.6281	1.627E-03
G5	5.250	25.50	0.000	39.26	1.313	418.2	0.375	434.0	48.97	26.35	0.00	30.35	195.70	0	0	1.1488	2.975E-03
G6	5.250	25.50	0.000	39.26	0.802	418.2	0.229	434.0	27.00	26.35	0.00	30.35	0	0	0	0.6281	1.627E-03
G7	5.250	25.50	0.000	39.26	0.000	0	0.000	0	48.97	26.35	0.00	30.35	0	13.53	0	0.2549	6.603E-04
G8	5.250	25.50	0.000	39.26	0.000	0	0.000	0	27.00	26.35	0.00	30.35	0	0	0	0.1932	5.003E-04
G9	2.625	25.50	2.333	39.26	0.000	0	0.000	0	8.97	26.35	19.75	30.35	0	0	379.68	0.6079	1.574E-03
H1	2.625	25.50	2.333	39.26	0.000	0	0.000	0	0.00	26.35	28.00	30.35	0	0	0	0.2294	5.941E-04
H2	5.250	25.50	0.000	39.26	0.000	0	0.000	0	0.00	26.35	0.00	30.35	0	0	0	0.1339	3.467E-04
H3	5.250	25.50	0.000	39.26	0.000	0	0.000	0	0.00	26.35	0.00	30.35	0	0	0	0.1339	3.467E-04
H4	5.250	25.50	0.000	39.26	3.208	434.0	0.000	0	0.00	26.35	0.00	30.35	0	0	0	1.5263	3.953E-03
H5	5.250	25.50	0.000	39.26	5.250	434.0	0.000	0	28.00	26.35	0.00	30.35	0	0	0	2.4739	6.408E-03
H6	5.250	25.50	0.000	39.26	3.208	434.0	0.000	0	0.00	26.35	0.00	30.35	0	0	0	1.5263	3.953E-03
H7	5.250	25.50	0.000	39.26	0.000	0	0.000	0	28.00	26.35	0.00	30.35	0	0	0	0.1954	5.060E-04
H8	5.250	25.50	0.000	39.26	0.000	0	0.000	0	0.00	26.35	0.00	30.35	0	0	0	0.1339	3.467E-04
H9	2.625	25.50	2.333	39.26	0.000	0	0.000	0	0.00	26.35	28.00	30.35	0	0	0	0.2294	5.941E-04
I1	2.625	25.50	2.333	39.26	0.000	0	0.000	0	0.00	26.35	28.00	30.35	0	0	0	0.2294	5.941E-04
I2	5.250	25.50	0.000	39.26	0.000	0	0.000	0	0.00	26.35	0.00	30.35	0	0	0	0.1339	3.467E-04
I3	5.250	25.50	0.000	39.26	0.000	0	0.000	0	0.00	26.35	0.00	30.35	0	0	0	0.1339	3.467E-04
I4	5.250	25.50	0.000	39.26	3.208	434.0	0.000	0	0.00	26.35	0.00	30.35	0	0	0	1.5263	3.953E-03
I5	5.250	25.50	0.000	39.26	5.250	434.0	0.000	0	28.00	26.35	0.00	30.35	0	0	0	2.4739	6.408E-03
I6	5.250	25.50	0.000	39.26	3.208	434.0	0.000	0	0.00	26.35	0.00	30.35	0	0	0	1.5263	3.953E-03
I7	5.250	25.50	0.000	39.26	0.000	0	0.000	0	28.00	26.35	0.00	30.35	0	0	0	0.1954	5.060E-04
I8	5.250	25.50	0.000	39.26	0.000	0	0.000	0	0.00	26.35	0.00	30.35	0	0	0	0.1339	3.467E-04
I9	2.625	25.50	2.333	39.26	0.000	0	0.000	0	0.00	26.35	28.00	30.35	0	0	0	0.2294	5.941E-04

Table C.2 Nodal Weights and Masses on 2nd Floor of Phase 2 Specimen Model (continued)

Node	Source of Weight and Mass															Total Nodal Weight	Total Nodal Mass
	Interior Slab		Exterior Slab		Added Weight				Steel Beam				Brace Framing to Beam	Beam-to-Beam Joints	Column		
					Item 1		Item 2		Item 1		Item 2						
	A_T	Unit Wt.	A_T	Unit Wt.	A_T	Unit Wt.	A_T	Unit Wt.	L_T	Unit Wt.	L_T	Unit Wt.					
	(ft^2)	(psf)	(ft^2)	(psf)	(ft^2)	(psf)	(ft^2)	(psf)	(in.)	(lb/ft)	(in.)	(lb/ft)	(lbs)	(lbs)	(lbs)	(kips)	(kip-sec/$in.^2$)
J1	2.625	25.50	2.333	39.26	0.000	0	0.000	0	9.64	26.35	28.00	30.35	0	6.77	0	0.2573	6.664E-04
J2	5.250	25.50	0.000	39.26	0.000	0	0.000	0	27.00	26.35	0.00	30.35	0	0	0	0.1932	5.003E-04
J3	5.250	25.50	0.000	39.26	0.000	0	0.000	0	27.00	26.35	0.00	30.35	0	0	0	0.1932	5.003E-04
J4	5.250	25.50	0.000	39.26	3.208	434.0	0.000	0	27.00	26.35	0.00	30.35	0	0	0	1.5856	4.107E-03
J5	5.250	25.50	0.000	39.26	5.250	434.0	0.000	0	38.49	26.35	0.00	30.35	0	6.77	0	2.5037	6.485E-03
J6	5.250	25.50	0.000	39.26	3.208	434.0	0.000	0	0.00	26.35	0.00	30.35	0	0	0	1.5263	3.953E-03
J7	5.250	25.50	0.000	39.26	0.000	0	0.000	0	28.00	26.35	0.00	30.35	0	0	0	0.1954	5.060E-04
J8	5.250	25.50	0.000	39.26	0.000	0	0.000	0	0.00	26.35	0.00	30.35	0	0	0	0.1339	3.467E-04
J9	2.625	25.50	2.333	39.26	0.000	0	0.000	0	0.00	26.35	28.00	30.35	0	0	0	0.2294	5.941E-04
K1	2.625	25.50	2.333	39.26	0.000	0	0.000	0	0.00	26.35	28.00	30.35	0	0	0	0.2294	5.941E-04
K2	5.250	25.50	0.000	39.26	0.000	0	0.000	0	0.00	26.35	0.00	30.35	0	0	0	0.1339	3.467E-04
K3	5.250	25.50	0.000	39.26	0.000	0	0.000	0	0.00	26.35	0.00	30.35	0	0	0	0.1339	3.467E-04
K4	5.250	25.50	0.000	39.26	3.208	434.0	0.000	0	0.00	26.35	0.00	30.35	0	0	0	1.5263	3.953E-03
K5	5.250	25.50	0.000	39.26	5.250	434.0	0.000	0	28.00	26.35	0.00	30.35	0	0	0	2.4739	6.408E-03
K6	5.250	25.50	0.000	39.26	3.208	434.0	0.000	0	0.00	26.35	0.00	30.35	0	0	0	1.5263	3.953E-03
K7	5.250	25.50	0.000	39.26	0.000	0	0.000	0	28.00	26.35	0.00	30.35	0	0	0	0.1954	5.060E-04
K8	5.250	25.50	0.000	39.26	0.000	0	0.000	0	0.00	26.35	0.00	30.35	0	0	0	0.1339	3.467E-04
K9	2.625	25.50	2.333	39.26	0.000	0	0.000	0	0.00	26.35	28.00	30.35	0	0	0	0.2294	5.941E-04
L1	2.625	25.50	2.333	39.26	0.000	0	0.000	0	0.00	26.35	28.00	30.35	0	0	0	0.2294	5.941E-04
L2	5.250	25.50	0.000	39.26	0.000	0	0.000	0	0.00	26.35	0.00	30.35	0	0	0	0.1339	3.467E-04
L3	5.250	25.50	0.000	39.26	0.000	0	0.000	0	0.00	26.35	0.00	30.35	0	0	0	0.1339	3.467E-04
L4	5.250	25.50	0.000	39.26	3.208	434.0	0.000	0	0.00	26.35	0.00	30.35	0	0	0	1.5263	3.953E-03
L5	5.250	25.50	0.000	39.26	5.250	434.0	0.000	0	28.00	26.35	0.00	30.35	0	0	0	2.4739	6.408E-03
L6	5.250	25.50	0.000	39.26	3.208	434.0	0.000	0	0.00	26.35	0.00	30.35	0	0	0	1.5263	3.953E-03
L7	5.250	25.50	0.000	39.26	0.000	0	0.000	0	28.00	26.35	0.00	30.35	0	0	0	0.1954	5.060E-04
L8	5.250	25.50	0.000	39.26	0.000	0	0.000	0	0.00	26.35	0.00	30.35	0	0	0	0.1339	3.467E-04
L9	2.625	25.50	2.333	39.26	0.000	0	0.000	0	0.00	26.35	28.00	30.35	0	0	0	0.2294	5.941E-04

Table C.2 Nodal Weights and Masses on 2nd Floor of Phase 2 Specimen Model (continued)

Node	Source of Weight and Mass															Total Nodal Weight	Total Nodal Mass
	Interior Slab		Exterior Slab		Added Weight				Steel Beam				Brace Framing to Beam	Beam-to-Beam Joints	Column		
					Item 1		Item 2		Item 1		Item 2						
	A_T	Unit Wt.	A_T	Unit Wt.	A_T	Unit Wt.	A_T	Unit Wt.	L_T	Unit Wt.	L_T	Unit Wt.					
	(ft^2)	(psf)	(ft^2)	(psf)	(ft^2)	(psf)	(ft^2)	(psf)	(in.)	(lb/ft)	(in.)	(lb/ft)	(lbs)	(lbs)	(lbs)	(kips)	(kip-sec/$in.^2$)
M1	2.719	25.50	2.417	39.26	0.000	0	0.000	0	19.34	26.35	9.38	30.35	0	0	376.06	0.6064	1.571E-03
M2	5.438	25.50	0.000	39.26	0.000	0	0.000	0	27.00	26.35	0.00	30.35	0	0	0	0.1979	5.127E-04
M3	5.438	25.50	0.000	39.26	0.000	0	0.469	351.4	38.99	26.35	0.00	30.35	0	6.77	0	0.3957	1.025E-03
M4	5.438	25.50	0.000	39.26	0.802	434.0	1.688	351.4	27.00	26.35	0.00	30.35	0	0	0	1.1390	2.950E-03
M5	5.438	25.50	0.000	39.26	1.313	434.0	1.688	351.4	49.97	26.35	0.00	30.35	195.70	0	0	1.6067	4.161E-03
M6	5.438	25.50	0.000	39.26	0.802	434.0	1.688	351.4	27.00	26.35	0.00	30.35	0	0	0	1.1390	2.950E-03
M7	5.438	25.50	0.000	39.26	0.000	0	0.469	351.4	49.97	26.35	0.00	30.35	0	13.53	0	0.4266	1.105E-03
M8	5.438	25.50	0.000	39.26	0.000	0	0.000	0	27.00	26.35	0.00	30.35	0	0	0	0.1979	5.127E-04
M9	2.719	25.50	2.417	39.26	0.000	0	0.000	0	19.34	26.35	9.38	30.35	0	0	376.06	0.6064	1.571E-03
N1	2.813	25.50	2.500	39.26	0.000	0	0.000	0	30.00	26.35	0.00	30.35	0	0	0	0.2357	6.106E-04
N2	5.625	25.50	0.000	39.26	0.000	0	0.000	0	0.00	26.35	0.00	30.35	0	0	0	0.1434	3.715E-04
N3	5.625	25.50	0.000	39.26	1.563	351.4	0.000	0	30.00	26.35	0.00	30.35	0	0	0	0.7584	1.964E-03
N4	5.625	25.50	0.000	39.26	5.625	351.4	0.000	0	0.00	26.35	0.00	30.35	0	0	0	2.1200	5.491E-03
N5	5.625	25.50	0.000	39.26	5.625	351.4	0.000	0	30.00	26.35	0.00	30.35	0	0	0	2.1859	5.662E-03
N6	5.625	25.50	0.000	39.26	5.625	351.4	0.000	0	0.00	26.35	0.00	30.35	0	0	0	2.1200	5.491E-03
N7	5.625	25.50	0.000	39.26	1.563	351.4	0.000	0	30.00	26.35	0.00	30.35	0	0	0	0.7584	1.964E-03
N8	5.625	25.50	0.000	39.26	0.000	0	0.000	0	0.00	26.35	0.00	30.35	0	0	0	0.1434	3.715E-04
N9	2.813	25.50	2.500	39.26	0.000	0	0.000	0	30.00	26.35	0.00	30.35	0	0	0	0.2357	6.106E-04
O1	2.813	25.50	2.500	39.26	0.000	0	0.000	0	29.72	26.35	0.00	30.35	0	0	274.10	0.5092	1.319E-03
O2	5.625	25.50	0.000	39.26	0.000	0	0.000	0	27.00	26.35	0.00	30.35	0	0	0	0.2027	5.251E-04
O3	5.625	25.50	0.000	39.26	0.469	351.4	0.000	0	50.97	26.35	0.00	30.35	0	13.53	0	0.4336	1.123E-03
O4	5.625	25.50	0.000	39.26	1.688	351.4	2.292	447.4	27.00	26.35	0.00	30.35	0	0	0	1.8211	4.717E-03
O5	5.625	25.50	0.000	39.26	1.688	351.4	2.813	447.4	50.97	26.35	0.00	30.35	195.70	0	0	2.3024	5.963E-03
O6	5.625	25.50	0.000	39.26	1.688	351.4	2.292	447.4	27.00	26.35	0.00	30.35	0	0	0	1.8211	4.717E-03
O7	5.625	25.50	0.000	39.26	0.469	351.4	0.000	0	50.97	26.35	0.00	30.35	0	13.53	0	0.4336	1.123E-03
O8	5.625	25.50	0.000	39.26	0.000	0	0.000	0	27.00	26.35	0.00	30.35	0	0	0	0.2027	5.251E-04
O9	2.813	25.50	2.500	39.26	0.000	0	0.000	0	29.72	26.35	0.00	30.35	0	0	274.10	0.5092	1.319E-03

Table C.2 Nodal Weights and Masses on 2nd Floor of Phase 2 Specimen Model (continued)

Node	Source of Weight and Mass															Total Nodal Weight	Total Nodal Mass
	Interior Slab		Exterior Slab		Added Weight				Steel Beam				Brace Framing to Beam	Beam-to-Beam Joints	Column		
					Item 1		Item 2		Item 1		Item 2						
	A_T	Unit Wt.	A_T	Unit Wt.	A_T	Unit Wt.	A_T	Unit Wt.	L_T	Unit Wt.	L_T	Unit Wt.					
	(ft^2)	(psf)	(ft^2)	(psf)	(ft^2)	(psf)	(ft^2)	(psf)	(in.)	(lb/ft)	(in.)	(lb/ft)	(lbs)	(lbs)	(lbs)	(kips)	(kip-sec/$in.^2$)
P1	2.813	25.50	2.500	39.26	0.000	0	0.000	0	30.00	26.35	0.00	30.35	0	0	0	0.2357	6.106E-04
P2	5.625	25.50	0.000	39.26	0.000	0	0.000	0	0.00	26.35	0.00	30.35	0	0	0	0.1434	3.715E-04
P3	5.625	25.50	0.000	39.26	0.000	0	0.000	0	30.00	26.35	0.00	30.35	0	0	0	0.2093	5.421E-04
P4	5.625	25.50	0.000	39.26	4.583	447.4	0.000	0	0.00	26.35	0.00	30.35	0	0	0	2.1942	5.683E-03
P5	5.625	25.50	0.000	39.26	5.625	447.4	0.000	0	30.00	26.35	0.00	30.35	0	0	0	2.7261	7.061E-03
P6	5.625	25.50	0.000	39.26	4.583	447.4	0.000	0	0.00	26.35	0.00	30.35	0	0	0	2.1942	5.683E-03
P7	5.625	25.50	0.000	39.26	0.000	0	0.000	0	30.00	26.35	0.00	30.35	0	0	0	0.2093	5.421E-04
P8	5.625	25.50	0.000	39.26	0.000	0	0.000	0	0.00	26.35	0.00	30.35	0	0	0	0.1434	3.715E-04
P9	2.813	25.50	2.500	39.26	0.000	0	0.000	0	30.00	26.35	0.00	30.35	0	0	0	0.2357	6.106E-04
Q1	1.406	25.50	3.375	39.26	0.000	0	0.000	0	28.00	26.35	0.00	30.35	66.04	0	0	0.2959	7.664E-04
Q2	2.813	25.50	2.250	39.26	0.000	0	0.000	0	27.00	26.35	0.00	30.35	0	0	0	0.2193	5.681E-04
Q3	2.813	25.50	2.250	39.26	0.000	0	0.000	0	38.99	26.35	0.00	30.35	0	6.77	0	0.2524	6.538E-04
Q4	2.813	25.50	2.250	39.26	4.125	447.4	0.000	0	27.00	26.35	0.00	30.35	0	0	0	2.0650	5.349E-03
Q5	2.813	25.50	2.250	39.26	5.063	447.4	0.000	0	38.99	26.35	0.00	30.35	0	6.77	0	2.5175	6.521E-03
Q6	2.813	25.50	2.250	39.26	4.125	447.4	0.000	0	27.00	26.35	0.00	30.35	0	0	0	2.0650	5.349E-03
Q7	2.813	25.50	2.250	39.26	0.000	0	0.000	0	38.99	26.35	0.00	30.35	0	6.77	0	0.2524	6.538E-04
Q8	2.813	25.50	2.250	39.26	0.000	0	0.000	0	27.00	26.35	0.00	30.35	0	0	0	0.2193	5.681E-04
Q9	1.406	25.50	3.375	39.26	0.000	0	0.000	0	28.00	26.35	0.00	30.35	66.04	0	0	0.2959	7.664E-04

Table C.3 Nodal Weights and Masses on Roof of Phase 2A Specimen Model

Node	Source of Weight and Mass										Total Nodal Weight	Total Nodal Mass
	Roof Deck		Added Weight (Stoppers Only)	Steel Beam				Brace Framing to Beam	Beam-to-Beam Joints	Column		
				Item 1		Item 2						
	A_T	Unit Wt.		L_T	Unit Wt.	L_T	Unit Wt.					
	(ft^2)	(psf)	(lbs)	(in.)	(lb/ft)	(in.)	(lb/ft)	(lbs)	(lbs)	(lbs)	(kips)	(kip-sec/$in.^2$)
A1	2.4375	2.30	0	7.450	17.00	6.850	17.00	0	0	549.05	0.5749	1.489E-03
A2	4.8750	2.30	0	0	17.00	27.000	17.00	0	0	0	0.0495	1.281E-04
A3	4.8750	2.30	0	0	17.00	27.000	17.00	0	0	0	0.0495	1.281E-04
A4	4.8750	2.30	0	0	17.00	27.000	17.00	0	0	0	0.0495	1.281E-04
A5	4.8750	2.30	0	11.495	17.00	27.000	17.00	203.99	0	0	0.2697	6.986E-04
A6	4.8750	2.30	0	0	17.00	27.000	17.00	0	0	0	0.0495	1.281E-04
A7	4.8750	2.30	0	0	17.00	27.000	17.00	0	0	0	0.0495	1.281E-04
A8	4.8750	2.30	0	0	17.00	27.000	17.00	0	0	0	0.0495	1.281E-04
A9	2.4375	2.30	0	7.450	17.00	6.850	17.00	0	0	549.05	0.5749	1.489E-03
B1	2.6250	2.30	0	28.000	17.00	0	17.00	0	0	0	0.0457	1.184E-04
B2	5.2500	2.30	0	0	17.00	0	17.00	0	0	0	0.0121	3.128E-05
B3	5.2500	2.30	0	0	17.00	0	17.00	0	0	0	0.0121	3.128E-05
B4	5.2500	2.30	0	0	17.00	0	17.00	0	0	0	0.0121	3.128E-05
B5	5.2500	2.30	40.220	28.000	17.00	0	17.00	0	0	0	0.0920	2.382E-04
B6	5.2500	2.30	0	0	17.00	0	17.00	0	0	0	0.0121	3.128E-05
B7	5.2500	2.30	0	0	17.00	0	17.00	0	0	0	0.0121	3.128E-05
B8	5.2500	2.30	0	0	17.00	0	17.00	0	0	0	0.0121	3.128E-05
B9	2.6250	2.30	0	28.000	17.00	0	17.00	0	0	0	0.0457	1.184E-04
C1	2.6250	2.30	0	28.000	17.00	10.995	17.00	0	4.34	0	0.0656	1.700E-04
C2	5.2500	2.30	0	0	17.00	27.000	17.00	0	0	0	0.0503	1.303E-04
C3	5.2500	2.30	9.630	0	17.00	27.000	17.00	0	0	0	0.0600	1.553E-04
C4	5.2500	2.30	4.050	0	17.00	27.000	17.00	0	0	0	0.0544	1.408E-04
C5	5.2500	2.30	22.350	28.000	17.00	21.990	17.00	0	8.68	0	0.1139	2.951E-04
C6	5.2500	2.30	4.050	0	17.00	27.000	17.00	0	0	0	0.0544	1.408E-04
C7	5.2500	2.30	9.630	0	17.00	27.000	17.00	0	0	0	0.0600	1.553E-04
C8	5.2500	2.30	0	0	17.00	27.000	17.00	0	0	0	0.0503	1.303E-04
C9	2.6250	2.30	0	28.000	17.00	10.995	17.00	0	4.34	0	0.0656	1.700E-04

Table C.3 Nodal Weights and Masses on Roof of Phase 2A Specimen Model (continued)

Node	Source of Weight and Mass										Total Nodal Weight	Total Nodal Mass
	Roof Deck		Added Weight (Stoppers Only)	Steel Beam				Brace Framing to Beam	Beam-to-Beam Joints	Column		
				Item 1		Item 2						
	A_T	Unit Wt.		L_T	Unit Wt.	L_T	Unit Wt.					
	(ft^2)	(psf)	(lbs)	(in.)	(lb/ft)	(in.)	(lb/ft)	(lbs)	(lbs)	(lbs)	(kips)	(kip-sec/$in.^2$)
G1	2.6250	2.30	0	19.750	17.00	8.965	17.00	0	0	191.61	0.2383	6.173E-04
G2	5.2500	2.30	0	0	17.00	27.000	17.00	0	0	0	0.0503	1.303E-04
G3	5.2500	2.30	0	0	17.00	27.000	17.00	0	0	0	0.0503	1.303E-04
G4	5.2500	2.30	0	0	17.00	27.000	17.00	0	0	0	0.0503	1.303E-04
G5	5.2500	2.30	0	22.990	17.00	27.000	17.00	208.48	0	0	0.2914	7.547E-04
G6	5.2500	2.30	0	0	17.00	27.000	17.00	0	0	0	0.0503	1.303E-04
G7	5.2500	2.30	0	0	17.00	27.000	17.00	0	0	0	0.0503	1.303E-04
G8	5.2500	2.30	0	0	17.00	27.000	17.00	0	0	0	0.0503	1.303E-04
G9	2.6250	2.30	0	19.750	17.00	8.965	17.00	0	0	191.61	0.2383	6.173E-04
H1	2.6250	2.30	0	28.000	17.00	0	17.00	0	0	0	0.0457	1.184E-04
H2	5.2500	2.30	0	0	17.00	0	17.00	0	0	0	0.0121	3.128E-05
H3	5.2500	2.30	0	0	17.00	0	17.00	0	0	0	0.0121	3.128E-05
H4	5.2500	2.30	0	0	17.00	0	17.00	0	0	0	0.0121	3.128E-05
H5	5.2500	2.30	34.220	28.000	17.00	0	17.00	0	0	0	0.0860	2.226E-04
H6	5.2500	2.30	0	0	17.00	0	17.00	0	0	0	0.0121	3.128E-05
H7	5.2500	2.30	0	0	17.00	0	17.00	0	0	0	0.0121	3.128E-05
H8	5.2500	2.30	0	0	17.00	0	17.00	0	0	0	0.0121	3.128E-05
H9	2.6250	2.30	0	28.000	17.00	0	17.00	0	0	0	0.0457	1.184E-04
I1	2.6250	2.30	0	28.000	17.00	10.995	17.00	0	4.34	0	0.0656	1.700E-04
I2	5.2500	2.30	0	0	17.00	27.000	17.00	0	0	0	0.0503	1.303E-04
I3	5.2500	2.30	8.265	0	17.00	27.000	17.00	0	0	0	0.0586	1.518E-04
I4	5.2500	2.30	5.415	0	17.00	27.000	17.00	0	0	0	0.0557	1.444E-04
I5	5.2500	2.30	28.350	28.000	17.00	21.990	17.00	0	8.68	0	0.1199	3.106E-04
I6	5.2500	2.30	5.415	0	17.00	27.000	17.00	0	0	0	0.0557	1.444E-04
I7	5.2500	2.30	8.265	0	17.00	27.000	17.00	0	0	0	0.0586	1.518E-04
I8	5.2500	2.30	0	0	17.00	27.000	17.00	0	0	0	0.0503	1.303E-04
I9	2.6250	2.30	0	28.000	17.00	10.995	17.00	0	4.34	0	0.0656	1.700E-04

Table C.3 Nodal Weights and Masses on Roof of Phase 2A Specimen Model (continued)

Node	Source of Weight and Mass										Total Nodal Weight	Total Nodal Mass
	Roof Deck		Added Weight (Stoppers Only)	Steel Beam				Brace Framing to Beam	Beam-to-Beam Joints	Column		
				Item 1		Item 2						
	A_T	Unit Wt.		L_T	Unit Wt.	L_T	Unit Wt.					
	(ft^2)	(psf)	(lbs)	(in.)	(lb/ft)	(in.)	(lb/ft)	(lbs)	(lbs)	(lbs)	(kips)	(kip-sec/$in.^2$)
J1	2.6250	2.30	0	28.000	17.00	0	17.00	0	0	0	0.0457	1.184E-04
J2	5.2500	2.30	0	0	17.00	0	17.00	0	0	0	0.0121	3.128E-05
J3	5.2500	2.30	0	0	17.00	0	17.00	0	0	0	0.0121	3.128E-05
J4	5.2500	2.30	0	0	17.00	0	17.00	0	0	0	0.0121	3.128E-05
J5	5.2500	2.30	0	28.000	17.00	0	17.00	0	0	0	0.0517	1.340E-04
J6	5.2500	2.30	0	0	17.00	0	17.00	0	0	0	0.0121	3.128E-05
J7	5.2500	2.30	0	0	17.00	0	17.00	0	0	0	0.0121	3.128E-05
J8	5.2500	2.30	0	0	17.00	0	17.00	0	0	0	0.0121	3.128E-05
J9	2.6250	2.30	0	28.000	17.00	0	17.00	0	0	0	0.0457	1.184E-04
K1	2.6250	2.30	0	28.000	17.00	10.995	17.00	0	4.34	0	0.0656	1.700E-04
K2	5.2500	2.30	0	0	17.00	27.000	17.00	0	0	0	0.0503	1.303E-04
K3	5.2500	2.30	8.265	0	17.00	27.000	17.00	0	0	0	0.0586	1.518E-04
K4	5.2500	2.30	5.415	0	17.00	27.000	17.00	0	0	0	0.0557	1.444E-04
K5	5.2500	2.30	28.350	28.000	17.00	21.990	17.00	0	8.68	0	0.1199	3.106E-04
K6	5.2500	2.30	5.415	0	17.00	27.000	17.00	0	0	0	0.0557	1.444E-04
K7	5.2500	2.30	8.265	0	17.00	27.000	17.00	0	0	0	0.0586	1.518E-04
K8	5.2500	2.30	0	0	17.00	27.000	17.00	0	0	0	0.0503	1.303E-04
K9	2.6250	2.30	0	28.000	17.00	10.995	17.00	0	4.34	0	0.0656	1.700E-04
L1	2.6250	2.30	0	28.000	17.00	0	17.00	0	0	0	0.0457	1.184E-04
L2	5.2500	2.30	0	0	17.00	0	17.00	0	0	0	0.0121	3.128E-05
L3	5.2500	2.30	0	0	17.00	0	17.00	0	0	0	0.0121	3.128E-05
L4	5.2500	2.30	0	0	17.00	0	17.00	0	0	0	0.0121	3.128E-05
L5	5.2500	2.30	34.220	28.000	17.00	0	17.00	0	0	0	0.0860	2.226E-04
L6	5.2500	2.30	0	0	17.00	0	17.00	0	0	0	0.0121	3.128E-05
L7	5.2500	2.30	0	0	17.00	0	17.00	0	0	0	0.0121	3.128E-05
L8	5.2500	2.30	0	0	17.00	0	17.00	0	0	0	0.0121	3.128E-05
L9	2.6250	2.30	0	28.000	17.00	0	17.00	0	0	0	0.0457	1.184E-04

Table C.3 Nodal Weights and Masses on Roof of Phase 2A Specimen Model (continued)

Node	Source of Weight and Mass										Total Nodal Weight	Total Nodal Mass
	Roof Deck		Added Weight (Stoppers Only)	Steel Beam				Brace Framing to Beam	Beam-to-Beam Joints	Column		
				Item 1		Item 2						
	A_T	Unit Wt.		L_T	Unit Wt.	L_T	Unit Wt.					
	(ft^2)	(psf)	(lbs)	(in.)	(lb/ft)	(in.)	(lb/ft)	(lbs)	(lbs)	(lbs)	(kips)	(kip-sec/$in.^2$)
M1	3.0208	2.30	0	19.750	17.00	10.465	17.00	0	0	191.61	0.2414	6.251E-04
M2′	6.0417	2.30	0	0	17.00	30.000	17.00	0	0	0	0.0564	1.461E-04
M3′	5.4375	2.30	21.870	12.495	17.00	27.000	17.00	0	4.34	0	0.0947	2.452E-04
M4′	4.8333	2.30	0	0	17.00	24.000	17.00	0	0	0	0.0451	1.169E-04
M5	4.8333	2.30	52.200	23.990	17.00	24.000	17.00	208.48	0	0	0.3398	8.801E-04
M6′	4.8333	2.30	0	0	17.00	24.000	17.00	0	0	0	0.0451	1.169E-04
M7′	5.4375	2.30	21.870	12.495	17.00	27.000	17.00	0	4.34	0	0.0947	2.452E-04
M8′	6.0417	2.30	0	0	17.00	30.000	17.00	0	0	0	0.0564	1.461E-04
M9	3.0208	2.30	0	19.750	17.00	10.465	17.00	0	0	191.61	0.2414	6.251E-04
N1	3.1250	2.30	0	30.000	17.00	0	17.00	0	0	0	0.0497	1.287E-04
N2′	6.2500	2.30	0	0	17.00	0	17.00	0	0	0	0.0144	3.723E-05
N3′	5.6250	2.30	0	30.000	17.00	0	17.00	0	0	0	0.0554	1.436E-04
N4′	5.0000	2.30	0	0	17.00	0	17.00	0	0	0	0.0115	2.979E-05
N5	5.0000	2.30	0	30.000	17.00	0	17.00	0	0	0	0.0540	1.399E-04
N6′	5.0000	2.30	0	0	17.00	0	17.00	0	0	0	0.0115	2.979E-05
N7′	5.6250	2.30	0	30.000	17.00	0	17.00	0	0	0	0.0554	1.436E-04
N8′	6.2500	2.30	0	0	17.00	0	17.00	0	0	0	0.0144	3.723E-05
N9	3.1250	2.30	0	30.000	17.00	0	17.00	0	0	0	0.0497	1.287E-04
O1	2.8125	2.30	0	10.375	17.00	10.465	17.00	0	0	185.96	0.2220	5.749E-04
O2′	5.6250	2.30	0	0	17.00	30.000	17.00	0	0	0	0.0554	1.436E-04
O3′	5.0625	2.30	21.870	12.495	17.00	27.000	17.00	0	4.34	0	0.0938	2.430E-04
O4′	4.5000	2.30	0	0	17.00	24.000	17.00	0	0	0	0.0444	1.149E-04
O5	4.5000	2.30	52.200	12.495	17.00	24.000	17.00	0	4.34	0	0.1186	3.072E-04
O6′	4.5000	2.30	0	0	17.00	24.000	17.00	0	0	0	0.0444	1.149E-04
O7′	5.0625	2.30	21.870	12.495	17.00	27.000	17.00	0	4.34	0	0.0938	2.430E-04
O8′	5.6250	2.30	0	0	17.00	30.000	17.00	0	0	0	0.0554	1.436E-04
O9	2.8125	2.30	0	10.375	17.00	10.465	17.00	0	0	185.96	0.2220	5.749E-04

Table C.4 Nodal Weights and Masses on Roof of Phase 2B Specimen Model

Node	Source of Weight and Mass										Total Nodal Weight	Total Nodal Mass
	Roof Deck		Added Weight (Stoppers Only)	Steel Beam				Brace Framing to Beam	Beam-to-Beam Joints	Column		
				Item 1		Item 2						
	A_T	Unit Wt.		L_T	Unit Wt.	L_T	Unit Wt.					
	(ft^2)	(psf)	(lbs)	(in.)	(lb/ft)	(in.)	(lb/ft)	(lbs)	(lbs)	(lbs)	(kips)	(kip-sec/$in.^2$)
A1	2.4375	2.30	0	7.450	17.00	6.850	17.00	0	0	549.05	0.5749	1.489E-03
A2	4.8750	2.30	0	0	17.00	27.000	17.00	0	0	0	0.0495	1.281E-04
A3	4.8750	2.30	0	0	17.00	27.000	17.00	0	0	0	0.0495	1.281E-04
A4	4.8750	2.30	0	0	17.00	27.000	17.00	0	0	0	0.0495	1.281E-04
A5	4.8750	2.30	0	11.495	17.00	27.000	17.00	203.99	0	0	0.2697	6.986E-04
A6	4.8750	2.30	0	0	17.00	27.000	17.00	0	0	0	0.0495	1.281E-04
A7	4.8750	2.30	0	0	17.00	27.000	17.00	0	0	0	0.0495	1.281E-04
A8	4.8750	2.30	0	0	17.00	27.000	17.00	0	0	0	0.0495	1.281E-04
A9	2.4375	2.30	0	7.450	17.00	6.850	17.00	0	0	549.05	0.5749	1.489E-03
B1	2.6250	2.30	0	28.000	17.00	0	17.00	0	0	0	0.0457	1.184E-04
B2	5.2500	2.30	0	0	17.00	0	17.00	0	0	0	0.0121	3.128E-05
B3	5.2500	2.30	0	0	17.00	0	17.00	0	0	0	0.0121	3.128E-05
B4	5.2500	2.30	0	0	17.00	0	17.00	0	0	0	0.0121	3.128E-05
B5	5.2500	2.30	40.220	28.000	17.00	0	17.00	0	0	0	0.0920	2.382E-04
B6	5.2500	2.30	0	0	17.00	0	17.00	0	0	0	0.0121	3.128E-05
B7	5.2500	2.30	0	0	17.00	0	17.00	0	0	0	0.0121	3.128E-05
B8	5.2500	2.30	0	0	17.00	0	17.00	0	0	0	0.0121	3.128E-05
B9	2.6250	2.30	0	28.000	17.00	0	17.00	0	0	0	0.0457	1.184E-04
C1	2.6250	2.30	0	28.000	17.00	10.995	17.00	0	4.34	0	0.0656	1.700E-04
C2	5.2500	2.30	0	0	17.00	27.000	17.00	0	0	0	0.0503	1.303E-04
C3	5.2500	2.30	9.630	0	17.00	27.000	17.00	0	0	0	0.0600	1.553E-04
C4	5.2500	2.30	4.050	0	17.00	27.000	17.00	0	0	0	0.0544	1.408E-04
C5	5.2500	2.30	22.350	28.000	17.00	21.990	17.00	0	8.68	0	0.1139	2.951E-04
C6	5.2500	2.30	4.050	0	17.00	27.000	17.00	0	0	0	0.0544	1.408E-04
C7	5.2500	2.30	9.630	0	17.00	27.000	17.00	0	0	0	0.0600	1.553E-04
C8	5.2500	2.30	0	0	17.00	27.000	17.00	0	0	0	0.0503	1.303E-04
C9	2.6250	2.30	0	28.000	17.00	10.995	17.00	0	4.34	0	0.0656	1.700E-04

Table C.4 Nodal Weights and Masses on Roof of Phase 2B Specimen Model (continued)

Node	Source of Weight and Mass											Total Nodal Weight	Total Nodal Mass
	Roof Deck		Added Weight		Steel Beam				Brace Framing to Beam	Beam-to-Beam Joints	Column		
					Item 1		Item 2						
	A_T	Unit Wt.	A_T	Unit Wt.	L_T	Unit Wt.	L_T	Unit Wt.					
	(ft^2)	(psf)	(ft^2)	(psf)	(in.)	(lb/ft)	(in.)	(lb/ft)	(lbs)	(lbs)	(lbs)	(kips)	(kip-sec/$in.^2$)
A1	2.4375	2.30	0	0	7.450	17.00	6.850	17.00	0	0	549.05	0.5749	1.489E-03
A2	4.8750	2.30	0	0	0	17.00	27.000	17.00	0	0	0	0.0495	1.281E-04
A3	4.8750	2.30	0	0	0	17.00	27.000	17.00	0	0	0	0.0495	1.281E-04
A4	4.8750	2.30	0	0	0	17.00	27.000	17.00	0	0	0	0.0495	1.281E-04
A5	4.8750	2.30	0	0	11.495	17.00	27.000	17.00	203.99	0	0	0.2697	6.986E-04
A6	4.8750	2.30	0	0	0	17.00	27.000	17.00	0	0	0	0.0495	1.281E-04
A7	4.8750	2.30	0	0	0	17.00	27.000	17.00	0	0	0	0.0495	1.281E-04
A8	4.8750	2.30	0	0	0	17.00	27.000	17.00	0	0	0	0.0495	1.281E-04
A9	2.4375	2.30	0	0	7.450	17.00	6.850	17.00	0	0	549.05	0.5749	1.489E-03
B1	2.6250	2.30	0	0	28.000	17.00	0	17.00	0	0	0	0.0457	1.184E-04
B2	5.2500	2.30	0	0	0	17.00	0	17.00	0	0	0	0.0121	3.128E-05
B3	5.2500	2.30	0.153	292.3	0	17.00	0	17.00	0	0	0	0.0567	1.469E-04
B4	5.2500	2.30	0.750	292.3	0	17.00	0	17.00	0	0	0	0.2313	5.991E-04
B5	5.2500	2.30	0.750	292.3	28.000	17.00	0	17.00	0	0	0	0.2710	7.018E-04
B6	5.2500	2.30	0.750	292.3	0	17.00	0	17.00	0	0	0	0.2313	5.991E-04
B7	5.2500	2.30	0.153	292.3	0	17.00	0	17.00	0	0	0	0.0567	1.469E-04
B8	5.2500	2.30	0	0	0	17.00	0	17.00	0	0	0	0.0121	3.128E-05
B9	2.6250	2.30	0	0	28.000	17.00	0	17.00	0	0	0	0.0457	1.184E-04
C1	2.6250	2.30	0	0	28.000	17.00	10.995	17.00	0	4.34	0	0.0656	1.700E-04
C2	5.2500	2.30	0	0	0	17.00	27.000	17.00	0	0	0	0.0503	1.303E-04
C3	5.2500	2.30	1.069	292.3	0	17.00	27.000	17.00	0	0	0	0.3629	9.400E-04
C4	5.2500	2.30	5.250	292.3	0	17.00	27.000	17.00	0	0	0	1.5848	4.105E-03
C5	5.2500	2.30	5.250	292.3	28.000	17.00	21.990	17.00	0	8.68	0	1.6261	4.212E-03
C6	5.2500	2.30	5.250	292.3	0	17.00	27.000	17.00	0	0	0	1.5848	4.105E-03
C7	5.2500	2.30	1.069	292.3	0	17.00	27.000	17.00	0	0	0	0.3629	9.400E-04
C8	5.2500	2.30	0	0	0	17.00	27.000	17.00	0	0	0	0.0503	1.303E-04
C9	2.6250	2.30	0	0	28.000	17.00	10.995	17.00	0	4.34	0	0.0656	1.700E-04

Table C.4 Nodal Weights and Masses on Roof of Phase 2B Specimen Model (continued)

Node	Source of Weight and Mass											Total Nodal Weight	Total Nodal Mass
	Roof Deck		Added Weight		Steel Beam				Brace Framing to Beam	Beam-to-Beam Joints	Column		
					Item 1		Item 2						
	A_T	Unit Wt.	A_T	Unit Wt.	L_T	Unit Wt.	L_T	Unit Wt.					
	(ft^2)	(psf)	(ft^2)	(psf)	(in.)	(lb/ft)	(in.)	(lb/ft)	(lbs)	(lbs)	(lbs)	(kips)	(kip-sec/$in.^2$)
D1	2.6250	2.30	0	0	28.000	17.00	0	17.00	0	0	0	0.0457	1.184E-04
D2	5.2500	2.30	0	0	0	17.00	0	17.00	0	0	0	0.0121	3.128E-05
D3	5.2500	2.30	1.069	292.3	0	17.00	0	17.00	0	0	0	0.3247	8.409E-04
D4	5.2500	2.30	5.250	292.3	0	17.00	0	17.00	0	0	0	1.5466	4.006E-03
D5	5.2500	2.30	5.250	292.3	28.000	17.00	0	17.00	0	0	0	1.5862	4.108E-03
D6	5.2500	2.30	5.250	292.3	0	17.00	0	17.00	0	0	0	1.5466	4.006E-03
D7	5.2500	2.30	1.069	292.3	0	17.00	0	17.00	0	0	0	0.3247	8.409E-04
D8	5.2500	2.30	0	0	0	17.00	0	17.00	0	0	0	0.0121	3.128E-05
D9	2.6250	2.30	0	0	28.000	17.00	0	17.00	0	0	0	0.0457	1.184E-04
E1	2.6250	2.30	0	0	28.000	17.00	10.995	17.00	0	4.34	0	0.0656	1.700E-04
E2	5.2500	2.30	0	0	0	17.00	27.000	17.00	0	0	0	0.0503	1.303E-04
E3	5.2500	2.30	1.069	292.3	0	17.00	27.000	17.00	0	0	0	0.3629	9.400E-04
E4	5.2500	2.30	5.250	292.3	0	17.00	27.000	17.00	0	0	0	1.5848	4.105E-03
E5	5.2500	2.30	5.250	292.3	28.000	17.00	21.990	17.00	0	8.68	0	1.6261	4.212E-03
E6	5.2500	2.30	5.250	292.3	0	17.00	27.000	17.00	0	0	0	1.5848	4.105E-03
E7	5.2500	2.30	1.069	292.3	0	17.00	27.000	17.00	0	0	0	0.3629	9.400E-04
E8	5.2500	2.30	0	0	0	17.00	27.000	17.00	0	0	0	0.0503	1.303E-04
E9	2.6250	2.30	0	0	28.000	17.00	10.995	17.00	0	4.34	0	0.0656	1.700E-04
F1	2.6250	2.30	0	0	28.000	17.00	0	17.00	0	0	0	0.0457	1.184E-04
F2	5.2500	2.30	0	0	0	17.00	0	17.00	0	0	0	0.0121	3.128E-05
F3	5.2500	2.30	0.153	292.3	0	17.00	0	17.00	0	0	0	0.0567	1.469E-04
F4	5.2500	2.30	0.750	292.3	0	17.00	0	17.00	0	0	0	0.2313	5.991E-04
F5	5.2500	2.30	0.750	292.3	28.000	17.00	0	17.00	0	0	0	0.2710	7.018E-04
F6	5.2500	2.30	0.750	292.3	0	17.00	0	17.00	0	0	0	0.2313	5.991E-04
F7	5.2500	2.30	0.153	292.3	0	17.00	0	17.00	0	0	0	0.0567	1.469E-04
F8	5.2500	2.30	0	0	0	17.00	0	17.00	0	0	0	0.0121	3.128E-05
F9	2.6250	2.30	0	0	28.000	17.00	0	17.00	0	0	0	0.0457	1.184E-04

Table C.4 Nodal Weights and Masses on Roof of Phase 2B Specimen Model (continued)

Node	Source of Weight and Mass											Total Nodal Weight	Total Nodal Mass
	Roof Deck		Added Weight		Steel Beam				Brace Framing to Beam	Beam-to-Beam Joints	Column		
					Item 1		Item 2						
	A_T	Unit Wt.	A_T	Unit Wt.	L_T	Unit Wt.	L_T	Unit Wt.					
	(ft^2)	(psf)	(ft^2)	(psf)	(in.)	(lb/ft)	(in.)	(lb/ft)	(lbs)	(lbs)	(lbs)	(kips)	(kip-sec/$in.^2$)
G1	2.6250	2.30	0	0	19.750	17.00	8.965	17.00	0	0	191.61	0.2383	6.173E-04
G2	5.2500	2.30	0	0	0	17.00	27.000	17.00	0	0	0	0.0503	1.303E-04
G3	5.2500	2.30	0	0	0	17.00	27.000	17.00	0	0	0	0.0503	1.303E-04
G4	5.2500	2.30	0	0	0	17.00	27.000	17.00	0	0	0	0.0503	1.303E-04
G5	5.2500	2.30	0	0	22.990	17.00	27.000	17.00	208.48	0	0	0.2914	7.547E-04
G6	5.2500	2.30	0	0	0	17.00	27.000	17.00	0	0	0	0.0503	1.303E-04
G7	5.2500	2.30	0	0	0	17.00	27.000	17.00	0	0	0	0.0503	1.303E-04
G8	5.2500	2.30	0	0	0	17.00	27.000	17.00	0	0	0	0.0503	1.303E-04
G9	2.6250	2.30	0	0	19.750	17.00	8.965	17.00	0	0	191.61	0.2383	6.173E-04
H1	2.6250	2.30	0	0	28.000	17.00	0	17.00	0	0	0	0.0457	1.184E-04
H2	5.2500	2.30	0	0	0	17.00	0	17.00	0	0	0	0.0121	3.128E-05
H3	5.2500	2.30	0.026	375.7	0	17.00	0	17.00	0	0	0	0.0217	5.622E-05
H4	5.2500	2.30	0.246	375.7	0	17.00	0	17.00	0	0	0	0.1045	2.708E-04
H5	5.2500	2.30	0.246	375.7	28.000	17.00	0	17.00	0	0	0	0.1442	3.735E-04
H6	5.2500	2.30	0.246	375.7	0	17.00	0	17.00	0	0	0	0.1045	2.708E-04
H7	5.2500	2.30	0.026	375.7	0	17.00	0	17.00	0	0	0	0.0217	5.622E-05
H8	5.2500	2.30	0	0	0	17.00	0	17.00	0	0	0	0.0121	3.128E-05
H9	2.6250	2.30	0	0	28.000	17.00	0	17.00	0	0	0	0.0457	1.184E-04
I1	2.6250	2.30	0	0	28.000	17.00	10.995	17.00	0	4.34	0	0.0656	1.700E-04
I2	5.2500	2.30	0	0	0	17.00	27.000	17.00	0	0	0	0.0503	1.303E-04
I3	5.2500	2.30	0.547	375.7	0	17.00	27.000	17.00	0	0	0	0.2558	6.626E-04
I4	5.2500	2.30	5.250	375.7	0	17.00	27.000	17.00	0	0	0	2.0230	5.240E-03
I5	5.2500	2.30	5.250	375.7	28.000	17.00	21.990	17.00	0	8.68	0	2.0642	5.346E-03
I6	5.2500	2.30	5.250	375.7	0	17.00	27.000	17.00	0	0	0	2.0230	5.240E-03
I7	5.2500	2.30	0.547	375.7	0	17.00	27.000	17.00	0	0	0	0.2558	6.626E-04
I8	5.2500	2.30	0	0	0	17.00	27.000	17.00	0	0	0	0.0503	1.303E-04
I9	2.6250	2.30	0	0	28.000	17.00	10.995	17.00	0	4.34	0	0.0656	1.700E-04

Table C.4 Nodal Weights and Masses on Roof of Phase 2B Specimen Model (continued)

Node	Source of Weight and Mass											Total Nodal Weight	Total Nodal Mass
	Roof Deck		Added Weight		Steel Beam				Brace Framing to Beam	Beam-to-Beam Joints	Column		
					Item 1		Item 2						
	A_T	Unit Wt.	A_T	Unit Wt.	L_T	Unit Wt.	L_T	Unit Wt.					
	(ft^2)	(psf)	(ft^2)	(psf)	(in.)	(lb/ft)	(in.)	(lb/ft)	(lbs)	(lbs)	(lbs)	(kips)	(kip-sec/$in.^2$)
J1	2.6250	2.30	0	0	28.000	17.00	0	17.00	0	0	0	0.0457	1.184E-04
J2	5.2500	2.30	0	0	0	17.00	0	17.00	0	0	0	0.0121	3.128E-05
J3	5.2500	2.30	0.547	375.7	0	17.00	0	17.00	0	0	0	0.2176	5.635E-04
J4	5.2500	2.30	5.250	375.7	0	17.00	0	17.00	0	0	0	1.9847	5.141E-03
J5	5.2500	2.30	5.250	375.7	28.000	17.00	0	17.00	0	0	0	2.0244	5.243E-03
J6	5.2500	2.30	5.250	375.7	0	17.00	0	17.00	0	0	0	1.9847	5.141E-03
J7	5.2500	2.30	0.547	375.7	0	17.00	0	17.00	0	0	0	0.2176	5.635E-04
J8	5.2500	2.30	0	0	0	17.00	0	17.00	0	0	0	0.0121	3.128E-05
J9	2.6250	2.30	0	0	28.000	17.00	0	17.00	0	0	0	0.0457	1.184E-04
K1	2.6250	2.30	0	0	28.000	17.00	10.995	17.00	0	4.34	0	0.0656	1.700E-04
K2	5.2500	2.30	0	0	0	17.00	27.000	17.00	0	0	0	0.0503	1.303E-04
K3	5.2500	2.30	0.547	375.7	0	17.00	27.000	17.00	0	0	0	0.2558	6.626E-04
K4	5.2500	2.30	5.250	375.7	0	17.00	27.000	17.00	0	0	0	2.0230	5.240E-03
K5	5.2500	2.30	5.250	375.7	28.000	17.00	21.990	17.00	0	8.68	0	2.0642	5.346E-03
K6	5.2500	2.30	5.250	375.7	0	17.00	27.000	17.00	0	0	0	2.0230	5.240E-03
K7	5.2500	2.30	0.547	375.7	0	17.00	27.000	17.00	0	0	0	0.2558	6.626E-04
K8	5.2500	2.30	0	0	0	17.00	27.000	17.00	0	0	0	0.0503	1.303E-04
K9	2.6250	2.30	0	0	28.000	17.00	10.995	17.00	0	4.34	0	0.0656	1.700E-04
L1	2.6250	2.30	0	0	28.000	17.00	0	17.00	0	0	0	0.0457	1.184E-04
L2	5.2500	2.30	0	0	0	17.00	0	17.00	0	0	0	0.0121	3.128E-05
L3	5.2500	2.30	0.026	375.7	0	17.00	0	17.00	0	0	0	0.0217	5.622E-05
L4	5.2500	2.30	0.246	375.7	0	17.00	0	17.00	0	0	0	0.1045	2.708E-04
L5	5.2500	2.30	0.246	375.7	28.000	17.00	0	17.00	0	0	0	0.1442	3.735E-04
L6	5.2500	2.30	0.246	375.7	0	17.00	0	17.00	0	0	0	0.1045	2.708E-04
L7	5.2500	2.30	0.026	375.7	0	17.00	0	17.00	0	0	0	0.0217	5.622E-05
L8	5.2500	2.30	0	0	0	17.00	0	17.00	0	0	0	0.0121	3.128E-05
L9	2.6250	2.30	0	0	28.000	17.00	0	17.00	0	0	0	0.0457	1.184E-04

Table C.4 Nodal Weights and Masses on Roof of Phase 2B Specimen Model (continued)

Node	Source of Weight and Mass											Total Nodal Weight	Total Nodal Mass
	Roof Deck		Added Weight		Steel Beam				Brace Framing to Beam	Beam-to-Beam Joints	Column		
					Item 1		Item 2						
	A_T	Unit Wt.	A_T	Unit Wt.	L_T	Unit Wt.	L_T	Unit Wt.					
	(ft^2)	(psf)	(ft^2)	(psf)	(in.)	(lb/ft)	(in.)	(lb/ft)	(lbs)	(lbs)	(lbs)	(kips)	(kip-sec/$in.^2$)
M1	3.0208	2.30	0	0	19.750	17.00	10.465	17.00	0	0	191.61	0.2414	6.251E-04
M2′	6.0417	2.30	0.486	156.2	0	17.00	30.000	17.00	0	0	0	0.1323	3.427E-04
M3′	5.4375	2.30	1.875	156.2	12.495	17.00	27.000	17.00	0	4.34	0	0.3656	9.470E-04
M4′	4.8333	2.30	1.667	156.2	0	17.00	24.000	17.00	0	0	0	0.3054	7.910E-04
M5	4.8333	2.30	1.667	156.2	23.990	17.00	24.000	17.00	208.48	0	0	0.5479	1.419E-03
M6′	4.8333	2.30	1.667	156.2	0	17.00	24.000	17.00	0	0	0	0.3054	7.910E-04
M7′	5.4375	2.30	1.875	156.2	12.495	17.00	27.000	17.00	0	4.34	0	0.3656	9.470E-04
M8′	6.0417	2.30	0.486	156.2	0	17.00	30.000	17.00	0	0	0	0.1323	3.427E-04
M9	3.0208	2.30	0	0	19.750	17.00	10.465	17.00	0	0	191.61	0.2414	6.251E-04
N1	3.1250	2.30	0	0	30.000	17.00	0	17.00	0	0	0	0.0497	1.287E-04
N2′	6.2500	2.30	1.458	156.2	0	17.00	0	17.00	0	0	0	0.2421	6.271E-04
N3′	5.6250	2.30	5.625	156.2	30.000	17.00	0	17.00	0	0	0	0.9339	2.419E-03
N4′	5.0000	2.30	5.000	156.2	0	17.00	0	17.00	0	0	0	0.7924	2.052E-03
N5	5.0000	2.30	5.000	156.2	30.000	17.00	0	17.00	0	0	0	0.8349	2.162E-03
N6′	5.0000	2.30	5.000	156.2	0	17.00	0	17.00	0	0	0	0.7924	2.052E-03
N7′	5.6250	2.30	5.625	156.2	30.000	17.00	0	17.00	0	0	0	0.9339	2.419E-03
N8′	6.2500	2.30	1.458	156.2	0	17.00	0	17.00	0	0	0	0.2421	6.271E-04
N9	3.1250	2.30	0	0	30.000	17.00	0	17.00	0	0	0	0.0497	1.287E-04
O1	2.8125	2.30	0	0	10.375	17.00	10.465	17.00	0	0	185.96	0.2220	5.749E-04
O2′	5.6250	2.30	0.486	156.2	0	17.00	30.000	17.00	0	0	0	0.1314	3.402E-04
O3′	5.0625	2.30	1.875	156.2	12.495	17.00	27.000	17.00	0	4.34	0	0.3648	9.448E-04
O4′	4.5000	2.30	1.667	156.2	0	17.00	24.000	17.00	0	0	0	0.3046	7.890E-04
O5	4.5000	2.30	1.667	156.2	12.495	17.00	24.000	17.00	0	4.34	0	0.3267	8.461E-04
O6′	4.5000	2.30	1.667	156.2	0	17.00	24.000	17.00	0	0	0	0.3046	7.890E-04
O7′	5.0625	2.30	1.875	156.2	12.495	17.00	27.000	17.00	0	4.34	0	0.3648	9.448E-04
O8′	5.6250	2.30	0.486	156.2	0	17.00	30.000	17.00	0	0	0	0.1314	3.402E-04
O9	2.8125	2.30	0	0	10.375	17.00	10.465	17.00	0	0	185.96	0.2220	5.749E-04

Table C.5 Calculation of Section Properties for Collectors

(a) for Axial Action and Strong-Axis Flexure

Material Properties									
Steel			Concrete Slab			Added RC Block			
E_s = 29000 ksi			E_{c1} = 2473 ksi n_1 = 11.727			E_{c2} = 3605 ksi n_2 = 8.044			
Calculation of Section Properties for Composite Collectors									
Collector Designation (Beam Element Designation)			Frame N				Frame S		
			N1 (AG1)	N2 (GM1)	N3 (MO1)	N4 (OQ1)	S1 (AG9)	S2 (GM9)	S3 (MO9)	S4 (OQ9)
Steel Beam Section Properties	Shape		W14x30	W14x30	W14x26	W14x26	W14x30	W14x30	W14x26	W14x26
	A_s	(in.^{2})	8.85	8.85	7.69	7.69	8.85	8.85	7.69	7.69
	$I_{x,s}$	(in.^{4})	291	291	245	245	291	291	245	245
	$A_{vy,s}$	(in.^{2})	3.726	3.726	3.545	3.545	3.726	3.726	3.545	3.545
	d_s	(in.)	13.8	13.8	13.9	13.9	13.8	13.8	13.9	13.9
Bottom-Layer Concrete Dimensions	w_{cb}	(in.)	13.3375	14.25	10.9375	10.9375	9.1	10.9	7.5	7.5
	t_{cb}	(in.)	1.5	1.5	1.5	1.5	1.5	1.5	1.5	1.5
Top-Layer Concrete Dimensions	w_{ct}	(in.)	19.6	22	15	15	20.2	24	15	15
	t_{ct}	(in.)	2	2	2	2	2	2	2	2
y-coordinates	y_s	(in.)	6.9	6.9	6.95	6.95	6.9	6.9	6.95	6.95
	y_{cb}	(in.)	14.55	14.55	14.65	14.65	14.55	14.55	14.65	14.65
	y_{ct}	(in.)	16.3	16.3	16.4	16.4	16.3	16.3	16.4	16.4
Effective Concrete Section Properties	A_{cb}/n_1	(in.^{2})	0	2	1.399	1.399	1.164	1.394	0.959	1
	A_{ct}/n_1	(in.^{2})	3.343	3.752	2.558	2.558	3.445	4.093	2.558	2.558
	$I_{x,cb}/n_1$	(in.^{4})	0	0	0.262	0.262	0.218	0.261	0.180	0
	$I_{x,ct}/n_1$	(in.^{4})	1.114	1.251	0.853	0.853	1.148	1.364	0.853	0.853
Fully Composite Section Properties	$\bar{y}$	(in.)	9.48	10.31	9.95	9.95	9.97	10.33	9.77	9.77
	A_{tr}	(in.^{2})	12.19	14.42	11.65	11.65	13.46	14.34	11.21	11.21
	$I_{x,tr}$	(in.^{4})	507	563	453	453	538	567	442	442
Avg. Properties of Composite Section	A_{avg}	(in.^{2})	10.52	11.64	9.67	9.67	11.15	11.59	9.45	9.45
	$I_{x,avg}$	(in.^{4})	399	427	349	349	415	429	344	344
Model Input Properties	A_{ipt}	(in.^{2})	10.52	11.64	9.67	9.67	11.15	11.59	9.45	9.45
	I_{ipt}	(in.^{4})	399	427	349	349	415	429	344	344
	$A_{vy,ipt}$	(in.^{2})	3.726	3.726	3.545	3.545	3.726	3.726	3.545	3.545

Table C.5 Calculation of Section Properties for Collectors (continued)

(b) for Torsion and Weak-Axis Flexure

Material Properties									
Steel			Concrete Slab			Added RC Block			
E_s =	29000	ksi	E_{c1} =	2473	ksi	E_{c2} =	3605	ksi	
			n_1 =	11.727		n_2 =	8.044		

Calculation of Section Properties for Composite Collectors										
Collector Designation (Beam Element Designation)			Frame N				Frame S			
			N1 (AG1)	N2 (GM1)	N3 (MO1)	N4 (OQ1)	S1 (AG9)	S2 (GM9)	S3 (MO9)	S4 (OQ9)
Steel Beam Section Properties	Shape		W14x30	W14x30	W14x26	W14x26	W14x30	W14x30	W14x26	W14x26
	$I_{y,s}$	(in.^{4})	19.6	19.6	8.91	8.91	19.6	19.6	8.91	8.91
	$A_{vx,s}$	(in.^{2})	3.455	3.455	2.817	2.817	3.455	3.455	2.817	2.817
	J_s	(in.^{4})	0.380	0.380	0.358	0.358	0.380	0.380	0.358	0.358
Bottom-Layer Concrete Dimensions	w_{cb}	(in.)	13.3375	14.25	10.9375	10.9375	9.1	10.9	7.5	7.5
	t_{cb}	(in.)	1.5	1.5	1.5	1.5	1.5	1.5	1.5	1.5
Top-Layer Concrete Dimensions	w_{ct}	(in.)	19.6	22	15	15	20.2	24	15	15
	t_{ct}	(in.)	2	2	2	2	2	2	2	2
Effective Concrete Section Properties	$I_{y,cb}/n_1$	(in.^{4})	25.3	30.8	13.9	13.9	8.0	13.8	4.5	4.5
	$I_{y,ct}/n_1$	(in.^{4})	107.0	151.3	48.0	48.0	117.1	196.5	48.0	48.0
	J_{cb}/n_1	(in.^{4})	1.189	1.276	0.959	0.959	0.782	0.955	0.629	0.629
	J_{ct}/n_1	(in.^{4})	4.171	4.716	3.125	3.125	4.307	5.171	3.125	3.125
Model Input Properties	$I_{y,ipt}$	(in.^{4})	151.9	201.8	70.8	70.8	144.8	229.9	61.4	61.4
	$A_{vx,ipt}$	(in.^{2})	3.455	3.455	2.817	2.817	3.455	3.455	2.817	2.817
	J_{ipt}	(in.^{4})	5.739	6.373	4.441	4.441	5.469	6.506	4.111	4.111

Table C.6 Calculation of Section Properties for Chords and Floor Beams

(a) for Axial Action and Strong-Axis Flexure

Material Properties													
Steel				Concrete Slab				Added RC Block					
E_s =	29000	ksi		E_{c1} =	2473	ksi		E_{c2} =	3605	ksi			
				n_1 =	11.727			n_2 =	8.044				

Calculation of Section Properties for Composite Floor Beams													
Beam Location			Longitudinal Beams						Transverse Beams				
			AG5, GM5	AG7, GM7	MO5	MO3, MO7	OQ5	OQ3, OQ7	A19	G19, D15, J15, M19, O19	M19*, O19*	Q19	Q19*
Steel Beam Section Properties	Shape		W14x26	W14x26	W14x26	W14x26	W14x26	W14x26	W14x26	W14x26	W14x26	W14x26	W14x26
	A_s	(in.^{2})	7.69	7.69	7.69	7.69	7.69	7.69	7.69	7.69	7.69	7.69	7.69
	$I_{x,s}$	(in.^{4})	245	245	245	245	245	245	245	245	245	245	245
	$A_{vy,s}$	(in.^{2})	3.545	3.545	3.545	3.545	3.545	3.545	3.545	3.545	3.545	3.545	3.545
	d_s	(in.)	13.9	13.9	13.9	13.9	13.9	13.9	13.9	13.9	13.9	13.9	13.9
Bot.-Layer Concrete Dimensions	w_{cb}	(in.)	0	0	0	0	0	0	12	0	0	12	12
	t_{cb}	(in.)	1.5	1.5	1.5	1.5	1.5	1.5	1.5	1.5	1.5	1.5	1.5
Top-Layer Concrete Dimensions	w_{ct}	(in.)	42	42	15	15	15	15	25.5	27	27	39	39
	t_{ct}	(in.)	2	2	2	2	2	2	2	2	2	2	2
Added RC Block	w_{add}	(in.)	60	0	48	24	71	0	0	0	27	0	39
	t_{add}	(in.)	33.5	0	24	24	29	0	0	0	24	0	29
y-coordinates	y_s	(in.)	6.95	6.95	6.95	6.95	6.95	6.95	6.95	6.95	6.95	6.95	6.95
	y_{cb}	(in.)	14.65	14.65	14.65	14.65	14.65	14.65	14.65	14.65	14.65	14.65	14.65
	y_{ct}	(in.)	16.4	16.4	16.4	16.4	16.4	16.4	16.4	16.4	16.4	16.4	16.4
Effective Concrete Section Properties	A_{cb}/n_1	(in.^{2})	0	0	0.000	0.000	0.000	0.000	1.535	0	0	1.535	1.535
	A_{ct}/n_1	(in.^{2})	7.163	7.163	2.558	2.558	2.558	2.558	4.349	4.605	4.605	6.652	6.652
	$I_{x,cb}/n_1$	(in.^{4})	0	0	0.000	0.000	0.000	0.000	0.288	0	0	0.288	0.288
	$I_{x,ct}/n_1$	(in.^{4})	2.388	2.388	0.853	0.853	0.853	0.853	1.450	1.535	1.535	2.217	2.217
Fully Composite Section Properties	$\bar{y}$	(in.)	11.51	11.51	9.31	9.31	9.31	9.31	10.85	10.49	10.49	11.65	11.65
	A_{tr}	(in.^{2})	14.85	14.85	10.25	10.25	10.25	10.25	13.57	12.29	12.29	15.88	15.88
	$I_{x,tr}$	(in.^{4})	579	579	417	417	417	417	520	504	504	581	581
Avg. Properties of Composite Section	A_{avg}	(in.^{2})	11.27	11.27	8.97	8.97	8.97	8.97	10.63	9.99	9.99	11.78	11.78
	$I_{x,avg}$	(in.^{4})	412	412	331	331	331	331	382	374	374	413	413
Added RC Block Section Properties	A_{add}/n_2	(in.^{2})	250	0	143	72	256	0	0	0	80.55	0	140.59
	$I_{x,add}/n_2$	(in.^{4})	23367	0	6874	3437	17938	0	0	0	3867	0	9853
Model Input Properties	A_{ipt}	(in.^{2})	11.27	11.27	8.97	8.97	8.97	8.97	10.63	9.99	9.99	11.78	11.78
	$I_{x,ipt}$	(in.^{4})	23779	412	7205	3768	18269	331	382	374	4241	413	10266
	$A_{vy,ipt}$	(in.^{2})	3.545	3.545	3.545	3.545	3.545	3.545	3.545	3.545	3.545	3.545	3.545

Table C.6 Calculation of Section Properties for Chords and Floor Beams (continued)

(b) for Torsion and Weak-Axis Flexure

Material Properties									
Steel			Concrete Slab			Added RC Block			
E_s =	29000	ksi	E_{c1} =	2473	ksi	E_{c2} =	3605	ksi	
			n_1 =	11.727		n_2 =	8.044		

Calculation of Section Properties for Composite Floor Beams													
Beam Location			Longitudinal Beams						Transverse Beams				
			AG5, GM5	AG7, GM7	MO5	MO3, MO7	OQ5	OQ3, OQ7	A19	G19, D15, J15, M19, O19	M19*, O19*	Q19	Q19*
Steel Beam Section Properties	Shape		W14x26	W14x26	W14x26	W14x26	W14x26	W14x26	W14x26	W14x26	W14x26	W14x26	W14x26
	$I_{y,s}$	(in.^{4})	8.91	8.91	8.91	8.91	8.91	8.91	8.91	8.91	8.91	8.91	8.91
	$A_{vx,s}$	(in.^{2})	2.817	2.817	2.817	2.817	2.817	2.817	2.817	2.817	2.817	2.817	2.817
	J_s	(in.^{4})	0.358	0.358	0.358	0.358	0.358	0.358	0.358	0.358	0.358	0.358	0.358
Bot.-Layer Concrete Dimensions	w_{cb}	(in.)	0	0	0	0	0	0	12	0	0	12	12
	t_{cb}	(in.)	1.5	1.5	1.5	1.5	1.5	1.5	1.5	1.5	1.5	1.5	1.5
Top-Layer Concrete Dimensions	w_{ct}	(in.)	42	42	15	15	15	15	25.5	27	27	39	39
	t_{ct}	(in.)	2	2	2	2	2	2	2	2	2	2	2
Added RC Block	w_{add}	(in.)	60	0	48	24	71	0	0	0	27	0	39
	t_{add}	(in.)	33.5	0	24	24	29	0	0	0	24	0	29
Effective Concrete Section Properties	$I_{y,cb}/n_1$	(in.^{4})	0.0	0.0	0.0	0.0	0.0	0.0	18.4	0.0	0.0	18.4	18.4
	$I_{y,ct}/n_1$	(in.^{4})	1053.0	1053.0	48.0	48.0	48.0	48.0	235.7	279.7	279.7	843.1	843.1
	J_{cb}/n_1	(in.^{4})	0.00	0.00	0.00	0.00	0.00	0.00	1.06	0.00	0.00	1.06	1.06
	J_{ct}/n_1	(in.^{4})	9.26	9.26	3.12	3.12	3.12	3.12	5.51	5.85	5.85	8.58	8.58
Added RC Block Section Properties	$I_{y,add}/n_2$	(in.^{4})	74959.1	0.0	27495.4	3436.9	107522.3	0.0	0.0	0.0	4893.6	0.0	17820.4
	J_{add}/n_2	(in.^{4})	60858.0	0.0	12951.2	3984.5	36585.2	0.0	0.0	0.0	4977.4	0.0	14694.1
Model Input Properties	$I_{y,ipt}$	(in.^{4})	76021	1062	27552	3494	107579	56.9	263	289	5182	870	18691
	$A_{vx,ipt}$	(in.^{4})	2.817	2.817	2.817	2.817	2.817	2.817	2.817	2.817	2.817	2.817	2.817
	J_{ipt}	(in.^{4})	60868	9.622	12955	3988	36589	3.483	6.931	6.211	4984	10.00	14704

Appendix D. Quality Check for Shake Table Tests

This Appendix presents the quality check for several selected shake table tests. The measured responses from the key instruments for measuring the global responses of the test specimens are presented. These key sensors included the string potentiometers used to measure the absolute displacement of the foundation, 2nd floor and roof levels and the accelerometers placed on the 2nd floor and roof levels. In addition, the comparisons among the displacement or acceleration responses measured form the sensors at the same levels are presented as well. Figure D.1 through Figure D.6 show the quality check for Test 1-3; Figure D.7 through Figure D.16 show the quality check for Test 2A-5; Figure D.17 through Figure D.26 show the quality check for Test 2B-5; and Figure D.27 through Figure D.36 show the quality check for Test 3-6.

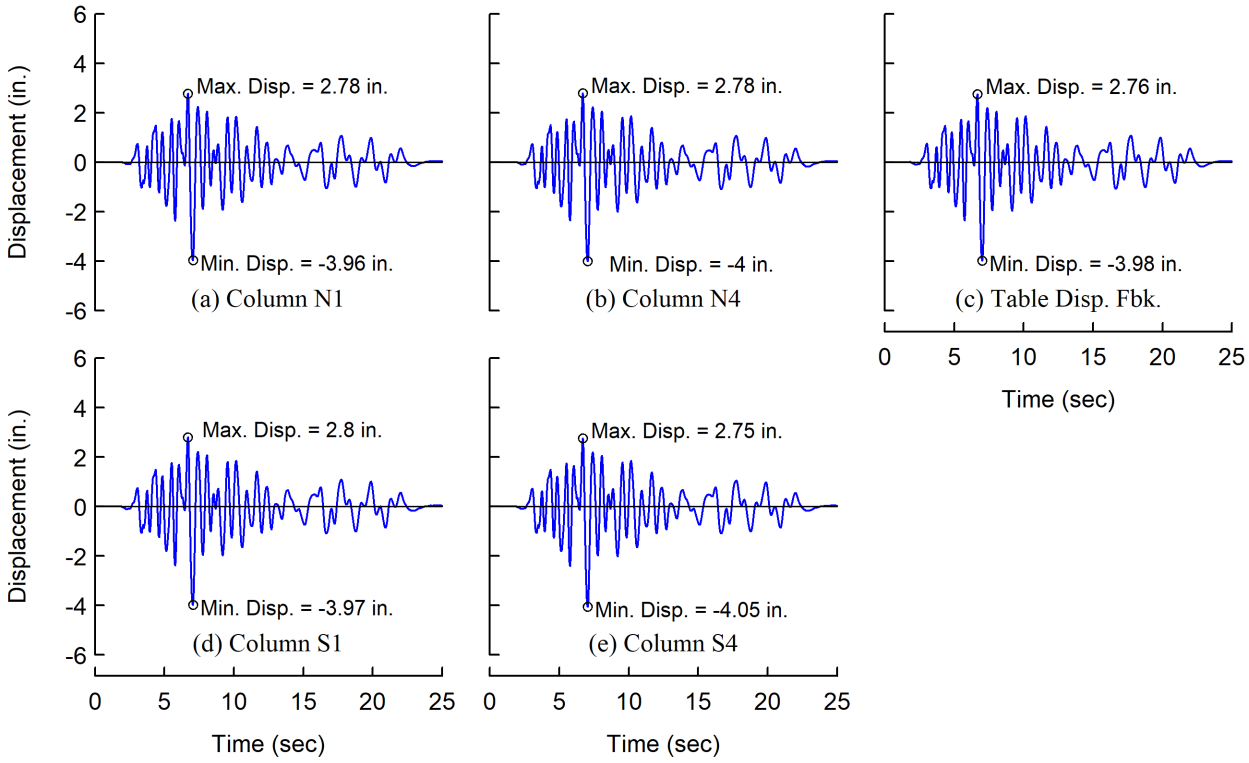

Figure D.1 Test 1-3: Measured Displacements at Various Locations on Footing Level

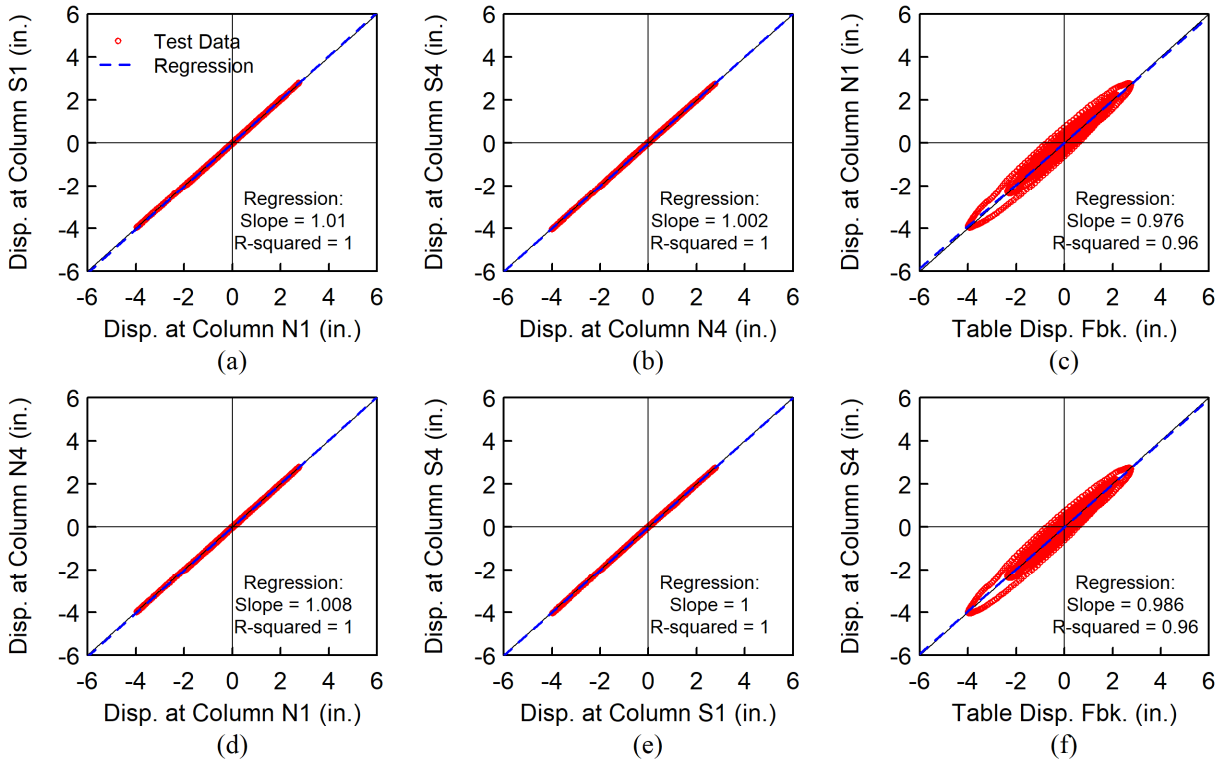

Figure D.2 Test 1-3: Comparisons of Displacements at Various Locations on Footing Level

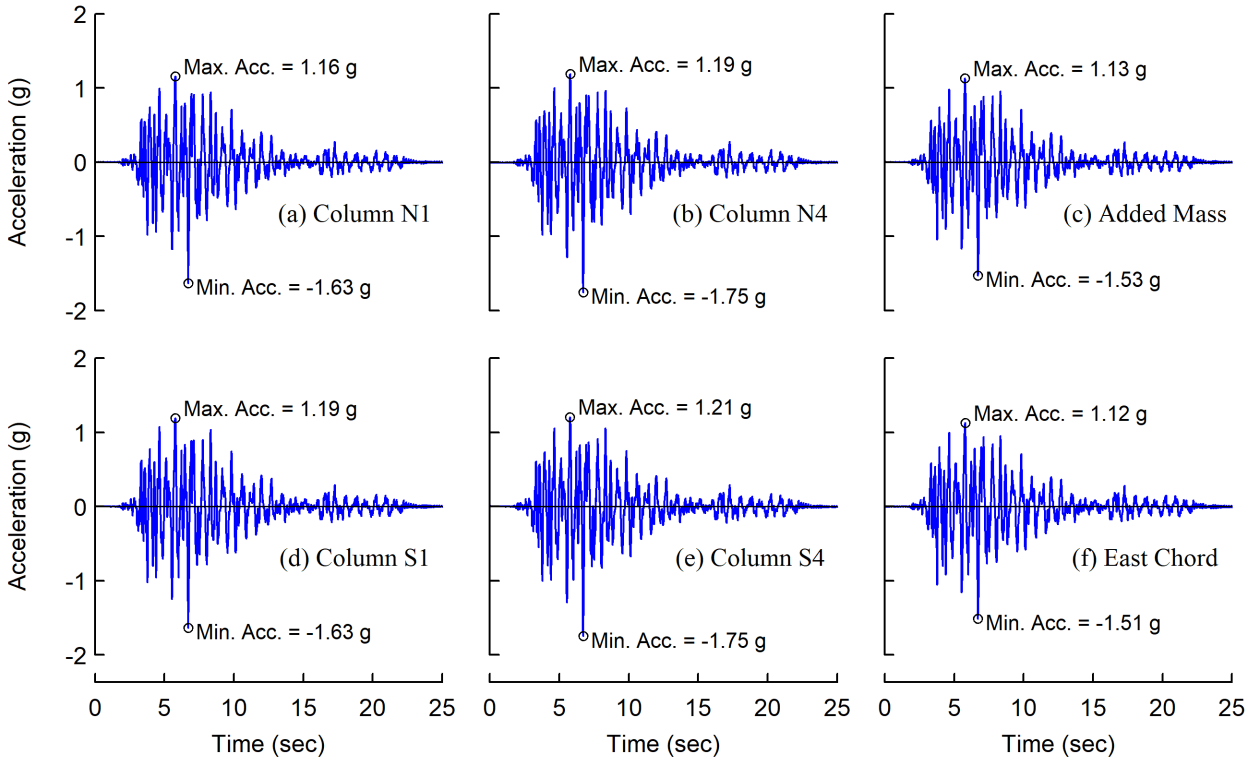

Figure D.3 Test 1-3: Measured Accelerations at Various Locations on 2nd Floor

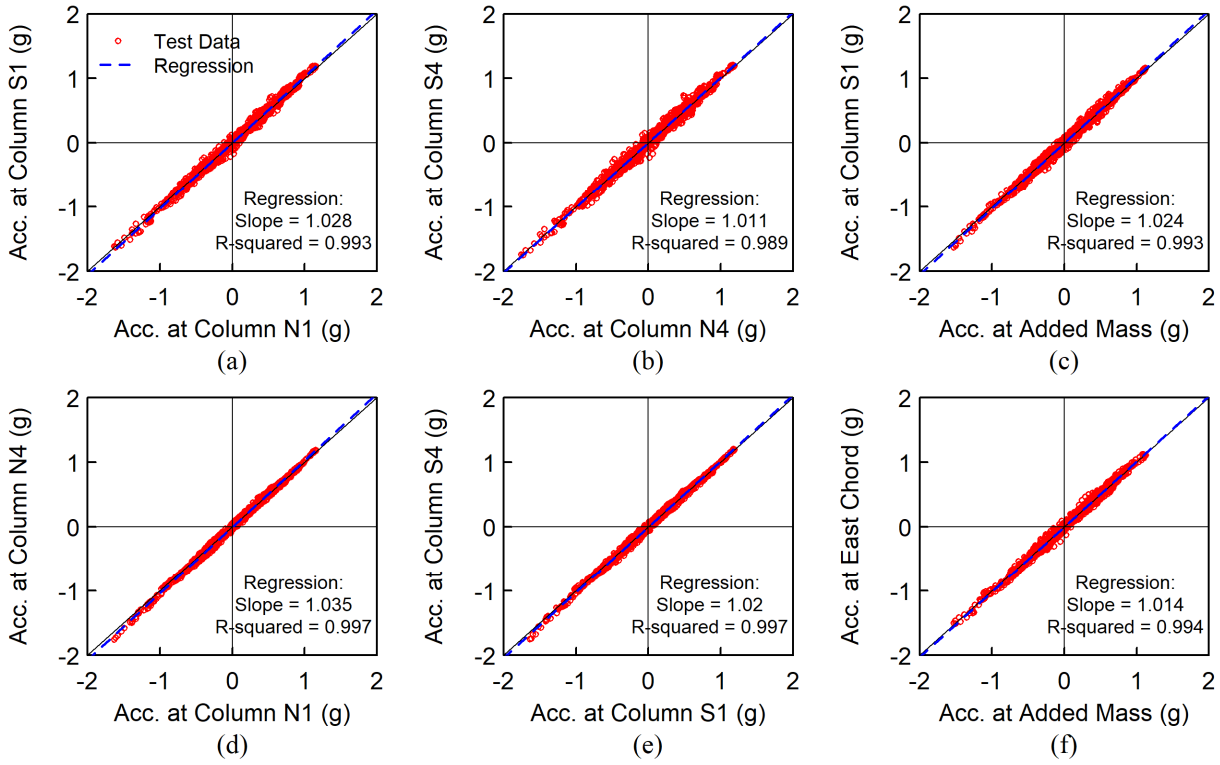

Figure D.4 Test 1-3: Comparisons of Accelerations at Various Locations on 2nd Floor

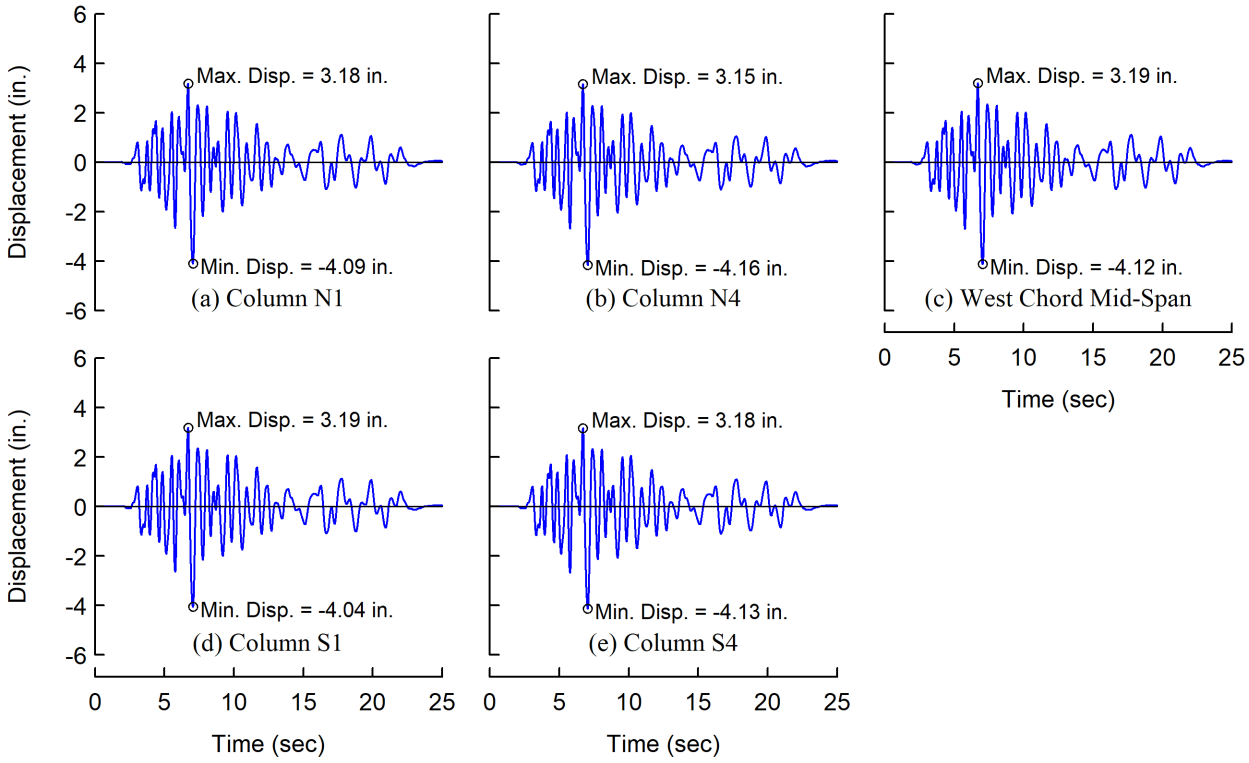

Figure D.5 Test 1-3: Measured Displacements at Various Locations on 2nd Floor

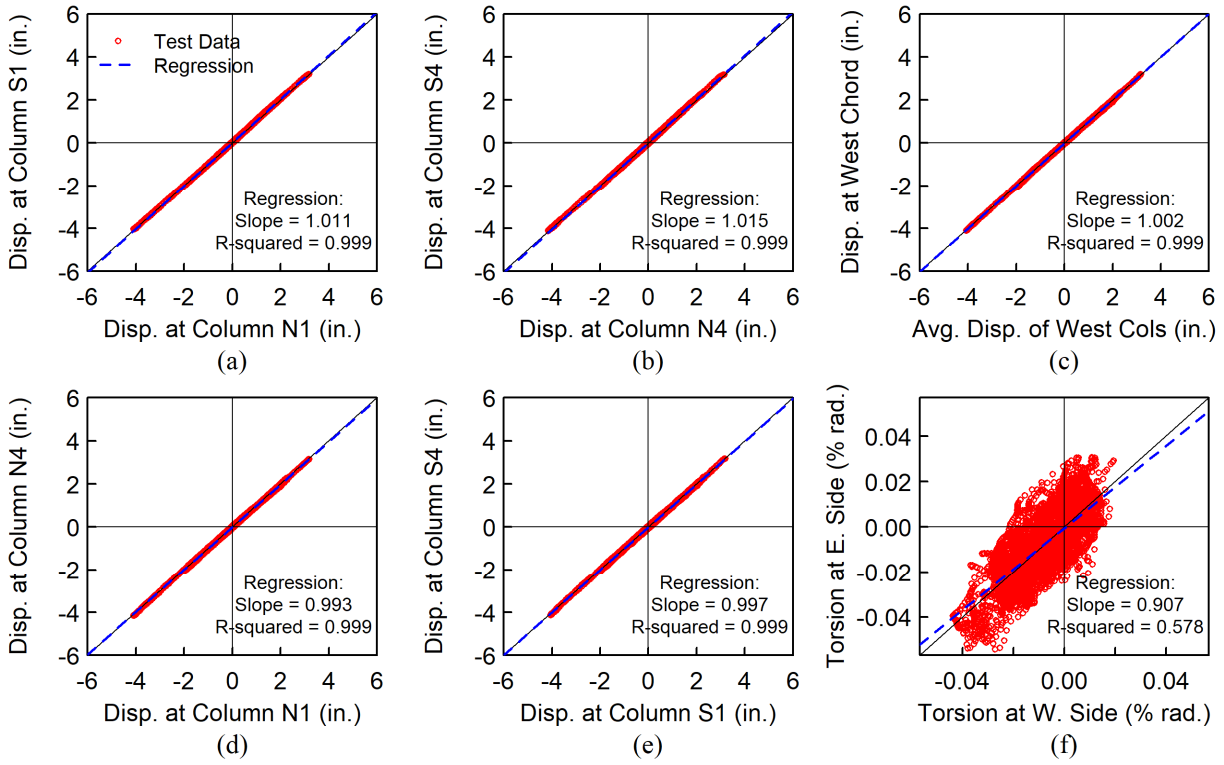

Figure D.6 Test 1-3: Comparisons of Displacements at Various Locations on 2nd Floor

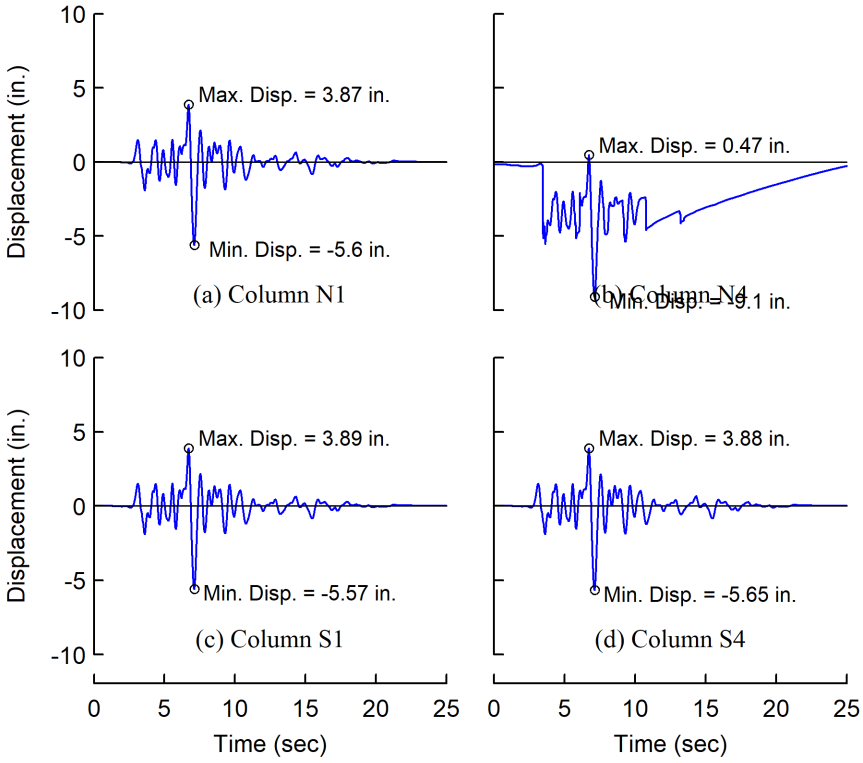

Figure D.7 Test 2A-5: Measured Displacements at Various Locations on Footing Level

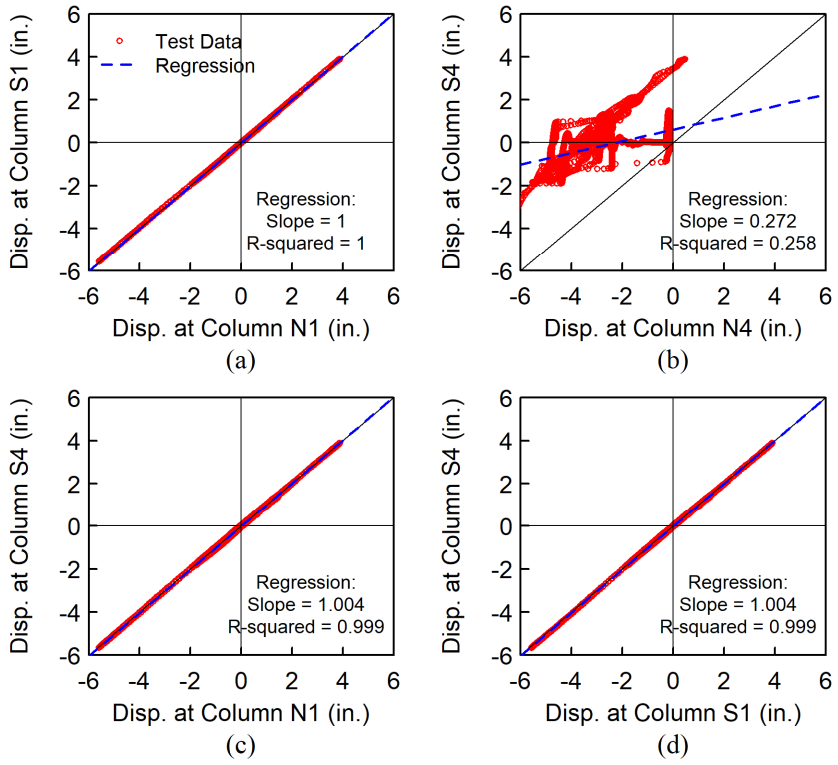

Figure D.8 Test 2A-5: Comparisons of Displacements at Various Locations on Footing Level

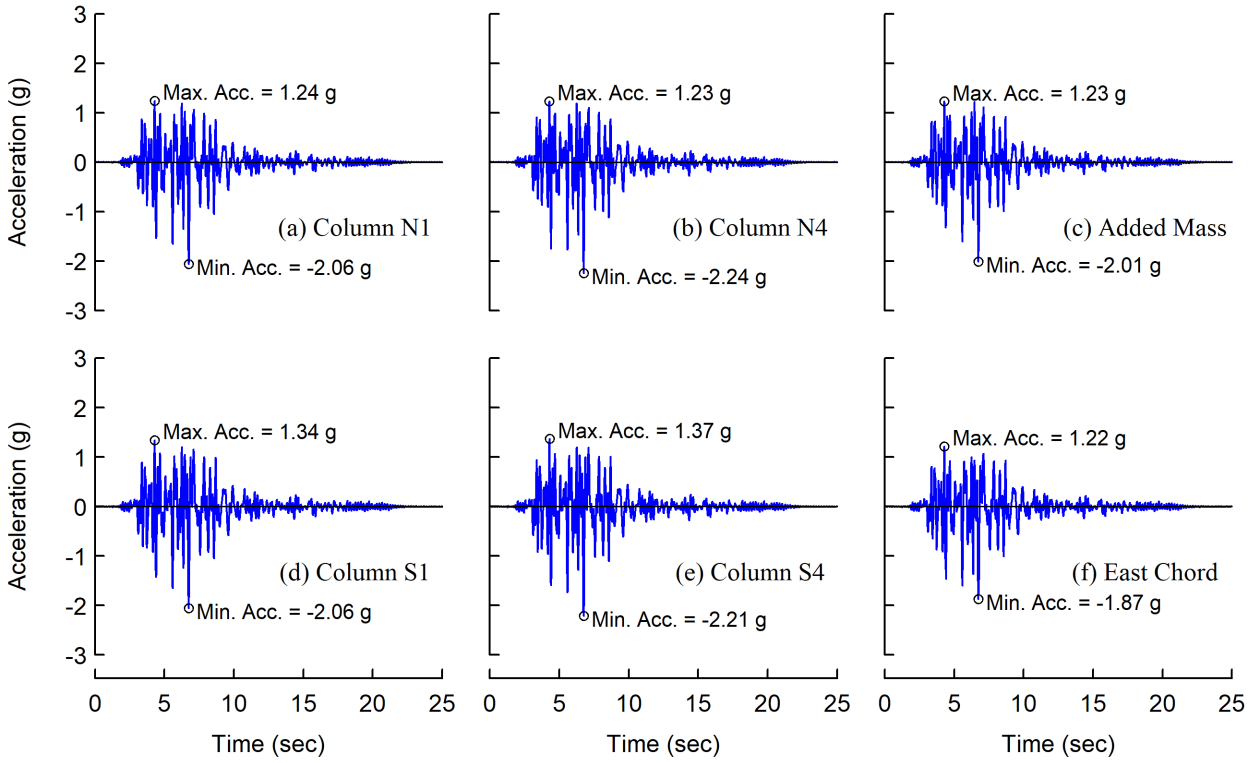

Figure D.9 Test 2A-5: Measured Accelerations at Various Locations on 2nd Floor

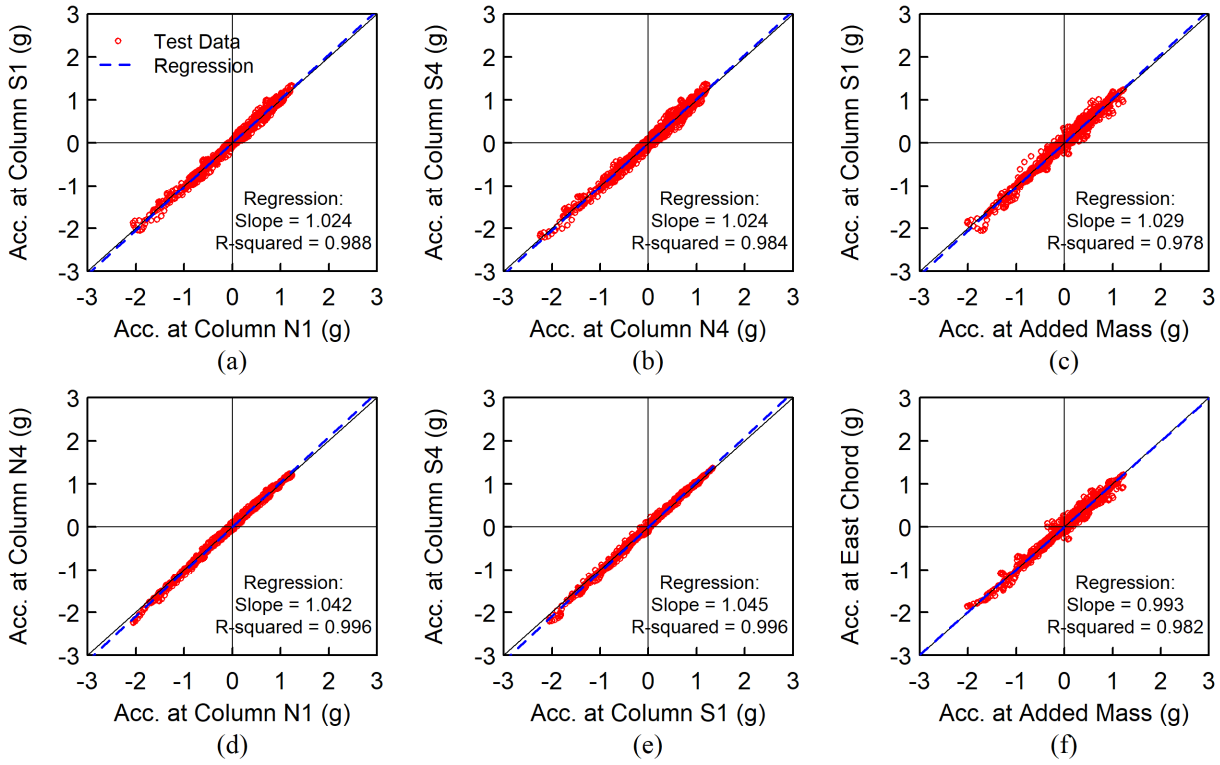

Figure D.10 Test 2A-5: Comparisons of Accelerations at Various Locations on 2nd Floor

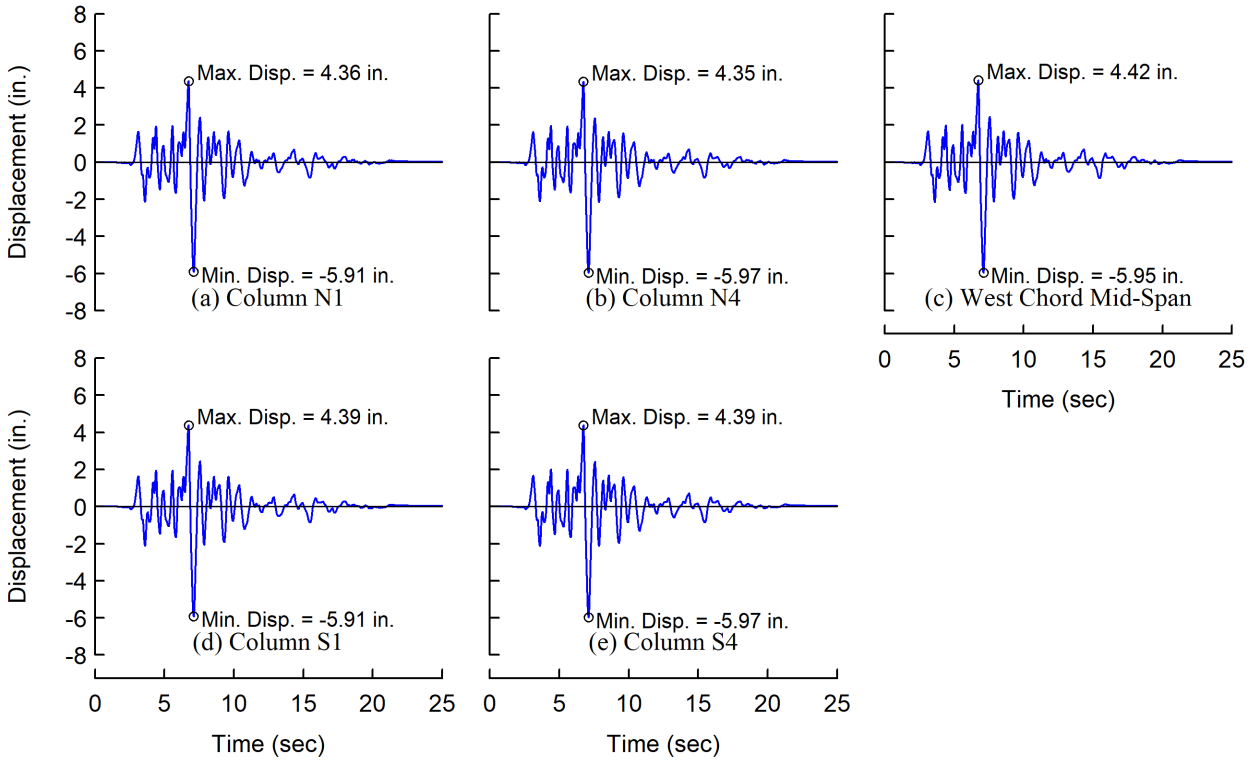

Figure D.11 Test 2A-5: Measured Displacements at Various Locations on 2nd Floor

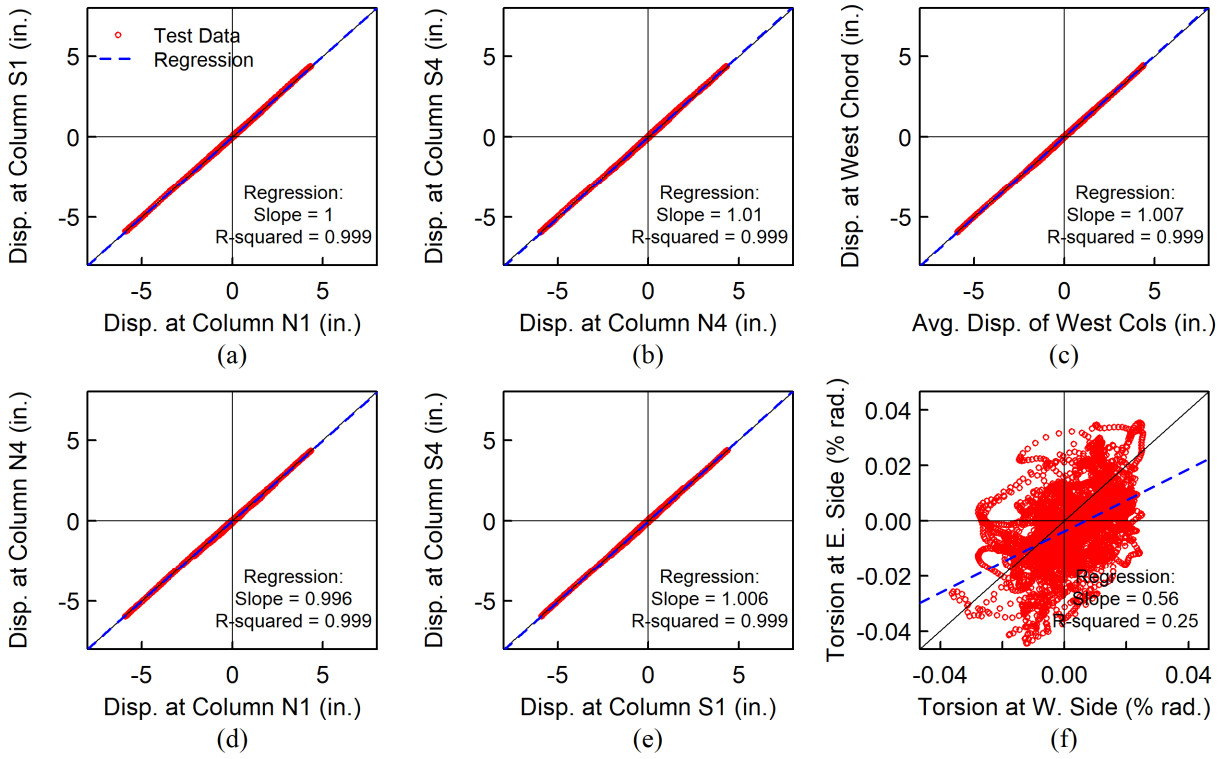

Figure D.12 Test 2A-5: Comparisons of Displacements at Various Locations on 2nd Floor

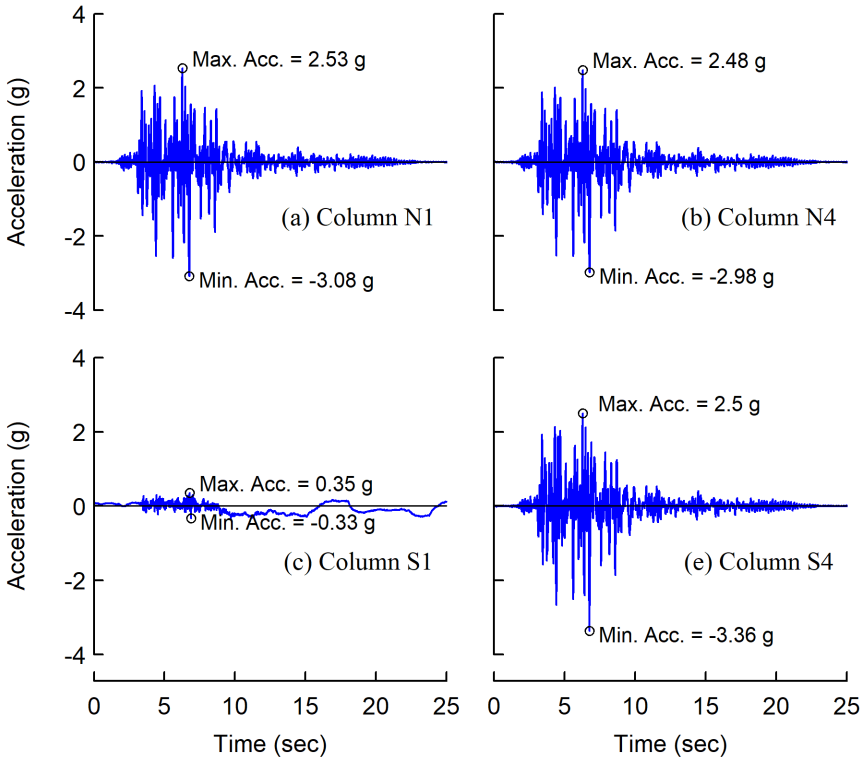

Figure D.13 Test 2A-5: Measured Accelerations at Various Locations on Roof Level

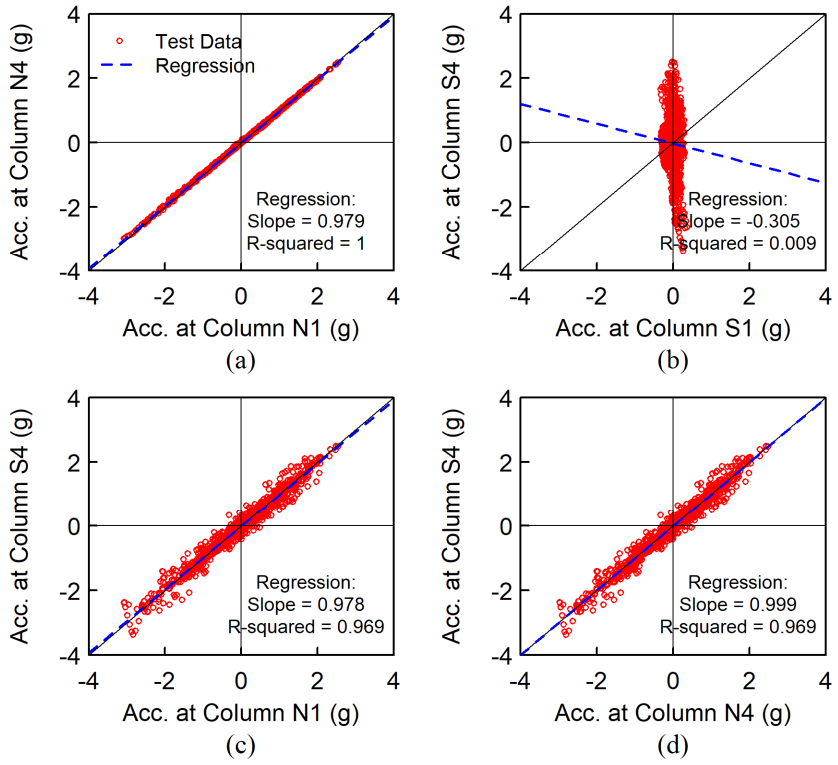

Figure D.14 Test 2A-5: Comparisons of Displacements at Various Locations on Roof Level

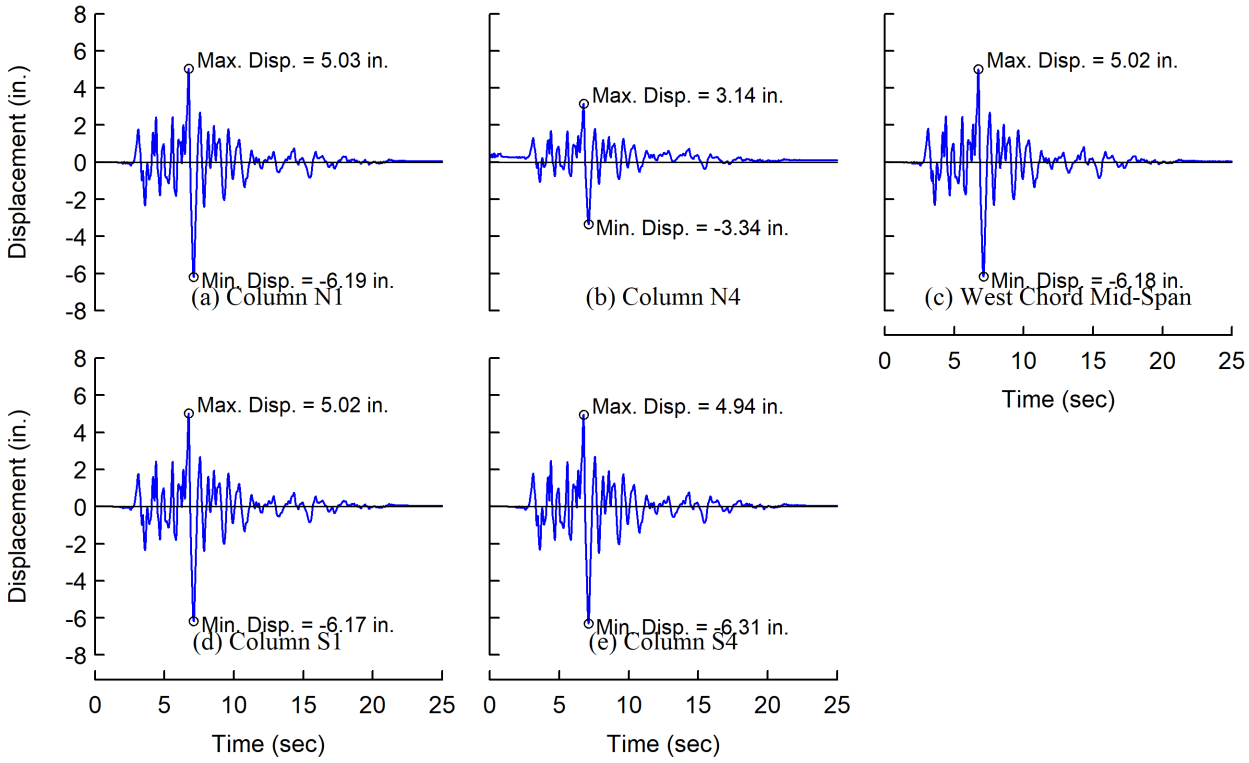

Figure D.15 Test 2A-5: Measured Displacements at Various Locations on Roof Level

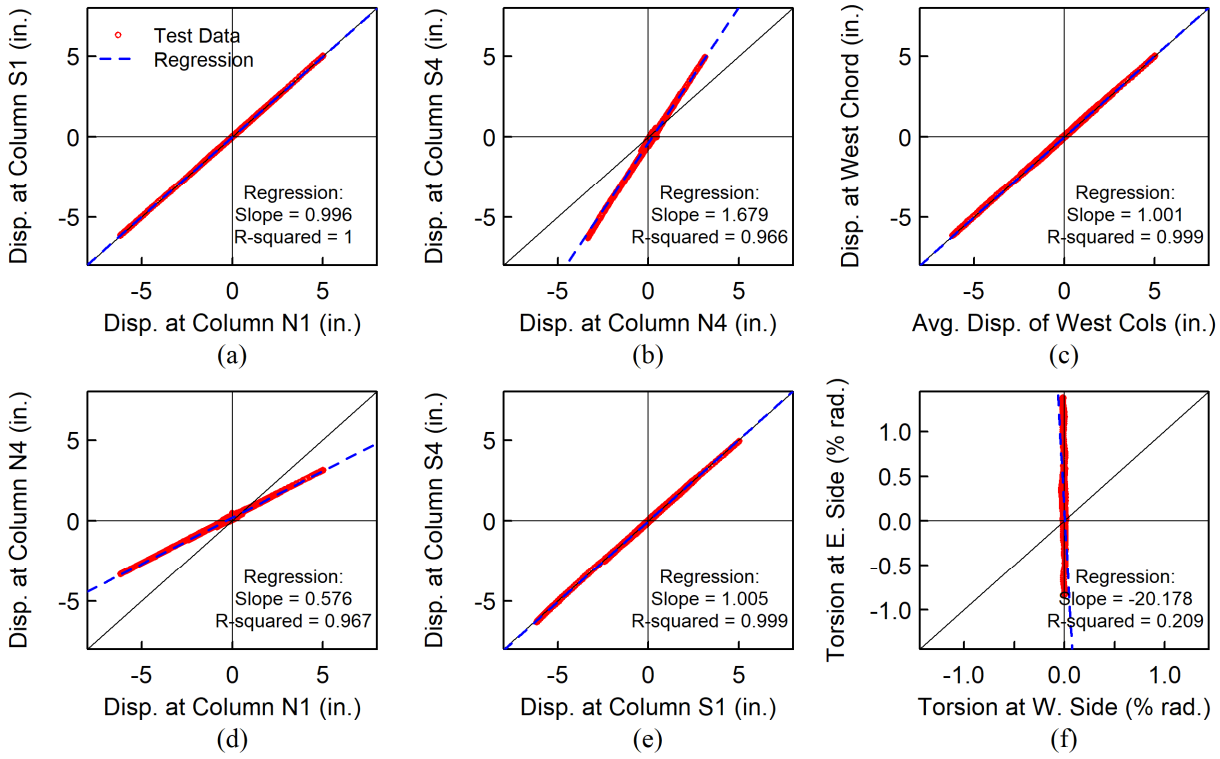

Figure D.16 Test 2A-5: Comparisons of Displacements at Various Locations on Roof Level

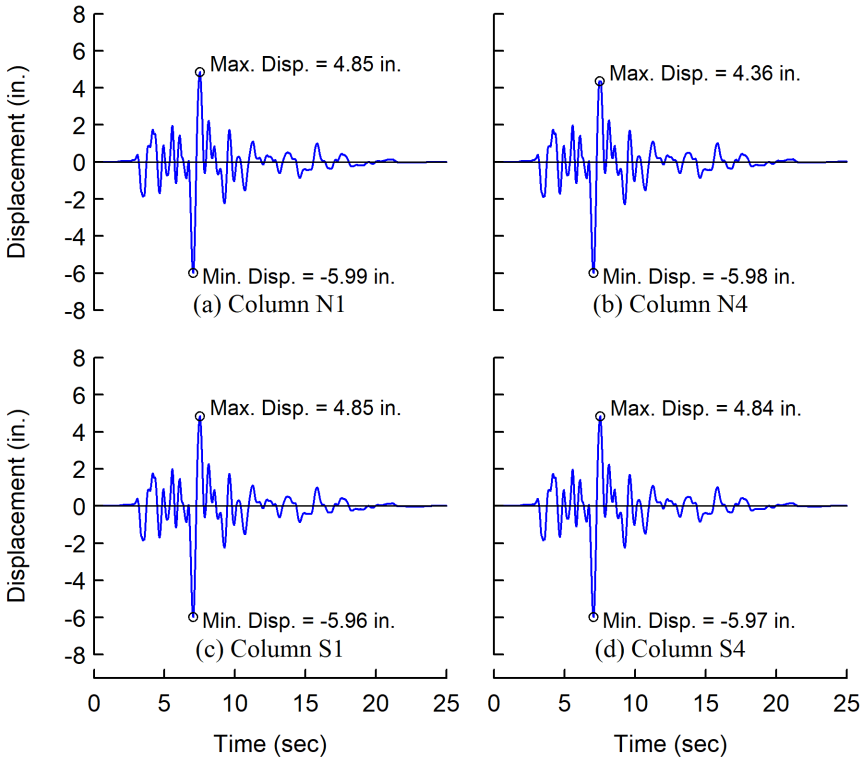

Figure D.17 Test 2B-5: Measured Displacements at Various Locations on Footing Level

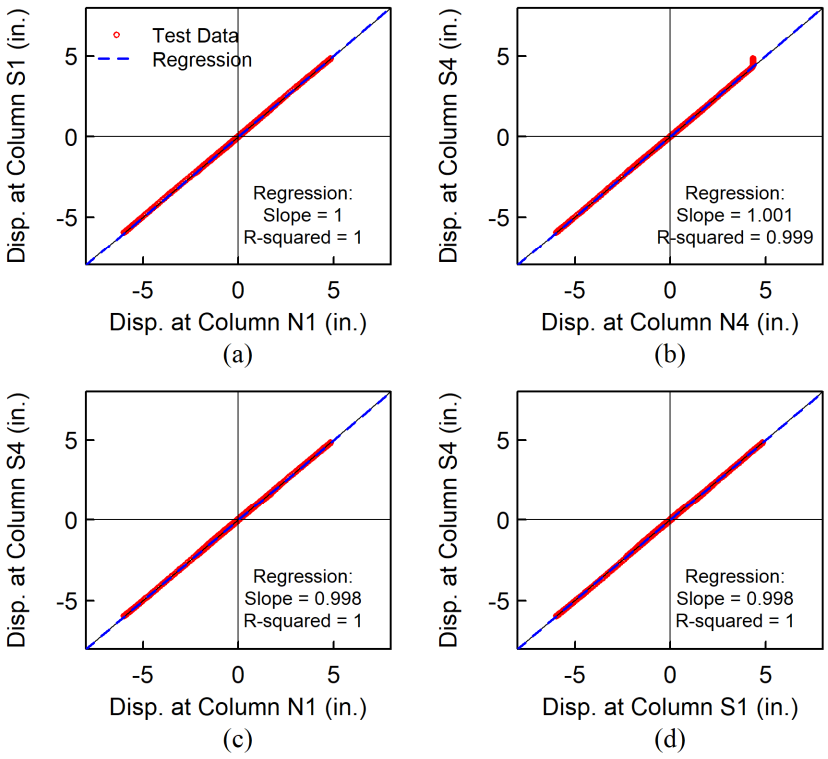

Figure D.18 Test 2B-5: Comparisons of Displacements at Various Locations on Footing Level

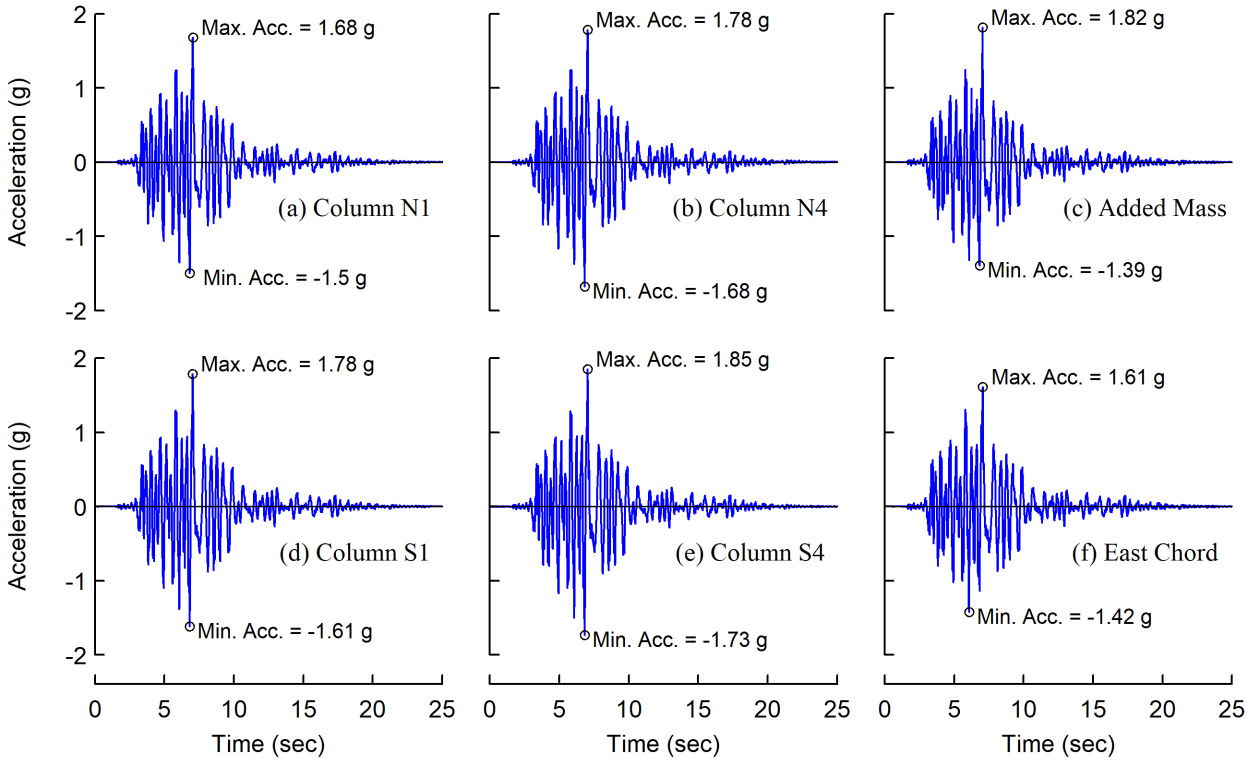

Figure D.19 Test 2B-5: Measured Accelerations at Various Locations on 2nd Floor

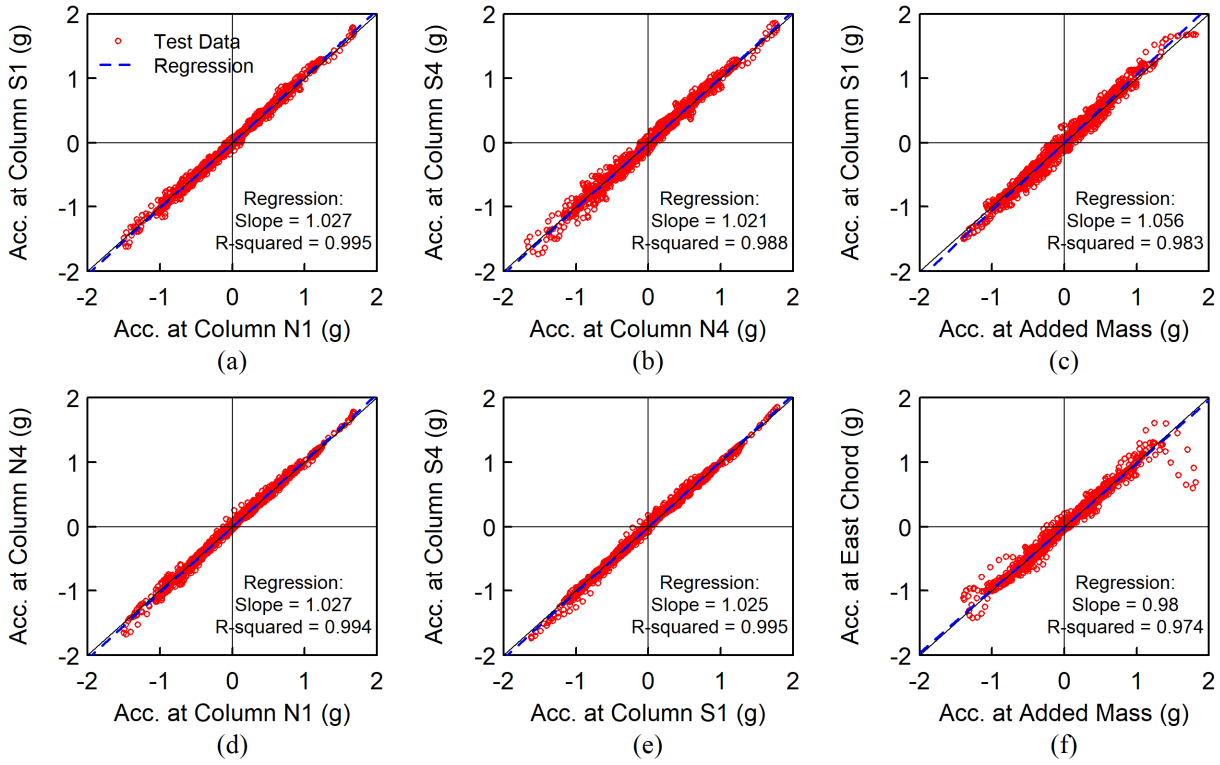

Figure D.20 Test 2B-5: Comparisons of Accelerations at Various Locations on 2nd Floor

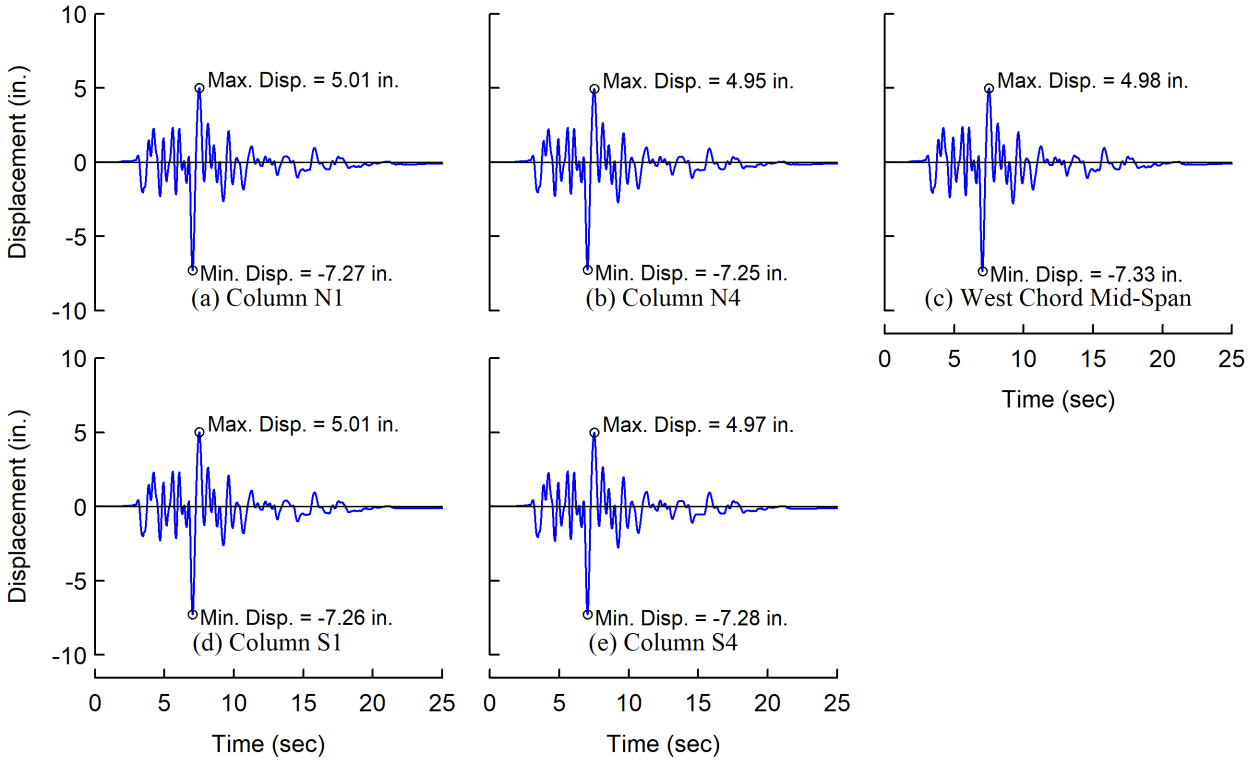

Figure D.21 Test 2B-5: Measured Displacements at Various Locations on 2nd Floor

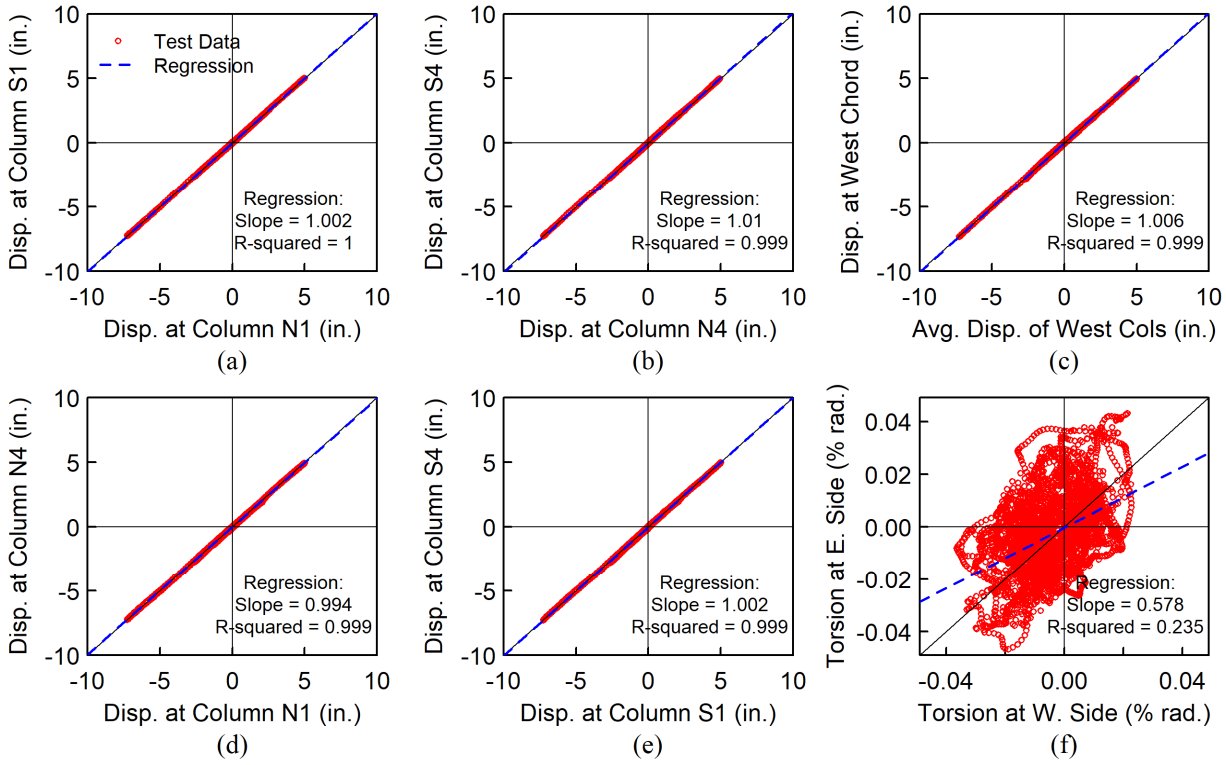

Figure D.22 Test 2B-5: Comparisons of Displacements at Various Locations on 2nd Floor

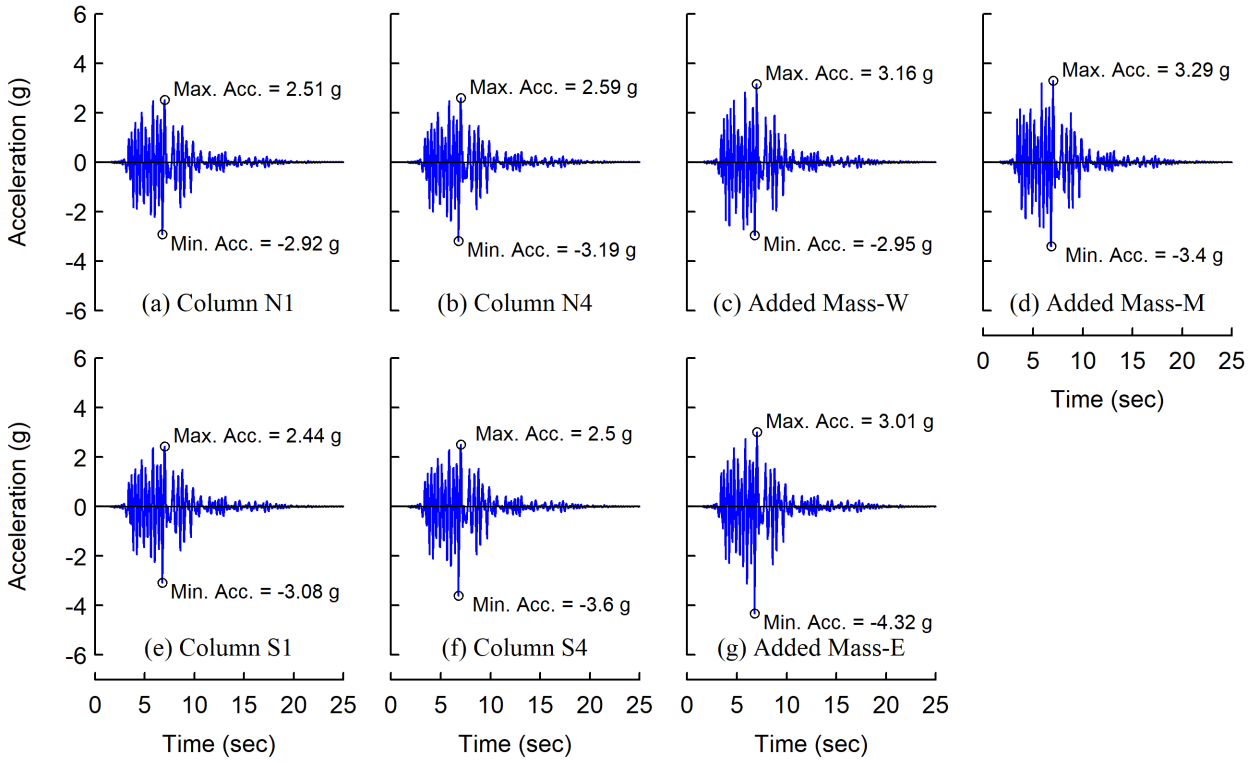

Figure D.23 Test 2B-5: Measured Accelerations at Various Locations on Roof Level

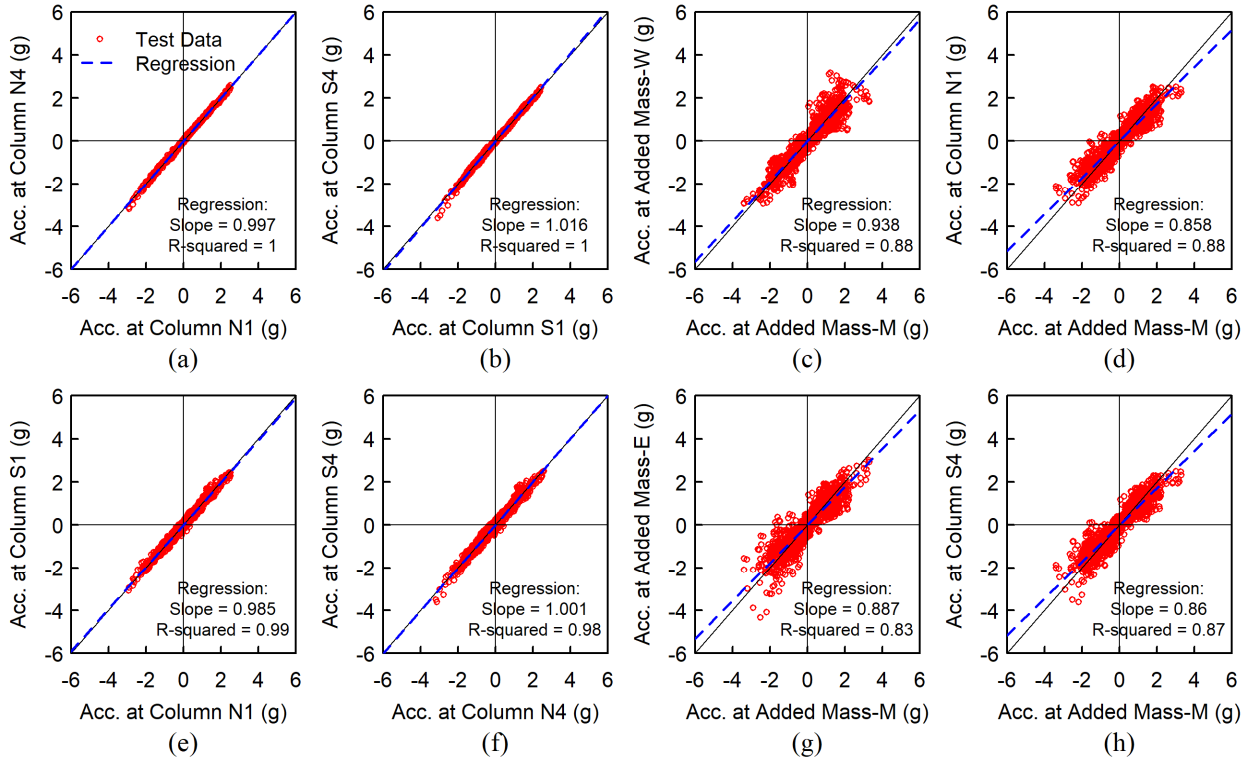

Figure D.24 Test 2B-5: Comparisons of Displacements at Various Locations on Roof Level

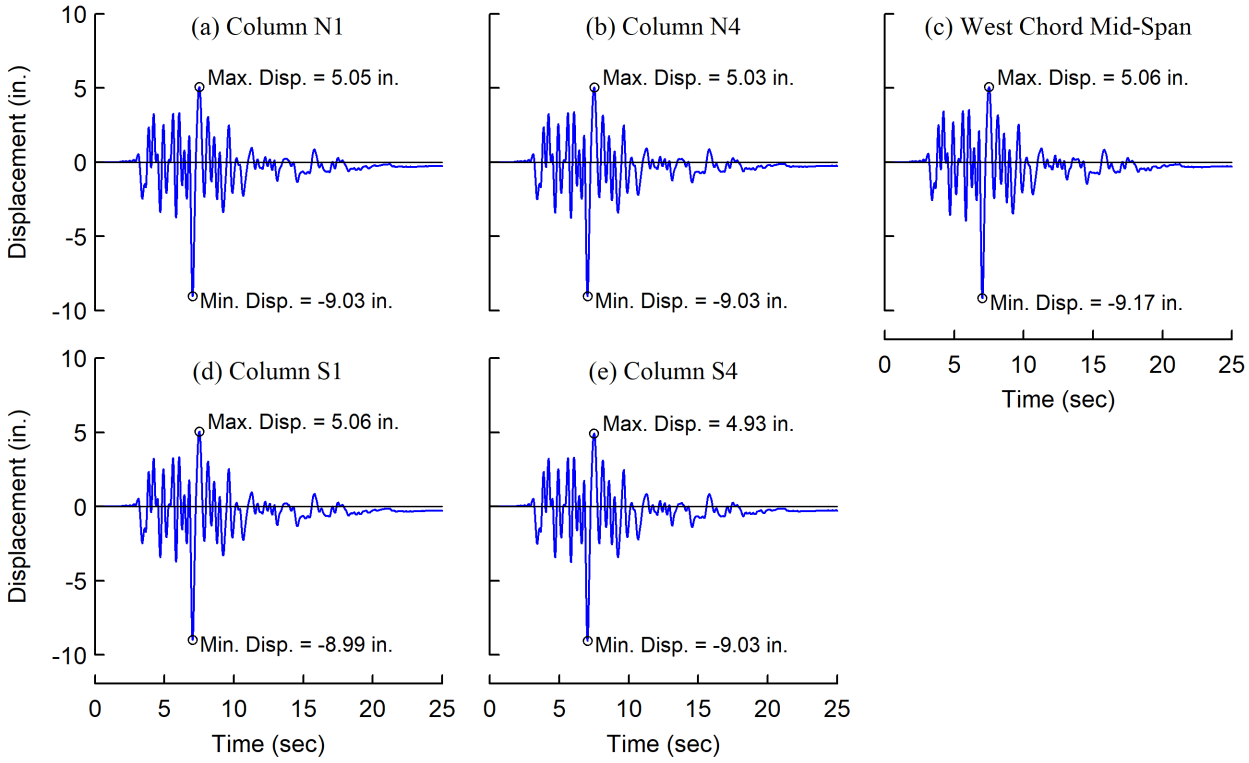

Figure D.25 Test 2B-5: Measured Displacements at Various Locations on Roof Level

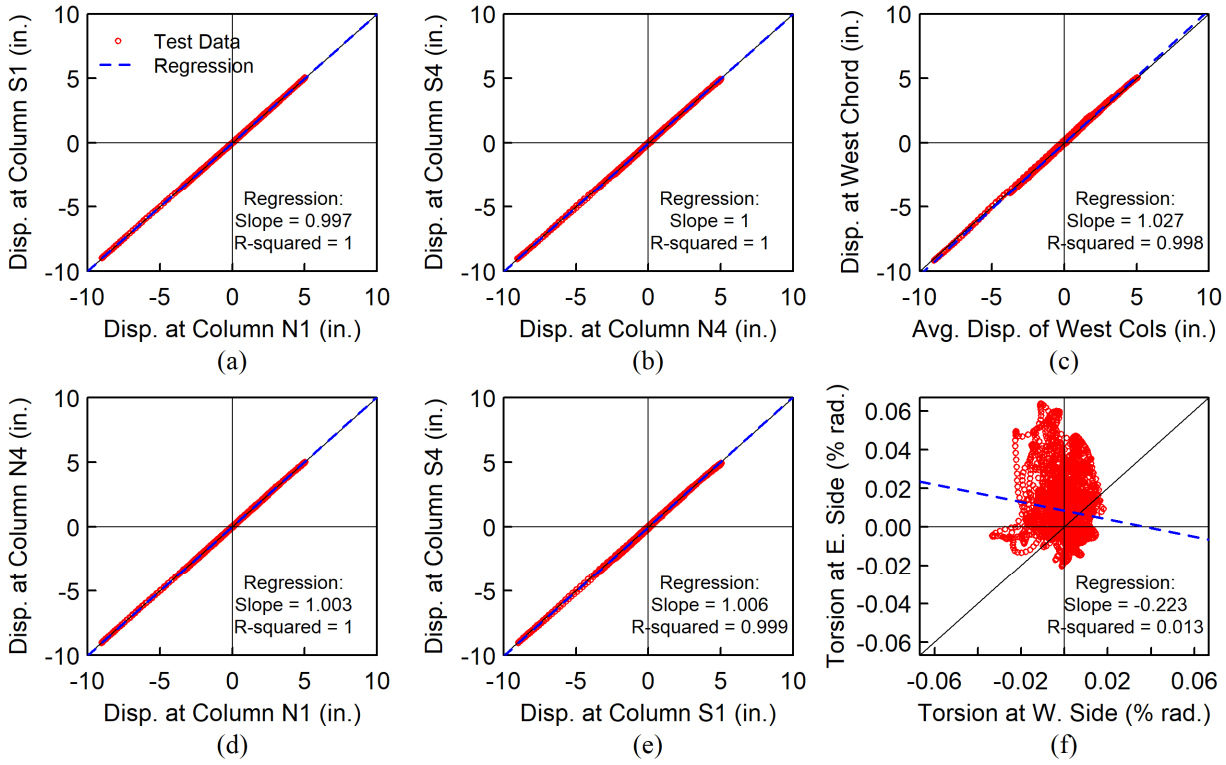

Figure D.26 Test 2B-5: Comparisons of Displacements at Various Locations on Roof Level

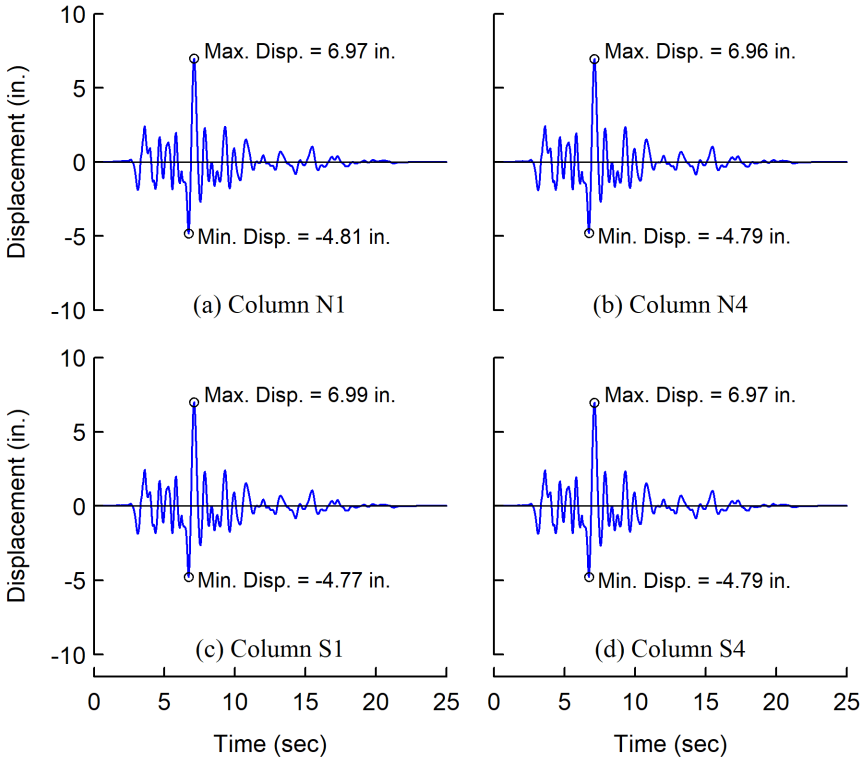

Figure D.27 Test 3-6: Measured Displacements at Various Locations on Footing Level

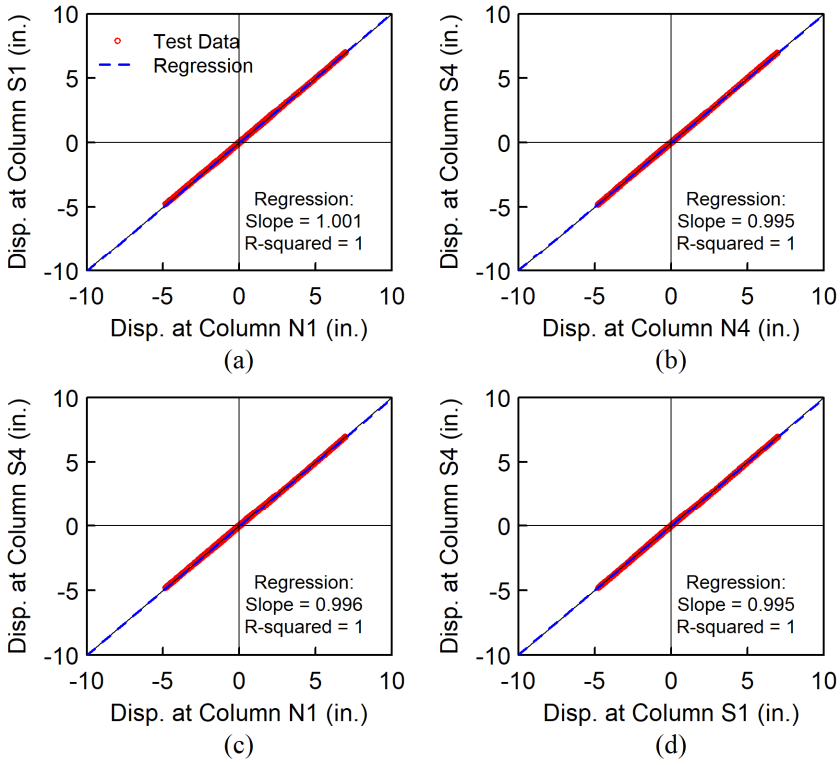

Figure D.28 Test 3-6: Comparisons of Displacements at Various Locations on Footing Level

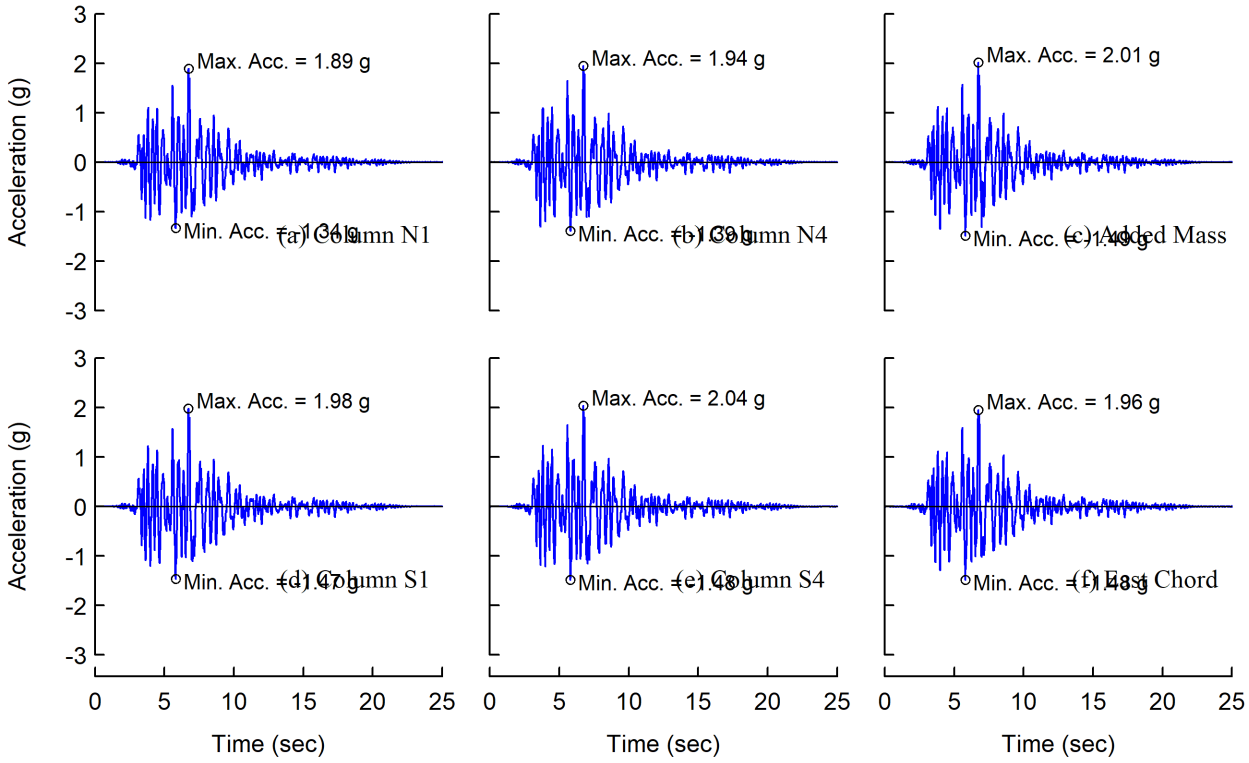

Figure D.29 Test 3-6: Measured Accelerations at Various Locations on 2nd Floor

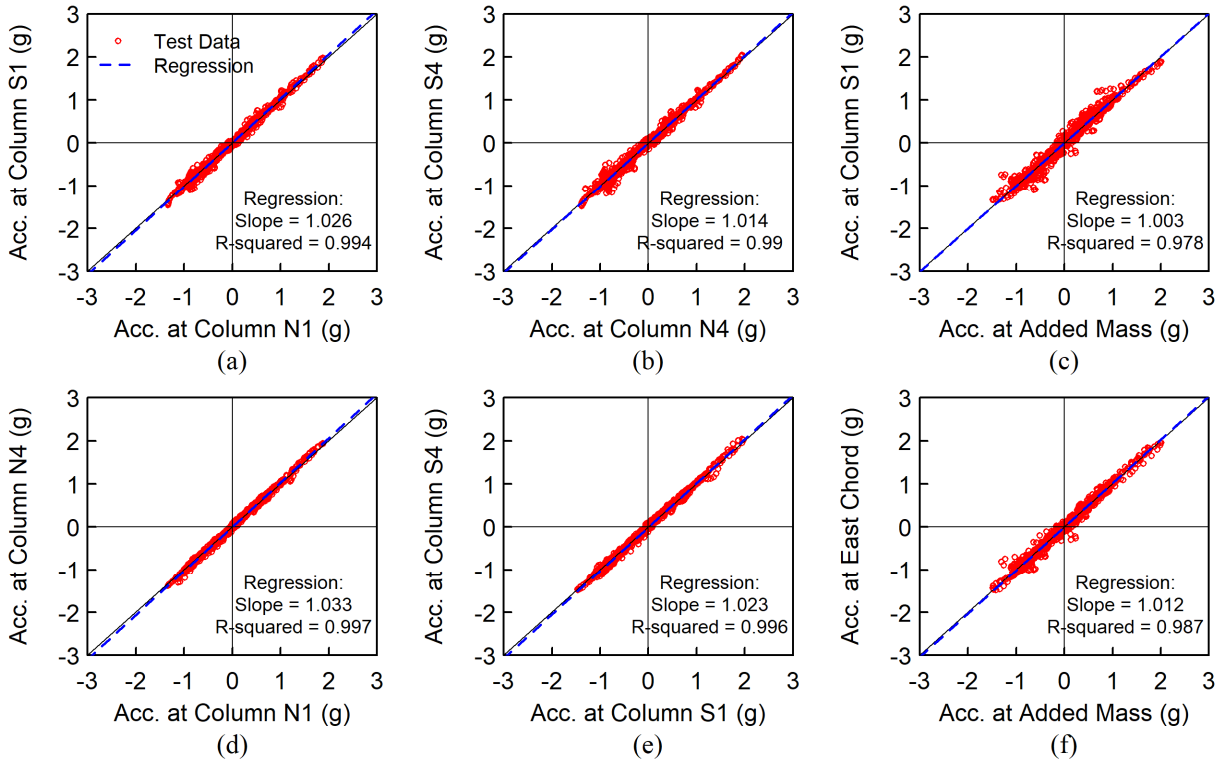

Figure D.30 Test 3-6: Comparisons of Accelerations at Various Locations on 2nd Floor

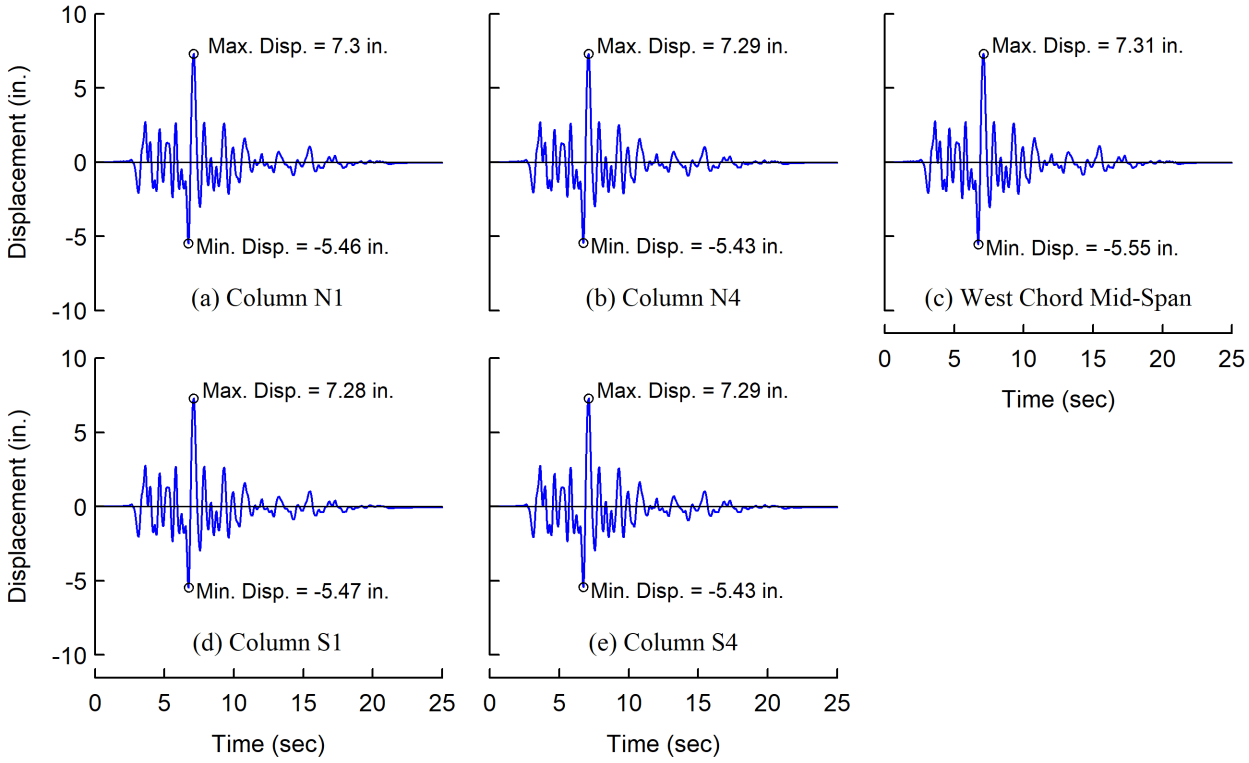

Figure D.31 Test 3-6: Measured Displacements at Various Locations on 2nd Floor

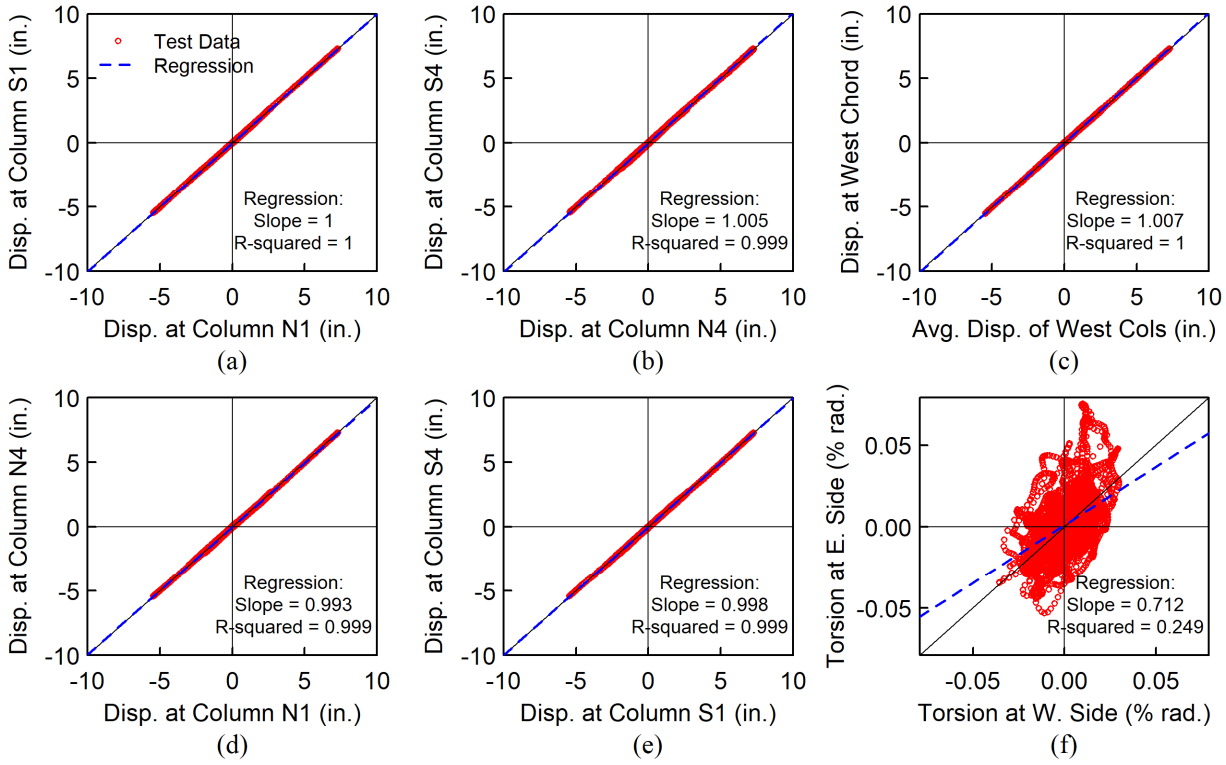

Figure D.32 Test 3-6: Comparisons of Displacements at Various Locations on 2nd Floor

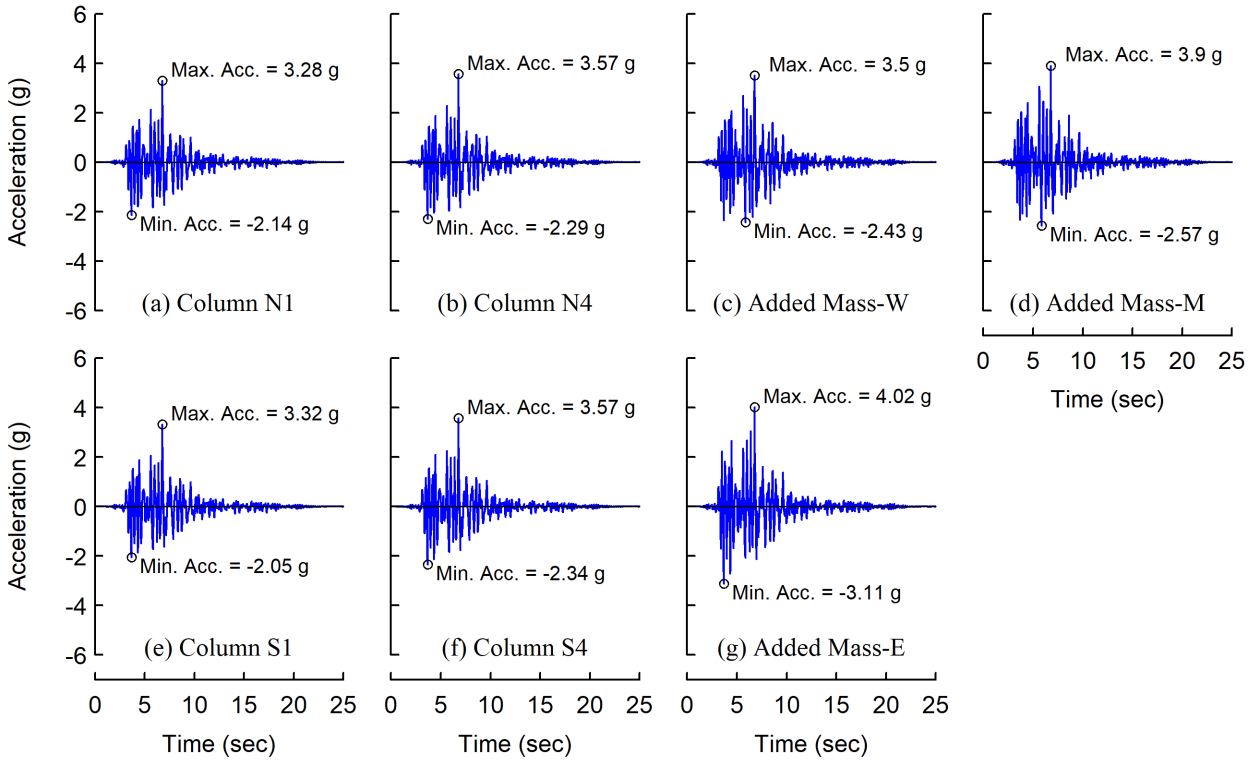

Figure D.33 Test 3-6: Measured Accelerations at Various Locations on Roof Level

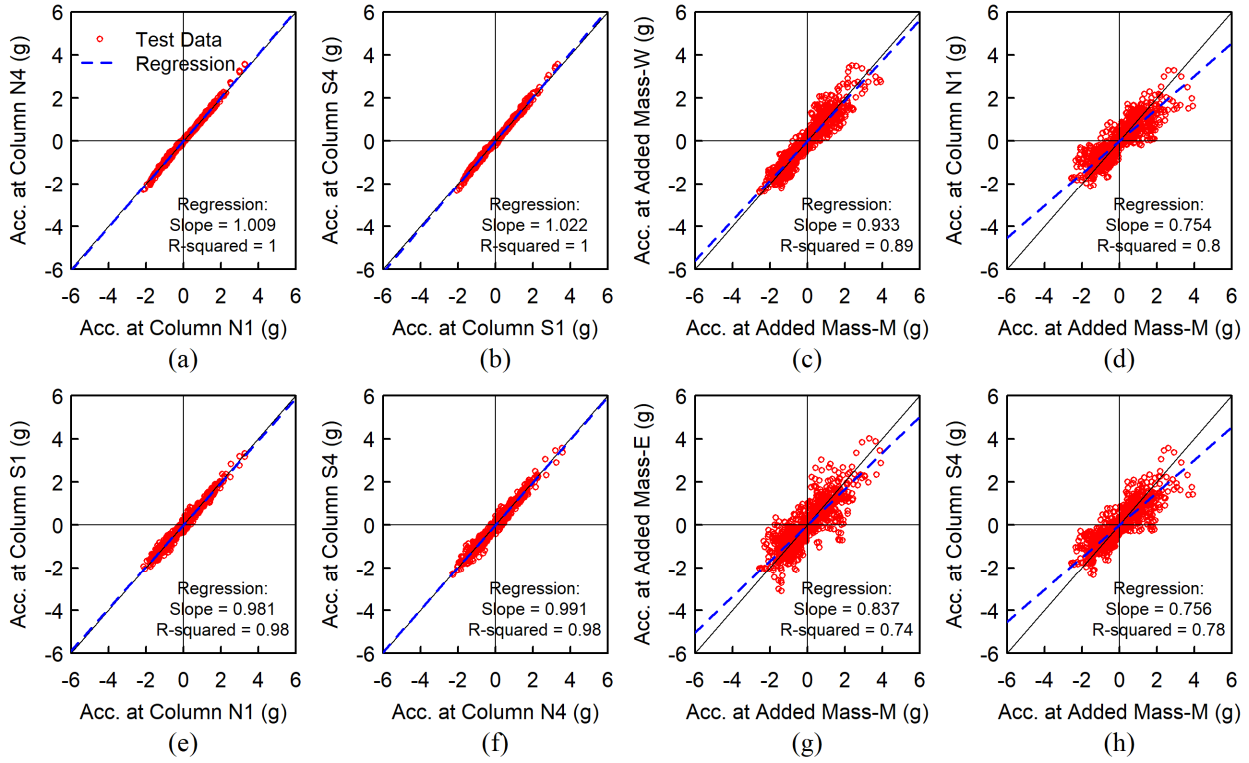

Figure D.34 Test 3-6: Comparisons of Displacements at Various Locations on Roof Level

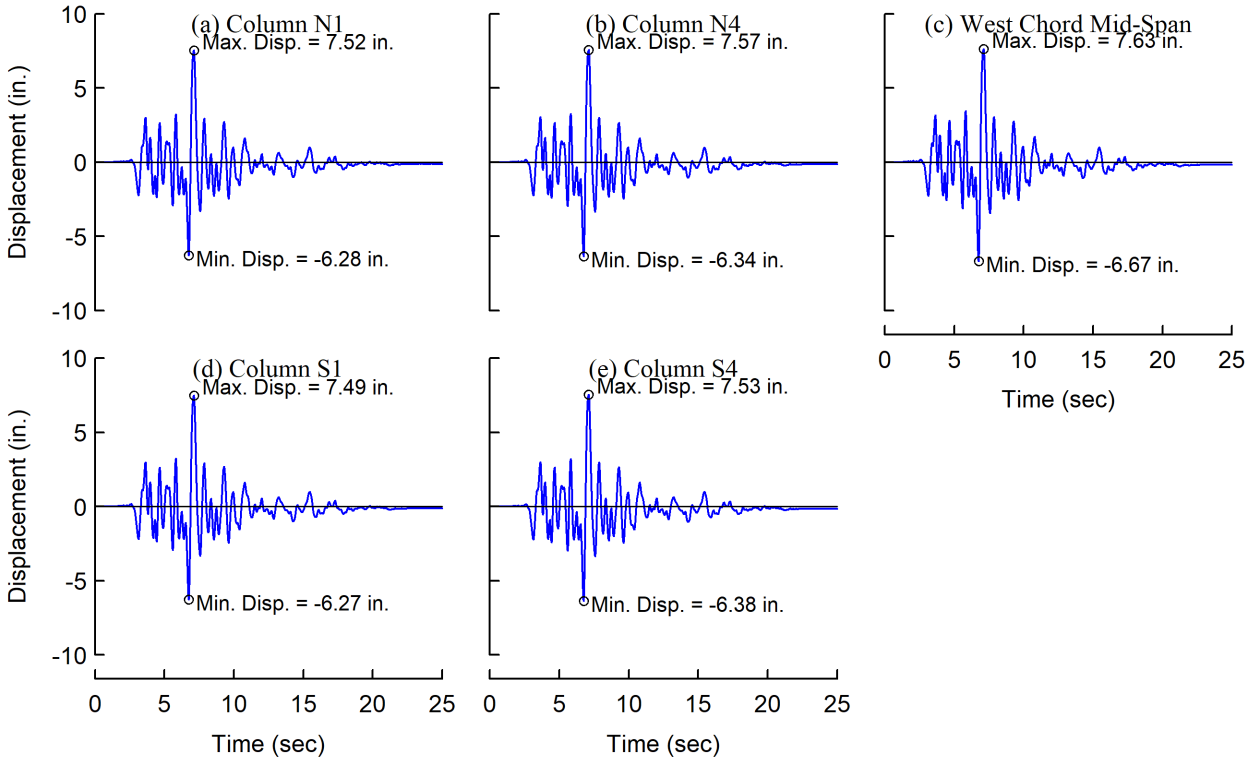

Figure D.35 Test 3-6: Measured Displacements at Various Locations on Roof Level

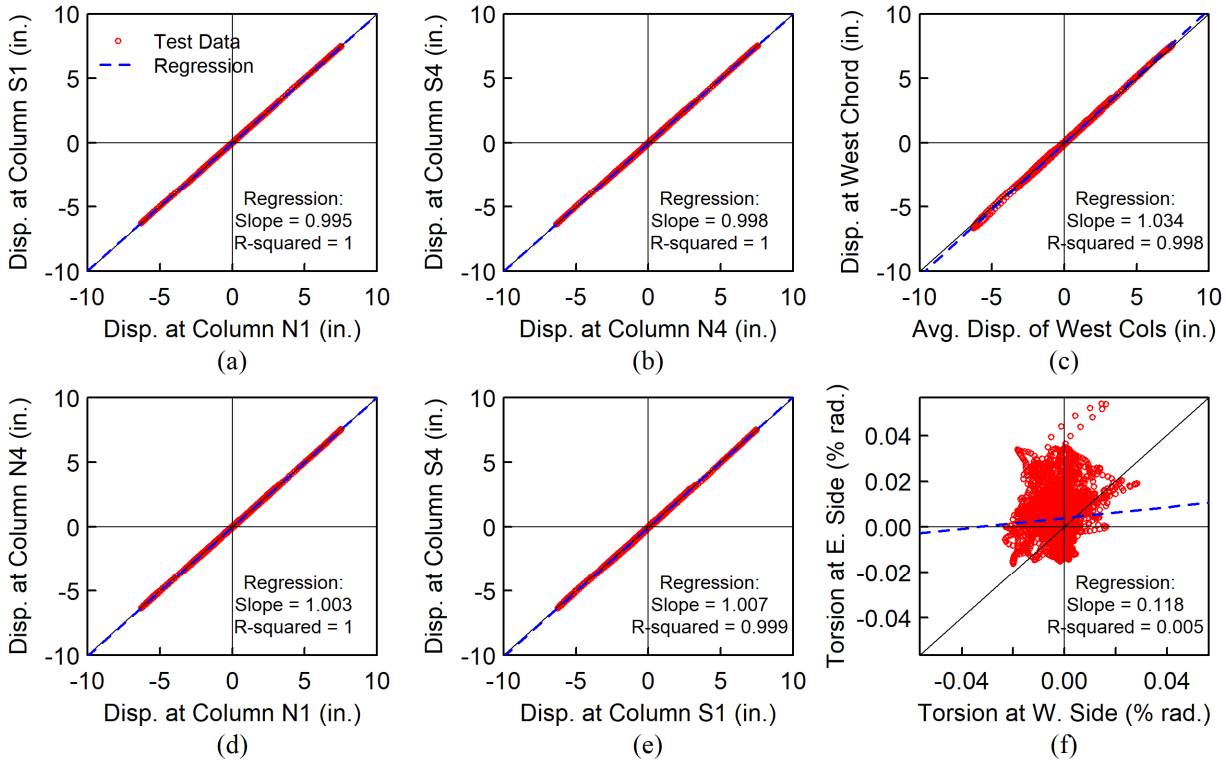

Figure D.36 Test 3-6: Comparisons of Displacements at Various Locations on Roof Level

Appendix E. Force Recovery of BRBs for Shake Table Tests

Braces S1 and N1 were installed in a two-story test frame and the test frame was subjected to seven earthquake simulation tests at LHPOST. In order to determine the brace axial forces induced by these shake table tests, a pair of uniaxial strain gauges were installed on the stiffeners of both lugs at the top end of each brace [see Figure 9.8(i)]. These gauges were placed in parallel with the axis of the brace to measure the axial strain at the start of the brace end section in front of the first row of bolts of the bolted connection. As the brace end section is designed to remain elastic, the strain, ε, measured at this location would be proportional to the brace axial force, P. This allows the brace axial force can be determined from measured strain based on the relationship as follows:

$$P = \gamma\varepsilon = \rho(E_s A_{end})\varepsilon \tag{E.1}$$

The slope, γ, for the linear P versus ε relationship can be expressed as the term $\rho(E_s A_{end})$, where E_s and A_{end} (=7.66 in.^{2}) are the Young's modulus of steel and the cross-sectional area of the brace end section, respectively. The factor, ρ, accounts for the uneven distribution of axial strain due to the shear lag phenomenon around the bolted connection and the imperfect placement of strain gauge in line with the longitudinal axis of the brace. Theoretically, the value of ρ factor would be larger than 1.0. A value of ρ equal to 1.0 represents a uniform distribution of axial strain and a perfect placement of the gauges.

The slope, γ, for the four BRBs in this test program were determined from the SRMD tests, in which the brace axial forces were measured from a load cell and a pair of strain gauges were installed on each brace at the same location as those for the LHPOST tests. Noted that the strain gauges used for Braces S1 and N1 in the LHPOST tests were removed when the braces were disconnected from the test frame at the LHPOST. New strain gauges were then installed on these

two braces for SRMD tests. Based on the SRMD test results (see Figure E.1 through Figure E.4), the values of γ for Braces S1, N1, S2, and N2, which were determined from the slope of the linear regression of experimental P versus ε relationship, were 235416, 235619, 236690, and 238165 kips/(in./in.), respectively. These four γ values respectively corresponded to a ρ factor of 1.060, 1.060, 1.065, and 1.072. As γ values were very similar among the four nominally identical braces, the strain test data are considered reliable. Assuming the P versus ε relationship for each brace is constant, the γ values measured from SMRD tests for Braces S1 and N1 were used for the brace axial force determination for the LHPOST tests.

Recognizing that a replacement of strain gauges took place between the LHPOST and SRMD tests, which would make the P versus ε relationship (i.e., the γ values) inconsistent between the tests, the elastic axial stiffness of the brace measured from the LHPOST tests was compared with that measured from the SRMD tests to justify the use of γ values determined from SRMD tests for the brace force determination for the LHPOST tests. Figure E.5 and Figure E.7 show the measured force versus displacement relationships for Braces S1 and N1, respectively, for Test 1 of Stage 1 testing at the LHPOST, in which the input ground motion was at an intensity of 50% design earthquake level and two braces were responding in the elastic range. Note that the brace forces herein were calculated by the γ values obtained from the SRMD tests. The measured elastic axial stiffness from the tensile excursions for Braces S1 and N1 were 270.9 and 277.9 kips/in., respectively. These two values are close to the measured stiffness (261.9 and 268.8 kips/in. for Braces S1 and N1, respectively) from the diagnostic tests conducted at the SRMD facility, in which the brace forces were measured by a load cell and the braces responded elastically to ±0.025% and ±0.05% core strains (see Figure E.6 and Figure E.8). For each brace, the stiffness measured from the LHPOST test is only higher than that measured from the SRMD test by about 3% to 4%. This

can be attributed to that the braces were cyclically loaded with respect to a tensile residual core strain about +0.12% during the diagnostic tests at SRMD, resulting in cyclic brace deformations on the tension side only. By contrast, the cyclic brace deformations induced by Test 1 at LHPOST were on both tension and compressive sides. Due to Poison's effect, the fiction force between steel core plate and outer casing in the shake table test would be higher than that in the diagnostic test for each brace, which agrees with that a higher stiffness was measured in the shake table test. The comparisons in the measured stiffness between Test 1 at LHPOST and diagnostic tests at SRMD confirmed the reliability of brace force determination for the LHPOST tests.

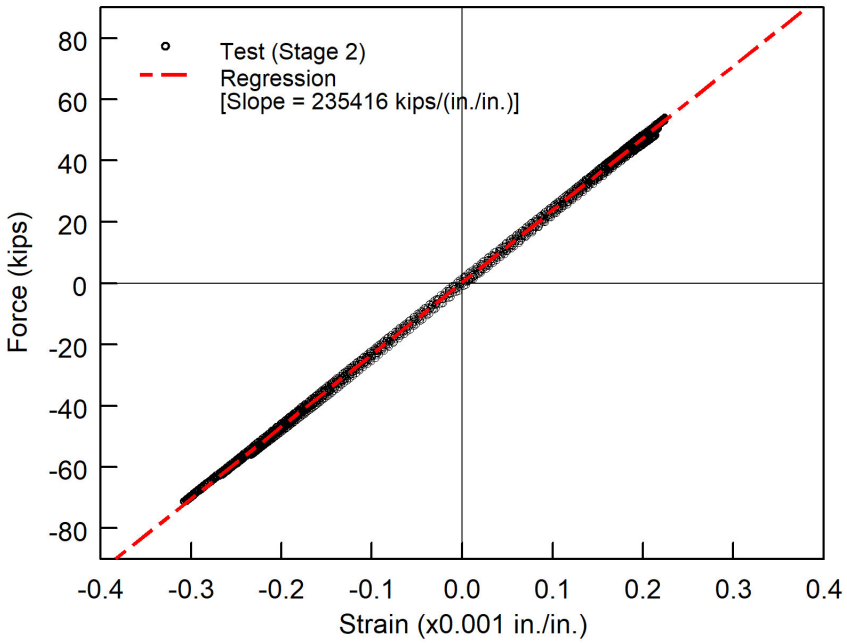

Figure E.1 Brace S1: Measured Axial Force versus Strain Relationship

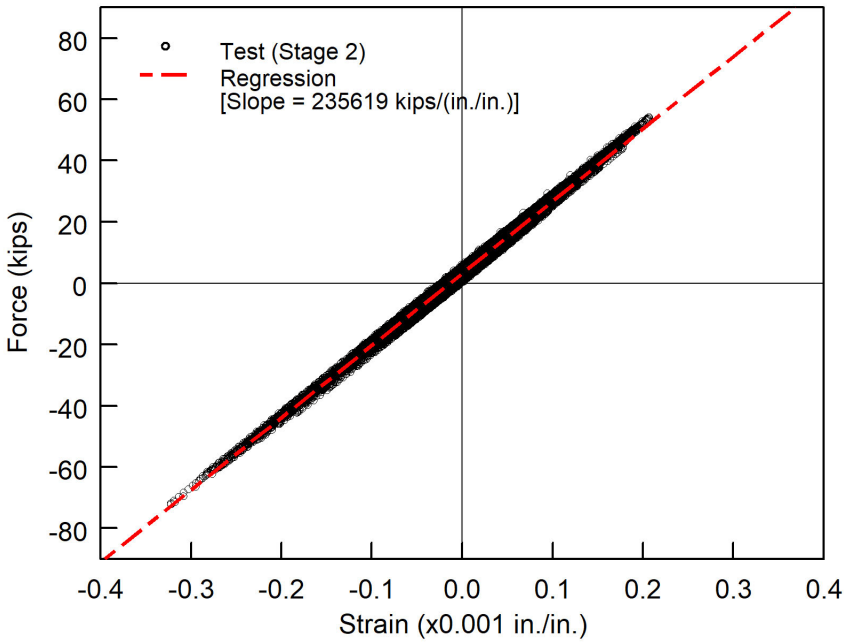

Figure E.2 Brace N1: Measured Axial Force versus Strain Relationship

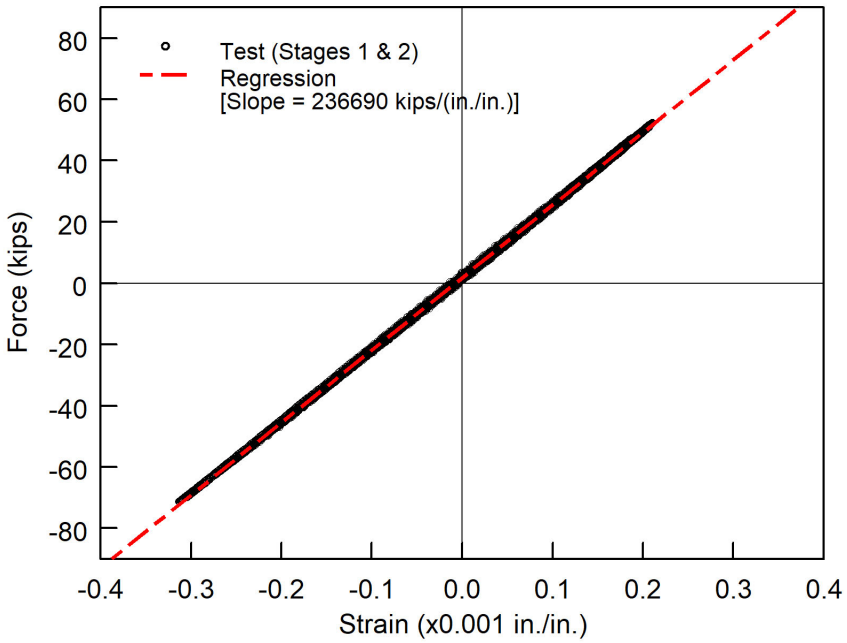

Figure E.3 Brace S2: Measured Axial Force versus Strain Relationship

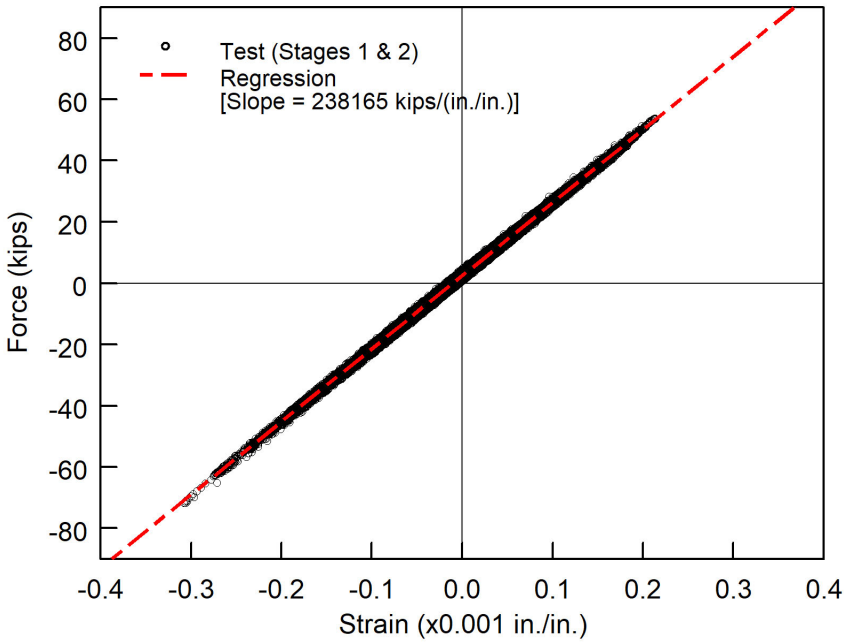

Figure E.4 Brace N2: Measured Axial Force versus Strain Relationship

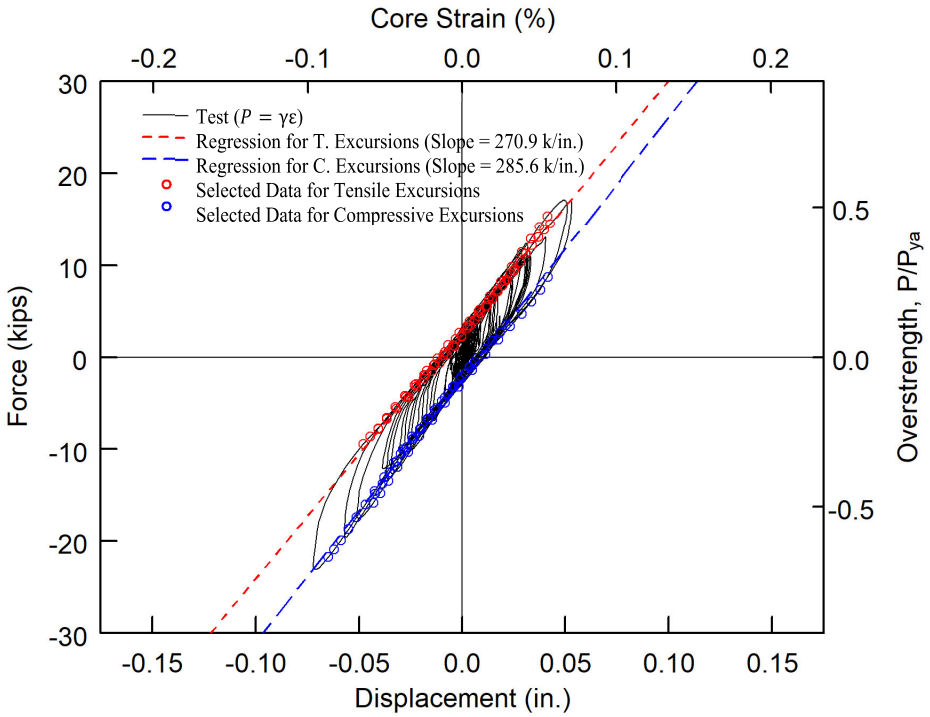

Figure E.5 Brace S1: Force versus Displacement Relationship for Test 1 of Stage 1 Testing at LHPOST

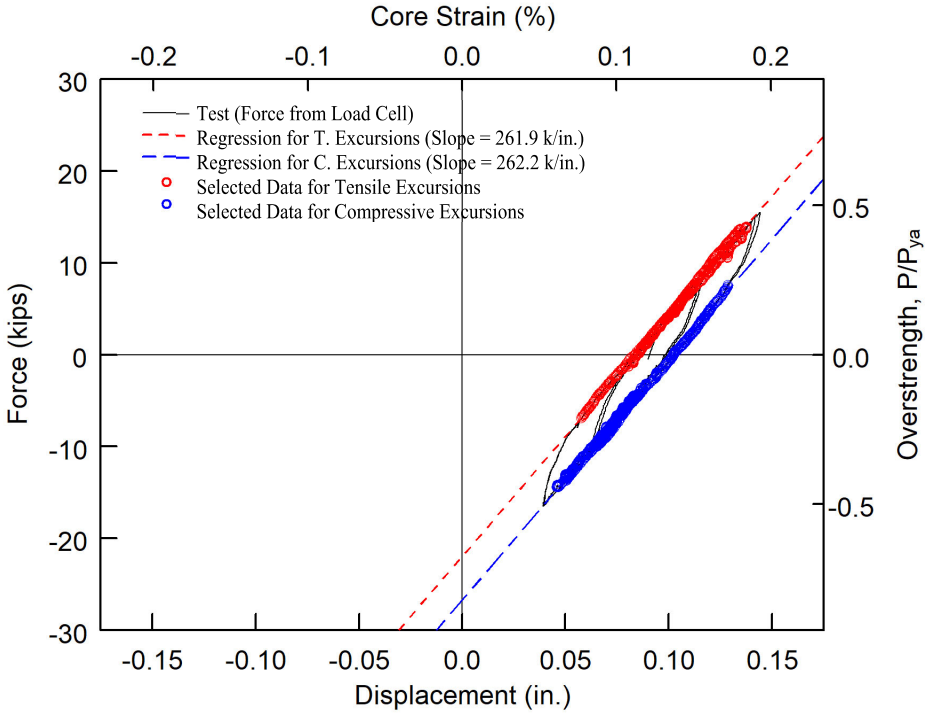

Figure E.6 Brace S1: Force versus Displacement Relationship for Elastic Test at SRMD

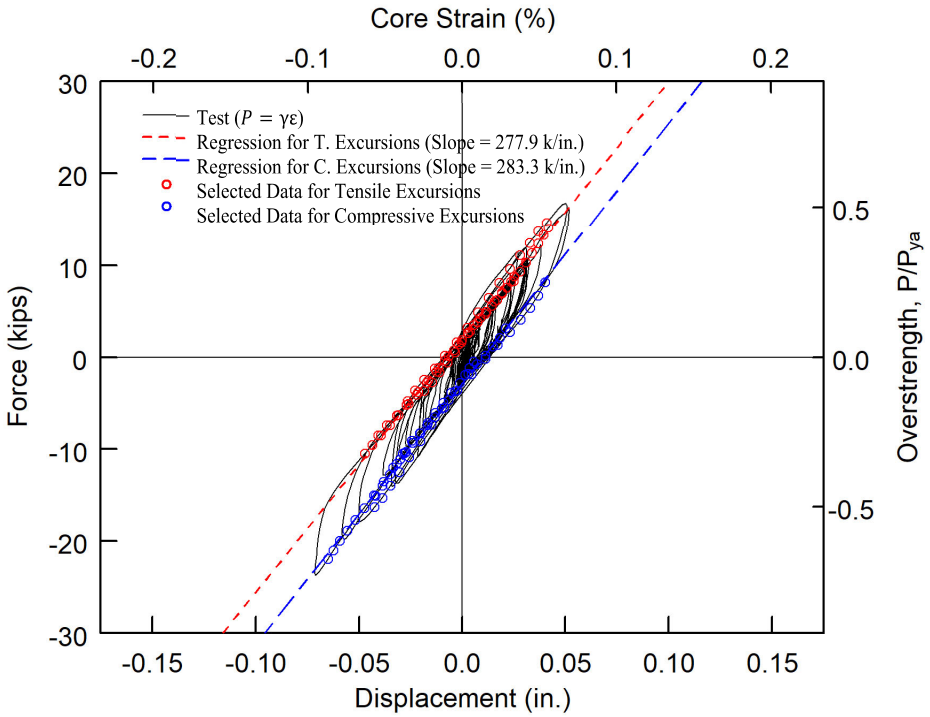

Figure E.7 Brace N1: Force versus Displacement Relationship for Test 1 of Stage 1 Testing at LHPOST

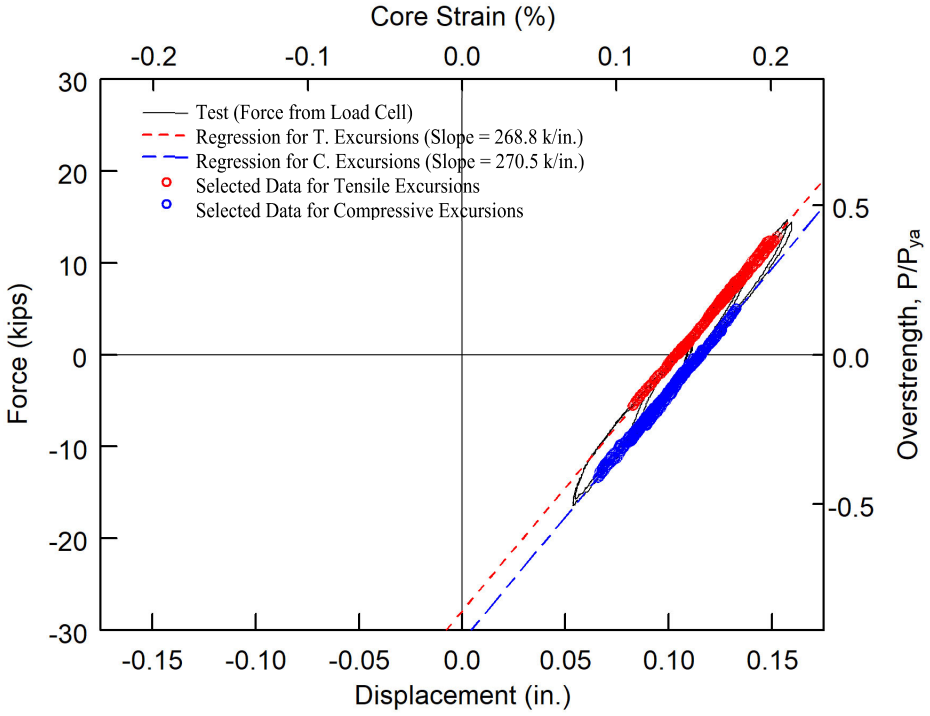

Figure E.8 Brace N1: Force versus Displacement Relationship for Elastic Test at SRMD

Appendix F. Description of Prototype Structure

A 12-story building with buckling restrained braced frames (BRBFs) for the seismic force-resisting system (SFRS) from the version 1.0 of the Steel Diaphragm Innovation Initiative (SDII) building archetypes (Torabian et al. 2017) was selected as the prototype structure for this research. As shown in Figure F.1 and Figure F.2, the building used a 100 ft by 300 ft plan area with a story height of 14 ft at the first story and 12.5 ft for a typical story. The parapet was 3 ft high. Four bays of BRBFs are located on the perimeter of the building at in each orthogonal direction. The bare steel deck roof while and composite concrete on steek deck floors are used. The composite slab consists of 4.5-in. deep normal weight concrete over 18-ga. thick and 3-in. deep metal deck. The beams and columns were made of A992 steel, while the core plates of BRBs were A36 steel (F_y = 42 ksi). Figure F.2 shows the member sizes for the beams, columns and BRBs. Table F.1 lists the stiffness modification factor (KF) and yield-to-length ratio (YLR) for BRBs.

The self-weights of the roof deck and composite slab were 3 psf and 75.5 psf, respectively. The superimposed dead loads considered for the roof and floors were 22 psf and 10 psf, respectively. The external walls weighted 40 psf. The partition load considered was 15 psf on the floors. The live loads on the roof and floors were taken as 20 psf and 50 psf, respectively. The total seismic weights on the roof and each floor were 1,271 kips and 3,415 kips, respectively.

The site location is at Irvine, California with a Class D soil. Risk Category II was considered, resulting in a seismic importance factor of I_e = 1.0. The associated parameters for the seismic design spectrum were: S_s = 1.545, S_1 = 0.569, F_a = 1.0 and F_v = 1.5, which lead to S_{DS} = 1.030 and S_{D1} = 0.569. In addition, as the building employed the BRBFs as the primary SFRS, the seismic design parameters were R = 8, Ω_0 = 2.5, and C_d = 2.5. Table F.2 lists three diaphragm design forces: (1) Conventional design forces, denoted as F_{px} for level x, computed by the

procedures prescribed in Section 12.10.1 of ASCE 7-16; (2) Alternative 1 forces, denoted as F'_{px} for level x, determined from the alternative procedures depicted in Section 12.10.3 of ASCE 7-16 with R_s = 3; and (3) Alternative 2 forces, denoted as F''_{px} for level x, calculated by the alternative procedures with R_s = 1.

Table F.1 Stiffness Modification Factor (KF) and Yield-to-Length Ratio (YLR) for BRBs

Story	BRBs in Longitudinal Direction			BRBs in Transverse Direction		
	A_{sc} (in.^{2})	KF	YLR	A_{sc} (in.^{2})	KF	YLR
12th	2	1.37	0.85	2	1.45	0.77
11th	7	1.37	0.85	5	1.45	0.77
10th	11	1.37	0.86	8	1.46	0.79
9th	13	1.37	0.86	10	1.46	0.79
8th	14	1.37	0.86	12	1.53	0.75
7th	14	1.37	0.86	14	1.53	0.75
6th	15	1.41	0.84	16	1.53	0.75
5th	15	1.41	0.84	17	1.53	0.75
4th	16	1.41	0.84	17	1.53	0.75
3rd	16	1.41	0.84	18	1.53	0.75
2nd	16	1.41	0.84	18	1.53	0.75
1st	17	1.41	0.84	19	1.51	0.76

Table F.2 Seismic Deign Force and Diaphragm Forces for Prototype Structure

Level, x	Seismic Weight	Seismic Force	Diaphragm Design Forces					
			Conventional		Alternative 1 (R_s=3)		Alternative 2 (R_s=1)	
	w_x (kips)	F_x (kips)	F_{px} (kips)	a_{flr}* (g)	F'_{px} (kips)	a_{flr}* (g)	F'_{px} (kips)	a_{flr}* (g)
Roof	1271	147	147	0.29	262	0.52	419	0.82
12th	3415	343	358	0.26	703	0.51	1126	0.82
11th	3415	394	331	0.24	703	0.51	1126	0.82
10th	3415	247	306	0.22	703	0.51	1142	0.84
9th	3415	204	283	0.21	703	0.51	1171	0.86
8th	3415	164	261	0.19	703	0.51	1200	0.88
7th	3415	128	240	0.18	703	0.51	1229	0.90
6th	3415	95	220	0.16	703	0.51	1258	0.92
5th	3415	66	202	0.15	703	0.51	1287	0.94
4th	3415	42	185	0.14	703	0.51	1316	0.96
3rd	3415	22	169	0.12	703	0.51	1345	0.98
2nd	3415	8	155	0.11	703	0.51	1374	1.01

*$a_{flr} = \frac{\Omega_0 F_{px}}{w_x}$, where F_{px} is replaced by F'_{px} and F''_{px} for Alternative 1 and Alternative 2 designs

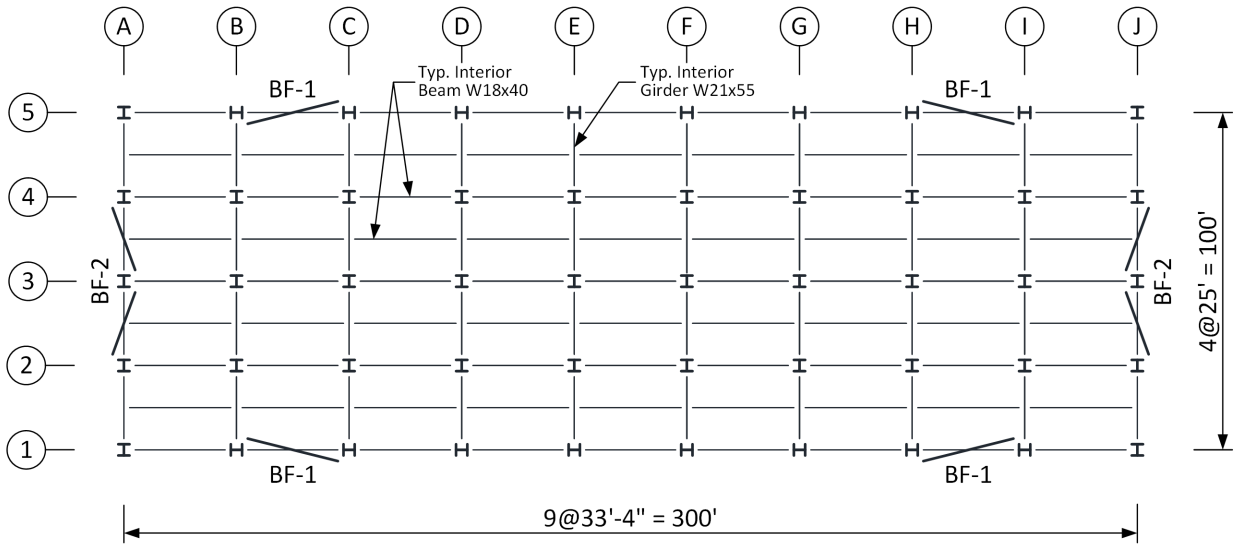

(a)

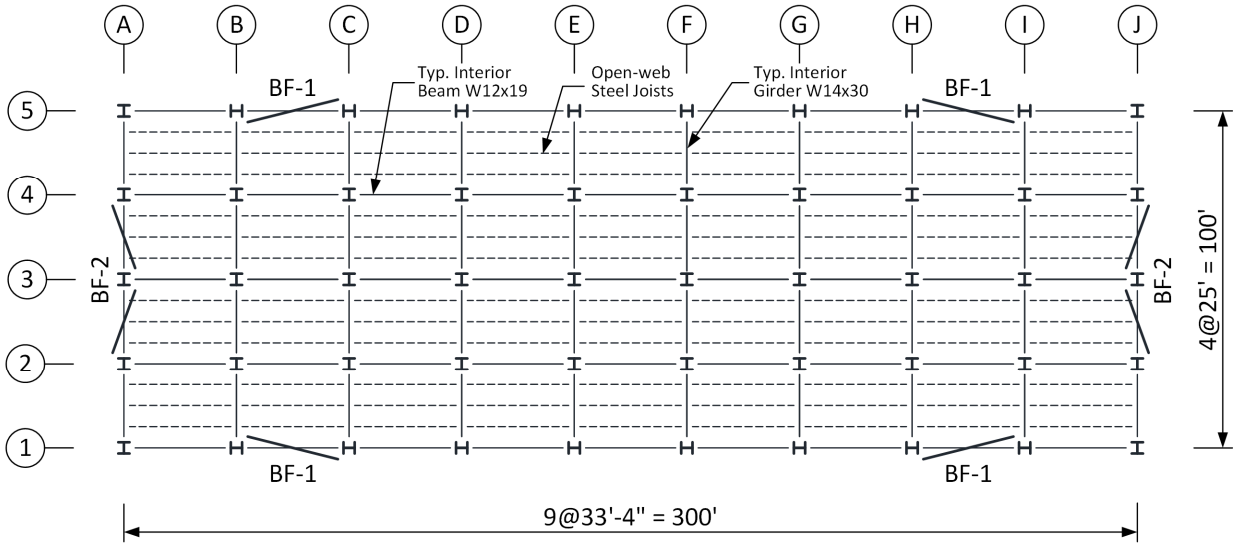

(b)

Figure F.1 Prototype Building Structure: (a) Typical Floor Plan and (b) Roof Plan

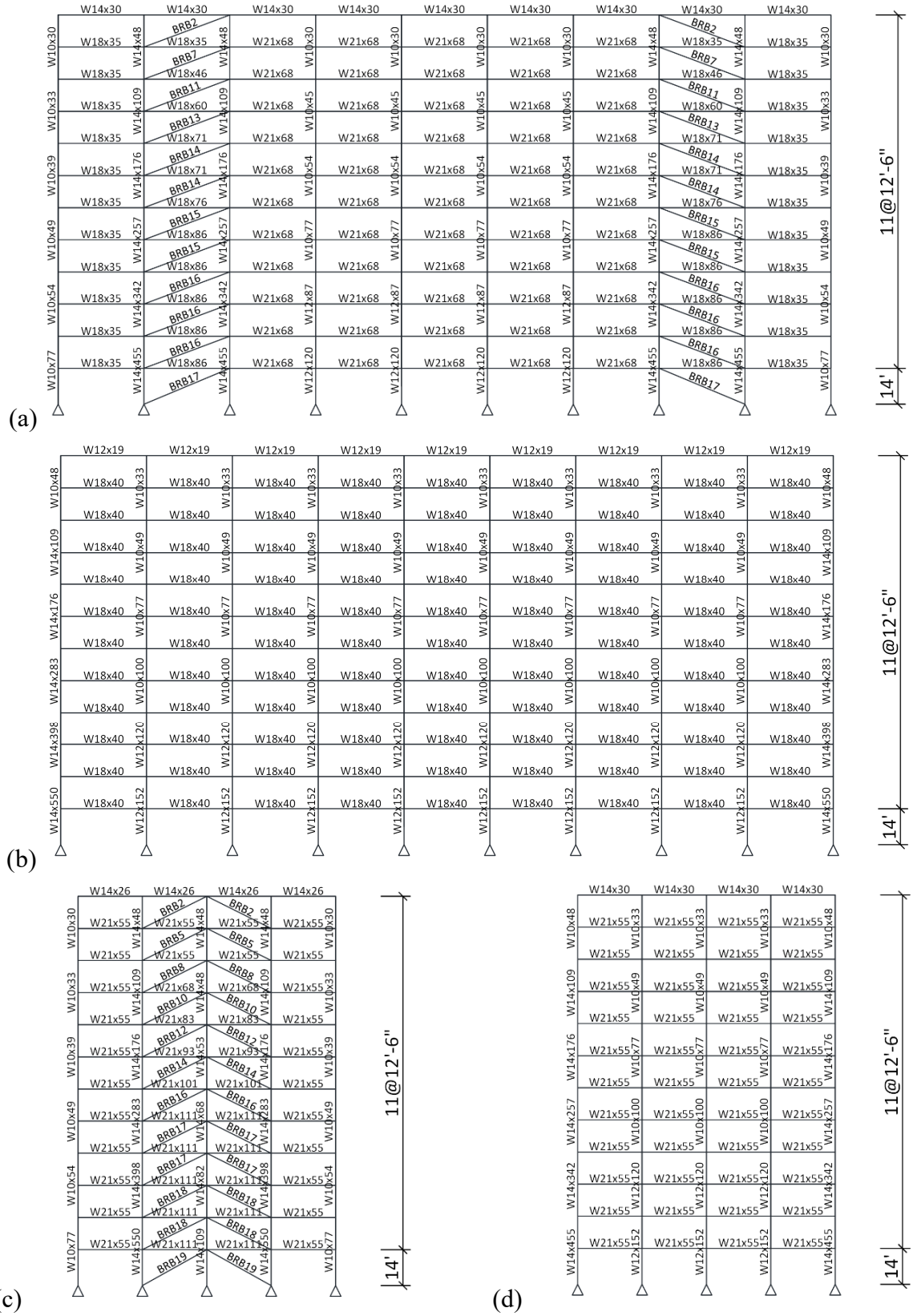

Figure F.2 Frame Elevations: (a) Exterior and (b) Interior Frames in Longitudinal Direction; and (c) Exterior and (d) Interior Frames in Transverse Direction

REFERENCES

ABAQUS (2014). Abaqus Standard User's Manual, Version 6.14, Dassault Systemes Simulia Corp.

AISC (2016a). *Prequalified Connections for Special and Intermediate Steel Moment Frames for Seismic Applications*, ANSI/AISC 358-16, American Institute of Steel Construction, Chicago, IL.

AISC (2016b). *Seismic Provisions for Structural Steel Buildings*, ANSI/AISC 341-16, American Institute of Steel Construction, Chicago, IL.

AISC (2016c). *Specification for Structural Steel Buildings*, ANSI/AISC 360-16, American Institute of Steel Construction, Chicago, IL.

AISC (2016d). *Steel Construction Manual*, 15th Ed., American Institute of Steel Construction, Chicago, IL.

AISC (2018). *Seismic Design Manual*, 3rd Ed., American Institute of Steel Construction, Chicago, IL.

AISI (2016a). *North American Specification for the Design of Cold-Formed Steel Structural Members*, AISI S100-16, American Iron of Steel Institute, Washington, DC.

AISI (2016b). *North American Standard for the Design of Profiled Steel Diaphragm Panels*, AISI S360-16, American Iron of Steel Institute, Washington, DC.

AISI (2017). *AISI Design Guide - Design Examples for the Design of Profiled Steel Diaphragm Panels Based on AISI S310-16*, AISI D360-17, American Iron of Steel Institute, Washington, DC.

Amadio, C., Fedrigo, C., Fragiacomo, M., and Macorini, L. (2004). "Experimental evaluation of effective width in steel–concrete composite beams." *Journal of Constructional Steel Research*, 60(2): 199–220. https://doi.org/10.1016/j.jcsr.2003.08.007

Amadio, C., and Fragiacomo, M. (2002). "Effective width evaluation for steel–concrete composite beams." *Journal of Constructional Steel Research*, 58(3): 373–388. https://doi.org/10.1016/S0143-974X(01)00058-X

Anshul, A., Lizarraga, D., Beedle, M., Li, C.-H., Fleischman, R., Sause, R. Ricles, J. and Uang, C.-M. (2018). "Investigation of seismic performance of collectors in steel building structures." *Proceedings, 11th U.S. National Conference on Earthquake Engineering (11NCEE)*, Los Angeles, CA.

ASCE (2013). *Seismic Evaluation and Retrofit of Existing Buildings*, ASCE/SEI 41-13, American Society of Civil Engineers, Reston, VA.

ASCE (2016). *Minimum Design Loads and Associated Criteria for Buildings and Other Structures*, ASCE/SEI 7-16, American Society of Civil Engineers, Reston, Reston, VA.

Astaneh-Asl, A., Call, S. M., and McMullin, K. M. (1989). “Design of single plate shear connections.” *Engineering Journal*, AISC, 26: 21–32.

Astaneh-Asl, A., Liu, J., and McMullin, K. M. (2002). “Behavior and design of single plate shear connections.” *Journal of Constructional Steel Research*, ASCE, 58: 1121–1141. https://doi.org/10.1016/S0143-974X(01)00101-8

ASTM (2021). *Standard Test Methods for Tension Testing of Metallic Materials*, ASTM E8/E8M-21, ASTM International, West Conshohocken, PA.

AWS (2015). *Structural Welding Code–Steel*, ANSI/AWS D1.1/D1.1M:2015, American Welding Society, Miami, FL.

AWS (2016). *Structural Welding Code–Seismic Supplement*, ANSI/AWS D1.1:2015, American Welding Society, Miami, FL.

Bazant, Z. P., and Planas, J. (1998). *Fracture and size effect in concrete and other quasibrittle materials*, CRC Press, Boca Raton, FL.

Belarbi, H., and Hsu, T. C. C. (1994), “Constitutive laws of concrete in tension and reinforcing bars stiffened by concrete.”, *ACI Structural Journal*, 91(4): 465–474.

Benjamin, I. A. (1965). “Composite beams of steel and lightweight concrete.” *Engineering Journal*, AISC, 2: 125–128.

Brosnan, D. P., and Uang, C.-M. (1995). “Effective width of composite L-beams in buildings.” *Engineering Journal*, AISC, 32: 73–80.

Castro, J. M., Elghazouli, A. Y., and Izzuddin, B. A. (2007). “Assessment of effective slab widths in composite beams.” *Journal of Constructional Steel Research*, 63(10): 1317–1327. https://doi.org/10.1016/j.jcsr.2006.11.018

CEN (2004a). *Eurocode 4*: *Design of Composite Steel and Concrete Structures – Part 1-1: General Rules and Rules for Buildings*, EN 1994-1-1:2004, Comité Européen de Normalisation, Brussels, Belgium.

CEN (2004b). *Eurocode 8*: *Design of Structures for Earthquake Resistance – Part 1: General Rules, Seismic Actions and Rules for Building*, EN 1998-1-1:2004, Comité Européen de Normalisation, Brussels, Belgium.

CERC (2012). “Final Report Volumes 6: Canterbury Television Building (CTV)”, prepared by Canterbury Earthquakes Royal Commission (CERC), Wellington, New Zealand.

Charney, F. A., and Marshall, J. (2006). “A comparison of the Krawinkler and scissors models for including beam column joint deformations in the analysis of moment resisting steel frames.” *Engineering Journal*, AISC, 43: 31–48.

Chiorean, C. G., and Buru, S. M. (2017). "Practical nonlinear inelastic analysis method of composite steel-concrete beams with partial composite action." *Engineering Structures*, 134: 74–106. https://doi.org/10.1016/j.engstruct.2016.12.017

Coleman, J., and Spacone, E. (2001). "Localization issues in force-based frame elements." *Journal of Structural Engineering*, ASCE, 127(11): 1422–1425. https://doi.org/10.1061/ (ASCE)0733-9445(2001)127:11(1257)

Crawford, S. F. and Kulak, G. L. (1971). "Eccentrically loaded bolted connections." *Journal of the Structural Division*, ASCE, 97(3): 765–783. https://doi.org/10.1061/JSDEAG.0002844

Crocker J. P., and Chambers J. J. (2004). "Single plate shear connection response to rotation demands imposed by frames undergoing cyclic lateral displacements" *Journal of Structural Engineering*, ASCE, 130(6): 934–941. https://doi.org/10.1061/(ASCE)07339445(2004)130:6(934)

Dafalias, Y. F., and Popov, E. P. (1976). "Plastic internal variables formalism of cyclic plasticity." *Journal of Applied Mechanics*, 43 (4): 645–651. https://doi.org/10.1115/ 1.3423948

Deierlein, G. G., Reinhorn, A. M., and Willford, M. R. (2010). *Nonlinear structural analysis for seismic design: A guide for practicing engineers*, NEHRP Seismic Design Technical Brief No. 4 (NIST GCR 10-917-5), produced by the NEHRP Consultants Joint Venture for the National Institute of Standards and Technology, Gaithersburg, MD.

Easterling, W. S., and Porter, M. L. (1994a). "Steel-deck-reinforced concrete diaphragms. I." *Journal of Structural Engineering*, ASCE, 120(2): 560–576. https://doi.org/ 10.1061/(ASCE)0733-9445(1994)120:2(560)

Easterling, W. S., and Porter, M. L. (1994b). "Steel-deck-reinforced concrete diaphragms. II." *Journal of Structural Engineering*, ASCE, 120(2): 577–596. https://doi.org/ 10.1061/(ASCE)0733-9445(1994)120:2(577)

Eatherton, M. R., O'Brien P. E., and Easterling, W. S. (2020). "Examination of ductility and seismic diaphragm design force-reduction factors for steel deck and composite diaphragms." *Journal of Structural Engineering*, ASCE, 146(11): 04020231. https://doi.org/10.1061/(ASCE)ST.1943-541X.0002797

Elkady, A., and Lignos, D. G. (2014). "Modeling of the composite action in fully restrained beam-to-column connections: implications in the seismic design and collapse capacity of steel special moment frames." *Earthquake Engineering and Structural Dynamics*, 43(13): 1935–1954. https://doi.org/10.1002/eqe.2430

Essa, H. S., Tremblay R., and Rogers, C. A. (2003). "Behavior of roof deck under quasistatic cyclic loading." *Journal of Structural Engineering*, ASCE, 129(12): 1658–1666. https://doi.org/10.1061/(ASCE)0733-9445(2003)129:12(1658)

Fang, C.-H., and Roberto, T. L. (2018). “Seismic behavior of symmetric and asymmetric steel structures with rigid and semirigid diaphragms.” *Journal of Structural Engineering*, ASCE, 144(10): 04018186. https://doi.org/10.1061/(ASCE)ST.1943-541X.0002123

FEMA (2000). *State of the Art Report on Connection Performance*, FEMA 355D, prepared by the SAC Joint Venture for the Federal Emergency Management Agency, Washington, DC.

FEMA (2015). *Seismic design of rigid wall-flexible diaphragm buildings: an alternative procedure*. FEMA P-1026, Federal Emergency Management Agency, Washington DC.

FEMA (2020). *NEHRP Recommended Seismic Provisions for New Buildings and Other Structures Volume 1: Part 1 Provisions, Part 2 Commentary*, FEMA P-2082-1, Federal Emergency Management Agency, Washington, DC.

Fisher, J.W. (1964). “On the behavior of fasteners and plates with holes.” *Fritz Engineering Laboratory Rep. No. 288.18*, Department of Civil Engineering, Lehigh University, Benthlehem, PA.

Fleischman, R. B., and Farrow, K. T. (2001). “Dynamic behavior of perimeter lateral-system structures with flexible diaphragms.” *Earthquake Engineering and Structural Dynamics*, 30(5): 745–763. https://doi.org/10.1002/eqe.36

Fleischman, R. B., Farrow, K. T., and Eastman, K. (2002). “Seismic performance of perimeter lateral system structures with highly flexible diaphragms.” *Earthquake Spectra*, 18(2): 251. http://dx.doi.org/10.1193/1.1490547

Geschwindner, L. F. and Gustafson, K. D. (2010). “Single-plate shear connection design to meet structural integrity requirements.” *Engineering Journal*, AISC, 47: 125–202.

Groper M. (1985) “Microslip and macroslip in bolted joints” *Experimental Mechanics*, 25: 171–174.

Hagood, T. A., Guthrie, L., and Hoadley, P. G. (1968). “An investigation of the effective concrete slab width for composite construction.” *Engineering Journal*, AISC, 5: 20–27.

Hajjar J. F., Leon R. T., Gustafson M. A., and Shield C. K. (1998). “Seismic response of composite moment-resisting connections. II: behavior.” *Journal of Structural Engineering*, ASCE, 124(8): 877–885. https://doi.org/10.1061/(ASCE)0733-9445(1998)124:8(877)

Huang, Y., Huang, D., Yang, Y., Yi, W., and Zhu, Z. (2016). “Element-based effective width for deflection calculation of steel-concrete composite beams.” *Journal of Constructional Steel Research*, 121: 163–172. https://doi.org/10.1016/j.jcsr.2016.02.010

IMPAO (2021). *Uniform Evaluation Service Report ER-2018*, International Association of Plumbing and Mechanical Officials, Ontario, California.

Karsan, I. D., and Jirsa, J. O. (1969). “Behavior of concrete under compressive loading.” *Journal of Structural Division*, ASCE, 95(ST12): 2443–2564

Kennedy J. (2018). "Developing diaphragm analysis." *Modern Steel Construction*, May, American Institute of Steel Construction, Chicago, IL.

Koduru, S. D., and Driver, R. G. (2014). "Generalized component-based model for shear tab connections." *Journal of Structural Engineering*, ASCE, 140(2): 04013041. https://doi.org/10.1061/(ASCE)ST.1943-541X.0000823

Koliou, M., Filiatrault A., Kelly, D. J., and Lawson, J. (2016a). "Buildings with rigid walls and flexible roof diaphragms. I: evaluation of current U.S. seismic provisions" *Journal of Structural Engineering*, ASCE, 142(3): 04015166. https://doi.org/10.1061/ (ASCE)ST.1943-541X.0001438

Koliou, M., Filiatrault A., Kelly, D. J., and Lawson, J. (2016b). "Buildings with rigid walls and flexible roof diaphragms. II: evaluation of a new seismic design approach based on distributed diaphragm yielding." *Journal of Structural Engineering*, ASCE, 142(3): 04015167. https://doi.org/10.1061/(ASCE)ST.1943-541X.0001439

Kwong, N. S., and Chopra, A. K. (2015). "Theory and application of experimental model analysis in earthquake engineering." *PEER Rep. No. 2015/11*, Pacific Earthquake Engineering Research Center, Berkeley, CA.

Lee, C. H., Jung, J. H., Kim., S. Y., and Kim, J. J. (2016). "Investigation of composite slab effect on seismic performance of steel moment connections." *Journal of Constructional Steel Research*, 117: 91–100. https://doi.org/10.1016/ j.jcsr.2015.10.004

Leon R. T., Hajjar J. F., and Gustafson M. A. (1998). "Seismic response of composite moment-resisting connections. I: performance." *Journal of Structural Engineering*, ASCE, 124(8): 868–876. https://doi.org/10.1061/(ASCE)0733-9445(1998)124:8(868)

Li, C.-H. and Uang, C.-M. (2020). "Strain Aging Effect on Cyclic Response of Buckling-Restrained Braces," *Report No. TR-20/06*, University of California, San Diego, La Jolla, CA.

Lin, B.-Z., Chuang, M.-C., and Tsai, K.-C. (2009). "Object-oriented development and application of a nonlinear structural analysis framework." *Advances in Engineering Software*, 40 (1): 66–82. https://doi.org/10.1016/j.advengsoft.2008.03.012

Liu, J., and Astaneh-Asl. A. (2000). "Cyclic testing of simple connections including effects of slab." *Journal of Structural Engineering*, ASCE, 126(1): 32–39. https://doi.org/10.1061/(ASCE)0733-9445(2000)126:1(32)

Liu, J., and Astaneh-Asl, A. (2004). "Moment-rotation parameters for composite shear tab connections." *Journal of Structural Engineering*, ASCE, 130(9): 1371–1380. https://doi.org/10.1061/(ASCE)0733-9445(2004)130:9(1371)

Lu, Y., and Panagiotou, M. (2012). "Three-dimensional nonlinear cyclic beam-truss model for non-planar reinforced concrete walls." *Rep. UCB/SEMM-2012/01*, Earthquake Engineering Research Center, Univ. of California, Berkeley.

Lu, Y., and Panagiotou, M. (2014). "Three-dimensional cyclic beam-truss model for nonplanar reinforced concrete walls." *Journal of Structural Engineering*, ASCE, 140(3): 04013071. https://doi.org/10.1061/(ASCE)ST.1943-541X.0000852

Ma, L. and Bocchini, P. (2019) "Hysteretic model of single-bolted angle connections for lattice steel towers." *Journal of Engineering Mechanics*, ASCE, 145(8): 04019052. https://doi.org/10.1061/(ASCE)EM.1943-7889.0001630

Main, J. A., and Sadek, F. (2012). "Robustness of steel gravity frame systems with single-plate shear connections." *Rep. No. NIST-TN-1749*, National Institute of Standards and Technology, U.S. Dept. of Commerce, Gaithersburg, MD. http://dx.doi.org/10.6028/ NIST.TN.1749

Main, J. A., and Sadek, F. (2014). "Modeling and Analysis of Single-Plate Shear Connections under Column Loss." *Journal of Structural Engineering*, ASCE, 140(3): 04013070. https://doi.org/10.1061/(ASCE)ST.1943-541X.0000866

Mander, J. B., Priestley, M. J. N., and Park, R. (1988). "Theoretical stress-strain model for confined concrete." *Journal of Structural Engineering*, ASCE, 114(8): 1804–1826. https://doi.org/10.1061/(ASCE)0733-9445(1988)114:8(1804)

Masoudnia, R. (2020). "State of the art of the effective flange width for composite T-beams." *Construction and Building Materials*, 244: 118303. https://doi.org/ 10.1016/j.conbuildmat.2020.118303

Massone L. M., Orakcal K., and Wallace, J. W. (2006), "Modeling flexural/shear interaction in RC walls." *ACI-SP-236: Deformation Capacity and Shear Strength of Reinforced Concrete Members under Cyclic Loadings*, American Concrete Institute, Farmington Hills, MI, pp. 127–150.

Mathew R., Redi E., and Uang C.-M. (2021) "Effect of bolt-hole clearance on the ultimate strength of eccentrically loaded bolt groups." *Journal of Structural Engineering*, ASCE, 147(1): 04020285. https://doi.org/10.1061/(ASCE)ST.1943-541X.0002863

MathWorks (2019), MATLAB, Version 2019a, The MathWorks, Inc., Natick, MA.

McGarraugh, J. B., Baldwin, Jr., and James, W. (1971). "Lightweight concrete-on-steel composite beams." *Engineering Journal*, AISC, 8: 90–98.

McKenna, F., Fenves, G. L., and Scott, M. H. (2000). "Open system for earthquake engineering simulation", http://opensees.berkeley.edu

Menegotto, M., and Pinto, P. E. (1973). "Method of Analysis for Cyclically Loaded Reinforced Concrete Plane Frames Including Changes in Geometry and Nonelastic Behavior of Elements Under Combined Normal Force and bending." *IABSE Symposium on Resistance and ultimate Deformability of Structures Acted on by Well-Defined Repeated Loads*, Final Report, Lisbon.

Miranda, E., and Taghavi, S. (2005). "Approximate floor acceleration demands in multistory buildings. I: Formulation." *Journal of Structural Engineering*, ASCE, 131(2): 203–211. https://doi.org/10.1061/(ASCE)0733-9445(2005)131:2(203)

Moehle, J. (1994). "Preliminary Report on the Seismological and Engineering Aspects of the January 17, 1994, Northridge Earthquake," *Report No. UCB/EERC-94/01*, Earthquake Engineering Research Center, University of California at Berkeley, Berkeley, CA.

Moehle, J. P., Hooper, J. D., Kelly, D. J., and Meyer, T. (2010). *Seismic design of cast-in-place concrete diaphragms, chords, and collectors: A guide for practicing engineers*, NEHRP Seismic Design Technical Brief No. 3 (NIST GCR 10-917-4), produced by the NEHRP Consultants Joint Venture for the National Institute of Standards and Technology, Gaithersburg, MD.

Moncarz, P. D., and Krawinkler, H. (1981). "Theory and application of experimental model analysis in earthquake engineering." *Technical Rep. 50*, John A. Blume Earthquake Engineering Center, Stanford, CA.

Naeim F. and Boppana R. R. (2001) "Seismic Design of Floor Diaphragms." *The Seismic Design Handbook*. Springer, Boston, MA, pp. 373–407. https://doi.org/10.1007/978-1-4615-1693-4_8

Neuenhofer, A. and Filippou, F. C. (1997), "Evaluation of nonlinear frame finite element models.", *Journal of Structural Engineering*, 123(7): 958–966. https://doi.org/10.1061/ (ASCE)0733-9445(1997)123:7(958)

Nikolaidou, V., Latreille P., Lignos, D. G., and Rogers, C. A. (2018). "Seismic performance characterization of wood-sheathed and cold-formed steel framed floor and roof diaphragm structures." *Journal of Structural Engineering*, ASCE, 144(2): 04017215. https://doi.org/10.1061/(ASCE)ST.1943-541X.0001962

Nilson, A. H. (1960). "Shear diaphragms of light gage steel." *Journal of the Structural Division*, ASCE, 86(11): 111–140. https://doi.org/10.1061/JSDEAG.0000582

NIST. (2017). *Guidelines for Nonlinear Structural Analysis for Design of Buildings Part I – General*, NIST GCR 17-917-46v1, prepared by the Applied Technology Council for the National Institute of Technology and Standards, Gaithersburg, MD. https://doi.org/10.6028/NIST.GCR.17-917-46v1

NIST. (2017). *Guidelines for Nonlinear Structural Analysis for Design of Buildings Part IIa – Steel Moment Frames*, NIST GCR 17-917-46v2, prepared by the Applied Technology Council for the National Institute of Technology and Standards, Gaithersburg, MD. https://doi.org/10.6028/NIST.GCR.17-917-46v2

O'Brien, P., Eatherton, M. R., and Easterling, W. S. (2017). "Characterizing the load-deformation behavior of steel deck diaphragms using past test data." *Cold-Formed Steel Research Consortium Report Series, CFSRC R-2017-02*.

Ozkula G., Uang C.-M., and Harris J. (2021) "Development of enhanced seismic compactness requirements for webs in wide-flange steel columns." *Journal of Structural Engineering*, ASCE, 147(7): 04021100. https://doi.org/10.1061/(ASCE)ST.1943-541X.0003036

Panagiotou, M., Restrepo, J. I., Schoettler, M., and Kim, G. (2012). "Nonlinear cyclic truss model for reinforced concrete walls." *ACI Structural Journal*, 109(2): 205–214.

Popovics, S. (1973). "A numerical approach to the complete stress strain curve for concrete." *Cement and concrete research*, 3(5): 583–599. https://doi.org/10.1016/0008-8846(73)90096-3

Rex, C. O., and Easterling, W. S. (2003). "Behavior and modeling of a bolt bearing on a single plate." *Journal of Structural Engineering*, ASCE, 129(6): 792–800. https://doi.org/10.1061/(ASCE)0733-9445(2003)129:6(792)

Richard, M. R. and Abbott, B. J. (1975). "Versatile Elastic-Plastic Stress-Strain Formula." *Journal of the Engineering Mechanics Division*, 101(4): 511–515. https://doi.org/10.1061/JMCEA3.0002047

Rodriguez, M. E., Restrepo, J. I., and Carr, A. J. (2002). "Earthquake-induced floor horizontal accelerations in buildings." *Earthquake Engineering and Structural Dynamics*, 31(3): 693–718. https://doi.org/10.1002/eqe.149

Rodriguez, M. E., Restrepo, J. I., and Blandón, J. J. (2007). "Seismic design forces for rigid floor diaphragms in precast concrete building structures." *Journal of Structural Engineering*, ASCE, 133(11): 1604–1615. https://doi.org/10.1061/(ASCE)0733-9445(2007)133:11(1604)

Rogers, C. A., and Tremblay R. (2003a). "Inelastic seismic response of side lap fasteners for steel roof deck diaphragms." *Journal of Structural Engineering*, ASCE, 129(12): 1637–1646. https://doi.org/10.1061/(ASCE)0733-9445(2003)129:12(1637)

Rogers, C. A., and Tremblay R. (2003b). "Inelastic seismic response of frame fasteners for steel roof deck diaphragms." *Journal of Structural Engineering*, ASCE, 129(12): 1647–1657. https://doi.org/10.1061/(ASCE)0733-9445(2003)129:12(1647)

Sabelli R., Pottebaum, W., and Dean, B. (2009). "Diaphragms for seismic loading." *Structural Engineer*, Part 1, January, pp. 24–29, Part 2, February 2009, pp. 22–23.

Sabelli, R., Sabol, T. A., and Easterling, W. S. (2011). *Seismic design of composite steel deck and concrete-filled diaphragms: A guide for practicing engineers*, NEHRP Seismic Design Technical Brief No. 5 (NIST GCR 11-917-10), produced by the NEHRP Consultants Joint Venture for the National Institute of Standards and Technology, Gaithersburg, MD.

Sadek, F., El-Tawil, S., and Lew, H. S. (2008). "Robustness of composite floor systems with shear connections: modeling, simulation, and evaluation." *Journal of Structural Engineering*, ASCE, 134(11): 1717–1725. https://doi.org/10.1061/(ASCE)0733-9445(2008)134:11(1717)

SDI (2016). *Diaphragm design manual*, 4th ed., Steel Deck Institute, Canton, OH.

Shimizu, N., Kanno, R., Ikarashi, K., and Sato, K. (2013). "Cyclic behavior of corrugated steel shear diaphragms with end failure." *Journal of Structural Engineering*, ASCE, 139(5): 796–806. https://doi.org/10.1061/(ASCE)ST.1943-541X.0000669

Sim H.-B., Ballantyne G., Chen A., and Uang C.-M. (2017) "Effect of beam tension on cyclic performance of WUF-W steel moment connection." *Journal of Structural Engineering*, ASCE, 143(9): 04017102. https://doi.org/10.1061/(ASCE)ST.1943-541X.0001833

Spacone, E., Ciampi, V., and Filippou, F. C. (1996), "Mixed formulation of nonlinear beam finite element." *Computer and Structures*, 58: 71–83. https://doi.org/10.1016/0045-7949(95)00103-N

Taghavi, S., and Miranda, E. (2005). "Approximate floor acceleration demands in multistory buildings. II: Applications." *Journal of Structural Engineering*, ASCE, 131(2): 212–220. https://doi.org/10.1061/(ASCE)0733-9445(2005)131:2(212)

Thomas, D. L., Wilson, J. M., and Wilson, R. R. (1973). "Timoshenko beam finite elements." *Journal of Sound and Vibration*, 31(3), 315–330. https://doi.org/10.1016/S0022460X(73)80276-7

Torabian, S., Eatherton, M. R., Easterling, W. S., Hajjar, J. F., and Schafer, B. W. (2017). *SDII building archetype design v1.0*. JScholarship. https://jscholarship.library.jhu.edu/handle/1774.2/40638

Torabian, S., Eatherton, M. R., Easterling, W. S., Hajjar, J. F., and Schafer, B. W. (2019). "SDII building archetype design v2.0." *Cold-Formed Steel Research Consortium Report Series, CFSRC R-2019-04*. http://jhir.library.jhu.edu/handle/1774.2/62106

Torabian, S., and Schafer, B. W. (2021). "Cyclic experiments on sidelap and structural connectors in steel deck diaphragms." *Journal of Structural Engineering*, ASCE, 147(4): 04021028. https://doi.org/10.1061/(ASCE)ST.1943-541X.0002981

Tremblay R., Martin, E., Yang, W., and Rogers, C. A. (2004). "Analysis, testing and design of steel roof deck diaphragms for ductile earthquake resistance." *Journal of Earthquake Engineering*, 8(5): 775–816. https://doi.org/10.1080/13632460409350509

Turmo, J., Lozano-Galant, J. A., Mirambell, E., and Xu, D. (2015). "Modeling composite beams with partial interaction." *Journal of Constructional Steel Research*, 114: 380–393. https://doi.org/10.1016/j.jcsr.2015.07.007

Uang C.-M., Sato A., Hong J.-K., and Wood K. (2010) "Cyclic testing and modeling of cold-formed steel special bolted moment frame connections. II: behavior." *Journal of Structural Engineering*, ASCE, 136(8): 953–960. https://doi.org/10.1061/(ASCE)ST.1943541X.0000190

Uang, C.-M., Yu, Q.-S., Shane, N. and Gross, J. (2000). "Cyclic testing of steel moment connections rehabilitated with RBS or welded haunch." *Engineering Journal*, AISC, 126(1): 57–68. https://doi.org/10.1061/(ASCE)0733-9445(2000)126:1(57)

Vallenilla, C. R., and Bjorhovde, R. (1985). “Effective width criteria for composite beams.” *Engineering Journal*, AISC, 22: 169–175.

Vecchio, F. J., and Collins, M. P. (1986). “The modified compression-field theory for reinforced concrete elements subjected to shear.” *ACI Journal Proceedings*, 83(2): 219–231.

Wei, G., Eatherton, M. R., Foroughi, H., Torabian, S., and Schafer, B.W. (2020). “Seismic behavior of steel BRBF buildings including consideration of diaphragm inelasticity.” *Cold-Formed Steel Research Consortium Report Series, CFSRC R-2020-04*. https://jscholarship.library.jhu.edu/handle/1774.2/62366

Weigand, J. M. (2017). “Component-based model for single-plate shear connections with pretension and pinched hysteresis.” *Journal of Structural Engineering*, ASCE, 143(2): 04016178. https://doi.org/10.1061/(ASCE)ST.1943-541X.0001662

Wen, R., Akbas, B., and Shen, J. (2013). “Practical moment–rotation relations of steel shear tab connections.” *Journal of Constructional Steel Research*, 88: 296–308. https://doi.org/10.1016/j.jcsr.2013.05.018

Yim, H. C., and Easterling, T. (2012). “Mechanical properties of single-plate shear connections under monotonic, cyclic, and blast loads.” *Engineering Structures*, 37: 24–35. https://doi.org/10.1016/j.engstruct.2011.12.041

Yu, Y.-J., Tsai, K.-C., Li, C.-H., Weng, Y.-T., and Tsai, C.-Y. (2012). “Earthquake response analyses of a full-scale five-story steel frame equipped with two types of dampers.” *Earthquake Engineering and Structural Dynamics*, 42(9): 693–718. https://doi.org/ 10.1002/eqe.149

Zhu, L., Nie, J.-G., Li, F.-X., and Ji, W.-Y. (2015). “Simplified analysis method accounting for shear-lag effect of steel–concrete composite decks.” *Journal of Constructional Steel Research*, 115: 62–80. https://doi.org/10.1016/j.jcsr.2015.08.020